Rajdeep Singh Rawat *Editor*

Plasma Science and Technology for Emerging Economies

An AAAPT Experience

Springer

Plasma Science and Technology for Emerging Economies

Rajdeep Singh Rawat
Editor

Plasma Science and Technology for Emerging Economies

An AAAPT Experience

Springer

Editor
Rajdeep Singh Rawat
Natural Sciences and Science Education,
National Institute of Education
Nanyang Technological University
Singapore
Singapore

ISBN 978-981-10-4216-4 ISBN 978-981-10-4217-1 (eBook)
DOI 10.1007/978-981-10-4217-1

Library of Congress Control Number: 2017948218

Printed on acid-free paper

This Springer imprint is published by Springer Nature
The registered company is Springer Nature Singapore Pte Ltd.
The registered company address is: 152 Beach Road, #21-01/04 Gateway East, Singapore 189721, Singapore

Contents

Chapter 1
Asian African Association for Plasma Training (AAAPT)—History, Network, Activities, and Impact

Rajdeep Singh Rawat

1.1 Introduction to Asian African Association for Plasma Training (AAAPT)

The Asian African Association for Plasma Training (AAAPT) is an association or network of plasma research groups from emerging economies in Asia and Africa. AAAPT was founded on June 7, 1988, in Kuala Lumpur during the Third Tropical College on Applied Physics and the Second United Nation University—International Centre for Theoretical Physics (UNU/ICTP) Training Programme on Plasma and Laser Technology with an aim to provide facilities for plasma research for small research groups in developing countries in Asian and African region. Professor Lee Sing from University Malaya, Malaysia was elected as the Founding President of AAAPT along with four Vice Presidents Prof. T. El Khalafawy (Atomic Energy Authority, Egypt), Prof. Ghulam Murtaza (Quaid-i-Azam University, Pakistan), Prof. Mahesh Prasad Srivastava (University of Delhi, India), and Prof. Tsai Shih Tung (Chinese Academy of Sciences, China) in its inaugural meeting on June 7, 1988. At the time of its formation, the AAAPT consisted of 16 institutions from 12 countries; who became the founding members of AAAPT. The AAAPT Secretariat was formed comprising of Prof. Lee Sing (President), Assoc. Prof. Moo Siew Pheng (Vice President), Assoc. Prof. Wong Chiow San (Honorary Secretary) and Assoc. Prof. Chew Ah Chuan (Honorary Treasurer). By June 1, 1993, the membership list grew to 30 Institutions from 19 countries and by October 2012, it grew further to 46 institutions from 22 countries. Currently, AAAPT has 54 member institutes (including two associate members) in 24 countries which clearly indicates its increasing strength and cooperation.

R.S. Rawat (✉)
National Institute of Education, Nanyang Technological University,
Singapore 637616, Singapore
e-mail: rajdeep.rawat@nie.edu.sg

R.S. Rawat (ed.), *Plasma Science and Technology for Emerging Economies*,
DOI 10.1007/978-981-10-4217-1_1

Soon after its formation the AAAPT became an affiliated network of the Abdus Salam International Centre for Theoretical Physics (ICTP), Trieste, Italy and received funding for its collaborative activities, workshops, exchange programmes, etc., for several years. It also received assistance in the form of travel and other fellowships from the Third World Academy of Sciences (TWAS), UNESCO and several other organizations for several years from 1988 to about 2003–2004. It was somewhere around year 2004 when the ICTP decided to provide funding based on itemized request and not as a lump sum fund on regular basis. This meant that regular funds were stopped but AAAPT could still request for funds to Office of External Activities of ICTP, based on the activities and the funds it would be directly given to the institution involved in the activity rather than being provided to AAAPT Secretariat which was maintained at University Malaya, Kuala Lumpur, Malaysia ever since its inception. This therefore still helped the AAAPT to continue to survive, thrive, and organize various network activities. However, since 2014 even this type of itemized funding requests to ICTP, made mainly to organize annual AAAPT network activity, for organization of AAAPT annual conference has been unsuccessful. The AAAPT network group, however, has not only continued to survive but also actively engaged in several collaborative activities to promote cooperation in plasma science and technology.

The bulk of the contributions for AAAPT activities have started coming from the scientists of the member institutions in terms of their expertise, time, and effort and also in sharing of technical and academic expertise sharing along with infrastructural support for inter-AAAPT institute collaborations. The AAAPT continues to excel and thrive, as will be evident from the plethora of activities that have been organized under its wings, due to strong sense of cooperation and culture of helping each other. A large number of institutes, universities, organizations, facilities, and events will be referenced in the remaining part of the chapter by their acronyms due to their repeated used. The list of acronyms is provided in Table 1.1.

1.2 Missions, Goals, and Impact of AAAPT

As defined in the Constitution of AAAPT, its **key missions are**:

(a) to promote the initiation and strengthening of plasma research, especially experimental, in developing countries in Asia and Africa, and
(b) to promote cooperation and technology sharing among plasma physicists in the developing countries in Asia and Africa region.

In the light of above-mentioned missions, AAAPT over almost three decades of it history set many goals for itself which evolved over the time due to changing situations. The missions included in its initial stage of formation included:

Table 1.1 List of frequently used acronym in this chapter

Acronym	Institute/University/Organization/Facility/Event	City and Country
AAAPT	Asian African Association for Plasma Training	–
AAAPT R & T	AAAPT Research & Training Centre	Beijing, China
AEC	Atomic Energy Authority	Cairo, Egypt
CAS	Chinese Academy of Sciences	Beijing, China
CU	Chulalongkorn University	Bangkok, Thailand
DU	University of Delhi	Delhi, India
DXS	Diode X-ray Spectrometer	–
IAEA	International Atomic Energy Agency	Vienna, Austria
ICPSA	International Conference on Plasma Science and Applications	Various places
ICTP	Abdus Salam International Centre of Theoretical Physics	Trieste, Italy
IMFP	International Meeting on Frontier of Physics	Malaysia
IP-CAS	Institute of Physics, Chinese Academy of Sciences	Beijing, China
IPFS	Institute for Plasma Focus Studies	Melbourne, Australia
IWPDA2009	International Workshop on Plasma Diagnostics and Applications, 2009	Singapore
IWPCA2008	International Workshop on Plasma Computation and Applications, 2008	Malaysia
KSU	Kansas State University	USA
KU	Kathmandu University	Dhulikhel, Nepal
NIE/NTU	National Institute of Education, Nanyang Technological University	Singapore
PECVD	Plasma enhanced chemical vapor deposition	–
PFF	Plasma Focus Facility	–
QIAU	Quaid-i-Azam University	Islamabad, Pakistan
TWAS	Third World Academy of Sciences	Trieste, Italy
UM	University Malaya	Kuala Lumpur, Malaysia
UNESCO	United Nations Educational, Scientific and Cultural Organization	Paris, France
UNU	United Nation University	Tokyo, Japan
UNU/ICTP PFF	United Nation University/International Centre of Theoretical Physics Plasma Focus Facility	–
UTM	Universiti Teknologi Malaysia	Johor, Malaysia

(a) to hold a series of coordinated training programmes and colleges specially designed for effective training on selected aspects of plasma physics (experimental, technological, and theoretical),
(b) to develop and maintain relations among its member institutions carrying out research or having an interest to start research in plasma physics, especially experimental plasma physics,
(c) to develop a coordinated scientist/fellow exchange scheme with the aim of technology sharing and acquisition and also consultancy in theory and experiments, and
(d) to develop relationship with agencies such as IAEA, ICTP, UNESCO, TWAS, and others to obtain financial and fellowship support.

The AAAPT over last 28 years has not only successfully achieved all its missions and goals which it had initially envisioned during its formation but has gone far beyond. A brief summary of its activities/accomplishments includes:

1. Several coordinated training and attachment programmes, colleges, workshops (including online internet workshops), symposiums, conferences, etc.
2. Publications of large number of theses, reports, journal papers, conference papers, conference and workshop proceedings, etc.
3. Promoted numerous research collaborations among its member institutions with transfer and sharing of technology, equipment, simulation package, knowledge, and skills. This has led to a large number of collaborative published work (cited later).
4. Good number of fellowships from various local and international resources.

1.3 Events Leading to the Formation of AAAPT

The account of series of events that led to the formation of the AAAPT is provided by Professor Lee Sing, the Founding President of AAAPT, when I started to prepare the webpage of AAAPT at http://www.aaapt.org/home in 2012. The summary of those events is briefly described here, more details can be found at AAAPT webpage [1]. The AAAPT was not formed overnight and it took more than 5 years of intense planning, hard work, several rounds of group discussions, and experimental activities under the leadership of Professor Lee Sing. It all started at the 1983 Spring College on Plasma Physics at ICTP, Trieste, Italy, where a group of scientists from developing countries met in the evenings to discuss about the difficulties faced in trying to start experimental research. They realized a need for small plasma devices that could be built easily and yet offer challenging plasma physics along with advanced technical know how on which fruitful and sustained research could be carried out.

The Spring College on Plasma Physics at ICTP, Trieste in 1983 was almost immediately followed by another major meeting called “The First Tropical College

on Applied Physics" from December 26, 1983, to January 14, 1984, at the University of Malaya, Kuala Lumpur, refer photographs of tropical college participants in Fig. 1.1. The college was directed by Professor Lee Sing with 2 weeks of intensive hands-on laboratory work and numerical experiments on electromagnetic shock tube, plasma focus, glow discharge, and lasers for 34 participants from the region. The activities of this tropical college were published in a book [2] and also set the tone for the rigors and standards of the future AAAPT collaboration programmes. In 1984, the white paper of the proposal on "Research Transfer as an Educational Process—A Model and Some Experience" was formally prepared and presented to various international agencies. The proposal was to use the facilities and resources of an existing group in a developing country to prepare a programme to transfer its total research technology in a specific topic to other groups in the region having an interest and commitment in the specific subject area offered. The proposal provided the basis for (i) the identification of the Host Centre with experience, infrastructure, and willingness to run the training programme; and (ii) identification of participants with a strong physics and technical background along with the backing of their home institute to carry the project successfully after training and technology transfer. More details about the proposal can be found in reference [3].

On the recommendations of University Malaya Vice-Chancellor Royal Professor Ungku Aziz, the UNU, Tokyo, Japan agreed to fund a training programme. Prof. Lee Sing in early 1985, as the programme's initiator and director, visited several institutions in Asia and Africa (refer Fig. 1.2) and also interviewed several candidates at 1985 Spring College, ICTP. Finally, eight candidates from six countries were selected and eventually awarded the UNU Fellowships. The selected candidates were Dr. M.A. Eissa (Egypt), Dr. S. Sapru (India), S. Mulyodrono, Suryadi and Widdi Usada (Indonesia), Dr. A.V. Gholap (Nigeria), M. Zakaullah (Pakistan), and Dr. Augustine J. Smith (Sierra Leone).

Fig. 1.1 Photographs of participants and activities at "The First Tropical College on Applied Physics", December 26, 1983, to January 14, 1984, at the University of Malaya, Kuala Lumpur. *Photo Courtesy* From personal collection of Professor Lee Sing with his kind permission. Also available at http://www.aaapt.org/home/formative-years-of-aaapt at public domain

Fig. 1.2 Site Visits to PPNY (Indonesia), Quaid-i-Azam University (Pakistan) and AEC Cairo and Al Azhar University (Egypt). *Photo Courtesy* From personal collection of Professor Lee Sing with his kind permission. Also available at http://www.aaapt.org/home/formative-years-of-aaapt at public domain

A 6-month UNU Training Programme in Plasma and Laser Technology was conducted at the University Malaya, Malaysia under the leadership of Prof. Lee Sing from October 1985 to April 1986. During the first 3 months of training programme, the UNU Fellows attended lectures and did experiments on glow discharge, electromagnetic shock tube, plasma focus, computation packages on circuit and plasma dynamics, and various laser systems. Fellows also carried out system planning, design and construction, and development of all the subsystems that they needed for the device they chose to install back at their home institute. Most of the Fellows chose the plasma focus device for its ability to produce wide-ranging intense plasma conditions and also due to its capability of enabling research in nuclear fusion and advanced plasma diagnostics. The Training Programme led to the design of a practical compact plasma focus device based on a single capacitor as the pulsed power source. The school participants planned and decided to build almost all parts of the plasma focus facility (PFF) including a high voltage charger, a high-precision triggering system, and diagnostic instrumentation such as neutron detectors and a nanosecond laser shadowgraphic system from readily available materials and components [4]. The development, assembly, and testing of the first version of the UNU/ICTP (PFF) were carried out. Prof. Abdus Salam, Director of the ICTP, visited the programme on January 20, 1986 (refer Fig. 1.3) and after seeing the activities offered to provide US$15,000 funds. With funds secured, six sets of UNU/ICTP PFF were assembled during the last phase of the programme and full operational testing

including focusing characteristics in various gases and fusion neutrons diagnostics with paraffin-wax moderated silver activation counter were completed. By end of March 1986, reports and preparation for shipment of equipment were completed (refer Fig. 1.3). Some research papers were presented at the Second Tropical College on Applied Physics (17 March–5 April 1996).

Based on the work done during this First UNU Training Program, six research papers were written and eventually published, including two in international journals. One of the papers [5] is now among the top 3 most highly cited plasma focus papers. Dr. Walter Shearer represented the UNU in a ceremony in early April 1986 at which the equipment, in 7 consignments (6 UNU-ICTP PFF, 1 nitrogen laser) over 1000 kg, was handed over to the Fellows. During this handing over ceremony Prof. Lee Sing stressed that the "***success of the programme will depend on the work achieved by the Fellows back at the home institutes in the years to come***".

Fig. 1.3 Visit by Prof. Abdus Salam, Director ICTP, to UNU Training Programme in Plasma and Laser Technology in January 1986 (*upper right*). Fellows working on plasma focus device and its assembly and finally taking back the follow-up equipment to home institution. *Photo Courtesy* From personal collection of Professor Lee Sing with his kind permission. Also available at http://www.aaapt.org/home/formative-years-of-aaapt at public domain

In 1988, a second UNU/ICTP Training Programme was conducted during which a Sequenced Nitrogen Laser was invented [6]. The start of this Training Programme was timed to coincide with the Third Tropical College on Applied Physics and the formation of the AAAPT on June 7, 1988. Though AAAPT was formally formed in June 1988 but the core group of AAAPT under the leadership of Prof. Lee Sing was carefully planning and executing various activities that would later ensure the success of AAAPT.

1.4 Overview of AAAPT Activities

The leadership of AAAPT during its initial formative stage decided to choose a plasma device which would be suitable for plasma training for interested researchers in developing countries. The plasma training facility thus needed to be cost-effective and simple but rich in plasma phenomena with good educational value so that it could be used not only for educational training in plasma science and technology but also for competitive research. From the First UNU Training Programme, mentioned above, it became clear that the (PFF) with fusion relevant features and complex rich plasma and radiation environment would be the right facility for plasma training for Asian and African fraternity under AAAPT network. Ever since its inception in 1988, the AAAPT organized or co-organized numerous activities; with most of them focused on PFF-related research and training. These activities can be classified into several categories which highlight the breadth and depth of involvement and commitment of AAAPT leadership to establish and promote the plasma science and technology among its member institutes and others. Different activities or programmes that were/are being run by AAAPT catered/cater to different needs of the plasma researchers in its member institutes. These activities were/are supported not only by the institutes and experts from AAAPT network group from but also by organizations and experts from all around the globe. Some of the key activities and programmes are listed below under different categories.

1.4.1 Group Training Programmes and Colleges Organized and Supported by AAAPT

The success of intensive 6-month long training at Host Centre (Physics Department, UM, Kuala Lumpur, Malaysia) through First and Second UNU Training Programmes on PFF and related diagnostics highlighted the importance of intensive and longer duration theme based programmes. The AAAPT, in years to come, organized many such activities under Colleges, Schools and Training Programmes. Some of the important ones are listed below:

- *Beijing College on Plasma Physics and Diagnostics, Beijing, China, 30 October–9 November 1989*: The activity was funded by UNESCO, ICTP, Institute of Physics, and CAS Beijing as AAAPT network activity. There were 39 participants from nine countries and it featured lectures and hands-on experiments. The college was directed by Prof. Tsai Shi Tung.
- *Regional College on Plasma Applications, Songkla, Thailand, 7–13 January 1990*: It focused on basic plasma physics and applications of plasmas for industry. It had five invited lecturers and 55 participants from 15 countries and was funded mainly by UNESCO, ICTP, International Science Programme Uppsala University, ISSS Australia and Songkla University. The college was directed by Prof. Chaivitya Silawatshananai.
- *Third ICTP-UM Training Programme in Plasma and Pulse Technology, Kuala Lumpur, Malaysia, December 1989–June 1990*: Participants were Jalil Ali (Malaysia), M.A. Alabraba (Nigeria), Mohamad Nisar (Pakistan), Rajdeep Singh Rawat (India), A.V. Gholap (Zimbabwe), Mario Favre Domiguez (Chile), Feng Xian-Ping (China), and A.G. Warmate (Nigeria). The training focused on assembly of (PFF) and designing of simple nitrogen laser shadowgraphy system for plasma dynamics studies on the UNU-ICTP PFF. Other studies conducted were electron beam studies (XP Feng) and X-ray studies (M. Favre-Dominguez). Follow-up equipment of Laser shadowgraphic systems was taken back to Port Harcourt (Nigeria), Islamabad (Pakistan), and Delhi (India). The research in this training programme resulted in 3 research papers [7–9]. The Third ICTP-UM Training Programme was Funded by ICTP, UNESCO, TWAS, ICAC-UM and University Malaya and was directed by Prof. Lee Sing.
- *Basic Course on Plasma Physics Theory, Islamabad, Pakistan, 22 September–24 December 1990*: The course was directed by Prof. G. Murtaza with nine lectures on basic concepts of plasma, kinetic theory, Boltzmann equation, Fokker Planck Equation, controlled fusion magnetic and inertial confinement, and special topics. The activity was funded by AAAPT, ICAC-QIA, QIAU, and Dr. A.Q. Khan Research Laboratory. The course was attended by Feng Xian-Ping (China), M.N. Bhuiyun (Bangladesh), Suryadi (Indonesia) and M.A. Khan, Yousaf Zai, Noor Abbas Din Khattak, M.H. Nasim, S.R. Khan, Tanveer, and Ziaullah (Pakistan) and several postgraduate students of QIAU Plasma Group.
- *Nitrogen Laser Training Programme, Kuala Lumpur, Malaysia, 15 October–10 November 1990*: The training programme was comprised of lectures and hands-on activities on pulse technology, and physics and technology of gas and dye lasers. Each participant built a nitrogen laser (1 ns pulse) including the high voltage power supply and control electronics and then took the working laser system back to their home institutions. The participants, basically students and researchers from AAAPT network institutes, were Homnath Paudyal (Nepal), Zarin Ahmad (Bangladesh), Shahid Mahmud (Pakistan), Ampon Wongjamran (Thailand), and Widdi Usada (Indonesia). The programme was sponsored by ICAC-UM, University of Malaya, AAAPT, Malaysia Institute of Physics and ICTP and was directed by Prof. Lee Sing and Dr. K.H. Kwek.

- *Fifth Training Programme on Plasma Lab Techniques, Beijing, China, 15 April–4 May 1991*: 5 participants from AAAPT member institutes attended the 3-week training in plasma laboratory techniques. The programme was sponsored by APSC, Institute of Physics, CAS and AAAPT and was directed by Prof. Li Yin-an.
- *Sixth ICTP-UM Training Programme on Plasma Focus and Pulsed X-ray Technology, Kuala Lumpur, Malaysia March–15 April 1992*: This activity was sponsored by ICAC-UM, AAAPT, ICTP, and IFM and was directed by Prof. C.S. Wong. The participants were Prof. Min Han (China), Dr. C. Silawatshananai (Thailand), Jiang Zhiming (China), and Smruti R. Mohanty (India). During this programme, the participants were trained on 5-channel filtered diode X-ray spectrometer (DXS) for measurement of X-rays from the UNU-ICTP PFF. As follow-up, 3 units of 5-channel DXS were given to the participants from Thailand, India and China.
- *Fourth AAAPT College on Plasma Technology—Training on Plasma Diagnostics, Cairo, Egypt, 24 April–5 May 1993*: The activity was sponsored by the Plasma Physics and Nuclear Fusion Department of the Atomic Energy Authority of Egypt and participants from AAAPT network group received training on the plasma focus, glow discharge and theta-z pinch particularly on low-cost diagnostics.
- *ICTP-UM Training Programme on the Technology and Applications of the Plasma Focus, Kuala Lumpur 13 March–23 April 1995*: The programme consisted of elementary and advanced research on plasma focus and associated diagnostics with participation of Pius Adjardo (Liberia), Suryadi (Indonesia), Prof. Chaivitya Silawatshananai and Yuthana (Thailand), Dr. C. Deminitscu-Zoita (Romania), Prof. Peter Choi (UK), Prof. V.A. Gribkov (Russia) and staff of the Plasma Research Lab and Pulse Technology and Instrumentation Lab of University of Malaya. The training programme was sponsored by ICAC-UM, University of Malaya and AAAPT and was directed by Prof. C.S. Wong.

In addition to the above-mentioned larger scale activities of AAAPT which were organized for training of group of young researchers on advanced plasma devices, diagnostics, and theory, the AAAPT was involved and associated with the organization of several other major events. This include (i) Fourth Tropical College on Applied Physics, Kuala Lumpur, Malaysia, 28 May–16 June 1990, (ii) Third Summer School on Plasma Physics, Tsingdao, China, August 1990, (iii) Research sessions using the ICTP/UM PFF at the ICTP 1991 Spring College on Plasma Physics, Trieste, Italy, May–June 1991, and (iv) Regional Course on Plasma Physics, QIAU, Islamabad, Pakistan 12–30 November 1994.

1.4.2 Activities at AAAPT Training Centres [1991–2003]

Initial intensive training activities of AAAPT were conducted at the Host Centre at University of Malaya, Malaysia and through the second and third training programmes, in 1988 and 1990, respectively, 24 UNU Fellows were trained up to November 1990 [10]. By 1991 several UNU Fellows, who had earlier taken back UNU/ICPT Plasma Focus and other diagnostics facilities back home, established these facilities successfully at home institutes/universities with the help of active local support. Some of these institutes/universities also had already existing plasma facilities and research programme which catalyzed the faster growth of experimental plasma research and laboratories at these places. From 1991 onwards, many other AAAPT network activities, mostly for individual plasma researchers, were conducted through other centers at University of Delhi (India), Quaid-i-Azam University (Pakistan), Atomic Energy Authority (Egypt), AAAPT Research and Training Centre (China), and Nanyang Technological University (Singapore), while the Host Centre at UM continued its training programme. Some of the training activities conducted at these centers have already been mentioned in previous section.

- *Regional Attachment Centre @ University of Delhi, India*: The regional attachment center at Plasma Research Laboratory, Department of Physics and Astrophysics, University of Delhi, India was coordinated by Prof. M.P. Srivastava. The major objective of "Delhi Attachment Programme" was to provide exposure and training on dense plasma focus device operation and fabrication of associated diagnostics including nitrogen laser shadowgraphy. The programme started in November 1991 and trained 13 visiting scientists and researchers from different parts of India by July 1997. The participants in attachment programme were paid return rail fare and local expanses out of AAAPT allocation to Regional Centre at Delhi. Most of the attachments were of 4-week duration. The first week focused on literature survey on UNU/ICTP PFF and associated diagnostics along with detailed discussion of work plan. In the second week, they would learn the assembly and disassembly of the device and the diagnostics followed by operation of the (PFF) with electrical and optical diagnostics and analysis of data obtained in third and fourth week along with the report writing. The list of names of 13 participants trained under Delhi Regional Centre training programme of AAAPT and details of other research activities at University of Delhi, India until 1997 can be found in reference [11].
- *Regional Attachment Centre @ Quaid-i-Azam University, Pakistan*: The Regional Attachment Centre at Department of Physics, Quaid-i-Azam University, Islamabad, Pakistan was coordinated by Prof. G. Murtaza. The center over the period of 1991–1997 trained many overseas and local visiting scientists and researcher with 1-month attachment programme. The overseas visiting researchers include Feng Xianping (SIOFM China), M.A. Alabraba (Nigeria), A.G. Warmate (Nigeria), F.E. Opara (Nigeria), K.D. Alagoa (Nigeria), Abdul Rahim Omar (Malaysia), and Manny Mathuthu (Zimbabwe).

Dr. M. Zakaullah from Quaid-i-Azam University, Pakistan made a follow-up to UTM Malaysia to help with diagnostics of the UTM plasma focus. The center's activities were sponsored by AAAPT. Some of this work resulted in publication of highly cited research paper on effects of anode shape on plasma focus operation with argon [12] and also on neutron and X-ray emission with stainless steel anode [13].

- *Attachment at Atomic Energy Authority, Cairo, June–December 1996*: This programme was coordinated by Prof. T. El Khalafawy and carried out with the participation of several scientists from several countries in the region including Dr. Walid Sahyouni (Syria) who received training sponsored by AAAPT and the Plasma Physics and Nuclear Fusion Department of the AEA Egypt.
- *Attachments for research and training at University Malaya Host Centre*: In addition to group training programmes mentioned in previous section, the UM hosted several smaller or individual training/attachment programmes which include (i) attachment for George Ishiekwene of Liberia from December 1990 to January 1991 on Nitrogen Laser and shadowgraphy of spark discharges, (ii) training programme on Plasma Experiments from January to March 1991 for a group of researchers from Tajura Nuclear Research Centre, Tripoli, Libya which was directed by Prof. Lee Sing for ICAC-UM in association with AAAPT [14]: (iii) attachment of Dr. Wahid Sahyouni (Al Baath University, Syria), Prof. Sharif Al-Hawat (Atomic Energy Commission, Syria) and Prof. A. Blagoev (Sofia University, Bulgaria) in May–June 1999 on the plasma focus; (iv) attachment of researchers from PPNY, Yogyakarta, Indonesia on plasma ozonizer in 2000; (v) collaborative work with Prof. C. Silawatshananai (Songkla University, Thailand) on plasma immersion ion implantation; (vi) several research visits of Yuthana Tirawanichakul of PSU, Thailand for his Ph.D. sandwich programme and (vii) several attachment visits of Dusit of Chulalongkorn University, Thailand for his M.Sc. sandwich programme.
- *AAAPT Research and Training Center, Institute of Physics, Beijing, China, 1995*: The AAAPT Research & Training Centre (AAAPT R & T), Beijing was established on 24 May 1995 with Prof. Tsai Shih Tung as its Director and with Prof. Li Yin-an and Prof. Lee Sing (representing AAAPT) as its Associate Directors. Prof. Yang Guo-zhen (Director Institute of Physics, Chinese Academy of Sciences; IP-CAS) and Prof. G. Denardo (Office of External Activity, ICTP) were its Advisors. The center started a sandwich Ph.D. programme which provided combined resources with parts of Ph.D. programme done at home institution (from AAAPT network) and at the AAAPT R & T Center. The financial help for the candidates involved in sandwich Ph.D. programme was provided from the CAS-TWAS South-South Fellowship, IP-CAS, AAAPT, and ICTP. The programme covered a very wide area of research that included theta pinch, RF plasma sources, coaxial plasma gun, plasma source ion implantation, Tokamak, steady-state plasma devices, and plasma-aided materials processing for experimental research and plasma theory, fusion, space, and dusty plasmas in theoretical research.

- Arun K. Sharma from Institute of Advanced Study in Science and Technology, Guwahati, India attended a 3 months attachment from 18 September to 15 December 1996 to study the ECR plasma using Faraday Cup energy analyzer.
- Manny Mathuthu from Physics Department, University of Zimbabwe, Zimbabwe spent 3 months (May to August 1997) at Tsinghua University, Beijing, China as part sandwich Ph.D. programme. He was trained on X-ray production and detection from the pseudo-spark, gas-puff Z-pinch, and the plasma focus.
- Pejman Khorshid from Plasma Physics Research Center, Iran, attended attachments on tokamak studies in 1999 and 2000 totaling 6 months.
- Two researchers from Jiangxi Normal University were given hands-on training at the AAAPT R & T Center on RF plasma device in 1995–96. The device also transferred to Jiangxi Normal University to start the teaching of experimental plasma physics.

- *Scientific Exchanges and attachments at National Institute of Education, NTU, Singapore*: In 1991, Prof. Lee Sing, the founding President of AAAPT, joined the National Institute of Education, Nanyang Technological University (NIE/NTU) in Singapore. He started a Plasma Radiation Source Lab at NIE/NTU and initiated several exchange and attachment programmes under the umbrella of AAAPT network. Some of the activities carried out under his leadership at NIE/NTU are listed below:

  - AAAPT sponsored visit of Prof. V.A. Gribkov in April 1995 and started a major research collaboration between Prof. Gribkov's team and NTU/NIE leading to the development of the NX1 plasma focus as high-performance soft X-ray source and the publication of joint research papers [15, 16].
  - Prof. Tsai Shih Tung (China) visited on AAAPT-initiated research collaboration for 3 months from December 1995 to March 1996 to work on plasma focus radiation [17].
  - Suriyakan Vongtrakul (Chiangmai University, Thailand) was attached for plasma training (April–June 1999).
  - Dr. Rajdeep Singh Rawat was attached to NTU/NIE under AAAPT-initiated and partially sponsored research collaboration in two visits in 1999 and 2000. This visit led to the development of plasma focus materials deposition programme at the NIE/NTU Plasma Radiation Source Lab [18–20].
  - Prof. Li Yin-an visited NTU/NIE for research collaboration for a total period of 2.5 years (1999–2001) resulting from AAAPT collaboration. This visit led to the development of several important projects including deposition of "harder than diamond" materials [21].
  - Vikas Aggarwal (IIT Mumbai, India) carried out research on TiO_2 deposition using dense plasma focus during June–July 2003. The work was later moved forward by another AAAPT researcher, M. Hassan, and ultimately led to a research publication [22].

1.4.3 AAAPT Network Activities 2005 Onwards

The attachment and training programmes listed in previous two subsections were possible because as an affiliated network of the Abdus Salam International Centre for Theoretical Physics (ICTP), Italy, the AAAPT received regular lump sum funding from ICTP for several years from 1988 to around 2003. It also received assistance in the form of travel and other fellowships from the Third World Academy of Sciences (TWAS), UNESCO and several other organizations. In the 20th Executive Council meeting held at Kuala Lumpur, Malaysia during International Meeting on Frontier of Physics (IMFP) the AAAPT President, Prof. C.S. Wong, informed that the ICTP decided to provide the funding based on itemized request towards a particular objective and not as a lump sum fund anymore. He informed that the first request from AAAPT to ICTP for the Satellite Plasma Meeting during IMFP2005 and partial sponsorship for IMFP2005 was successful and 5000 Euros were received from ICTP for this activity. Similar itemized funding supports were received afterwards from ICTP which helped AAAPT network members to continue to help each other through technology transfer and targeted training. Since 2014, even this type of itemized funding requests to ICTP has been unsuccessful. The AAAPT network group, however, has not only continued to survive but also actively engaged in several collaborative activities to promote cooperation in plasma science and technology. Following are the examples of the activities that were conducted after year 2005 with or without ICTP funding.

- Dr. Rattachat Mongkolnavin successfully set up the theta pinch system at CU, Bangkok, Thailand in 2004–2005 with the help of Prof. Li Yin-an and Prof. Ye Moufu who stayed at CU for 1 month. Prof. Chai, Songkla University, Thailand, also helped them. Prof. Lee Sing also visited to help them develop the code for theta pinch. Prof. Jiang Nan, CAS, provided three capacitors to Dr. Rattachat's group to support the dense plasma focus device research.
- Mr. Tamer Emara from Atomic Energy Authority, Egypt was on 3-month attachment at UM from 26 April to 25 July 2006 to work on X-ray diagnostic techniques. He was doing sandwich Ph.D. programme with UM, Malaysia and AEC, Egypt. He received financial support from ICTP for his travel and accommodation.
- Mr. Mohammad Ali Mohammadi from Tabriz University Iran was on 3 months attachment at NIE/NTU, Singapore from January 4 to April 4, 2007, to work on Laser shadowgraphy techniques for plasma diagnostics. He received support from ICTP for travel, accommodation, and laser shadowgraphy equipment. The attachment was later extended to 6 months with 3 months financial support from NIE/NTU, Singapore. Mr. Mohammadi was co-supervised by Prof. Samad Sobhanian, University of Tabriz, Iran and Dr. Rajdeep Singh Rawat, NIE/NTU, Singapore under a joint Ph.D. programme. Two papers were published based on the work done during the 6 months attachment [23, 24]. He took the laser shadowgraphy system back to Tabriz, University. The collaboration between Dr. Mohammadi Ali Mohammadi (now Assistant Professor at University of

Tabriz, Iran) and Dr. Rajdeep Singh Rawat, NIE/NTU, Singapore continued even afterwards and resulted in more joint publications [25–27].

- Mr. Ujjwal M. Joshi from Kathmandu University (KU), Nepal was on 3 months attachment at University Malaya, Malaysia from June 19 to September 10, 2007, to work on dielectric barrier discharge. His attachment was supported by ICTP. KU, Nepal later became member institute of AAAPT in 2009 and actively participated in and organized several AAAPT activities described later. He completed his Ph.D. successfully and is currently working as Assistant Professor at Kathmandu University, Nepal.
- Mr. Isarawut, a Ph.D. student from CU, Bangkok, Thailand, was on research attachment from March to May 2009 at University Malaya. He was supervised by Prof. C.S. Wong to work on "plasma treatment of gelatin surface for biomedical application" under the spirit of AAAPT as collaboration between AAAPT network institutes. Mr. Isarawut was supported by CU and later he successfully completed his Ph.D. programme.
- One of most intensive and productive AAAPT network experimental research collaboration that has happened in recent years is between the Government College, Lahore, Pakistan, QIAU, Islamabad, Pakistan and NIE/NTU, Singapore. The collaboration was initiated by Prof. Riaz Ahmad (Government College, Lahore) when he proposed a series of long-term attachments of his Ph.D. student to NIE/NTU, Singapore with financial support from Higher Education Commission of Pakistan to work mostly on hard coatings using plasma focus device. The students were hosted by Dr. Rajdeep Singh Rawat at NIE/NTU, Singapore as the non-graduating students. The Ph.D. students, enrolled in Government College, Lahore, irradiated and synthesized samples at Plasma Lab in Government College, Lahore and also at Plasma Radiation Source Lab of NIE/NTU, and then did extensive characterization at NIE/NTU, Singapore. The irradiated/deposited samples were taken back by the participants for completion of remaining characterization. All participating students were given training on many material characterization techniques such as scanning electron microscopy, Energy Dispersive X-ray spectroscopy, and Raman, FTIR and UV-Visible spectroscopy at NIE/NTU. The collaboration between three AAAPT network institutes resulted in successful completion of 4 Ph.D. and several research papers [28–51], refer Table 1.2.
- Mr. Eslam Gharshebani a Ph.D. student of Prof. Samad Sobhanian, University of Tabriz, Tabriz, Iran was on 6-month attachment from February to July 2000 to Plasma Radiation Source Lab of NIE/NTU, Singapore and worked on "Hard coatings using plasma focus" under the supervision of Dr. Rajdeep Singh Rawat. He later successfully completed his Ph.D. The collaboration resulted in two research papers in international journals [50, 51]. He was supported by Ministry of Science (Iran), NIE/NTU (Singapore) and AAAPT.
- Dr. Mohammed Akel from Syria visited Physics Department, UM, Malaysia in the spirit of AAAPT network activity, from July 5, 2009, for 1 month to design and learn the use of Diode X-ray Spectrometer (DXS) from the research group

Table 1.2 List of participants from Government College, Lahore on attachment at Plasma Radiation Sources Lab of NIE/NTU under the AAAPT collaboration

Participants	Duration	Project	Refs.
Muhammad Hassan	3 months; May–July 2007	Synthesis of various thin films such as ZrN, TiC, TiN, and TiO_2 using plasma focus device	[22, 28–31]
Ijaz Ahmed Khan	6 months; September 2008–March 2009	Synthesis of various thin films such as AlN, ZrON, Zirconia, ZrSiN, and ZrCN using plasma focus device	[32–41]
Zeshan A Umar	6 months; October 2011–April 2012	Synthesis of various carbides thin films such as TiC, AlC, NiC, CuC, and CN using plasma focus device	[42–46]
Ali Hussanain	6 months; July 2012–January 2013	Synthesis of tungsten nitride thin films on SS and irradiation studies on zirconium	[47–49]

of Prof. C.S. Wong. Dr. Akel successfully completed the activity at UM and took back a five channel DXS.

- A 2-week collaborative activity was held at INTI International University, Nilai, Malaysia from August 15 to August 27, 2010 during which Dr. Rajdeep Singh Rawat and Dr. Alireza Talebitaher (both from NIE/NTU, Singapore) trained INTI researchers on designing and use of diode X-ray spectrometer on INTI focus. The experiments on X-ray emissions from pure Neon and Krypton seeded Neon were conducted at INTI [52, 53]. The activity was supported by INTI International University, NIE/NTU Singapore, and AAAPT.
- A Ph.D. student of Prof. Amrollahi, Mr. Mohsen Mardani successfully completed his 4 months research attachment at NIE/NTU Singapore under the supervision of Dr. Rajdeep from May to August 2013. During this attachment, Mr. Mardani (now Dr. Mohsen Mardani) worked on laser shadowgraphic studies of plasma focus device as collaborative AAAPT activity between Amir Kabir University, Iran and NIE/NTU, Singapore.
- A student, Ms. Mahsa Mahtab from Amir Kabir University, Tehran, Iran was invited by Dr. Rajdeep to NTU Singapore for 2 months (June–July 2014) under AAAPT network activity to work on graphene synthesis using PECVD.
- Dr. Mohan V. Jacob from James Cook University, Australia (which has recently become the Associate Member of AAAPT) spent 5 months sabbatical in NIE/NTU, Singapore from July to November 2014. During this time, Dr. Mohan helped to establish the plasma polymerization research activity at NIE/NTU and also conducted collaborative research experiments with Dr. Rajdeep Singh Rawat on graphene synthesis using non-synthetic products using PECVD. Several high impact factor papers have been published out of this collaboration [54–56]
- Ms. Sepide Javadi a Ph.D. student of Prof. M. Ghoraneviss from Islamic Azad University, Tehran, Iran was invited by Dr. R.S. Rawat to NIE/NTU Singapore

for 6 months (May–October 2015) research attachment under AAAPT network activity to work on stainless steel and tungsten irradiation and ion beam measurements in plasma focus device. The attachment resulted in one publication [57] while another publication will come out in the future soon. The attachment was financially supported by NIE/NTU, Singapore.

- Mr. Daniel Grant, a Ph.D. student of Dr. Mohan V. Jacob, James Cook University, Australia, spent 5 months on research attachment at NIE/NTU, Singapore from January to June 2016 to work on ion irradiation studies on polymer thin films. Few publications are expected to come out this work in near future.

1.4.4 Facilities Transferred or Developed After Training Programmes or Collaborative Visits Under AAAPT Network Activities

Main reasons for the success of UNU Training Program on Plasma and Laser Technology according to Prof. Takaya Kawabe of United Nations University Institute of Advanced Studies (UNU/IAS), Tokyo, Japan in his review report of programme after 12 years in 1998 were leadership, proper selection of theme, unique idea of bringing back experimental equipment to the respective home institutes to continue research, good financial support and networking among the trainees after their return to home institution [58, 59]. The outstanding success of AAAPT and its ability to grow continuously is largely due to the facilities that were/are transferred or developed through the attachment programme and collaborative work between its member institutes. The list of facilities transferred after training and attachment programme through UNU Training Program during the formative years of AAAPT and after the formal start of AAAPT in 1988 is provided in Refs. [4 and 10]. The list, however, has been growing continuously and is updated in Table 1.3.

1.4.5 Numerical Simulation Workshops

The Lee model code, developed by Prof. Lee Sing with contributions from many over past three decades, is highly successful in numerical simulation of many aspects of plasma focus device. The Lee Code has been used for designing and calibration of plasma focus device, and also for studying and estimating plasma dynamics, post-pinch fast plasma streams, ions, X-rays, and neutrons. The Lee Code and its applications in different areas are described in great detail in Chap. 3. Due to immense interest by many researchers from across the globe, Prof. Lee Sing and Prof. S.H. Saw have conducted several face-to-face and Internet-based

Table 1.3 Facilities transferred after UNU/ICTP Training Program or developed locally with support from AAAPT member institutes

Institution	UNU/ICTP PFF	EM Shock Tube (EMST) flow simulator	Nitrogen laser system	Laser shadowgraph system	Diode X–ray spectrometer	Low-Temperature plasma system
Al Azhar University, Cairo, Egypt	❶ ❸		❶	❶		
University of Rajasthan, Jaipur, India	❶		❶			
University of Delhi, Delhi, India	❶ ❸		❶ ❸	❶ ❸	❶ ❸	
Sri Pratap College, Srinagar, India			❶			
LAPAN (Space Research), Jakarta, Indonesia		❶ ❸				
PPNY (Nuclear Research), Jakarta, Indonesia	❶ ❸		❶ ❸	❶		❶
Quaid-i-Azam University, Islamabad, Pakistan	❶ ❸		❶ ❸	❶		
River State University of Science and Technology, Port Harcourt, Nigeria	❶ ❸		❶ ❸	❶		
Njala University College, Freetown, Sierra Leone	❶ ❸					
Prince of Songkla University, Hatyai, Thailand	❶ ❸		❶		❶	
University of Zimbabwe, Harare, Zimbabwe	❷ ❸					
Chulalongkorn University, Bangkok, Thailand	❷ ❸					
MLAB, ICTP, Trieste, Italy	❶ ❷					
Government College, Lahore, Pakistan	❷ ❸					

(continued)

Table 1.3 (continued)

Institution	UNU/ICTP PFF	EM Shock Tube (EMST) flow simulator	Nitrogen laser system	Laser shadowgraph system	Diode X–ray spectrometer	Low-Temperature plasma system
University of Tabriz, Tabriz, Iran			❶ ❸	❶ ❸		
Atomic Energy Commission, Syria					❶	
INTI International University, Nilai, Malaysia	❶ ❸				❶ ❸	
Thammasat University, Thailand	❷					
National Institute of Education, NTU, Singapore	❷ ❸		❷ ❸	❷ ❸	❷ ❸	❶ ❷
Kansas State University, USA	❷ ❸					

❶ Received facility through UNU Training Programme or UNU/ICTP funded programmes
❷ Developed facility locally with support from AAAPT member institutes
❸ Have produced Ph.D./M.Sc. theses using these facilities

numerical simulation workshops and courses as AAAPT network activity to teach the Lee Code. The information about some of these workshops organized by Prof. Lee Sing and Prof. S.H. Saw is listed below:

- Workshop on Plasma Focus Computation, NIE/NTU, Singapore, June 2000: Participants from 10 countries worked on numerical modeling of the plasma focus during this workshop. This workshop marks a point when the numerical code, originally developed for the UNU-ICTP PFF, comes of age, assembled together as a package applicable universally to all Mather-type plasma focus and its strength is fully realized.
- Prof. Lee Sing and Prof. S.H. Saw organized two Internet-based Workshops as AAAPT affiliated activity for 4 weeks from April 14 to May 19, 2008 and from July to end of August 2009. These two courses were attended by 30 participants from countries including Malaysia, Russia, Serbia, Syria, Turkey, Egypt, Iran, Poland, Chile, Singapore, Thailand, and India.
- Five hands-on courses were run in Ankara and Turunc in Turkey in September–October 2009, at Kansas State University, USA in May–June 2010 and at the ICTP, Trieste, Italy.
- A 2-week activity from September 26 to October 8, 2013 was organized on "The Numerical Experiment Workshop on Plasma Focus" at KU, Dhulikhel, Nepal as collaborative project between KU, INTI International University, IPFS, and AAAPT.
- One-day pre-conference workshop on September 21, 2014, just before the start of ICPSA2014, was organized in collaboration with Prof. Deepak Subedi and Dr. Raju Khanal at KU, Dhulikhel, Nepal. The workshop was attended by about 25 participants. This was a research training workshop, with an Internet section starting 1 month before the final face-to-face hands-on session on September 21. Three PFF from Singapore were simulated, generating new and exciting research results. Similar special session or Internet-based workshop on numerical simulation experiments was also conducted during other AAAPT annual workshops and conferences such as IWPCA2008, IWPDA2009, ICPSA2013, and ICPSA2016.

To date, more than 130 participants from 23 countries have completed these courses and workshops. A DIY course is also available from the IPFS website [60]. The impact of these courses is very significant and has resulted in collaborative interaction by IPFS and INTI IU with groups in Turkey, Syria, Chile, Malaysia, Singapore, and Iran. This has resulted in large number of joint publications lead by Prof. Lee Sing and Prof. S.H. Saw with various groups from AEC Syria, NTU/NIE Singapore, KSU USA, TU & KU Nepal, UTM Malaysia, and IAU Iran [61–95].

1.4.6 Symposia, Workshops, and Conferences Organized or Co-organized by AAPPT

One of the ways by which AAAPT network has kept itself alive and going is by organizing or co-organizing regular meetings in the forms of symposia, workshops, and conferences which provided the platform for status updates, scientific discussions, collaboration exploration, and to decide future directions. The AAAPT, ever since its formation in 1988, has found means and ways to organize one or the other activities every year where it would also hold its Executive Council meetings and its 30th Executive Council meeting was recently held at Langkawi, Malaysia during the 9th ICPSA 2016 organized by AAAPT together with UTM, Johor, Malaysia. The details of some of the key events organized or co-organized by AAAPT are listed below.

- *Workshop on Plasma Sources and Applications, Kuala Lumpur, Malaysia, 17–18 August 1992*: Organized as a post-conference event of 5th Asia Pacific Physics Conference (5APPC) with 20 participants from nine countries to discuss the exchange research and collaborative experience. The workshop was sponsored by ICAC-UM, AAAPT, and UM.
- *International Symposium on Laser-Plasma Interactions, Shanghai, China, 9–12 November 1992*: The event was co-sponsored by Shanghai Institute of Optics and Fine Mechanics, ICTP, AAAPT, Chinese Optical Society, Chinese Physics Society, and APSC. It was well attended by local and foreign participants. The topic covered in the symposium included laser fusion, X-ray lasers, radiation and hydrodynamics of laser plasmas, target design, diagnostics, plasma accelerators, magnetic confined and ion beam fusion, astrophysical plasmas, and anomalous nuclear phenomena in glow discharge plasmas
- *One-day Workshop on Elements of Plasma Physics and Applications, UM, Kuala Lumpur, 3 July 1993*: 57 participants were given general introduction to plasma physics and application. It was sponsored by ICAC-UM, Plasma Physics and Pulse Technology Groups of University of Malaya, AAAPT and Hisco (M) Sdn Bhd. Directed by C.S. Wong
- *International Workshop on Thin Films and Plasma Applications in Thin Film Technology, National University of Science and Technology, Bulawayo, Zimbabwe July–Aug 1997*: It was organized by Prof. A.V. Gholap and sponsored by AAAPT.
- *Regional Meeting on Plasma Research in 21 Century, CU, Bangkok, Thailand, 7–12 May 2000*: It was held in conjunction with AAAPT Council Meetings and establishment of the AAAPT Research and Training Centre at CU, Bangkok, Thailand.
- *First Cairo Conference on Plasma Physics and Applications, Cairo, Egypt, 11–15 October 2003*: The conference was sponsored by Egyptian AEA, ICTP, and AAAPT and was attended by participants from 25 countries. AAAPT Council meetings and the Third General Meeting of AAAPT was held during CCPPA.

This 3rd AAAPT General Meeting failed to elect a new Council and the election was rescheduled as a postal ballot to be conducted by Dr. Brian Stewart from his office at the ICTP—co-sponsored by AAAPT. This was duly completed in 2004 electing Prof. C.S. Wong as New President of the Fifth Council of the AAAPT. More details about the CCPPA can be found from the proceedings of the conference [96].

- *NIE-AAAPT Expert Meeting, NIE/NTU, Singapore, 21–22 August 2004*: Besides the NIE/NTU Plasma Group, the meeting was attended by Prof. C.S. Wong (UM, Malaysia), Dr. Rattachat Mongkolnavin (CU, Thailand), Prof. M. Zakaullah (QIAU, Pakistan), Dr. S.M. Mohanty (Centre for Plasma Physics, India), and Dr. Ashok Aggarwal (Indian Institute of Technology, Delhi, India). The meeting was supported by AAAPT and NIE/NTU, Singapore.
- *Workshop and Training School in Cheap Plasma Technology Applications in Industry and Environment, Nasr City, Cairo, Egypt, 8 to 14 November 2005*: Supported by AAAPT.
- *Workshop on Initiation of Fusion Programme in Thailand, Bangkok, Thailand, 15–18 June 2006*: AAAPT co-organized this meeting with CU, Thailand.
- *International Symposium on Plasma Focus, INTI International University, Nilai, Malaysia, 12 June 2013*: It was supported by IAEA and AAAPT with many renowned international plasma physicists gave invited talks on recent research results on plasma focus. The symposium was organized by Prof. S.H. Saw.
- Conference on Plasma Focus (COPF 2014) *INTI International University, Nilai, Malaysia, 20 June 2014*: One-day conference was organized by Prof. S.H. Saw and was attended by all plasma focus groups in Malaysia and Australia. There were 20 participants and 14 papers were presented.

In addition to above-mentioned events, it was realized in 2008 that the AAAPT needs to provide a platform to the young researchers from AAAPT community to showcase their research results and to have close interaction with experienced researchers from AAAPT community through an annual activity. Since 2008, the AAAPT Network has started a new series of annual workshops/conferences and has successfully organized nine international workshops, some of the participants of these events are shown in Figs. 1.4, 1.5, 1.6, 1.7, 1.8 and 1.9. The 10th ICPSA is planned from 23 to 25 October 2017 in Walailak University, Thailand and it will be chaired by Dr. Mudtorlep Nisoa.

1st International Workshop on Plasma Computation and Applications, 14–15 July 2008, Nilai and Kuala Lumpur, Malaysia: IWPCA2009 was chaired by Dr. Saw Sor Heoh. There were about 40 participants with 16 overseas participants from 14 countries and 24 local participants. About 20 presentations were made in five scientific sessions with three keynote addresses and 17 invited presentations and one hands-on session on Numerical Experiments. A 100-page proceeding of IWPCA2008 [97] was sent to all the participants of IWPCA2009 and AAAPT Council members. The IWPDA2009 was first of the recently organized series of

Fig. 1.4 Participants of IWPCA 2008 visiting the Plasma Lab at UM, Kuala Lumpur, Malaysia

Fig. 1.5 Opening ceremony of IWPDA 2009 at NIE/NTU, Singapore

workshops and served as the ice-breaker. The IWPCA2008 was supported by INTI International University, University Malaya, AAAPT, and ICTP.

2nd International Workshop on Plasma Diagnostics and Applications (IWPDA2009), 2–3 July 2009, Nanyang Technological University, Singapore: IWPDA2009 was chaired by Dr. Rajdeep Singh Rawat. There were about 70 participants with 46 overseas participants from 14 countries and 24 local participants. More than 60 presentations were made in 11 scientific sessions with one

Fig. 1.6 Opening ceremony of ICPSA 2013 at NIE/NTU, Singapore

Fig. 1.7 Participants of ICPSA 2014 at KU, Dhulikhel, Nepal

keynote address, 19 invited presentations, 17 contributory presentations, and 24 poster presentations on various aspects of plasma diagnostics, mostly for pulsed plasma, plasma simulations and plasma applications. A 260-page proceeding of IWPDA2009 was published [98]. The IWPDA2009 was supported by NIE/NTU, AAAPT, ICTP, Lee Foundation, Institute of Physics Singapore, INTI International University, and PerkinElmer Singapore.

Fig. 1.8 Participants of ICPSA 2015 at I. Azad University, Najafabad Branch, Isfahan, Iran

Fig. 1.9 Participants at closing ceremony of ICPSA 2016, Langkawi, Malaysia

3rd International Workshop on Plasma Science and Applications (IWPSA2010), 25–26 October 2010, Xiamen University, Xiamen, China: IWPSA2010 was chaired by Prof. S.Z. Yang. There were about 70 participants with 18 overseas participants from 10 countries. A total of 65 papers, with 18 invited, 12 contributed and 35

posters were presented. The IWPSA2010 was the third of the series of Workshop/Conference which started as the IWPCA2008 at INTI-UC and UM Malaysia and continued as the IWPDA2009 at NTU/NIE in Singapore. The IWPSA2010 was organized by the Institute of Physics, Chinese Academy of Sciences in cooperation with Fujian Key Laboratory for Plasma and Magnetic Resonance, School of Physics and Mechanical & Electrical Engineering, Xiamen University and was supported by ICTP and AAAPT.

4th International Workshop on Plasma Science and Applications (IWPSA2011), 27–28 October 2011, Amirkabir University, Tehran, Iran: IWPSA2010, the fourth AAAPT network workshop activity, was chaired by Prof. R. Amrollahi. There were about 106 participants. A total of 75 papers, with 11 Invited and Plenary talks, 9 Oral talks, and 55 posters were presented. The whole workshop was organized into Plenary, four Technical and Poster Session, and Panel discussion session. A visit to laboratories equipped with Tokamak and Plasma focus device was also arranged. The activity was organized by Faculty of Nuclear Engineering and Physics, the Amirkabir University of Technology in Tehran, Islamic Republic of Iran and supported by AAAPT.

5th International Conference on Plasma Science and Applications (ICPSA2012), 4–5 October 2012, Chulalongkorn University, Bangkok, Thailand: The fifth AAAPT network series workshop, IWPSA2012, was chaired by Dr. R. Mongkolnavin. There were about 35 participants. A total of about 19 invited and contributory presentations were made. The activity was supported by Chulalongkorn University, AAAPT, and ICTP. The 5th General Meeting of AAAPT was also organized along with it.

6th International Conference on Plasma Science and Applications (ICPSA2013), 4–6 December 2013, National Institute of Education, NTU, Singapore: The ICPSA2013 was co-organized by NIE/NTU, Singapore, and AAAPT. It was chaired by Dr. Rajdeep Singh Rawat. The ICPSA2013 received generous support by (i) The Abdus Salam International Centre for Theoretic Physics (ICPT), Trieste, Italy, (ii) Institute of Advanced Studies (IAS), NTU, Singapore, (iii) Asian Photonic Research Institute (APRI), GIST, Korea and (iv) Institute of Advanced Studies, Singapore. The ICPSA2013 celebrated the 25 years of formation of AAAPT. The ICPSA2013 focused on fundamentals of plasmas, plasma sources development and optimizations, plasma diagnostics, and applications of plasmas in different fields such as fusion education and training facility, X-ray/EUV radiations source, neutron source, lithography, plasma processing of biological subjects, solar cells, spintronics and magnetic materials, plasma-based nanofabrication, and plasma polymerization. The ICPSA2013 was attended by 125 participants from 27 countries and there were 3 Plenary, 8 Keynote, 44 Invited, and 26 Contributory talks along with over 60 poster presentations. The online open access proceedings of ICPSA2013 are available [99].

7th International Conference on Plasma Science and Applications (ICPSA2014), 22–24 September 2014, Kathmandu University, Dhulikhel, Nepal: The ICPSA2014 was co-organized by Department of Natural Sciences, School of Science, Kathmandu University, Nepal; Central Department of Physics, Tribhuvan

University, Nepal and Asian African Association for Plasma Training (AAAPT) network. The ICPSA2014 was coordinated by Prof. Deepak Subedi and Dr. Raju Khanal and was chaired by Prof. L.N. Jha. A one-day workshop on Numerical Experiments Workshop (Research) on Plasma Focus (NEW-PF-2014) was also organized on September 21, 2014, as a pre-conference event. There were 24 participants in this workshop. Prof. S. Lee and Prof. S.H. Saw were the resource persons for the workshop. The ICPSA2014 focused on the fundamentals, sources, diagnostics, and applications of various types of plasmas that include low-pressure low-temperature plasmas, high-pressure atmospheric plasmas, high energy density laser plasmas, and hot-dense magnetized plasma. There were about 70 participants from 10 different countries.

8th International Conference on Plasma Science and Applications (ICPSA2015), 8–10 September 2015, I. Azad University (Najafabad Branch), Isfahan, Iran: The ICPSA2015 was Co-chaired by Prof. R. Amrollahi of Amirkabir University of Technology, Tehran Polytechnic and Prof. M. Ghoranneviss of Islamic Azad University, Iran. The ICPSA2015 was co-organized by Plasma Physics Research Center of I. Azad University, Tehran, Iran and Department of Energy Engineering and Physics of Amirkabir University, Tehran, Iran. The conference had 7 Plenary, 13 Oral, and 76 poster presentations with participations from 6 countries.

9th International Conference on Plasma Science and Applications (ICPSA2016), 28–29 November 2016, Langkawi, Malaysia: The ICPSA2016 was organized at beautiful Langkawi Lagoon Resort, Langkawi and chaired by Prof. Jalil Ali from Physics Department, Faculty of Science, Universiti Teknologi Malaysia 81310 Skudai, Johor Bahru-Malaysia. The conference had 4 Plenary, 4 Invited, 40 Oral, and 20 poster presentations with participations from 8 countries.

1.5 Summarizing Success of AAAPT

Central to the success of AAAPT was to help and promote experimental plasma research using UNU/ICTP PFF and associated diagnostics in AAAPT networked institutes and universities. The total technology transfer along with taking back the equipment after UNU training/attachment programmes or through the help in developing the experimental facility locally with the help of AAAPT networked institutes resulted in either establishment or strengthening of about 20 research labs listed in Table 1.3 which itself is a testimony of AAAPT enormous effort and success. In his review of 12 years of UNU/ICPT PFF in 1998 [10], Prof. Lee Sing writes “Over the twelve years the training, transfer and follow-up activities cost an estimated total of USD500,000 in international funds and contributions from training institutions, not counting the contributions of the home institutions”. The funding, particularly from ICTP, continued for some more years on regular basis and later on for itemized request towards a particular objective or activity and also from several other resources and may have doubled the number by 2016.

Most important parameter that can be used to gauge the success of AAAPT network activity is the number of PhDs and Masters produced and the research papers published. By 1998, based on the research work carried on UNU/ICTP PFF or similar locally developed facility in AAAPT member institutes, the numbers stood at 16 PhDs, 31 Masters, and more than 160 research papers. The list was compiled by Prof. Lee Sing in reference [10]. Based on the information that can be gathered from Internet and personal contacts from AAAPT network institutes, the numbers continue to grow after 1998 and are mentioned in Table 1.4. It may be noted that the list in Table 1.4 only includes the information about research related to experimental and simulation work on plasma focus device, mostly centered about UNU/ICTP PFF.

Another remarkable contribution from AAAPT network is the development of deceptively simple Lee Model Code by Prof. Lee Sing which runs as a macro in Microsoft Excel to couple the plasma and current sheath dynamics, thermodynamics and radiation with electric circuit equations to simulate outstandingly large number of parameters of interest for PFF. The Lee Model code, initially developed as the computational package for UNU/ICTP PFF, today is one of the mostly wide used tools to model or operate any existing, past, and planned dense (PFF). The code is freely available as "The Universal Plasma Focus Laboratory RADPF5.515b" can be downloaded from Internet [100]. Its success on several fronts and its popularity is evident from the fact that about 50 journal papers (the number estimated through careful search and counting on Web of Science) have been published using Lee code, most of which are included in references 61–95 at the end of this chapter. The Lee Model code and its utility and applications are described in great length in Chap. 3 by Prof. Lee Sing and Prof. Sor Heoh Saw.

The hot and dense transient pinch plasma of plasma focus device is a well-known source of multiple radiations such as ions, electron, soft and hard X-rays, and neutrons which led to its intensive exploration for several applications in a variety of fields such as lithography, radiography, imaging, activation analysis, radioisotopes production, etc. The application of pulsed high energy density pinch plasmas, accompanied by energetic high flux instability accelerated ion beams, from a UNU/ICTP PFF for material processing and synthesis was another milestone contribution of AAAPT network group. The characteristics of the plasma focus device set it apart from other conventionally used plasma-based material processing and synthesis devices. The first work on the processing of thin film, lead-zirconate-titanate thin film, by argon ion beam using UNU/ICTP PFF was reported in 1992 by Rawat et al. [101] at AAAPT Regional Centre at University of Delhi, India under the leadership of Prof. M.P. Srivastava. This was followed by number of other novel applications of UNU/ICTP PFF in material processing and synthesis at University of Delhi, India [102–105]. The substantially different physical characteristics of plasma focus device, compared to conventional plasma devices used, offer novel and unique opportunities in processing and synthesis of nano-phase materials, which are highlighted in review papers by Rawat [106–108]. This area of research and application has been picked by almost all AAAPT network affiliated and others labs around the globe that have plasma focus devices

Table 1.4 List of candidates from AAAPT member institutes, after the year 1998, who did PhDs or Masters on experimental and numerical simulation work on plasma focus device only

Institute /University	Ph.D.	M.Phil. /M.Sc.	Publications
All AAAPT Member Institutes—by 1998 from reference [10]	16	31	>160 including 85 Journal papers
NIE/NTU Singapore—after 1998	Shan Bing (2000) Alin Patran (2002) Darren Wong (2005) Tao Zhang (2007) Rishi Verma (2009) M.V. Roshan (2010) Pan Zhen Ying (2011) Alireza Talebitaher (2012) Seng Yeow Sing (2016) S.M.P. Kalaiselvi (2016) K.S. Tan (2017)	Loh Lian Seng (2009) Tan Li Ching Claudia (2010)	**Total number of papers found on Web of Science[a] from Year 2000 to Jan 2017 from research groups mentioned in column 1** Journal Articles→ 213 Proceeding papers→ 38
UM, Kuala Lumpur, Malaysia—after 1998	Yap Seong Ling (2007) Muhammad Zubair Khan (2016) Lim Lian Kuang (2016)	Low Yoon Keong (2003) Poh Hun Seng (2007) Lim Lian Kuang (2011) Lee Seng Huat (2011) Foo Chien Shin (2011) Ngoi Siew Chien (2011) P.N.N. Elumalai (2015)	
QIAU, Islamabad, Pakistan—after 1998	Khalid Alamgir (2003) Muhammad Shafiq (2003) Safdar Hussain (2005) Sarfraz Ahmad (2006) Mahboob Sadiq (2006) M. Sharif (2006) Shaista Zeb (2007) Syed Salman Hussain (2010)	Ather Rasool (2000) Sarfaraz Ahmad (2002) Abdul Qyyum (2002) Muhammad Hassan (2002) Shaista Zeb (2002) Shujaat Ali (2003) Ikramullah (2005) Atiq-ur-Rehman (2005)	

(continued)

Table 1.4 (continued)

Institute /University	Ph.D.	M.Phil. /M.Sc.	Publications
	Hamadullah (2010) Ghulam Murtaza (2011)	Syed Salman Hussain (2006) Kashif Shahzad (2007) Aftab Ahmad Khan (2008)	
DU, Delhi, India—after 1998	Priti Agarwala (2002) Ruby Gupta (2005) Yashi Malhotra (2012) Bilasini Devi Naorem (2014) Onkar Mangla (2015)		
GC, Lahore, Pakistan—after 1998	Muhammad Hassan (2007) Ijaz A Khan (2010) Tousif Hussain (2012) Zeshan A Umar (2015) Ali Hussnain (2016)	Azeem Mir (2002) Hafiz Atiqur Rehman (2006) Aamir Islam (2006) Ijaz A Khan (2007) Saqid Jabbar (2007) Tausif Hussain (2008) Jamil Siddiqi (2008) Zeshan A Umar (2009) Haroon ur Rashid (2010) Sumaira Noreen (2011) Hafiz M Siddiq (2014) Falak Sher (2015) Hafiz M Zeeshan (2015)	
INTI International University, Nilai, Malaysia—after 1998	Arwinder Singh Jigri Singh (2016) Vahid Damideh (2016)		
University of Tabriz, Iran—after 1998	Mohammad A Mohammadi (2009) Eslam Gharshebani (2013) Sepide Javadi (2017)		
Total	16 (before 1998) + 39 (after 1988) = **55**	31 (before 1998) + 33 (after 1988) = **64**	**>400**

Note There may be other PhDs, Masters, and publications from AAAPT member institutes on plasma focus facility, numerical simulations, and other plasma devices; so the impact/success is even greater

[a]Using Advanced Search thread "TS = plasma focus device AND (AU = Lee S OR AU = Rawat R.S OR AU = Zakaullah M OR AU = Srivastava M.P OR AU = Lee P OR AU = Roy S OR AU = Wong C.S OR AU = Yap S L)". **Hence there can be more papers**

leading to more than 100 journal publications some which were listed earlier as collaboration between AAAPT networked institutes [18–20, 22, 28–51]. The application of PFF for materials processing and synthesis are described in great details in Chaps. 2 and 7.

In addition to above three specific high impact cases, i.e., (i) help and promote experimental plasma research using UNU/ICTP PFF and associated diagnostics, (ii) development, training, and distribution of Lee Model code through workshops and Internet-based courses, and (iii) collaborations on extensive use of PFF for materials processing and synthesis including applications in hard coatings and nano-fabrications, there are indeed lots of other success stories of AAAPT collaborations and coordination. For example, Dr. Mudtorlep Nisoa from Walailak University, Thailand (AAAPT member) along with his two students visited Plasma Lab NIE/NTU, Singapore for 3 weeks in May–June 2011 and set up two low-temperature plasma systems of 100 W 100 kHz RF discharge and 1.5 kW Microwave plasma. RF plasma system was later upgraded with commercial 13.56 MHz RF power supply and then in 2014 in collaboration with Dr. Mohan Jacob from James Cook University, Australia (AAAPT Associate member), a highly successful research programme on vertical graphene synthesis and its application to resistive random access memory and energy storage device started at NIE/NTU, Singapore [54–56]. There are indeed many other such stories of successful cooperation which might not be known to many of us, as sometimes we just help each other and work together in the true spirit AAAPT.

Acknowledgements Author would like to acknowledge the information and photographs provided by Prof. Lee Sing, founding President (1988–2004) and currently Advisor of AAAPT, about the formation of AAAPT and also about plethora of activities during the pre-2004 period. Information for post-2004 period is extracted from the minutes of meetings of AAAPT when the author was the initially serving as Honorary Secretary with Prof. Chiow San Wong as President (2004–2012) and later as President (2012 onwards) of AAAPT. Many others from AAAPT network institutes have also contributed to the information included in this chapter and the author acknowledges their help and support.

References

1. Link for homepage of AAAPT http://www.aaapt.org/home/formative-years-of-aaapt
2. S. Lee, Research transfer as an educational process—a model and some experience. J. Mosc. Phys. Soc. (Series B) Phys. High. Educ. Russia. 1, 99–126 (1995)
3. *Laser and Plasma Technology* (World Scientific, Singapore, 1985). ISBN 9971-978-27-X
4. S. Lee, C.S. Wong, *Initiating and Strengthening Plasma Research in Developing Countries* (Physics Today, USA, 2006), pp. 31–36
5. S. Lee, T.Y. Tou, S.P. Moo, M.A. Elissa, A.V. Gholap, K.H. Kwek, S. Mulyodrono, A. J. Smith, Suryadi, W. Usada, M. Zakaullah, A simple facility for the teaching of plasma dynamics and plasma nuclear fusion. Am. J. Phys. **56**, 62–68 (1988)
6. S. Lee, K.H. Kwek, J. Ali, M.V.H.V. Prabhakar, Y.S. Shishodia, A.G. Warmate, Sequenced Nitrogen Lasers. J. Appl. Phys. **65**, 4133–4137 (1989)

7. S. Lee, M.A. Alabraba, A.V. Gholap, S. Kumar, K.H. Kwek, M. Nisar, R.S. Rawat, J. Singh, A simple shadowgraphic setup and some results. J. Phys. Malays. **11**, 1–11 (1990)
8. S. Lee, M.A. Alabraba, A.V. Gholap, S. Kumar, K.H. Kwek, M. Nisar, R.S. Rawat, J. Singh, Effects of targets on plasma focus dynamics. IEEE Trans. Plasma Sci. **18**(6), 1028–1032 (1990)
9. S. Lee, A sequential plasma focus. IEEE Trans. Plasma Sci. **19**(5), 912–919 (1991)
10. S. Lee, in Twelve Years Of UNU/ICTP PFF—A Review. *Proceedings of Satellite Meeting of the International Meeting on Frontiers of Physics*, ICTP Preprint IC/98/231 (1998), pp. 5–34
11. M.P. Srivastava, Studies on Dense Plasma Focus at Delhi University—A Review, in Twelve Years of UNU/ICTP PFF—A Review. *Proceedings of Satellite Meeting of the International Meeting on Frontiers of Physics*, ICTP Preprint IC/98/231 (1998), pp. 58–66
12. M. Zakaullah, I. Ahmad, A. Omar, G. Murtaza, M.M. Beg, Plasma Sources Sci. Technol. **5**, 544 (1996)
13. M. Zakaullah, I. Ahmad, M. Shafique, S. Khanam, A.R. Omar, M. Mathuthu, G. Murtaza, M.M. Beg, Phys. Scr. **56**, 649 (1997)
14. S. Lee, S.H. Saw, A.A. Elfetouri, A.M. Shengher, E.O. Shumaki, N.A. Hassan, Magnetic reynold number and current sheet structure. J. Fizik Malays. **12**, 25 (1991)
15. S. Lee, P. Lee, G. Zhang, X. Feng, V.A. Gribkov, M. Liu, A. Serban, T.K.S. Wong, High rep rate high performance plasma focus as a powerful radiation source. IEEE Trans. Plasma Sci. **26**(4), 1119–1126 (1998)
16. S. Lee, G.X. Zhang, V.A. Gribkov, X. Feng, A.V. Dubrovsky, S.V. Springham, A repetitive compact plasma soft X-ray source. Singap. J. Phys. **12**(1), 69–76 (1996)
17. S.T. Tsai, S. Lee, J.L. Hu, Y.P. Chen, Time averaged spontaneous power radiation in plasma focus. ACTA Phys. Sinica (Overseas Ed) **6**, 690–696 (1997)
18. R.S. Rawat, P. Arun, A.G. Videshwar, Y.L. Lam, P. Lee, M.H. Liu, S. Lee, A.C.H. Huan, Effect of argon ion on antimony telluride thin films in dense plasma focus device. Bull. Mater. Res. **35**(3), 477–486 (2000)
19. R.S. Rawat, P. Lee, T. White, L. Ying, S. Lee, Room temperature deposition of titanium carbide thin film using dense plasma focus device. Surf. Coat. Technol. **138**(2–3), 159–165 (2001)
20. Y.L. Lam, P. Lee, M.H. Liu, S.Lee, R.S. Rawat, P. Arun, A.G. Videshwar, A.C.H. Huan, in Argon ion induced changes on antimony telluride thin films using dense plasma focus device, ed. by P. Pavlo. *Proceeding International Congress on Plasma Physics, Prague, Czech Republic*, vol. 22C (1998), pp. 2793–2797
21. S. Xu, S. Kumar, Y.A. Li, N. Jiang, S. Lee, Low-temperature synthesis of highly transparent carbon nitride thin films. J. Phys. Condens. Matter **12**(6), L121 (2000)
22. R.S. Rawat, V. Aggarwal, M. Hassan, P. Lee, S.V. Springham, T.L. Tan, S. Lee, Nano-phase titanium dioxide thin film deposited by repetitive plasma focus: ion irradiation and annealing based phase transformation and agglomeration. Appl. Surf. Sci. **255**(5), 2932–2942 (2008)
23. M.A. Mohammadi, S. Sobhanian, C.S. Wong, S. Lee, P. Lee, R.S. Rawat, The effect of anode shape on neon soft X-ray emissions and current sheath configuration in plasma focus device. J. Phys. D Appl. Phys. **42**, 045203 (2009)
24. M.A. Mohammadi, R. Verma, S. Sobhanian, C.S. Wong, S. Lee, S.V. Springham, T.L. Tan, P. Lee, R.S. Rawat, Neon soft X-ray emission studies from UNU-ICTP plasma focus operated with longer than optimal anode length. Plasma Sources Sci. Technol. **16**(4), 785–790 (2007)
25. M.A. Mohammadi, S. Sobhanian, M. Ghomeishi, E. Ghareshabani, M. Moslehi-fard, S. Lee, R.S. Rawat, Current sheath dynamics and its evolution studies in sahand filippov type plasma focus. J. Fusion Energy **28**(4), 371–376 (2009)
26. M.A. Mohammadi, S. Sobhanian, R.S. Rawat, Neutron production with mixture of deuterium and krypton in sahand filippov type plasma focus facility. Phys. Lett. A **375**, 3002–3006 (2011)

27. M. Valipour, M.A. Mohammadi, S. Sobhanian, R.S. Rawat, Increasing of hardness of titanium using energetic nitrogen ions from sahand as a filippov type plasma focus facility. J. Fusion Energy **31**(1), 65–72 (2012)
28. M. Hassan, R.S. Rawat, P. Lee, S.M. Hassan, A. Qayyum, R. Ahmed, G. Murtaza, M. Zakaullah, Synthesis of nanocrystalline multiphase titanium carbide/a-C thin films by UNU/ICTP and NX2 plasma focus devices. Appl. Phys. A Mater. Sci. Process. **90**(4), 669–677 (2008)
29. M. Hassan, A. Qayyum, R. Ahmad, R.S. Rawat, P. Lee, S.M. Hassan, G. Murtaza, M. Zakaullah, Dense plasma focus ion-based titanium nitride coating on titanium. Nucl. Instrum. Methods B **267**, 1911–1917 (2009)
30. M. Shafiq, M. Hassan, K. Shahzad, A. Qayyum, S. Ahmad, R.S. Rawat, M. Zakaullah, Pulsed ion beam-assisted carburizing of titanium in methane discharge. Chin. Phys. B **19**(1), 012801 (2010)
31. M. Hassan, A. Qayyum, S. Ahmad, S. Mahmood, M. Shafiq, M. Zakaullah, P. Lee, R.S. Rawat, DLC coating on stainless steel by pulsed methane discharge in repetitive plasma focus. Appl. Surf. Sci. **303**, 187–195 (2014)
32. I.A. Khan, M. Hassan, R. Ahmad, A. Qayyum, G. Murtaza, M. Zakaullah, R.S. Rawat, Nitridation of zirconium using ion beam delivered by plasma focus discharges. Thin Sol. Films **516**(23), 8255–8263 (2008)
33. I.A. Khan, M. Hassan, R. Ahmad, G. Murtaza, M. Zakaullah, R.S. Rawat, P. Lee, Synthesis of zirconium oxynitride (ZrON) nanocomposite films on zirconium substrate by dense plasma focus. Int. J. Mod. Phys. B **22**(23), 3941–3955 (2008)
34. I.A. Khan, M. Hassan, T. Hussain, R. Ahmad, M. Zakaullah, R.S. Rawat, Synthesis of nano-crystalline zirconium aluminium oxynitride (ZrAlON) composite films by dense plasma focus device. Appl. Surf. Sci. **255**(12), 6132–6140 (2009)
35. I.A. Khan, S. Jabbar, T. Hussain, M. Hassan, R. Ahmad, M. Zakaullah, R.S. Rawat, Deposition of zirconium carbonitride composite films using ion and electron beams emitted from plasma focus device. Nucl. Instrum. Methods Phys. Res. B **268**, 2228–2234 (2010)
36. I.A. Khan, R.S. Rawat, R. Verma, G. Macharaga, R. Ahmad, Role of charge particles irradiation on the deposition of AlN films using plasma focus device. J. Cryst. Growth **317** (1), 98–103 (2011)
37. I.A. Khan, R.S. Rawat, R. Verma, G. Macharaga, R. Ahmad, Z.A. Umar, M.A.K. Shahid, Role of ion beam irradiation and annealing effect on the deposition of AlON nanolayers by using plasma focus device. Plasma Sci. Technol. **15**(11), 1127–1135 (2013)
38. I.A. Khan, R.S. Rawat, R. Verma, R. Ahmad, M.A.K. Shahid, Post-annealing effect on the structural and mechanical properties of zirconia films deposited by plasma focus device. Chin. Phys. B **22**(12), 127306 (2013)
39. R. Ahmad, T. Hussain, I.A. Khan, R.S. Rawat, Synthesis of ZrSiN composite films using a plasma focus device. Chin. Phys. B **23**(6), 065204 (2014)
40. I.A. Khan, U. Ikhlaq, A. Farid, R.S. Rawat, R. Ahmad, Role of nitrogen pressure on the structural and mechanical properties of ZrON composite films deposited by plasma focus device. J. Fusion. Energy **34**(6), 1284–1296 (2015)
41. I.A. Khan, B. Freeha, U. Ikhlaq, R.S. Rawat, R. Ahmad, Structural and mechanical properties of zirconia film deposited by plasma focus device. J. Fusion. Energy **34**(4), 930–940 (2015)
42. Z.A. Umar, R.S. Rawat, K.S. Tan, A.K. Kumar, R. Ahmad, C. Kloc, Z. Chen, L. Shen, Z. Zhang, Hard TiCx/SiC/a-C: H nanocomposite thin films using pulsed high energy density plasma focus device. Nucl. Instrum. Methods Phys. Res. B **301**, 53–61 (2013)
43. Z.A. Umar, R.S. Rawat, R. Ahmad, A.K. Kumar, Y. Wang, T. Hussain, Z. Chen, L. Shen, Z. Zhang, Mechanical properties of Al/a-C nanocomposite thin films synthesized using plasma focus device. Chin. Phys. B (IOP Sci. Pub) **23**(2), 025204 (2014)
44. Z.A. Umar, R. Ahmad, R.S. Rawat, A. Hussnain, N. Khalid, Z. Chen, L. Shen, Z. Zhang, T. Hussain, Influence of different CH4/N2 ratios on structural and mechanical properties of a-CNx: H film synthesized using plasma focus. J. Fusion Energy **33**(6), 640–647 (2014)

45. Z.A. Umar, R. Ahmad, R.S. Rawat, M. Baig, J. Siddiqui, T. Hussain, Structural and mechanical properties of Al–C–N films deposited at room temperature by plasma focus device. Chin. Phys. B. **25**(7), 075201 (2016)
46. Z.A. Umar, R.S. Rawat, R. Ahmad, Z. Chen, Z. Zhang, J. Siddiqui, A. Hussnain, T. Hussain, M.A. Baig, Structural, compositional and hardness properties of hydrogenated amorphous carbon nitride thin films synthesized by dense plasma focus device. Surf. Interface Anal. (in press, 2017)
47. A. Hussnain, R.S. Rawat, R. Ahmad, T. Hussain, Z.A. Umar, U. Ikhlaq, Z. Chen, L. Shen, A study of structural and mechanical properties of nano-crystalline tungsten nitride film synthesis by plasma focus. Radiat. Eff. Defects Solids **170**(2), 7383 (2015)
48. A. Hussnain, R.S. Rawat, K.S. Tan, R. Ahmad, T. Hussain, P. Lee, Z. Chen, L. Shen, Z. Zhang, Study of structural and mechanical properties of WN/a-Si_3N_4 hard coatings grown by plasma focus. J. Fusion Energy **34**(2), 435–442 (2015)
49. A. Hussnain, R.S. Rawat, R. Ahmad, T. Hussain, Z.A. Umar, U. Ikhlaq, Z. Chen, L. Shen, Synthesis of nano-structure tungsten nitride thin films on silicon using Mather-type plasma focus. Radiat. Eff. Defects Solids **170**(7–8), 557–566 (2015)
50. E. Gharshebani, R.S. Rawat, S. Sobhanian, R. Verma, S. Karamat, Z.Y. Pan, Synthesis of nanostructured multiphase Ti(C, N)/a-C films by a plasma focus device. Nucl. Instrum. Methods Phys. Res. B **268**, 2777–2784 (2010)
51. E. Gharshebani, R.S. Rawat, R. Verma, S. Karamat, S. Sobhanian, Low energy repetitive miniature plasma focus device as high deposition rate facility for synthesis of DLC thin films. Appl. Surf. Sci. **256**(16), 4977–4983 (2010)
52. S.H. Saw, R.S. Rawat, P. Lee, A. Talebitaher, A.E. Abdou, P.L. Chong, F. Roy Jr., J. Ali, S. Lee, SXR measurements in INTI PF operated in neon to identify typical (normal N) Profile for shots with good yield. IEEE Trans. Plasma Sci. **41**(11), 3166–3172 (2013)
53. S. Lee, S.H. Saw, R.S. Rawat, P. Lee, R. Verma, A. Talebitaher, S.M. Hassan, A.E. Abdou, M. Ismail, A. Mohamed, H. Torreblanca, S. Al Hawat, M. Akel, P.L. Chong, F. Roy, A. Singh, D. Wong, K. Devi, Measurement and processing of fast pulsed discharge current in plasma focus machines. J. Fusion Energy **31**, 198–204 (2012)
54. M.V. Jacob, R.S. Rawat, B. Ouyang, K. Bazaka, D.S. Kumar, D. Taguchi, M. Iwamoto, R. Neupane, O.K. Varghese, Catalyst-free plasma enhanced growth of graphene from sustainable sources. Nano Lett. **15**(9), 5702–5708 (2015)
55. B. Ouyang, M.V. Jacob, R.S. Rawat, Free standing 3D graphene nano-mesh synthesis by RF plasma CVD using non-synthetic precursor. Mater. Res. Bull. **71**, 61–66 (2015)
56. M.V. Jacob, D. Taguchi, M. Iwamotob, K. Bazakaa, R.S. Rawat, Resistive switching in graphene-organic device: charge transport properties of graphene-organic device through electric field induced optical second harmonic generation and charge modulation spectroscopy. Carbon **112**, 111–116 (2017)
57. S. Javadi, M. Ghoranneviss, R.S. Rawat, A.S. Elahi, Topographical, structural and hardness changes in surface layer of stainless steel-AISI 304 irradiated by fusion-relevant high energy deuterium ions and neutrons in a low energy plasma focus device. Surf. Coat. Technol. **313**, 73–81 (2017)
58. T. Kawabe, Review of the UNU training program on plasma and laser technology, http://archive.unu.edu/capacitybuilding/Pg_microproc/UNU-ICTP-PFF.html
59. H. van Ginkel, Preface in Twelve Years of UNU/ICTP PFF—A Review. *Proceedings of Satellite Meeting of the International Meeting on Frontiers of Physics*, ICTP Preprint IC/98/231 (1998), pp. 4
60. http://www.plasmafocus.net
61. S. Lee, P. Lee, S.H. Saw, R.S. Rawat, Numerical experiments on plasma focus pinch current limitation. Plasma Phys. Controlled Fusion **50**(6), 065012 (2008)
62. S. Lee, S.H. Saw, P.C.K. Lee, R.S. Rawat, H. Schmidt, Computing plasma focus pinch current from total current measurement. Appl. Phys. Lett. **92**(11), 111501 (2008)
63. S. Lee, S.H. Saw, P. Lee, R.S. Rawat, Numerical experiments on plasma focus neon soft X-ray scaling. Plasma Phys. Controlled Fusion **51**, 105013 (2009)

64. S.H. Saw, P. Lee, R.S. Rawat, S. Lee, Optimizing UNU/ICTP PFF plasma focus for neon soft X-ray operation. IEEE Trans. Plasma Sci. **37**(7), 1276–1282 (2009)
65. S. Lee, R.S. Rawat, P. Lee, S.H. Saw, Soft X-ray yield from NX2 plasma focus. J. Appl. Phys. **106**, 023309 (2009)
66. S. Lee, S.H. Saw, L. Soto, S.V. Springham, S.P. Moo, Numerical experiments on plasma focus neutron yield versus pressure. Plasma Phys. Controlled Fusion **51**, 075006 (2009)
67. M. Akel, Sh Al-Hawat, S. Lee, Numerical experiments on soft X-ray emission optimization of nitrogen plasma in 3 kJ plasma focus SY-1 using modified Lee model. J. Fusion Energy **28**, 355–363 (2009)
68. M. Akel, Sh Al-Hawat, S. Lee, Pinch current and soft X-ray yield limitation by numerical experiments on nitrogen plasma focus. J. Fusion Energy **29**, 94–99 (2010)
69. M. Akel, Sh Al- Hawat, S.H. Saw, S. Lee, Numerical experiments on oxygen soft X-ray emissions from low energy plasma focus using Lee model. J. Fusion Energy **29**, 223–231 (2010)
70. S.H. Saw, S. Lee, F. Roy, P.L. Chong, V. Vengadeswaran, A.S.M. Sidik et al., In situ determination of the static inductance and resistance of a plasma focus capacitor bank. Rev. Sci. Instrum. **81**(5), 053505 (2010)
71. S. Lee, S.H. Saw, R.S. Rawat, P. Lee, A. Talebitaher, A.E. Abdou et al., Correlation of measured soft X-ray pulses With modeled dynamics of the plasma focus. IEEE Trans. Plasma Sci. **39**, 3196–3202 (2011)
72. M. Akel, S. Al-Hawat, S. Lee, Neon soft X-ray yield optimization from PFSy-1 plasma focus device. J Fusion Energy **30**(1), 39–47 (2011)
73. S. Lee, S.H. Saw, A.E. Abdou, H. Torreblanca, Characterising plasma focus devices—role of static inductance—instability phase fitted by anomalous resistance. J. Fusion Energy **30** (4), 277–282 (2011)
74. S. Al-Hawat, M. Akel, S. Lee, Numerical experiments on neon soft X-ray optimization of AECS-PF2 plasma focus Device. J. Fusion Energy **30**, 494–502 (2011)
75. A.E. Abdou, M.I. Ismail, A.E. Mohamed, S. Lee, S.H. Saw, R. Verma, Preliminary results of kansas state university dense plasma focus. IEEE Trans. Plasma Sci. **40**, 2741–2744 (2012)
76. S. Al-Hawat, M. Akel, S. Lee, S.H. Saw, Model parameters versus gas pressure in two different plasma focus devices operated in argon and neon. J. Fusion Energy **31**, 13–20 (2012)
77. M. Akel, S. Lee, Dependence of plasma focus argon soft X-ray yield on storage energy, total and pinch currents. J. Fusion Energy **31**, 143–150 (2012)
78. M. Akel, S. Lee, Practical optimization of AECS PF-2 plasma focus device for argon soft X-ray operation. J. Fusion Energy **31**, 122–129 (2012)
79. S. Lee, S.H. Saw, R.S. Rawat, P. Lee, A. Talebitaher, A.E. Abdou, P.L. Chong, F. Roy, A. Singh, D. Wong, K. Devi, Correlation of measured soft X-ray pulses with modeled dynamics of the plasma focus. IEEE Trans. Plasma Sci. **39**(11), 3196–3202 (2012)
80. S. Lee, S.H. Saw, R.S. Rawat, P. Lee, R. Verma, A. Talebitaher, S.M. Hassan, A.E. Abdou, M. Ismail, A. Mohamed, H. Torreblanca, S. Al Hawat, M. Akel, P.L. Chong, F. Roy, A. Singh, D. Wong, K. Devi, Measurement and processing of fast pulsed discharge current in plasma focus machines. J. Fusion Energy **31**, 198–204 (2012)
81. S. Javadi, M. Habibi, M. Ghoranneviss, S. Lee, S.H. Saw, R.A. Behbahani, Investigation of structural properties of chromium thin films prepared by a plasma focus device. Phys. Scr. **86**, 025801 (2012)
82. A.E. Mohamed, A.E. Abdou, M.I. Ismail, S. Lee, S.H. Saw, Current sheet axial dynamics of 2.5 KJ KSU-DPF under high pressure regime. IEEE Trans. Plasma Sci. **40**, 2736–2740 (2012)
83. S.H. Saw, M. Akel, P.C.K. Lee, S.T. Ong, S.N. Mohamad, F.D. Ismail, N.D. Nawi, K. Devi, R.M. Sabri, A.H. Baijan, J. Ali, S. Lee, Magnetic probe measurements in INTI plasma focus to determine dependence of axial speed with pressure in neon. J. Fusion Energy **31**, 411–417 (2012)

84. S. Lee, S.H. Saw, J. Ali, Numerical experiments on radiative cooling and collapse in plasma focus operated in krypton. J. Fusion Energy **32**, 42–49 (2013)
85. S. Lee, S.H. Saw, P. Lee, R.S. Rawat, K. Devi, Magnetic reynolds number and neon current sheet structure in the axial phase of a plasma focus. J. Fusion Energy **32**, 50–55 (2013)
86. M. Akel, S.A. Salo, S. Ismael, S.H. Saw, S. Lee, Interaction of the high energy deuterons with the graphite target in the plasma focus devices based on Lee model. Phys. Plasmas **21** (7), 072507 (2014)
87. M. Akel, S.A. Salo, S.H. Saw, S. Lee, Properties of ion beams generated by nitrogen plasma focus. J. Fusion Energy **33**, 189–197 (2014)
88. S. Lee, S.H. Saw, H. Hegazy, J. Ali, V. Damideh, N. Fatis et al., Some generalised characteristics of the electro-dynamics of the plasma focus in its axial phase: illustrated by an application to independently determine the drive current fraction and the mass swept-up fraction. J. Fusion Energy **33**, 235–241 (2014)
89. S. Lee, S.H. Saw, P.C.K. Lee, M. Akel, V. Damideh, N.A.D. Khattak et al., A model code for the radiative theta pinch. Phys. Plasmas **21**, 072501 (2014)
90. S.H. Saw, D. Subedi, R. Khanal, R. Shrestha, S. Dugu, S. Lee, Numerical experiments on PF1000 neutron yield. J. Fusion Energy **33**, 684–688 (2014)
91. P. Gautam, R. Khanal, S.H. Saw, S. Lee, Comparison of measured soft X-ray yield versus pressure for NX1 and NX2 plasma focus devices against computed values using Lee model code. J. Fusion Energy **34**, 686–693 (2015)
92. D. Piriaei, T.D. Mahabadi, S. Javadi, M. Ghoranneviss, S.H. Saw, S. Lee, The study of pinch regimes based on radiation-enhanced compression and anomalous resistivity phenomena and their effects on hard X-ray emission in a Mather type dense plasma focus device (SABALAN2). Phys. Plasmas **22**, 123507 (2015)
93. S.H. Saw, P. Lee, R.S. Rawat, R. Verma, D. Subedi, R. Khanal et al., Comparison of measured neutron yield versus pressure curves for FMPF-3, NX2 and NX3 plasma focus machines against computed results using the Lee model code. J. Fusion Energy **34**, 474–479 (2015)
94. M. Akel, S. Ismael, S. Lee, S.H. Saw, H.J. Kunze, Effects of power terms and thermodynamics on the contraction of pinch radius in plasma focus devices using the Lee model. J. Fusion Energy **35**, 807–815 (2016)
95. M. Akel, S.A. Salo, S. Ismael, S.H. Saw, S. Lee, Deuterium plasma focus as a tool for testing materials of plasma facing walls in thermonuclear fusion reactors. J. Fusion Energy **35**, 694–701 (2016)
96. H.-J. Kunze, T. El-Khalafawy, H. Hegazy (eds.), *Proceedings of First Cairo Conference on Plasma Physics and Applications*, vol. 34 (Forchungszentrum Julich GmbH as Bilateral Seminars of the International Bureau, 2004). ISSN 1433-5581
97. S.H. Saw, C.S. Wong, S. Lee, R.S. Rawat, S.L. Yap (eds.), *Proceedings of International Workshop on Plasma Computation and Applications.* (INTI College Press, 2009). ISBN 978967506563-7
98. R.S. Rawat, P. Lee, T.L. Tan, S.V. Springham (eds.), *Proceedings of International Workshop on Plasma Diagnostics and Applications.* (National Institute of Education, Nanyang Technological University, 2010). ISBN 978-983-44947-2-8
99. R.S. Rawat, P. Lee (eds.), *Proceedings of the International Conference on Plasma Science and Applications (ICPSA 2013)*, vol 32, National Institute of Education, Nanyang Technological University, Singapore, 4–6 December 2013 (Int. J. Mod. Phys. Conf. Ser., World Scientific, 2014). Online ISSN: 2010-1945
100. Lee Model Code Package: The Universal Plasma Focus Laboratory RADPF5.15b, http://www.plasmafocus.net/IPFS/modelpackage/UPF.htm
101. R.S. Rawat, M.P. Srivastava, S. Tandon, A. Mansingh, Crystallization of amorphous lead zirconate titanate thin film by dense plasma focus. Phys. Rev. B **47**(9), 4858–4862 (1993)
102. M.P. Srivastava, S.R. Mohanty, S. Annapoorni, R.S. Rawat, Diode like behaviour of ion irradiated polyaniline film. Phys. Lett. A **215**(1–2), 63–67 (1996)

103. C.R. Kant, M.P. Srivastava, R.S. Rawat, Thin carbon film deposition using energetic ions of dense plasma focus. Phys. Lett. A **226**(3–4), 212–216 (1997)
104. P. Aggarwal, S. Annapoorni, M.P. Srivastava, R.S. Rawat, P. Chauhan, Magnetite phase due to energetic argon ion irradiation from dense plasma focus on hematite thin film. Phys. Lett. A **231**(5–6), 434–438 (1997)
105. C.R. Kant, M.P. Srivastava, R.S. Rawat, Dense plasma focus energetic ions based fullerene films on Si(111) substrate. Physics Letters A **239**(1–2), 109–113 (1998)
106. R.S. Rawat, High-energy-density pinch plasma: A unique non-conventional tool for plasma nanotechnology. IEEE Trans. Plasma Sci. **41**(4), 701–715 (2013)
107. R.S. Rawat, High energy density pulsed plasmas in plasma focus: novel plasma processing tool for nanophase hard magnetic material synthesis. Nanosci. Nanotechnol. Lett. **4**, 251–274 (2012)
108. R.S. Rawat, Dense plasma focus—from alternative fusion source to versatile high energy density plasma source for plasma nanotechnology, ed. by I. VargasBlanco, Herrera Velazquez. *Proceedings of 15th Latin American Workshop on Plasma Physics (LAWPP)/ 21st IAEA TM on Research Using Small Fusion Devices (RUSFD), San Jose, COSTA RICA*, 27–31 Jan 2014, vol 591, Article Number: 012021(IOP Publishing Ltd., England, J. Phys. Conf. Ser., 2015)

Chapter 2
Dense Plasma Focus—High-Energy-Density Pulsed Plasma Device Based Novel Facility for Controlled Material Processing and Synthesis

Rajdeep Singh Rawat

2.1 Introduction

Plasma, a term that Irving Langmuir ascribed in 1928 to a volume of ionized gas, consists of positive and negative charge particles and neutrals which are generated from the physical process of gas discharge or ionization of a gas. Plasma seems simple as it is largely governed by physical laws known to nineteenth-century physicists. Yet the sophisticated and often mysterious behavior of plasma is anything but simple. One of the greatest virtues of plasma is that this seemingly simple ionized fluid exhibits bewildering variety and complexity. Currently, the plasma science is at the edge of embarking into a new era where is poised to make significant breakthroughs in next decade in the field of nuclear fusion research which uses the high-temperature high-density plasmas. For example, the International Thermonuclear Experimental Reactor (ITER), currently being built at Cadarache, France with huge international collaboration, is expected to go for deuterium–tritium operation [1] with full-scale electricity-producing fusion reactor while the National Ignition Facility (NIF), US aims to ignite the fusion capsule [2]; as a critical step to commercial fusion in future. At the same time, the low-temperature plasma applications are already creating new products and techniques that are changing our everyday lives.

The ever-expanding scope of plasma science and technology is creating a plethora of new scientific opportunities and challenges. The plasma science and technologies are playing increasingly important and critical roles in the economy, energy security, energy efficiency, environmental safety, health care and fundamental scientific knowledge and discoveries.

R.S. Rawat (✉)
National Institute of Education, Nanyang Technological University,
Singapore 637616, Singapore
e-mail: rajdeep.rawat@nie.edu.sg

R.S. Rawat (ed.), *Plasma Science and Technology for Emerging Economies*,
DOI 10.1007/978-981-10-4217-1_2

- *Economy and Plasmas*: The economic impact of plasmas is evident through its extensive use in etching tiny features onto a semiconductor wafer for microelectronic industry. The semiconductor industry uses plasmas for surface hardening, texturing or coating and simply cannot exist without the support of plasma science and technology. The low-temperature cold plasmas have also established a market base in several industries that include textile industry (finishing, printing, and sterilization), polymer and paper industry (surface treatment, printability, and adhesion), and food and agriculture industry (packaging decontamination, food surface decontamination, seed germination and wastewater treatment).
- *Energy Security*: The thermonuclear fusion using hot dense deuterium plasmas has been identified as one of the future sustainable and clean energy source to provide energy security for mankind. Great progress has been made in heating and confinement of plasmas for fusion and according to ITER's timeline; it will start exploring deuterium–tritium plasmas by 2027. The success of these experiments will very much decide the fate of fusion as long-term energy security for mankind.
- *Energy-Efficient Processes*: The plasma science is also contributing to innovations in energy-efficient technologies for various applications. The energy that is not consumed does not have to be generated! Plasma-based processes are replacing old energy-intensive manufacturing processes with new energy-efficient processes. For example, the drying stage in conventional, wet chemistry processes consumes many times more energy compared to the dry, inline plasma process through energy-efficient surface pretreatment. Similarly, material synthesis and processing using plasma-assisted or plasma-enhanced approaches are energy- and cost-efficient. Another example of higher energy efficiency of the plasma-based product is that of plasma lighting system (plasma lamp). It is a proven fact that the plasma lighting systems have a longer life, higher efficacy, better lumen maintenance, improved color rendering, and enhanced dimming performance compared to conventional high-intensity discharge lighting systems. Even compared to the new technology of light-emitting diode systems, the plasma lighting systems have higher light output and lower overall system price while maintaining a small optical package and high system efficiency.
- *Environmental Applications*: There is a growing use of plasmas for various environmental applications. These applications mostly include air pollutant treatment, wastewater and drinking water decontamination, and thermal disposal of solid waste using thermal and non-thermal plasmas (defined later). These applications exploit the ability of plasmas, which is composed of excited species, free radicals, electrons, ions and/or UV photons, to break down harmful chemicals and kill microbes to purify water and destroy pollutants.
- *Biomedical Applications*: The biomedical applications of plasmas in healthcare industry is on the rise with plasmas being used for sterilization, surface treatment of human implants, plasma-aided surgery and more recently for plasma cosmetics. Plasmas are a rich source of reactive neutral species and UV light which can destroy biological activity providing local sterilization. Plasma

treatment also makes surgical implants biocompatible by either depositing material or modifying the surface of the implant. The plasma knives (plasma streamers) are already in use for long to cut and cauterize tissue. More recently, the cold plasma jet is now being used for the cosmetic purpose for the treatment of facial skin to make it brighter, clearer and tighter. The other applications include wound healing, blood coagulation, dentistry, cancer treatment, and others.

- *Contribution to Other Sciences and Discoveries*: In addition, the development and studies in plasma science have also bred new avenues of basic science. Plasma physicists were among the first to open up and develop the new and profound science of chaos and nonlinear dynamics which has found its applications in many fields that include electronics, robotics, fluid dynamics, communication, etc. Plasma science has also contributed greatly to studies of wave phenomena, instabilities, and turbulences, important for flow, transport, and other applications. In addition, new discoveries in understanding extremely cold plasmas created from laser-cooled atoms are unleashing a flood of new ideas in atomic physics, particle acceleration through laser-plasma wakefield for future tabletop particle accelerators, the study of high-intensity laser interactions, new highly efficient lighting systems etc.

The brief introduction given above highlights the versatility and diversity of plasma applications. The focus of this chapter is the application of non-conventional high-energy-density pulsed plasma generated in dense plasma focus device for controlled synthesis and processing of a variety of materials.

2.2 Material Synthesis and Processing

Materials with different properties, shapes, and sizes are fundamental to different functional structures ranging from the smallest integrated circuit to the largest man-made structure. In almost every technology, the performance, reliability, or cost is determined by the materials used. As a result, there is always a relentless drive to develop new materials and processes (or to improve existing ones). Understanding the relationships among the structures, properties, processing, and performance of materials are crucial to optimize their functional performance and equally important is the continuous development of technologies that can provide new tools for materials processing and synthesis. The material processing and synthesis technologies help in the development of new novel materials with better properties. For example, the surface engineering of metal surface can help to protect it against all forms of wear. The surface engineering of metals can be achieved either through coatings (material syntheses/depositions) or through surface/material processing, as shown in Fig. 2.1. It may be noticed in Fig. 2.1 that two key material deposition or synthesis methods are chemical vapor deposition (CVD) [3] and physical vapor deposition (PVD) [4] methods. Since plating is mostly common to

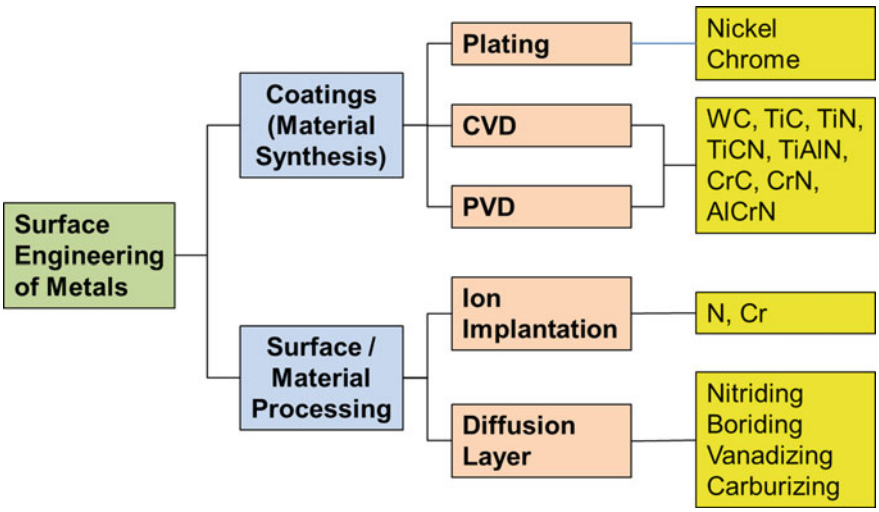

Fig. 2.1 Material synthesis/deposition and processing as tools for surface engineering of metals to protect them against different kinds of wear. *Note* CVD and PVD stand for chemical and physical vapor deposition methods

metals only, we will not discuss that. The typical setups of CVD and PVD systems are shown in Fig. 2.2.

Chemical Vapor Deposition (CVD): The CVD process involves the formation of a non-volatile solid thin film or nano-structured morphology on the substrate placed in heated reactor zone by the reaction of vapor phase chemicals (reactants) that contain the required constituents. As shown in Fig. 2.2a the cold gaseous or vapor precursor(s) of the reactant(s) are introduced into the heated reaction chamber that are decomposed and reacted at the heated substrate surface to form the thin film. The controlled transport of the reactants, controlled by mass flow controllers and evacuation pumping speed, is further forced by convection to the deposition region which is a heated substrate in heated reactor region. The reactants are decomposed by the heat or any other energy source such as plasma discharge or radiation energy and are transported by diffusion from the main gas/vapor stream to the substrate surface. At the substrate surface, many different processes take place which include (i) further chemical decomposition or reaction of the reactants, (ii) surface adsorption or nucleation at certain nucleation or attachment sites which are atomic-level ledges, kinks or grain boundaries, and (iii) surface migration and other surface reactions. Some of the byproducts get desorbed from the surface and transported back to the main gas stream by diffusion and are finally evacuated by the vacuum pump. The schematic of the process is shown in Fig. 2.2a. There exists a very large variety of CVD systems which are named either on the basis of method/type of precursor injection or on the basis of the method of precursor gas/vapor decomposition. The names of these CVD systems are self-explanatory such as Aerosol-Assisted CVD (AACVD) [5], Direct Liquid Injection CVD

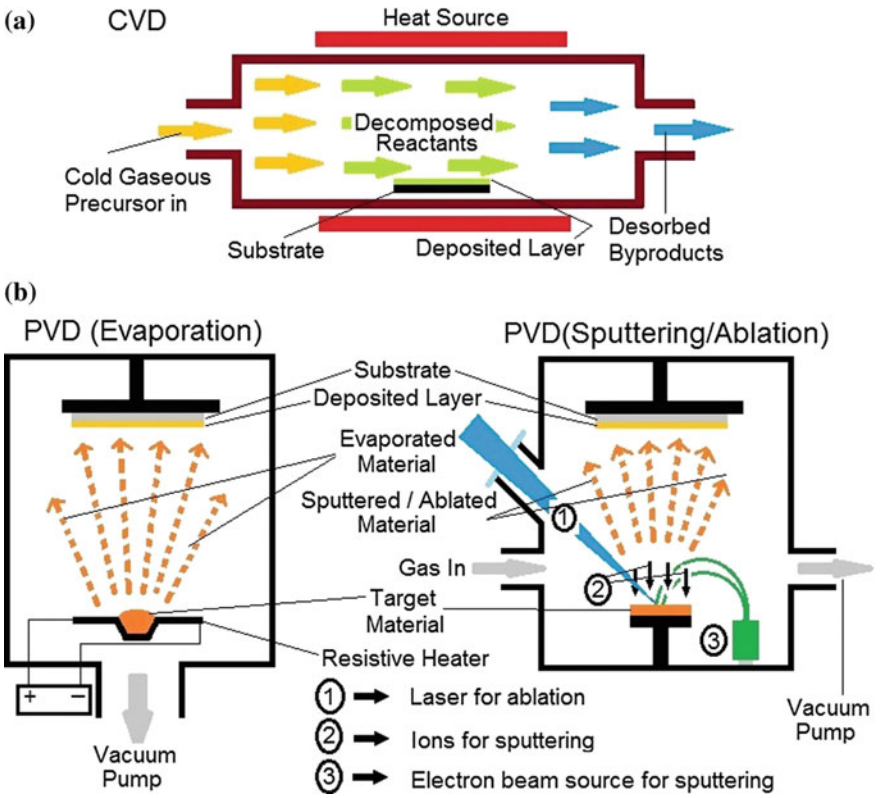

Fig. 2.2 Material synthesis/deposition methods. **a** Chemical vapor deposition (CVD), and **b** physical vapor deposition (PVD) methods

(DLICVD) [6], Plasma-Enhanced CVD (PECVD) [7], Hot Wire CVD (HWCVD) [6], Atomic Layer CVD (ALCVD) [8], Rapid Thermal CVD (RTCVD) [9], Combustion CVD (CCVD) [10], Hybrid Physical-Chemical VD (HPCVD) [11], etc. Among these, PECVD systems are becoming increasingly popular as the use of plasma discharge based decomposition of precursor gas is much more efficient compared to purely thermal decomposition in other CVD systems. This allows PECVD systems to operate at relatively less reactor zone temperature and in relatively shorter time scale, making them energy- and cost-efficient. The CVD-based thin films deposition systems have the advantages of the possibility of high growth rate synthesis, good reproducibility and ability to grow epitaxial thin films. The disadvantages of CVD include the typical use of high temperatures (though in PECVD the temperature can be lower), complex processes and toxic and corrosive gases.

Physical Vapor Deposition (PVD): The PVD is fundamentally a vaporization coating technique involving the transfer of material on an atomic level. The PVD process is quite similar to CVD except for the usage of the different physical form

of raw material. In PVD, the material that is being deposited starts out in solid form rather than in gaseous form. In addition to vaporization of solid raw material by heating normally using resistive heater (left configuration in Fig. 2.2b), other methods of vaporization such as sputtering of the solid target by plasma or ions and ablation by an intense laser pulse or energetic electron beam are also used in PVD as shown in configuration on the right in Fig. 2.2b. Various different types of PVD systems which use different evaporation methods are cathodic arc PVD [12], electron beam PVD, evaporative PVD, pulsed laser PVD, magnetron sputtering PVD, etc. [13]. The PVD is carried out under vacuum conditions with three key steps involved: evaporation, material transport, and deposition. The evaporation/sputtering/ablation stage of PVD involves either the direct resistive heating of solid material or the bombardment or irradiation of solid target by a high energy source such as a beam of electrons or ions, or plasma or concentrated laser light beam. During this stage, the atoms in neutral and ionized form are dislodged from the target surface. Evaporation is followed by transportation of vaporized material species from the target to the substrate surface. Finally, the impinging material is deposited in the form of coating at the substrate surface which may be heated or kept at room temperature. The thin films of various different materials such as metals, bi-metals, metal nitrides/oxides/carbides, etc. can be deposited using the PVD system with above-mentioned three processes using the corresponding targets in same exact stoichiometry. For example, the coating of Al or AlN can be deposited using targets of Al or AlN with inert gases being used as the background gas in the PVD chamber. The PVD system can also be used as hybrid physical-chemical vapor deposition system where an additional step of the chemical reaction is introduced by using reactive background medium. For example, to deposit AlN thin film on a substrate the Al solid target is vaporized by plasma or ions or electrons or laser and reactive background gas containing nitrogen, such as molecular N_2 or ammonia, is used to obtain nitrogen atoms. The atoms of Al metal will then react with nitrogen atoms during the transport stage from target to the substrate to form AlN coating on the substrate. If the heated substrate is used then the chemical reaction can also take place between the vaporized target material and decomposed reactive background gas at the substrate surface. The advantages of PVD are (i) ability to produce high-quality hard coatings with better corrosion and abrasion resistance, (ii) ability to utilize any type of inorganic and organic target material for deposition on an equally diverse group of substrates, and (iii) little damage to the target and the substrate. The disadvantages are (i) line of sight transfer and deposition in most PVD process making it difficult to coat undercuts and similar surface features, (ii) to require high vacuum conditions and high temperatures and hence resource requirements are stringent, and (iii) deposition rates of coatings are usually quite low.

Material Processing: In the context of this chapter, the material synthesis simply refers to creating new thin films or coatings on substrates using CVD or PVD processes, while the material processing refers to the modification of the preexisting material, either in bulk or thin film, by thermally activated diffusion, ion implantation or plasma exposure. As an example, the deposition of thin film of ZnO

on Si substrate using pulsed laser ablation of solid ZnO target is an example of material synthesis. The ZnO thin films synthesized in this fashion are mostly oxygen deficient and exhibit n-type behavior. The annealing of oxygen-deficient ZnO thin film in a furnace at a suitable temperature with partial oxygen flow can reduce the oxygen deficiency in ZnO due to oxygen diffusion. Alternatively, one can bombard oxygen-deficient ZnO with nitrogen ions to implant nitrogen in ZnO lattice to convert it to p-type material. Both, the thermal treatment in oxygen ambiance and nitrogen ion implantation which modify the physical properties of ZnO, in this case, are the examples of material processing. The material processing, however, is not just limited to ion implantation or changing the chemical or stoichiometric composition of the thin film as mentioned in the example above but it is also referred to a much wider range of processes shown in Fig. 2.3. This includes (i) etching to make nano- or micro-structures by chemical or plasma-based processes particularly for device fabrication as is normally used in microelectronic industry, (ii) doping of suitable atoms by thermal diffusion or ion implantation or plasma treatments to change material properties, (iii) changing the crystal structure and surface facet of the material by various processing methods, (iv) surface functionalization of material to make it behave differently for different applications,

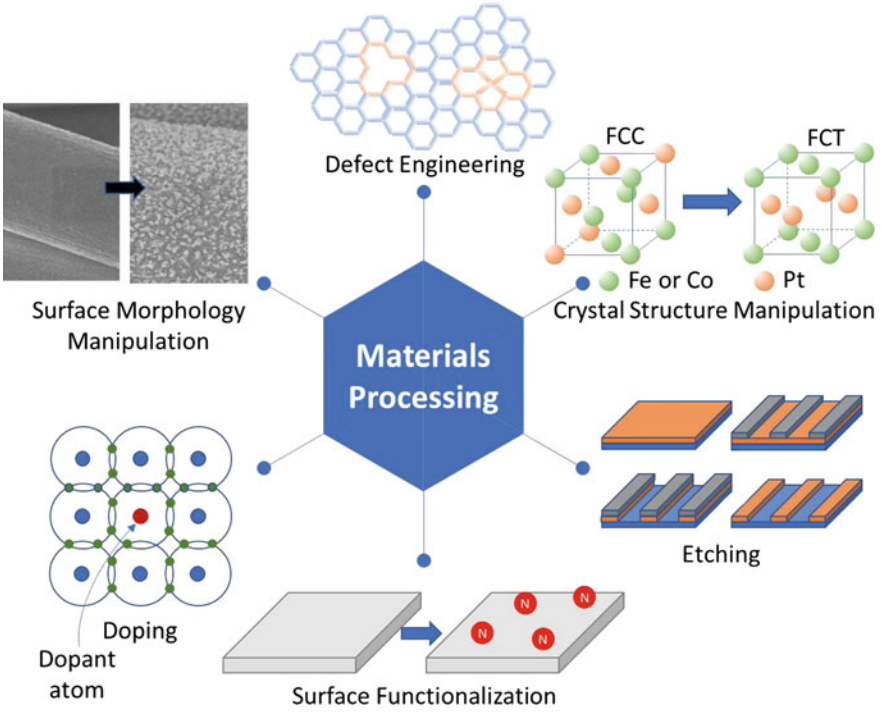

Fig. 2.3 Various types of material processing which changes the material characteristics and materials functional behavior

(v) surface morphological manipulation to increase the surface for the materials which is beneficial for many applications, (vi) defect engineering of materials, etc.

2.3 Plasmas for Material Synthesis and Processing

Plasma, the ionized gas, can be formed when an external energy source is introduced to the matter in gaseous, liquid, or solid form. External energy sources include heat, concentrated light such as in a laser, electric, and electromagnetic field. The solid, liquid, and gas can be either converted directly into plasma state or may go through other intermediate states before being converted into plasma when the energy is provided as shown in Fig. 2.4. For example, the solid can directly be ablated in a plasma state by focused laser light or electron/ion beams or the solid may first change into the liquid state followed by vaporization of the liquid to gas phase and finally the decomposition of a significant fraction of atoms into electrons and positive ions. The energy sources can be used in a controlled way to achieve plasma conditions with specific outcomes. If the energy received by atoms or molecules of the matter is sufficient enough to release the outermost electron(s) and create a significant number of ions and electrons then "plasma" is said to be formed. The temperature required to form plasmas from substances in thermal equilibrium range from 4000 K for easy-to-ionize elements like cesium to 20,000 K for hard-to-ionize elements like helium. In addition to ions and electrons, the plasma contains neutrals, excited neutrals, excited ions, and photons.

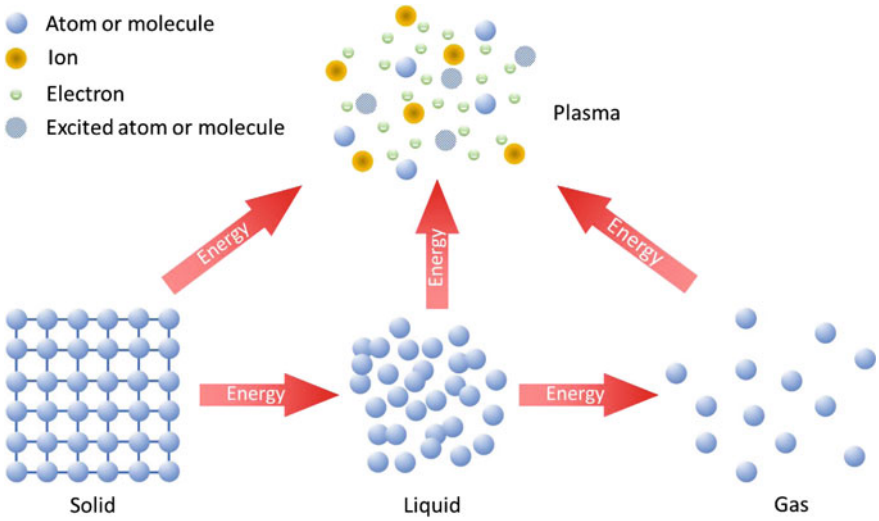

Fig. 2.4 Plasma formation from solid, liquid and gases upon delivery of energy

The easiest way to generate plasma is by applying the electric field across the gas. Normally, gases are electrical insulators but there is a negligibly small fraction of gas that is ionized due to bombardment by energetic cosmic radiations. The charges, specifically light electrons, can be accelerated by the applied electric field, which then collide with neutral particles producing an avalanche of electrons and ions breaking down the neutral gas into plasma. The electric field needed for gas breakdown can be setup simply using a pair of electrodes, or with an "electrodeless" radio frequency induction coil, or with a laser, or with charged or neutral particle beam. Heating of solids, usually alkali metals, in the evacuated chamber can not only evaporate them but also ionize them to form plasmas. Similarly, many chemical processes can also cause ionization forming plasmas. The ionization fraction of a plasma is given by $f_{iz} = n_i/(n_i + n_g)$, where n_i and n_g are ion and neutral gas density respectively. The f_{iz} is near unity for fully ionized plasmas and is $\ll 1$ for weakly ionized plasmas.

More precisely, plasma is a quasineutral gas which exhibits collective behavior [14]. The quasineutrality simply means that plasma is neutral enough so that one can take the number of densities of ions, electrons, and neutrals almost equal to each other but not so neutral that all interesting electromagnetic forces vanish. The collective behavior means that the motion of plasma species depends not only on local conditions, such as collisions among the species but also on the state of plasma in the remote region. The plasmas can occur naturally or are man-made. They exist over a very wide range of temperature and density, as shown in Fig. 2.5.

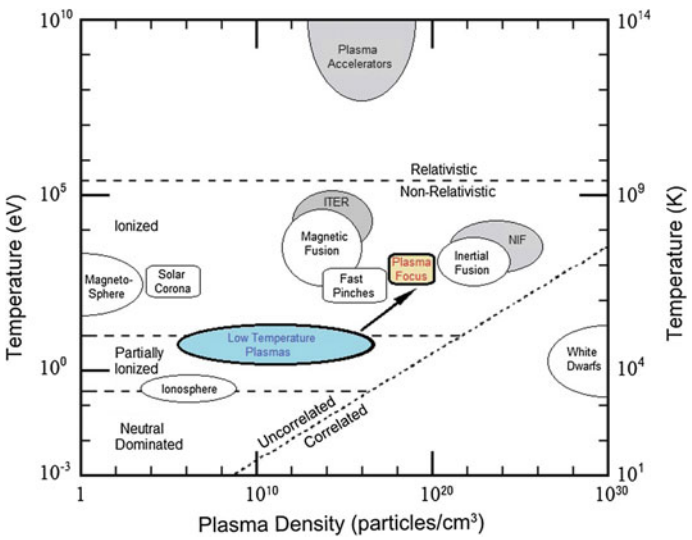

Fig. 2.5 Natural and man-made plasmas existing over a very wide range of temperature and density. Note the difference in temperature and density of low-temperature plasmas, conventionally used for material synthesis and processing, and the plasmas of dense plasma focus (DPF) devices used and discussed in this chapter

The **density**, **temperature**, and **composition** of plasma are its key parameters. The **density**, number of particular species per unit volume, is described by the electron density n_e, the ion density n_i, and the neutral or the gas density n_g. For multiple ion species in complex plasma one may describe the ion and neutral/gas density of species x as n_{ix}, and n_{gx}. Additionally, many plasmas contain positive (after neutrals loose an electron) and negative (after an electron is attached to neutral particle) ions. The density is usually a function of time, position, applied field/power, etc. Another important quantity that is needed to characterize a plasma, as evident in Fig. 2.5, is the **temperature** of the individual component of the plasma; and can be designated as the electron temperature T_e, the ion temperature T_{ix} of species x, and the neutral/gas temperature T_{gx} of species x. The multiple temperatures for different components of plasma can exist in a situation where plasma components are not able to equilibrate with each other. Like density, the plasma temperature is also not usually constant in space or time. The **composition** of plasma is one of the most important parameter, particularly for material synthesis. Knowing composition, particularly the mass numbers of all ions and neutral species as the function of space, time and feeding gas stock is handy for better control over the material synthesis and processing. Based on these three key parameters the plasmas can be classified in many different categories. However, for the sake easy classification we will simply classify the plasmas into two broad categories from the point of view of their applications for material synthesis and processing: (i) the low and (ii) the high-temperature plasmas. The dense plasma focus (DPF) device, which is the focus of this chapter, falls into the category of high-temperature plasma which also has high density (refer Fig. 2.5) while most of the plasmas commonly used for material synthesis and processing are low-temperature plasmas with density varying over a very wide range but still at least about two to three orders of magnitude lower than DPF pinch plasmas.

2.3.1 Low-Temperature Plasmas (LTPs) for Material Synthesis and Processing

The low-temperature plasmas (LTPs) are characterized by low electron kinetic temperatures ranging from fractions to tens of eV with low ionization fraction. A large fraction of the gas in LTPs actually remains in the neutral state. The LTPs are mainly produced by low-current AC or DC electric gas discharge or by gas discharges initiated by RF or microwave electromagnetic fields or by concentrating intense laser/ion/electron beams on the solid targets etc. The low-temperature plasmas are the backbone of material synthesis and processing industry. The LTPs are grouped in the blue box in Fig. 2.5. Low-temperature plasmas can be further classified into non-equilibrium and equilibrium (thermal) plasmas. The equilibrium (thermal) plasmas are formed in high-pressure gas discharges where due to higher densities and sufficiently long durations of plasma existence, the electron and ions

and neutrals have frequent and sufficient collisions among them resulting in equilibration of temperatures among the charged and neutral species, i.e., $T_e \sim T_i \sim T_g$; where T_e, $T_{i,}$ and T_g are temperatures of electrons, ions, and background gas (neutrals) species, respectively, and represent their mean kinetic energies. The non-equilibrium plasmas, on the other hand, are formed when (i) either the low operating pressures with lower electrons/ions/neutrals densities result in insufficient collisions between electrons and ions and neutrals disallowing the thermal equilibrium to be achieved; or (ii) even for high operating pressure plasmas which have higher collision rates among different species but the plasmas are short-lived (e.g., in pulsed electric discharge) interrupting the equilibration process as the plasma existence duration is less than temperature equilibration time. They are described by relation $T_e \gg T_i = T_g$.

The low temperature, equilibrium and non-equilibrium type, cold plasmas have been used extensively in synthesis and processing of materials due to their interesting combination of electrical, thermal, and chemical properties making them indispensable and versatile tool in many industries. In plasma, the neutral species or radicals are unpaired electron gas particles that are chemically reactive and electrically neutral. The result of ionization of a gaseous species leads to a plethora of active species and is the basis for plasma chemistry. This mixture of reactive gas species offers enhanced reactions and creates new chemical pathways not found in room temperature chemistry. The ease of forming a plasma discharge is an added incentive since active species can commence and be sustained at a wide range of electron temperature values ranging from 1 eV to several tens to hundreds of eV while maintaining vacuum at a wide range of pressure values. Various gas mixtures and plasma intensity deepen the processing technique further allowing a wide array of conditions or chemical pathways to be made available. In addition, the presence of highly concentrated energetic and chemically active species leads to higher processing efficiencies at low bulk plasma temperature. Thus, processes exceeding thermodynamic equilibrium can exist which intensifies traditional chemical processes [15].

The wide range of density, temperature, and composition of LTPs has largely contributed to the long and expanding list of applications for material synthesis and processing as a result of both scientific and economic drivers. The temperature, energy, and density range of the neutral and/or ionized species allow heat and particle control to sputter, etch, clean, melt, cut, functionalize, coat, and grow materials at macro-, micro- and nanoscale via the so-called “plasma processing and synthesis”. This allows thousands of applications of LTPs in different industries

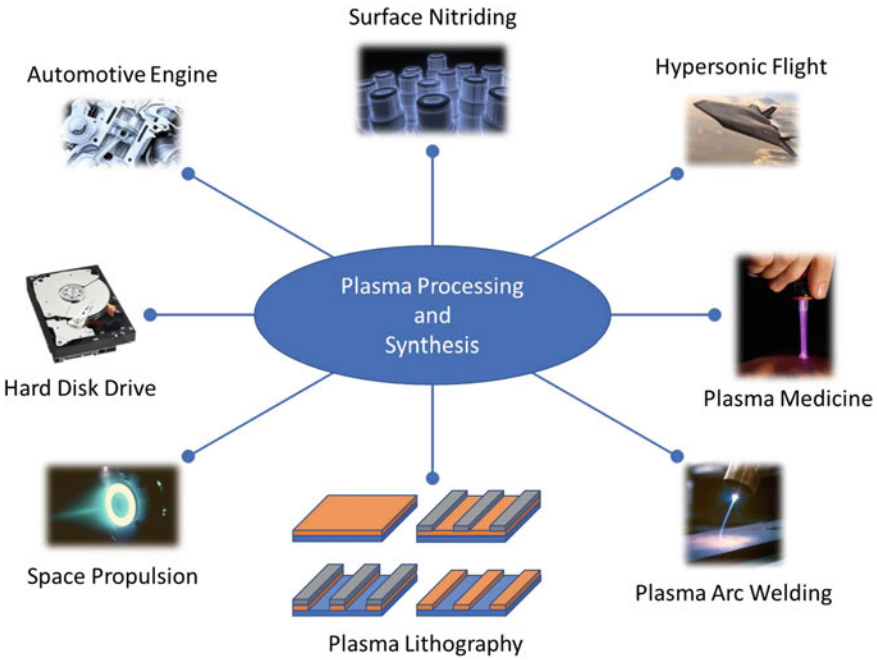

Fig. 2.6 Plasma material processing and synthesis in the industry

[16], refer Fig. 2.6. Some of the most prominent industrial applications are listed below.

- Plasma etching in fabrication of microelectronic chips;
- Plasma light sources such as discharge lamps, low-pressure lamps, field emitter arrays, lasers and plasma displays;
- Plasma deposition of (i) silicon nitride for surface passivation and insulation, (ii) amorphous silicon films for solar cells, (iii) diamond thin films, (iv) ceramic or metal alloy coatings used for protection against wear or corrosion in aircraft and automotive engines, (v) high-temperature superconductors and refractory materials, (vi) biocompatible coatings for body implants, (vii) magnetic films and carbon overcoats for hard disk drive for data storage etc.;
- Surface oxidation used in fabrication of silicon-based microelectronic circuits;
- Plasma switches such as electric power switches, pulsed power, etc.;
- Plasma nitriding, which is used to harden the surface of steel;
- Plasma melting and refining of alloys;
- Plasma-assisted manufacture of optical fibers used in communications;
- Plasma welding and cutting;
- Plasma volume processing such as flue gas flue gas treatment, metal recovery, waste treatment, water purification, etc.;
- Plasma sterilization in medical industry;

- Plasma thruster for space propulsion;
- etc.

It would not be wrong to say that low-temperature plasma-based processing and synthesis technologies are ruling the industrial applications of plasmas. Science and technology of low-temperature plasmas are quite well understood and developed, though there is still an enormous scope and potential to master it further particularly for manipulation and synthesis of materials at the nanoscale. However, since the focus of this chapter is hot and dense high-energy-density plasma in dense plasma focus device, we will next introduce the high-temperature plasmas.

2.3.2 *High-Temperature Plasmas for Material Synthesis and Processing*

High-temperature plasmas are synonymous with fusion plasmas. They have temperatures ranging from few hundred eV to several keV making the plasma to be in the almost fully ionized state. As can be seen from Fig. 2.5, these plasmas are obtained in magnetic and inertial fusion devices as well as in high-current powerful pinch discharge devices. They not only have high temperatures but also have high densities. Historically, these high-temperature fusion plasmas were not used for any practical application in material synthesis and processing. The thermonuclear fusion facilities such as ITER and NIF, in near future, will be performing D-T fusion experiments to demonstrate ignition and energy gain. These experiments will result in enormous plasma, radiation, and heat load on reactor chamber wall. One of the key issues still to be resolved in the quest for fusion energy production is the characterization, qualification (testing), and development of advanced plasma facing materials capable of withstanding the extreme radiation and heat loads expected in fusion reactors. Fundamental understanding of plasma-material surface interaction (PSI) processes in magnetic and inertial confinement fusion devices is one of the key areas of research in fusion material science and engineering. There are many gaps in the knowledge related to the PSI area which must be addressed in order to build up a validated predictive capability in support of the design of plasma facing components for ITER and a fusion demonstration power plant (DEMO). While a number of unresolved issues in plasma edge physics in magnetic confinement devices (e.g., scrape-off layer plasma widths, flows and turbulent transport) can only be addressed using tokamaks and stellarators, issues related to the impact of transient heat loads on materials, erosion, and re-deposition mechanisms, fuel retention, dust formation, as well as new material concepts can be explored using dedicated testbed devices such as plasma focus, plasma guns, plasma and particle accelerators, etc.

The focus of this chapter is however not about the fusion plasmas or the similar testbed facilities to investigate the plasma-material interaction processes on candidate materials for fusion reactor wall chamber but on relatively less-explored area of application of high-temperature high-energy-density dense plasma focus (DPF) device for material processing and synthesis. The dense plasma focus device,

in Fig. 2.5, is seen to have plasma temperature similar to that magnetic and inertial fusion plasmas but the density is in between the two of them. The high-energy-density plasmas, by definition, refers to the plasmas which are heated and compressed to extreme energy densities, exceeding 10^{11} J/m^3 (the energy density of a hydrogen molecule) [17]. The magnitude of physical parameters associated with high-energy-density physics is enormous: shock waves at hundreds of km/s (approaching a million km per hour), temperatures of millions of degrees, and pressures that exceeds 100 million atmospheres. The plasmas with energy densities in the range of (1–10) $\times$ 10^{10} J/m^3 are also now classified as high-energy-density plasmas. There are many facilities which fall in the category and they include high-energy long-pulsed (nanosecond range) lasers and high-power very short pulse (femtosecond range) TW or PW laser-based laser-plasma systems [2, 18], and fast high-current pulsed power Z–pinch [19]. The energy density of DPF devices, estimated by dividing the energy stored in the DPF capacitor bank by the volume of the final pinch column, is reported to be in the range of (1.2–9.5) $\times$ 10^{10} J/m^3 making it a high-energy-density plasma facility [20].

In addition to DPF devices, the other two high-temperature high-energy-density devices that have been extensively used for material synthesis and processing include plasma accelerator (such as QSPA Kh-50 in Kharkov, Ukraine) and PHEDP plasma gun in Ukraine and China, respectively. The QSPA Kh-50 (Quasi-Stationary Plasma Accelerator, Kh-50) [22, 23] consists of two stages, refer Fig. 2.7 [21]. The first one is used for plasma production and pre-acceleration. The second stage (main accelerating channel) is a coaxial system of shaped active electrodes-transformers with magnetically screened elements. The total energy stored in capacitor bank is about 2.2 MJ at the charging voltage of 25 kV. The amplitude and time duration of discharge current is up to 700 kA and 300 ms, respectively. The main characteristics of plasma streams depending on operations regime and distance from accelerator output can be varied in a wide range: density of plasma $10^{15} - 8 \times 10^{16}$ cm^{-3}, velocity up to 4.2 $\times$ 10^7 cm/s, energy density of

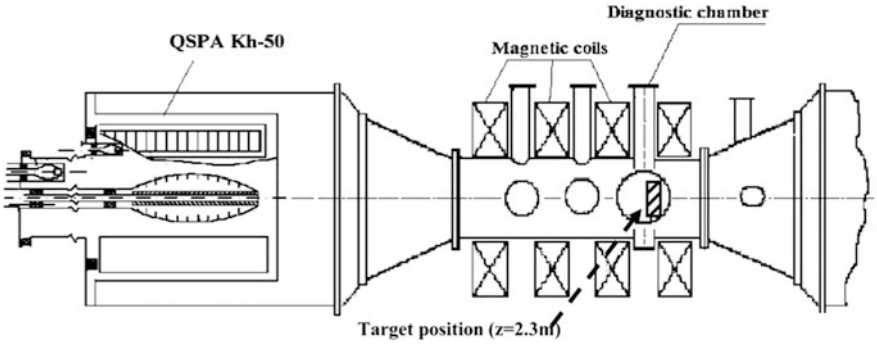

Fig. 2.7 Schematic of quasi-stationary plasma accelerator (QSPA Kh-50) which has been extensively used for material research for plasma facing components of fusion reactors. Reprinted from Garkusha et al. [21], Copyright (2009), with permission from Elsevier Ltd

plasma stream 5 J/cm^2–2 kJ/cm^2, and total energy in plasma stream up to 600 kJ. The high-energy-density plasma stream generated by QSPA can be injected into the vacuum chamber of 10 m in length and 1.5 m in diameter. Average plasma stream diameter is about 0.5 m at the distance of 1 m and it is up to 1 m at the distance >3 m from accelerator output. This enormous device, therefore, has the capability to test full-scale prototypes of tokamak divertor cassette. Most of the studies done on QSPA are limited to processing of fusion relevant material at high–temperature and high-energy-density which is not the focus of this chapter and hence is not discussed in detail.

Another high-temperature plasma device which has been used occasionally by the group led by Prof Si-Ze Yang at Beijing National Laboratory for Condense Matter Physics, Chinese Academy of Sciences is a plasma gun which has been referred in their reported work as Pulsed High-Energy-Density Plasma (PHEDP) facility [24–32]. This device has been used for film deposition and surface modification. The typical setup of PHEDP is shown in Fig. 2.8 [30]. As shown in Fig. 2.8, it consists of three sections: (i) the fast pulse electromagnetic valve driven by the discharge of a stored capacitance Cp (2 kV, 180 mF) through a driving coil to introduce the working gas into the vacuum chamber; (ii) the coaxial PHEDP gun which is powered by a capacitor bank Cg (5 kV, 1.11 mF) connected between the outer and inner electrodes; and (iii) the vacuum chamber, where films are deposited. Other parameters like the distance between substrate and gun, the number of pulses and base pressure, etc., all influence the properties of the film. Other most important features of PHEDP [33] are high electron temperature (about 10–100 eV), high plasma density (about 10^{14}–10^{16} cm^{-3}), very high axial velocity (about 10–50 km s^{-1}), and the energy density of 1–10 J cm^{-2}. Yang and his coworkers have used the PHEDP facility for a variety of applications which include deposition of (Ti,Ta)N [25] and Ta(c)N [26] thin films, titanium carbonitride [27, 29] and titanium nitride [30] films on cemented carbide cutting tools, surface metallization of alumina ceramics [31], titanium coatings on Si_3N_4 [32], etc.

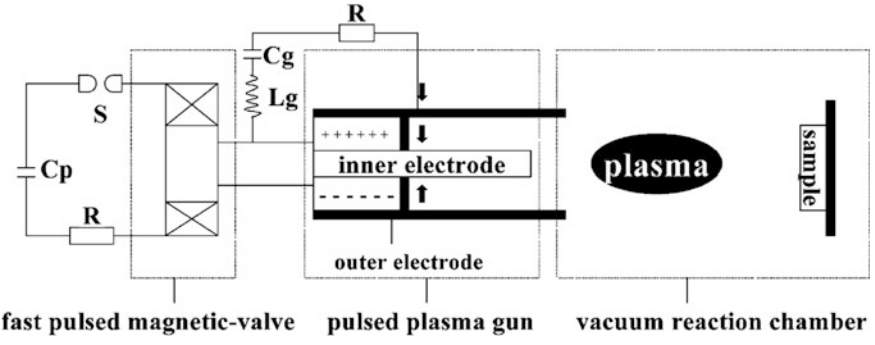

Fig. 2.8 Schematic of PHEDP facility at Chinese Academy of Sciences used for thin film deposition and surface modification. Reprinted from [30], Copyright (2003), with permission from Elsevier Ltd

The PHEDP facility, used by Yang and his coworkers, is quite similar to DPF device except that it does not have compression/pinch phase and hence the plasma is relatively not as hot and dense as one can obtain in DPF device due to efficient pinch. This book has several chapters that deal with various aspects of DPF devices ranging from simulation and modeling of DPF devices, X-ray, and neutron emissions studies from DPF devices and application of DPF devices for hard coatings. In this chapter, we will discuss the application for DPF device for material processing and synthesis under Sect. 2.5. The next section is devoted to the detailed introduction to DPF devices providing device details, the principle of operation and its key characteristics.

2.4 Dense Plasma Focus (DPF) Device: Introduction, Principle, and Characteristics

The dense plasma focus (DPF) device, refer Fig. 2.9, is a coaxial electrode gun in which plasma discharge is initiated at the closed end of the electrode assembly as the electrical energy stored in a high-voltage fast discharging capacitor bank is transferred across the electrodes. The discharge soon evolves into an axially accelerated plasma sheath which finally compresses into a hot and dense pinch plasma column at the top of the central electrode (anode). The coaxial gun primarily consists of a central conducting electrode typically a metal rod surrounded by a solid cage or an array of conducting electrodes in a squirrel cage configuration. Typically, the central electrode acts as the anode and the outer electrode (connected to chamber wall) acts as the ground electrode. One end of the coaxial electrode

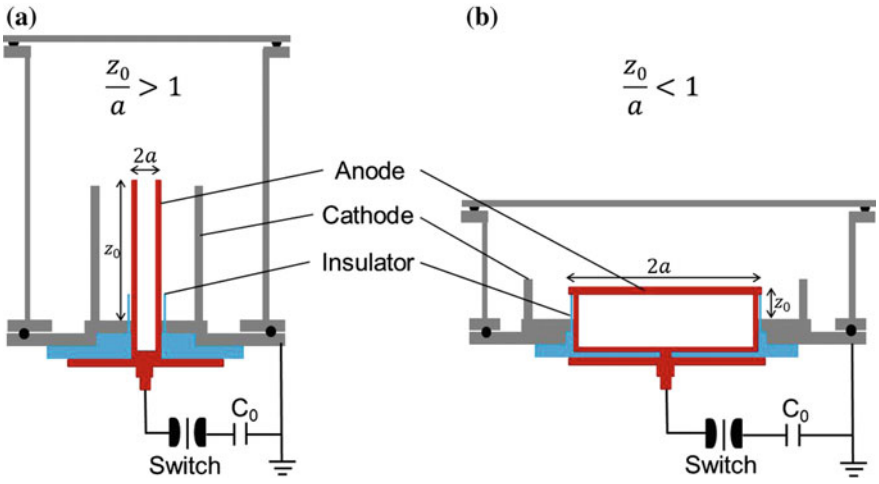

Fig. 2.9 Schematic of dense plasma focus (DPF) device. **a** Mather-type and **b** Filipov-type configuration

assembly is open, whereas the other end where the discharge is initiated is closed. The volume of DPF chamber where the coaxial electrode assembly is placed is comprised of desired operating gas at a suitable pressure. This configuration is one of the simplest and efficient methods in producing pinch plasma capable of providing avenues to conduct fusion relevant research in a relatively small and simple device [34, 35].

In the 60s, the design of this device was derived from a predecessor with similar purpose called a z-pinch device which generated a column of plasma that self-compresses when a high current flows through the plasma resulting in a high-temperature and dense plasma at the axis of the electrode. Two different electrode assembly geometries of DPF devices were developed independently with different anode aspect ratio (anode length upon its diameter). The Mather-type [36] DPF devices, developed by J.W. Mather, are the one with an anode aspect ratio typically in a range from 5 to 10 (i.e., anode aspect ratio >1) and the Filipov-type [37] devices, developed by N.V. Filipov, have the anode aspect ratio <1. In Filipov-type DPF devices the anode radius is much larger compared to its axial dimension and hence the plasma current sheath is accelerated in the radial direction towards the axis of the anode whereas in Mather geometry the sheath is accelerated mostly along the axial direction. The two geometries are shown in Fig. 2.9.

2.4.1 DPF Device Details

The coaxial electrode assembly of a DPF device resides inside a vacuum chamber and the whole system is operated at the pressure of about 10 mbar and less or at optimal pressure ranges which satisfy the focusing or pinching of the plasma sheath at the final stage. The vacuum condition allows for reliable sheath formation in the initial stage as the minimum breakdown voltage depends on the pressure according to the Paschen's law. Another important factor in the reliable operation of the DPF device is the insulator sleeve placed around the base of the anode and the presence of which allows proper formation of the plasma sheath in the initial breakdown phase and leads to efficient pinching [38]. To operate the plasma focus, high-voltage (typically greater than ten kV) and high-current (>10 kA) electrical pulses of few hundred ns to few μs duration are required. The most economic and simple way to generate these pulses is to charge a capacitor to a suitable voltage and discharge it through load viz. the plasma focus. However, to get high current pulses, the capacitors, and the connections from the capacitors to the load are specially designed. The typical working gases used in most DPF devices are hydrogen, deuterium, inert gases, and reactive gases such as oxygen, nitrogen, methane, acetylene, etc. Most studies that require the production of radiation (X-rays or neutrons) sources using the DPF device will utilize inert or deuterium gas while there is no restriction on gases used for material synthesis or treatment unless a specific material outcome is required. Gases used in material synthesis involving reactive gases such as oxygen and nitrogen will yield ceramic materials such as zinc

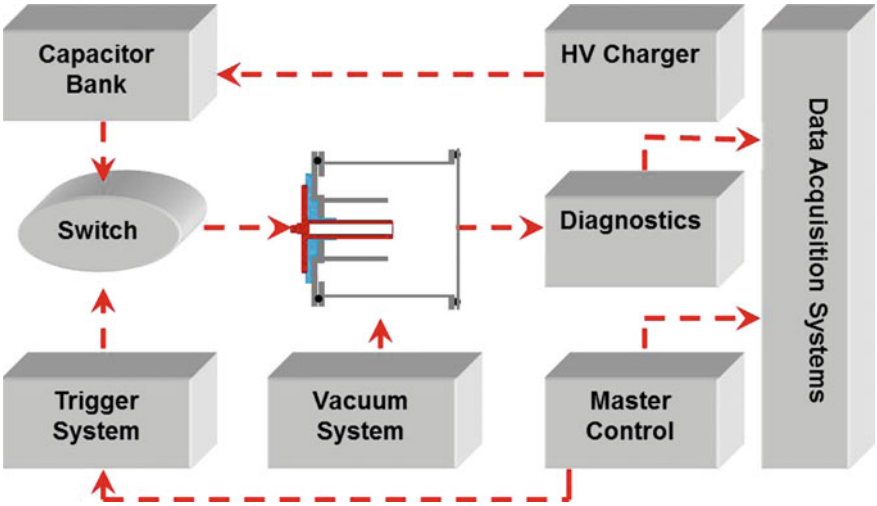

Fig. 2.10 Block diagram representation of the DPF device

oxide, titanium nitride, etc. The inert gases, such as neon, argon, etc. will yield deposited material derived from the anode tip material. The overall layout of DPF device with its various subsystems is shown in block diagram in Fig. 2.10.

Capacitor Bank: A single capacitor or a bank of capacitors, based on desired energy storage capacity, is used to store the electrical energy needed for the operation of the DPF device. The capacitors used for DPF devices are high-energy-density fast-discharging capacitors which are capable of delivering high currents needed for efficient acceleration and compression of the current sheath. The capacitor bank value, for the DPF devices available in author's Plasma Radiation Sources Lab, NTU, Singapore, is decided based on the typical operating voltage range of 12–15 kV for ease of transmission line designing. We use commercially available energy storage class of capacitors which are rated typically up to 30 kV with shot life of $>10^5$ charge/discharge cycles withstanding 80% voltage reversal. By operating the capacitors at 40–50% of their maximum charging voltage, life expectancy improves significantly and can be used for $>10^6$ charge/discharge cycles. The selection of capacitors for DPF device also depends on the intended repetition rate of the device. The single 30 μF/15 kV capacitor used in UNU-ICTP DPF device is not designed for repetitive operation, therefore for 10 Hz FMPF-3 device we used a total of eight low inductance 0.3 μF/30 kV plastic case capacitors (Model No. #37323), procured from General Atomics, USA. These capacitors specifically feature repetitive mode of operation.

Triggerable High Current Switch: A triggerable high-current switch(es) in a capacitor bank is/are incorporated to transfer energy from the bank to the load (electrode assembly in DPF chamber) at a preset voltage and time. For a fast discharge in low inductance system, the switch should have (i) low inductance, (ii) low erosion at high current levels, (iii) minimum breakdown time delay (also

referred as jitter), and (iv) reliable operation. The simplest and the most economical switch is the sparkgap switch. The sparkgaps are available in various configurations such as trigatron, direct over-volted gaps, field distortion gaps, railgaps, etc.; though some configuration like railgaps can be quite expensive. The DPF devices operated in author's lab use swinging cascade spark gap switch [34] for UNU-ICPT DPF devices while other devices such as NX2 [39], NX3 [40], and FMPF-series [41] DPF devices use pseudo-sparkgap switches.

Trigger System: Switches used in DPF devices need to endure high-voltage and high-current operation along with precise timing but its switching performance is mainly decided by applied trigger pulse characteristics produced by the trigger system/module. A major factor that affects the performance of the switch is trigger pulse rise time applied to the switch. The simple swinging cascade spark gap switches used in UNU-ICTP DPF device uses relative simple low-voltage and high-voltage silicon-controlled rectifier circuits generating a negative pulse of about 600 V which is amplified by commercially available HV TV transformer by about 60–70 times to about 35–42 kV [34]. The trigger system used for pseudospark switches [42] are slightly more complex but can be easily assembled and used for reliable switching of capacitor bank energy to the DPF tube.

The DPF Chamber: The capacitor bank, high-current low jitter switch(es), and a trigger system form the pulse power driver while the DPF chamber with coaxial electrode assembly is the load where the plasma is formed and compressed to high temperature and density. The DPF chamber normally is fabricated from stainless steel of wall thickness of 3–5 mm with several vacuum parts, gas inlets, and diagnostics ports. The electrode assembly comprises of an anode as central electrode surrounded by cathode which can either be the chamber wall [43] or several rods in squirrel cage fashion mounted on backwall plate [44, 45], shown in Fig. 2.11. The anode and cathode, at the closed end, are separated by an insulator sleeve. Low erosion characteristic is one of the most important factors in the selection of anode material. In conventional DPF device experiments selection of anode material is based on low spark erosion characteristics, good mechanical and thermal properties, availability and low cost. Spark erosion rates of various materials that are used as anode have been shown in Table 2.1. The erosion results are presented in terms of the volume of eroded material per coulomb of charge transferred ($\mu\ cm^3\ C^{-1}$) [46]. The "Elkonite", the Cu–W alloy, has the lowest erosion rate but it is very costly and not easy to machine. "Aluminum" is the cheapest option but it has the highest erosion rate of all the materials along with poor mechanical strength. So many DPF devices normally use stainless steel, because of its relatively lower cost, good mechanical, and thermal properties though copper is also another good choice which has been routinely used in our UNU-ICTP and NX2 DPF devices. Similarly, the selection of insulator sleeve material is primarily done on the basis of the dielectric constant of the material as a study done by Beg et al. [47] indicated a significant enhancement in neutron yield with use of high dielectric constant sleeve material. Dielectric constants of various sleeve materials have been compared in Table 2.2. Although ceramic has highest

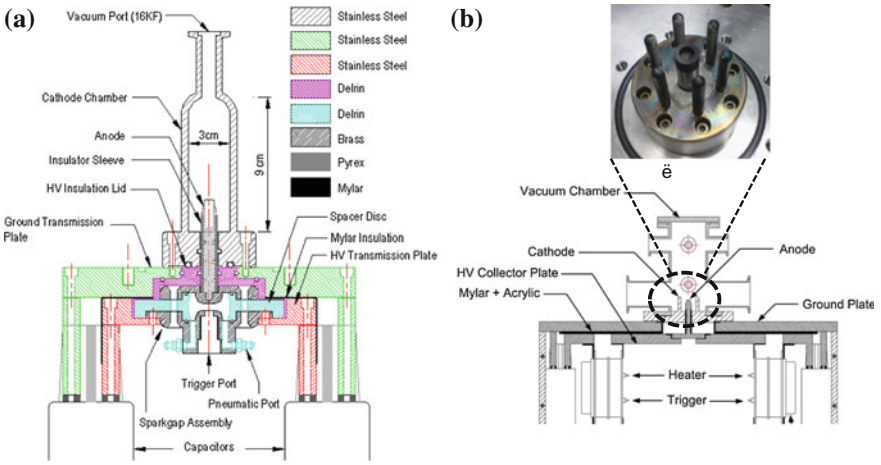

Fig. 2.11 Schematics of **a** FMPF-1 device with chamber wall as cathode, and **b** FMPF-3 device with cathode rods in squirrel cage fashion. Reprinted from **a** Verma et al. [43], Copyright (2008), with permission from IOP Publishing; **b** Reprinted from Verma et al. [44], Copyright (2010), with permission from Elsevier Ltd and Verma et al. [45], Copyright (2013), with permission from Springer

Table 2.1 Spark erosion rate of various anode materials

Material	Erosion rate ($\mu cm^3\ C^{-1}$)
Elkonite (Cu–W)	5.44
Brass	7.59
Stainless steel (SS)	9.14
Aluminum	17.37

Table 2.2 Dielectric constants and densities of various insulator sleeve materials

Material	Dielectric constant	Density ($g\ cm^{-3}$)
Alumina/ceramic	4.5–8.4	4.14
Pyrex	4.5–6.0	2.05
Nylon	3.55	1.09
Perspex	2.76–3.12	1.08
Teflon	2.04	2.04
Quartz	3.7–4.1	2.17

dielectric constant, but as a compromise between electric characteristics, easy availability and low cost; in all our DPF devices, "Pyrex" has been used.

The choice of anode material and anode type (solid v/s hollow anode) for application of DPF devices for material processing and synthesis are very critical. For applications in material processing where the intended target material, placed down the anode stream, is required to be processed by high-energy ions of filling gas species or hot dense decaying plasma, the hollow anode with thin wall and

made up of material which erodes less is highly desirable. Otherwise, in addition to processing of bulk material, the undesirable deposition of impurity material from the ablation of anode material will also take place. The application requiring the use of DPF device as deposition facility may need to use the solid anode of suitable material with suitable background gas.

High Voltage Charger: A high-voltage power supply with suitable voltage and current rating is required to charge the capacitor bank. The electrical characteristics of the high-voltage power supply will depend on the repetition rate of DPF device. For single shot operations, with the significantly large time interval between the shots, a simple home-made power supply utilizing a step-up transformer with diode chain for rectification would suffice. This was the kind of HV charger that was assembled and given to the trainees participating in UNU-ITCP training program mentioned in Chap. 1. They worked pretty well for all kind of DPF operation. The repetitive operation of DPF devices, however, requires HV chargers with much large charge transfer rate to achieve fast charging of the capacitors. The repetitive NX2 and FMPF-series DPF devices in our lab use constant power charger "EMI HVPS 802L" (procured from M/s a.l.e. Systems, USA) for fast charging of the modular capacitor bank. The HVPS 802 is especially designed for fast charging of energy storage capacitors used in various pulsed power applications, with an average power exceeding 8000 W. The HVPS 802 power supply incorporates a high-frequency IGBT series-resonant inverter for efficient generation of the output power. A high-performance control module precisely regulates the output voltage, automatically compensating for line, load, temperature, repetition rate, and program voltage variations along with inbuilt overload and short-circuit protection. The output voltage of the HVPS 802 is fully adjustable over the whole range 1–40 kV.

Vacuum System: The typical pressure range in which DPF devices operate with best focusing efficiency is from about 1–10 mbar with heavier gases requiring lower pressure and lighter gases requiring higher operating pressures. The pressure range can also be manipulated with a change in anode dimensions and designs, e.g., longer anode will require smaller filling gas pressures while the tapered anode with reducing radius at the top can operate at higher filling gas pressures. Since the operating pressure is of the order of few mbar, typically a rotary vane pump capable of producing a base pressure of about 10^{-2} mbar is good enough for most operations. However, for application of DPF device in materials-related work it is advisable to use turbo molecular or any other high capacity pump which can produce a much lower base pressure of about 10^{-5}–10^{-6} mbar to reduce the gaseous impurities in the chamber. Adequate vacuum gauges should be used to reliably read the filling gas pressure of the chamber. It is important to note that the DPF devices generate strong EM noise and shock waves during their operation, so for the safety of electronic pressure gauges (i) mechanical isolation using valves, and (ii) electronic isolation by switching off the gauge and detaching its cable to gauge controller are important safety procedures.

Diagnostic System: The DPF device is a rich source of many fundamental plasma phenomena and radiations. The fundamental plasma phenomena of interest include breakdown across electrodes at the closed end of the electrode assembly;

formation of plasma sheath; lift-off, axial acceleration and radial compression of plasma sheath; shock formation; plasma instabilities and turbulences; ionization wavefront formations; magnetic field structures; plasma decays, etc. The radiation of interest include soft and hard X-rays, relativistic electrons, instability-accelerated high-energy ions, and neutrons (for deuterium operated DPF). The availability of a large range of fundamental plasma physics phenomena and radiation yields which can be used for applications allows DPF to be a test-bed facility for many diagnostics making it an outstanding playground for fundamental research. Over the years a large number of electrical, magnetic, optical, spectroscopic, radiation, charge particles, and neutron diagnostics have been developed, tested, and explored on DPF device. For the material synthesis and processing application of DPF device, most of these diagnostics are actually not required but they create the knowledge and database and understanding of the device operation and characteristic features which help its operator to master its material-related application. Even though most diagnostics are not required for materials-related application of DPF device, basic electrical diagnostics comprising of a Rogowski coil and a resistive divider voltage probes to monitor the pinching efficiency and a Faraday cup (biased ion collector) to deduce the ion emission characteristics of the DPF device are normally employed.

Data Acquisition System: Most DPF devices operate with capacitor banks that produce electrical discharges with a quarter period (T/4) in the range of 500 ns to 4 μs. Hence, a fast data acquisition system is required to record the signals from applied diagnostics. The digital storage oscilloscopes have sampling speed of about 1GS/s and bandwidth of 1 GHz with multiple channels (four channels) is more than sufficient for most works. The synchronization of signals is very important because the data processing requires comparison on the same time base.

2.4.2 Principle of Operation: Plasma Dynamics in DPF Device

The DPF chamber is first evacuated to base pressure using rotary vane pump or with the combination of turbo molecular and rotary vane pump. The working gas is then filled in right operating pressure range which is different for different gases (typically about few mbar). The capacitor bank is first charged to high voltages (typically in 10–30 kV range) using a high-voltage power supply. The electrical energy stored in the capacitor bank is then transferred to the electrode assembly by activating low-inductance high-current fast switches resulting in gas breakdown in DPF device chamber which undergoes through several phases shown in Fig. 2.12. If the operating pressure is within right working range then gas breakdown, phase ❶ in Fig. 2.12, is initiated across the insulator sleeve at the closed end of the electrode assembly. In the breakdown phase, the ionization of the background gas grows exponentially as predicted by the Townsend law which states that an electron

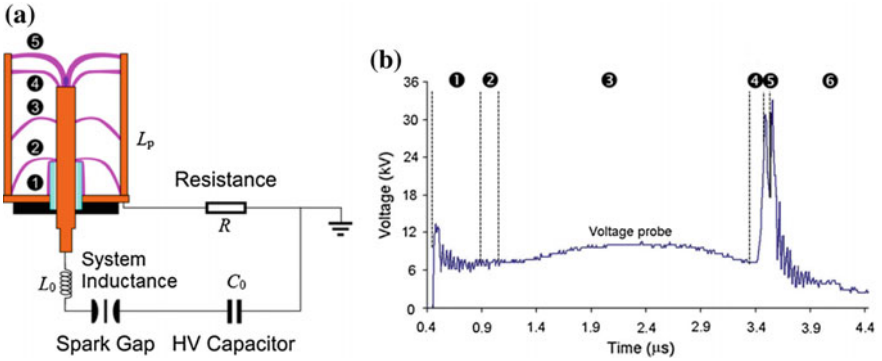

Fig. 2.12 **a** Different phases of plasma dynamics from (i) breakdown and current sheath formation ❶, (ii) lift off or inverse pinch ❷, (iii) axial acceleration ❸, (iv) radial compression ❹, and (v) pinch ❺ phase. The post pinch phase ❻ is not shown here. **b** The oscilloscope trace of the typical voltage probe signal with approximate timing duration marked on it

avalanche is produced when a free electron under the influence of an electric field ionizes a neutral particle and releases bound electron which become free electron for subsequent ionization. The formation of the initial discharge is heavily influenced by the gas pressure, type of filling gas used in the DPF chamber where the behavior resembles Paschen's law, and the inter-electrode distance. This discharge then evolves into a well-defined sheath of plasma. The time duration required for the formation of the well-defined axisymmetric plasma current sheath is about 100–500 ns for DPF devices having the quarter time period of about 500 ns and 3 μs, respectively [48, 49]. This is followed by lift-off phase in which current sheath is lifted away from the insulator sleeve in an inverse pinch manner, phase ❷ in Fig. 2.12, to the outer electrode, the cathode, due to a radially outward component of $\boldsymbol{J} \times \boldsymbol{B}$ force. The magnetic field $\boldsymbol{B}$ generated by discharge current I flowing through the anode and then through the current sheath to the ground electrode is responsible for this $\boldsymbol{J} \times \boldsymbol{B}$ Lorentz force (where $\boldsymbol{J}$ is the current density). This phase is relatively short, probably about several tens of ns to hundreds of ns, and is easily recognized when the plasma sheath widens on backwall from the base away from the insulator surface and takes on a shape of a curve or parabola, caused by the radial magnetic pressure that drifts along the anode axis while maintaining electrical contact with both electrodes [50]. Zhang et al. [49], using laser shadowgraphy, showed that the curvature steepness or angle of the plasma sheath is influenced by the length of the insulator sleeve mounted at the closed end of the anode. An increase in the insulator sleeve length was found to increase the steepness angle which affected the focusing efficiency. The optimized focusing of the DPF device was found to be closely related to the current sheath steepness angle which can be adjusted through the length of the insulator sleeve, thus highlighting another important aspect of the insulator sleeve.

Driven by the axial component of $\boldsymbol{J} \times \boldsymbol{B}$ force, the current sheath then accelerates along the electrode assembly in what is commonly referred as axial acceleration phase, phase ❸ in Fig. 2.12. The radial component of $\boldsymbol{J} \times \boldsymbol{B}$ force pushes the sheath outwards, leading to the mass loss through the open squirrel cage cathode. Both components of $\boldsymbol{J} \times \boldsymbol{B}$ force cause the plasma sheath to be canted as it moves axially forming an axis-symmetric parabolic shape. In this stage, the magnetic field strength is described as a smooth sinusoidal curve with field strength reaching the maximum value, owing to a maximum value of discharge current, as the current sheath reaches the open end of the assembly before entering the radial collapse phase [51]. The typical current sheath speed in axial acceleration phase is reported to be about 4–6 cm/μs though it can range from 2 to 10 cm/μs.

As the current sheath reaches the open end of the anode and starts to roll over anode, it is said to enter into radial acceleration phase ❹ where it collapses on the anode axis. This fast collapse causes a sudden increase in the circuit inductance and produces anomalous electrical resistance [51]. The radial speed of current sheath in radial compression phase is about 2–2.5 time the speed in axial phase which results in extremely fast moving shock. The abrupt change in plasma characteristics in this stage is due to plasma heating mechanism and several other major contributors include shock heating, magnetic compression, and viscous heating [52]. The magnetic compression and Joule heating of the imploding current sheath also cause the heating of the plasma sheath due to the intense current flowing through it. Another major effect is the viscous heating where collisional ion–ion interaction in a dense plasma volume results in self-heating.

The fast-moving shock front ahead of the collapsing current sheath can result in plasma temperature of about several hundred electron volts; while the reflected shock at the axis, together with the magnetic compression, can finally raise this temperature to around 1–2 keV. The outgoing reflected shock from the electrode axis hits the incoming plasma current sheath slowing it down and resulting in formation elongated stable pinch plasma column. This is referred as pinch phase, depicted as ❺ in Fig. 2.12. During the pinch phase, ion density increases from 10^{20-22} m^{-3} to the order of 10^{24-26} m^{-3} in pinch plasma column, increasing by a factor of 10^{4-6}, due to the densification and further ionization of a wide plasma sheath converging into a narrow column driven by the magnetic compression and secondary ionization [53]. Soon after the formation of pinched plasma columns, it breaks up due to $m = 0$ and $m = 1$ instabilities. The $m = 0$ mode instabilities (also referred as plasma diode formation in literature) accelerate the ions of the filling gas species to very high energies, up to MeV range, towards the top of the chamber and accelerate electrons to relativistic energies (100 keV and above) towards the positively charged anode.

The pinched plasma column finally breaks up and disintegrates leading to the decay of hot and dense plasma. The plasma dynamics in DPF device now can be labeled as being entering into post pinch phase; not shown in Fig. 2.12a but is

labeled as ❻ in Fig. 2.12b. A fast-moving axial ionization wavefront, produced by the ionization caused by energetic ions, later develops into a bubble-like structure [54]. The ionizing front coincides with the beginning of the hard X-ray emission due to the interaction of energetic electrons with anode tip material and also the neutron pulses for deuterium-filled DPF device. It may be noted that the number of studies performed for post pinch phase is rather limited and almost all of those studies are limited to the time scale of the order of few tens to hundreds of ns only, though the phase may last several tens of microseconds. Martínez-Fuentes et al. [55] used a triple Langmuir probe to measure the velocity, electron density, and temperature of the plasma in the expansion discharge phase (after pinch formation) at distances between 16 and 24 cm in 4.8 kJ FN-II DPF device filled with 2.5 Torr pure deuterium gas. The values of velocity, electron density, and temperature of the plasma were reported to be 5.5×10^5 m/s, 10^{20-21} m^{-3}, and 30–60 eV, respectively. Another study on 481 kJ DPF device (PF-1000) at 3.5 kPa pure deuterium showed that the free-propagating plasma stream (plasma after pinch phase) has an electron density of about 10^{23} m^{-3} and 10^{22} m^{-3} at 15 cm and 30 cm, respectively, from the electrode outlet [56]. For more details about DPF devices, readers are advised to refer to excellent reviews written by Tendys [57], Bernard et al. [58], Gribkov et al. [59], and Krishnan [60]. A detailed review highlighting several applications of DPF device in plasma nanotechnology can also be found in reference [61].

2.4.3 Key Characteristics of DPF Device

The optimized DPF devices operating across entire energy range from few J to MJ exhibit many typical parameters and characteristic features of pinch plasmas, current sheath dynamics, various radiations, and energetic charged particles that are very similar and are not affected by the dimensions of coaxial electrode assembly, capacitor bank energy, peak discharge current, and the operating gas type. This has been referred as "the unique universality of plasma focus devices" by Rawat [61]. The typical values of various key parameters of interest for **optimized** DPF devices are given below.

(i) The typical time required for the breakdown and formation of the well-defined current sheath at the start of the discharge pulse is approximately one-fifth to one-sixth of the quarter time period of discharge.
(ii) The current sheath speed in axial acceleration phase is typically in the range of 2–10 cm/μs [62, 63] which shock-heats the plasmas to electron and ion temperatures of about 100 and 300 eV, respectively, at the end of the axial acceleration phase [64].
(iii) The current sheath speed in radial compression phase is typically about 2–2.5 times that of the axial speed [62] and hence it can reach as high as 25 cm/μs (i.e., 250 km/s).

(iv) The radius of the pinch plasma column, formed in the pinch phase, is approximately about 1/10th of the anode radius [65].

(v) For DPF devices using solid anodes, the length of pinch plasma column is approximately the same as anode radius [65]. However, for the DPF device with hollow anode, the length of pinch plasma column is approximately double of the anode radius as half of the pinch plasma column is inside the anode and another half above the anode.

(vi) The energy parameter, defined as E/V_p, where E is the energy of the charged capacitor bank and V_p the volume of the pinched plasma column, is (1–10) $\times$ 10^{10} J/m^3 for the DPF devices operating at energies between 50 J and 1 MJ [20].

(vii) The drive parameter, also referred as speed factor, $I_0/\left(ap^{1/2}\right)$ has an average value of 89 $\pm$ 8 kA cm^{-1} torr$^{-1/2}$ for neutron-optimized DPF device, I_0 where is peak discharge current, a is the anode radius and p is ambient gas density of deuterium [66].

(viii) The electron/ion densities in pinch plasmas are in the range of 5 $\times$ 10^{24}–10^{26} m^{-3} [53, 67].

(ix) The electron and ion temperatures of pinch plasmas are in the range of 200 eV–2 keV [54] and 300 eV–1.5 keV [67], respectively.

(x) The energies of instability-accelerated electrons, which moves towards the anode, are in the range of few tens of keV to few hundreds of keV [68, 69].

(xi) The energies of instability-accelerated ions, which mostly move axially along the anode axis towards the top of the DPF chamber, are in the range of tens of keV to few MeV [70, 71]. The ions are mostly forward directed with most of the ions being emitted in the narrow angle of 20° with respect to the anode axis.

(xii) The UV, soft, and hard X-rays with photon energies ranging from hundreds to several hundred thousands of eV have been measured in DPF device [49, 72–75].

The DPF devices are essentially LCR circuits, refer Fig. 2.12a, involving the transient discharge of a capacitive driver, C_0, into an inductive-resistive load with the inductance L comprising of fixed system inductance L_0 and dynamic plasma inductance L_p and the resistance due to circuit connections. The characteristic transient discharge duration, given by $\sqrt{LC_0}$, typically ranges from few hundred ns for low energy sub-kJ DPF devices to over 10 μs for high-energy hundreds of kJ or MJ large DPF devices. Hence the durations of pinch plasma, radiation and energetic particles in DPF devices, which are typically some fraction of characteristic discharge duration, are of the order of tens of ns to about hundred or several hundred ns. This makes most phenomena of interest in DPF device being highly transient in nature. Hence, "*in DPF devices the very high densities and temperatures of pinch plasmas, very high number and energy densities of high energy instability accelerated ions and electrons, intense energetic radiations such as soft x-rays and neutrons (for deuterium operated devices), fast moving shock and hot-dense decaying plasma combined with their transient nature offers a kind of plasma and*

radiation environment that is drastically different from the ambience of low temperature plasmas conventionally used for material synthesis and processing".

2.4.4 Plasma Lifetime in DPF Device and Some Features of Post Pinch Phase

It may be highlighted that Sect. 2.4.3 concentrates on or refers to the intense plasma and radiation phenomena associated with DPF device during pinch phase, phase ❺ in Fig. 2.12, and only first few hundreds of ns of post pinch phase, the phase ❻ in Fig. 2.12b. However, as the DPF operation is an LCR discharge, the discharge current or DPF tube voltage has damped sinusoid profile lasting over several discharge cycles as shown in Fig. 2.13a. This allows the DPF plasma to last much longer than what has been explored by almost all DPF researchers as there is sufficient electromagnetic energy available during subsequent half cycles of damped sinusoidal LCR discharge circuit of DPF.

The plasma lifetime and other features of post pinch phase in DPF device can be deduced from the optical emission spectroscopy results discussed by T. Zhang in his Ph.D. thesis [76], carried under author's supervision. An Acton 750 spectrometer was used for end-on optical emission spectroscopy to study temporal absorption/emission characteristics of primary gas (hydrogen) plasma of the filling gas species and secondary Fe/Co plasma ablated from FeCo anode top in the NX2 DPF device. One of the exit ports of the spectrometer was coupled to an intensified CCD camera which could be gated down to durations of 10 ns using Programmable Pulse Generator PG200 from Princeton Instrument. The other exit port was coupled to PMT. The spectroscopic setup on plasma focus device is shown in Fig. 2.13b. The spectra were obtained at central wavelengths of 656.1 and 526 nm, corresponding to H and Fe emission/absorption lines at different time instants with respect to the peak of the voltage probe signal and are shown in Fig. 2.13c,d, respectively.

The hydrogen spectra, with central wavelength 656.1 nm, obtained at different delays with respect to the first voltage probe peak (corresponding to first compression phase), shown in Fig. 2.13c, were obtained at 12 mbar hydrogen at 12 kV NX2 DPF operation. It is needed to point out that relatively stronger intensities at a later time are due to the use of wider gate width for the spectrometer. The spectra recorded up to 0.7 μs show that the whole 13 nm spectral window is covered with the strong continuum, almost saturating the CCD camera. It may be important to mention here that the spectra that appear to be like that of the continuum are actually a Stark-broadened hydrogen line at 656.1 nm because of high plasma density in pinch plasma column at the anode top. It is a well-known fact that the plasma density in focused plasma column can be of the order of 10^{24}–10^{26} m^{-3} [53, 67]. Such high plasma density results in FWHM of the Stark-broadened line to be more than 15 nm, resulting in complete coverage of the observing window of the

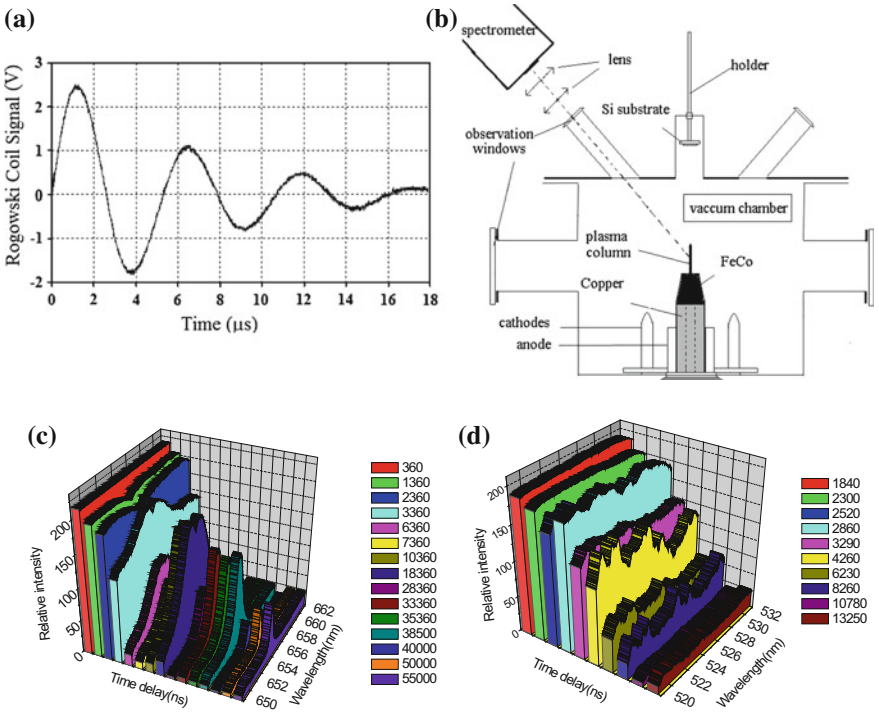

Fig. 2.13 **a** Discharge current signal taken using Rogowski coil at a high operating pressure of 25 mbar argon in NX2 DPF device showing multiple half-cycles. **b** Optical emission spectroscopy setup on NX2 DPF device with anode fitted with FeCo top and device operated with hydrogen as the filling gas [76]. **c** H emission spectra when NX2 is operated at 12 kV and 12 mbar hydrogen [76]. **d** Fe emission spectra from NX2 DPF device [76]. The delay time in colored bars in (**c**) and (**d**) are in ns. Reprinted from Zhang [76]. Permission not needed

spectrometer. The decay of focused plasma column will result in a reduction in plasma density and correspondingly the FWHM of Stark-broadened spectral line will decrease as can be seen in Fig. 2.13c with a clear emergence of the emission peak from 3.3 μs spectrum and with its continuous sharpening as time evolves. Another noticeable feature in hydrogen spectra recorded from 1.3 μs onward is the emergence of H absorption line (seen as a depression in the center of spectral peak). This absorption line is caused by the resonance absorption of hydrogen emission line emitted from hot-focused hydrogen plasma column by the bulk of the background neutral hydrogen gas (at 12 mbar) between the focused plasma column and the chamber wall. The absorption line must be there from the beginning of focused plasma column formation, but it is not observable because of the saturation of the ICCD camera. It becomes prominent when the focused plasma column starts to decay/expand decreasing the plasma density and temperature and hence reducing

the emission line intensity. The absorption line seems to disappear at about 3.9 μs which can be attributed to the continuous reduction of neutral hydrogen zone between the focused plasma column and the exit window of the chamber because of fast expansion of the ionization wavefront [77] which while expanding pushes away the neutral gas in front of it. A reasonably strong hydrogen emission peak can still be observed as late as 55 μs; and it can probably last tens of microsecond more.

In addition to the plasma of the filling (hydrogen) gas species there will be ablated plasma of anode top material which in this case is that of Fe and Co, refer Fig. 2.13b. The time evolution of the Fe emission/absorption spectra is shown in Fig. 2.13d. Please note that Co optical emission/absorption spectra are not shown and the discussion from Fe spectra should suffice. The spectra are shown from 1.8 μs onwards as spectra captured before that show a continuum in the 13 nm spectral window of the spectrometer indicating the very high density of ablated Fe plasma. The observation of continuum, followed by absorption and finally conversion to emission line spectra of Fe can be explained as follows. The hot dense pinch plasma coupled with the instability-accelerated intense and energetic electron beam ablates the anode top resulting in the formation of hot and dense Fe/Co plasma. The ablation of FeCo anode top probably lasts several microseconds because the electron emission duration in plasma focus has been found to be longer than 1 μs and in some cases even a second electron emission period was observed [78]. The initial ablated plasma is formed from the ablation of the solid target material and hence its density is expected to be very high. This was also observed in laser shadowgraphy results obtained by Soh et al. [77], shown in Fig. 2.14, for graphite anode top where the density of the carbon plasma ablated from graphite top is so high that it was opaque to nitrogen laser light. The hot and high-density ablated Fe/Co plasma produces emission spectra, which due to very high plasma density initially is Stark-broadened resulting in completing coverage of 13 nm spectral window for spectra captured up to 1.8 μs (not included in Fig. 2.13d). The ablated Fe/Co plasma continues to expand with time and so the plasma density and hence the corresponding Stark broadening reduces and hence the emission spectral lines are expected in the spectra. However, Fe/Co absorption lines were observed which is due to absorption of emission line (generated from plasma that is still being generated at the anode top because of long electron beam pulse duration and also due to prolonged thermal ablation time of the anode) by the relatively less hot expanding part of the Fe/Co plasma envelope. The spectra from 4 μs onwards show only the emission lines which are attributed to the fact that the electron beam hitting and ablation of the anode ceases by this time and therefore there is no background emission source to generate absorption spectra. It can be noticed that the Fe emission lines were observed even at 13 μs after the pinch plasma phase indicating that even the plasma ablated from the anode top, which is much lower temperature plasma as compared to compressed pinch plasma of filling gas species, lasts significantly longer to the time scale of greater than 10 μs.

The lifetime of the plasma ablated from the anode top or the plasma of the filling gas species also depends on the operating gas pressure of DPF device. It was found

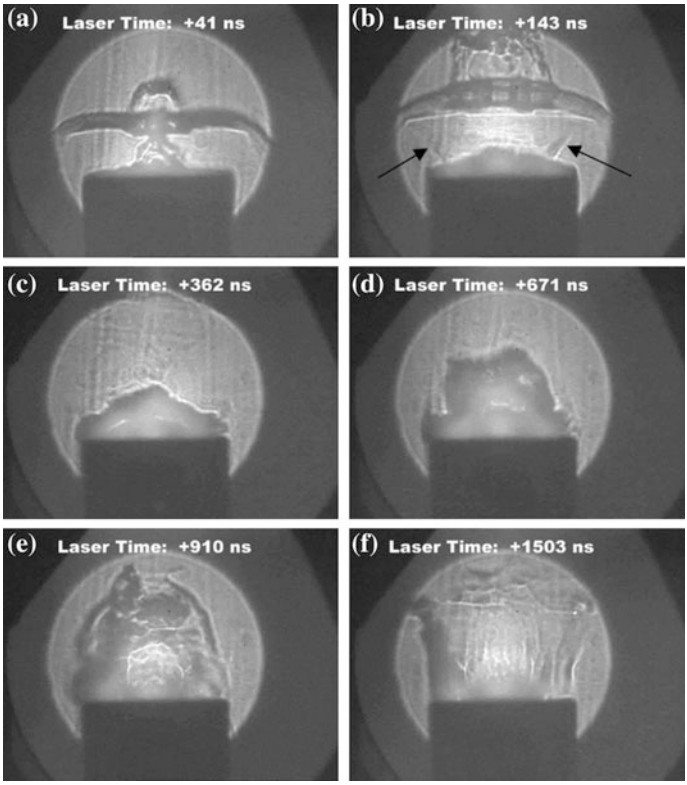

Fig. 2.14 Laser shadowgraphic images graphite anode ablation. Initially, ablated plasma is so dense that laser cannot pass through it. Ionization wavefront resulting in bubble formation can be seen in (**a**) and (**b**). Reprinted with permission from Soh et al. [77], Copyright (2004), with permission from IEEE

that the lifetime of the plasma of the filling gas species increases with the increasing gas pressure (with the pressure increase limited to the range where strong focusing or pinching efficiency can still be maintained) while that of plasma ablated from anode top decreases. The increase in the lifetime of the plasma of the filling gas species with an increase in pressure can be attributed to the increase in pinch (or hot dense plasma) volume and pinch being delayed. The increase in pressure, however, is known to adversely affect the formation and efficiency of $m = 0$ instabilities resulting a reduction in instability-accelerated electron and hence the anode ablation. Another reason could be enhanced collision between the ablated plasma and background neutral gas resulting in relatively faster collisional cooling of the ablated plasma reducing its lifetime.

2.5 Material Processing and Synthesis Using DPF Device—Timeline of Milestones

The evolutionary progress on the application of the DPF device for material processing and synthesis is shown in Fig. 2.15. The timeline of the important milestones for different materials-related application in different possible ways is shown in Fig. 2.15.

Processing of bulk target surface—the first report (1988): The first ever materials-related work using DPF was reported by Feugeas et al. [79]. in 1988 on the processing of bulk AISI 304 stainless steel substrate by the implantation of energetic nitrogen ions produced by BD-1 DPF device at the Instituto de Fisica Rosario, Argentina for surface nitriding. They used nitrogen as the working gas for the implantation of nitrogen ions into the stainless steel substrate. The DPF-nitrided stainless steel sample showed a wear reduction by a factor of 42 times compared to virgin stainless steel. It was found through XPS that the implantation of nitrogen ions by 30 exposures generated Fe_2N thin film as deep as 300 nm from the surface. Based on the nitrogen concentration in the irradiated sample, the depth of nitrogen implantation in the sample they estimated that total ion flux was about 1.3×10^{17} cm^{-2} over 30 DPF discharge with ion energy range up to 500 keV. This initial work showed promising application for DPF as a material processing device as the

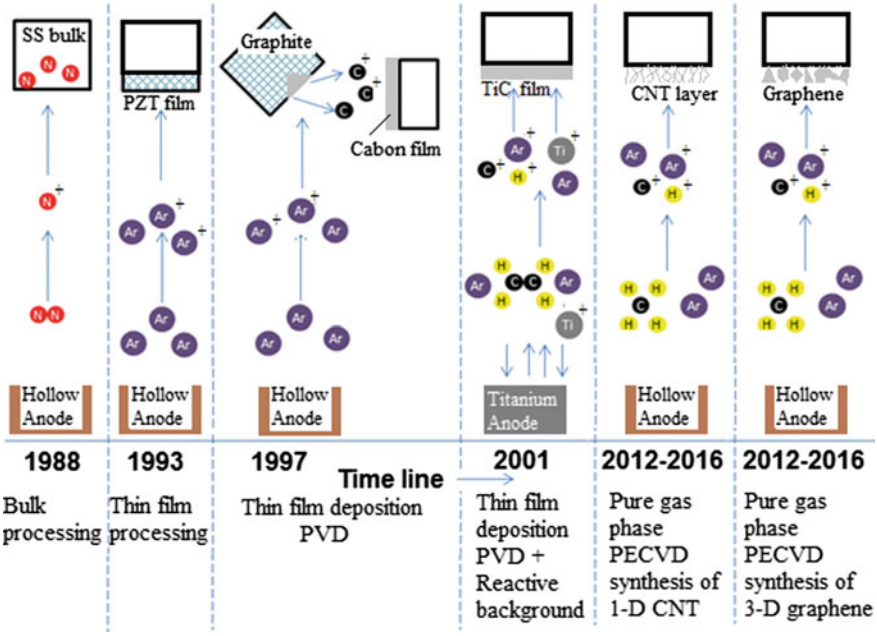

Fig. 2.15 The evolutionary progress of material process and synthesis using DPF device. Feugeas et al. [79], Rawat et al. [80, 82], Kant et al. [81], Tan et al. [83, 84]

surface of a particular material can be modified to have ceramic behavior such as Fe_2N, a wear-resistant ceramic material. The artistic impression the setup is shown in Fig. 2.16a.

Processing of thin film—the first report (1993): The first ever application in the processing of thin film, deposited by another deposition scheme, was reported by Rawat et al. [80] in 1993 using 3.3 kJ DPF device at University of Delhi, India. A material science research group at the University of Delhi was working on ferroelectric thin films of lead zirconate titanate (PZT). The group had an interest in depositing thick PZT thin film using rf magnetron sputtering. As-deposited PZT thin films were amorphous in nature and had to be annealed for transformation to the crystalline phase. However, it was found by the group that about 1 μm thick films of PZT were not crystallized even after 10 h of annealing. Many different strategies were adopted to achieve the crystallization of micron thick PZT film including the irradiation using very high-energy ion beam at the nuclear accelerator, but they all failed. Finally, 3.3 kJ UNU-ICTP DPF device was used to irradiate 0.9 μm thick PZT films by Rawat et al. [80]. The crystalline PZT was achieved by a single exposure of DPF-operated argon as the working gas although the device required minor optimization in operating parameters such as the exposure distance and operating gas pressure to prevent removal of the thin film and to achieve significant crystallization. The 0.9 μm PZT sample was successfully crystallized at an optimized distance of 4.0–4.4 cm from the anode. The setup of irradiation or processing experiment is shown in Fig. 2.16a which is similar to the processing of bulk target material discussed earlier. The crystallization of PZT was deduced to be caused by the intense and rapid heating of the amorphous material surface by pulsed

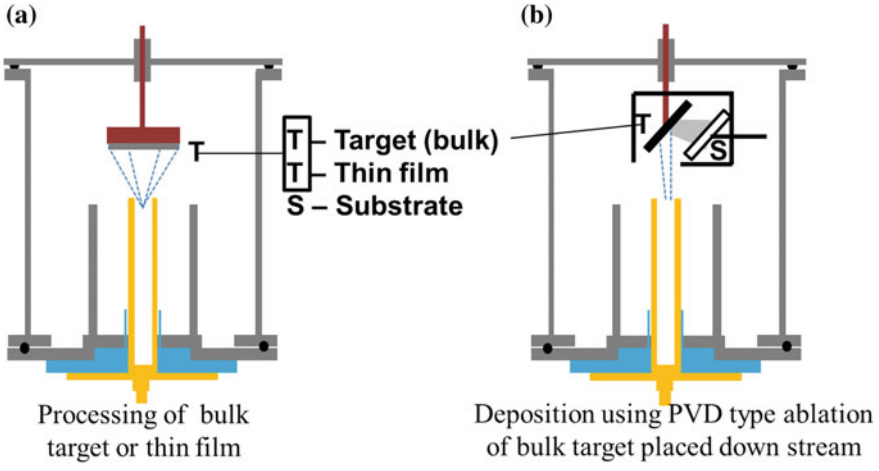

Fig. 2.16 The DPF device configurations for **a** processing of bulk target or thin film and **b** deposition or synthesis of a thin film by ablation/sputtering of a bulk target placed down the anode stream; by instability accelerated energetic ions and hot dense decaying plasma. *Note* Hollow anodes were used to minimize impurity ablation from the anode

energetic ion beam leading to a melted state. The heat from the melted surface propagates through the entire film until it reaches the film–substrate interface. Upon cooling, the entire film crystallizes. In other words, unlike both the post-processing techniques which require high temperature and prolonged processing duration, the DPF was able to produce the same effect of PZT crystallization at room temperature as well as in a short span of time.

The first synthesis of thin film—target ablation in pure PVD mode (1997): The applications stated in two previous illustrations were related to the first ever reported use of DPF device as a materials processing device for bulk and thin film material. On the deposition front, the first ever application of DPF for deposition of materials was reported by Kant et al. [81] in 1997. They were able to deposit carbon thin films by ablating the graphite target placed down the anode stream using energetic argon ions produced by the DPF device. The schematic of the experimental setup is shown in Fig. 2.16b. A substrate, S, was placed in shielded enclosure to avoid its direct exposure to energetic ions and hot dense decaying plasma. They established that the DPF was able to produce 100–150 nm thick crystalline graphitic thin films on silicon and quartz substrates with a number of DPF shots ranging from 10 to 30 shots. The mechanism used in their approach is identical to physical vapor deposition (PVD) in RF sputtering device where ions, typically argon ions, from capacitively coupled plasma are accelerated towards target due to the electric field of the sheath region on the target surface resulting in sputtering of the target material which is then deposited on the substrate surface. In the case of a DPF device, the instability-accelerated energetic argon ions and hot dense argon plasma from pinch plasma column is accelerated towards the top of the chamber and ablated the graphite target placed downstream to deposit the ablated carbon on the substrate surface. The difference is that the DPF acts like pulsed PVD facility with a sputtering process much more intense than in conventional RF sputtering system thus allowing more efficient ablation of material.

The first synthesis of thin film by the anode ablation in PVD mode with reactive background gas (2001): Rawat et al. [82] in 2001 reported the first ever use of background reactive gas, containing the carbon precursor, along with the PVD type ablation of solid anode of titanium to synthesize nano-structured TiC thin film using 3.3 kJ UNU-ICTP DPF device. No external heating arrangement was used and the substrates were kept at room temperature and the anode top or anode inert was ablated by instability-accelerated electrons and hot dense pinch plasma much like in a PVD system. The suitable background gas was made reactive by intense DPF discharge. We still refer it as DPF in PVD mode with reactive background gas. For deposition of TiC films, the conventionally used central hollow copper anode was changed to a solid titanium one whereas the outer cathode rods were kept the same as shown in Fig. 2.17a. The argon-acetylene admixture was used as the working gas. Throughout the experiment, the filling gas pressure of argon-acetylene admixture, in the ratio 7:3, was kept at 1.5 mbar. This work opened a new era of DPF device application whereby many kinds of ceramic materials such as metal nitrides, metal carbides, metal oxides, etc., were deposited using anode of

suitable material and with desired working gases such as nitrogen, methane or acetylene, and oxygen.

In many of the works reported later instead of replacing the entire anode by solid anode, many of the researchers either replaced only the anode top by machining and attaching the desired material piece, shown in Fig. 2.17b, or by using a relatively small anode insert as shown in Fig. 2.17c. The strategy of replacing the anode top by desired material piece [77], Fig. 2.17b, has the advantages of using a smaller amount of material in comparison to the full solid anode and avoiding any impurity from anode material as the ablation occurs only at the anode top. This configuration, however, can be used only for metallic or graphite as anode top which are conductive in nature and does not affect the plasma dynamics of DPF device as seen in shadowgraphic images in Fig. 2.14 where graphite anode top was used. The strategy of using the material to be ablated as anode insert [85], totally inside conventional hollow anode as shown in Fig. 2.17c, has advantages of (i) using very small amount of material, (ii) no machining requirement, and (iii) even non-conducting materials can be used. However, this strategy suffers from a major drawback that the anode rim, which is a different material, also ablates and contributes to impurities in deposited layer. The impurity ablation from anode rim, however, can be minimized by making anode wall very thin.

The first synthesis of pure gaseous precursor based process—pure PECVD mode (2012–2016): Carbon nano-structures such as nanotubes, nanowalls, and graphenes have been regarded as an advance material due to their vast and unique properties with great potential in many commercial applications. Many apparatus and techniques have been employed in producing and commercializing carbon nano-structures. Currently, the preferred method of preparing them is chemical

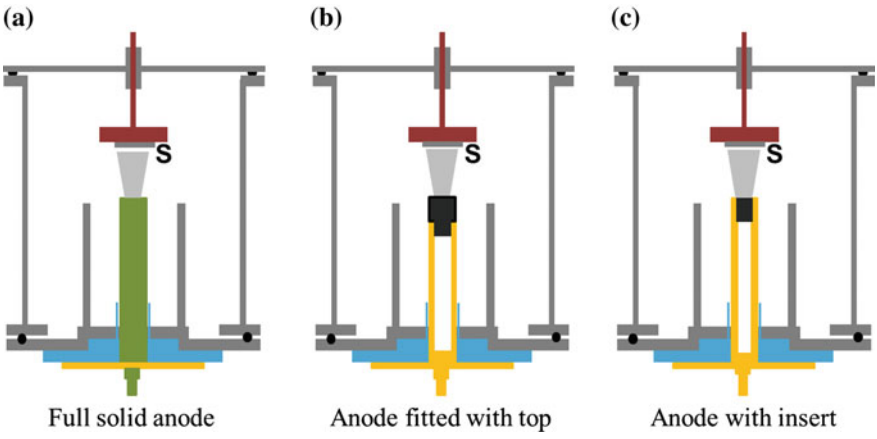

Fig. 2.17 Different type of anode configuration used for deposition of thin film synthesis which relies on ablation of anode material by backward moving energetic electrons and hot dense plasma of DPF pinch

vapor deposition (CVD) where a carbon feedstock, process gas, and catalyst are fed into a furnace at high temperature which decomposes the carbon feedstock while allowing for the catalyst to initiate the CNTs growth. The Plasma-Enhanced CVD (PECVD) systems where a CVD system is improved by using a microwave discharge, or a capacitive discharge, or an inductive discharge are becoming popular as they allow the chemical reaction to take place at a lower temperature. Our group at PRSL, NIE/NTU, Singapore, has successfully synthesized vertically aligned carbon nanotube at very high instantaneous growth rates at low substrate temperatures through the use of DPF with the assistance of a catalyst coated substrate and a substrate heater. It is demonstrated that 2 μm long vertically aligned carbon nanotube can be successfully grown using pulsed plasma that lasts for a maximum of about 100 μs in a single DPF shot giving rise to the enormous instantaneous growth rate of about 2 cm/s. The same device with different operating conditions can be tailored to produce graphene nanoflower structures. This pioneering was done by K.S. Tan during his Ph.D. program at Nanyang Technological University, Singapore [83, 84]. This work highlights the first ever use of DPF device in pure PECVD (plasma-enhanced CVD) mode with the use of hollow copper anode, heated substrate surface and pure gas based (using carbon-containing gaseous precursor) synthesis of one-dimensional CNT and three-dimensional graphene nanoflowers. More details are provided later.

Other strategies for material synthesis and processing using DPF devices: It may be important to mention that there may be other processing and deposition strategies that might have been developed or used but are not included in timeline and milestone developmental work listed in Fig. 2.15. This can be purely incidental or may be due to very limited use of those methods. For example, Zhang et al. [68] reported the optimization and application of NX2 DPF device as pulsed electron beam source for deposition of thin film FeCo. The arrangement of their experimental setup is shown in Fig. 2.18a where the electron beam was extracted through the hole in the anode in the lower deposition chamber attached to the anode and high voltage flange. The pulsed electron beam was used to ablate the FeCo target and the nano-structured FeCo thin films were deposited on the substrate placed across. They used CCD based magnetic electron energy spectrometer to deduce that hydrogen should be the first choice as filling gas for DPF operation for electron-based target ablation for thin film deposition as it produces highest electron beam charge and higher energy (from 50 to 200 keV) electrons. They claim the first ever thin film deposition using PFPED (Plasma Focus assisted Pulsed Electron Deposition) using hydrogen operated NX2 DPF device. Similarly, Mohanty et al. fabricated the network of polyaniline nanowires at room temperature in microsecond timescale by using the pulsed electron beam of a plasma focus device [86]. The experimental setup used by them is shown in Fig. 2.18b.

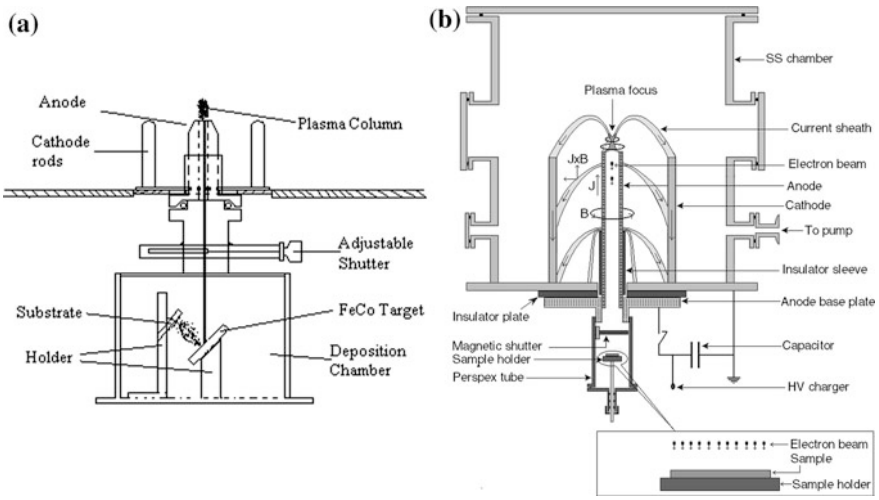

Fig. 2.18 **a** Pulsed electron beam based deposition of thin films in deposition chamber attached to the lower end of the NX2 DPF device. **b** Schematic of experimental setup for electron beam processing of polyaniline thick films; with magnified view of electron beam interaction process with film. Reprinted from **a** Zhang et al. [68], Copyright (2007), with permission from IOP Publishing; and **b** Mohanty et al. [86], Copyright (2009), with permission from Elsevier Ltd

2.6 Material Processing Using DPF Device

The typical DPF setup for the processing of bulk or thin film samples used is the UNU-ICTP facility in our lab in NTU, Singapore is shown in Fig. 2.19a. For efficient processing of samples in DPF device, one should take note of following characteristics of DPF device and use the appropriate strategies according to the requirement or proceedings of the experiment

(i) The DPF devices, like any other plasma device, lacks the exact reproducibility, i.e., there is variation in device performance (and hence the radiation and charged particle yield) from one shot to another. To minimize the shot-to-shot variation in performance of the DPF device it should be conditioned to achieve efficient pinching. Unwarranted exposure of the sample to the less-efficient conditioning shots is avoided using a mechanical shutter between the anode top and the sample, as shown in Fig. 2.19a. The conditioning of DPF ensures reliable shot-to-shot operation of DPF device. Once the good focusing efficiency, monitored by current and/or voltage probe, is achieved then the shutter is removed and the sample is exposed or deposited in subsequent DPF shots. The conditioning process needs to be repeated for each fresh loading of a new sample.

(ii) As mentioned earlier, in each DPF shot the irradiated sample is processed by a complex mix of instability-accelerated energetic ions, high-energy

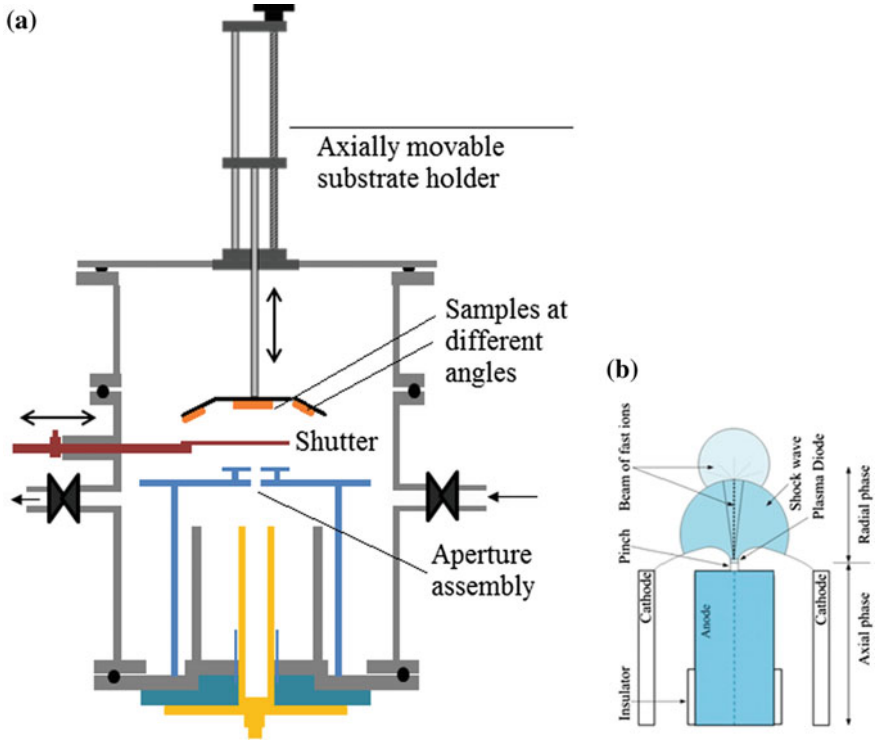

Fig. 2.19 **a** Schematic of DPF as a bulk and thin film processing facility. **b** The pinch column above anode acts like a point source of the fast ion beam and hot-dense decaying plasma. The schematic in (**b**) is reprinted from Nawi et al. [88] (Open access no permission needed)

high-flux photons, fast moving ionization wavefront, strong shock wave, and hot and dense decaying plasma. The source of above-mentioned energetic plasma, ions and radiation source is the pinch plasma column which from the end-on direction behaves like a point source [87]. Energetic ions and plasma emitted from a point source (tip of pinched plasma column) spread out and expand as shown in Fig. 2.19b. Moreover, this flux of energetic ions and hot dense decaying plasma is forward directed with the highest number and energy densities along the anode axis. The number and energy density of ions and decaying plasma decrease in radial direction with increasing angle from the anode axis. This angular dependence of number and energy density of energetic ions and plasma species plays the key role in controlling the processing conditions of the irradiated target surface and deposition features on the substrate surface. The angular variation is much more evident at a smaller distance of material processing or deposition. This leads to greater inhomogeneity in processing or deposition at smaller distances. However, as the distance is increased, the area within the same solid angle increases

leading to greater homogeneity in processing or deposition over a larger area at a larger distance from anode top. Hence, with the increasing distance of exposure, the ions/radiation/plasma flux will decrease or in other words the energy flux delivered at different distances of exposure is different. This gives the possibility of a different degree of processing of the sample by simply changing its exposure distance from the anode top and also by using a different number of DPF exposure shots. The exposure distance and angular position of the sample can simply be changed using an axially moveable sample holder with mounting positions along the axis as well as at different radial position from the anode axis as shown in Fig. 2.19a.

(iii) Depending on the application, one should carefully choose the gas to be used as the operating media. Inert gases such as neon and argon have been used in many studies where the aim was to simply process the material to change its physical characteristics without affecting its composition. For the fusion relevant studies, where the aim is to test the performance of the first wall candidate material, one needs to use deuterium as the filling gas. This provides 2.45 meV D-D fusion neutrons along with other intense radiations. To simulate more realistic fusion reactor type irradiation conditions it will be desired to have 14 meV fusion neutrons by operating the DPF device with 1:1 D-T gas mixture. The handling and procurement of tritium, however, is not trivial and only certain selected groups only can probably do these experiments. The processing of bulk or thin films for the purpose of doping or the nitride, oxide, and carbide formation will require the use of reactive gas environment such as nitrogen, oxygen, acetylene, methane, etc., in DPF chamber.

2.6.1 Mechanism and Physical Processes for Material Processing in DPF Device

The processing of bulk or thin/thick film material in DPF device is a very complex process due to a complex mix of energetic ions, hot decaying plasma, radiation, and shock, shown in Fig. 2.19b. The mechanism of material processing in DPF device **is not unique** as it strongly depends on the exposure position and distance of the material from the anode top. Five different material processing positions and distances from the anode top are possible which are marked in Fig. 2.20a as position "1" to position "5". These five positions are: (1) within the pinch region, (2) very close to the exit point of the pinch, (3) at moderate distance from the anode top (surface melting possible), (4) large distance from the anode top (no surface melting), and (5) below the anode top inside the hollow anode or in the chamber attached to the anode.

The sample placed within pinch region: The sample placed at the position marked as "1", in Fig. 2.20a, can be placed in two different orientations: horizontal

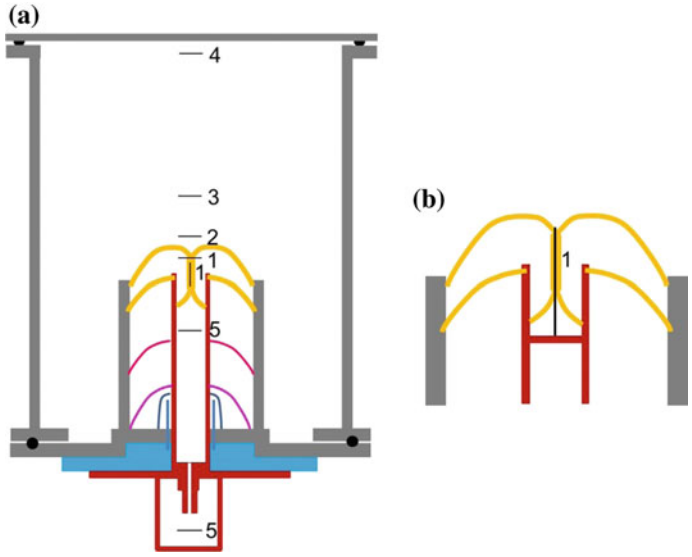

Fig. 2.20 **a** Five different material processing positions in DPF device. Note two different orientations for position marked as "1" inside the pinch region. **b** Wire type sample mounted along the anode axis using support

or vertical. For the planar sample, both these orientations at position "1" obstruct and interfere with pinching plasma. The shadowgraphic study of plasma dynamics showed that any target/sample placed at a distance less than the anode radius, i.e., within the pinch region, will severely affect the plasma dynamics [89] and will not allow the pinch to take place and hence all subsequent phases of plasma focus are disrupted. Sample exposure at this position does not allow the sample to be exposed to the fast ion beam, hot dense plasma, and strong shock. Hence it is not advisable to expose planar samples at this position. However, thin cylindrical wire type sample can be exposed at this position by mounting them using a support as shown in Fig. 2.20b. In an unpublished work done at the University of Delhi, India, the group conducted experiments of Langmuir probe measurements in dense plasma focus device by mounting tungsten wire probe tip at many positions including the position 1 shown in Fig. 2.20b. The pinching efficiency of DPF device was not affected by tungsten wire along the anode axis, but the plasma was so intense that the tip did not last for more than three–five shots.

The sample placed very close to the exit point of the pinch: The exposure of target sample placed very close the exit point of the pinch, marked as position "2" in Fig. 2.20a and also shown in Fig. 2.21d, is discussed in great detail by Gribkov et al. [90]. With the help of extensive fast gated imaging and time-resolved interferometry, they demonstrated the generation of cumulative plasma stream (referred as a jet) at the conical compression of the imploding pinch plasma current sheath shown in Fig. 2.21b. The plasma jet is guided by the axial magnetic field (B_z)

formed by the compression of Earth's magnetic field and residual field of construction material of DPF chamber by the imploding current sheath by the azimuthal (B_φ) magnetic field, refer Fig. 2.21a. The fast-moving plasma jet produces a shock wave (SW) in the residual gas above the pinch shown in Fig. 2.21c. They estimated the speed of deuterium hot plasma stream (plasma jet + SW) to be about $\sim 3\times10^7$ cm s^{-1} with the energy of about 1 keV. If the target sample is placed very close to the pinch exit point, Fig. 2.21d, then this hot plasma stream (plasma jet + SW) hits the target surface with the power density of about $P_{pl} \approx 10^{10}$ W cm^{-2} for PF-1000 DPF device over the sample surface of about few cm^2. This results in intense head load on target surface leading to surface melting and generation of secondary plasma (SP) which starts moving in the direction opposite to the incoming primary plasma. They estimated the temperature of this secondary plasma, produced by hot plasma stream, of the order of 10 eV. It may be noted over here that the above-mentioned physical processes are taking place before the pinch disruption, i.e., when the pinch is stable and the instability-accelerated fast ions have not been generated yet. This shows the strong ablative/sputtering effect of hot plasma stream at very close distance of exposure. This secondary plasma which is moving toward the anode/pinch may or may not interfere with the pinching plasma

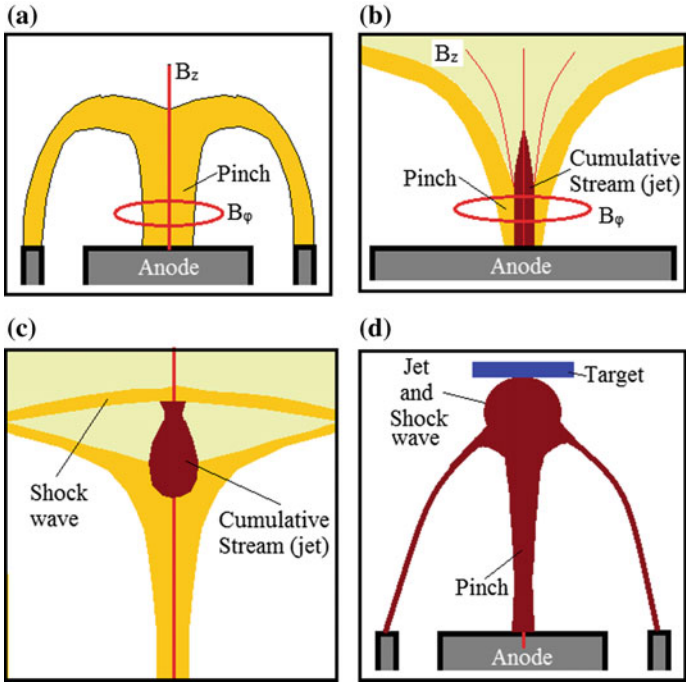

Fig. 2.21 **a** Implosion phase of the DPF plasma and magnetic field dynamics, **b** generation of plasma jet/stream, **c** plasma jet and shock wave produced by jet, and **d** target sample placed very close to the exit point of the pinch

dynamics depending on target distance from pinch exit point. Assuming that the pinch dynamics is not affected then the kinetic stage of DPF dynamics follows.

The kinetic stage of DPF device consists of "current abruption", plasma diode formation (a term normally used by Gribkov et al. [90] which is referred as $m = 0$ instability formation in this chapter earlier and by others as well) and generation of fast energetic beam of ions and electrons. The plasma diode (or $m = 0$ instability), shown in Fig. 2.22, results in a very strong local electric field of the order of 10 MV cm^{-1} resulting in acceleration of ions and electrons in opposite directions. The ions have been observed to have energies from several tens of keV to several MeV [70, 71]; while the electrons have energies from several ten to several hundred keV [68, 69]. According to Gribkov et al. [90], the fast ion beam has two components; the first component is magnetized in the combined B_φ/B_z magnetic field and escapes from the pinch within cone of angle of about 25–30° (shown by cone in Fig. 2.19b) and the second component, the main part, propagates in a relatively narrow cone of 5° along the line of singularity of B_φ field, i.e., the anode axis where $B_\varphi = 0$. The narrow main part of the fast ion beam, comprising of ions of average energy of the order of 100 keV, results in small spot size of the order of few mm^2 on the irradiated target surface with very high-power density [90] of about $10^{12} - 10^{13}$ W cm^{-2}. Such high-power density of fast ions results in the generation of another set of secondary plasma from the targets placed at closer distances to the pinch. This secondary plasma was observed to be moving at a speed of $\sim 10^7$ cm s^{-1} with the

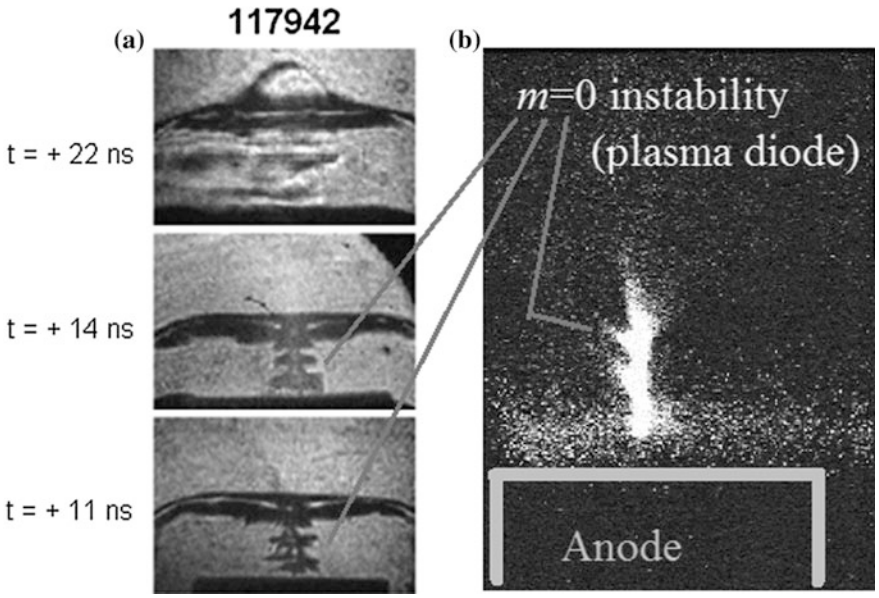

Fig. 2.22 **a** 1-ns three laser sequenced shadowgrams, and **b** time integrated soft X-ray image; all showing plasma diode ($m = 0$ instability) formation in DPF device. **a** Reprinted from Rafique et al. [93], Copyright (2010), with permission from Springer

energy of about hundreds of eV. Recently, ion beam fluences and flux for various gases, at the exit point of the pinch, in a DPF device have been numerically estimated and reported by Lee and Saw [91, 92]. Hence the target/substrate sample placed nearer to the pinch exist point suffers greater ablative/sputtering damage as both the hot plasma stream (comprising of keV plasma jet and SW during stable pinch phase) and instability generated fast energetic ions (comprising of ions of tens of keV to MeV energy during the pinch abruption phase) result in secondary plasmas from irradiated surface. It may, however, be noted that the power densities of hot plasma stream and fast ions beam mentioned above are specific to the large PF-1000 device. For smaller DPF devices the pinch volume, and hence energy content in pinch, is much smaller as they scale on anode radius. Hence the effects on sample surface will be different.

The ablative/sputtering generation of secondary plasma will have two different effects on the irradiated surface: (i) the surface reconstruction and (ii) thin film formation if a reactive background gas is used. This will be explained with the help of suitable examples in later sections. In addition to material melting and ablation in the form of secondary plasma, the high-energy fast ions (>100 keV ions) are capable of moving deep inside the bulk target surface, from several hundred nm to micrometer distance, with the ability to dislodge bulk atoms from their lattice positions creating vacancy defects in crystalline structure. The penetration depth of ions and vacancy defects in bulk or thin film targets of various materials can be estimated using SRIM© [94].

Sample at a moderate distance from the anode top (surface melting possible): This exposure position is marked as "3" in Fig. 2.20a. The instability generated beam of fast ions initially propagates behind the shock wave as it is generated later in time and does not spread much, as seen in Fig. 2.19b. However, as it pierces through the shock wavefront, the ions find themselves in neutral gas with density same as that of the ion beam. The fast ions escaping the shock front, supported/guided by diverging B_z field due to increased distance from pinch regions, turn in the direction of grounded chamber walls resulting in the greater spread of fast ions as shown in Fig. 2.19b. The increasing spread of fast ions will reduce the fluence on the target surface with increasing distance of exposure. The mean free path of very high-energy ions, say hydrogen ions of >100 keV, will be greater than 60 cm in hydrogen at 6 mbar. The very high-energy ions, hence, will not be able to ionize the working gas before they hit the target or the chamber wall.

At moderate distances of exposures, the delivery of high flux and high-energy instability-accelerated ions, energetic radiations, shock exposure and hot dense decay plasmas in a very short time (with different events lasting from few tens of ns to several μs) results in the processing of material in DPF device which is equivalent to ultra-fast annealing. Sanchez and Feugeas [95] estimated the generation of intense transient heating slopes and heating speeds as high as ~ 3600 K μm^{-1} and ~ 40 K ns^{-1} respectively, on various metal sample surface confirming the ultra-fast annealing rate in DPF device. The rapid surface temperature rise, beyond evaporation point, followed by the rapid cooling results in a strong thermal effect on the material exposed at a moderate distance which brings out the changes in their

several physical properties and compositional characteristics. In addition, the high-energy ions can also induce defect in crystalline structure of irradiated materials.

Sample at large distance from the anode top (no surface melting possible): At large distances from the pinch region, marked as position "4" in Fig. 2.20a, due to the conical geometry of ion beam, the number and energy density of ions are greatly reduced on the sample surface. This leads to insignificant processing of the irradiated sample surface.

The sample placed inside the hollow anode or in the chamber attached to the anode: These positions are marked as "5" in Fig. 2.20a and also shown in Fig. 2.18b. In this case, the sample is essentially processed by instability-accelerated energetic electrons which move in a downward direction through the annular hollow space of the anode. Roshan et al. [96], though, demonstrated the existence of backward moving high-energy ions in NX2 DPF device using the direct and unambiguous technique of nuclear activation. They conducted a 30 shot sequence at 1 Hz repetition rate in NX2 DPF device at 8 mbar deuterium and showed significant activation of graphite mounted as an insert inside the anode top by high-energy deuterons moving in the backward direction. Their estimates showed 1.3×10^{11} backward deuterons per shot per steradian with energies higher than 500 keV. They estimated that the number of backward deuterons was about one order of magnitude less than the forward ones. Hence, for the samples placed at position "5" mainly electrons and to some extent ions will be responsible for processing. At smaller distances of exposure below the anode top, in the negative direction, the charge particle number and energy flux will be strong enough to cause rapid thermal melting and re-solidification of the sample surface. The effect obviously will decrease with the increasing negative distance. Based on self-luminescence and laser interferometric images of plasma diode formation, it was deduced that after that an acceleration of electrons in plasma diode by the vortex electric field takes place followed by the self-focusing of the electron beam inside the pinch during its propagation to the anode [90]. Moreover, it was inferred from Rogowski coil and magnetic spectrometry measurements that electrons from pinch region are accelerated towards the anode over a relatively long period of microseconds and that too in several bunches [78, 97]. Hence, the sample irradiated by electrons in downward direction depending on the distance of exposure will have nonuniform irradiation with electrons bunch focusing at a different place on the irradiated sample. This was observed on polyaniline thick films irradiated by electron beams in DPF device where polyaniline nanowires were observed to form at scattered locations and not uniformly on the entire irradiated surface [86].

Next, we will illustrate the application of DPF device for material processing by a transient complex mix of radiation, shock, plasma, and charged particle using selected examples.

2.6.2 *Selective Examples of Material Processing*

This section is divided into two subheadings (i) processing of bulk substrates and (ii) processing of thin films.

2.6.2.1 Processing of Bulk Substrate Surface

The first experiment on processing of bulk substrate of AISI 304 stainless steel using DPF device was reported in 1988 [79] and after that several experiments have been conducted on processing of many different bulk substrate materials, such as titanium [95, 98–103], different types of stainless steel [95, 104–106], silicon [107–113], aluminum [114–116], zirconium [117–123], zirconia [124], tungsten [125], tantalum [126], boron nitride [127], alumina [127], PET [128], etc. This shows that wide range of materials such as metals, semiconductors, ceramics, and polymers have been processed using DPF devices. Some of the key features of DPF-based processing are discussed under following subheadings.

Surface Reconstruction: Fig. 2.23 shows typical SEM (scanning electron microscopy) images of the Ti and W samples before and after being processed by DPF. The bulk samples were processed at smaller distances from the anode top using different DPF devices (UNU-ICTP and PF-6 devices, respectively, in this case). The processed samples show the surface reconstruction with nano-structures being formed on them. The surfaces of the unexposed Ti and "Eurofer" ferritic steel substrates are shown in Fig. 2.23a, d, respectively. The low-magnification image in Fig. 2.23a shows linear scratch marks on unexposed Ti sample surface formed during mechanical polishing by abrasive silicon carbide paper. As discussed in the previous section, the exposure of bulk substrate samples to an efficiently pinching DPF shot at lower distances of exposure causes an extreme transient temperature rise of the top few micron thick layer of the sample surface which results in sputtering, melting, and re-solidification of the top layer. This melting and re-solidification result in surface reconstruction, as seen in Fig. 2.23b, with the removal of initial mechanical polishing marks along with substantial smoothening of the Ti sample surface which was irradiated at an axial distance of 5 cm using nitrogen operated 30 shots in UNU-ICTP type device. In addition to the surface smoothening, one can also observe the crack formation in Fig. 2.23b. The crack formation can be attributed to the stress formed between the bulk cold solid substrate and transiently melted and re-solidified top surface layer upon DPF exposure [129]. Similar surface reconstruction has been observed in several other processing experiments using DPF devices, such as the one reported recently by Chernyshova et al. [130] and is shown in Fig. 2.23e, f. The ferritic steel "Eurofer" sample showed surface reconstruction within one shot in PF-6 DPF device, refer Fig. 2.23e, with the wavelike structure on the surface with initial traces microcrack nucleation. The wavelike structures, cracks, and craters were strongly developed on the sample surface after five shots, as seen in Fig. 2.23f.

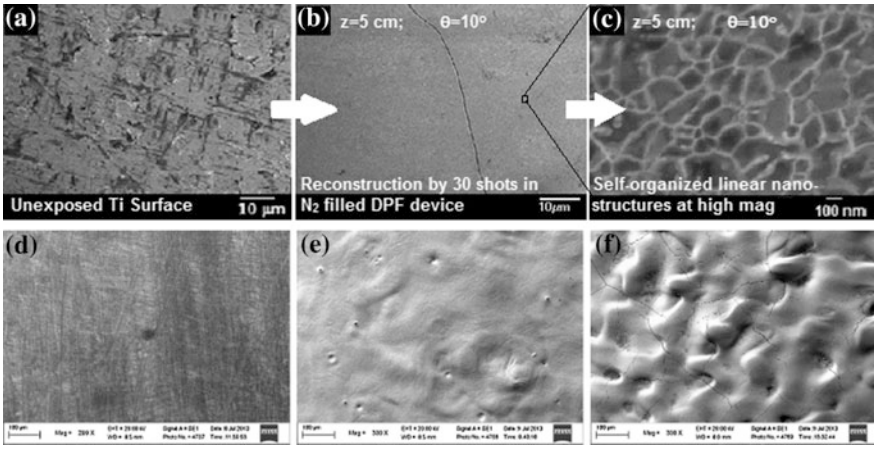

Fig. 2.23 **a** Virgin Ti sample surface, **b** Ti sample surface after exposure to 30 DPF shots in at axial distance of 5 cm at angular position of 10° with respect to anode axis, **c** magnified image of part of image in (**b**), **d** virgin ferritic steel "Eurofer" sample, (**e**, **f**) exposed to 1 and 5 shots in PF-6 device. Reprinted from **a**–**c** Rawat [129], IOP Publishing (Open Access paper no permission needed); and **d**–**f** Chernyshova et al. [130], Copyright (2016), with permission from Elsevier Ltd

Surface Nano-structurization: Fig. 2.23c, the SEM image at higher magnification on DPF processed Ti sample surface, shows the formation of self-organized linear nano-structures. It may be mentioned that the dark gray islands observed in Fig. 2.23c are not large grains but itself composed of very small nanoparticles (not visible at this magnification) within the boundaries of these linear nano-structures.

Figure 2.24a–c shows the SEM images of bulk Ti substrate processed by two different methane-operated DPF devices; 190 kA, 3.2 kJ single shot UNU/ICTP and 430 kA, 3.1 kJ NX2 devices. The comparison of SEM images in Fig. 2.24a, c shows the formation of titanium oxycarbide nanoparticles on the substrate surface exhibiting the reproducibility of the results from two independent devices. The size of nanoparticles is about 35–50 and 20 nm in Fig. 2.24a, c respectively. The bigger size of nanoparticles in Fig. 2.24a is attributed to the higher energy and material flux due to exposure at a lower distance as well as the being conducted along the anode axis. The off-axis irradiation at an angular position of 10° with respect to anode axis as well as at a higher distance of 9 cm results in lower ion number and energy flux at the irradiated substrate surface leading to smaller nanoparticle size for SEM image shown in Fig. 2.24c. The SEM image of the Ti substrate exposed along anode axis in the NX2 device, shown in Fig. 2.24b, exhibits features similar to the one observed in Fig. 2.23c with linear nano-structures. The greater details about the structure, composition and hardness of the nano-structured nanocomposite titanium oxycarbide layer formed on DPF irradiated Ti substrate surface can be found in our paper [100]. The Fig. 2.24d–f shows SEM images of the unexposed and irradiated tungsten samples. The high magnification image of unexposed W samples, Fig. 2.24d, shows variable sized and shaped grains and pits on the rough surface but it does not

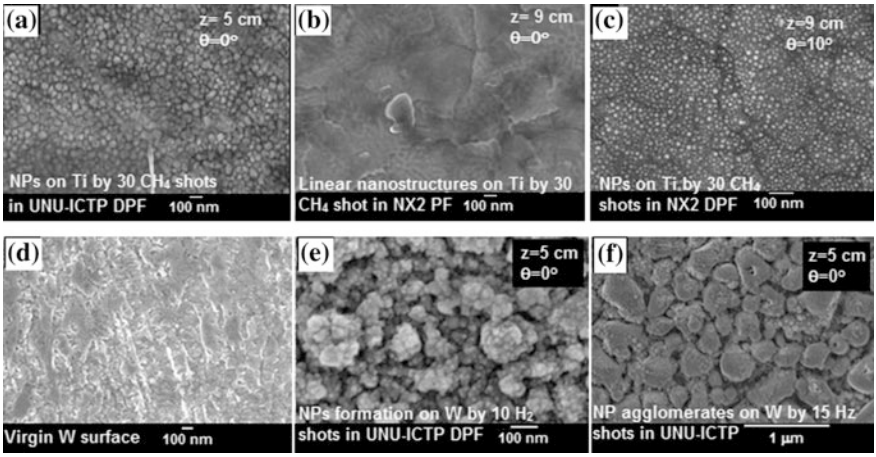

Fig. 2.24 **a–c** SEM images of Ti samples processed in methane operated UNU-ICTP and NX2 DPF devices at different distance and angular positions. **d–f** Virgin and irradiated *W* samples. The distance (z) and angular position (θ) of the samples, the number of DPF irradiation shots and DPF operating gas for each of the exposure experiment are mentioned in SEM images. Reprinted from Rawat [129], Copyright (2015), IOP Publishing (Open Access paper no permission needed)

show any nano-structures. The SEM images of 10 and 15 shot irradiations in hydrogen operated UNU/ICTP DPF device, shown in Fig. 2.24e–f respectively, exhibit the formation of nanoparticles and nanoparticle agglomerates on the irradiated tungsten surface. The size of nanoparticles is about 15–20 nm for 10 shot irradiation and they also agglomerate resulting in particle agglomerates with size varying from 100 to 300 nm. The tungsten sample irradiated with 15 shots shows mostly particle agglomerates of about 200–800 nm in size. These big size particle agglomerates are made up of 40–60 nm sized nanoparticles. The increase in nanoparticle and particle agglomerate size with the greater number of irradiation shots can be attributed to enhanced transient thermal treatment of the sample surface.

Changes in properties of processed materials: In addition to morphological changes, several other properties of the processed sample may change which includes (i) surface layer composition, (ii) lattice structure, (iii) hardness, etc. The changes in crystal structure, hardness, and other physical properties are discussed in detail in Chap. 7 on hard coating synthesis using DPF device so we will not touch on those aspects over here. However, the processes or the reasons for the change in surface properties are discussed over here. For the examples cited in the previous paragraph, the use of background reactive gases such as nitrogen and methane results in TiN [101] and nanocomposite titanium oxycarbide (TiC_xO_y) [100] layer formation, respectively, on the Ti substrate surface. For the sake of illustration, we will discuss the formation of a TiN layer on Ti substrate processed in nitrogen operated DPF device on the basis of physical processes discussed in Sect. 2.6.1. The DPF discharge results in fast primary nitrogen plasma stream, shock wave, and fast energetic nitrogen ion beam based sputtering of Ti substrate surface resulting in

the formation of a secondary plasma of Ti in front of the irradiated substrate surface. This secondary titanium plasma interacts with background nitrogen plasma to form TiN in the gas phase or on Ti substrate to fabricate a nitride layer. Thus the gas phase nucleation may be the first step towards TiN layer growth, assisted by the direct ion-assisted compound layer formation due to implantation of energetic nitrogen ions interstitially. In a dynamic process like plasma focus based nitriding, ion implantation and ion sputtering take place simultaneously which results in surface modification and grain formation. The dimension of grains/crystallites depends on the lattice structure of the resultant TiN compound, reaction kinetics, diffusion rate of nitrogen, and mass loss due to ion sputtering. The thickness of the TiN coating is dependent (i) on the depth of ion implantation in the substrate which depends on the highest energy nitrogen ions in fast ion beam and (ii) on TiN compound layer formation by re-deposition of gas phase nucleated titanium and nitrogen plasma mix. As the processing was done using multiple DPF shots, the successive ion pulses will process the pre-deposited TiN layer to improve the quality of TiN layer with possible re-sputtering as well. The temperature evolution during irradiation also enhances the reactivity of the nitrogen already introduced during the preceding shots. This provides the additional energy required for surface diffusion and migration of nitrogen, and thus enhances the crystallinity of the TiN layer. The TiN layer formed on top of the Ti substrate surface results in different crystalline structure and hardness properties as shown in Fig. 2.25 [101]. Similar changes in surface stoichiometry, crystalline structure, and other physical properties (hardness, electrical conductivity, surface energy, water contact angle, etc.) are observed for other processed materials.

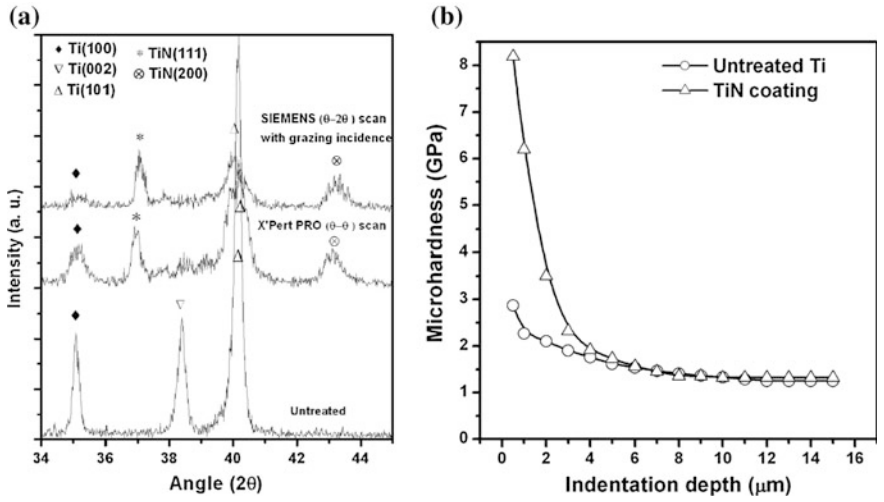

Fig. 2.25 Change in crystalline structure (**a**) and hardness (**b**) of titanium substrate upon being processed by nitrogen operated DPF device due to TiN layer formation. Reprinted from Hassan [101], Copyright (2009), with permission from Elsevier Ltd

2.6.2.2 Processing of Thin/Thick Films

A good number of thin/thick films have been processed using DPF devices though the amount of work done in this field is rather limited compared to processing of bulk material. Thin films processed by DPF include PZT [80], CdS [131], hematite [132], Sb_2Te_3 [133], CdI_2 [134], ZnO [135] and FePt [136–138], and thick films of polyaniline [86, 139]. The processing of thin film is much more interesting as changes in many different types of properties such as crystallinity, grain size, stoichiometric, optical, electrical, and magnetic properties have been reported. While Rawat et al. [80] reported the crystallization of amorphous PZT thin films, the amorphization of crystalline thin films of CdS was reported by Sagar and Srivastava [131]. The non-magnetic α-Fe_2O_3 (hematite) thin films were exposed to argon ion beam at different distances from the anode top by Agarwala et al. [132]. At a particular distance, at 10 cm in Fig. 2.26a, hematite film was converted completely to magnetite (Fe_3O_4) form which is ferromagnetic in nature. The transformation was attributed to the loss of oxygen from the irradiated iron oxide film resulting in decreased amount of oxygen relative to iron leading to Fe_3O_4 (with 1.33 oxygen atom per iron atom) formation from α-Fe_2O_3 (with 1.5 oxygen atom per iron atom). The change in magnetic property was thus due to stoichiometric variation in the irradiated sample. A substantial reduction in film thickness was observed for DPF processing performed at smaller distance indicating the significant sputtering of material, in line with changes observed for bulk material. Another demonstration of stoichiometric variation in DPF irradiated thin films was demonstrated by Rawat et al. [133] for antimony telluride. Vacuum evaporation based as-deposited films of antimony telluride contained mixed phase comprising of both stoichiometric (Sb_2Te_3) and antimony-rich non-stoichiometric (Sb_3Te_2) phases. The processing of mixed-phase antimony telluride film at lower distances by high-energy ion flux broke chemical bonds resulting in further enhancement of Sb-rich non-stoichiometric phase and oxidation in the film. A higher distance of exposure with a right dose of lower ion energy flux led the conversion of mixed-phase antimony telluride thin film to single stoichiometric (Sb_2Te_3) phase

Rawat et al. investigated the processing of CdI_2 thin films by argon ions in UNU-ICTP DPF device [134]. The as-grown film, deposited by a thermal evaporation method, were essentially 4H polytype (002) oriented CdI_2 stoichiometric films. The argon ion irradiation changed the orientation to (110) at certain moderate irradiation distances as shown in Fig. 2.26b. The diffraction peaks shifted towards higher 2θ values from their corresponding powder data indicating uniform compressive stress. The estimation of grain size from SEM and residual stress from diffractograms showed a linear increase in grain size (shown in Fig. 2.26c) and residual stress with increasing irradiation distance (or decreasing ion energy). The morphology of the films with (002) preferred orientation was found to be similar to each other but with different grain sizes. The films with (110) orientation, however, was found to have different morphology. The direct optical energy gap, E_g, of the ion-irradiated films was found in the range of 3–3.3 eV. The E_g was found to increase linearly at the rate of 15 μ eV/atm with the compressive stress.

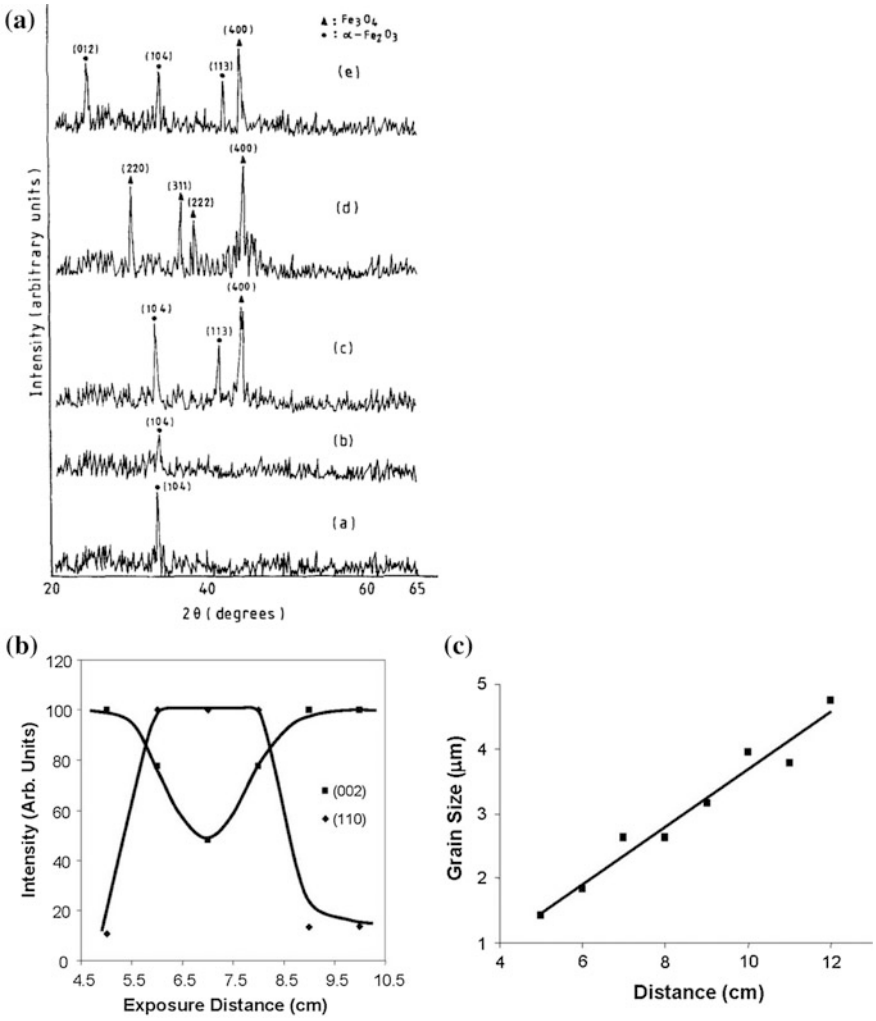

Fig. 2.26 **a** XRD patterns of virgin iron oxide (**a**) thin film and ion irradiated samples at 8, 9, 20 and 11 cm from (**b**–**e**). Variation in crystalline orientation from (002) to (110) plane (**b**) and grain size (**c**) of CdI_2 thin films at certain distances of exposures. Reprinted from **a** Agarwala et al. [132], Copyright (1997), permission from Elsevier Ltd and **b**, **c** Rawat et al. [134], Copyright (2004), with permission from AIP Publishing

One of the most interesting applications of DPF device in thin film processing is the nano-structurization of thin/thick films. The nano-structuring of FePt thin films in hydrogen operated DPF device [136–138] and polyaniline thick film in nitrogen operated DPF device [86] has been demonstrated. The FePt thin films were processed in conventional forward direction by hydrogen ions whereas the polyaniline (PA) thick films were processed by backward moving relativistic electron beam

after being extracted through the hollow anode in a separate chamber attached to the bottom exit point of the anode as shown in Fig. 2.18b. The 67 nm thick FePt thin films samples were grown using pulsed laser deposition method and processed in 3 kJ hydrogen operated UNU-ICTP DPF device by Jiaji et al. [136] at a distance of the 5 cm from the anode top, while the few tens of micrometer thick PA films prepared by chemical oxidation method were exposed in 2.2 kJ Mather-type nitrogen operated DPF device [70] by Mohanty et al. [86]. The SEM images in Fig. 2.27a show the change in surface morphology from the smooth uniform film for the as-deposited sample to the film with uniform and isolated nanoparticles after a single DPF shot exposure with an average size of about 9.1 ± 2.3 nm. The DPF irradiation using two shots resulted in agglomeration of FePt nanoparticles to about 51.3±7.4 nm sized agglomerates. Z.Y. Pan et al. repeated the experiments with 100 nm thick PLD grown FePt thin films and were able to reproduce nano-structuring of FePt thin films, refer Fig. 2.27(d), in hydrogen operated UNU-ICTP DPF device using different number of focus shots [137] as well as different exposure distances (5, 6, and 7 cm) [138]. The mechanism of nano-structuring of the DPF exposed thin film can be understood from the characteristics of instability-accelerated ions of the filling gas species. Though the ion energy is found to vary over a very big range from few tens of keV to few MeV, the mean energy of the bulk of the H^+ ions in UNU-ICTP DPF has been estimated to be 124 keV [136]. The projected range of the H^+ ions of this mean energy is about half-micrometer in FePt, as estimated from SRIM®. Therefore, most of the H^+ ions stop and deposit the bulk of their energy in the silicon substrate at the Bragg peak position as the thickness of FePt thin films was only about 67 or 100 nm. This would result in heating of silicon substrate to a very high temperature in a very short span of time. The thermal energy is then conducted to the FePt thin films and causes the diffusion of metal atoms either through the lattice or along grain boundaries. The diffusion releases the thermal expansion mismatch stresses between the silicon oxide layer of the silicon substrate surface and the PLD coated FePt thin film, leading to the formation of nanoparticles at the surface layer of FePt thin films. One of the biggest advantages of nano-structuring using a DPF device is that it can achieve nano-structuring of the thin film in single shot exposure with ion pulse duration of the order of a few hundred ns compared with hours of irradiation time required for other reported continuous ion sources [140].

Figure 2.27d shows the TEM bright-field image for the single shot ion irradiation sample after 400 °C annealing. The image shows relatively uniform size distribution for nanoparticles with average particle size of about 11.6 ± 3.4 nm. The selected area electron diffraction (SAED) pattern, in the inset of Fig. 2.27d, shows that FePt nanoparticles are in polycrystalline fct phase. It may be important to mention over here that ion irradiation has assisted not only in the FePt nanoparticles formation (from FePt thin films) but also in lowering the phase transition temperature to 400 °C. The phase transition at lower temperature, for single focus shot irradiation, has restricted nanoparticles grain size growth and agglomeration resulting in relatively small and well separated magnetically hard fct phase FePt nanoparticles; much needed for higher magnetic data storage density. Figure 2.27e

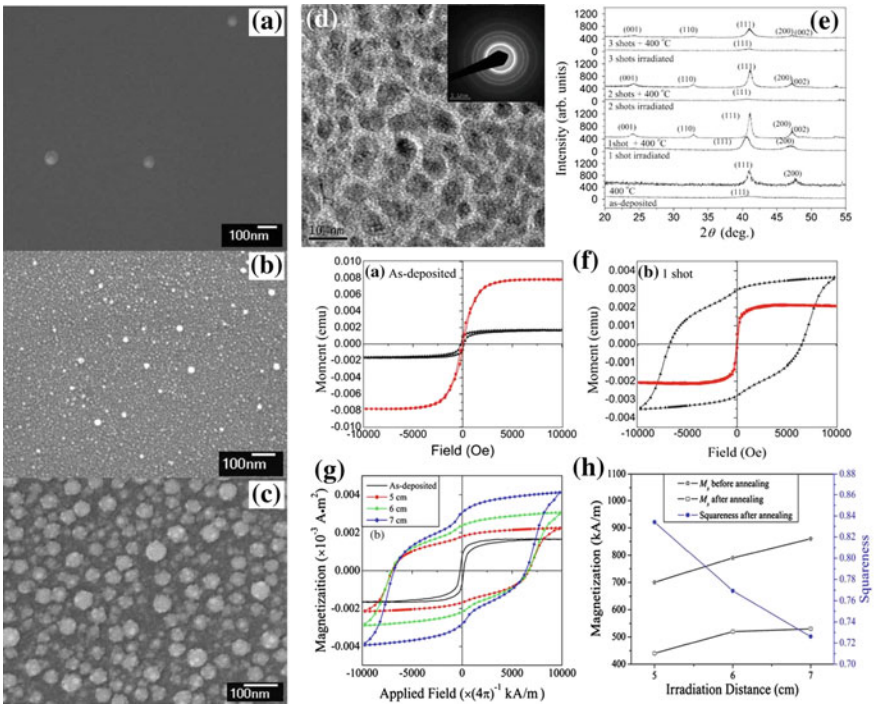

Fig. 2.27 SEM images of **a** as-deposited and DPF irradiated FePt thin films at 5 cm from anode top using one (**b**) and two (**c**) DPF shots; the nanoparticle formation was observed on irradiated films. **d** TEM image of FePt nanoparticles formed in single DPF irradiation at 4 cm distance. **e** XRD patterns of as-deposited and DPF processed FePt film samples before and after 400°C annealing. **f** An enormous increase in magnetic hardness (higher coercivity) of DPF processed and annealed sample. **g**, **h** Variation in magnetic properties such as coercivity, magnetization and squareness of FePt samples irradiated at different distances. Reprinted from (**a**–**c**) Lin et al. [136], Copyright (2007), permission from IOP publishing; **d**–**f** Pan et al. [137], Copyright (2009), with Springer; and **g**, **h** Pan et al. [138], Copyright (2009), with permission from Elsevier Ltd

shows the XRD patterns of (i) as-deposited, (ii) annealed at 400 °C (without ion irradiation), (iii) ion irradiated (without annealing) and (iv) ion-irradiated samples after annealing at 400 °C. The as-deposited FePt sample exhibits fcc phase with a broad and weak peak of (111) which after annealing at 400 °C remains in fcc phase but with significantly improved (111) peak intensity and emergence of (200) peak. The sample after single plasma focus irradiation shot, without annealing, shows almost similar XRD patterns as the FePt sample after 400 °C annealing with (111) and (002) fundamental peaks of fcc phase. This implies that single shot of pulsed plasma focus ion irradiation provides almost equal amount energy that is offered by conventional thermal annealing for 1 h at 400 °C. The average crystallite size for single shot ion-irradiated sample, as estimated from the (111) peak using Scherrer formula, is smaller than that of average crystallite size of sample annealed at 400 °C. The smaller average crystallite size can be attributed to transient

annealing by pulsed ion irradiation. With the increase in the number of plasma focus irradiation shots to two and three, the crystallinity of the irradiated alone samples decreases and reverses to that of as-deposited sample. Increased number of irradiation shots provided more than required energy inducing more defects (both the vacancy and interstitial) and lattice distortion leading to lattice disordering. The annealing of all ion-irradiated samples at 400 °C led to the phase transition in the FePt film from disordered fcc structure to chemically ordered fct structured $L1_0$ phase, confirmed by the appearance of the superlattice tetragonal (001), (110) and (002) peaks. However, with the increase in the number of ion irradiation shots the intensity of the superlattice peaks of fct phase become weaker, suggesting that the ordering of the fct crystallite lattice is reduced. The sample irradiated by one shot and annealed at 400 °C exhibited an enormous increase in its magnetic hardness (coercivity) as seen in Fig. 2.27f as compared to as-deposited sample. A similar increase in magnetic hardness (coercivity) was also observed for FePt thin films samples processed at different distances from the anode top, Fig. 2.27g, indicating very high reliability in reproducing results. Figure 2.27h shows that other magnetic properties of the FePt thin film samples also change with the change in processing distance from the anode top due to change in number and energy flux of the ions.

2.7 Material Synthesis/Deposition Using DPF Device

The material syntheses or depositions using DPF devices are mainly in the form of thin films of many different types [44, 68, 77, 82, 120, 123, 141–156]. The large variation in the type of thin films deposited using DPF devices is due to various possible configurations that have been used and were discussed in detail in Sect. 2.5 and summarized in Fig. 2.15. In this section, we will highlight advantages and criticism of DPF devices based syntheses and depositions.

2.7.1 Advantages of DPF-Based Depositions

The main advantages of DPF device as deposition facilities are as follows:

1. High deposition rates.
2. Ability to grow crystalline thin films at room temperature substrates.
3. Superior physical properties.
4. Versatile deposition facility with variety of deposition options.

2.7.1.1 High Deposition Rates

The deposition rates in DPF devices can be extremely high, much higher than other deposition methods. We will illustrate this with the help of selected examples. Figure 2.28 shows the cross-sectional SEM images and thickness of CoPt thin films deposited using a different number of shots in NX2 DPF device at a low operating voltage of 8 kV with a stored energy of the capacitor bank in sub-kJ range (~88 J) [146]. It clearly shows that the thickness of the as-deposited samples increases continuously with increasing number of plasma focus deposition shots with the thicknesses of the as-deposited samples about 44.0 ± 2.0, 72.5 ± 4.0, 208.1 ± 8.0, 294.5 ± 14.0 and 331.7 ± 12.0 nm for the 25, 50, 100, 150, and 200 shots deposition samples, respectively. The curve of the variation of the thickness of the deposited sample with varying number of plasma focus shots is plotted in Fig. 2.28f, which is linearly fitted to estimate the deposition rate of the nano-structured CoPt thin films at a fixed distance of 25 cm and the filling hydrogen gas pressure fixed at 6 mbar. The slope of the linear fitted curve reveals the average growth rate of CoPt nanoparticle deposition when the other operation parameters were fixed. It is estimated to be about 1.78 nm/shot. This deposition rate is more than 30 times higher as compared with that of conventional PLD which is found to be about 0.50 Å/shot by Lin et al. [157]. It may also be mentioned over here that the target to substrate distance in case of PLD deposition by PLD was only 3 cm [157], much less compared to that of 25 cm for DPF deposition. This clearly indicated that deposition rates in DPF are actually may be more than two orders of magnitude higher than that of PLD device.

The extremely high deposition rate of ZnO thin film has been demonstrated by Tan et al. [158] using zinc top fitted anode in UNU-ICTP device with pure oxygen being used as the operating gas. Figure 2.28g shows the cross-sectional SEM image of ZnO film deposited using 30 focus shots at 15 cm from anode top with a film thickness of about 2.82 ± 0.32 μm. They estimated the ZnO deposition rate to be about 100 nm per shot at the deposition distance of 15 cm. In 3 kJ UNU/ICTP device, the ablation plume of graphite anode top was found to last for about 2 μs for DLC thin film deposition experiments [77]. Even if we assume the anode top ablation duration to be about 10 μs, the estimated transient ZnO thin film deposition rate would be a staggering 10 mm/s. However, the transient deposition rate is not as important as the average growth rate, which depends on the repetition rate (operating frequency) of the DPF device, and will be lower as DPF devices have limited repletion rates. Tan et al. performed ZnO synthesis in single shot mode with one shot per minute, which is the standard practice for UNU/ICTP device to avoid overheating of the electrical system and anode target which may change the DPF operational characteristics. This accounts for an average growth rate of about 0.1 μm/min in their study, similar to the reported growth rate found in RF magnetron sputtering devices [159, 160]. On the other hand, when the DPF system operates in repetitive mode, multiple exposures can be made within a second and this leads to the assumption of increased deposition rate. One such DPF device that can perform such operation is the high-performance high repetition rate NX2

plasma focus facility. The NX2 is a 3 kJ, 27.6 μF Mather-type DPF device with a repetition rate of up to 16 Hz and has routinely been operated between 1 to 10 Hz operation for X-ray lithography related work [161]. As for material synthesis, the device in repetitive mode has been demonstrated to work for the synthesis of bimetallic FeCo nanoparticles at 1 Hz repetition rate [68]. The deposition of ZnO thin film in NX2 plasma focus device at 1 Hz repetition rate operation will lead to a time averaged deposition rate of 6 μm/min, which could further be enhanced to 60 μm/min at 10 Hz operation. Operating beyond the 10 Hz operations would surpass the highest known deposition rate of an inductively coupled microplasma system [162]. These deposition rates are expected to surpass any existing device, along with material synthesis at room temperature substrates. Additionally, in DPF device even the room temperature deposition provides a polycrystalline ZnO thin film without any need for post-deposition annealing which is invariably needed for ZnO thin film depositions in other devices. Further improvements of the DPF device in terms of growth rate can be expected since a 50 Hz repetitive DPF device has been developed [163]. However, high repetition rate operation creates several design considerations as the plasma focus anode will require a cooling arrangement for thermal load management due to high heat dissipation to the anode by pinch

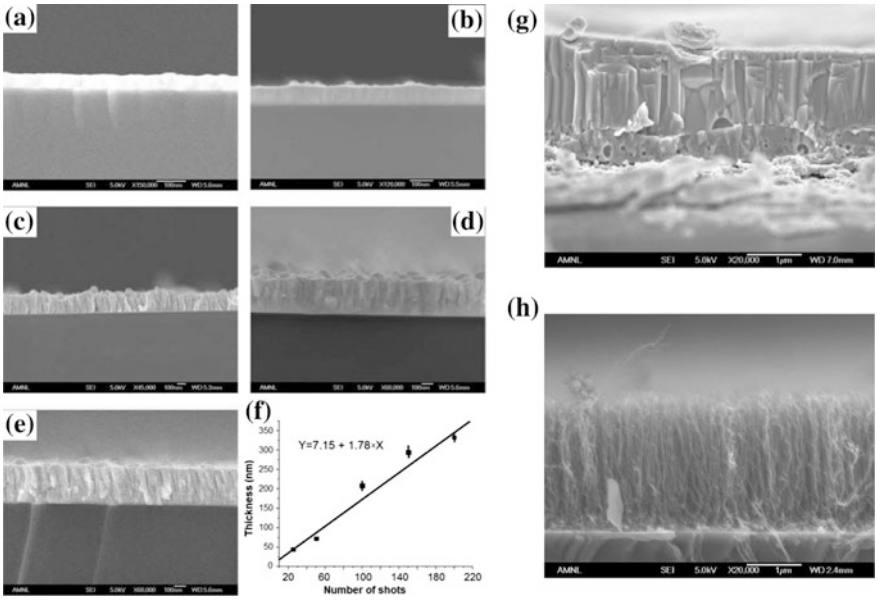

Fig. 2.28 **a**–**e** Cross-sectional SEM images of CoPt thin films deposited using 25, 50, 100, 150 and 200 NX2 DPF shots, respectively, at 25 cm from anode top. **f** Film thickness variation with the number of deposition shots. **g** Cross-sectional SEM of ZnO thin film deposited using 30 shots in UNT-ICTP DPF at 15 cm from anode top. **h** Single shot synthesis of carbon nanotube in UNU-ICTP DPF device. Reprinted from **a**–**f** Pan et al. [146], Copyright (2009) with permission from IOP publishing; and **g, h** Tan [83, 84] (Permission not needed)

plasma. This would require significant modification to the anode design with water cooling arrangement before the high repetition rate experiments can actually be performed.

It may be noted that while CoPt thin film synthesis (Fig. 2.28a–e) was purely PVD-type deposition by the ablation of CoPt anode top, the ZnO synthesis was PVD synthesis with reactive background gas of oxygen. Figure 2.28h shows the pure gas phase PECVD synthesis of carbon nanotube (CNT) in single UNU-ICTP DPF shot [83, 84]. The length of CNT is about 2 μm in single shot synthesis in Fig. 2.28h. So if assume the discharge plasma duration to be of the order of 100 μs (refer to the discussion of plasma lifetime in Sect. 2.4.4 where the H plasma emission peak is observed even at 55 μs in Fig. 2.13c) then the CNT transient growth rate is staggering 20 mm/s, double that of ZnO transient growth mentioned above, and far more greater than CNT growth rate in any other device.

2.7.1.2 Ability to Grow Crystalline Thin Films at Room Temperature

In almost all the experiments conducted using DPF devices, it has been demonstrated that thin films can be deposited directly into crystalline phase at room temperature substrate. No in situ annealing was required to achieve the crystalline phase. Figure 2.29 shows XRD patterns of TiN [141], ZnO [158] and TiO_2 [145] thin films deposited using DPF device on room temperature substrates. The ability to deposit thin films directly in crystalline phase at room temperature substrate highlights the critical role played by high-energy-density plasma and energetic ion processing during the deposition process

Figure 2.29a shows the XRD patterns of TiN thin film samples deposited at fixed distance of 7 cm using different numbers (10, 20, and 30) of DPF shots at different angular positions. Not only the films deposited along the anode axis (labeled as "Centre") but also the one deposited at off-axis positions at different angular positions (labeled as "Off-centre" and "outermost") were all crystalline in nature. The crystallinity, however, was highest for the samples deposited along the anode axis and it decreased with increasing deposition angle. The crystallinity was also found to increase with the increasing number of shots.

The XRD of ZnO thin films, in Fig. 2.29b, also demonstrate the deposition of highly crystalline thin films with (002) preferred orientation at room temperature substrate. Author's group at NTU has done a good amount of work on a dilute magnetic semiconductor for transition metal doped ZnO synthesis [135, 164–168]. The ZnO thin films for those studies were synthesized using PLD deposition method and were mostly amorphous or very weakly crystalline at room temperature deposition conditions; and either in situ or post-deposition annealing was required to get the a good crystalline film.

Figure 2.29c shows XRD spectra of the as-deposited TiO_2 (titania) thin films on Si substrate at room temperature for a different number of DPF deposition shots viz. 25, 50, 75, and 200. In the notation of Miller indices, "A" indicates anatase-type crystal, and "R" indicates rutile-type crystal. The XRD spectra reveal that the film

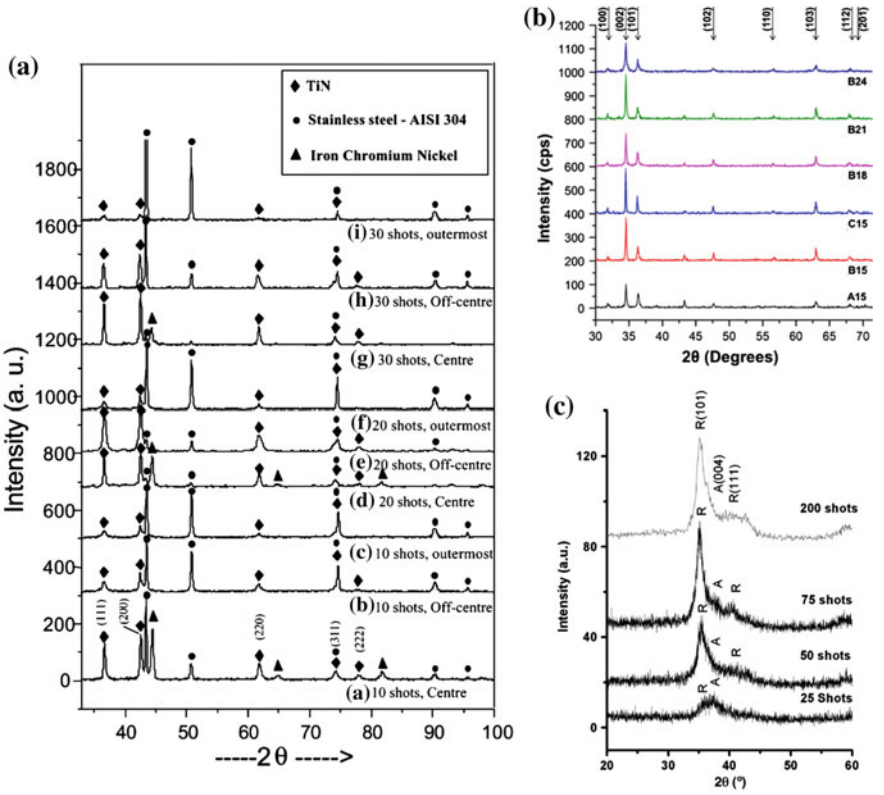

Fig. 2.29 Direct crystalline phase synthesis at room temperature substrates for various thins films, **a** TiN, **b** ZnO and **c** TiO_2. Reprinted from **a** Rawat et al. [141], Copyright (2003) with permission from Elsevier Ltd; **b** Tan et al. [158], Copyright (2015), with permission from IEEE; and **c** Rawat et al. [145], Copyright (2008) with permission from Elsevier Ltd

deposited with 25 shots is anatase with a broad diffraction peak. The film deposited with 50 shots shows the presence of a weak (111) and a strong (101) rutile peaks along with the anatase (004) peak shoulder. For the films deposited with 75 and 100 shots, only rutile phase is evolved with (101) preferred orientation. The crystalline nature of the as-deposited titania thin films using multiple focus shots at room temperature substrate made DPF-based deposition different from most of the studies reporting amorphous titania thin films grown on substrates at room temperature [169, 170]. The crystallization from amorphous to anatase and from anatase to rutile usually occurs in the temperature ranges of 450–550 and 600–700 °C, respectively. But in DPF-based deposition, we achieved both anatase and rutile phase in as-deposited titania samples at room temperature deposition with multiple shots. This confirms the highly energetic deposition process or strong in situ transient thermal annealing in DPF device which allows room temperature crystalline phase formation. Hence DPF-based deposition can be used for direct crystalline phase thin

film depositions on soft substrate materials such acrylic, plastics, or other polymers which cannot be annealed at a higher temperature for phase transformation purposes.

2.7.1.3 Superior Physical Properties

There are numerous examples whereby superior physical properties are exhibited by DPF-deposited thin films compared to the films deposited by other methods. In order to illustrate this, we will use few selected examples. For example, one of the best depositions of oxygen-rich ZnO thin films by PLD method in author's lab is reported in a paper by Usman et al. [166] whose XRD and PL (photoluminescence) spectra are shown in Fig. 2.30a, b. Chemically synthesized oxygen-rich ZnO power (with Zn/O ratio of 0.71) was used for PLD pellet preparation. The ZnO target rotating at 33 revs/min was ablated by second harmonic Nd:YAG laser (532 nm, 26 mJ) at pulse repetition rate of 10 Hz. The ZnO thin films were deposited on Si (100) substrate for constant ablation duration of 90 min in the ultra high vacuum of 10^{-6} Torr. Post-deposition annealing was carried out at different temperatures ranging from 500 to 800 °C for 4 h in air. The XRD of all annealed samples exhibited polycrystalline wurtzite structure; as-grown films were weakly crystalline. A typical ZnO PL spectral is known to exhibit characteristic UV (centered about 3.37 eV or about 370 nm) and defects-related deep level green-yellow (1.8–2.8 eV range) emissions. The UV band emission, centered at about 3.37 eV originates from the exciton recombination corresponding to NBE exciton emission of the wide bandgap ZnO. The DLE in green and yellow emission spectra is related to the variation in intrinsic defects of ZnO thin films, such as zinc vacancy (V_{Zn}), oxygen vacancy (V_o), interstitial zinc (Zn_i), and interstitial oxygen (O_i) [171]. The room temperature PL spectrum of PLD grown ZnO thin films annealed at 700 °C, shown in Fig. 2.30b, exhibited small NBE UV emission peak at ∼385 nm (3.23 eV) and relatively stronger and broad DLE defect (green) emission centered at ∼520 nm (2.39 eV). The DLE spectrum, as seen in Fig. 2.30b, can be deconvoluted with four peaks centered which correspond to zinc vacancy (V_{Zn}), oxygen vacancy (V_o), interstitial zinc (Zn_i) and interstitial oxygen (O_i) defects. The presence of much stronger DLE peak indicates that intrinsic defects are quite high in PLD grown ZnO thin films. All other samples also exhibited similar PL spectra. In comparison, the PL spectra of DPF grown ZnO thin film samples, shown in Fig. 2.30d, exhibit quite contrasting nature with much stronger NBE emission compared to DLE emission indicating a low concentration of intrinsic defects [158]. The samples deposited at 15 cm with increasing number of deposition shots (A15, B15, and C15) show a gradual blue shift of NBE peak from 3.23 to 3.28 eV and gradual decrease in relative intensity of defects-related broad green-yellow DLE band. The sample C15, deposited with 30 focus shots at 15 cm, does not exhibit DLE emission band that indicates intrinsic defects-free ZnO thin film in this sample. The gradual decrease in

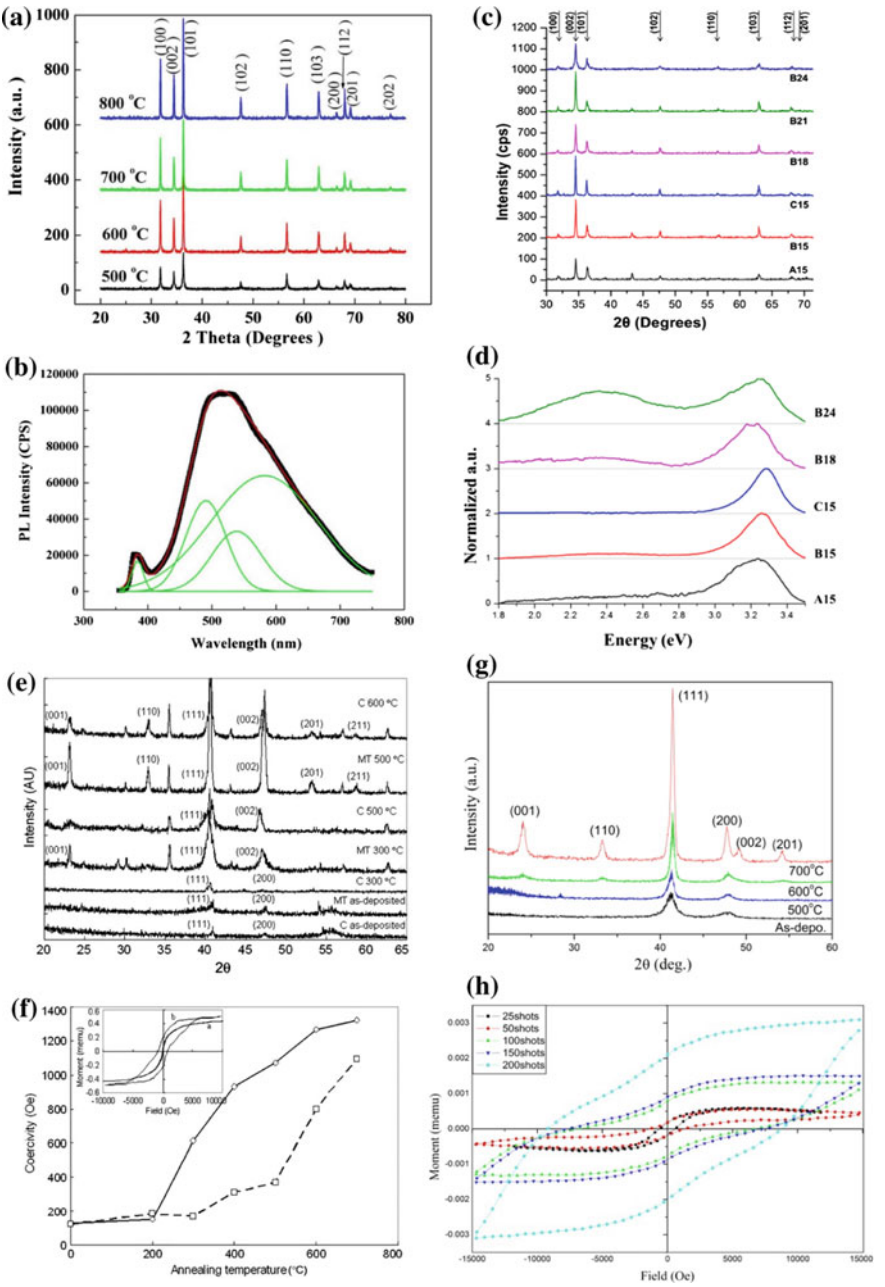

Fig. 2.30 XRD and PL spectra of PLD (**a**, **b**) and DPF (**c**, **d**) grown ZnO thin films. XRD and VSM results of PLD grown FePt:Al2O3 composite (**e**, **f**) and DPF grown CoPt thin films (**g**, **h**). Reprinted from **a**, **b** Ilyas et al. [166], Copyright (2011) with permission from AIP publishing; **c**, **d** Tan et al. [158], Copyright (2015), with permission from IEEE; **e**, **f** Lin et al. [172], Copyright (2008) with permission from IOP publishing; and **g**, **h** Pan et al. [146], Copyright (2009) with permission from IOP publishing

intrinsic defects with increasing number of focus deposition shots was caused by a greater amount of transient annealing of the deposited ZnO. This demonstrates superior structural properties (defect-free) exhibited by DPF grown ZnO films compared to PLD-grown films.

Another example that we would like to highlight is that of the magnetic thin film deposited by PLD [172] and DPF [146] and shown in Fig. 2.30e–h. The PLD grown, refer Fig. 2.30e, f, as-deposited FePt thin films were very weakly crystalline and soft magnetic in nature with a coercivity of about 100 Oe. With post-deposition annealing, the samples became hard magnetic with coercivity increasing gradually to a maximum of about 1300 Oe with increasing annealing temperature due to transition from face centered cubic (fcc) to face centered tetragonal (fct) phase. But one thing to notice in Fig. 2.30e is the presence of a large number of unidentified (non-labeled) XRD peaks which were associated with impurity phase formation which did not allow the formation of very hard magnetic phase [173]. It took lots of effort to eliminate the impurity phase formation in PLD grown thin films to be finally able to achieve very hard magnetic phase in FePt thin films with a coercivity of the order of 7.7 kOe. The CoPt thin films grown by DPF were having better crystallinity but still in chemically disordered fcc phase. The crystallinity improved significantly with annealing and converted to highly crystalline chemically ordered desired fct phase as seen in Fig. 2.30g. One of the most important facts to note is that no unidentified peaks were observed in XRD spectra of DPF grown CoPt thin films implying that no impurity phases were formed. This resulted in the very hard magnetic film for the sample deposited with 200 DPF shots with coercivity value approaching almost to 10 kOe, refer Fig. 2.30h [146]. Even the sample deposited with 100 and 150 shots were highly crystalline and depicted very hard magnetic phase with a coercivity of the order of 7–8 kOe. The reader may be questioning the comparison of DPF grown CoPt films with PLD grown FePt thin films, as they are different materials. Both materials have similar magnetic properties and phase transition temperature and that is the why the comparison is fair. Author's group has also deposited CoPt thin films using PLD and the results are discussed in paper by Pan et al. [174]. The PLD grown CoPt thin films were less crystalline compared to the DPF grown films, moreover the highest coercivity obtained was about 3.7 kOe, significantly lower than that of 10 kOe obtained for DPF grown CoPt films. This highlights the superior crystalline and magnetic properties obtained for DPF-grown films.

2.7.1.4 Versatile Deposition Facility with a Variety of Deposition Options

The versatility of DPF device as deposition facility is reflected through many types of depositions that have been achieved in many different investigations which include

(i) use of DPF device as pure PVD or hybrid PVD-CVD or pure CVD type deposition facility as depicted in Fig. 2.15,
(ii) the DPF device can be operated in different configurations, shown in Figs. 2.16, 2.17 and 2.18, to utilize its different components such as ions, electrons and hot dense plasma for material synthesis,
(iii) ability to deposit a wide variety of materials that include metal, bi-metals, metal nitrides, metal oxides, metal carbide, metal oxy-nitrides, metal carbo-nitrides, and a large number of carbon-based materials, and
(iv) ability to deposit nanoparticle (0-dim), nanowires (1-dim), flat thin films (2-dim) and vertical graphene (3-dim) materials.

2.7.2 *Understanding Mechanisms of Material Synthesis in DPF Device*

The mechanisms of material synthesis are different for different types of depositions that have been performed in DPF device. We have broadly classified these different mechanisms in three broad categories based on materials and morphology of the deposited materials.

Mechanism for deposition of metallic, bimetallic, and carbon thin films: The depositions of thin films of Fe, Cu, FeCo, CoPt, FePt, diamond-like carbon, etc., are primarily done in inert gases (neon or argon) or hydrogen as filling gas with central electrode replaced or fitted with relevant material (metal, bimetal, or graphite). The substrate on which deposition is done can be kept at different distances from solid anode top and/or angular positions with respect to anode axis to control the deposition rate and uniformity of the thin films. Most depositions are done using multiple DPF shots to achieve higher thickness and size of nanoparticles on the surface of the film. During each DPF deposition shot two different plasmas, one of filling gas species and the other one of plasma of anode top ablated material, are primarily created. The plasma of filling gas species (which in the present case is that of either inert or hydrogen gas) is created right from the initiation of discharge and its density and temperature reach the highest during the pinch phase. In addition to plasma of filling gas species, as mentioned earlier, energetic ions of filling gas species in the range of 10 keV to few MeV are also generated by instabilities and they are the one which would reach the substrate much before ablated plasma of anode top material. Actually, short ion pulses of high-energy-density can cause sputtering as well as very rapid heating of the substrate surface depending on the nature of the surface layer and the energy density (which depends on the distance and the angular position of the substrate) of the incident ions of filling gas species. This may cause the ablation/sputtering of the substrate forming the momentary substrate surface plasma at the substrate surface. This leads to the cleaning of the substrate surface before the deposition of desired thin film material, which may result in improved adhesion of the deposited films. At the same time, it may

introduce the undesirable impurities of substrate material in the deposited thin material. The problem of substrate material ablation can be avoided by increasing the distance of deposition to avoid its impurities in the film. This is followed by the arrival and deposition of anode top ablated material plasma over the much longer duration of several microseconds. Since all depositions performed in DPF devices are multiple shot deposition, during the next DPF shot the energetic ions of filling gas species will process the film deposited in previous shot leading to its densification and in situ intense transient annealing. This in situ transient annealing is the reason for most DPF depositions to directly go into a crystalline phase without the need of post-deposition annealing.

Mechanism for deposition of metal-nitride, -carbide, -oxide, etc*., thin films*: The mechanism of depositions of MX thin films (with M = metal and X = nitride/carbide/oxide) is slightly different as though the central electrode is fitted with relevant metal as before but the filling gas is reactive. The filling gas is either nitrogen or oxygen or carbon-containing gas such as methane or acetylene. For example, hard coating of TiN can be deposited using DPF fitted with Ti anode and by operating the DPF in nitrogen ambiance. High-pinch plasma temperature causes the complete ionization of the filling gas species (nitrogen) resulting formation of nitrogen ions, atoms, and molecules. The interaction of hot dense pinch plasma and instability generated backward moving relativistic electrons causes the ablation of Ti anode material forming the Ti plasma which then reacts with ambient nitrogen plasma resulting in TiN formation on the substrate placed down the anode axis. Once again, during the next shot, the material deposited in previous shot is transiently annealed by instability-accelerated energetic nitrogen ions leading to crystalline TiN phase. In addition to transient annealing, the energetic nitrogen ions exposure can also add on the TiN formation by implantation of nitrogen ions in the previously deposited TiN layer. Similarly, for TiC coating the Ti anode fitted DPF just needs to be operated with a gas containing carbon such as methane or acetylene. It has however been found that the DPF operation in these gases is non-reliable and inconsistent. It is for this reason these gas are normally used as an admixture with inert gases such as argon or neon. Thus, the deposition of thin films of carbides, nitrides or oxides of any metal can simply be achieved using suitable reactive background gases such nitrogen, acetylene, methane, and oxygen or their combinations.

Mechanism for deposition of carbon nanotube or graphene thin films: The mechanism presented here for the deposition of carbon nanotube (CNT) and graphene nanoflakes (GNF) in DPF device is based on the research findings presented by K.S. Tan in his Ph.D. thesis [84]. The successful growth of CNT required simultaneously the presence of three important parameters while GNF required only one important parameter for the successful synthesis in a DPF device. The first important parameter for CNT growth was the presence of heated substrate (> 500 °C) which provided the energy necessary for the enhancement of the dissolution of carbon into metal catalyst due to lowering of activation energy for CNT growth at the heated substrate. The assistance of the DPF discharge plasma is the second important parameter which enhances/substitutes the role of thermal decomposition.

Although it is well known that carbon dissolution into Fe results in formation of iron carbide above 500 °C, what explains the absence of carbon nanotube growth is due to the lack of iron carbide converting into a α-Fe phase which is an active graphite precipitation phase. This phase increases the production of CNT rapidly and begins to form between 500 and 750 °C while stabilizing at the temperature above 750 °C through exothermic precipitation. Even without the assistance of a heat source the carbon nano-structures such as graphene nanoflakes were formed without thermal decomposition of carbon feedstock as the presence of active carbon species was sufficiently made available via energetic DPF discharge plasma decomposition for the growth of this material. Thus, the results hint that GNF synthesis does not require catalytic decomposition but the presence of a catalyst improves the synthesis outcome towards graphene-like nano-structures. Additionally, the formation of highly dense carbonaceous plasma was more than sufficient for GNF synthesis. However, the CNT growth without the presence of a catalyst was not possible. In other words, the presence of catalyst plays as the third important factor/parameter which provided a low-activation energy pathway for the successful low-temperature plasma-assisted growth of CNT. The transient effect of the dense plasma focus forms the α-Fe phase nanoparticles on the irradiated Fe-coated silicon substrate, providing active catalytic carbon nucleation sites of a right size allowing the growth of CNT on the catalyst substrate.

2.8 Scalability of DPF Devices for Material Processing and Synthesis

One of the major issues that DPF device faces as processing and deposition facility is its suitability as reliable and possibly a potential research/industrial facility is the scalability of the device for large area and uniform processing/deposition. In order to understand how scalability of DPF device can be achieved we need to understand the basic characteristics/features of DPF device and its pinch plasma. Electrically, the DPF device is an inductive load connected to a capacitor bank C_0. The total inductance of the DPF device during its operation is the sum of fixed system inductance L_0 (comprising of the inductances of the capacitor bank, fast switches, transmission line, and input flanges) and the variable plasma inductance L_p due to plasma dynamics in axial and radial phase. The bulk of the DPF inductance is due to L_0 and is used to define the quarter time period $T/4 = \pi\sqrt{L_0 C_0}/2$ of the discharge current in DPF device, the time instant at which the discharge current reaches the maximum. For most efficient magnetic compression and resistive Joule heating of the pinch plasma column the radial compression phase is required to occur at or near maximum discharge current (at about $\sim T/4$). As mentioned in Sect. 2.4.3 the typical current sheath speed in axial phase for maximum compression efficiency is in a limited range of about few cm/μs which together with the requirement of achieving the radial compression near or at the quarter time period

of the discharge current for maximum current to flow through pinch plasma, controls the dimension of the central electrode (anode). Therefore most plasma focus devices are designed using anode with lengths, which is approximately equal to the multiplication of the typical average value of axial current sheath speed (say 5 cm/μs) by the quarter time period of the short-circuit discharge current.

The anode radius is another crucial parameter which is decided on the basis of speed parameter value defined by Lee and Serban [66]. Most of the neutron optimized plasma focus devices have been found to have the typical speed factor, $I_0/a\sqrt{P}$, value of about 90 kA cm^{-1} Torr$^{-1/2}$ where I_0, a and P denote the short-circuit peak discharge current in kA, anode radius in cm and deuterium filling gas pressure in Torr, respectively. Using the short-circuit peak discharge current and approximate deuterium operating pressure of say 5 Torr, one can estimate the approximate anode radius. The peak short-circuit discharge current for a given charging voltage of V_0 depends on the capacitance of the capacitor bank as $I_0 = V_0/\sqrt{L_0/C_0}$ In other words, the dimensions (length and radius) of the anode of DPF devices are different for devices of difference capacitor bank (storage energy). The higher the capacitance of the capacitor bank the bigger is the dimension (length as well as the radius) of the anode. According to the established scaling laws [66] and performed optical investigations [175], the final pinch radius and the maximum pinch length are proportional to anode radius a ($\sim 0.12a$ and $\sim 0.8a$, respectively). Thus, the final plasma volume V_p is of the order of $\pi(0.12a^2) \times (0.8a) \approx 0.036a^3$. Another important parameter is the time duration of various transient phenomena in DPF devices. For example, the pulse duration of energetic ion beam, which is one of the main component that is responsible for energetic processing of material placed down the anode stream, depends on pinch phase duration of plasma focus device which in turn depends on the characteristic time ($\sim\sqrt{L_0C_0}$) of the device. In low- and mid-energy DPF devices, the duration of energetic ion beam is of the order of several tens to about hundreds of ns while in bigger plasma focus device it might be several hundred ns.

It can, therefore, be concluded that DPF devices with larger storage energy use larger capacitance and hence also have a larger quarter time period and the large dimensions of the coaxial electrode assembly leading to the larger volume of the dense hot plasma and that too for longer durations. Hence, the increase in anode radius a from about 1 cm in 3 kJ UNU-ICTP DPF device to about 11.5 cm in 1 MJ PF1000 device not only increases the final-pinch plasma volume by 1000 times but the hot dense plasma and other associated phenomena are also of significantly long durations. So even though increasing the storage energy and correspondingly the physical dimensions of electrode assembly do not increase the temperature and the density of the pinch plasmas, providing the unique universality in the basic nature of the DPF devices, but the increase in final pinch plasma volume and time durations of all associated transient phenomena leads to the increase in yields of energetic charged particles and radiations which points to the scalability of the DPF device. The large volume of pinch plasma will allow a large area of uniform deposition with even high deposition rate, which makes the DPF facility scalable.

However, making DPF devices with larger bank energy and electrode dimensions will come at increased cost and lower repetition rate operation. For example, the hugely expensive 1 MJ PF1000 device is operated on an average of 1 shot per 20 min, whereas low-cost kJ range UNU-ICTP device can be operated twice in 1 min.

Another solution to improve the scalability, large area uniform deposition/processing, of the DPF device is to increase the distance of deposition from the anode top. This normally results in significant reduction in deposition rate but the uniformity of films improves significantly. It may also be pointed out that now high repetition rate DPF devices are available, operating at 1–50 Hz. This in principle allows the repetitive DPF device to be used just like repetitive PLD (pulsed laser deposition) facility where the uniformity of deposited material can be achieved by rotating the substrate.

2.9 Conclusions

The major aim of this chapter was to establish that the DPF device based high-energy-density pulsed plasma facility has enormous potential for controlled material processing and synthesis for a wide range of material types in wide range nano-structural features ranging from zero-dimensional nanoparticles to three-dimensional graphene nanoflowers. The versatility of DPF-based deposition was established by demonstrating that how over the years the depositions have evolved from pure PVD type to hybrid PVD-CVD to purely CVD type depositions. The processing and synthesis of nanoscale materials in DPF have been successfully performed by many different research groups across the globe using both "top–down" and "bottom–up" approaches. In "top–down" approach, which relies on the successive fragmentations or processing of macro-scale materials to smaller nano-sized objects, the bulk and thin film samples were exposed to different numbers of DPF shots at different distances from the anode top. It was found that while the nano-structurization and property modification of the entire thickness of the thin film can be achieved by its exposure to DPF shots but for bulk material, only the top surface layer of the bulk sample is processed and nano-structurized by its exposure to DPF shots. In "bottom-up" approach, which relies on nanoscale materials being assembled atoms and molecules, several thin film deposition configurations, in term of target-substrate orientation and placement, use of different ablative components, and pure gas-based synthesis have been used in DPF devices for nano-structured material syntheses. The DPF device has the enormous flexibility of being operated in many different possible configurations whereby its different components such as ions, electrons, and hot dense plasma can be used for material synthesis or processing. Each of the DPF-based deposition configurations has its own limitations and disadvantages but based on our extensive experience and survey of results from different groups, we conclude that most versatile and efficient for thin film deposition setup is where the target material (to be ablated) is used

either as anode insert or as anode tip with background inert/reactive gas is used in the DPF chamber and the substrate (on which thin film is deposited) is placed downstream either along or at some angle with respect to the anode axis. This setup allows deposition of nano-structured metallic, bimetallic, carbide, nitride, oxide, and composite thin films. Using the hollow anode, a pure gas-based synthesis of carbon nanotube has also been successfully demonstrated which extends the application domain of DPF device to PECVD (plasma-enhanced CVD). This opens a very wide area of application of DPF facility for other pure gas-based depositions though limitations and issues need to be explored in greater details. The DPF device has also been used successfully for the synthesis of zero-, one-, two- and three-dimensional nano-structures proving its immense potential in plasma nanoscience and nanotechnology. In addition, the device has the added advantage of high deposition rates, the ability to grow crystalline thin films directly at room temperature without any need for post-deposition annealing (though through post-deposition annealing material properties can be tuned additionally), and other superior physical properties in deposited materials. The DPF device offers a complex mixture of high-energy ions of the filling gas species, immensely hot and dense decaying plasma, fast-moving ionization wavefront and a strong shockwave that provides a unique plasma and physical/chemical environment that is completely unheard of in any other conventional plasma-based deposition or processing facility making it a novel and versatile facility with immense potential for high-energy-density pulsed plasma-based material processing and depositions.

References

1. ITER. *Phases Ahead*. https://www.iter.org/construction/timeline (2017)
2. NIF. *Ignition Experiments at NIF*. https://lasers.llnl.gov/science/ignition/ignition-experiments (2017)
3. K.L. Choy, Chemical vapour deposition of coatings. Prog. Mater Sci. **48**, 57–170 (2003). doi:10.1016/s0079-6425(01)00009-3
4. J.E. Mahan, *Phys. Vapor Deposition Thin Films.* (Wiley, USA, 2000)
5. S.S. Meysami, A.A. Koos, F. Dillon, M. Dutta, N. Grobert, Aerosol-assisted chemical vapour deposition synthesis of multi-wall carbon nanotubes: III. Towards upscaling. Carbon **88**, 148–156 (2015). doi:10.1016/j.carbon.2015.02.045
6. G. Papadimitropoulos, D. Davazoglou, Copper films deposited by hot-wire CVD and direct liquid injection of CupraSelect. Chem. Vap. Deposition **13**, 656–662 (2007). doi:10.1002/cvde.200706621
7. S.G. Ansari et al., Effect of RF plasma power and deposition temperature on the surface properties of tin oxide deposited by modified plasma enhanced chemical vapor deposition. Sci. Adv. Mat. **1**, 254–261 (2009). doi:10.1166/sam.2009.1052
8. G.L. Doll, B.A. Mensah, H. Mohseni, T.W. Scharf, Chemical vapor deposition and atomic layer deposition of coatings for mechanical applications. J. Therm. Spray Technol. **19**, 510–516 (2010). doi:10.1007/s11666-009-9364-8
9. S.A. Amer, S. Magnaudeix, P. Duverneuil, On the behavior of rapid thermal cvd reactors. J. Phys. IV **3**, 35–42 (1993). doi:10.1051/jp4:1993304

10. I. Zunke et al., Conductive zinc oxide thin film coatings by combustion chemical vapour deposition at atmospheric pressure. Thin Solid Films **532**, 50–55 (2013). doi:10.1016/j.tsf.2012.11.151
11. Y.Z. Wang, et al., MgB2 superconducting whiskers synthesized by using the hybrid physical-chemical vapor deposition. J. Am. Chem. Soc. **131**, 2436–2437, doi:10.1021/ja8087828 (2009)
12. A. Anders, *Cathodic Arcs: From Fractal Spots to Energetic Condensation*. (Springer, Berlin, 2008)
13. Harsha, K. S. S. *Principles of Physical Vapor Deposition of Thin Films*. (Elsevier, Netherlands, 2006)
14. F.F. Chen, *Introduction to Plasma Physics and Controlled Fusion*. (Springer, Berlin, 1984)
15. A. Fridman, *Plasma Chemistry*. (Cambridge University Press, UK, 2008)
16. Panel on Plasma Processing of Materials, National Research Council (US), *Plasma processing of materials: Scientific opportunities and technological challenges*. 88 (National Academy Press (US), 1991)
17. Committee on High Energy Density Plasma Physics, P. S. C., *National Research Council Frontiers in High Energy Density Physics: The X-Games of Contemporary Science*. (National Academies Press, USA, 2003)
18. Laboratory for Laser Energetics. http://www.lle.rochester.edu/omega_facility/omega/
19. Sandia National Laboratories. http://www.sandia.gov/z-machine/
20. L. Soto, New trends and future perspectives on plasma focus research. Plasma Phys. Controlled Fusion **47**, A361–A381 (2005). doi:10.1088/0741-3335/47/5a/027
21. I.E. Garkusha et al., Experimental study of plasma energy transfer and material erosion under ELM-like heat loads. J. Nucl. Mater. **390–91**, 814–817 (2009). doi:10.1016/j.jnucmat.2009.01.215
22. V.A. Makhlaj, I.E. Garkusha, N.N. Aksenov, O.V. Byrka, I. Landman, S.I. Lebedev, P.B. Shevchuk, Plasma-surface interaction and mechanisms of dust production in ITER ELM simulation experiments with QSPA Kh-50. Prob Atomic Sci Technol, # 6, Ser "Plasma Phys" **18**, 55–57 (2012)
23. S.V. Bazdyreva, I.E. Garkusha, V.A. Makhlaj, S.V. Malykhin, S.V., A.T. Pugachov, The influence of irradiation by hydrogen plasma on the structure and phase composition of Ti-Zr-Ni alloys containing quasicrystalline Phase. Prob Atomic Sci Technol, # 6, Ser "Plasma Phys" **18**, 226–228 (2012)
24. W.R. Feng, H. Zhou, S.Z. Yang, Gas pressure dependence of composition in Ta-Ti-N films prepared by pulsed high energy density plasma. Mater. Chem. Phys. **124**, 287–290 (2010). doi:10.1016/j.matchemphys.2010.06.033
25. W.R. Feng et al., Characteristics of (Ti, Ta)N thin films prepared by using pulsed high energy density plasma. J. Phys. D-Appl. Phys. **40**, 4228–4233 (2007). doi:10.1088/0022-3727/40/14/018
26. W.R. Feng et al., Preparation of Ta(C)N films by pulsed high energy density plasma. J. Phys. D-Appl. Phys. **40**, 2132–2137 (2007). doi:10.1088/0022-3727/40/7/041
27. W.R. Feng et al., Titanium carbonitride films on cemented carbide cutting tool prepared by pulsed high energy density plasma. Appl. Surf. Sci. **253**, 4923–4927 (2007). doi:10.1016/j.apsusc.2006.10.069
28. D. Wu et al., Numerical study of dynamic effects and evaporation of target material under irradiation of intense pulsed ion beam. Acta Physica Sinica **55**, 3501–3505 (2006)
29. H.Z. Miao et al., Nanometer grain titanium carbonitride coatings with continuously graded interface onto silicon nitride cutting tools by pulsed high energy density plasma. Mat Sci Eng A-Struct Mat Prop Microstruct Process **384**, 202–208 (2004). doi:10.1016/j.msea.2004.06.005
30. Z.J. Peng, H.Z. Miao, L.H. Qi, S. Yang, C.Z. Liu, Hard and wear-resistant titanium nitride coatings for cemented carbide cutting tools by pulsed high energy density plasma. Acta Mater. **51**, 3085–3094 (2003). doi:10.1016/s1359-6454(03)00119-8

31. C. Rong, J.Z. Zhang, C.Z. Liu, S.Z. Yang, Surface metallization of alumina ceramics by pulsed high energy density plasma process. Appl. Surf. Sci. **200**, 104–110 (2002). doi:10.1016/s0169-4332(02)00874-7
32. B. Liu et al., Investigation of titanium coating on Si3N4 by using a pulsed high energy density plasma (PHEDP) gun. Mater. Chem. Phys. **57**, 219–223 (1999). doi:10.1016/s0254-0584(98)00219-3
33. B. Liu, C.Z. Liu, D.J. Cheng, R. He, S.Z. Yang, Pulsed high energy density plasma processing silicon surface. Thin Solid Films **390**, 149–153 (2001). doi:10.1016/s0040-6090(01)00927-0
34. S. Lee et al., A simple facility for the teaching of plasma dynamics and plasma nuclear fusion. Am. J. Phys. **56**, 62 (1988)
35. J.O. Pouzo, M.M. Milanese, Applications of the dense plasma focus to nuclear fusion and plasma astrophysics. IEEE Trans. Plasma Sci. **31**, 1237–1242 (2003). doi:10.1109/tps.2003.821475
36. J.W. Mather, Formation of a high-density deuterium plasma focus. Phys. Fluids **8**, 366–377 (1965). doi:10.1063/1.1761231
37. N.V. Filipov, T.I. Filipova, V.P. Vinogradov, *Nuclear Fusion* 2, 577 (1962)
38. J.N. Feugeas, The influence of the insulator surface in the plasma focus behavior. J. Appl. Phys. **66**, 3467–3471 (1989). doi:10.1063/1.344102
39. V.A. Gribkov, A. Srivastava, P.L.C. Keat, V. Kudryashov, S. Lee, Operation of NX2 dense plasma focus device with argon filling as a possible radiation source for micro-machining. IEEE Trans. Plasma Sci. **30**, 1331–1338 (2002). doi:10.1109/tps.2002.802156
40. R. Verma et al., Neutron emission characteristics of NX-3 plasma focus device: speed factor as the guiding rule for yield optimization. IEEE Trans. Plasma Sci. **40**, 3280–3289 (2012). doi:10.1109/tps.2012.2220569
41. A. Talebitaher et al., Laser Shadowgraphic study of the influence of krypton-seeding, switch synchronization and electrode geometry on plasma dynamic in plasma focus device. J. Fusion Energy **34**, 794–801 (2015). doi:10.1007/s10894-015-9888-5
42. A. Gribkov et al., Pseudosparks in the nanosecond range of operation: firing, jitter, and current disruption. J. Phys. D-Appl. Phys. **37**, 2107–2111 (2004). doi:10.1088/0022-372737/15/009
43. R. Verma, et al., Compact sub-kilojoule range fast miniature plasma focus as portable neutron source. Plasma Sources Sci. Technol. **17**, 045020, doi:10.1088/0963-0252/17/4/045020 (2008)
44. E. Ghareshabani, R.S. Rawat, R. Verma, S. Karamat, S. Sobhanian, Low energy repetitive miniature plasma focus device as high deposition rate facility for synthesis of DLC thin films. Appl. Surf. Sci. **256**, 4977–4983 (2010). doi:10.1016/j.apsusc.2010.03.012
45. R. Verma, R.S. Rawat, P. Lee, S.V. Springham, T.L. Tan, High performance high repetition rate miniature plasma focus device: record time averaged neutron yield at 200 J with enhanced reproducibility. J. Fusion Energy **32**, 2–10 (2013). doi:10.1007/s10894-012-9517-5
46. J.M. Koutsoubis, S.J. MacGregor, Electrode erosion and lifetime performance of a high repetition rate, triggered, corona-stabilized switch in air. J. Phys. D-Appl. Phys. **33**, 1093–1103 (2000). doi:10.1088/0022-3727/33/9/309
47. F.N. Beg, M. Zakaullah, G. Murtaza, M.M. Beg, Effect of insulator sleeve material on neutron emission from a plasma-focus. Phys. Sci. **46**, 152–154 (1992). doi:10.1088/0031-8949/46/2/008
48. S.M. Hassan et al., Pinching evidences in a miniature plasma focus with fast pseudospark switch. Plasma Sources Sci. Technol. **15**, 614–619 (2006). doi:10.1088/0963-0252/15/4/004
49. T. Zhang et al., Current sheath curvature correlation with the neon soft x-ray emission from plasma focus device. Plasma Sources Sci. Technol. **14**, 368–374 (2005). doi:10.1088/0963-0252/14/2/020
50. J.W. Mather, P.J. Bottoms, Characteristics of the dense plasma focus discharge. Phys. Fluids **11**, 611–618 (1968)

51. S. Al-Hawat, Axial velocity measurement of current sheath in a plasma focus device using a magnetic probe. IEEE Trans. Plasma Sci. **32**, 764–769 (2004)
52. A.J. Toepfer, D.R. Smith, E.H. Beckner, Ion heating in the dense plasma focus. Phys. Fluids **14**, 52–61 (1971)
53. V.A. Gribkov et al., Plasma dynamics in the PF-1000 device under full-scale energy storage: II. Fast electron and ion characteristics versus neutron emission parameters and gun optimization perspectives. J. Phys. D Appl. Phys. **40**, 3592–3607 (2007). doi:10.1088/0022-3727/40/12/008
54. A. Bernard, A. Coudeville, A. Jolas, J. Launspach, J.D. Mascureau, Experimental studies of plasma focus and evidence for non-thermal processes. Phys. Fluids **18**, 180–194 (1975). doi:10.1063/1.861101
55. M. Martínez-Fuentes, et al., Dynamics of the expansion discharge originated by a dense plasma focus. *J. Phys.: Conf. Ser.* **370**, doi:10.1088/1742-6596/370/1/012059(2012)
56. E. Skladnik-Sadowska, et al., 365–368
57. J. Tendys (ed) (Lucus Heights Research Establishment, Sydney, Australia) (1976)
58. A. Bernard et al., Dense plasma focus—high intensity neutron source. Nuclear Instrum. Methods **145**, 191–218 (1977). doi:10.1016/0029-554x(77)90569-9
59. V.A. Gribkov, in *Plasma and Fusion Science*, vol. 996, ed. by C. Varandas, C. Silva. Aip Conference Proceedings, pp. 51–64 (2008)
60. M. Krishnan, The dense plasma focus: a versatile dense pinch for diverse applications. IEEE Trans. Plasma Sci. **40**, 3189–3221 (2012). doi:10.1109/tps.2012.2222676
61. R.S. Rawat, High-energy-density pinch plasma: a unique nonconventional tool for plasma nanotechnology. IEEE Trans. Plasma Sci. **41**, 701–715 (2013). doi:10.1109/tps.2012.2228009
62. S. Lee, S.H. Saw, P. Lee, R.S. Rawat, Numerical experiments on plasma focus neon soft x-ray scaling. *Plasma Phys. Controll Fusion* **51**, 105013, doi:10.1088/0741-3335/51/10/105013 (2009)
63. H. Krompholz, F. Ruhl, W. Schneider, K. Schonbach, G. Herziger, A scaling law for plasma-focus devices. Phys. Lett. A **82**, 82–84 (1981). doi:10.1016/0375-9601(81)90944-0
64. A.J. Toepfer, D.R. Smith, E.H. Beckner, Ion heating in dense plasma focus. Bull. Am. Phys. Soc. **14**, 1013 (1969)
65. R.S. Rawat et al., Effect of insulator sleeve length on soft x-ray emission from a neon-filled plasma focus device. Plasma Sources Sci. Technol. **13**, 569–575 (2004)
66. S. Lee, A. Serban, Dimensions and lifetime of the plasma focus pinch. IEEE Trans. Plasma Sci. **24**, 1101–1105 (1996)
67. N. Qi, S.F. Fulghum, R.R. Prasad, M. Krishnan, Space and time resolved electron density and current measurements in a dense plasma focus z-pinch. IEEE Trans. Plasma Sci. **26**, 1127–1137 (1998)
68. T. Zhang et al., Optimization of a plasma focus device as an electron beam source for thin film deposition. Plasma Sources Sci. Technol. **16**, 250–256 (2007). doi:10.1088/0963-0252/16/2/006
69. P. Choi, C. Deeney, H. Herold, C.S. Wong, Characterization of self-generated intense electron beams in a plasma focus. Laser Part. Beams **8**, 469–476 (1990)
70. H. Bhuyan, S.R. Mohanty, T.K. Borthakur, R.S. Rawat, Analysis of nitrogen ion beam produced in dense plasma focus device using Faraday Cup. Indian J. Pure Appl. Phys. **39**, 698–703 (2001)
71. M.V. Roshan, S. Springham, A. Talebitaher, R.S. Rawat, P. Lee, Magnetic spectrometry of high energy deuteron beams from pulsed plasma system. *Plasma Phys. Controlled Fusion* **52**, 085007, doi:10.1088/0741-3335/52/8/085007 (2010)
72. V. Raspa et al., Plasma focus as a powerful hard x-ray source for ultrafast imaging of moving metallic objects. Braz. J. Phys. **34**, 1696–1699 (2004)
73. M. Zakaullah et al., Characteristics of x-rays from a plasma focus operated with neon gas. Plasma Sources Sci. Technol. **11**, 377–382 (2002)

74. H. Bhuyan, S.R. Mohanty, N.K. Neog, S. Bujarbarua, R.K. Rout, Comparative study of soft x-ray emission characteristics in a low energy dense plasma focus device. J. Appl. Phys. **95**, 2975–2981 (2004). doi:10.1063/1.1647269
75. M. Barbaglia, H. Bruzzone, H. Acuna, L. Soto, A. Clausse, Experimental study of the hard x-ray emissions in a plasma focus of hundreds of Joules. *Plasma Phys. Controlled Fusion* **51**, 045001, doi:10.1088/0741-3335/51/4/045001 (2009)
76. T. Zhang, *Electron emission from plasma focus for nano phase FeCo thin film deposition*, PhD thesis, Nanyang Technological University, (2007)
77. L.Y. Soh, P. Lee, X. Shuyan, S. Lee, R.S. Rawat, Shadowgraphic studies of DLC film deposition process in dense plasma focus device. IEEE Trans. Plasma Sci. **32**, 448–455 (2004). doi:10.1109/tps.2004.826031
78. A. Patran et al., Spectral study of the electron beam emitted from a 3 kJ plasma focus. Plasma Sources Sci. Technol. **14**, 549–560 (2005). doi:10.1088/0963-0252/14/3/018
79. J.N. Feugeas, E.C. Llonch, C.O. De González, G. Galambos, Nitrogen implantation of AISI 304 stainless steel with a coaxial plasma gun. J. Appl. Phys. **64**, 2648–2651 (1988). doi:10.1063/1.341604
80. R.S. Rawat, M.P. Srivastava, S. Tandon, A. Mansingh, Crystallization of an amorphous lead zirconate titanate thin film with a dense-plasma-focus device. Phys. Rev. B **47**, 4858–4862 (1993). doi:10.1103/PhysRevB.47.4858
81. C.R. Kant, M.P. Srivastava, R.S. Rawat, Thin carbon film deposition using energetic ions of a dense plasma focus. Phys. Lett. Sect A: General, At. Solid State Phys. **226**, 212–216 (1997)
82. R.S. Rawat, P. Lee, T. White, L. Ying, S. Lee, Room temperature deposition of titanium carbide thin films using dense plasma focus device. Surf. Coat. Technol. **138**, 159–165 (2001)
83. K.S. Tan, *High Growth Rate Synthesis of Zinc Oxide and Carbon Based Nanostructured Materials Using Dense Plasma Focus Device* PhD thesis, Nanyang Technological University (2017)
84. K.S. Tan, B. Ouyang, R.S. Rawat, in *10th Asian-European International Conference on Plasma Surface Engineering (AEPSE2015)* (Jeju, Republic of Korea, 2015)
85. S. Zeb, M. Sadiq, A. Qayyum, G. Murtaza, M. Zakaullah, Deposition of diamond-like carbon film using dense plasma focus. Mater. Chem. Phys. **103**, 235–240 (2007)
86. S.R. Mohanty et al., Self-organized transformation to polyaniline nanowires by pulsed energetic electron irradiation in a plasma focus device. Phys. Lett. A **373**, 1962–1966 (2009). doi:10.1016/j.physleta.2009.03.062
87. V.N. Pimenov et al., Damage and modification of materials produced by pulsed ion and plasma streams in dense plasma focus device. Nukleonika **53**, 111–121 (2008)
88. N.D. Nawi, R. Farma, S.T.Ong, K.T. Chaudhary, J. Ali, Saktioto, Numerical studies on pinching radius effects to current densities of NX2 Plasma Focus. *KnE Engineering* **2016**, 6, doi:10.18502/keg.v1i1.515 (2016)
89. S. Lee et al., Effect of targets on plasma focus dynamics. IEEE Trans. Plasma Sci. **18**, 1028–1032 (1990)
90. V.A. Gribkov, Physical processes taking place in dense plasma focus devices at the interaction of hot plasma and fast ion streams with materials under test. *Plasma Physics and Controlled Fusion* **57**, doi:10.1088/0741-3335/57/6/065010 (2015)
91. S. Lee, S.H. Saw, Plasma focus ion beam fluence and flux-Scaling with stored energy. *Physics of Plasmas* **19**, doi:10.1063/1.4766744 (2012)
92. S. Lee, S.H. Saw, Plasma focus ion beam fluence and flux-For various gases. *Physics of Plasmas* **20**, doi:10.1063/1.4811650 (2013)
93. M.S. Rafique, P. Lee, A. Patran, R.S. Rawat, S. Lee, Radiation emission correlated with the evolution of current sheath from a deuterium plasma focus. J. Fusion Energy **29**, 295–304 (2010). doi:10.1007/s10894-010-9276-0
94. J.F. Ziegler, *SRIM—The Stopping and Range of Ions in Matter*. http://www.srim.org/

95. G. Sanchez, J. Feugeas, The thermal evolution of targets under plasma focus pulsed ion implantation. J. Phys. D-Appl. Phys. **30**, 927–936 (1997)
96. M.V. Roshan, et al. Backward high energy ion beams from plasma focus. *Phys. Plasmas* **16**, 074506, doi:10.1063/1.3183715 (2009)
97. A. Patran et al., A magnetic electron analyzer for plasma focus electron energy distribution studies. J. Fusion Energy **25**, 57–66 (2006). doi:10.1007/s10894-006-9005-x
98. R. Gupta, M.P. Srivastava, Carbon ion implantation on titanium for TiC formation using a dense plasma focus device. Plasma Sources Sci. Technol. **13**, 371–374 (2004). doi:10.1088/0963-0252/13/3/002
99. M. Hassan, A. Qayyum, R. Ahmad, G. Murtaza, M. Zakaullah, Nitriding of titanium by using an ion beam delivered by a plasma focus. J. Phys. D-Appl. Phys. **40**, 769–777 (2007). doi:10.1088/0022-3727/40/3/013
100. M. Hassan et al., Synthesis of nanocrystalline multiphase titanium oxycarbide (TiC_xO_y) thin films by UNU/ICTP and NX2 plasma focus devices. Appl. Phys. A-Mat. Sci. Process. **90**, 669–677 (2008). doi:10.1007/s00339-007-4335-8
101. M. Hassan et al., Dense plasma focus ion-based titanium nitride coating on titanium. Nucl. Instrum. Methods Phys. Res. Sect. B-Beam Interact. Mat. Atoms **267**, 1911–1917 (2009). doi:10.1016/j.nimb.2009.03.102
102. H. Bhuyan, et al., High energy ion beam irradiation on titanium substrate in a pulsed plasma device operating with methane. J. Phys. D-Appl. Phys. **42**, 205207, doi:10.1088/0022-3727/42/20/205207 (2009)
103. M. Valipour, M.A. Mohammadi, S. Sobhanian, R.S. Rawat, Increasing of hardness of titanium using energetic nitrogen ions from sahand as a filippov type plasma focus facility. J. Fusion Energy **31**, 65–72 (2012). doi:10.1007/s10894-011-9432-1
104. V.A. Gribkov et al., Interaction of high temperature deuterium plasma streams and fast ion beams with stainless steels in dense plasma focus device. J. Phys. D-Appl. Phys. **36**, 1817–1825 (2003)
105. M. Shafiq et al., Dense plasma focus-assisted nitriding of AISI-304. Radiat. Eff. Defects Solids **163**, 729–736 (2008). doi:10.1080/10420150701365664
106. J. Feugeas et al., Austenite modification of AISI 316L SS by pulsed nitrogen ion beams generated in dense plasma focus discharges. Surf. Coat. Technol. **204**, 1193–1199 (2010). doi:10.1016/j.surfcoat.2009.10.034
107. M. Sadiq, M. Shafiq, A. Waheed, R. Ahmad, M. Zakaullah, Amorphization of silicon by ion irradiation in dense plasma focus. Phys. Lett. A **352**, 150–154 (2006). doi:10.1016/j.physleta.2005.11.058
108. M. Sadiq, S. Ahmad, M. Shafiq, M. Zakaullah, Nitrogen ion implantation of silicon in dense plasma focus. Nuclear Instrum. Methods Phys. Res. Sect. B-Beam Interact. Mat. Atoms **252**, 219–224 (2006). doi:10.1016/j.nimb.2006.08.020
109. H. Bhuyan et al., Effect of high energy ion irradiation on silicon substrate in a pulsed plasma device. Appl. Surf. Sci. **254**, 197–200 (2007). doi:10.1016/j.apsusc.2007.07.029
110. H. Bhuyan et al., Formation of hexagonal silicon carbide by high energy ion beam irradiation on Si(100) substrate. J. Phys. D-Appl. Phys. **40**, 127–131 (2007). doi:10.1088/0022-3727/40/1/003
111. Z.R. Wang, H.R. Yousefi, Y. Nishino, H. Ito, K. Masugata, Preparation of silicon carbide film by a plasma focus device. Phys. Lett. A **372**, 7179–7182 (2008). doi:10.1016/j.physleta.2008.10.062
112. S. Jabbar, I.A. Khan, R. Ahmad, M. Zakaullah, J.S. Pan, Carbonitriding of silicon using plasma focus device. J. Vac. Sci. Technol., A **27**, 381–387 (2009). doi:10.1116/1.3085720
113. M. Ahmad, S. Al-Hawat, M. Akel, Porous structure formation on silicon surface treated by plasma focus device. J. Fusion Energy **32**, 471–478 (2013). doi:10.1007/s10894-013-9596-y
114. M.V. Roshan et al., High energy ions and energetic plasma irradiation effects on aluminum in a Filippov-type plasma focus. Appl. Surf. Sci. **255**, 2461–2465 (2008). doi:10.1016/j.apsusc.2008.07.152

115. Z.S. Rad, M. Shahriari, F.A. Davani, Investigation of spatial distribution of hydrogen and argon ions and effects of them on aluminum samples in a 2.5 kJ mater type plasma focus device. J. Fusion Energy **30**, 358–366 (2011). doi:10.1007/s10894-011-9405-4
116. M. Afrashteh, M. Habibi, Study of dense nitrogen plasma irradiation of aluminum targets by APF plasma focus device. J. Fusion Energy **31**, 223–226 (2012). doi:10.1007/s10894-011-9463-7
117. L. Rico, B.J. Gomez, J. Feugeas, O. de Sanctis, Crystallization of amorphous zirconium thin film using ion implantation by a plasma focus of 1 kJ. Appl. Surf. Sci. **254**, 193–196 (2007). doi:10.1016/j.apsusc.2007.07.028
118. I.A. Khan et al., Nitridation of zirconium using energetic ions from plasma focus device. Thin Solid Films **516**, 8255–8263 (2008). doi:10.1016/j.tsf.2008.03.012
119. I.A. Khan et al., Synthesis of zirconium oxynitride (ZrON) nanocomposite films on zirconium substrate by dense plasma focus device. Int. J. Mod. Phys. B **22**, 3941–3955 (2008)
120. I.A. Khan et al., Synthesis of nano-crystalline zirconium aluminium oxynitride (ZrAlON) composite films by dense plasma Focus device. Appl. Surf. Sci. **255**, 6132–6140 (2009). doi:10.1016/j.apsusc.2009.01.066
121. I.A. Khan et al., Deposition of zirconium carbonitride composite films using ion and electron beams emitted from plasma focus device. Nucl. Instrum. Methods Phys. Res. Sect. B-Beam Interact. Mat. Atoms **268**, 2228–2234 (2010). doi:10.1016/j.nimb.2010.03.030
122. G. Murtaza et al., Carburizing of zirconium using a low energy Mather type plasma focus. Surf. Coat. Technol. **205**, 3012–3019 (2011). doi:10.1016/j.surfcoat.2010.11.015
123. I.A. Khan, R.S. Rawat, R. Ahmad, M.A.K. Shahid, Deposition of alumina stabilized zirconia at room temperature by plasma focus device. Appl. Surf. Sci. **288**, 304–312 (2014). doi:10.1016/j.apsusc.2013.10.025
124. S.R. Mohanty et al., Energetic ion irradiation of American diamond in a plasma focus device and characterization of irradiated material. Nucl. Instrum. Methods Phys. Res. Sect. B-Beam Interact. Mat. Atoms **243**, 113–118 (2006). doi:10.1016/j.nimb.2005.07.199
125. M. Bhuyan, S.R. Mohanty, C.V.S. Rao, P.A. Rayjada, P.M. Raole, Plasma focus assisted damage studies on tungsten. Appl. Surf. Sci. **264**, 674–680 (2013). doi:10.1016/j.apsusc.2012.10.093
126. J. Siddiqui et al., Growth and study of plasma assisted nanostructured hard tantalum nitride thin films. J. Fusion Energy **34**, 1193–1202 (2015). doi:10.1007/s10894-015-9943-2
127. V.A. Gribkov, et al., Experimental studies of radiation resistance of boron nitride, C2C ceramics Al2O3 and carbon-fiber composites using a PF-1000 plasma-focus device. *Physica Scripta* **83**, doi:10.1088/0031-8949/83/04/045606 (2011)
128. M. Habibi, M.H.S. Alavi, Argon ion beam interaction on polyethylene terephthalate surface by a 4 kJ plasma focus device. Pramana-J. Phys. **86**, 599–607 (2016). doi:10.1007/s12043-015-1024-6
129. R.S. Rawat, Dense plasma focus—from alternative fusion source to versatile high energy density plasma source for plasma nanotechnology. *15th Latin American Workshop on Plasma Physics (Lawpp 2014) and 21st Iaea Tm on Research Using Small Fusion Devices (Rusfd)* **591**, doi:10.1088/1742-6596/591/1/012021 (2015)
130. M. Chernyshova et al., Interaction of powerful hot plasma and fast ion streams with materials in dense plasma focus devices. Fusion Eng. Des. **113**, 109–118 (2016). doi:10.1016/j.fusengdes.2016.11.003
131. R. Sagar, M.P. Srivastava, Amorphization of thin film of CdS due to ion irradiation by dense plasma focus. Phys. Lett. A **183**, 209–213 (1993)
132. P. Agarwala, S. Annapoorni, M.P. Srivastava, R.S. Rawat, P. Chauhan, Magnetite phase due to energetic argon ion irradiation from a dense plasma focus on hematite thin film. Phys. Lett. A **231**, 434–438 (1997)

133. R.S. Rawat et al., Effect of argon ion irradiation on Sb2Te3 films in a dense plasma focus device. Mater. Res. Bull. **35**, 477–486 (2000)
134. R.S. Rawat, P. Arun, A.G. Vedeshwar, P. Lee, S. Lee, Effect of energetic ion irradiation on CdI2 films. J. Appl. Phys. **95**, 7725–7730 (2004). doi:10.1063/1.1738538
135. S. Karamat et al., Nitrogen doping in pulsed laser deposited ZnO thin films using dense plasma focus. Appl. Surf. Sci. **257**, 1979–1985 (2011). doi:10.1016/j.apsusc.2010.09.038
136. J.J. Lin, et al., FePt nanoparticle formation with lower phase transition temperature by single shot plasma focus ion irradiation. J. Phys. D-Appl. Phys. **41**, doi:10.1088/0022-3727/41/13/135213 (2008)
137. Z.Y. Pan et al., Nanostructuring of FePt thin films by plasma focus device: pulsed ion irradiation dependent phase transition and magnetic properties. Appl. Phys. A-Mat. Sci. Process. **96**, 1027–1033 (2009). doi:10.1007/s00339-009-5138-x
138. Z.Y. Pan et al., Lowering of L1(0) phase transition temperature of FePt thin films by single shot H + ion exposure using plasma focus device. Thin Solid Films **517**, 2753–2757 (2009). doi:10.1016/j.tsf.2008.11.113
139. M.P. Srivastava, S.R. Mohanty, S. Annapoorni, R.S. Rawat, Diode like behaviour of an ion irradiated polyaniline film. Phys. Lett. A **215**, 63–68 (1996)
140. D.E. Alexander, L.E. Rehn, P.M. Baldo, Y. Gao, Appl. Phys. Lett. **62**, 1597 (1993)
141. R.S. Rawat, W.M. Chew, P. Lee, T. White, S. Lee, Deposition of titanium nitride thin films on stainless steel - AISI 304 substrates using a plasma focus device. Surf. Coat. Technol. **173**, 276–284 (2003). doi:10.1016/s0257-8972(03)00628-5
142. R. Gupta, M.P. Srivastava, V.R. Balakrishnan, R. Kodama, M.C. Peterson, Deposition of nanosized grains of ferroelectric lead zirconate titanate on thin films using dense plasma focus. J. Phys. D-Appl. Phys. **37**, 1091–1094 (2004). doi:10.1088/0022-3727/37/7/022
143. R.S. Rawat, T. Zhang, K.S.T. Gan, P. Lee, R.V. Ramanujan, Nano-structured Fe thin film deposition using plasma focus device. Appl. Surf. Sci. **253**, 1611–1615 (2006). doi:10.1016/j.apsusc.2006.02.047
144. T. Zhang, K.S.T. Gan, P. Lee, R.V. Ramanujan, R.S. Rawat, Characteristics of FeCo nano-particles synthesized using plasma focus. J. Phys. D-Appl. Phys. **39**, 2212–2219 (2006). doi:10.1088/0022-3727/39/10/033
145. R.S. Rawat et al., Nano-phase titanium dioxide thin film deposited by repetitive plasma focus: Ion irradiation and annealing based phase transformation and agglomeration. Appl. Surf. Sci. **255**, 2932–2941 (2008). doi:10.1016/j.apsusc.2008.08.055
146. Z.Y. Pan, et al., Nanostructured magnetic CoPt thin films synthesis using dense plasma focus device operating at sub-kilojoule range. J. Phys. D-Appl. Phys. **42**, 175001, doi:10.1088/0022-3727/42/17/175001 (2009)
147. Y. Malhotra, S. Roy, M.P. Srivastava, C.R. Kant, K. Ostrikov, Extremely non-equilibrium synthesis of luminescent zinc oxide nanoparticles through energetic ion condensation in a dense plasma focus device. J. Phys. D-Appl. Phys. **42**, 155202, doi:10.1088/0022-3727/42/15/155202 (2009)
148. E. Ghareshabani et al., Synthesis of nanostructured multiphase Ti(C, N)/a-C films by a plasma focus device. Nucl. Instrum. Methods Phys. Res. Sect. B-Beam Interact. Mat. Atoms **268**, 2777–2784 (2010). doi:10.1016/j.nimb.2010.06.027
149. Z.Y. Pan et al., Miniature plasma focus as a novel device for synthesis of soft magnetic FeCo thin films. Phys. Lett. A **374**, 1043–1048 (2010). doi:10.1016/j.physleta.2009.12.037
150. G. Macharaga et al., TiO_2 nano-cluster thin films by dense plasma focus and ion implantation effect on its photocatalytic activity. J. Adv. Oxid. Technol. **14**, 308–313 (2011)
151. G.R. Etaati, M.T. Hosseinnejad, M. Ghoranneviss, M. Habibi, M. Shirazi, Deposition of tungsten nitride on stainless steel substrates using plasma focus device. Nucl. Instrum. Methods Phys. Res. Sect. B-Beam Interact. Mat. Atoms **269**, 1058–1062 (2011). doi:10.1016/j.nimb.2011.02.083

152. M.T. Hosseinnejad, M. Ghoranneviss, G.R. Etaati, M. Shirazi, Z. Ghorannevis, Deposition of tungsten nitride thin films by plasma focus device at different axial and angular positions. Appl. Surf. Sci. **257**, 7653–7658 (2011). doi:10.1016/j.apsusc.2011.03.155
153. S. Javadi, M. Ghoranneviss, A. Hojabri, M. Habibi, M.T. Hosseinnejad, Deposition of chromium thin films on stainless steel-304 substrates using a low energy plasma focus device. J. Fusion Energy **31**, 242–248 (2012). doi:10.1007/s10894-011-9461-9
154. S.K. Ngoi et al., Formation of nano-crystalline phase in hydrogenated amorphous silicon thin film by plasma focus ion beam irradiation. J. Fusion Energy **31**, 96–103 (2012). doi:10.1007/s10894-011-9435-y
155. M.T. Hosseinnejad, M. Shirazi, Z. Ghorannevis, M. Ghoranneviss, F. Shahgoli, Using mather-type plasma focus device for fabrication of tungsten thin films. J. Fusion Energy **31**, 426–431 (2012). doi:10.1007/s10894-011-9488-y
156. Z.A. Umar et al., Hard TiC_x/SiC/A-C: H nanocomposite thin films using pulsed high energy density plasma focus device. Nucl. Instrum. Methods Phys. Res. Sect. B-Beam Interact. Mat. Atoms **301**, 53–61 (2013). doi:10.1016/j.nimb.2013.03.007
157. J.J. Lin, et al., Backward plume deposition as a novel technique for high deposition rate Fe nanoclusters synthesis. *Nanotechnology* **18**, doi:10.1088/0957-4484/18/11/115617 (2007)
158. K.S. Tan, R.J. Mah, R.S. Rawat, Dense plasma focus device based high growth rate room temperature synthesis of nanostructured zinc oxide thin films. IEEE Trans. Plasma Sci. **43**, 2539–2546 (2015). doi:10.1109/tps.2015.2445055
159. L. García-Gancedo et al., Room-temperature remote-plasma sputtering of c-axis oriented zinc oxide thin films. J. Appl. Phys. **112**, 014907 (2012)
160. C. Sima et al., Porous nanostructured ZnO films deposited by picosecond laser ablation. Mater. Sci. Eng., B **177**, 1188–1193 (2012)
161. S. Lee et al., High rep rate high performance plasma focus as a powerful radiation source. IEEE Trans. Plasma Sci. **26**, 1119–1126 (1998)
162. S. Stauss, Y. Imanishi, H. Miyazoe, K. Terashima, High rate deposition of ZnO thin films by a small-scale inductively coupled argon plasma generated in open air. J. Phys. D Appl. Phys. **43**, 155203 (2010)
163. C. James, B. Bures, R. Madden, M. Krishnan, R. Adler, in *2011 IEEE Pulsed Power Conference*, pp. 1522–1525 (IEEE)
164. U. Ilyas et al., Enhanced ferromagnetic response in ZnO: Mn thin films by tailoring composition and defect concentration. J. Magn. Magn. Mater. **344**, 171–175 (2013). doi:10.1016/j.jmmm.2013.05.040
165. U. Ilyas et al., Alteration of Mn exchange coupling by oxygen interstitials in ZnO: Mn thin films. Appl. Surf. Sci. **258**, 6373–6378 (2012). doi:10.1016/j.apsusc.2012.03.043
166. U. Ilyas, et al., Oxygen rich p-type ZnO thin films using wet chemical route with enhanced carrier concentration by temperature-dependent tuning of acceptor defects. J. Appl. Phys. **110**, doi:10.1063/1.3660284 (2011)
167. S. Karamat et al., Ferromagnetism in ZnCoO thin films deposited by PLD. Appl. Phys. A-Mat. Sci. Process. **101**, 717–722 (2010). doi:10.1007/s00339-010-5928-1
168. S. Karamat et al., Structural, optical and magnetic properties of $(ZnO)(1-x)(MnO_2)(x)$ thin films deposited at room temperature. Appl. Surf. Sci. **254**, 7285–7289 (2008). doi:10.1016/j.apsusc.2008.05.318
169. D. Mardare, A. Stancu, On the optical constants of TiO2 thin films. Ellipsometric stud. Mat. Res. Bull. **35**, 2017–2025 (2000). doi:10.1016/s0025-5408(00)00408-6
170. D. Mardare, M. Tasca, M. Delibas, G.I. Rusu, On the structural properties and optical transmittance of TiO_2 r.f. sputtered thin films. Appl. Surf. Sci. **156**, 200–206 (2000). doi:10.1016/s0169-4332(99)00508-5
171. B. Lin, Z. Fu, Y. Yia, Appl. Phys. Lett. **79**, 943 (2001)

172. J.J. Lin, et al., FePt: Al_2O_3 nanocomposite thin films synthesized by magnetic trapping assisted pulsed laser deposition with reduced intergranular exchange coupling. J. Phys. D-Appl. Phys. **41**, doi:10.1088/0022-3727/41/9/095001 (2008)
173. Y. Wang et al., Elimination of impurity phase formation in FePt magnetic thin films prepared by pulsed laser deposition. Appl. Surf. Sci. **288**, 381–391 (2014). doi:10.1016/j.apsusc.2013.10.036
174. Z.Y. Pan et al., Oriented growth of CoPt nanoparticles by pulsed laser deposition. Appl. Phys. A-Mat. Sci. Process. **101**, 609–613 (2010). doi:10.1007/s00339-010-5937-0
175. J. Moreno, P. Silva, L. Soto, Optical observations of the plasma motion in a fast plasma focus operating at 50J. Plasma Sources Sci. Technol. **12**, 39–45 (2003)

Chapter 3
The Plasma Focus—Numerical Experiments, Insights and Applications

S. Lee and S.H. Saw

3.1 Introduction

3.1.1 Introduction to the Plasma Focus—Description of the Plasma Focus. How It Works, Dimensions and Lifetimes of the Focus Pinch

The Plasma Focus is a compact powerful-pulsed source of multi-radiation [1–3]. Even a small table top sized 3 kJ plasma focus produces an intense burst of radiation with extremely high powers. For example when operated in neon, the X-ray emission power peaks at 10^9 W over a period of tens of nanoseconds. When operated in deuterium the fusion neutron burst produces rates of neutron typically 10^{15} neutrons per second over burst durations of tens of nanosecond. The emission comes from a point-like source making these devices among the most powerful laboratory pulsed radiation sources in the world. These sources are plasma-based. There are two main types of plasma focus classified according to the aspect ratio of the anode. The Filippov type [4] has an anode with a radius larger than its length. The Mather type [5] has a radius smaller than its length. In this chapter, we discuss the Mather-type plasma focus.

S. Lee (✉) · S.H. Saw
Institute for Plasma Focus Studies, 32 Oakpark Drive, Melbourne, VIC, Australia
e-mail: leesing@optusnet.com.au

S. Lee · S.H. Saw
Nilai University, 71800 Nilai, Malaysia

S. Lee
University of Malaya, Kuala Lumpur, Malaysia

S. Lee · S.H. Saw
INTI International University, 71800 Nilai, Malaysia

R.S. Rawat (ed.), *Plasma Science and Technology for Emerging Economies*,
DOI 10.1007/978-981-10-4217-1_3

When matter is heated to a high enough temperature, it ionizes and becomes plasma. It emits electromagnetic radiation. The spectrum depends on the temperature and the material. The higher the temperature and the denser the matter, the more intense is the radiation. Beams of electrons and ions may also be emitted. If the material is deuterium, nuclear fusion may take place if the density and temperature are high enough. In that case, neutrons are also emitted. Typically the temperatures are above several million K and compressed densities above atmospheric density starting with a gas a hundredth of an atmospheric density.

One way of achieving such highly heated material is by means of an electrical discharge through gases. As the gas is heated, it expands, lowering the density and making it difficult to heat further. Thus it is necessary to compress the gas whilst heating it, in order to achieve sufficiently intense conditions. An electrical discharge between two electrodes produces an azimuthal magnetic field which interacts with the column of current, giving rise to a self-compression force which tends to constrict (or pinch) the column. In order to 'pinch', or hold together, a column of gas at about atmospheric density at a temperature of 1 million K, a rather large pressure has to be exerted by the pinching magnetic field. Thus an electric current of at least hundreds of kA is required even for a column of small radius of say 1 mm. Moreover, the dynamic process requires that the current rises very rapidly, typically in under 0.1 μs in order to have a sufficiently hot and dense pinch. Such a pinch is known as a super fast super dense pinch, and requires special MA fast-rise (ns) pulsed-lines. These lines may be powered by capacitor banks, and suffer the disadvantage of conversion losses and high cost due to the cost of the high technology pulse-shaping line, in addition to the capacitor banks.

A superior method of producing the super dense and super hot pinch is to use the plasma focus. Not only does this device produce superior densities and temperatures, moreover its method of operation does away with the extra layer of technology required by the expensive and inefficient pulse-shaping line. A simple capacitor discharge is sufficient to power the plasma focus.

The plasma focus

The Mather-type plasma focus is divided into two sections, the axial and the radial sections (see Fig. 3.1). The function of the axial (pre-pinch) section is primarily to delay the pinch until the capacitor discharge (rising in a distorted sinusoidal fashion) approaches its maximum current. This is done by driving a current sheet down an axial (acceleration) section until the capacitor current approaches its peak. Then the current sheet is allowed to undergo transition into a radial compression phase. Thus the pinch starts and occurs at the top of the current pulse. This is equivalent to driving the pinch with a super fast rising current without necessitating the fast line technology. Moreover, the intensity which is achieved is superior to the line driven pinch.

The simplified two-phase mechanism of the plasma focus [6] is shown in Fig. 3.1. The inner electrode (anode) is separated from the outer concentric cathode by an insulating back wall. The electrodes are enclosed in a chamber, evacuated and

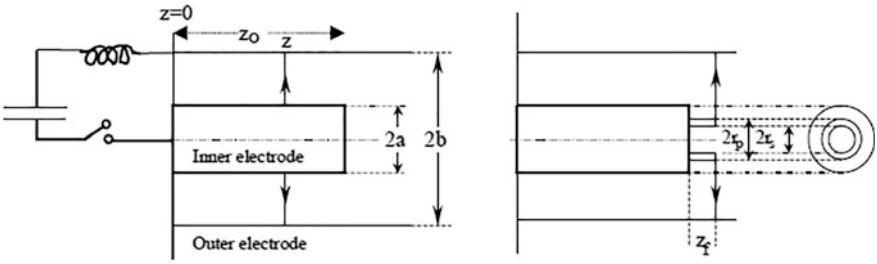

Fig. 3.1 Schematic cross sections of the axial and radial phases. The *left section* depicts the axial phase, the *right section* depicts the radial phase. In the *left section*, z is the effective position of the current sheath-shock front structure. In the *right section* r_s is the position of the inward moving shock front driven by the piston at position r_p. Between r_s and r_p is the radially imploding slug, elongating with a length z_f. The capacitor, static inductance and switch powering the plasma focus are shown for the axial phase schematic only

typically filled with gas at about 1/100 of atmospheric pressure. When the capacitor voltage is switched onto the focus tube, breakdown occurs axisymmetrically between the anode and cathode across the back wall. The 'sheet' of current lifts off the back wall as the magnetic field (B_θ) and it's inducing a current (J_r) rises to a sufficient value.

Axial phase: The $\boldsymbol{J}_r \times \boldsymbol{B}_\theta$ force then pushes the current sheet, accelerating it supersonically down the tube. This is very similar to the mechanism of a linear motor. The speed of the current sheet, the length of the tube and the rise time of the capacitor discharge are matched so that the current sheet reaches the end of the axial section just as the discharge reaches its quarter cycle. This phase typically lasts 1–3 μs for a plasma focus of several kJ.

Radial Phase: The part of the current sheet in sliding contact with the anode then 'slips' off the end 'face' of the anode forming a cylinder of current, which is then pinched inwards. The wall of the imploding plasma cylinder has two boundaries (see Fig. 3.1 radial phase). The inner face of the wall, of radius r_s is an imploding shock front. The outer side of the wall, of radius r_p is the imploding current sheet, or magnetic piston. Between the shock front and the magnetic piston is the annular layer of plasma. Imploding inwards at higher and higher speeds, the shock front coalesces on-axis and a super dense, super hot plasma column is pinched onto the axis (see Fig. 3.2). This column stays super hot and super dense for typically tens of ns for a small focus. The column then breaks up and explodes. For a small plasma focus of several kJ, the most intense emission phase lasts for the order of several tens of ns. The radiation source is spot-like (1 mm diameter) when viewed end-on.

Figure 3.3 shows a drawing of a typical plasma focus, powered by a single capacitor, switched by a simple parallel-plate spark gap [7]. The anode may be a hollow copper tube so that during the radial pinching phase the plasma not only elongates away from the anode face but also extends and elongates into the hollow anode (see Fig. 3.2). Figure 3.3 shows the section where the current sheet is

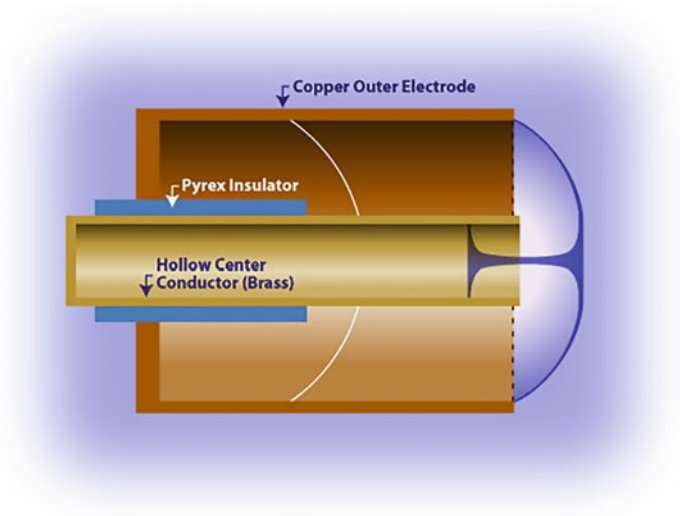

Fig. 3.2 Dense plasma focus device. *Source* Focus Fusion Society [202]

accelerated axially and also the radial section. Also shown in the same figure are shadowgraphs [8] taken from the actual radially imploding current sheet-shock front structure. The shadowgraphs are taken in a sequence, at different times. The times indicated on the shadowgraphs are relative to the moment judged to be the moment of maximum compression. That moment is taken as $t = 0$. The quality of the plasma compression can be seen to be very good, with excellent axisymmetry, and a very well compressed dense phase. In the lower left of Fig. 3.3 are shown the current and voltage signatures of the radial implosion [9], occurring at peak current. The implosion speeds are measured and have a peak value approaching 30 cm/μs.

This agrees with modelling, and by considering shock wave theory together with modelling [10] of subsequent reflected shock wave and compressive effects, a temperature of 6 million K (0.5 keV) is estimated for the column at peak compression, with a density of 10^{19} ions per cm^3. The values quoted here are for the UNU/ICTP PFF 3 kJ device [7]. Dimensions and lifetimes of the pinch are indicated by these images.

An observed property of plasma focus machines is that they operate at similar speeds. A sub-kJ focus [11] has about the same peak axial speed and the same (higher) peak radial speed as a 1 MJ focus [12]. Since the square of speed represents energy density (energy per unit mass) this means the machines achieve similar temperatures in each of their dynamical phases and also similar highest temperatures in the plasma focus pinch. This is a remarkable scaling property of the plasma focus which will be discussed further in this chapter.

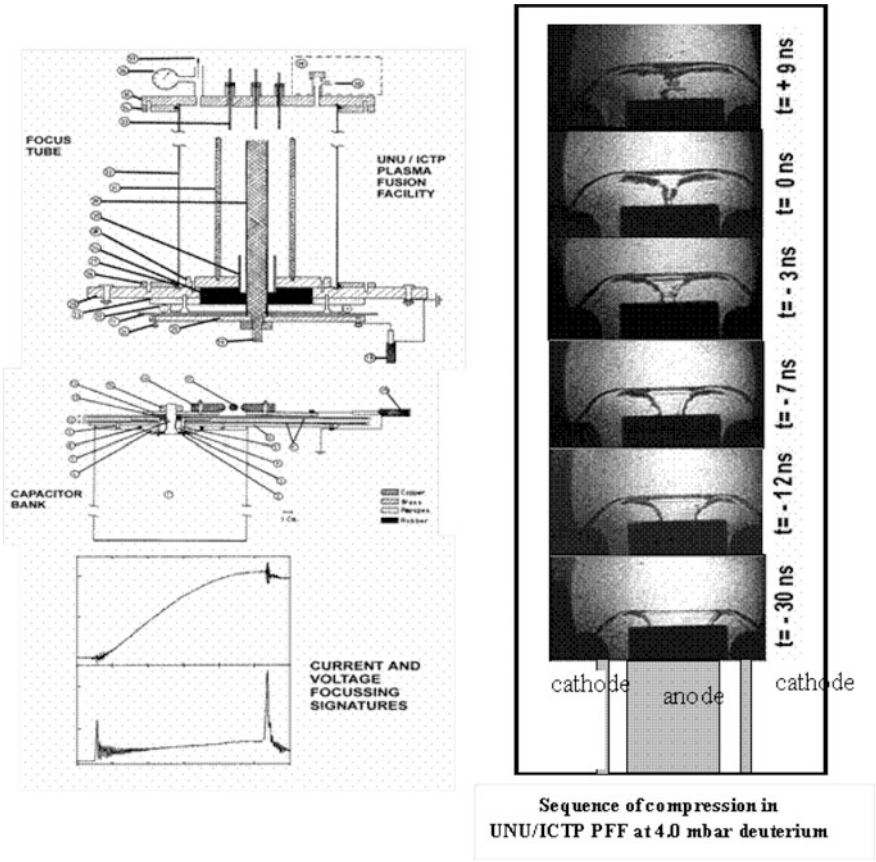

Fig. 3.3 UNU/ICTP PFF—design, signatures and dynamics [8, 9]

3.1.2 Review of Models and Simulation

Observations of the axial acceleration phase of the plasma focus show that typically the current sheath travels at greater than Mach 10 speeds over more than 95% of the axial phase. Thus the axial phase is in the strong-shock electromagnetic regime and may be approximated by a snowplow model essentially considering a thin sheath trapping all encountered mass which is driven by the self-generated electromagnetic force of the current flowing through the ionized sheath. Such a model was used by Rosenbluth [13].

Such one-fluid formulation of a thin (impermeable piston-like 'snowplow') current sheath was also presented by various authors [14–16] justifiable on assumptions of small ion–electron collision times, ion–ion collision lengths being short compared to shock layer thickness, and infinite conductivity or at least large magnetic Reynolds number. Shock conservation equations in 2-D were used.

A similar one-fluid time-dependent model was solved by Amsden [17] by the particle-in-cell method with good agreement with experimental results of the shape of the sheath for a coaxial gun with no outer electrode. The one-fluid model has a serious limitation, as it does not consider the effects of ionization. Whilst that may not affect the equation of conservation of momentum it certainly affects the calculation of temperature and of the structure of layers near the interaction zones with the electrodes.

Two-dimensional two-fluid models [18, 19] were developed for MHD modelling of an entire plasma focus discharge (until the final pinch phase) assuming a thin fully ionized plasma layer as an initial condition. Potter's work [18] was used to discuss many aspects of flow dynamics within the plasma focus pinch. Cylindrical symmetry is assumed so that each dependent variable is a function of r, z, t radius, axial position and time, respectively. The plasma is described by six dependent variables namely ρ, $\rho \boldsymbol{v}$, B_o, $\rho\varepsilon_e$ and $\rho\varepsilon_i$ where ρ is the plasma density, $\boldsymbol{v}$ is the centre of mass velocity with two components, B_o is the azimuthal magnetic field and $\varepsilon_{e,}$ ε_i are the thermal energy densities per unit fluid mass for the electrons and ions, respectively. The MHD equations are the conservation of mass, momentum and magnetic flux appropriately for the dependent variables ρ, $\rho \boldsymbol{v}$, B_o, respectively, with the total pressure tensor in the momentum equation being written as the sum of the scalar pressure with electron and ion contributions and the current density $\boldsymbol{j}$ in the momentum equation calculated from the curl of B_o. The conservation of energy is written in the form of two separate equations for the electron and ion thermal energy densities in which terms due to Joule heating, bremsstrahlung radiation, equipartition of energy between electrons and ions, viscous heating, electron and ion heat conduction are included. The thermal energy densities of the electrons and ions are, respectively, written in terms of the electron temperature and the ion temperature using the specific heat ratio. Quasi-neutrality is assumed which defines the electron velocity in terms of the ion or ambipolar plasma velocity. Maxwell's equations and the generalized Ohm's law, defining the electric field, complete the set of MHD equations. In the process of solving the equations variable transport coefficients for the electron and ion heat conductivities, resistivity, viscosity and equipartition times are used. Ion orbiting effects are included incorporating finite Larmor radius effects. Boundary conditions are specified and the domain of dependence is coupled with an external L–C circuit. The equations are integrated over small time steps, using second-order two-step Lax-Wendroff method. To increase the spatial resolution in the focus stage a fine scale mesh is introduced at the end of the centre electrode. The results of the computation show three main regions in the focus pinch: an anode cold source, a hot pinch region and an axial shock. The observed anomalously long lifetime of the plasma focus is shown to be the result of axial flow with stabilization of MHD modes through the ion stress tensor in the intermediate collisionless, collision-dominated regime.

For explaining the experimental results of D–D neutron yield from the specific plasma focus device, Potter used a thermonuclear mechanism. Potter extracted results based on the computed temperature and density profiles. Although his visualization of the two-dimensional flows within the pinch column had several

points of agreement with experimental observations, his conclusion of a mainly thermonuclear fusion mechanism within pinch column was presumably affected by computed flow velocities of too high a value. The consensus view today from generations of experiments is that the fusion mechanism of the plasma focus has a main component which is beam-plasma target [1, 2, 12, 20–22].

A three-fluid MHD model by Bazdenkov and Vikhrev took into account the initial ionization [23]. In a similar manner, Behler and Bruhns [24] extended the two-fluid Potter code to a three-fluid model. With the three-fluid treatment, neutral gas was added to the plasma components to incorporate the effects of recombination and ionization. Additional mass, momentum and energy conservation equations were written for the neutral component of the fluid. Treating the elastic processes in a similar way as Potter's work, for the inelastic processes Behler and Bruhns considered electron impact ionization from the ground state, radiative recombination, three-body Auger recombination and charge exchange. Various approximations were also made in adjustments of the coefficients of these processes. The sheet dynamics were studied including residual gas (or plasma) density behind the current sheet in the run-down phase leading to the occurrence of leak currents.

Behler and Bruhns [24] applied the resultant three-fluid model to SPEED 1 with an initial (starting) current of 1 kA assumed to flow along the insulator. Subsequent current was determined by the circuit equation. The results show the dynamics of the lift-off and the structure of the residual neutral density, followed by the dynamics of the current sheath. At 250 ns the sheet has almost reached the end of the centre electrode (the anode) with an axial speed of 20 cm/μs about 8% faster than the two-fluid model. During this time a neutral density of up to 2×10^{16} cm^{-3} is left behind, the maximum is close to the anode at z = 4–6 cm). Beyond the tip of the anode, the accelerated sheet continues to move axially. The radial velocity attains 12.5 cm/μs, leading to a total time of 510 ns from breakdown to maximum compression compared to experimentally observed of 470 ns. The calculated maximum current of 780 kA occurs at 380 ns compared to 770 kA appearing at 370 ns. However, the current dip is less pronounced in the computation than observed experimentally and the computed pinch radius remains much larger than inferred from Schlieren pictures. The late pinch phase could not be simulated due to the finite mesh size and the inapplicability of the MHD model. The model code was also applied to SPEED 2, the 250 kJ high-speed Poseidon and the large Frascati PF (1 MJ). Their conclusion is that there is a comparatively good agreement in all cases between the calculated overall features of the discharges and experiments. In particular, the three-fluid 2-D model could provide the leakage currents and had points of agreement in the axial and radial dynamics in both the dynamics and structure of the current sheet. The computation could not be completed to the later part of the pinch.

Magnetohydrodynamic codes face this same problem. In a paper by Nukulin and Polukhin [25] the MHD computed current waveform of PF1000 using the Vikhrev MHD code [26] was also compared with the measured current waveform. The computed waveform agrees well with the measured down to about a third of the current dip. The computed current had a value of 1.6 MA at peak compression

compared to a measured value of 1.1 MA at peak compression, indicating that the MHD treatment was unable to correctly describe the current waveform for a large part of the pinch which occurs at the end of the pinch towards maximum compression and beyond.

The failure of MHD codes to describe this crucial part of the pinching process is due to the breakdown of the assumptions used in calculating the transport coefficients. To avoid such failures one way is to use the kinetic method. The fluid MHD approach considers each dependent variable as a function of space and time (4 independent variables for 3-D simulation and 3 independent variables for 2-D simulation) with the velocity distribution of each species assumed to be Maxwellian everywhere so that it may be uniquely specified by only one number, the temperature T [27]. The kinetic method being a fundamental approach makes no such assumption so that each dependent variable is a function of space, velocity space and time (7 independent variables for 3-D simulation and 5 independent variables for 2-D simulation). The plasma is described by a distribution function which is a function of space, velocity space and time. The basic conservation law is described by Liouville Theorem which in the form of Boltzmann Equation enables to follow the evolution of the distribution function with time. Once the distribution function is obtained at any time at any point of space, any macroscopic quantity may be obtained by integrating the product of that quantity with the velocity distribution function over all velocity space.

A. Schmidt et al. used fully kinetic simulations applied to a kJ plasma focus [28, 29]. They demonstrated that both kinetic ions and kinetic electrons are needed to reproduce experimentally observed features, such as charged-particle beam formation and anomalous resistivity. A. Schmidt et al. extended the method to megajoule-scale plasma focus devices [30] specifically for the Gemina. The cathode (outer electrode) was simulated by a conducting boundary at $r = 10$ cm to represent the set of 24 rectangular rods arranged in a circular pattern with gaps in between where gas can escape. The experimental anode was 57 cm long. To reduce simulation run time the calculation was initialized with 2-D MHD simulation using ALEGRA [31]. The fluid simulation began with the plasma sheath at the insulator and proceeded into the sheath run-in radial phase at 6.6 μs, when the plasma profiles were transferred to the particle-in-cell (PIC) code large scale plasmas (*LSP*) [32] for kinetic simulation with time step dynamically varied from 2.5×10^{-4} to 8×10^{-6} ns to resolve the electron cyclotron frequency. Densities at $z < 9.5$ cm were set to 0 to reduce the total number of particles in the simulation. The kinetic simulation was then run for a total of 26 ns; 11 ns prior to the formation of the pinch and for an additional 15 ns of the pinch. The voltage drive was modelled with a prescribed incoming voltage wave travelling the length of the anode, with a reflected wave travelling back. The voltage was ramped up during the first 10 ns of the simulation and then kept constant for the remainder of the simulation, resulting in a steady state current of 1.94 MA before the pinch formation. At the end of the 26 ns of kinetic simulation, the pinch had not completely stopped producing neutrons. The simulation was stopped due to computing resource limitations and the remaining yield was extrapolated from the simulated yield curve. Extrapolated

estimates of the neutron yield are 1.5–2 $\times$ 10^{11} at 3.6 Torr which is consistent with an experimentally measured yield of 1.5 $\times$ 10^{11} at 3.5 Torr. The 26 ns of kinetic simulation also predicted ion and neutron spectra, neutron anisotropy, neutron spot size of 0.7 mm for Gemini DPF and time history of neutron production. In the forward direction 5 ns after the start of the pinch, the bulk of ions had energies below 100 eV with a high-energy tail extending to 1 meV. Preliminary measurements of ion beam energies on the Gemini DPF using a Faraday cup time of flight (TOF) measurement observed deuterons with energies up to 310 keV. The main neutron production appeared to be produced from the pinch region (r = 0–2.5 mm) and was apparently dominated by beam-target fusion, producing a wide spread in energies around a central peak at 2.45 meV. Outside this region, neutrons were predominantly produced at 2.45 meV with an 11 keV width, characteristic of thermonuclear fusion or low-energy beam-target fusion. The results also indicated anomalously high plasma resistivity during the pinch with plasma resistance rising to 0.7 Ω at peak neutron production.

The fully kinetic simulation of Schmidt et al. [28–30] may be the most advanced simulation so far carried out for the plasma focus pinch. This work has demonstrated the capability of such fundamental methods to show details of the pinch plasmas. However considerable theoretical sophistification and computing resources are required as can be seen in the work of Schmidt et al. [30] for just 26 ns of simulation. Hence the technique is not available for general use on any machine.

On the other hand, simple methods with varying degrees of utility may be used in attempts to look at experimental neutron yields. For example, Moreno et al. [33] and Gonzalez et al. [34] applied modelling codes based on thermonuclear fusion mechanism by adjusting axial and radial mass sweeping factors in their particular plasma focus devices until acceptable matching between computed neutron yield Y_n and measured Y_n. In addition, their method of calculating shock speeds was based upon an old version of Lee Model Code (pre-1995) [6, 35] which did not include the important properties of 'communication delay' between the shock front and driving magnetic piston in the radial plasma slug [36]. That pre-1995 version over-estimated the shock speed by factor 2, shock temperature by factor 4 and D-D fusion cross section by factors exceeding 1000. After 1995, the Lee Model Code [10, 37] has included this 'communication delay; and its results in terms of dynamics and radiation yields have an acceptable correlation with experimental results.

In 2009, Gonzalez et al. [38] used Von Karman approximations of radial velocity and density profiles to fit the experimental Y_n versus gas pressure curve of the seven plasma focus devices using thermonuclear mechanism. Four parameters namely axial and radial shape parameters, velocity profile exponent and density profile exponent were used to describe this model and these values were adjusted until the Y_n versus pressure curve for each machine fitted the measured Y_n versus pressure curve. It appears that that is the sole purpose of this modelling. There is no discussion that this model has any predictive value, especially in the case of neutron emission yield.

From the above review, it is seen that much of the numerical work that has been carried out is motivated by a desire to simulate the plasma focus to obtain a computed picture of flow dynamics and the density and temperature structure of the

plasma focus pinch. There has been a particular motivation to simulate the Y_n to determine the mechanism of neutron production and to have a method to predict the Y_n of a machine. Additionally, several studies towards other uses and applications may also be noted here.

Trunk carried out a numerical study of the parameters of the plasma focus machines at Stuttgart [39] using MHD equations coupled to the electrical circuit. The influence of varying circuit parameters, focus apparatus dimensions, and filling pressure on the discharge characteristics, especially the maximum current, and the plasma variables in the pinch phase were examined and compared with experimentally determined neutron outputs. An experimentally derived scaling law for the dependence of maximum neutron output on bank energy, filling pressure and length of the inner electrode was confirmed by the results of the MHD computations. In the process, Trunk observed that the optimum conditions for the focus experiment "NESSI" occurred at an external inductance L_0 of 20 nH.

The harnessing of nuclear fusion energy has been described as indispensable to the salvation of our planet [40], indeed the next giant step of Mankind [41]. In this context, early work on the plasma focus generated great excitement in demonstrating that fusion yield was proportional to stored energy squared in the plasma focus. Conditions for plasma focus to achieve energy breakeven had been a topic of discussion. The currents required for breakeven fusion was a highly optimistic 10 MA as predicted by Imshennick et al. [42] using a similarity calculation. Vikhrev and Korolev [43] predicted a more realistic though still highly optimistic value of 30 MA. In the context of very large machines, an attempt had been made to discuss neutron saturation in terms of a proportional relationship between tube inductance and storage capacitance [21, 25, 44]. Using a completely different approach Lerner et al. [45] proposed to achieve controlled fusion with hydrogen-boron (p-B^{11}) fuel in the dense plasma focus. The proposal is based on a theory of plasmoids within the plasma focus pinch. The theory envisages the trapping of magnetic energy within the plasmoid and plasma instability conditions relating to electron gyro-frequency, and ion and electron plasma frequencies. Estimates of dimension, magnetic field, ion density and lifetime of these plasmoids are made resulting in a favourable picture to support aneutronic fusion. The concept is being tested in the Focus-Fusion-1 [46].

An enterprising ongoing project to obtain so-called 'global optimization' has been discussed recently by Auluck [47] regarding the use of the Gratton-Vagras 2-D electromechanical model for the construction of an appropriate design tool to search for a globally optimized "best possible" design to maximize quantitative performance criteria per unit of stored energy. According to Auluck, the Gratton-Vargas model [48] can currently calculate optimality parameters of designs at the rate of 150,00 designs a day with considerable scope for further improvements in speed. This model maps the 10 parameters of a DPF installation—capacitance, inductance, resistance, voltage, anode radius, anode length, insulator radius, insulator length and gas pressure—on to 7 dimensionless model parameters, out of which 5 are relevant for optimization. This circumstance enables generation of a database of a limited set of optimality properties (such as average power transfer efficiency, electromagnetic work, energy per particle, a fraction of energy dissipated in circuit resistance, etc.) of

Mather-type DPF devices in a practically relevant range of parameters. The cases presented by Auluck do not include variation in thermodynamics or the effect of radiation. Therefore the 'global optimisation' could not have an application in most of plasma focus operation which spans not just plasma focus of varied geometry and electrical parameters but also many gases in which the variations of thermodynamics and the effects of radiation on the dynamics and compression are significant, even dominant. Without including these effects even the dynamics is not accurately computed and electromagnetic work, energy and power transfer efficiencies are incorrectly scaled for most of the gases in which plasma focus machines operate.

3.1.3 A Universal Code for Numerical Experiments of the Mather-Type Plasma Focus

The Lee model code [10, 37] uses the snowplow model [13] in the axial phase, the slug model [36] with 'communication delay' and thermodynamics in the early radial phase and a radiation-coupled compression in the pinch phase; all the phases being rigorously circuit-coupled so as to be energy and charge consistent.

The code has on the one hand been successful in developing a number of deep insights and on the other hand has been successful in applications ranging from correlation with experiments in dynamics, neutron and soft X-ray (SXR) yields, in fast ion beams (FIB) and fast plasma streams (FPS) properties and in designing plasma focus and variants. Its success on so many fronts appears to be due to its use of 4 parameters (fitted to a measured current waveform) which in one sweep incorporates all the mechanisms and effects occurring in the plasma focus including mechanisms and effects difficult to compute or even as yet unknown.

The simple treatment of the axial and early radial phases has nevertheless produced several important insights into plasma focus such as an optimum static inductance [49] and current and neutron scaling and yield deterioration (for which a misnomer would be the word 'saturation') [21, 44]. The radiation-coupled equation of motion used in the pinch phase has enabled pioneering work on radiative collapse in the plasma focus [50–54].

On a more practical level, SXR experiments using Pin Diode system in INTI PF operated in Ne to correlate typically measured profile with dynamics computed from the code have been demonstrated [55, 56] and optimization of UNU/ICTP PFF plasma focus guided by the code for Ne soft X-ray operation has been presented [57]. A recent extension of the code to compute ion beam has pioneered the establishment of reference units and numbers for fast ion beams (FIB) and fast plasma streams (FPS) from the dense plasma focus device [58, 59]. These numerical computations of FIB and FPS properties have been incorporated into studies for damage assessment of prospective materials for plasma facing walls of fusion reactors [60] using conventional fast focus mode (FFM), and additionally generated a concept of running the plasma focus in a slow focus mode (SFM) to produce less damaging FIB and FPS with bigger and more uniform interaction with targets for materials fabrication [61–63].

Such a wide range of insights and applications has not been demonstrated by any other single model or code. Its features include the following [10, 37]:

- Numerical Experimental Facility
- Simulate any Mathers-type plasma focus, computes axial and radial dynamics
- Design new plasma focus machines
- Thermodynamics included; H, D, Ne, Ar, Xe, He, N, Kr and D-T
- Model parameters to fit experimental axial, radial phase times implicit in measured current traces
- Radiative phase computes bremsstrahlung, line radiation, recombination and total radiation power yield. Computes neutron yield for D and D-T operation; based on a combined thermonuclear and beam-target model. Computes FIB properties and FPS properties. Plasma self-absorption incorporated in the code
- Code computes radiative cooling and collapse
- Code includes choice of tapered anode and has been approximated to curved electrodes and also SPF (spherical plasma focus).

3.2 Lee Model Code

3.2.1 The Physics Foundation and Wide-Ranging Applications of the Code

In the early 1960s, Filippov [4] and Mather [5] independently invented the plasma focus and carried out groundbreaking research establishing the Filippov- and Mather-type devices. In 1971, D. Potter published his *Numerical Studies of the Plasma Focus*, a two-dimensional fluid model which estimated neutron yield concurring with experimental yields, and concluded that these neutrons were the result of thermally reacting deuterons in the hot pinch region [18]. Since then some five decades of research have been conducted, computing and measuring all aspects of the plasma focus [1, 2]: imaging for dynamics, interferometry for densities, spectroscopy for temperatures, measurements on neutrons and radiation yields, and MeV particles. The result is the commonly accepted picture today that mechanisms within the focus pinch, such as micro- and MHD instabilities, acceleration by turbulence and 'anomalous' plasma resistance are important to plasma focus behaviour and that the bulk of the emitted neutrons do not originate from thermonuclear reactions.

In conjunction with the development of the plasma focus known as the UNU/ICTP PFF [7, 9] during the UNU Training Programme in Plasma and Laser Technology in 1985 [7, 9, 64] a 2-phase code had been developed [6, 7, 10, 65] to describe and optimize the design of the plasma focus. The code [10] couples the electrical circuit with PF dynamics, thermodynamics and radiation. It is energy-, charge- and mass-consistent. It was used in the design and interpretation of experiments [7, 20, 66–69]. An improved 5-phase code [10, 37] incorporating finite small

disturbance speed [36] and radiation-coupled dynamics evolved and this version was used [49–63, 70–81], and was first web-published [82] in 2000. Plasma self-absorption was included [10, 37] in 2007. It has been used extensively as a complementary facility in several machines, for example: UNU/ICTP PFF [7, 9, 20, 62, 70–76], NX2 [74, 78–80, 83, 84], NX1 [74, 78], and modified for Filippov configuration for DENA [85]. It has also been used in several machines for design, optimization [7, 10, 55–57, 62, 83, 84, 86–89] and interpretation including sub-kJ PF machines [90], FNII [91], the UBA hard X-ray source [92], KSU PF [89] and a cascading plasma focus [93]. Information computed includes axial and radial dynamics [7, 62, 68–81, 94, 95], SXR emission characteristics and yield [55–57, 73–79, 83, 87, 88, 96–99] for various gases and applications including as a source for microelectronics lithography [74, 78], adaptation in the form of ML (Modified Lee) to Filippov-type plasma focus devices [85]. Speed-enhanced PF [70–72] was demonstrated. Plasma focus neutron yield calculations [21, 37, 44, 100–102], current and yield limitations [49, 102–104], deterioration of neutron scaling (neutron saturation) [21, 44], radiative collapse [50–54], current-stepped PF [105], extraction of diagnostic data [106–109] and anomalous resistance data [110–112] from current signals have been studied using the code [10, 37] or variants. Yield enhancement effects of high operational pressure and voltage have been studied [44]. It has recently been used to produce reference numbers for deuteron beam number and energy fluence and flux and scaling trends for these with PF storage energy; and subsequently extended for beam ion calculations for all gases [58, 59]. Fast ion beams FIB and fast plasma streams FPS for damage studies have been simulated [60] and calculations for the production of short-lived radioisotopes have been made [113]. Radiation and particle yields scaling laws [21, 22, 44, 77, 98, 100, 114–123] have been deduced. Arwinder Singh [77] has used the code as a tool to tabulate the characteristics and properties of 44 machines collated from all over the world, including sealed, small and big plasma focus devices. Considerable effort has also been made to collect neutron and SXR data for comparison with computed results using the code [124–129]. The code opens up so many fronts in plasma focus numerical experiments that it has been proposed as an advanced training system for the fusion energy age [130] to further advance the successful international training programmes established by the Asian African Association for Plasma Training (AAAPT) [9, 64]. The range and scope of this Model code is shown in the following Fig. 3.4.

The code has been continuously developed over the past 3 decades and in recent years many details, as they evolve, are described in the website of the Institute for Plasma Focus Studies [10]. This section presents the complete description of the Lee Model code in its basic 5-phase version. The chapter also briefly describes the development into the 6-phase version for Type-2 (high inductance plasma focus) machines which have been found to be incompletely fitted with the 5-phase model due to a dominant anomalous resistance phase [110].

This model has been developed for Mather-type [5] plasma focus machines. It was developed for the 3 kJ machine known as the UNU/ICTP PFF [7, 9] (United Nations University/International Centre for Theoretical Physics Plasma Focus

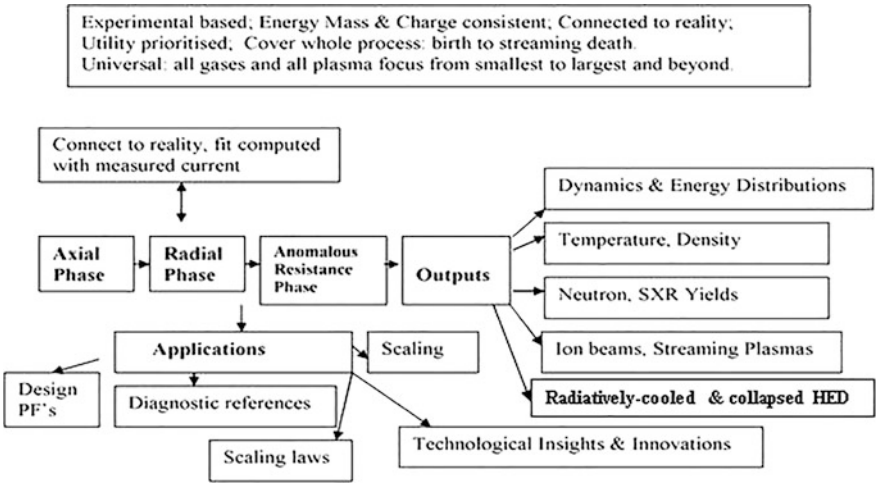

Fig. 3.4 The philosophy, the phases, the outputs and applications of the Lee model code

facility), which now forms an international network. However, it has since been generalized to all machines. In principle there is no limit to energy storage and electrode configuration, though house-keeping may need to be carried out in extreme cases, in order to keep within efficient ranges, e.g. of graph plotting.

3.2.2 The Five Phases of the Plasma Focus

A brief description of the five phases is summarized as follows:

1. Axial Phase (see Fig. 3.1): This is described by a snowplow model with an equation of motion which is coupled to a circuit equation. The equation of motion incorporates the axial phase model parameters: mass and current factors f_m and f_c [55, 131–133]. The mass swept-up factor f_m accounts for not only the porosity of the current sheet but also for the inclination of the moving current sheet-shock front structure, boundary layer effects and current shunting and fragmenting and all other unspecified effects which have effects equivalent to increasing or reducing the amount of mass in the moving structure, during the axial phase. The current factor, f_c accounts for the fraction of current effectively flowing in the moving structure (due to all effects such as current shedding at or near the back wall, current sheet inclination). This defines the fraction of current effectively driving the structure, during the axial phase.
2. Radial Inward Shock Phase (see Figs. 3.1 and 3.6): Described by 4 coupled equations using an elongating slug model. The first equation computes the radial inward shock speed from the driving magnetic pressure. The second equation computes the axial elongation speed of the column. The third equation computes the speed of the current sheath (CS), also called the magnetic piston, allowing

the current sheath to separate from the shock front by applying an adiabatic approximation. The fourth is the circuit equation. Thermodynamic effects due to ionization and excitation are incorporated into these equations (as well as for all radial phases), these effects being especially important for gases other than hydrogen and deuterium. Temperature and number densities are computed during this phase. A communication delay between shock front and current sheath due to the finite small disturbance speed is crucially implemented in this phase. The model parameters, radial phase mass swept-up and current factors, f_{mr} and f_{cr}, are incorporated in all three radial phases. The mass swept-up factor f_{mr} accounts for all mechanisms including current sheet curvatures and necking leading to axial acceleration and ejection of mass, and plasma/current disruptions. These effects may give rise to localized regions of high density and temperatures. The detailed profile of the discharge current is influenced by these effects and during the pinch phase also reflects the Joule heating and radiative yields. At the end of the pinch phase, the total current profile also reflects the sudden transition of the current flow from a constricted pinch to a large column flow. Thus the discharge current powers all dynamic, electrodynamic, thermodynamic and radiation processes in the various phases of the plasma focus. Conversely, all the dynamic, electrodynamic, thermodynamic and radiation processes in the various phases of the plasma focus affect the discharge current. It is then no exaggeration to say that the discharge current waveform contains information on all the dynamic, electrodynamic, thermodynamic and radiation processes that occur in the various phases of the plasma focus which have effects equivalent to increasing or reducing the amount of mass in the moving slug, during the radial phase. The current factor f_{cr} accounts for the fraction of current effectively flowing in the moving piston forming the back of the slug (due to all effects). This defines the fraction of current effectively driving the radial slug.

3. Radial Reflected Shock (RS) Phase: When the shock front hits the axis (Fig. 3.6), because the focus plasma is collisional, a reflected shock RS develops which moves radially outwards, whilst the radial current sheath (CS) piston continues to move inwards. Four coupled equations are also used to describe this phase, these being for the RS moving radially outwards, the piston moving radially inwards, the elongation of the annular column and the circuit. The same model parameters, f_{mr} and f_{cr}, are used as in the previous radial phase. The plasma temperature behind the RS undergoes a jump by a factor nearly 2.
4. Slow Compression (Quiescent) or Pinch Phase (Fig. 3.6): When the outgoing RS hits the incoming piston the compression enters a radiative phase in which for gases such as Ne, Ar, Kr and Xe, radiation emission may strongly enhance the compression where we have included energy loss/gain terms from Joule heating and radiation losses into the piston equation of motion. Three coupled equations describe this phase; these being the piston radial motion equation, the pinch column elongation equation and the circuit equation, incorporating the same model parameters as in the previous two phases. Thermodynamic effects [134] are incorporated into this phase. Radiation yields are computed incorporating the effects of plasma self-absorption. Thermonuclear and beam-gas target

components of neutron yields are computed as are properties of fast ion beams (FIB) and fast plasma streams (FPS) exiting the focus pinch [56–58, 135]. The duration of this slow compression phase is set as the time of transit of small disturbances across the pinched plasma column. The computation of this phase is terminated at the end of this duration.

5. Expanded Column Phase: To simulate the current trace beyond this point, we allow the column to suddenly attain the radius of the anode, and use the expanded column inductance for further integration. In this final phase, the snowplow model is used, and two coupled equations are used; similar to the axial phase above. This phase is not considered important as it occurs after the focus pinch.

We note that the transition from Phase 4 to 5 is observed in laboratory measurements to occur in an extremely short time with plasma/current disruptions resulting in localized regions of high densities and temperatures. These localized regions are not modelled in the code, which consequently computes only an average uniform density and an average uniform temperature which is considerably lower than measured peak density and temperature. We have investigated profiling techniques to estimate these peaks [136]. However, because the 4 model parameters are obtained by fitting the computed total current waveform to the measured total current waveform, the model incorporates the energy and mass balances equivalent, at least in the gross sense, to all the processes which are not even specifically modelled. Hence the computed gross features such as speeds and trajectories and integrated soft X-ray yields have been extensively tested in numerical experiments for many machines across the range of machines and are found to be comparable with measured values. The statements in this paragraph apply to both Type-1 (low inductance) and Type-2 (high inductance) plasma focus machines [110]. However it has been found that whilst Type-1 current waveforms can be fitted adequately with the 5-phase code, the current waveform of a Type-2 machine typically contains current dip with a first portion that is well fitted by the 5-phase code. Beyond the first portion of the dip, there is an extended dip which cannot be fitted by the 5-phase model however much the model parameters are stretched. Therefore for Type-2 machines, an additional sixth phase (termed Phase 4a) has been coded occurring between Phase 4 and 5 above which is fitted by assuming anomalous resistance terms [110]. Despite the need for this additional phase for Type-2 machines it is found that the dynamics up to the slow compression (pinch) phase and neutron and soft X-ray yields for the same Type-2 machines are correctly described by the 5-phase code which already incorporates a compensatory feature for the neutron yield, basically a multiplier to the beam deuteron energy deduced from inductive voltage and fitted with global experimental data (see section on neutron calculation below). The conclusion is that the anomalous resistance phase which dominates an additional phase after the pinch phase is needed to fit the current trace but otherwise is likely not needed for the description of the dynamics up to the pinch phase or for the estimation of the neutron, SXR and other yields.

We proceed to a detailed description of the basic 5-phase model code.

3.2.3 The Equations of the Five Phases

3.2.3.1 Axial Phase (Snowplow Model)

We refer to the left image of Fig. 3.1:

Rate of change of momentum at current sheath, position z, is

$$\frac{\mathrm{d}}{\mathrm{d}t}\left(\left[\rho_0\pi(b^2-a^2)z\right]f_\mathrm{m}\frac{\mathrm{d}z}{\mathrm{d}t}\right)=\rho_0\pi\left(c^2-1\right)a^2f_\mathrm{m}\frac{\mathrm{d}}{\mathrm{d}t}\left(z\frac{\mathrm{d}z}{\mathrm{d}t}\right)$$

Magnetic force on current sheath is

$$\int_a^b\left[\left(\frac{\mu I f_\mathrm{c}}{2\pi r}\right)^2/(2\mu)\right]2\pi r\mathrm{d}r=\frac{\mu f_\mathrm{c}^2}{4\pi}\ln(c)I^2$$

where f_m = fraction of mass swept down the tube in the axial direction; f_c = fraction of current flowing in piston (or current sheet CS); $c = b/a$ = cathode radius/anode radius, ρ_0 = ambient density, I = time-varying circuit current, μ = permeability.

Equation of Motion

From the above equating rate of change of momentum to the magnetic force, we derive:

$$\frac{\mathrm{d}^2z}{\mathrm{d}t^2}=\left[\frac{f_\mathrm{c}^2}{f_\mathrm{m}}\frac{\mu(\ln c)}{4\pi^2\rho_0(c^2-1)}\left(\frac{I}{a}\right)^2-\left(\frac{\mathrm{d}z}{\mathrm{d}t}\right)^2\right]/z \tag{3.1}$$

Circuit (Current) Equation

We ignore $r_\mathrm{p}(t)$, plasma resistance, hence not shown in the circuit diagram of Fig. 3.5. This is the approximation which is generally used for electromagnetic drive. Using the C_0–L_0–$L(t)$–r_0 mesh of Fig. 3.5 we derive the circuit equation as follows:

$$\begin{aligned}\frac{\mathrm{d}}{\mathrm{d}t}\left[(L_0+Lf_\mathrm{c})I\right]+r_0I&=V_0-\int\frac{I\mathrm{d}t}{C_0}\frac{\mathrm{d}I}{\mathrm{d}t}\\&=\left[V_0-\frac{\int I\mathrm{d}t}{C_0}-r_0I-If_\mathrm{c}\frac{\mu}{2\pi}(\ln c)\frac{\mathrm{d}z}{\mathrm{d}t}\right]/\left[L_0+\frac{f_\mathrm{c}\mu}{2\pi}(\ln c)z\right]\end{aligned} \tag{3.2}$$

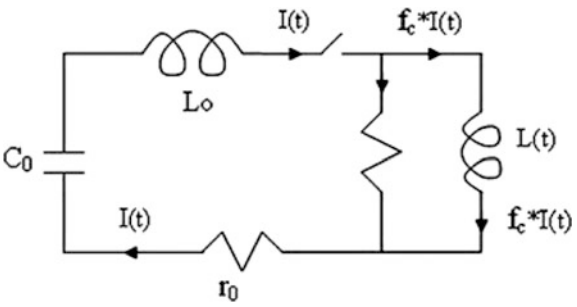

Fig. 3.5 Plasma focus circuit: the inductance of the plasma focus tube is treated as a time-dependent inductance $L(t)$, neglecting the plasma resistance r_p. The resistance parallel to the $L(t)$ mesh is a schematic representation of a leakage current $(1 - f_c)I(t)$ which limits the effective drive current to $f_c I(t)$

Equations (3.1) and (3.2) are the Generating Equations of the axial model. They contain the physics built into the model. They are coupled equations. The equation of motion is affected by the electric current I. The circuit equation is affected by the current sheath motion dz/dt and position z.

Normalizing the Generating Equations to Obtain Characteristic Axial Transit Time, Characteristic Axial Speed and Speed Factor S; and Scaling Parameters of Times, α and Inductances β

Replace variables t, z, and I by non-dimensionalised quantities as follows:

$$\tau = t/t_0, \zeta = z/z_0 \text{ and } \imath = I/I_0$$

where the normalizing quantities z_0 = the length of the anode, $t_0 = (L_0 C_0)^{0.5}$ (note that $2\pi t_0$ is the periodic time of L_0–C_0 discharge circuit) and $I_0 = V_0/Z_0$ where $Z_0 = (L_0/C_0)^{0.5}$ is the surge impedance.

Normalizing, we have equation of motion:

$$\frac{d^2\zeta}{d\tau^2} = \left[\frac{f_c^2}{f_m}\frac{\mu \ln c}{4\pi^2\rho_0(c^2-1)}\left(\frac{I_0}{a}\right)^2\frac{t_0^2}{z_0^2}\imath^2 - \left(\frac{d\zeta}{d\tau}\right)^2\right] \Big/ \zeta$$

which we write in the following form

$$\frac{d^2\zeta}{d\tau^2} = \frac{\left[\alpha^2\imath^2 - \left(\frac{d\zeta}{d\tau}\right)^2\right]}{\zeta} \tag{3.3}$$

with

$$\alpha^2 = t_0^2/t_a^2 \tag{3.4}$$

and

$$t_a = \left[\frac{4\pi^2(c^2-1)}{\mu \ln c}\right]^{1/2} \frac{\sqrt{f_m}}{f_c} \frac{z_0}{(I_0/a)/\sqrt{\rho}} \tag{3.5}$$

which is identified as the characteristic axial transit time of the CS for the anode axial phase.

$$\alpha = (t_0/t_a) \tag{3.6}$$

is identified as the first scaling parameter being the ratio of characteristic electrical discharge time to the characteristic axial transit time. This scaling parameter is seen as an indicator of the matching of electrical drive time to the axial transit time for efficient energy transfer.

We further identify a characteristic axial transit speed $v_a = z_0/t_a$ where

$$v_a = \left[\frac{\mu \ln c}{4\pi^2(c^2-1)}\right]^{1/2} \frac{f_c}{\sqrt{f_m}} \frac{(I_0/a)}{\sqrt{\rho}} \tag{3.7}$$

The quantity $(I_0/a)/\rho^{0.5}$ is the all-important S (speed or drive) factor [137] of the plasma focus axial phase and as we shall see also the radial phase; and indeed for all electromagnetically driven devices.

Normalizing the circuit (current) Equation, we have:

$$\frac{d\imath}{d\tau} = \left(1 - \int \imath d\tau - \beta\imath \frac{d\zeta}{d\tau} - \delta\imath\right) \Big/ (1 + \beta\zeta) \tag{3.8}$$

where

$$\beta = (L_a/L_0) \tag{3.9}$$

and $L_a = f_c(\mu/2\pi)(\ln c)z_0$ is the inductance of the axial phase when CS reaches anode end at $z = z_0$.

Thus this second scaling parameter has a great effect on the electrodynamics of the system.

The third scaling parameter $\delta = r_0/Z_0$ is the ratio of circuit stray resistance to surge impedance. This has a damping effect on the current.

Equations (3.3) and (3.8) are the Generating Equations (in normalized form) that are integrated step-by-step for the time variation of current $\imath$ and axial position ζ.

Calculate Voltage Across Input Terminals of Focus Tube

$$V = \frac{\mathrm{d}}{\mathrm{d}t}(LIf_c) = f_c I\frac{\mathrm{d}L}{\mathrm{d}t} + f_c L\frac{\mathrm{d}I}{\mathrm{d}t} \quad \text{where } L = \frac{\mu}{2\pi}(\ln c)z \tag{3.10}$$

Normalised to capacitor voltage V_0:

$$\upsilon = \frac{V}{V_0} = \beta\imath\frac{\mathrm{d}\zeta}{\mathrm{d}\tau} + \beta\zeta\frac{\mathrm{d}_c}{\mathrm{d}\tau} \tag{3.11}$$

Integration Scheme for Normalized Generating Equations

Define initial conditions:

$$\tau = 0,\ \mathrm{d}\zeta/\mathrm{d}\tau = 0,\ \zeta = 0,\ \imath = 0,\ \int \imath\mathrm{d}\tau = 0,\ \mathrm{d}\imath/\mathrm{d}\tau = 1,\ \mathrm{d}^2\zeta/\mathrm{d}\tau^2 = (1/2)^{0.5}\alpha$$

Set time increment: $D = 0.001$; Increment time: $\tau = \tau + D$

Next step values (LHS) are computed from current-step values (RHS) using the following linear approximations:

$$\begin{aligned} \frac{\mathrm{d}\zeta}{\mathrm{d}\tau} &= \frac{\mathrm{d}\zeta}{\mathrm{d}\tau} + \frac{\mathrm{d}^2\zeta}{\mathrm{d}\tau^2}D \\ \zeta &= \zeta + \frac{\mathrm{d}\zeta}{\mathrm{d}\tau}D \\ \imath &= \imath + \frac{\mathrm{d}\imath}{\mathrm{d}\tau}D \\ \int \imath\mathrm{d}\tau &= \int \imath\mathrm{d}\tau + \imath D \end{aligned} \tag{3.12}$$

Use new values of $\mathrm{d}\zeta/\mathrm{d}\tau$, ζ, $\imath$ and $\int \imath\mathrm{d}\tau$ to calculate new generating values of $\mathrm{d}\imath\mathrm{d}\tau$ and $\mathrm{d}^2\zeta/\mathrm{d}\tau^2$ using generating Eqs. (3.3) and (3.8). Increment time again and repeat calculations of next step values and new generating values. Continue procedure until $\zeta = 1$. Then go on to radial phase inward shock.

3.2.3.2 Radial Inward Shock Phase (Slug Model)

The snowplow model is used for axial phase just to obtain axial trajectory and speed (from which temperature may be deduced) and to obtain a reasonable current profile. As the plasma structure is assumed to be infinitesimally thin, no information of density is contained in the physics of the equation of motion, although an estimate of density may be obtained by invoking additional mechanisms, e.g. using shock wave theory [138, 139].

In the radial phase, however, a snowplow model (with infinitesimally thin structure) would lead to all current flowing at $r = 0$, with infinite inductance and density. This is obviously unrealistic.

We thus replace the snowplow model by a slug model [10, 36]. In this model, the magnetic pressure drives a shock wave ahead of it, creating a space for the magnetic piston (also called current sheet CS) to move into. The speed of the inward radial shock front (see the left image of Fig. 3.1) is determined by the magnetic pressure (which depends on the drive current value and CS position r_p). A radius-time representation of the slug model is shown in Fig. 3.6.

The speed of the magnetic piston (CS) is determined by the first law of thermodynamics applied to the effective increase in volume between shock front (SF) and CS, created by the incremental motion of the SF. The compression is treated as an elongating pinch.

Four generating equations are needed to describe the motion of (a) radial SF (see right image of Fig. 3.1); (b) radial CS; (c) pinch elongation and (d) the electric current; in order to be integrated for the four variables r_s, r_p, z_f and I.

Motion of Shock Front

From shock theory [138, 139], shock pressure

$$P = 2\rho_0 v_s^2/(\gamma + 1) \tag{3.13}$$

where shock speed v_s into ambient gas ρ_0 causes the pressure of the shocked gas (just behind the shock front) to rise to value P (see Fig. 3.7); γ is the specific heat ratio of the gas.

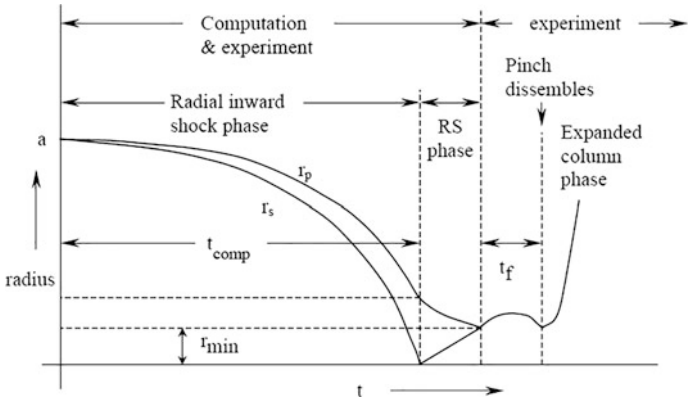

Fig. 3.6 Schematic of the radial phase—in radius versus time format

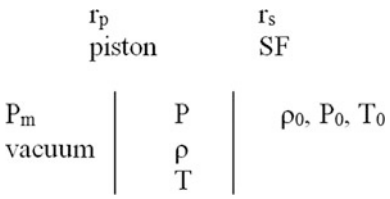

Fig. 3.7 Relationship between ambient conditions (quantities with subscript 0), slug and driver properties

If we assume that this pressure is uniform from the SF to the piston or CS (infinite acoustic, or small disturbance speed approximation) then across the piston (Fig. 3.7), we may apply $P = P_m$ where

$$P_m = \left(\mu I f_c / 2\pi r_p\right)^2 / 2\mu v_s^2 = \frac{\mu (I f_c)^2}{8\pi^2 r_p^2} \times \frac{\gamma + 1}{2\rho_0 f_{mr}} \tag{3.13a}$$

where I is the circuit current and If_c is the current flowing in the cylindrical CS, taken as the same f_c as in the axial phase, and $\rho_0 f_{mr}$ is the effective mass density swept into the radial slug; where f_{mr} is a different (generally larger) factor than f_m of the axial phase.

Thus

$$\frac{dr_s}{dt} = -\left[\frac{\mu(\gamma+1)}{\rho_0}\right]^{1/2} \frac{f_c}{\sqrt{f_{mr}}} \frac{I}{4\pi r_p} \tag{3.14}$$

Elongation Speed of CS (Open-Ended at Both Ends)

The radial compression is open-ended. Hence an axial shock is propagated in the z-direction, towards the downstream anode axis. We take z_f as the position of the axial CS. The pressure driving the axial shock is the same as the pressure driving the inward radial shock. Thus the axial shock speed is the same as the radial shock speed. The CS speed is slower, from shock wave theory, by an approximate factor of $2/(\gamma + 1)$. Thus axial elongation speed of CS is:

$$\frac{dz_f}{dt} = -\left(\frac{2}{\gamma+1}\right) \frac{dr_s}{dt} \tag{3.15}$$

Radial Piston Motion

We inquire: for an incremental motion, dr_s, of the shock front, at a driving current I, what is the relationship between plasma slug pressure P and plasma slug volume Vol?

We assume an adiabatic relationship [10, 36, 37] (assuming infinite small disturbance speed for which we will apply a correction subsequently) to a **fixed mass of gas** in the slug during the incremental motion dr_s. We have $PVol^{\gamma}$ = constant or

$$\frac{\gamma d(Vol)}{(Vol)} + \frac{dP}{P} = 0 \tag{3.16}$$

where slug pressure $P \sim v_s^2$ (see Eq. 3.13); so $\frac{dP}{P} = \frac{2dv_s}{v_s}$ but $v_s \sim \frac{I}{r_p}$ (see Eq. 3.13a); so

$$\frac{dP}{P} = 2\left(\frac{dI}{I} - \frac{dr_p}{r_p}\right) \tag{3.16a}$$

Now slug volume $Vol = \pi(r_p^2 - r_s^2)z_f$.

Here we note that although the motion of the piston dr_p does not change the mass of gas in the slug, the motion of the shock front, dr_s, **does** sweep in an amount of ambient gas. This amount swept in is equal to the ambient gas swept through by the shock front in its motion dr_s. This swept-up gas is compressed by a ratio $(\gamma + 1)/(\gamma - 1)$ and will occupy part of the increase in volume dVol.

The actual increase in volume available to the original mass of gas in volume *Vol* does not correspond to increment dr_s but to an effective (reduced) increment $dr_s(2/(\gamma + 1))$. (Note γ is specific heat ratio of the plasma, e.g. $\gamma = 5/3$ for atomic gas, $\gamma = 7/5$ for molecular gas; for strongly **ionizing** argon γ has value closer to 1, e.g. 1.15.) The specific heat ratio and effective charge $Z_{eff,}$ where needed are computed from a corona model and placed in the code in the form of a series of polynomials. This is described in Sect. 3.2.3.4 slow compression phase below. Thus:

$$dVol = 2\pi\left(r_p dr_p - \frac{2}{\gamma+1} r_s dr_s\right) z_f + \pi\left(r_p^2 - r_s^2\right) dz_f$$

and we have:

$$\frac{\gamma dVol}{Vol} = \frac{2\gamma\left(r_p dr_p - \frac{2}{\gamma+1} r_s dr_s\right) z_f + \gamma\left(r_p^2 - r_s^2\right) dz_f}{z_f\left(r_p^2 - r_s^2\right)} \tag{3.16b}$$

From Eqs. (3.16), (3.16a) and (3.16b); (and taking effective increment of dz_f as $dz_f(2/(\gamma+1)$ for the same reason as explained above for effective increment of dr_s) we have

$$\frac{dr_p}{dt} = \frac{\frac{2}{\gamma+1}\frac{r_s}{r_p}\frac{dr_s}{dt} - \frac{r_p}{\gamma I}\left(1 - \frac{r_s^2}{r_p^2}\right)\frac{dI}{dt} - \frac{r_p}{(\gamma+1)z_f}\left(1 - \frac{r_s^2}{r_p^2}\right)\frac{dz_f}{dt}}{\frac{\gamma-1}{\gamma} + \frac{1}{\gamma}\frac{r_s^2}{r_p^2}} \tag{3.17}$$

Circuit Equation During Radial Phase

The inductance of the focus tube now consists of the full inductance of the axial phase and the inductance of the radially imploding and elongating plasma pinch. Thus

$$L = \frac{\mu}{2\pi}(\ln c)z_0 + \frac{\mu}{2\pi}\left(\ln\frac{b}{r_p}\right)z_f \tag{3.18}$$

where both z_f and r_p vary with time.

Thus the circuit (current) equation is obtained as:

$$\frac{dI}{dt} = \frac{V_0 - \frac{\int I dt}{C_0} - r_0 I - f_{cr}\frac{\mu}{2\pi}\left(\ln\frac{b}{r_p}\right)I\frac{dz_f}{dt} + f_{cr}\frac{\mu}{2\pi}\frac{z_f}{r_p}I\frac{dr_p}{dt}}{L_0 + f_{cr}\frac{\mu}{2\pi}(\ln c)z_0 + f_{cr}\frac{\mu}{2\pi}\left(\ln\frac{b}{r_p}\right)z_f} \tag{3.19}$$

The four Generating Eqs. (3.14), (3.15), (3.17) and (3.19) form a closed set of equations which are integrated for r_s, r_p, z_f and I.

Normalizing the Generating Equations to Obtain Characteristic Radial Transit Time, Characteristic Radial Transit Speed and Speed Factor S; and Scaling Parameters for Times α_1 and Inductances β_1; also Compare Axial to Radial Length Scale, Time Scale and Speed Scale

For this phase, the following normalization is adopted.

$\tau = t/t_0$, $\imath = I/I_0$ as in axial phase but with $\kappa_s = r_s/a$, $\kappa_p = r_p/a$, and $\zeta_f = z_f/a$, i.e. distances are normalized to anode radius, instead of anode length.

After normalization we have:

Radial shock speed

$$\frac{d\kappa_s}{d\tau} = -\alpha\alpha_1\imath/\kappa_p \tag{3.20}$$

Axial column elongation speed (both ends of column defined by axial piston)

$$\frac{d\zeta_f}{d\tau} = -\frac{2}{\gamma+1}\frac{d\kappa_s}{d\tau} \tag{3.21}$$

Radial piston speed:

$$\frac{d\kappa_p}{d\tau} = \frac{\frac{2}{\gamma+1}\frac{\kappa_s}{\kappa_p}\frac{d\kappa_s}{d\tau} - \frac{\kappa_p}{\gamma\imath}\left(1-\frac{\kappa_s^2}{\kappa_p^2}\right)\frac{d\imath}{d\tau} - \frac{1}{\gamma+1}\frac{\kappa_p}{\zeta_f}\left(1-\frac{\kappa_s^2}{\kappa_p^2}\right)\frac{d\zeta_f}{d\tau}}{(\gamma-1)/\gamma + (1/\gamma)(\kappa_s^2/\kappa_p^2)} \tag{3.22}$$

Current:

$$\frac{\mathrm{d}\iota}{\mathrm{d}\tau} = \frac{1 - \int \iota \mathrm{d}\tau + \beta_1 \left[\ln(\kappa_p/c)\right] \iota \frac{\mathrm{d}\zeta_f}{\mathrm{d}\tau} + \beta_1 \frac{\zeta_f \iota}{k_p} \frac{\mathrm{d}\kappa_p}{\mathrm{d}\tau} - \delta\iota}{\left\{1 + \beta - (\beta_1)\left[\ln\left(\kappa_p/c\right)\right]\zeta_f\right\}} \tag{3.23}$$

where **scaling parameters** are

$$\beta_1 = \beta/(F \ln c) \tag{3.24}$$

and

$$\alpha_1 = \left[(\gamma+1)\left(c^2-1\right)/(4\ln c)\right]^{1/2} F[f_m/f_{mr}]^{1/2}[f_{cr}/f_c]. \tag{3.24a}$$

We note that $F = z_0/a$ (the length/radius ratio of the anode) may be considered to be the controlling parameter of β_1 and α_1. In other words, β_1 and α_1 may not be independently assigned, but should be assigned as a pair with the value of each fixed by the value of F.

Note that whereas we interpret $\alpha = t_0/t_a$, (Eq. 3.6) we may interpret

$$\alpha_1 = t_a/t_r \tag{3.25}$$

where t_r is the characteristic radial transit time.

$$t_r = \frac{4\pi}{[\mu(\gamma+1)]^{1/2}} \frac{\sqrt{f_{mr}}}{f_{cr}} \frac{a}{(I_0/a/\sqrt{\rho})} \tag{3.26}$$

The **product** $\alpha\alpha_1$ may then be interpreted as $\alpha\alpha_1 = \frac{t_0}{t_a} = t_0/t_r$

The characteristic speed of the radial inward shock to reach focus axis is:

$$v_r = a/t_r = \frac{[\mu(\gamma+1)]^{1/2}}{4\pi} \frac{f_{cr}}{\sqrt{f_{mr}}} \frac{(I_0/a)}{\sqrt{\rho}} \tag{3.27}$$

The ratio of characteristic radial and axial speeds is also essentially a geometrical one, modified by thermodynamics. It is

$$v_r/v_a = \left[\frac{(c^2-1)(\gamma+1)}{4\ln c}\right]^{1/2} [f_m/f_{mr}]^{1/2}[f_{cr}/f_c]. \tag{3.28}$$

with a value typically 2.5 for a small deuterium plasma focus with $c \sim 3.4$, and $\gamma = 5/3$. We note [137] that the radial characteristic speed has same dependence as axial transit speed on the all-important drive factor (see Eq. 3.7). $S = (I_0/a)/\sqrt{\rho}$.

Calculate Voltage V Across PF Input Terminals

As in the axial phase, the tube voltage is taken to be inductive: $V = \mathrm{d}(LI)/\mathrm{d}t$

$$L = \frac{\mu}{2\pi}(\ln c)z_0 + \frac{\mu}{2\pi}\left(\ln\frac{b}{r_\mathrm{p}}\right)z_\mathrm{f}$$

where

$$V = \frac{\mu}{2\pi}\left[(\ln c)z_0 + \left(\ln\frac{b}{r_\mathrm{p}}\right)z_\mathrm{f}\right]\mathrm{f}_\mathrm{cr}\frac{\mathrm{d}I}{\mathrm{d}t} + \frac{\mu}{2\pi}\left[\left(\ln\frac{b}{r_\mathrm{p}}\right)\frac{\mathrm{d}z_\mathrm{f}}{\mathrm{d}t} - \frac{z_\mathrm{f}}{r_\mathrm{p}}\frac{\mathrm{d}r_\mathrm{p}}{\mathrm{d}t}\right]\mathrm{f}_\mathrm{cr}I \tag{3.29}$$

We normalize to the capacitor charging voltage V_0; so that $\upsilon = V/V_0$

$$\upsilon = \left[\beta - \beta_1\left(\ln\frac{\kappa_\mathrm{p}}{c}\right)\zeta_\mathrm{f}\right]\frac{\mathrm{d}\imath}{\mathrm{d}\tau} - \beta_1\imath\left[\left(\frac{\zeta_\mathrm{f}}{\kappa_\mathrm{p}}\right)\frac{\mathrm{d}\kappa_\mathrm{p}}{\mathrm{d}\tau} + \left(\ln\frac{\kappa_\mathrm{p}}{c}\right)\frac{\mathrm{d}\zeta_\mathrm{f}}{\mathrm{d}\tau}\right] \tag{3.30}$$

Integrating for the Radial Inward Shock Phase

The 4 normalized generating Eqs. (3.20)–(3.23) may now be integrated using the following initial conditions: τ = the time at which the axial phase ended, $\kappa_\mathrm{s} = 1$, $\kappa_\mathrm{p} = 1$; $\zeta_\mathrm{f} = 0$ (taken as a small number such as 0.00001 to avoid numerical difficulties for Eq. (3.21); $\imath$ = value of current at the end of the axial phase; $\int \imath\mathrm{d}\tau$ = value of 'flowed charge' at the end of the axial phase.

Smaller time increments of $D = (0.001/100)$ are taken.

$\frac{\mathrm{d}\kappa_\mathrm{s}}{\mathrm{d}\tau}, \frac{\mathrm{d}\zeta_\mathrm{f}}{\mathrm{d}\tau}, \frac{\mathrm{d}\kappa_\mathrm{p}}{\mathrm{d}\tau}$ and $\frac{\mathrm{d}\imath}{\mathrm{d}\tau}$ are sequentially calculated from generating Eqs. (3.20)–(3.23).

Then using linear approximations we obtain next step values (LHS) from current (RHS) values as follows:

$$\kappa_\mathrm{s} = \kappa_\mathrm{s} + D\mathrm{d}\kappa_\mathrm{s}/\mathrm{d}\tau.\ \zeta_\mathrm{f} = \zeta_\mathrm{f} + D\mathrm{d}\zeta_\mathrm{f}/\mathrm{d}\boldsymbol{\tau}'$$

$$\kappa_\mathrm{p} = \kappa_\mathrm{p} + D\mathrm{d}\kappa_\mathrm{p}/\mathrm{d}\tau;\ \imath = \imath + D\mathrm{d}\imath/\mathrm{d}\tau \text{ and } \int \imath\mathrm{d}\tau = \int \imath\mathrm{d}\tau + \imath D$$

Time is then incremented by D, and the next step value of $\mathrm{d}\kappa_\mathrm{s}/\mathrm{d}\tau$, $\mathrm{d}z_\mathrm{f}/\mathrm{d}\tau$, $\mathrm{d}\kappa_\mathrm{p}/\mathrm{d}\tau$ and $\mathrm{d}\imath/\mathrm{d}\tau$ are computed from Eqs. (3.20)–(3.23) followed by linear approximation for κ_s, ζ_f, κ_p, $\imath$ and $\int \imath\mathrm{d}\tau$.

The sequence is repeated step-by-step until $\kappa_\mathrm{s} = 0$.

Correction for Finite Acoustic (Small Disturbance) Speed

In the slug model above we assume that the pressure exerted by the magnetic piston (current I, position r_p) is instantaneously felt by the shock front (position r_s). Likewise, the shock speed dr_s/dt is instantaneously felt by the piston (CS). This assumption of infinite small disturbance speed (SDS) is implicit in Eqs. (3.14) and (3.17) [or in normalized form Eqs. (3.20) and (3.22)].

Since the SDS is finite, there is actually a time lapse Δt communicating between the SF and CS. This communication delay has to be incorporated into the model. Otherwise, for the PF, the computation will yield too high values of CS and SF speed.

Consider the instant t, SF is at r_s, CS at r_p, the value of current is I. SF actually feels the effect of the current not of value I but of a value I_{delay} which flowed at time $(t - \Delta t)$, with the CS at $r_{p\text{-}delay}$. Similarly, the piston 'feels' the SF speed is not dr_s/dt but $(dr_s/dt)_{delay}$ at time $(t - \Delta t)$.

To implement this finite SDS correction we adopt the following procedure:

Calculate the SDS, taken as the acoustic speed.

$$\text{SDS} = \left(\frac{\gamma P}{\rho}\right)^{1/2} \text{ or } \left(\frac{\gamma R_0}{M} D_c T\right)^{1/2} \text{ or } \left(\frac{\gamma D_c k T}{\text{Mm}_i}\right)^{1/2} \tag{3.31}$$

M = Molecule Weight, R_0 = Universal Gas constant = 8×10^3 (SI units); m_i = mass of proton, k = Boltzmanns constant. D_c = departure coefficient = DN (1 + Z); where Z, here, is the effective charge of the plasma $Z = \sum_r^J r\alpha_r$, summed over all ionization levels $r = 1, \ldots, J$. This is computed using a corona model [140]. The procedure is described in more details in the description of the pinch phase.

DN = dissociation number, e.g. for deuterium DN = 2, whereas for argon DN = 1.

From shock theory, the shocked plasma temperature T is:

$$T = \frac{M}{R_0 D} \frac{2(\gamma - 1)}{(\gamma + 1)^2} \left(\frac{dr_s}{dt}\right)^2 \tag{3.32}$$

The communication delay time is then:

$$\Delta T = (r_p - r_s)/\text{SDS} \tag{3.33}$$

In our programme using the Microsoft EXCEL VISUAL BASIC, data of the step-by-step integration is stored row-by-row, each step corresponding to one row. Thus the ΔT may be converted to Δ(row number) by using Δ(row number) = ΔT/(timestep increment); this Δ(row number) being, of course, rounded off to an integer.

The correction then involves 'looking back' to the relevant row number to extract the corrected values of I_{delay}, $r_{p\text{-}delay}$ and $(dr_s/dt)_{delay}$. Thus in the actual

numerical integration, in Eq. (3.20) $\imath$ and κ_p are replaced by $\imath_{delay}$ and $\kappa_{p\text{-}delay}$ and in Eq. (3.22) $d\kappa_s/d\tau$ is replaced by $(d\kappa_s/d\tau)_{delay}$.

3.2.3.3 Radial Reflected Shock (RS) Phase

When the inward radial shock hits the axis, $\kappa_s = 0$. Thus in the computation, when $\kappa_s \leq 1$ we exit from radial inward shock phase. We start computing the RS phase. The RS is given a constant speed of 0.3 of on-axis inward radial shock speed [37].

In this phase, computation is carried out in real (SI) units.

Reflected Shock Speed

$$\frac{dr_r}{dt} = -0.3\left(\frac{dr_s}{dt}\right)_{on-axis} \tag{3.34}$$

Piston Speed

$$\frac{dr_p}{dt} = \frac{-\frac{r_p}{\gamma I}\left(1-\frac{r_s^2}{r_p^2}\right)\frac{dI}{dt} - \frac{r_p}{(\gamma+1)z_f}\left(1-\frac{r_s^2}{r_p^2}\right)\frac{dz_f}{dt}}{\frac{\gamma-1}{\gamma}+\frac{1}{\gamma}\frac{r_s^2}{r_p^2}} \tag{3.35}$$

Elongation Speed

$$\frac{dz_f}{dt} = -\left(\frac{2}{\gamma+1}\right)\left(\frac{dr_s}{dt}\right)_{on-axis} \tag{3.36}$$

Circuit Equation

$$\frac{dI}{dt} = \frac{V_0 - \frac{\int I dt}{C_0} - r_0 I - f_{cr}\frac{\mu}{2\pi}\left(\ln\frac{b}{r_p}\right)I\frac{dz_f}{dt} + f_{cr}\frac{\mu}{2\pi}\frac{z_f}{r_p}I\frac{dr_p}{dt}}{L_0 + f_{cr}\frac{\mu}{2\pi}(\ln c)z_0 + f_{cr}\frac{\mu}{2\pi}\left(\ln\frac{b}{r_p}\right)z_f} \tag{3.37}$$

The integration of these 4 coupled generating Eqs. (3.34)–(3.37) is carried out step-by-step as in the radial inward shock phase.

Tube Voltage

The tube voltage uses Eq. (3.29) above as in the radial inward shock phase.

In this phase as the RS (position r_r) moves outwards, the piston (position r_p) continues moving inwards. When the RS position reaches that of the piston the RS phase ends and the slow compression (pinch) phase begins.

3.2.3.4 Slow Compression (Pinch) Phase

Radiation-Coupled Dynamics (Piston) Equation

In this phase the piston speed is:

$$\frac{\mathrm{d}r_p}{\mathrm{d}t} = \frac{\frac{-r_p}{\gamma I}\frac{\mathrm{d}I}{\mathrm{d}t} - \frac{1}{\gamma+1}\frac{r_p}{z_f}\frac{\mathrm{d}z_f}{\mathrm{d}t} + \frac{4\pi(\gamma-1)}{\mu\gamma z_f}\frac{r_p}{f_{cr}^2 I^2}\frac{\mathrm{d}Q}{\mathrm{d}t}}{\frac{\gamma-1}{\gamma}} \tag{3.38}$$

Here we have included energy loss/gain terms into the equation of motion. The plasma gains energy from Joule heating; and loses energy through bremsstrahlung and line radiation. A positive power term $\mathrm{d}Q/\mathrm{d}t$ will tend to push the piston outwards whilst a power loss term will have the opposing effect. The specific heat ratio γ is taken as 5/3 for H, D, T and He gases. For other gases such as Ne, N, O, Ar, Kr, Xe, a sub-routine [140] based on a corona model is used to compute γ as a function of temperature; and for faster computing the values of γ for each gas are represented by a series of polynomials incorporated into the code. At the same time the charge number Z is also computed and included as another series of polynomials and incorporated into the code.

Joule Heating Component of $\mathrm{d}Q/\mathrm{d}t$

The Joule term is calculated from the following:

$$\frac{\mathrm{d}Q_J}{\mathrm{d}t} = RI^2 f_{cr}^2 \tag{3.39}$$

where plasma resistance R is calculated using the Spitzer form [141]:

$$R = \frac{1290 Z z_f}{\pi r_p^2 T^{3/2}} \tag{3.40}$$

And using Bennett [142] formula:

$$T = \frac{\mu}{8\pi^2 k} I^2 f_{cr}^2 / (\mathrm{D}N_0 a^2 f_{mr}) \tag{3.41}$$

Radiation Components of dQ/dt

The bremsstrahlung loss term may be written as:

$$\frac{\mathrm{d}Q_B}{\mathrm{d}t} = -1.6 \times 10^{-40} N_i^2 \left(\pi r_\mathrm{p}^2\right) z_\mathrm{f} T^{1/2} Z^3 \tag{3.42}$$

$$N_0 = 6 \times 10^{26} \frac{\rho_0}{M}; \quad N_\mathrm{i} = N_0 \mathrm{f}_\mathrm{mr} \left(\frac{a}{r_\mathrm{p}}\right)^2 \tag{3.43}$$

Z_n = atomic number, N_0 = ambient number density, N_i = ion number density.
The line loss term may be written as:

$$\frac{\mathrm{d}Q_L}{\mathrm{d}t} = -4.6 \times 10^{-31} N_\mathrm{i}^2 Z Z_n^4 \left(\pi r_\mathrm{p}^2\right) z_\mathrm{f} / T \tag{3.44}$$

And

$$\mathrm{d}Q/\mathrm{d}t = \mathrm{d}Q_J/\mathrm{d}t + \mathrm{d}Q_B/\mathrm{d}t + \mathrm{d}Q_L/\mathrm{d}t \tag{3.45}$$

where dQ/dt is the total power gain/loss of the plasma column. In the standard code, recombination radiation is similarly incorporated into dQ/dt.

By this coupling, if, for example, the radiation loss dQ/dt is severe, this would lead to a large value of dr_p/dt inwards. In the extreme case, this leads to radiation collapse [50], with r_p going rapidly to such small values that the plasma becomes opaque to the outgoing radiation, thus stopping the radiation loss.

This radiation collapse occurs at a critical current of 1.6 MA (the Pease-Braginski current) for deuterium [143, 144]. For gases such as Ne or Ar, because of intense line radiation, the critical current is reduced to even below 100 kA, depending on the plasma temperature [50, 145].

Plasma Self-absorption and Transition from Volumetric Emission to Surface Emission

Plasma self-absorption [10, 146, 147] and volumetric (emission described above) to surface emission of the pinch column are implemented in the following manner.

The photonic excitation number is written as follows:

$$M = 1.66 \times 10^{-15} r_\mathrm{p} Z_n^{0.5} n_\mathrm{i} / (Z T^{1.5}) \tag{3.46}$$

with T in eV, rest in SI units.

The volumetric plasma self-absorption correction factor A:

$$A_1 = \left(1 + 10^{-14} n_i Z\right) / \left(T^{3.5}\right); A_2 = 1/_1; A = A_2^{(1+M)} \tag{3.47}$$

Transition from volumetric to surface emission occurs when the absorption correction factor goes from 1 (no absorption) down to $1/e$ ($e = 2.718$) when the emission becomes surface-like given by:

$$\frac{dQ_L}{dt} = -\text{const} Z^{0.5} Z_n^{3.5} r_p z_f T^4 \tag{3.48}$$

where the constant '*const*' is taken as 4.62×10^{-16} to conform with numerical experimental observations that this value enables the smoothest transition, in general, in terms of power values from volumetric to surface emission.

Neutron Yield

Neutron yield is calculated with two components, thermonuclear term and beam-target term. The thermonuclear term is taken as:

$$dY_{th} = 0.5 n_i^2 \pi r_p^2 z_f \langle \sigma v \rangle (\text{time interval}) \tag{3.49}$$

where $\langle \sigma v \rangle$ is the thermalized fusion cross section-velocity product corresponding to the plasma temperature [148], for the time interval under consideration. The yield Y_{th} is obtained by summing up over all intervals during the focus pinch.

The beam-target term is derived using the following phenomenological beam-target neutron generating mechanism [12], incorporated in the code version RADPFV5.13 and later. A beam of fast deuteron ions is produced by diode action in a thin layer close to the anode, with plasma disruptions generating the necessary high voltages. The beam interacts with the hot dense plasma of the focus pinch column to produce the fusion neutrons. In this modelling, each factor contributing to the yield is estimated as a proportional quantity and the yield is obtained as an expression with a proportionality constant. The yield is then calibrated against a known experimental point.

The beam-target yield is written as: $Y_{b-t} \sim n_b n_i (r_p^2 z_p)(\sigma v_b)\tau$

where n_b is the number of beam ions per unit plasma volume, n_i is the ion density, r_p is the radius of the plasma pinch with length z_p, σ the cross section of the D–D fusion reaction, n-branch [148], v_b the beam ion speed and τ is the beam-target interaction time assumed proportional to the confinement time of the plasma column. Total beam energy is estimated [12] as proportional to $L_p I_{pinch}^2$, a measure of the pinch inductance energy, with L_p being the focus pinch inductance. Thus the number of beam ions is $N_b \sim L_p I_{pinch}^2 / v_b^2$ and n_b is N_b divided by the focus pinch volume. Note that $L_p \sim \ln(b/r_p) z_p$, that [137] $\tau \sim r_p \sim z_p$, and that $v_b \sim U^{1/2}$

where U is the disruption-caused diode voltage. Here b is the cathode radius. We also assume reasonably that U is proportional to $V_{\max}$, the maximum voltage induced by the current sheet collapsing radially towards the axis.

Hence:

$$Y_{\mathrm{b-t}} = C_n n_{\mathrm{i}} I_{\mathrm{pinch}}^2 z_{\mathrm{p}}^2 \left(\ln\left(b/r_{\mathrm{p}}\right)\right)\sigma / V_{\max}^{1/2} \tag{3.50}$$

where I_{pinch} is the current flowing through the pinch at start of the slow compression phase; r_{p} and z_{p} are the pinch dimensions at end of that phase. Here C_{n} is a constant which in practice we will calibrate with an experimental point.

The D–D cross section is highly sensitive to the beam energy so it is necessary to use the appropriate range of beam energy to compute σ. The code computes $V_{\max}$ of the order of 20–50 kV. However, it is known [12], from experiments that the ion energy responsible for the beam-target neutrons is in the range 50–150 keV, and for smaller lower-voltage machines the relevant energy [149] could be lower at 30–60 keV. Thus to align with experimental observations the D–D cross section σ is reasonably obtained by using beam energy fitted to 3 times $V_{\max}$.

A plot of experimentally measured neutron yield Y_{n} versus I_{pinch} was made combining all available experimental data [7–10, 21, 44, 100, 150, 151]. This gave a fit of $Y_{\mathrm{n}} = 9 \times 10^{10} I_{\mathrm{pinch}}^{3.8}$ for I_{pinch} in the range 0.1–1 MA [21, 37, 44, 100]. From this plot, a calibration point was chosen at 0.5 MA, $Y_{\mathrm{n}} = 7 \times 10^9$ neutrons. The model code [10] from version RADPFV5.13 onwards was thus calibrated to compute $Y_{\mathrm{b\text{-}t}}$ which turns out to be typically the same as Y_{n} since the thermonuclear component is typically negligible.

Column Elongation

Whereas in the radial RS phase we have adopted a 'frozen' elongation speed model, we now allow the elongation to be driven fully by the plasma pressure.

$$\frac{\mathrm{d}z_{\mathrm{f}}}{\mathrm{d}t} = \left[\frac{\mu}{4\pi^2(\gamma+1)\rho_0}\right]^{1/2} \frac{I f_{\mathrm{cr}}}{r_{\mathrm{p}}} \tag{3.51}$$

Circuit Current Equation

$$\frac{\mathrm{d}I}{\mathrm{d}t} = \frac{V_0 - \frac{\int I \mathrm{d}t}{C_0} - \frac{\mu}{2\pi}\left(\ln\frac{b}{r_{\mathrm{p}}}\right)\frac{\mathrm{d}z_{\mathrm{f}}}{\mathrm{d}t} I f_{\mathrm{cr}} + \frac{\mu}{2\pi}\frac{z_{\mathrm{f}}}{r_{\mathrm{p}}}\frac{\mathrm{d}r_{\mathrm{p}}}{\mathrm{d}t} I f_{\mathrm{cr}} - I(R f_{\mathrm{cr}} + r_0)}{L_{\mathrm{o}} + \frac{\mu}{2\pi} f_{\mathrm{cr}}\left((\ln c) z_0 + \left(\ln\frac{b}{r_{\mathrm{p}}}\right) z_{\mathrm{f}}\right)} \tag{3.52}$$

Voltage Across Plasma Focus Terminals

$$V = \frac{\mu f_{cr}}{2\pi} I \left[\left(\ln \frac{b}{r_p} \right) \frac{dz_f}{dt} - \frac{z_f}{r_p} \frac{dr_p}{dt} \right] + \frac{\mu f_{cr}}{2\pi} \left[\left(\ln \frac{b}{r_p} \right) z_f + (\ln C) z_0 \right] \frac{dI}{dt} + RIf_{cr} \quad (3.53)$$

Pinch Phase Dynamics and Yields of Neutrons, Soft X-rays, Ion Beams and Fast Plasma Stream

Equations (3.38), (3.51) and (3.52) are the coupled Generating Equations integrated for r_p, z_f and I. At each step the value of dQ/dt is also evaluated as above using Eqs. (3.39)–(3.45) with the effect of plasma self-absorption implemented using Eqs. (3.46)–(3.48). Soft X-rays of various gases are computed using Eq. (3.44) modified by the effect of plasma self-absorption. Neutron yield is computed using Eqs. (3.50) and (3.49). In the latest version RADPFV5.15FIB fast ion beam (FIB) fluence and flux, energy fluence and flux, power flow and damage factors as well as fast plasma streams (FPS) exiting the pinch are also computed [58, 59].

The step-by-step integration is terminated at the end of a period related to the transit time of small disturbance speed across the plasma pinch column.

3.2.3.5 Expanded Column Axial Phase

We model the expanded column axial phase [10] in the following manner. In the expanded column phase we assume that the current flows uniformly from anode to cathode in a uniform column having the same radius as the anode and a length of z.

The normalized equations (same normalization as in axial phase):

Circuit current:

$$\frac{d\imath}{d\tau} = \frac{1 - \int \imath d\tau - \beta\imath \frac{d\zeta}{d\tau} e - \delta\imath}{1 + \beta + \beta(\zeta - 1)e} \quad (3.54)$$

where

$$e = \left(\ln c + \frac{1}{z} \right) / \ln c$$

Motion:

$$\frac{d^2\zeta}{d\tau^2} = \frac{\alpha^2 \imath^2 e_1 - h^2 \left(\frac{d\zeta}{d\tau} \right)^2}{1 + h^2(\zeta - 1)} \quad (3.55)$$

with

$$h = \left[c^2/(c^2-1)\right]^{1/2}$$
$$e_1 = \left(\ln c + \frac{1}{4}\right)/(\ln c)$$

The initial conditions for $\imath$ and $\int \imath d\tau$ are the last values of $\imath$ and $\int \imath d\tau$ from the last phase. The initial value of ζ is $\zeta = 1 + \zeta_f$ where ζ_f is the last length of the focus column, but normalized to z_0, rather than a. This phase is terminated when the discharge has proceeded to a half cycle. The purpose of computing this phase is to allow the fitting of the computed current to the measured to the point when the current has dropped to low levels beyond interest. This completes the integration of all five phases.

3.2.4 Procedure for Using the Code

The Lee model code is configured [10, 37, 152] to work as any plasma focus by inputting into the configuration panel of the code (see Fig. 3.8a for the main Sheet of the code and guide diagram Fig. 3.8b-block 1 is the configuration panel):

Bank parameters L_0, C_0 and stray circuit resistance r_0;
Tube parameters b, a and z_0;
Model parameters f_m, f_c, f_{mr} and f_{cr} (either fitted or trial values) and
Operational parameters V_0 and P_0 and the fill gas.

The computed total current waveform is fitted to a measured waveform by varying model parameters f_m, f_c, f_{mr} and f_{cr} sequentially, until the computed waveform agrees with the measured waveform [10, 37].

First, the axial model factors f_m, f_c are adjusted (fitted) until the features in Fig. 3.9: **'1'** computed rising slope of the total current trace; **'2'** the rounding off of the peak current, as well as **'3'** the peak current itself, is in reasonable (typically very good) fit with the measured total current trace (see Fig. 3.9, measured trace fitted with computed trace).

Then we proceed to adjust (fit) the radial phase model factors f_{mr} and f_{cr} until features **'4'** the computed slope and **'5'** the depth of the dip agree with the measured values. Note that the fitting of the computed trace with the measured current trace is done up to the end of the radial phase which is typically at the bottom of the current dip. Fitting of the computed and measured current traces beyond this point is not done. If there is significant divergence of the computed with the measured trace beyond the end of the radial phase, this divergence is not considered important.

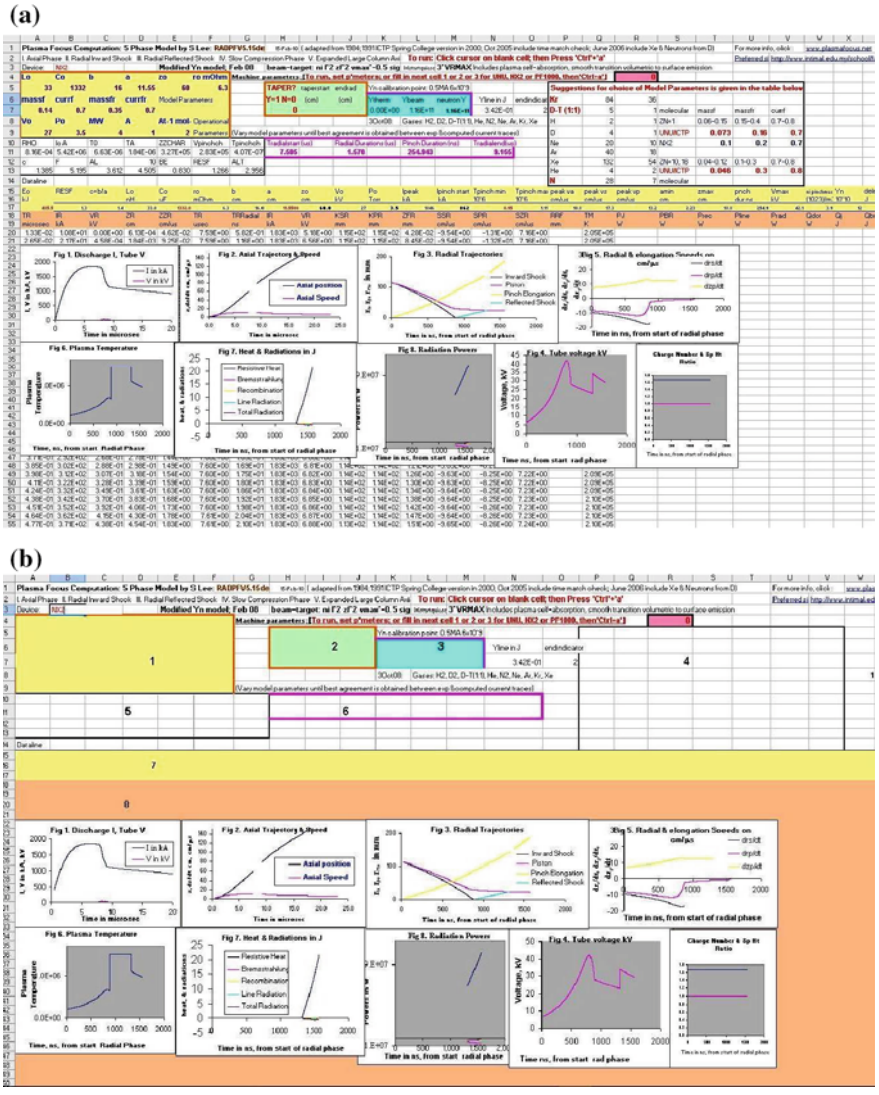

Fig. 3.8 **a** Showing the blocks of sheet 1 of RADPFV5.15—showing display after run—refer 3.8b for guide dividing the data display in blocks (details are deliberately blurred out). **b** Guide to sheet 1: Block 1 (see above *labelled 1* in *gold*) = main configuration panel; Block 2 (see above *labelled 2* in *green*) = taper configuration sub-panel; Block 3 (see above *labelled 3* in *blue*) = neutron yields; (cell *R4* in *pink*) = selection of 1 of three reference machines; Block 4 (*labelled 4 not coloured*) = data of applicable gases and suggested model parameters; Block 5 (*labelled 5*, *not coloured*) = some computed useful parameters; Block 6 (*labelled 6*, *not coloured*) = start and end of phases; Block 7 (*labelled 7*, in *gold*) = row (17) of computed results (dataline); Block 8 (*labelled 8*, in *brown*, shown partially above) = from row 20 downwards for typically several thousand rows: computed point by point data for various quantities described in the headings of rows 18 and 19

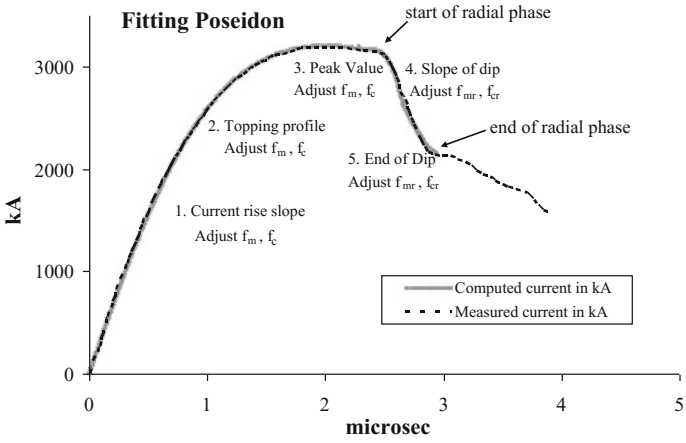

Fig. 3.9 The 5-point fitting of computed current trace to measured (reference) current trace. *Point 1* is the current rise slope. *Point 2* is the topping profile. *Point 3* is the peak value of the current. *Point 4* is the slope of the current dip. *Point 5* is the bottom of the current dip. Fitting is done up to *point 5* only. Further agreement or divergence of the computed trace with/from the measured trace is only incidental and not considered to be important

In this example (Poseidon plasma focus), after fitting the five features **'1'** to **'5'** above, the following fitted model parameters are obtained: $f_m = 0.277$, $f_c = 0.6$, $f_{mr} = 0.47$ and $f_{cr} = 0.44$.

Typically refinements to the fitting process require adjustments to L_0 and r_0, as well as the discharge start time and measured peak value. Because the code is charge consistent, once the measured waveform is accurately fitted, the correct peak current is the computed value which is then be used to calibrate the measured peak current. For Poseidon, we fitted the value of $L_0 = 17.7$ nH and $r_0 = 1.7$ mΩ.

Once fitted the code outputs in tabular and graphical forms [10, 37] realistic data of the following: axial and radial dynamics (positions and speeds), pinch length and minimum pinch radius, temperatures and densities, bremsstrahlung and line yields, thermonuclear and beam-target neutron yields. Also, energy distributions and thermodynamics properties are found to be realistic representations of the actual machines.

An extended code also gives fast ion beam flux and fluence, energy flux and fluence, power flow and damage factors, fast plasma stream energies and speeds [58, 59]. This concludes the description of the standard 5-phase Lee Model code. This 5-phase code has been used to fit all low L_0 plasma focus with adequate accuracy (an example is given in Fig. 3.10 [12]). However, it was found necessary for high L_0 plasma focus devices to include a 6-phase (phase 4a) in order to achieve a complete fit. The development of the code variant version (RADPFV6.1b) [10] for phase 4a is described in the following section.

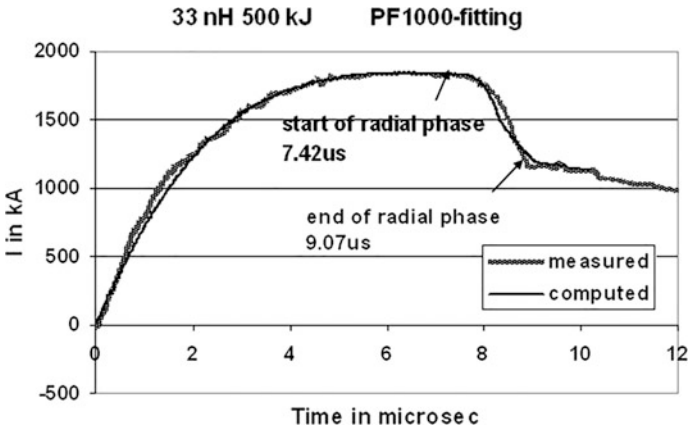

Fig. 3.10 A typical 5-phase fit of a low inductance PF; showing reasonable agreement between computed and measured waveforms. This current trace is digitized from PF1000 [12]. Reprinted from Lee et al. [110]. Copyright (2011), with permission from Springer Science+Business Media, LLC

3.2.5 Adding a 6th Phase: From Pinch (Slow Compression) Phase to Large Volume Plasma Phase-Transition Phase 4a

From experiments, it is well known that after a brief period (few ns for a small plasma focus), the quiescent column is rapidly broken up by instabilities. One effect is a huge spike of voltage, partially observed at focus tube terminals. This voltage spike is responsible for driving ion beams (forward direction) and relativistic electron beam, REB, (negative direction, towards the anode) with energies typically 200 keV. The final result of this instability mechanism is the breaking up of the focus pinch into a large expanded current column.

3.2.5.1 The 5-Phase Model Is Adequate for Low Inductance L_0 Plasma Focus Devices

The 5-phase Lee code does not model the transition from Phase 4 to Phase 5. Nevertheless it has been found to be adequate for modelling all the well-known plasma focus with low static inductance L_0 [10, 12, 21, 74] which we have fitted; in the sense that the computed current traces can be fitted to the measured current trace by adjustment of the model parameters f_m, f_c, f_{mr} and f_{cr}. This has been the case for the PF1000, PF400J, NX1, NX2, DPF78, Poseidon [106], FMPF1 [153–155], and FN-II [91]. The case of a low inductance machine (Poseidon) is already shown in Fig. 3.9. Another example of a typical 5-phase fit is shown in Fig. 3.10.

Amongst the well-published plasma focus devices only the UNU/ICTP PFF [7–9] which has relatively higher L_0 of 110 nH presented a problem in the fitting. This was due to a very small computed current dip and a measured current dip that has always been masked by very large oscillations taken to be noise; although when operated in unusually low-pressure regime, a clear discrepancy was noted between the computed and measured current trace [156, 157].

In 2012 a current trace from the then newly commissioned KSU DPF (Kansas State University Dense Plasma Focus) [89, 110] which had an even higher L_0, was obtained by numerically integrating the output of a dI/dt coil [108]. An analysis of the frequency response of the coil system and the digital storage oscilloscope (DSO) signal acquisition system showed that noise frequencies below 200 MHz were removed by the numerical integration. The resultant waveform is clean and clearly shows an extended current dip with good depth and duration (see Fig. 3.11, the darker trace). The KSU DPF shows very consistent operation with more than 95% of the shots showing current dips with similar depth and duration.

Following the usual procedure of the Lee model code, an attempt was made to fit the computed current trace with the measured. The computed current trace has only a small dip as is characteristic of the computed current dip of a device with large static inductance L_0. All possible adjustments were made to the model parameters but the computed current dip could not be made to fit the whole measured current dip. The best fit is shown in Fig. 3.11; which shows that the computed dip does fit the first small part of the measured current dip. But the measured dip continues on in both depth and duration far beyond the computed dip.

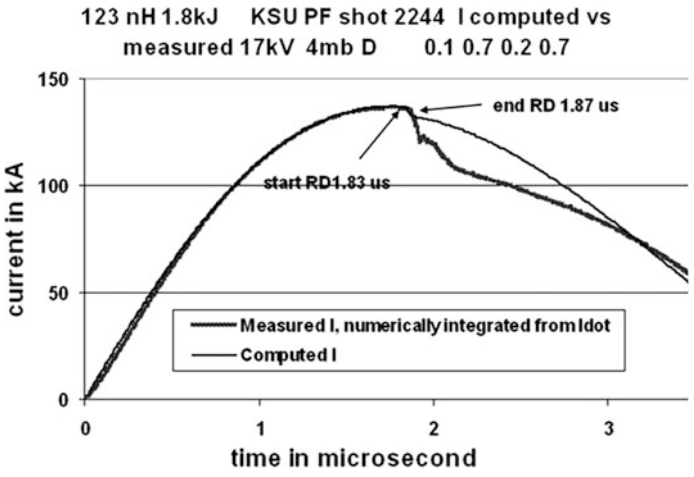

Fig. 3.11 Computed current trace (*lighter trace*) with best attempt to fit the measured current trace (*darker trace*) of the KSU PF. Reprinted from Lee et al. [110]. Copyright (2011), with permission from Springer Science+Business Media, LLC

3.2.5.2 Factors Distinguishing the Two Types of Plasma Focus Devices

The code models the electrodynamic situation using the slug model and a reflected shock for the radial phase, ending the radial phase in phase 4. Let's call the radial phase modelled in that manner as the REGULAR radial phase. This REGULAR radial phase, in increasing sharply the inductance of the system (constituting also a dynamic resistance [21, 37, 44]) causes a dip on the current trace. Call this the regular dip, RD. At the end of the REGULAR radial phase, experimental observations point to another phase (phase 4a) of 'instabilities' manifesting in anomalous resistance [1]. These effects would also extract energy from the magnetic field and hence produce further current dips. These effects are not modelled specifically in the code. Call this the extended current dip, ED.

However, it may be argued that as long as the model parameters can be stretched sufficiently to have the computed current dip agree with the measured current dip, then in a gross sense, the modelling is energetically and mass-wise equivalent to the physical situation. Then the resulting gross characteristics from the model would give a fair representation of the actual plasma properties, even though the model has not specifically modelled ED. In other words, RD is able to be stretched to also model ED, with equivalent energetics and mass implications. Whether RD can be stretched sufficiently to cover ED depends on the relative sizes of the two effects. If RD is already a big dip, then this effect may dominate and it is more likely that RD may be stretched sufficiently to cover the less prominent ED. If RD is only a miniscule dip and ED is a big dip, then it is unlikely that the RD can be stretched enough to encompass the ED.

We looked at the inductance L_0 and the ratio of L_0 with various inductances inherent in the system. We considered the inductance ratio $R_L = (L_0 + L_a)/L_{pinch}$ where L_{pinch} is the inductance of the focus pinch at the end of the REGULAR radial phase, L_0 the bank static inductance and L_a the inductance of the axial part of the focus tube. We also considered the remnant energy ratio $R_{EL} = (E_{L0} + E_{La})/E_{Lpinch}$ where E_{L0} = energy stored in L_0 at end of the RD, E_{La} = energy stored in L_a at end of the RD and E_{Lpinch} = energy stored inductively in the pinch at end of RD.

Computing the values of these two quantities [110] for PF1000, Poseidon, DPF78, NX2, PF400J, FMPF-1, FNII, UNU/ICTPPFF and KSU PF, we have a range of devices from very big (MJ) to rather small (sub-kJ) of which we have well-documented fittings.

The results show that the smaller is the ratio R_L, the bigger is the regular current dip (RD). When this ratio is large (primarily due to a large L_0 in the numerator), like in the case of KSU PF, the REGULAR radial phase RD is minuscule. Likewise, the trend is also observed for the ratio R_{EL}. The smaller this energy ratio, the bigger is the current dip.

On the basis of these two ratios, we have divided the plasma focus devices into two types: T1 and T2. Type T1 is for plasma focus devices with relatively small L_0 with large RD's and with relatively small ratios R_L and R_{EL}. These T1 focus devices are well-fitted using the Lee model code. The computed current traces (with radial phase computed only as a regular dip RD) are well-fitted to the whole measured

current trace. Type T2 is for plasma focus devices with relatively large L_0 with small RD's and with relatively large ratios of R_L and R_{EL}. These T2 focus devices are not well-fitted using the Lee model code. The computed current trace shows only a small dip which is fitted to the first portion of the measured current dip, but the measured current dip has an extended portion which is not well-fitted using the 5-phase Lee model code.

Next, we note that the magnetic energy per unit mass at the start of the radial phase is the same across the whole range of devices [137]. Thus T1 with a big RD drops the current a lot and strongly depletes the magnetic energy per unit mass at the end of the RD, leading to a small ED. Consequently, T1 are completely fitted using a model that computes only the RD, stretching the model parameters until the large RD covers also the small ED. Conversely, a T2 plasma focus has a small RD, consequently a large ED and cannot be completely fitted with the computed RD. Thus a big RD drops the current a lot and strongly depletes the magnetic energy per unit mass at the end of the REGULAR radial phase. Hence a device with small R_L produces a big RD and ends up with relatively less energy per unit mass at the end of the REGULAR phase when compared to a device with a big value of R_L. Therefore a big RD generally tends to lead to a small ED; whereas a small RD is more conducive to lead to a larger ED.

From the above we summarized that T1 plasma focus has a big RD, consequently, a small ED and hence can be completely fitted using a model that computes only the RD, which is able to stretch its RD by stretching the model parameters until the large RD covers also the small ED. Moreover energetically and mass-wise the fitting is correct. On the other hand, T2 plasma focus has a small RD, consequently a large ED. T2 plasma focus cannot be completely fitted with the RD computed from the code, no matter how the model parameters are stretched. To fit the computed current trace to the measured current for T2, a phase 4a needs to be included into the model in order to progress the current dip beyond the small RD into the large ED part of the current dip.

One way to simulate the current ED is to assign the phase 4a period with an anomalous resistance term such as:

$$R = R_0[\exp(-t/t_2) - \exp(-t/t_1)] \tag{3.56}$$

where R_0 could be of the order of 1 Ω, t_1 is a characteristic time representative of the rise time of the anomalous resistance and t_2 is characteristic of the fall time of the anomalous resistance (Fig. 3.12).

We have applied this technique to the KSU current waveform (Fig. 3.11). We note that using the 5-phase code, the computed RD does not follow the measured current dip which goes on to an ED. Following that first current dip in this particular case, the dip continues in a second portion which is almost flat then followed by a third section which is less steep than the first dip but of slightly longer duration. We applied a resistance term to each of the 3 sections. We adjusted the parameters R_0, t_2 and t_1 for each of the section as well as a fraction (*endfraction*) which terminates the term. The fitted parameters are as follows in Table 3.1:

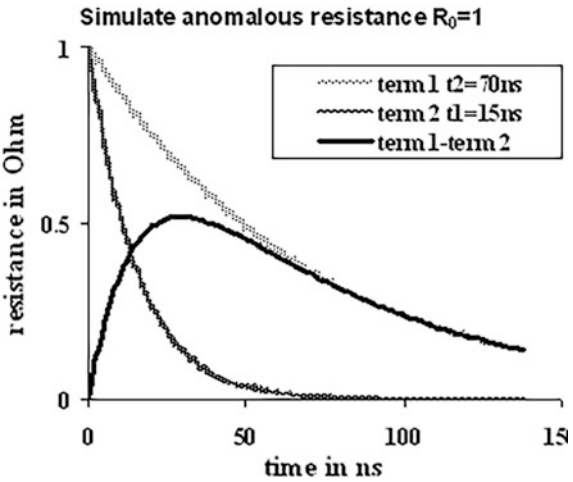

Fig. 3.12 Simulating anomalous resistance. *Term 1* and *term 2* refer to the two terms on the right-hand side of Eq. (3.56). Reprinted from Lee et al. [110]. Copyright (2011), with permission from Springer Science+Business Media, LLC

Table 3.1 Anomalous resistances used for the fitting

ED	R_0 (Ω)	t_2 (ns)	t_1 (ns)	Endfraction
Dip 1	1.0	70	15	0.53
Dip 2	0.2	70	40	0.4
Dip 3	0.5	70	25	1.0

With these parameters, it is found that the computed current dip now fits the measured current dip all the way to the end of the current dip at 2.1 μs (see Fig. 3.11) and even beyond to 2.6 μs where the computation ends as we are not interested in the fitting beyond phase 4a. The fitting involved the fitting of the RD followed by the ED of the first dip, then the second and third dips treated as ED's each requiring a separate anomalous resistance function of the type Eq. (3.56).

The resistance functions used for the fitting are also shown in Fig. 3.13 (dashed trace, with the resistance values magnified 200 times in order to be visible on the scale of Fig. 3.13). The computed voltage waveform is also shown (trace labelled 2) compared with the measured voltage waveform (trace labelled 1). The correspondence of the computed voltage waveform and the measured is seen clearly. The lower measured values of voltage may be attributed to the inadequate frequency response of the resistive divider voltage probe.

3.2.5.3 Procedure for Using 6-Phase Code—Control Panel for Adding Anomalous Phases

The code is extended to the 6-phase version RADPFV6.1b. The corresponding control is by way of an additional panel for the anomalous resistances (default

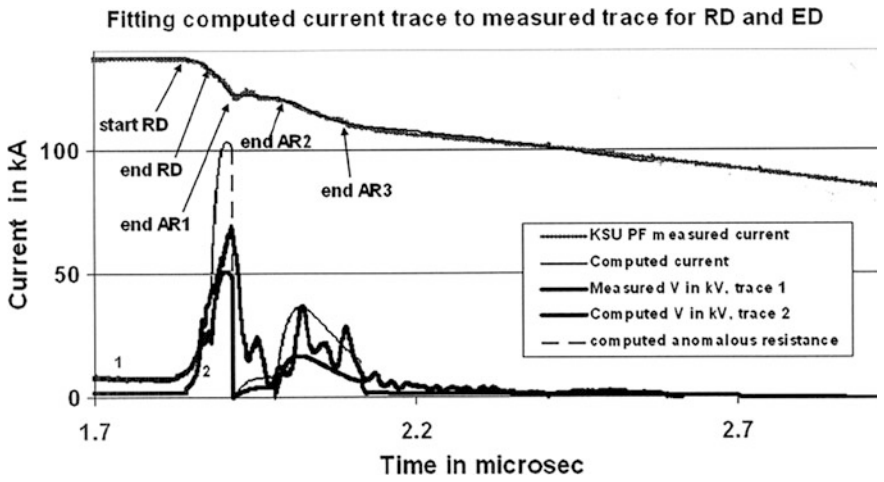

Fig. 3.13 Computed current (dip region only and expanded to see details) fitted to measured current with the inclusion of Phase 4a. Note that the computed current trace is fitted so well to the measured current trace that the two traces lie very closely on top of each other, these being the topmost traces (overlapping). Note also that the computed trace is stopped at 2.6 μs which is beyond the end of the AR3. *Note*: *AR* stands for "anamolous resistance". Reprinted from Lee et al. [110]. Copyright (2011), with permission from Springer Science+Business Media, LLC

design is a 3-step AR). The main sheet (sheet 1) of the 6-phase code is the same as the 5-phase code depicted in Fig. 3.8b; except for an additional panel inserted below block 6 (see Fig. 3.8a and b for the location of block 6).

3.2.6 Conclusion for Description of the Lee Model Code

We presented the complete 5-phase Lee Model code, which is found to be adequate for fitting the computed current waveform and the measured waveform of each low L_0 (Type T1) plasma focus by varying two pairs of mass and current factors, one each for the axial and radial phases. Once fitted the code outputs in tabular and graphical forms realistic axial and radial dynamics (positions and speeds), pinch length and minimum pinch radius, temperatures and densities, bremsstrahlung and line yields, thermonuclear and beam-target yields, fast ion beam flux and fluence, energy flux and fluence, power flow and damage factors, fast plasma stream energies and speeds. All tests to date of computed with measured quantities have shown good agreement. The next section reviews the considerable results of the code of designing and optimizing machines, providing expected neutron, soft X-rays (various gases) and ion beams (various gases) yields, giving insights into current and neutron yield limitations, deterioration of neutron scaling (neutron saturation), radiative collapse, speed-enhanced PF, current-stepped PF and

extraction of diagnostic data and anomalous resistance data from current signals. Yield scaling laws for neutron, soft X-rays and ion beams are obtained from the code. In one respect the 5-phase code has been found wanting. For high L_0 (Type T2) PF devices it is able to fit the computed current trace to the first part of the measured current trace; but the measured current then exhibits a much larger 'extended' dip which the computed current cannot be fitted; although the 5-phase code does produce reasonable values of neutron and soft X-rays yields in comparison with measured yields even for the high L_0 cases. The section concludes with an extended 6-phase code in order to complete the current fitting for high L_0 machines. An important use of the 6-phase code is for gathering data on the anomalous resistance of the plasma focus.

3.3 Scaling Properties of the Plasma Focus Arising from the Numerical Experiments

3.3.1 Various Plasma Focus Devices

In Fig. 3.14 (upper left) is shown the UNU ICTP PFF 3 kJ device [7–9, 57] mounted on a 1 m × 1 m × 0.5 m trolley, which was wheeled around the International Centre for Theoretical Physics (ICTP) for the 1991 and 1993 Plasma Physics Colleges during the experimental sessions. The single capacitor is seen in the picture mounted on the trolley. In contrast, the upper right image in Fig. 3.14 shows on approximately the same scale, the PF1000, the 1 MJ plasma focus device [12] at the International Centre for Dense Magnetized Plasmas (ICDMP) in Warsaw, Poland. Only the chamber and the cables connecting the plasma focus to the capacitors are shown. The capacitor bank with its 288 capacitors, switches and chargers are located in a separate hall.

The comparison of physical dimensions of the devices is shown, refer lower part of the image in Fig. 3.14, in the shadowgraphs of the focus pinches of the two devices, on the same scale for comparison of the pinch dimensions. Each dimension of each pinch scales according to the anode radius of the corresponding device. It will be shown later that the anode radius scales to the peak current available to drive the plasma focus.

3.3.2 Scaling Properties (Mainly Axial Phase)

Table 3.2 shows the characteristics of three plasma focus devices including the two shown in Fig. 3.14 [7, 11, 12]. These characteristics are taken from the code after using model parameters resulting from the fitting of computed current waveform with the corresponding measured current waveform.

Above: A small PF (3kJ UNU ICTP PFF) on same scale for comparison with a large PF (1 MJ PF1000)
Below: Shadowgraphs of the pinches of the two machines placed on the same scale.

Anode radius	1 cm	11.6 cm
Pinch Radius:	1 mm	12 mm
Pinch length:	8 mm	90 mm
Lifetime	~10ns	~100 ns

Fig. 3.14 Comparing physical sizes and pinch sizes for a small PF (3 kJ) and a large PF (1 MJ)

In Table 3.2 we look at the PF1000 and study its properties at typical operation with energy storage at 500 kJ level. We compare this big focus (MJ) with two small devices at the kJ and sub-kJ level. The storage energy of the three devices covers a range over four orders of magnitude. In a survey of existing machines in 1996, it was noted [137] that machines, when optimized for neutron yield all, had axial speeds close to 10 cm/μs. Observations since then have not changed this view. The reason for a lower limit of speed is due to ionization and the need for a sufficiently large magnetic Reynold number to achieve efficient electromagnetic drive. The upper limit has been postulated [137] as due to a separation of centre of force field from the centre of mass field which would render the electromagnetic drive to become inefficient as the dynamics transitions from axial to radial phase. From Table 3.2 we note:

Table 3.2 Characteristics of three PF devices covering energy range over four orders of magnitude

PF devices	E_0 (kJ)	A (cm)	Z_0 (cm)	V_0 (kV)	P_0 (Torr)	I_{peak} (kA)	v_a (cm/μs)	ID (kA/cm)	SF [(kA cm^{-1})/Torr$^{0.5}$]	Y_n (10^8n)
PF1000	486	11.6	60	27	4	1850	11	160	85	1100
UNUPFF	2.7	1.0	15.5	14	3	164	9	173	100	0.20
PF400J	0.4	0.6	1.7	28	7	126	9	210	82	0.01

1. Voltage and pressure do not have particular relationship to E_0.
2. Peak current I_{peak} increases with E_0.
3. Anode radius 'a' increases with E_0.
4. ID (current per *cm* of anode radius), I_{peak}/a, is in a narrow range from 160 to 210 kA/cm.
5. SF (speed or drive factor), $(I_{peak}/a)/P_0^{0.5}$, is 82–100 kA cm^{-1}/Torr$^{0.5}$ deuterium gas [137].
6. Peak axial speed v_a is in the narrow range 9–11 cm/μs.
7. Neutron yield Y_n ranges from 10^6 neutrons/shot for the smallest device to 10^{11} neutrons/shot for PF1000.

We stress that whereas the ID and SF are practically constant at around 180 kA/cm and (90 kA/cm)/Torr$^{0.5}$ for deuterium gas operation throughout the range of small to big devices, Y_n changes over 5 orders of magnitude.

The data of Table 3.2 is generated from numerical experiments and most of the data has been confirmed by actual experimental measurements and observations.

We note that the speed factor SF is inherent in the equations of motion (see Sections "Normalizing the Generating Equations to Obtain Characteristic Axial Transit Time, Characteristic Axial Speed and Speed Factor S; and Scaling Parameters of Times, α and Inductances β" and "Normalizing the Generating Equations to Obtain Characteristic Radial Transit Time, Characteristic Radial Transit Speed and Speed Factor S; and Scaling Parameters for Times α1 and Inductances β1; also Compare Axial to Radial Length Scale, Time Scale and Speed Scale)". $(SF)^2$ is a measure of the kinetic energy per unit mass. Soto [158] has proposed an empirical 'stored energy per unit volume parameter' $28E_0/a^3$ as another constant for plasma focus machines with a range of (0.4–80) × 10^{10} J m^{-3}. The wide range of that parameter is because it is a "storage energy density" which translates into plasma energy density with different efficiency depending on the widely differing performance of different machines. Thus to result in the necessary plasma energy density (which is found to be a near constant for optimized neutron production) requires widely differing initial storage density. It is important to distinguish that whereas the Speed Factor is a fundamental scaling quantity derived inherently from the axial and radial phase equations, the 'stored energy per unit volume' parameter is an empirical parameter with a wide range of values.

3.3.3 Scaling Properties (Mainly Radial Phase)

Table 3.3 compares the properties of the same three plasma focus devices [159] related to the radial phase and pinch.

From Table 3.3 we note:

1. The pinch temperature T_{pinch} is strongly correlated to the square of the radial pinch speed v_p.
2. The radial pinch speed v_p itself is closely correlated to the value of v_a and $c = b/a$; so that for a constant v_a, v_p is almost proportional to the value of c. Thus it is noted that whereas the PF1000 has largest v_a of the 3 machines, it has the lowest v_p of the 3 machines. This is entirely due to its low value of c; as can be seen from Eq. (3.28).
3. The dimensions and lifetime of the focus pinch scale as the anode radius 'a'.
4. The r_{min}/a is almost constant at 0.14–0.17.
5. The z_{max}/a is almost constant at 1.5. (*N*ote: z_{max} is twice the visible length of the pinch.)
6. Pinch duration has a relatively narrow range of 8–14 ns per cm of anode radius.
7. The pinch duration per unit anode radius is correlated to the inverse of T_{pinch}.

This summary shows that the computed dimensions and lifetime of the pinch agree with the measured values depicted in Fig. 3.14.

T_{pinch} itself is a measure of the energy per unit mass. It is quite remarkable that this energy density at the focus pinch varies so little (factor of 5) over a range of device energy four orders of magnitude.

This practically constant pinch energy density (per unit mass) is related to the constancy of the axial speed moderated by the effect of the values of c on the radial speed.

The constancy of r_{min}/a suggests that the devices also produce the same compression of ambient density to maximum pinch density; with the ratio (maximum pinch density)/(ambient density) being proportional to $(a/r_{min})^2$. So for two devices of different sizes starting with the same ambient fill density, the maximum pinch density would be the same.

Note that Table 3.3 is for operation in deuterium over the range of machines. The deuterium is fully ionized and behaves like an ideal gas under the high

Table 3.3 Properties of the pinches of the three plasma focus devices operated in deuterium

PF devices	$c = b/a$	a (cm)	T_{pinch} (10^6/K)	v_p (cm/μs)	r_{min} (cm)	z_{max} (cm)	Pinch duration (ns)	r_{min}/a	z_{max}/a	Pinch duration/a (ns/cm)
PF1000	1.4	11.6	2	13	2.2	19	165	0.17	1.6	14
UNU PFF	3.4	1.0	8	26	0.13	1.4	7.3	0.14	1.4	8
PF400 J	2.6	0.6	6	23	0.09	0.8	5.2	0.14	1.4	9

temperature operation of the plasma focus. In gases that are freely ionizing the compressions are affected by the thermodynamics of ionization and also line radiation. These effects will be further discussed in Sect. 3.5.

3.3.4 Scaling Properties: Rules of Thumb

From the above discussion, we may put down as rule-of-thumb the following scaling relationships, subject to minor variations caused primarily by the variation in c (cathode to anode radius ratio).

1. Axial phase energy density (per unit mass): constant
2. Radial phase energy density (per unit mass): constant
3. Pinch to anode radius ratio: constant
4. Pinch to anode length ratio: constant
5. Pinch duration per unit anode radius: constant.

Summarizing

1. The dense hot plasma pinch of a small E_0 plasma focus and that of a big E_0 plasma focus have essentially the same energy density, and the same mass density.
2. The big E_0 plasma focus has a bigger physical size and a bigger discharge current. The size of the plasma pinch scales proportionately to the current and to the anode radius, as does the duration of the plasma pinch.
3. The bigger E_0, the bigger 'a', the bigger I_{peak}, the larger the plasma pinch and the longer the duration of the plasma pinch. The larger size and longer duration of the big E_0 plasma pinch are essentially the properties leading to the bigger neutron yield compared to the yield of the small E_0 plasma focus. The well-known yield $\sim I^4$ rule-of-thumb may be ascribed to the following: yield $\sim$ product of volume and lifetime of the hot plasma; and each dimension of the volume as well as the lifetime is proportional to the current.

Numerical experiments have provided the following summary in Table 3.4.

Table 3.4 Dimensions and lifetime of plasma focus machines operated in deuterium and neon

Plasma focus pinch parameters	Deuterium	Neon (for SXR)
Minimum radius, r_{min}	$0.15a$	$0.05a$
Max length (hollow anode), z	$1.5a$	$1.6a$
Radial shock transit, t_{comp}	$5 \times 10^{-6}a$	$4 \times 10^{-6}a$
Pinch lifetime, t_p	$10^{-6}a$	$10^{-6}a$

Unit of time is in s when 'a' the anode radius is in m

In Table 3.4, the times are in s, and the value of anode radius, a, is in m. For the neon calculations, radiative terms are included, and the stronger compression (smaller radius) is due to thermodynamic and radiation effects.

The above description of the plasma focus combines data from numerical experiments and is consistent with laboratory observations some of which is summarized and depicted in Fig. 3.14.

3.3.5 *Designing an Efficient Plasma Focus: Rules of Thumb [10]*

The Lee Model code may be used to aid the design of a new conventional machine.

First, use the following rule of thumb procedure [use SI units].

1. What capacitance (C_0) are you planning?
2. How low is the inductance (L_0) you expect to attain?
3. What maximum voltage (V_0) do you expect to operate?
4. For the stray (circuit) resistance, take 1/4 the value of $(L_0/C_0)^{1/2}$.
5. Estimate the undamped peak current using the formula $I_0 = V_0/(L_0/C_0)^{1/2}$.
6. Use (I_0/a) = 250 kA max undamped current per cm to assign the value of centre electrode (anode) radius 'a'.
7. Put in double this value for outer electrode radius 'b'.
8. The length of the electrode may be assigned as 5 times the value of $1.6(L_0C_0)^{1/2}$. This length is in cm when the value of $(L_0C_0)^{1/2}$ is expressed in μs. This gives a length which will provide an average axial speed of 5 cm/μs which typically gives a peak speed at end of axial phase of 8 cm/μs. For operation in H_2 or D_2 20% longer (electrode length) may be better; for neon operation to get suitable line radiation (12–13.5 Å) for SXR microlithography purposes, 20% shorter may be better as we require a lower speed to get to the correct level of ionization stages. The focus is normally operated so that the start of current dip (signifying the end of the axial phase) occurs at or just after peak current. For argon to generate characteristic argon SXR a high speed (much higher than calculated above for deuterium or neon) is required so use the same length as for H_2. For xenon, if the aim is for EUV (around 13 nm) for experiments for NGL (next generation lithography) the model has predicted a requirement for very low speeds, around 1.3 cm/μs. So it appears one needs very short anodes, at least 5 times shorter than that needed for D_2. However, there is not much experimental experience accumulated so far for xenon.
9. For pressure values assign as follows: D: 4 Torr; Ne: 1.5 Torr; Ar: 0.7 Torr. For xenon, runs on the code suggest several Torr go with the very short anode length.

The above rule of thumb design gives the complete specifications for planning a plasma focus.

The rule of thumb can be checked and fine tuned with the Lee Model code. First ask the question: is your PF fat or thin? (According to the ratio length of the centre electrode divided by diameter; for NX2 this ratio is 1.2, "fat"; for UNU/ICTP PFF this ratio is 17, "thin".)

If it is "fat" use the model parameters suggested for the NX2. These suggested values are tabulated at the top right of the active sheet which appears when you open the RADPF code which is available online at www.plasmafocus.net.

If it is "thin" assign the model parameters closer to the UNU/ICTP PFF which are also included in the online code.

Configure the standard code using the parameters you have from the above rule of thumb estimates. Run the computation and from results make an adjustment to '*a*', '*b*', length z_0 (V_0 may also easily be varied, especially reduced since we have started with max V_0; C_0 also, use more or less capacitors). We need to be careful with L_0, normally make L_0 as small as possible, but be realistic. For a single capacitor with internal inductance of 40 nH, the value of L_0 could be put as 100 nH since L_0 is the total static inductance which includes the inductance of the capacitor bank plus that of the switch and connecting plates and or cable bunch plus the inductance of the PF collector plates usually forming the head of the PF tube. Adjust parameters for best results over a range of pressures and gases. Best results could mean a number of different (not necessarily concurrent) things for example strong current dip or best neutron yield (when operating with deuterium) or biggest line emission in the case of neon, which is useful for developing microlithography SXR sources.

3.3.6 Tapered Anode, Curved Electrodes, Current-Stepped PF, Theta Pinch

3.3.6.1 Tapered Anode

The code has incorporated tapered anode. The default value of taper configuration panel (see Sect. 3.2.4, Fig. 3.8b-block 2) is zero for no taper. If the anode is tapered, set the value to 1 and input the taper parameters: the position where taper starts and the radius of the end of the anode (i.e. at end of taper). The code has a branch which computes the inductance of the tapered anode geometry. Computations give reasonable results when compared to measured results.

3.3.6.2 Curved Electrodes

Bora Plasma Focus

For curved anodes such as NX1 [74, 78] or Bora [160] or the spherical plasma focus (SPF) [161, 162] the standard code is used and an 'equivalent straight length' technique is adopted. In effect, the curved electrodes are treated as straight electrodes and an equivalent length is estimated so as to use the standard code. A properly selected 'equivalent' anode length will give the correct run-down time. However, the change of inductance with distance travelled will not be correct since the inductance of the curved electrodes will have dependence with axial distance which is not strictly linear as is the case of a straight anode. This effect appears to be secondary since our experience is that a reasonable fit is obtained between the computed and the measured current waveforms with necessary adjustments being made to the equivalent straight length.

For example, for Bora, some details are given in a report by Gribkov et al. [160] from which the following diagram (Fig. 3.15) of the Bora plasma focus tube is obtained. A current waveform is also gleaned from that report as is explained in the manual by Saw [163].

We use the following configuration shown in Table 3.5:

The final fitted parameters $\boldsymbol{L_0}$, $\boldsymbol{r_0}$, $\boldsymbol{z_0}$, $\boldsymbol{f_m}$, $\boldsymbol{f_c}$, $\boldsymbol{f_{mr}}$ and $\boldsymbol{f_{cr}}$ are shown in the fitting table (taken from fitted control panel) above.

The computed current waveform using the configuration of Table 3.5 gives the computed current waveform which is shown in Fig. 3.16.

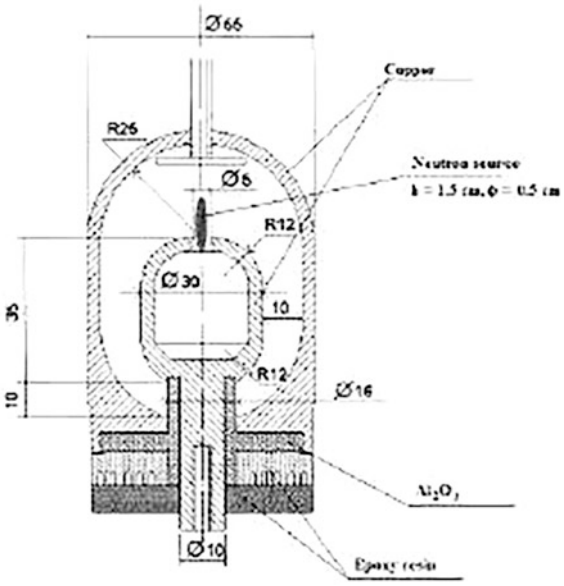

Fig. 3.15 The geometry of Bora [160]

Table 3.5 Fitted configuration of Bora corresponding to relevant shot-values

L_0 (nH)	C_0 (μF)	b (cm)	a (cm)	z_0 (cm)	r_0 (mΩ)
54[a]	24.4	2.5	1.5	6[a]	6[a]
Massf	Currf	Massfr	Currfr		
0.201[a]	0.7[a]	0.55[a]	0.69[a]		
V_0 (kV)	P_0 (Torr)	MW	A	At = 1 mol = 2	
17	7.6	4	1	2	

[a]Fitted using measured d*I*/d*t*; other values are given

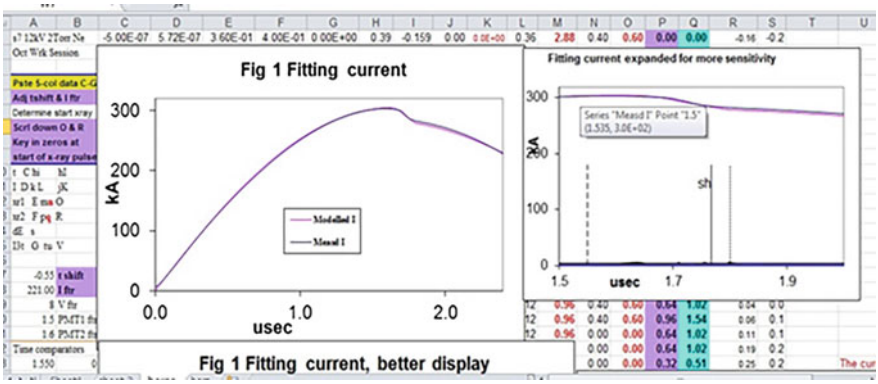

Fig. 3.16 Final fitting of the computed current waveform with the measured current waveform of Bora [160, 163]. Note that the two traces overlap very well in the *left picture* and also well in the expanded picture on the *right*, showing just the current dip

The computed neutron yield is 1.9×10^8 with a peak current of 304 kA. These compare well with their measured peak current of 300 kA and their estimated neutron yield of 10^8 neutrons.

Spherical Plasma Focus, KU200

We had also applied the 'equivalent straightened electrode' technique to the KPU200 SPF [161, 162]. A diagram is given in Fig. 3.17.

We use the configuration shown in Table 3.6.

The final fitted parameters $\boldsymbol{L_0}$, $\boldsymbol{r_0}$, $\boldsymbol{z_0}$, $\boldsymbol{f_m}$, $\boldsymbol{f_c}$, $\boldsymbol{f_{mr}}$, and $\boldsymbol{f_{cr}}$ are shown in the fitting Table 3.6 (taken from fitted control panel) above.

The computed current waveform using the configuration of Table 3.6 gives the computed current waveform which is shown as follows:

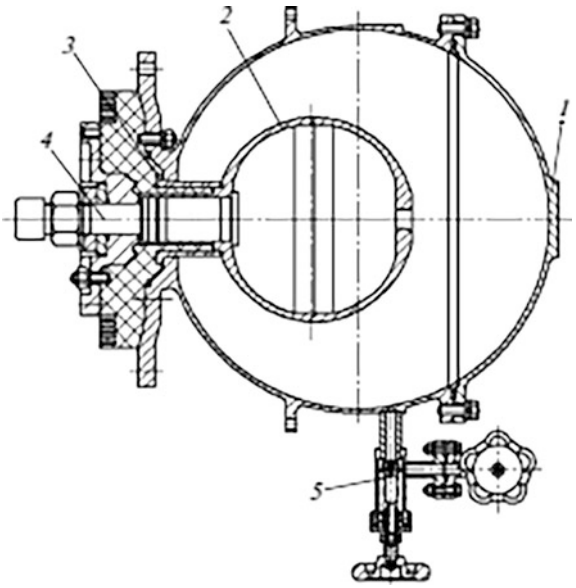

Fig. 3.17 Geometry of KPU200 [161]; *1* cathode housing, *2* anode, *3* insulator, *4* anode lead-in, *5* valves for pumping and filling the chamber with gas. Reprinted from V.V. Maslov et al [161]. Copyright (2014) with permission from Pleiades Publishing Ltd, 2014. Original Russian text published in Pribory i tekhnika Eksperimenta, 2014, No 2 pp 43–47

Table 3.6 Fitted configuration of KPU corresponding to relevant shot-values

L_0	C_0	B	A	z_0	r_0 (mΩ)
36[a]	432	15	8	21.3[a]	1.2[a]
Massf	Currf	Massfr	Currfr	Model parameters	
0.0635[a]	0.7[a]	0.14[a]	0.7[a]		
V_0	P_0	MW	A	At = 1 mol = 2	Operational
25	14.3	5	1	2	Parameters

[a]Fitted using measured current; other values are given

The fit of computed current trace with the experimental current signal is shown in Fig. 3.18. The fitted peak circuit current is 1.6 MA giving a D-T $Y_n = 1.44 \times 10^{13}$ neutrons per shot. These compare with measured values of the peak current of 1.5 MA and D–T $\boldsymbol{Y_n = 1.26 \times 10^{13}}$ as reported in [162].

At 17.3 Torr in D-T, we computed 1.66 MA and 1.34×10^{13} D-T neutrons. These compare well with their measured values of 1.65 MA and 1.2×10^{13} D-T neutrons.

Operating in 12 Torr D at 25 kV, we computed peak current of 1.5 MA and D–D $Y_n = 7.5 \times 10^{10}$ neutrons per shot. These compared with their measured value of 1.4 MA and D–D $Y_n = (7.5–8.0 \times 10^{10}$ D–D neutrons per shot). The results for these 3 cases are summarized and compared in Table 3.7. The agreement is reasonable.

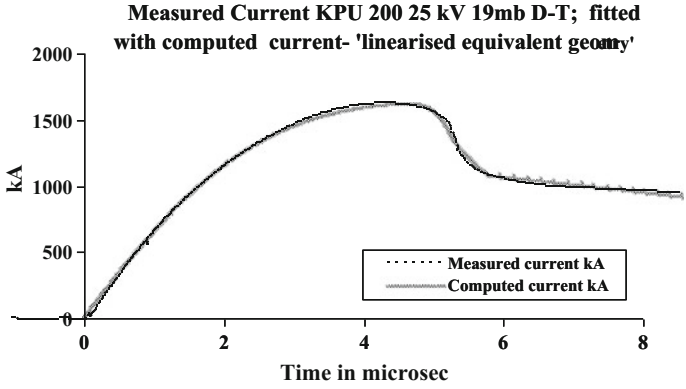

Fig. 3.18 Final fitting of the computed current waveform (*dashed trace*) with the measured current waveform of KPU200 [162]. Note that the two traces overlap reasonably well

Table 3.7 Computed I_p and Y_n for KPU200 compared to measured values

Voltage (kV)	Gas	Pressure (Torr)	Measured I_p (MA)	Computed I_p (MA)	Measured Y_n	Computed Y_n
25	D-T	14.3	1.50	1.60	1.26×10^{13}	1.44×10^{13}
25	D-T	17.3	1.65	1.66	1.2×10^{13}	1.34×10^{13}
25	D-D	12.0	1.50	1.40	$7.5–8 \times 10^{10}$	7.5×10^{10}

A Note on the 2-D Model of Abdul Al-Halim et al.

In relation to the spherical plasma focus SPF, Abd Al-Halim has used a 2-D MHD model to obtain the dynamics of the spherical plasma focus [164], essentially modifying the Lee Model code to include curvature in the current sheet with the ability to follow curved electrodes. More recently his group has [165] extended the code to obtain neutrons, radiation and beam ions properties of the SPF. For the KPU200 they reported a computed value of 1.13×10^{13} D-T neutrons for 14.3 Torr. Their computed value also agrees reasonably with the measured value.

3.3.6.3 Current-Stepped Plasma Focus

Lee [166] had predicted based on basic energy and pressure considerations that a linear Z-pinch would have improved compression characteristics if a current is stepped rather than increased in the usual near sinusoidal fashion, even if it were just a faster sinusoid placed near the top of a slower sinusoid. This concept was tested by Saw in the laboratory using a current-stepped pinch [167, 168]. This same energy and pressure considerations, being fundamental, should already be inbuilt in the Lee Model code which is energy- and momentum-consistent. A two-circuit

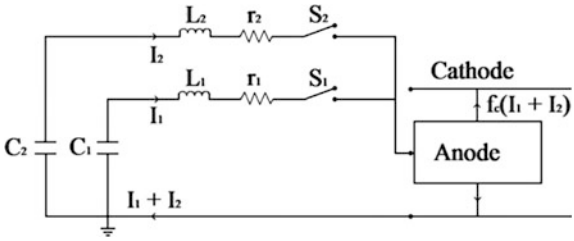

Fig. 3.19 Schematic of the current-stepped PF. The main bank with components C_1, L_1 and r_1 is switched by S_1 onto the anode, with mesh current I_1. The current taking part in the plasma dynamics is $f_c I_1$ with $(1 - f_c)I_1$ being a leakage current. Just before peak I_1, the current-step bank with C_2, L_2 and r_2 is switched by S_2 onto the anode, with mesh current I_2. The total current flowing into the anode is $I = I_1 + I_2$. The current taking part in the plasma dynamics is $f_c(I_1 + I_2)$; shown in this figure flowing in the axial phase. The leakage path of remnant current $(1 - f_c)(I_1\ I_2)$ is not shown. Mesh 2 has smaller L_2–C_2 time constant than L_1–C_1 and C_2 is charged to a higher voltage than C_1. Reprinted from Lee and Saw [105]. Copyright (2012) with permission from Springer Science+Business Media, LLC

system was proposed for a plasma focus [105] to provide a stepped current (see Fig. 3.19).

A plasma focus with b = 23.4 cm, a = 16.9 cm and z_0 = 35 cm operating at 10 Torr was designed. For a 50 kV, 1 MJ, 6 μs rise-time bank, the current-step from a 200 kV, 0.4 MJ, 0.8 μs rise-time bank maintains the pinch current at 2.2 MA, enhances compression by 1.9 and increases the neutron yield by a factor of 4 from 2.5×10^{12} to 1.03×10^{13}. The current-step is switched when the r_p = 0.4 a. The increase is attributed mainly to the step nature of the current which favourably shifts the end-point of compression; rather than to the scaling in terms of energy or current.

3.3.6.4 Procedure to Use Lee Code for the Above Devices

For application of the 'straight electrode equivalent' technique the standard 5-phase code is used. For the current-stepped computations, a separate code is required designated as the CS-RADPF05.15d (available from either author).

3.3.6.5 Theta Pinch Version of the Code

There is a version of the code written for the radiative theta pinch [169] which has the capacitor current coupled into the plasma via a single turn air-core loop. With this difference in the drive, the rest of the code is adapted from the radial phase of the Lee Model code. This code for the theta pinch is designated (May 2014) theta002.

3.4 Insights and Scaling Laws of the Plasma Focus Arising from the Numerical Experiments

3.4.1 Using the Lee Model Code as Reference for Diagnostics

The Lee Model code [10, 37] is configured [22, 152] to work as any plasma focus by inputting:

Bank parameters L_0, C_0 and stray circuit resistance r_0;
Tube parameters b, a and z_0;
Operational parameters V_0 and P_0 and the fill gas.

The computed total current waveform is fitted to the measured waveform by varying model parameters f_m, f_c, f_{mr} and f_{cr} one by one until the computed waveform agrees with the measured waveform as described earlier in Sect. 3.2.4.

During every adjustment of each of the model parameters, the code goes through the whole cycle of computation. In the last adjustment, when the computed total current trace is judged to be reasonably well-fitted in all 5 waveform features, computed time histories are presented, in Fig. 3.20a–n as an example, as follows: for the NX2 operated at 11 kV, 2.6 Torr Ne.

Thus the code after fitting to a measured current trace provides the dynamics and energetics of the plasma focus and properties of the plasma pinch. One important use of the code is to provide values that may act as a reference for diagnostic purposes.

3.4.1.1 Comments on Computed Quantities by Lee Model Code

1. The computed total discharge current trace typically is fitted very well with the measured trace. The end of the radial phase is indicated in Fig. 3.20a. Plasma currents are rarely measured. We had done a comparison of the computed plasma current with measured plasma current for the Stuttgart PF78 which shows good agreement of our computed to the measured plasma current [106]. The computed plasma current in this case of the NX2 is shown in Fig. 3.20b.
2. The computed tube voltage is difficult to compare with measured tube voltages in terms of peak values, typically because of the poor response time of voltage dividers used for voltage measurements. However the computed waveform shape in Fig. 3.20c is general as expected.
3. The computed axial trajectory and speed (Fig. 3.20d), agree with experimentally obtained time histories. Moreover, the behaviour with pressure, running the code at different pressures, agrees well with experimental results. The radial trajectories and speeds are difficult to measure. The computed radial trajectories Fig. 3.20e agrees with the scant experimental data available. The length of the

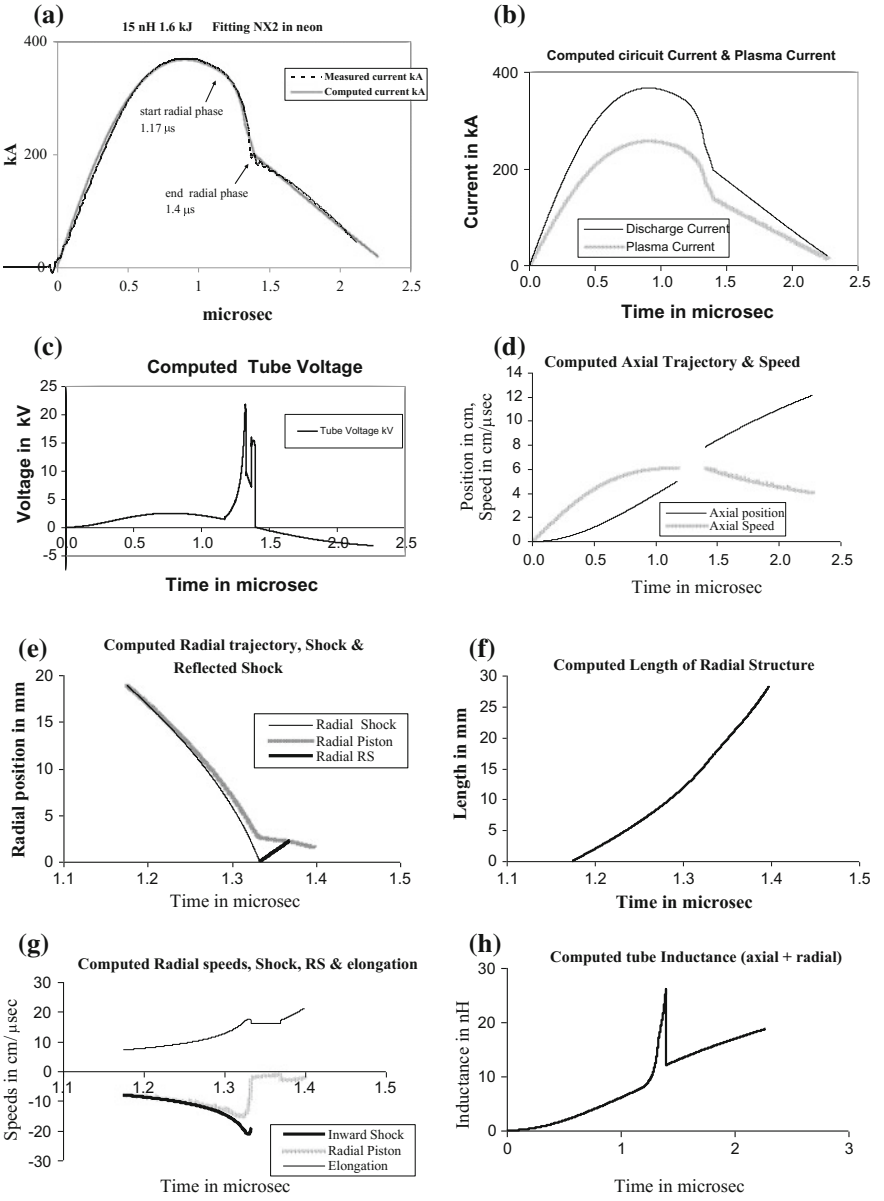

Fig. 3.20 **a**. Fitted computed I_{total}. **b** Computed I_{total} or $I_{\text{discharge}}$ and I_{plasma}. **c** Tube voltage. **d** Axial trajectory and speed. **e** Radial trajectories. **f** Length of elongating structure. **g** Speeds in radial phases. **h** Tube inductance-both phases. **i** Total inductive energy. **j** Piston work and DR energy; traces overlap. **k** Peak and averaged uniform n_i. **l** Peak and averaged uniform n_e. **m** Plasma temperature T. **n** Neon soft X-ray power

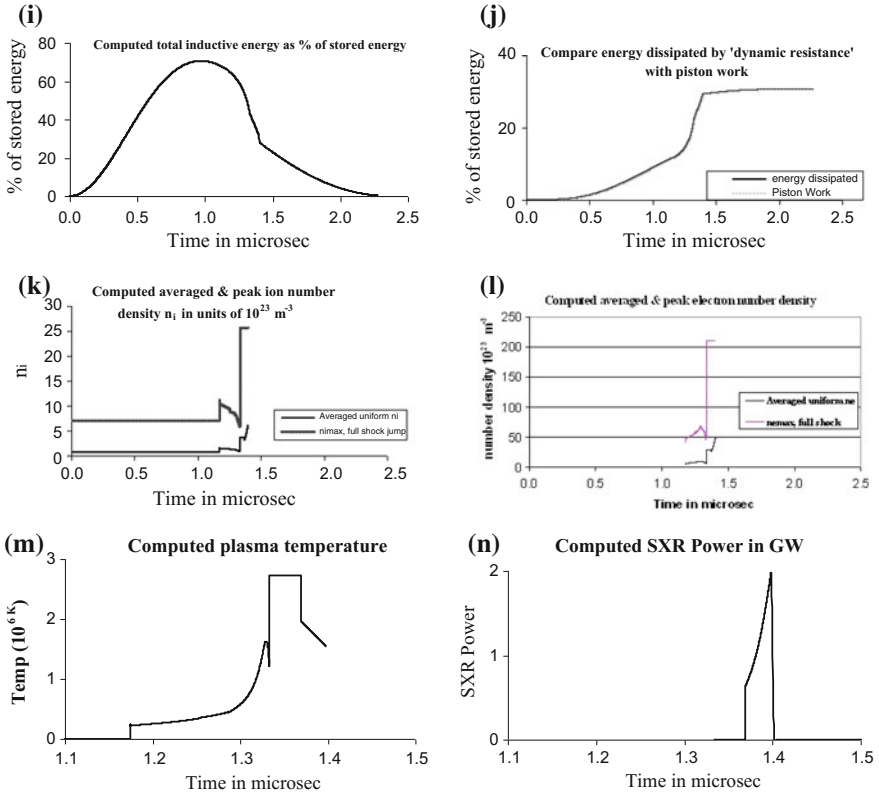

Fig. 3.20 (continued)

radial structure is shown in Fig. 3.20f. Computed speeds, radial shock front and piston speeds and speed of the elongation of the structure, are shown in Fig. 3.20g.

4. The computed inductance (Fig. 3.20h) shows a steady increase of inductance in the axial phase, followed by a sharp increase (rising by more than a factor of 2 in a radial phase time interval about 1/10 the duration of the axial phase for the NX2).
5. The inductive energy ($0.5LI^2$) peaks at 70% of initial stored energy and then drops to 30% during the radial phase, as the sharp drop of current more than offsets the effect of sharply increased inductance (Fig. 3.20i).
   In Fig. 3.20j is shown the work done by the magnetic piston, computed using force integrated over distance method. Also shown is the work dissipated by the dynamic resistance, computed using dynamic resistance power integrated over

time. We see that the two quantities and profiles agree exactly. This validates the concept of half L_{dot} as a dynamic resistance DR. The piston work deposited in the plasma increases steadily to some 12% at the end of the axial phase and then rises sharply to just below 30% in the radial phase. The values of the DR in the axial phase, together with the bank surge impedance, are the quantities that determine I_{peak}.

6. The ion number density has a maximum value derived from shock-jump considerations, and an averaged uniform value derived from overall energy and mass balance considerations. The computed number density is averaged over the assumed flat profile, hence can be expected to be considerably lower than measured peak density. The time profiles of these are shown in Fig. 3.20k. The electron number density (Fig. 3.20l) has similar profiles to the ion density profile but is modified by the effective charge numbers due to ionization stages reached by the ions.
7. Plasma temperature too has a maximum value and an averaged uniform value derived in the same manner; are shown in Fig. 3.20m. Computed neon soft X-ray power profile is shown in Fig. 3.20n. The area of the curve is the soft X-ray yield in J. Pinch dimensions and lifetime may be estimated from Fig. 3.20e, f.
8. The code also computes the neutron yield, for operation in deuterium, using a phenomenological beam-target mechanism [10, 37] added on to a much smaller thermonuclear component. The code does not compute a time history of the neutron emission, only a yield number Y_n.

Thus as demonstrated above, the Lee Model code when properly fitted is able to realistically model any plasma focus and act as a guide to diagnostics of plasma dynamics, trajectories, energy distribution and gross plasma properties. Radiation yields and properties of FIB fast ion beams and FPS fast plasma streams are also computed. These are treated in other sections later.

3.4.1.2 Correlating Computed Plasma Dynamics with Measured Plasma Properties—A Very Powerful Diagnostic Technique

A measured current waveform is usually available together with measured time profiles of plasma properties. In such cases, the fitted code has been used to compare the computed dynamics with a measured streak photograph [95] and to correlate the computed dynamics with neon SXR time profiles [55, 56, 76] and Faraday Cup signals [81]. An example of such a correlation is shown in Fig. 3.46 in Sect. 3.5.6.7. This is a very powerful technique particularly when incorporated into a customized template. More widespread use will generate new data to further the understanding of the plasma focus.

Besides providing reference quantities for diagnostics, series of numerical experiments have been systematically carried out to look for behaviourial patterns of the plasma focus. Insights uncovered by the series of numerical experiments include:

1. Pinch current limitation effect, and associated yield limitation, as static inductance is reduced;
2. Scaling laws for neutron, SXR, fast ion beams and fast plasma strteams; and
3. The nature and a fundamental cause of neutron saturation (being a misnomer for neutron scaling deterioration).

3.4.2 *Insight 1—Pinch Current Limitation Effect as Static Inductance Is Reduced Towards Zero*

There was expectation [12] that the large MJ plasma focus PF1000 in Warsaw could increase its discharge current, and its pinch current, and consequently neutron yield by a reduction of its external or static inductance L_0. To investigate this point, experiments were carried out using the Lee Model code. Unexpectedly, the results indicated that whilst I_{peak} indeed progressively increased with a reduction in L_0, no improvement may be achieved due to a pinch current limitation effect [49]. Given a fixed C_0 powering a plasma focus, there exists an optimum L_0 for maximum I_{pinch}. Reducing L_0 further will increase neither I_{pinch} nor Y_n. The numerical experiments leading to this unexpected result is described below.

A measured current trace of the PF1000 with $C_0 = 1332$ μF, operated at 27 kV, 3.5 Torr deuterium, has been published [12], with cathode and anode radii $b = 16$ cm and $a = 11.55$ cm and anode length $z_0 = 60$ cm. In the numerical experiments, we fitted external (or static) inductance $L_0 = 33.5$ nH and stray resistance $r_0 = 6.1$ mΩ (damping factor $RESF = r_0/(L_0/C_0)^{0.5} = 1.22$). The fitted model parameters are $f_m = 0.13$, $f_c = 0.7$, $f_{mr} = 0.35$ and $f_{cr} = 0.65$. The computed current trace [10, 49] agrees very well with the measured trace [12] through all the phases, axial and radial, right down to the bottom of the current dip indicating the end of the pinch phase as shown in Fig. 3.21.

We carried out numerical experiments for PF1000 using the machine and model parameters determined from Fig. 3.21. Operating the PF1000 at 35 kV and

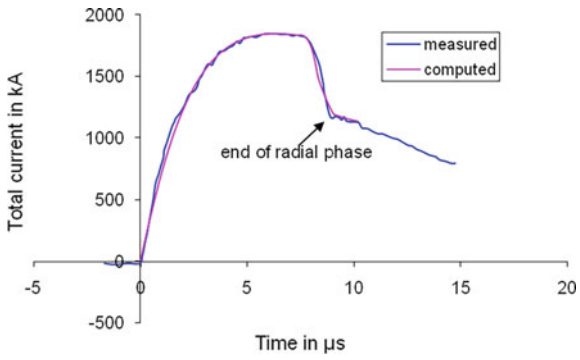

Fig. 3.21 Fitting computed current to measured current traces to obtain fitted parameters $f_m = 0.13$, $f_c = 0.7$, $f_{mr} = 0.35$ and $f_{cr} = 0.65$. The measured current trace was for the PF1000 at 27 kV, storage capacity of 1332 μF and fitted static inductance of 33.5 nH

3.5 Torr, we varied the anode radius a with the corresponding adjustment to b to maintain a constant $c = b/a = 1.39$ and in order to keep the peak axial speed at 10 cm/μs. The anode length z_0 was also adjusted to maximize I_{pinch} as L_0 was decreased from 100 nH progressively to 5 nH.

As expected, I_{peak} increased progressively from 1.66 to 4.4 MA. As L_0 was reduced from 100 to 35 nH, I_{pinch} also increased, from 0.96 to 1.05 MA. However, then unexpectedly, on further reduction from 35 to 5 nH, I_{pinch} stopped increasing, instead of decreased slightly to 1.03 MA at 20 nH, to 1.0 MA at 10 nH, and to 0.97 MA at 5 nH. Y_{n} also had a maximum value of 3.2×10^{11} neutron per shot at 35 nH.

To explain this unexpected result, we examine the energy distribution in the system at the end of the axial phase (see Fig. 3.21) just before the current drops from peak value I_{peak} and then again near the bottom of the almost linear drop to the pinch phase indicated by the arrow pointing to 'end of radial phase'. The energy equation describing this current drop is written as follows:

$$0.5I_{\text{peak}}^2(L_0 + L_a f_c^2) = 0.5I_{\text{pinch}}^2(L_0/f_c^2 + L_a + L_p) + \delta_{\text{cap}} + \delta_{\text{plasma}}, \tag{3.57}$$

where L_a is the inductance of the tube at full axial length z_0, δ_{plasma} is the energy imparted to the plasma as the current sheet moves to the pinch position and is the integral of $0.5(\text{d}L/\text{d}t)I^2$. We approximate this as $0.5L_pI_{\text{pinch}}^2$ which is an underestimate for this case. δ_{cap} is the energy flow into or out of the capacitor during this period of current drop. If the duration of the radial phase is short compared to the capacitor time constant, the capacitor is effectively decoupled and δ_{cap} may be put as zero. From this consideration we obtain

$$I_{\text{pinch}}^2 = I_{\text{peak}}^2(L_0 + 0.5L_a)/(2L_0 + L_a + 2L_p) \tag{3.58}$$

where we have taken $f_c = 0.7$ and approximated f_c^2 as 0.5.

Generally, as L_0 is reduced, I_{peak} increases; a is necessarily increased leading [49] to a longer pinch length z_p, hence a bigger L_p. Lowering L_0 also results in a shorter rise time, hence a necessary decrease in z_0, reducing L_a. Thus, from Eq. (3.58), lowering L_0 decreases the fraction $I_{\text{pinch}}/I_{\text{peak}}$. Secondly, this situation is compounded by another mechanism. As L_0 is reduced, the L–C interaction time of the capacitor bank reduces while the duration of the current drop increases due to an increasing a. This means that as L_0 is reduced, the capacitor bank is more and more coupled to the inductive energy transfer processes with the accompanying induced large voltages that arise from the radial compression. Looking again at the derivation of Eq. (3.58) from Eq. (3.57) a nonzero δ_{cap}, in this case, of positive value, will act to decrease I_{pinch} further. The lower the L_0 the more pronounced is this effect.

Summarizing this discussion, the pinch current limitation is not a simple effect but is a combination of the two complex effects described above, namely, the interplay of the various inductances involved in the plasma focus processes abetted by the increasing coupling of C_0 to the inductive energetic processes, as L_0 is reduced.

3.4.3 Neutron Yield Limitations Due to Current Limitations as L_0 Is Reduced

From the pinch current limitation effect, it is clear that given a fixed C_0 powering a plasma focus, there exists an optimum L_0 for maximum I_{pinch}. Reducing L_0 further will increase neither I_{pinch} nor Y_n. The results of the numerical experiments carried out are presented in Fig. 3.22 and Table 3.8.

With large L_0 = 100 nH it is seen (Fig. 3.22) that the rising current profile is flattened from what its waveform would be if unloaded; and peaks at around 12 μs (before its unloaded rise time, not shown, of 18 μs) as the current sheet goes into the radial phase. The current drop, less than 25% of peak value, is sharp compared with the current rise profile. At L_0 = 30 nH the rising current profile is less flattened, reaching a flat top at around 5 μs, staying practically flat for some 2 μs before the radial phase current drop to 50% of its peak value in a time which is still short compared to the rise time. With L_0 of 5 nH, the rise time is now very short, there is hardly any flat top; as soon as the peak is reached, the current waveform

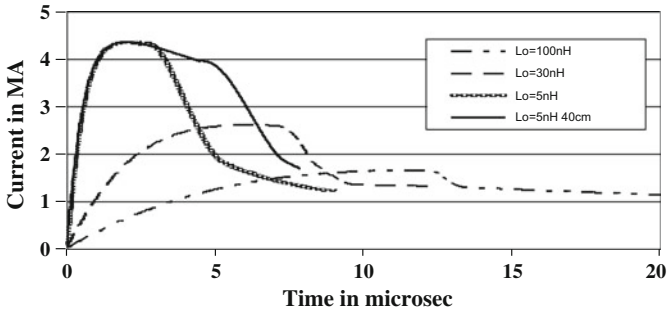

Fig. 3.22 PF1000 current waveforms computed at 35 kV, 3.5 Torr D_2 for a range of L_0 showing the changes in waveforms as L_0 varies. Reprinted from Lee et al. [102]. © IOP Publishing. Reproduced with permission. All rights reserved

Table 3.8 Currents and ratio of currents as L_0 is reduced-PF1000 at 35 kV, 3.5 Torr deuterium

L_0 (nH)	b (cm)	a (cm)	z_0 (cm)	I_{peak} (MA)	I_{pinch} (MA)	Y_n (10^{11})	I_{pinch}/I_{peak}
100	15.0	10.8	80	1.66	0.96	2.44	0.58
80	16.0	11.6	80	1.81	1.00	2.71	0.55
60	18.0	13.0	70	2.02	1.03	3.01	0.51
40	21.5	15.5	55	2.36	1.05	3.20	0.44
35	22.5	16.3	53	2.47	1.05	3.20	0.43
30	23.8	17.2	50	2.61	1.05	3.10	0.40
20	28.0	21.1	32	3.13	1.03	3.00	0.33
10	33.0	23.8	28	3.65	1.00	2.45	0.27
5	40.0	28.8	20	4.37	0.97	2.00	0.22

drops significantly. There is a small kink on the current waveform of both the L_0 = 5 nH, z_0 = 20 cm and the L_0 = 5 nH, z_0 = 40 cm. This kink corresponds to the start of the radial phase which, because of the large anode radius, starts with a relatively low radial speed, causing a momentary reduction in dynamic loading. Looking at the three types of traces it is seen that for L_0 = 100–30 nH, there is a wide range of z_0 that may be chosen so that the radial phase may start at peak or near peak current, although the longer values of z_0 tend to give better energy transfers into the radial phase.

The optimized situation for each value of L_0 is shown in Table 3.8. The table shows that as L_0 is reduced, I_{peak} rises with each reduction in L_0 with no sign of any limitation. However, I_{pinch} reaches a broad maximum of 1.05 MA around 40–30 nH. Neutron yield Y_n also shows a similar broad maximum peaking at 3.2×10^{11} neutrons. Figure 3.23 shows a graphical representation of this I_{pinch} limitation effect. The curve going up to 4 MA at low L_0 is the I_{peak} curve. Thus I_{peak} shows no sign of limitation as L_0 is progressively reduced. However, I_{pinch} reaches a broad maximum. From Fig. 3.23 there is a stark and important message. One must distinguish clearly between I_{peak} and I_{pinch}. In general, one cannot take I_{peak} to be representative of I_{pinch}.

We carried out several sets of experiments on the PF1000 for varying L_0, each set with a different damping factor. In every case, an optimum inductance was found around 30–60 nH with I_{pinch} decreasing as L_0 was reduced below the optimum value. The results showed that for PF1000, reducing L_0 from its present 20–30 nH will increase neither the observed I_{pinch} nor the neutron yield, because of the pinch limitation effect. Indeed, the I_{pinch} decreases very slightly on further reduction to very small values. We would add that we have used a set of model

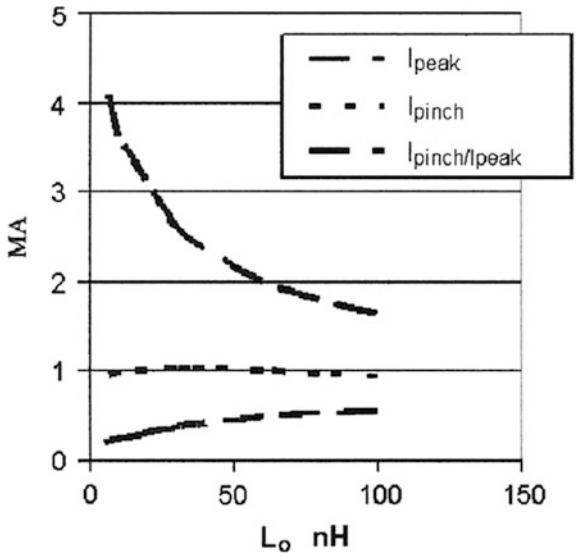

Fig. 3.23 Currents and current ratio (computed) as L_0 is reduced PF1000, 35 kV, 3.5 Torr D_2. Reprinted from [102]. © IOP Publishing. Reproduced with permission. All rights reserved

parameters which in our experience is the most reasonable to be used in these numerical experiments. Variations of the model parameters could occur but we are confident that these variations are not likely to occur with such a pattern as to negate the pinch current limitation effect. Nevertheless, these variations should be actively monitored and any patterns in the variations should be investigated.

Similar series of numerical experiments have been carried out for SXR yields [98, 103] which indicate that the same current limiting effect also applies to optimizing the yields of neon SXR, and likely to other yields including FIB and FPS as well.

3.4.4 *Insight 2—Scaling Laws for Neutron—Scaling Laws for Neutrons from Numerical Experiments Over a Range of Energies from 10 kJ to 25 MJ*

We apply the Lee Model code to the MJ machine PF1000 over a range of C_0 to study the neutrons emitted by PF1000-like bank energies from 10 kJ to 25 MJ.

As shown earlier the PF1000 current trace has been used to fit the model parameters, with very good fitting achieved between the computed and measured current traces (Fig. 3.10). Once the model parameters have been fitted to a machine for a given gas, these model parameters may be used with some degree of confidence when operating parameters such as the charging voltage are varied [10, 132]. With no measured current waveforms available for the higher megajoule numerical experiments, it is reasonable to keep the model parameters that we have got from the PF1000 fitting.

The optimum pressure for this series of numerical experiments is 10 Torr and the ratio $c = b/a$ is retained at 1.39. For each C_0, anode length z_0 is varied to find the optimum. For each z_0, anode radius a_0 is varied so that the end-axial speed is 10 cm/μs. The numerical experiments were carried out for C_0 ranging from 14 to 39,960 μF corresponding to energies from 8.5 kJ to 24.5 MJ [44].

For this series of experiments we find that the Y_n scaling changes from $Y_n \sim E_0^{2.0}$ at tens of kJ to $Y_n \sim E_0^{0.84}$ at the highest energies (up to 25 MJ) investigated in this series. This is shown in Fig. 3.24.

From Figs. 3.24 and 3.25, over wide ranges of energy, optimizing pressure, anode length and radius, the scaling laws for Y_n [21, 44, 100, 114–116] obtained through numerical experiments are listed here:

$Y_n = 3.2 \times 10^{11} I_{pinch}^{4.5}$
$Y_n = 1.8 \times 10^{10} I_{peak}^{3.8}$; I_{peak} (0.3–5.7) in MA, I_{pinch} (0.2–2.4) in MA.
$Y_n \sim E_0^{2.0}$ at tens of kJ to
$Y_n \sim E_0^{0.84}$ at MJ level (up to 25 MJ).

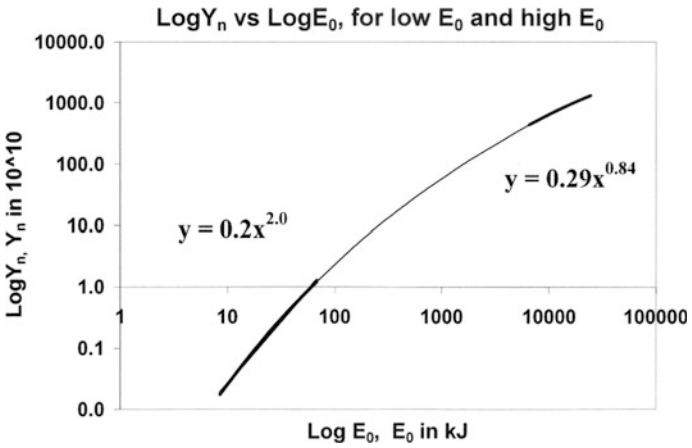

Fig. 3.24 Y_n plotted as a function of E_0 in log–log scale, showing Y_n scaling changes from $Y_n \sim E_0^{2.0}$ at tens of kJ to $Y_n \sim E_0^{0.84}$ at the highest energies (up to 25 MJ). This scaling deterioration is discussed in Sect. 4.7. Reprinted from Lee [44]. © IOP Publishing. Reproduced with permission. All rights reserved

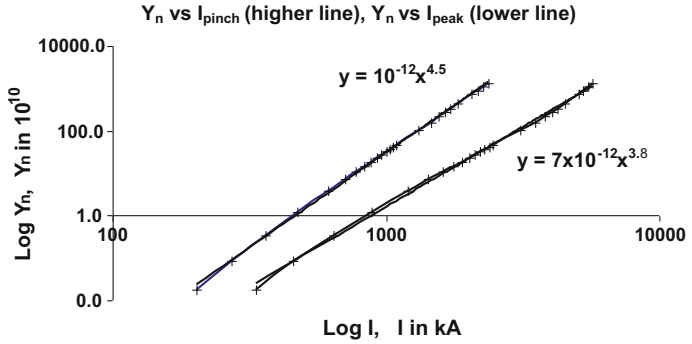

Fig. 3.25 Log(Y_n) scaling with Log(I_{peak}) and Log(I_{pinch}), for the range of energies investigated, up to 25 MJ. Reprinted from Lee [44]. © IOP Publishing. Reproduced with permission. All rights reserved

These laws provide useful references and facilitate the understanding of present plasma focus machines. More importantly, these scaling laws are also useful for design considerations of new plasma focus machines particularly if they are intended to operate as optimized neutron sources.

3.4.5 Insight 3—Scaling Laws for Soft X-ray Yield

3.4.5.1 Computation of Neon SXR Yield

We note that the transition from Phase 4 to Phase 5 is observed in laboratory measurements to occur in an extremely short time with plasma/current disruptions resulting in localized regions of high densities and temperatures. These localized regions are not modelled in the code, which consequently computes only an average uniform density, and an average uniform temperature which is considerably lower than measured peak density and temperature. However, because the 4 model parameters are obtained by fitting the computed total current waveform to the measured total current waveform, the model incorporates the energy and mass balances equivalent, at least in the gross sense, to all the processes which are not even specifically modelled. Hence the computed gross features such as speeds and trajectories and integrated soft X-ray yields have been extensively tested in numerical experiments for several machines and are found to be comparable with measured values.

In the code [10, 37], neon line radiation Q_{L} is calculated:

$$\frac{\mathrm{d}Q_L}{\mathrm{d}t} = -4.6 \times 10^{-31} n_{\mathrm{i}}^2 Z Z \left(\pi r_{\mathrm{p}}^2\right) z_{\mathrm{f}} / T \tag{3.59}$$

where for the temperatures of our interest we take the SXR yield $Y_{\mathrm{sxr}} = Q_{\mathrm{L}}$, Z_n is the atomic number.

Hence the SXR energy generated within the plasma pinch depends on the properties: number density n_{i}, effective charge number Z, pinch radius r_{p}, pinch length z_{f} and temperature T. It also depends on the pinch duration since in our code Q_{L} is obtained by integrating over the pinch duration.

This generated energy is then reduced by the plasma self-absorption which depends primarily on density and temperature; the reduced quantity of energy is then emitted as the SXR yield. These effects are included in the modelling by computing volumetric plasma self-absorption factor A derived from the photonic excitation number M which is a function of Z_n, n_{i}, Z and T. However, in our range of operation, the numerical experiments show that the self-absorption is not significant. It was first pointed out by Liu [73, 75] that a temperature around 300 eV is optimum for SXR production. Subsequent work [55–57, 76–79] and further experience through numerical experiments suggest that around 2×10^6 K (below 200 eV) or even a little lower could be better. Hence unlike the case of neutron scaling, for SXR scaling there is an optimum small range of temperatures (T windows) to operate.

3.4.5.2 Scaling Laws for Neon SXR Over a Range of Energies from 0.2 kJ to 1 MJ

We next use the Lee Model code to carry out a series of numerical experiments over the energy range 0.2 kJ–1 MJ [117]. In this case, we apply it to a proposed modern fast plasma focus machine with optimized values for c the ratio of the outer to inner electrode radius and L_0 obtained from our numerical experiments.

The following parameters are kept constant : (i) the ratio $c = b/a$ (kept at 1.5, which is practically optimum according to our preliminary numerical trials); (ii) the operating voltage V_0 (kept at 20 kV); (iii) static inductance L_0 (kept at 30 nH, which is already low enough to reach the I_{pinch} limitation regime [49] over most of the range of E_0 we are covering) and; (iv) the ratio of stray resistance to surge impedance RESF (kept at 0.1, representing a higher performance modern capacitor bank). The model parameters [132] f_{m}, f_{c}, f_{mr} and f_{cr} are also kept at fixed values 0.06, 0.7, 0.16 and 0.7. We choose the model parameters so they represent the average values from the range of machines that we have studied. A typical example of a current trace for these parameters is shown in Fig. 3.26.

The storage energy E_0 is varied by changing the capacitance C_0. Parameters that are varied are operating pressure P_0, anode length z_0 and anode radius a. Parametric variation at each E_0 follows the order; P_0, z_0 and a until all realistic combinations of P_0, z_0 and a are investigated. At each E_0, the optimum combination of P_0, z_0 and a is found that produces the biggest Y_{sxr}. In other words at each E_0, a P_0 is fixed, a z_0 is chosen and a is varied until the largest Y_{sxr} is found. Then keeping the same values of E_0 and P_0, another z_0 is chosen and a is varied until the largest Y_{sxr} is found. This procedure is repeated until for that E_0 and P_0, the optimum combination of z_0 and a is found. Then keeping the same value of E_0, another P_0 is selected. The procedure for parametric variation of z_0 and a as described above is then carried out for this E_0 and new P_0 until the optimum combination of z_0 and a is found. This procedure is repeated until for a fixed value of E_0, the optimum combination of P_0, z_0 and a is found.

The procedure is then repeated with a new value of E_0. In this manner after systematically carrying out some 2000 runs, the optimized runs for various energies are tabulated in Table 3.9. We plot Y_{sxr} against E_0 as shown in Fig. 3.27.

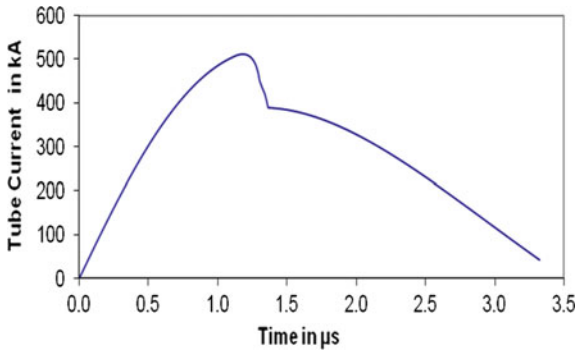

Fig. 3.26 Computed total curent versus time for $L_0 = 30$ nH and $V_0 = 20$ kV, $C_0 = 30$ µF, RESF = 0.1, $c = 1.5$ and model parameters $f_{\text{m}}, f_{\text{c}}, f_{\text{mr}}, f_{\text{cr}}$ are fixed at 0.06, 0.7, 0.16 and 0.7 for optimized $a = 2.285$ cm and $z_0 = 5.2$ cm

Table 3.9 Optimized configuration found for each E_0

E_0 (kJ)	C_0 (μF)	a (cm)	z_0 (cm)	P_0 (Torr)	I_{peak} (kA)	I_{pinch} (kA)	v_a (cm/μs)	v_s (cm/μs)	v_p (cm/μs)	Y_{sxr} (J)
0.2	1	0.58	0.5	4.0	100	68	5.6	22.5	14.9	0.44
1	5	1.18	1.5	4.0	224	143	6.6	23.3	15.1	7.5
2	10	1.52	2.1	4.0	300	186	6.8	23.6	15.2	20
6	30	2.29	5.2	4.2	512	294	8.1	24.5	15.6	98
10	50	2.79	7.5	4.0	642	356	8.7	24.6	15.7	190
20	100	3.50	13	4.0	861	456	9.6	24.6	16.0	470
40	200	4.55	20	3.5	1109	565	10.3	24.7	16.2	1000
100	500	6.21	42	3.0	1477	727	11.2	24.8	16.4	2700
200	1000	7.42	63	3.0	1778	876	11.4	24.8	16.5	5300
400	2000	8.70	98	3.0	2079	1036	11.4	24.9	16.5	9400
500	2500	9.10	105	2.9	2157	1086	11.5	25.1	16.7	11000
1000	5000	10.2	160	3.0	2428	1261	11.4	25.2	16.7	18000

Optimisation carried out with RESF = 0.1, c = 1.5, L_0 = 30 nH and V_0 = 20 kV and model parameters f_m, f_c, f_{mr}, f_{cr} are fixed at 0.06, 0.7, 0.16 and 0.7, respectively. The v_a, v_s and v_p are the peak axial, radial shock and radial piston speeds, respectively

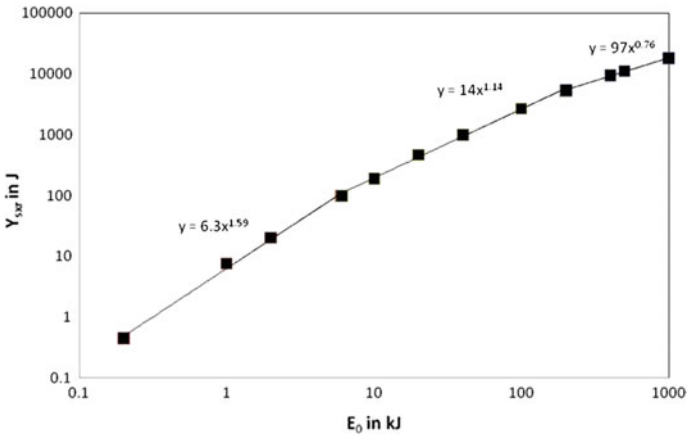

Fig. 3.27 Y_{sxr} versus E_0. The parameters kept constants are: RESF = 0.1, c = 1.5, L_0 = 30 nH and V_0 = 20 kV and model parameters f_m, f_c, f_{mr}, and f_{cr} at 0.06, 0.7, 0.16 and 0.7, respectively. The scaling deterioration observed in this figure is similar to that for neutron yield and is discussed in Sect. 3.4.7. Reprinted from Lee et al. [117]. © IOP Publishing. Reproduced with permission. All rights reserved

We then plot Y_{sxr} against I_{peak} and I_{pinch} and obtain SXR yield scales as

$$Y_{sxr} \sim I_{pinch}^{3.6} \text{ and}$$
$$Y_{sxr} \sim I_{peak}^{3.2}.$$

The I_{pinch} scaling has less scatter than the I_{peak} scaling. We next subject the scaling to further test when the fixed parameters RESF, c, L_0 and V_0 and model parameters f_m, f_c, f_{mr}, f_{cr} are varied. We add in the results of some numerical experiments using the parameters of several existing plasma focus devices including the UNU/ICTP PFF (RESF = 0.2, c = 3.4, L_0 = 110 nH and V_0 = 14 kV with fitted model parameters f_m = 0.05, f_c = 0.7, f_{mr} = 0.2, f_{cr} = 0.8), the NX2 (RESF = 0.1, c = 2.2, L_0 = 20 nH and V_0 = 11 kV with fitted model parameters f_m = 0.10, f_c = 0.7, f_{mr} = 0.12, f_{cr} = 0.68), and PF1000 (RESF = 0.1, c = 1.39, L_0 = 33 nH and V_0 = 27 kV with fitted model parameters f_m = 0.1, f_c = 0.7, f_{mr} = 0.15, f_{cr} = 0.7). These new data points (white data points in Fig. 3.28) contain wide ranges of c, V_0, L_0 and model parameters. The resulting Y_{sxr} versus I_{pinch} log–log curve remains a straight line, with the scaling index 3.6 unchanged and with no more scatter than before. However, the resulting Y_{sxr} versus I_{peak} curve now exhibits considerably larger scatter and the scaling index has changed slightly (note the change is not shown/obvious here).

We would like to highlight that the consistent behaviour of I_{pinch} in maintaining the scaling of $Y_{sxr} \sim I_{pinch}^{3.6}$ with less scatter than the $Y_{sxr} \sim I_{peak}^{3.2}$ scaling particularly when mixed-parameters cases are included, strongly supports the conclusion that

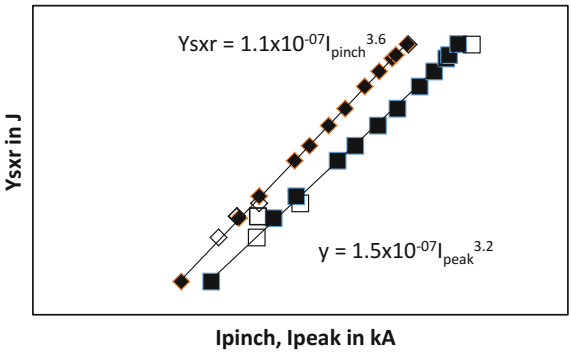

Fig. 3.28 Y_{sxr} is plotted as a function of I_{pinch} and I_{peak}. The parameters kept constant for the *black data points* are: RESF = 0.1, c = 1.5, L_0 = 30 nH and V_0 = 20 kV and model parameters f_m, f_c, f_{mr}, f_{cr} at 0.06, 0.7, 0.16 and 0.7, respectively. The *white data points* are for specific machines which have different values for the parameters c, L_0 and V_0.

I_{pinch} scaling is the more universal and robust one. Similarly, conclusions on the importance of I_{pinch} in plasma focus performance and scaling laws have been reported [106].

It may also be worthy of note that our comprehensively surveyed numerical experiments for Mather configurations in the range of energies 0.2 kJ–1 MJ produce an I_{pinch} scaling rule for Y_{sxr} not compatible with Gates' rule [170]. However it is remarkable that our I_{pinch} scaling index of 3.6, obtained from a set of comprehensive numerical experiments over a range of 0.2 kJ–1 MJ, on Mather-type devices, is within the range of 3.5–4 postulated on the basis of sparse experimental data, (basically just two machines one at 5 kJ and the other at 0.9 MJ), by Filippov et al. [171], for Filippov configurations in the range of energies 5 kJ–1 MJ.

It must be pointed out that the results represent scaling for comparison with baseline plasma focus devices that have been optimized in terms of electrode dimensions. It must also be emphasized that the scaling with I_{pinch} works well even when there are some variations in the actual device from L_0 = 30 nH, V_0 = 20 kV and c = 1.5.

Summary of Soft X-ray scaling laws found by numerical experiments:

Over wide ranges of energy, optimizing pressure, anode length and radius, the scaling laws for neon SXR found by numerical experiments are:

$Y_{sxr} = 8.3 \times 10^3 \times I_{pinch}^{3.6}$;

$Y_{sxr} = 600 \times I_{peak}^{3.2}$; I_{peak} (0.1 to 2.4), I_{pinch} (0.07 to 1.3) in MA.

$Y_{sxr} \sim E_0^{1.6}$ (kJ range) to $Y_{sxr} \sim E_0^{0.8}$ (towards MJ).

These laws provide useful references and facilitate the understanding of present plasma focus machines. More importantly, these scaling laws are also useful for design considerations of new plasma focus machines particularly if they are intended to operate as neon SXR sources.

In a similar fashion, scaling laws for several other gases, e.g. nitrogen, oxygen, argon have been computed [98, 119, 120].

3.4.6 *Insight 4—Scaling Laws for Fast Ion Beams and Fast Plasma Streams from Numerical Experiments*

3.4.6.1 Computation of Beam Ion Properties

The Lee code has been extended (RADPFV5.15FIB) and computes the flux of the ion beams:

$$J_b = n_b v_b \tag{3.60}$$

where n_b = number of beam ions N_b divided by the volume of plasma traversed is derived from pinch inductive energy considerations; and v_b = effective speed of the beam ions is derived from the accelerating voltage taken as diode voltage U. All quantities are expressed in SI units, except where otherwise stated.

3.4.6.2 The Ion Beam Flux and Fluence Equations

We derive n_b from the beam kinetic energy BKE and pinch inductive energy PIE considerations.

The BKE is contributed from the total number of beam ions N_b where each beam ion has a mass Mm_p and speed v_b and is represented by $BKE = (1/2)N_b Mm_p v_b^2$. The mass of the proton m_p is 1.673×10^{-27} kg and M is the mass number of ion, e.g. neon ion has a mass number $M = 20$.

This BKE is imparted by a fraction f_e of the PIE represented by $PIE = (1/2)L_p I_{pinch}^2$ where $L_p = (\mu/2\pi)\left(\ln\left[b/r_p\right]\right)z_p$ is the inductance of the focus pinch; $\mu = 4\pi \times 10^{-7}$ Hm^{-1}; b = outer electrode of the plasma focus carrying the return current; r_p = pinch radius carrying the current through the plasma; z_p = length of the pinch and I_{pinch} is the pinch current value taken at start of pinch.

Thus: $(1/2)N_b Mm_p v_b^2 = f_e(1/2)(\mu/2\pi)(\ln[b/r_p])z_p I_{pinch}^2$

This gives:

$$n_b = N_b/(\pi r_p^2 z_p) = (\mu/[2\pi^2 m_p])(f_e/M)\{(\ln[b/r_p])/r_p^2)\}(I_{pinch}^2/v_b^2) \tag{3.61}$$

Next, we proceed to derive v_b from the accelerating voltage provided by the diode voltage U to an ion. Each ion with effective charge Z_{eff} is given kinetic energy of $(1/2)Mm_p v_b^2$ by diode voltage U. Thus:

$(1/2)\mathrm{Mm_p}v_\mathrm{b}^2 = Z_\mathrm{eff}\mathrm{eU}$ where e is the electronic (or unit) charge 1.6×10^{-19} C; Hence

$$v_\mathrm{b} = (2e/m_\mathrm{p})^{1/2}(Z_\mathrm{eff}/M)^{1/2}U^{1/2} \tag{3.62}$$

Now, we substitute n_b and v_b from Eqs. (3.61) and (3.62) into Eq. (3.60); and noting that $(\mu/[2.83\pi^2(em_\mathrm{p})^{1/2}]) = 2.75 \times 10^{15}$, we have the flux equation:

$$\mathrm{Flux} = J_\mathrm{b} = 2.75 \times 10^{15}\left(f_\mathrm{e}/[MZ_\mathrm{eff}]^{1/2}\right)\left\{\left(\ln[b/r_\mathrm{p}]\right)/(r_\mathrm{p}^2)\right\}\left(I_\mathrm{pinch}^2\right)/U^{1/2} \tag{3.63}$$

in units of (ions m^{-2} s^{-1})

where M = ion mass, Z_eff = average effective charge of the ion in the pinch, b = cathode radius, r_p = pinch radius and I_pinch = pinch current. The parameter f_e is the fraction of energy converted into beam energy from the inductive energy of the pinch. Analyzing neutron yield data [58, 59] and pinch dimensional-temporal relationships we estimate $f_\mathrm{e} = 0.14$ and use the approximate scaling [137]: $\tau = 10^{-6}z_\mathrm{p}$. This condition $f_\mathrm{e} = 0.14$ is equivalent to ion beam energy of 3–6% E_0 in the case when the pinch inductive energy holds 20–40% of E_0. Our extensive study of high performance low inductance PF classified [110] as Type T1 shows that this estimate of f_e is consistent with data.

The value of the ion flux is deduced in each situation by computing Z_eff, r_p, I_pinch and U from the code.

The fluence is the flux multiplied by pulse duration τ. Thus:

$$\mathrm{Fluence(ions\ m^{-2})} = 2.75 \times 10^{15}\tau\left(f_\mathrm{e}/[MZ_\mathrm{eff}]^{1/2}\right)\left\{\left(\ln[b/r_\mathrm{p}]/(r_\mathrm{p}^2)\right)\right\}\left(I_\mathrm{pinch}^2\right)/\mathrm{U}^{1/2} \tag{3.64}$$

For deuteron where $M = 2$ and $Z_\mathrm{eff} = 1$; and if we take $f_\mathrm{e} = 0.14$ (ie 14% of PIE is converted into BKE) then we have for deuterons:

$$\mathrm{Fluence(ions\ m^{-2})} = J_b\tau = 8.5 \times 10^8 I_\mathrm{pinch}^2 z_\mathrm{p}\left\{\left(\ln\left[b/r_p\right]\right)/\pi r_p^2 U^{1/2}\right\} \tag{3.65}$$

Equation (3.65) is exactly equivalent to Eq. (3.5) first derived in [58].

In other words starting from first principles we have derived exactly the same equation using empirical formula derived with quantities all with proportional constants finally calibrated at a 0.5 MJ point of neutron yield. In this present derivation from first principles, we need only one additional condition $f_\mathrm{e} = 0.14$ (the fraction of energy converted from PIE into BKE) and the approximate scaling $\tau = 10^{-6}z_\mathrm{p}$. This additional condition of $f_\mathrm{e} = 0.14$ is equivalent to ion beam energy of 3–6% E_0 for cases when the *PIE* holds 20–40% of E_0 as observed for Type *T*1 or low inductance plasma focus device. We also conclude that the flux Eq. (3.63)

derived here is the more basic equation to use as it does not have to make any assumptions about the ion beam pulse duration.

According to Eqs. (3.63) and (3.64) the flux and fluence are dependent on $(MZ_{\text{eff}})^{-1/2}$, if all other pinch properties remain equal. From this simple dependency one would expect the flux and fluence to reduce as we progress from H_2 to D_2, He to Kr and Xe. However, the pinch properties, primarily the pinch radius do change drastically for different gases at different regimes of operation; due to thermodynamic and radiative effects. The change in r_p and associated and consequential changes in pinch dynamics and other properties, as computed from the code we use in this chapter, have profound effects on modifying this simple dependence.

We summarize the assumptions:

1. Ion beam flux J_b is $n_b v_b$ with units of ions m^{-2} s^{-1}.
2. Ion beam is produced by diode mechanism [12].
3. The beam is produced uniformly across the whole cross section of the pinch.
4. The beam speed is characterized by an average value v_b.
5. The BKE is a fraction f_e of the PIE, taken as 0.14 in the first instance; to be adjusted as numerical experiments indicate.
6. The beam ion energy is derived from the diode voltage U.
7. The diode voltage U is $U = 3V_{\max}$ taken from data fitting in extensive earlier numerical experiments [10, 100], where $V_{\max}$ is the maximum induced voltage of the pre-pinch radial phase. However for cases exhibiting strong radiative collapse, the strong radiative collapse generates an additional induced voltage V^*_{max}. This voltage is very large and from extensive numerical experiments appears to be a reasonable estimate of the beam ion energy from the point of view of the various energy distributions including the ion beam energy relative to the fast plasma stream energy. Hence the feedback from our extensive examinations of the data suggests that we take, in such cases [58–60] $U = V^*_{max}$.

The value of the ion flux is deduced in each situation for specific machine using specific gas by computing the values of Z_{eff}, r_p, I_{pinch} and U by configuring the Lee Model code with the parameters of the specific machine and specific gas. The code and the procedure are discussed in more detail in a later section.

3.4.6.3 Consequential Properties of the Ion Beam [59]

Once the flux is determined, the following quantities are also computed:

1. Energy flux or power density flow (Wm^{-2}) is computed from $\boldsymbol{J_b} \times Z_{\text{eff}}U$ noting the need to multiply by 1.602×10^{-19} to convert eV to J;
2. Power flow (W) is computed from Energy flux × pinch cross section;
3. Current density (A m^{-2}) is computed from J_b × ion charge eZ_{eff};
4. Current (A) is computed from Current density × pinch cross section;
5. Ions per sec (ions s^{-1}) is computed from J_b × pinch cross section;

6. Fluence (ions m^{-2}) is computed from $J_b \times \tau$;
7. Energy fluence (J m^{-2}) is computed from $J_b \times \tau \times Z_{eff}U$;
8. Number of ions in beam (ions) is computed from Fluence × pinch cross section;
9. Energy in beam (J) is computed from Number of ions in beam × $Z_{eff}U$;
10. Damage Factor (Wm^{-2} $s^{0.5}$) is computed from $J_b \times Z_{eff}U \times \tau^{1/2}$;
11. Energy of fast plasma stream (J)

Experimentally it is found that as the focus pinch starts to break-up a fast shock wave exits the plasma focus pinch in the axial direction preceding the ion beams which rapidly catches up and overtakes it. Associated with this fast post-pinch axial shock wave is a fast plasma stream (FPS) [59]. We estimate the energy of the FPS by computing the work done by the magnetic piston through the whole radial phase from which is subtracted twice the ion beam energy (the second count being for the oppositely directed relativistic electron beam which we assume to have the same energy as the ion beam) and from which is further subtracted the radiation yield of the plasma pinch.

3.4.6.4 Fast Ion Beam and Fast Plasma Stream Properties of a Range of Plasma Focus Devices—Investigations of Damage to Plasma Facing Wall Materials in Fusion Reactors

Each of twelve machines of an IAEA CRP (Coordinated Research Program F13013—"Investigations on materials under high repetition and intense fusion pulses") [172] was fitted using parameters (bank, tube and operation) supplied with a measured current trace. Where necessary the fitting of the code output current waveform to the measured current waveform also entailed adjustments to the values of static inductance L_0 and stray resistance r_0. The results of the fitting are a set of model parameters f_m, f_c for the axial phase and f_{mr} and f_{cr} for the radial phase. Once fitted the dynamics in terms of axial and radial speeds and trajectories are found, as are the plasma axial phase and radial phase and pinch plasma properties such as temperatures and densities and neutron yields (in deuterium). Also computed are the properties (number and energy fluence and flux, power flow and damage factors, ion energy and current) of the fast ion beam (FIB) and the energies and properties of the fast plasma stream (FPS). The most important of the computed properties of the IAEA CRP plasma focus machines are listed in Table 3.10.

The most important features regarding the scaling of ion beam properties that are observed from Table 3.10 are as follows:

- FIB Properties independent of machine size: Number fluence, damage factor and speed factor
- FIB Properties dependent on machine size: Beam size (footprint-cross sectional radius), beam pulse length, number of ions per shot, beam current, total beam energy per shot and power flow (W)

Table 3.10 The parameters of the IAEA CRP PF machines

Machine		PF1000	NX3	BARC	PF6	Bora	INTI	NX2T	PF12	Sofia	PF5M	PF400J	FMPF3
E_0	kJ	486	14.5	11.5	6.2	3.5	3.4	3.0	2.6	2.6	2.0	0.4	0.2
C_0	μF	1332	100	40.0	28.0	24.4	30.0	29.0	20.0	20.0	16.0	1.0	2.4
L_0	nH	33.0	50.0	65.0	21.0	54.0	110	20.0	80.0	80.0	33.0	40.0	34.0
r_0	mΩ	6.3	2.3	5.0	2.9	6.0	12.0	2.7	6.0	6.5	6.0	10.0	11.0
b	cm	16.0	5.2	6.1	5.1	2.5	3.2	3.8	2.7	3.1	2.6	1.6	1.5
a	cm	11.6	2.6	3.0	3.0	1.5	1.0	1.6	0.9	1.0	1.5	0.6	0.6
b/a		1.4	2.0	2.0	1.7	1.7	3.4	2.5	3.0	3.1	1.7	2.7	2.5
z_0	cm	60.0	16.0	7.7	4.0	6.0	16.0	4.5	7.2	14.5	5.0	1.7	1.7
V_0	kV	27.0	17.0	24.0	21.0	17.0	15.0	14.5	16.0	16.0	16.0	28.0	13.0
P_0	Torr	3.5	11.0	3.0	4.0	7.6	3.5	15.2	3.5	4.0	2.0	6.6	3.4
t_{rise}	μs	10.4	3.51	2.53	1.20	1.80	2.85	1.20	1.99	1.99	1.14	0.31	0.45
I_{peak}	kA	1846	564	482	584	305	180	402	187	198	258	129	96
I_{pinch}	kA	862	347	279	314	196	122	233	128	127	165	84	63
T_{pinch}	10^6 K	1.1	1.6	1.6	1.3	1.0	7.2	1.7	5.4	6.2	7.4	6.5	1.4
n_{ipinch}	10^{23} m^{-3}	3.9	13.8	6.6	7.2	21.7	3.5	22.5	5.6	3.9	2.1	4.2	9.8
r_{min}	cm	2.23	0.40	0.46	0.54	0.23	0.13	0.23	0.12	0.14	0.22	0.09	0.1
z_{max}	cm	18.8	4.0	5.0	5.1	2.6	1.4	2.2	1.4	1.5	2.3	0.8	1.1
t_{pinch}	ns	255	46	52	60	33	7.6	33	8.3	8.7	12	5.1	11
V_{max}	kV	126	84	81.8	79.2	43.2	75.5	54.6	73.3	69.0	97.3	53.4	18.5
Y_n	10^8 n	1157	27.6	13.1	15.4	1.87	0.11	3.52	0.19	0.13	0.34	0.013	0.001
Fluence	10^{20} m^{-2}	5.75	8.29	4.79	4.31	7.77	2.14	10.7	2.73	2.37	1.41	1.68	2.98
Flux	10^{27} m^{-2} s^{-1}	2.3	18.1	9.3	7.2	23.6	28.1	32.7	32.8	27.3	11.6	33.0	27.2
U	keV	126	84	82	79	43.2	74.1	54.6	73.3	66.3	97.3	53.4	18.5
En fluence	10^7 J m^{-2}	1.16	1.12	0.63	0.55	0.54	0.25	0.94	0.32	0.25	0.22	0.14	0.09

(continued)

Table 3.10 (continued)

Machine		PF1000	NX3	BARC	PF6	Bora	INTI	NX2T	PF12	Sofia	PF5M	PF400J	FMPF3
En flux	10^{13} W m^{-2}	4.56	24.5	12.1	9.18	16.4	33.4	28.6	38.6	29.0	18.1	28.3	8.08
P flow	10^{10} W	7.14	1.23	0.79	0.85	0.26	0.18	0.48	0.19	0.18	0.28	0.07	0.02
Ions	10^{15}	899	41.5	31.3	40.0	12.5	1.15	18.1	1.33	1.45	2.21	0.39	0.77
En Bm	J	18201	561	410	508	86.4	13.6	159	15.6	15.4	34.4	3.3	2.3
I_{ion}	kA	564	145	97	107	60.7	24.1	88.6	25.6	26.7	29.0	12.2	11.2
DamFac	10^{10} W m^{-2} s$^{0.5}$	2.30	5.24	2.76	2.24	2.97	2.91	5.17	3.52	2.70	1.99	2.02	0.84
v_{ion}	cm/μs	347	284	279	275	203	266	228	265	252	305	226	133
FPS En	J	27214	1509	571	572	172	269	289	124	290	143	21.3	12.4
FPS En	% E_0	5.6	10.4	5.0	9.3	4.9	8.0	9.5	4.8	11.3	7.0	5.4	6.1
FPS sp	cm/μs	18.2	24.2	32.8	25.8	29.4	47.4	23.5	52.1	43.0	48.5	35.6	35.2
SF	kA cm^{-1} Torr$^{-0.5}$	85.5	65.4	92.8	97.4	73.7	102	66.6	111	99.1	121	83.5	86.8
Peak v_a	cm/μs	10.8	7.7	6.6	8.2	6.5	9.5	7.0	9.4	9.9	11.8	8.9	7.0
Peak v_s	cm/μs	17.3	17.8	18.0	17.9	13.8	36.1	14.4	31.3	33.6	37.9	35.1	16.5
Peak v_p	cm/μs	13.2	12.3	12.0	11.9	9.2	24.9	10.0	21.3	23.3	25.7	23.5	11.0
EINP	J	63616	2631	1391	1588	344	296	606	155	321	212	28.0	16.9
f_m		0.14	0.10	0.18	0.20	0.20	0.08	0.11	0.10	0.08	0.15	0.08	0.15
f_c		0.70	0.70	0.61	0.70	0.70	0.70	0.70	0.70	0.70	0.70	0.70	0.70
f_{mr}		0.35	0.25	0.43	0.50	0.55	0.16	0.38	0.26	0.16	0.20	0.11	0.55
f_{cr}		0.70	0.70	0.64	0.70	0.69	0.70	0.70	0.70	0.70	0.70	0.70	0.70
Machine		PF1000	NX3	BARC	PF6	Bora	INTI	NX2T	PF12	Sofia	PF5M	PF400 J	FMPF3

- FIB properties with minor dependence on machine size: Number flux, number fluence, energy flux and energy per ion
- FPS properties, practically independent of machine size: equivalent damage factor, FPS energy as fraction of E_0 and flow speed.

Validation of our computations in regards to FIB and FPS properties in relation to the damage testing is presented in reference [60]. In particular, our computed values of damage factor, power flow density and FPS energy [58] for the case of PF-400J agree with those reportedly measured by Soto et al. [173]. Related recent work on target interaction and damage testing has been reported [113, 174–176]. Numerical experiments [58, 59] have already established that the fluence and flux and energy fluence and flux and damage factors have similar values within a narrow range for all plasma focus whether big or small. Thus small plasma focus devices produce as much damage as a big plasma focus; except that the damage produced in a small plasma focus is over a smaller area compared to the bigger target area that the big plasma focus irradiate on a per shot basis. However, exposure frequencies of >1 Hz are achieved in small plasma focus devices aggregating thousands of shots in a few minutes [74]. Thus the damage accumulated over a number of shots can be achieved much more rapidly in a small plasma focus fired repetitively than in a big focus which is a single shot. Therefore, important progress could be achieved in materials damage testing for plasma facing walls of fusion reactors using small plasma focus devices as plasma sources.

3.4.6.5 Slow Focus Mode SFM Versus Fast Focus Mode FFM-Advantage of SFM for Fast Plasma Stream Nano-materials Fabrication: Selection of Energy of Bombarding Particles by Pressure Control [63]

As a source of neutrons, X-rays and charged-particle beams the plasma focus PF is typically operated in the time-matched regime (TMR) where maximum energy is pumped into the radial shock waves and compression, resulting in large inductive voltages, high temperatures and copious multi-radiations. In this Fast Focus Mode (FFM) of operation, targets placed in front of the anode are subjected to strong bursts of fast ion beams (FIB), post-pinch fast plasma streams (FPS) followed by materials exploded off the anode by relativistic electron beams (REB); in that order of time sequence. In the INTI PF in hydrogen, as the operational pressure is increased beyond the TMR, the dynamics slows, the minimum pinch radius ratio increases, peak inductive voltages V_{max} decreases, the FIB reduces in energy per ion U, in beam power flow P_{FIB} and in damage factor D_{FIB}, as operation moves away from FFM into the Slow Focus Mode (SFM). This is the same pattern for D, He, N and Ne; but for the highest radiative gases Ar, Kr and Xe, radiative collapse becomes dominant, past the time-matched point; and the points of highest V_{max}, P_{FIB} and D_{FIB} shift to relatively higher pressures. However in all gases in all machines, as operational pressure is increased further, there comes a point (slowest

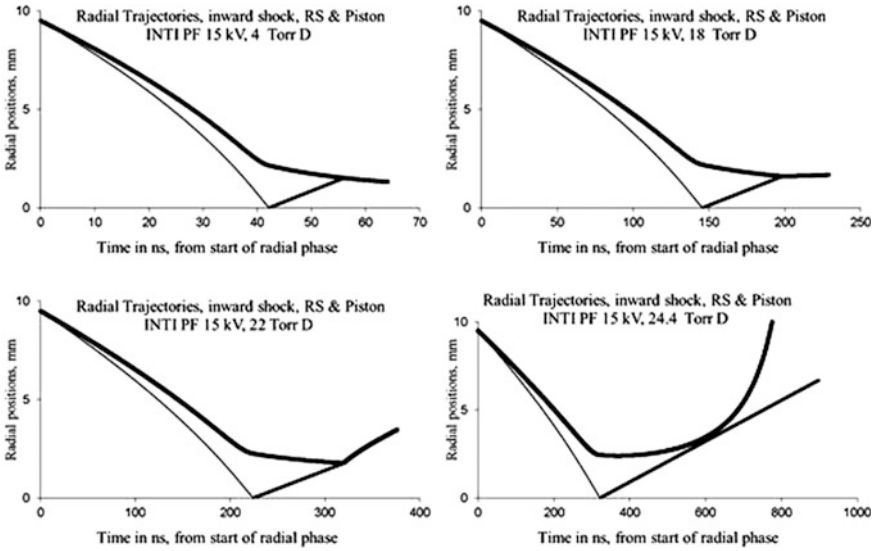

Fig. 3.29 Comparing the pinch radius at FFM (4 Torr) with that at SFM (around 22 Torr)

SFM or SSFM point) where compression is so weak that outgoing reflected shock barely reaches the incoming piston ie the focus pinch barely forms (see Fig. 3.29, case of 24.4 Torr). We consider this point (at 24.4 Torr) as hypothetical and would rather take the case of 22 Torr for discussion. In any case, because we have taken the model parameters as fixed throughout the whole range of pressure we expect that in practice the choice of SFM regime would likely be shifted towards higher pressure since from experiments we find the tendency is for f_m and f_{mr} to be larger as pressure moves towards the SFM regime. Thus the approach the SSFM point would be reached at a lower pressure than shown in this discussion.

At this SSFM point the pinch radius ratio is at its largest (typically > twice that of the FFM), the V_{max} (see Fig. 3.30), P_{FIB} and D_{FIB} (see Fig. 3.31) are very low and we expect a great reduction of anode boil-offs due to reduction of REB's [63].

However, FPS energy is near its highest level. Operation near this SSFM point reduces ion beam damage and anode materials on-target and allows the largest area of interaction, primarily with the FPS (Fig. 3.32).

The above is surmised from results using RADPF FIB code. Recent laboratory experiments with targets in INTI PF [81] confirm experimental indications [177] that such high pressure operations produce a bigger area of more uniform target interaction. This should produce better results in production of nano-materials such as carbon nano-tubes on graphite substrate. Moreover, numerical experiments suggest that operational pressure may be used to select FPS particle energy (see Fig. 3.33) [63].

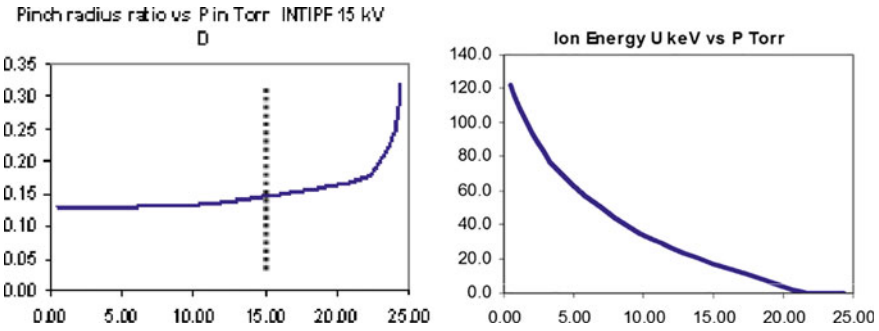

Fig. 3.30 Radius ratios versus *P* (*left*) and FIB ion energy versus *P* in Torr (*right*)

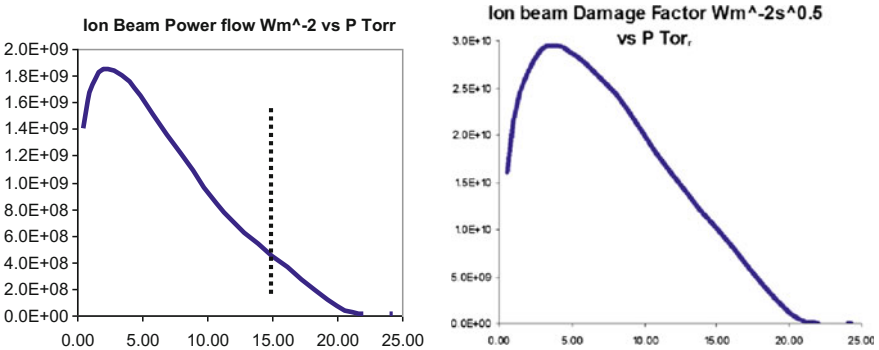

Fig. 3.31 Ion beam power versus *P* (*left*) and ion beam damage factor versus *P* (*right*)

Fig. 3.32 FPS energy versus *P*

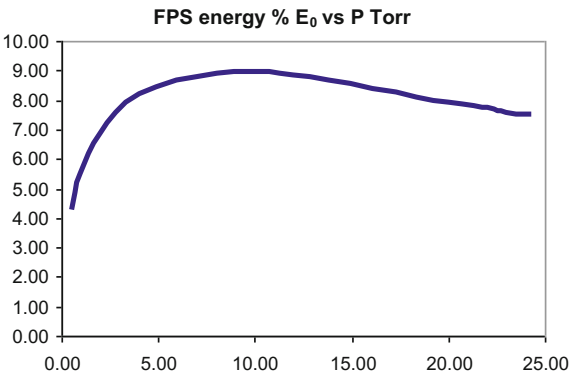

This ability to control and select bombarding particle energy, particularly in the range from tens to hundreds of eV will contribute to making PF materials technology more of a science than the present state-of-the-art.

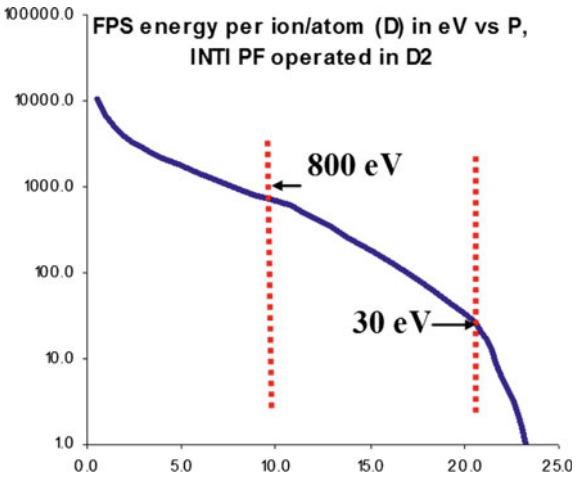

Fig. 3.33 FPS energy per ion/atom versus P

3.4.6.6 The Dual PF (DuPF)—Optimizing FFM and SFM in One Machine [61]

In the above section we have demonstrated operating FFM and SFM in the INTI PF, and in similar fashion can demonstrate both regimes in any other plasma focus. However, it is more efficient, given a capacitor bank, to have two sets of electrodes, one designed for FFM (smaller anode radius) and the other set designed for SFM (larger anode radius).

The key to the production of these two distinct regimes of operation of the plasma focus, the intense pinch regime and the plasma flow regime, is the speed parameter which may be expressed as $(I_{peak}/a)/\sqrt{P}$ where 'a' is the radius and P is the pressure in Torr. For plasma focus operated in intense neutron-optimized regime in deuterium the speed factor is known to be in the region of (90 kA/cm)/Torr$^{0.5}$ [137]. At typical operation of 4 Torr deuterium the required current density may be taken to be 180 kA/cm of 'a'. On the other hand we expect that at a speed factor < (50 kA/cm)/Torr$^{0.5}$ a PF will typically be not operating at optimized intense pinch. The radiation and ion beam emission from the low speed parameter pinch will be reduced. The design of a plasma focus that operate interchangeably in both regimes will hinge on designing it to operate efficiently in two different speed factors one of which is large of the order of (90 kA/cm)/Torr$^{0.5}$ and the other less than half that value.

Starting with available 6 × 450 μF capacitors rated at 11 kV (10% reversal), numerical experiments indicate safe operation at 9 kV, more than 1 Torr deuterium with FFM anode of 5 cm radius; producing intense ion beam and streaming plasma pulses which would be useful for studies of potential fusion reactor wall materials. On the other hand operating at 5 kV, near 10 Torr deuterium with SFM anode of 10 cm radius leads to long duration uniform flow of larger interacting cross sections with low damage factors which could be more suitable for synthesis of nano-materials.

Table 3.11 Results of numerical on 160 kJ DuPF operated with deuterium at different pressures during FFM operation; 9 kV deuterium, b = 8 cm, a = 5 cm, z_0 = 70 cm, C_0 = 2700 μF, L_0 = 50 nH, r_0 = 1 mΩ [81]

P_0 (Torr)	3	4	8	12
I_{peak} (kA)	750	795	903	966
I_{pinch} (kA)	458	485	550	586
v_a (cm/μs)	11.4	10.5	8.6	7.6
v_s (cm/μs)	26.4	24.2	19.4	16.9
v_p (cm/μs)	18.9	17.4	13.9	12.1
I/a (kA/cm)	150	159	181	193
SF [kA/(cm$\sqrt{\text{Torr}}$)]	87	79	64	56
FIB ion energy (keV)	113	110	99	91
FIB beam energy (J)	1360	1637	2495	3119
FIB energy flux ($\times 10^{14}$ W m^{-2})	1.2	1.3	1.6	1.7
FIB damage ftr ($\times 10^{10}$ Wm^{-2} s$^{0.5}$)	2.9	3.4	4.6	5.3
PS energy (kJ)	7.9	8.8	10.9	12.1
FPS speed exit (cm/μs)	31	29	23	20
Plasma footprint radius (mm)	7.7	7.7	7.8	7.8
J_b flux ions ($\times 10^{28}$ m^2 s^{-1})	0.66	0.75	1.0	1.2
Fluence ions ($\times 10^{21}$ m^{-2})	0.40	0.49	0.83	1.1
EINP %	10	11	14	17
EINP work on pinch (kJ)	10.6	12.0	15.9	18.4
Ion current (kA)	199	227	306	362
Current density ($\times 10^9$ A m^{-2})	1.1	1.2	1.6	1.9
Numb ions per shot ($\times 10^{17}$)	0.75	0.93	1.6	2.1
Number of Neutrons ($\times 10^{10}$)	0.49	0.72	1.7	2.7
FPS energy per ion (eV)	1033	867	554	417
FPS energy % E_0	7.2	8.0	9.9	11.1
PS energy/FIB energy	6	5.3	4.4	3.9
FPS speed to v_a ratio	2.75	2.73	2.68	2.64

The results shown in Tables 3.11 and 3.12 confirm that the FFM configuration of the DuPF in the range 2–12 Torr produces intense pulses suitable for damage testing whilst the SFM configuration in the range 3–10 Torr produces less damaging larger area streams with characteristics likely to be suitable for advanced materials fabrication. Schematics of the DuPF and the interchangeable electrodes for SFM and FFM are shown in Figs. 3.34, 3.35 and 3.36 [178]. Typical current waveforms [178] of the DuPF in FFM and in SFM are shown in Fig. 3.37.

Table 3.12 Results of numerical experiments on 160 kJ DuPF operated with deuterium at different pressures during SFM operation: 5 kV, deuterium, b = 8 cm, a = 5 cm, z_0 = 70 cm, C_0 = 2700 μF, L_0 = 50 nH, r_0 = 1 mΩ [81]

P_0 (Torr)	3	4	6	8	10
I_{peak} (kA)	657	681	714	736	753
I_{pinch} (kA)	330	328	309	280	243
v_a (cm/μs)	5.4	4.8	4.1	3.5	3.2
v_s (cm/μs)	10.3	8.9	7.0	5.6	4.5
v_p (cm/μs)	7.7	6.6	5.2	4.2	3.4
I/a (kA/cm)	66	68	71	74	75
SF [kA/(cm$\sqrt{\text{T}}$orr)]	38	34	29	26	24
FIB energy (keV)	30	25	18	12	7
FIB energy (J)	1896	1967	1848	1491	993
FIB energy flux ($\times 10^{11}$ W m^{-2})	54	46	29	15	4.7
FIB damage ftr ($\times 10^{10}$ W m^{-2} s$^{0.5}$)	0.32	0.29	0.21	0.12	0.44
PS energy (kJ)	5.5	5.7	5.9	6.2	6.5
FPS speed exit (cm/μs)	9	8	6	4	2
Plasma footprint radius (mm)	18.0	18.4	19.6	22.2	27.8
Jb flux ions ($\times 10^{26}$ m^2 s^{-1})	11	11	10	7.6	4.1
Fluence ions ($\times 10^{20}$ m^{-2})	3.8	4.6	5.4	5.1	3.5
EINP %	27	28	28	27	25
EINP1 work on pinch (kJ)	9.3	9.6	9.6	9.1	8.4
Ion current (kA)	181.9	193.4	199.3	188.0	159.9
Current density ($\times 10^8$ A m^{-2})	1.8	1.8	1.6	1.2	0.66
Numb ions per shot ($\times 10^{17}$)	3.9	4.8	6.5	7.8	8.6
FPS energy per ion (eV)	94	66	34	16	6
FPS energy % E_0	16.2	16.8	17.5	18.3	19.1
PS energy/FIB energy	2.9	2.9	3.2	4.1	6.5
FPS speed to v_a ratio	1.8	1.6	1.4	1.1	0.8

3.4.7 *Insight 5—Neutron Saturation*

Besides being accurately descriptive and related to wide-ranging experimental reality, desirable characteristics of a model include predictive and extrapolative scaling. Moreover, a useful model should be accessible, usable and user-friendly and should be capable of providing insights. Insight, however, cannot be a characteristic of the model in isolation but is the interactive result of the model with the modeler or model user.

It was observed early in plasma focus research [1, 179] that neutron yield $Y_n \sim E_0^2$ where E_0 is the capacitor storage energy. Such scaling gave hopes of possible development as a fusion energy source. Devices were scaled up to higher E_0. It was then observed that the scaling deteriorated, with Y_n not increasing as much as suggested by the E_0^2 scaling. In fact, some experiments were interpreted as

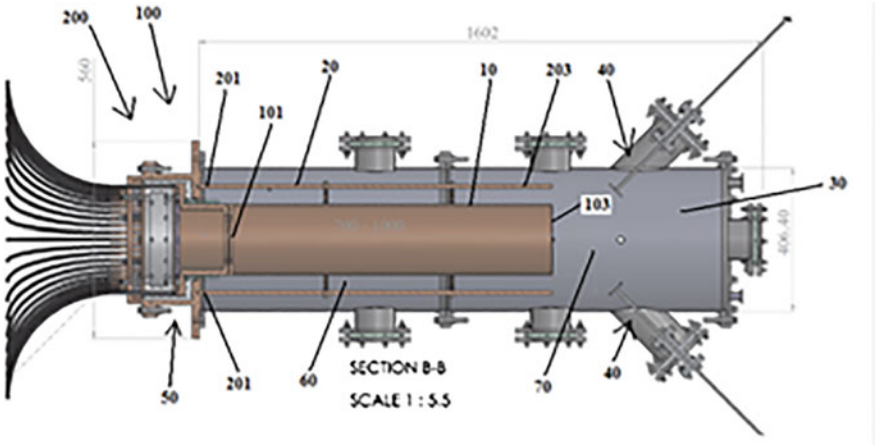

Fig. 3.34 Main design presentation of the DuPF, using SolidWorks software

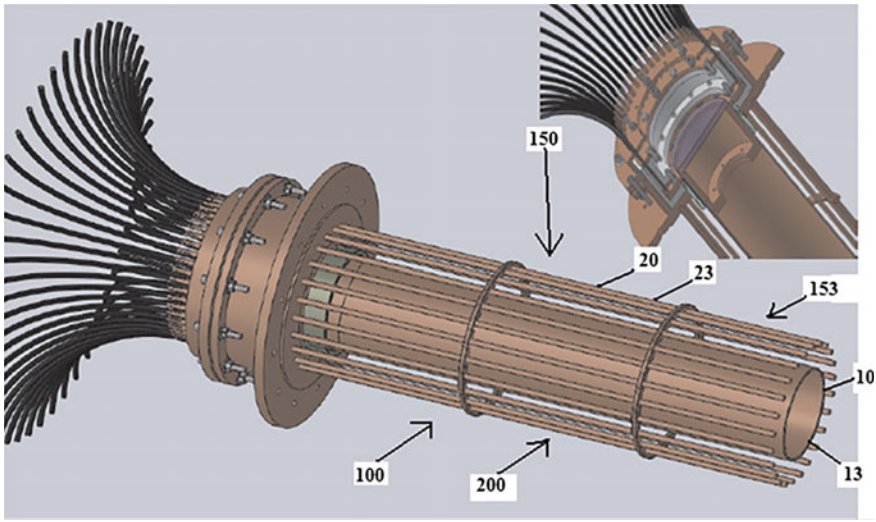

Fig. 3.35 Design of the SFM electrodes

evidence of a neutron saturation effect [1] as E_0 approached several hundreds of kJ. As recently as 2006 Krauz [180] and 2007 Scholz [181] have questioned whether the neutron saturation was due to a fundamental cause or to avoidable machine effects such as the incorrect formation of plasma current sheath arising from impurities or sheath instabilities. We should note here that the region of discussion (several hundreds of kJ approaching the MJ region) is in contrast to the much higher energy region discussed by Schmidt at which there might be expected to be a decrease in the role of beam-target fusion processes [1].

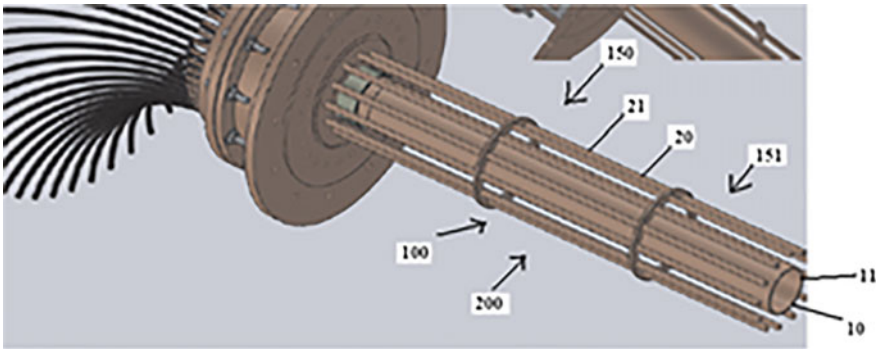

Fig. 3.36 Design of the FFM electrodes

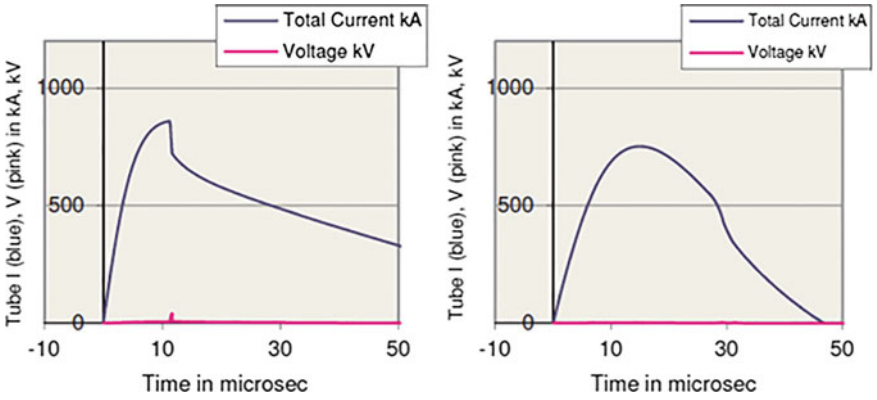

Fig. 3.37 Current waveforms (*left*) in FFM 9 kV, 6 Torr and (*right*) in SFM 5 kV, 10 Torr

3.4.7.1 The Global Neutron Scaling Law

Recent extensive numerical experiments [10, 21, 22, 44, 100] also showed that whereas at energies up to tens of kJ the $Y_n \sim E_0^2$ scaling held, deterioration of this scaling became apparent above the low hundreds of kJ. This deteriorating trend worsened and tended towards $Y_n \sim E_0^{0.8}$ at tens of MJ. The results of these numerical experiments are summarized in Fig. 3.38, with the solid line representing results from numerical experiments. Experimental results from 0.4 kJ to MJ, compiled from several available published sources are also included. The combined experimental and numerical experimental results [10, 21, 44] (see Sect. 3.4.4) appear to have general agreement particularly with regards to the $Y_n \sim E_0^2$ at energies up to 100 kJ, and the deterioration of the scaling from low hundreds of kJ to the 1 MJ level. The global data of Fig. 3.38 suggests that the apparently observed neutron saturation effect is overall not at significant variance with the deterioration of the scaling shown by the numerical experiments.

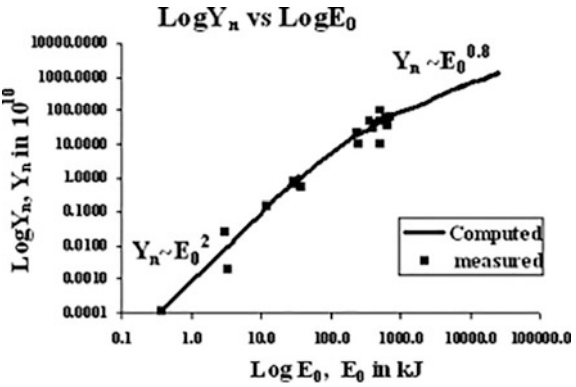

Fig. 3.38 Y_n scaling deterioration observed in numerical experiments from 0.4 kJ to 25 MJ (*solid line*) using the Lee model code, compared to measurements compiled from publications (*squares*) of various machines from 0.4 kJ to 1 MJ. Reprinted from Lee [21]

3.4.7.2 The Dynamic Resistance

A simple yet compelling analysis of the cause of this neutron saturation has been published [21]. In Fig. 3.1 (see Sect. 3.1.1) on the left side is shown a schematic of the plasma dynamics in the axial phase of the Mather-type plasma focus with the current sheet shown to go from the anode to the cathode perpendicularly. Experimental observations show that there is actually a canting of the current sheet and also that only a fraction (typically 0.7) of the total current participates in driving the current sheet. These points are accounted for in the modelling by model parameters f_m and f_c. We have represented the plasma focus circuit in Fig. 3.5.

We consider only the axial phase. By surveying published results of all Mather-type experiments we find that all deuterium plasma focus devices operate at practically the same speeds [137] and are characterized by a constancy of energy density (per unit mass) over the whole range from the smallest sub-kJ to the largest MJ devices. The time-varying tube inductance is $L = (\mu/2\pi)\ln(c)z$ where $c = b/a$ and μ is the permeability of free space. The rate of change of inductance is $dL/dt = 2 \times 10^{-7}\ln(c)(dz/dt)$ in SI units. Typically on switching, as the capacitor discharges, the current rises towards its peak value, the current sheet is accelerated, quickly reaching nearly its peak speed and continues accelerating slightly towards its peak speed at the end of the axial phase. Thus for most of its axial distance, the current sheet is travelling at a speed close to the end-axial speed. In deuterium, the end-axial speed is observed to be about 10 cm/μs over the whole range of devices [6]. This fixes the rate of change of inductance dL/dt as 1.4×10^{-2} H/s for all the devices, if we take the radius ratio $c = b/a = 2$. This value of dL/dt changes by at most a factor of 2, taking into account the variation of c from low values of 1.4 (generally for larger machines) to 4 (generally for smaller machines). The typical value of dL/dt is about 14 mΩ.

We need now to inquire into the nature of the change in the inductance $L(t)$.

Consider instantaneous power P delivered to $L(t)$ by a change in $L(t)$
Induced voltage:

$$V = \mathrm{d}(LI)/\mathrm{d}t = I(\mathrm{d}L/\mathrm{d}t) + L(\mathrm{d}I/\mathrm{d}t) \tag{3.66}$$

Hence instantaneous power into $L(t)$:

$$P = VI = I^2(\mathrm{d}L/\mathrm{d}t) + LI(\mathrm{d}I/\mathrm{d}t) \tag{3.67}$$

Next, consider instantaneous power associated with the inductive energy (½LI^2):

$$P_L = \mathrm{d}(1/2LI^2)/\mathrm{d}t = 1/2I^2(\mathrm{d}L/\mathrm{d}t) + LI(\mathrm{d}I/\mathrm{d}t) \tag{3.68}$$

We note that P_L of Eq. (3.68) is not the same as P of Eq. (3.67).

The difference = $P - P_\mathrm{L}$ = (½)(dL/dt)I^2 is not associated with the inductive energy stored in L. We conclude that whenever $L(t)$ changes with time, the instantaneous power delivered to $L(t)$ has a component that is not inductive. Hence this component of power (½)(dL/dt)I^2 must be resistive in nature; and the quantity (½)(dL/dt) also denoted as half L_dot is identified as a resistance, due to the motion associated with dL/dt; which we call the dynamic resistance DR [10, 21, 37, 44]. Note that this is a general result and is independent of the actual processes involved. In the case of the plasma focus axial phase, the motion of the current sheet imparts power to the shock wave structure with consequential shock heating, Joule heating, ionization, radiation, etc. The total power imparted at any instant is just the amount (½)(dL/dt)I^2, with this amount powering all consequential processes. We denote the dynamic resistance of the axial phase as DR_0.

We have thus identified for the axial phase of the plasma focus a typical dynamic resistance of 7 mΩ due to the motion of the current sheet at 10 cm/μs. It should be noted here that similar ideas of the role of dL/dt as a resistance were discussed by Bernard et al. [1]. In that work, the effect of dL/dt was discussed only for the radial phase. In our opinion, the more important phase for the purpose of neutron saturation is actually the axial phase for the Mather-type plasma focus.

3.4.7.3 The Interaction of a Constant Dynamic Resistance with a Reducing Generator Impedance Causes Deterioration in Current Scaling

We now resolve the problem into its most basic form as follows. We have a generator (the capacitor charged to 30 kV), with an impedance of $Z_0 = (L_0/C_0)^{0.5}$ driving a load with a near constant resistance of 7 mΩ. We also assign a value for stray resistance of $0.1Z_0$. This situation is shown in Table 3.11 where L_0 is given a typical value of 30 nH. We also include in the last column the results from a circuit (L–C–R) computation, discharging the capacitor with initial voltage of 30 kV into a fixed resistance load of 7 mΩ simulating the effect of the DR_0 and a stray resistance of value $0.1Z_0$ (Table 3.13).

Table 3.13 Discharge characteristics of equivalent PF circuit, illustrating the 'saturation' of I_{peak} with an increase of E_0 to very large values

E_0 (kJ)	C_0 (μF)	Z_0 (m Ω)	DR_0 (m Ω)	Z_{total} (m Ω)	$I_{peak} = V_0/Z_{total}$ (kA)	I_{peak}, L–C–R (kA)
0.45	1	173	7	197	152	156
4.5	10	55	7	67	447	464
45	100	17	7	26	1156	1234
135	300	10	7	18	1676	1819
450	1000	5.5	7	12.9	2321	2554
1080	2400	3.5	7	10.8	2781	3070
4500	10000	1.7	7	8.8	3407	3722
45000	100000	0.55	7	7.6	4209	4250

The last column presents results using circuit (L–C–R) computation, with a fixed resistance load of 7 mΩ, simulating the effect of the DR_0 and a stray resistance of value $0.1Z_0$

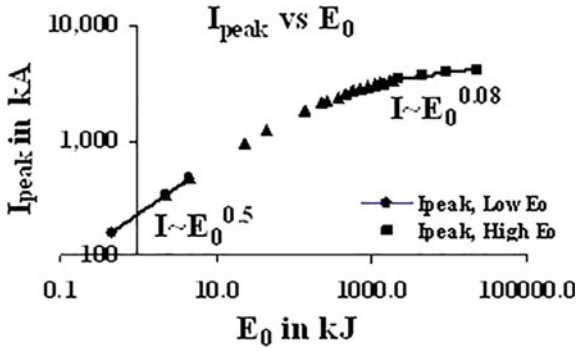

Fig. 3.39 I_{peak} versus E_0 on log–log scale, illustrating I_{peak} 'saturation' at large E_0. Reprinted from Lee [21]

Plotting the peak current as a function of E_0 we obtain Fig. 3.39, which shows the tendency of the peak current towards saturation as E_0 reaches large values; the deterioration of the curve becoming apparent at the several hundred kJ level. This is the case for $I_{peak} = V_0/Z_{total}$ and also for the L–C–R discharge with simulated value of the DR_0. In both cases it is seen clearly that a capacitor bank of voltage V_0 discharging into a constant resistance such as DR_0 will have a peak current I_{peak} approaching an asymptotic value of $I_{peak} = V_0/DR_0$ when the bank capacitance C_0 is increased to such large values that the value of $Z_0 = (L_0/C_0)^{0.5} \ll DR_0$. Thus DR_0 causes current 'saturation'.

3.4.7.4 Deterioration in Current Scaling Causes Deterioration in Neutron Scaling

In Sect. 3.4.4 we had shown the following relationships between Y_n and I_{peak} and I_{pinch} as follows:

$$Y_n \sim I_{pinch}^{4.5}$$
$$Y_n \sim I_{peak}^{3.8}$$

Hence saturation of I_{peak} will lead to saturation of Y_n.

At this point, we note that if we consider that only 0.7 of the total current takes part in driving the current sheet, as typically agreed upon from experimental observations, then there is a correction factor which reduces the axial dynamic resistance by some 40%. That would raise the asymptotic value of the current by some 40%; nevertheless, there would still be 'saturation'.

Thus we have shown that current 'saturation' is inevitable as E_0 is increased to very large values by an increase in C_0, simply due to the dominance of the axial phase dynamic resistance. This makes the total circuit impedance tend towards an asymptotic value which approaches the dynamic resistance at infinite values of E_0. The 'saturation' of current inevitably leads to a 'saturation' of neutron yield. Thus the apparently observed neutron 'saturation' which is more accurately represented as a neutron scaling deterioration is inevitable because of the dynamic resistance. In line with current plasma focus terminology, we will continue to refer to this scaling deterioration as 'saturation'. The above analysis applies to the Mather-type plasma focus. The Filippov-type plasma focus does not have a clearly defined axial phase. Instead, it has a lift-off phase and an extended pre-pinch radial phase which determine the value of I_{peak}. During these phases, the inductance of the Filippov discharge is changing, and the changing $L(t)$ will develop a dynamic resistance which will also have the same current 'saturation' effect as the Filippov bank capacitance becomes big enough.

The same scaling deterioration is also observed in the yield of Neon SXR (see Fig. 3.27) and we expect the same for other radiation yields as well. The speed restriction for a plasma focus operating in neon is not the same as that in deuterium. Nevertheless, there is a speed window related to the optimum temperature window. This again requires fixing the dynamic resistance of the axial phase for the neon plasma focus within certain limits typically the dynamic resistance equivalent to an axial speed range of 5–8 cm/μs. This dynamic resistance and its interaction with the capacitor bank impedance, as storage energy is increased, is again the cause of the scaling deterioration.

3.4.7.5 Beyond Presently Observed Neutron Saturation Regimes

Moreover, the 'saturation' as observed in presently available data is due also to the fact that all tabulated machines operate in a narrow range of voltages of 15–50 kV. Only the SPEED machines, most notably SPEED II [182] operated at low hundreds of kV. No extensive data have been published from the SPEED machines. Moreover, SPEED II, using Marx technology, has a large bank surge impedance of 50 mΩ which itself would limit the current. If we operate a range of such high voltage machines at a fixed high voltage, say 300 kV, with ever larger E_0 until the

surge impedance becomes negligible due to the very large value of C_0, then the 'saturation' effect would still be there, but the level of 'saturation' would be proportional to the voltage. Moreover operation at higher pressures beyond 60 Torr [44] would further increase the neutron yield. In this way we can go far above presently observed levels of neutron 'saturation'; moving the research, as it were into presently beyond-saturation regimes.

Could the technology be extended to 1 MV? That would raise I_{peak} to beyond 15 MA and I_{pinch} to over 6 MA. Also multiple Blumleins at 1 MV, in parallel, could provide driver impedance of 100 mΩ, matching the radial phase dynamic resistance and provide fast-rise currents peaking at 10 MA with I_{pinch} value of perhaps 5 MA. Bank energy would be several MJ. The push to higher currents may be combined with proven neutron yield enhancing methods such as doping deuterium with low % of krypton [183]. Further increase in pinch current might be by fast current injection near the start of the radial phase. This could be achieved with charged-particle beams or by circuit manipulation such as current-stepping [105]. The Lee model is ideally suited for testing circuit manipulation schemes.

3.4.7.6 Neutron Scaling—Its Relationship with the Plasma Focus Properties

In Sect. 3.4.7.1 we had discussed the global scaling law for neutron yield as shown in Fig. 3.1 which was compiled with data from experiments and numerical experiments. Figure 3.38 shows that whereas at energies up to tens of kJ the $Y_n \sim E_0^2$ scaling held, deterioration of this scaling became apparent above the low hundreds of kJ. This deteriorating trend worsened and tended towards $Y_n \sim E_0^{0.8}$ at tens of MJ. The global data of Fig. 3.38 suggests that the apparently observed neutron saturation effect is overall not in significant variance with the deterioration of the scaling shown by the numerical experiments.

3.4.7.7 Relationship with Plasma Focus Scaling Properties

Now we link up this neutron scaling law deterioration and subsequent saturation with the scaling properties of the plasma focus discussed in Sect. 3.3. This scaling law deterioration and saturation are due to the constancy of the speed factor SF and energy density, as E_0 increases. The constancy of the axial speed or SF causes the deterioration of current scaling, requiring that the anode radius 'a' is not increased as much as it would have been increased if there were no deterioration. This implies that the size and duration of the focus pinch are also restricted by the scaling deterioration. Ultimately at high tens of MJ, I_{peak} saturates, the anode radius of the focus should not be increased anymore with E_0. The size and duration of the focus pinch no longer increase with E_0 and Y_n also saturates. We now have the complete picture.

We may consider the other effects such as the current limiting effect as inductance is reduced and the scaling laws of plasma focus for SXR yield. These are all related to the behaviour of the scaling properties and the interaction of these scaling properties, particularly the dynamic resistance with the capacitor bank impedance.

3.4.8 Summary of Scaling Laws

Numerical experiments carried out using the universal plasma focus laboratory facility based on the Lee Model code give reliable scaling laws for neutrons production and neon SXR yields for plasma focus machines. The scaling laws obtained are summarized in Table 3.14.

These laws provide useful references and facilitate the understanding of present plasma focus machines. More importantly, these scaling laws are also useful for design considerations of new plasma focus machines particularly if they are intended to operate as an optimized neutron or neon SXR sources. More recently, the scaling of Y_n versus E_0 as shown above has been placed in the context of a global scaling law with the inclusion of available experimental data. From that analysis, the cause of scaling deterioration for neutron yield versus energy as shown in Fig. 3.38 (which has also been given the misnomer 'neutron saturation') has been uncovered as due to a current scaling deterioration caused by an almost constant axial phase 'dynamic resistance' interacting with a reducing bank impedance as energy storage is increased by increasing capacitance of energy bank at essentially constant voltage. The deterioration of soft X-ray yield with storage energy as shown in Fig. 3.27 could also be ascribed to the same axial phase 'dynamic resistance' effect. This deterioration of scaling will also appear in the scaling trends (with stored energy) of beam ions.

Table 3.14 Summary of radiation scaling laws for the plasma focus

For neutron yield: (yield in number of neutrons per shot)
$Y_n = 3.2 \times 10^{11} I_{pinch}^{4.5}$; $Y_n = 1.8 \times 10^{10} I_{peak}^{3.8}$; I_{peak} (0.3–5.7), I_{pinch} (0.2–2.4) in MA
$Y_n \sim E_0^{2.0}$ at tens of kJ to $Y_n \sim E_0^{0.84}$ at MJ level (up to 25 MJ)
For neon soft X-rays: (yield in J per shot)
$Y_{sxr} = 8.3 \times 10^3 I_{pinch}^{3.6}$; $Y_{sxr} = 6 \times 10^2 I_{peak}^{3.2}$; I_{peak} (0.1–2.4), I_{pinch} (0.07–1.3) in MA
$Y_{sxr} \sim E_0^{1.6}$ (kJ range) to $Y_{sxr} \sim E_0^{0.8}$(towards MJ)
For beam ions at exit of a deuterium plasma pinch: (yield in J per shot)
$Y_{beamions}$=$4.8 \times 10^{-7} I_{pinch}^{3.6}$ $Y_{beamions} = 9.7 \times 10^{-7} I_{peak}^{3.2}$ where $Y_{beamions}$ is in J; currents in kA
$Y_{beamions} = 18.2 E_0^{1.2}$ where $Y_{beamions}$ is in J and E_0 is in kJ; averaged over 1 kJ–1 MJ

We emphasise here that the scaling laws with I_{pinch} are the more fundamental and robust one compared to I_{peak}. This is because although the PF is reasonably consistent in its operations, there will be occasions when even the best-optimized machines may not focus or poorly focused although having a high I_{peak} with no neutrons. However, I_{pinch} being the current actually flowing in the pinch is more consistent in all situations.

The numerical experiments give robust scaling laws for PFs covering a wide range of energies from sub-kJ to tens of MJ. It supplements the limited (non-existent in the case of beam ions) scaling laws available to predict PF radiations yields. Now, we have on stronger footing the useful scaling laws for neutron, SXR and ion yields from PF machines.

3.5 Radiative Cooling and Collapse in Plasma Focus

3.5.1 Introduction to Radiative Cooling

The Plasma Focus has wide-ranging applications due to its intense radiation of SXR, XR, electron and ion beams and fusion neutrons [1]. The use of gases such as Ne and Xe for generation of specific SXR or EUV lines for microlithography applications [1, 2, 74, 78] has been widely discussed in the literature as has the use of N and O to generate the lines suitable for water-window microscopy [184, 185]. Recently Ar has been considered for micro-machining due to the harder characteristic line radiation [186]. Various gases including Kr have been discussed and used for fusion neutron yield enhancement [183] due arguably to mechanisms such as thermodynamically enhanced pinch compressions.

In a Z-pinch, compressed by large electric currents to high densities and temperatures [187], an equilibrium state may be envisaged when the plasma kinetic pressure rises to balance the compressing magnetic pressure, resulting in the pinch achieving an equilibrium pinch radius. This is the pressure balance basis of the Bennett equation [188]. During the compression, work is done on the column leading to a rise in internal energy. By applying energy balance additionally to pressure balance the equilibrium radius of the pinch may in principle be computed [189], as might also the density ratio of a compression driven by radiation pressure [190]. This minimum pinch radius was computed to be 0.3 [189] for a deuterium Z-pinch compared to Imperial College observation of 1/3 [191]. For Ar, the energy balance and pressure balance method [134] computed the radius ratio as 0.18, compared to observations of 0.17 at temperatures of 2×10^7 K for the Imperial College low-pressure high-speed Ar Z-pinch. The radius ratio is somewhat temperature-dependent due to the compressibility of the gas dependent on the specific heat ratio γ of the plasma. The above is for the situation in which the pinch is assumed to be purely electromagnetic with energy input into the pinch arising only through electromagnetic motional effect. When Joule heating and radiation

emission are considered, these will modify pinch dynamics and pinch configuration. Joule heating will increase internal energy allowing a bigger equilibrium pinch radius whilst radiation emission will oppose this trend. The power loss due to emitted radiation may exceed the gain due to Joule heating. In such a situation the magnetic pressure associated with the electric current continues to exert a radially inward squeezing (pinching) force, but the kinetic (resisting) pressure drops due to the excess radiation power loss (emitted radiation power minus the Joule power gain). This radiation cooling effect, if sufficient, will lead to a sharp enhancement of compression to the very small radius, which could be far smaller than envisaged in the case of the electromagnetic pinch.

In the case of hydrogen pinch, the plasma is typically far above fully ionized temperature and the dominant radiation is free-free transitions (bremsstrahlung). The bremsstrahlung power P_{brem} is proportional to $T^{1/2}$ whilst plasma resistive heating P_{joule} is proportional to $T^{-3/2}$; implying an increase in P_{brem} and decrease in P_{joule} with increasing plasma temperature. Thus as pinch current is increased and pinch temperature rises, there comes a point when P_{brem} exceeds P_{joule}. Pease [143] and Braginskii [144] separately showed that in hydrogen this point may be defined by a critical pinch current referred to as $I_{\text{P-B}}$ of 1.4 MA. In such a pinch at equilibrium when pinch current is raised above 1.4 MA, radiation collapse may occur.

As the temperature drops due to excessive emitted radiation the kinetic pressure is reduced and hence the pinch compressed density increases, the plasma self-absorption [146, 147] sets in limiting the emission of radiation. Radiation collapse will stop. This mechanism will place a lower limit on the radius of the pinch.

The possibility of intense radiation leading to extreme compressions in a Z-pinch and the implications of such a mechanism for the development of radiation sources has recently been reviewed [187]. Shearer [142] considered an equilibrium model of the Z-pinch based on Bennett relation, radiation losses and Ohmic heating to explain the highly localized X-ray sources observed in plasma focus experiments. Vikhrev [192] considered the dynamics of a Z-pinch contraction in deuterium with appreciable radiative loss taking into account decreased current due to pinch inductance and resistance; the viscous heat and anomalous resistive heat release; transition of plasma bremsstrahlung into blackbody surface radiation; the pressure of the degenerate electron gas and the thermonuclear heat release. A neutron yield of 10^{14} is found from a highly compressed plasma of a 2 MJ system. With a 1% mixture of xenon with a fully ionized plasma at 10 MA, the enhanced compression to a density of 10^{27} cm^{-3} leads to a neutron yield of 1.5×10^{16}. Using a mixture of deuterium and tritium the neutron yield reached 10^{18} per discharge with an input energy of 2 MJ, reaching breakeven according to their calculations. Koshelev et al. [193] considered the formation of radiation enhanced micropinches as a source of highly ionized atoms. It is known that in gases undergoing intense line radiation the radiation-cooled threshold current is considerably lowered [194].

We show that the equations of the Lee Model code [10, 37] may be used to compute this lowering. The model is correctly coupled between the plasma

dynamics and the electrical circuit which is an advantageous feature when compared to computations which use a fixed current or a current which is not correctly associated with the electric circuit interacting with the plasma dynamics. The model treats the pinch as a column. Our computations show that the radial collapse of the column is significantly enhanced by the net energy loss due to radiation and joule heating with consideration of plasma opacity. This radiatively enhanced compression of the plasma column would, in reality, mean that as the column breaks up into localized regions (hot spots) the radiative collapse would be further enhanced. Thus the calculated radiative collapse of the column would be an underestimate of the more realistic 'line of hot spots' situation [195]. Nevertheless, the Lee Model code does give useful information since it incorporates the time history of the axial and radial phases. Earlier work has already suggested that the neutron enhancement effect of seeding [183] could at least in part be due to the enhanced compression caused by radiation cooling.

3.5.2 The Radiation-Coupled Dynamics for the Magnetic Piston

The code uses Eq. (3.38) for the piston position r_p derived from the first law of thermodynamics applied to the pinch volume (For convenience of the readers we reproduce this equation here):

$$\frac{dr_p}{dt} = \frac{\frac{-r_p}{\gamma I}\frac{dI}{dt} - \frac{1}{\gamma+1}\frac{r_p}{z_f}\frac{dz_f}{dt} + \frac{4\pi(\gamma-1)}{\mu\gamma z_f}\frac{r_p}{f_c^2 I^2}\frac{dQ}{dt}}{\frac{\gamma-1}{\gamma}} \tag{3.38}$$

where I is the total discharge current in the circuit, f_{cr} is the fraction of current flowing into the pinch, z_f is the time-varying length of the PF pinch and γ is the specific heat ratio (SHR) of the plasma. When dQ/dt (sum of Joule heating and radiation energy loss) is negative, energy is lost from the plasma adding a negative component to dr_p/dt which tends to reduce the radius r_p.

3.5.3 The Reduced Pease-Braginskii Current

Following Lee et al. [50, 52] we write the reduced P-B current $I_{\text{P-Breduced}}$ as:

$$I^2_{\text{P-Breduced}} = I^2_{\text{P-B}} \times \frac{1}{K} \times Z' \tag{3.69}$$

with

$$Z' = (1/4)\frac{(1+\mathrm{Z_{eff}})^2}{\mathrm{Z_{eff}^2}}\,;K = \left[\frac{(\mathrm{d}Q_{\mathrm{line}}/\mathrm{d}t)+(\mathrm{d}Q_{\mathrm{Brem}}/\mathrm{d}t)}{(\mathrm{d}Q_{\mathrm{Brem}}/\mathrm{d}t)}\right] \tag{3.70}$$

We consider the following powers (all quantities in SI units unless otherwise stated): respectively, Joule heating, Bremsstrahlung and Line radiation generated in a plasma column of radius r_{p}, length l at temperature T (rewriting Eqs. (3.32)–(3.45) so that the powers are functions of the pinch current written as I from this point onwards without reference to fractions f_{cr}):

$$\frac{\mathrm{d}Q_J}{\mathrm{d}t} = C_J T^{-3/2}\frac{l}{\pi r_\rho^2}\mathrm{Z_{eff}}I^2 \quad \text{where } \mathrm{C_J} \cong 1300 \text{ and } T \text{ is in Kelvin} \tag{3.71}$$

$$\frac{\mathrm{d}Q_{\mathrm{Brem}}}{\mathrm{d}t} = C_1 T^{1/2} n_{\mathrm{i}}^2 Z_{\mathrm{eff}}^3 \pi r_{\mathrm{p}}^2 l \quad \text{where } n_{\mathrm{i}} \text{ is in m}^{-3} \text{ and } \mathrm{C_1} = 1.6\times10^{-40} \tag{3.72}$$

$$\frac{\mathrm{d}Q_{\mathrm{line}}}{\mathrm{d}t} = C_2 T^{-1} n_{\mathrm{i}}^2 Z_n^4 Z_{\mathrm{eff}}^2 \pi r_{\mathrm{p}}^2 l \quad \text{where } \mathrm{C_2} = 4.6\times10^{-31} \tag{3.73}$$

So that we write the total power adding the three terms as follows:

$$\begin{aligned}\frac{\mathrm{d}Q}{\mathrm{d}t} = &-\pi\left[C_1 b^{1/2}\right]\frac{Z_{\mathrm{eff}}^3}{(1+Z_{\mathrm{eff}})^{1/2}} n_{\mathrm{i}}^{3/2} r_{\mathrm{p}} l I \\ &-\frac{\pi C_2}{b}(1+Z_{\mathrm{eff}})Z_{\mathrm{eff}} Z_n^4 n_{\mathrm{i}}^3 r_{\mathrm{p}}^4 \frac{l}{I^2} + \frac{C_J}{\pi b^{3/2}}(1+Z_{\mathrm{eff}})^{3/2} Z_{\mathrm{eff}} n_{\mathrm{i}}^{3/2} r_{\mathrm{p}} \frac{l}{I}\end{aligned} \tag{3.74}$$

For He the factor $Z' = 0.56$. This factor alone reduces the Pease-Braginskii currentto 1.2 MA, even if we assume that He is completely ionized with insignificant line radiation so that $K = 1$. When line radiation becomes dominant the calculation of K is complicated by the dependence of P_{line} on density and temperature; so that there is no one value for reduced Pease-Braginskii current, $I_{\text{P-Breduced}}$.

3.5.3.1 The Reduced Pease-Braginskii Current for PF1000 at 350 kJ

We take some likely points of operation in PF1000 for the gases Ne, Ar, Kr and Xe and estimate typical values of $I_{\text{P-Breduced}}$ for these gases; shown in Table 3.15. In the example for Ne we take a typical point of operation for intense line radiation at $Z_{\mathrm{eff}} \sim 9$ so that $Z' \sim 0.31$. At this point of operation P_{line} is found to be 20 P_{brem}; so we have $I_{\text{P-Breduced}} \sim 190$ kA. It is emphasized that unlike the value for H or D which is derived by balancing P_{Joule} and P_{brem} resulting in a value dependant only on the pinch current, when higher Z gases are considered with line radiation that needs to be included in the factor K, then there is no one value for the $I_{\text{P-Breduced}}$. Table 3.15 thus gives only indicative values of $I_{\text{P-Breduced}}$ with the trend as the

Table 3.15 Reduced Pease-Braginskii current for various gases; PF1000 operating conditions

Gases	P_0 (Torr)	$I_{\text{P-Breduced}}$ (kA)	T (10^6 K)
D2	3.0	1562	4.3
He	2.0	1175	4.8
Ne	0.44	187	9.0
Ar	0.178	110	11.1
Kr	0.060	87	22.6
Xe	0.017	66	32.5

Z-number increases, a lower value of $I_{\text{P-Breduced}}$ may be expected. In particular, He may have a smaller $I_{\text{P-Breduced}}$ than indicated in Table 3.15 which for simplicity has only considered bremsstrahlung for He.

We note that in deriving Table 3.15 the radiation powers are considered at the source. The derived $I_{\text{P-Breduced}}$ is indicative of the situation when the plasma is assumed to be completely transparent to the radiation.

3.5.3.2 The Reduced Pease-Braginskii Current for INTI PF at 2 kJ

Similarly, we compute indicative values of $I_{\text{P-Breduced}}$ for INTI PF at 12 kV [196]. We select some possible points of operation for the gases Ne, Ar, Kr and Xe and estimate typical values of $I_{\text{P-Breduced}}$ for these gases in Table 3.16. In the example for Ne we take a typical point of operation for intense line radiation at $Z_{\text{eff}} \sim 8.5$ so that $Z' \sim 0.31$. At this point P_{line} is found to be 136 P_{brem}; so we have $I_{\text{P-Breduced}} \sim 76$ kA. Note that this much smaller value of $I_{\text{P-Breduced}}$ (compared to the corresponding neon value for PF1000 in Table 3.15) is obtained by selecting a lower operating temperature conducive to a higher ratio of P_{line} to $P_{\text{brem.}}$ Table 3.16 gives attainable values of $I_{\text{P-Breduced}}$ in INTI PF.

3.5.4 Effect of Plasma Self-absorption

We also note that the above consideration has not taken into account the effect of plasma self-absorption. Taking that into consideration the emission power will be

Table 3.16 Reduced Pease-Braginskii current for various gases; at typical INTI PF operating conditions

Gases	P_0 (Torr)	$I_{\text{P-Breduced}}$ (kA)	T (10^6 K)
D	NA	NA	NA
He	NA	NA	NA
Ne	1.2	76	3.5
Ar	0.17	47	5.8
Kr	0.025	23	5.6
Xe	0.007	15.4	7.5

reduced, effectively reducing the value of K thus raising the threshold current from that value computed in Eq. (3.69).

Plasma self-absorption included in the code is already discussed in Section "Plasma Self-Absorption and Transition from Volumetric Emission to Surface Emission" which shows the method for computing the plasma self-absorption correction factor A.

When there is no plasma self-absorption $A = 1$. When A goes below 1, plasma self-absorption starts. When a sizeable fraction of the photons is re-absorbed, e.g. value of A reaches $1/e$, plasma radiation is considered to switch over from volume radiation to surface radiation and is computed accordingly in the model.

Summarizing: The code computes the amount of radiation emitted, computes plasma self-absorption effects and incorporates these effects into the plasma dynamics.

3.5.5 Characteristic Times of Radiation

In a recent paper, Lee et al. [52] argue that $I_{\text{P-B}}$ or $I_{\text{P-Breduced}}$ is only one condition for the occurrence of radiative collapse. Another condition would be the magnitude of the excess radiative power $\mathrm{d}Q/\mathrm{d}t$ (which we call $Qdot$, where Q = total energy radiated out of the pinch plasma less Joule heat released in the pinch plasma) acting to reduce the energy in the pinch E_{pinch}. We define a characteristic radiative time as $t_{\text{rad}} \sim E_{\text{pinch}}/Qdot$ which is the time required for all the pinch energy to be radiated away at the rate $Qdot$.

We preface our argument by reviewing the work of Robson on the Z-pinch. Robson [146] considered this situation for the case of the hydrogen and helium Z-pinch including the effects of opacity. Robson considered a circuit which provided a constant voltage until the pinch collapsed to its minimum radius limited by opacity; at which point the voltage is set to zero. Robson assigned line densities of 10^{17}, 10^{18} and 10^{19} ions per cm at applied voltages of 65–380 kV per cm of pinch length with initial established fully ionized pinch of radius 1 mm. For a typical case in hydrogen of 10^{18} ions per cm, $L_0 = 25$ nH with applied 190 kV per cm driving initial $\mathrm{d}I/\mathrm{d}t$ of 5 kA per ns, the current reaches 1.81 MA in 440 ns. The radius which has reduced over the current rise time relatively 'gradually' to 10^{-3} cm at this time, abruptly plunges to 2×10^{-5} cm in a time of 0.06 ns whilst the current drops precipitously from 1.8 to 0.8 MA.

According to Table 3.15, our calculations show that for He the reduced P-B current ($I_{\text{P-Breduced}}$) is 1.2 MA considering only the charge factor; though there may be a further reduction due to line radiation. However running the code for PF1000 at 40 kV (in principle the maximum operating voltage of PF1000) in He the pinch current exceeds 1.2 MA but there is no sign of radiative collapse. Even hypothetically increasing the PF1000 operating voltage to 100 kV when the pinch current exceeds 2 MA, there is still no sign of a sharp drop in pinch radius ratio which is the most indicative sign of radiative collapse. To explain this we develop

an expression for the characteristic time required to radiate away all the pinch energy through bremsstrahlung and also for the characteristic time for line radiation. The numerical experiments show that the pinch duration has to be of the order (typically at least 0.1) of the characteristic time of radiation (t_{rad}) in order for that radiation to cause significant radiative cooling resulting in radial collapse.

3.5.5.1 Definition-Pinch Energy/Radiation Power

We write down the thermal energy in the pinch as the total number of particles in the pinch multiplied by the thermal energy per particle:

$$E_{\mathrm{pinch}} = [kT/(\gamma - 1)]n_{\mathrm{i}}(1 + Z_{\mathrm{eff}})\pi r_{\mathrm{p}}^2 z_{\mathrm{p}}, \tag{3.75}$$

where γ is the specific heat ratio which may be written in terms of the degree of freedom f as $\gamma = (2+f)/f$; so that $1/(\gamma - 1) = f/2$.

In Eq. (3.75) the energy of the pinch is written in a form suitable for high-Z gases in which the energy expended in ionization is not insignificant when compared to the translational modes even at the high temperatures concerned. Note that for a fully ionized gas at such a high temperature that the expanded ionization energies are already insignificant compared to the translation energy then $f = 3$ and $[kT/(\gamma - 1)] = 3(kT/2)$ per particle, $k = 1.38 \times 10^{-23}$ J/K being the Boltzmann constant. As examples: for gases such as Ne in the PF pinch, the temperature may typically be high enough for it to be approaching full ionization; the specific heat ratio computes [134] to be 1.5 so that $f = 4$ and $[kT/(\gamma - 1)] = 4(\mathrm{kT}/2)$ per particle. In Kr, operating at a temperature of 10^6 K, $Z_{\mathrm{eff}} \sim 14$, $\gamma \sim 1.3$, $f \sim 6.7$ and $[kT/(\gamma - 1)] = 6.7(kT/2)$ per particle.

We divide the pinch energy by the radiation power to give us a measure of the characteristic time it would take the pinch to have its energy radiated away by that radiation power taken as constant over the whole duration. We call this the characteristic depletion time of radiation.

3.5.5.2 Characteristic Depletion Time for Bremsstrahlung

From Eqs. (3.75) and (3.72) we derive t_{brem}:

$$\begin{aligned} t_{\mathrm{brem}} &= E_{\mathrm{pinch}}/P_{\mathrm{brem}} = \left[kT^{1/2}/(C_1 n_0 f_n)\right](1 + Z_{\mathrm{eff}})/[Z_{\mathrm{eff}}^3(\gamma - 1)], \\ t_{\mathrm{brem}} &= \left(kb^{1/2}/C_1\right)\left[I/\left(n_0^{3/2} f_n^{3/2} r_{\mathrm{p}}\right)\right](1 + Z_{\mathrm{eff}})^{1/2}/[Z_{\mathrm{eff}}^3(\gamma - 1)]. \end{aligned} \tag{3.76}$$

Here we have eliminated T by using Bennett equation for a pinch in which magnetic pressure balances the kinetic pressure:

$T = b\frac{I^2}{\left(n_i r_p^2\right)(1+Z_{\text{eff}})}$, where $b = \mu/(8\pi^2 k)$ and $\mu = 4\pi \times 10^{-7}$ H/m is the permeability of free space so that $b = 1.15 \times 10^{15}$.

The pinch number density n_i is written in terms of the initial number density n_0 by writing:

$n_i = n_0 f_n$ where $f_n = (a/r_p)^2 f_{mr} f_g$, accounting not only for the area compression $(a/r_p)^2$ but also for the mass fraction swept-in f_{mr} and a geometrical factor f_g due to the elongation of the radial collapse.

To get an estimate of the size of t_{brem} we put in typical numbers for operation at pinch current higher than the Pease-Braginskii current for D into Eq. (3.75) as follows:

$I = 2.1 \times 10^6$ operated at 3 Torr D so that $n_0 = 10^{23}$, $a = 0.2$, $r_p = 3 \times 10^{-2}$ (i.e. $k_{min} = 0.15$), $f_m = 0.2$, $f_g = 1/3$, so that $f_n \sim 3$; $\gamma = 5/3$and $Z_{\text{eff}} = 1$.

For these parameters, $t_{brem} \sim 1 \times 10^{-3}$ s. This means that the magnitude of P_{brem} at a constant value is such that it would take 10^{-3} s to radiate away all the pinch thermal energy. Even to radiate away 10% would take 100 μs. The lifetime of such a PF pinch (e.g. PF1000) may typically be estimated as 0.2 μs. Thus in the lifetime of such a plasma focus, it is unlikely that the radiation would affect the dynamics. Looking at Eq. (3.75) we could possibly increase the effect of bremsstrahlung by increasing the ambient pressure within a range suitable for operation. Careful examination of a large range of numerical experiments shows no sign of radiative cooling in D in which the radiation is dominated by bremsstrahlung, although the code includes bremsstrahlung, line and recombination radiation.

3.5.5.3 Characteristic Depletion Time for Line Radiation

From Eqs. (3.75) and (3.73) we derive:

$$t_{\text{line}} = E_{\text{pinch}}/P_{\text{line}} = (k/C_2)\left[T^2/(n_0 f_n)\right](1+Z_{\text{eff}})/\left[(Z_{\text{eff}} Z_n^4(\gamma-1)\right]$$

and eliminating T:

$$t_{\text{line}} = (kb^2/C_2)I^4/\left[(n_0^3 f_n^3 r_p^4)(1+Z_{\text{eff}})Z_{\text{eff}} Z_n^4(\gamma-1)\right] \tag{3.77}$$

The above equation shows how depletion times for t_{line} for typical plasma focus operation may be computed.

3.5.5.4 Characteristic Depletion Time t_Q for PF1000

In the same way, the nett depletion time t_Q may also be computed from Eqs. (3.75) and (3.74) where t_Q is the ratio $E_{\text{pinch}}/Qdot$ where $Qdot$ or $dQ/dt = P_{\text{line}}+P_{\text{brem}} - P_J$. The latter is the time which is more applicable. In Table 3.17 we show an example of computations of depletion times in D, He, Ne, Ar, Kr and

Table 3.17 Depletion times in D, He, Ne, Ar, Kr and Xe for various conditions in PF1000

Gas	a (cm)	V_0 (kV)	P_0 (Torr)	I_{pinch} (kA)	Ab	Z_{eff}	SHR	t_Q (μs)	t_Q^* (τ_{pinch})
D	20.0	90	3.5	2125	0.80	1.0	1.67	3200	32,000
He	20.0	90	3.5	2094	0.91	2.0	1.64	88	880
Ne	5.0	14	1.0	514	0.99	8.3	1.49	0.26	2.6
Ar	11.6	23	0.5	674	0.65	11.9	1.36	0.028	0.28
Kr	11.6	23	0.3	670	0.89	14.2	1.33	0.0024	0.02
Xe	11.6	23	0.2	657	0.56	16.6	1.27	0.001	0.01

Xe for some conditions shown to be practicable PF operation in the numerical experiments. We model the PF configuration after the PF1000. For D and He, we operate at 90 kV in order to reach pinch current in excess of 2 MA. For the other gases, we operate the numerical experiments at 23 kV which is a voltage that is currently used in actual PF1000 operation.

In Table 3.17 we calculate depletion times t_Q and also t_Q^* which is t_Q expressed in units of a characteristic pinch time τ_{pinch}. We take the pinch time as proportional to anode radius [137] with a figure of 10 ns per cm (rounding τ_{pinch} to 100 ns). From Table 3.17 it may be surmised that even though the PF is operated with currents above the reduced P-B, nevertheless there would be no radiative collapse to be expected from operation in H and He. In Ne with a significant proportion of pinch energy radiated away within one τ_{pinch}, radiative cooling should be expected, leading to considerable reduction in minimum radius ratio. In Ar, Kr and Xe one would expect a strong radiative collapse. It is stressed that these numbers act only as a rough guide since the pinch system is non-static and the various properties are interacting continuously. Moreover, all the above estimates are based on radiative terms at source without consideration of plasma opacity which in those cases when the plasma is not completely transparent would reduce the energy loss from the plasma.

3.5.5.5 Characteristic Depletion Time t_Q for INTI PF

For comparison, we also calculate indicative values of the depletion times for the 2 kJ INTI PF [196] in Table 3.18.

Table 3.18 Depletion times in Ne, Ar, Kr and Xe for various conditions (*Ab* absorption correction factor at peak emission) in INTI PF

Gas	a (cm)	V_0 (kV)	P_0 (Torr)	I_{pinch} (kA)	Ab	Z_{eff}	SHR	t_Q (ns)	t_Q^* (τ_{pinch})
Ne	0.95	12	2.5	79	0.72	8	1.35	700	70
Ar	0.95	12	1.1	84	0.30	16	1.33	30	3
Kr	0.95	12	0.47	87	0.13	23	1.40	0.7	0.07
Xe	0.95	12	0.25	92	0.16	30	1.43	0.15	0.015

From Table 3.18 it may be surmised that in INTI PF at the selected attainable point of operation in Ne, with less than 2% of pinch energy radiated away within one τ_{pinch}, radiative cooling should be hardly apparent leading to at most a small reduction in minimum radius ratio. In Ar, Kr and Xe one expects a strong radiative collapse in the small INTI PF as likely as in the big PF1000.

To confirm these indicative results we next carry out numerical experiments with the code in which *Q* and *Qdot* and plasma self-absorption effect are all included with a smoothened transition from opacity-corrected volume emission to surface emission when opacity effects exceed a set limit. The code models all these effects and properties in properly coupled interactive fashion.

3.5.6 *Numerical Experiments on PF1000 and INTI PF*

3.5.6.1 *Fitting* for Model Parameters in PF1000

We have a recently measured current waveform for the PF1000 operated at 23 kV at 1.5 Torr deuterium. In order to obtain the model parameters we use the following configuration for the PF1000:

Bank parameters: L_0 = 33 nH (fitted), C_0 = 1332 μF, r_0 = 3 mΩ (fitted),
Tube parameters: b = 16 cm, a = 11.55 cm, z_0 = 60 cm,
Operating parameters: V_0 = 23 kV, P_0 = 1.5 Torr deuterium

We achieved a reasonably good fit [52] (Fig. 3.40), confirming the above bank and tube parameters and obtaining the following model parameters: f_m = 0.11, f_c = 0.7, f_{mr} = 0.26, f_{cr} = 0.68.

We then used these model parameters and the above-mentioned configuration for a series of numerical experiments. For all the gases we operated the numerical experiments at 23 kV which is a voltage that is currently used in actual PF1000 operation.

3.5.6.2 *PF* 1000 *in Deuterium and Helium—Pinch Dynamics* Showing no Sign of Radiative Cooling or Collapse

Figure 3.41a shows the total discharge current rising to a peak value of 1836 kA. The pinch current I_{pinch} at the start of pinch (time of start of pinch is shown with the right-pointing arrow) is calculated as 853 kA dropping to 796 kA at the end of the pinch (left-pointing arrow). Figure 3.41b shows the trajectories in the radial phase. The piston trajectory delineates the pinch radius after the piston meets the reflected shock (RS). For this shot, the pinch lasts for 206 ns. The code computes the radial trajectory up to this point. Figure 3.41b shows a very slow compression (radius decreases barely perceptibly), typical of an efficiently operated pinch with no

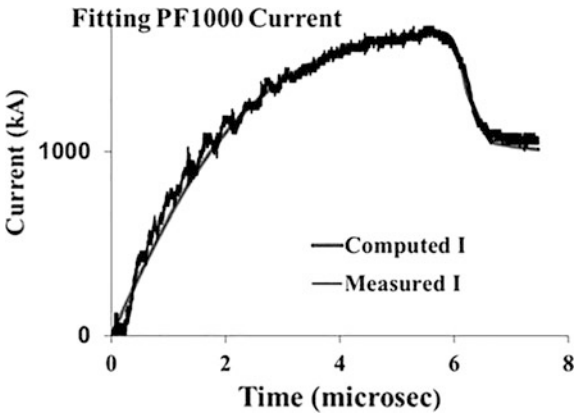

Fig. 3.40 Fitting the computed current trace to the measured current trace of PF1000 at 23 kV, 1.5 Torr deuterium. *Note* the two curves have a close fit except after the bottom of the current dip. Fitting is done only up to the bottom of the dip, so any agreement or divergence of the computed and measured traces after the bottom of the dip has no significance. Reprinted from Lee et al. [52]. Copyright (2012) with permission from IEEE

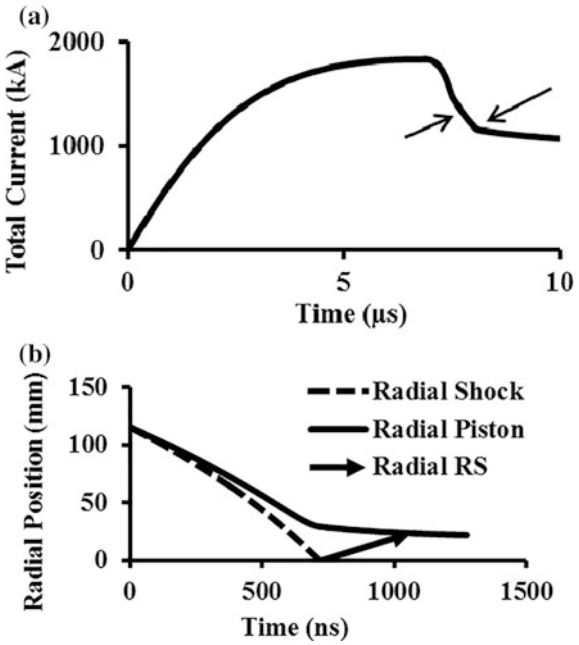

Fig. 3.41 **a** Computed total current of PF1000 at 23 kV, 3 Torr D; *right-pointing arrow* shows start of pinch and *left-pointing arrow* shows end of pinch. Reprinted from Lee et al. [52]. Copyright (2012) with permission from IEEE. **b** Radial dynamics on PF1000 plasma focus at 23 kV, 3 Torr D. Reprinted from Lee et al. [52]. Copyright (2012) with permission from IEEE

radiation compression or significant cooling. A careful study of the computed properties agrees with Table 3.15 (and Table 3.17) showing that the radiation power is too small to affect the trajectory. The minimum radius is 22.2 mm, with radius ratio $r_{min}/a = 0.19$. In an extension to this exercise we have increased the

charging voltage in this experiment to a hypothetical PF1000-like configuration of 90 kV with $a = 20$ cm, $b = 28$ cm and $P_0 = 3.5$ Torr. The pinch current is 2.1 MA. This experiment and other numerical experiments carried out earlier confirmed that despite the P-B current being far exceeded, there is no sign of radiative collapse in the D focus pinch in PF1000.

The results for He (at 23 kV 3 Torr and hypothetical 90 kV) are very similar to the case of D. The minimum radius is 20.5 mm with $r_{min}/a = 0.18$ which is a little smaller than that achieved in the very similar D discharge. This is in agreement with Table 3.15 (and Table 3.17) showing that the radiation power in He is not sufficient to severely affect the pinch compression but is larger than that of D and perhaps enough to reduce the minimum radius slightly from that of the case of D.

3.5.6.3 *PF 1000 in Neon* 23 *kV,* 1 *Torr—Pinch Dynamics* Showing Signs of Radiative Cooling and Enhanced Compression

In Ne, the effect of radiation on the radial compression of the pinch is unmistakable in both the current waveform (Fig. 3.42a) and the radial piston trajectory (Fig. 3.42b). The total discharge current shows an additional steepening in the final part of the dip (perceptible even without magnifying the relevant region) from a pinch current value of 819 kA at 9.021 μs (right-pointing arrow) to a value of 673 kA at 9.243 μs (left-pointing arrow). Detailed study of the code outputs shows

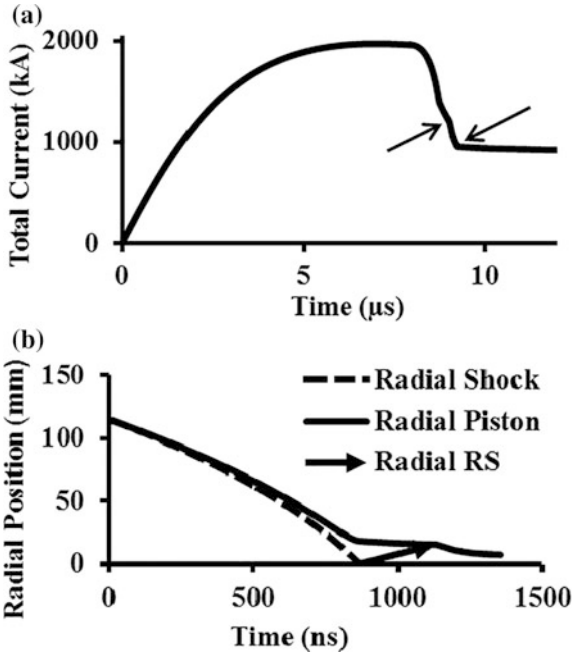

Fig. 3.42 **a** Computed total current of PF1000 at 23 kV, 1 Torr Ne. Reprinted from Lee et al. [52]. Copyright (2012) with permission from IEEE. **b** Radial dynamics of PF1000 at 23 kV, 1 Torr Ne. Reprinted from Lee et al. [52]. Copyright (2012) with permission from IEEE

that over this pinch period of 222 ns the pinch compressed from 15.8 to 7.3 mm, reaching $r_{min}/a = 0.06$. These features also correlate with emission power time profile. Undoubtedly in PF1000, strong radiative cooling is exhibited in the Ne pinch plasma leading to a substantial reduction of pinch radius.

3.5.6.4 *PF1000 in Argon, Krypton and Xenon—Pinch Dynamics Showing Strong Radiative Collapse*

At 23 kV, in argon, krypton and xenon, respectively, at 0.5, 0.3 and 0.2 Torr, the numerical experiments show current waveform, radial trajectories and net power dQ/dt or $Qdot$ emissions consistent with strong radiative collapse. For illustration, we show here the case of xenon obtained from the numerical experiments. An analysis of all the gases is summarized in Table 3.19.

The current and radial trajectories for operation in Xe are shown in Fig. 3.43a, b. Figure 3.43b shows dramatically the collapse of the radius of the column.

These traces are presented in magnified scale in Fig. 3.43c to show details of the 50 ns which includes the radiative phase up to maximum compression and a little beyond. Figure 3.43c correlates the time profiles of current I, piston position r_p and $Qdot$. Each of these is normalized (as described in the caption of Fig. 3.43c) so that the 3 traces may be presented in the one figure. At the start of the pinch, r_p is 16.1 mm at 1272 ns dropping sharply to 1.43 mm at 1274 ns and then further dropping less sharply to 0.48 mm at 1275 ns and then to a minimum radius of 0.388 mm ($r_{min}/a = 0.0034$) at 1278 ns. Over this time period, the pinch current drops from 843 to 483 kA. The value of $Qdot$ rises from 3.1×10^{12} W at the start of pinch to peak value of 6.0×10^{13} W at 1274 ns and then drops sharply as plasma self-absorption which has been rising rapidly causes the emission to transiton from volumetric emission to surface emission. The value has dropped to 4×10^{12} W at 1275 ns and further to 2×10^{11} W at 1278 ns. The value of Q at 1278 ns is 33.4 kJ (9.5%) and at end of pinch 1480 ns is 37.0 kJ (10.5%); whilst r_p

Table 3.19 Summary of numerical experiments of PF1000 radiative collapse in various gases

Gas	I_{ps} (kA)	I_{pe} (kA)	t_{min} (ns)	t_p (ns)	r_{ps} (mm)	k_{min} (r_p/a)	$-Qdot_{peak}$ (10^{11} W)	−Q (%E)	$-E_{rad}$ (%E)
D	853	789	206	206	23.8	0.192	−0.0005	−0.00002	0.000003
He	833	768	190	190	21.9	0.178	0.0008	0.00004	0.00008
Ne	819	650	222	222	15.4	0.063	0.72	2.63	2.76
Ar	820	530	130	208	14.8	0.016	7.6	6.8	9.2
Kr	848	307	20	206	16.4	0.007	116	9.0	19.9
Xe	847	168	6	209	16.1	0.003	600	10.5	22.9

Key I_{ps} current at start of pinch, I_{pe} current at end of pinch, t_{min} time to min radius, t_p time to end of pinch, r_{ps} pinch radius at start of pinch, k_{min} min radius ratio, $-Qdot_{peak}$ peak value of −dQ/dt, Q energy radiated from pinch less Joule heat energy deposited in pinch; E_{rad} energy radiated for whole pinch duration

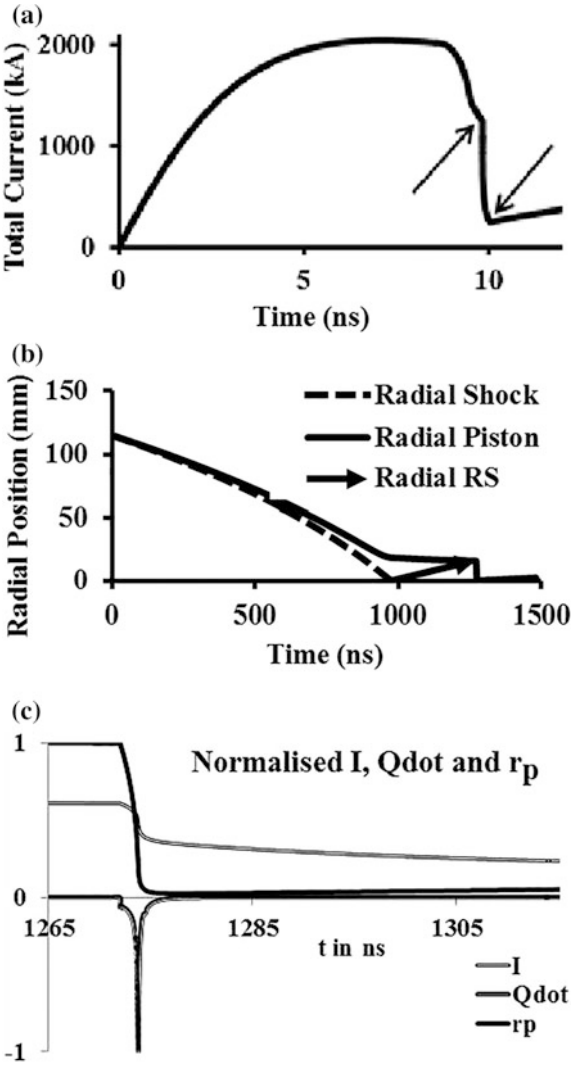

Fig. 3.43 **a** Computed total current of PF1000 at 23 kV, 0.2 Torr Xe. Copyright (2012) with permission from IEEE. **b** Radial dynamics on PF1000 at 23 kV, 0.2 Torr Xe. Reprinted from Lee et al. [52]. Copyright (2012) with permission from IEEE. **c** Time history of discharge current I, nett power emission dQ/dt ($Qdot$) and piston path (r_p): I is normalized to I_{peak} 2048 kA; $Qdot$ to peak 6×10^{13} W; r_p to piston radius at start of pinch, 16.1 mm. Start of radial phase is at 0 ns; start of pinch at 1272 ns. PF1000 at 23 kV, 0.2 Torr xenon. Reprinted from Lee et al. [52]. Copyright (2012) with permission from IEEE

has expanded to 2.6 mm (not shown in Fig. 3.37c, see Fig. 3.37b). The resistive heat liberated in the pinch over the pinch period is 43.6 kJ whilst 80.6 kJ (22.9% of E_0) of radiation is emitted from the pinch over the period of the pinch, one-third of this amount within the first 3 ns.

3.5.6.5 PF 1000 in Various Gases—Summary of Radiative Pinch Dynamics

The data [52] is summarized in Table 3.19.

In this table, the values of peak $-Qdot$, $-Q$ and $-E_{rad}$ are shown in the last three columns. Positive values in the $-Qdot$ and $-Q$ columns indicate that the radiation exceeds the Joule heating in the pinch so that the net power works in the direction of radiation cooling and collapse. The values of these two quantities for D are negative indicating that joule heating exceeds radiation. For all the other gases these terms act to radiatively cool the pinch although in the case of He the power is so small and the heat loss is such a small percentage of bank energy (also of pinch energy) that the effect is almost negligible; although the combined effect of SHR and dQ/dt in the He pinch does show a perceptible increased compression of the pinch with pinch radius ratio k_{min} of 0.178 compared to that of D of 0.192. In Ne the radiative cooling is unmistakable with k_{min} of 0.063. Argon with k_{min} of 0.016 shows a time t_{min} of 130 ns to minimum radius and then a small expansion over the rest of the pinch period. In Kr, t_{min} is only 20 ns to a k_{min} of 0.007. In Xe, t_{min} reduces further to 6 ns with k_{min} = 0.003, pinch radius of 0.35 mm; and in the rest of the pinch duration over some 203 ns the pinch expands back to almost 2 mm.

3.5.6.6 Comparison of r_{min} from Experiments and Simulation in PF1000

Estimates of minimum radius r_{min} were obtained of the PF1000 pinch from multiframe interferometric measurements of the plasma column employing the second harmonic (527 nm) of a Nd:YLF laser of less than 1 ns duration. The laser pulse was split by mirrors into fifteen separated beams which passed through a Mach-Zehnder interferometer [54, 197, 198]. The experimental results consisting of r_{min} in neon operated in a narrow range of pressures are compared with our numerical experiments of r_{min}, with and without (hypothetically) radiative losses (see Fig. 3.44).

3.5.6.7 Six Regimes of the PF Pinch Characterized by Relative Dominance of Joule Heating Power, Radiative Power and Dynamic Power Terms

As the PF is operated at different pressure, the significance of Joule heating power, radiative power and dynamic power terms relative to each other varies. To characterize the pressure ranges at which each combination of power terms dominates the following four scenarios for the total radiative power $Qdot$ may be computed:

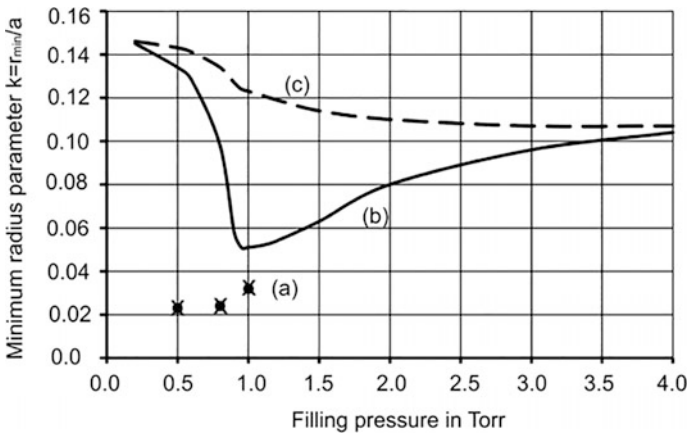

Fig. 3.44 Radius ratio r_{min}/a for Ne discharges in PF1000: **a** experimental values, **b** simulation with radiative losses, **c** simulation without radiative losses. Reprinted from Akel et al. [54]

S1: With the total radiative power *Qdot* = PJ + PRAD
S2: Without Joule heating and radiative losses *Qdot* = 0
S3: With the Joule heating effect only *Qdot* = PJ
S4: With radiative losses only *Qdot* = PRAD.

Plotting the curves corresponding to these four scenarios on the same chart, there are found to be six possible combinations distinguishable by the order of the magnitude of values calculated with the four scenarios.

1. Both PJ and PRAD significant (mod PJ > mod PRAD): order of values: S3 highest, then S1, then S2, then S4 lowest.
2. Both PJ and PRAD significant (mod PJ < mod PRAD): order of values: S3 highest, then S2, then S1, then S4 lowest.
3. Both PJ and PRAD significant (mod PJ = mod PRAD): order of values: S3 highest, then S2 = S1 (or very close together), then S4 lowest.
4. PJ significant and PRAD insignificant: order of values: S3 = S1 (or very close together) these being higher than S2 = S4 (or S2 slightly greater than S4)
5. PJ insignificant and PRAD significant: order of values: S3 = S2 (or S3 slightly greater than S2) these being higher, then S1 = S4 (or these values being very close to each other).
6. Both PJ and PRAD insignificant: order of values: S1 = S2 = S3 = S4 (all 4 values being the same.

Thus by looking at the relative positions of the 4 curves plotted from S1 to S4, not only can we obtain information about the pressures at which radiative cooling and collapse occur, but we can differentiate further the six regimes of operation across the pressure range. This is another application of the code on which work has just commenced with the publication of a paper [199].

3.5.6.8 Experiments of INTIPF Showing Radiative Collapse and High-Energy Density (HED)

We have carried out series of experiments in INTI PF in various gases to obtain information on radiative collapse from the current waveform [200]. A fitting of the computed current waveform to the measured is carried out. Once fitted, the radial trajectory of the piston is obtained giving the value of r_{min}. An example is given here [196] for comparison with the numerical experiments of the PF1000 given above in Sect. 3.5.6.4.

We use a measured current waveform for the INTI PF operated at 12 kV 0.5 Torr Kr (Shot 631). We fitted the current waveform using Lee 6-phase Radiative code:

Bank parameters: L_0 = 124 nH (fitted), C_0 = 30 μF, r_0 = 13 mΩ (fitted),
Tube parameters: b = 3.4 cm, a = 0.95 cm, z_0 = 16 cm,
Operating parameters: V_0 = 12 kV, P_0 = 0.5 Torr and gas parameters (for Kr) are 84 (molecular weight), 36 (atomic number) and 1 (for atomic gas).

Fitted model parameters: f_m = 0.0434, f_{mr} = 0.11 and $f_c = f_{cr}$ = 0.7and fitted anomalous resistance parameters are as follows (shown in Table 3.20).

The fitted waveforms are shown in Fig. 3.45. An expanded view is shown in Fig. 3.46, which also correlates the expanded current waveform with computed dynamics, fitted anomalous resistances and measured quantities including tube voltage and Faraday cup waveforms.

Having fitted the computed current trace to the measured current trace, the resulting radial trajectory indicates strong radiative collapse, as shown in Fig. 3.47.

The peak compression region is magnified and shown in Fig. 3.48. The current values are normalized by 145 kA, the P_{line} is normalized by 3.7×10^{12} W and the radius ratio $k_p = r_p/a$ is multiplied by 20 for a good display. The pinch compresses to a radius of 0.0013 cm corresponding to a radius ratio (pinch radius normalized to anode radius) of 0.0014. The radiative collapse is ended when plasma self-absorption attenuates the intense line radiation. The rebound of the pinch radius is also evident in Fig. 3.48. The line radiation leaving the plasma is correlated to the trajectory in order to show the effect of the radiation on the compression. This intense compression, despite the low mass swept in the factor of f_{mr} = 0.11 (fitted), reaches 3.7×10^{26} ions m^{-3}, which is 15 times atmospheric density (starting from less than 1/1000 of an atmospheric pressure). Moreover, the energy pumped into the pinch is 250 J whilst 41 J is radiated away in several ns, most of the radiation occurring in a tremendous burst over 50 ps at peak compression with a peak

Table 3.20 Anomalous resistance parameters of fit

	Ran1	Ran2	Ran3
R_0 (Ω)	0.20	0.10	0.08
τ_2 (ns)	80.0	100.0	280.0
τ_1 (ns)	5.0	8.0	10.0
End time	2.80	0.10	3.50

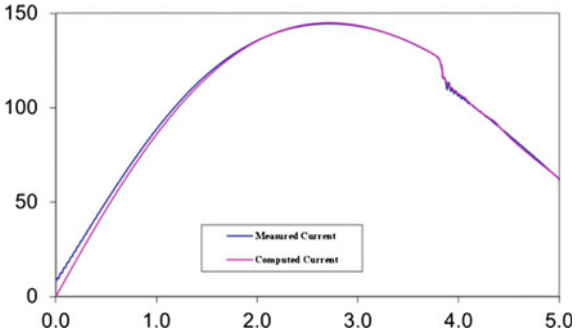

Fig. 3.45 Fitting the computed current trace to the measured current trace of INTI PF at 12 kV 0.5 Torr Kr (shot 631). *Note* the two curves have a close fit from the top of the current profile and down to the bottom of the current dip. Reprinted from Saw and Lee [200]. Copyright (2012) with permission from Springer Science+Business Media, LLC

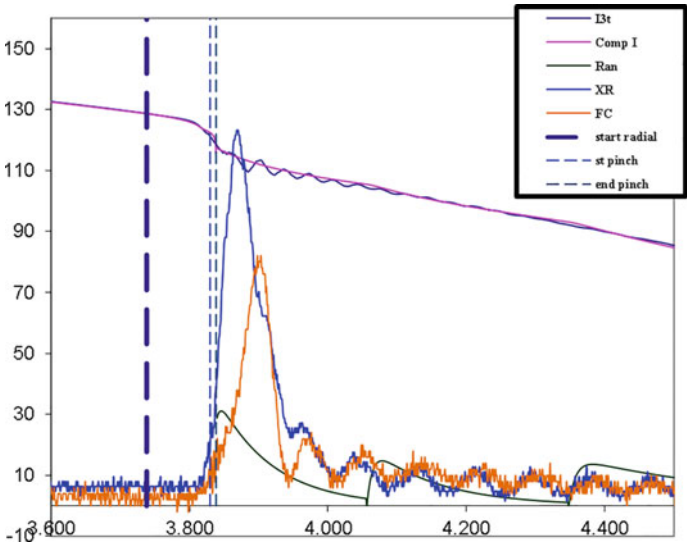

Fig. 3.46 Expanded view of the fitting, correlating the start of the radial phase (*dark vertical dashed line*) and the start and end of the pinch phase (*lighter vertical pair of lines*) with current trace and signals of XR and FC detectors and simulated anomalous resistances. Reprinted from Saw and Lee [200]. Copyright (2012) with permission from Springer Science+Business Media, LLC

radiation power of almost 4×10^{12} W. The energy density at peak compression is 4×10^{13} J m^{-3} or 40 kJ mm^{-3}. Thus even in this 2 kJ plasma focus intense HED is achieved with impressive radiation power. This radiation power is ¼ of that of PF1000 for Kr discussed in Sect. 3.5.6.4 and summarized in Table 3.19; and 1/15

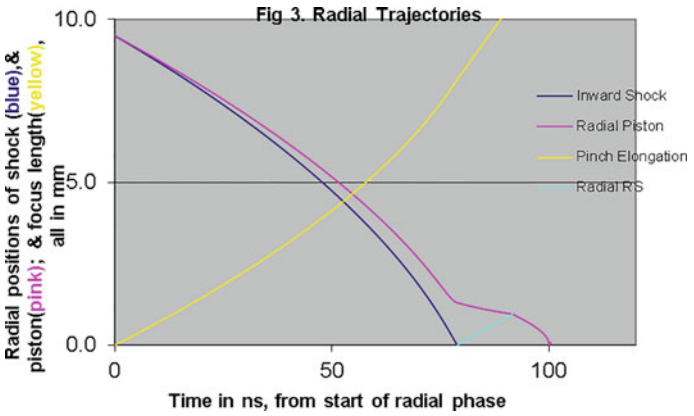

Fig. 3.47 Radial trajectory corresponding to the fitting of the current waveform of Fig. 3.45 for INTI PF 12 kV, 0.5 Torr Kr. Reprinted from Saw and Lee [200]. Copyright (2012) with permission from Springer Science+Business Media, LLC

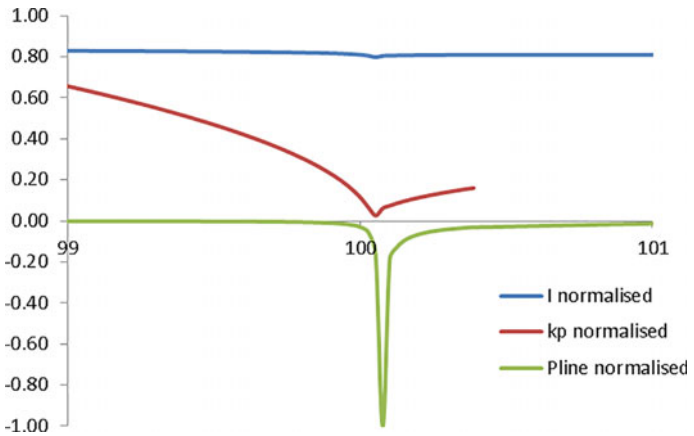

Fig. 3.48 Normalized pinch current, piston radius ratio and P_{line} at peak compression region. Reprinted from Saw and Lee [200]. Copyright (2012) with permission from Springer Science +Business Media, LLC

that of PF1000 for Xe discussed above. The outperformance in emission power of this PF storing 2 kJ compared to the PF1000 storing 350 kJ is due to the greater compression (fitted radius ratio of 0.0014) compared to the compression of PF1000 (computed radius ratio of 0.007 in Kr and 0.003 in Xe using assumed model parameters).

3.5.7 *Conclusion for Section on Radiative Collapse*

In this section, we have derived indicative values of the reduced P-B currents for various gases from D to Xe. We have also derived radiation levels from PF operations in these gases and from these we have estimated characteristic depletion times of pinch energy due to radiation less Joule heating. These depletion times indicate that D and He will have little or no radiation cooling; that Ne will show radiation cooling leading to some radiative compression for both large (PF1000) and small (INTI PF) plasma focus machines; and that Ar, Kr and Xe will have a severe radiative collapse. These results (Tables 3.15, 3.16, 3.17 and 3.18) are estimated without considering plasma opacity (plasma self-absorption). The numerical experiments, summarized in Table 3.19 include self-absorption demonstrating substantial moderating effects of self-absorption, nevertheless, confirm the indications of these tables. Some experimental results are presented. We note that the code assumes that the pinch is compressed as a column. In actual operation, break-up of the column into a line of spots have been observed particularly, but not exclusively in the heavier gases [195]. Such break-ups and indeed more detailed structures as described recently [201] will likely lead to localized enhanced compression and may tend to make it easier for the radiative collapse to occur. Moreover, the action of beams will also remove energy from the pinch [58, 59]. If beams are emitted even partially within the pinch time, this could also lead to beam-enhanced radiative collapse.

3.6 Conclusion

In this chapter, we have reviewed our experience in numerical experiments using the Lee Model code. This review describes the contributions made by this code in the past 30 years in the light of overall work on computations and simulations already carried out and documented in the area of plasma focus. The plasma focus is indeed a multi-faceted device with interesting phenomena ranging from electromagnetically driven dynamics to copious radiation including ions, electrons, X-rays, characteristic soft X-rays, fusion neutrons to fast ion beams (FIB) and fast plasma streams (FPS) to anomalous resistivity resulting from a range of plasma instabilities to plasma states of extreme high-energy density (HED) achieved in the focus pinch through radiative cooling and collapse. The Lee Model code is successful in modelling most of these multi-faceted aspects of the plasma focus. The Lee Model code developed originally as a simple code to complement the AAAPT inspired UNU ICTP PFF 3 kJ plasma focus has over the past 30 years been continuously developed. It is still a relatively simple tool. Its simplicity and sound fundamental grounding enable it to have a long and wide reach to compute gross plasma dynamics and properties, to obtain data on anomalous resistivity, to pick out fundamental scaling properties and design rules-of-thumb, recognize scaling trends

and scaling laws and develop insights into optimum inductance, current saturation, deterioration of neutron and radiation scaling in relation to energy and to understand some conditions for radiative collapse.

The physics and equations of the code are explained in detail in this chapter, as are the contributions of the code. A survey of the results of myriad simulations including MHD and kinetic methods show that the scope of the Lee Model code in the range of results and insights is unmatched. It is desirable to ask the following question. Why has such a simple model been so successful in interpreting so many aspects of plasma focus behaviour? The following may be the answer.

Its success on so many fronts is due to its use of 4 parameters (fitted to a measured current waveform) which in one sweep incorporates all the mechanisms and effects occurring in the plasma focus including mechanisms and effects difficult to compute or even as yet unrecognized. The simple premise is that the sum total effect of all these mechanisms and phenomena is represented in net result by mass field and force field distributions which in the gross sense are represented by a mass swept-up factor f_m and a effective current factor f_c in the axial phase and two corresponding factors in the radial phase, up to the end of the focus pinch.

Continuing this argument, the exact time profile of the total current trace is governed by the bank parameters, by the focus tube geometry and the operational parameters. It also depends on the fraction of mass swept-up and the fraction of sheath current and the variation of these fractions through the axial and radial phases. These parameters determine the axial and radial dynamics, specifically the axial and radial speeds which in turn affect the profile and magnitudes of the discharge current. There are many underlying mechanisms in the axial phase such as shock front and current sheet structure, porosity and inclination, boundary layer effects and current shunting and fragmenting which are not simply modelled; likewise in the radial phase mechanisms such as current sheet curvatures and necking leading to axial acceleration and ejection of mass, and plasma/current disruptions. These effects may give rise to localized regions of high density and temperatures. The detailed profile of the discharge current is influenced by these effects and during the pinch phase also reflects the Joule heating and radiative yields. At the end of the pinch phase, the total current profile also reflects the sudden transition of the current flow from a constricted pinch to a large column flow. Thus the discharge current powers all dynamic, electrodynamic, thermodynamic and radiation processes in the various phases of the plasma focus. Conversely, all the dynamic, electrodynamic, thermodynamic and radiation processes in the various phases of the plasma focus affect the discharge current.

It is then no exaggeration to say that the discharge current waveform contains information on all the dynamic, electrodynamic, thermodynamic and radiation processes that occur in the various phases of the plasma focus. The simplification of the model is that all these processes may in the gross sense be incorporated into the four model parameters f_m, f_c, f_{mr} and f_{cr} up to the end of the pinch indicated on the current waveform by the regular dip and beyond that in the extended of the current waveform by anomalous resistance functions.

This explains the importance attached to matching the computed total current trace to the measured total current trace in the procedure adopted by the Lee model code. Once matched, the fitted model parameters assure that the computation proceeds with all physical mechanisms accounted for, at least in the gross energy and mass balance sense.

Acknowledgements The authors acknowledge the contributions of students, colleagues and collaborators who have in one way or another contributed to the development of this code over the past three decade.

References

1. A. Bernard, H. Bruzzone, P. Choi, H. Chuaqui, V. Gribkov, J. Herrera, K. Hirano, A. Krejei, S. Lee, C. Luo, F. Mezzetti, M. Sadowski, H. Schmidt, K. Ware, C.S. Wong, V. Zoita, Scientific status of plasma focus research. J. Moscow Phys. Soc. **8**(2), 93–170 (1998)
2. M. Krishnan, The dense plasma focus: A versatile dense pinch for diverse applications. Plasma Sci IEEE Trans **40**(12), 3189–3221 (2012)
3. J. Tendys, Dense plasma focus-a literature review. Internal report of Australian Atomic Energy Commission Research Establishment, Lucas Heights, Australia, No. AAEC/E334 (Jan 1976). ISBN 64299696 2
4. N.V. Fillipov, T.I. Fillipova, V.P. Vinogradov, Dense high temperature plasma in a non-cylindrical Z-pinch compression. Nucl. Fusion Suppl. **2**, 577–587 (1962)
5. J.W. Mather, Investigation of the high-energy acceleration mode in the coaxial gun. Phys. Fluids Suppl. **7**(11), S28–S34 (1964)
6. S. Lee, Plasma focus model yielding trajectory and structure. in *Radiations in Plasmas*, ed. by B. Mcnamara. Proceedings of Spring College in Plasma Physics 1983, ICTP, Trieste, (World Scientific Pub Co, Singapore, 1984), pp. 978–987. ISBN 9971-966-37-9
7. S. Lee, T.Y. Tou, S.P. Moo, M.A. Eissa, A.V. Gholap, K.H. Kwek, S. Mulyodrono, A. J. Smith, S.W. Usala, M. Zakaullah, A simple facility for the teaching of plasma dynamics and plasma nuclear fusion. Am. J. Phys. **56**, 62–68 (1988). doi: http://dx.doi.org/10.1119/1.15433
8. M.S. Rafique, Compression dynamics and radiation emission from a deuterium plasma focus. PhD Thesis, NTU, Singapore (2000)
9. S. Lee, S.P. Moo, C.S. Wong, A.C. Chew, Twelve years of UNU/ICTP PFF—A review. IC/98/231, ICTP preprint (International Centre for Theoretical Physics, Trieste, Italy, 1998), 101 pages
10. S. Lee, Radiative dense plasma focus computation package: RADPF. http://www.plasmafocus.net/IPFS/modelpackage/File1RADPF.htm
11. P. Silva, J. Moreno, L. Soto, L. Birstein, R.E. Mayer, W. Kies, Neutron emission from a fast plasma focus of 400 Joules. Appl. Phys. Lett. **83**, 3269 (2003)
12. V.A. Gribkov, A. Banaszak, B. Bienkowska, A.V. Dubrovsky, I. Ivanova-Stanik, L. Jakubowski, L. Karpinski, R.A. Miklaszewski, M. Paduch, M.J. Sadowski, M. Scholz, A. Szydlowski, K. Tomaszewski, J. Phys. D **40**, 3592 (2007)
13. M. Rosenbluth, in *Magnetohydrodynamics*, ed. by R.K.M. Landshoff (Stanford University Press, 1957), p. 57
14. F.J. Fishman, H. Petscheck, Phys. Fluids **11**, 632 (1962)
15. T.D. Butler, I. Henins, F.C. Jahoda, J. Marshall, R.L. Morse, Phys. Fluids **12**, 1904 (1969)
16. K.V. Roberts, D.E. Potter, *Methods of Computational Physics* (Academic, New York, 1970)
17. A.A. Amsden, LA-3466 (1966)

18. D.E. Potter, Numerical studies of the plasma focus. Phys. Fluids **14**(9), 1911–1925 (1971). doi: 10.1063/1.1693700
19. S. Maxon, J. Eddelman, Phys. Fluids **21**, 1856 (1978)
20. S.P. Moo, C.K. Chakrabarty, S. Lee, An investigation of the ion beam of a plasma focus using a metal obstacle and deuterated target. Plasma Sci IEEE Trans **19**(3), 515–519 (1991)
21. S. Lee, Neutron yield in plasma focus: a fundamental cause. Appl. Phys. Lett. **95**(151503) (2009)
22. S.H. Saw, S. Lee, Scaling laws for plasma focus machines from numerical experiments. Energy Power Eng. **2**(1), 65–72 (2010)
23. S.V. Bazdenkov, V.V. Vikhrev, Sov. J. Plasma Phys. **1**, 250 (1975)
24. K. Behler, H. Bruhns, Three-fluid magnetohydrodynamical simulation of plasma focus discharges. Phys. Fluids **30**(12), 3767–3776 (1987)
25. V.Ya. Nukulin, S.N. Polukhin, Plasma Phys. Rep. **33**, 271–277 (2007)
26. V.V. Vikhrev, V.V. Ivanov, G.A. Rosanova, Nucl. Fusion **33**, 311 (1993)
27. F F Chen Introduction to Plasma Physics. Plenum Press, New York (1974)
28. A. Schmidt, V. Tang, D. Welch, Fully kinetic simulations of dense plasma focus Z-pinch devices. Phys. Rev. Lett. **109**(20), 205003 (2012)
29. A. Schmidt, A. Link, D. Welch, J. Ellsworth, S. Falabella, V. Tang, Comparisons of dense-plasma-focus kinetic simulations with experimental Measurements. Phys. Rev. E **89** (6), 061101 (2014)
30. A. Schmidt, A. Link, D. Welch, B.T. Meehan, V. Tang, C. Halvorson, M. May, E.C. Hagen, Fully kinetic simulations of megajoule-scale dense plasma focus. Phys. Plasmas **21**, 102703 (2014)
31. B. Allenm, C. Thomas, D. Susan, G. Richard, G. Christopher, H. Thomas, H. Thomas, H. Heath, L. David, L. Duane, L. Raymond, L. Edward, M. Christopher, N. Stewart, O. John, P. Curtis, R. Sharon, S.William, O. Guglielmo, S. Strack, T. Randall, V. Timothy, W. Weirs, M.A. Thomas, Alegra: an arbitrary Lagrangian-Eulerian multimaterial multiphysics code. in *46th AIAA Aerospace Sciences Meeting and Exhibit* (American Institute of Aeronautics And Astronautics, 2008)
32. D.R. Welch, D.V. Rose, M.E. Cuneo, R.B. Campbell, T.A. Mehlhorn, Integrated simulation of the generation and transport of proton Beams from laser-target interaction. Phys. Plasmas **13**(6), 063105 (2006)
33. C. Moreno, H. Bruzzone, J. Martínez, A. Clausse, Conceptual engineering of plasma focus thermonuclear pulsors. IEEE Trans. Plasma Sci **28**(5), 1735–1741 (2000)
34. José H. González, Alejandro Clausse, Horacio Bruzzone, Pablo C. Florido, A lumped parameter model of plasma focus. Plasma Sci. IEEE Trans. **32**(3), 1383–1391 (2004)
35. S. Lee, B.C. Tan, C.S. Wong, A.C. Chew, laser and plasma technology. in *Proceedings of First Tropical College on Applied Physics 26th Dec 1983–14th Jan 1984* (World Scientific Publishing Co., Kuala Lumpur, 1985), pp. 38–62. ISBN 9971–978-27-X
36. D. Potter, The formation of high-density z-pinches. Nucl. Fusion **18**(6), 813–823 (1978)
37. S. Lee, Plasma focus radiative model: review of the lee model code. J. Fusion Energy **33**(4), 319–335 (2014)
38. J.H. González, F.R. Brollo, A. Clausse, Modeling of the dynamic plasma pinch in plasma focus discharges based in Von Karman approximations. IEEE Trans. Plasma Sci. **37**(11), 2178–2185 (2009)
39. M. Trunk, Numerical parameter studies for the dense plasma focus. Plasma Phys. **17**(4), 237–248 (1975)
40. F. Chen, in *An Indispensable Truth—How Fusion Power Can Save the Planet* (Springer, New York, 2011). doi:10.1007/978-1-4419-7820-2
41. S. Lee, S.H. Saw, Nuclear fusion energy-mankind's giant step forward. J. Fusion Energy **30** (5), 398–403. doi: 10.1007/s10894-011-9390-7
42. V.S. Imshennik, N.V. Fillipov, T.I. Fillipova, Similarity theory and Increased neutron yield in a plasma focus. Nucl. Fusion **13**(6), 929–934 (1973)

43. V. Vikhrev, V.D. Korolev, Neutron generation from Z-pinches. Plasma Phys. Rep. **33**(5), 356–380 (2007) (Pleiades Publ., Ltd)
44. S. Lee, Current and neutron scaling for megajoule plasma focus machines. Plasma Phys. Controlled Fusion **50**(10), 105005 (2008)
45. E.J. Lerner, S. Krupakar Murali, A. Haboub, Theory and experimental program for the p-B11 fusion with the dense plasma focus. J Fusion Energ **30**, 367–376 (2011). doi:10.1007/s10894-011-9385-4
46. http://lppfusion.com/focus-fusion-1-works/
47. S.K.H. Auluck, Dense plasma focus: a question in search of answers, a technology in search of applications. Plasma Sci. Appl Int. J. Mod. Phys. Conf. Ser. **32**, 1460315 (11 pages) (2014). doi:10.1142/S2010194514603159 (ICPSA 2013)
48. S.K.H. Auluck, Phys. Plasmas **20**, 112501 (2013)
49. S. Lee, S.H. Saw, Pinch current limitation effect in plasma focus. Appl. Phys. Lett. **92**(2), 021503 (2008)
50. S. Lee, S.H. Saw, J. Ali, Numerical experiments on radiative cooling and collapse in plasma focus operated in krypton. J. Fusion Energy **32**(1), 42–49 (2012)
51. M. Akel, S. Lee, Radiative collapse in plasma focus operated with heavy noble gases. J. Fusion Energy **32**, 111–116 (2013). doi:10.1007/s10894-012-9535-3
52. S. Lee, S.H. Saw, M. Akel, H.-J. Kunze, P. Kubes, M. Paduch, Conditions for radiative cooling and collapse in plasma focus illustrated with numerical experiments on the PF1000. IEEE Trans. Plasma Sci. **44**(2), 165–173 (2016). doi:10.1109/TPS.2015.2497269
53. D. Piriaei, T.D. Mahabadi, S. Javadi, M. Ghoranneviss, S.H. Saw, S. Lee, The investigation of pinch regimes in a Mather type dense plasma focus device and their effects on hard X-ray emission. Phys. Plasmas **22**, 123507 (2015). doi:10.1063/1.4936801
54. M. Akel, J. Cikhardt, P. Kubes, H.J. Kunze, S. Lee, M. Paduch, S.H. Saw, Experiments and simulations on the possibility of radiative contraction/collapse in the plasma focus PF-1000-. Nukleonika **61**(2), 145–148 (2016). doi:10.1515/nuka-2016-0025
55. S. Lee, S.H. Saw, R.S. Rawat, P. Lee, A. Talebitaher, A.E. Abdou, P.L. Chong, F. Roy, A. Singh, D. Wong, K. Devi, Correlation of soft X-ray pulses with modeled dynamics of the plasma focus. IEEE Trans. Plasma Sci. **39**(11), 3196–3202 (2011)
56. S.H. Saw, R.S. Rawat, P. Lee, A. Talebitaher, A.E. Abdou, P.L. Chong, F. Roy, J. Ali, S. Lee, SXR measurements in INTI PF operated in neon to identify typical (normal N) profile for shots with good yield. IEEE Trans. Plasma Sci. **41**(11), 3166–3172 (2013)
57. S.H. Saw, P.C.K. Lee, R.S. Rawat, P. Lee, Optimizing UNU/ICTP PFF plasma focus for neon soft X-ray operation. IEEE Trans. Plasma Sci. **37**(7), 1276–1282 (2009)
58. S. Lee, S.H. Saw, Plasma focus ion beam fluence and flux—scaling with Stored Energy. Phys. Plasmas **19**(11), 2703 (2012)
59. S. Lee, S.H. Saw, Plasma focus ion beam fluence and flux—for various gases. Phys. Plasmas **20**(062702) (2013)
60. M. Akel, S. Alsheikh Salo, Sh Ismael, S.H. Saw, S. Lee, Deuterium plasma focus as a tool for testing materials of plasma facing walls in thermonuclear fusion reactors. J. Fusion Energy **35**(4), 694–701 (2016). doi:10.1007/s10894-016-0092-z
61. S.H. Saw, V. Damideh, P. Lee, R.S. Rawat, S. Lee, A 160 kJ dual plasma focus (Dupf) for fusion-relevant materials testing and nano-materials fabrication, plasma science and applications (ICPSA 2013). Int. J. Mod. Phys. Conf. Ser. **32**, 1460322 (10 pages) (2014). doi:10.1142/S2010194514603226
62. S.H. Saw, V. Damideh, P.C.K. Lee, R.S. Rawat, S. Lee, Comparative study of fast and slow focus modes in INTI plasma focus for deuterium, neon and argon operation. (submitted for publication)
63. S. Lee, S.H. Saw, The slow focus mode in plasma focus for fast plasma stream nano-materials fabrication: selection of energy of bombarding particles by pressure control. J. Sci. Eng. Technol. **10**(11), 17–23 (2014)
64. S. Lee, C.S. Wong, Initiating and strengthening plasma research in developing countries. Phys. Today (USA), pp. 31–36 (May 2006)

65. S. Lee, Plasma focus experiment. published *in Laser and Plasma Technology. Part I, Experiment II*, ed. by S. Lee, B.C. Tan, C.S. Wong, A.C. Chew. Proceedings of First Tropical College on Applied Physics 26th Dec 1983–14th Jan 1984, Kuala Lumpur (World Scientific Publishing Co., Singapore, 1985), pp. 37–62. ISBN 9971-978-27-X (680 pages)
66. T.Y. Tou, S. Lee, K.H. Kwek, Non-perturbing plasma focus measurements in the run down phase. IEEE Trans. Plasma Sci. **17**, 311–315 (1989)
67. T.Y. Tou, Pinch radius ratio of the plasma focus. PhD thesis. UM, Malaysia (1987)
68. K.H. Kwek. Pinch structure of a plasma focus. PhD thesis, UM, Malaysia (1989)
69. J.B. Ali, Development and studies of a small plasma focus. PhD thesis, UTM, Malaysia (1990)
70. A. Serban, Anode geometry and focus characteristics. PhD thesis, NTU, Singapore (1995)
71. A. Serban, S. Lee, The effect of high axial sheath velocity on neutron yield in plasma focus. Fusion Technol. **35**, 54–61 (1999)
72. A. Serban, S. Lee, Experiments on Speed-enhanced neutron yield from a small plasma focus. J. Plasma Phys. **60**(1), 3–15 (1998)
73. M.H. Liu, X.P. Feng, S.V. Springham, S. Lee, Soft X-ray yield Measurement in a small plasma focus operated in neon. IEEE Trans. Plasma Sci. **26**, 135 (1998)
74. S. Lee, P. Lee, G. Zhang, X. Feng, V.A. Gribkov, M. Liu, A. Serban, T. Wong, High rep rate, high performance plasma focus as a powerful radiation source. IEEE Trans. Plasma Sci. **26**, 1119 (1998)
75. M.H. Liu, Soft X-rays from compact plasma focus. PhD thesis, NTU, Singapore (1997)
76. F. Roy Jr., Investigation and optimisation of neon soft X-ray of the INTI plasma focus at 12 kV. PhD thesis, INTI International University, Malaysia (2015)
77. A. Singh, Comparative study of plasma focus machines. PhD thesis, INTI International University, Malaysia (2015)
78. G.X. Zhang. Plasma soft x-ray source for microelectronic lithography. PhD thesis. NTU, Singapore (1999)
79. B. Shan, Comparative study: dynamics and SXR emission of several plasma focus devices. PhD thesis, NTU, Singapore (2000)
80. Alin Constantin Pătran, Electron and medium energy X-ray emission from a dense plasma focus. PhD thesis, NTU, Singapore (2002)
81. V. Damideh, A comparative study of fast focus mode and slow focus mode in plasma focus devices. PhD thesis, INTI International University, Malaysia (2016)
82. S. Lee in http://ckplee.home.nie.edu.sg/plasmaphysics/ (archival website) (2013)
83. D. Wong, P. Lee, T. Zhang, A. Patran, T.L. Tan, R.S. Rawat, S. Lee, An improved radiative plasma focus model calibrated for neon-filled NX2 using a tapered anode. Plasma Sour. Sci. Tech. **16**, 116 (2007)
84. J.M. Koh, R.S. Rawat, A. Patran, T. Zhang, D. Wong, S.V. Springham, T.L. Tan, S. Lee, P. Lee, Optimization of the high pressure operation regime for enhanced neutron yield in a plasma focus device. Plasma Sour. Sci. Technol. **14**, 12 (2005)
85. V. Siahpoush, M.A. Tafreshi, S. Sobhanian, S. Khorram, Plasma Phys. Controlled Fusion **47**, 1065 (2005)
86. T. Zhang, R.S. Rawat, S.V. Springham, V.A. Gribkov, T.L. Tan, J. Lin, S.M. Hassan, S. Mahmood, P. Lee, S. Lee, Drive parameter as a design consideration for mather and filippov types of plasma focus. IEEE Trans. Plasma Sci. (USA) **34**, 2356 (2006)
87. M. Akel, S. Hawat, S. Lee, Numerical experiments on Soft X-ray emission optimization of nitrogen plasma in 3 kJ plasma focus SY-1 using modified Lee model. J Fusion Energy **28**, 355 (2009). doi: 10.1007/s10894-009-9203-4
88. M. Akel, S. Lee, Practical optimization of AECS PF-2 plasma focus device for argon soft X-ray operation. J. Fusion Energy **31**, 122–129 (2012)
89. A.E. Abdou, M.I. Ismail, A.E. Mohamed, S. Lee, S.H. Saw, R. Vermam, Preliminary results of Kansas State University dense plasma focus. IEEE Trans. Plasma Sci. **40**(10), 2741–2744 (2012). doi:10.1109/TPS.2012.2209682

90. L. Soto, P. Silva, J. Moreno, G. Silvester, M. Zambra, C. Pavez, L. Altamirano, H. Bruzzone, M. Barbaglia, Y. Sidelnikov, W. Kies, Brazilian J. Phys. **34**, 1814 (2004)
91. H. Acuna, F. Castillo, J. Herrera, A. Postal, Int. Conf. Plasma Sci. p. 127 (1996)
92. C. Moreno, V. Raspa, L. Sigaut, R. Vieytes, Appl. Phys. Lett. **89** (2006)
93. S. Lee, A sequential plasma focus. IEEE Trans. Plasma Sci. USA **19**, 912–919 (1991)
94. S.H. Saw, M. Akel, P.C.K. Lee, S.T. Ong, S.N. Mohamad, F.D. Ismail, N.D. Nawi, K. Devi, R.M. Sabri, A.H. Bajian, J. Ali, S. Lee, Magnetic probe measurements in INTI plasma focus to determine dependence of axial speed with pressure in neon. J. Fusion Energy **31**, 411–417 (2012). doi:10.1007/s10894-011-9487-z
95. L.H. Lim, S.L. Yap, L.K. Lim, M.C. Lee, H.S. Poh, S.S. Yap, S. Lee comparison of measured and computed radial trajectories of plasma focus devices. Phys. Plasmas **22**, 092702 (2015). doi:10.1063/1.4929856
96. S. Lee, R.S. Rawat, P. Lee, S.H. Saw, Soft X-ray yield from NX2 plasma focus. J. Appl. Phys. **106**, 023309 (2009)
97. M. Akel, Sh. Al-Hawat, S.H. Saw, S. Lee, Numerical experiments on oxygen Soft X-ray emissions from low energy plasma focus using lee model. J. Fusion Energy **29**:223–231 (2010). doi:10.1007/s10894-009-9262
98. M. Akel, S. Lee, S.H. Saw, Numerical experiments in plasma focus operated in various gases. IEEE Trans. Plasma Sci. **40**(12), 3290–3297 (2012). doi:10.1109/tps.2012.2220863
99. M. Akel, Sh Al-Hawat, S. Lee, Neon soft X-ray yield optimization from PF-SY1 plasma focus device. J. Fusion Energy **30**, 39–47 (2011). doi:10.1007/s10894-010-9338-3
100. S. Lee, S.H. Saw, Neutron scaling laws from numerical experiments. J. Fusion Energy **27**, 292–295 (2008)
101. S. Lee, S.H. Saw, L. Soto, S.V. Springham, S.P. Moo, Numerical experiments on plasma focus neutron yield versus pressure compared with laboratory experiments. Plasma Phys. Control. Fusion **51**, 075006 (11 pp) (2009)
102. S. Lee, P. Lee, S.H. Saw, R.S. Rawat, Numerical experiments on plasma focus pinch current limitation. Plasma Phys. Control. Fusion **50**, 065012 (2008)
103. M. Akel, Sh Al-Hawat, S. Lee, Pinch current and soft X-ray yield limitation by numerical experiments on nitrogen plasma focus. J. Fusion Energy **29**, 94–99 (2010)
104. M. Akel, S. Hawat, S. Lee, Pinch current and soft X-ray yield limitation by numerical experiments on nitrogen plasma focus. J. Fusion Energ, **29**, 94–99 (2010)
105. S. Lee, S.H. Saw, Current-step technique to enhance plasma focus compression and neutron yield. J. Fusion Energy **31**, 603–610 (2012). doi:10.1007/s10894-012-9506-8
106. S. Lee, S.H. Saw, P.C.K. Lee, R.S. Rawat, H. Schmidt, Computing plasma focus pinch current from total current measurement. Appl. Phys. Lett. **92**, 111501 (2008)
107. S.H. Saw, S. Lee, F. Roy, P.L. Chong, V. Vengadeswaran, A.S.M. Sidik, Y.W. Leong, A. Singh, In-situ determination of the static inductance and resistance of a plasma focus capacitor bank. Rev. Sci. Instrum. **81**, 053505 (2010)
108. S. Lee, S.H. Saw, R.S. Rawat, P. Lee, R. Verma, A. Talebitaher, S.M. Hassan, A.E. Abdou, M. Ismail, A. Mohamed, H. Torreblanca, Sh. Al Hawat, M. Akel, P.L. Chong, F. Roy, A. Singh, D. Wong, K.K. Devi, Measurement and processing of fast pulsed discharge current in plasma focus machines. J. Fusion Energy **31**, 198–204 (2012)
109. S. Lee, S.H. Saw, P.C.K. Lee, R.S. Rawat, K. Devi, Magnetic Reynolds number and neon current sheet structure in the axial phase of a plasma focus. J Fusion Energy **32**, 50–55 (2013). doi:10.1007/s10894-012-9521-9
110. S. Lee, S.H. Saw, A.E. Abdou, H. Torreblanca, Characterizing plasma focus devices—role of the static inductance—instability phase fitted by anomalous resistances. J. Fusion Energy **30**, 277–282 (2011). doi:10.1007/s10894-010-9372-1
111. R.A. Behbahani, F.M. Aghamir, J. Appl. Phys. **111**(4), 043304, 043304–5 (2012)
112. R.A. Behbahani, F.M. Aghamir, Phys. Plasmas **18**, 103302 (2011). doi:10.1063/1.3647958
113. M. Akel, S. Alsheikh Salo, Sh. Ismael, S.H. Saw, S. Lee, Interaction of the high energy deuterons with the graphite target in the plasma focus devices based on Lee model. Phys. Plasmas **21**, 072507 (2014)

114. S. Lee, S.H. Saw, in *"Fusion Energy" Numerical Experiments Providing New Insights into Plasma Focus Fusion Devices—Special Edition on "Fusion Energy" Energies*, vol. 3, pp. 711–737. doi:10.3390/en3040711-Published (12 Apr 2010)
115. S.H. Saw, S. Lee, Scaling the plasma focus for fusion energy considerations. Int. J. Energy Res. **35**, 81–88 (2011). doi:10.1002/er.1758S
116. S. Lee, S.H. Saw, The plasma focus- trending into the future. Int. J. Energy Res. **36**, 1366–1374 (2012). doi:10.1002/er.1918
117. S. Lee, S.H. Saw, P. Lee, R.S. Rawat, Numerical experiments on neon plasma focus soft X-rays scaling. Plasma Phys. Controlled Fusion **51**, 105013 (8 pp) (2009)
118. S.H. Saw, S. Lee, Multi-scaling of the dense plasma focus. J. Phys. Conf. Ser. **591**, 012022 (2015). doi:10.1088/1742-6596/591/1/012022
119. M. Akel, S. Lee, Dependence of plasma focus argon soft X-ray yield on storage energy, total and pinch currents. J. Fusion Energy **31**, 143–150 (2012)
120. M. Akel, S. Lee, Scaling laws of nitrogen soft X-ray yields from 1–200 kJ plasma focus. J Fusion Energy **32**, 107–110 (2013). doi: 10.1007/s10894-012-9537-1
121. S.H. Saw, S. Lee, The plasma focus scaled for neutrons, soft X-rays, fast ion beams and fast plasma streams. J. Sci. Eng. Technol. **10**(11), 42–49 (2014)
122. A. Singh, S. Lee, S.H. Saw, Numerical experiments to obtain the scaling laws for neutron yield on mather-type plasma focus machines below 500 Joules. J. Sci. Eng. Technol. **10**(11), 35–41 (2014)
123. F. Karami, M.V. Roshan, M. Habibi, P. Lee, S.H. Saw, s Lee, Neutron yield scaling with inductance in plasma focus. IEEE Trans. Plasma Sci. **43**(7), 2155–2159 (2015). doi:10.1109/TPS.2015
124. S.T, Ong, K. Chaudhary, J. Ali, S. Lee, Numerical experiments on neutron yield and soft X-ray study of a ~100 kJ plasma focus using the current profile fitting technique. Plasma Phys. Controlled Fusion **56**, 075001 (6 pp) (2014). doi:10.1088/0741-3335/56/7/075001
125. S.H. Saw, D. Subedi, R. Khanal, R. Shrestha, S. Dugu, S. Lee, Numerical experiments on pf1000 neutron yield. J. Fusion Energy **33**, 684–688 (2014). doi:10.1007/s10894-014-9731-4
126. A. Singh, S. Lee, S.H. Saw, Numerical experimentation on focusing time and neutron yield in GN1 plasma focus machine, plasma science and applications (ICPSA 2013). Int. J. Mod. Phys. Conf. Ser. **32**, 1460325 (6 pages) (2014). doi:10.1142/S2010194514603251
127. S.H. Saw, P. Lee, R.S. Rawat, R. Verma, D. Subedi, R. Khanal, P. Gautam, R. Shrestha, A. Singh, S. Lee, Comparison of measured neutron yield versus pressure curves for FMPF-3, NX2 and NX3 plasma focus machines against computed results using the lee model code. J. Fusion Energy **34**, 474–479 (2015). doi:10.1007/s10894-014-9824-0
128. L.K. Lim, S.L. Yap, L.H. Lim, Y.S. Neoh, M.Z. Khan, S.K. Ngoi, S.S. Yap, S. Lee, Parametric optimisation of plasma focus devices for neutron production. J. Fusion Energy **35**, 274–280 (2016). doi: 10.1007/s10894-015-0014-5
129. P. Gautam, R. Khanal, S.H. Saw, S. Lee, Comparison of measured Soft X-ray yield versus pressure for NX1 and NX2 plasma focus devices against computed values using lee model code. J. Fusion Energy **34**, 686–693 (2015). doi:10.1007/s10894-015-9872-0
130. S. Lee, Developing a plasma focus research training system for the fusion energy age, plasma science and applications (ICPSA 2013). Int. J. Mod. Phys. Conf. Ser. **32**, 1460313 (12 pages) (2014). doi:10.1142/S2010194514603135
131. S.P. Chow, S. Lee, B.C. Tan, Current sheath studies in a coaxial plasma focus gun. J. Plasma Phys. UK **8**, 21–31 (1972)
132. Sh Al-Hawat, M. Akel, S.H. Saw, S. Lee, Model parameters vs gas pressure in two different plasma focus devices operated in Argon and Neon. J. Fusion Energy **31**, 13–20 (2012). doi:10.1007/s10894-011-9414-3-3

133. S. Lee, S.H. Saw, H. Hegazy, J. Ali, V. Damideh, N. Fatis, H. Kariri, A. Khubrani, A. Mahasi, Some generalised characteristics of the electro-dynamics of the plasma focus in its axial phase-illustrated by an application to independently determine the drive current fraction and the mass swept-up fraction. J. Fusion Energy **33**, 235–241 (2014). doi:10.1007/s10894-013-9658-1
134. S. Lee, Radius ratio of argon pinches. Australian. J. Phys. **36**, 891–895 (1983)
135. V.N. Pimenov, A.V. Dubrovsky, E.V. Demina, V.A. Gribkov, S.V. Latyshev, S.A. Maslyaev, I.P. Sasinovskaya, M. Scholz, Innovative powerful pulsed technique, based on a plasma accelerator, for simulation of radiation damage and testing of materials for nuclear systems (IAEA). Published in http://www-pub.iaea.org/MTCD/publications/PDF/P1433_CD/datasets/papers/at_p5-04.pdf (2013)
136. P.L. Chong, S. Lee, S.H. Saw, Estimating ratio of peak to uniform values of various profiles of relevance to plasma focus pinch columns. J. Eng. Sci. Tech. **8**(1), 27–33 (2013)
137. S. Lee, A. Serban, Dimensions and lifetime of plasma focus pinch. IEEE Trans. Plasma Sci. **24**, 1101–1105 (1996). doi: 10.1109/27.533118
138. R.A. Gross, Rev. Mod. Phys. **37**, 724–743 (1965)
139. S. Lee, Transverse ionizing shock waves in a planar electromagnetic shock tube, PhD thesis, ANU, Australia (1970)
140. www.plasmafocus.net/IPFS/modelpackage/Corona%20Calculations/c1coronaintroduction.htm
141. L. Spitzer, in *Physics of Fully Ionised Gases, Interscience Tracts on Physics and Astronomy*, 2nd rev. edn. (Interscience Publication, New York, 1965)
142. J.W. Shearer, Phys. Fluids **19**, 1426 (1976). doi:10.1063/1.861627
143. R. Pease, Procs. Phys. Soc. **70**, 11 (1957)
144. S. Braginskii, Zh. Eksp. Teor. Fiz. **33**, 645 (1957)
145. K. Koshelev, N. Pereira, J. Appl. Phys. **69**, 21–44 (1991)
146. A.E. Robson, Phys. Fluid **B3**, 1481 (1991)
147. N.A.D. Khattak, anomalous heating (LHDI). http://www.plasmafocus.net/IPFS/modelpackage/File3Appendix.pdf (2011)
148. J.D. Huba (2006) Plasma formulary, pg 44. http://wwwppd.nrl.navy.mil/nrlformulary/NRL_FORMULARY_07.pdf
149. S.V. Springham, S. Lee, M.S. Rafique, Correlated deuteron energy spectra and neutron yield for a 3 kJ plasma focus. Plasma Phys. Controlled Fusion **42**(10), 1023
150. W. Kies, in *Laser and Plasma Technology*, ed. by S. Lee, B.C. Tan, C.S. Wong, A.C. Chew, K.S. Low, H. Ahmad, Y.H. Chen, Proceedings of Second Tropical College (World Scientific, Singapore, 1988), pp. 86–137. ISBN 9971-50-767-6
151. H. Herold, in *Laser and Plasma Technology*, ed. by C.S. Wong, S. Lee, B.C. Tan, A.C. Chew, K.S. Low, S.P. Moo, Proceedings of Third Tropical College (World Scientific, Singapore, 1990), pp. 21–45. ISBN 981-02-0168-0
152. S. Lee, S.H. Saw, *Course on Plasma Focus Numerical Experiments Manual*, 200 p. Joint ICTP-IAEA workshop on dense magnetized plasmas and plasma diagnostics, 15–26 Nov 2010, Trieste, Italy—Course on plasma focus numerical experiments manual, 200 p. http://indico.ictp.it/event/a09172/session/46/contribution/28/material/1/0.pdf
153. A. Patran, R.S. Rawat, J.M. Koh, S.V. Springham, T.L. Tan, P. Lee, S. Lee, A high flux pulsed neutron source using dense plasma focus. in 31st EPS Conference on Plasma Physics, London, 2004 ECA, vol. 28G, P-4.213 (2004)
154. R. Verma, M.V. Roshan, F. Malik, P. Lee, S. Lee, S.V. Springham, T.L. Tan, M. Krishnan, R.S. Rawat, Compact sub-kilojoule range fast miniature plasma focus as portable neutron source. Plasma Sour. Sci. Technol. **17**(4), 045020 (2008)
155. V. Rishi, R.S. Rawat, P. Lee, S. Lee, S.V. Springham, T.L. Tan, M. Krishnan, Effect of cathode structure on neutron yield performance of a miniature plasma focus device. Phys. Lett. A **373**, 2568–2571 (2009)
156. M. Favre, S. Lee, S.P. Moo, C.S. Wong, X-ray emission in a small plasma focus operating with H_2–Ar mixtures. Plasma Sour. Sci. Technol. **1**(2), 122 (1992)

157. S.L. Yap, S.H. Lee, L.K. Lim, C.S. Wong, in *Proceedings International Workshop on Plasma Computations and Applications (IWPCA2008)*, ed. by S.H. Saw et al. (INTI Publishing House Sdn Bhd, Malaysia, 2008), pp 51–54. 14–15 July 2008. ISSN 165-0284
158. L. Soto, New trends and future perspectives on plasma focus research. Plasma Phys. Control. Fusion **47**, A361–A381 (2005). doi:10.1088/0741-3335/47/5A/027
159. S. Lee, S.H. Saw, The plasma focus-scaling properties to scaling laws. Joint ICTP-IAEA workshop on dense magnetized plasmas and plasma diagnostics, 15–26 Nov 2010, Trieste, Italy-invited lecture. The plasma focus-scaling properties to scaling laws. http://www.plasmafocus.net/IPFS/2010%20Papers/2168-1%20lee%20scaling%20prop%20to%20scaling%20laws.pdf
160. V.A. Gribkov, M.V. Chernyshova, A. Cicuttin, M.L. Crespo, R.A. Miklaszewski, M. Scholz, A.E. Shapiro, K. Tomaszewsk, C. Tuniz, Dense plasma focus "bora" operational at The Abdus Salam International Centre for Theoretical physics and experiments provided with the device. http://mlab.ictp.it/uploads/C1/cK/C1cKba2XDKJNeoN26x5GmA/Dense-Plasma-Focus-BoraICTP.pdf
161. V.V. Maslov, V.G. Rumyantsev, V.F. Basmanov, D.V. Budnikov, A.V. Garin, I.Yu. Drozdov, D.A. Ershov, D.S. Korkin, N.G. Makeev, D.A. Molodtsev, N.I. Moskvin, S.T. Nazarenko, O.N. Petrushin, A.P. Falin, V.A. Yukhnevich, A KPU_200 movable capacitor installation. instruments and experimental techniques, vol. 57, No. 2, pp. 131–134 (© Pleiades Publishing, Ltd., 2014. Original Russian text published in Pribory i Tekhnika Eksperimenta, 2014, No. 2, pp. 43–47)
162. N.V. Zavyalov, V.V. Maslov, V.G. Rumyantsev, I.Yu. Drozdov, D.A. Ershov, D.S. Korkin, D.A. Molodtsev, V.I. Smerdov, A.P. Falin, A.A. Yukhimchuk, A source with a 10^{13} DT neutron yield on the basis of a spherical plasma focus chamber plasma physics reports, vol. 39, No. 3, pp. 243–247 (2013) (© Pleiades Publishing, Ltd., 2013. Original Russian Text, published in Fizika Plazmy, 2013, vol. 39, No. 3, pp. 276–280)
163. S.H. Saw. Plasma focus numerical experiments and BORA—2370-6 school and training course on dense magnetized plasma as a source of ionizing radiations, their diagnostics and applications, Abdus Salam International Centre for theoretical physics, 8–12 Oct 2012. http://indico.ictp.it/event/a11188/session/24/contribution/15/material/0/
164. M.A. Abd Al-Halim, Simulation of plasma focus devices with hemisphere electrodes. J. Fusion Energy **29**, 134–140 (2009). doi: 10.1007/s10894-009-9245–9247
165. Y. Ay, M.A. Abd Al-Halim, M.A. Bourham, MHD simulation for neutron yield, radiations and beam-ion properties in the spherical plasma focus. J. Fusion Energy **35**, 407–414 (2016) doi: 10.1007/s10894-015-0046-x
166. S. Lee, A current-stepping technique to enhance pinch compression. J. Phys. D Appl. Phys. **17**, 733–739 (1984) https://doi.org/10.1088/0022-3727/17/4/012
167. S.H. Saw, C.S. Wong, S. Lee, The design, construction and performance studies of a Z-pinch for current-stepping experiments. in Proceedings of symposium on small scale laboratory plasma experiments, spring college on plasma physics, small plasma physics experiments (World Scientific, 1988), pp. 116–128
168. S.S. Heoh, experimental studies of a current-stepped Z-pinch. PhD thesis, University of Malaya (1990)
169. S. Lee, S.H. Saw, P.C.K. Lee, M. Akel, V. Damideh, N.A.D. Khattak, R. Mongkolnavin, B. Paosawatyanyong, A model code for the radiative theta pinch. Phys. Plasmas **21**, 072501 (2014). doi:10.1063/1.4886359
170. D.C. Gates, in *1978 Proceedings of the 2nd International Conference on Energy Storage, Compression and Switching, Venice*, vol. 2 (Plenum Press, New York, 1983) p. 3239
171. N.V. Filippov, T.I. Filippova, I.V. Khutoretskaia, V.V. Mialton, V.P. Vinogradov, Megajoule scale plasma focus as efficient X-ray source. Phys. Lett. A **211**(3), 168–171 (1996)
172. http://cra.iaea.org/crp/project/ProjectDetail?projectId=1754

173. L. Soto, C. Pavez, J. Moreno, J. Moreno, M.J. Inestrosa-Izurieta, F. Veloso, G. Gutierrez, J. Vergara, A. Clausse, H. Bruzzone, F. Castillo, L.F. Delgado-Aparicio, Phys. Plasmas **21**, 122703 (2014)
174. V. Gribkov, M.S. Ladygina, E. Skladnik-Sadowska, D.R. Zaloga, K. Malinowski, M. J. Sadowski, M. Kubkowska, E. Kowalska-Strzeciwilk, M. Paduch, E. Zielinska, R. Miklaszewski, Study of tungsten surface interaction with plasma streams at DPF-1000U. Plasma Phys. Control Fusion **57**(6) (2015) doi:10.1088/0741-3335/57/6/065010
175. A. Cicuttin, M.L. Crespo, V.A. Gribkov, J. Niemela, C.Tuniz, C. Zanolli, M. Chernyshova, E.V. Demina, S.V. Latyshev, V.N. Pimenov, A.A. Talab, Nuclear Fusion **55**(6), 063037 (2015). doi:10.1088/0029-5515/55/6/063037
176. M.J. Inestrosa-Izurieta, E. Ramos-Moore, L. Soto, Morphological and structural effects on tungsten targets produced by fusion plasma pulses from a table top plasma focus. Nucl. Fusion **55**, 093011 (8 pp) (2015). doi:10.1088/0029-5515/55/9/093011
177. R.S. Rawat, Dense plasma focus—from alternative fusion source to versatile high energy density plasma source for plasma nanotechnology. J. Phys. Conf. Ser. **591** (2015) [15th Latin American Workshop on Plasma Physics (LAWPP2014)]
178. S.H. Saw, S. Lee, V. Damideh, Plasma focus apparatus and system. Malaysia patent application no. PI 2015702605 (filed 2015) (2015)
179. H. Rapp, Phys. Lett. A **43A**, 420–422 (1973)
180. V.I. Kraus, Progress in plasma focus research and applications. Plasma Phys. Control. Fusion **48**, B221–B229 (2006) (33rd EPS Conference on Plasma Physics, Rome, 20 June 2006)
181. M. Scholz, *Report at ICDMP Meeting* (ICDMP, Warsaw, Poland, 2007)
182. G. Decker, W. Kies, R. Nadolny, P. Röwekamp, F. Schmitz, G. Ziethen, K.N. Koshelev, YuV Sidelnikov, Plasma Sour. Sci. Technol. **5**, 112–118 (1996)
183. R. Verma, P. Lee, S. Lee, S.V. Springham, T.L. Tan, R.S. Rawat, M. Krishnan, Order of magnitude enhancement in neutron emission with deuterium-krypton admixture operation in miniature plasma focus device. Appl. Phys. Lett. **93**, 101501 (2008)
184. M. Akel, S. Lee, Soft X-ray emission in the water window region with nitrogen filling in a low energy plasma focus. J. Fusion Energy **32**, 121–127 (2013). doi:10.1007/s10894-012-9536-2
185. R. Lebert, W. Neff, D. Rothweiler, J. X-ray Sci. Tech. **6**(2) (1996)
186. V.A. Gribkov, A. Srivastava, P.C.K. Lee, V. Kudryashov, S. Lee, IEEE Trans. Plasma Sci. **30**, 1331–1338 (2002)
187. M.G. Haines, Plasma Phys. Control. Fusion **53**, 093001 (2011). doi:10.1088/0741-3335/53/9/093001
188. W.H. Bennett, Phys. Rev. **45**, 890 (1934)
189. S. Lee, Plasma Phys. **25**(5), 571 (1983)
190. S. Lee, Density ratios in compressions driven by radiation pressure. Laser Part Beams **6**, 597–606 (1988)
191. M.G. Haines, Phil. Trans. R. Soc. Lond. **A300**, 649 (1981)
192. V. Vikhrev, Pis'ma Zh Elsp Teor Fiz **27**(2), 104–107 (1978)
193. K.N. Koshelev, YuV Sidelnikov, Nucl. Instrum. Methods Phys. Res. **B9**, 204–205 (1985)
194. K.N. Koshelev, V.I. Krauz, N.G. Reshetniak, R.G. Salukvadze, YuV Sidelnikov, EuV Khautiev, J. Phys. D Appl. Phys. **21**, 1827 (1988)
195. F.N. Beg, I. Ross, A. Lorenz, J.F. Worley, A.E. Dangor, M.G. Haines, J. Appl. Phys. **88**, 3225–3230 (2000)
196. S.H. Saw, S. Lee, Radiative cooling and collapse in the plasma focus, in 22nd IAEA Technical Meeting (TM) on Research Using Small Fusion Devices, 12–14 Oct 2015, Prague, Czech Republic
197. E. Zielinska, M. Paduch, M. Scholz, Sixteen-frame interferometer for a study of a pinch dynamics in PF-1000 device. Contrib. Phys. **51**, 279–283 (2011)

198. P. Kubes, M. Paduch, J. Cikhardt, J. Kortanek, B. Cikhardtova, K. Rezac, D. Klir, J. Kravarik, E. Zielinska, Filamentary structure of plasma produced by compression of puffing deuterium by deuterium or neon plasma sheath on plasma-focus discharge. Phys. Plasmas **21**, 122706 (2014)
199. M. Akel, Sh. Ismael, S. Lee, S.H. Saw, H.J. Kunze, Effects of power terms and thermodynamics on the contraction of pinch radius in plas ma focus devices using the Lee Model. J. Fusion Energy **35**, 807–815 (2016). doi: 10.1007/s10894-016-0108-8
200. S.H. Saw, S. Lee, Measurement of radiative collapse in 2.2 kJ PF: achieving high energy density (HED) conditions in a small plasma focus. J Fusion Energy **35**, 702–708 (2016). doi:10.1007/s10894-016-0095-9
201. P. Kubes, M. Paduch, J. Cikhardt, D. Klir, J. Kravarik, K. Rezac, B. Cikhardtova, J. Kortanek, E. Zielinska, Plasma Phys. Control. Fusion **58**, 045005 (2016). doi:10.1088/0741-3335/58/4/045005
202. Glenn Millam Focus Fusion Society

Chapter 4
X-ray Diagnostics of Pulsed Plasmas Using Filtered Detectors

Paul Lee and Syed M. Hassan

4.1 Introduction

Measurements of X-rays can give information about a plasma. X-ray emission from high-temperature, high-density, transient plasmas like plasma focus, z-pinches and laser-produced plasmas can be easily observed using simple and cost-effective diagnostics. This chapter provides the details of how filtered detectors can be used to find the rough spectrum of X-ray emission. The physics is very well known but we will work through a few examples to help us design and implement a filtered detector for X-ray measurements. It is instructive to go through some fundamentals which will help us in our design and data analysis. The design of the diagnostics depends on the type of X-ray spectrum being observed and on the objective of the experiment. For example, the design can be quite different for the following cases of various experimental objectives:

(a) The spectrum is known and the diagnostic seeks to measure the total yield.
(b) The spectrum is unknown and the diagnostic seeks to get an idea of X-rays in various spectral ranges.
(c) The form of the spectrum is known and the diagnostic seeks to get an idea of how the X-ray parameters change when other variables are changed.

The design may also change depending on practical reasons. Some examples of variation in design could be

P. Lee (✉) · S.M. Hassan
NSSE, National Institute of Education, Nanyang Technological University, Singapore 637616, Singapore
e-mail: paul.lee@nie.edu.sg

S.M. Hassan
LPP Fusion Inc, Middlesex, NJ 08846, USA

R.S. Rawat (ed.), *Plasma Science and Technology for Emerging Economies*,
DOI 10.1007/978-981-10-4217-1_4

(a) Variation due to X-ray energy range.
(b) Cost-effective filter availability.

4.1.1 X-ray Sources—Traditional and Plasma

In 1895, German physicist Wilhelm Conrad Röntgen discovered that X-rays were produced when cathode rays impinged upon an anode [1]. The same principle is used in many industrial and medical X-ray sources. It is used for X-ray imaging to take chest X-rays, dental X-rays, mammograms, screening baggage and people in the airport, and product inspection. It is also used for X-ray diffractometers. This source of X-rays, called the X-ray tube (Fig. 4.1a) is very well characterized with well-known yields and spectrum. The form of the spectral distribution from bremsstrahlung is given by Kramers' law, and the minimum wavelength is given by the maximum photon energy or tube voltage and is called the Duane–Hunt law. Figure 4.1b illustrates Kramers' law for low and high accelerating voltages.

From Kramers' law we find that roughly 90% of the X-ray energy is in photons with energy less than 70% of that provided to electrons moving through the tube voltage, V. The average energy of the photons is about 30% of the tube voltage. Therefore, the high-energy end of X-ray spectrum in keV can only be numerically equal to the maximum tube voltage in kV (kilovolts). An empirical formula can be found for the efficiency of the X-ray tube. From NRL formulary [2]

$$\text{Efficiency} = \frac{\text{X-ray power}}{\text{beam power}} = 7 \times 10^{-10} ZV, \tag{4.1}$$

where Z is the atomic number and V is the X-ray tube voltage in V and the power is

$$P_b = 7 \times 10^{-10} ZiV^2, \tag{4.2}$$

where i is the beam current. The formula is valid for applied potential of less than 5 MV.

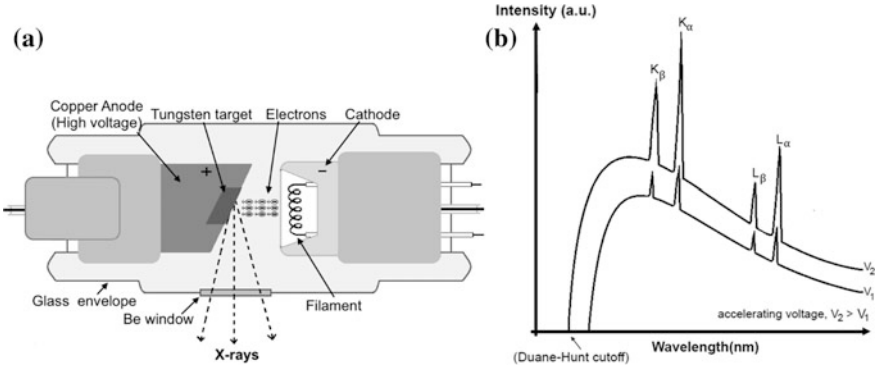

Fig. 4.1 **a** Schematic of an X-ray tube, and **b** Kramer's law for different voltages

It is instructive to work the formula through with a few values. Using a very high peak voltage of about 5 MV and an anode of a very large atomic number, e.g., tungsten, $Z = 74$, it is possible to get high efficiencies of $\sim 30\%$. Of course, it should never be possible to get more than 100% efficiency and therefore it is clear that the formula breaks down at very high voltages. On the other hand, for soft X-rays at ~ 1 keV the efficiency is only 0.007% with tungsten when we try to obtain low-energy X-rays by bremsstrahlung with a tube voltage of 1.3 kV. If we try to use an element with characteristic X-rays close to ~ 1 keV, then from Moseley's law

$$E_{pk} = 10.2(Z - 1)^2 \tag{4.3}$$

with $Z = 11$ (sodium) or more realistically $Z = 13$ (aluminum), the bremsstrahlung efficiency is only 0.001%. Note that Moseley's law does not work for low-Z materials such as hydrogen and the energy, E_{pk}, is in eV.

For soft X-rays, it is possible to make use of *K*, *L*, *M*… line radiation.

The power of the *K*-alpha (K_α) line fits the formula

$$P_\mathrm{k} = 1.7 \times 10^{-9} I(V - V_i)^{1.5} \tag{4.4}$$

Therefore

$$\frac{P_\mathrm{k}}{P_\mathrm{b}} = C\frac{(V - V_i)^{1.5}}{V^2} \tag{4.5}$$

and maximum *K-shell* radiation is obtained when electron energy of the electron beam is four times more than the *K*-edge energy where the characteristic radiation yield is about 25% of the bremsstrahlung yield. The power in the K_α set of lines is usually 5–10 times more than the K_β and much stronger than the rest.

In addition to X-ray tubes, there are some modern ways for producing X-rays, such as via synchrotrons and dense plasma focus devices.

Plasma focus as a pinch device that produces a broad spectrum of X-rays with a duration of tens of nanoseconds. At the open end of a coaxial electrode system, rapid magnetic compression of a plasma column is formed by the discharge current itself. Low-energy X-rays of a few keV can be formed from the plasma while the high-energy X-rays are emitted from the anode surface. The X-ray spectrum and intensity can be varied by changing the external parameters, such as the input energy by changing the charging voltage of a machine, gas pressure and its composition, and the electrodes material and shape. As a non-destructive diagnostic technique, X-rays provide information about the plasma electron temperature and its density, the energy of the electron beams and fast ions, and most importantly the dimensions of the emitting regions and their locations.

4.1.2 X-ray Detectors—Spectral, Spatial and Temporal Resolution

The choice of a detector for X-rays depends to a considerable extent on the source and the information required. X-ray intensities are usually measured with photographic plates, windowless photomultipliers, gas counters, a combination of scintillators with standard photomultipliers, or with semiconductor detectors. More complex systems for X-ray detection in plasma include X-ray streak cameras and microchannel plates. However, each detection system has a different range of applicability because of differences in sensitivity, time constants, linearity, wavelength dependence, dark current, and response to scattered light.

Spectral Resolution

Pinch plasma has a hot-spot or intense radiation zone which emits short wavelength radiation. X-rays spectrometers can give spectra of a few Å in a single shot depends upon the radiating body temperature and material. A simple spectrometer requires a dispersive element (crystal or grating) and an X-ray sensitive detector [3–6] as shown in Fig. 4.2. The advantage of a crystal spectrometer is that it can cover a large wavelength range, useful for the soft X-rays with photon energy $E < 15$ keV.

The compact size and high spectral resolution are some of the requirements to install a spectrometer close to the X-rays source inside the vacuum chamber of a pulsed plasma machine. The bent crystal spectrometer is simple to design for a broader range of X-rays as shown in Fig. 4.2. If the line broadening due to a finite rocking curve of the convex crystal is disregarded then the line width, W, on the detector is related to the size of the source, S, by the expression [4]

$$W = \frac{S}{\sin\theta_d}\left(\frac{L_1 + R_{cry}\sin\theta_B}{L + R_{cry}\sin\theta_B}\right), \tag{4.6}$$

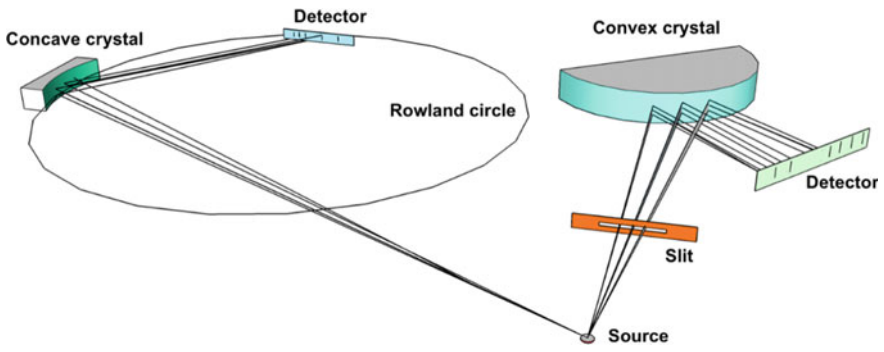

Fig. 4.2 Bent crystal spectrometers

where R_{cry} = crystal's radius of curvature, L is the distance from plasma to the point of reflection, θ_d is an angle at detector, θ_B is an angle of radiation follows Braggs law and L_1 is the distance from the point of reflection to the detector.

Typically, the pinch plasma from the pulsed power machine is in a cylindrical shape, and the location of a source size fluctuates from shot to shot. For simplicity, a plasma source size of about a millimeter is considered for numerical calculation of linewidth with a miniature spectrometer of 25 mm crystal radius and the result is shown in Fig. 4.3. It is important to mention that the width of the line does not depend on the order of reflection but it decreases with increasing wavelength.

Another important parameter of a crystal spectrometer is the resolution which depends on the geometrical shape of source, half-width of its rocking curve, the order of reflection and the position of crystal from source and detector [3]. This resolution for a small crystal radius can simply be related to a larger distance L between the crystal center and the radiation source of a size S [5], such as

$$R_s = \delta\lambda/\lambda = \cot\theta_B S/2L \tag{4.7}$$

Figure 4.3 shows the resolution for the source size of 1 mm in the first through third orders of reflection. It is obvious that the resolution at 7 Å in the second order is equal to the resolution at 14 Å in the first order of reflection. The resolution at 7 Å in the first order of reflection is twice as good as the resolution at 7 Å in the second order.

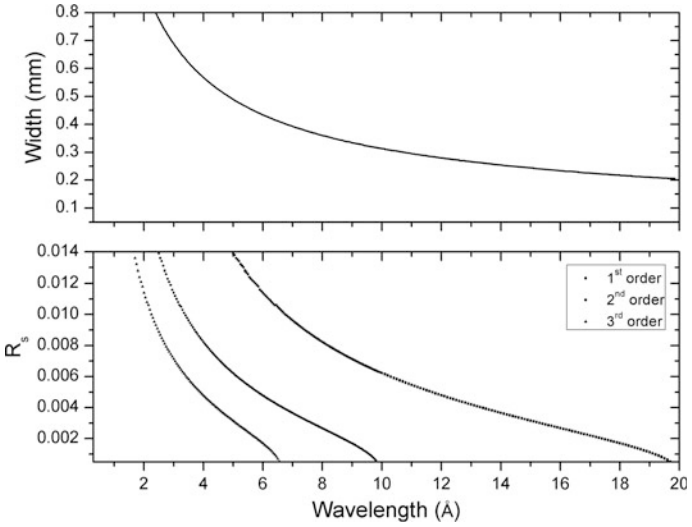

Fig. 4.3 Linewidth calculation and spectral resolution for first three reflection orders of mica convex crystal

If there is no space limitation around the plasma chamber, a high-resolution grating spectrometer with a large radius of curvature of few meters should be used for diagnosing the emission condition of plasmas. However, a good X-ray spectrum, other than the dispersive element, is highly dependent on the X-ray detection system. For a data analysis, an X-ray sensitive film (or a cooled, low-noise, X-ray sensitive charge-coupled device) is required to convert absorption spectra into useful quantitative emission spectra. The analysis includes the processing of raw data to extract lineouts, applying wavelength calibration to lineouts, and converting the film density to an intensity unit (i.e., photons per μm^2). Also, the film response needs to be checked by performing background subtraction; as an important procedure, this can be done by developing a blank piece of film or recording a blank image without a shot at the same time of experimental data. Subsequently, wavelength-related corrections to account for filter transmission, crystal and slit imperfections and detector response can be applied. Once the background continuum is collected, then a recorded spectrum should be divided by this continuum to generate the transmission spectra. If there is a system of multiple slits or pinholes for imaging the same shots, then there exists the opportunity of averaging over the nominally identical measurements for time-integrated spectra to enhance the signal-to-noise ratios.

Spatial Resolution

Imaging of radiative plasmas is complicated due to non-availability of refractive materials for lenses in the X-rays region. The advancement of multilayer (ML) mirrors for soft X-rays has enabled the analysis of plasma region, but they are expensive and their reflectivity is easily degraded by the deposition of charged and neutral particles. Curved crystal spectrometers can record simultaneously the spatially and spectrally images [6] by using filtered pinhole. This lensless technique is a simple and the most reliable plasma diagnostic device for X-ray imaging. A pinhole camera can give the time-integrated, space resolved X-ray measurements of the plasma. However, it can also be used to obtain time-resolved images by employing microchannel plate detector [7]. The main parameters of a pinhole camera are magnification, resolution, and its diffraction limit. The magnification of a pinhole camera, $M = b/a$, simply depends upon the distance, b, from pinhole-to-detector and the distance, a, from source-to-pinhole. For a pinhole of a diameter d, the resolution R of an image is given by:

$$R = d(1 + 1/M) \tag{4.8}$$

For an excellent resolution, it is necessary to increase the magnification and decrease the pinhole size, but there are certain limitations. For example, too high a magnification may give a low-intensity image on the detector, and small pinholes

increase the diffraction effects. The pinhole diameter can be adjusted until radiation diffraction at the pinhole is less, i.e., the angle of diffraction becomes much smaller than the angle under which the pinhole can be seen by any point of an object

$$\lambda/d \ll d/a, \quad \text{i.e., } d \gg \sqrt{\lambda.a} \tag{4.9}$$

Temporal Resolution

The extremely dense-pulsed plasma produces short-lived X-rays. X-ray streak camera and microchannel plates in the sub-picosecond resolution are available to couple with X-ray spectrometer for obtaining information about plasma mainly its temperatures, densities, ionic distributions, polarization, and electromagnetic fields. The semiconductor X-ray spectrometer based on Si-PIN diodes is a cost-effective system for obtaining time-resolved and space-integrated X-ray measurements from nanosecond pulsed plasma. In addition to superior energy resolution, semiconductor solid-state detectors can have several other excellent features. Among these are compact size, relatively fast timing characteristics, ruggedness, insensitivity to the magnetic field and detection area which can be designed to match the requirements of the application. Some limitation to its use includes the small sizes, lack of internal gain and performance degradation due to temperature and radiation-induced damage. Semiconductors-based photon detection are available for extremely low-energy photons with amplification mechanism up to the direct detection of X-rays in 1–100 keV energy range. Photons interact in the intrinsic by means of the photoelectric effect and the Compton scattering and the resulting secondary recoiling electrons lose energy in the intrinsic silicon by forming electron–hole pairs. The motion of these charges in the applied field results in a current flowing through an external load connected to the oscilloscope. The output voltage across the load reproduces the temporal properties of the source while the integral of the voltage is proportional to the absorbed energy. The temporal resolution requires a thinner detector but too thin detector will increase the capacitance of a detector which can also be increased by increasing area. The performance of a diode as a radiation detector is highly dependent on its size and temporal properties of the source.

4.1.3 X-ray Production Mechanisms

The plasma temperature is high enough in pulsed power plasma device that the wavelengths of spectral interest fall in the X-ray region. These radiations are the usual bremsstrahlung and recombination continua of ionized gases or target materials and line emission from different ionic species which are not fully stripped. Studying the details of the spectra, such as the time history, the continuum shape, and the identification and measurement of the intensities and profiles of different lines provide information about the electron and ion temperatures and temperature

histories, the plasma composition and density, and the degree of thermalization. The plasma X-ray spectrum is more complex than that produced by the typical X-ray tube in which bremsstrahlung and line radiations are the radiation mechanisms. For plasmas, there is also the possibility of recombination and line radiation from ions.

Free–Free (Bremsstrahlung) Radiation

Bremsstrahlung radiation is emitted when an electron makes a transition between two free energy levels of an ion which gives continuum spectrum of the radiation. In the classical picture, this radiation emission occurs because a moving charge is either accelerated or retarded. Such acceleration of electrons is mainly caused by the Coulomb field of ions, and the spectrum of the radiation is continuous because both the initial and final states are continuous.

The bremsstrahlung emission in a unit frequency interval, from N_e electrons/cm^3 with temperature T_e interacting with N_i ions/cm^3 of effective nuclear charge Z_i, is [8]

$$\frac{dE_{ff}}{dv} = C \sum_i N_e N_i \left(\frac{\chi_H}{kT_e}\right)^{1/2} g_{ff} \exp\left(\frac{-hv}{kT_e}\right), \tag{4.10}$$

where $C = 1.7 \times 10^{-40}$ erg cm^3, χ_H = hydrogen ionization potential, and g_{ff} = free–free Gaunt factor [9].

In terms of emission per unit wavelength interval, $dE/d\lambda$ shows a maximum at

$$\lambda_{max}(\text{nm}) = \frac{620}{T_e(\text{eV})} \tag{4.11}$$

A property of the free–free emission is that for long wavelengths [$\lambda \gg hc/(kT_e)$], the spectral shape is independent of T_e. However, for short wavelengths [i.e., $\lambda \leq hc/(kT_e)$] the spectrum is strongly dependent on T_e and its analysis can be used to determine the plasma electron temperature.

Free-Bound (Recombination) Radiation

The capture of free electrons into a bound state of an ion, with the accompanying emission of radiation of energy

$$hv = 1/2\, mv^2 + \chi_n \tag{4.12}$$

produces a continuous spectrum of radiation for $hv > \chi_n$. The radiation energy or the emission in a unit frequency interval from recombination into the nth shell of a hydrogen like ion of charge i ($n_{i+1} + e \rightarrow n_{i,n} + hv$) is

$$\frac{dE_{fb}}{dv} = C \sum_i N_e N_{i+n} \left(\frac{\chi_H}{kT_e}\right)^{3/2} \left(\frac{\chi_{i,n}}{\chi_H}\right)^2 \frac{\zeta_n}{n} g_{fb} \exp\left(\frac{\chi_{i,n} - hv}{kT_e}\right), \tag{4.13}$$

where $\chi_{i,n}$ is an ionization potential of the final state, ζ_n states a number of places in the nth shell which can be occupied by the captured electron, g_{fb} is the free-bound Gaunt factor [8], and all other terms are the same as in equation for bremsstrahlung radiation.

Recombination radiation may have edges in its spectrum due to binding energies associated with the different atomic states of plasma species. This type of radiation is also useful to estimate the plasma parameters such as the electron density, electron temperature, and ionic charge.

The ratio of the spectrally integrated recombination and bremsstrahlung energy densities can be expressed as $W_r/W_B \approx 2.4\, Z^2\, E_H/(k_B T_e)$ [10]. This shows that for low-Z or high-temperature plasmas bremsstrahlung overcomes recombination radiation.

Bound–Bound Transition (Line Radiation)

Line radiation occurs due to electronic transitions between the discrete or bound energy levels in atoms, molecules, or ions. When an ion, an atom, or a molecule is in the excited state, it will undergo a transition from its present state to the ground state through spontaneous or stimulated emission. The energy of the emitted photon γ is given by the difference of energies between the initial E_i and the final levels E_f. Thus, the energy of the emitted photon can be written as $h\nu = (E_i - E_f)$. Since the energy levels inside the atom are quantized, this emission appears as a discrete packet of energy, or "lines", therefore it is also known as the characteristic radiation and represents the characteristic properties of the emitting ion, atom, or molecule. For the intermediate and high-Z plasmas, line emission is considered as the most important radiation process particularly for the plasmas in which the ions are not fully ionized. The spectrum from such plasma contains many closely spaced lines exhibiting spacing smaller than their linewidths and thus forms an unresolved transition array (UTA) [11].

4.1.4 Filter and Detector Absorption Mechanisms

X-ray Absorption Process

As X-ray photons pass through a material, it interacts with the material and energy is lost to the material. This random process based mainly on three mechanisms: the photoelectric effect, Compton scattering, and pair production. Other scattering mechanisms and absorption (e.g., Rayleigh/Thomson scattering) is usually unimportant for X-rays and will not be considered here, along with photonuclear absorption (similar to the photoelectric effect but with the nucleus). We may think of the absorption process simply as removing photons based on a cross-sectional area of the material "atoms"—like throwing darts at a dartboard with areas marked out. Although photons are not actually removed by Compton scattering, but scattered and reduced in energy, we will use the same cross-section

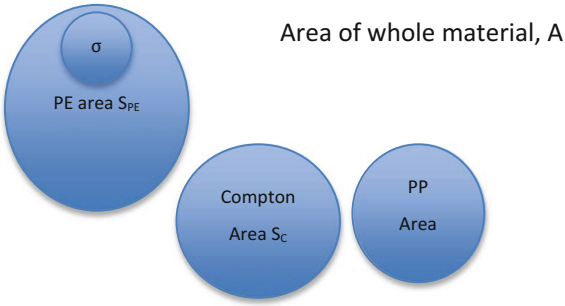

Fig. 4.4 Illustration of three main X-rays interaction mechanisms within a material A as cross-sectional areas

idea which will allow us to estimate the amount of X-rays absorbed. This is probably a good estimate if the number of photons is large.

As illustrated in Fig. 4.4, for a thin slab of material with area A and thickness Δz, the probability of a photon entering the area to be absorbed is

$$\frac{S_{\mathrm{PE}}(E_{\mathrm{p}}) + S_{\mathrm{C}}(E_{\mathrm{p}}) + S_{\mathrm{PP}}(E_{\mathrm{p}})}{A} = \frac{nA\Delta z\left(\sigma_{\mathrm{PE}}(E_{\mathrm{p}}) + \sigma_{\mathrm{C}}(E_{\mathrm{p}}) + \sigma_{\mathrm{PP}}(E_{\mathrm{p}})\right)}{A}, \quad (4.14)$$

where photoelectric, Compton and pair production cross-sections are σ_{PE}, σ_{C}, and σ_{PP}, respectively. Also, n is the number density of atoms such that total area S is made up of smaller areas with $\sigma[\mathrm{m}^{-2}]$ of each atom.

If the number of photons with energy E_{p} is N, the change in the number of photons = expected number of photons absorbed, given as

$$\Delta N = -Nn\Delta z\left(\sigma_{\mathrm{PE}}(E_{\mathrm{p}}) + \sigma_{\mathrm{C}}(E_{\mathrm{p}}) + \sigma_{\mathrm{PP}}(E_{\mathrm{p}})\right) \quad (4.15)$$

integrating the above equation, we get the number of photons

$$N = N_0 \mathrm{e}^{-n\sigma(E_{\mathrm{p}})z}, \quad (4.16)$$

where N_0 is the initial number of photons. This also means that

$$I = I_0 \mathrm{e}^{-n\sigma(E_{\mathrm{p}})z} \quad (4.17)$$

Attenuation Coefficients

Although we have described the absorption process as a cross-section, it is possible to use other ways to characterize the absorption mathematically. For example, the atomic photoelectric cross-section σ can be related to the atom forward scattering factors f_2

$$\sigma = 2r_0\lambda f_2, \tag{4.18}$$

where r_0 is the classical atomic radius and λ is the X-ray wavelength.

The absorption may also be characterized, for example in Fig. 4.6 by the linear attenuation coefficient $\mu = n\sigma[\mathrm{m}^{-1}]$, by using the mass attenuation coefficient (also called mass absorption coefficient) $= \frac{\mu}{\rho}\left[\mathrm{m}^2\,\mathrm{kg}^{-1}\right]$, attenuation length $= \frac{1}{\mu}[\mathrm{m}]$ and half value thickness $= \frac{\ln(2)}{\mu}[\mathrm{m}]$.

Photoelectric Effect

When a photon interacts with an atom, it may transfer its energy to an electron, thus freeing the electron and giving it kinetic energy. The photon is said to be absorbed and this mechanism is called the photoelectric effect. This mechanism is dominant at low photon energies; low meaning not much higher than the binding energy of the electron. In fact, the photoelectric effect does not happen at low photon energies if the photon is unable to supply the energy required to remove the electron. This effect gives rise to transmission curves for transmission against photon energy which increases until an "absorption edge" is encountered, where the transmission drops suddenly and after that starts increasing again until the next edge. The edges are related to the energy required to remove the *K*, *L*, *M*… shell electrons. Due to this behavior, a filter made of a certain element will not absorb the characteristic lines of the cold element as the characteristic line (e.g., *L–K* will have slightly lower energy than ∞*–K)*. Fig. 4.5 shows the typical K- and L- absorption edges of a filter. However, if the element is ionized, the magnitude of its energy levels will increase, and a plasma of the element may produce lines which are well absorbed by the cold filter made of the same element.

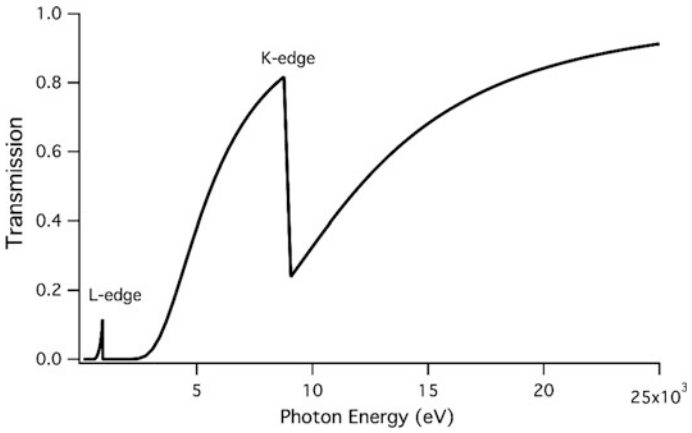

Fig. 4.5 Illustration of typical transmission against photon energy. Transmission falls suddenly at *L*- and *K*-edges due to photoelectric effect

Since an electron is removed from the atom, the photoelectric effect may cause X-ray fluorescence. Where, for example, the *L* shell electron falls to fill the *K*-shell electron which was ejected. The K_α fluorescence will be able to penetrate through the filter easily as described above. The probability of fluorescence increases with increasing atomic number. For this reason, sometimes when dealing with hard X-rays, it is good to have a low-Z material after the high-Z filter to reabsorb fluorescence from the filter and to keep the detector some distance from the filter so that the fluorescence may escape in angles not directed at the detector. This will allow us to calculate the absorption without taking into account the fluorescence.

Compton Scattering

When an X-ray photon with energy much higher than the electron binding energy interacts with the atom, we may treat the interaction as if the X-ray photon is interacting only with the electron. Unlike the photoelectric case where energy and momentum can be conserved when the photon gives all its energy to the electron as the atom can have a substantial momentum change even with negligible energy change, in Compton scattering the amount of energy transferred is controlled by the conservation of energy and momentum in the two-body collision. The Compton effect becomes more important at intermediate energy, high above the *K*-edge of the material and lower than the energy required for pair production.

Although the Compton effect reduces photon energy and scatters the photons, to make it easier to take the Compton effect into account, it is preferable to have the filter some distance from the detector so that the scattered photons do not fall directly on the detector similarly to the precaution taken to avoid fluorescence. Pair production is a dominant phenomenon at high energy greater than 1.22 MeV which can also be ignored for most of the pulsed plasmas X-rays production. Taking a common filter material, Fig. 4.6 illustrates the mass attenuation coefficient of aluminum as a function of photon energy.

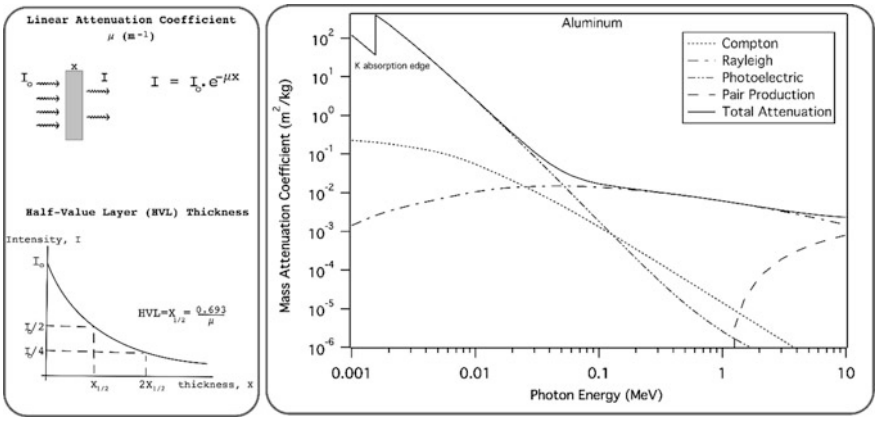

Fig. 4.6 Filter absorption and attenuation mechanisms

4.2 Experimental Setup

Easy and Cost-Effective Detectors

A conducting surface in a high vacuum will emit photoelectrons. When appropriately biased, the photoelectrons can be made to flow in a circuit, and the measured current from the vacuum diode will allow this device to be used as an X-ray detector. Only electrons from the surface with sufficient energy and will have a good probability to leave the surface.

If X-rays penetrate deep into the metal, the resulting photoelectrons will not contribute to the photocurrent. This means that the vacuum photodiode is effective for UV to soft X-rays and not very sensitive to higher energy X-rays. Furthermore, the surface condition strongly affects the photoelectron emission, and it is not easy to predict a theoretical sensitivity which may degrade over time as surface conditions change with oxidation, deposition of other materials.

The PIN (or *p-i-n*) diode is widely used for X-ray detection [12, 13]. Fig. 4.7 illustrates a typical PIN diode structure made of a wide intrinsic semiconductor region for photon absorption sandwiched between a P-type semiconductor plus surface material as a top layer and an N-type semiconductor layer as a bottom region. The PIN diode does not require vacuum operation and the sensitivity of its active region does not degrade much with time. This makes it a more reliable for absolute measurements than vacuum X-ray diodes [14, 15]. The BPX65 photodiode has been used for X-rays as a low-cost alternative to diodes for X-rays. This diode was popularized by C.S. Wong's group [16] and has been used for many plasma experiments by many groups in the AAAPT network. The PIN diode with different filters is sensitive to X-rays at various energy ranges although its sensitivity is not particularly good for very soft X-rays due to the dead layer. An array of filtered PIN diodes can be used as a low resolution but calibrated X-ray spectrometer.

Dead Layer—Characteristics

The dead layer consists of any anti-reflection, metallized, heavily doped semiconductor, or doped semiconductor region which blocks the active region from the

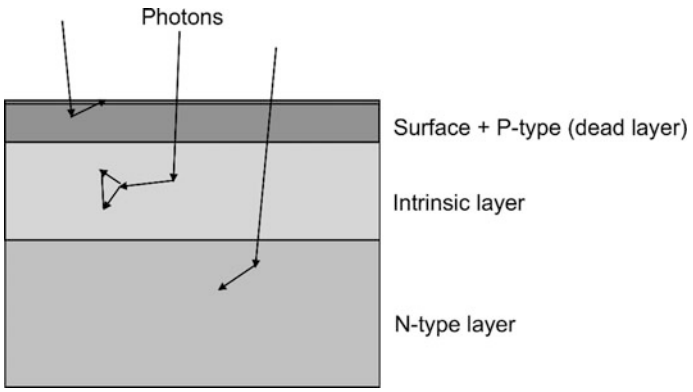

Fig. 4.7 Layers of the PIN diode

X-rays. If photodiodes are used, then this layer must by necessity be very thin for visible light to penetrate to the active layer. The X-ray photon transmission through the dead layer is given by

$$T_{\mathrm{d}}(E_{\mathrm{p}}) = \exp\left(-\sigma(E_{\mathrm{p}})n_{\mathrm{d}}l_{\mathrm{d}}\right), \tag{4.19}$$

where n_{d} is number of atoms per unit volume, and l_{d} is the thickness of the dead layer.

Active Layer—Characteristics

The active layer is the region where absorbed photons create electron–hole pair which leads to a signal which can be recorded. In a negatively biased PIN diode, the active layer may be taken to be the depletion region. When a photon generates electron–hole pairs within the depletion region, the high electric field across the depletion region causes a current to flow through the circuit. In practice, electron–hole pairs generated outside the depletion layer may also contribute to the current but this current will not be directly proportional to the incident X-ray power at any instant as the diffusion of the charges may happen on a longer time scale. A PIN diode which can be used as a good X-ray diode should have a thick intrinsic layer as shown in Fig. 4.7. This allows for higher efficiency in absorbing photons and also a good reproducibility in the calibration factor. As the thickness of the depletion layer depends on the applied reverse bias voltage, the sensitivity of the PIN diode also varies with the reverse bias voltage.

The X-ray absorption in the depletion region can be expressed as

$$A_{\mathrm{a}}(E_{\mathrm{p}}) = 1 - \exp\left(-\sigma(E_{\mathrm{p}})n_{\mathrm{a}}l_{\mathrm{a}}\right) \tag{4.20}$$

where l_{a} is the thickness of the intrinsic silicon wafer.

Spectral Response Curve of a PIN Diode

The sensitivity can be calculated from the low-energy X-ray interaction coefficients given by Henke [17]. The fraction of photons absorbed by the diode is $T_{\mathrm{d}}A_{\mathrm{a}}$. When a semiconductor detector absorbs an X-ray photon of energy $E_{\mathrm{p}} = hv$, then hv/w number of electron–hole pairs are produced where w is the average energy needed to create an electron–hole pair.

For silicon, $w = 3.6$ eV, the photon detection efficiency is given by

$$Q_{\mathrm{p}}(E_{\mathrm{p}}) = \frac{E_{\mathrm{p}}}{w}\exp\left(-\sigma(E_{\mathrm{p}})n_{\mathrm{d}}l_{\mathrm{d}}\right)\cdot\left(1 - \exp\left(-\sigma(E_{\mathrm{p}})n_{\mathrm{a}}l_{\mathrm{a}}\right)\right), \tag{4.21}$$

where Q is the output number of electrons from the PIN diode for one photon.

The sensitivity of a diode at a given wavelength or incident energy is a measure of the effectiveness of the light power (P) into electrical current (I_{p}). It is also known as responsivity (A/W) of a detector and can be measured as

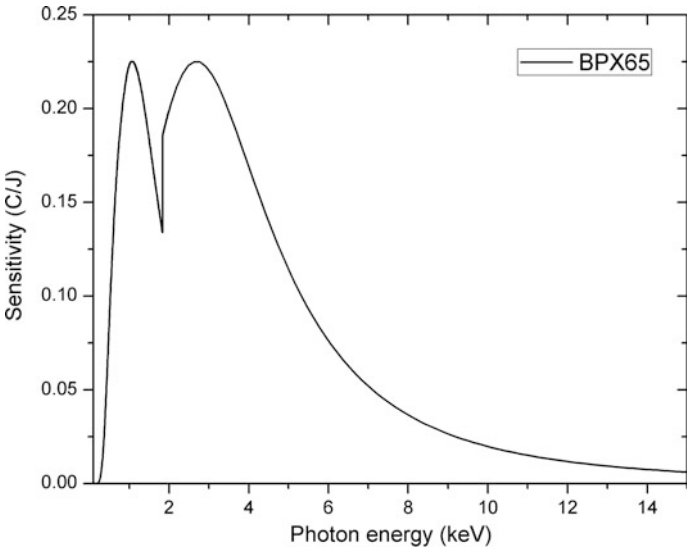

Fig. 4.8 Sensitivity of the windowless BPX65 PIN diode detector

$$S(E) = \frac{I_\mathrm{p}}{P} = \frac{Q_\mathrm{p}(E_\mathrm{p})e}{E_\mathrm{i}}, \tag{4.22}$$

where E_i is the incident photon energy and e is the electronic charge.

The BPX65 photodiode has intrinsic and dead layer thicknesses of about 10 and 0.5 μm, respectively. The typical sensitivity of a windowless BPX65 photodiode to X-ray fluence in the range 1–15 keV without any filter is shown in Fig. 4.8.

Circuit—Characteristics

For the photodiode to work with a good time response, dynamic range, and a well-known and reproducible spectral response, an appropriate circuit should be used with the photodiode. An example circuit is shown in Fig. 4.9. The circuit needs to supply a constant negative bias to the diode to maintain a well-defined and constant active layer. This is accomplished by using the voltage supply or battery together with capacitor C. When a photocurrent flows through the diode D, the same current will flow through resistor R assuming that the bias resistor, $R_B \gg R$. A voltage thus develops across R which can be measured.

The capacitance of C must be large enough that the photo charge should not significantly discharge it. Also, C must be large enough to ensure that $1/(\omega C)$ is negligible as compared to R, as R should be chosen to match the impedance of the transmission line T_L to avoid reflections. However the time constant $R_\mathrm{B}C$ must be much smaller than the time between shots so that the capacitor has time to be charged up. A practical consideration would also be to minimize stray inductances and capacitances to avoid ringing and obfuscation of the signal.

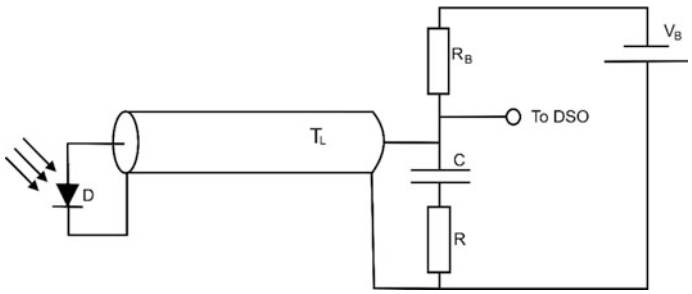

Fig. 4.9 Example circuit to bias and connect the diode circuit to external measurement such as a digital sampling oscilloscope

Worked Example

Design the biasing circuit based on the following specifications: the RG-58 coaxial cable is used to connect the diode with 50 V bias to the oscilloscope. Signals of about 100 ns, 0.1 A are expected from a 1 kHz rate X-ray source. Choose suitable values for R_B, R, and C.

The value of R must be chosen to match the impedance of the coaxial cable. Since the nominal value for the coaxial cable is 50 or 52 Ω, R should be close to 50 Ω as well. Standard resistor values are 47 and 51 Ω. It is also possible to use two standard 100 Ω resistors in parallel or three standard 150 Ω resistors in parallel. At 0.1 A and 50 Ω, the voltage expected is 5 V and the power is 0.5 W. The power is very sensitive to the maximum current and voltage. For example, if in some shots 10 V signals are obtained, then the maximum power dissipation becomes 2 W. However due to the short timescale of the X-ray pulse and the relatively low repetition rate, the average power is 10,000 times less, so standard 1/8 W resistors may be used. Small (in dimensional size) resistors are preferred for their low stray capacitance; low inductance resistors are also preferred.

We may choose C such that the bias voltage does not change significantly during the shot. The charge flow for the typical signal is 10 nC. Let us say we want the voltage drop to be less than 10% of the typical signal, i.e., 0.5 V, then the capacitance should be at least 20 nF. We may choose for example a 100 nF capacitor so that we do not have to worry about any correction factors even for larger than usual signals.

The bias resistor R_B must be much more than 50 Ω to avoid recalculating the value of the terminating resistor R as R_B will be effectively in parallel with R if the impedance of C and the battery are small. To recharge the 0.5 V between every shot, 10 nC must flow within 1 ms, so the resistance should be less than 50 kΩ. If we take the geometric mean of 50 Ω and 50 kΩ, we get a value of 1.5 kΩ. This would make a 3% difference in the value of the terminating resistance and will recharge 30 × faster than required.

Time Response

The practical time response of the photodiode can be estimated as RC_D, where C_D is the capacitance of the photodiode. The photodiode has a capacitance due to its "capacitor-like" structure, i.e., two conductors (p- and n-layers) separated by an insulator (active intrinsic layer).

In addition, charges generated outside the depletion layer may also diffuse into the depletion layer and contribute to the signal. As the electric field outside the depletion region is very small, this diffusion takes a long time. This gives a typical microsecond "background" to the observed signal. For short pulses of X-rays, this extra slow signal may be subtracted, but for time-integrated measurements this effect will add a systematic overestimate to the X-ray yield measurements.

Saturation

When a large X-ray flux falls on the detector, the detector or its current may get saturated in the time-resolved measurements.

We may attribute this to several mechanisms. A simplistic way of understanding this saturation is to consider the external circuit in Fig. 4.9 where the voltage across the bias capacitor is equal to the voltage across the diode and output resistor, $V_C = V_R + V_D$. From this analysis, the maximum output voltage can be V_C and this is made worse if the capacitor discharges significantly during the measurement. In this case the saturation current is V_C/R and is independent of the diode and X-ray characteristics. However, the observed situation is worse than the above analysis. For example, with the BPX65 diode biased at 50 V, signals/optical power become nonlinear for UV light at diode voltages of about 1 and $\sim$10 V for X-rays hard enough to penetrate the whole active layer. To explain this, we may think of the charges generated by the X-rays as changing the electric field distribution and structure of the diode as they are generated in such a way as to reduce the current flow. If a lot of charges are generated in a particular region the electric field is "shielded" in that region, this causes the mobility of the charges to drop and in the extreme case, a situation similar to that described in the time response occurs where charges drift slowly across the "shielded" region. This changes the current measured by the oscilloscope, but fortunately the total charge collected by the measurement system may still be correct as long as the time scale of charge flow is much shorter than the recombination time for the charges [13].

Basic Checks

If multiple photodiodes are used it is important to check that they have similar characteristics. One way is to test their response to visible light. It is preferable to make a few tests with various filters to check if the response is the same at different X-ray energies.

4.2.1 Determination of Detector Active Layer

In some cases, it is possible to obtain information about the photodiode's active and dead layers from the manufacturer. However, for low-cost diodes it may not be possible to do so or to have confidence that the quoted values are constant for various batches. But it is possible to find the thickness of active layer using a simple experiment. As a diode in reverse bias behaves like a capacitor (this effect may also be used for producing electrically controlled capacitors for tuning circuits) we may find a close approximation to the active layer thickness by finding the capacitance. Such an exercise will also allow us to know how the active layer thickness changes with bias voltage and help in deciding on an appropriate diode and also the negative biasing voltages to be used during actual experiment. A good diode which has a stable spectral response must also have a stable active layer.

As mentioned, the time response of the diode depends mostly on the diode capacitance. A simple way to estimate thickness of the active layer involves measurements of the RC time constant to determine the capacitance and thus obtain the thickness of the insulator region.

4.2.2 Detector—Choice of Filters

Ideal Filters

In principle ideal filters with a bandpass characteristic would make data analysis simple. If the detector has a flat spectral response, then a filter with a spectral transmission would allow the amount of X-rays to be measured between E_1 and E_2 with a single detector, refer Fig. 4.10. If n number of detectors are used with filters for different ranges, then it is easy to obtain the spectrum. It may be possible to make such a filter with multiple layers in a way similar to multilayer mirrors in optics, but that would be very difficult as the wavelengths are very small.

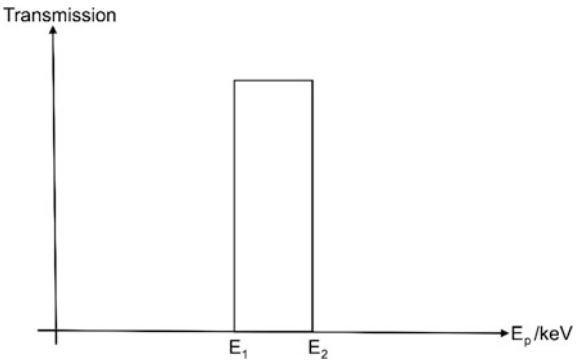

Fig. 4.10 Filter with flat transmission between two photon energies and transmission of 0 at all other energies to facilitate easy data analysis

Ross-Filter Pair

A simple way to approximate the ideal X-ray filter was proposed by Ross [18]. In this method a pair of filters is used to make up one "detector". Figure 4.11 illustrates the idea behind the Ross-filter method. For convenience, a typical detector sensitivity is considered with the filter transmission. This is important as the detectors may exhibit variations in sensitivity with photon energy, and an ideal sensitivity depends not only on the filters and detector but also on the gas fill between the detectors and the plasma source.

Analysis of the raw data to obtain an X-ray yield is simple. For example, if I_1 = 125 mA is measured flowing through the detector with Co filter and I_2 = 100 mA flows through the detector with the Fe filter, then using the sensitivity of 0.025 C/J from the Fig. 4.11, we estimate that the X-ray power incident in the range (7–8 keV) on the detector is 1 W. The exact form of the spectrum is unimportant.

It can be seen in the Fig. 4.11 that neither of the filtered detector has a sensitivity close to ideal. However when the sensitivity of the 16.5 μm Fe filtered detector is subtracted from the 13.5 μm Co filtered detector, a situation very close to that obtained by the ideal detector and filter is obtained.

Care must be taken however when Ross-filter pairs are used. Figure 4.12 illustrates the effect of introducing a gas in the path of the X-rays between the source and the detector pair. If the path is long or the density of the gas is high such as the krypton or xenon, then the behavior of the filter pair is significantly altered.

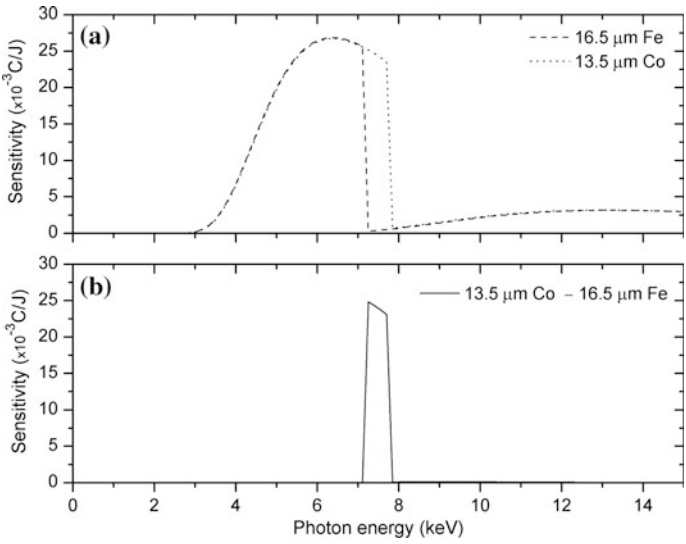

Fig. 4.11 **a** Sensitivity of two diodes filtered with 16.5 μm Fe and 13.5 μm Co. **b** The difference between the two filtered detectors

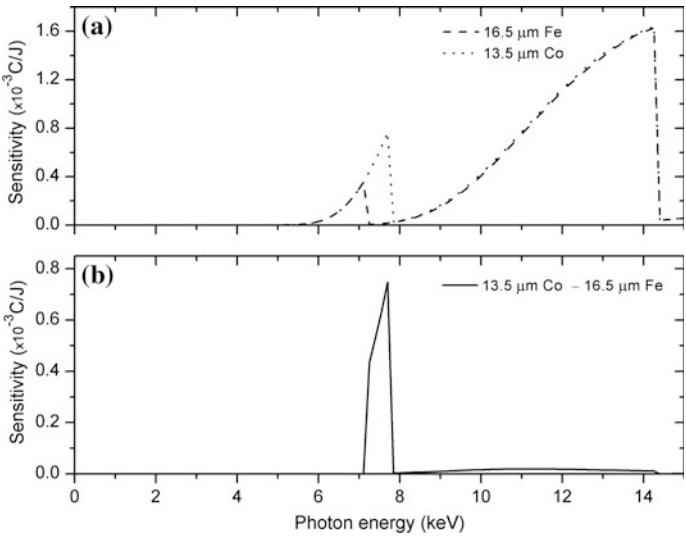

Fig. 4.12 Same filters as in Fig. 4.11 but with a "long" & "high-pressure" gas path between the source and detectors. **a** Sensitivity of two diodes filtered with 16.5 μm Fe and 13.5 μm Co. **b** The difference between the two filtered detectors

The same effect may occur when an additional material is placed between the detector and the source or if the detector characteristics are changed.

In this case, analysis of the raw data to obtain an X-ray yield is not so simple if the spectrum is not known. For example, if I_1 = 26 mA of current is measured flowing through the detector with Co filter and I_2 = 20 mA flows through the detector with the Fe filter, then using the "average" sensitivity of 0.6 mC/J from Fig. 4.12, we find that the X-ray power incident in the range of 7–8 keV on the detector is 10 W. In this case, the exact form of the spectrum is important. If the X-ray is from line radiation at 7.2 keV, then the yield will be closer to 14 W and if the X-ray is from line radiation close to the 8 keV end then the yield is 8 W. There is also the possibility that the X-ray is from above the 8 keV range. This example also demonstrates another difficulty in choosing good Ross-filter pairs is that it is not always possible for the sensitivity to be exactly same for energies above and below the energy range of interest, and a decision needs to be made as to which one can be matched well based on the expected spectrum. It is also difficult to get the exact filter thickness to be manufactured.

Choice of Thickness

For the same two materials, the energy band is defined and it is possible to obtain filter pairs for different pairs of thicknesses. If the filters are too thick or thin, then the problems mentioned above where the sensitivity is not constant to apply. In addition, there are other practical problems. For example, if the filters are too thick, signals obtained from both detectors in the pair will be small with a correspondingly

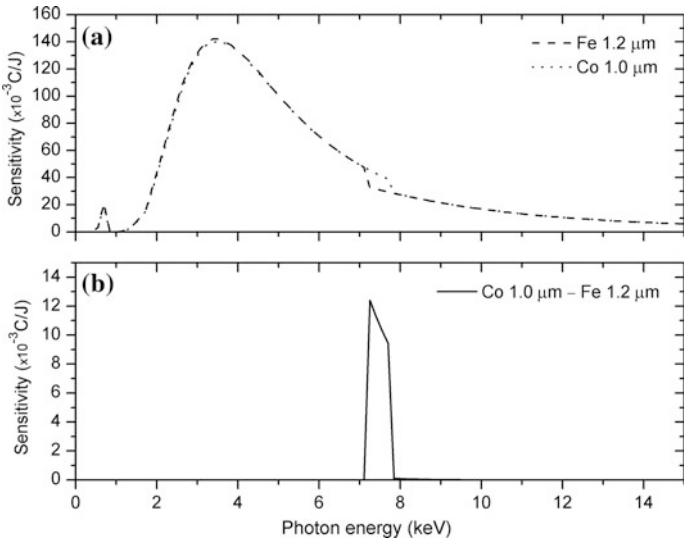

Fig. 4.13 Same material filters as in Fig. 4.11 but thinner. **a** Sensitivity of two diodes filtered with 1.2 μm Fe and 1.0 μm Co. **b** The difference between the two filtered detectors

poor signal-to-noise ratio. If the filters are too thin, then the dynamic range of the detection system is important. Figure 4.13 illustrates the sensitivity of the Ross-filter pair when very thin filters are chosen. It can be seen that the sensitivity of each of the individual filters is increased but the sensitivity of the "difference" is reduced as compared to the "optimum" filter above. The *L*-edge can be seen for very thin filters but if the amount of radiation in that range is known to be negligible, then this is not a problem.

Choice of Material

Usually solid non-reactive metals are chosen as filters as it is easier to manufacture these to the correct thickness. Plastic materials are also used for the same reason. If a spectral resolution is required, then filters with *K*, *L*-edges in the energy range to be investigated should be chosen.

Cost-Effective Filters

It is possible to get almost any filter manufactured nowadays but sometimes it is difficult to purchase the exact filters. One way of minimizing cost is to share filters with other labs as the amount of material required is very small but a minimum order is usually required to manufacture the filters. In some cases, no metallic elements are available, though it is still possible to make filters in these cases. For example if the edges of phosphorus, sulfur, and chlorine are required, it is possible to use compounds where the other elements in the compound are of much lower atomic number. If the compound is not completely opaque, it is usually possible to

add a thin layer of aluminized mylar without significantly changing the transmission.

However it may be more cost effective to consider using more easily available filters, despite the associated increase in the complexity of the analysis. It is possible to get aluminum and mylar foils from packaging of consumable goods or mylar capacitors. Figure 4.14 shows how filters made only from aluminum and mylar can give two broad ranges of energy.

Obtaining X-ray Attenuation Data

X-ray data has been tabulated for many applications. Data from Henke et al. [17], NIST [19], and other calculated data can be found from many sources on the internet which makes the X-ray data collection very easy [20].

Combining Mass Attenuation Data

After obtaining the attenuation coefficients, we will need to process the data if we want to work with several different materials. The data obtained from the above websites will typically list the coefficients at various energies. The energy scale for different elements will be similar yet distinct as each element has X-ray absorption edges at a different energy. This means that the data for aluminum, for example, would also have several coefficients for its *K*-edge at smaller intervals of energy around 1.5 keV. The data may be processed such that all filters have coefficients given on the same energy scale so that if a spreadsheet is used to combine the values, it will be easier. This may be done manually if only a few materials are chosen as filters or a program may be written to achieve this.

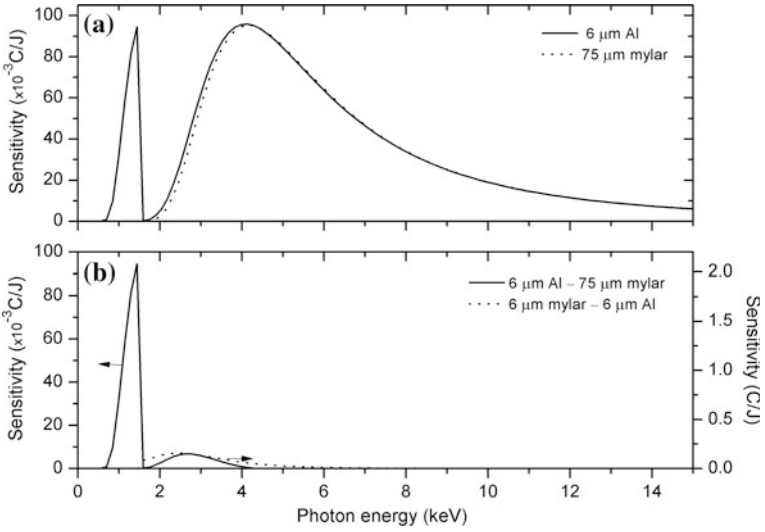

Fig. 4.14 Filters made from mylar and aluminum foil by using multiple layers of the two materials

A program created in Excel could have the following steps:

1. Make a "complete list" of energy values
   (a) Combine the energy values from all filters into one column
   (b) Remove duplicates
   (c) Sort energy values in ascending order
2. For each element interpolate values of coefficients for the "complete list" of energy values
   (a) Compare the energy value, row by row with the complete list. If the coefficient is available copy it over. If not, perform a linear interpolation of the value from the two nearest values.

4.2.3 Construction of Detector Housing

For X-ray time-integrated image recording, a pinhole camera is a simple detector to be mounted on one diagnostic port of the plasma vacuum chamber, mainly along the radial direction for plasma focus device. The pinhole camera can be used to provide an image of the plasma source as well as the size of the hot spots or bright spots. Typically, a pinhole with a diameter of 5–100 μm with a light tight filter is used. If it is a single pinhole camera, then any vacuum port size can be used such as the NW40 or CF2.73 inches flange with a metallic tube of a length according to the best magnification and resolution. Figure 4.15 shows a schematic of the pinhole camera, which can be made with a standard vacuum flanges. For a multiple pinhole camera, a large diameter vacuum flange can be used to record multiple images of many shots without breaking the vacuum inside the plasma chamber [21].

In case of the crystal spectrometer, a light tight metallic box can serve as a compact spectrometer. Its basic element can be a bent crystal, for example a mica crystal ($2d$ = 19.8 Å) in a convex shape (Fig. 4.15), with radii of a few tens of mm for soft X-rays detection. Crystal spectrometer has a slit covered by metallic filter. A debris filter or other debris mitigation techniques are required to protect the filter from plasma if the spectrometer is placed inside the vacuum chamber. The

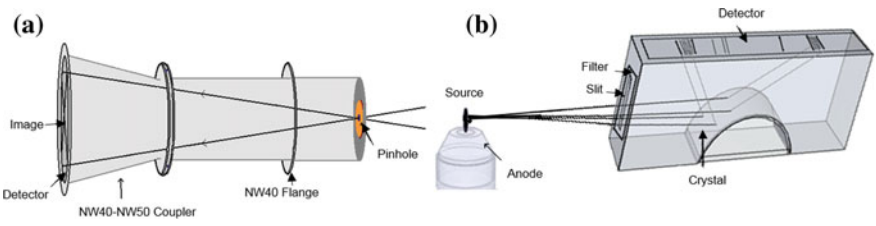

Fig. 4.15 Schematics of the **a** pinhole camera and **b** crystal spectrometer

time-integrated spectra can be recorded on high sensitive photographic film or an X-ray sensitive electronic detector. For a PIN diode as an X-ray detector, a filter holder is required to place in front of this windowless detector. Typically, a PIN diode detector is also required to place inside the vacuum chamber, therefore, its filter holder should not be a vacuum sealed but just a light tight.

4.2.4 Debris Mitigation

The conditions inside a plasma device may be extreme due to other radiations and debris occurring in addition to the presence of X-rays. For example, there may be neutrons, ions of various energies, electrons, visible and UV light, molten droplets, and particulates of various sizes—all of which may damage or coat filters. To maintain the integrity of the filters, various arrangements may need to be implemented for mitigating the effects of plasma and debris on the filters and detectors.

As most detectors are chosen due to their sensitivity to X-rays, they should be placed at a distance where the X-ray flux is appropriately low. If very soft X-rays are to be measured and absorption through the ambient gas needs to be avoided, filters may be placed much nearer to the plasma.

We may estimate the energy density required to completely melt a 1 μm aluminum filter, using equation below, to be about 2.5 mJ/mm^2, where ρ and C are the density and specific heat, L is the fusion latent heat, ΔT is the temperature change, and z is the thickness of a material.

$$E_{\text{melting}} = (C\Delta T + L)\rho z \tag{4.23}$$

Plasma flow may be in certain angles. For example in laser produced plasmas, plasma and debris tend to flow in the direction normal to the surface.

Magnetic Fields and Pinholes for Debris Mitigation

Magnetic fields may be used as a simple way to deflect charged particles. This may even be done from outside the vacuum chamber. Strong neodymium magnets can be easily obtained to give magnetic fields on the order of 0.1 T over several centimeters. This gives the Larmor radius of a charged particle and other parameters related to magnetic deflection as shown in Fig. 4.16.

Consider a charged particle q of mass m is moving with velocity v with kinetic energy K in a region of uniform magnetic induction B. For motion in the plane perpendicular to B, we can write the particles gyro-radii as:

$$r_1 = \frac{V_\perp}{\omega_c} = \frac{mV_\perp}{|q|B} = \frac{\sqrt{2Km}}{|q|B} \tag{4.24}$$

For 10 keV deuterium plasma in the magnetic field of 1 T, the Larmor radius of ions is 20 mm, and the electrons has Larmor radius of about 0.34 mm. The circular motion of charged particle in a uniform magnetic field requires to consider the thickness w along with the length L and separation d of the magnets for mitigation purposes.

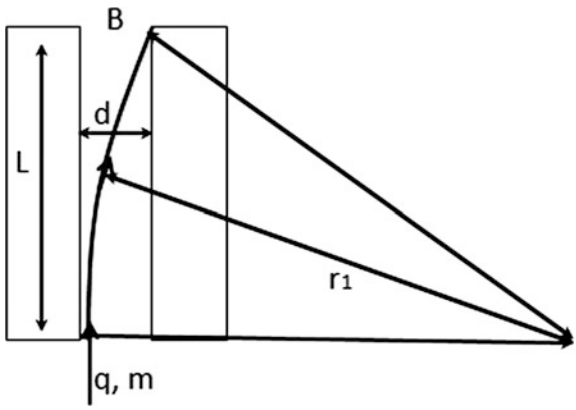

Fig. 4.16 Trajectories of plasma charged particles under the influence of a magnetic field

Another simplest mitigation technique is the pin holes to deflect sound waves and materials carried by for low temperature plasmas. An effective pinhole which separates X-rays from plasma would have its diameter much bigger than the detector but much smaller than the sound wavelength.

Foil Trap

Another simple mitigation technique is the use of a foil trap [22] as shown in Fig. 4.17.

To analyze the effect of a foil trap, consider the geometrical transmission of the comb filter is t then the total number of energetic ions, I_i, arrive at detection or collector system are following the same trajectory as the photons [23]. In this case

$$I_i = I_o t \tag{4.25}$$

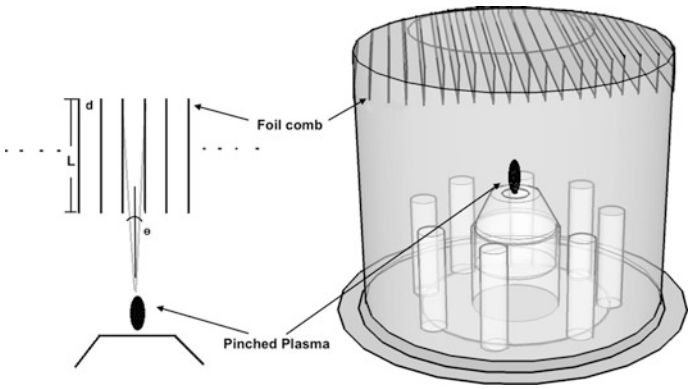

Fig. 4.17 Schematic of a foil trap and mitigation technique for a pinched plasma

If the average spacing between thin plates is d and the depth of the foil comb plates is L, then the total number of particles, $A_{r,}$ to arrive at detector are

$$A_r = A_o t \frac{d}{L}, \tag{4.26}$$

where A_o is the total number of energetic particles arriving at detector without any filter. In above equation, the geometrical factor d/L is due to the acceptance angle of the foil trap for small angles, i.e., tan θ = sin θ = θ. This angle is independent of the distance between the plasma source and detector system, however, if this distance is increased but L and d remain constant, then the number of slots in the foil comb has to be increased. For an efficient system, the t value needs to be as high as 80%, and a typical d/L ratio for the foil trap of about 1:40 gives protection factors of about 50 for the sputtered atoms and reflected atoms, but only 1.25 for fast ions [23].

4.3 Analysis Method

As described in the previous sections, a filtered diode has a sensitivity (C/J) which changes for photons of various energies. Analysis may be done in terms of total energy if the time response is not important or it may be done on a power basis if time is important. The analysis may be of the following types with the aim to obtain:

(i) the X-ray yield in a single range of photon energy,
(ii) the X-ray yield of a source with a known spectrum,
(iii) a characteristic "temperature" of a source with a known form of the spectrum, and
(iv) the X-ray yield in several ranges and thus a spectrum.

Type (iv) is thus an extension of type (i).

We will give examples of how to use various methods to do each type of analysis. Type (i) analysis may be done by the Ross-filter method, type (ii) may be done using type (i) and back calculation, type (iii), by ratio or fitting method, and type (iv) by the matrix method.

4.3.1 Rose Filter Method

Type (i) analysis: in this case we use at least two filters to make a well-defined range. We first discuss a simple case where we have an X-ray source in vacuum and two filters are chosen, e.g., 16.5 μm Fe and 13.5 μm Co, to form a Ross-filter pair such that photons with energy below the K-edge of Fe the transmission of both

filters are the same. Above the *K*-edge of Fe and below the *K*-edge of Co filter the photon transmission window forms an ideal Ross-filter system. Also, above the *K*-edge energy of Co both filters have the same transmission. In this case we may assign a single value of sensitivity of $\Delta_{21} = S_2 - S_1 = 25$ mC/J to the difference of the two signals.

Let us try theoretically for 922 and 1022 eV X-rays from neon pinch plasma. For this range of photon energy, Fig. 4.18 illustrates that the materials with the nearest *K*-edges are Ne (*K*-edge at 0.874 keV) and Na (*K*-edge at 1.080 keV).

Alternatively, the *L*-edge may be used as shown in Fig. 4.19. In this case, the nearest filters could be Fe and Cu with *L*-edges at 0.846 and 1.09 keV, respectively. If the lines are to be separated, two pairs could be used: (a) Fe (*L*-edge $\sim$ 0.846 keV) and Co (*L*-edge $\sim$ 0.929 keV), and (b) Ni (*L*-edge $\sim$ 1.016 keV) and Cu (*L*-edge $\sim$ 1.09 keV). Unfortunately, the filters need to be very thin and the *K*-edge forms another band pass. This can be corrected for by having yet another set of filters where the X-rays near the *L*-edge are filtered off, perhaps using beryllium or organic filters to get only the X-rays in the *K*-edge band. This can then be subtracted from the filters which pass both the *K*- and *L*-edge bands.

It must be noted that the proposed filters are not easily implemented. Furthermore, the self-absorption from neon would significantly change the sensitivities and thus must be eliminated.

Worked Example

Suppose the filters in Fig. 4.12 were used with a neon plasma and there was an additional e-beam copper X-ray from a plasma focus discharge. Signals were

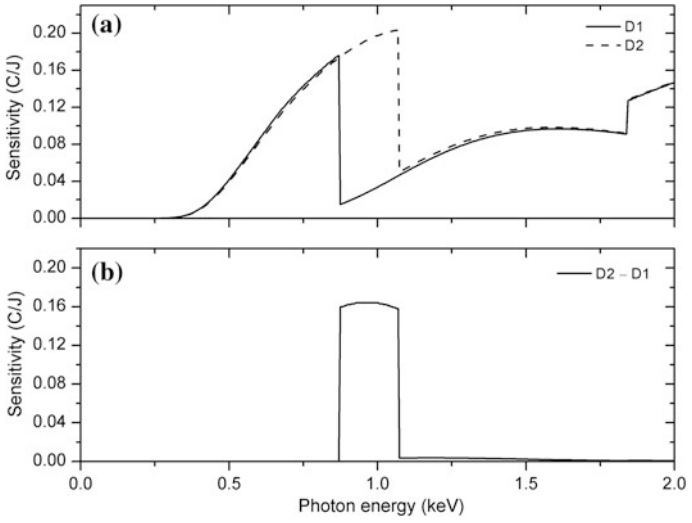

Fig. 4.18 "Ross filters" using *K*-edge D_1 is 0.3 cm-atm Ne and D_2 is 2 μm Na with Si detector **a** sensitivities, **b** difference

simulated for two situations: shot 1 and shot 2. The charges collected by the four X-rays detectors for these two shots are given in Table 4.1. In shot 1 we had 50% of X-rays in the 1 keV range and 1% of X-rays in the 8 keV range, whereas in shot 2 it was 50% in the 1 keV range and 49% in the 8 keV range. The remainder was simulated as a continuous spectrum with an exponential form with characteristic energy of 700 eV.

The sensitivities taken as the average are $\Delta_{21} = 0.12$ C/J and $\Delta_{43} = 0.0023$ C/J. Table 4.2 summarizes the results for X-rays at 1 keV and 8 keV.

This example illustrates some of the difficulties associated with getting accurate and precise measurements. If the signals are large compared to the difference, the detection system may not have sufficient dynamic range to give precise results. For example, for shot 1 the X-rays at 8 keV were found to be zero even though the signals were calculated with 1% X-rays in the 8 keV range. For shot 2 even though the signals were given to two significant figures, the difference signals were only one significant figure.

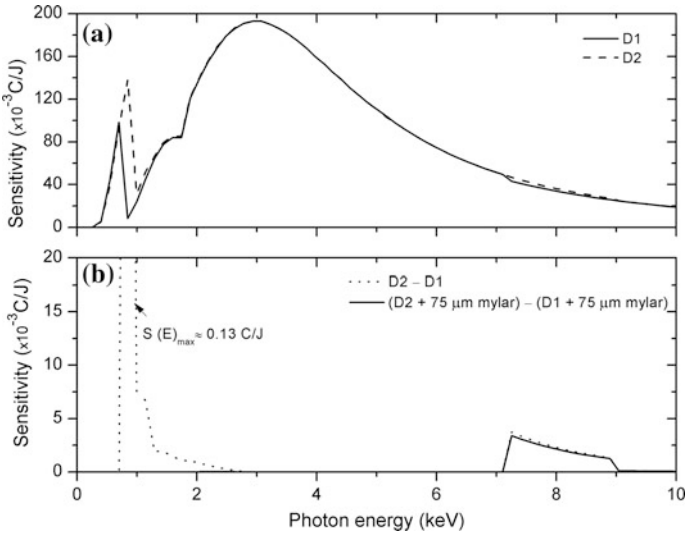

Fig. 4.19 "Ross filters" using *L*-edge D1 is 0.31 μm Fe and D2 is 0.2 μm Cu with Si detector **a** sensitivities, **b** differences with and without additional 75 μm mylar on both filters

Table 4.1 Charge collected by detectors for two different plasma focus shots

	Detector charge (nC)	
	Shot 1 (50,1)	Shot 2 (50,49)
D1	4.9	21
D2	9.7	27
D3	0.75	18
D4	0.75	19

4.3.2 Calculation of Expected Detector Signals Based on Known Spectra

Taking an example of two points: $J(E_1)/J_{\text{total}} = R_1$, and $J(E_2)/J_{\text{total}} = R_2$ where R_1 and R_2 are constants, J corresponds to X-rays incident energy in Joules on the filtered detector, and E_1 and E_2 are the photon energy. Then the charge C is measured as

$$C = S(E_1)J(E_1) + S(E_2)J(E_2) = (S(E_1)R_1 + S(E_2)R_2)J_{\text{total}} \tag{4.27}$$

Thus,

$$J_{\text{total}} = C/(S(E_1)R_1 + S(E_2)R_2), \tag{4.28}$$

where S is the sensitivity of the detector in Coulombs/Joule, which can be extended to any number of points.

This implies that if the spectrum is known then a single detector is sufficient to calculate the X-ray yield. We can get the information about lines from http://physics.nist.gov/PhysRefData/ASD/lines_form.html.

In the examples, the sensitivity to lower energy X-rays is low with the low-cost Al filter. Even with the beryllium (Be) filter, the sensitivity to the lower energy X-rays is low and worse when there is more intervening gas. Table 4.3 gives the sensitivities of the filtered detectors in presence of an intervening gas, for example, a neon (Ne). We can theoretically investigate the effect of a changing spectrum. If a single detector is used, there is no way to detect if the spectrum is changed.

If we have the expected spectrum, then 1 J of X-rays will produce 1.51, 125 and 2.35 mC for the above-filtered detectors (Table 4.3). We calculate the X-ray yield

Table 4.2 Results from analysis

	Difference signal (nC)		Energy on detector (nJ)	
	Shot 1	Shot 2	Shot 1	Shot 2
E (~1 keV)	4.8	5	40	42
E (~8 keV)	0	1	0	435

Table 4.3 Example: filtered detectors and gas fill

Spectrum	Energy (keV)	Sensitivity (mC/J) 25 μm Al (10 mbar-cm Ne)	Sensitivity (mC/J) 5 μm Be (10 mbar-cm Ne)	Sensitivity (mC/J) 5 μm Be (100 mbar-cm Ne)
44%	0.922	0.009	100	0.05
20%	1.022	0.110	126	0.37
36%	1.300	4.11	158	6.88
Average		1.51	125	2.35

for various scenarios with different spectrum to see how we may over or under-estimate the X-ray yield.

There is also possible to combine spectrum with detector sensitivity to obtain useful information about the plasma state such as the electron density and plasma temperature. Assume the number of photons N absorbed at the energy E_p then a spectrum is defined by

$$\frac{dN}{dE_p} = Ae^{-\frac{E_p}{T_e}} \tag{4.29}$$

$$\frac{dN}{dE_p} = BE_p^{-x} \tag{4.30}$$

Fold the spectrum with the response from at least two different filters with negligible sensitivity to low-energy photons.

For these methods, it is possible to make use of the low-cost filters. Unfortunately, it is not easy to interpret the results from this type of analysis. Using the spectrum, it is possible to get an idea of the "temperature". However, if we have a spatially or temporally non-uniform plasma then it is not easy to interpret the meaning of average temperature. In this case, the spectrum obtained by using more than two filters will be reasonable to conclude about the temperature or electron density. For example with three filters, we may calculate two ratios which will allow us to see if the results are consistent . Fig. 4.20 illustrates the spectrum of seven filters made of aluminum.

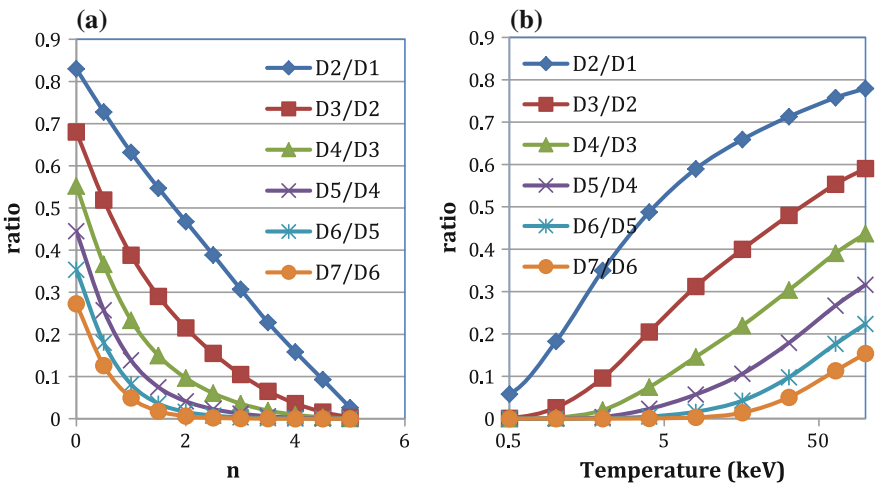

Fig. 4.20 **a** Plot of E_p^{-n} spectrum with 7 filters starting with 25 μm Al, and each subsequent filter thereafter with double the Al thickness. **b** Spectrum ratios versus the temperature

4.3.3 The Inverse Problem: Calculating the Spectra from Detector Signals

In this situation, we have a lot of filters and diodes with known sensitivities, but the spectrum is unknown. In such case, we can deduce the relationship between the X-ray energy spectrum and PIN diode output signals. The signal from the PIN diode is the integral of the X-rays with an energy range determined by the filters. So for a five-channel spectrometer, five intervals are obtained within the energy spectrum, and they can be expressed mathematically as shown,

$$\begin{aligned} S_{11}E_1 + S_{12}E_2 + S_{13}E_3 + S_{14}E_4 + S_{15}E_5 &= Q_{d1} \\ S_{21}E_1 + S_{22}E_2 + S_{23}E_3 + S_{24}E_4 + S_{25}E_5 &= Q_{d2} \\ S_{31}E_1 + S_{32}E_2 + S_{33}E_3 + S_{34}E_4 + S_{35}E_5 &= Q_{d3} \\ S_{41}E_1 + S_{42}E_2 + S_{43}E_3 + S_{44}E_4 + S_{45}E_5 &= Q_{d4} \\ S_{51}E_1 + S_{52}E_2 + S_{53}E_3 + S_{54}E_4 + S_{55}E_5 &= Q_{d5}, \end{aligned} \tag{4.31}$$

where E_i is the energy due to interval i within the energy spectrum range, S_{dj} is the integrated signal from diode j, and A_{ji} is the sensitivity coefficient of diode j in spectral interval i. The units of S_{ji}, E_i and Q_{dj} are C/J, J, and C, respectively.

To obtain the spectrum of the X-ray, we need to solve for E_i, and to do so we can write the above equation in matrix form as

$$SE = Q, \quad \text{hence } E = S^{-1}Q \tag{4.32}$$

Taking the example of the Type (i)—"ideal filters" the solution is simple

$$\begin{aligned} S_{11}E_1 + 0 + 0 + 0 + 0 &= Q_{d1} \\ 0 + S_{22}E_2 + 0 + 0 + 0 &= Q_{d2} \\ 0 + 0 + S_{33}E_3 + 0 + 0 &= Q_{d3} \\ 0 + 0 + 0 + S_{44}E_4 + 0 &= Q_{d4} \\ 0 + 0 + 0 + 0 + S_{55}E_5 &= Q_{d5} \end{aligned} \tag{4.33}$$

$$S = \begin{pmatrix} S_{11} & 0 & 0 & 0 & 0 \\ 0 & S_{22} & 0 & 0 & 0 \\ 0 & 0 & S_{33} & 0 & 0 \\ 0 & 0 & 0 & S_{44} & 0 \\ 0 & 0 & 0 & 0 & S_{55} \end{pmatrix} \tag{4.34}$$

And the inverse matrix is

$$S^{-1} = \begin{pmatrix} S_{11}^{-1} & 0 & 0 & 0 & 0 \\ 0 & S_{22}^{-1} & 0 & 0 & 0 \\ 0 & 0 & S_{33}^{-1} & 0 & 0 \\ 0 & 0 & 0 & S_{44}^{-1} & 0 \\ 0 & 0 & 0 & 0 & S_{55}^{-1} \end{pmatrix} \tag{4.35}$$

And therefore,

$$E_n = \frac{Q_{dn}}{S_{nn}} \tag{4.36}$$

Using Type (ii) filters, i.e., Ross-filter pairs such that filters 1 and 2 make a Ross-filter pair, 2 and 3 make a pair and so on, we can simulate the "ideal filters" situation by converting the n signals into $n - 1$ signals with each new signal given by:

$$D_i = S_{di+1} - S_{di} \tag{4.37}$$

And the spectrum can be obtained as in the "ideal filter" case but with one less energy range.

$$S = \begin{pmatrix} S_{11} & S_{12} & S_{13} & S_{14} & S_{15} \\ S_{21} & S_{22} & S_{23} & S_{24} & S_{25} \\ S_{31} & S_{32} & S_{33} & S_{34} & S_{35} \\ S_{41} & S_{42} & S_{43} & S_{44} & S_{45} \\ S_{51} & S_{52} & S_{53} & S_{54} & S_{55} \end{pmatrix} \tag{4.38}$$

It may be difficult to obtain exact Ross-filter pairs over a large energy range. To match the transmission from one filter to another requires selecting specific thicknesses which may not be easily available. One method for doing so involves the creative use of adding foils together to make one composite filter. This is difficult however when very soft X-rays are to be detected using the thinnest possible foils. As a last option, we may use Type (iii) filters where there is no obvious way of analysis. However, filter ranges have to be chosen very carefully to avoid singular matrices. These filters must have spectral response shapes which are significantly different from each other in the energy range of interest. The inverse matrix may be found using the Excel function MINVERSE.

4.3.4 Error Analysis

Some basic sources of errors in X-rays yield measurements can be categorized into three major categories (1) analysis errors, (2) measurement and equipment errors, and (3) physical assumption errors.

Analysis errors: designing the X-ray spectrometer based on the Ross-filtering technique often leads to an error in X-rays yield measurement due to tails in S (E) of a detector at the desired range of X-rays. This error can be calculated by

$$\delta = \left(\int_{E_{min}}^{E_{k1}} |S| \mathrm{d}E + \int_{E_{k2}}^{E_{max}} |S| \mathrm{d}E \right) / Q, \tag{4.39}$$

where $Q = \int_{E_{k1}}^{E_{k2}} |S| \mathrm{d}E$ is from a Ross-pair filter with K-edge energies of E_{k1} and E_{k2}. Take the example of an X-ray source in a vacuum and its detection with two filters 16.5 μm Fe and 13.5 μm Co as a Ross-filter pair. This is a situation very close to that obtained by the ideal detector and filter in the range of soft X-rays, i.e., $E_{\min}$ = 1 keV and $E_{\max}$ = 15 keV. However, the effect of tails is about 3% below and 6% above the passband sensitivity of a detector as shown in Fig. 4.21.

The effect of tails in error calculation can be minimized by adding a thin filter into a second filter also known as a compensation filter in a Ross-pair system [24]. Another source of error in X-ray analysis is the X-ray cross-section table database itself, which includes uncertainty in the cross-section, photon energy and the resolution.

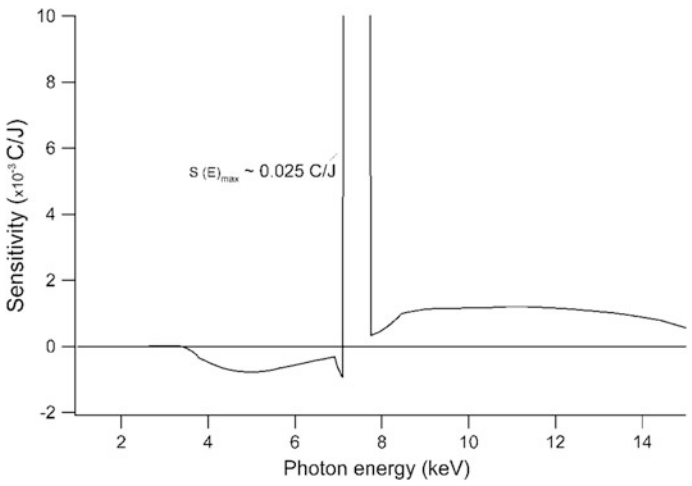

Fig. 4.21 Sensitivity of a Ross-pair filter system (16.5 μm Fe and 13.5 μm Co)

Table 4.4 Comparison of different detector systems (D1 and D2) to errors in spectrum analysis

Spectrum (assumed, actual)	Energy (keV)	D1 sensitivity (mC/J)	D1 error (%)	D2 sensitivity (mC/J)	D2 error (%)
44%, 33%	0.922	0.009	90	100	46
20%, 15%	1.022	0.110	90	126	46
36%, 52%	1.300	4.11	1	158	25
Total			43		9
Average		1.51		125	

D1 has 25 μm Al filter with 10 mbar-cm Ne gas and D2 has 5 μm Be with 10 mbar-cm Ne gas

Measurement and equipment errors: the X-ray filtered detector has some uncertainties in its system such as uncertainty of the filter thickness, dead layer thickness uncertainty, and uncertainty of measurements (detector readings). X-ray detection from pulsed power plasma sources such as plasma focus is more complicated due to the background gas fill pressure. Background gas fill pressure may make significant contributions to X-rays error analysis if self-absorption is important.

Assumption errors: another source of error in X-ray analysis of plasma is uncertainty in source size, shape, and location assumptions. The assumed spectrum may have additional peaks due to impurities, and the spectrum may change due to changes in temperature and density.

In general, to do the error analysis, it makes sense to identify the major sources of uncertainty to reduce complexity. Due to the complexity of measurement and analysis methods, we will give an example of analysis for one specific scenario. In this example, we investigate the effect of a 25% difference in the assumed spectrum. We consider the use of one filter to measure X-rays from neon, and compare the sensitivity to errors in the spectrum with other filters, i.e., 25 or 5 μm Al.

Table 4.4 summarizes the results. If there is a 25% decrease in the amount of X-rays at 922 and 1022 eV, the analysis of the 25 μm Al filter shows that we will overestimate the 922 and 1022 eV lines by 90%, underestimate the 1300 eV band by 1% and overestimate the total yield by 43%. This uncertainty may not be a lot if we are interested in the total yield, or the 1300 eV band. However, if we are interested in the in-band yield of only the 922 eV line, then it is a big uncertainty.

With the 5 μm Be filter we can see that the uncertainties are not as pronounced as they are with the 25 μm Al filter for the low-energy lines because of the filter sensitivity to these X-ray energies.

4.4 Summary and Conclusion

The combination of high density and temperature that occurs during the compression phase makes pulsed plasma focus device a very attractive source for the production of intense X-ray radiation in the pinching mode. The spectrum and

intensity of the emission can be controlled by changing external parameters such as current, voltage, dimensions of the device, and the composition and pressure of a filling gas of the plasma focus. In this chapter, we discussed different techniques for detecting X-ray radiation with a specific aim to provide a convenient way to diagnose the plasma without disturbing it. The simplest time-integrated X-ray detector is a pinhole imaging camera which consists of either single or multiple pinholes. These pinholes are covered with light blocking filters with known X-ray transmission characteristics. For a plasma focus device, the field of view of the imaging camera needs to include the pinch region as well as the anode end rim. Using metallic coated plastic filters such as silver- and aluminized mylar combined with a ratio method, several tens of eV temperatures can be measured with a good accuracy.

Bremsstrahlung and recombination are the main mechanisms for X-rays emission from hot plasmas. Line radiation also presents depending on the species and temperature of a plasma. In plasma focus device, the main source of line radiation is the interaction of the electron beam from the focus region with the anode, which is typically made of copper. When electrons of energy 10–100 keV are directed onto a Cu target, the dominant line radiation is Kα, which is of energy 8.05 keV. The temperature of the pinch plasma typically lies in the range of 0.5–10 keV. The spectrum consists of X-ray flux of different energy photons can be evaluated with careful selection of filtering technique. Detectors such as PIN diodes or photographic film do not discriminate the energy of the incident photons and instead, they exhibit energy-integrated behavior. Thus, a PIN diode signal at any given instant represents photons of different energies originating from the plasma. A pair of filters (i.e., Ross filter) is a simple technique to give a crude analysis of the X-ray regime. The sensitivity of a detector such as that of PIN diode is not the same for photons of different energy. It is important to include the detector's response to a specific energy of the photon. For an accurate interpretation of the X-ray signal, several error analysis techniques should be applied during an evaluation of the X-ray data.

References

1. L.E. Etter, Am. J. Roentgenol Radium Ther. **54**, 547 (1945)
2. www.nrl.navy.mil/ppd/content/nrl-plasma-formulary
3. T.P. Donaldson, R.J. Hatcheon, M.H. Key, R.J. Urguhart, J. Phys. B **9**, 1645 (1976)
4. M. Swartz, S. Kastner, E. Rothe, W. Neupert, J. Phys. B **4**, 1747 (1971)
5. M. Gersten, J.E. Rauch, J. Appl. Phys. **53**, 1297 (1982)
6. E. Baronova, B. Bucher, D. Haas, D. Fedin, A. Stepanenko, F.N. Beg, Rev. Sci. Inst. **77**, 103104 (2006)
7. K. Hirano, N. Hisatome, T. Yamamoto, K. Shimoda, Rev. Sci. Instrum. **65**, 3761 (1994)
8. R.H. Huddlestone, S.L. Leonard, *Plasma Diagnostic Techniques* (Academic Press, New York, 1965), p. 362
9. V.M. Geoffrey, *Plasma Spectroscopy* (Elsevier Publishing Company, London, 1968), p. 221
10. D. Giulietti, L.A. Gizzi, Rivista del Nuovo Cimento **21**, 1 (1998)

11. I.Y. Tolstikhina, S.S. Churilov, A.N. Ryabtsev, K.N. Koshelev, in *EUV Sources for Lithography,* ed. by V. Bakshi (SPIE Book, Bellingham, 2006), p. 118
12. W. Wang, A. Patran, S. Lee, P. Lee, Sing. J. Phys. **17**, 27 (2001)
13. D. Wong, A. Patran, T.L. Tan, R.S. Rawat, P. Lee, IEEE Trans. Plasma Sci. **32**(6), 2227 (2004)
14. T.K. Borthakur, S.R. Mohanty, H. Bhuyan, V.N. Rai, Indian J. Phys. **75**, 455 (2001)
15. J.M. Bayley, G. Decker, W. Kies, M. Malzig, F. Muller, P. Rowekamp, J. Westheide, Y.V. Sidelnikov, J. Appl. Phys. **69**, 613 (1991)
16. C.S. Wong, *Five Channel Diode X-ray Spectrometer, Instruction Manual, ICACUM/DXS-3*, (University of Malaya, Malaysia, 1992)
17. B.L. Henke, E.M. Gullikson, J.C. Davis, At. Data Nucl. Data Tables **54**, 181 (1993)
18. D.J. Johnson, Rev. Sci. Instrum. **45**, 191 (1974)
19. http://physics.nist.gov/PhysRefData/XrayMassCoef/cover.html
20. http://henke.lbl.gov/optical_constants/
21. S. Hussain, M. Shafiq, M. Zakaullah, Appl. Phys. Lett. **96**, 031501 (2010)
22. L.A. Shmaenok, C.C. de Bruijn, H.F. Fledderus, R. Stuik, A.A. Schmidt, D.M. Simanovski, A.V. Sorokin, T.A. Andreeva, F. Bijkerk, in *Proceedings of SPIE 3331*, 1998, p. 90
23. D.N. Ruzic, in *EUV Sources for Lithography*, ed. by V. Bakshi (SPIE Book, Bellingham, 2006), p. 970
24. I.V. Khutoretsky, Rev. Sci. Inst. **66**(1), 773 (1995)

Chapter 5
Pulsed Plasma Sources for X-ray Microscopy and Lithography Applications

Syed M. Hassan and Paul Lee

5.1 Introduction

The use of high-energy photons ranging from vacuum ultraviolet to hard X-rays is emerging as an area of primary importance in both research and industry for many fields such as biology, biochemistry, crystallography, micro-lithography, non-destructive control, ballistics, cine-radiography, studies of plasma dynamics, etc. The generation of an electromagnetic (EM) wave with short wavelengths directly from a transient motion of electrons needs the acceleration of these electrons to be large to create a fast, electric field transient. Radiation from synchrotrons, undulators and wigglers are based on the acceleration of the relativistic electrons [1]. These are excellent systems to produce photons for the whole or part of the energy range with characteristics of a short pulse duration, high flux and high brilliance. Though best scientific and technological systems for X-ray generation, these devices are expensive and do not meet the criteria of compactness and easy access. Dense plasmas with high temperature are sources of ionized media that can give rise to X-ray emission. Photons with wavelength in the range of few nanometers are also known as extreme ultraviolet radiation (EUV). Technological advancement in the pulsed power, particularly in the energy storage and fast switching areas, made the discharge-based plasma devices an interesting alternative to both coherent and incoherent radiation sources. Discharge plasma devices also fulfil the requirement of compactness that can be operated easily for the study and development of plasma-based radiation sources.

Measurements of X-rays can give information about plasmas. The emission of X-rays from pulsed plasma is characterized by high intensity, extremely short

S.M. Hassan · P. Lee (✉)
NSSE, National Institute of Education, Nanyang Technological University, Singapore 637616, Singapore
e-mail: paul.lee@nie.edu.sg

S.M. Hassan
LPP Fusion Inc, Middlesex, NJ 08846, USA

R.S. Rawat (ed.), *Plasma Science and Technology for Emerging Economies*,
DOI 10.1007/978-981-10-4217-1_5

duration of radiation emission and wide spectral range. The pinched plasma structure emitting X-rays has some distinct characteristics which are suitable to be used as a pulsed point source for some special applications such as X-rays radiography, X-rays microscopy and X-rays lithography. In this chapter, we highlight some of the most important applications of X-ray emission from dense plasma focus.

5.1.1 Pinch Plasma X-ray Sources

Emission of radiation at shorter wavelengths such as EUV and X-rays demands hot and dense plasma, which is not possible by an ordinary lamp discharge, a spark or flash. However, the self-compression of cylindrical plasma by the azimuthal magnetic field generated by the axial discharge current can convert a low-temperature and low-density plasma to the hot, and high-density plasma. Such phenomenon of compression of plasma by magnetic fields is called the pinch effect, and the compressed plasma is known as pinch plasma. The pinch plasma column in the steady state can be derived by setting the velocity and time-derivatives to zero in the ideal magnetohydrodynamic (MHD) equation [2] and in Maxwell equations. Magnetostatic equations for perfectly conducting plasma are:

$$\vec{\nabla}P - \vec{J} \times \vec{B} = 0,\ \vec{\nabla} \times \vec{B} = \mu_o \vec{J},\ \vec{\nabla} \cdot \vec{B} = 0 \tag{5.1}$$

where P is the momentum, $\vec{J}$ represents current density and $\vec{B}$ is the magnetic field. In the cylindrically symmetric plasma column, all the quantities are the function of r. Substituting $\vec{J}$ from second equation into the momentum equation if there is no external magnetic field, i.e. $B_z = 0$, we obtain

$$\frac{\mathrm{d}}{\mathrm{d}r}\left(P + \frac{B_\varphi^2}{2\mu_0}\right) + \frac{1}{r}\frac{B_\varphi^2}{\mu_0} = 0 \tag{5.2}$$

In above equation, the derivative terms are the plasma kinetic pressure and the magnetic pressure, and the second term describes the tension force generated by the curvature of the magnetic field lines. Applying the Ampere's law, $B_\varphi(r) = \frac{\mu_0 I(r)}{2\pi r}$, we get

$$\frac{\mathrm{d}P}{\mathrm{d}r} + \frac{\mu_0}{8\pi^2 r^2}\frac{\mathrm{d}I^2(r)}{\mathrm{d}r} = 0 \tag{5.3}$$

Assuming the uniform current density J_z in the plasma column, I_o the total current flowing through the pinch with the radius R of the pinch plasma column. Integration simplifies the above equation to

$$\frac{\mu_o I_o}{8\pi} = 2\pi \int_0^R P(r) r \mathrm{d}r \tag{5.4}$$

Taking the Bennett temperature [3] relation, we have

$$T_{\mathrm{B}}(eV) = \frac{2\pi}{N_i(1+Z_{\mathrm{eff}})} \int_0^R P(r) r \mathrm{d}r \tag{5.5}$$

where Z_{eff} is the average degree of ionization and N_i ($= 2\pi \int_0^R n_i(r) r \mathrm{d}r$) is the ion line density.

From above equations, the Bennett condition of equilibrium can be described as

$$T_{\mathrm{B}} N_i (1+Z_{\mathrm{eff}}) = \frac{\mu_o I_o}{8\pi} \tag{5.6}$$

It is clear that the pinch plasma column under the steady state condition is a force balance between plasma thermal pressure and magnetic field pressure. The isothermal plasma temperature ($T_{\mathrm{B}} = T_e = T_i$) in such magnetic self-focusing plasma with electrical current flow (I) can be expressed as

$$T_e = \frac{\mu_0 I^2}{8\pi(Z_{\mathrm{eff}}+1)N_i} \tag{5.7}$$

The minimum requirement for generation of soft X-ray of wavelength of about 13 nm or EUV for lithography purposes is a plasma temperature T_e of 20 eV. For this temperature, the current I is required to be 20 kA for a gas such as xenon [4], and the plasma cylinder must be compressed to about 1 mm diameter sphere by a pressure of 2000 bar generated by the magnetic field of 20 T. It is important to note that a stable plasma cylinder has a resistance of 50 mΩ heated with some 10 MW due to its ohmic resistance. The heating of the plasma decreases the current significantly after several hundred nanoseconds. Thus, the operation of plasma device should be in a pulsed regime with a total energy of 10 J for 20 kA discharge current for EUV radiation.

Plasma focus as a pinch device produces a broad spectrum of X-rays in tens of nanosecond duration. At the open end of a coaxial electrode system, rapid magnetic compression of a plasma column is formed by the discharged current itself. Low energy X-rays of few hundreds of eV can be formed from the plasma while the high-energy X-rays are emitted from the anode surface by the interaction of fast electron beam with the anode material. The spectrum and intensity of X-rays emission are mainly dependent on the composition of a seed gas, discharge current

and dimensions of the device. X-ray as a non-destructive diagnostic technique provides the information of plasma and most importantly the dimension of the emitting regions and their locations.

5.1.2 X-ray Production and Evaluation Mechanisms

X-rays produced in high-energy plasmas are the usual Bremsstrahlung and recombination continua of ionized gases and line emission of the 'optical' spectral type. When the plasma temperature exceeds few hundreds of eV, the wavelengths of radiation becomes shorter and falls in the X-ray region. Considering only the continuum (Bremsstrahlung) radiation, the maximum wavelength is given by

$$\lambda_{\max}(\dot{A}) = \frac{6200}{k_B T_e(eV)} \tag{5.8}$$

A property of the free–free emission is that for long wavelength ($\lambda \gg hc/k_BT_e$), the spectral shape is independent of T_e, however, for short wavelength (i.e. $\lambda \leq hc/k_BT_e$ or $h\nu \geq k_BT_e$) the spectrum is strongly temperature dependent, at T_e = 1 keV, the spectrum peaks at $\lambda_{\max}$ = 6.2 Å, which is in the soft X-ray region.

For high-Z focus plasma, the characteristic line emission also falls in the soft X-ray region. For example, for highly ionized argon and neon plasma at a sufficiently high temperature, the wavelengths of K_α lines are 4.2 and 12.13 Å, respectively.

The emission of X-rays from plasma was first observed [5] around 1930 in high-voltage vacuum sparks. The Plasma Focus (PF) device as a coaxial plasma gun has been studied in many countries since 1960s. This gun is usually filled to a pressure of few Torr with some suitable gas and is driven by a high voltage (>10 kV) and high-current (>50 kA) capacitor bank. During operation, intense X-ray bursts are emitted from plasma focus devices. The plasma focus emits both soft (thermal) as well as hard (non-thermal) X-rays as described in previous X-ray diagnostics chapter. The emission of thermal X-rays in plasma focus can be divided into three processes: bremsstrahlung, recombination and line radiation. Bremsstrahlung gives a continuum spectrum due to free–free transition of electrons and ions interacting in the Coulomb field; recombination radiation also falls into continuum spectrum of X-rays when free electron loses its energy on recombination with an ion; and line radiation gives the characteristic of material when a bound electron loses energy by falling into a lower ionic energy state. The relative strengths of the emission depend on the temperature and gas species of the plasma. The continuum emission dominates for high-Z plasma and line emission is stronger from low-Z plasma. Therefore, X-rays detection is considered an important diagnostic tool for studying the properties of plasmas. Analysis of the X-ray spectrum related to the time history, the continuum shape and the identification and measurement of the intensities and profiles of different lines provides information about

the electron and ion temperatures and temperature histories, the plasma composition and density, and the degree of thermalization. The emission of X-rays from the plasma focus is studied with various diagnostic techniques: these include pinhole cameras (with one or multiple pinholes covered with appropriate filters) for recording the time-integrated spatial/spectral distribution of the X-ray emitting region; microchannel plates in conjunction with pinhole cameras for resolved spatial distribution of soft X-rays; semiconductor detectors with appropriate filters for space-integrated temporal/spatial distribution of the soft X-ray emission; crystal X-ray spectrographs for space-resolved line spectrum analysis; X-ray streak photography for temporal distribution of the X-rays in one space dimension (radial or axial); and X-ray films resists and X-ray pulse calorimeters for absolute soft X-ray yield measurements.

For effective use of dense plasma focus (DPF) device for X-ray applications, it is essential that different parameters should be investigated systematically and comprehensively. Zakaullah research group [6] reported that the good radiation yield is strongly dependent on the anode shape and filling gas. Several efforts have been made to study hard X-ray emission in the plasma focus devices including the insertion of high-Z materials at the anode tip. The hard X-ray pulses produced by the interaction of localized electron beams at the anode tip. The X-ray emission from Ne operated plasma focus is many times more intense than that measured for operation in pure deuterium. Scaling laws relating the soft X-ray yield to peak discharge current and peak axial velocity have been reported by Serban et al. [7]. Several research groups [8–10] reported the scaling laws for either total X-ray yield or soft X-ray yield. Table 5.1 summarizes X-ray yield scaling to peak discharge current and capacitor bank energy. A general soft X-ray scaling is given by the numerical experiments based on the Lee Model Code [11] and is described in the next section.

5.1.3 Numerical Simulation—Tools for Radiation Source Optimization

The X-ray emission from DPF (Dense Plasma Focus) is characterized by high intensity and a wide spectral range which can be controlled by following the scaling law of X-rays. In the last few years, various research groups tried to enhance the X-ray yield in the range of 0.25–50 keV photons by changing various experimental parameters such as bank energy, discharge current [11], electrode configuration (shape and material) [6, 12], insulator material and dimensions [13, 14], gas composition and filling gas pressure [15, 16] and pre-ionization assisted breakdown [17]. Any practical plasma-based radiation source needs an optimization for its peak performance. For example, computer simulation of DPF needs the link between the computation and physical reality by fitting the computed current waveform to a measured current waveform due to non-perfect mass swept up. The Lee

Table 5.1 X-ray scaling law for different plasma foci

Researchers [Ref.]	Anode/material insert	Gas	Bank energy	Scaling Law	
				K-radiation (J)	Total X-ray (J)
Serban and Lee [7]	Cu	D_2	3 kJ	$\sim Y_{sxr} \sim I^{2.0–4.0}$	
Filippov et al. [8]	…	Ne	0.9 MJ		$\sim I_{pinch}^{3.5–4.0}$
Sharif et al. [9]	Cu	Ar	0.6–1.8 kJ	$\sim [I(100\ \text{kA})]^{3.5–4.5}$ $\sim [E\ (\text{kJ})]^{3.5–4.5}$	$\sim [I(100\ \text{kA})]^{4.5–5.5}$ $\sim [E\ (\text{kJ})]^{4.5–5.5}$
	Cu	Ar	2.3–4.6 kJ	$\sim [I(100\ \text{kA})]^{2.9–3.3}$ $\sim [E\ (\text{kJ})]^{2.1–2.2}$	$\sim [I(100\ \text{kA})]^{4.3–4.8}$ $\sim [E\ (\text{kJ})]^{2.8–3.7}$
Sharif et al. [10]	Mo	Ar	2.3–4.6 kJ	$\sim [I(100\ \text{kA})]^{2.4–3.0}$ $\sim [E\ (\text{kJ})]^{1.8–1.9}$	$\sim [I(100\ \text{kA})]^{4.2–4.6}$ $\sim [E\ (\text{kJ})]^{2.7–3.6}$
	W	H	2.3–5.3 kJ	....	$\sim [I(100\ \text{kA})]^{3.3–3.9}$ $\sim [E\ (\text{kJ})]^{2.4–2.5}$

computational models of DPF developed by the Sing Lee have been successfully used for several projects [18, 19].

Lee model code uses a five phase model: an axial phase treated as snow-plow; a radial inwards shock phase using slug model; a radial reflected shock phase with the reflected shock moving to hit radially incoming current sheath 'piston'; followed by a radiative slow compression phase also known as pinch phase and finally, an evolution of discharge current waveform is completed by an expansion phase in axial direction. The transitions from axial to radial phases and vice versa is the most complicated part in modelling. The discharge current waveform is the necessary diagnostics tool which contains information on all the dynamics and radiation processes that occur in the various phases of the DPF. This multi-phase Lee model code requires physical dimensions of the electrodes, information about input energy and operating gases. It was initially designed to optimize the operation of UNU/ICTP DPF [20, 21], but later extended to NX2 [11], NX1 [22], FMPF3 [23] and many other plasma foci around the globe. The Lee code can give important plasma parameters of DPF operating with various gases such as D, D–T, N, He, Ne, Ar, Kr and Xe. Radiation-coupled motion and radiation absorptions are included in the modelling to extend the DPF device for X-rays. A recent development includes soft X-ray [22] scaling laws over a wider range of energies. The radiation from plasma is the usual bremsstrahlung and recombination continua of ionized gases or target materials and line emission from different ionic species which are not fully stripped. The total power emission in the form of radiation from plasma is highly dependent on various assumptions made about the state of plasma. The spectral radiation data in the soft X-ray region from neon operated 3.3 kJ UNU-ICTP

plasma focus device is reported to 64% in the line radiations at 922 eV (Ly-α) and 1022 eV (He-α) in the spectral range 1–1.3 nm and the remaining spectrum falls mainly in the category of recombination radiations. The contribution of line radiation from NX2 plasma focus device is about 80%. In the Lee model, neon soft X-ray (Y_{sxr}) is simply equivalent to line radiation yield (Q_L):

$$\frac{\mathrm{d}Q_L}{\mathrm{dt}} = -4.6 \times 10^{-31} n_i^2 Z Z_n^4 \left(\pi r_{\mathrm{p}}^2\right) z_{\mathrm{f}} / T \tag{5.9}$$

The X-ray yield generated by pinch plasma is the integration over the entire pinch duration. It is obvious that the radiation yield from DPF is dependent on the plasma properties such as the effective charge number Z, gas atomic number Z_n, number density n_i, pinch length z_{f}, pinch radius r_{p}, temperature T, and the pinch duration.

Liu et al. [24] and Bing et al. [25] have shown that a pinch compression reaching to a temperature about 200–500 eV is suitable for a high neon soft X-ray yield. By using Lee model, Lee et al. [11] and Saw et al. [22] figured out numerically the optimum configuration of the electrodes for the 3.3-kJ UNU/ICTP-PFF capacitor system that can give a yield of Y_{sxr} = 9.5 J, a two- to three-fold increase in the Y_{sxr} from the standard UNU/ICTP-PFF. Scaling laws for neon X-ray have been defined for plasma focus machines with storage energy E from 0.2 kJ to 1 MJ. The soft X-ray yield from low energy plasma machines is $Y_{\mathrm{sxr}} \sim E^{1.6}$. At higher DPF device storage energy of about 1 MJ, the radiation yield saturation starts and soft X-ray scales as $Y_{\mathrm{sxr}} \sim E^{0.8}$. The scaling laws for plasma focus machines are typically defined by its peak discharge current I_{peak}, but numerically it is possible to define it by focus pinch current I_{pinch}. For soft X-ray, Y_{sxr} scaling laws are found as $Y_{\mathrm{sxr}} \sim I_{\mathrm{peak}}^{3.2}$ (0.1–2.4 MA) and $Y_{\mathrm{sxr}} \sim I_{\mathrm{pinch}}^{3.6}$ (0.07–1.3 MA) [11].

5.2 Pinch Plasma Sources for X-ray Microscopy

Generating X-rays of short pulse duration and a wide range in photon energy gained importance in past few years due to advancement in pulsed power technologies. These pulsed sources are used for various applications, for example, radiography of live biological specimen, dynamical studies of biomedical systems, non-destructive testing of material structures, the performance testing of electronic devices in the harsh environment, sterilization of food, crops and/or biologically active tissues, time-resolved analysis of atomic and molecular systems, various transmutation of organic material and fluorescence studies.

In plasma focus device, the production of hard X-ray of few nanosecond duration is attributed to a bombardment of the central electrode from instability accelerated energy electron beams. The high power of the X-ray pulses makes the

plasma focus device the best choice for X-ray radiography and microscopy due to its simplicity, versatility, compactness, cost-effectiveness and easy maintenance.

5.2.1 Soft X-ray Radiography

The UNU/ICTP plasma focus (PF) facility [7] with the typical parameters C_0 = 30 μF, L_0 = 119 nH, V_0 = 14 kV and I_0 = 170 kA has been widely used to study a variety of plasma phenomena. The 3 kJ PF device with neon and argon filling gases has been studied by the Zakaullah et al. [12]. X-ray generation with wall plug efficiency of 4% was obtained. At Plasma Radiation Sources Laboratory (PRSL), National Institute of Education, Nanyang Technological University, Singapore [26], soft X-ray emission efficiency up to 5.6% from 3 kJ low inductance/high-current PF system has been achieved. Rawat et al. [27] used 3 kJ PF machine with neon fill for imaging the insect and other biological objects. A CCD-based soft X-ray pinhole (35 μm) camera system, as shown in Fig. 5.1, was used to obtain images of the soft X-ray emitting zone of focused plasma column.

The details of the various parts of an insect as the biological sample were obtained by using neon soft X-rays of energy (900–1550 eV) from plasma device. The head, prothorax and antennae of the insect can be seen in X-rays images as shown in Fig. 5.2. It is clear that the capacity of soft X-rays by pulsed DPF device can be used to get X-ray images of small objects which are too thin to be imaged by hard X-rays. Better resolution in the image is highly dependent on the pinhole size and base pressure in the X-ray detection chamber.

Another example of soft X-ray imaging is the radiograph of the epidermal peel of the Crassula leaf joins with the thicker area of the sample, as shown in Fig. 5.3. The epidermis region is clearly visible but the soft X-ray is completely absorbed by the grass blade. The variable contrast in the radiograph is clearer in the area of uneven peeling of the epidermal layer of Crassula leaf.

5.2.2 Hard X-ray Radiography

A pulsed plasma device can also be used to take clear radiographs of metallic objects, either moving or stationary. The major advantage of X-rays from pulsed plasma is the extremely short duration of radiation emission in nanoseconds time duration which gives the exposure time of about six orders of magnitude shorter than conventional X-ray sources. The controllable parameters of X-rays emission from plasmas and together with the degree of penetration of the radiation contribute to high-quality X-ray images of thick objects. The main mechanism of hard-ray production from plasma focus device is the bremsstrahlung radiation produced by

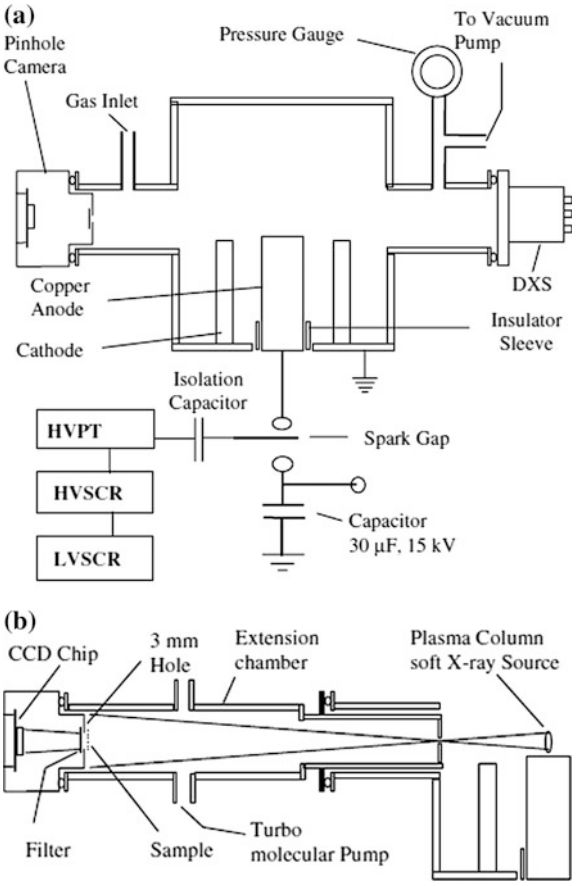

Fig. 5.1 **a** Schematic of plasma focus device for soft X-ray pinhole imaging of focused plasma column. **b** Modification of experimental arrangement for soft X-ray projection imaging. Reprinted from Rawat et al. [27] Soft X-ray Imaging using a Neon Filled Plasma Focus X-ray Source, Copyright (2005), with permission from Springer Publishing Company

the collision of a collimated electron beam with the anode bottom. Further enhancements of hard X-ray emission from a low energy DPF (e.g. UNU/ICTP machine) requires a high-Z material insert such as lead, tungsten or molybdenum at the tip of a solid anode. A lead blanket at the bottom of an anode region can also serve as a high-Z target for the electron beam. An exhaustive study on X-ray characteristics from a plasma focus device in a range of 3 kJ (UNU/ICTP-PFF device, AAAPT) has been conducted by a group of researchers led by Zakaullah [28]. This group investigated X-ray emission from a 2.3 kJ plasma focus device, energized by a 32 μF single capacitor charged at 12 kV, with high-Z inserts at the anode tip. Specifically, the X-ray emission in the 5–9 and 13–25 keV energy ranges were studied. The maximum value of the total X-ray emission in 4π-geometry was reported around 29.4±0.2, 4.00±0.02 and 3.43±0.05 J with a Pb, Mo and W inserted anode, respectively, and the corresponding wall plug efficiencies were 1.28, 0.20 and 0.15%. However, for a radiographic purpose, a high voltage of more

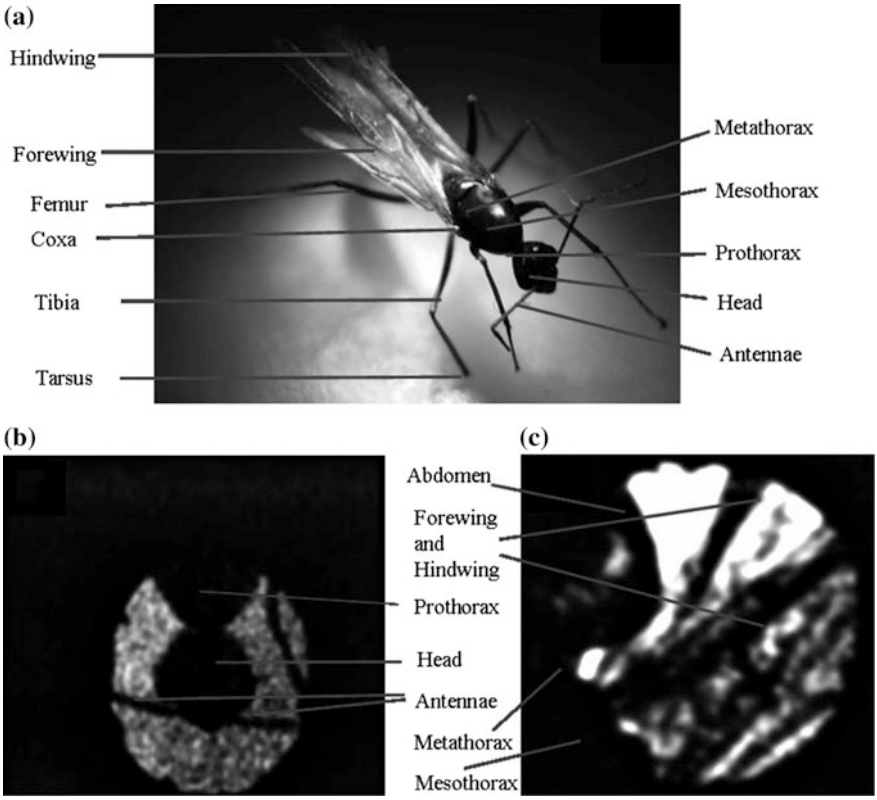

Fig. 5.2 **a** Visible light photo of an insect, **b** soft X-ray image of frontal part of insect and **c** soft X-ray image of abdomen and wings of the insect. Reprinted from Rawat et al. [27] Soft X-ray Imaging using a Neon Filled Plasma Focus X-ray Source, Copyright (2005), with permission from Springer Publishing Company

than 15 kV was required to operate the pinch plasma device. By increasing the charging voltage, the contribution of high-energy X-rays increased abruptly. Hussain et al. [29] reported 0.025% efficiency in the X-ray window 13–25 keV with 12 kV charging voltage but recorded an increase by an order of magnitude to a value of 0.25% at 20 kV charging voltage. Even a low energy PF device with kilojoules, but capable of operating with a high voltage (>20 kV) can generate a higher yield of pulsed X-ray. A conventional PF anode is made of copper but high reproducible X-ray with less damages to the anode by electron bombardments is possible with high-Z insert. This observation clearly shows an effective way of pulsed X-ray emission from a high-Z target in comparison to a compact diode [30]. It is speculated that the plasma contains high-Z vapours which significantly contributes to high X-ray emission. The latter explanation is supported by the measurement of high X-ray emission from a PF when a small amount of a high-*Z* gas is

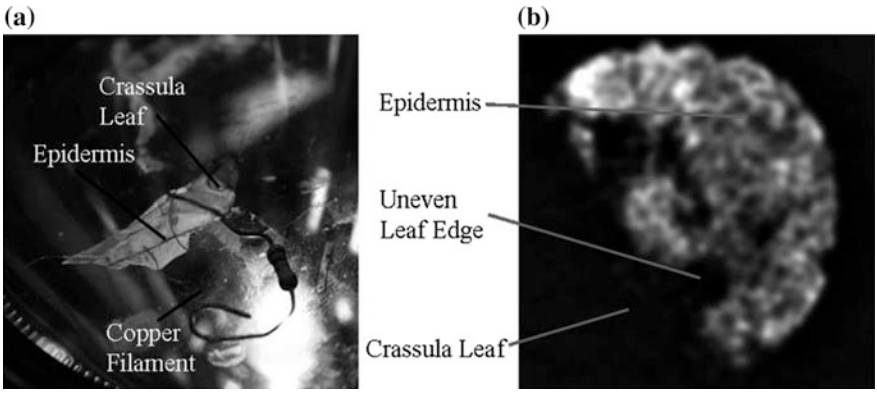

Fig. 5.3 **a** Visible photograph and **b** X-ray radiograph of Crassula leaf. Reprinted from Rawat et al. [27], Soft X-ray Imaging using a Neon Filled Plasma Focus X-ray Source, Copyright (2005), with permission from Springer Publishing Company

introduced. Figure 5.4 shows the experimental setup for a high X-ray yield from a low energy PF (1.8 kJ, 20 kV) with various shapes of lead (Pb) inserted anode. The X-ray flux was measured as a function of the filling gas pressure for each anode shape in windows of 5–9, 7.7–9 and 13–25 keV energy ranges. At 0.75 and 0.5 mbar hydrogen, the maximum X-ray flux of 1.36±0.06 and 2.70±0.11 J/sr were estimated for cylindrical and tapered anodes with a 75° cut at the tip, respectively. Without any cut in anode but still tapered, the maximum value of the energy integrated X-ray flux was reported to be about 2.17±0.09 J/sr. In 4π-geometry, the maximum X-ray emission was estimated to 17.09±0.75, 27.25±1.13, 27.91±1.28 J with the cylindrical anode with a 75° cut at the tip, the tapered anode without any cut and the tapered anode with a 75° cut at the tip, respectively. This X-ray analysis corresponded to the much lower 0.95% wall plug efficiency of X-ray generation with the cylindrical anode with a 75° cut at the tip in comparison to 1.5% with a tapered anode with and without 75° cut at the tip of these anodes. The pinhole images of the anode (see Fig 5.5) and plasma suggest that the hard X-ray emission could be due to electron bombardment of the anode tip.

The results could be useful in developing a DPF device for enhanced X-ray production. Fig. 5.5 shows the importance of an anode shape. Anodes with a 75° cut at the tip enhance X-ray flux in the side-on direction to be helpful in designing the DPF for X-ray diffraction and microscopy (Fig 5.5).

Figure 5.6b, c shows radiographs of a motorbike spark plug and an integrated circuit obtained with one shot of X-rays flashed by the tapered anode with a 75° cut at the tip. The radiographs were recorded on Fuji medical X-ray film by placing the specimens in the side-on direction at 29±0.1 cm from the X-ray source. Figure 5.6c shows the radiograph of an electrolytic capacitor recorded on Fuji medical X-ray film with single-shot exposure. This image was obtained with the tapered anode without any cut at 20 kV charging PF system. The electrolytic

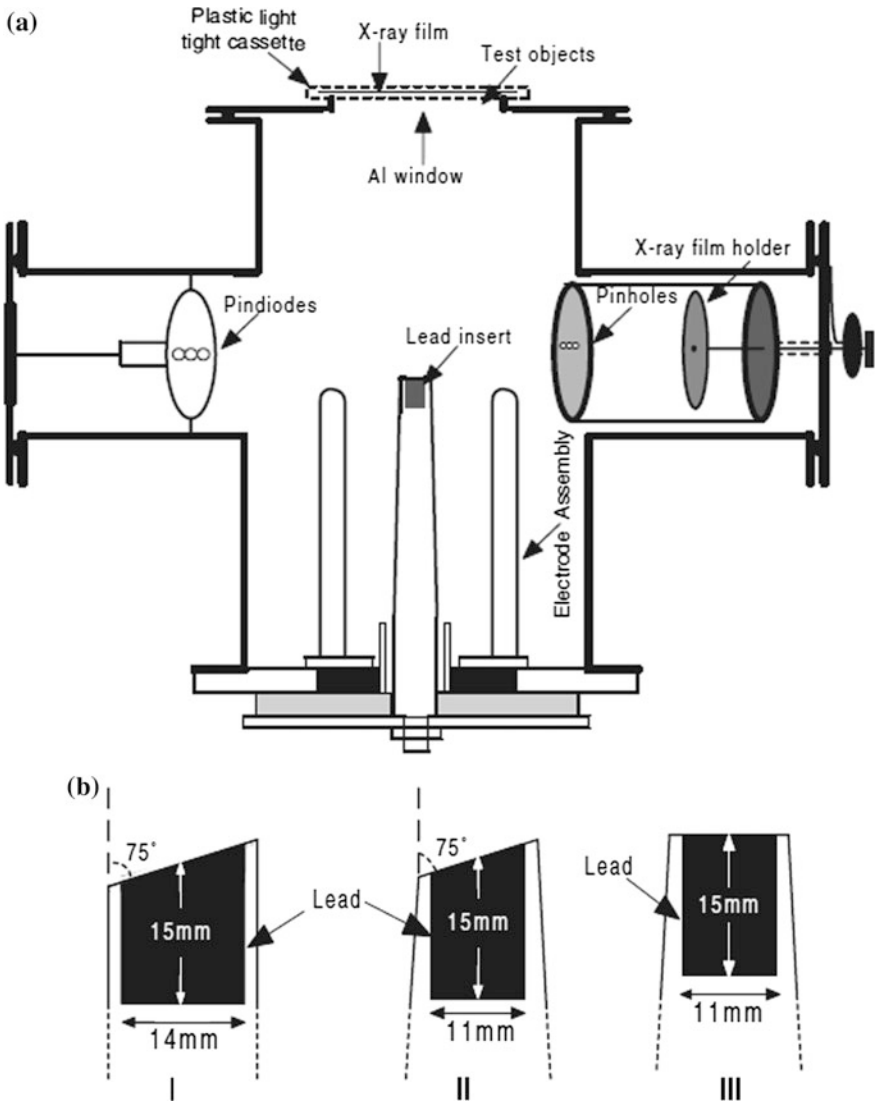

Fig. 5.4 **a** A schematic of the DPF electrodes and X-rays diagnostics. **b** The three anode shapes; (I) cylindrical anode with a 75° cut at the tip with respect to the anode axis; (II) tapered anode with a 75° cut at the tip with respect to the anode axis; (III) tapered anode without any cut. Reprinted from Hussain et al. [29] Plasma focus as a possible X-ray source for radiography, Copyright (2005), with permission from IOP Publishing Ltd.

capacitor was placed at 27±0.1 cm from the X-ray source in the end-on direction. These high contrast radiographs of different materials are the evidence of extended applications of radiation from pulsed plasmas with different photon energies.

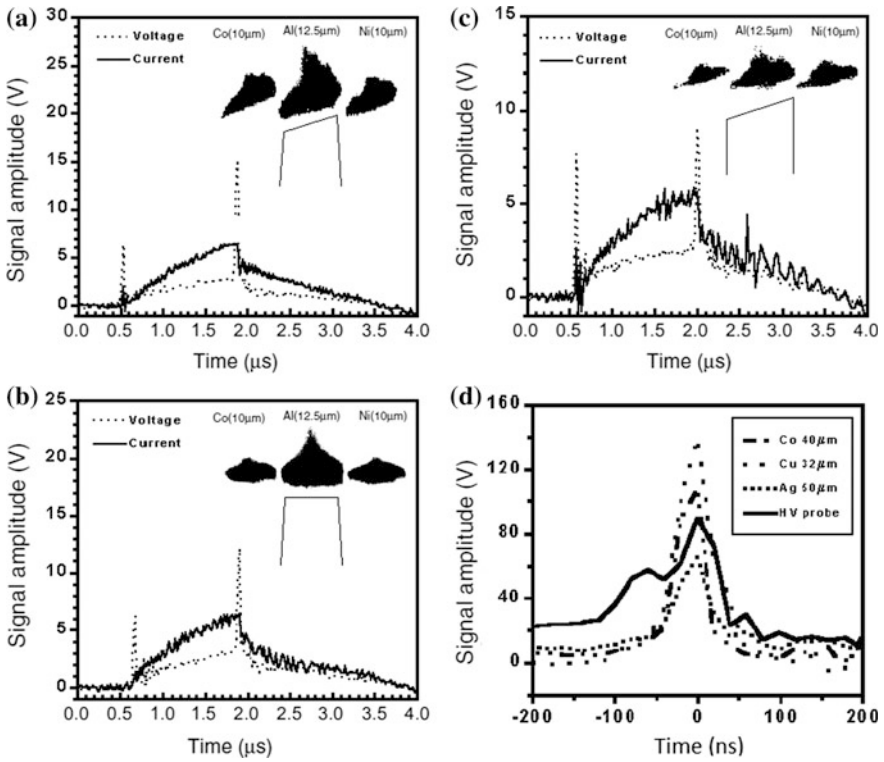

Fig. 5.5 The typical HV probe, Rogowski coil signals and soft X-ray pinhole images recorded with Co (10 μm), Al (12.5 μm) and Ni (10 μm) filters for **a** tapered anode with a 75° cut; **b** tapered anode without any cut; and **c** cylindrical anode with a 75° cut. **d** Oscillogram of a typical shot showing HV probe and PIN-diode signals at 0.5 mbar of hydrogen for tapered anode with a 75° cut. Reprinted from Hussain et al. [29] Plasma focus as a possible X-ray source for radiography, Copyright (2005), with permission from IOP Publishing Ltd.

Later, the same research group studied the performance of a 5.3 kJ plasma focus operated in argon for hard X-ray emission [31]. The hard X-rays came from electron beams having a pulse duration of 15–20 ns and a source size 1 mm. In Fig. 5.7 the major skeletal structure fine bones and soft tissues of the fish demonstrates a clear example of the ability of DPF as a hard X-ray source. The radiograph was obtained at 27 cm from anode tip outside the chamber on Fuji medical X-ray film. The spatial resolution was about 50 μm, restricted mainly by the penumbral blurring due to the estimated source size of about 1 mm.

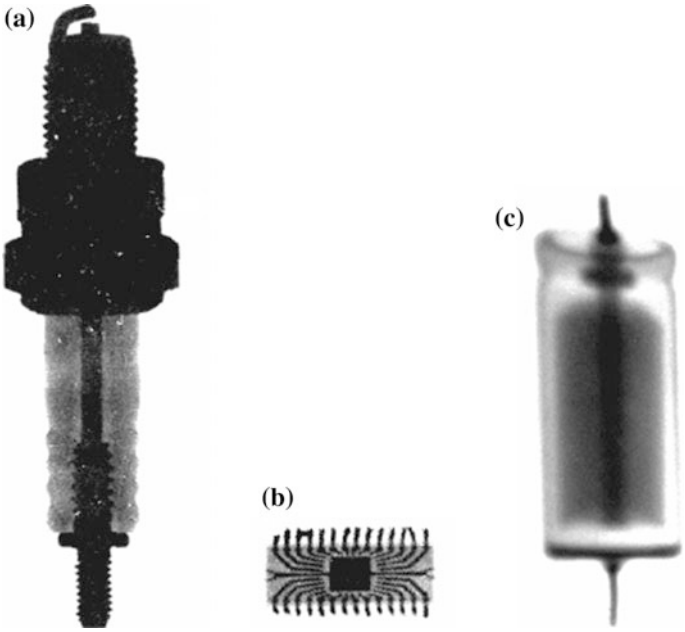

Fig. 5.6 Radiographic images of test objects: **a** motorbike spark plug; **b** integrated circuit; and **c** electrolytic capacitor. Recorded by placing the components outside the chamber. Reprinted from Hussain et al. [29], Plasma focus as a possible X-ray source for radiography, Copyright (2005), with permission from IOP Publishing Ltd.

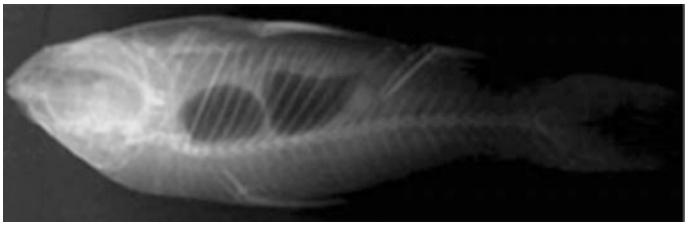

Fig. 5.7 Radiograph image of a fish recorded on Fuji medical X-ray film using X-rays with energy above 15 keV by placing the specimens outside the chamber with objects within 2 mm of the film. Reprinted from Hussain et al. [31], Tailoring a plasma focus as hard X-ray source for imaging, Copyright (2010), with permission from AIP Publishing LLC

5.2.3 X-ray Microscopy of Living Biological Specimen

Higher energy X-rays from plasma focus device (NX2) were used to take the hard X-ray images of living biological objects [32]. It is noted that these X-rays can pass through the 2 cm thick objects, a useful tool to radiograph small living species. The NX2 machine can be operated in a repetitive mode of up to 16 Hz for a short

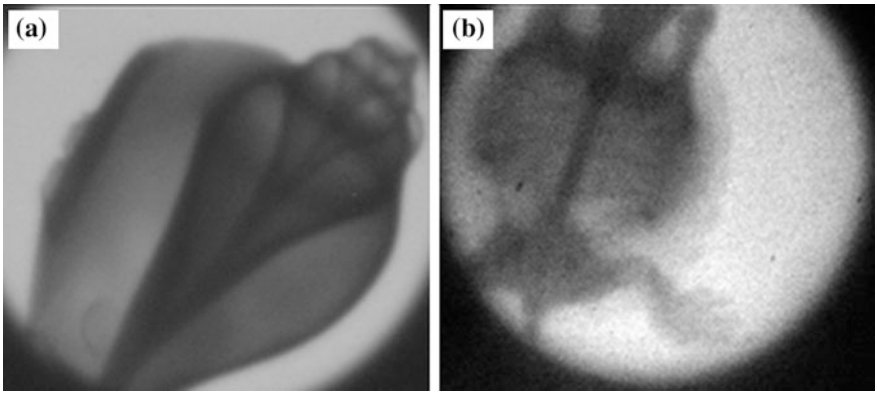

Fig. 5.8 Hard X-ray images using plasma focus. **a** sea-shell and **b** a live terrapin. Reprinted from Rawat et al. [32], Applications of Dense Plasma Device, Copyright (2005), with permission from IFM

duration, giving an opportunity to record an X-ray movie of a living object such as a terrapin.

Figure 5.8 shows the radiograph obtained of a sea-shell and a live terrapin. The authors attributed this high-quality radiograph to the two factors: the very short duration of the emission, and the small (less than 1 mm) size of the source.

5.3 Plasma Focus as X-ray Source for Lithography

In the semiconductor industry, lithography is the leading technology that is used to print the basic patterns that define integrated circuits (ICs) onto semiconductor wafers. The fabrication of smaller sized component requires a shorter wavelength radiation source. From last two decades, a variety of radiation sources has been developed for medical and industrial applications particularly in the wavelength band from about several tenths to several tens of nanometers. Each source concept has its specific advantages regarding its radiation characteristics such as intensity, spectral and spatial distribution, and source operation characteristics such as its conversion efficiency and repetition rate. Each source concept has several disadvantages in particularly non-radiation related effects like the particle or debris emission and EM-field production.

Pulsed radiation sources in the soft X-rays region are considered to fabricate next-generation lithographic structures. Dense plasma focus (DPF) device as an intense X-ray source has been studied for the fabrication of micro-sized structures with high aspect ratio. At plasma radiation sources lab (PRSL), National Institute of Education, Nanyang Technological University [33], a special lithographic chamber

was designed with a separation valve to allow for convenient replacement of the sample without the need for the entire vacuum chamber to be pumped down each time. The anode, modified for water cooling, of length 51 mm was operated at p = 6 mbar and V = 12.5 kV under 1 Hz repetition mode. The average X-ray yield was 82 J/shot for 800 shots in the same gas filling and the best average wall plug efficiency obtained under repetitive mode was 4%. Various X-ray yield optimization studies with argon and neon as filling gases were performed under different conditions of charging voltage, filling pressure, anode length and insulator sleeve lengths. The X-ray yield was computed using appropriate filters and a two-channel PIN-diode spectrometer. Silicon photodiodes (BPX65) were used as X-ray detectors, and the exposure dose was computed by integrating the oscilloscope signals from the focus after considering geometrical factors, the filter characteristics and the filling gas self-absorption. When operated in neon ($\lambda \sim 1$ nm), the optimum soft X-ray yield in 4π geometry was reported to 140 J/shot which corresponded to a wall plug efficiency of about 6%. Operation in argon ($\lambda \sim 0.4$ nm) gave the soft X-ray yield up to 1.5 J/shot.

A chemically amplified resist (CAR) was characterized for X-ray lithographic applications (Fig. 5.9) by studying, the resist's cross-linking process under different conditions of resist thickness (3.5–15 μm) and X-ray exposure dose. For the necessary exposure dose (0.1–1.6 J/cm^2) required for the cross-linking analysis of thick resists, the DPF device was operated repetitively using neon as a filling gas for a range of 100–1500 shots.

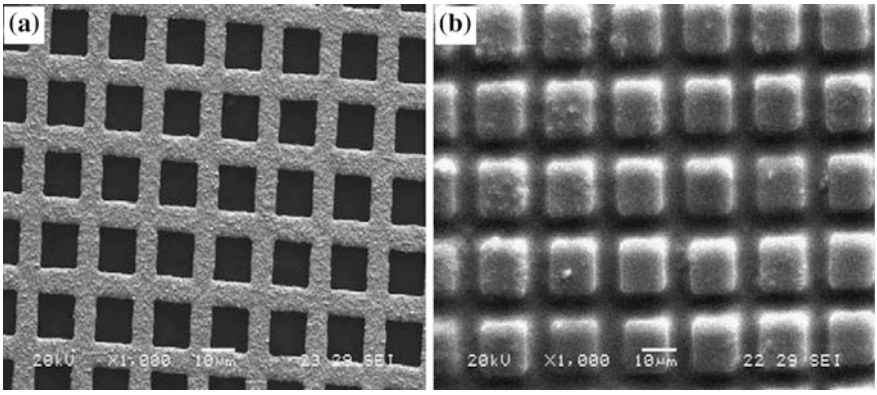

Fig. 5.9 SEM micrographs of: **a** gold mesh, and **b** SU-8 resist test structures. Reprinted from Wong et al. [30], Study of X-ray lithographic conditions for SU-8 by Fourier transform infrared spectroscopy, Copyright (2006), with permission from Elsevier Publishing Company

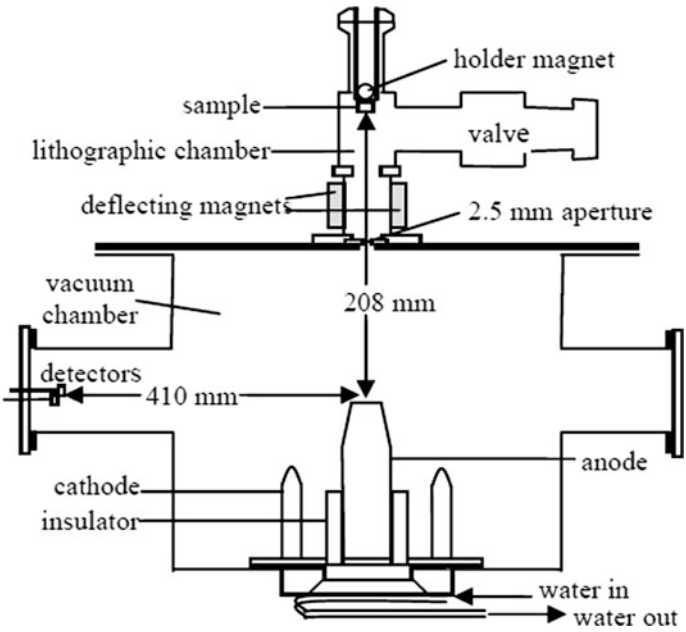

Fig. 5.10 The schematic of the NX2 experimental setup for micro-machining. Reprinted from Wong et al. [33], Repetitive Operation of A Dense Plasma Soft X-ray Source for Micromachining, Copyright (2006), with permission from AIP Publishing LLC

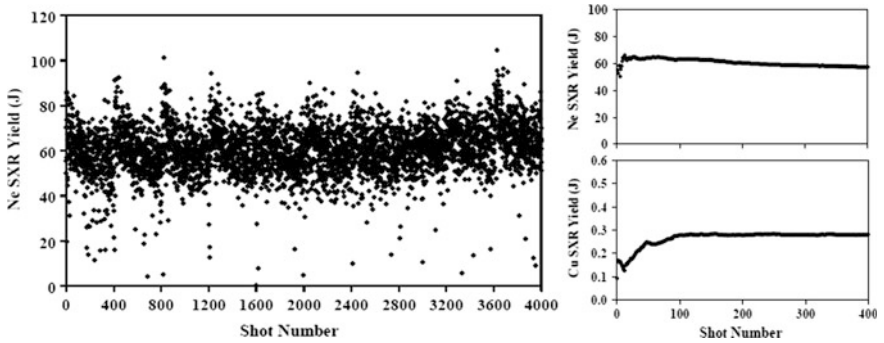

Fig. 5.11 Soft X-ray (SXR) yield for neon-filling under repetitive firing. Reprinted from Wong et al. [33], Repetitive Operation of A Dense Plasma Soft X-ray Source for Micromachining, Copyright (2006), with permission from AIP Publishing LLC

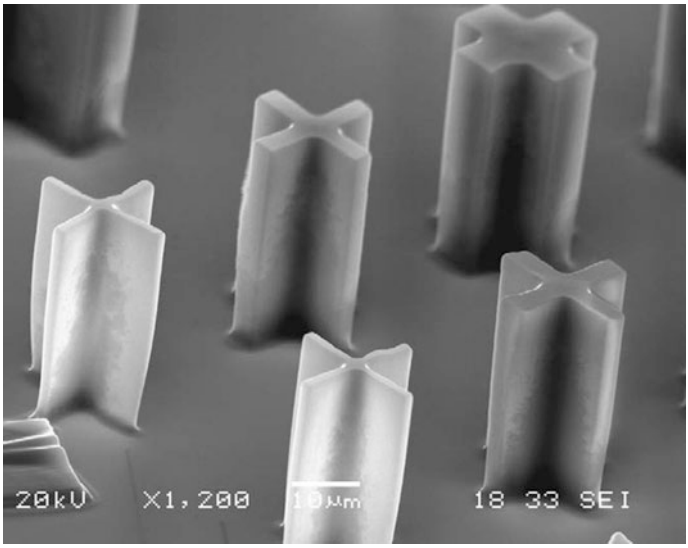

Fig. 5.12 SEM micrograph showing a close-up view of test structures with an aspect ratio of up to 20:1 on 25 micron-thick SU-8 resist. Reprinted from Wong et al. [30] Study of X-ray lithographic conditions for SU-8 by Fourier transform infrared spectroscopy, Copyright (2006), with permission from Elsevier Publishing Company

5.3.1 Repetitive Mode of Operation

The NX2 device (Fig. 5.10): a 27.6-μF, 15-kV, 430-kA DPF, at the PRSL, has been demonstrated as a soft X-ray source for micro-machining [30, 33]. A neon gas was used to produce X-rays in a narrow spectral range of 0.9–1.6 keV. For the lithographic purpose, a stable pulsed operation is required to give constant radiation yield. The NX2 radiation was measured using a multi-channel soft X-ray spectrometric system based on filtered BPX65 PIN diodes. A radiative source was monitored by pulse shaping electronics—A/D converter, a microcontroller, integrator, sample and peak holder, and analogue switch. The system was designed to give shot-to-shot statistical analysis at adjustable preset trigger frequencies. The machine was operated at 0.5 Hz for 4000 shots under the same gas fill. An average radiation yield of 60 J/shot and a maximum single-shot yield of more than 100 J were recorded as shown in Fig. 5.11. The experimental setup as shown in Fig. 5.10 was used for contact micro-machining by placing a sample in an axial direction. Some microstructures with an excellent aspect ratio of up to 20:1 on 25 μm SU-8 resist are shown in Fig. 5.12.

5.3.2 Miniature Plasma Focus as a Lithography Source

Modern semiconductor technology is based on optical projection technique and state-of-the-art 193 nm wavelength lasers to manufacture high-volume integrated circuits. After more than a decade of research, the optics for the shorter wavelength of radiation made extreme ultraviolet (EUV) with a wavelength of 13.5 nm and beyond EUV (BEUV) with 6.6 nm as leading contenders to become next-generation lithographic techniques. The sources emitting nanometers wavelength radiation are based on the high-Z plasma. Characteristics radiation from high-Z plasma contains many lines that are closely spaced and thus forms an unresolved transition array (UTA). Such UTA structure has been observed in the EUV and BEUV emitting material spectra such as Sn, Xe and Li. To achieve high production throughput the radiation source needed to be almost spherical of about 1 mm diameter. Plasma focus as a gas discharge produced plasma device was a strong candidate for the EUV lithography (EUVL) [34]. A 10 J PF device was studied for EUVL at repetition rates of 20 Hz in Xenon [35]. The strongest EUV emission in the 13.5 nm band was reported at the electron temperature of about 30 eV. This sets a minimum requirement of a current necessary to generate the plasma temperature of 20 eV in pinch device of about 20 kA. Pulsed power device for the EUV and BEUV photons production needs two orders of magnitude lower temperatures as compared to typical X-ray, electron, ion or neutron production from these devices. Earlier efforts to study small DPF as an EUVL source includes the usage of a reliable all-solid-state pulsed power drivers and advanced thermal management of water-cooled electrodes for few kHz operation [34]. Taking advantages of previous extensive research on medium DPF, a plasma research group at PRSL, NIE, NTU developed 50 kA small plasma focus for EUV radiation [36]. A less than 1% conversion efficiency (CE) was reported with tin-insert copper anode [37]. For lithography purpose the intrinsic conversion efficiency (ICE) of a source, i.e. the plasma energy conversion into the desired spectral band of radiation for the discharge produced plasma devices can be achieved up to 2% with pre-ionization setup. Pre-ionization system was also found useful for stable operation of a machine with less pulse-to-pulse fluctuations in radiation yield. The EUV yield (Y_{EUV}) and the peak current (I_{peak}) flowing through the pinch column indicate the EUV scaling law of $Y_{EUV} \propto I_{peak}^{4.2}$ for the pinch plasma focus devices. The EUV radiation increases significantly after 25 kA of discharge current due to high magnetic compression and Joule heating of plasma. The current sheath dynamics within the discharge tube plays a significant role to obtain an optimum condition for enhanced radiation. The source size in the EUV band is reported about 3.5 mm full-width (FW $1/e^2$) and 1.15 mm full-width at half maximum (FWHM) at the pinch region. However, it is well known that pinch size varies with seed gas pressures.

The source capable of stable operation over a longer time at the repetition rate of tens of kHz operation is the basic requirement for EUV and X-ray lithography. The source with a low electrical-to-radiation efficiency, high-level debris, heat

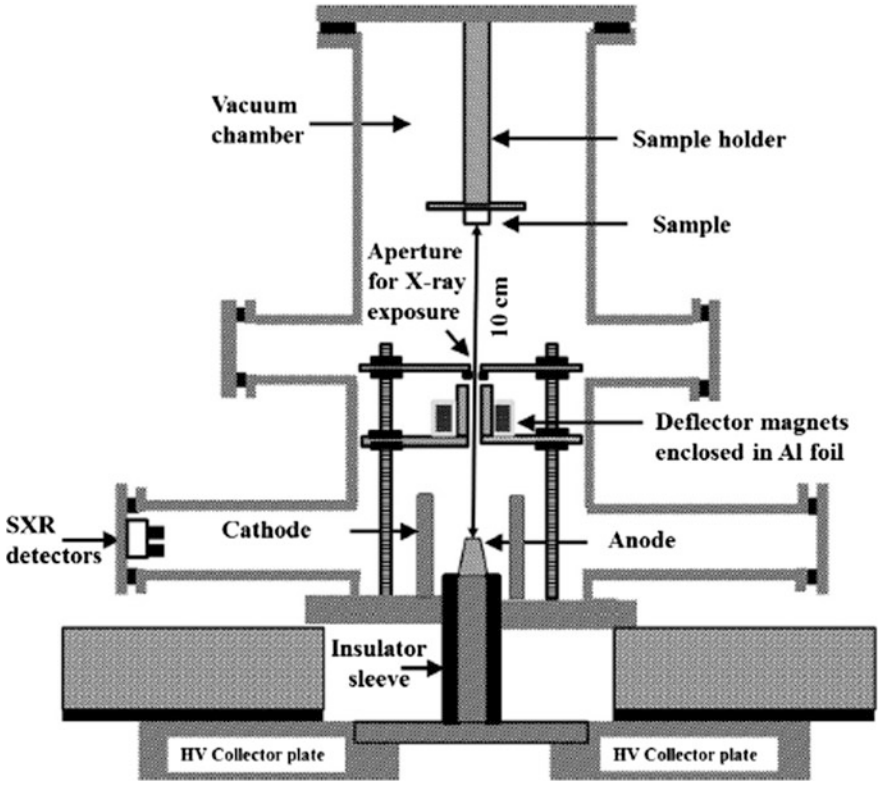

Fig. 5.13 Lithography set up inside the vacuum chamber of FMPF. Reprinted from Kalaiselvi et al. [38] X-ray lithography of SU-8 photoresist using fast miniature plasma focus device and its characterization using FTIR spectroscopy, (copyright 2014), with permission from Elsevier Publishing Company

generation, operation in high-Z gases and pulse-to-pulse fluctuations in the radiation yield made pulsed plasma radiation sources less attractive in comparison with existing lasers technology as a commercial EUV source for lithography.

Pulsed X-ray or beyond EUV (smaller than 6.67 nm photons) lithography is also under investigation for future lithographic techniques. Fast miniature plasma focus (FMPF) of 200 J developed at PRSL, NIE, NTU (with typical setup shown in Fig. 5.13) can be a possible source for X-ray lithography regarding portability, tunable design parameters for optimal operation, low-input energy requirement, generation of bright and smaller point source for generation of high-resolution micro-components and high throughput [38]. The accomplishment of X-ray lithography using FMPF are reported by the usage of stencil mask, reduction of a distance between sample and anode to 10 cm inside the chamber, and finally the achievement of the cross-linking of photoresist, just with 200 mJ/cm^2 instead of 800 mJ/cm^2 for the fabrication of desired micro-patterns, shown in Fig. 5.14. This

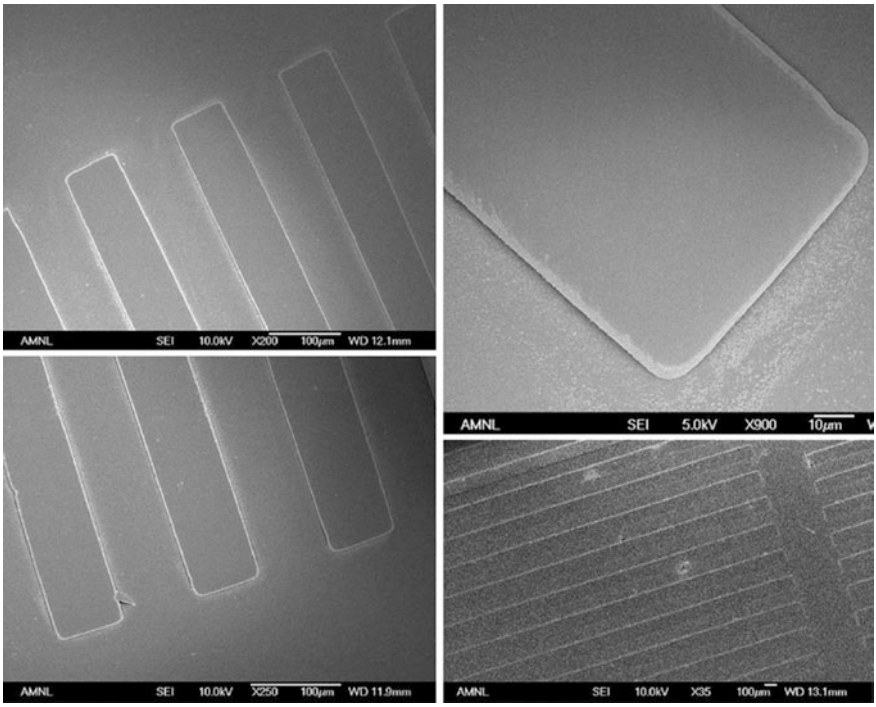

Fig. 5.14 SEM image of SU-8 micro-patterns exposed with FMPF radiation. Reprinted from Kalaiselvi et al. [38] X-ray lithography of SU-8 photoresist using fast miniature plasma focus device and its characterization using FTIR spectroscopy, (copyright 2014), with permission from Elsevier Publishing Company

in turn significantly reduced the number of shots required to sufficiently cross-linked the photoresist SU-8, but a thicker structure would not be possible to expose with such a lower dosage.

5.3.3 MHD Simulation—Tools for Radiation Source Optimization

For many applications of X-ray radiation, the size and the location of a radiation emitting region is an important issue which depends on the electrode geometry and the initial density profiles within the discharge tube. The plasma characteristics of a DPF can be achieved both experimentally and by Lee model as described in a previous section. The discharge current development within a plasma device is a time dependence parameter of plasma. Magnetohydrodynamics (MHD)-based simulation can give high resolution, electromagnetic simulations of plasma sheath creation, its acceleration, pinching and the MHD instabilities for obtaining the high

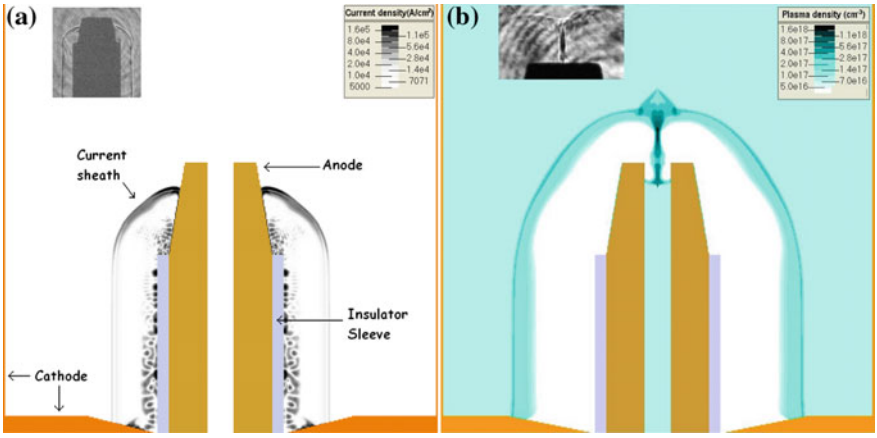

Fig. 5.15 The MHD simulation results: **a** Current density during axial acceleration phase, and **b** Plasma density at maximum compression. Small windows correspond to the images obtained by laser probing technique

temperature and density distribution of plasma. A two-dimensional single fluid MHD code [39] is used to analysis the discharge plasma. By solving the equations describing laws of conservation of mass, energy and momentum coupled with circuit and Maxwell's equations, we have obtained the time dependent spatial distributions of plasma parameters. The two-dimensional single fluid MHD code simulates faster by assuming the axisymmetric geometry of the DPF device. As an example, a small 50 kA plasma focus known as MPF is simulated with an MHD codes by considering solid outer electrode with a diameter of 48 mm [37]. Inner electrode with a hole of 3 mm in diameter having a length 29.5 mm and a diameter of 11.5 mm acts as an anode. This tapered anode has a tip of diameter 8 mm. Insulator sleeve of diameter 14 mm with a length of 19.5 mm makes the effective length of an anode about 10 mm.

During axial acceleration phase, the current sheath has a velocity of about 5.6 cm/μs at the middle of anode's effective length, as shown in Fig. 5.15. At the peak value of discharge current of about 50 kA, a shock wave is generated after the compression phase. The heating of plasma continues due to ions in the shock wave and by the Joule heating. The plasma temperature rises due to increase in electrons temperature. Since the magnetic field pressure ($B^2/2\mu$) has an inverse square dependence on the radius of the current sheath, thus the higher velocity of a current sheath of about 12 cm/μs is estimated at the tip of a tapered anode.

At pinch time, the plasma column reduces to a diameter $\sim$0.25–0.3 mm a so called 'neck' by the high magnetic field pressure. The outflow of plasma from the high-pressure neck causes the pinch column to become hydromagnetically unstable to axial perturbations. Subsequently, the sausage mode instability creates the conditions for radiative collapse. During this time, the radiation emission rises exponentially to several MW. This is due to the rapid conversion of the plasma

kinetic energy into thermal energy causing the sudden rise in plasma temperature. The duration of radiation can be estimated by considering the sausage instability lifetime due to plasma outflow: $\tau \approx \gamma r/V_s$, where γ is the sausage aspect ratio (length/radius) which is approximately constant (2–5), V_s is the ionic sound velocity in the plasma and r is the radius of the pinch column.

5.4 Summary and Conclusion

Plasma X-ray spectrum is more complex than the typical X-ray tube in which bremsstrahlung and line radiation are the radiation emission mechanisms. For plasmas, there is also the possibility of recombination and line emission from ions. A plasma focus device as an intense X-ray source has been studied for more than two decades. The major studies include the characterization of soft X-rays from the hot-spots at the tip of an anode and the hard X-rays from the interactions of energetic electron beams impacting on the anode. It proves advantageous in terms of cost-effectiveness, portability, tunable design parameters for optimal operation, low-input energy requirement, generation of bright and reliable X-rays, pulsed source and smaller point source for generation of high-resolution micro-components and high throughput. The plasma focus geometry with a coaxial cylindrical electrode configuration has several advantages for X-ray lithography, radiography and microscopy, such as its working in gases mixture and open end anode/cathode system of the source in principle enables collection of radiation over an angle of 2π sr. It has been successfully demonstrated that these sources can indeed be employed for X-ray imaging and lithography.

References

1. P.S. Yadav, Y.S. Kashyap, T. Roy, P.S. Sarkar, A. Sinha, J. Synchrotron. Radiat. **15**, 100 (2008)
2. M.A. Liberman, J.S. De Groot, A. Toor, R.B. Spielman, *Physics of High Density Z-Pinch Plasmas* (Springer, New York, 1999), p. 31
3. W.H. Bennett, Phys. Rev. **45**, 890 (1934)
4. U. Stamm, J. Phys. D: Appl. Phys. **37**, 3244 (2004)
5. H. Friedman, S.W. Lichtman, E.T. Byram, Phys. Rev. **83**, 1025 (1951)
6. M. Zakaullah, I. Ahmed, A.R. Omer, G. Murtaza, M.M. Beg, Plasma Sources Sci. Technol. **5**, 544 (1996)
7. A. Serban, S. Lee, Plasma Sources Sci. Technol. **6**, 78 (1997)
8. N.V. Filippov, T.I. Filippova, I.V. Khutoretskaia, V.V. Mialton, V.P. Vinogradov, Phys. Lett. A **211**, 168 (1996)
9. M. Sharif, S. Hussain, M. Zakaullah, A. Waheed, Plasma Sources Sci. Technol. **13**, B7 (2004)
10. M. Sharif, S. Ahmad, M. Zakaullah, S. Hussain, A. Waheed, J. Appl. Phys. **100**, 073301 (2006)
11. S. Lee, S.H. Saw, P. Lee, R.S. Rawat, Plasma Phys. Control Fusion **51**, 105013 (2009)

12. M. Zakaullah, K. Alamgir, M. Shafiq, S.M. Hassan, M. Sharif, S. Hussain, A. Waheed, Plasma Sources Sci. Technol. **11**, 377 (2002)
13. R.S. Rawat, T. Zhang, C.B.L. Phua, J.X.Y. Then, K.A. Chandra, X. Lin, A. Patran, P. Lee, Plasma Sources Sci. Technol. **13**, 569 (2004)
14. S. Hussain, M. Shafiq, M.A. Badar, M. Zakaullah, Phys. Plasmas **17**, 092705 (2010)
15. F.N. Beg, I. Ross, A. Lorenz, J.F. Worley, A.E. Dangor, M.G. Haines, J. Appl. Phys. **88**, 3225 (2000)
16. M. Zakaullah, K. Alamgir, G. Murtaza, A. Waheed, Plasma Sources Sci. Technol. **9**, 592 (2000)
17. S. Ahmad, M. Sadiq, M. Shafiq, A. Waheed, P. Lee, M. Zakaullah, Plasma Sources Sci. Technol. **15**, 314 (2006)
18. S. Lee, Plasma focus model yielding trajectory and structure, in *Radiation in Plasmas*, vol. II, ed. by B. McNamara (World Scientific, Singapore, 1984), pp. 978–987
19. S. Lee, P. Lee, S.H. Saw, R.S. Rawat, Plasma Phys. Control Fusion **50**(6), 065012 (2008)
20. S. Lee, P. Lee, G. Zhang, X. Feng, V.A. Gribkov, M. Liu, A. Serban, T.K.S. Wong, IEEE Trans. Plasma Sci. **26**(4), 1119 (1998)
21. S. Lee, *Twelve Years of UNU/ICTP PFF—A Review* (Abdus Salam ICTP, Trieste IC/98/231, 1998), pp. 5–34
22. S.H. Saw, P.C.K. Lee, R.S. Rawat, S. Lee, IEEE Trans. Plasma Sci. **37**(7), 1276 (2009)
23. R. Verma, R.S. Rawat, P. Lee, A.T.L. Tan, H. Shariff, G.J. Ying, S.V. Springham, A. Talebitaher, U. Ilyas, A. Shyam, IEEE Trans. Plasma Sci. **40**(12), 3280 (2012)
24. M. Liu, *Soft X-rays from Compact Plasma Focus*, Ph.D. dissertation, (NIE, Nanyang Technological University, Singapore, 1996) http://hdl.handle.net/10497/1571
25. S. Bing, *Comparative Study of Dynamics and X-ray Emission of Several Plasma Focus Devices*, Ph.D. dissertation, (NIE, Nanyang Technological University, Singapore, 2000) http://hdl.handle.net/10497/1607
26. D. Wong, A. Patran, T.L. Tan, R.S. Rawat, P. Lee, IEEE Trans. Plasma Sci. **32**(6), 2227 (2004)
27. R.S. Rawat, T. Zhang, G.J. Lim, W.H. Tan, S.J. Ng, A. Patran, S.M. Hassan, S.V. Springham, T.L. Tan, M. Zakaullah, P. Lee, S. Lee, J. Fusion Energy **23**(1), 49 (2004)
28. M. Zakaullah, K. Alamgir, M. Shafiq, S.M. Hassan, M. Sharif, A. Waheed, Appl. Phys. Lett. **78**, 877 (2001)
29. S. Hussain, M. Shafiq, R. Ahmad, A. Waheed, M. Zakaullah, Plasma Sources Sci. Technol. **14**, 61 (2005)
30. D. Wong, T.L. Tan, P. Lee, R.S. Rawat, A. Patran, Microelectron. Eng. **83**, 1912 (2006)
31. S. Hussain, M. Shafiq, M. Zakaullah, Appl. Phys. Lett. **96**, 031501 (2010)
32. R.S. Rawat, T. Zhang, P. Lee, A. Patran, S.M. Hassan, D. Wong, S.V. Springham, T.L. Tan, S. Lee, J. Fiz. Malaysia **26**, 17 (2005)
33. D. Wong, T.L. Tan, A. Patran, S.M. Hassan, T. Zhang, S.V. Springham, S. Lee, R.S. Rawat, P. Lee, AIP Conf. Proc. **808**, 227 (2006)
34. I.V. Fomenkov, N. Bowering, C.L. Rettig, S.T. Melnychuk, I.R. Oliver, J.R. Hoffman, O.V. Khodykin, R.M. Ness, W.N. Partlo, J. Phys. D: Appl. Phys. **37**, 3266 (2004)
35. N. Bowering, M. Martins, W.N. Partlo, I.V. Fomenkov, J. Appl. Phys. **95**, 16 (2004)
36. S.M. Hassan, T. Zhang, A. Patran, R.S. Rawat, S.V. Springham, T.L. Tan, D. Wong, W. Wang, S. Lee, V.A. Gribkov, S.R. Mohanty, P. Lee, Plasma Sources Sci. Technol. **15**, 614 (2006)
37. S.M. Hassan, *Development and Studies of Plasma EUV Sources for Lithography*, Ph.D. dissertation, (NIE, Nanyang Technological University, Singapore, 2010), http://hdl.handle.net/10497/18201
38. S.M.P. Kalaiselvi, T.L. Tan, A. Talebitaher, P. Lee, S.P. Heussler, M.B.H. Breese, R.S. Rawat, Phys. Lett. A **379**, 560 (2015)
39. V.V. Vikhrev, V.V. Ivanov, G.A. Rozanova, Nucl. Fusion **33**, 311 (1993)

Chapter 6
Neutron and Proton Diagnostics for Pulsed Plasma Fusion Devices

Alireza Talebitaher and Stuart V. Springham

6.1 Introduction

There are several pulsed plasma devices which can be used for fusion reaction such as Tokamak, Stellarator, pinch plasmas, etc., which work on the basis of magnetic confinement and also laser or ion beam-driven fusion systems which work on the basis of inertial confinement. The dense plasma focus (DPF) can be used as a magnetic fusion device due to its high plasma density and temperature, intense fusion products and simple structure. Based on the authors' experiences in DPFs in different range of storage energy from sub-kJ to MJ devices, for neutron and proton diagnostics from pulsed plasma fusion devices, this chapter is mainly focused on deuterium–deuterium (DD) fusion reaction in DPF.

The DPF device is a pulsed electrical discharge in different gases which was discovered independently by Mather [1] and Filippov [2]. Although these two systems were different in terms of constructional geometries, they were very similar as regards the dynamics of the current sheath and in the scaling laws [3] for neutron yield, X-ray and other kinds of emission. Since then, DPF devices have been built with energies ranging from a few joules to a few mega-joules with a consequent variation in the physical size. The main difference between Mather-type and Filippov-type DPF is in the electrode dimension and the aspect ratio (diameter/length) of the anode. The Mather-type device has an anode aspect ratio less than 1 (typically 0.25), while for the Filippov-type device the typical aspect ratio is around 5.

Physicists are interested in the Plasma Focus (PF) because of the high $n\tau$ value for the pinched plasma (where n is the particle density $\sim 10^{19}$ cm^{-3} and τ is the confinement time ~ 50 ns, giving $n\tau = 5 \times 10^{11}$ s cm^{-3}), and bursts of fusion neutrons when operated in deuterium. However, to reach ignition in a thermonu-

A. Talebitaher (✉) · S.V. Springham
National Institute of Education, Nanyang Technological University, Singapore, Singapore
e-mail: mtalebi69@yahoo.com

R.S. Rawat (ed.), *Plasma Science and Technology for Emerging Economies*,
DOI 10.1007/978-981-10-4217-1_6

clear reaction requires fulfilling the Lawson Criterion of $n\tau$ greater than 3×10^{14} s cm^{-3}. Also the hot ($\sim$1 keV) dense plasma emits abundant soft and hard X-rays, especially when operated with high-Z gases like neon or argon.

The PF has a very complex behavior and exhibits a rich variety of plasma phenomena. The PF is essentially a two-dimensional Z-pinch formed on, or near, the axis at the end of a coaxial plasma accelerator. The Filippov machine was developed as a modification of the straight Z-pinch and the Mather-type device was modified from the coaxial plasma gun.

6.1.1 Fusion Reactions in Plasmas

Among all of the possible fusion reactions which are shown in Table 6.1, DT reaction is the best candidate for future power plant based on fusion; however, obtaining and handling tritium is not easy for all plasma fusion labs. By contrast, deuterium is readily available commercially. Moreover, due to the high-energy neutron production from DT reaction, it needs a lot of insulation and safety regulation which leads most of the research labs including the authors to select DD reaction for their nuclear fusion investigation.

The ^{2}H(d, n)^{3}He and ^{2}H(d, p)^{3}H reactions are of interest for fusion energy applications when deuterium is the working gas. The DD fusion reactions are:

$$D + D \rightarrow n\,(2.45\,\text{MeV}) + {}^3\text{He}(0.82\,\text{MeV}) \sim 50\%$$

$$D + D \rightarrow p(3.02\,\text{MeV}) + {}^3T(1.01\,\text{MeV}) \sim 50\%$$

Table 6.1 List of the most favorable fusion reactions. [4]

1.	D + T	→	^{4}He (3.5 MeV) + n (14.1 MeV)
2.	D + D	→	T (1.01 MeV) + p (3.02 MeV) (50%)
		→	^{3}He (0.82 MeV) + n (2.45 MeV) (50%)
3.	D + ^{3}He	→	^{4}He (3.6 MeV) + p (14.7 MeV)
4.	T + T	→	^{4}He + 2n + 11.3 MeV
5.	^{3}He + ^{3}He	→	^{4}He + 2 p
6.	^{3}He + T	→	^{4}He + p + n + 12.1 MeV (51%)
		→	^{4}He (4.8 MeV) + D (9.5 MeV) (43%)
		→	^{4}He (0.5 MeV) + n (1.9 MeV) + p (11.9 MeV) (6%)
7.	D + ^{6}Li	→	2 ^{4}He + 22.4 MeV
8.	p + ^{6}Li	→	^{4}He (1.7 MeV) + ^{3}He (2.3 MeV)
9.	^{3}He + ^{6}Li	→	2 ^{4}He + p + 16.9 MeV
10.	p + ^{11}B	→	3 ^{4}He + 8.7 MeV

Classically, the energy required to overcome the Coulomb barrier which is due to electrostatic repulsion, so that DD fusion takes place is

$$E = \frac{1}{4\pi\epsilon_0}\frac{Z_1 Z_2 e^2}{R_0}$$

where Z_1 and Z_2 are the atomic number of two nucleus and R_0 is the distance between nuclei centers at which the short-range nuclear force exceeds long-range repulsive Coulomb force. However, according to quantum mechanics, there is a finite probability that two nuclei will fuse even though they do not have sufficient energy to overcome the Coulomb barrier. The penetration probability for a given nuclear fusion reaction increases as the energy of the fusing nuclei approaches the top of the barrier. Fusion reactors such as Tokamak are expected to operate at temperatures in the range $kT = 1$ to 30 keV [5].

6.1.2 Reaction Cross Sections and Kinematics

By looking at the cross section of different fusion reaction shown in Fig. 6.1 from Ref. [4], it can be realized that for the ranges of less than 100 keV for incident particles' kinetic energy, DT and DD reactions have the highest fusion cross section. However, as it is mentioned before, working with tritium is not straightforward for most of the research labs, so we will focus on DD fusion reaction kinematics and elaborate them in this chapter.

The principal mechanisms for fusion production in plasma focus device can be categorized as thermonuclear and non-thermonuclear.

Thermonuclear Reaction

In thermonuclear mechanism, the ions are approximately in thermal equilibrium with one another. If the thermal plasma is considered to have an isotropic Maxwellian ion-energy distribution, then the energy spectra are independent of proton emission angle, and FWHM of proton line will be significant. Concerning the proton fluence anisotropy, for a stationary isotropic Maxwellian energy distribution, the proton intensity is spatially isotropic. One characteristic of a thermonuclear reaction is that the reacting center of mass of any two deuterons should be statistically stationary in the laboratory frame of reference. This is in contrast to the case of an accelerated beam striking a target, in which case the reaction center of mass has a directed momentum equal to the incident particle momentum in the beam. The resulting velocity of the reacting system results in a non-isotropic velocity distribution (in the laboratory frame).

An accelerated ion beam incident upon a cold target cannot produce useful (positive net output) thermonuclear power because the irreversible energy loss of slowing down in the target is always greater than the reaction energy produced. In this case, the bulk of the kinetic energy of the impinging beam is dissipated

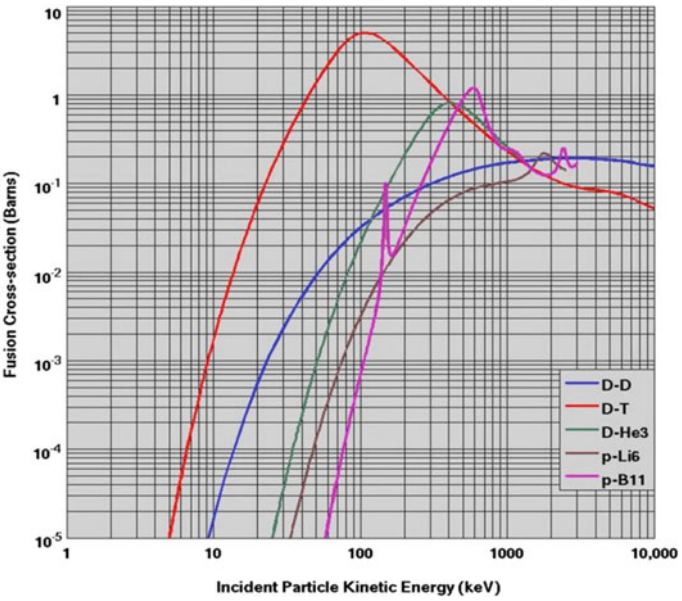

Fig. 6.1 Cross sections versus center of mass energy for key fusion reactions [4]

uselessly by ionization, radiation, and energy transfer to the atomic electrons of the target [6].

Approximately one-half of the thermonuclear reactions produce protons, so the number of protons (and neutrons) in thermal mechanism, is

$$Y_p = Y_n = \left(\frac{1}{2}\times\frac{1}{2}\right) n_{d-\text{pinch}}^2 \langle\sigma v\rangle_{DD} \times \text{volume} \times \text{reaction time}$$
$$= \frac{1}{4} n_d^2 \langle\sigma v\rangle_{DD-\text{th}} \left(\pi r_{\text{pinch}}^2 h_{\text{pinch}}\right)\tau$$

where $n_d \approx 3\times 10^{18}\text{cm}^{-3}$ is the deuteron density inside the pinch, $\langle\sigma v\rangle \approx 2\times 10^{-22}\text{cm}^3\text{s}^{-1}$ is the cross-sectional velocity product of DD fusion reaction at $\sim$1 keV. Also $r_{\text{pinch}} \approx 0.1$ cm and $h_{\text{pinch}} \approx 1$ cm are the pinch radius and height, respectively, for NX2 plasma focus device (as an example). By replacing the $\tau \approx 50$ ns as neutron emission time, the neutron yield will be in order of 10^6.

This model was rejected very soon with observing the relatively high anisotropy in neutron emission. Moreover, the actual neutron yield is much higher (2 order of magnitude) than calculated yield based on plasma temperature ($\sim$1 keV) in pinch plasma.

Beam-Target Mechanism

In order to explain the neutron energy spectrum, several models for acceleration mechanisms have been considered for energetic electrons and ions (in our case,

deuteron) beams. However, mechanisms for ion acceleration and the formation of intense ion beams have still not been enough clarified yet. Some of the proposed mechanisms are fluid-like and others are kinetic in nature. An important test of any hypothetical theory is whether total axial momentum is conserved during the ion beam formation.

With regard to the ion/deuteron beam, Bernard et al. [8] claim that it is the main source of neutrons, as the deuterons bombard both the dense plasma and the ionized but relatively cold gas bubble between the ionization-front and the shock-front.

The non-thermonuclear (beam target) model considers a high current of charged particles accelerated in an electromagnetic field giving a different proton and neutron production mechanism. In this mechanism, the accelerated deuterons strike ions at rest. The beam-target yield is written in the form:

$$Y_p = Y_n = \frac{1}{2} n_b n_i \sigma_{DD-b\_t} v \left(\pi r_{\text{pinch}}^2 h_{\text{pinch}} \right) \tau$$

where $n_b \approx 10^{16} \text{cm}^{-3}$ is the number of beam ions per unit plasma volume for NX2 PF device, $n_i = n_d \approx 3 \times 10^{18}\,\text{cm}^{-3}$ is the target ion density, $\sigma \approx 0.02$ barn = $2 \times 10^{-26}\,\text{cm}^2$ is the cross section of DD fusion reaction and $v \approx 3 \times 10^8\,\text{cm s}^{-1}$ at ~ 100 keV. So the total neutron yield will be in the order of 10^8 which is matched with the experimental result from NX2.

Moving Boiler Model

This model, based on thermonuclear mechanism, tries to explain the anisotropy in neutron production where it is assumed that the plasma center of mass is moving along the axis of plasma focus device [7]. The required velocity to produce anisotropy of 1.5 is about 5×10^8 cm/s. However, it is in contrary to many experimental results such as optical observation which indicates a velocity of 5×10^7 cm/s. Moreover, the neutron emission interval time (50–100 ns) gives us a fusion source length around 25–50 cm which is very unrealistic (the average length of fusion source in NX2 is about 1 cm). In addition, the neutron energy spectrum shows a large range of energy (2.2–2.9 MeV) which indicates the involvement of high-energy deuterons in neutron production.

Gyrating Particle Model (GPM)

In a generalized beam-target model GPM, the trajectories of trapped high-energy deuterons are simulated in the time varying structure pinch plasma column. It is assumed that the deuteron source is a series of local point source positioned on the axis. The main difference between conventional beam-target model and GPM is the stretching of deuteron path by gyro-motion in GPM against a straight and un-scattered axial beam in the original version. Jager shows the results of this new model [9] in comparison with spectrally and spatially resolved measurements of

fusion protons (pinhole imaging) and accelerated deuterons in POSEIDON plasma focus device (W_0 = 280 kJ, U_0 = 60 kV, Mather type).

Cross-Field Acceleration Model
Bernstein and Comisar [10] proposed another generalized beam-target model which assumes: (1) high-energy deuterons have angular distributions consistent with a cross-field acceleration mechanism and have velocity vectors distributed anisotropically in space and energy and (2) these energetic deuterons undergo fusion collisions primarily with stationary target ions. The principle assumption is that the azimuthal magnetic field diffuses rapidly toward the axis of self-pinching discharge.

Plasma Diode Model
The study of ion-induced pinch and enhancement of ion current by pinched electron flow in relativistic diodes was done by Goldstein and Lee [11]. In this model, the initial motion of the ions, accelerated from the anode plasma, forms an ion sheath which modifies the electric field. When an electron enters the ion sheath with grazing incidence, it will be reflected back into the diode by the unaffected magnetic field but reduced electric field. The necessary ion-sheath thickness to provide such electron reflection is reached in times which are short enough (<1 ns) to explain the fast collapsing pinch. The electric field in the diode is of order $\sim$1 MV/cm.

Double-Layer Pulse Current Model
Hora et al. developed a new model [12] for the mechanism of the plasma focus based on the assumption that the space charge term in Maxwell's equation (usually neglected) is dominating due to the double layer of discharge. The model assumes that the current pulse is being produced during the several nanoseconds in the focus by the charge separation in the double layer between the collapsing plasma and the remaining gas in the focus.

Surfing Model
The simulation of high-energy proton production by fast magneto-sonic shock waves in pinched plasma focus was done by Mizuguchi et al. [13]. It is focused on the shock formation and the shock acceleration during the pinched current. Some protons are trapped in the electrostatic potential produced near the shock front can be accelerated to a few MeV by surfatron acceleration mechanism.

Collective Focusing Model
Recently, the collective focusing of intense ion beam pulses model was proposed by Dorf et al. [14]. The main concept is that a weak magnetic lens (several hundred gauss) can provide a strong focusing of an intense ion beam pulse carrying a neutralizing electron background. Note that for a single-species non-neutral ion beam, a several Tesla magnetic field would be required to achieve the same focal length. Collective focusing will only occur if no background plasma or secondary electrons are present inside the lens.

6.1.3 Overview of Neutron and Proton Detectors

Because of the same cross section of DD fusion reaction, the neutron and proton yields are the same. So by measuring the neutron yield, we can estimate the total protons for each shot and vice versa. However, the techniques for neutron and proton detection are completely different. Neutron is electrically neutral and has very low interaction with matters and so its detection is based on an indirect method such as absorption or activation, whereas a proton is positively charged and deposits its energy in matter in a short range. Using the solid-state nuclear track detector (SSNTD) is a common method to record the high-energy charged particles such as fusion protons; although it is a very time-consuming method and needs several post-processes such as etching, scanning the detector, and analyzing the images. Also, specifically for plasma focus as a magnetized plasma device, the trajectory of protons in plasma current magnetic field must be taken into account, whereas, the magnetic field does not influence on neutron path.

Another difficulty with neutron detection is the influence of wall-scattered neutron on its yield measurement. Most of the thermal neutron detectors which use a moderator to reduce the neutron energy suffer from this problem. A good neutron detector should be sensitive only to the specific range of energy (in case of DD fusion reaction, around 2.5 MeV) and ignores all scattered neutrons with lower energy.

Sensitivity of a neutron detector to the high-energy gamma-ray is another issue which must be considered. For instance, plastic scintillators (which are commonly used for neutron detector) are quite sensitive to gamma-ray which must be rejected with some techniques such as pulse shape discrimination. Instead, SSNTD for proton detection is insensitive to gamma-ray.

In the next two sections, the different techniques for neutron and proton detections are explained and their detection efficiency and sensitivity to the background noises are compared.

6.2 Neutron Diagnostics

In 1932, James Chadwick bombarded beryllium with α particles leading to the emission of a previously unknown particle. In order to explain his experimental results, he postulated the existence of a "new" neutral particle, which he named the neutron. Hence, the nuclear reaction he observed was $^{9}\mathrm{Be} + {}^{4}\alpha \rightarrow {}^{12}\mathrm{C} + {}^{1}\mathrm{n}$. These days, neutron measurements have become an essential part of any experiment or technique involving nuclear fission or fusion.

Neutron detection techniques are based on indirect methods. Typically, a nuclear reaction with, or a neutron scattering from, a target nucleus produces one or more energetic charged particles, and the ionization or excitation resulting from the

transit of the charged particles is processed by the detection system. Detectors which rely on neutron absorption are generally more sensitive to thermal neutrons (0.025 eV), and are orders of magnitude less sensitive to high-energy neutrons. On the other hand, organic scintillation detectors, which rely on elastic scattering of fast neutrons to transfer kinetic energy to hydrogen nuclei, have difficulty in registering low-energy neutrons. This illustrates the principle that different approaches are required for detecting neutrons of different energy groups. Thermal neutrons are usually detected by absorption/capture methods which can be divided into prompt detectors employing ^{3}He, ^{6}Li, ^{10}B (examples of these are ^{3}He filled proportional counters, lithium-iodide (LiI) scintillator crystals, and ^{10}B-enriched-boron-trifluoride ($^{10}BF_3$) filled proportional counters); and activation detectors employing silver (Ag) [15], indium (In), or rhodium (Rh) [16]. Fast neutrons can be detected by organic scintillation [17]; activation by inelastic scattering from certain chemical elements, such as indium (In) [18, 19], arsenic (As) [20], or yttrium (Y) [21]; or by moderation to thermal energies followed by capture by a suitable chemical element that emits charged particles.

6.2.1 Thermal Neutron Detectors

There are common requirements for slow neutron detection. As in photon detection, the interaction cross section must be as large as possible to achieve a high efficiency.

Neutrons always produce secondary gamma-rays by interacting either with detector materials or with surrounding materials. Thus, the Q-value of the interaction should be large to make the gamma-ray discrimination easy. The third requirement is that the kinetic energies of the interaction products should be fully absorbed (Table 6.2).

Boron Detector

BF_3 proportional counter is a boron-based neutron detector. The gas acts as both a proportional counter and a neutron detection material. BF_3 has a high concentration of boron and its gas multiplication performance is good as well. The intrinsic

Table 6.2 Q-value and products kinetic energy for three useful interactions [54]

	^{10}B(n, α)	^{6}Li(n, α)	^{3}He(n, p)
Abundance and cross section	19.9% 3837 barns	7.6% 937 barns	0.014% 5330 barns
Products and Q-value	^{7}Li + α (2.79 MeV) (6%) ^{7}Li* + α (2.31 MeV) (94%)	^{3}H + α (4.78 MeV)	^{3}H + p (0.76 MeV)
Kinetic E	α: 1.47 MeV ^{7}Li: 0.84 MeV	α: 2.05 MeV ^{3}H: 2.73 MeV	p: 0.57 MeV ^{3}H: 0.19 MeV

efficiency of a 30 cm long detector (96% enriched ^{10}B) filled to 600 torr is 92% at thermal neutron energies (25 MeV).

Hellium-3 Detector

The Hellium-3 based gas neutron proportional counter is the most popular type due to the natural property of helium. They are sensitive to thermal neutrons and are normally used in conjunction with a moderator material. For applications where the surrounding medium acts as a moderator, the detectors can be used un-moderated. They utilize the ^{3}He(n, p)^{3}H reaction for the detection of thermal neutrons. The energy of reaction is carried away as kinetic energy of the products, which move in opposite direction. This detector provides an output pulse that is proportional to 764 keV (reaction Q-value) for thermal neutrons. The cross section of He-3 for thermal neutrons is 5330 barns. The cross section follows an inverse proportionality with neutron velocity up to about 200 keV. The ionization potential of helium is about 25 eV.

Compared to the ^{10}B(n, α) interaction, the ^{3}He(n, p) reaction has a bigger cross section, which makes the ^{3}He proportional counter an attractive alternative to the BF_3 proportional counter. The lower Q-value of the ^{3}He(n, p) reaction makes gamma-ray discrimination more difficult than for a BF_3 counter.

Lithium Detector

Because a lithium-containing gas is not available, scintillation detectors are common as lithium-iodide (LiI) based slow neutron detectors. LiI is chemically similar to NaI, and therefore its scintillation performance is reasonably good. As an activator for LiI, Europium (Eu) is doped.

A LiI(Eu) crystal thickness of tens of microns is sufficient to fully stop the products particles (alpha particle and triton) from the neutron absorption. Thus, each neutron interaction event can make a signal pulse height equivalent to 4.78 MeV. When a gamma-ray with similar energy makes an interaction of full-energy deposition, the resultant pulse height is the same as the pulse height of the neutron event. Accordingly, the gamma-ray discrimination of LiI(Eu) neutron detectors is inferior to gas neutron detectors.

Indium Foil Activation Detector

Natural indium consists of ^{115}In (95.8% abundance) and ^{113}In (4.2%). The activation cross section is about 200 barns. The thermal neutrons are captured predominantly by ^{115}In within an indium foil, making it beta radioactive as described by the following reaction:

$$^{115}\mathrm{In} + n \rightarrow {}^{116}\mathrm{In}^{*} + \gamma \rightarrow {}^{116}\mathrm{Sn} + \beta^{-}$$

The activated ^{116}In has three separate half-lives: 14.1 s, 54.15 min, 2.18 s associated with the ground state and two isomeric levels. For the indium activation detector used in NX2 plasma focus experiments, only the beta decay with the half-life of 14.1 s (and with end-point energy of 3.3 MeV) are counted. The beta particles are counted by the Geiger-Muller tube detector (or plastic scintillator with

photomultiplier). This detector can be calibrated by ^{252}Cf fission source (positioned temporarily at the top of the anode of the PF device).

Silver Activation Detector
Natural silver consists of ^{107}Ag (51.35% abundance) and ^{109}Ag (48.65%). Both isotopes have a sufficiently high activation cross section for thermal neutrons and a relatively short decay time. The activation cross sections for thermal neutrons are 35 and 92 barns, respectively. When ^{109}Ag is activated with thermal neutrons, ^{110}Ag (half-life of 24.2 s) and ^{110m}Ag (half-life of 270 days) are produced which undergo beta decay to ^{110}Cd. Activation of ^{107}Ag results in the generation of ^{108}Ag with a half-life of 2.3 min. So the total activity is the sum of the activities of ^{110}Ag and ^{108}Ag.

6.2.2 Fast Neutron Detectors

The neutron interaction with matter occurs in three different ways:

1. The fast neutron can be thermalized by using a moderator such as paraffin or polyethylene (energy will be reduced) and then be detected by above mentioned thermal neutron detector. However, there are some direct methods to detect fast neutrons such as elastic scattering from proton at high energy.
2. The incoming neutron is scattered by a nucleus. If the recoil nucleus acquires sufficient energy from the neutron, it ionizes the matter surrounding the interaction site. This type of interaction facilitates fast neutron (typically with energy of >100 keV) detection and is efficient for neutrons interacting with lighter nuclei such as H and He.
3. Activation processes: neutrons may be detected by reacting with absorbers in a radiative capture, spallation, or similar reaction, producing reaction products that then decay at some later time, releasing beta particles or gammas. Selected materials have extremely large cross sections for the capture of neutrons within a very narrow band of energy: (^{9}Be(n, α)^{6}He), (^{56}Fe(n, p)^{56}Mn), (^{27}Al(n, α)^{24}Na), (^{93}Nb(n, 2n)^{92m}Nb), and (^{28}Si(n, p)^{28}Al).

Scintillation Detection
Plastic and liquid (organic) scintillators are often used for fast-neutron detection because of their fast response and modest cost. The major disadvantage of organic scintillators in nondestructive assay applications is their high gamma-ray sensitivity.

Neutron Detection Mechanism: Fast neutrons interact in scintillators through elastic scattering with the nuclei present (C and H). Most of the useful scintillator light comes from recoiling protons because a neutron can transfer 100% of its energy in an elastic scattering interaction (only 28% can be transferred to a recoiling ^{12}C). The kinetic energy of the recoiling protons is absorbed by the scintillator and is ultimately converted to heat and visible light. The visible light can be collected in

a photomultiplier tube (PMT) or Avalanche Photo Diode (APD) optically coupled to the scintillator and converted to an electronic pulse whose magnitude is related to the kinetic energy of the recoiling proton.

Gamma Detection Mechanism: Gamma-rays (and X-rays) also interact in scintillators and part of its energy is transferred to the recoiling electron (Compton Scattering) which results in a decrease in energy (increase in wavelength) of the photon.

A good neutron detector must have high sensitivity to neutron and less sensitivity to gamma. A good scintillation material for radiation detection has:

- Relatively high efficiency for converting recoil particle energy to fluorescent radiation.
- Good transparency to its own radiation.
- Good matching of the fluorescent light spectrum to the photomultiplier tube response.
- And specifically for fast neutron scintillation, it must be rich in hydrogen.

Fast neutrons are detected in hydrogen-rich organic scintillators and significant absorption volume is required. They have continuous spectrum and neutron/gamma separation by pulse shape discriminator (PSD) is needed.

Neutron Activation

Neutron activation methods are well suited to make accurate measurements of neutron fluence in environments with high backgrounds of gamma-rays or other forms of radiation. For many chemical elements, neutron-induced nuclear reactions lead uniquely to a specific radioactive product which no other form of radiation can produce. The half-life of the radioactive product allows measuring (in some way) of both the neutron fluence and the background radiation; and then the essence of the activation technique is that the neutron fluence during exposure can be inferred from a measurement of the activity of the product nuclide after exposure. In this way, the influence of even an intense background of non-neutron radiation is very effectively eliminated.

Several different chemical elements and activation schemes have been employed in a wide variety of experimental situations. In practical terms, the half-life of the induced activity must be long enough so that the target can be recovered (if necessary) and counted before the activity decays away, but not so long as to make the counting interval impractically long. Many other factors come into the selection of a particular target element and reaction, including the natural abundance of the relevant isotope, the reaction cross section, the chemical and physical forms of the element available, the type and energy of the decay radiation, and the branching ratio for the relevant decay mode. For some targets (e.g., rhodium), cost can also be an important consideration. The type and energy of the decay radiation strongly influence its detection efficiency, discrimination against interfering radiations, and self-absorption in the activation target. To reduce self-absorption of the decay radiation, the target is often in the form of a foil or sheet, and its lateral dimensions are chosen to match the active area of the detection system. In situations where the

high background radiation is more or less continuous, the activated target is typically transported to a shielded low-background area where it is "counted". Automated foil activation systems with pneumatic target transfer (or sometimes activation of a flowing liquid or gas) are important neutron diagnostics for large fusion devices [22–25]. If relatively long half-life activations are chosen, then several different foils may be activated over the same exposure period and measured individually with a single remote counting system.

For pulsed neutron sources, it is often advantageous to measure the activity in situ after the burst of background radiation associated with the neutron pulse has died away. The detector and activation target are therefore kept in close proximity, and together form a single instrument referred to as an "activation counter" [17]. Unlike foil activation schemes, no transfer-time is involved, and short half-lives (typically milliseconds to minutes) are preferred. Both thermal neutron and fast neutron activation detectors have been developed. Rhodium and silver, for which (n, γ) neutron capture reactions lead to β radioactive products, are the most suitable elements for thermal neutron activation counters. Naturally, with the addition of a moderator, the fast neutrons can also be detected. However, the bulky nature of the moderator, mutual interference between nearby moderating detectors, and the lack of neutron energy discrimination are potential disadvantages of such detectors.

For fast neutron activation counters, a considerably wider group of elements have been employed, including: arsenic [20], beryllium [26], fluorine [27], indium [18, 19], lead [28], neon [25], oxygen [24], praseodymium [29], sodium [30], yttrium [21], and zirconium [28]. Fast neutron activation of these elements occurs via one of the reactions: (n, n'), $(n, 2n)$, (n, p) or (n, α). In each case, the reaction has a definite threshold energy which is useful for differentiating between neutrons of different energy groups, such as DD and DT fusion neutrons, or discriminating against room scattered neutrons (which will have lower energies than the source). For fast DD neutron activation detectors, the most suitable elements (with half-lives) are: arsenic (17.6 ms), beryllium (807 ms), indium (4.49 h), and yttrium (15.7 s). The half-life for arsenic activation is too short to properly exclude the influence of capture gamma-rays from the room, making beryllium a good choice of activation target for moderate repetition-rate sources. Fast neutron activation detectors have proven well suited for neutron fluence measurements on pulsed devices such as ICF, Z-pinch, and plasma focus sources.

Beryllium Detector

This is a fast neutron detector, so neutron moderation is not required. Important advantages of beryllium activation are its short decay half-life (0.807 s), maximum sensitivity at 2.8 MeV neutrons, and practically no sensitivity to the neutrons with energies less than 1 MeV (due to cross section). Consequently, the detector has good sensitivity to $\sim$2.5 MeV neutrons from DD fusion, while largely rejecting room-scattered neutrons, which are predominantly <1 MeV. It is also insensitive to hard X-ray. It employs a beryllium sheet sandwiched between two proportional counters using xenon gas. The relevant reaction $^{9}\mathrm{Be}(n, \alpha)^{6}\mathrm{He}$ has a threshold energy of 670 keV and a peak cross section of 105 mb for 2.8 MeV neutrons. The

^{6}He beta decay (100% β^{-} to ^{6}Li) has a half-life of 0.807 s and end-point energy of 3.5 MeV [31]. This high end-point energy means that a relatively thick beryllium sheet (5 mm) can be used as the activation target with a substantial fraction of the emitted beta particles still being able to escape from the metal sheet. So in terms of detector sensitivity, the high beta end-point energy and low atomic number of the target compensate for the relatively modest reaction cross section. Moreover, the half-life of ^{6}He enables this detector to be used with moderate repetition rate sources (<0.2 Hz) such as plasma focus devices.

Figure 6.2 shows a plot of the cross section from the Evaluated Nuclear Data File (ENDF), National Nuclear Data Center (NNDC) [32], where the main source for experimental cross-sectional data for energies up to 4.4 MeV is a reference [33]. The $^{9}\mathrm{Be}(n,\alpha)^{6}\mathrm{He}$ cross section at 14 MeV is approximately 10 mb, so the detector has much lower sensitivity for the detection of DT fusion neutrons.

A prototype of the beryllium detector was previously constructed [31], with a 2 mm thick Be sheet and proportional counters which required a flowing gas mixture (90% Ar + 10% CH_4) at a rate of about 1.2 L/min. For the new detector, the beryllium sheet is sandwiched between two sealed xenon-filled proportional counters. There are two main advantages of xenon- over argon-filling for the proportional counters. First, xenon has a higher electron density (a factor of 3 for the same gas pressure), and therefore higher energy loss for the beta particles traversing the gas layer. Second, xenon has much higher X-ray absorption than argon enabling the proportional counters to be energy-calibrated using standard X-ray sources. Of course, the xenon-filled proportional counters are also sensitive to the hard X-rays emitted during and after the maximum compression of the plasma focus pinch. However, since this is an activation detector, a delay of a few milliseconds following the shot, eliminates the influence of the hard X-rays and there is sufficient time for the proportional counters to recover (i.e. to clear the gas-ionization and recharge to the applied bias voltage) before counting of beta particles begins.

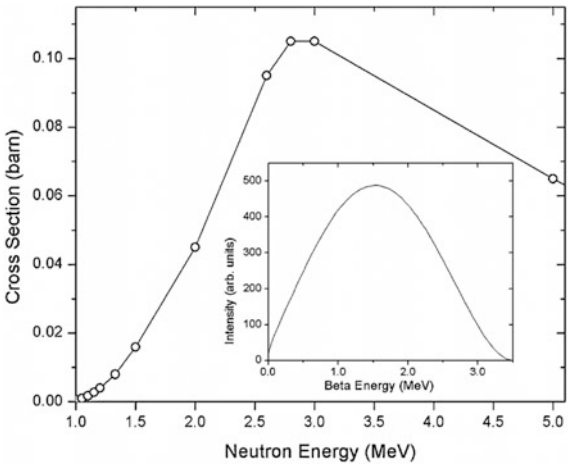

Fig. 6.2 Plot of the $^{9}\mathrm{Be}(n,\alpha)^{6}\mathrm{He}$ reaction cross section as function of neutron energy. *Inset* beta-particle energy spectrum for the decay of ^{6}He. (Data for both plots from NNDC database). Reprinted from Talebitaher and Springham [51] with permission from Elsevier publishing company

The goals for developing the new Be activation detector were: (i) to eliminate the inconvenience of flowing gas in the proportional counters, (ii) to obtain a high β particle count (typically several thousand counts for NX2 PF shots of $\sim 10^8$ neutrons), and thereby achieve good statistical accuracy in the measured neutron fluence, and (iii) attain an absolute calibration using the method described in the next sections.

Bubble Detector

It is a reusable and passive dosimeter that allows instantly visible detection of neutron emission. It can be used to calibrate the other neutron detectors. It consists of droplets of a superheated liquid dispersed throughout an elastic polymer. When neutrons strike these droplets, they form small gaseous bubbles that remain fixed in the polymer and hence providing a real time and immediate visual record of the dose that is directly proportional to the number of bubbles. Neutron elastically scatters from a nucleus, e.g., ^{35}Cl, in a superheated drop; the recoil of nucleus provides energy to nucleate the boiling of the droplet. The number of neutrons per square centimeter equivalent to a dose of 1 rem for 2.5 MeV DD neutrons from plasma focus is $\sim 3 \times 10^7$ n/cm^2 [34].

6.2.3 Fluence Anisotropy Measurements

Neutron anisotropy measurements are amongst the most informative of diagnostics for the deuterium-filled plasma focus as they afford explicit evidence of the nature of the fusion mechanism [35, 36]. It is well known that thermonuclear fusion is characterized by isotropic emission of neutrons with a narrow spread (some keV) of energies around 2.45 MeV. However, numerous experiments conducted by different groups using PF devices covering a wide range of capacitor-bank energies [38–43] show that the emitted neutrons exhibit both fluence and energy anisotropy: the neutron fluence is greater in the axial (0°) direction than in the radial (90°) direction, and the average neutron energy at 0° is significantly higher ($\sim$2.8 MeV) than it is at 90° ($\sim$2.5 MeV). The fusion cannot, therefore, be straightforward thermonuclear fusion within the hot plasma pinch column. In the moving-boiler model [44], ions and electrons within the 'boiler' are thermalized at energies of a few keV (typical of thermonuclear fusion), and the observed neutron emission anisotropy results from center of mass (CM) motion of the whole plasma-containing 'boiler'. However, this model provides no explanation for the intense forwardly directed D^+ ion beam that has been consistently observed for numerous PF devices. D^+ ions ejected from the pinch have a wide spectrum of energies ranging up to a few MeV. However, deuterons with energies < 100 keV are responsible for the bulk of the neutron yield [45–47]. These observations are consistent with the beam-target mechanism [48–50] in which an intense forwardly

directed D^+ ion beam bombards stationary deuterons within the pinch column and the surrounding deuterium gas.

In order to perform anisotropy measurements on the PF device, two identical beryllium activation detectors were fabricated. The DD fusion neutron yield and anisotropy were measured on a shot-to-shot basis for the NX2 plasma focus device using these two detectors at 0° and 90° to the PF axis. Measurements were performed for deuterium gas pressures in the range 6–16 mbar, and positive correlations between neutron yield and anisotropy were observed at all pressures.

Figure 6.3 presents a group of plots containing the main results from this experimental series. As seen in the top-right plot, the highest average neutron yield was obtained for a deuterium gas pressure of 12 mbar. The MCNP derived calibration gives the average neutron yield at 12 mbar to be about 3×10^8 per shot, but a sizeable neutron yield was obtained over the whole 6–16 mbar pressure range. The top-left plot shows that the average count-anisotropy $\langle A_{n\mathrm{Be}} \rangle$ decreases steadily with increasing gas pressure. The other plots in Fig. 6.3 show that for each of the six experimental pressures there is a positive correlation between the count-anisotropy ($A_{n\mathrm{Be}}$) and net neutron count at 0° ($C^0_{n\mathrm{Be}}$) (i.e. higher yielding shots tend to have higher count-anisotropy).

Subsequently, the contribution to the fusion yield produced by the forwardly directed D^+ ion beam, emitted from the plasma pinch, was investigated by using a circular Pyrex plate to obstruct the beam and suppress its fusion contribution. Neutron measurements were performed with the obstacle positioned at two distances from the anode tip (3.0 and 6.0 cm), and also without the obstacle. Two identical beryllium activation detectors were positioned at 0° and 90° to the PF axis, respectively. The distance from the anode tip to the mid-point of each Be plate was 250 mm. The gross count was integrated over a 3.0 s interval (=3.7 half-lives) following each PF shot, and the background count was subtracted to give the net count: denoted $C^0_{n\mathrm{Be}}$ and $C^{90}_{n\mathrm{Be}}$ for the 0° and 90° beryllium detectors, respectively. A schematic diagram of the experimental setup is shown in Fig. 6.4.

Figure 6.5 shows the variability of the neutron yield in plasma focus shots. An estimate of the fraction of the neutron yield Y_n originating within the pinch can be made by averaging the 0° and 90° count values for the two cases: without-obstacle and with-obstacle ($z = 3.0\,\mathrm{cm}$ or $6.0\,\mathrm{cm}$). The estimated pinch fusion contribution is then $\sim 80\%$.

6.2.4 Neutron Energy Measurements

As previously mentioned, the neutron energy spectrum in DD fusion reaction in plasma focus device shows a large range of energy (2.2–2.9 MeV) due to the high-energy deuteron involvement in neutron production.

Plastic scintillator can be employed for fast neutron measurements. Some of the neutrons entering the plastic scintillator will undergo elastic scattering collisions

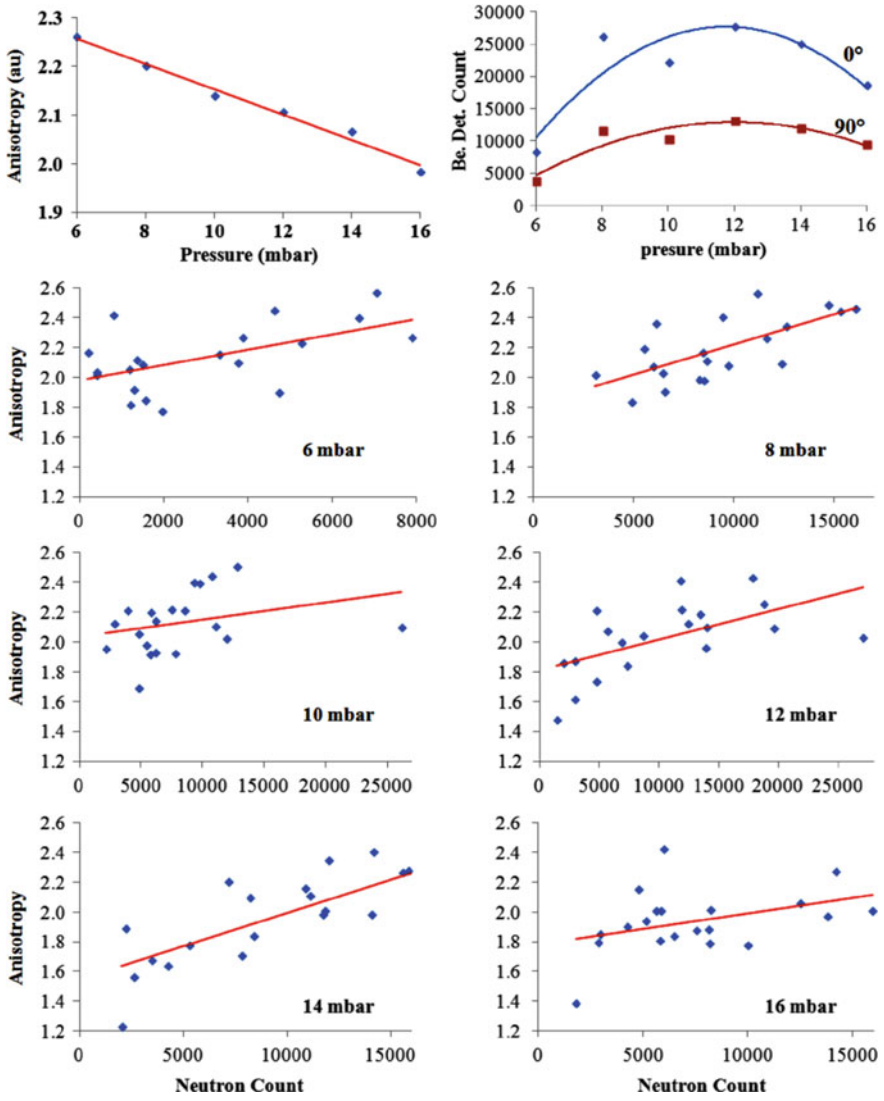

Fig. 6.3 *Top right* Average Be detector count (0° and 90°) vs. D2 gas pressure; *Top left* Average neutron count-anisotropy vs. D2 gas pressure; (other panels) individual shot count-anisotropy for different D2 gas pressures. Reprinted from Talebitaher and Springham [37] with permission from Elsevier publishing company

with hydrogen nuclei (i.e. protons) which comprise part of the polymer chain in the plastic scintillator. The colliding neutron transfers some of its kinetic energy to the proton in one collision. The fraction of kinetic energy given to the proton varies between $\sim$ 0 and $\sim$1 depending on the scattering angle, and averaging one-half of

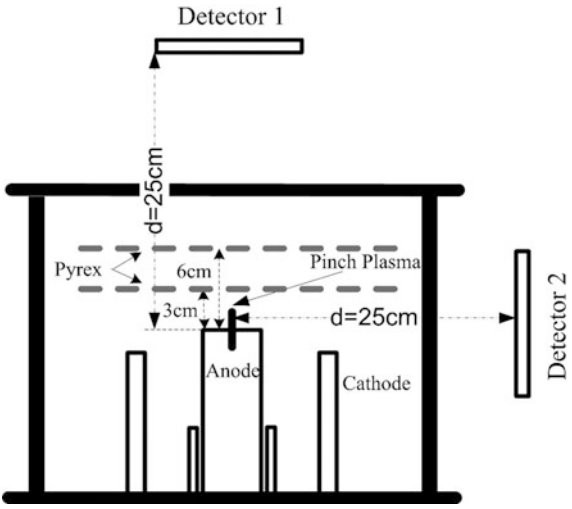

Fig. 6.4 Schematic diagram (not to scale) of the NX2 plasma focus device and beryllium activation detectors for neutron yield and anisotropy measurements. *Dashed lines* indicate the two alternative positions for the circular Pyrex-obstacle (when used). Reprinted from Talebitaher and Springham [37] with permission from Elsevier publishing company

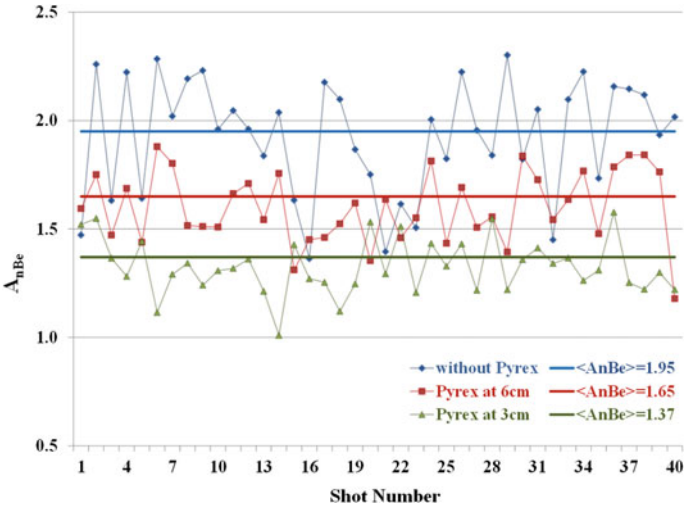

Fig. 6.5 Individual shot count-anisotropies ($A_{n\mathrm{Be}}$) over 40 shot series, without the Pyrex obstacle and with the Pyrex obstacle at positions: $z = 3.0$ or 6.0 cm. Statistical uncertainties in $A_{n\mathrm{Be}}$ values are typically $\sim 2\%$, and therefore too small to indicate as error bars. Reprinted from Talebitaher and Springham [37] with permission from Elsevier publishing company

the neutron energy. As a result, the scintillator material gains energy from the proton and the excited scintillating molecule will produce light photons during the de-excitation process. The light photons are then detected by a photomultiplier tube. The scintillation decay-time is approximately 2 ns for most types of plastic scintillator.

It is possible to obtain a few nanoseconds resolution with the combination of a fast multiplier and a selected scintillation material. The detection efficiency for fast neutrons in a plastic scintillator depends upon the neutron energy, the geometry, and the scintillation material. Figure 6.6 shows the various components of an assembled plastic scintillator and photomultiplier-tube combination; a 14-stage high gain photo-multiplier tube, Thorn EMI 9813BK coupled with NE-102A scintillator (of 40 mm length and 52 mm diameter) having decay time constant of $\sim$2.4 ns [55].

The neutrons produced from the DD fusion reaction are non-relativistic since they have energy of 2.45 MeV which is much less than 940 MeV (rest mass energy of neutrons). The energy resolution is given by

$$\frac{\Delta E}{E} = \frac{2\Delta t}{\tau}, \quad \tau = \frac{x}{v}$$

where Δt is the emission duration, and τ is the average time of flight of the neutron from the source to the detector. The scintillation decay-time can be neglected as it is so much shorter than the neutron emission time in the plasma focus. Then the neutron velocity can be calculated by

$$v = \left(\frac{2E}{m}\right)^{1/2}$$

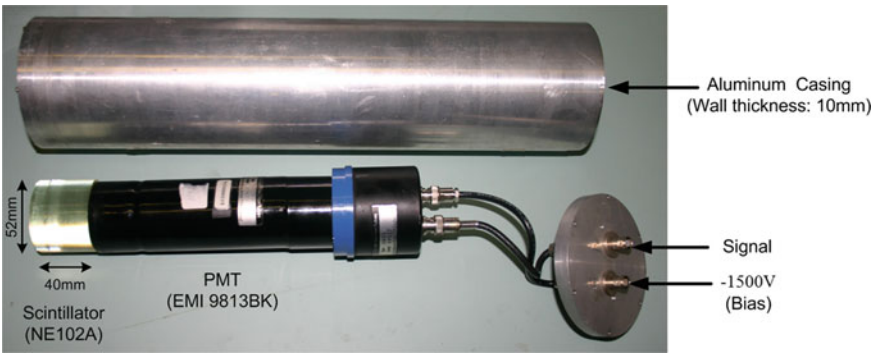

Fig. 6.6 Components of Scintillator-PMT combination [56]

6.2.5 Monte Carlo Simulation for Neutron Detector

Simulations necessary for the absolute efficiency calibration of the beryllium activation detector were performed with the Monte Carlo radiation transport code MCNP5. The overall simulation of the detector response was conducted in two parts: first, the neutron interaction in the Be and the production of ^{6}He; and second, the path of the emitted β particle and its energy-deposition (if any) in one of the Xe gas layers. The simulated geometry was simplified to three cuboids representing beryllium and xenon cells with the same dimensions and densities as for the physical detector. A parallel neutron beam of 1 n/cm^2 fluence was taken to be normally incident on the (largest area) face of the detector. The probability of a β particle escaping from the Be sheet and entering one of the xenon cells is clearly greater if it originates close to the surface of the Be sheet. For this reason, in the MCNP simulation, the beryllium sheet is divided into five layers (sub-cells), each of 1-mm thickness, and the neutron-induced production of ^{6}He within each layer is determined separately. Simulations were performed over the range of neutron energies 2.0–4.0 MeV in steps of 0.2 MeV. The neutron energy 2.45 MeV which is characteristic of DD thermonuclear fusion was also simulated. This energy range is sufficiently wide to cover neutrons from almost any DD fusion device. From the first part of the simulation η-values $(\eta_1(E_n), \ldots, \eta_5(E_n))$, representing the number of ^{6}He atoms produced in each layer for a neutron beam of energy E_n and 1 n/cm^2 fluence, were calculated. As examples, η-values found for a selection of four of the neutron energies simulated are shown in Table 6.3. In these MCNP5 simulations, the neutron beam is incident on the "layer 1 side" of the Be cell.

In the second part of the MCNP simulation, the probability of a β particle, originating in a given layer, reaching a Xe gas cell and depositing energy E_{dep} is tallied. The ^{6}He β energy spectrum used for this simulation, and plotted in Fig. 6.7,

Table 6.3 Beryllium layers (each 1 mm) contribution to ^{6}He production

Layer	E_n = 2.0 MeV	2.2 MeV	2.4 MeV	2.45 MeV	2.6 MeV	2.8 MeV
η_1	0.1279	0.1763	0.2246	0.2366	0.2776	0.3037
η_2	0.1274	0.1751	0.2219	0.2334	0.2732	0.3022
η_3	0.1264	0.1733	0.2185	0.2294	0.2676	0.2993
η_4	0.1251	0.1709	0.2146	0.2249	0.2612	0.2953
η_5	0.1234	0.1679	0.2099	0.2198	0.2536	0.2898
η_{tot}	0.6302	0.8636	1.089	1.144	1.333	1.490
Layer	E_n = 3.0 MeV	3.2 MeV	3.4 MeV	3.6 MeV	3.8 MeV	4.0 MeV
η_1	0.3033	0.2921	0.2806	0.2697	0.2589	0.2478
η_2	0.3019	0.2905	0.2788	0.2679	0.2569	0.2457
η_3	0.2991	0.2877	0.2759	0.2649	0.2538	0.2425
η_4	0.2952	0.2838	0.2719	0.2609	0.2497	0.2384
η_5	0.2900	0.2787	0.2669	0.2557	0.2445	0.2334
η_{tot}	1.489	1.433	1.374	1.319	1.263	1.208

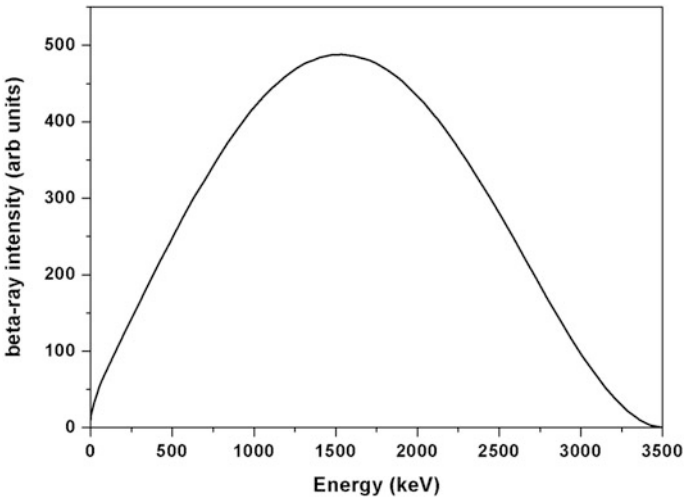

Fig. 6.7 β-particle energy spectrum for the decay of ^{6}He [56]

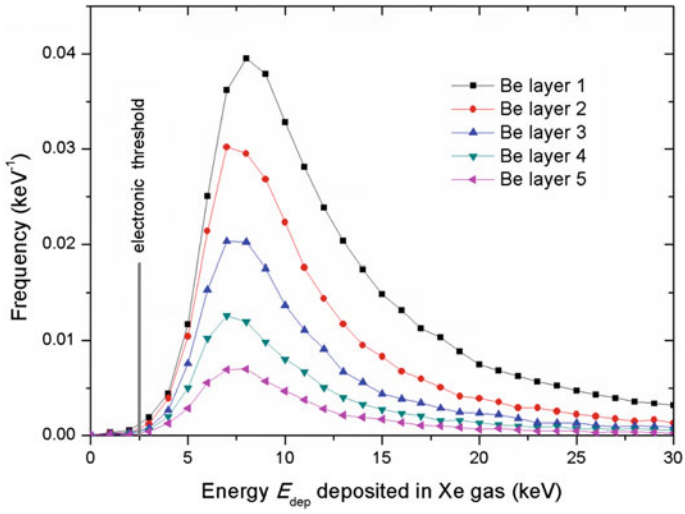

Fig. 6.8 MCNP simulation results of frequency distribution of energy deposition in PC xenon gas layer (12.7 mm depth) by ^{6}He β particles which escape from Be sheet and enter PC. Separate curves are for ^{6}He β particles originating in each 1 mm thick layer of the 5 mm thick Be sheet. In this simulation a PC is located on one side only of the Be sheet, and adjacent to layer 1. Reprinted from Talebitaher and Springham [51] with permission from Elsevier publishing company

was taken from the NNDC database [32]. The probability distributions obtained from this part of the simulation are plotted in Fig. 6.8. The summed probabilities for $E_{\mathrm{dep}} > 2.5$ keV (denoted $\kappa_1, \ldots, \kappa_5$) is shown in the first part of Table 6.3.

Since, however, as the xenon cells are placed symmetrically on the either side of the Be cell, this probability distribution can be folded as shown in the second part of Table 6.3. It can be seen that approximately 40% of the ^{6}He β particles are detected in one of the proportional counters.

Then the overall calibration, or response function, of the detector is given by

$$R(E_n) = \sum_{l=1}^{5} R_l(E_n) = \sum_{l=1}^{5} \eta_l(E_n) \times (\kappa_l + \kappa_{6-l})$$

where η_l is the neutron energy dependent production of ^{6}He in layer l of the Be sheet, and κ_l is the probability of a β particle originating in layer l depositing more than 2.5 keV of energy in one xenon gas cell.

Making use of above equation with values from Table 6.3 (expanded for all E_n) and Table 6.4: the calculated response function $R(E_n)$ of the detector for a parallel beam of 1 neutron/cm^2 is presented in Table 6.5. These values of $R(E_n)$ are also plotted in Fig. 6.9, along with the contributions $R_L(E_n)$ from each of the 5 layers modeled in MCNP5. The largest contribution to the uncertainties in these values comes from the experimental cross-sectional measurements. From Fig. 6.2 of Ref. [33], it is apparent that the shape (or relative cross section vs. energy) of the ^{9}Be(n, α)^{6}He cross section is very well determined. Table 6.2 of the same reference lists the six absolute cross-sectional points around the 2–4 MeV region relevant to this work, and the mean relative uncertainty for these cross sections is 9.6%. Consequently, the shape of the response function in Fig. 6.9 should be correspondingly accurate, but the absolute values across the curve as a whole, have an estimated uncertainty of ±10%.

To consider the response function for point sources, it is convenient to keep the number of neutrons incident on the Be plate the same as for the parallel beam of 1 neutron/cm^2, and therefore numerically equal to the plate area (in cm^2) of 21 × 10.6 = 222.6. Then the response factor is affected only by the spread of angles of incidence. Also useful is the formula for the solid angle subtended by a right rectangular pyramid:

$$\Omega_{\text{rrp}} = 4\arctan\left(\frac{ab}{2\text{d}\sqrt{4d^2 + a^2 + b^2}}\right)$$

Table 6.4 Sum of frequencies of β particle originating in each 1 mm layer of the Be cell entering a Xe cell and depositing energy >2.5 keV

Beryllium layer	κ_1	κ_2	κ_3	κ_4	κ_5
Sum of frequency	0.416	0.264	0.167	0.102	0.058
Folded Be layer	$\kappa_1 + \kappa_5$	$\kappa_2 + \kappa_4$	$2\kappa_3$		
Folded frequency	0.473	0.366	0.335		

Table 6.5 Counts from layers for a parallel neutron beam fluence of 1 neutron/cm^2

Layer	E_n = 2.0 MeV	2.2 MeV	2.4 MeV	2.45 MeV	2.6 MeV	2.8 MeV
R_1	0.0605	0.0835	0.1064	0.1121	0.1314	0.1438
R_2	0.0466	0.0641	0.0812	0.0854	0.0999	0.1106
R_3	0.0423	0.0580	0.0732	0.0768	0.0896	0.1002
R_4	0.0458	0.0625	0.0785	0.0823	0.0956	0.1080
R_5	0.0584	0.0795	0.0994	0.1041	0.1201	0.1372
R_{total}	0.2537	0.3476	0.4386	0.4607	0.5367	0.5999
Layer	E_n = 3.0 MeV	3.2 MeV	3.4 MeV	3.6 MeV	3.8 MeV	4.0 MeV
R_1	0.1436	0.1383	0.1329	0.1277	0.1226	0.1173
R_2	0.1105	0.1063	0.1020	0.0980	0.0940	0.0899
R_3	0.1002	0.0964	0.0924	0.0887	0.0850	0.0812
R_4	0.1080	0.1039	0.0995	0.0955	0.0914	0.0872
R_5	0.1373	0.1320	0.1264	0.1211	0.1158	0.1105
R_{total}	0.5996	0.5770	0.5532	0.5311	0.5088	0.4862

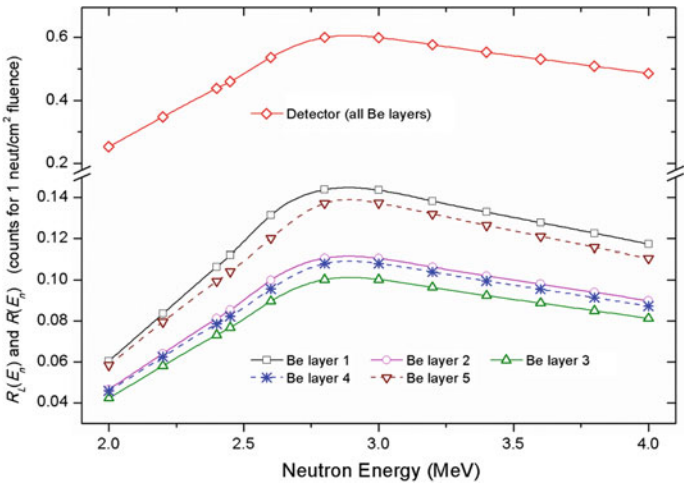

Fig. 6.9 Response function $R(E_n)$ of beryllium neutron activation detector for a parallel neutron beam of fluence 1 neutron/cm^2, and contributions $R_L(E_n)$ from each 1 mm thick layer of the Be sheet. Note that the vertical axis is broken and the two parts are scaled differently. The absolute $R(E_n)$ values across the curve as a whole, have an estimated uncertainty of ±10%. Reprinted from Talebitaher and Springham [51] with permission from Elsevier publishing company

where a and b are the dimensions of the Be plate and d is the distance from the point source to the midplane of the plate. Hence, for the above scaling, the emittance of the source is $(222.6/\Omega_{Be})$ n/sr. MCNP simulations were performed for a point source of 2.45 MeV neutrons located at d = 15, 20, 25, 30, 40, and 50 cm. The simulation results were processed in an analogous way to that described above, and scaled to 222.6 neutrons incident on the plate midplane. Figure 6.10 shows a

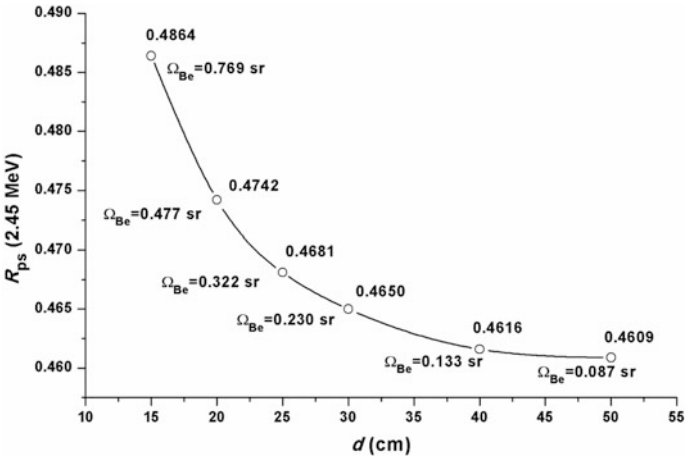

Fig. 6.10 Beryllium neutron detector response function $R_{ps}(E_n = 2.45\,\text{MeV})$ for a point source at distance d. Reprinted from Talebitaher and Springham [51] with permission from Elsevier publishing company

plot of point source response function $R_{ps}(E_n = 2.45\,\text{MeV})$ versus distance d. It can be seen that for larger d, the response tends asymptotically towards the value (0.4607) obtained for a parallel beam. To obtain the response function in terms of neutrons per steradian, a R_{ps} value can be interpolated from the graph and multiplied by the factor $(\Omega_{Be}/222.6)$.

Special Calibration for NX2 Plasma Focus Device

To approach the numerical absolute efficiency calibration of the activation detector, the accurate reaction cross section is needed which is related to the incoming neutron energy and this in turn is determined by the kinematics of the DD fusion reaction, e.g. for beam-target reactions, it depends on the energy of the incoming deuteron and the angle of neutron emission.

For the first step, we need the angular differential cross section of $D(d, n)^3\text{He}$ reaction as a function of deuteron energy. The most suitable references are IAEA Technical Report [52] and Brown-Jarmie [53]. Both data have been fitted by using a polynomial function of $\cos(\theta)$, because the DD differential cross sections are symmetric about 90°. We have chosen the IAEA result in the form of Legendre polynomial:

$$\sigma(\theta) = S_0\left[A_0 + \frac{A_2}{2}\left(3\cos^2\theta - 1\right) + \frac{A_4}{8}\left(35\cos^4\theta - 30\cos^2\theta + 3\right)\right]$$

where S_0 is Center of Mass (CM) differential cross section at 0°, A_0, A_2, and A_4 are reduced Legendre coefficients. Figure 6.11 shows the angular distribution of CM cross section of DD reaction.

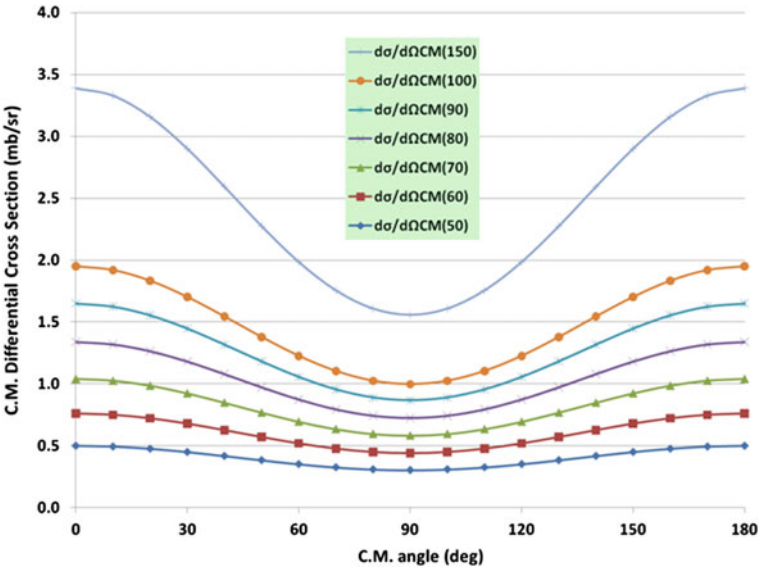

Fig. 6.11 Center of Mass (C.M.) cross section for DD reaction with the deuteron energy (in keV) as a parameter [56]

But as the measurement is performed in the Lab Frame (LF), the data must be changed to the lab frame regarding to these followed formulas:

$$\theta_{\mathrm{Lab}} = \tan^{-1}\left(\frac{\sin\,\theta_{\mathrm{CM}}}{\gamma + \cos\,\theta_{\mathrm{CM}}}\right) \quad \text{where:} \quad \gamma = \left(\frac{\mathrm{E_d}}{3E_{\mathrm{d}} + 6Q}\right)^{1/2} \quad \text{and}$$
$$Q = 3.27\,\mathrm{MeV}$$

$$\text{so,} \quad \left(\frac{\mathrm{d}\sigma}{\mathrm{d}\Omega}\right)_{\mathrm{Lab}} = \frac{(1 + 2\gamma\cos\,\theta_{\mathrm{CM}} + \gamma^2)^{3/2}}{|1 + \gamma\cos\,\theta_{\mathrm{CM}}|}\left(\frac{\mathrm{d}\sigma}{\mathrm{d}\Omega}\right)_{\mathrm{CM}}$$

The result is shown in Fig. 6.12.

In the second step, we need the angular distribution of neutron energy from $D(d, n)\,^3\mathrm{He}$ reaction with different deuteron energy. Using accepted atomic masses of $m_D = 2.014102(u)$, $m_n = 1.008665(u)$, and $m_{\mathrm{He3}} = 3.016029(u)$, the energy released in the $D(d, n)^3\mathrm{He}$ reaction is $Q = \Delta m \times 931.5 = 3.27\,\mathrm{MeV}$ and the neutron energy is given by the kinematic formulae below, and plotted in Fig. 6.13 for the deuteron energy range $E_D = 50$ to 150 keV.

$$E_n = \left(u + \sqrt{u^2 + w}\right)^2$$

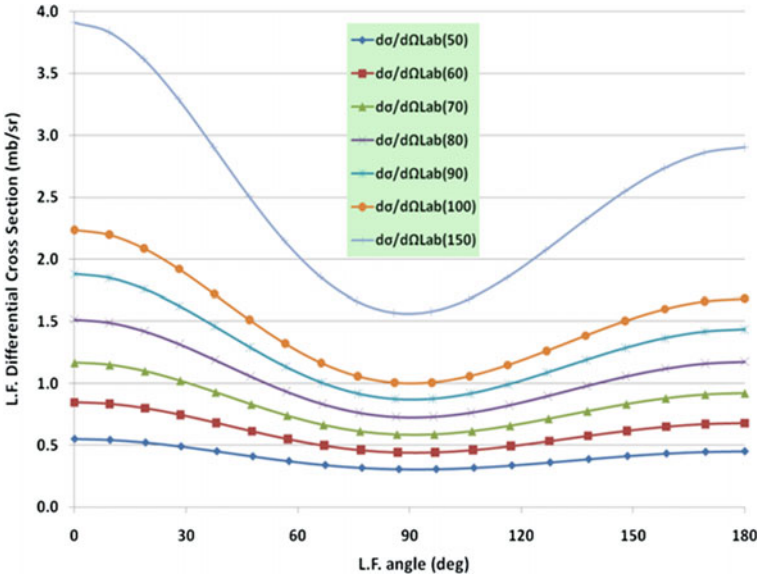

Fig. 6.12 Lab frame cross section for DD reaction with the deuteron energy (in keV) as a parameter [56]

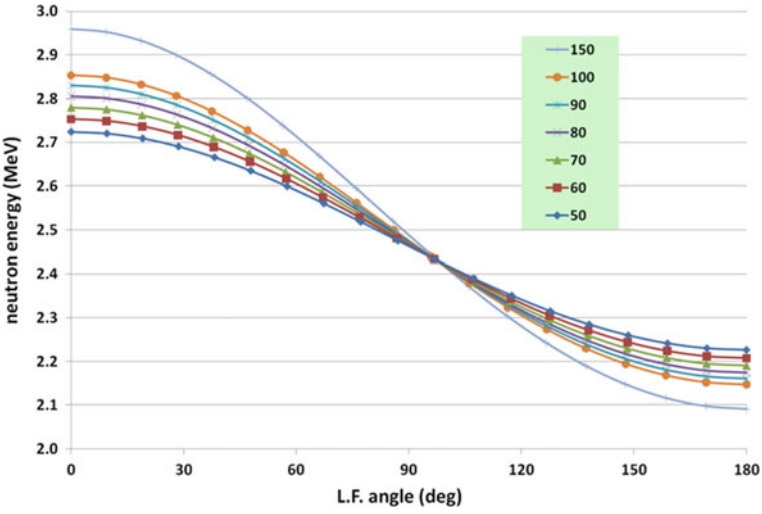

Fig. 6.13 Lab frame (L.F.) neutron energy distribution for DD reaction with the deuteron energy (in keV) as a parameter [56]

where

$$w = \frac{Q \times M_{\mathrm{He3}} + E_D(M_{\mathrm{He3}} - M_D)}{M_{\mathrm{He3}} + M_n} = E_D(90^{\mathrm{o}})$$

$$u = \frac{(M_D M_n E_D)^{1/2}}{M_{\mathrm{He3}} + M_n} \cos\theta_{\mathrm{Lab}}$$

To find the accurate beryllium count factor or efficiency for a special device like NX2 plasma focus device, the system geometry has been simulated in Monte-Carlo *N*-Particle code (MCNP5-visual version). The chamber's size and material, all flanges and plates, xenon proportional counters and beryllium plate of neutron detector have been arranged carefully. The distances between detectors and anode tip are 25.0 cm as it is in real experiment. Figure 6.14 shows the 3D image of simulation design.

Moreover, the source has been considered as a cylinder with 10 mm height and 2 mm diameter (the same as deuteron source shape or pinch region in NX2 plasma focus device). The angular distribution of lab-frame cross section and neutron energy have been calculated (as it is explained in introduction) and put as SDEF

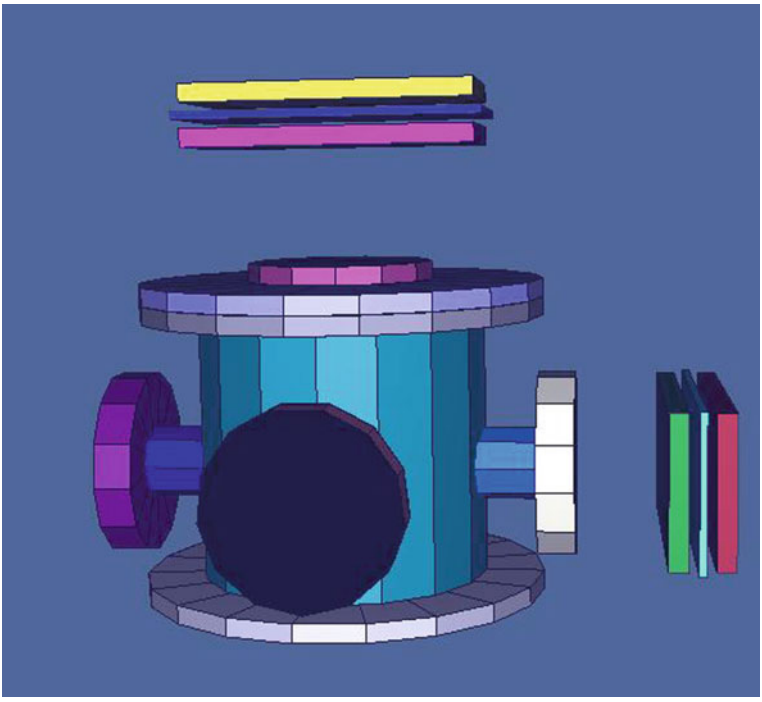

Fig. 6.14 Simulation of NX2 chamber and beryllium detectors in MCNP-visual [56]

input data for MCNP. The SDEF inputs include Source Information (SI) $(\cos(\theta_{\text{Lab}}))$, Source Probabilities (SP) (Cross Section), and Distribution Source (DS) (Energy).

The real deuteron angular and energy distributions within the pinch column are not known, but as a model we assumed the physically reasonable case [57] of deuterons with directions distributed isotropically within a forwardly directed 30° cone, and with positions distributed uniformly throughout a cylinder of 2 mm diameter and 10 mm length (at the pinch location). The deuterons were assumed to be mono-energetic, and this value of energy was varied as a parameter. The DD kinematics were entered into SDEF cards in the MCNP simulation as outlined above, so that the outgoing neutron energy and relative angular fluence were in accordance with the differential cross section (for the selected energy) and the reaction kinematics. Since the response of the beryllium detectors varies with neutron energy, the purpose of this simulation was to find the beryllium detector count/anisotropy as a function of deuteron energy within the DD fusion model described above. In order to make the correspondence with the experimental situation as close as possible, the simulation includes the effects of neutron scattering and absorption, in the chamber wall and top-plate, etc.

The simulation was performed for a range of deuteron energies as shown in Table 6.6. The count factors given in this table represent the number of counts per source neutron for the beryllium detectors located at 0° and 90°, based on the source model described above. It can be seen that the modeled anisotropy increases as the deuteron energy increases. It should be emphasized that values in the last column represent a mixture of fluence anisotropy and energy anisotropy as it affects the count from the beryllium detectors. The first row of the table labeled '0 keV' represents thermonuclear fusion, for which the neutron yield is perfectly isotropic and the neutron energy is 2.45 MeV. The simulated anisotropy value of 1.140 is, therefore, the result of neutron scattering and absorption in the chamber materials. For comparison, the simulation was also performed in absence of the chamber and all other materials (done by setting their densities to zero). In this case, the thermonuclear '0 keV' modeled anisotropy is 1.00, as expected.

Figure 6.15 shows the efficiency or response factor for both side-on and end-on situations. Also, Table 6.7 compares the effect of scattering in different deuteron

Table 6.6 Efficiency and anisotropy for different deuteron energy

E_D (keV)	Be count factor (0°) [/n]	Be count factor (90°) [/n]	Anisotropy
0	4.34×10^{-5}	3.81×10^{-5}	1.140
50	7.08×10^{-5}	3.49×10^{-5}	2.030
60	7.36×10^{-5}	3.44×10^{-5}	2.140
70	7.64×10^{-5}	3.42×10^{-5}	2.235
80	7.96×10^{-5}	3.43×10^{-5}	2.324
90	8.24×10^{-5}	3.40×10^{-5}	2.423
100	8.24×10^{-5}	3.38×10^{-5}	2.435
150	8.72×10^{-5}	3.32×10^{-5}	2.624

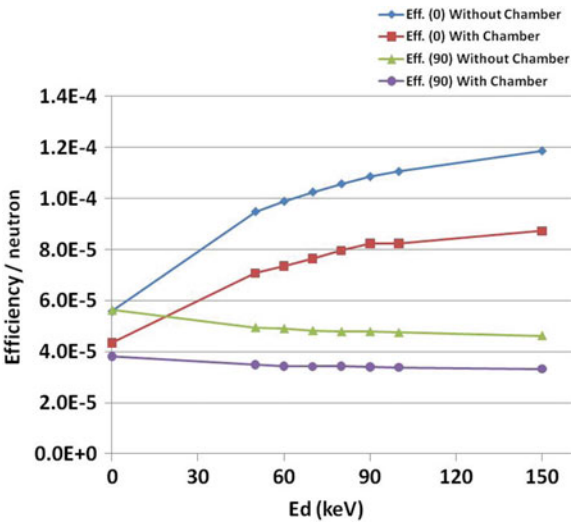

Fig. 6.15 Total efficiency of neutron detector in axial and radial direction at 25.0 cm from anode tip [56]

Table 6.7 Changing percentage of efficiency and anisotropy by scattering effect

E_D (keV)	Eff. (0°) %	Eff. (90°) %	Anisotropy %
0	−22.3	−32.4	14.9
50	−25.4	−29.5	5.8
60	−25.6	−29.9	6.1
70	−25.5	−29.2	5.2
80	−24.7	−28.4	5.2
90	−24.1	−28.9	6.8
100	−25.5	−28.6	4.5
150	−26.4	−28.1	2.3

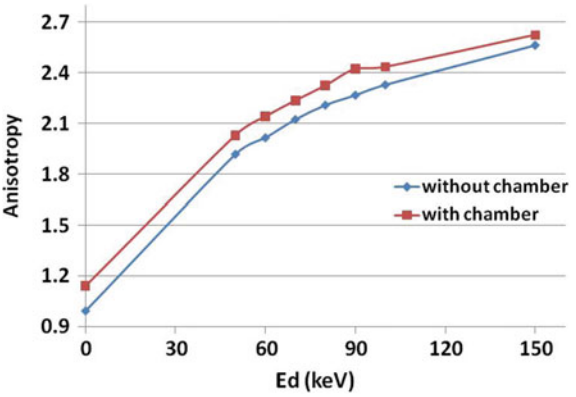

Fig. 6.16 The result of neutron anisotropy versus deuteron energy by MCNP [56]

energy. It can be seen that counts in both beryllium detectors are reduced as a result of neutron scattering, but more so for the side-on detector (at 90°) than for the end-on (0°) detector. Figure 6.16 shows the anisotropy versus deuteron energy in presence and absence of the chamber. It is worth mentioning that for calculating the efficiency factor for a different device, the simulation must be repeated with regarding the actual geometry and material of the device. Even for NX2 plasma focus device, to measure the neutron yield at different distances, the simulation must be repeated for them.

MCNP simulations also confirmed that for the best estimation of neutron yield, both detectors should be positioned at the same distances from the PF pinch, and for all experimental measurements this distance was 25 cm. Since anisotropy refers to particular deuteron energy, with calculating the ratio and referring to Fig. 6.16, the average deuteron energy in that experiment can be found. Finally to refer the efficiency plot in Fig. 6.15, and find the proper count factor (or just refer to Table 6.6 and find it by interpolation), the final neutron yield can be calculated by dividing the output count by efficiency. With this assumption, the results from both angles give almost the same numbers.

Moreover, MCNP simulation was applied to find the neutron fluence versus energy at different angles in the range of 0°–180° (with 30° interval) to find the neutron energy spectrum in plasma focus device. It was assumed that 30° forward cone deuteron beam is coming from pinch region with constant energy (100 keV) based on beam-target mechanism for DD reaction. The point detector was kept at 1 m from the center of pinch.

The simulation was run for two different situations, without chamber (void command) shown in Fig. 6.17 and with complete NX2 chamber shown in

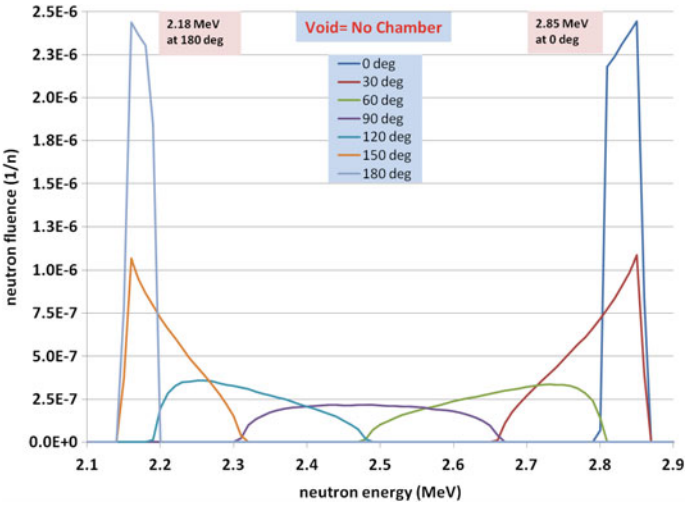

Fig. 6.17 Neuron fluence verusu energy at different angles with 100 keV deuteron energy 30° forward cone at r = 100 cm from center of pinch, without chamber. [56]

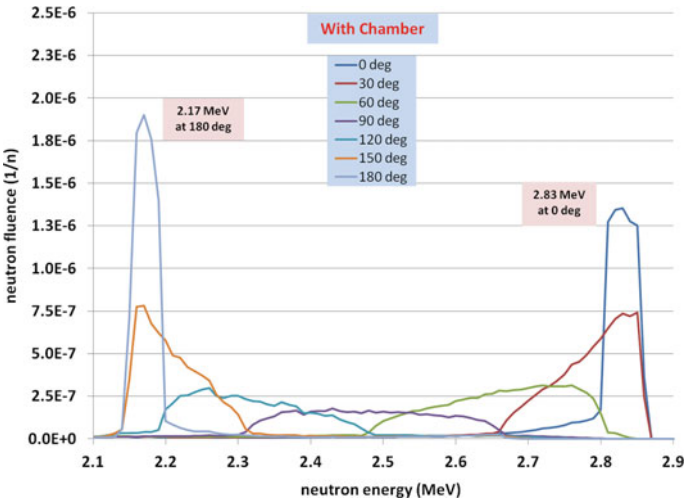

Fig. 6.18 Neuron fluence versus energy at different angles with 100 keV deuteron energy 30° forward cone at r = 100 cm from center of pinch, with NX2 chamber. [56]

Fig. 6.18. The result clearly shows the shifting of neutron energy by changing the angle for both situations. Regarding to the thermonuclear DD reaction, the neutron energy which is 2.45 MeV, at side-on (90°) the neutron fluence will remain almost constant in the range of 2.30–2.65 MeV, however, for 180° it has a peak around 2.18 MeV (∼0.3 MeV less) and for end-on (0°) it has a peak around 2.85 MeV (∼0.4 MeV more). As the beryllium neutron reaction cross section is depended to the neutron energy, this energy spectrum must be taken in account for response factor calculation.

It is worth referring to the simulation which was done by Bernstein [10]. In Fig. 6.4 of mentioned paper, there are two sharp spikes at both sides of neutron energy spectra for θ_n (neutron detector is placed at 90°). It is in contrast to our simulation which shows zero at the end sides (see the purple line). The reason is in his assumption, that the deuterons are emitted at 90° trajectories with respect to the PF axis (single angle θ_d = 90°). However, we have assumed that deuterons are going via a 30° cone with respect to the PF axis.

6.3 Proton Diagnostics

The ion energy and yield investigation in plasma focus device can be done by different methods. The most common method is using a Faraday Cup to find the number (fluence) of arriving ions. Mixing it with a magnetic system introduces the ion magnetic spectroscopy. Silicon-based detectors such as silicon PIN diode also

can be used for proton yield and energy measurement using the magnetic and electric fields.

However, the most efficient (almost 100%) system for ion detection is using the nuclear track detector. When a particle (in our case, proton or deuteron) crosses the nuclear track detector, it produces polymer chain scission damage within a cylindrical region extending to a few tens of μm, forming the so-called latent track. They can be made visible under an optical microscope by etching the exposed detector sheets with appropriate chemical solutions. During the etching, the material is removed along the latent track and conical etch-pits are formed. They are also insensitive to gamma-ray.

6.3.1 Polymer Nuclear Track Detectors

Poly-Allyl-Diglycol-Carbonate (PADC), marketed under the commercial name CR-39, is an excellent material for the detection and measurement of low and medium energy charge particles such as protons and alphas due to its dielectric properties, which makes it resistive to annealing [58]. With the advent of research in plasma technologies, it has been used as a Solid State Nuclear Track Detector (SSNTD) in detecting charged particles emitted from plasma devices. It is worth emphasizing that linearity of detector response and high spatial resolution (ideally sub-pixel) are key factors for the successful application of the coded aperture imaging (CAI) technique. In both these respects, CR-39 is an excellent detector: track-counting ensures very good linearity and the spatial resolution is of the order of microns.

When hit by heavy ionizing particles, invisible latent tracks of cleaved polymer chains are created. These latent tracks are developed by chemically etching the PADC, hence fixing the tracks for subsequent studies. The formation of tracks through etching is dependent on the track etch rate V_T, being greater than the bulk etch rate V_B which produces tracks or pits at the position of the latent tracks. CR-39 is a transparent thermo-set polymer with chemical formula $C_{12}H_{18}O_7$. The structure of the monomer is given below:

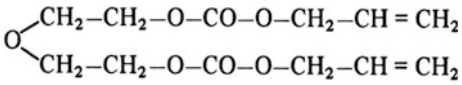

Table 6.8 Characteristic of CR-39 elements for stopping power calculation

CR-39 (PM-355) with ρ = 1.3 g/cm^3				
Element symbol	Atomic number (Z)	Formula number	Ionization pot. (eV)	No. density n (cm^{-3})
H	1	18	20.4	5.14E+22
C	6	12	73.8	3.43E+22
O	8	7	115.7	2.00E+22

6.3.2 Proton Stopping-Power and Range

To compute the Stopping Power for a compound using the Bethe-Bloch formula, we must sum the contributions for each element in the compound as below:

$$S(E) = \left(-\frac{dE}{dx}\right)_{tot} = \frac{z^2 e^4}{4\pi\varepsilon_0^2 m_0 v^2} \sum_i n_i Z_i \ln\left(\frac{2m_0 v^2}{I_i}\right)$$

where Z_i is the atomic number for the ith element, I_i is the mean ionization and excitation potential for that element (given by Tsoulfanidis-1995 [59]) and n_i is the associated atomic number density (1.3 g/cm^3) (see Table 6.8).

Stopping Powers were calculated from the equation given above for proton energies in the range 1–18 MeV, and the value plotted in Fig. 6.19. The Stopping Power calculation shows the expected approximately inverse relationship between proton energy and stopping power. It is convenient to consider the kinetic energy of 3 MeV to be characteristic of $D(d, p)^3$H fusion protons, and these protons have a stopping power of 14.83 keV/μm in CR-39. Polymer nuclear track detectors registered the arrival positions of the particles passing through the mask. The detection efficiency of CR-39 for charge particles incident at near normal incidence is effectively 100%.

The Stopping and Range of Ions in Matter (SRIM) Monte Carlo Simulation can be used for calculating the stopping power which demonstrates good agreement with graph. Using this simulation, we can determine the depth penetration range of the various charged particles emitted from the plasma focus. Figure 6.20 shows the output screen of SRIM program which is run by 3 MeV protons passing through a CR-39 layer. It illustrates that these protons can go 118 μm deep in CR-39 detectors. As CR-39 characteristics are not in the SRIM library, we have to include it in a new layer with element formula number as given in Table 6.8 with density = 1.31 g/cm^3.

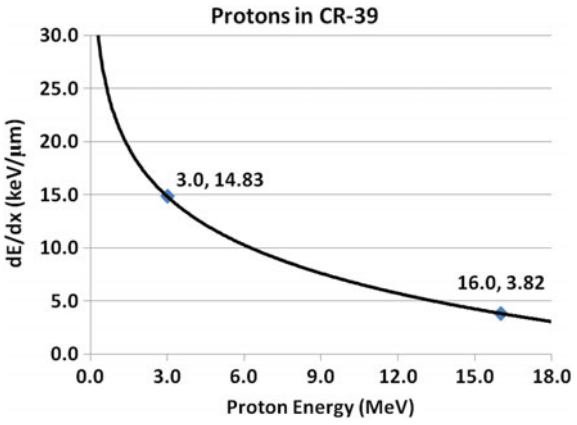

Fig. 6.19 Stopping power graph for protons in CR-39 [56]

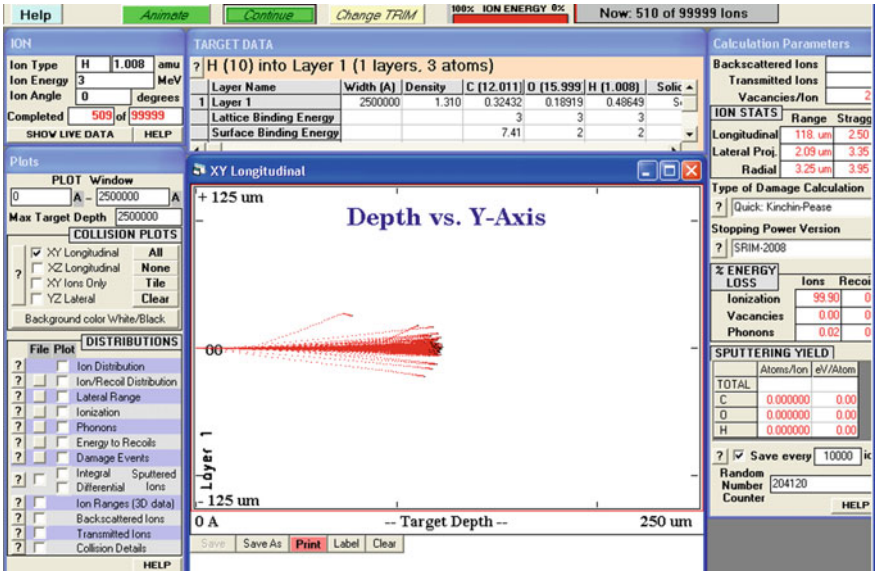

Fig. 6.20 The SRIM simulation result by 3 MeV proton pass through the CR-39 with 250 μm thickness [56]

6.3.3 *Proton Energy Spectroscopy Based on Range*

As mentioned earlier, the most efficient (almost 100%) system for ion detection is using the nuclear track detector [65]. When a particle crosses the nuclear track detector it forms latent track which is made visible under an optical microscope by etching the exposed detector foils with appropriate chemical solutions. During the etching, the material is removed along with the latent track at velocity V_T and isotropically at velocity V_B from the bulk of the material, if $V_T > V_B$ then conical etch-pits are formed.

Etching Criteria

After exposure, the CR-39 detector is chemically etched to reveal an etch-pit (also referred to as a track) where the energetic charged particle entered the detector. This enables us to extract an 'image' of the fusion within the plasma focus in a reliable and efficient fashion. For explaining the nature of charged particle tracks, we can use the Restricted Energy Loss (REL) model. When charge particles pass through nuclear tracks detectors, they leave trails of damage along their tracks. This damage (in the form of a trail of broken polymer chains and free radicals) represents a latent track for each incident particle. The amount of local damage is related to the local rate at which energy is lost by the particle. Non-local forms of energy loss (e.g. bremsstrahlung) are insignificant for protons at these energies; hence REL is essentially equivalent to the stopping power as given by the Bethe–Bloch formula. From Fig. 6.19 and also the Bragg peak in Fig. 6.21, it is clear that the damage

along the trail is lowest as the particle enters the detectors, and highest at the end of its track. Hence, in principle, it is evident that the rate of chemical attack on the damaged trail will not be strictly constant. However to simplify the details of the etch pit geometry, we can assume the rate of chemical attack to be constant. It is common that this rate of chemical attack on the damage trail to be called the "track etch rate", V_T. For areas that have not been damaged by incident charged particles, the chemical attack rate on the surface is constant and is often called the "bulk etch rate", V_B. The main etching parameters are:

- Etchant chemistry [NaOH, KOH, $Ba(OH)_2$ aqueous solution].
- Molarity.
- Temperature.
- Etching time.

Using a simplified model, when the track etch rate is greater than the bulk etch rate, we can predict that a conical pit will be formed if the particle is incident normally to the surface. This is shown in Fig. 6.22. The more general and complicated case is when the particle is not normally incident on the surface which has been discussed in [61].

As we have mentioned earlier about stopping power, the protons with the higher energy (like 14.7 MeV for the case of the $^3He(d, p)^4He$ reaction) lose at the beginning of the track much less than that of lower energy (like 3 MeV for the case

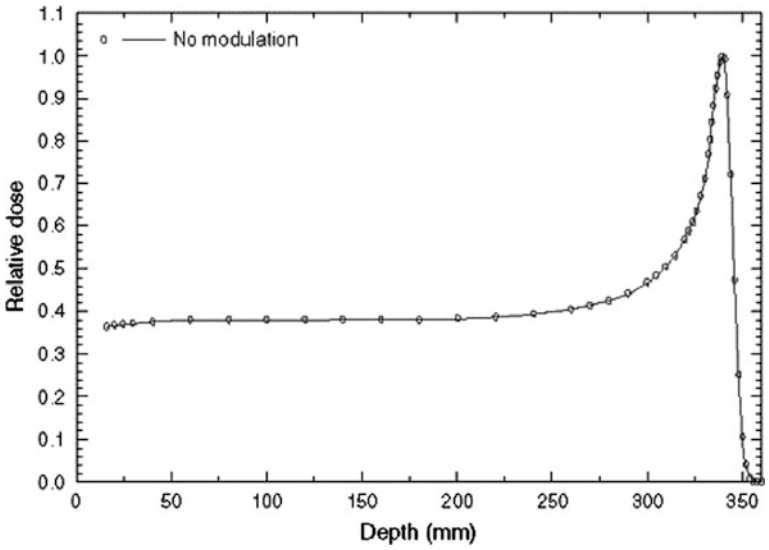

Fig. 6.21 Bragg curve for proton particle. The relative dose (*y*-axis) and depth (*x*-axis) are arbitrary unit. Reprinted from Miller [65] with permission from American Association of Physics Medicine

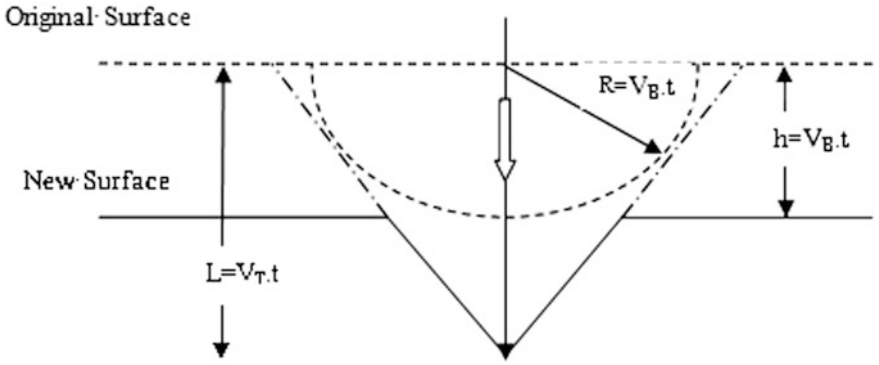

Fig. 6.22 Etching speed and normal track shape [56]

of the $^{2}H(d, p)^{3}H$ reaction). This is based on the predictions of the Bethe–Bloch formula. The formula predicts that when non-relativistic particles have the same charge, the specific energy loss varies approximately inversely with the particle energy. As the amount of damage in the material is directly related to the track etch rate, we can infer that the V_T in the case of the higher energy protons is lower.

But the sensitivity, $V = V_T/V_B$ has much more important role to identify the etching solution; higher sensitivity is depended to higher V_T and lower V_B. The response function of V has been defined by three groups:

Green et al. [62] $V = 1 + \left(11.45e^{-0.339R} + 4.0e^{-0.044R}\right) \times \left(1 - e^{-0.58R}\right)$

Brun et al. [63] $V = 1 + e^{-0.1R+1} - e^{-R+1.27} + e^{1.27} - e^{1}$

Nikezic et al. [64] $V = 1 + e^{-0.06082R+1.119} - e^{-0.8055R+0.8055}$

where R is residual range.

Based on these formulas, a program (NRU) has been written by Nikezic and Yu [64] (City University of Hong Kong) which calculates the track parameters, major and minor axes and depth. Then it plots the track profile and track opening contour. By specification of detector (CR-39 or LR-115), α-particle energy (MeV), etching time (hour), bulk etch rate (μm/h), incident angle and choosing a formula, it shows the tracks shape and its specifications. Figure 6.23 demonstrates the result of a track for 5 MeV α particle which is etched 5 h and bulk etch rate of solution is 1.6 μm/h (for 6.25 n NaOH which we use usually) [60, 66], incident angle 90° by choosing the formula number 1 given by Green et al. [62] (from three suggested empirical formulas in NRU program). It indicates a conic track shape which it can be seen a dark cone under microscope; however, if we increase the etching time, the shape becomes shallow with the appearance of a bright end point when viewed under an optical microscope; these shallow tracks, therefore, have poor contrast with the bright background in the microscope image (see Fig. 6.24).

If the etching time is defined properly for proton tracks, they will appear like a dark end cone circle while deuterons tracks will be a bright end cone circles, because they have been over etched. This is a good approach to distinguish the

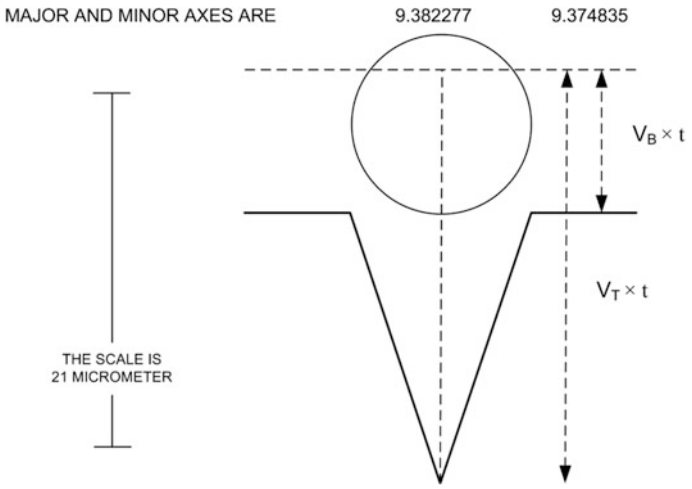

Fig. 6.23 NRU program output shows the 5 MeV α track size after 5 h etching [56]

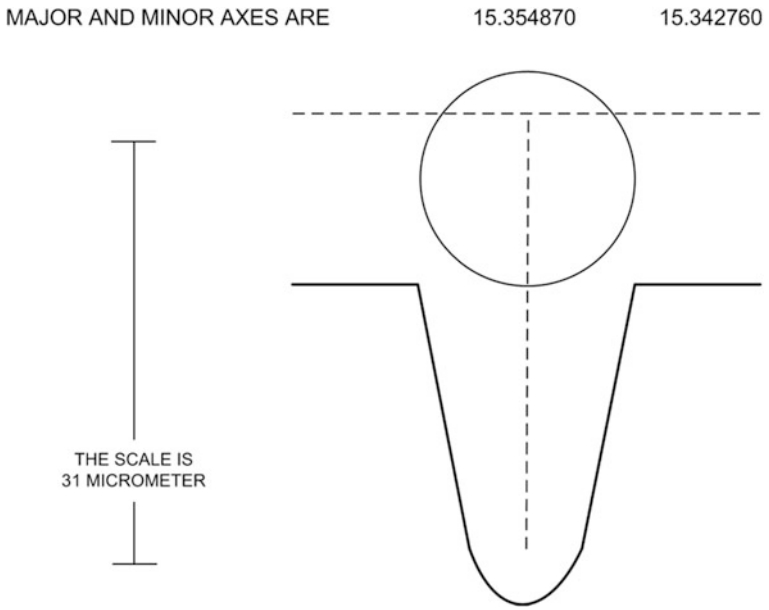

Fig. 6.24 Over etched track shape is shallow and appears like bright circle [56]

genuine proton tracks and high-energy deuteron tracks. Figure 6.25a, b has been taken by Confocal microscope which shows the normal and over etched tracks and Fig. 6.25c shows the difference between proton and deuteron tracks.

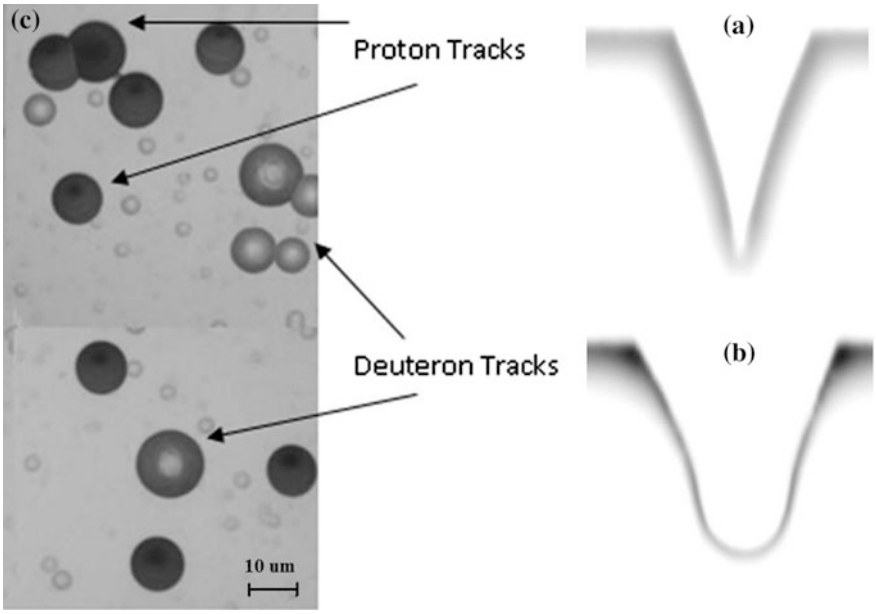

Fig. 6.25 Normal track (**a**) and over etched track (**b**) taken by confocal microscope. **c** Distinguishing between usual proton and deuteron tracks under microscope. Reprinted from Talebitaher et al. [67] with permission from Springer publishing company

6.3.4 Proton Imaging of the Fusion Source

In DD fusion proton imaging, we are interested in recording 3 MeV protons, however, all charged particles (mostly high-energy deuterons) would enter the detector and make a track in the detector, so after etching, the desirable protons position and number cannot be recognized. It leads us to use a proper filter to prevent passing the other charge particles mostly deuterons.

Kapton film of 75 μm thickness was used to filter (i.e., stop) the energetic deuterons. Table 6.9 shows the minimum energy of charge particles (proton and deuteron) to pass the Kapton filter layer with different thickness (50, 75, 100 μm) using SRIM simulation. Although the results show the best thickness is 100 μm for 3 MeV protons, however, in plasma focus device, the DD reaction mostly relies on beam-target model and so because of collision and momentum conservation, the

Table 6.9 Minimum energy of proton and deuteron to pass the Kapton filter

	Proton min. energy (MeV)	Deuteron min. energy (MeV)
Kapton (50 μm)	1.8	2.3
Kapton (75 μm)	2.3	3.0
Kapton (100 μm)	2.7	3.6

fusion product protons have a wider energy range (roughly ±10%). To avoid missing some lower energy range protons, 75 μm Kapton is preferred.

Using the same method it can be realized that the residual energy of 3 MeV protons after passing the Kapton is 1.6 MeV and they can penetrate 41 μm in CR-39, instead all deuteron particles with energy less than 3 MeV will be stopped by Kapton. It is worth emphasizing that the 4 MeV deuterons (if any) can go the same depth as 3 MeV protons and make the same track shape on CR-39. Fortunately, the magnetic spectroscopy results predict the quantity of such high-energy deuterons drops dramatically, much less than the fusion protons in NX2 plasma focus device [68].

To acquire the images of CR-39 surface, an Optical Microscope (Olympus BX51) has been used together with a motorized stage (PRIOR Scientific H138) controlled by Stage-Pro software (Media Cybernetics). The detector scanning system also comprises a (PRIOR Scientific) motorized microscope stage controlled by Image-Pro software (Media Cybernetics). The CMOS camera produced 8 bit monochrome images, transferred to a computer by IEEE 1394 (FireWire) interface.

To obtain the best focusing on detector, we have two choices; automatic laser-focusing and software auto-focusing. In auto-focus option, the program allows the system to scan the frame in different focusing state (z-position) and choose the best one (maximum local contrast) and goes to new position (if it is set). The number of stage and step size for finding the best focus must be identified by user. In laser focusing option (using Prior Scientific LF100 laser auto-focus), the system sends a laser wave to detector surface and detects the reflected wave and finds the best focus stage. Although it is much faster than software auto-focusing but for using this option the detector surface must be highly reflective, it needs to be coat by Silver or Indium before scanning. Actually Silver has the best reflectivity, but it gets oxidized fast and the tracks disappear. The problem of Indium is that it cannot be bonded on CR-39, so, it must be coated first by Chromium because of its good adhesiveness. In our case, we coat the detectors with 2 μm Chromium and 2.5 μm Indium using the thermal evaporator.

Moreover, suppose we have different energy ranges of incident particle, in our case 2.7–3.3 MeV protons and so the tracks have slightly different diameters. Figure 6.26 shows the proton tracks from DD fusion reaction in a typical NX2 discharge.

6.3.5 *Coded Aperture Imaging*

Coded Aperture Imaging (CAI) is a technique originally developed for X-ray and γ-ray astronomy, where typical imaging problems are characterized by far-field geometry and an object comprising many point sources distributed over a mainly dark background. These conditions provide, respectively, the basis of artifact-free and high Signal to Noise Ratio (SNR) imaging. Coded aperture techniques were first proposed in 1961 by Mertz and Young [69, 70]. The aperture they proposed

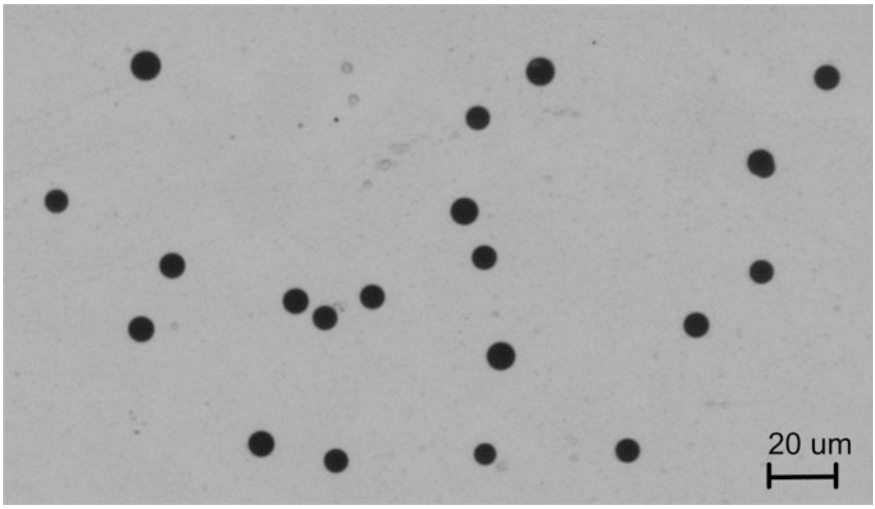

Fig. 6.26 Proton tracks with different energy in the range of 2.7–3.3 MeV have slightly different diameters [56]

was a Fresnel Zone Plate (FZP), in theory a circularly symmetric mask of continuously varying transmittance. The advent of more manageable apertures gave new momentum to the field. In 1968, Dicke [71] and Ables [72] independently pointed out that a square arrangement of randomly distributed square openings (a random array) has reasonable self-correlation properties.

In 1971, the Non Redundant Arrays (NRAs) were proposed [73–75]. These arrays are compact but have ideal properties only on a small field of view and contain a small number of holes, which prevents great improvements in the SNR. The difficulty was overcome in 1978, when Fenimore and Cannon [76] introduced the rectangular Uniformly Redundant Arrays (URAs), which have an ideal Point Spread Function (PSF) and are finite. A decade later URAs were followed by the Modified URAs (MURAs), which have the additional convenience of being square. Meanwhile, a number of other apertures were discovered. A coded mask pattern of 95×95 elements formed by a replicated 53×53 MURA basic pattern (Gottesman and Fenimore [78]) is shown in Fig. 6.27.

Since its invention, the most salient applications of the CAI technique have been in X-ray and gamma-ray astronomy [79, 80]. However in recent years, the CAI technique has also been investigated for a broader range of applications. For example, in medical imaging, it may be a means of obtaining high-resolution images while decreasing the radiation dose for patients [81]. And its uses for particle-source imaging include Coded Aperture Fast Neutron Analysis (CNFNA) [82, 83] and Inertial Confinement Fusion (ICF) neutron and proton imaging [84–86].

The two most essential components of a CAI camera are a position-sensitive detector and a patterned mask of alternately transparent and opaque areas

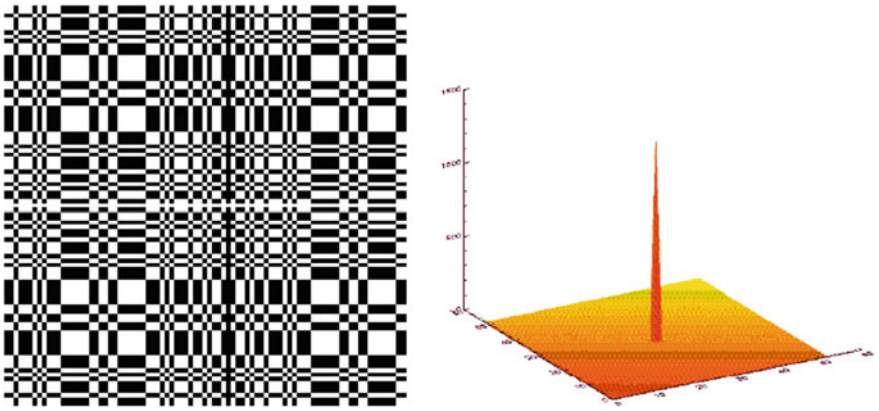

Fig. 6.27 Coded mask pattern of 95 × 95 elements formed by a replicated 53 × 53 MURA basic pattern (*left*) whose cyclic autocorrelation (*right*) is a δ function. Reprinted from Goldwurm et al. [77] with permission from Astronomy and Astrophysics

(or pixels). The detector and mask planes are arranged to be parallel, and the pixels are usually square or hexagonal. In essence, all CAI schemes are a form of multiplexed pinhole imaging. The pinhole is, of course, the simplest and earliest known method of imaging, and its limitations, in terms of resolution versus signal, are well known. As the pinhole size is increased, the signal increases but the axial resolution decreases [87]. However, it is still important for types of radiation for which coherent imaging is not practicable (e.g., vacuum-ultraviolet, X-rays (>30 keV), gamma-rays, etc.). The basic concept of the CAI technique is to open multiple small pinholes, thereby maintaining good angular resolution, while achieving the high signal throughput of a large aperture.

It is notable that all the apertures that in far-field ensure artifact-free imaging, deviate significantly from ideality when used in near-field [89]. The goal of devising a rational design procedure for the coded aperture is now expanding to include near-field artifact reduction. Also, among the many apertures that provide ideal far-field imaging, some types have a SNR significantly superior to others, which are preferred to use.

Coded apertures try to achieve the good resolution of small pinholes while maintaining a high signal throughput. The basic idea is to overcome photon (or, in our case proton) shortage by opening many small pinholes to give the same effective open area as a large pinhole. A large pinhole necessarily results in a loss of resolution [57, 88]. These many small pinholes are placed in specially designed arrays called patterns. The coded aperture (or mask) is the physical realization of a pattern. The detector and mask, together, form the coded aperture camera. The design of a coded aperture system for charged particles such as protons and deuterons requires work on two components: a position and energy sensitive detector and the coded aperture. The complexity of the CAI system requires theoretical investigation together with verification by numerical and experimental simulations.

In order to design a suitable CAI mask and camera, it is necessary to have an understanding of the trade-offs between various imaging parameters such as field-of-view, resolution, collection efficiency, and signal-to-noise ratio. Clearly, for a detector of reasonable size, and a mask of a useful open fraction, there will be considerable overlap of the multiple (inverted) pinhole images. Therefore, a deconvolution step is necessary to extract the final image, known as the decoded image. The unprocessed image from the detector is referred to as the coded image.

It is worth mentioning that single pinhole imaging is quite sufficient for high neutron (proton) yield device such as the 1 MJ Frascati, plasma focus with the $Y_n \approx 10^{11}$ per shot [81]. However, in our case with NX2 PF with $Y_n \approx 10^8$ neutrons per shot, the precise fusion imaging can only be done by coded aperture imaging technique.

2D Imaging

An image is a mapping over space of some distribution, in our case that of a proton source. A pinhole is the simplest imaging device, being a sheet of material through which light or charged particles cannot pass, which is punctured by a small (ideally dimensionless) hole. As every ray (or proton) emitted from the object passes through the pinhole following a straight line trajectory (see Fig. 6.28-left), every point of the detector plane is related to a point in the source. Another simple imaging system is the collimator: an array of narrow parallel tubes placed side by side, and aligned perpendicular to the detector plane. Then protons must arrive from directions perpendicular to the detector surface (see Fig. 6.28-right), which effectively identifies the place of emission. The image is directly the proton distribution recorded by the detector. So a one-to-one correspondence between object and image is the property of ideal pinholes and collimators [89]. Also, in both cases, for a given source point, only protons traveling in a single direction are collected.

In theory, the resolution obtainable with an ideal dimensionless pinhole is perfect, in the sense that two point sources arbitrarily close to one another in the object will always be separated on the detector. However, an ideal pinhole results in no counts at all on the detector, as the ideal pinhole has zero area. Real pinholes must have a finite size to allow some protons to pass, but the problem is if two point sources are very close, their projections on the detector would not be distinct. As the

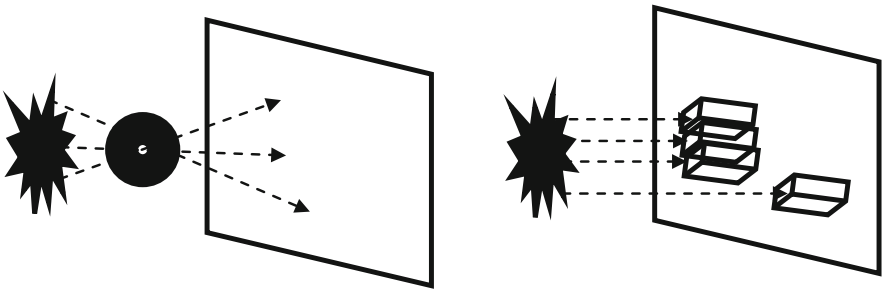

Fig. 6.28 Pinhole imaging (*left*) and collimator imaging (*right*) systems

blue lines show, (see Fig. 6.29-right) light rays from the same source point can hit the detectors over a small region. In the same way, the red lines show that the light rays from different points on the object can hit the same point on the film. Light from the same point on the object hits a circular area on the film, creating a so-called "circle of confusion". The larger the hole, the larger the circle of confusion, and the blurrier the photograph becomes. In conclusion, the pinhole (or collimator) hole size cannot be increased indefinitely to increase efficiency because some resolution limit will be reached.

Concept of Coded Aperture Imaging

For a coded aperture arrangement, the number of protons passing through each pinhole is independent of all the others; each pinhole producing an inverted image on the detector. Therefore, the tracks collected on the detector are, the superposition of many shifted copies of the object by different pinholes. In a far-field approximation, the projection process follows the equation:

$$O^{*}A = R$$

where O is the number of emitted protons per unit area from the object, A is the transmission function of the coded aperture (mask), R is the counts recorded on the detector, and * indicates non-periodic correlation.

As the mask can have a large number of pinholes, R does not resemble O. When O is replaced with Dirac's delta function (δ):

$$R = \delta^{*}A = A$$

Therefore, each point of the object will project a pattern on the detector, rather than a point. Different point sources are characterized by a pattern shift. So a point source is counted once for every pinhole of the pattern, which is expected to increase the counting statistics and, consequently, improve the SNR. The second thing is that each point of detector presents information about many points of the source. In this sense, information is multiplexed. The third consequence is that the

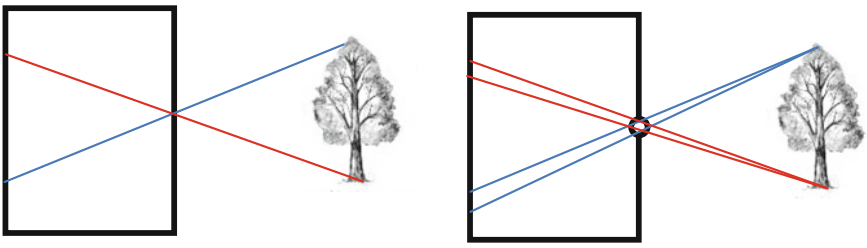

Fig. 6.29 Pinhole camera limitation: ideal zero dimension pinhole (*left*) and practical pinhole camera (*right*)

recorded pattern R must be decoded to obtain an image by separating the overlapped copies through an associated decoding pattern G such that

$$A \otimes G = \delta$$

where $\otimes$ indicates periodic correlation. Given the linearity of correlation operations one can write

$$\widehat{O} \equiv R \otimes G = (O \times A) \otimes G = O^*(A \otimes G)$$

where $\widehat{O}$ is the reconstructed image. This shows that the output of the imaging system is not directly the object, but as in all linear systems, it is a convolution of the object with a kernel, in this case $A \otimes G$ also called the Point Spread Function (PSF):

$$\widehat{\mathbf{O}} = O * \mathrm{PSF}$$

From equations above, in coded aperture imaging:

$$\mathrm{PSF} = A \otimes G$$

We can design and generate pairs of A and G somehow to satisfy the criteria and have perfect imaging properties:

$$\widehat{\mathbf{O}} = O^* \delta = \mathrm{O}$$

which means that if the *PSF* is a δ function, the reconstruction is perfect. Naturally, the choice of aperture pattern A and decoding function G have a large influence on the quality of the final image [90, 91].

In conclusion, coded aperture imaging is able to produce a high precision copy of the object via a two-step process, which is a physical projection of the source through the aperture pattern, followed by computational decoding. The motivation to go through this complication is the potential of achieving a higher SNR than for a small pinhole of equivalent angular resolution.

Coded Aperture Geometry

The most important parameters in coded aperture imaging are shown in Fig. 6.30. The analysis can be carried out from 1D to 2D, because it is assumed that the mask and detector planes are parallel.

The image or detector pixel size is:

$$P_{x\mathrm{Det}} = \frac{d_1 + d_2}{d_1} \times P_{x\mathrm{Mask}}$$

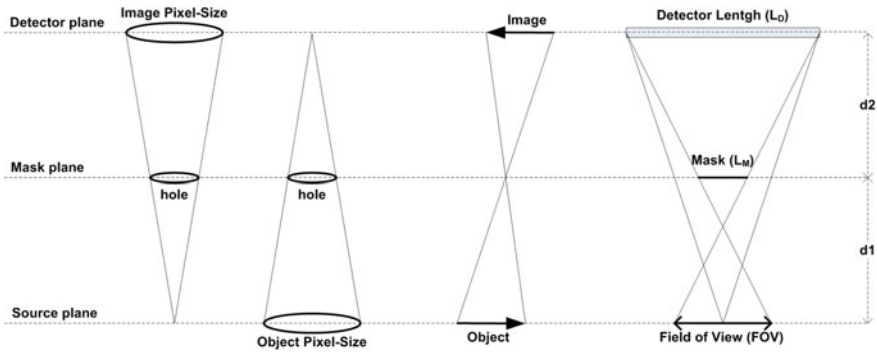

Fig. 6.30 CAI geometry to identify the magnification, object pixel size (resolution), image pixel size and field of view. [56]

where $P_{x\mathrm{Det}}$ and $P_{x\mathrm{Mask}}$ are pixel size of detector and mask, respectively, d_1 is the distance between the object (source) and mask and d_2 is the distance between detector (image) and mask.

The resolution of system is defined by object pixel size ($P_{x\mathrm{Obj}}$):

$$P_{x\mathrm{Obj}} = \frac{d_1 + d_2}{d_2} \times P_{x\mathrm{Mask}}$$

The Image size can be recognized by assumption of an ideal (dimensionless) pinhole:

$$\text{Image size} = \frac{d_2}{d_1} \times \text{Object size}$$

The linear dimensions of mask and detector determine the CAI Field of View (FOV) which is the maximum object size that can be fully coded on the detector:

$$FOV = \frac{d_1 L_D - (d_1 + d_2) L_M}{d_2}$$

where L_D and L_M are the lengths of the detector and mask sides, respectively. With $L_\mathrm{M} = 0$, the pinhole's field of view will be

$$\mathrm{FOV} = \frac{d_1}{d_2} L_\mathrm{D}$$

This means that the FOV for pinhole imaging system is bigger than that of a CAI system with the same size of the detector. In applications such as the plasma focus in which the source is relatively compact, the reduction in the FOV (by comparison with a pinhole) is not a problem.

Singer Set Array, a New Approach for Coded Aperture Imaging

As it was mentioned before, Coded Aperture Imaging is a linear technique. If $O(x, y)$ is the two-dimensional object distribution, $A(x, y)$ is the aperture transmission function and $N(x, y)$ is the signal independent noise, then the spatial distribution of the detected fluence (or coded image) is given by:

$$R(x,y) = A(x,y)^{*}O(x,y) + N(x,y)$$

where * is the correlation operator. Then using the correlation method of decoding, $\widehat{O}(x,y)$, the estimate of the object or reconstructed image is defined by:

$$\widehat{O}(x,y) = G(x,y)^{*}R(x,y) = G(x,y)^{*}A(x,y)^{*}O(x,y) + G(x,y)^{*}N(x,y)$$

where $G(x, y)$ is the decoding function. From this equation, it can be seen that the Point Spread Function, PSF $= G^{*}A$, should ideally be a delta function for the best image reconstruction.

A Cyclic Difference Set (CDS) is a set of h positive numbers $[a_1 = 0, a_2, a_3, \ldots, a_s] < p$, with the property that all differences $(a_i - a_j)$ modulo p for $i \neq j$, occur the same number of times (λ), corresponding to a flat autocorrelation side-lobe. The $i = j$ condition clearly occurs h times, corresponding to the autocorrelation peak. The numbers p and h are referred to as the modulus and size of the CDS, respectively. So the important parameters for any CDS can be abbreviated to (p, h, λ). Among the CDS, there are two subclasses which are particularly suitable for generating masks for multiplex imaging:

1. Singer sets [92, 93] for which

$$p = \frac{t^{m+1} - 1}{t - 1} \quad h = \frac{t^{m} - 1}{t - 1} \quad \lambda = \frac{t^{m-1} - 1}{t - 1}$$

with t being a prime number, or a prime power,

2. Hadamard sets [94, 95] for which

$$p = 4t - 1 \quad h = 2t - 1 \quad \lambda = t - 1$$

with t being an integer.

To form a two-dimensional mask, the CDS is wrapped onto a rectangular array, where the sides of the rectangle are factors of p. Hence, p represents the total number of pixels in the mask, and h is the number of open pixels (holes). Considering these two sets, it can be seen that Hadamard masks have an open fraction, very close to 50%:

$$\rho_H = h/p = (2t-1)/(4t-1)$$

whereas those based on Singer sets have a variable open fraction:

$$\rho_S = (t^m - 1)/\left(t^{m+1} - 1\right) \approx 1/t$$

Since t is a prime number, the obtainable open fractions with Singer sets are:

$$\rho_S \cong \frac{1}{2}, \frac{1}{3}, \frac{1}{4}, \frac{1}{5}, \frac{1}{7}, \frac{1}{8}, \frac{1}{9}, \frac{1}{11} \cdots$$

Note that $\frac{1}{8}$ open fractions are obtainable because $8 = 2^3$, and t is therefore a prime power. But open fractions of $\frac{1}{6}$ and $\frac{1}{10}$, etc., are not obtainable as they are not prime number.

The simplest modulo is "Binary Field" or modulo 2 which produce $a \sim 50\%$ open area Singer set pattern. The irreducible polynomial for modulo 2 is $x^3 + x + 1$ and the parameters of this set are (7, 3, 1) which can be found by putting $t = 2$ and $m = 2$. Figure 6.31 shows a one-dimensional analog of the CAI technique using the $(v, k, \lambda) = (15, 7, 3)$ set. It includes 15 pixels, 7 holes, and 3 side lobes which represent about 50% open area.

Figure 6.32 also shows the final image reconstruction procedure which is called "Deconvolution" algorithm.

If with the same modulo (modulo 2 with 50% open area) one wants to increase the number of pixels and holes, one has to apply an irreducible polynomial of a higher order. For making the Singer set with parameter (15, 7, 3) ($t = 2$ and $m = 3$),

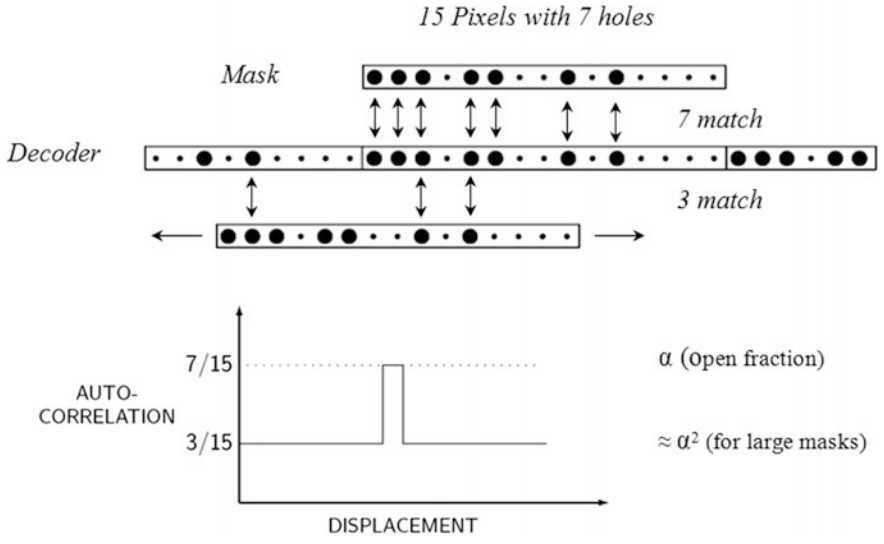

Fig. 6.31 1D cyclic difference singer set in modulo 2 [56]

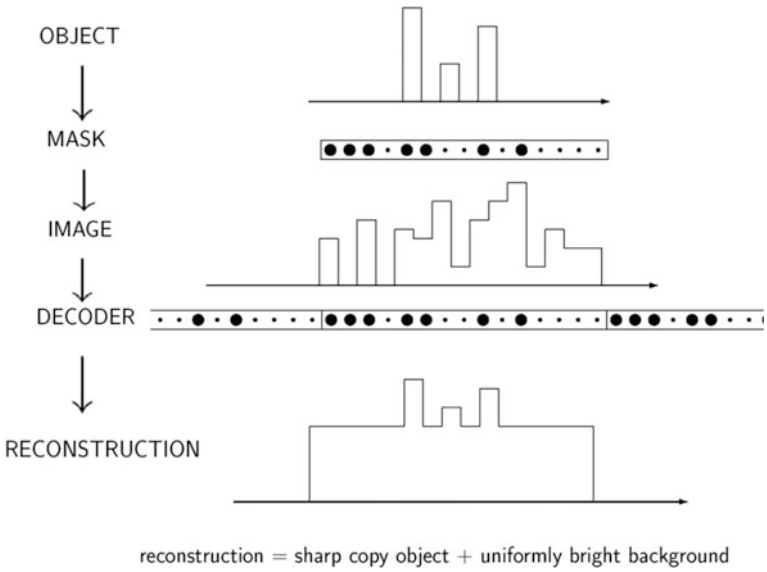

Fig. 6.32 Schematic of reconstruction algorithm (Deconvolution) [56]

the polynomial $x^4 + x + 1$ must be used as the irreducible factor. For our first mask design, a modulo 7 with parameter (400, 57, 8) has been used ($t = 7$ and $m = 4$) where the irreducible polynomial is $x^4 + 2x^3 + 6x^2 + 3x + 6$. From these parameters, it is clear that the mask comprises 400 pixels in a 2D pattern (20 × 20), 57 holes and a side lobe value of 8. The open fraction is $57/400 \cong 14.3\%$.

It is known in the literature that for maximum SNR, the optimum mask open fraction decreases as the spatial extent of the source increases [96, 97]. However, attempts to reduce the effective open fraction of Hadamard set masks have not been successful [98]. Hence for imaging extended sources, the wide range of open fractions attainable with Singer sets is an important advantage, enabling the mask to be designed to achieve near optimum SNR.

Signal-to-Noise Ratio (SNR) in Coded Aperture Imaging

Fenimore [96] and Accorsi et al. [98] have compared the SNR for different Hadamard families and pinholes for a series of simulated sources using the standard "balanced" method of decoding. However, their definition of SNR corresponds to the variation in brightness of a given fixed pixel between hypothetically many exposures for a source with assumed constant intensity, which simplifies the statistical analysis at the cost of a loss of intuition. Also, balanced decoding, while relatively simple in the Hadamard case (the matrix G consists of +1 where A has a hole and −1 where it does not) becomes more complicated in the Singer case. In this work, it was considered more meaningful to define SNR in terms of the variation in brightness across different pixels within a single exposure, more precisely as follows:

$$\mathrm{SNR} = \frac{\text{signal from given pixel}}{\sqrt{\text{variance of signal across image}}}$$

As well as being closer to our intuition, this within-exposure definition of SNR has the added advantage of being more readily compared with the results of experiment. And in cases of non-repeatability, where a single-exposure is the only thing available, it may be the only possibility. We shall also find it more convenient to use direct decoding, where the decoding matrix $G = A$, the aperture itself, which, although differing from balanced decoding by overall constants and scaling, separates the terms involved in a way which makes the statistical analysis more straightforward.

Direct decoding, where we take $G = A$, the aperture itself, uses the defining property of a CDS-based coded aperture, namely that if two copies of the aperture are cyclically displaced relative to each other then the resulting open fraction, that is, where the holes of the two copies happen to coincide, is ρ^2 independent of the displacement, except of course when the two copies themselves coincide, in which case the open fraction is just ρ again. In other words, as the aperture A passes across the encoded image R we will pick up the signal from the object pixel matching that position but attenuated by a factor ρ, together with the signal from all other object pixels but attenuated by a factor ρ^2. More specifically, let N be the total number of particles incident on the mask, and $N' = \rho N$ the number which pass through the mask, and let n be the number of particles incident on the mask which arrive from a direction associated with a particular object pixel, and $n' = \rho n$ those passing through the mask, and let the object comprise m bright (illuminated) pixels. Then, when the decoding matrix is aligned with that particular pixel, the decoded signal will be $n' + \rho(N' - n') = \rho n + \rho^2(N - n)$, while if the decoding matrix is aligned with any other pixel in the field of view not corresponding to a pixel on the object the decoded signal will be $\rho N' = \rho^2 N$. So direct decoding produces a sharp image of the object but superimposed on an approximately uniformly bright background, where the average background brightness is $\rho N'$. Subtracting this average background brightness, we recover a signal $\rho n + \rho^2(N - n) - \rho^2 N = \rho n - \rho^2 n = \rho(1 - \rho)n$ against an approximately uniformly zero background. It is then not difficult to show that, up to an overall scaling factor of $1/(1 - \rho)$ the resulting decoded image is identical with that obtained from balanced decoding.

Including this overall $1/(1 - \rho)$ scaling, in which case the reconstructed signal is just ρn has the advantage that the total particle count in the reconstructed image is identical with the number of particles actually detected. Since the SNR is invariant under overall scaling of the data, however, direct decoding allows us to neglect it for the purposes of the statistical analysis. An additional advantage of direct decoding, at least in the case where SNR is defined within-exposure, is that the overall constant $\rho N'$ subtracted also does not affect the computation of the variance and can be neglected, whereas in the case where SNR is defined exposure-to-exposure it does vary. To compute the SNR within-exposure, it only remains therefore to compute the variance of the signal $n' + \rho(N' - n') = \rho n + \rho^2(N - n)$. It is a property of CDS -based coded apertures

that the second term represents a pseudo-random sampling of the detected particles with probability ρ and so follows binomial statistics. If we make the simplifying assumption that the m object pixels are uniformly bright, then the first term also follows binomial statistics with probability ρ. Neglecting the covariance between the two terms, and using the standard result that a $B(N, \rho)$ random variable of N trials with probability success p and failure $q = 1 - p$ has expectation Np and variance Npq, the variance of the directly decoded signal as the decoder moves across the coded image is

$$\rho(1-\rho)n + \rho(1-\rho)(N'-n') = \rho(1-\rho)n + \rho(1-\rho)\rho(N-n)$$

Substituting this into our earlier formula defining the within-exposure SNR we obtain:

$$\mathrm{SNR} = \frac{\rho(1-\rho)n}{\sqrt{\rho(1-\rho)n + \rho^2(1-\rho)(N-n)}} = \frac{\sqrt{\rho(1-\rho)}n}{\sqrt{n + \rho(N-n)}}$$

Then putting $m = \frac{N}{n}$: $\quad \mathrm{SNR} = \sqrt{\frac{N\rho(1-\rho)}{m(1+\rho(m-1))}}$

This expression happens to coincide with the formula derived by Fenimore [96] although under quite different assumptions, i.e., exposure-to-exposure variance, and later shown by Accorsi [98] to be in error in that case. These formulae are, however, approximations. A truly complete SNR analysis for the within-exposure case has, to our knowledge, not yet been reported.

Again using the simplification that the m bright pixels are considered to be equally bright, and differentiating the SNR function with respect to ρ, gives the optimum open fraction in terms of the number of bright pixels:

$$\rho_{\mathrm{opt}} = \frac{1}{1+\sqrt{m}} \quad \text{and} \quad \mathrm{SNR}_{\max} = \rho_{\mathrm{opt}}\sqrt{\frac{N'}{m}} = \rho_{\mathrm{opt}}\sqrt{n'} = \sqrt{\rho_{\mathrm{opt}}n}$$

Hence, for a mask of constant size (and therefore constant N'), both ρ_{opt} and $\mathrm{SNR}_{\max}$ decrease as the source becomes more extended and illuminates more pixels; or alternatively, as the pixel-size shrinks and the number of pixels increases. Figure 6.33 shows a plot of SNR versus ρ for different numbers of bright pixels $m = 8, 16, 32$ and 64. This calculation is for a mask of the dimensions used for our first experimental study (8×8 mm^2) with a total of 400 pixels and an isotropic source of 10^8 particles located at a distance of 45 mm from the center of the mask.

The solid angle subtended by the mask is 0.0314 sr, and the number of particles hitting the mask is $N' = 2.5 \times 10^5$. Open circles in Fig. 6.33 represent values of ρ_{opt} for each curve. The vertical lines on the plot represent the values of $\left(\rho_S \cong \frac{1}{t} = \frac{1}{2}, \frac{1}{3}, \frac{1}{4}, \frac{1}{5}, \frac{1}{7}, \frac{1}{8}, \frac{1}{9}, \frac{1}{11}\right)$ attainable with Singer set masks, while the circle symbols represent values of ρ_{opt} for each curve. Hadamard masks, being restricted to $\rho_H \cong 0.5$, are best suited to situations with very few bright pixels.

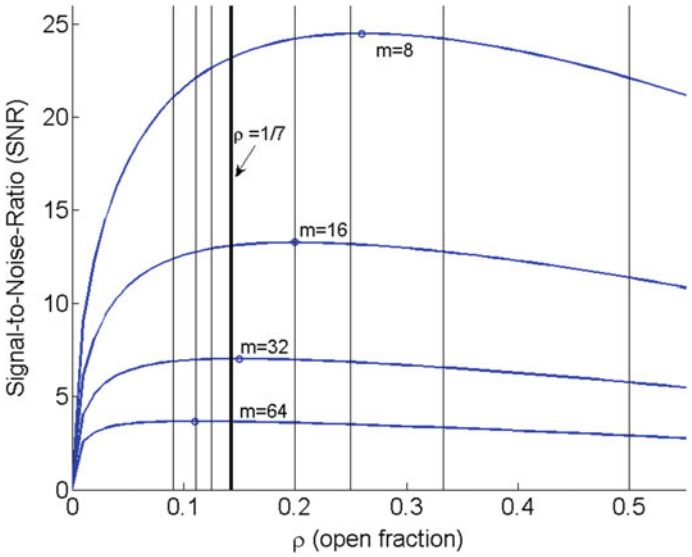

Fig. 6.33 SNR versus open fraction (ρ) for objects (of the same total brightness) which illuminate different numbers of pixels (m) the *vertical black lines* represent the possible open fraction for Singer Set. Reprinted from Talebitaher et al. [99] with permission from Elsevier publishing company

Also for pinhole imaging, the SNR is simply:

$$\mathrm{SNR_{ph}} = \frac{n}{\sqrt{n}} = \sqrt{n}$$

It should be remembered that the value of n for a CAI is h times greater than that for a pinhole of the same angular resolution. Hence the optimum enhancement of a CAI mask over a pinhole (i.e. always with a mask of optimum open fraction ρ_{opt}) is given by

$$\left(\mathrm{SNR_{max}}/\mathrm{SNR_{ph}}\right)_{\mathrm{opt}} = \sqrt{h\rho_{\mathrm{opt}}} = \rho_{\mathrm{opt}}\sqrt{p} = \frac{\sqrt{p}}{1+\sqrt{m}}$$

It is clear from this formula that the SNR advantage of CAI over pinhole imaging decreases as the source becomes more extended, until the limit at which the source fills the entire field of view ($m \approx p$) when CAI offers essentially no SNR advantage over pinhole imaging. As a rule of thumb, CAI can be considered advantageous, and worth the additional complexity, in cases where the source occupies no more than 10% of the field of view (FOV).

Experimentally it is usually the case (and certainly so for the plasma focus) that the precise number of bright pixels is not known prior to the exposure. It is probably best, therefore, to use a mask with ρ somewhat larger than ρ_{opt} for the

anticipated value of m. As can be seen from Fig. 6.31, the SNR penalty for using a moderately larger value of ρ is slight. Also, for experiments using CR-39 detectors, the signal independent noise $N(x, y)$ is primarily due to flaws, scratches, alpha tracks from background radon, which are always present to some extent on the etched CR-39 surface. With proper handling of the material, this background is relatively low and uniform across the detector surface, resulting in a slightly degraded SNR in the decoded image.

6.3.6 Proton Gyration in Magnetic Field

It was anticipated that the fusion source dimension would be somewhat larger than the size of the pinch: the reason being that medium energy deuterons ($\sim$20–50 keV) gyrate within, and around, the pinch column due to the high magnetic field. On this basis, for NX2 PF device, we roughly predicted the size of the fusion source to be about 3 mm in diameter and 11 mm in length.

For proton imaging, it is essential to consider the curvature of proton trajectories due to the magnetic field in and around the pinch column, and its influence on the images recorded by the CAI camera. For this purpose, a program was written in MATLAB to calculate trajectories of DD fusion protons that impinge on the CAI mask, and to calculate the apparent source position. It was assumed that current through the PF pinch plasma column is parallel to the PF axis and uniformly distributed throughout the pinch column (i.e. disregarding breaking and kink instabilities), and also that the current flows uniformly out of the pinch in a fountain shaped current sheath. Then the magnetic field is purely toroidal and given by

$$\begin{aligned} B_\phi &= \frac{\mu_0 I_\mathrm{p} r}{2\pi R_\mathrm{p}^2} \quad \left(r \le R_\mathrm{p}\right) \\ B_\phi &= \frac{\mu_0 I_\mathrm{p}}{2\pi r} \quad \left(R_\mathrm{P} < r \le R_{cs}(z)\right) \\ B_\phi &= 0 \quad \left(r > R_\mathrm{cs}(z)\right) \end{aligned}$$

where R_p is the radius of the pinch column and I_p is the current flowing through it. The radius of the current sheath (CS) is given by an empirical function $R_\mathrm{cs}(z)$ which follows the observed shape of the CS. The acceleration of protons in the magnetic field is

$$\frac{d\vec{v}}{dt} = \frac{\vec{F}}{m} = \frac{e}{m}\vec{v} \times \vec{B} = (v_r\hat{\boldsymbol{z}} - v_z\hat{\boldsymbol{r}})eB_\phi/m$$

and this ordinary differential equation is solved in MATLAB by numerical integration (Runge–Kutta method) to determine the proton trajectory for a given point of origin and initial velocity. When the proton exits from magnetic field region

($r \leq R_{cs}(z)$), it follows a straight line path. For simplicity, a 3 MeV proton source was assumed to be positioned on-axis ($x = y = 0$) and the z position within the plasma pinch column was selected randomly ($0 \leq z \leq l$) where l is the length of the column. The program then follows the trajectories of protons emitted over a range of angles, to find those that are incident on the coded mask. Figure 6.34 shows calculated proton trajectories for the geometry of the CAI exposures, and a pinch current $I_P = 300\,\text{kA}$.

For these mask-incident trajectories, the program determines the apparent position of the proton source by extrapolation of the straight section of the trajectory back to the pinch. Table 6.10 shows the z displacements of protons emitted over a range of angles which impinge on the coded mask (with the same 45° positioning as used experimentally). The mean z displacement δz_m is −3.0 mm. More importantly, the range of z displacements is 0.08 mm which is only 8% of the object pixel size (∼1 mm) and the standard deviation is 0.02 mm. Hence for a mono-energetic proton point source, the effect of the magnetic field amounts simply to a displacement (in the negative z direction) of the apparent source position. Figure 6.35 shows $|\delta z_m|$ as a function of the point source height z_s within the pinch column, and it can be seen that the relationship is almost linear. Since δz_m is negative, the overall affect of magnetic curvature of proton trajectories is that the fusion source image is linearly stretched (by a factor of $S_z = 1.6$) in the axial z direction, but no other significant distortion of the image occurs.

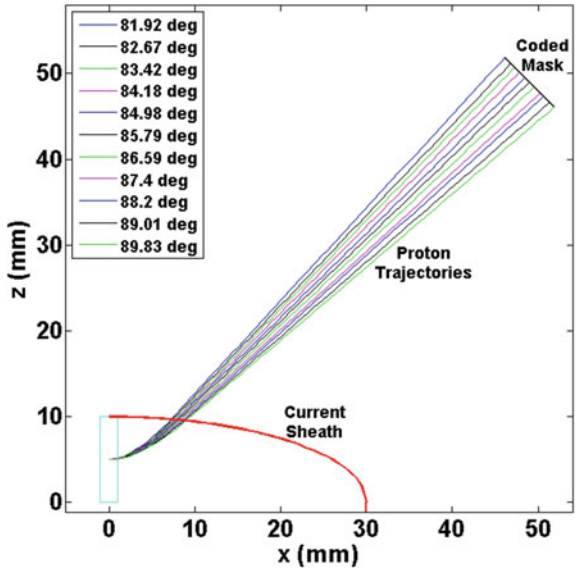

Fig. 6.34 Trajectories of 3 MeV protons (which impinge on coded mask at 45°) in plasma pinch magnetic field. Reprinted from Talebitaher et al. [67] with permission from Springer publishing company

Table 6.10 Displacements of apparent proton source position versus emission angle, for trajectories which impinge on coded mask at 45°

Angle (°)	Mask position (mm)	Displacement (mm)
81.92	4.1	−3.11
82.67	3.1	−3.06
83.42	2.5	−3.09
84.18	1.7	−3.09
84.98	0.8	−3.06
85.79	0	−3.08
86.59	−0.8	−3.09
87.4	−1.8	−3.05
88.2	−2.3	−3.13
89.01	−3.3	−3.09
89.83	−4.1	−3.11
Average Displacement (mm)	−3.09	
Maximum Displacement Range (mm)	0.08	
Standard Deviation (mm)	0.02	

Actual source position is mid-pinch: $z = 5$ mm

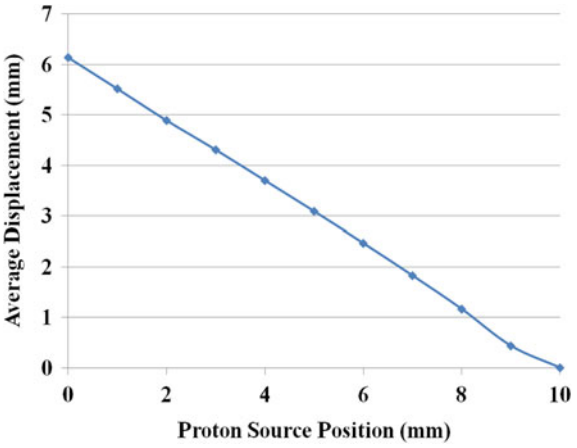

Fig. 6.35 Magnitude of mean displacement of apparent source position $|\delta z_m|$ versus actual z position of source within the pinch for mask-400 at 45°. Reprinted from Talebitaher et al. [67] with permission from Springer publishing company

6.3.7 Some Experiments and Results

The Coded Aperture Imaging (CAI) technique has been used to investigate the spatial distribution of DD fusion in NX2 Plasma Focus device operated in, alternatively, pure deuterium or a deuterium-krypton admixture. Fusion images were obtained for single PF shots with a neutron yield of 1–3 $\times$ 10^8 neutrons per shot. The coded 91 $\times$ 15 mask pattern is based on a Singer Cyclic Difference Set with

341 square holes of 300 μm side, giving a total open area of 30.69 mm^2 (see Fig. 6.36 which shows this experimental setup).

CR-39 nuclear track detectors were employed to register the tracks of protons from the D(d, p)T reaction. A 75 μm thick Kapton film was placed immediately in front of the CR-39 detectors to stop all energetic charged particles (mostly deuterons) other than the ~3 MeV protons. The CAI camera system was located inside the NX2 vacuum chamber close to the radial direction.

The source-to-mask and mask-to-detector distances were $d_1 = 44$ mm and $d_2 = 40$ mm, respectively, giving an open solid angle of 1.32×10^{-2} sr. The dimensions of the CR-39 detectors used were 67 (horiz) × 77 (vert) mm^2 giving a fully coded field of view (FOV) in the source plane of 2.8×1.7 cm^2. Hence, the anticipated $\sim 1.0 \times 0.3$ cm^2 fusion source of the NX2 lies easily within this FOV. The resolution of CAI camera (i.e., the magnified pixel size in the source plane) for this geometry is 0.63 mm. The internal angle of the conical anode tip is 130°, and the coded mask spans the angular range of 60°–90° relative to the PF axis.

The pinch current for good shots was close to 300 kA, and hence the deflection of proton trajectories in the magnetic field around the dense plasma column was analogous to that described in Ref. [67]. The anode cone-angle and CAI camera position were chosen based on these proton trajectory calculations to ensure that protons emitted from the upstream end of the pinch column could reach the CAI camera unobstructed.

An X-ray pinhole camera was employed to record the time-integrated image of the hot (~keV) plasma X-ray source for each shot. It comprised a 1/3 in. CCD sensor with 768 × 576 pixels, and a laser-drilled pinhole through 50 μm thick tungsten foil. The demagnification for this pinhole camera was 4.5. For pure deuterium operation, the pinhole was covered with a 20 μm Be filter to cut all photons with energies below ~700 eV. For deuterium–krypton operation, a

Fig. 6.36 Mask, its pattern and holder (*left*) and its position in front of anode top inside the plasma focus (*right*). [56]

12.5 μm Ti plus 50 μm Be filter combination was used. Both sets of filters transmit the Cu K_α and K_β X-rays of energies $\sim$8 and 8.9 keV, which permits the position of the copper anode tip to be observed in many of the X-ray images.

To measure the time-integrated neutron yield and anisotropy, two beryllium fast-neutron activation counters [51] were positioned 25 cm from the anode tip in the axial and radial directions, respectively (shown in Fig. 6.37).

For the pure D2 series of shots, the NX2 plasma focus was operated in its neutron yield optimized regime (13 mbar, 11 kV/1.6 kJ). Several CR-39 detectors were exposed to single PF shots: these being the first shot fired after evacuating the chamber and filling with deuterium gas, so that there should be no significant effect from the gas impurities, which usually accumulate over a series of shots. In spite of different neutron yields and anisotropies, the fusion source images showed quite similar spatial distributions.

We have selected one "good shot" (1365-I23-A) as an example. This shot had a high neutron yield of 3.2×10^8, but in other respects is fairly typical of the results obtained. The high neutron anisotropy of 2.4 indicates a high average energy for deuterons producing fusion via the beam-target interaction. For this shot, Fig. 6.38-right shows a cone-shaped fusion source of $\sim$11 mm length. The source width is $\sim$2 mm near the anode, and widens to $\sim$5 mm near the top of the cone, with the

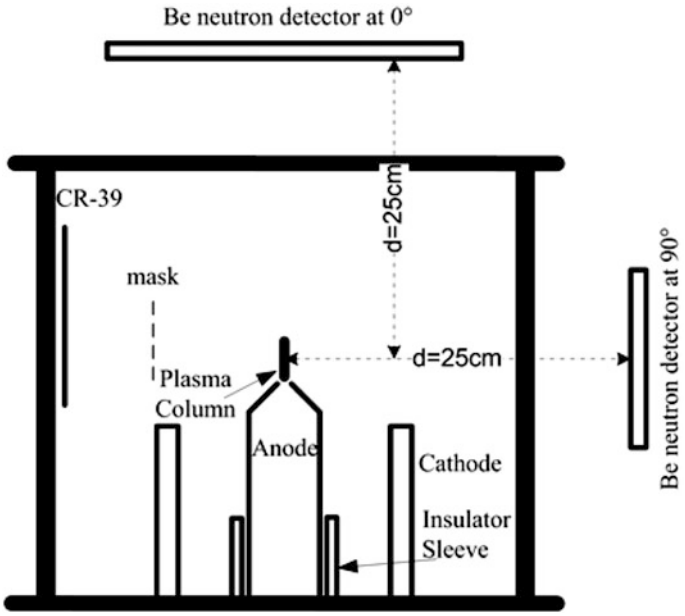

Fig. 6.37 Schematic of experimental setup showing: NX2 plasma focus, CAI mask, CR-39 detector, and two beryllium neutron activation counters (positioned axially and radially). The X-ray pinhole imaging system is not shown. Reprinted from Springham et al. [100] with permission from AIP publishing

highest fusion density occurring at z = 3 mm. The high SNR value of 21.8 for this image is a consequence of the high number of proton tracks ($\sim$174,000) recorded on the CR-39 detector. The corresponding X-ray image, Fig. 6.38-left, shows a hot dense pinch region (of $\sim$4 mm length and $\sim$0.5 mm width) above the anode tip. It also shows considerable X-ray emission from the copper anode tip due to bombardment by the energetic electron beam emitted from the pinch.

Comparison of the X-ray and fusion proton images indicates that the zone with the highest concentration of DD fusion occurs close to the downstream end of the hot dense plasma column. This can be understood in terms of deuterons being accelerated (predominantly in the +z direction) by the rapidly constricting magnetic field around the pinch, and so reaching their highest kinetic energies at the downstream end of the pinch column, where they produce fusion reactions with the approximately stationary and relatively high-density deuterium gas within the "fountain" at this end of the pinch. This cone-shaped fusion zone at the end of the pinch column is consistent with the more extended conical distribution of fusion, due to forwardly directed deuteron beams, observed in another plasma focus device [57]. Of course, there is also a concentration of fusion production along the length of the pinch column (where the ion density is at its highest) before the accelerated deuterons have attained their maximum energy.

The CAI fusion source images clearly show the different size and density of the fusion emission zones for pure D_2 and D_2-Kr admixture (98% D_2 + 2% Kr by vol.) operation. The NX2 was operated with the same parameters as for D_2 (i.e., 13 mbar, 11 kV/1.6 kJ).

The majority of fusion source images in the D_2-Kr admixture case show a similar structure. For the selected illustrative shot, 1365-I28-A, the neutron yield was 4.1×10^8. The relatively low neutron anisotropy of 2.17 indicates a lower average energy of beam deuterons involved in the fusion reactions. The image of fusion

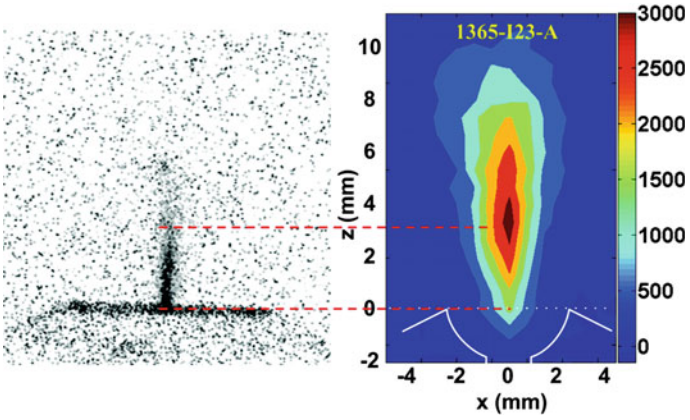

Fig. 6.38 Proton CAI fusion source image (*right*) and X-ray image (*left*) for pure D_2 gas operation (shot 1365-I23-A). Reprinted from Springham et al. [100] with permission from AIP publishing

source in Fig. 6.39-right appears as a prolate ellipsoid of ~2 mm width and ~6 mm length, with the highest concentration of fusion near the geometrical center (z = 6.5 mm). A very high SNR value of 50.8 for this image is due to the high number of proton tracks (~187 000) and compact geometry of the source. The corresponding X-ray image (Fig. 6.39-left) clearly shows the existence of high-density hot spots possibly associated with $m = 0$ instabilities in the final compression. The pinch column length is only ~3 mm. The hot plasma is distributed quite evenly along the z-axis. The $m = 0$ and $m = 1$ instability structures responsible for the break-up of the pinch column are not evident in the fusion source images, which indicate that the deuterons are accelerated along the pinch column and react mostly above the pinch.

In conclusion, the fusion source in pure deuterium appears cone-shaped, narrower near the anode, and wider at the top, but most concentrated in the central region of the pinch. There is no evidence for the existence of hot spots or $m = 0$ instabilities in the fusion source image or even in the pinch X-ray region. The observed neutron anisotropy values (>2.0) together with the lack of axial structure in the fusion proton images are a strong indication that beam-target fusion is distributed along the length of the pinch column, and to a lesser extent, within the fountain-shaped region of high gas density at the downstream end of the column. The lack of spatial correlation between the regions of fusion and X-ray emissions for the D_2-Kr shots shows that any contribution from thermonuclear fusion is relatively small. Moreover, the downstream displacement of the fusion source relative to the X-ray source shows that, although it is not associated with $m = 0$ instabilities or micro-pinches, the zone of deuteron acceleration is quite compact and located within the X-ray emitting region.

In contrast to the pure deuterium case, Kr-doped operation produces a prolate ellipsoidal fusion source, which is smaller and more concentrated in the center. The

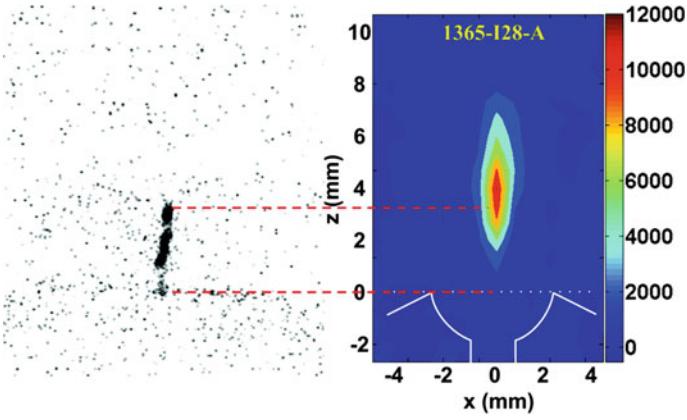

Fig. 6.39 Proton CAI fusion source image (*right*) and X-ray image (*left*) for D_2-Kr gas admixture operation (shot 1365-I28-A). Reprinted from Springham et al. [100] with permission from AIP publishing

X-ray images clearly show the existence of hot spots/micro-pinches in the final compression phase, and the resultant radiation cooling leads to this compact highly compressed plasma pinch.

6.4 Conclusion

In this chapter, some of the methods and diagnostics which are applied for neutron and proton detection especially produced from DD reaction in plasma focus device, have been explained. Also some results based on experiments which were done in Plasma Radiation Source Lab at NIE, NTU, Singapore have been shared and discussed.

The new developed neutron detector based on beryllium activation has good sensitivity and a high signal-to-background ratio, enabling neutron fluence measurements above 3×10^4 n/cm^2 to be made with statistical uncertainties better than 1%. Very large pulsed neutron fluences can be measured by interposing a known delay before the counting interval begins. Another useful aspect of this detector is its lack of sensitivity to neutrons with energies <1 MeV, which provides good discrimination against room-scattered DD neutrons.

The reliability of the calibration methodology relies primarily on (i) the evaluated ^{9}Be (n, α) ^{6}He reaction cross-sectional data from the ENDF database, (ii) energy calibration of the xenon-filled proportional counters and the measurement of their relative gas-gain as a function applied bias voltage using standard X-ray sources, and (iii) the accuracy of the neutron and electron transport physics incorporated in the MCNP5 code. The largest contribution to the uncertainty in the response function arises from (i), and this represents $\pm 10\%$ uncertainty across the R (En) curve as a whole.

The constructed detectors are quite compact, enabling them to be positioned close to the pulsed neutron source with negligible mutual interference. The relevant half-life of ~ 0.8 s is shorter than that for most types of neutron activation detector, enabling them to be used for moderate repetition-rate sources (<0.2 Hz). The experimental tests performed with the NX2 plasma focus show that interfering activations of detector materials are negligible, and that the responses of the two constructed beryllium activation detectors are, for practical purposes, identical.

The DD fusion imaging in plasma focus device using a newly developed coded aperture technique was also described. A cyclic difference Singer set coded aperture was applied to investigate the spatial distribution of the fusion source in the NX2 PF device by recording the 3 MeV protons from DD reaction on CR-39 polymer nuclear track detector.

It is evident from the results, that the CAI system has superior SNR and fidelity by comparison with pinhole imaging; these masks have a good resolution as well as a significantly large open solid angle which should yield better precision images. After chemical etching, the positions of several proton tracks were successfully read from the surface of CR-39 by an automated scanning system. The list of track

coordinates was processed by a de-convolution algorithm to produce a final image of the pinch fusion source for each CAI camera.

From the CAI images, the fusion reaction source in the NX2 devise appears to be a "cigar shaped" cylindroid. It is interesting to observe that the size of the fusion source is larger than the pinch column itself, although the highest fusion densities are concentrated in the pinch column. It is also interesting that there is no indication of sausage or kink instabilities which are typically observed in shadographic images of PF pinches.

Acknowledgements The authors are grateful to the National Institute of Education, Nanyang Technological University, Singapore, for AcRF grant and also the provision of a research scholarship for one of the authors, Alireza Talebitaher.

They are also thankful to the Plasma Radiation Source Lab member at NIE, NTU including Prof. Lee Sing, A/P Rajdeep Singh Rawat, A/P Paul Lee, A/P Augustine Tan and other researchers and graduate students for their help and collaboration in these projects.

References

1. J.W. Mather, Phys. Fluids **3**, 135 (1960)
2. N.V. Filippov, T.I. Filippova, V.P. Vinogradov, Nucl. Fus. Suppl. **2**, 577 (1962)
3. S. Lee, *Scaling of the Plasma Focus, Plasma Dynamic Viewpoint, International Workshop on Plasma Focus Research (PF98)* (Kudova, Poland, 1998), p. 1998
4. M. Kikuchi, K. Lackner, M.Q. *Tran* (Fusion Physics International Atomic Energy Agency, 2012), p. 22. ISBN 9789201304100
5. R.E. Brown, N. Jarmie, Phys. Rev. C **41**, 1391 (1990)
6. R.F. Post, Rev. Mod. Phys. **28**, 338 (1956)
7. J.H. Lee, L.P. Shomo, K.H. Kim, Phys. Fluids **15**, 2433 (1972)
8. A. Bernard, et al. (1979) in Plasma Physics Controlled Nuclear Fusion Research (1978) Innsbruck, p. 159
9. U. Jager, H. Herold, Nucl. Fusion **27**, 407 (1987)
10. M.J. Bernstein, G.G. Comisar, Phys. Fluids **15**, 700–707 (1972)
11. S.A. Goldstein, R. Lee, Phys. Rev. Lett. **35**(16), 1079–1082 (1975)
12. Heinrich Hora, Reinhard Hopfl, G.H. Miley, Plasma Phys. Contr. Fusion **36**, 1075–1079 (1994)
13. Y. Mizuguchi, J.-I. Saka, H.R. Yousefi Phys Plasmas **14**, 032704 (2007)
14. M.A. Dorf, I.D. Kaganovich, E.A. Startsev, R.C. Davidson, Phys. Plasmas **18**, (2011). doi: http://dx.doi.org/10.1063/1.3557894
15. D.R. Slaughter, W.L. Pickles, Nucl. Instrum. Methods Phys. Res. A **160**, 87–92 (1979)
16. C.A. Ekdahl, Rev. Sci. Instr. **50**, 941–948 (1979)
17. G.F. Knoll, *Radiation Detection and Measurement*, 3rd ed. (Wiley, New York, 1999)
18. C.L. Ruiz, R.J. Leeper et al., Rev. Sci. Instr. **63**, 4889–4891 (1992)
19. L. Bertalot, M. Damiani et al., Rev. Sci. Instr. **68**, 528–531 (1997)
20. E.L. Jacobs, S.D. Bonaparte, P.D. Thatcher, Nucl. Instrum. Methods **213**, 387–392 (1983)
21. M.V. Roshan et al., Rev. Sci. Instrum. **81**(8), 083506 (2010)
22. G.W. Cooper, C.L. Ruiz, Rev. Sci. Instr. **72**, 814–817 (2001)
23. C.W. Barnes et al., Rev. Sci. Instr. **66**, 888–890 (1995)
24. T. Nishitani et al., Rev. Sci. Instr. **74**, 1735–1738 (2003)
25. YuA Kaschuck et al., Fusion Sci. Technol. **43**(2), 176–183 (2003)
26. M.S. Rowland, J.C. Robertson, Nucl. Instrum. Methods **224**, 322–323 (1984)

27. A. Wolf, R. Moreh, Nucl. Instrum. Methods **148**, 195–197 (1978)
28. L. Ruby, J.B. Rechen, Nucl. Instrum. Methods **224**, 322–323 (1984)
29. B.T. Meehan et al., Nucl. Instrum. Methods **620**, 397–400 (2010)
30. V.E. Lewis, T.B. Ryves, Nucl. Instrum. Methods **257**, 462–466 (1987)
31. S. Mahmud et al., Rev. Sci. Instrum. **77**, 713–722 (2006)
32. National Nuclear Data Center (NNDC). http://www-nds.iaea.org/exfor/endf.htm
33. P.H. Stelson, E.C. Campbell, Phys. Rev. **106**(6), 1252–1255 (1957)
34. H. Ing, R.A. Noulty, T.D. McLean, Radiat. Meas. **27**, 1 (1997)
35. J.H. Lee et al., Phys. Fluids **14**(10), 2217–2223 (1971)
36. H. Kelly, A. Marquez, Plasma Phys. Control Fusion **38**, 1931–1942 (1996)
37. A. Talebitaher, S.V. Springham, R.S. Rawat, P. Lee, Nucl. Instrum. Methods Phys. Res. A **848**, 60–65 (2017)
38. Rishi Verma et al., Plasma Physics Control Fusion **51**, 16 (2009)
39. I. Tiseanu, N. Mandache, V. Zambreanu, Plasma Phys. Control. Fusion **36**, 417–432 (1994)
40. J. Koh, Plasma Source Sci. Tech. **14**, 12–18 (2005)
41. M. Zakaullah et al., Plasma Sources Sci. Tech. **12**, 443–448 (2003)
42. M. Scholz et al., Plasma Sci. IEEE Trans. **30**(2), 476–481 (2002)
43. J.H. Lee et al., Phys. Fluids **15**(12), 2433–2438 (1972)
44. K. Hübner, H. Bruhns, K. Steinmetz, Phys. Lett. A **69**(4), 269–272 (1978)
45. R.L. Gullickson, H.L. Sahlin, Appl. Phys. **49**, 1099 (1978)
46. S.V. Springham, S. Lee, M.S. Rafique, Plasma Phys. Contr. Fusion **42**, 1023–1032 (2000)
47. M.V. Roshan et al., Phys. Lett. A **373**, 851–855 (2009)
48. A. Cebanu, et al., *8th International Plasma Physics and Controlled Nuclear Fusion Research IAEA*, Brussels, p. 197 (1980)
49. A. Mozer et al., J. Appl. Phys. **13**, 2929 (1977)
50. H. Krompholz et al., Appl. Phys. **13**(1), 29–35 (1977)
51. A. Talebitaher, S.V. Springham, R.S. Rawat, P. Lee, Nucl. Instrum. Methods Phys. Res. A **659**, 361 (2011)
52. IAEA Technical Report, *Handbook on Nuclear Activation Data*, pp. 111–115 (1987)
53. R.E. Brown, N. Jarmie, Phys. Rev. C **41**(4), 1391–1396 (1989)
54. Med Phys 4R06/6R03 Radioisotopes and Radiation Methodology, Chapter 9 Neutron Detectors, McMaster University, http://fumblog.um.ac.ir/gallery/170/note9.pdf
55. R. Verma, PhD thesis, NIE, NTU, Singapore (2010)
56. A. Talebitaher, PhD thesis, NIE, NTU, Singapore (2012)
57. S.V. Springham, S. Lee, S.P. Moo, Braz. J. Phys. **32**(1), 172–178 (2002)
58. R.L. Fleischer, in *Radon Measurements by Etched Track Detectors: Appl. Rad. Prot. Earth Sci. Env.*, ed. by S.A. Durrani, R. Ilić (World Scientific, Singapore, 1997), pp. 285–299
59. N. Tsoulfanidis, *Measurement and Detection of Radiation*, 2nd edn. (1995)
60. S.V. Springham et al., Radiat. Meas. **44**, 173–175 (2009)
61. S.T. Haur, PhD thesis, NIE, NTU, Singapore (2004)
62. Green, et al., Nucl. Instrum. Methods **157**(1), 185–193 (1978)
63. Brun, et al., Radiat Meas **31**, 89–98 (1999)
64. D. Nikezic, K.N. Yu, Comput. Phys. Commun. **174**(2), 160–165 (2006)
65. D.W. Miller, Medial Physics **22**(11), 1943–1954 (1995)
66. D. Nikezic, K.N. Yu, Mat. Sci. Eng. **46**(3–5), 51–123 (2004)
67. A. Talebitaher, S.V. Springham, P.M.E. Shutler, P. Lee, R.S. Rawat, J. Fusion Energy **31**(3), 234 (2012)
68. M.V. Roshan et al., Plasma Phys. Control Fusion **52**, 17 (2010)
69. L. Mertz, N.O. Young, *Fresnel Transformation of Images, International Conference on Optical Instrument and Technology* (Chapman and Hall, London, 1961) p. 305
70. H. Barrett, J. Nucl. Med. **13**(6), 382–385 (1972)
71. R.H. Dicke, Astrophys. J. **153**(2), 101–106 (1968)
72. J.G. Ables, Astron Soc Aust **1**(4), 172–173 (1968)
73. M.J.E. Golay, J. Opt. Soc. Am. **61**, 272 (1971)

74. E.E. Fenimore, T.M. Cannon, Opt. Eng. **19**(3), 283–289 (1980)
75. E.D. Nelson, M.L. Fredman, J. Opt. Soc. Am. **60**(12), 1664–1669 (1970)
76. E.E. Fenimore, T.M. Cannon, Appl. Opt. **17**, 337–347 (1978)
77. A. Goldwurm et al., Astron. Astrophys. **411**, L223–L229 (2003)
78. S.R. Gottesman, E.E. Fenimore, Appl. Opt. **28**, 4344–4352 (1989)
79. E. Caroli et al., Space Sci. Rev. **45**, 349–403 (1987)
80. G.K. Skinner, in *22nd Moriond Astrophysics Meeting*. arXiv:astro, Vietnam (2003)
81. F. Garibaldi et al., IEEE Trans. Nuclear Science **52**, 573–579 (2005)
82. L. Zhang, R.C. Lanza, IEEE Trans. Nuclear Science **46**, 1913–1915 (1999)
83. R. Accorsi, R.C. Lanza, in *16th Intl. Conf. Appl. of Accel. Res. & Indust.* pp. 491–494 (2001)
84. Yen-Wei Chen et al., Optics Commun. **73**, 337–341 (1989)
85. U. Jager et al., Rev. Sci. Instrum. **56**, 77–79 (1985)
86. C.A. Barrera, E.C. Morse, Rev. Sci. Instr. **77**, 716–725 (2006)
87. W.T. Mason, *Fluorescent and Luminescent Probes for Biological Activity*, Edition 2 (Academic Press, USA, 1999)
88. S.V. Springham et al., Jpn. J. Appl. Phys. **44**, 4177–4121 (2005)
89. R. Accorsi, PhD thesis, Massachusetts Institute of Technology (2001)
90. G. Groh, G.S. Hayat, G.W. Stroke, Appl. Optics **11**, 931 (1972)
91. C. Brown, J. Appl. Phys. **45**, 1806–1811 (1974)
92. J. Singer, Trans. Amer. Math. Soc. **43**, 377–385 (1938)
93. L.D. Baumert, *Cyclic Difference Sets. Lecture Notes in Mathematics* (Springer, New York, 1971), p. 182
94. M. Hall, Combinatorial Theory, ed. G. Co., London, Blaisdell
95. L.D. Baumert, M. Hall, Bull. Amer. Math. Soc. **71**, 169–170 (1965)
96. E.E. Fenimore, Appl. Opt. **17**(22), 3562–3570 (1978)
97. J.J.M. In't Zand, J. Heise, R. Jager, Astron. Astrophys. **288**, 665–674 (1994)
98. R. Accorsi, F. Gasparini, R.C. Lanza, Nucl. Instrum. Methods Phys. Res. A **474**, 273–284 (2001)
99. A. Talebitaher, P.M.E. Shutler, S.V. Springham, R.S. Rawat, P. Lee, Radiat Meas **47**(10), 992–999 (2012)
100. S.V. Springham et al., Appl. Phys. Lett. **101**, 114104 (2012)

Chapter 7
Plasma Focus Device: A Novel Facility for Hard Coatings

R. Ahmad, Ijaz A. Khan, Tousif Hussain and Z.A. Umar

7.1 Introduction

Thin films are the layers of materials on other materials and its thickness can be varied from few nanometers to several micrometres. These films are developed to address the novel applications in various areas because the properties of thin films can be tailored by using different methods. Hard thin films or coatings are deposited to resist the harsh conditions of working environments such as temperature, pressure, radiation, etc. It has various applications in fields such as optics, mechanics, chemistry, electronics, magnetism, etc. The hardness of thin film can be measured using Vickers indenter in units of HV or GPa. Various techniques are being used to develop a wide range of advanced functional properties, such as physical, chemical, electrical, electronic, magnetic, mechanical, wear resistant and corrosion resistant properties at the required substrate surface. Almost all types of materials including metals, ceramics, polymers and composites can be deposited onto similar or dissimilar materials.

R. Ahmad (✉) · T. Hussain
Centre for Advanced Studies in Physics, GC University, Lahore 54000, Pakistan
e-mail: ahriaz@hotmail.com

T. Hussain
e-mail: tousifhussain@gmail.com

I.A. Khan
Department of Physics, GC University, Faisalabad 38000, Pakistan
e-mail: ijazahmad@gcuf.edu.pk

R. Ahmad
Department of Physics, GC University, Lahore 54000, Pakistan

Z.A. Umar
Atomic and Laser Physics Department, National Centre for Physics,
Islamabad 45320, Pakistan
e-mail: imnotshani@gmail.com

R.S. Rawat (ed.), *Plasma Science and Technology for Emerging Economies*,
DOI 10.1007/978-981-10-4217-1_7

Nanocomposite thin films having higher hardness are a new kind of coatings which also exhibit excellent mechanical, electronic, optical and magnetic properties because of their dependence on size and morphological structures of the thin films. Three basic steps in the formation of a hard coating on any given substrate are given below [1, 2]:

- Production of the depositing species for synthesis
- Transport from source to substrate
- Deposition onto the substrate and subsequent growth of film

These steps can completely be separated from each other or can be superimposed on each other depending on the process under consideration.

A large number of deposition techniques are being used to deposit thin films. Techniques based on the deposition from a vapour of some kind are more common. These techniques can be subdivided further into two broad categories of Physical Vapour Deposition (PVD) and Chemical Vapour Deposition (CVD).

(a) **Physical Vapour Deposition (PVD) Processes**

The term PVD is generally used to describe a variety of methods to deposit thin solid films by the condensation of a vapourized form of the solid material onto various surfaces and hence covers a wide range of vapour-phase technologies. The process of PVD involves physical ejection of material as atoms or molecules (sputtering), evaporation and condensation resulting in nucleation of these atoms onto a substrate (Fig. 7.1). This can only be explained on the basis of momentum transfer theory which was proposed by Wehner et al. [3] on the basis of earlier work. Sputtering strongly depends on the energy of ions but not on the flux of ions.

The ratio of atoms sputtered to the number of high-energy incident particles is known as sputtering yield. It depends on the binding energy of incident ion and on the angle of incidence and is written as under [4, 5]

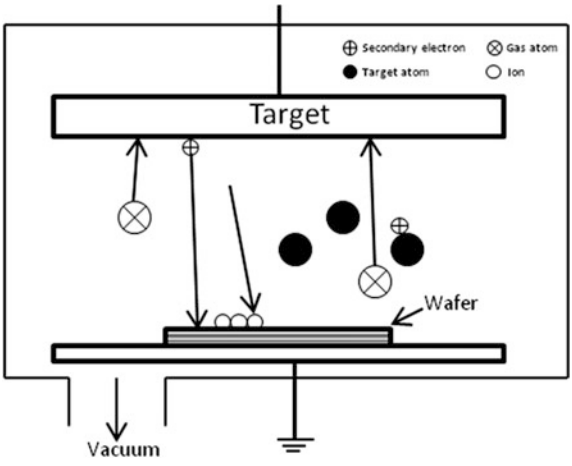

Fig. 7.1 Physical vapour deposition typical arrangement

$$Y = \frac{3\alpha}{4\pi^2} \frac{4m_i m_t}{(m_i + m_t)^2} \frac{E}{U}$$

where

m_i the atomic mass of the bombarding incident ion,
m_t the atomic mass of the target,
U the binding energy of the surface atom of the target,
E the energy of the incident ion, and
α depends on striking/incident angle.

The vapour-phase material consisting of ions or plasma often reacts chemically with gases introduced into the vapour, called reactive deposition, to form new compounds. The main categories of PVD processing are vacuum evaporation, sputter deposition and ion plating. A variety of other processes like reactive ion plating, reactive sputtering, unbalanced magnetron sputtering, High Power-Pulsed Magnetron Sputtering (HPPMS), and filtered cathodic arc deposition are derived forms of these basic PVD processes:

- *Vacuum evaporation* is a process in which material from a thermal vapourization source reaches the substrate. Trajectory of the evaporated material is 'line of sight'. There is little or no collision with gas molecules in the space between the source and substrate.
- *Molecular Beam Epitaxy (MBE)* uses evaporation to grow crystalline thin films in ultrahigh vacuum (UHV) with precise control of thickness, composition and morphology from well-controlled deposition rates.
- *Reactive evaporation (RE)* is a process in which metal atoms are evaporated from the target with a partial pressure of a reactive gas present in the chamber. The evaporated material reacts chemically with the gas forming a compound and deposited onto the substrate.
- *Activated Reactive Evaporation (ARE)* is the reactive evaporation process carried out in plasma which converts some of the neutral atoms into ions or energetic neutrals thus enhancing reaction probabilities and rates to deposit refractory compounds.
- *Biased Activated Reactive Evaporation (BARE)* is the same process as ARE with the substrate held at a negative bias voltage.
- *Sputter Deposition* is the deposition of particles vapourized from a surface (target), by the physical sputtering process. Physical sputtering is a non-thermal vapourization process where surface atoms are physically ejected from a solid surface by momentum transfer from an atomic-sized energetic bombarding particle which is usually gaseous ion accelerated from plasma. These ejected

atoms from the solid surface can be condensed on a substrate to form a surface coating.

- *Reactive Sputter Deposition* is a sputter deposition that involves a partial pressure of a reactive gas which reacts with the sputtered material to form a compound surface coating.
- *Ion Beam Deposition* process involves an ion beam gun of the material to be deposited which generates a beam of ions. This ions beam impinges on the substrate and deposition is achieved.
- *Ion Beam Assisted Deposition* is similar to the above. However, it sputters target material and deposits them on to the substrate. In dual ion beam assisted deposition an ion beam is used to sputter a target and a second beam is used to bombard the growing film to change the structure and properties.
- In *Ion Implantation* process, all of the depositing material is ionized having much higher accelerating energies. The result is that the depositing ions are able to penetrate the substrate surface and be implanted in the substrate rather than depositing on it.

(b) **Chemical Processes**

- When a volatile compound of the substance to be deposited is vapourized via heating, and the vapour is thermally decomposed into atoms or molecules, and/or reacted with other gases, vapours, or liquids at the substrate surface to produce the desired thin film onto substrate, the process is called thermal chemical vapour deposition (CVD). Thermally activated CVD processes are initiated only with the thermal energy of the resistance heating, RF heating or by infrared radiation. While in some cases enhanced CVD methods are employed, which includes plasma-enhanced CVD (PECVD), laser-induced CVD (LCVD), photo CVD (PCVD) and so on [5].
- Plasma-Enhanced Chemical Vapour Deposition (PECVD) is a process in which species to be deposited are generated in the plasma. As a result, deposition using the same source gases takes place at lower wafer temperature than in conventional CVD which requires high temperature to break bonds and to release desired species from input gases. The plasma is generally created by RF or DC discharge between two electrodes, space between which is filled with the reacting gases.

(c) **Magnetron sputtering**

The magnetron is heavily used as a system to deposit thin film because of its versatility [5]. It uses the static magnetic field and electric field to confine the electrons through Hall drift closer to the substrate area. The magnetic field is located parallel to the cathode surface. This confinement increases plasma density through ionization by these energetic electrons trapped in the electric and magnetic field lines (Fig. 7.2). These increased ions collide with the target. This results in a higher rate of deposition. Magnetron sputtering can also have balanced and unbalanced electrode systems which have their own advantages.

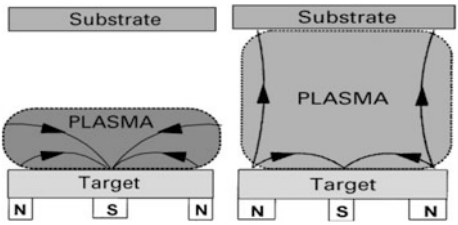

Fig. 7.2 Balanced and unnbalanced Sputtering gun

In balanced magnetron sputtering the plasma is confined in the range of few tens of mm on the surface of target, and the substrate remains outside of the system and some of the secondary electrons may escape the trapped area producing less dense plasma near the substrate. This plasma provides electron/ion current which heats the substrate by the bombardment which would affect the structure of the film. Due to this limitation, unbalanced magnetron is designed as shown Fig. 7.2. In this configuration, the plasma is extended from the target to the substrate due to the strengthening of the outer pole of the magnetron. This plasma column extending to the substrate leads to a significant increase in substrate ion current density and electron current density measurable at the substrate. This leads to better transport of ions to the substrate with better adherence of thin film [6].

In case of reactive sputtering, arcing occur which results in the reduced ionization. Therefore, it cannot handle the growth of insulating materials. The main disadvantage of using a single unbalanced magnetron for thin film deposition is the anode problem and the inhomogeneity of plasma at the substrate. These problems can be overcome by employing two or more magnetron systems and by using moving substrates. Various methods were used to increase ionization in magnetron but with the coming of HIPIMS (High Power Impulse Magnetron Sputtering) system, the problems are resolved.

HIPIMS was first reported in 1999 by Kouznetsov et al. [7, 8] and they explicitly outlined the possibility to operate a planar magnetron at high power density leading to deposition of the target material from the plasma. HIPIMS combines the advantages of high ionization like arc evaporation with the advantages of magnetron sputtering. The basis of the technique is to increase the plasma density in front of a sputtering source, and, thereby, decreasing the mean ionization distance for the sputtered particles. The plasma density is increased simply by applying a higher pulsed power. However, the electron utilization efficiency during sputtering is rather low and the metal particle ionization rate needs to be considerably improved to allow for a large-scale industrial application. Therefore, Li and Tian [9] enhanced the HIPIMS technique by simultaneously applying an electric field (EF-HIPIMS). The major focus of this chapter is, however, a dense a plasma focus device which is introduced in the next section.

(d) Dense Plasma Focus—A potential Surface Coating Technique

Dense plasma focus (DPF) device was developed initially as a feasible fusion scheme [10, 11]. However, later on whole interests were diverted in using this

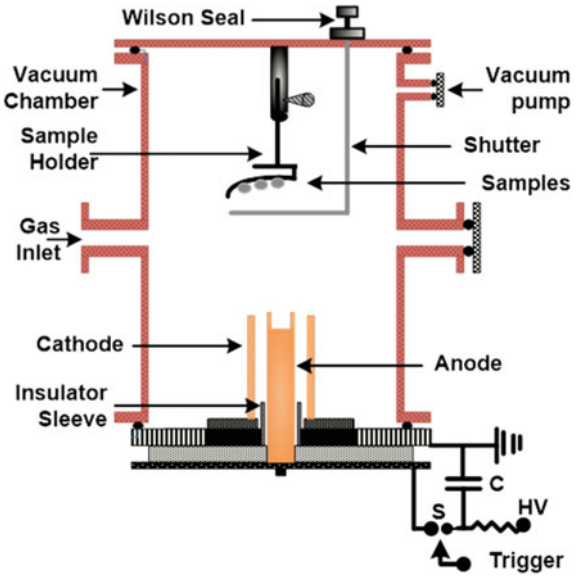

Fig. 7.3 Schematic of plasma focus device for materials processing

device as a copious source of multi-radiations which include neutrons, X-rays, fast electrons and ions [11]. The DPF is a device that can generate, accelerate and pinch plasma by electromagnetic forces. The short-lived pinched plasma column ($\sim 10^{-7}$ s) is sufficiently hot ($\sim$1–2 keV) and dense ($\sim 10^{25}$–10^{26} m^{-3}) to enhance nuclear fusion reaction [11], even with high threshold energies, which make it a multi-radiation source. DPF works in pulsed mode since the whole discharge lasts for a few tens of microsecond and is a pulsed ionizing radiation source for many applications. DPF as an abundant source of neutrons has been used earlier as pulsed neutron activation analysis [12, 13] and as a wide range of X-ray source for lithography and radiography [14–17]. The highly energetic ion and electron beams emitted in DPF have also been used for processing of materials in the form of surface modification and thin film coatings [18–24]. The nature of gases and the electrodes material inside DPF chamber determine the emission of different kind of radiations.

The DPF has been used for nitrogen ion implantation on stainless steel [25], titanium [26] and high carbon steel. Figure 7.3 shows the schematic of typical DPF device as material processing facility where the samples to be processed are mounted on sample holder down the anode stream. Kant et al. [27, 28] used nitrogen ions of the DPF for fabrication of carbon nitride coating on a graphite substrate. Others have reported ion induced structural and morphological changes of a variety of thin films [28–33]. When compared with other surface modification and thin film deposition techniques, plasma processing and deposition with DPF has several attractive features which are listed below.

Advantages of Surface Coatings Using DPF

Several prominent features of DPF which make it an attractive candidate for thin film coatings when compared with other coating techniques are as follows:

- DPF combines the feature of three different techniques which are the PVD sputtering process, electron beam evaporation and plasma-enhanced chemical vapour deposition and hence is a hybrid deposition technique.
- The deposition rates in DPF device are extremely high in comparison to most of the other plasma based depositions due to intense ablation of anode material by energetic electron beam generated from high-energy density pinch plasmas.
- To deposit thin films no external heating of the substrate is required as highly energetic ions (40 keV–2 MeV) emanated in DPF heats up the substrate surface transiently to high temperatures.
- DPF operation requires low working gas pressure and static gas fill mode rather than flowing gas operation and hence the gas consumption is low as compared to other deposition techniques.
- DPF can be energized by a simple fast discharge capacitor.
- Short duration ion pulse is used to deposit composite thin films.
- Adhesion between the deposited films and substrate is good due to the treatment of substrate surface by ions of filling gas species.

7.2 Studies of Ions Emitted from Plasma Focus

Plasma focus device is a rich source of ions with a broad range of energies. These ions are being used to deposit a thin film or to modify the surface of the substrate. Therefore, characterization of ions generation in plasma focus is of great importance to understand the processes happening in plasma focus devices. Various studies [34–45] were made over the years by using various techniques such as SSNTDs [36–38], photodiode [39, 40], Faraday cup [41–45] and simulations [46]. The fast radial collapse induces very high local electric field accelerating the ions and electrons in opposite direction with high velocities. The ions are accelerated towards the top of the chamber in a conical fashion with energies ranging from tens of keV to few MeV. Various mechanisms were proposed for ion acceleration in the plasma focus [47, 48].

Kelly et al. [35] studied the spectrum of ions by operating the device with nitrogen. A Faraday cup operating in the secondary electron emission mode was used. Jakubowski et al. [49] investigated the energetic ion beams and their correlation with a pulsed relativistic electron beam. The measurements were performed with pinhole camera equipped with solid-state nuclear track detectors (SSNTDs) and with a scintillation detector, allowing determination of the ion energy spectrum on the basis of the time of flight technique. Takao et al. [50] studied ion beams and

their energy spectra with a Thomson parabola spectrometer. From the measurement, the proton beam energy was found to be distributed from 0.15 to 2 MeV. Takao et al. [51] investigated the anode configuration to improve the purity of ion beams produced in a PF. The purity of nitrogen ion was enhanced up to 91% with an engraving of anode face.

(a) Ions Studies Using SSNTDs

A solid-state nuclear track detector or SSNTD is plastic material to record tracks of neutrons or charged particles. These tracks are revealed after etching. The commonly used plastic material is polyallyl diglycol carbonate (PADC) which is also known as CR-39.

The characteristics of ion beams of hydrogen and nitrogen with different filling pressures emitted from the 2.3 kJ plasma focus device have been investigated by author's group [52]. CR-39 SSNTDs are employed for the registration of tracks of ions. The exposed detectors are etched in 6 N NaOH solution at 70 °C and then examined with an optical microscope. The ion flux is estimated to be of the order of $10^{5–6}$ tracks/cm^2 (Fig. 7.4).

The flux with the radial position does not exhibit any regular pattern of variation. This is attributed to the generation of micro-beams at the anode tip, which are scattered on passing through pinch region under the influence of intense electromagnetic field [52, 53]. This scattering is stronger for nitrogen because ion beams find sufficient time to interact with neutral species or ionized gas in the pinch region. The irregular behaviour can also be attributed to the shot-to-shot fluctuations of the ion emission.

Moreno et al. [54] used SSNDT to detect the ions and found that average energy of hydrogen ions is around 40 keV.

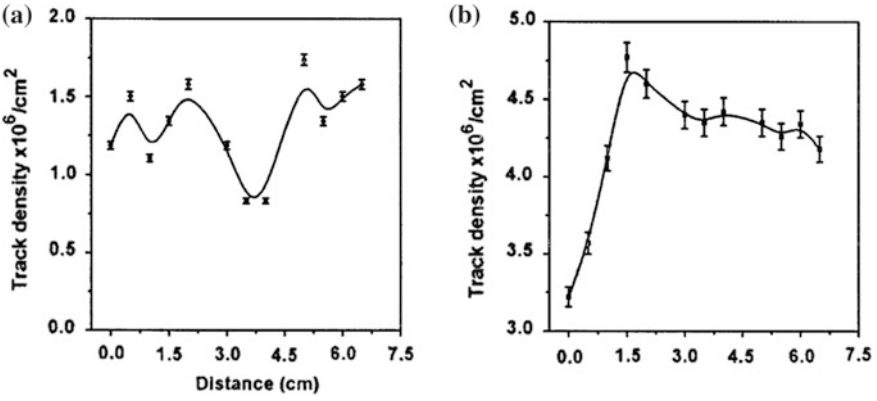

Fig. 7.4 **a** Variation of hydrogen ion's flux with distance from the focus axis at 1 mbar. **b** Variation of nitrogen ion's flux with distance from the focus axis at 2 mbar. Reprinted from Ahmad et al. [52] (copyright 2002), with permission from Springer

(b) **Measurements Using Photodiode**

Photodiodes are conventionally designed to operate for light but these are also used to detect the charged particles directly [55]. Thickness of intrinsic layer of BPX 65 photodiode is large so that charged particles dissipate their energy along a linear track. The energy dissipation results in the generation of electron hole pair by means of coulomb interaction between ions and electrons. A number of electron–hole pair generation depends on the incident ion energy. The amount of electron–hole pair generated can be estimated by detecting the amount of this charge.

The ion beam signals emanated during the radial collapse phase of PF operation are recorded with BPX65 photodiode detector in order to measure the ion beam parameters like ion velocity, ion energy and ion number density.

The protective glass of BPX65 photodiode detector is removed allowing the ions and soft X-rays to reach the active area of photodiode. The photodiode has a response time of about 12 ns, whereas an aperture (diameter = 600 μm and area 0.28 mm^2) is made in the active layer of thickness (10 μm) which limits the ion beam flux striking the detection area of the photodiode. The ion beam signal is recorded through coaxial cable (resistance = 50 Ω) with the help of oscilloscope attached to the computer.

Time of flight technique [44] is employed to measure the ion beam parameters like ion velocity, ion energy and ion number density. The ion velocity can be calculated by using the relation:

$$V_{\text{ion}} = \frac{d}{t} \tag{7.1}$$

where d is the distance (from source to detector) and t is the flight time of ions. Flight time is measured by comparing the ion beam signal with the X-ray signal emitted during the same focus shot of PF device. The estimated ions velocity is used to further calculate the ion beam parameters like energy (E_{ion}) and ion number (N_{d}) density through the following relations, respectively.

$$E = \frac{1}{2}mv^2 \tag{7.2}$$

$$N_{\text{d}} = \frac{V}{RqAv} \tag{7.3}$$

where m is the atomic mass of ions or mass of ion of the filling gas species and N_{d} is the ion number density, A is the area of aperture through which ions are entered and reached to the active area of photodiode detector, v is the ion velocity, q is the charge and V is the voltage developed by ion current across the resistor R.

In order to confirm the results obtained with the help of BPX65 photodiode detector, spectral law $\frac{\mathrm{d}N}{\mathrm{d}E} = \alpha E^{-X}$ is employed to estimate different parameters (Eqs. 7.2 and 7.3) of ion beam signals [56]. Where N is the total number of ions

emitted during one focus shot (one ion beam signal) having energy E, the value of exponent X is ranged from 2 to 5 and the proportionality constant "α" is equal to 1.12×10^{19} a.u. If we divide the total number of ions emitted during one shot of PF operation to the ion beam cross-section, it gives us the ion beam fluence denoted by ($f_i = N/\sigma_l$), this ion beam fluence is estimated by using the expression given in Ref. [56].

A typical ion beam signal recorded with BPX65 photodiode detector placed at 9 cm from the anode tip along with high voltage probe signal is shown in Fig. 7.5. The first and second peaks of diode signal (solid line) indicate an X-ray pulse due to its high sensitivity for X-rays and the desired ion pulse, respectively. The discrimination of X-rays and ion pulses has been confirmed by masking the detector with a thin foil allowing the X-rays to pass while stopping the ions. Such ion beam pulses have already been reported by Kelly [44] and Nunomura [57].

Two photodiodes (one photodiode has glass window while the second photodiode has a copper foil with small hole at its centre) were used to differentiate the existence of X-ray peak and ion pulse recorded by BPX65 photodiode. Both the BPX65 photodiodes are placed at 10 cm from the anode. The recorded signal was the light signal because UV and visible light have the ability to pass through the glass window.

Now the ion energy flux emanated during each focus shot is determined for 9 and 14 cm positions. For 9 cm axial position, the estimated values of ion energy (E) and ion number density (N_d) are ranged from 40 keV to 1.2 MeV and 9.7×10^{19} to 1.8×10^{19} m^{-3} and 140 to 847 keV and 5.3×10^{19} to 2.2×10^{19} m^{-3}, respectively [58]. These estimated values of ion energy and ion number density agreed well with the reported values [59]. This shows that the ion

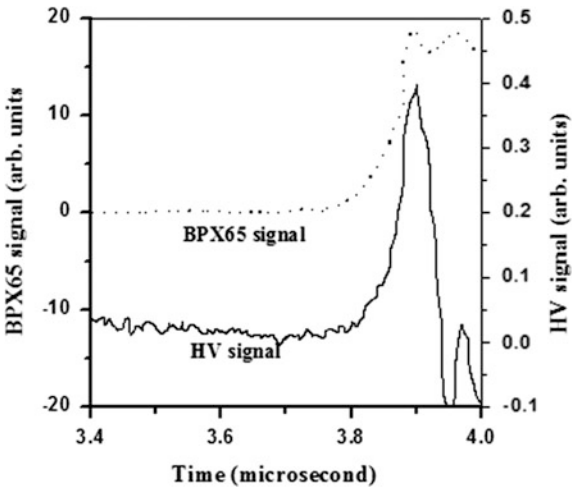

Fig. 7.5 Typical ion beam signal recorded with BPX65 photodiode detector along with high voltage signal

energies and ion number densities are decreased with the increase of axial distance. Most of the ions are emitted in a small solid angle (along the anode axis) and their flux decreases with the increase of angular position. Therefore, it is concluded that as we go away from the pinched plasma region (source point); either along the anode axis or away from the anode axis at different angular positions; the energy and number density of ions reached at the detector surface is decreased.

(c) **Faraday Cup**

A Faraday cup (FC) is a conductive cup designed to detect charged particles in vacuum. FCs have been used as a measurement tool for charged particle beam parameters such as current and current density profile. Various designs of FCs have been reported for different applications [42, 58–60].

The electric current of the FC is dependent on the incident particle beam current. These charged particles may be backscattered and may result in the ejection of secondary electrons. These secondary electrons may escape from the FC aperture. Care must be taken to minimize these electrons. The escaping of secondary electrons results in the current overestimation for positively charged particle beams and current underestimation for electrons and other negative charged particle beams from the true values of current. To avoid this problem, cylindrical FC designs have employed either coaxial electrostatic fields or magnetic fields to recapture the ejected secondary electrons.

A negative voltage is applied to the electrostatic guard ring which produces the coaxial electrostatic fields to prevent electrons from escaping. For high-energy ejected electrons, a voltage with rather a large magnitude should be used which may cause difficulties. A new design was proposed by Thomas et al. [61] to solve this problem. This design was based on the addition of a long bevel to the entrance end of the cylindrical inner cup (IC) of a traditional coaxial electrostatic FC. The simulation and experimental results showed an improvement in the FC performance.

Time of flight (TOF) is used to determine the velocity of the ions which in turn provide us the energy of ions. The dimensions of the electrodes and the insulation material between them are chosen such that a characteristic impedance of 50 Ω is achieved according to the expression [60]

$$Z = \frac{138.2}{\sqrt{K}} \log_{10} \frac{D}{d} \tag{7.4}$$

where D = 28 mm is the internal diameter of the anode, d = 8 mm is the external diameter of the cathode and K = 2.269 is the dielectric constant of Teflon. An electrically insulated perforated circular disc of brass having a cross-sectional area of 3.92 mm^2 acts as an entrance window, and also avoids escaping of charged particles once they entered the FC.

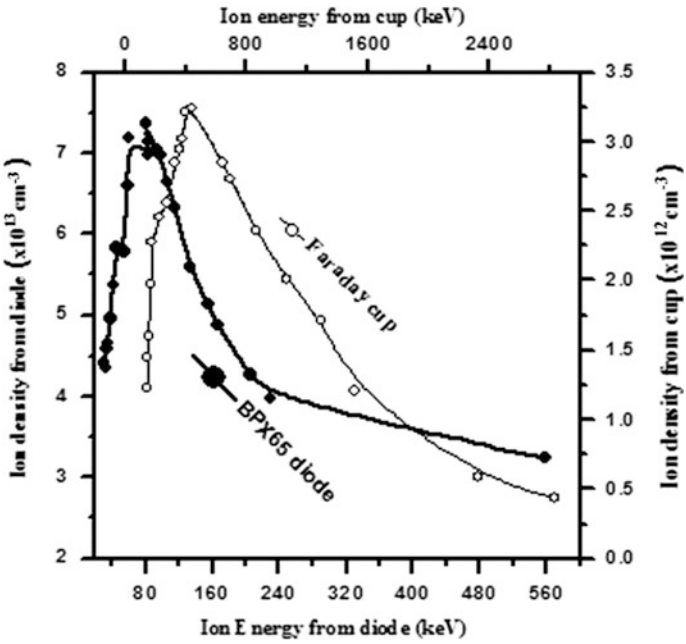

Fig. 7.6 Distribution of ion number density (cm^{-3}) as a function of ion energy (keV) estimated with BPX65 photodiode and Faraday cup

The ion number density N_d having velocity v and charge q can be estimated using Eq. 7.2. The ion beam current density J is also estimated from FC signals using simple expression

$$J = \frac{I}{A} \tag{7.5}$$

where $I = \frac{dQ}{dt}$ is the ion current and $Q = \int \frac{V}{R} dt$ is the charge collected at the collector.

Figure 7.6 shows that ion density determined by Faraday cup and the photodiode is significantly different as techniques are different and therefore have inherent errors.

After discussing various ion measurement techniques that we have used in plasma focus device we will now provide details of various hard coatings that have been deposited by our group using this device.

7.3 Deposition of Nitride and Carbide Coatings

Plasma nitriding/carbiding is a well-established technique for surface modification of metal alloys, improving the mechanical and chemical properties of the materials. The nitrogen/carbon chemical potential is the driving force in the diffusion process, i.e. the concentration gradient determines the species diffusion into the bulk material. Important processes in plasma nitriding/carbiding are implantation, sputtering and diffusion. These phenomena are energy dependent. As we know plasma focus device has the wide range of energies for ions (45 keV–2 MeV), all of these phenomena occurred but dominant phenomena are sputtering and ion implantation.

Ions coming from plasma focus device have been used for the surface modification of a variety of metals. These ions have much energy which is transferred to the material's surface raising its surface temperature (discussed above). Feugeas et al. [25] reported that this change in temperature is much significant in materials with plasma focus. Several surface treatment processes like annealing of crystal lattice defects, formation of new phases and quenching can be performed by this process. It can also cause to penetrate the ions beyond the normal range through cascade collision and because of the energetic ions.

Titanium nitride is a member of the refractory transition metal nitrides family showing characteristics of both covalent and metallic compounds [62]. For a few decades, TiN coatings have been applied to tools, dies and many mechanical parts to increase their lifetime and performance owing to their excellent mechanical, thermal and electronic properties, such as good thermal stability, high corrosion resistance and low electrical resistivity. Therefore, they have many applications ranging from coatings on cutting tools to diffusion barriers in microelectronic applications. However, TiN coating is degraded by oxidation at high temperature during working. So, it is important to improve its oxidation resistance for successful use. As a possible solution to this problem, aluminium atoms have been added to the TiN material considering that both TiN and TiAlN have the same crystallographic structure (fcc). In high-temperature applications, a dense and strongly adhesive Al_2O_3 film is observed because of diffusion of Al atoms to the surface, which stops further oxidation. TiAlN is expected to be a promising candidate as a hard coating layer because it shows excellent properties, especially for high-temperature use [63, 64].

Amorphous carbon (a-C) films are known due to their extraordinary properties such as high hardness, wear resistance, chemical resistance and good tribological properties [63]. The a-C thin films are generally hard (about 18–80 GPa) but brittle. Metal/amorphous carbon (Me/a-C) thin films improve the toughness of the thin films [63], with moderately high hardness and therefore are important engineering materials for surface protection [64].

The Al/a-C nanocomposite thin films are synthesized on Si substrates using Mather-type plasma focus device. For the deposition of Al/a-C nanocomposite thin films, the central hollow copper anode was replaced by an engraved copper anode

with solid aluminium top placed as an insert at the anode tip. The optimized CH_4:Ar admixture filling gas pressure was found to be about 1.5 mbar. We used the CH_4/Ar admixture ratio of 3:7 for the synthesis of Al/a-C thin films on Si substrate placed at a distance of 10 cm above the anode tip along the anode axis.

Titanium Carbide (TiC) is very well known as a hard refractory ceramic material used in protecting coating. TiC shows high hardness, high melting point, remarkably chemical stability, high oxidation resistance, excellent wear resistance and low coefficient of friction. It also has metallic properties such as high electric and thermal conductivity [65]. Hydrogenated amorphous carbon (a-C:H) films have been studied widely for about three decades because of their excellent mechanical and tribological properties [65]. Carbon based nanocomposites such as (TiC/a-C:H) where TiC nanocrystalline is embedded into a-C:H matrix is more attractive because of their potential as high-strength material [66].

The TiC/SiC/a-C:H nanocomposite structure shows high hardness and Young's modulus values as well as low friction similar to that of the Ti_3SiC_2 phase [67–69]. These nanocomposite films share a combination of properties such as superior corrosion resistance SiC, wear resistance and low friction a-C:H, and mechanical enhancement due to the nc-TiC [70]. Koutzaki et al. [71] and Krzanowski et al. [72] deposited films using RF magnetron co-sputtering of TiC and SiC targets and they observed increase in hardness from 10 GPa of silicon-free TiC film to 20–22 GPa for films containing 15–30 atomic percent (at.%) Si. These outstanding properties of the Ti-Si-C nanocomposite coatings make them a suitable candidate for various applications, such as protective coatings [70, 73, 74], diffusion barriers [73] and material for solar cells [75]. Different techniques have been used for the synthesis of TiC_x/SiC/a-C:H thin films such as RF magnetron sputtering [74, 75], DC magnetron sputtering [76], CVD [77], etc.

Experimental Details

The synthesis of zirconium nitride, zirconium oxy-nitride, zirconium carbonitride, zirconium aluminium oxy-nitride, titanium carbide, titanium aluminium nitride, aluminium carbide and alumina stabilized zirconia films are accomplished with Mather-type PF facility energized by a single capacitor with maximum storage energy [78], whose schematic is shown in Fig. 7.3. The electrode system comprises of copper anode surrounded by six equidistant copper rods forming a cathode. The anode is engraved 15 mm deep at the tip to reduce the copper (anode material) impurities [51].

1. Synthesis of the TiAlN thin films was done using polished aluminium substrates and a titanium target fitted at the top of the anode. The deposition was performed in a Mather-type DPF device powered by a single 32 μF, 15 kV capacitor for 10–50 focus shots.

2. For zirconium nitride: the zirconium samples (about 10 × 10 × 5 mm^3) are polished with SiC abrasive papers of different grids and subsequently washed in an ultrasonic water bath for 30 min. The vacuum chamber is filled with nitrogen gas at 1.25 mbar pressure. The polished zirconium samples are mounted at 9 cm above the anode tip with the help of sample holder but at different angular positions (0°, 10° and 20°) with respect to anode axis. These samples are exposed to multiple focus shots (10, 20, 30 and 40) at various axial positions (5, 8, 11, 14 and 23 cm) with the help of an axially movable sample holder.
3. In the other experiment, graphite and aluminium materials were placed as an insert at the anode tip to deposit them onto the zirconium or titanium substrate. The samples were irradiated with multiple shots from 10 to 50.
4. Aluminium samples were deposited with carbon which is inserted in the anode tip for focus shots from 10 to 50.

These synthesized films were investigated by using different characterized techniques like X-ray diffractometer (XRD), field emission scanning electron microscope (FESEM), energy dispersive X-ray (EDX) spectrometer, Fourier transform infrared (FTIR) spectrometer, Raman spectrometer and Vickers micro-hardness indenter in order to explore the ion induced structural changes, crystallinity, crystallite size, residual stresses, surface morphology, elemental composition and micro-hardness.

7.3.1 Growth of TiAlN Coatings

Various methods are used to deposit thin films on a substrate for the improvement of hardness. Ait Djafer et al. [79] deposited the film using RF magnetron sputtering and found the maximum hardness of 25.75 GPa. Addition of aluminium improved the wear, corrosion resistance and can be used for orthopaedic [79] and mechanical applications. These treated samples are characterized by using X-ray diffractometer, scanning electron microscope and micro-hardness [80].

7.3.1.1 Phase Identification

Figure 7.7 shows the XRD peak patterns, ranging from 30° to 85°, of coatings for various focus shots. XRD patterns showed the development of two phases: one with fcc NaCl B1 structure similar to TiN structure and the other with AlN (fcc phase). Differentiation of the TiN and TiAlN phases using the diffraction method is impossible because of their isomorphous nature, as TiAlN is, in fact, the secondary solid solution based on titanium nitride. The diffraction patterns exhibit a pattern of crystalline TiAlN with orientations of (111), (200), (220) and (311) and AlN with orientations of (111), (200) and (220). Native oxide of aluminium, is removed

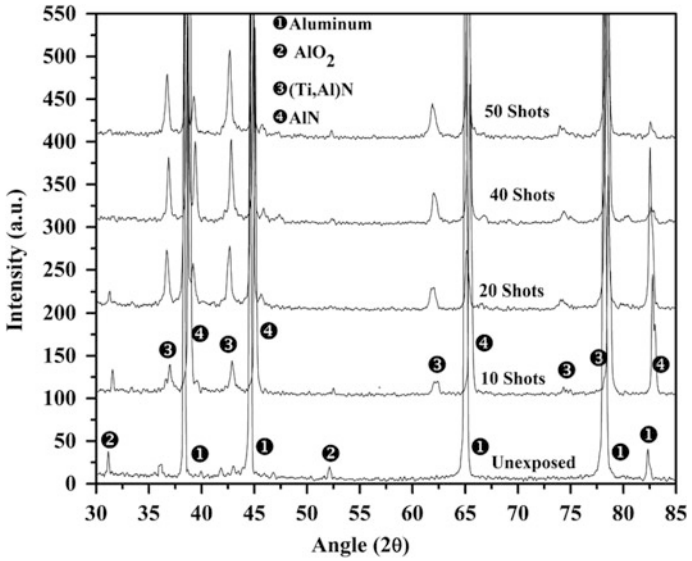

Fig. 7.7 XRD patterns obtained for TiAlN coatings deposited at a distance of 9 cm at zero angular positions for various number of focus shots. Reprinted from Hussain et al. [80] (copyright 2011), with permission from Taylor & Francis

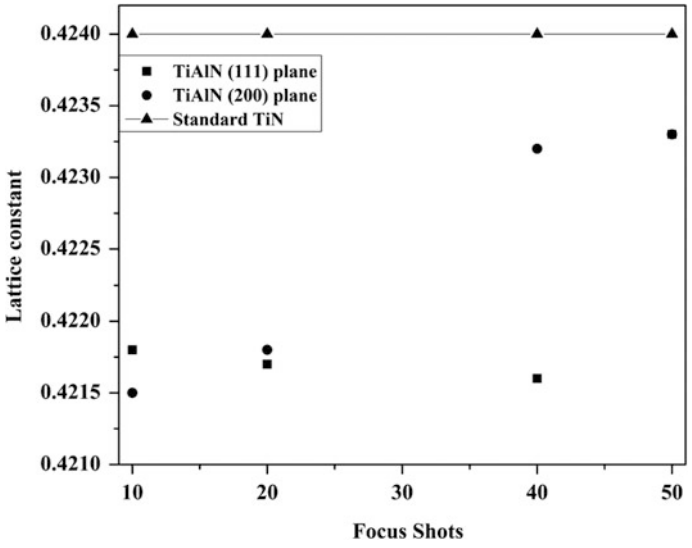

Fig. 7.8 Lattice constant with varying number of focus shots. Reprinted from Hussain et al. [80] (copyright 2011), with permission from Taylor & Francis

Table 7.1 Crystallite/Grain size as a function of the number of focus shots

Number of focus shots	Crystallite size (nm) of TiAlN (111) plane
10	48.7
20	41.6
40	36.5
50	29.2

gradually with the increase in the number of focus shots. The observed intensity of the TiAlN planes for TiAlN coatings showed an increasing trend when the number of focus shots is increased (Fig. 7.7). The intensity of diffraction peaks is improved with the increase in energy and flux of ions that are impinging on the film surface with the increase in a number of focus shots.

In order to further investigate the microstructural changes of plasma focus deposited TiAlN coatings, the lattice constants were calculated. The peak position revealed a nonlinear variation of the lattice parameter (Fig. 7.8), which is considered to result from the composite nature of the ternary nitrides and the substrate high heating effect during deposition. The reported lattice parameter of TiN is 0.424 nm. It is clear from Fig. 7.8 that the lattice parameter of (111) and (200) planes are less than the reported lattice parameter of TiN. The smaller lattice parameter was related to the formation of a solid solution structure where Al atoms substitute Ti atoms in the TiN cubic lattice (remaining still fcc structure), since the aluminium's atomic radius (0.143 nm) is smaller than that of Ti (0.146 nm). This leads to shrinkage in the lattice parameter and hence a shift in 2θ value in the XRD pattern.

From the figure, it is observed that peaks are broadening; using the broadening of the peaks, it is possible to determine the grain size from the Scherrer formula [81]. Crystallite size (D) of TiAlN (111) plane is estimated from the following equation:

$$D = \frac{0.9\lambda}{\beta \cos\theta} \tag{7.6}$$

where β is the full width at half-maximum (FWHM) of the diffraction peak, λ is the wavelength of the incident Cu Kα X-ray (1.514 Å) and θ is the diffraction angle. The grain size curve (Table 7.1) is influenced by the number of focus shots; when increasing the focus shots, the crystallite size was found to decrease linearly. With the reduction in the crystallite size, the dislocation activity is restricted and crack propagation along grain boundaries is prevented.

Surface Morphology

The surface morphological studies of the plasma focus deposited TiAlN coatings that exhibit good crystallinity were observed by SEM as shown in Fig. 7.9. The sample exposed to 10 focus shots showed dense and fine-grained morphology with

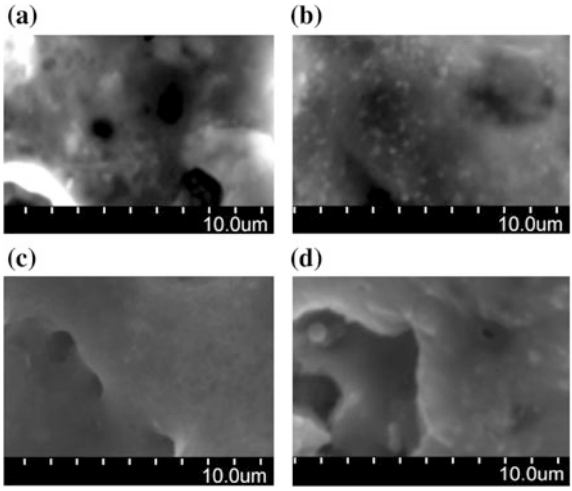

Fig. 7.9 SEMs of the TiAlN coatings synthesized at **a** 10 focus shots; **b** 20 focus shots; **c** 40 focus shots and **d** 50 focus shots. Reprinted from Hussain et al. [80] (copyright 2011), with permission from Taylor & Francis

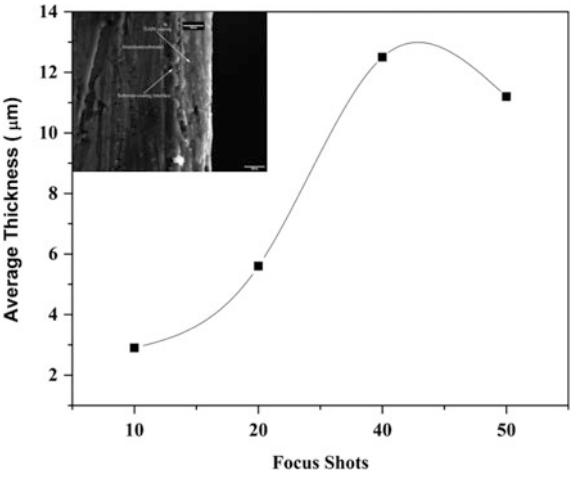

Fig. 7.10 Thickness as a function of the number of focus shots (*inset* cross-sectional SEM of TiAlN coating synthesized with 40 focus shots). Reprinted from Hussain et al. [80] (copyright 2011), with permission from Taylor & Francis

few pit holes and crater present throughout the TiAlN coating. It is noticeable that there is no trace of columnar growth in any of the TiAlN coatings. The columnar growth results by self-shadowing during the deposition process and is the characteristic feature for evaporation and sputter deposition [82, 83]. For sufficiently high energies, the impacting cluster compresses and anneals the area directly, hindering the columnar growth. The energetic cluster also leads to a self-smoothing of the surface [84, 85].

The average thicknesses of the samples synthesized using various focus shots can be measured from the corresponding cross-sectional SEM images as shown in Fig. 7.10. The results showed that the deposition thickness of the TiAlN coatings in

a plasma focus system is in some way linear with the typical deposition rate of about 276 ± 50 nm per shot at focus bank storage energy of 2.3 kJ. It may be noted that the deposition rate achieved in plasma focus is high compared with the deposition rates obtained in other devices. It may also be noted that energetic ions also sputtered the substrate.

7.3.1.2 Micro-hardness

The Vickers micro-hardness (HV) as a function of imposed load for plasma focus deposited TiAlN coatings is shown in Fig. 7.12. Four hardness measurements at 25, 50, 100 and 200 gf loads, applied for dwell time of 5 s, for each sample were used for micro-hardness profile. The hardness of untreated aluminium sample is also presented for comparison. The hardness was observed to increase with the increase in focus shots except for 50 focus shots. A steep fall in the micro-hardness values in the near-surface region of the samples exposed to focus shots suggests a concentration gradient towards the bulk. The microstructure severely affects the hardness of the material [86]. The increase in the micro-hardness values may be credited to increase in ion flux and incorporation of titanium and nitrogen ions into the deposited TiAlN coatings [26].

There are many factors that may affect the measured hardness of TiAlN coatings, including the crystallite size, residual stresses and densification of coatings. A hardening (H) because of a decrease in the average crystallite size (d) according to the Hall–Patch relationship $H \propto 1/d^{1/2}$ might also be included in the present case. This can be deduced from the observation that hardness increases as the crysallite size decreases from about 49 to 29 nm (Fig. 7.11).

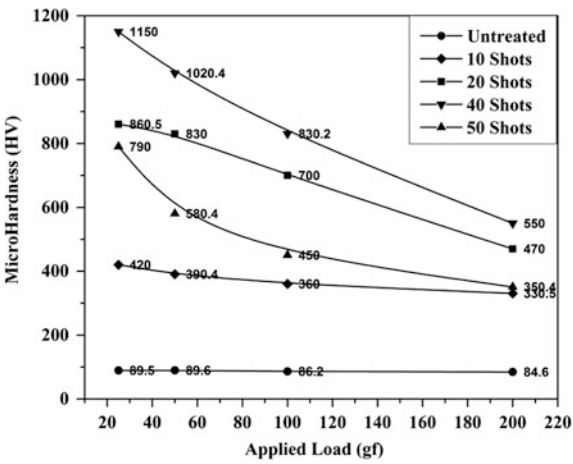

Fig. 7.11 Micro-hardness as a function of the applied load and the number of focus shots. Reprinted from Hussain et al. [80] (copyright 2011), with permission from Taylor & Francis

7.3.2 Synthesis of Zirconium Nitride Films

The intense nitrogen ion energy fluxes emanated during the radial collapse phase of PF operation irradiate the surface of zirconium samples resulting in the formation of sputtered zirconium plasma [87] which react with the background ionized nitrogen plasma to form zirconium nitride which is deposited in the form of thin film. The zirconium nitride films are deposited by multiple (10, 20, 30 and 40) focus shots ion irradiation process. These deposited zirconium nitride films are characterized by induced structural change, phase identifications, crystallinity, crystallite size, dislocation density, lattice parameters, surface morphology and micro-hardness by employing XRD, FESEM attached with EDX and Vickers micro-hardness tester.

Structural Analysis

Figure 7.12(a) reveals the XRD patterns of zirconium nitride films deposited for multiple (10, 20, 30 and 40) focus shots ion irradiations when the zirconium samples are placed at a distance of 9 cm from the top of the central anode. The XRD pattern shows that the peak intensity of zirconium is decreased whereas the peak intensity of newly formed zirconium nitride phase is increased with the increase in a number of focus irradiation shots. This shows that the ion irradiation process sputtered the zirconium surface creating zirconium plasma which reacts with energetic nitrogen ions to form zirconium nitride. The XRD patterns confirm the development of various diffraction peaks related to ZrN and Zr_2N compounds which grow along different orientations. However, their peak intensities are increased with increasing focus shots. The increase in peak intensity means the increase in crystallinity or growth of respective phase. Moreover, the increasing growth of zirconium nitride along various orientations is due to the increase of total

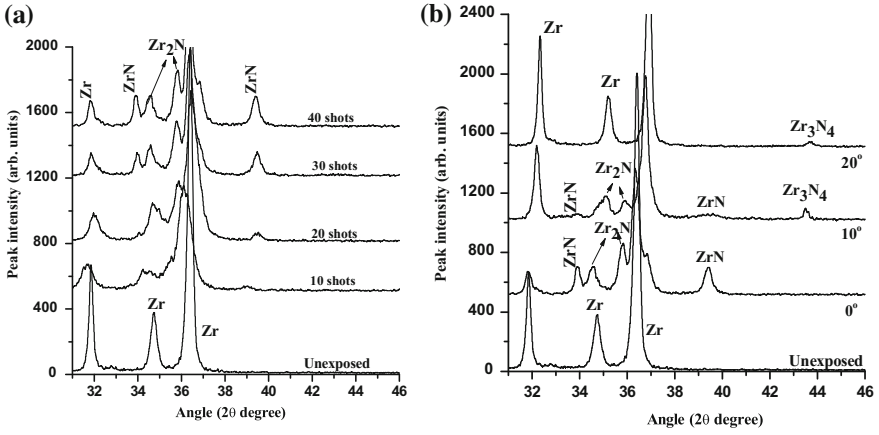

Fig. 7.12 XRD patterns of ZrN films deposited for **a** multiple (10, 20, 30 and 40) focus shots at zero-degree angular position and **b** 40 focus shots at different angular positions. Reprinted from Khan et al. [87] (copyright 2008), with permission from Elsevier

ion energy flux delivered to the zirconium samples and the total number of ion energy flux is associated with the total number of focus shots. It may be interesting to note that the intensity of Zr_2N planes is stronger than that of ZrN planes. This indicates that the amount of Zr_2N phase is more than ZrN phase. It was concluded that the PF assisted ZrN film formation is due to the combination of two different processes (i) ion implantation and (ii) re-deposition of zirconium nitride phases [87].

Figure 7.12b shows the XRD patterns of zirconium samples treated at different angular positions (0°, 10° and 20°) for 40 focus shots ion irradiation process. The respective positions of observed zirconium nitride peaks corresponding to ZrN, Zr_2N and Zr_3N_4 phases are in agreement with the literature [88–90] as well as Inorganic Crystal Structure Database (ICSD). It is observed that the growth of zirconium nitride (both ZrN and Zr_2N compounds) is decreased with the increase of sample angular positions along with the formation of Zr_3N_4 phase of zirconium nitride. It is concluded that the main features of XRD patterns are: (i) with the increase in angular sample position, the diffraction peaks of zirconium start to regain their intensity to the same level as that of the untreated zirconium sample, (ii) the crystallinity of ZrN and Zr_2N degrades with increasing angle of exposure and (iii) the appearance of Zr_3N_4 (340) phase at 2θ values of 43.5°, which is identified as the insulating phase of zirconium nitride [91]. It is observed that the insulating phase of zirconium nitride is formed at lower surface temperature whereas conducting phase of zirconium nitride is formed at comparatively higher surface temperature because the rise in surface temperature is associated with the total number of incorporated nitrogen ions and the total numbers of incorporated ions are increased with the increase of focus shots.

Figure 7.13 exhibits the variation of crystallite size of ZrN (200) and Zr_2N (121) planes and the corresponding peak intensity of respective diffraction peaks as a function of a number of focus shots when the zirconium samples are irradiated at zero-degree angular position. The crystallite size of ZrN (200) plane is increased from $\sim 36 \pm 2$ nm to $\sim 54 \pm 2.5$ nm when the ion dose is increased from 10 to 40 focus shots, respectively. These crystallite sizes are of the order of nanoscale dimensions which are agreed well with the FESEM microstructure measurements [87].

It is clear that both the crystallite size and peak intensity increased with the increase in a number of focus shots. The increasing number of focus shots results in the increase of ion energy flux delivered to the zirconium sample and hence greater transient annealing of zirconium sample surface which in turn increases the growth of zirconium nitride film.

7.3.2.1 Microstructural Analysis

Figures 7.14 and 7.15 exhibit the FESEM microstructures of zirconium nitride films deposited for 10 and 40 focus shots at 0°, 10° and 20° angular positions. The microstructure of zirconium nitride film deposited at zero-degree angular position

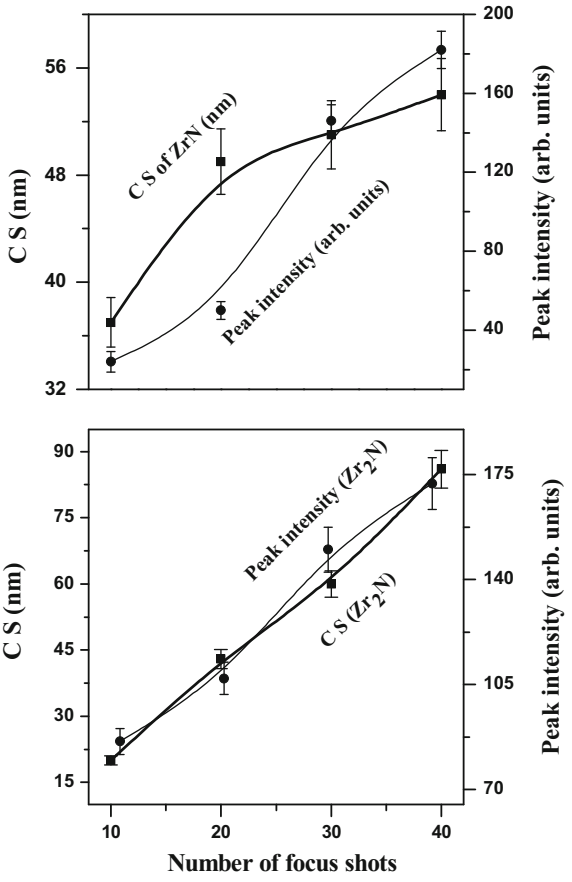

Fig. 7.13 Variation of crystallite size (C S) and peak intensity of ZrN (200) and Zr_2N (121) planes as a function of focus shots

exhibits a significant surface damage, showing pits of various shapes on the top surface owing to melting which may be due to the normal incidence of maximum ion energy flux. However, the crystallite and nanoparticles of zirconium nitride film formed during the ion irradiation process are increased by increasing the number of focus irradiation shots. A granular surface morphology is observed when zirconium nitride film is deposited at 10° angular position showing homogeneous distribution of nanoparticles which may be due to lower ion energy flux. It means that lower ion energy flux and hence lower surface transient temperature are suitable for the uniform distribution of nanoparticles and their growth. The estimated size of nanoparticles (by using linear interception method) is increased from 40 ± 2 nm to 50 ± 2.5 nm when the number of focus shots is increased from 10 to 40. This means that the growth of nanoparticles is associated with the increase in a number of focus shots. The microstructures of zirconium nitride films deposited for 10 and 40 focus shots but at 20° angular position show a slight restructuring which may be due to lowest ion energy flux and corresponding lowest surface transient temperature [87]. However, again a granular surface morphology is observed showing

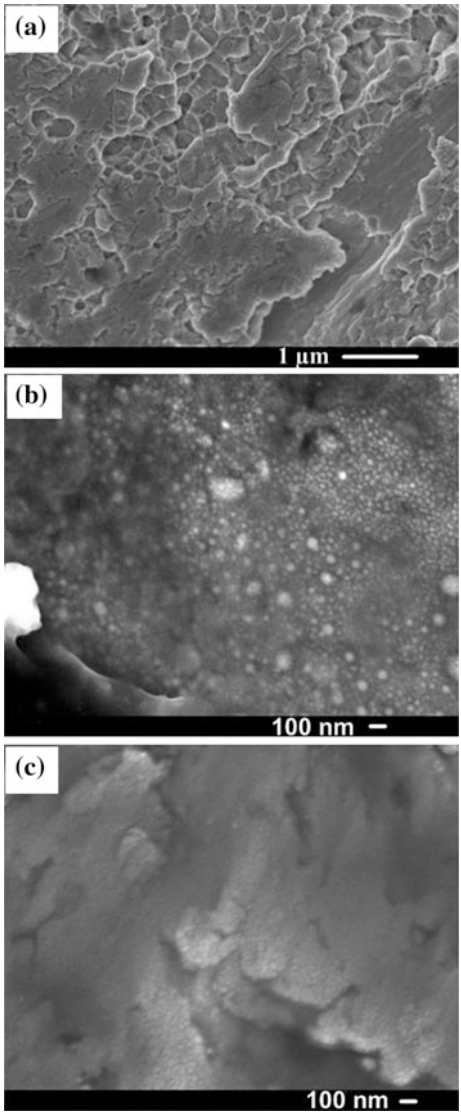

Fig. 7.14 SEM microstructures for 10 shots at **a** 0°, **b** 10° and **c** 20° angular positions. Reprinted from Khan et al. [87] (copyright 2008), with permission from Elsevier

comparatively smaller nanoparticles making wave-like double-layer structure (10 shots) and a cluster of nanoparticles (40 shots).

Moreover, the microstructure of zirconium nitride film deposited for 10 focus shots show polishing marks whereas the zirconium nitride film [87] deposited for 40 focus shots reveals the presence of a cluster of particles of nano-dimensions. These clusters probably consist of Zr_3N_4 phase coagulated with the oxide layer left un-sputtered due to lowest ion energy flux at higher degree angular position. It is well known that the surface morphology is attributed with the surface roughness

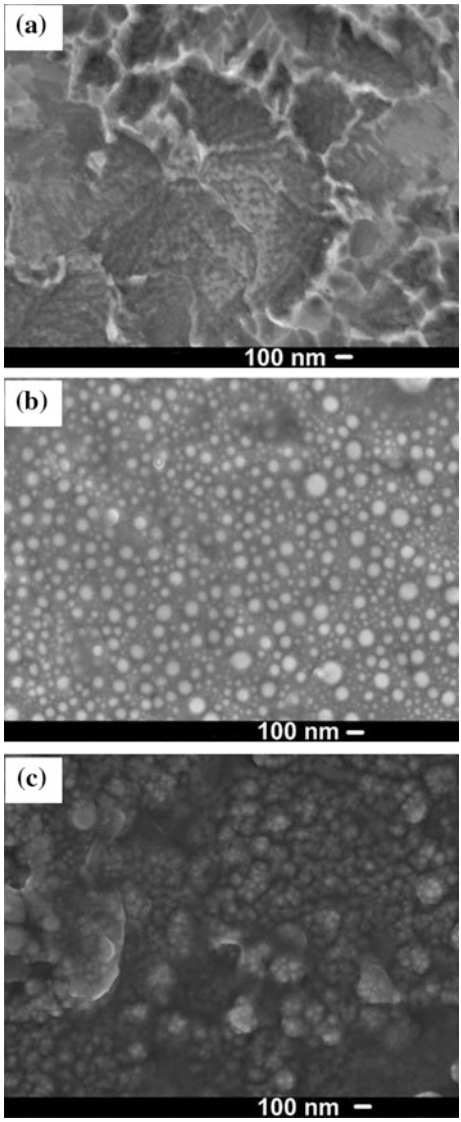

Fig. 7.15 SEM microstructures for 40 shots at **a** 0°, **b** 10° and **c** 20° angular positions. Reprinted from Khan et al. [87] (copyright 2008), with permission from Elsevier

which is increased with the increase in a number of focus shots but it is decreased with the increase of sample's axial positions. Therefore, the surface roughness of zirconium nitride films deposited along the anode axis for higher number of focus shots is more than the zirconium nitride films deposited for lower number of focus shots at all angular positions.

The surface morphology of zirconium nitride films deposited with a different number of focus shots at different angular positions revealed that the film surface quality is better at 10° as compared to 0° angular position. The significant melting,

surface damaging and presence of large pits on the surface at zero-degree angular position actually decrease the film surface quality and therefore the film surface quality at 10° angular position is better comparatively because a smoother, uniform and crack free microstructure is observed.

7.3.2.2 Micro-hardness Analysis

Figure 7.16a shows the Vickers micro-hardness of zirconium nitride films deposited for different number of focus shots as a function of depth (micrometre) of ZrN films at various imposed loads (10, 25, 50, 100 and 200 gf). The maximum micro-hardness of zirconium nitride film deposited for 40 focus shots is found to be 6.3 GPa which is four times the micro-hardness of virgin zirconium sample up to the depth of 1.01 μm of zirconium nitride film. The micro-hardness of zirconium nitride films is divided into three domains. Domain-I indicates the steep fall while domain-II shows the slow fall of micro-hardness values of zirconium nitride films. The third domain reveals the saturation in micro-hardness values; however, the saturation level of micro-hardness (domain-III) is still greater than the micro-hardness of the virgin sample up to the penetration depth of 10 μm. This steep and slow decrease in micro-hardness values with increasing depth of zirconium nitride film shows the formation of a thick film. Even the micro-hardness value of zirconium nitride is twice compared to the virgin zirconium sample up to the penetration depth of 10 μm.

Actually, during energetic nitrogen ion irradiation process, the zirconium lattice is distorted by the incorporation of nitrogen ions interstitially and ions induced collision cascades produce point defects. This lattice distortion of zirconium and the

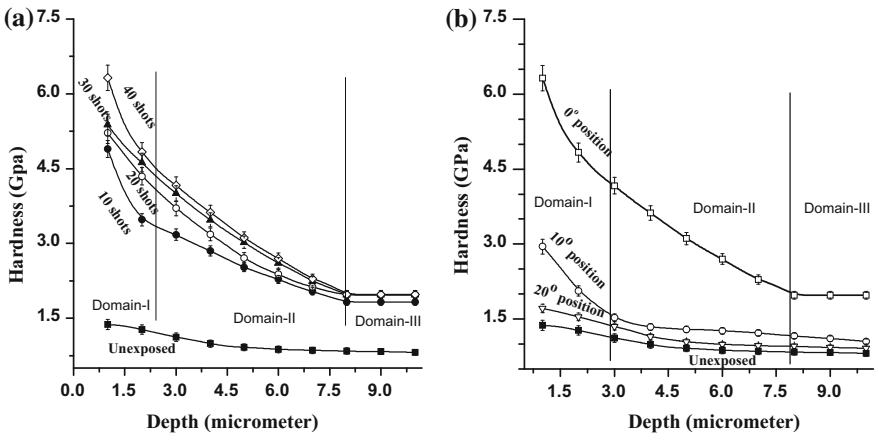

Fig. 7.16 Variation of surface hardness as a function of depth (micrometre) of ZrN films deposited **a** for multiple number of focus shots at zero-degree angular position and **b** at 0°, 10° and 20° angular positions for 40 focus shots

creation of defects improve the micro-hardness of zirconium nitride films [87]. These defects and lattice distortion are increased with the increase of total incorporated nitrogen ions which directly depend on the total number of focus shots. The total ion energy flux delivered to the substrate surface increases the substrate surface transient temperature which in turn improves the crystallinity or growth of various phases. The increasing growth behaviour or crystallinity of zirconium nitride phases actually decreases the micro-hardness. However, the main reason for increasing the micro-hardness is the total amount of nitrogen ions delivered to the substrate surface and the amount of nitrogen ions is increased with the increase in number of focus shots. This shows that the micro-hardness of zirconium nitride films is increased with the increase in number of focus shots. Therefore, the hardest zirconium nitride film deposited for 40 focus shots is due to the presence of maximum nitrogen content along with nitride compound layer although having minimum stresses.

Figure 7.16b shows the Vickers micro-hardness profile of zirconium nitride films deposited for 40 focus shots at various (0°, 10° and 20°) angular positions. Again the micro-hardness is divided into three domains. It is obvious that the micro-hardness of zirconium nitride film decreases with increasing angular position of deposition. The incorporation rate of nitrogen ions depends upon the nitrogen ion energy flux, which is highest at zero-degree angular position and decreases with the increase of sample's angular position. Moreover, the formation of nitride compounds (ZrN and Zr_2N) is also favoured at 0° due to maximum ablation and re-deposition of substrate surface. The formation of ZrN and Zr_2N hard compounds is the second reason to increase the micro-hardness of zirconium nitride. At higher angular positions, there is lower level of nitrogen ions implantation, defects formation and nitride compound formation because of lower ion energy flux. It is concluded that the micro-hardness of zirconium and zirconium nitrides decreases with the decrease of ion energy flux at higher angular positions.

7.3.3 Deposition of ZrON Composite Films

Recently, a new class of composite materials so called metal oxy-nitride (MeON) [Me = metal] is getting importance in diverse technological applications, especially for decorative purpose, coatings on medical and cutting tools and protective coatings. The oxygen plays a vital role in controlling the surface properties of nanocomposite thin films [92]. Zirconium oxy-nitride composite film on zirconium substrates at room temperature is deposited by using plasma focus with improved surface properties like change in crystal structure, surface morphology and micro-hardness of the deposited composite films [93].

7.3.3.1 Structural Analysis

Figure 7.17 exhibits the XRD patterns of virgin zirconium and polycrystalline zirconium oxy-nitride [P–ZrON] composite films deposited for various (0.5, 1, 1.5, 2 and 2.5 mbar) nitrogen pressures. The XRD pattern shows that virgin zirconium has preferential orientation along (101) plane as the intensity of diffraction peak corresponding to this plane is maximum. For 0.5 mbar nitrogen pressure, the peak intensity of Zr (101) plane is decreased whereas the Zr (100) and Zr (002) planes are disappeared due to the formation of nitride/oxide phases of zirconium on substrate surface. The XRD patterns confirm the evolution of various diffraction peaks related to ZrN (111), Zr_3N_4 (230), Zr_3N_4 (320), Zr_3N_4 (140), Zr_3N_4 (340) and ZrO_2 (200) planes. This confirms the deposition of P–ZrON composite films. The overlapping of diffraction peaks is due to their large FWHM (full width at half-maximum) which in turn can be attributed to small average crystallite size of polycrystalline regions. The amount of insulating phase of zirconium nitride (Zr_3N_4) is more because the peak intensity related to this phase is maximum. For 1 mbar nitrogen pressure, the peak intensity of Zr_3N_4 (320) and Zr_3N_4 (140) planes is increased while the peak intensity of Zr_3N_4 (340) plane is decreased along with the appearance of Zr_3N_4 (040) and ZrO_2 (102) diffraction planes. For 1.5 mbar nitrogen pressure, the intensity of various diffraction peaks observed in the previous P–ZrON composite films is increased significantly along with the development of ZrN (200) phase. For 2 mbar nitrogen pressure, a slight improvement in the intensity of various diffraction peaks is observed. For 2.5 mbar nitrogen pressure, the intensity of ZrN (111) and ZrN (200) planes is increased while it is decreased for all other phases. It is observed that the intensity of ZrN (111) and ZrN (200) diffraction peaks is maximum for 2.5 mbar nitrogen pressure whereas the

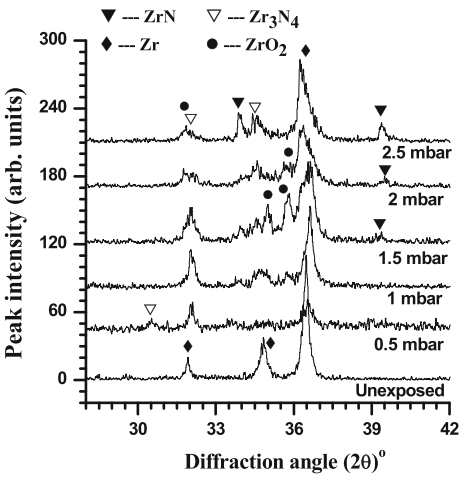

Fig. 7.17 XRD patterns of zirconium and P–ZrON composite films deposited for various nitrogen pressures

intensity of ZrO_2 (200) and (102) diffraction peaks is maximum for 1.5 mbar nitrogen pressure. The increased intensity of ZrN (200) plane for higher nitrogen pressure indicate the increased preferential growth along (200) plane for ZrN phase. It is concluded that the formation of new phases and their relative contents are associated with the ion energy fluxes delivered to the substrate surface which in turn depend on nitrogen pressure.

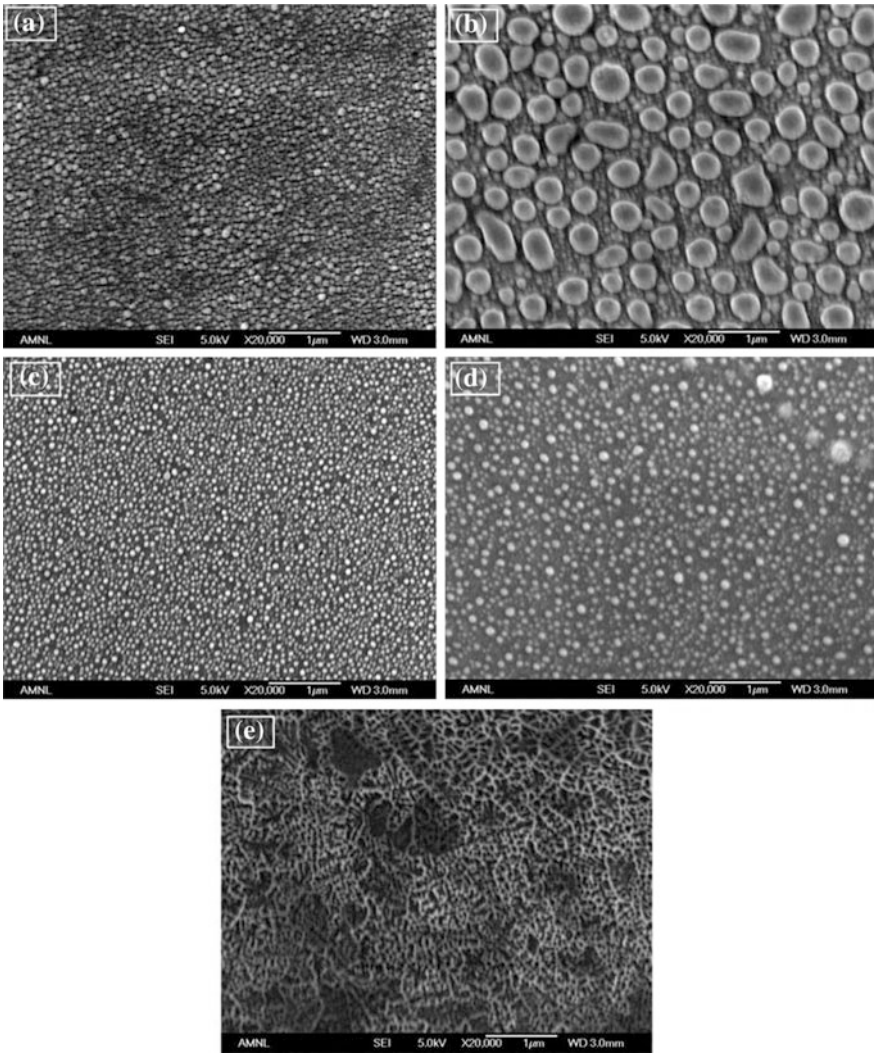

Fig. 7.18 FESEM microstructure of P–ZrON composite films deposited at **a** 0.5 mbar, **b** 1 mbar, **c** 1.5 mbar, **d** 2 mbar, **e** 2.5 mbar nitrogen pressures, respectively. The micron bar is 1 μm

7.3.3.2 Morphological Analysis

The FESEM microstructure can help to elucidate the growth behaviour and microstructure features of the P–ZrON composite films deposited at different nitrogen pressure. Figure 7.18 demonstrates the surface morphology of P–ZrON composite films deposited for various (0.5, 1.0, 1.5, 2.0 and 2.5 mbar) nitrogen pressure. For 0.5 mbar nitrogen pressure, the equiaxed nanoparticles (55–110 nm) are observed which are distributed uniformly. These equiaxed nanoparticles are separated from each other through their grain boundaries and the separation between the grains boundaries hinder the dislocation motion resulting in the increase of micro-hardness (discussed later). For 1 mbar nitrogen pressure, two types of particles (according to their dimensions) are observed. The sizes of equiaxed and elongated particles are ranged from 27 to 450 nm and 330 to 820 nm. The formation of particles of different dimensions makes the surface rough. The distribution of mixed particles (equiaxed and elongated) shows the formation of double-layer structure because it seems that the larger particles are located on the top of smaller particles. Therefore, the surface roughness and the formation of double-layer structure may hinder the dislocation motion resulting in the improvement of micro-hardness (discussed later). For 1.5 mbar nitrogen pressure, again equiaxed nanoparticles (30–60 nm) distributed uniformly are observed. The reduction in particle size confirms the grain refinement which is due to the bombardment of higher ion energy flux results in the creations of more micro-strains. However, the deposited P–ZrON composite film is more compact in nature. The surface roughness of P–ZrON composite film is more for 1.5 mbar than 1 mbar nitrogen pressure which is due to the grains of different dimensions; more ion energy flux strikes the substrate surface resulting in more separation between the grain boundaries. For 2 mbar nitrogen pressure, again equiaxed nanoparticles of different dimensions (ranged from 30 to 120 nm) distributed uniformly are observed. It is interesting to note that the microstructure pattern formed by these equiaxed nanoparticles is elegant and smooth. Up to 2 mbar nitrogen pressure, it is obvious from the microstructure appearance that equiaxed and elongated particles are formed, however, their distribution, size and gap between the grains boundaries depend strongly on the increase of nitrogen pressure [93].

For 2.5 mbar nitrogen pressure, the microstructure reveals the formation of complicated network of nanowires. Careful investigation reveals that many nanoparticles are attached on both sides of nanowires resulting in the formation of nanocombs. Actually, many nanocombs form joints with each other forming a complicated network of nanocombs. The bright and dark regions of the microstructure indicate the formation of double layer structure of nanocombs. The diameter of nanowires is found to be about 55 nm. It is concluded that the surface morphology of P–ZrON composite films can be controlled by controlling the nitrogen pressure. This change in microstructure appearance is associated with the total energy delivered to the substrate surface which in turn is controlled by changing the working gas pressures.

7.3.3.3 Mechanical Property Analysis

It is worth mentioning that the irradiated zirconium substrates exhibited better micro-hardness as compared to the virgin zirconium substrate. Figure 7.19 exhibits the micro-hardness of P–ZrON composite films deposited for various 0.5, 1, 1.5, 2 and 2.5 mbar nitrogen pressures. Five measurements are taken in order to estimate the average values of micro-hardness for the imposed load of 0.490 N. The maximum micro-hardness of P–ZrON composite film deposited for 1.5 mbar nitrogen pressures is found to be 8623 ± 0.96 MPa which is about 5.4 times the micro-hardness of the virgin substrate. The micro-hardness pattern of P–ZrON composite films is divided into two domains. In first domain (0.5–1.5 mbar), the micro-hardness values are increased sharply up to 1.5 mbar nitrogen pressures which is mainly due to the maximum (N + O)/Zr atomic ratio. In second domain (2–2.5 mbar), the micro-hardness values of P–ZrON composite film is decreased because the (N + O)/Zr atomic ratio present in the deposited film is decreased. The decrease in atomic ratio of the involved species is due to increase in nitrogen pressure. Generally, the increase in micro-hardness values of P–ZrON composite films up to 1.5 mbar nitrogen pressure can be interpreted in terms of lattice distortion, micro-strains and interstitial point defects which are associated with the coexistence of various crystalline phases and implantation of instability accelerated nitrogen ions into the top surface of zirconium substrate. It is concluded that the increasing contents of Zr, N and O species, overlapping of various diffraction planes, lattice distortion and point defects are responsible to enhance the micro-hardness of P–ZrON composite films up to 1.5 mbar nitrogen pressures whereas the decreasing contents of Zr, N and O species and decreasing probability of overlapping of diffraction planes are responsible for the reduction in micro-hardness of P–ZrON composite films. Vaz et al. [94] pointed out that the micro-hardness of the deposited films significantly decreases by increasing the oxygen content.

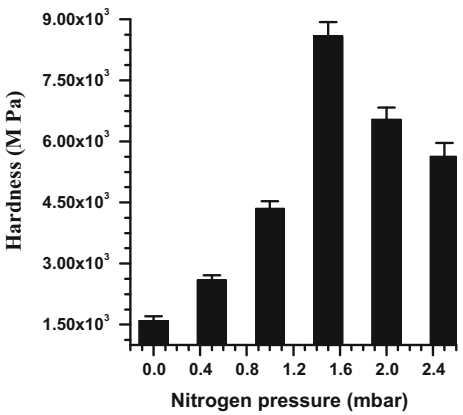

Fig. 7.19 Variation of hardness of P–ZrON composite films deposited for various nitrogen pressures

7.3.4 Growth of Nanocrystalline ZrAlO

Zirconium-based ternary transition metal nitrides composite films have been reported as promising hard coatings mainly in the field of protection technologies against wear and hot corrosion at high temperatures and superior resistance to abrasive and chemical wear [95, 96]. Incorporation of Al atoms into the ceramic nitride films provides higher hardness, oxidation and wear resistance. The nanocrystalline multiphase zirconium aluminium oxide (MP–ZrAlO) composite films are deposited on zirconium substrate by employing plasma focus device [97]. The deposited MP–ZrAlO composite films are characterized for different properties such as crystal structure, surface morphology, elemental distribution and micro-hardness.

7.3.4.1 XRD Analysis

Figure 7.20 shows the XRD patterns of nanocrystalline multiphase ZrAlO (MP–ZrAlO) composite films deposited for multiple (5, 15 and 25) number of focus deposition shots. The XRD patterns exhibit that virgin zirconium has four diffraction peaks. The development of oxides of zirconium and aluminium as well as zirconium aluminium oxide phases confirms the deposition of MP–ZrAlO composite films. However, the MP–ZrAlO composite film grows preferentially along (020) and (220) orientations of monoclinic zirconium oxide (m-ZrO_2) and

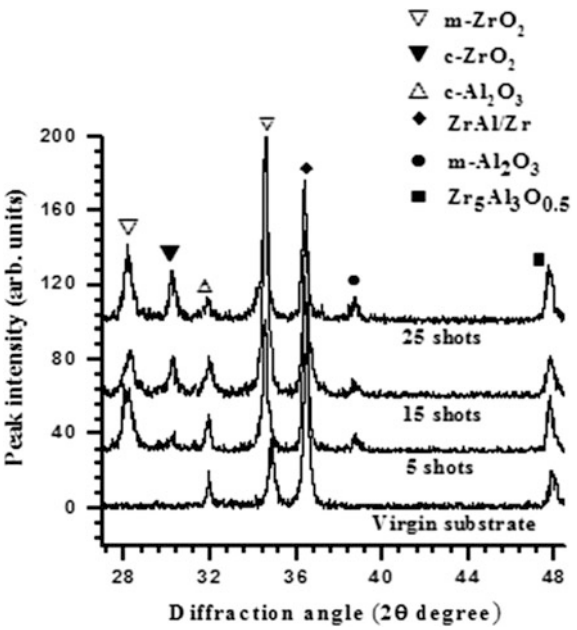

Fig. 7.20 XRD patterns of MP–ZrAlO composite films deposited for different (5, 15 and 25) focus shots at 2 mbar working gas pressures when the samples are placed at 10 cm in front of anode. Reprinted from Khan et al. [97] (copyright 2014), with permission from Elsevier

cubic aluminium oxide (c-Al_2O_3) phases, respectively. The XRD analysis reveals that the increase in crystallinity of above-mentioned phases is associated with the increase of focus deposition shots. The increasing number of focus shots actually increases the total ion energy flux delivered to the zirconium sample which is maximum along the anode axis and minimum as the sample moves away from the anode axis (means at higher degree angular positions). This shows that the crystallinity of various phases actually depends on the total amount of ion energy flux delivered to the zirconium samples. However, the crystallinity of zirconium oxide (zirconia) phase is better than the crystallinity of aluminium oxide (alumina) phase. This difference in the crystallinity of zirconia and alumina phases indicates that different ion energy fluxes are required for the better growth of zirconia and alumina phases.

The diffraction peak appeared at 2θ of about 36.4° is attributed to zirconium/zirconium aluminium (Zr/ZrAl) phase because according to JCPDS/ICDD reference card the diffraction peaks related to Zr and ZrAl are observed at the same diffraction angle. It is also hypothesized on the basis of the fact that the instability generated electron beam which moves towards the anode of plasma focus device ablate the energetic Al species which can substitute some of the Zr atoms in Zr lattice resulting in the formation of ZrAl phase. This also shows the formation of solid solution of Zr/ZrAl phase which plays a vital role in improving the micro-hardness of MP–ZrAlO composite films.

In order to examine the annealing effect on the surface properties like structural, morphological and mechanical of MP–ZrAlO composite film, we annealed the MP–ZrAlO composite film deposited for 5 focus shots at temperatures of 300 and 600 °C. Figure 7.21 demonstrates the annealing effect on the crystal growth of MP–ZrAlO composite films as a function of annealing temperature. For lower annealing

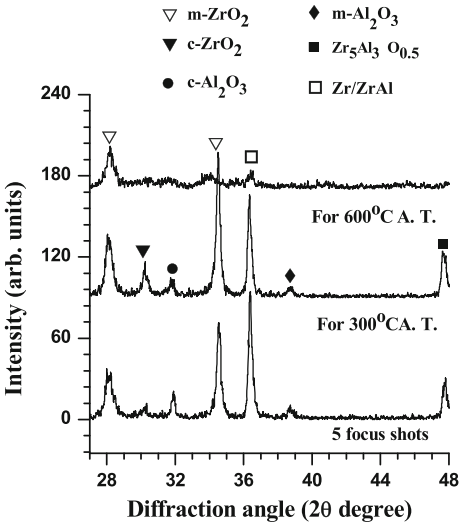

Fig. 7.21 XRD patterns of MP–ZrAlO composite films deposited for 5 focus shots and the films annealed for 300 °C and 600 °C temperature. Reprinted from Khan et al. [97] (copyright 2014), with permission from Elsevier

temperature, different phases of the deposited films show diverse behaviour like the crystallinity of zirconium oxide phase is increased while the crystallinity of aluminium oxide as well as zirconium aluminium phase is decreased. This shows that the monoclinic phase of zirconium oxide is stable while aluminium oxide and zirconium aluminium phases start to re-crystallize because the peaks are broadened. It is found that the monoclinic phase of zirconium oxide present in MP–ZrAlO composite film grows along (020) orientation preferentially which is due to its improved crystallinity. For higher annealing temperature, all phases except m-ZrO_2 (111) start to re-crystallize which shows that this phase is stable even at higher annealing temperature while all other phases are decomposed and re-crystallize resulting in the formation of nanocrystallites. The formation of more nanocrystallites increases the crystallite boundary area which hinders the dislocation of crystallite and hence plays a vital role in increasing the mechanical properties like the hardness of the deposited films. The stability of zirconium oxide phase growing along (111) direction which indicates that this phase may grow further with the increase of annealing temperature.

It is known that the decreasing crystallite size is associated with the phase transformation. In the deposition of MP–ZrAlO composite films and its annealing, the crystallite size is decreased with the increase of annealing temperature but no phase or orientation transformation occurs in zirconium oxide because zirconium oxide phases are embedded inside aluminium oxide which prevents the volume expansion of zirconium oxide phase since the Young's modulus of aluminium oxide is higher than zirconium oxide. The hindrance in the volume expansion of zirconium oxide and the development of rigid aluminium oxide matrix around zirconium oxide phases cause to develop local stresses which hinder the phase or orientation transformation of zirconium oxide. We have already reported that [32] phase or orientation transformation of zirconium oxide is attributed to the increase in a number of focus deposition shots and annealing temperature. It is concluded that the presence of aluminium oxide phase in the deposited MP–ZrAlO composite films is responsible to hinder the phase or orientation transformation of zirconium oxide phase. Therefore, the existence of aluminium oxide phase (in rigid matrix form) is responsible for stabilizing the zirconium oxide crystals at room temperature as well as at lower (300 °C) annealing temperature. The formation of monoclinic and cubic phase of zirconium oxide was observed for all focus shots as well as annealing temperatures. This reveals that the accessible ion energy flux and annealing temperature are appropriate not only for the nucleation and growth of monoclinic and cubic phase of zirconium oxide but also for the formation of aluminium oxide phase. However, the existence of aluminium oxide phase hinders the nucleation and growth of tetragonal zirconium oxide because no diffraction peak is observed related to the tetragonal phase of zirconium oxide.

7.3.4.2 SEM Analysis

Figure 7.22 illustrates the FESEM microstructural features of MP–ZrAlO composite films deposited for multiple 5, 15 and 25 focus shots at zero—degree angular position and only for 25 focus shots at 10° angular position. For 5 focus shots depositions, the FESEM image shows the formation of few dark regions indicated by an arrow; however, the overall nature of the composite film is compact. The film contains granular grains ranging from 50 to 100 nm that are closely packed to each other. The dark regions may be formed due to the removal of unbounded Zr, Al and O species resulting in the formation of the rough surface. For 15 focus shots, the density of dark regions decreases resulting in the formation of denser microstructure, decreasing the surface roughness. This increase in film compactness with increasing focus shots is due to the increase in crystallinity (XRD results) of alumina and zirconia phases. For 25 focus shots, the FESEM microstructure features abruptly changed showing the formation of lateral strips which are broadened from the centre (~ 750 nm), while narrowed (~ 333 nm) at the edges. These strips are laterally packed with each other forming denser film. The nanostrips separated through their boundaries having lengths ranging from 2.5 to 9 μm are also

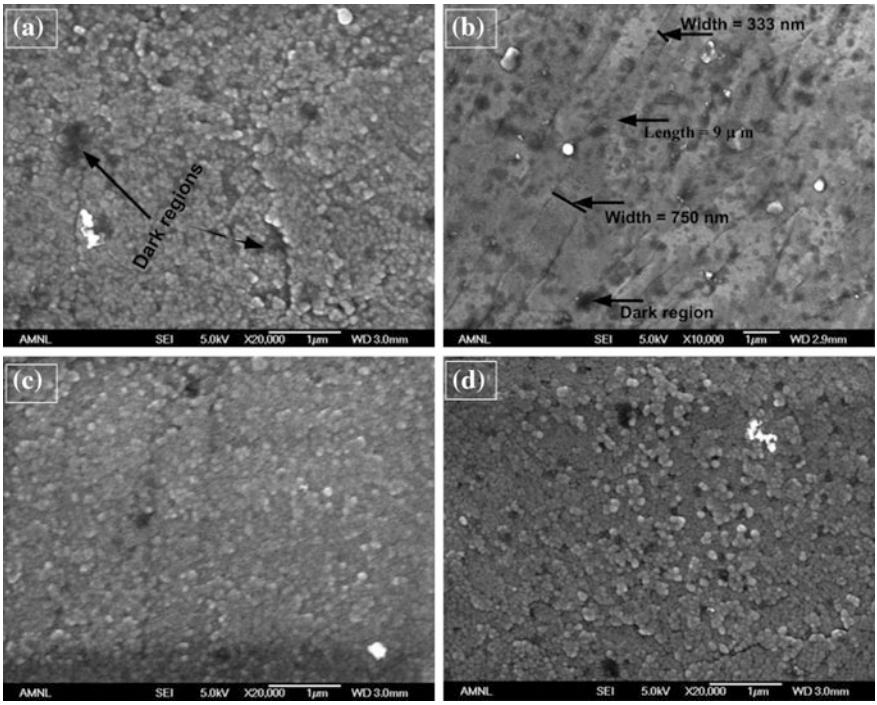

Fig. 7.22 The SEM images of MP–ZrAlO composite films deposited for 5, 15 and 25 FDS at 0° position and for 25 FDS at 10° angular positions [97]. The micron bar is 1 μm. Reprinted from Khan et al. [97] (copyright 2014), with permission from Elsevier

observed. The FESEM microstructure exhibits the granular surface morphology of MP–ZrAlO composite film when deposited for 25 focus shots at 10° angular position. These granular grains (ranging from 45 to 80 nm) are distributed uniformly on the whole scanned area. Careful investigation reveals that a film of equiaxed grains is formed in the background of the top surface layer. The deposited composite film contains more than one layer stacked one above the others. It is obvious that the surface morphology of MP–ZrAlO composite films changes from granular to strips and the formation of stacked layers containing granular grains which are attributed to the increase of focus shots and sample angular position. Thus, the surface morphology of MP–ZrAlO composite films depends on the total amount of incorporated ions and their energies. Therefore, strips are formed for greater ion energies and fluxes; whereas, stacked layers are formed for lower ion energies and fluxes.

Figure 7.23a, b reveals the surface morphology of MP–ZrAlO composite films annealed at 300 and 600 °C temperatures in oxygen environment for 1 h, respectively. For 300 °C annealing temperature, the FESEM image shows the uniform distribution of nanograins (size ranging from 60 to 120 nm) over the whole scanned surface area which is free from the dark regions. It is clear that the grain size increases during the annealing process. The dark regions observed in as deposited

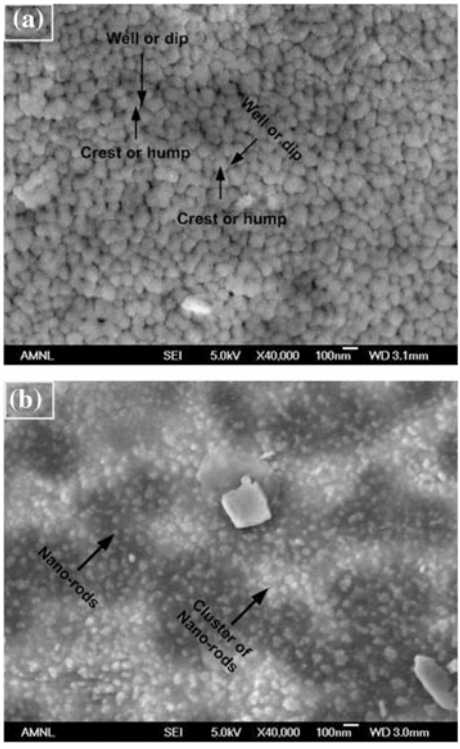

Fig. 7.23 SEM images of samples annealed at 300 and 600 °C [97]. The micron bar is 100 nm. Reprinted from Khan et al. [97] (copyright 2014), with permission from Elsevier

MP–ZrAlO composite films disappeared after annealing temperature. The grains distributed uniformly over the entire scanned surface area are separated through their grain boundaries and their close packing made the film dense. Consider a small portion of the same FESEM micrograph where one can observe the numbers of particles (not exactly rounded) spread over the surface and joined with each other (head to head). These closely packed nanoparticles are not well arranged like beaded string. The surface appearance of these nanoparticles exhibits crest/humps and wells/dips, as shown and marked in the FESEM micrograph. The combination of these humps and dips make the half wave-like structure, which is responsible to increase the surface roughness as well as hinder the dislocation motions resulting in the increase of micro-hardness of the deposited composite films. The roughened surface and the increase in grain boundary areas are probably responsible to improve the mechanical properties of the deposited film. For 600 °C annealing temperature, the surface morphology exhibits the formation of vertically growing nanorods which are located in the form of clusters (groups of nanorods). The diameter of nanorods ranges from 25 to 50 nm. The gap between the clusters decreases the film compactness. The formation of nanorods and porous film (because clusters of nanorods are not packed) is attributed to the re-crystallization of the previously deposited nanocrystalline MP–ZrAlO composite film (XRD results). These nanorods are related to monoclinic zirconia (m-ZrO_2) phase as only diffraction peak related to this phase is observed and grow perpendicular to the substrate surface (FESEM results). It is concluded that only m-ZrO_2 (111) phase is stable at higher annealing temperature while the others phases of alumina and zirconia are decomposed. The change in surface morphology (from equiaxed grains to nanorods) of MP–ZrAlO composite film is associated with the decomposition of alumina and zirconia phases during annealing at higher temperature. The porous film that consists of nanorods promotes the oxygen diffusion which is responsible for the distortion of the lattice and creation of point defects such as vacancies, which enhances the mechanical properties of the deposited film. However, the formation of dark and bright regions, large particles of different shapes (cubic and cylindrical) on the top surface of nanorods and porous film (due to re-crystallization of alumina and zirconia phases) make the surface rough. It is concluded that the surface morphology, grain size, distribution of grains and the formation of half wave-like structure made by grains are attributed with ion energy flux and continuous annealing.

7.3.4.3 Micro-Hardness Analysis

Figure 7.24 illustrates the surface hardness (GPa) of MP–ZrAlO composite films deposited for multiple (5, 15 and 25) focus shots at 2 mbar oxygen pressure when the samples are placed at 10 cm in front of the central electrode.

Five measurements (for 0.49033 N imposed load) were taken in order to estimate the average values of the hardness of MP–ZrAlO composite films deposited for multiple focus shots. It is found that the hardness of MP–ZrAlO composite films

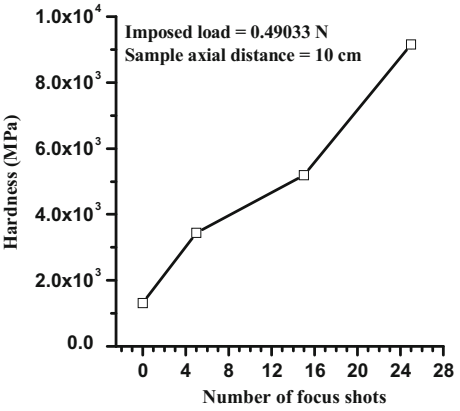

Fig. 7.24 Variation of hardness (MPa) of MP–ZrAlO composite films deposited for multiple 5, 15 and 25 focus shots at 2 mbar oxygen pressures when the samples are placed at 10 cm in front of central electrode anode. Reprinted from Khan et al. [97] (copyright 2014), with permission from Elsevier

is increased with the increase in number of focus shots. The maximum values of hardness of MP–ZrAlO composite films deposited for 25 focus shots is found to be 9140 ± 15 MPa which is approximately seven times the hardness of virgin zirconium substrate. We have already reported that the concentration of nitrogen in zirconium nitride film was increased with the increase of focus shots. Similarly, the concentration of oxygen in this case is increased with the increase in number of focus shots. Therefore, the total numbers of incorporated oxygen ions are associated with the increase of oxygen operating pressure and the increase in amount of oxygen present in the deposited films is the main reason for the improvement of hardness of MP–ZrAlO composite films. Moreover, the increase in hardness of MP–ZrAlO composite films could also be interpreted in terms of lattice distortion, point defects and vacancies which are associated with the total number of incorporated oxygen ions and their corresponding energies. Basically, the zirconium lattice is distorted by the incorporation of oxygen ions interstitially and ions induced collision cascades to create point defects. The doping of ablated Al into zirconium lattice also enhances the above-mentioned defects in the deposited composite films. The development of such defects inhibits the dislocation motions which improve the hardness of MP–ZrAlO composite films. Furthermore, the formation of multiphase zirconia embedded in alumina phase also improves the hardness of MP–ZrAlO composite films. The stability of zirconia phases for different focus shots which is due to the presence of alumina, the formation of nanocrystallites of zirconia and alumina phases and their coexistence also enhance the hardness of MP–ZrAlO composite films. The hardness of MP–ZrAlO composite film deposited for 5 focus shots (∼ 3441 ± 7 MPa) is increased up to approximately maximum value of hardness 7387 ± 11 MPa for lower annealing (300 °C) temperature and it is decreased again up to 5611 ± 9 MPa for higher annealing (600 °C) temperature (not shown). This increase in hardness for lower annealing temperature is due to the increase in crystallinity of zirconia and alumina phases. The change in weight fraction of zirconia phases and the formation of half wave-like microstructures actually hinders the dislocation motion which increases

the surface roughness as well as hardness of the deposited composite films. Moreover, besides the structural defects and the relatively stabilized zirconia content, the reduction in the hardness of MP–ZrAlO composite films annealed at higher temperature is also due to the film's increasing porosity but it is still higher than the hardness of virgin zirconium.

7.3.5 *Mechanical Properties of Nanocomposite Al/a-C*

Amorphous carbon films have extraordinary properties such as high hardness, wear resistance, chemical resistance and good tribological properties [98, 99]. The a-C thin films are generally hard (about 18–80 GPa) but have brittleness which can be improved by the formation of metal/amorphous carbon (Me/a-C) composite thin films [100] which are important engineering materials for surface protection. A lot of work has been done previously on Me/a-C or Me/DLC thin films using different techniques at room temperature such as sputter deposition [101, 102], plasma assisted chemical vapour deposition (CVD) [103], plasma focus [104] and vacuum arc deposition [105].

7.3.5.1 XRD Analysis

The XRD patterns of the nanocomposite Al/a-C thin films synthesized using a different number of focus deposition shots on silicon substrates are shown in Fig. 7.25. The XRD results show the formation of very weakly crystalline Al (111) plane for 10 focus shots and the intensity of this phase increases with

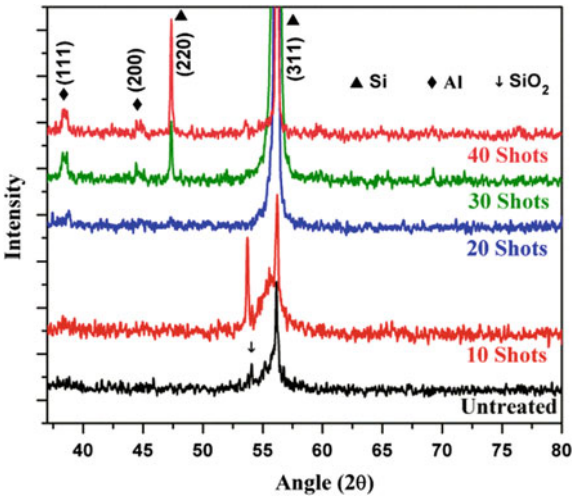

Fig. 7.25 XRD patterns of the deposited thin films using different number of focus shots with CH_4/Ar ratio of 3:7. Reprinted from Umar et al. [104] (copyright 2014), with permission from IOP Publishing

increasing number of focus deposition shots. The (200) phase of Al appears only for 30 and 40 focus deposition shots. The XRD patterns do not show any peak related to aluminium carbide. Moreover, the XPS results shown in Fig. 7.26 do not show any formation of aluminium carbide at the surface of thin film, which confirms the absence of aluminium carbide phase formation in nanocomposite thin films. The increase in the intensity of Al (111) phase with increasing number of focus deposition shots may be due to the increase in the thickness as well as the energetic processing of the nanocomposite thin film. The XRD spectrum of the virgin silicon substrate exhibits only (311) diffraction plane while the samples exposed to different numbers of focus deposition shots exhibit the formation of polycrystalline Si with additional Si diffraction peaks being observed. The accelerated energetic ions of filling gas species, decaying high-energy density pinched plasma column and fast moving shock wave in DPF increases the surface temperature of the silicon substrate placed down the anode stream [106], followed by the fast cooling may cause the formation of polycrystalline silicon on the substrate surface.

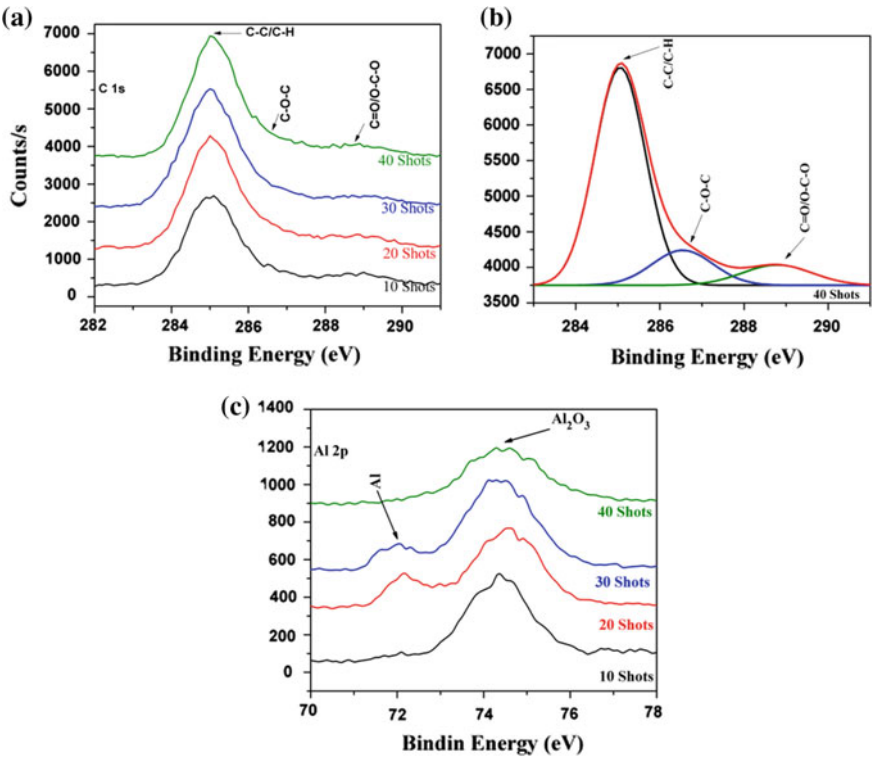

Fig. 7.26 XPS spectra of thin films deposited using different number of focus shots, **a** detailed scan of C 1s peak, **b** deconvoluted C 1s peak for the thin film deposited using 40 focus shots, and **c** detailed scan of Al 2p peak. Reprinted from Umar et al. [104] (copyright 2014), with permission from IOP Publishing

7.3.5.2 XPS Analysis

The XPS analysis of all the Al/a-C nanocomposite thin films synthesized using a different number of focus deposition shots were done to examine the elemental concentration and the bonding of the elements at the surface of thin films. Different elements present at the surface of composite thin films along with their atomic percentage are given in Table 7.2. The analysis shows increase in the atomic percentage of carbon with increasing number of focus deposition shots implying the increasing amount of carbon in the thin films.

The chemical states of carbon present at the surface of composite thin films synthesized with a different number of focus shots can be deduced from the C 1s spectra in Fig. 7.26a. The XPS spectra show the presence of carbon in C–C/C–H, C–O–C and O–C–O/C = O bonding with their peak binding energy values of about 285, 286.7 and 288.8 eV, respectively. The C 1s spectra do not show any peak in the range 281 to 283 eV for the nanocomposite thin films deposited with a different number of focus deposition shots, indicating that carbon is not making a bond with Al at the surface of the thin films to form carbide. The C 1s XPS spectra of one of the samples treated with 40 focus shots are deconvoluted to identify various compounds/phases that have been formed on the surface of the composite thin film shown in Fig. 7.26b. The deconvolution of the spectra shows the presence of C–C, C–O–C and C=O/O–C–O at the surface of the thin film. The presence of significant amount of oxygen on the nanocomposite thin film surface is due to the oxidation of metallic Al present at the surface when the samples were exposed to atmospheric conditions, as seen in Fig. 7.26c. So, from results obtained from XRD and XPS analysis, it is clear that composite Al/a-C thin film is formed on Si substrate without any Al–C bonding.

7.3.5.3 Raman Analysis

The Raman spectra of the nanocomposite thin films synthesized with a different number of focus shots are represented in Fig. 7.27. The spectra show the stretching vibrations due to D and G bonds which confirm the existence of carbon in sp^2 and sp^3 bonding configuration in composite thin films. The D and G peaks are appearing at about 1366 and 1600 cm^{-1} without any considerable shift in these

Table 7.2 Elemental composition and Al/C ratio of the deposited thin films using different number of focus shots

No. of focus shots	Al (at.%)	C (at.%)	O (at.%)	Al/C
10	19.6	44.3	36.1	0.44
20	15.4	53.8	30.8	0.29
30	11.3	58.6	30.1	0.19
40	12.6	60.6	26.8	0.21

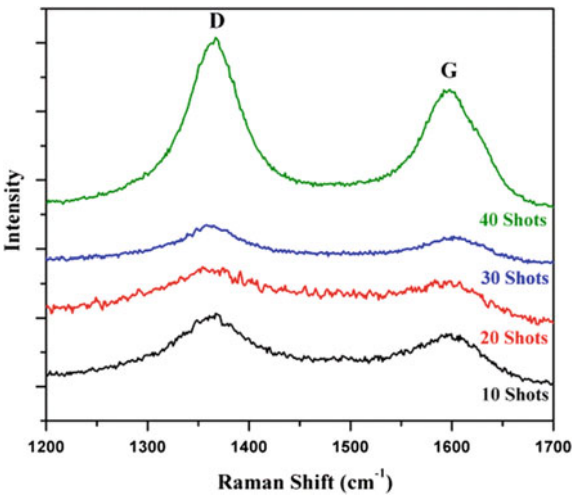

Fig. 7.27 Raman Analysis of the thin films deposited using different number of focus shots with fixed CH_4/Ar ratio of 3:7. Reprinted from Umar et al. [104] (copyright 2014), with permission from IOP Publishing

values for thin films deposited with a different number of focus deposition shots. The Raman spectra also show the variation in intensity of D and G peaks with different number of focus deposition shots. The pronounced intensity of D and G peaks for the samples treated with 40 focus deposition shots shows the increase in a-C in the thin film.

The variation in the integrated D and G peaks intensity ratios appearing for different thin films as a function of a number of focus deposition shots is also calculated. The I_D/I_G ratio is 1.26 and 1.27 for the films synthesized using 10 and 20 focus shots, respectively. I_D/I_G ratio increases to the values of 1.46 and 1.38 for the films synthesized using 30 and 40 focus shots, respectively. This shows greater amount of sp^3 content in the films deposited with 10 and 20 focus shots, as sp^3/sp^2 ratio is inversely related to I_D/I_G ratio. The variation in the ion flux and ion energies may be responsible for different sp^3 and sp^2 bonding content in the deposited thin films. Zeb et al. deposited diamond like carbon film at different axial positions using the DPF device and found the similar trend of I_D/I_G values with increasing ions flux and energies [107] as in our case.

7.3.5.4 Surface Morphology

The surface morphology of the nanocomposite thin films synthesized using a different number of focus deposition shots are shown in Fig. 7.28. The thin films synthesized with a different number of focus shots exhibit dense and smooth surface morphology without the presence of any cracks and voids and consist of nanoparticles and nanoparticle agglomerates. The round shaped nanoparticles on the surface of thin films deposited with a different number of focus deposition shots may be indicating the presence of amorphous carbon. The agglomerates size and

their number increased with increasing number of focus deposition shots. The agglomerates form a flower like structure for the film deposited with 40 focus deposition shots. The average size of these agglomerates for 30 and 40 focus deposition shots is more than 100 nm. The increase in a number of agglomerates and their size at higher number of deposition shots (30 and 40 shots) is attributed to the increase in ion energy and ion flux. The surface morphology of the thin film consists of nanoparticles and their agglomerates, which offer a large surface-to-volume ratio resulting in easy oxidation of metallic aluminium [108, 109], as observed earlier in XPS results.

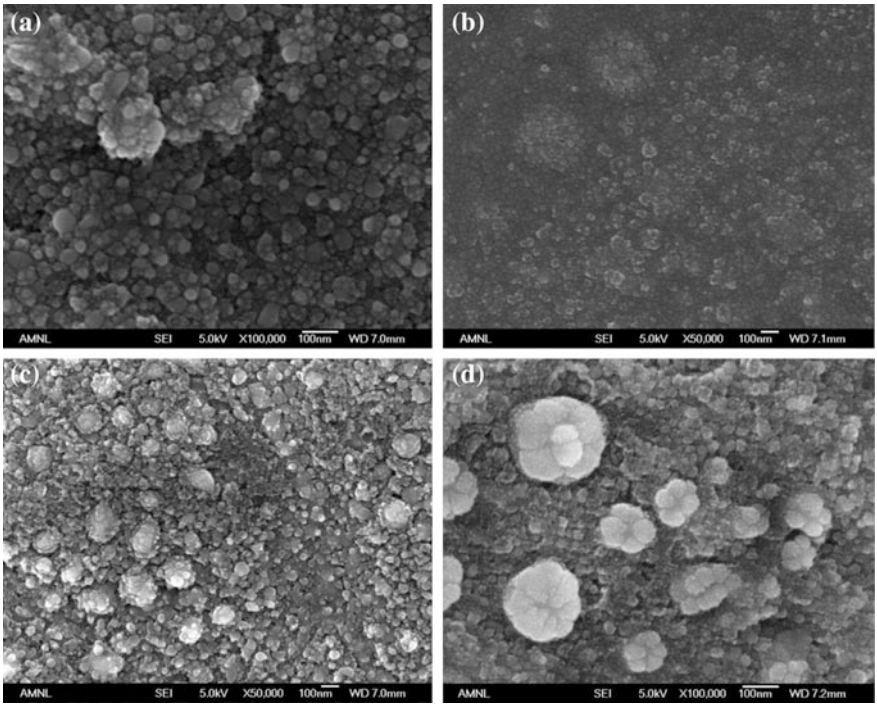

Fig. 7.28 Surface morphology of the thin films deposited using different **a** 10, **b** 20, **c** 30 and **d** 40 focus shots [104]. The micron bar is 100 nm. Reprinted from Umar et al. [104] (copyright 2014), with permission from IOP Publishing

Table 7.3 Hardness and elastic modulus values of the deposited thin films using different number of focus shots

No. of focus shots	Hardness (GPa)	Elastic modulus (GPa)
10	7.4 ± 0.24	155.1 ± 2.8
20	10.7 ± 0.27	189.2 ± 2.92
30	5 ± 0.29	115 ± 6.92
40	7.7 ± 0.59	170.2 ± 10.4

7.3.5.5 Mechanical Properties

The variation in hardness and elastic modulus values of Al/a-C thin films synthesized with varying number of focus deposition shots are shown in Table 7.3. The mechanical properties are analyzed in terms of their chemical composition and relative sp^3 content measured by XPS and Raman spectroscopy. The hardness and elastic modulus values of the films are taken at the depth of 100 nm to avoid the substrate effects to the measurement.

The processing of the film with a different number of focus shots gives different composition and structure due to the effect of ion beam flux and energy. It is evident from the results shown in Table 7.3 that the combination of Al/C ratio and sp^3 content in the film affect the mechanical properties. The hardness and elastic modulus values of the thin films are 7.4 and 155.1 GPa, respectively having Al/C ratio of 0.44 and I_D/I_G value of 1.26, for 10 focus shots. The hardness and elastic modulus values for 20 focus shots are highest (10.7 and 189.2 GPa). However, the sp^3 content in the film deposited with 20 focus shots with I_D/I_G value of 1.27 is almost same to that of 10 focus shots film but relatively lower Al/C ratio of 0.29 results in the increase of hardness and elastic modulus values. The film synthesized with 30 focus shots shows the lowest values of hardness and elastic modulus with I_D/I_G value of 1.46 and Al/C ratio of 0.19. The significant decrease in sp^3 content in this film sample resulted in reduced hardness and elastic modulus values. The hardness and elastic modulus values of the film synthesized with 40 focus shots increase again even though the Al/C ratio is almost same to 30 shots film. This increase in hardness and elastic modulus is due to the decrease in I_D/I_G value to 1.38 which implies the increase in sp^3 content in the film.

So, from above discussion, it is concluded that both Al/C ratio and sp^3 content play important role in achieving better mechanical properties in Al/a-C thin films. The low Al/C ratio and high sp^3 content in the film are the key features in attaining improved hardness and elastic modulus values.

7.3.6 Hard TiC_x/SiC/a-C:H Nanocomposite Thin Films

Titanium Carbide (TiC) is very well known as a hard refractory ceramic material used in protecting coating. TiC shows high hardness, high melting point, remarkably chemical stability, high oxidation resistance, excellent wear resistance and low coefficient of friction [110]. Hydrogenated amorphous carbon (a-C:H) films have been studied widely for about three decades because of their excellent mechanical and tribological properties [111, 112]. Carbon based nanocomposites such as (TiC/a-C:H) where TiC nanocrystalline is embedded into a-C:H matrix is more attractive because of their potential as high-strength material. The synthesis of composite thin films was performed using plasma focus [113].

7.3.6.1 XRD Results

The XRD patterns of the composite thin films synthesized using 20 focus shots at different CH_4:Ar admixture ratios of 1:9, 3:7 and 1:1 on the silicon substrates placed at the distance of 14 cm above the anode tip along the anode axis are shown in Fig. 7.29a. The XRD pattern of the film synthesized with CH_4:Ar admixture ratio of 1:9 shows only two diffraction peaks corresponding Si (311) and Si (200) at the 2θ values 56.13° and 47.35°, respectively. No diffraction peaks corresponding to TiC_x or SiC phases are observed indicating that the composite thin film is either amorphous or very weakly crystalline in nature. It may be highlighted that the XPS results, not shown, however confirm the formation of the carbides of Ti and Si on these samples. So even though the carbides of Ti and Si are observed in XPS results, which are a very sensitive surface analytical tool, the amount of these crystalline phases might be too low to be detected efficiently by XRD. The increase in CH_4 concentration to 30% in CH_4:Ar admixture (3:7 sample) results in the formation of crystalline TiC_x and SiC phases as seen in corresponding XRD spectrum in Fig. 7.29a. A further increase in CH_4 concentration to 50%, by using CH_4:Ar admixture ratio of 1:1, some of the diffraction peaks of the carbides of Ti and Si are observed but with a significantly reduced intensity which may be attributed to the formation of excessive amorphous carbon as discussed later through Raman analysis. This shows that for the formation of crystalline TiC_x/SiC composite thin films, the CH_4:Ar admixture ratio of 3:7 is the best. It may be pointed out that the XRD spectrum of virgin silicon substrate shows only the Si (311) diffraction peak. However, an additional diffraction peak of Si (200) appeared for all samples, synthesized either with different CH_4:Ar admixture ratio or a different number of focus shots, which shows that the single-crystalline silicon transforms into polycrystalline phase. The transient rise in surface temperature of the silicon substrate placed down the anode stream [26] (by the complex mix of intense flux of instability accelerated energetic ions of filling gas species, decaying

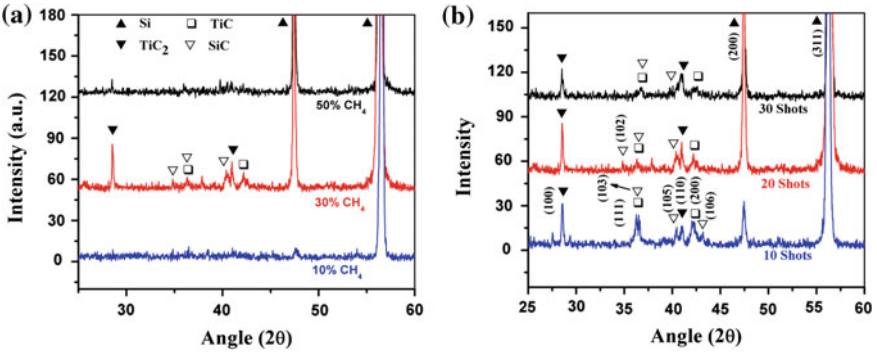

Fig. 7.29 XRD patterns of the deposited thin films using **a** different CH_4/Ar ratios for fixed 20 focus shots, and **b** different number of focus shots at fixed CH_4/Ar ratio of 3:7. Reprinted from Umar et al. [113] (copyright 2013), with permission from Elsevier

high-energy density pinched plasma column and fast moving shock wave) followed by the fast cooling may cause the formation of polycrystalline silicon on the substrate surface.

Figure 7.29b shows the XRD patterns of the composite thin films synthesized on the silicon substrates placed 14 cm above the anode tip along the anode axis using a different number of focus shots (10, 20 and 30) with fixed CH_4:Ar admixture ratio of 3:7. The results for 10 focus shots show the formation of polycrystalline TiC_x/SiC composite as diffraction peaks corresponding to TiC_2 (100), TiC_2 (110), TiC (111), TiC (200), SiC (103), SiC (105) and SiC (106) are observed. An additional phase of SiC (102) is found to appear for the film synthesized with 20 focus shots. The increase in a number of focus shots to 30 shots causes (i) the decrease in the intensity of most of the diffraction peaks and (ii) the disappearance of SiC phase. The decrease in diffraction peak intensities and disappearance of crystalline SiC phases may be attributed to the excessive processing of the synthesized composite thin film by energetic ions and high-energy density plasma flux which might be causing the amorphization of the deposited material.

7.3.6.2 SEM Results

The surface morphologies of the composite thin films synthesized (i) with different CH_4:Ar admixture ratio using fixed 20 focus shots and (ii) with a different number of focus shots for fixed CH_4:Ar filling gas ratio of 3:7; are shown in Figs. 7.30 and 7.31, respectively. Figures show that the films are made up of nanoparticles and nanoparticle agglomerates. The Fig. 7.30b, when viewed with digital magnification, shows that the composite thin film synthesized for CH_4:Ar ratio of 3:7 as it is composed of individual nanoparticles with the average size of 10.2 ± 2.6 nm as well as bigger sized nanoparticle agglomerates with an average size of 36.3 ± 9.2 nm. The images in Fig. 7.30a–c, however, show that the films synthesized for CH_4:Ar ratio of 1:9 and 1:1 essentially composed of nanoparticle agglomerates only. The average size of nanoparticle agglomerates was found to be 46.5 ± 10.7 nm and 40.0 ± 9.6 nm for the CH_4:Ar admixture ratio of 1:9 and 1:1, respectively. This indicates that if the methane concentration in admixture filling

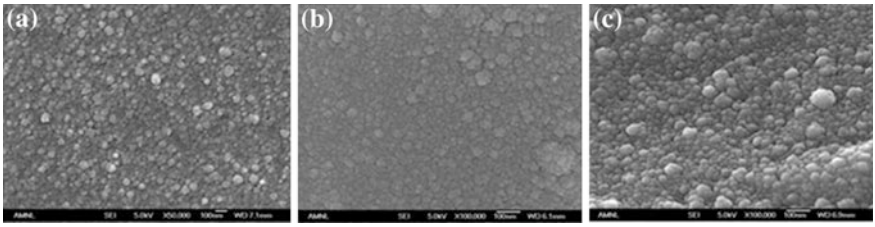

Fig. 7.30 Surface morphology of deposited thin films with fixed 20 focus shots at different CH_4 concentration of **a** 10%, **b** 30% and **c** 50% [113]. The micron bar is 100 nm. Reprinted from Umar et al. [113] (copyright 2013), with permission from Elsevier

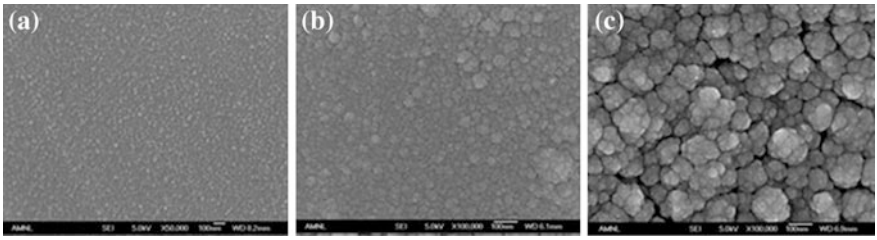

Fig. 7.31 Surface morphology of the deposited thin film using 30% CH_4 with increasing number of **a** 10, **b** 20, and **c** 30 focus shots [113]. The micron bar is 100 nm. Reprinted from Umar et al. [113] (copyright 2013), with permission from Elsevier

gas is either too low or if it is too high then the surface morphology of the synthesized film is affected.

The SEM image sequence shown in Fig. 7.31, shows the formation of nanoparticle agglomerates for all the thin films synthesized with a different number of focus shots. The average size of nanoparticle agglomerates are found to be 24.8 ± 1.3, 36.3 ± 9.2 and 83.9 ± 12.2 nm for 10, 20 and 30 focus shots, respectively. The increase in average size of the nanoparticle agglomerates with the increasing number of focus shots is due to the increase in the total energy transferred to the surface of the thin film and greater transient annealing at a higher number of focus shots.

Raman Analysis

Figure 7.32a and b show the Raman spectra of TiC_x/SiC/a-C:H composite thin films synthesized using different CH_4:Ar admixture ratio for fixed 20 focus shots and using a different number of focus shots for fixed CH_4:Ar admixture ratio of 3:7. The Raman spectra in figures have been roughly divided into three regions, demarcated by dotted lines, related to Si–Si, Si–C and C–C vibration modes [109]. It may be important to point out that the stoichiometric TiC does not have any Raman-active vibrational mode. Figure 7.32a shows the strong D and G peaks, at about 1340 and 1583 cm^{-1}, respectively, only for the film synthesized using 50% CH_4 which implies the presence of a-C as a separated layer. The D and G peaks are not present in the Raman spectra for the thin films synthesized with a lower methane concentration of 10% and 30% which indicates that most of the carbon in these films is bonded to titanium and silicon. A broad hump in the spectral range 150 to 1000 cm^{-1}, with a sharp peak at about 500 cm^{-1} (for deposition with 30% methane concentration), can be attributed to amorphous silicon and SiC [109]. The longitudinal optical (LO) phonon band of crystalline SiC is clearly observed only in the films synthesized with 30% methane.

The Raman spectrum of amorphous silicon can be divided into three regions: (i) low-frequency scattering below 200 cm^{-1} corresponding to transverse acoustical (TA) band, (ii) intermediate Raman band from 200 to 420 cm^{-1} corresponding to longitudinal acoustical (LA) and longitudinal optical (LO) peak range, and (iii) high frequency regime extending to 600 cm^{-1} corresponding to transverse optical

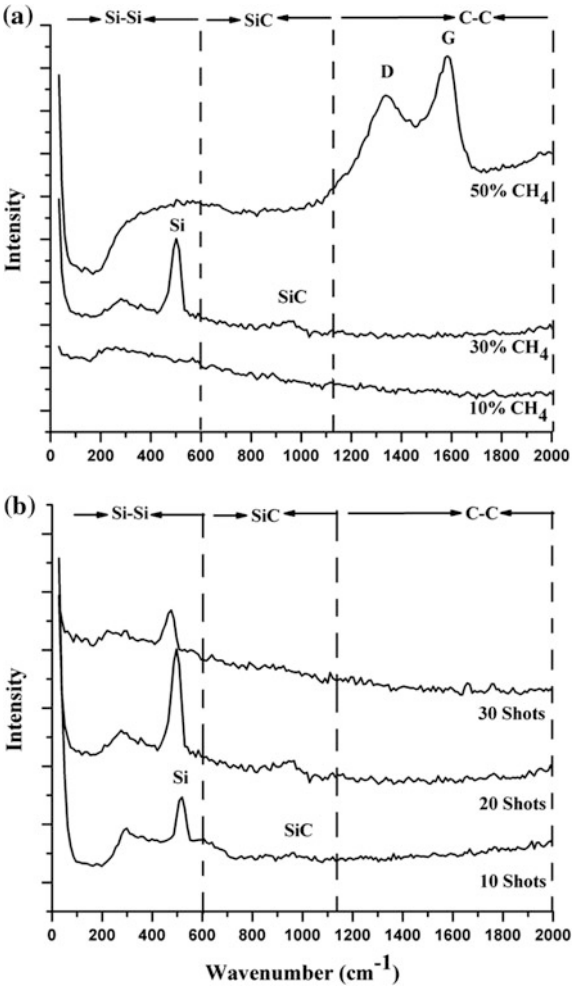

Fig. 7.32 Raman Analysis of the thin films synthesized with **a** different CH_4 concentration for fixed 20 focus shots and **b** different number of focus shots for fixed CH_4/Ar admixture ratio of 3:7. Reprinted from Umar et al. [113] (copyright 2013), with permission from Elsevier

(TO) band. A Raman peak at about 520 cm^{-1} is attributed to crystalline Si (c-Si) which shifts towards the lower wavenumber with the increasing disorder of the c-Si (110). The Fig. 7.32b shows a Raman peak at about 520, 500 and 473 cm^{-1} for thin film synthesized with 10, 20 and 30 focus shots. Since the thickness of the synthesized films varies between 0.8 and 2.1 μm for 10 and 30 shots it is not likely that the Raman spectrum is able to provide the information about the crystalline Si substrate or substrate-thin film interface as the laser light used in Raman spectrometer for non-transparent thin film samples typically can penetrate only up to about 50–100 nm. The observation of Raman peak at 520 cm^{-1} for thin film synthesized using 10 focus shots indicates that the Si ablated from silicon substrate surface by energetic ions of filling gas species re-deposited in crystalline form on the thin films surface. The increase in a number of focus shots to 20 increases the

intensity of the Raman peak corresponding to c-Si indicating the increase in the c-Si. However, the shift in peak's position towards the lower wavenumber of about 500 cm^{-1} indicates the increasing disorder in c-Si which can be attributed to the amorphization of c-Si due to increasing ion irradiation dose. The peak shifts further to 473 cm^{-1} for 30 focus shots which correspond to a-Si obviously because of increasing amorphization of the silicon due to higher ion irradiation dose. The LO phonon band of crystalline SiC was observed only in the film synthesized with 10 and 20 focus shots only.

7.3.6.3 Hardness Measurements

Table 7.4 shows the variation of the hardness and the elastic modulus (measure of the stiffness or the rigidity) of composite thin films, measured at the surface of the thin films, as a function of methane gas concentration for fixed 20 focus shots. For the films synthesized with fixed 20 focus shots but with different CH_4:Ar admixture ratio; the maximum values of the hardness and the elastic modulus of about 15 and 230 GPa, respectively, at the surface, were obtained for thin film synthesized with 30% methane concentration. This confirms that 30% methane concentration in CH_4: Ar admixture operating gas in plasma focus provides optimum mechanical properties for hard composite TiC_x/SiC/a-C:H coatings. The Raman results exhibited the abundance of a:C formation with the observation of graphitic D and G peak for the films synthesized with 50% methane; but this film does not show the maximum hardness implying thereby that the contribution to the hardness mainly comes from crystalline TiC phase formation which according to XRD results is maximum in the film synthesized with 30% methane.

The Table 7.5 shows the hardness and the elastic modulus of composite thin films synthesized using a different number of focus shots for fixed 30% methane

Table 7.4 The variation in hardness and elastic modulus of the deposited thin films using different CH_4:Ar ratio for fixed 20 focus shots

CH_4/Ar ratio	Hardness (GPa)	Elastic modulus (GPa)
1:9	3.9 ± 0.3	43.2 ± 11.9
3:7	15.3 ± 0.5	230.2 ± 14.9
1:1	2.2 ± 0.15	18.7 ± 2.4

Table 7.5 Variation in hardness and elastic modulus of the thin films deposited with different number of focus shots for fixed 30% CH_4

No. of focus shots	Hardness (GPa)	Elastic modulus (GPa)
10	4.0 ± 1.1	47.4 ± 17.1
20	15.3 ± 0.5	230.2 ± 14.9
30	22 ± 4.4	304.6 ± 37.6

concentration at the surface of the thin films. The general trend is that the hardness and the elastic modulus values are higher for the films synthesized with a higher number of focus shots at the surface. Maximum values of hardness and elastic modulus of about 22 and 305 GPa, respectively, were obtained at the surface of the composite thin film treated with 30 focus shots. XRD pattern (Fig. 7.29) show that the films synthesized with 10 and 20 focus shots have phases like TiC, TiC_2, and SiC whereas the films synthesized with 30 shots mainly has crystalline titanium carbide phase and hence the better mechanical properties for 30 focus shots once again confirms that they are mainly due to titanium carbide phases. A careful analysis of the position of the (100) TiC_2 and the (200) TiC peaks shows that they have shifted significantly compared to the positions mentioned in standard diffraction database for the film synthesized with 10 focus shots indicating thereby the biggest amount of stress in this thin film leading to lower hardness and elastic modulus. The peak positions shifted closer to the standard value, indicating thereby the stress relaxation and enhancement in mechanical properties, with the increase in the number of focus shots. The stress relaxation in the films synthesized with a greater number of focus shots can be related to greater thermal processing due to increased ion irradiation dose.

7.4 Conclusions

The DPF device is a simple, cost-effective and pulsed coaxial plasma accelerator that employs the self-generated magnetic field to squeeze the plasma column up to high density (10^{25}–10^{26} m^{-3}) and high-temperature ($\sim 1-2$ keV) in a short time ($\sim 10^{-7}$ s). The energetic ion and relativistic electrons emanated during the radial collapse phase of DPF operation are being used for material processing form the last few decades. The velocity, energy and flux of energetic ions have been estimated by employing various detectors like SSNTD, Faraday Cup and BPX65 photodiode. The estimated values of ions energy and ions number density by employing BPX65 photodiode detector ranged from 40 keV to 1.2 MeV and 9.7×10^{19} m^{-3} to 1.796×10^{19} m^{-3}, respectively when the BPX65 photodiode detector was placed at 9 cm in front of central anode. The ion energy and ion number densities are associated with the focusing efficiency of DPF device as well as sample axial and angular positions. It is found that the ion energy fluxes are decreased with the increased axial distance and angular position.

The deposition of TiAlN composite films on Al substrate was done by the irradiations of nitrogen ions emanated during the radial collapse phase of plasma focus operation. TiAlN composite films are deposited for different focus (10, 20, 30, 40 and 50) shots ion irradiation process. XRD analysis exhibits the development of various diffraction peaks related to TiAlN and AlN phases, respectively. The intensity of different diffraction peaks related to TiAlN and AlN phases was found to increase with the increase in a number of focus shots. The lattice parameters of

TiN were found to be lower which was associated with the formation of solid solution where Ti atoms are replaced by Al atoms without changing the crystal structure because Al atomic radius (0.143 nm) is smaller than the atomic radius of Ti (0.146 nm). The crystallite size of TiAlN (111) plane also decreased linearly with the increase in a number of focus shots which restricted the dislocation activity and crack propagation along grain boundaries. The surface morphology of TiAlN film was influenced by number of focus shots with the deposition rate of about 276 ± 50 nm per shot. Note that the deposition rate achieved in plasma focus is high as compared to the deposition rates obtained in other devices. The micro-hardness of TiAlN composite films increased with the increase in number of focus shots due to the increase in ions energy flux and incorporation of Ti and nitrogen in the deposited TiAlN composite films and Al substrate.

The ZrN films were deposited by the irradiation of energetic nitrogen ions from plasma focus on zirconium substrates placed at 9 cm in front of the central anode. The crystallinity of various planes of zirconium nitride phase and the grain size increased with the increase of a number of focus shots and decreased by increasing the sample angular position. The increased focus shot irradiation decreased the stresses developed in the deposited films. The ZrN film deposited at higher degree angular position was smooth and structured as compared to films deposited along the anode axis. The Vickers micro-hardness of ZrN film deposited for 40 focus shots is enhanced up to 400% as compared to an untreated substrate which can be attributed to greater lattice distortion produce in the substrate during ion irradiation process.

Polycrystalline ZrON composite films were deposited on zirconium substrates by the irradiation of energetic nitrogen ions using plasma focus at fixed distance of 10 cm for fixed 25 focus shots for various (0.5, 1, 1.5, 2 and 2.5 mbar) nitrogen pressures. The XRD pattern exhibits the development of zirconium nitride and oxide diffraction planes confirming the deposition of P–ZrON composite films. The (N + O)/Zr ratio present in P–ZrON composite strongly depends on nitrogen pressures. The average crystallite size and strain transformation observed in various diffraction planes were found to be associated with the increase of nitrogen pressures. The shape and size of nanoparticles and the formation of complex network of nanowires and nanocombs were coupled with the operating nitrogen pressures. The micro-hardness of P–ZrON composite film was found to be 5.4 times greater than the micro-hardness of virgin zirconium sample.

The MP–ZrAlO composite films are deposited on zirconium substrate by the irradiation of energetic oxygen ions and Al plasma from anode insert of plasma focus device. The XRD pattern showed that the growth of ZrO_2 and Al_2O_3 phases was better when MP–ZrAlO composite film was deposited for 15 focus shots whereas comparatively weak growth of MP–ZrAlO composite film was observed at higher degree angular positions. The crystallinity of monoclinic and cubic zirconium oxide (m-ZrO_2 and c-ZrO_2) phases was better at lower annealing temperature

while the re-crystallization of the above-mentioned phases of zirconium oxide at higher annealing temperature is obtained. The weight fractions of monoclinic and cubic phase of zirconium oxide were found to depend strongly on number of focus shots, angular position of sample and the annealing temperature. Similarly, the sample surface was found to be decorated with nanoparticles (45–100 nm in diameter), nanostrips (333–750 nm in width and 2.5–9 μm in length) and nanorods (25–50 nm in diameter) depending on the total ion energy flux delivered to the substrate surface, sample angular positions and annealing temperatures. For lower annealing temperature, the close packing of nanoparticles confirmed the development of half wave-like microstructures. The half wave microstructure played a significant role in surface roughness as well as hinders the dislocation motion which improved the mechanical properties like micro-hardness of MP–ZrAlO composite films. For higher annealing temperature, the decomposition of various phases present in MP–ZrAlO composite film was observed. The estimated values of micro-hardness of MP–ZrAlO composite films deposited for higher number of focus shots was about seven times greater than the micro-hardness of virgin zirconium.

The Al/a-C thin films were also successfully deposited on silicon substrates by the ions irradiation of various focus (10, 20, 30 and 40) shots. The XRD pattern does not show any diffraction peak related to aluminium carbide phase. The XPS analysis also confirms the absence of aluminium carbide phase. The Raman spectra showed the development of stretching vibrations D and G bonds (about 1366 and 1600 cm^{-1}) which confirmed the existence of carbon in sp^2 and sp^3 bonding configuration. It was shown that greater amount of sp^3 content was present in the deposited film for lower number of focus shots. The significant decrease in sp^3 content resulted in the decreased of micro-hardness and elastic modulus. However, the combination of Al/C ratio and sp^3 content in the deposited film influence the micro-hardness. On the other hand, the increase in micro-hardness and elastic modulus is due to the decrease in I_D/I_G ratio.

The TiC/a-C-H composite films were deposited different number of plasma focus deposition shots and also for various CH_4:Ar ratios of 1:9, 3:7 and 1:1 on silicon substrates placed at 14 cm. The best results were obtained for CH_4:Ar ratio of 3:7. For fixed CH_4:Ar (3:7) ratio samples showed deposition of polycrystalline TiC/SiC composite films. The crystallinity of these phases was strongly associated with the number of focus shots. For larger number of shots the SiC diffraction peak disappeared due to the excessive amount of energetic ions energy flux which caused the amorphization of deposited material. The SEM microstructure of the deposited films revealed the formation of nanoparticles and their agglomerates. The Raman analysis showed the strong D and G bands at about 1340 and 1583 cm^{-1}, respectively when the film was deposited for 50% concentration of carbon. These Raman bands did not appear for lower concentration of CH_4. Raman results also exhibited the shifting of SiC band position towards the lower wave numbers

indicating the disordering in crystalline silicon phase with increasing focus shots. The maximum values of micro-hardness and elastic modulus were found to be 22 and 305 GPa, respectively, when the film was deposited for 30 focus shots.

The DFP device has wide range of ion energy flux. The ion energy flux is associated with the focusing efficiency of DPF device; better the focusing efficiency more will be the ion energy flux. The focusing efficiency depends on working gas pressure as well as nature of the gas. The ion energy flux is tuned by adjusting the sample axial and angular positions. The total number of ion energy flux delivered to the substrate surface is associated with the total number of focus shots; more the focus shots, greater amount of ion energy flux incorporated to the substrate surface and more substrate surface transient temperature. Therefore, one can control the film surface properties just by tuning the total ion energy flux delivered to the substrate surface and their corresponding substrate surface transient temperature.

In short, the several prominent features which make DPF device an attractive, outstanding and potential candidate for the deposition of hard coatings as compared to other coating techniques are as follows: (i) the DPF device is a hybrid deposition technique for hard and soft coating materials because it comprises the feature of three different deposition techniques like PVD sputtering process, electron beam evaporation and plasma-enhanced chemical vapour deposition, (ii) it has comparatively higher deposition rate than other plasma deposition techniques, (iii) it has ability to incorporate the third element through the ablation process of anode material by the irradiation of relativistic electron beam generated from DPF device, (iv) no external heating to the substrate is required, (v) the DPF operation works on lower working gas pressure and also in static gas fills mode rather than flowing gas operation and thus the gas consumption is low comparatively, (vi) the DPF device is energized by a simple fast discharge capacitor, (vii) in DPF device, ion pulse of short duration is used to deposit various types of composite materials in the form of films, (viii) the deposited composite films of hard and soft materials have good adhesion with the substrate surface and (ix) the DPF device is capable to deposit hard and soft coating on various substrates at room temperature environment. Therefore, the DPF device is a versatile deposition technique to deposit hard and soft materials in the form of films of diverse surface properties at room temperature environment.

References

1. C. Donnet, A. Erdemir, Historical developments and new trends in tribological and solid lubricant coatings. Surf. Coat. Technol. **180–181**, 76–84 (2004)
2. R.F. Bunshah (ed.), *Handbook of Hard Coatings* (Noyes Publications/William Andrew Publishing, New York, 2001)
3. G.K. Wehner, Sputtering by ion bombardment. Adv. Electro. Electron Phys. **7**, 239–298 (1955)
4. P. Sigmund, Theory of sputtering. I. Sputtering yield of amorphous and polycrystalline targets. Phys. Rev. **184**, 383–416 (1969)

5. K. Wasa, I. Kanno, H. Kotera (eds.), *Handbook of Sputter Deposition Technology* (Elsevier Inc, 2012)
6. P.J. Kelly, R.D. Arnell, Magnetron sputtering: a review of recent developments and applications. Vac. **56**, 159–172 (2000)
7. V. Kouznetsov, K. Macak, J.M. Schneider, U. Helmersson, I. Petrov, A novel pulsed magnetron sputter technique utilizing very high target power densities. Surf. Coat. Technol. **122**, 290 (1999)
8. J. Bohlmark (ed.), Fundamentals of High Power Impulse Magnetron Sputtering. (Dissertation, Linköping Studies in Science and Technology, 2006)
9. C. Li, X. Tian, Novel high power impulse magnetron sputtering enhanced by an auxiliary electrical field. Rev. Sci. Instrum. **87**, 083507 (2016)
10. J.W. Mather, Formation of a high-density deuterium plasma focus. Phys. Fluids **8**(2), 366–377 (1965)
11. N.V. Filippov, T.I. Filippova, V.P. Vinogradov, Dense, high-temperature plasma in a noncylindrical Z-pinch. Nucl. Fusion Suppl. **2**, 577–587 (1962)
12. H. Conrads, Dense plasma focus as a neutron source for fusion research. Nucl. Sci. Eng. **106** (3), 299–307 (1990)
13. A. Serban, S. Lee, Experiments on speed-enhanced neutron yield from a small plasma focus. J. Plasma Phys. **60**, 3–15 (1998)
14. E.J. Lerner, S. Krupakar Murali, D. Shannon, A.M. Blake, F.V. Roessel, Fusion reaction from greater than 150 keV ions in a dense plasma focus plasmoid. Phys. Plasmas **19**, 032704 (2012)
15. S. Lee, P. Lee, G. Zhang, X. Feng, V.A. Gribkov, M. Liu, A. Serban, T.K. Wong, High rep rate high performance plasma focus as a powerful radiation source. IEEE Trans. Plasma Sci. **26**, 1119–1126 (1998)
16. S. Hussain, M. Shafiq, R. Ahmad, A. Waheed, M. Zakaullah, Plasma focus as a possible X-ray source for radiography. Plasma Sources Sci. Technol. **14**, 61–69 (2005)
17. M.A. Tafreshi, M.M. Nasseri, N. Nabipour, D. Rostamifard, A. Nasiri, Application of plasma focus device in fast industrial radiography. J. Fusion Energy **33**(6), 689–692 (2014)
18. M.J. Inestrosa-Izurieta, P. Jauregui, L. Soto, Deposition of materials using a plasma focus of tens of joules. J. Phys. Conf. Ser. **720**, 012045 (2016)
19. R.S. Rawat, V. Aggarwal, M. Hassan, P. Lee, S.V. Springham, T.L. Tan, S. Lee, Nano-phase titanium dioxide thin film deposited by repetitive plasma focus: ion irradiation and annealing based phase transformation and agglomeration. Appl. Surf. Sci. **255**, 2932–2941 (2008)
20. M. Sadiq, M. Shafiq, A. Waheed, R. Ahmad, M. Zakaullah, Amorphization of silicon by ion irradiation in dense plasma focus. Phys. Lett. A **352**, 150–154 (2006)
21. Z.P. Wang, H.R. Yousefi, Y. Nishino, H. Ito, K. Masugata, Preparation of silicon carbide film by a plasma focus device. Phys. Lett. A **372**, 7179–7182 (2008)
22. R.S. Rawat, M.P. Srivastava, S. Tandon, A. Mansingh, Crystallization of an amorphous lead zirconate titanate thin film with a dense-plasma-focus device. Phys. Rev. B **47**, 4858–4862 (1993)
23. Z.Y. Pan, R.S. Rawat, R. Verma, J.J. Lin, H. Yan, R.V. Ramanujan, P. Lee, S.V. Springham, T.L. Tan, Miniature plasma focus as a novel device for synthesis of soft magnetic FeCo thin films. Phys. Lett. A **374**, 1043–1048 (2010)
24. O. Mangla, S. Roy, K. Ostrikov, Dense plasma focus-based nanofabrication of III–V semiconductors: unique features and recent advances. Nanomaterials **6**, 4–16 (2016)
25. J.N. Feugeas, E.C. Llonch, C.O. de Gonzalez, G. Galambos, Nitrogen implantation of AISI 304 stainless steel with a coaxial plasma gun. J. Appl. Phys. **64**, 2648–2651 (1988)
26. R.S. Rawat, W.M. Chew, P. Lee, T. White, S. Lee, Deposition of titanium nitride thin films on stainless steel AISI 304 substrates using a plasma focus device. Surf. Coat. Technol. **173**, 276–284 (2003)
27. C.R. Kant, M.P. Srivastava, R.S. Rawat, Thin carbon film deposition using energetic ions of a dense plasma focus. Phys. Lett. A **226**(3–4), 212–216 (1997)

28. C.R. Kant, M.P. Srivastava, R.S. Rawat, Dense plasma focus energetic ions based fullerene films on a Si (111) substrate. Phys. Lett. A **239**, 109–114 (1998)
29. M. Omrani, R. Amrollahi, M. Habibi, The effect of TiN nanoparticles deposition with different number of shots on SS316L by plasma focus device. Radiat. Eff. Defects Solids **168**, 188–198 (2013)
30. A. Ghorbani, A. Sadighzadeh, M. Seifi, S.M.S. Kiai, A. Raeisdana, Amorphous hydrogenated carbon thin films deposited on stainless steel using high energy plasma focus device. Surf. Coat. Technol. **288**, 1–7 (2016)
31. J.G. Molleja, M. Milanese, B.J. Gómez, R. Moroso, M. Piccoli, J. Niedbalski, J. Bürgi, E. Bemporad, J. Feugeas, Behavior of nitrided and carburized AISI 904 L stainless steels under severe light ion beam irradiation with plasma focus. Surf. Interface Anal. **47**, 728–737 (2015)
32. S. Jabbar, I.A. Khan, R. Ahmad, M. Zakaullah, J.S. Pan, Carbonitriding of silicon using plasma focus device. J. Vac. Sci. Technol. A **27**, 381–387 (2009)
33. A. Hussnain, R.S. Rawat, T.K. Seng, R. Ahmad, T. Hussain, P. Lee, C. Zhong, S. Lu, Z. Zheng, Study of structural and mechanical properties of wn/a-si3n4 hard coatings grown by plasma focus. J. Fusion Energy **34**, 435–442 (2015)
34. M. Sohrabi, M. Habibi, H.R. Yousefi, G.H. Roshani, Angular distribution analysis of nitrogen ions in a low energy dense plasma focus device. Contrib. Plasma Phys. **53**, 592–598 (2013)
35. H. Kelly, A. Lepone, A. Márquez, Nitrogen ion spectrum from a low energy plasma focus device. IEEE Trans. Plasma Sci. **25**, 455 (1997)
36. R. Antanasijevic, J. Vukovic, S. Popovic, M. Popovic, Detection of light charged particles from plasma focus by CR-39. Int. J. Radiat. Appl. Instrum. D Nucl. Tracks Radiat. Meas. **19**, 555–556 (1991)
37. Z. Todorovic, R. Antanasijevic, D. Cevic, A. Zaric, D.J. Konjevic, J. Vukovic, J. Puric, M. Cuk, Discrimination of positive particles emitted in deuterium plasma focus device using SSNTD. Radiat. Meas. **25**, 265–266 (1995)
38. F. Castillo, J.J.E. Herrera, G. Espinosa, Energy study of accelerated ions from a dense plasma focus by means of CR-39 track detector. Nucl. Tracks Radiat. Meas. **22**, 551–553 (1993)
39. M. Hassan, A. Qayyum, R. Ahmad, R.S. Rawat, P. Lee, S.M. Hassan, G. Murtaza, M. Zakaullah, Dense plasma focus ion-based titanium nitride coating on titanium. Nucl. Instrum. Methods Phys. Res. B **267**, 1911–1917 (2009)
40. H.O. Funsten, S.M. Ritzau, R.W. Harper, Fundamental limits to detection of low-energy ions using silicon solid-state detectors. Appl. Phys. Lett. **84**, 3552–3554 (2004)
41. M. Akel, S.A. Salo, S.H. Saw, S. Lee, Properties of ion beams generated by nitrogen plasma focus. J. Fusion Energy **33**, 189–197 (2014)
42. L. Bertalot, H. Herold, U. Jager, A. Mozer, T. Oppenlander, M. Sadowski, H. Schmidt, Mass and energy analysis and space-resolved measurements of ions from plasma focus devices. Phys. Lett. A **79**, 389–392 (1980)
43. S.R. Mohanty, H. Bhuyan, N.K. Neog, R.K. Rout, E. Hotta, Development of multi faraday cup assembly for ion beam measurements from a low energy plasma focus device. Jpn. J. Appl. Phys. **44**, 5199–5205 (2005)
44. H. Kelly, A. Lepone, A. Marquez, M.J. Sadowski, J. Baranowski, E. Skladnik-Sadowska, Analysis of the nitrogen ion beam generated in a low-energy plasma focus device by a Faraday cup operating in the secondary electron emission mode. IEEE Trans. Plasma Sci. **26**, 113–117 (1998)
45. G.M. El-Aragi, Ion beam emission within a low energy focus plasma (0.1 kJ) operating with hydrogen. Z. Naturforsch. A **65**, 606–612 (2010)
46. F. Tang, X. Wang, L. Zhang, Z. Yan, Study on simulation and experiment of array micro Faraday cup ion detector for FAIMS. Sci. China Tech. Sci. **53**, 3225–3231 (2010)
47. D.E. Potter, Numerical studies of the plasma focus. Phys. Fluids **14**, 1911–1924 (1971)
48. S.P. Gray, F. Hohl, Ion kinematics in a plasma focus. Phys. Fluids **16**, 997–1002 (1973)

49. L. Jakubowski, M. Sadowski, J. Zebrowski, Measurements of charged particle beams from plasma focus discharges. Nucl. Fusion **41**, 755–760 (2001)
50. K. Takao, Y. Doi, S. Hirata, M. Shiotani, I. Kitamura, T. Takahashi, K. Masugata, Characteristics of ion beams produced in a plasma focus device. Jpn. J. Appl. Phys. **40**, 1013–1015 (2001)
51. K. Takao, T. Honda, I. Kitamura, K. Masugata, Purity of nitrogen ion beams produced in a plasma focus. Plasma Sources Sci. Technol. **12**, 407–411 (2003)
52. R. Ahmad, M. Hassan, G. Murtaza, A. Waheed, M. Zakaullah, Study of lateral spread of ions emitted from 2.3 kJ plasma focus with hydrogen and nitrogen gases. J. Fusion Energy **21**, 217–220 (2002)
53. M.G. Haines, Dense plasma in Z-pinches and the plasma focus. Phil. Trans. R. Soc. Lond. A **300**, 649–663 (1981)
54. J. Moreno, J. Pedreros, L. Soto, Measurements of ions emission using ToF method and CR39 SSNTD in a small plasma focus device of hundreds of joules. J. Phys. Conf. Ser. **511**, 012025 (2014)
55. https://www.hamamatsu.com/resources/pdf/ssd/e10_handbook_for_high_energy.pdf
56. M. Sadowski, J. Żebrowski, E. Rydygier, H. Herold, U. Jäger, H. Schmidt, Multi-spike structure of ion pulses generated by plasma focus discharges. Phys. Lett. A **113**, 25–31 (1985)
57. S. Nunomura, K. Koga, M. Shitarani, Y. Watanabe, Y. Morisada, N. Matsuki, S. Ikeda, Fabrication of nanoparticle composite porous films having ultralow dielectric constant. Jpn. J. Appl. Phys. **44**, L1509–L1552 (2005)
58. I.A. Khan, R.S. Rawat, R. Verma, G. Macharaga, R. Ahmad, Role of charge particles irradiation on the deposition of AlN films using plasma focus device. J. Cryst. Growth **317**, 98–103 (2011)
59. H. Bhuyan, H. Chuaqui, M. Favre, I. Mitchell, E. Wyndham, Ion beam emission in a low energy plasma focus device operating with methane. J. Phys. D Appl. Phys. **38**, 1164–1169 (2005)
60. G. Gerdin, W. Stygar, F. Venneri, Faraday cup analysis of ion beams produced by a dense plasma focus. J. Appl. Phys. **52**, 3269–3275 (1981)
61. J.D. Thomas, G.S. Hodges, D.G. Seely, N.A. Moroz, T.J. Kvale, Performance enhancement study of an electrostatic Faraday cup detector. Nucl. Instrum. Method **A536**, 11–21 (2005)
62. J. Feugeas, L. Rico, L. Nosei, B. Gómez, E. Bemporad, J. Lesage, J. Ferrón, Austenite modification of AISI 316L SS by pulsed nitrogen ion beams generated in dense plasma focus discharges. Surf. Coat. Technol. **204**, 1193–1199 (2010)
63. A. Grill, Diamond-like carbon: state of the art. Diam. Relat. Mater. **8**, 428–434 (1999)
64. A. Czyzniewski, Mechanical and tribological properties of Cr-DLC coatings deposited by arc-mag-rf PACVD hybrid method. Plasma Processes Polym. **4**, 5225–5230 (2007)
65. J. Li, D. Dzivenko, A. Zerr, C. Fasel, Y. Zhou, R. Riedel, Synthesis of nanocrystalline Zr_3N_4 and Hf_3N_4 powders from metal dialkylamides. Z. Anorg. Allg. Chem. **631**, 1449–1455 (2005)
66. R. Gupta, M.P. Srivastava, Carbon ion implantation on titanium for TiC formation using a dense plasma focus device. Plasma Sources Sci. Tech. **13**, 371–374 (2004)
67. P. Eklund, J. Emmerlich, H. Hogberg, O. Wilhelmsson, P. Isberg, J. Birch, R.O.A. Persson, U. Jansson, L. Hultman, Structural, electrical, and mechanical properties of nc-TiC/a-SiC nanocomposite thin films. J. Vac. Sci. Technol. B **23**, 2486–2495 (2005)
68. A.R. Phani, J.E. Krzanowski, J.J. Nainaparampil, Structural and mechanical properties of TiC and Ti–Si–C films deposited by pulsed laser deposition. J. Vac. Sci. Technol. A **19**, 2252–2258 (2001)
69. P. Eklund, C. Virojanadara, J. Emmerlich, L.I. Johansson, H. Hogberg, L. Hultman, Photoemission studies of Ti_3SiC_2 and nanocrystalline-TiC/amorphous-SiC nanocomposite thin films. Phys. Rev. B **74**, 045417 (2006)
70. D. Li, S. Hassani, S. Poulin, J.A. Szpunar, L. Martinu, J.E. Klemberg-Sapieha, Effect of Si and C concentration on the microstructure, and the mechanical, tribological and

electrochemical properties of nanocomposite TiC/a-SiC:H/a-C:H coatings prepared by plasma enhanced chemical vapor deposition. J. Appl. Phys. **111**, 043512 (2012)
71. S.H. Koutzaki, J.E. Krzanowski, J.J. Nainaparampril, Structure and mechanical properties of Ti–Si–C coatings deposited by magnetron sputtering. J. Vac. Sci. Technol. A **19**(4), 1912–1918 (2001)
72. J.E. Krzanowski, S.H. Koutzaki, Mechanical properties of sputter-deposited titanium–silicon–carbon films. J. Am. Ceram. Soc. **84**(3), 672–674 (2001)
73. T. Zehnder, J. Matthey, P. Schwaller, A. Klein, P.A. Steinmann, J. Patscheider, Wear protective coatings consisting of TiC–SiC–a-C:H deposited by magnetron sputtering. Surf. Coat. Technol. **163**, 238–244 (2003)
74. D. Munteanu, C. Ionescu, C. Olteanu, A. Munteanu, F. Davin, L. Cunha, C. Moura, F. Vaz, Influence of composition and structural properties in the tribological behavior of magnetron sputtered Ti–Si–C nanostructured thin films, prepared at low temperature. Wear **268**, 552–557 (2010)
75. A. Schuler, I.R. Videnovic, P. Oelhafen, S. Brunold, Titanium-containing amorphous hydrogenated silicon carbon fiilms (a-Si:C:H/Ti) for durable solar absorber coatings. Sol. Energ. Mat. Sol. C **69**, 271–284 (2001)
76. J.P. Palmquist, U. Jansson, T. Seppnen, P.O. Persson, J. Birch, L. Hultman, P. Isberg, Magnetron sputtered epitaxial single-phase Ti_3SiC_2 thin films. Appl. Phys. Lett. **81**, 835–837 (2002)
77. Y.-G. Jung, S.-W. Park, S.-C. Choi, Effect of CH_4 and H_2 on CVD of SiC and TiC for possible fabrication of SiC/TiC/C FGM. Mater. Lett. **30**, 339–345 (1997)
78. S. Lee, A. Serban, Dimensions and lifetime of the plasma focus pinch. IEEE Trans. Plasma Sci. **24**(3), 1101–1105 (1996)
79. A.Z. Ait-Djafer, N. Saoula, H. Aknouche, B. Guedouar, N. Madaoui, Deposition and characterization of titanium aluminum nitride coatings prepared by RF magnetron sputtering. Appl. Surf. Sci. **350**, 6–9 (2015)
80. T. Hussain, R. Ahmad, J. Siddiqui, N. Khalid, TiAlN coatings synthesised using a dense plasma focus system and varied focus shots. Radiat. Eff. Defects Solids **166**, 873–883 (2011)
81. B.D. Cullity, S.R. Stock, *Elements of X-ray Diffraction*, 3rd edn. (Prentice Hall, Englewood Cliffs, NJ, 2001)
82. J.A. Thornton, Influence of apparatus geometry and deposition conditions on the structure and topography of thick sputtered coatings. J. Vac. Sci. Technol. **11**, 666–670 (1974)
83. I. Dörfel, W. Österle, I. Urban, E. Bouzy, Microstructural characterization of binary and ternary hard coating systems for wear protection. Part I: PVD coatings. Surf. Coat. Technol. **111**, 199–209 (1999)
84. M. Moseler, O. Rattunde, J. Nordiek, H. Haberland, On the origin of surface smoothing by energetic cluster impact: molecular dynamics simulation and mesoscopic modeling. Nucl. Instrum. Methods B **164–165**, 522–536 (2000)
85. O. Rattunde, M. Moseler, A. Hafele, J. Kraft, D. Rieser, H. Haberland, Surface smoothing by energetic cluster impact. J. Appl. Phys. **90**, 3226–3231 (2001)
86. J. Adachi, K. Kurosaki, M. Uno, S. Yamanaka, A molecular dynamics study of zirconium nitride. J. Alloys Compd. **396**, 260–263 (2005)
87. I.A. Khan, M. Hassan, R. Ahmad, A. Qayyum, G. Murtaza, M. Zakaullah, R.S. Rawat, Nitridation of zirconium using energetic ions from plasma focus device. Thin Solid Films **516**(23), 8255–8263 (2008)
88. G. Lopez, M.H. Staia, High-temperature tribological characterization of zirconium nitride coatings Surf. Coat. Technol. **200**, 2092–2099 (2005)
89. K. Becker, F. Ebert, Die kristallstruktur einiger binarer carbide und nitride. Z. Phys. **31**, 268–272 (1925)

90. P. Klumdoung, P. Asanithi, S. Chaiyakun, P. Limsuwan, Variation of color in zirconium nitride films prepared by reactive dc magnetron sputtering. Adv. Mater. Res. **214**, 320–324 (2011)
91. D.A. Dzivenkoa, A. Zerr, G. Miehe, R. Riedel, Synthesis and properties of oxygen-bearing c-Zr_3N_4 and c-Hf_3N_4. J. Alloy. Compd. **480**, 46–49 (2009)
92. P. Carvalho, F. Vaz, L. Rebouta, L. Cunha, C.J. Tavares, C. Moura, E. Alves, A. Cavaleiro, Ph Goudeau, E. Le Bourhis, J.P. Riviere, J.F. Pierson, O. Banakh, Structural, electrical, optical, and mechanical characterizations of decorative ZrO_xN_y thin films. J. Appl. Phys. **98**, 023715 (2005)
93. I.A. Khan, M. Hassan, R. Ahmad, G. Murtaza, M. Zakaullah, R.S. Rawat, P. Lee, Synthesis of zirconium oxynitride (ZrON) nanocomposite films on zirconium substrate by dense plasma focus device. Int. J. Mod. Phys. B **22**(23), 3941–3955 (2008)
94. F. Vaz, P. Cerqueira, L. Rebouta, S.M.C. Nascimento, E. Alves, Ph Goudeau, J.P. Riviere, K. Pischow, J. De Rijk, Structural, optical and mechanical properties of coloured TiN_x O_y thin films. Thin Solid Films **447–448**, 449–454 (2004)
95. J. Musil, F. Hruby, Superhard nanocomposite Ti_{1-x} Al_x N films prepared by magnetron sputtering. Thin Solid Films **365**, 104–109 (2000)
96. R. Sanjines, C.S. Sandu, R. Lamni, F. Levy, Thermal decomposition of Zr_{1-x} Al_x N thin films deposited by magnetron sputtering. Surf. Coat. Technol. **200**, 6308–6312 (2006)
97. I.A. Khan, R.S. Rawat, R. Ahmad, M.A.K. Shahid, Deposition of alumina stabilized zirconia at room temperature by plasma focus device. Appl. Surf. Sci. **288**, 304–312 (2014)
98. J. Robertson, Diamond-like amorphous carbon. Mater. Sci. Eng. Reports **37**, 129–281 (2002)
99. H. Ronkainen, S. Varjus, J. Koskinen, K. Holmberg, Differentiating the tribological performance of hydrogenated and hydrogen-free DLC coatings. Wear **249**, 260–266 (2001)
100. Y. Pauleau, F. Thiery, P.B. Barna, F. Misjak, A. Kovacs, S.N. Dub, V.V. Uglov, A.K. Kuleshov, Nanostructured copper/hydrogenated amorphous carbon composite films prepared by microwave plasma-assisted deposition process from acetylene-argon gas mixtures. Rev. Adv. Mater. Sci. **6**, 140–149 (2004)
101. Y.T. Pei, D. Galvan, J.T.M. De Hosson, Nanostructure and properties of TiC/aC:H composite coatings. Acta Mater. **53**, 4505–4521 (2005)
102. G. Zhang, P. Yan, P. Wang, Y. Chen, J. Zhang, The preparation and mechanical properties of Al-containing a-C:H thin films. J. Phys. D Appl. Phys. **40**, 6748–6753 (2007)
103. Y. Pauleau, F. Thiery, Nanostructured copper–carbon composite thin films produced by sputter deposition/microwave plasma-enhanced chemical vapor deposition dual process. Mater. Lett. **56**, 1053–1058 (2002)
104. Z.A. Umar, R.S. Rawat, R. Ahmad, A.K. Kumar, Y. Wang, T. Hussain, Z. Chen, L. Shen, Z. Zhang, Mechanical properties of Al/aC nanocomposite thin films synthesized using a plasma focus device. Chin. Phys. B **23**, 025204 (2014)
105. P. Wang, X. Wang, Y. Chen, G. Zhang, W. Liu, J. Zhang, Appl. Surf. Sci. **253**, 3722–3726 (2007)
106. G. Murtaza, S.S. Hussain, M. Sadiq, M. Zakaullah, Thin Solid Films **517**, 6777–6783 (2009)
107. S. Zeb, M. Sadiq, A. Qayyum, G. Murtaza, M. Zakaullah, Mater. Chem. Phys. **103**, 235–240 (2007)
108. Z.A. Umar, R.S. Rawat, K.S. Tan, A.K. Kumar, R. Ahmad, T. Hussain, C. Kloc, Z. Chen, L. Shen, Z. Zhang, Nucl. Instrum. Methods Phys. Res. B **301**, 53–61 (2013)
109. E. Ghareshabani, R.S. Rawat, S. Sobhanian, R. Verma, S. Karamat, Z.Y. Pan, Synthesis of nanostructured multiphase Ti (C, N)/aC films by a plasma focus device. Nucl. Instum. Methods Phy. Res. B **268**, 2777–2784 (2010)
110. I. Zergioti, A. Hatziapostolou, E. Hontzopoulos, A. Zervaki, G.N. Haidemenopoulos, Pyrolytic laser-based chemical vapour deposition of TiC coatings. Thin Solid Films **271**, 96–100 (1995)

111. S. Scaglione, G. Emiliani, Mechanical properties (hardness and adhesion) of a-C:H thin films produced by dual ion beam sputtering. J. Vac. Sci. Technol. A **7**(3), 2303–2306 (1989)
112. F. Rabbani, Deposition and characterization of a-C:H coatings using a glow discharge. Surf. Coat. Technol. **187**, 54–62 (2004)
113. Z.A. Umar, R.S. Rawat, K.S. Tan, A.K. Kumar, R. Ahmad, T. Hussain, C. Kloc, Z. Chen, L. Shen, Z. Zhang, Hard TiC_x/SiC/a-C:H nanocomposite thin films using pulsed high energy density plasma focus device. Nucl. Instrum. Meth. Phys. Res. B **301**, 56–61 (2013)

Chapter 8
Research on IR-T1 Tokamak

Mahmood Ghoranneviss and Sakineh Meshkani

8.1 Introduction

According to estimates made by the Department of Economic and Social Affairs of the United Nations [1], the population of the world will keep increasing until it reaches 9 billion in 2050. Every one of these individuals needs access to energy resources. Furthermore, as the standards of living in third-world nations increase, the energy use per person will increase as well, causing an increase in the global need for energy that is even greater than the global increase in population. Taking this into account, the global energy usage may well increase to 30 TW, three times what is consumed today. At present, around 90% of the energy utilized by people is produced by burning fossil fuels (oil, coal, natural gas). Because of different economic and political interests, it is difficult to estimate the total reserves of these fossil fuels. It is estimated that the oil stores will last 20–30 years at the present rate of consumption, the natural gas reserves 50–60 years, and the coal 200 years. The uranium reserves on Earth, on the other hand, could last for over 2000 years at the present rate of consumption if breeder technology is employed [2]. The current record for the most efficient solar cell is 42% efficiency [3]. For a silicon solar cell, the record is 25% efficiency [4]. While research into high-efficiency solar cells continues, such cells may be uneconomical to produce in large quantities. Controlled thermonuclear fusion promises to provide a clean power source with sufficient fuel reserves to last far into the future [5].

M. Ghoranneviss · S. Meshkani (✉)
Plasma Physics Research Center, Science and Research Branch,
Islamic Azad University, Tehran, Iran
e-mail: s.meshkani@gmail.com

M. Ghoranneviss
e-mail: m_ghoranneviss29@yahoo.com; ghoranneviss@gmail.com

R.S. Rawat (ed.), *Plasma Science and Technology for Emerging Economies*,
DOI 10.1007/978-981-10-4217-1_8

8.2 Thermonuclear Fusion

It is a known fact that in nuclear fusion, two light nuclei fuse together to form a heavier nucleus and releases energy. For two nuclei to fuse, they must collide with enough energy to overcome the repulsive electrostatic force between them. In stars, hydrogen nuclei are fused due to high densities and long confinement times created by the intense pressure in the stellar core. In the laboratory, it is practically impossible to recreate the conditions necessary to fuse hydrogen. In order to control the nuclear fusion, a fuel mixture of deuterium and tritium needs to be heated to an adequately high temperature such that the thermal velocity of the cores is sufficiently high to overcome the Coulomb repulsion between them. To reach the deuterium-tritium fusion, the reaction cross section has the largest cross section of the possible fusion reactions in this energy and reaches a maximum at 100 keV (see Fig. 8.1). The reaction between deuterium and tritium can be shown as [6]:

$$ {}_1^2\mathrm{D} + {}_1^3\mathrm{T} \rightarrow {}_2^4\alpha\,(3.5\,\mathrm{MeV}) + {}_0^1\mathrm{n}\;(14.1\,\mathrm{MeV}) \tag{8.1} $$

This releases 17.6 meV in each reaction (Fig. 8.2). Though the cross section has a maximum at 100 keV, it is sufficient to heat the plasma to about 20 keV because the required reactions occur in the high-energy tail of the Maxwellian distribution. Additionally, due to the scaling of confinement time, the Lawson criterion is best met at plasma temperatures of around 10–20 keV. At temperatures of 20 keV, the fuel becomes a fully ionized plasma, where the electrostatic charge of the ions is balanced by that of electrons.

Deuterium is found mixed up (1 part in 6000) as heavy water (D_2O) in natural water. It is virtually inexhaustible. Tritium does not exist naturally because it has too

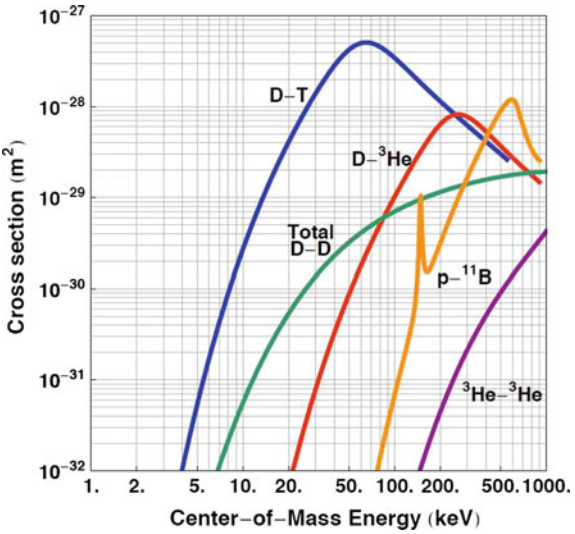

Fig. 8.1 Fusion cross sections of various fusion reactions as a function of center of mass energy [9]

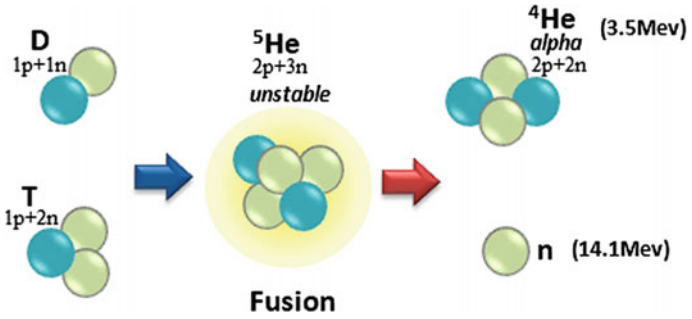

Fig. 8.2 Schematic of a D-T fusion reaction

many neutrons and undergoes β-decay with a half-life of 12.3 years. Therefore, the tritium necessary for fusion reactions must be reproduced by bombarding lithium with neutrons, as lithium is readily available in the Earth's crust and oceans [7]:

$$^{6}_{3}\mathrm{Li} + ^{0}_{1}\mathrm{n} \rightarrow ^{4}_{2}\mathrm{He} + ^{3}_{1}\mathrm{T} + 4.8\,\mathrm{MeV} \tag{8.2}$$

$$^{7}_{3}\mathrm{Li} + ^{0}_{1}\mathrm{n} \rightarrow ^{4}_{2}\mathrm{He} + ^{3}_{1}\mathrm{T} + ^{0}_{1}\mathrm{n} - 2.47\,\mathrm{MeV} \tag{8.3}$$

The ratio of ^{7}Li to ^{6}Li must be regulated in order to ensure that the amount of tritium bred exceeds that consumed in the reactor.

8.2.1 Confinement Fusion

To achieve the nuclear fusion on the Earth, a plasma of the fusion reactants with sufficiently high temperature and density needs to be achieved. Also, the plasma produced must be confined for a sufficiently long time away from any surrounding material walls. Inertial confinement fusion (ICF) and magnetic confinement fusion (MCF) are the two possible approaches to achieve this.

Inertial confinement fusion (ICF) is a type of fusion energy research that attempts to initiate nuclear fusion reactions by heating and compressing a small capsule of fuel by an intense pulse of laser light. The capsule is typically in the form of a pellet that most often contains a mixture of deuterium and tritium as follow [8]:

1. Laser beams of high-energy X-rays rapidly heat the surface of the fusion target, forming a surrounding plasma envelope (Fig. 8.3).
2. The fuel is compressed by the rocket-like blow-off of the hot surface material.
3. The fuel would ignite at 100–1,000,000 K when its density goes up to 20 times the density of the lead at the time of capsule breakdown.
4. Thermonuclear burn spreads rapidly through the compressed fuel, yielding many times the input energy.

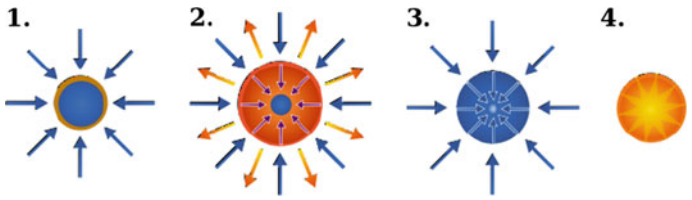

Fig. 8.3 Schematic of the stages of inertial confinement fusion using lasers. The *blue arrows* represent radiation; *orange* is blow-off; *purple* is inwardly transported thermal energy. Image made by Esham [8]

In magnetic confinement fusion, one utilizes the electromagnetic properties of the charged plasma particles to trap them away from material walls in a specifically designed magnetic field configuration called a magnetic bottle. This exploits the ability of a steady magnetic field to dramatically restrain the motion of the charged particles in a plasma across the magnetic lines of force, while allowing them to move freely along them. Research and development in the area of magnetic confinement fusion has given rise to a variety of confinement configuration concepts. Magnetic confinement fusion is the process of trapping the plasma particles by strong and non-uniform magnetic fields. The most successful configuration is a torus with the magnetic field pointing mainly in the toroidal direction based on the Tokamak concept.

8.3 Tokamak

The word Tokamak is an acronym for the Russian words for toroidal chamber with magnetic coils. In Tokamaks, the plasma is formed in the shape of a torus or a doughnut, through a specially designed magnetic field configuration. The main magnetic field is in a toroidal direction that is created by a solenoidal set of ring-like coils, the coils are placed around the torus toroidally. The curvature of the field lines leads to a charge separation and an electric field generation. Consequently, the plasma particles transport to the chamber wall. To confine the plasma particles, one needs an additional component of the magnetic field turning around on the minor cross section of the torus (poloidal magnetic field). This field is produced through the induced plasma current by the central solenoid (see Fig. 8.4).

The resultants of poloidal and toroidal magnetic field lines are the helical magnetic field lines that produce nested magnetic surfaces. In spite of the helical magnetic field, plasma particles expand toward the torus wall so a vertical field must be inserted into plasma. This field is provided through external coils (vertical field coils) and imposes a radial force on particles and moves them towards the chamber center; thus the plasma column achieves equilibrium. To raise the plasma temperature and D-T reaction rate, the plasma must be heated. There are three methods for plasma heating [9, 10]:

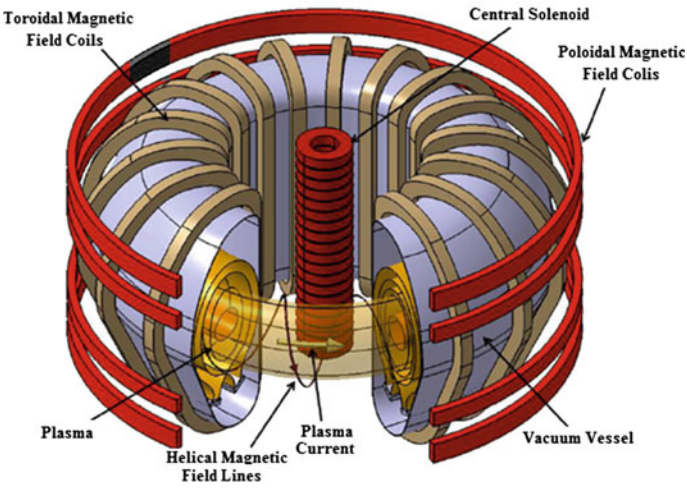

Fig. 8.4 Schematic representation of the magnetic field system of a Tokamak [10]

(1) Ohmic heating in intrinsic heating mechanism that is inherently produced through particle collisions. This is the main heating of all Tokamaks and can be effective in raising plasma temperatures only up to about 1 keV.
(2) Neutral beam injection (NBI) is a secondary heating in which energetic neutral particles are injected into the plasma and transfer energy to plasma particles to heat them to fusion temperatures.
(3) Radio frequency (RF) heating is a secondary method for plasma heating that includes electron cyclotron resonance heating (ECRH), lower hybrid range of frequencies (LHRF), ion cyclotron resonant heating (ICRH), and Alfvén waves.

8.4 IR-T1 Tokamak

IR-T1 is a small research Tokamak located at the Plasma Physics Research Center (PPRC). It is an air core Tokamak without a copper shell with major radius of $R = 45$ cm and a minor radius of $a = 12.5$ cm. This device consists of a vacuum vessel with a circular cross section that was made from a stainless steel welding structure with two toroidal breaks and a minor radius, $b = 15$ cm. The toroidal field in IR-T1 Tokamak is about 1 T and is produced by 16 coils that surround the torus toroidally [11]. The main parameters of IR-T1 Tokamak have been summarized in Table 8.1.

Table 8.1 The main parameters of IR-T1 Tokamak

Parameters	Value
Major radius	45 cm
Minor radius	12.5 cm
Toroidal field	<1.0 T
Plasma current	<40 kA
Discharge duration	<35 ms
Electron density	$0.7–1.5 \times 10^{13} cm^{-3}$
Toroidal field coils	16

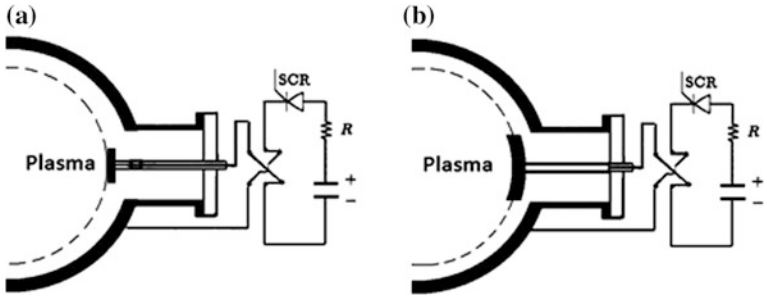

Fig. 8.5 Schematic of **a** electrode biasing and **b** limiter biasing in IR-T1

8.4.1 Biasing Systems in IR-T1 Tokamak

The biasing system in the Tokamak has played an important role in plasma confinement and in saving plasma energy by applying an electric field, especially at the edge of the plasma. The turbulence and particle transport are reduced by the radial current which is produced between the limiter biasing and the vacuum vessel [11]. IR-T1 Tokamak is equipped with three different types of biasing systems: (1) electrode biasing, (2) cold limiter biasing, and (3) emissive limiter biasing. These systems are illustrated in Fig. 8.5a, b. The electrode biasing consists of a circular disc with a diameter of 2 cm and thickness of 2 mm that is made of stainless steel (see Fig. 8.5a). Figure 8.5b is a limiter biasing system with a poloidal sector of stainless steel that has a thickness of 2 mm, a width of 2 cm and an arc length of 10 cm. Emissive limiter biasing and cold limiter biasing are the two types of limiter biasing that are being used in IR-T1 Tokamak. The difference between the cold and emissive biasing systems is determined by whether the tungsten filament inside the system is on or off. When turned on, the biasing system can heat the limiter biasing to a high temperature and can even cause electron emission into the plasma. When the filament is disconnected, the system is called cold limiter biasing. The schematic of emissive limiter biasing can be seen in Fig. 8.6.

The limiter or electrode biasing can be placed 1 cm into the Tokamak plasma to apply voltage ranges of −400 to +400 V and current ranges from −40 to +40 A between the vacuum chamber and the electrode.

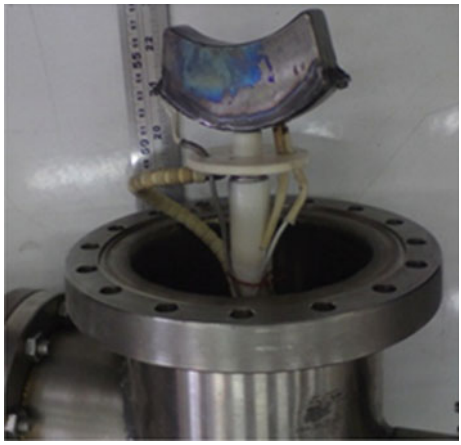

Fig. 8.6 Image of emissive limiter biasing in IR-T1

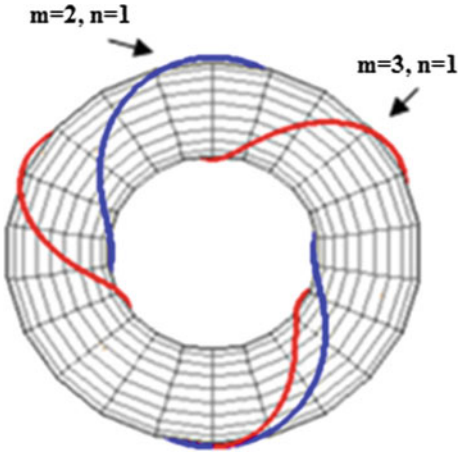

Fig. 8.7 Schematic of RHF on IR-T1

8.4.2 Resonant Helical Magnetic Field in IR-T1 Tokamak

Resonant helical magnetic field (RHF) is an external resonant helical magnetic field which can improve the Tokamak plasma confinement. The RHF in IR-T1 is created by two sets of local helical fields which are installed outside the vacuum vessel. This field is produced by two conductors with optimized geometry wound externally around the Tokamak torus with a given helicity. The ratio of the magnitude of the RHF perturbation to the main magnetic field is $\delta B/B = 1\%$. The minor radii of these helical windings are 22 cm ($L = 2$: $m = 2$, $n = 1$) and 23 cm ($L = 3$: $m = 3$, $n = 1$).

In the experiments presented here, the current through the helical windings was between 100 and 400 A, which is very low compared to the plasma current itself (25–30 kA). Figure 8.7 shows a typical schematic of RHF ($L = 2/1$ and $3/1$) on IR-T1 Tokamak [11].

8.5 Plasma Diagnostics in IR-T1 Tokamak

Plasma diagnostics is a novel branch of fusion science that requires understanding from all the physics fields. For magnetic confinement fusion, it is necessary to create the special experimental techniques for diagnostics. Generally, plasma diagnostic techniques are distinguished into two different classes: passive methods and active methods [10, 12]. Passive methods detect and study radiations that are emitted by the plasma while active methods measure plasma reactions to external stimuli. The performed measurements by former method give averaged information while latter method makes the local measurements. IR-T1 is an active Tokamak that performs extensive research into plasma diagnostic. There are many plasma diagnostics in IR-T1 Tokamak such as magnetic and electric diagnostics, and some of the diagnostics that measure based on passive methods are described in the following.

8.5.1 Magnetic Diagnostics

Tokamak is a magnetic device for plasma confinement, so magnetic measurements have played an important role in understanding plasma behavior. These measurements are performed using probes and coils that are sensitive to magnetic fields in different places within the plasma column.

8.5.1.1 Rogowski Coil

The Rogowski coil is a solenoid coil whose two ends are closed together and form a torus (Fig. 8.8) and can measure alternating current (AC). The Rogowski coil surrounds the Tokamak chamber and plasma column in the poloidal direction as the entire plasma current must pass through it. The plasma current produces a magnetic field around itself that induces an appropriate voltage in the Rogowski coil (Faraday's law of induction). According to the following equation, it is clear that the time evolution of the plasma current is proportional to the induced voltage [12]:

$$\frac{\mathrm{d}I}{\mathrm{d}t} = \frac{V}{NA\mu} \tag{8.4}$$

where A, N, μ, and V represent the cross-sectional area of the Rogowski coil, the number of solenoid turns, magnetic permeability of the material inside the solenoid, and the induced voltage in the Rogowski coil, respectively. The plasma current can be measured using an appropriate integrator which is connected to the coil.

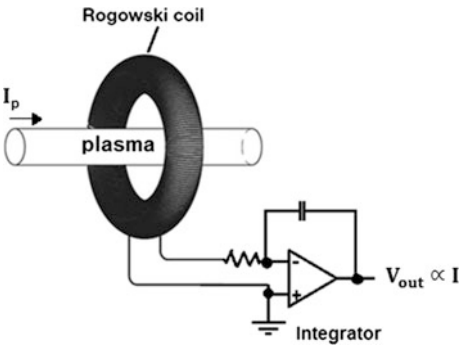

Fig. 8.8 Schematic representation of the Rogowski coil

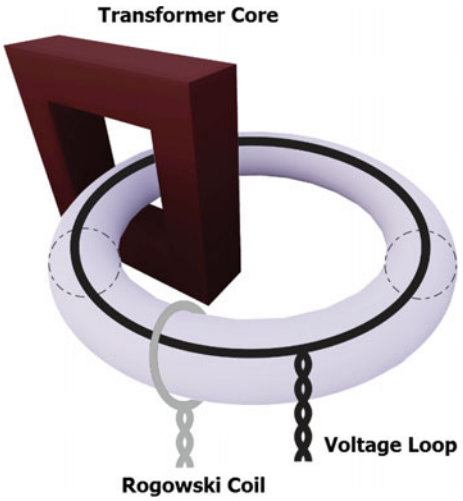

Fig. 8.9 Schematic of voltage loop and Rogowski coil installed on a Tokamak chamber

8.5.1.2 Loop Voltage

General information about the plasma impurities, plasma displacement, and plasma resistance can be obtained by the loop voltage. Toroidal loop voltage is often measured by a voltage loop that is a single wire placed along the Tokamak chamber (in the toroidal direction). In IR-T1 Tokamak, to increase the resolution of the loop voltage, four voltage loops are used at four angles of 0°, 90°, 180°, and 270°. Figure 8.9 illustrates a voltage loop and Rogowski coil installed on a Tokamak chamber.

8.5.1.3 Mirnov Coils

Mirnov oscillations and magneto hydrodynamic (MHD) instabilities in Tokamaks are detected using Mirnov coils. These coils are inductive sensors in the form of cylindrical coils that are placed in toroidal or poloidal configuration within a Tokamak. Variations in the magnetic flux density generated by moving charges induce voltage in the coils. Three different configurations of Mirnov coils have been placed in IR-T1 Tokamak. These configurations consist of an array of 12 poloidal Mirnov coils with a separation angle of 30°, an array of 8 poloidal Mirnov coils with a separation angle of 45° and an array of 12 radial Mirnov coils with a separation angle of 30°. These coils are installed inside the Tokamak chamber at a very small distance from the wall. Figure 8.10 presents the schematic of Mirnov coils installed in the Tokamak. In poloidal Mirnov coils, the axis of coils is in poloidal direction so the coils can detect poloidal fluctuations. Also, the axes of radial Mirnov coils are in the radial direction to sense radial magnetic fluctuations. Mirnov fluctuations play a very important role in the study of MHD instabilities, determination of plasma modes, and safety factor in Tokamaks.

Control of MHD Activity by Limiter Biasing System in IR-T1 Tokamak

MHD instabilities are responsible for various disruptions in plasma; these instabilities may cause destruction of magnetic surfaces and terminations of plasma discharges [13]. Consequently, the investigation and control of MHD phenomena in Tokamaks are of interest to researches around the world [14–16].

MHD instabilities are effective causes in radial dispersion of runaway electron, so IR-T1 group has performed many experiments to study and control MHD instabilities using singular value decomposition (SVD) and wavelet techniques [13]. To study the poloidal magnetic field fluctuations, dependent on the rotation of magnetic islands, one array of magnetic coils consisting of eight coils with a separation angle 45° is used. To investigate the external field effect on magnetic fluctuations, the emissive biased limiter is applied to the plasma. As mentioned in

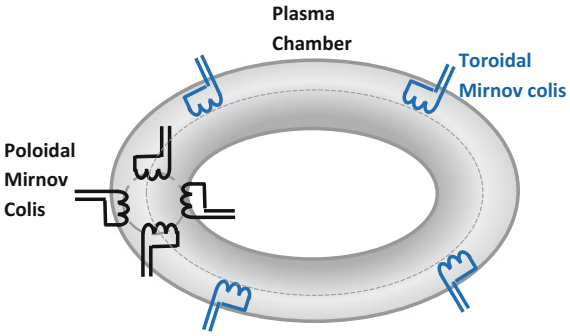

Fig. 8.10 Schematic of Mirnov coils in a Tokamak chamber

Sect. 8.4.1, an element is placed inside this limiter, which can regularly increase the temperature of the limiter using a separate DC power supply. If the power supply is turned on, the element with a heating current of 5 A will be heated and emit limiter electrons; consequently, the biased limiter is converted to an emissive biased limiter. If the power supply is off, then there will be a cold biased limiter. For this purpose, a biasing voltage with negative polarity (−200 V) is applied to the plasma when the plasma reaches relative stability. If the biasing voltage is applied before the plasma achieves stability, the plasma will collapse [11]. Then the signals detected by Mirnov coils are analyzed using SVD and wavelet techniques. In the following, wavelet and SVD techniques are described [17, 18]:

Wavelet Analysis

The wavelet transform method is a form of spectral analysis. A wavelet transformation decomposes a signal $x(t)$ into elementary functions $\psi_{a,b}(t)$ derived from a mother wavelet $\psi(t)$ by dilation and translation:

$$\psi_{a,b}(t) = \frac{1}{\sqrt{a}}\psi\left(\frac{t-b}{a}\right) \tag{8.5}$$

where b and $a > 0$ denote the position and the scale (dilation) of the wavelet, respectively. The wavelet transform of the signal $x(t)$ about the mother wavelet $\psi(t)$ is defined by the convolution integral:

$$W(a,b) = \frac{1}{\sqrt{a}}\int \psi^*\left(\frac{t-b}{a}\right)x(t)\mathrm{d}t \tag{8.6}$$

where ψ^* is the complex conjugate of $\psi(t)$ defined in the open time and scale real (b, a) half plane. There are many mother wavelets but the Morlet mother wavelet is very well suited to the experimental data analysis because it has a Gaussian envelope. It allows us to reach a reasonable compromise between the temporal and the frequency resolutions which is given by:

$$\psi_0(\eta) = \pi^{-\frac{1}{4}}\mathrm{e}^{i\omega_0\eta}\mathrm{e}^{\left(-\frac{\eta^2}{2}\right)} \tag{8.7}$$

where η is time and ω_0 is the wave number. The wave number is the number of oscillations within the wavelet itself. In this experiment, the Mirnov analysis was based on the use the Morlet wavelet [19, 20].

SVD Analysis

SVD is a powerful mathematical tool well suited to studying spatially extended systems. It detects the signal features which are relevant to the dynamics of the system as a whole. A brief description of the technique follows. Consider a time series of M-dimensional vectors $x(t) = [x_1(t), \ldots, x_M(t)]$, where the components $x_j(t)$ are simultaneous measurements of the same physical quantity at different position (channels). For practical objectives, the time series is sampled every T_s

seconds, which leads to the study of a set of N vectors $x(0)$, $x(T_s)$, …, $x((N-1)\,T_s)$. One can equivalently build an $N \times M$ rectangular matrix:

$$X = \frac{1}{\sqrt{N}} \begin{bmatrix} x(0) \\ x(T_s) \\ \cdot \\ \cdot \\ \cdot \\ x((N-1)T_s) \end{bmatrix} = \begin{bmatrix} x_1(0) & \cdots & x_M(0) \\ \vdots & \ddots & \vdots \\ x_1((N-1)T_s) & \cdots & x_M((N-1)T_s) \end{bmatrix} \tag{8.8}$$

whose components are then $x_{ij} = \frac{1}{\sqrt{N}} x_j((i-1)t_s)$ (row index and column index represent the time and channel, respectively). The singular value decomposition expresses X in terms of the following product of matrices [18]:

$$X = VSU^{\mathrm{T}} \tag{8.9}$$

where S is an $M \times M$ diagonal matrix:

$$S_{ij} = \delta_{ij} s_i \tag{8.10}$$

And the quantities $s_i \geq 0$ are called singular values of X, V is an $N \times M$ matrix with orthonormal columns $v^{(j)} = V_{ij}$, $v^{(j)} v^{(k)} = \delta_{jk}$.

U is an $M \times M$ orthonormal matrix. SVD is the analogue of the similarity transformation which diagonalizes a square matrix. The SVs are the analogue of the eigenvalues, while the U columns $u^{(j)} = U_{ij}$ are the analogue of the eigenvectors; therefore, Eq. (8.9) is equivalent to $X_{ij} = V_{ik} s_k U_{jk} = v_i^{(k)} s_k u_j^{(k)}$.

The vectors $u^{(j)}$, called principal axes, form an orthonormal basis on which the signal is decomposed. The projections of X along U (i.e., the product VS) are the principal components (PC) of X. They give the time evolution of the signal along the correspondent principal axis. This means that the original time series $X(t)$ is now described as a sum of time series each along the new coordinate axis $u^{(j)}$.

Fourier analysis and SVD are two common methods for mode detection in Tokamaks but when plasma activity and m (poloidal mode number) are relatively high ($m > 3$), the energy is balanced between modes and the phase of modes is close together. In this case, Fourier analysis is less capable than SVD for recognizing all modes [21, 22].

To study limiter biasing effects on plasma parameters, a long pulse is applied to the plasma at 10 ms for as long as the plasma persists. This study investigates how this long pulse (or DC pulse) affects MHD modes, time evolution and plasma rearrangement after that. Figure 8.11 shows the time evolution of plasma parameters such as plasma current (I_p), loop voltage (V_{loop}), biasing current ($I_{biasing}$), H-alpha radiation (H_α), and floating potential ($V_{fl.}$). As mentioned earlier, plasma current and loop voltage are measured by a Rogowski coil and voltage loop. H-alpha radiations and floating potential are measured by a single channel visible H_α

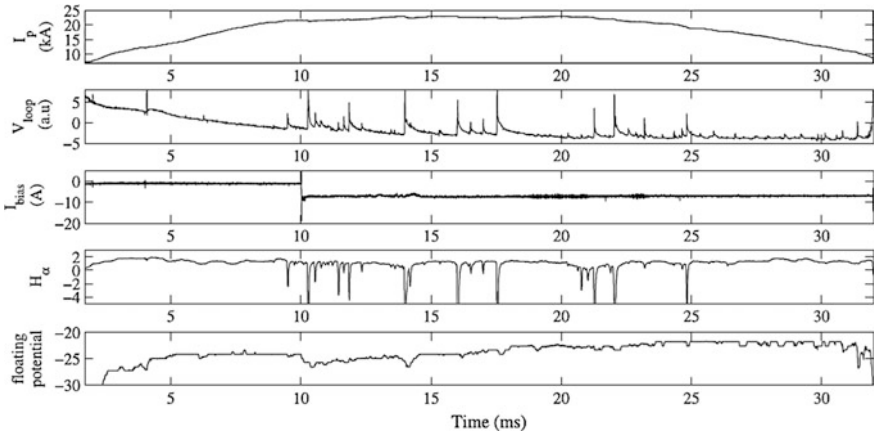

Fig. 8.11 The temporal evolution of plasma current (I_p), loop voltage (V_{loop}), biasing current ($I_{biasing}$), *H*-alpha radiation (H_α) and floating potential (V_f). Emissive biased voltage (−200 V) is applied at t = 10 ms

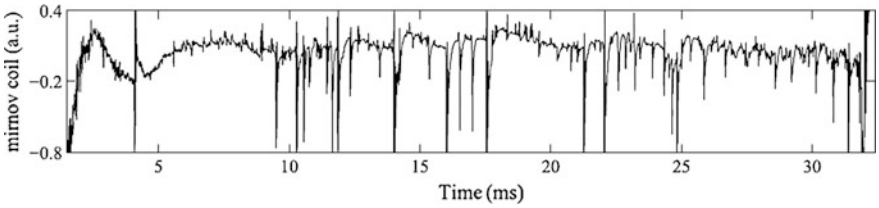

Fig. 8.12 The temporal evolution of magnetic fluctuations measured by a Mirnov coil

spectrometer and electric probes, respectively, as will be described later. The results show that the floating potential and consequently electric field are reduced after the application of a biasing voltage. The temporal evolution of magnetic fluctuations measured by a Mirnov coil is illustrated in Fig. 8.12. This signal is the same $x(t)$ input mentioned in Eq. (8.8). For this analysis, the time interval of 8–12 ms was chosen. As the sample rate of data acquisition is 0.5 l s, there were 8000 data points in this interval.

Figure 8.13a, b show the spectrum obtained from wavelet analysis in the time range of 8–12 ms without applying emissive biased limiter and after applying it, respectively. Figure 8.13b shows the effect of emissive biased limiter on MHD activity which is associated with the signal shown in Fig. 8.12 The comparison between Fig. 8.13a, b shows that the MHD frequency decreases from 45 to 25 kHz after applying the biasing voltage. This reduction can be due to mode suppression.

Mirnov fluctuations are analyzed by SVD method to investigate MHD mode energies. For this purpose, time intervals of 7–22 ms are divided into 15 smaller time intervals of 1 ms each, and SVD is run for all of the smaller intervals

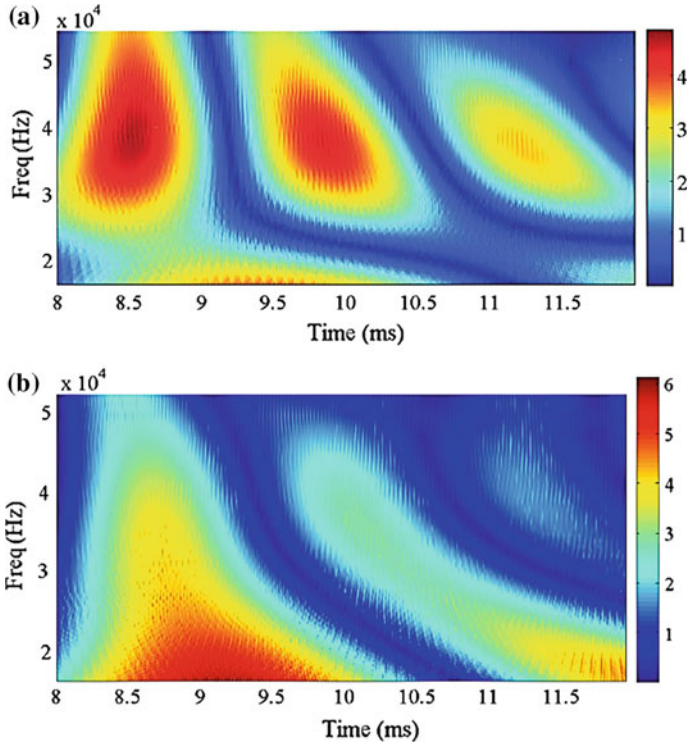

Fig. 8.13 Morlet wavelet spectrum of one Mirnov signal in the time range of 8–12 ms **a** without and **b** with applying emissive biased limiter. Biased voltage is applied at t = 10 ms

separately. SVD can extract the spatial features of MHD modes in the form of eigenvectors called principal axis (PAs). PAs of the dominant poloidal MHD modes and their temporal evolution are presented in Fig. 8.14 for 15 small time intervals. The toroidal mode number corresponds to n = 1 in this discharge, which is the typical case for most IR-T1 discharges [13].

The relative mode spectra of PAs for 15 small time intervals without applying biasing voltage are illustrated in Fig. 8.15 and Table 8.2. In all time intervals, the dominant mode is m = 3 and no mode suppression is observed. Relative mode spectra of PAs shows that the coupled mode of the first PA (7–8 ms) consists mainly of m = 3 mode (99.36%) and m = 4 mode (0.561%) as shown in Fig. 8.16 and Table 8.3. Other modes (i.e., m = 1 and m = 2) also appear in the spectrum with no significant contribution to the global mode amplitude. Subsequently, for the 14 other small time intervals, the energies of 1–4 modes are illustrated in Table 8.3.

As mentioned above, before applying the biasing voltage the dominant mode is m = 3; however, the biasing voltage causes an increase of the energy of mode m = 2 and at around 1 ms after applying biasing, the energy of mode m = 3 is suppressed and mode m = 2 becomes the dominant mode. It is clear that 5 ms after

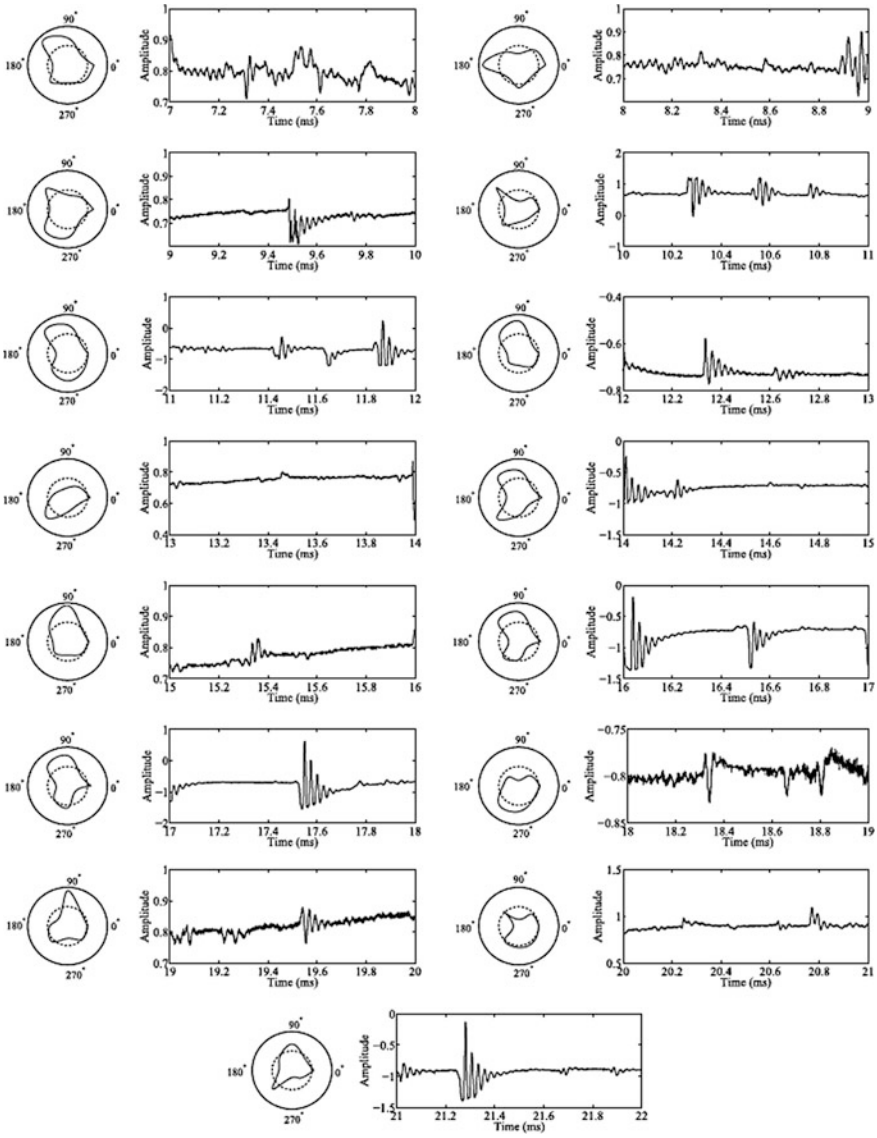

Fig. 8.14 Spatial and temporal structures of the dominant poloidal mode at 15 time windows. Emissive biased limiter is applied at t = 10 ms

applying the biasing voltage mode m = 2 is suppressed and mode m = 3 increased. The results demonstrate that an emissive biased limiter with negative voltage affects MHD modes.

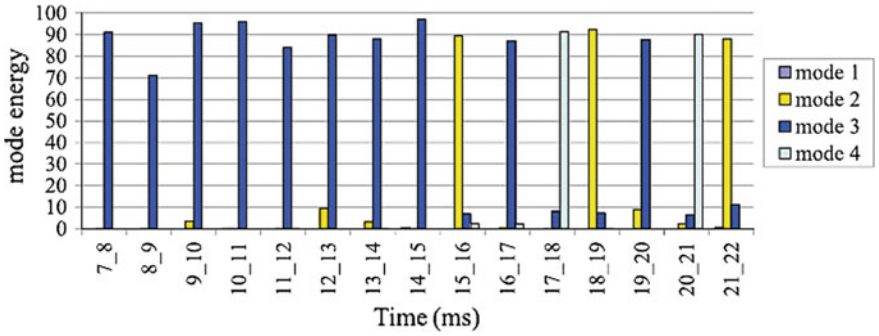

Fig. 8.15 Relative mode spectra of PAs for 15 small time intervals without applying biasing voltage. No mode suppression is observed

Table 8.2 MHD mode energies at 15 small time interval without applying biased voltage

Time (ms)	$m = 1$	$m = 2$	$m = 3$	$m = 4$
7–8	0	0.14	91.06	0
8–9	0	0.14	71.17	0
9–10	0	3.5	95.52	0
10–11	0.009	0.02	96.08	0
11–12	0	0.04	84.1	0.1
12–13	0	9.43	89.82	0
13–14	0	3.25	87.98	0.01
14–15	0.28	0.06	97.04	0
15–16	0	89.54	6.93	2.41
16–17	0	0.22	86.88	2.14
17–18	0	0.08	7.98	91.46
18–19	0	92.27	7.34	0.024
19–20	0	8.95	87.61	0
20–21	0	2.23	6.37	90.19
21–22	0.67	88.04	11.09	0

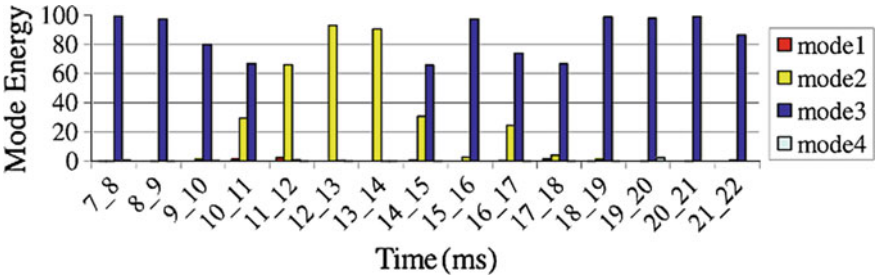

Fig. 8.16 Relative mode spectra of PAs for 15 small time intervals. To apply emissive biased limiter, dominant mode from $m = 3$ changes to $m = 2$

Table 8.3 MHD mode energies at 15 small time intervals in the presence of a biasing voltage

Time (ms)	$m = 1$	$m = 2$	$m = 3$	$m = 4$
7–8	0.006	0.053	99.36	0.561
8–9	0	0.008	97.07	0.042
9–10	0	1.09	79.63	0.347
10–11	1.124	29.264	66.481	0
11–12	1.98	65.867	0.848	0.022
12–13	0	92.728	0.195	0.0787
13–14	0	90.303	0.0455	0.025
14–15	0.714	30.579	65.455	0.024
15–16	0	2.64	97.07	0
16–17	0.35	24.46	73.97	0.0077
17–18	1.613	3.825	66.486	0.023
18–19	0.014	1.18	98.56	0.0022
19–20	0	0.058	97.85	2.03
20–21	0	0.0353	98.93	0
21–22	0	0.45	86.5	0

Study of Magnetic Islands Width in IR-T1 Tokamak

Macroscopic instabilities can affect Tokamak plasmas and lead to the reduction of their effectiveness [9]. One of these, tearing modes, is relatively slow growing instabilities which finally saturate with the process reconnecting magnetic flux surfaces to create magnetic islands. Magnetic islands cause a flow of heat and particles along field lines from inner to outer radii and finally the reduction of plasma confinement [23]. In fusion devices, magnetic islands mostly rotate at a kilohertz range of frequencies. Magnetic island rotation leads to rotating perturbations in the magnetic field, density, and temperature [24]. Since the amplitude and frequency depend on time evolution, the application of signal analysis techniques to capture the island dynamics is necessary. There are several experiments that demonstrate that the radial electric field induced by a biasing system can modify MHD activities [25, 26]. In the resistive plasma, the helical current $j_{\mathrm{h}} = \frac{v_{\mathrm{r}} B_\theta}{\eta_\parallel}$ is produced by $\vec{v}_{\mathrm{r}} \times \vec{B}_\theta$ where v_{r} is a radial flow of plasma across B_θ. The resulting Lorentz force $\left|\vec{j}_{\mathrm{h}} \times \vec{B}_\theta\right| \approx \frac{v_{\mathrm{r}}}{\eta_\parallel} B_\theta^2$ usually opposes the original fluid motion across the magnetic field and is finite in the limit that the plasma resistivity vanishes, $\eta_\parallel \to 0$. It may be considered as a mechanism of plasma field coupling or freezing of magnetic field lines and plasma embodied in the ideal Ohm's law, $\vec{E} + \vec{V} \times \vec{B} = 0$ [27].

Slipping of plasma through the field and the subsequent reconnection of the field can occur at the null layer centered on the resonant surface. As B_θ vanishes at the resonance even in the presence of small resistance, the restoring Lorentz force also vanishes and consequently fast diffusion, reconnection, and magnetic island formation are still feasible in a narrow resistive boundary layer about the rational

surface [28]. As the magnetic islands change the topology of the overall magnetic field and degrade plasma confinement when their width becomes greater, the complete loss of plasma can occur. So, determination of the width of magnetic islands and obtaining a proper technique to reduce them in plasma is a fundamental objective in Tokamaks. Therefore, in this section, the effect of limiter biased voltage on width and frequency of magnetic islands is studied. In the results reported in this experiment, the magnetic island width can be calculated from the following approximate formula [29]:

$$\frac{w}{r_s} = 2\sqrt{\frac{2}{m}\left(\frac{r_c}{r_s}\right)^m \frac{\delta B_\theta}{B_\theta}} \tag{8.11}$$

where r_s and m are mode rational surface radius and poloidal mode number, respectively. Also, $r_c = 18$ cm is the radius of the detecting Mirnov coil. It is customary to consider the relative amplitude, $\frac{\delta B_\theta}{B_\theta}$, where B_θ is the unperturbed poloidal field. To obtain δB_θ for the four different cases mentioned above, the time interval of 8–12.2 ms is divided into 14 smaller and equal time intervals of 300 μs; then in each of these intervals, one of the Mirnov coil signals (of relevant shot) is integrated over the time interval of 300 μs. The obtained result is used in relation (8.11). It is noticeable that the biasing voltage is applied at $t = 10$ ms. The poloidal mode number in relation (8.11) is obtained from SVD analysis of Mirnov coil signals (M8) in each of the time intervals of 300 s. r_s in this relation can be extracted from the following relation:

$$q = \frac{m}{n} = 5 \times 10^6 \times \frac{B_T r_s^2}{R I_p} \tag{8.12}$$

In this relation, B_T, I_P, R, q, and m are the toroidal magnetic field, the plasma current, the radius of Tokamak major, the safety factor, and the poloidal mode number, respectively. In order to investigate the frequency of magnetic islands, wavelet analysis of the Mirnov coil signal is used as mentioned earlier. In this section, the influence of the biased limiter in two situations (cold and emissive) on the magnetic island's width is investigated. For this purpose, the biasing voltage is exerted in two polarities: positive (+380 V) and negative (−380 V). Figure 8.17a–d illustrate the time evolution of plasma parameters such as plasma current, *H*-alpha radiation, loop voltage, and electron density in the presence of the cold biased limiter in positive polarity (+380 V), cold biased limiter in negative polarity (−380 V), emissive biased limiter in positive polarity (+380 V), and emissive biased limiter in negative polarity (−380 V), respectively. Clearly, it is observable that the emissive biased limiter is more effective in the reduction of loop voltage fluctuations and *H*-alpha radiation. On the other hand, positive polarity of the emissive biased limiter is much more effective in the reduction of loop voltage

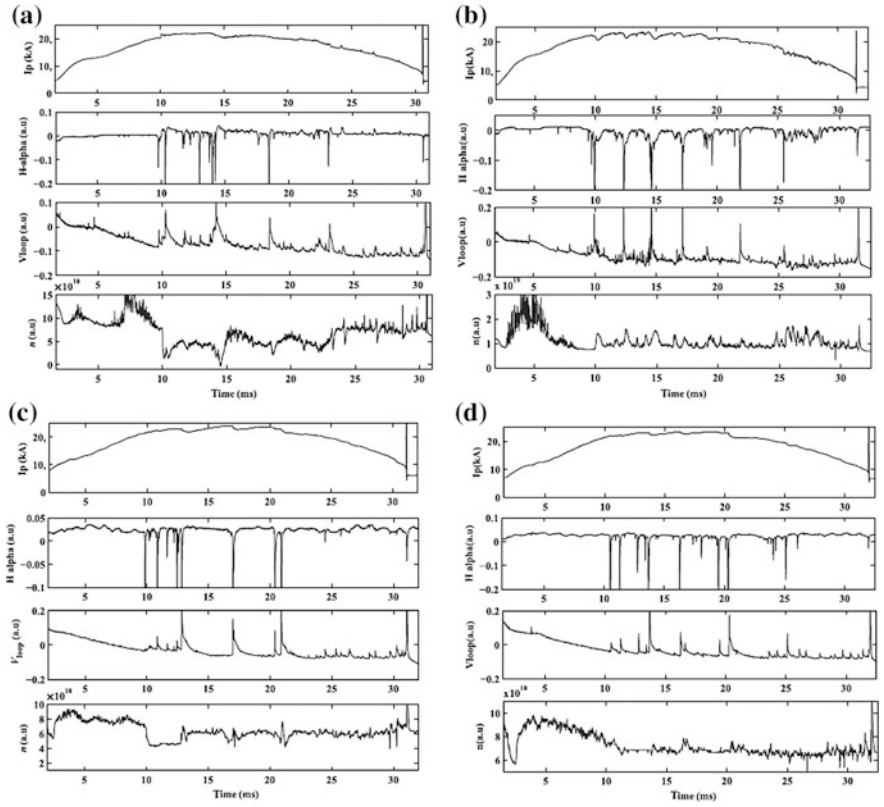

Fig. 8.17 The time evolution of plasma current, *H*-alpha radiation, V_{loop} and electron density in the presence of **a** cold biased limiter +380 V, **b** cold biased limiter −380 V, **c** emissive biased limiter +380 V and **d** emissive biased limiter −380 V. In all cases, the biasing voltage was applied at t = 10 ms until the end of the shot

fluctuations and *H*-alpha radiation and consequently plasma stability increases. Also, it can be seen that in presence of the cold biased limiter with negative voltage, *H*-alpha radiation is the highest value.

To study the biasing voltage effect on the rotation frequency of magnetic islands, a Mirnov signal from each of the conditions mentioned above, in the time interval 8–12 ms, is studied using wavelet analysis. The effect of limiter biasing on the rotation frequency of magnetic islands is investigated in Fig. 8.18a–d for different conditions. The results demonstrate that the emissive biased limiter with positive voltage is the most effective on the magnetic islands frequency (see Fig. 8.18c). This figure was taken 1 ms after applying the biasing voltage and shows that the magnetic island's frequency reduces from 50 to 25 kHz. Clearly, no reduction is found in the magnetic island's frequency after applying the cold biased limiter in negative polarity, as observed in Fig. 8.18b. It can be concluded that the emissive biased limiter has a greater effect on the reduction of magnetic island frequency

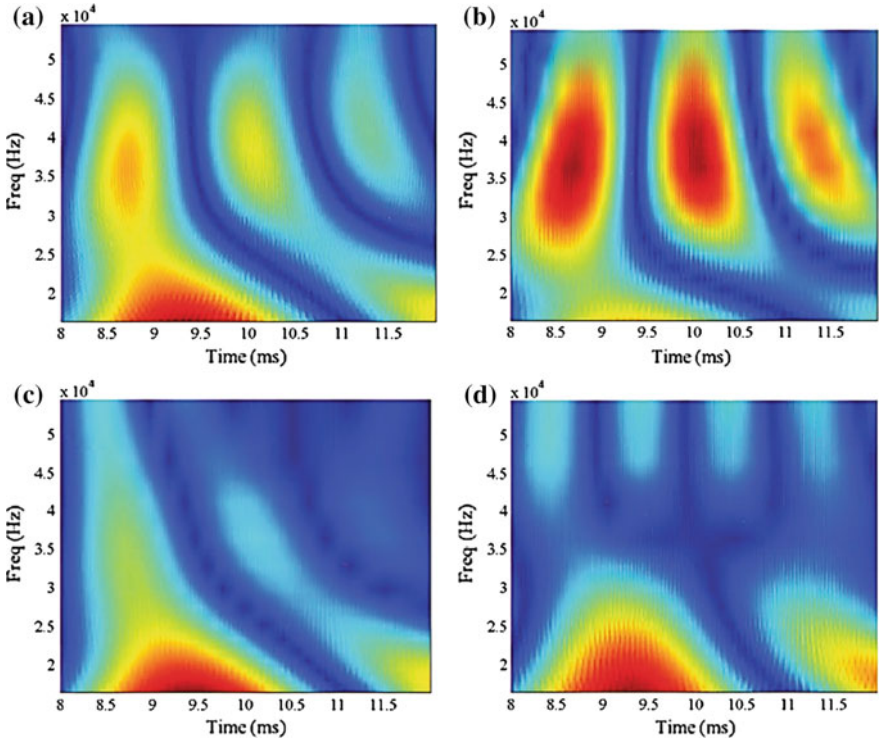

Fig. 8.18 Morlet wavelet spectrum of one Mirnov signal in the time range of 8–12 ms with applying **a** cold biased limiter with voltage +380 V, **b** cold biased limiter with voltage −380 V, **c** emissive biased limiter with voltage +380 V and **d** emissive biased limiter with voltage −380 V. Biased voltage is applied at $t = 10$ ms

compared to the cold biased limiter. Comparatively, between the positive and negative polarities of emissive biased limiter, the positive polarity is more influential.

To study the dominant poloidal MHD mode and temporal evolution of them in different conditions, a time interval of 8–12.2 ms for Mirnov fluctuations was chosen for SVD analysis (see Figs. 8.19, 8.20, 8.21 and 8.22). In order to investigate the limiter biased effect, Mirnov fluctuations were analyzed 2 ms before applying the biasing voltage and 2 ms after applying the biasing voltage. The time interval is divided into 14 smaller time intervals (of 300 μs each), and SVD is run for all of the smaller intervals individually. The effect of the cold biased limiter and the emissive biased limiter with positive and negative voltages on the dominant poloidal mode number (Dpmn), the dominant mode energy and magnetic island width in 14 time intervals are summarized in Table 8.4a–d. The results show that the emissive biased limiter with both negative and positive voltages immediately reduces the dominant poloidal mode number and the magnetic island's width.

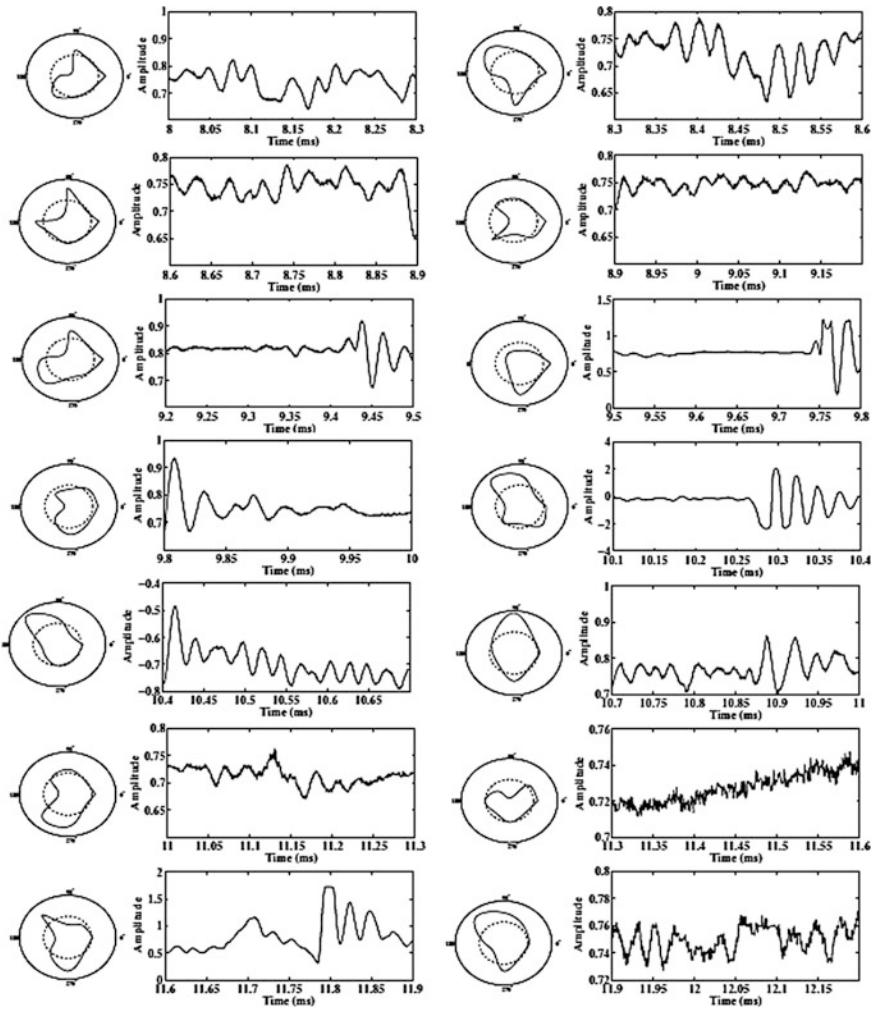

Fig. 8.19 Spatial and temporal structures of the dominant poloidal mode at 14 time windows. Cold biased limiter with positive voltage (+380 V) is applied at t = 10 ms

It is noticeable that the positive voltage is more effective than the negative voltage at reducing the magnetic island's width, as observed in Table 8.4c, d. Table 8.4a demonstrates that the magnetic island's width reduces around 1 ms after applying the cold biased limiter with positive voltage. It can be observed immediately after applying the biasing voltage that the energy mode m = 3 reduces while simultaneously the energy mode m = 4 increases (with energy 26.29 eV); however, in the following time interval the plasma goes to a more stable mode of m = 2, and these modifications have finally led to a reduction in the width of the magnetic islands. It is clear from Table 8.4b, that the cold biased limiter with negative

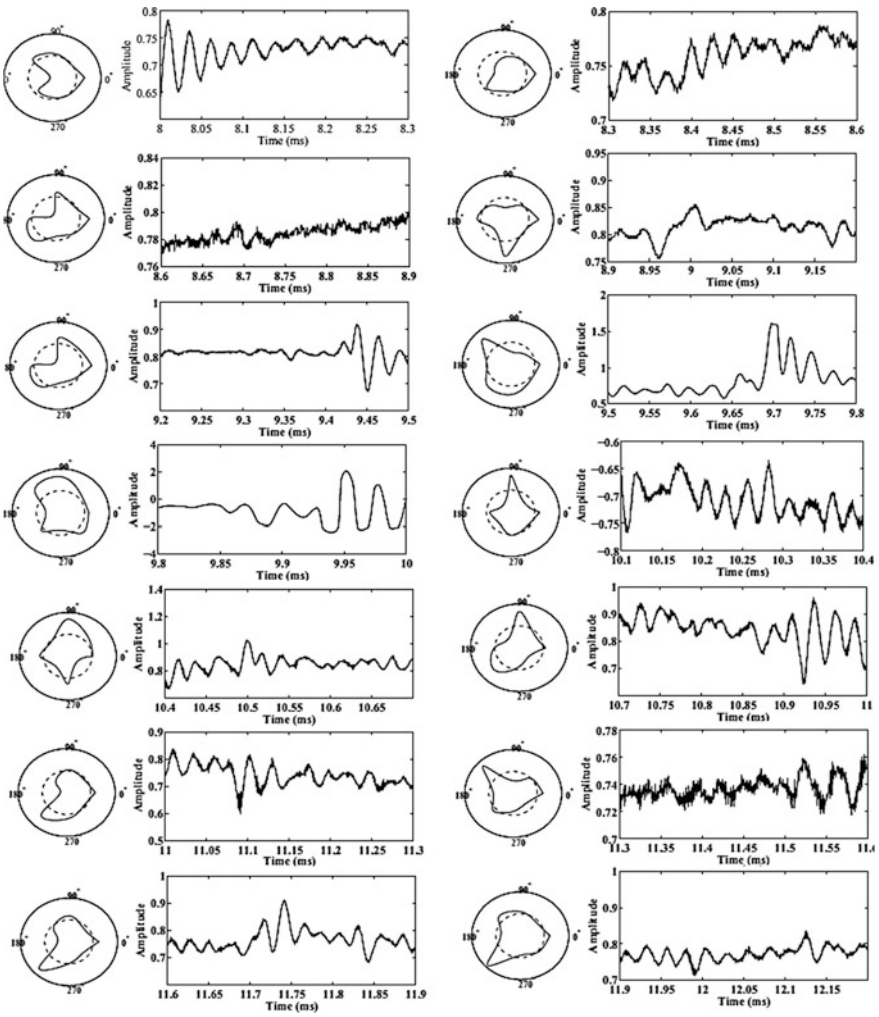

Fig. 8.20 Spatial and temporal structures of the dominant poloidal mode at 14 time windows. Cold biased limiter with negative voltage (−380 V) is applied at t = 10 ms

voltage causes an increase in the plasma instability. In the present case, immediately after applying the biasing voltage, mode m = 4 becomes the dominant mode and the magnetic island's width increases.

8.5.1.4 Magnetic Probes

To improve the plasma confinement, it is necessary to prevent contact between the plasma and Tokamak wall. Control of plasma position and stability can be studied

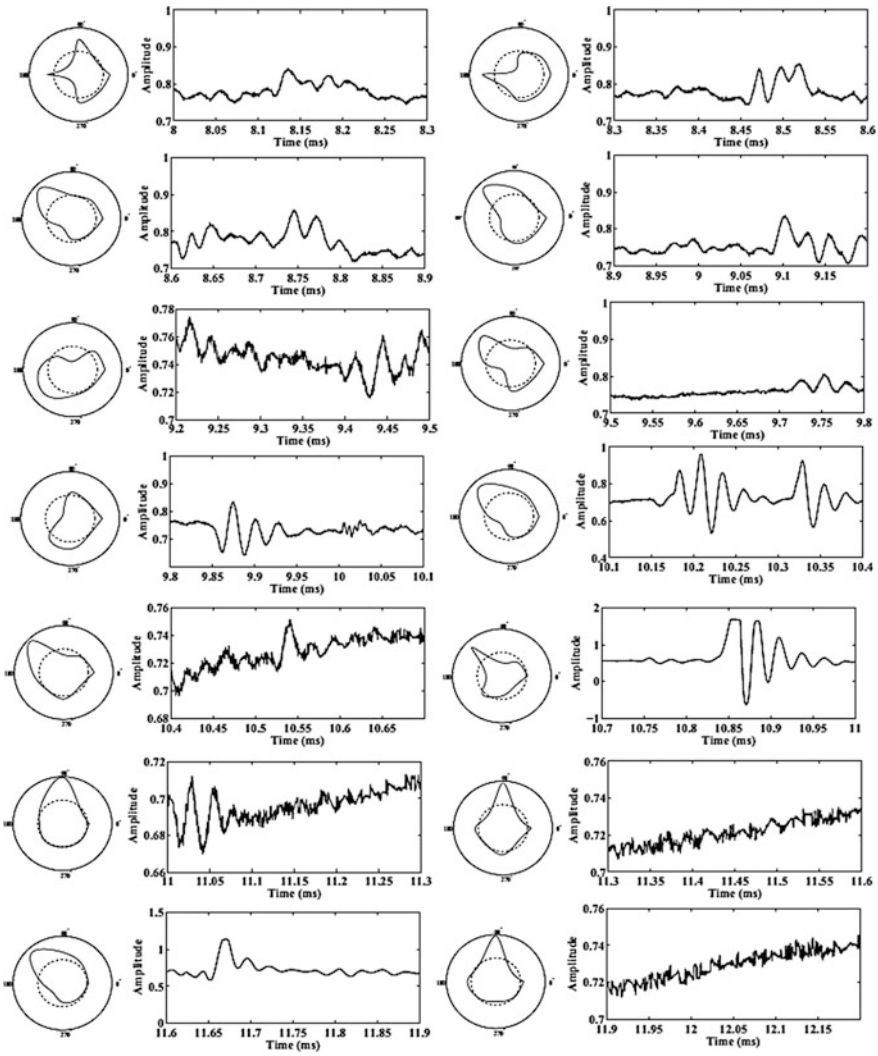

Fig. 8.21 Spatial and temporal structures of the dominant poloidal mode at 14 time windows. Emissive biased limiter with positive voltage (+380 V) is applied at t = 10 ms

using magnetic probes or diamagnetic loops that work based on Faraday's law. In IR-T1 Tokamak, an array of four magnetic probes has been installed in a circle with radius of 16.5 cm. Two magnetic probes were placed at angles of $\theta = 0$ rad and $\theta = \pi$ rad to determine the tangential magnetic field and two other probes were located at angles of $\theta = \frac{\pi}{2}$ rad and $\theta = 2\pi$ rad to determine the normal magnetic field [30]. The position of these probes is shown in Fig. 8.23.

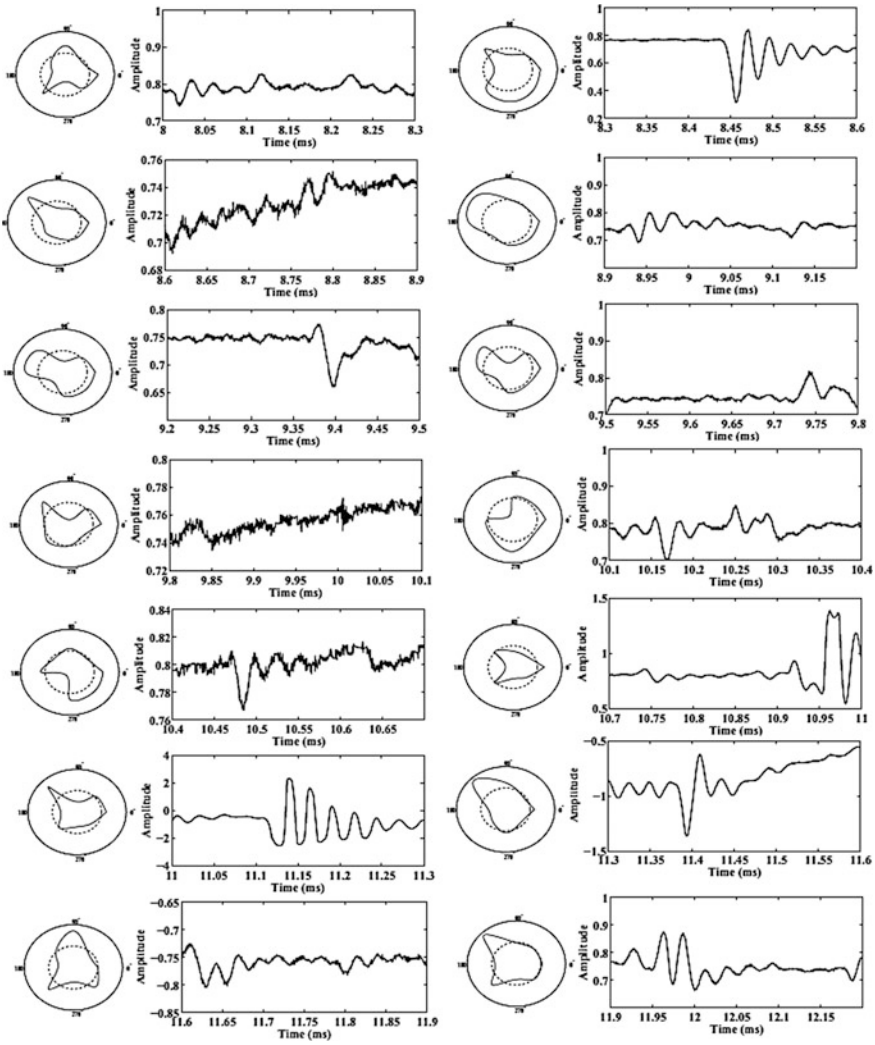

Fig. 8.22 Spatial and temporal structures of the dominant poloidal mode at 14 time windows. Emissive biased limiter with negative voltage (−380 V) is applied at t = 10 ms

Poloidal beta is an essential factor for determining optimized operation in Tokamaks. Poloidal beta can determine other parameters of a plasma such as internal inductance, plasma energy, and plasma confinement time. Poloidal beat is often specified by toroidal magnetic flux measured by a diamagnetic loop.

A diamagnetic loop is a simple wire loop that surrounds the Tokamak chamber in a poloidal direction as shown in Fig. 8.24. It is noticeable that this loop can be located either inside or outside of vacuum chamber. Intrinsically this loop will also detect the toroidal magnetic flux from the toroidal field coil and any current

Table 8.4 The dominant poloidal mode number (Dpmn), the dominant mode energy and magnetic island width in the presence of (a) cold biased limiter with positive polarity, (b) cold biased limiter with negative polarity, (c) emissive biased limiter with positive polarity and (d) emissive biased limiter with negative polarity

Time (ms)	Dpmn	Energy	Island width (cm)
(*a*)			
8–8.3	3	98.14	3.19
8.3–8.6	3	96.77	3.16
8.6–8.9	3	98.42	3.14
8.9–9.2	3	98.78	3.11
9.2–9.5	3	99.17	3.08
9.5–9.8	3/2	68.30/29.70	3.06
9.8–10.1	3	93.21	3.03
10.1–10.4	3/4	60.39/29.26	3.01
10.4–10.7	2	93.10	2.28
10.7–11	2	99.27	2.26
11–11.3	3	95.06	2.93
11.3–11.6	3	99.15	2.90
11.6–11.9	3/2	80.11/18.79	2.86
11.9–12.2	2	98.30	2.17
(*b*)			
8–8.3	3	94.73	3.06
8.3–8.6	3	98.74	3.04
8.6–8.9	3	99.67	3.02
8.9–9.2	3	98.10	2.99
9.2–9.5	3	91.48	2.97
9.5–9.8	3	80.01	2.94
9.8–10.1	3/4	73.52/15.91	2.92
10.1–10.4	4	93.13	3.52
10.4–10.7	4	98.99	3.49
10.7–11	3	98.92	2.84
11–11.3	3	96.02	2.80
11.3–11.6	3	98.43	2.79
11.6–11.9	3	91.68	2.75
11.9–12.2	3	98.001	2.72
(*c*)			
8–8.3	4	99.67	4.39
8.3–8.6	2	99.49	2.61
8.6–8.9	2	99.08	2.59
8.9–9.2	3	99.10	3.36
9.2–9.5	2	99.09	2.55
9.5–9.8	3	98.25	3.30
9.8–10.1	3	78.75	3.26

(continued)

Table 8.4 (continued)

Time (ms)	Dpmn	Energy	Island width (cm)
10.1–10.4	2	84.11	2.49
10.4–10.7	2	98.89	2.47
10.7–11	3/2	57.36/38.37	3.18
11–11.3	2	97.38	2.41
11.3–11.6	4	99.76	3.98
11.6–11.9	2/1	78.34/21.21	2.36
11.9–12.2	3	99.80	3.04
(*d*)			
8–8.3	3	99.75	2.06
8.3–8.6	2/3	65.57/32.52	2.16
8.6–8.9	2	99.39	2.15
8.9–9.2	2	98.34	2.13
9.2–9.5	2	97.35	2.11
9.5–9.8	3	98.41	2.56
9.8–10.1	3	97.93	2.53
10.1–10.4	2	97.16	2.06
10.4–10.7	2	97.95	2.04
10.7–11	3	79.70	2.46
11–11.3	3	73.15	2.44
11.3–11.6	2	90.16	1.98
11.6–11.9	3	99.43	2.39
11.9–12.2	3	97.35	2.36

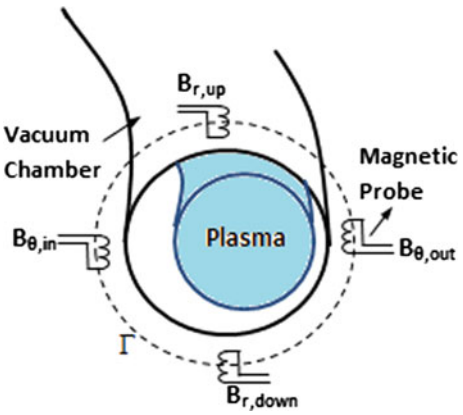

Fig. 8.23 Schematic of the position of the magnetic probes in IR-T1 Tokamak

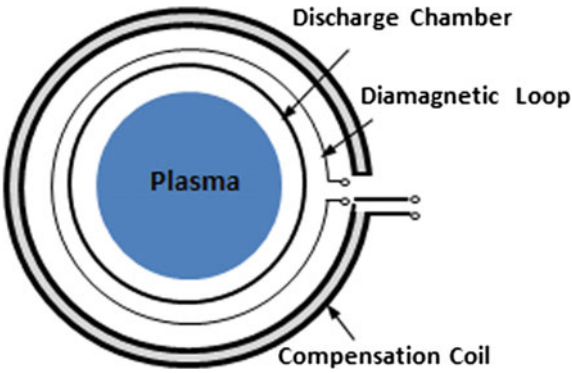

Fig. 8.24 Schematic presentation of the diamagnetic loop and compensation coil in IR-T1 Tokamak

Table 8.5 Design parameters of the magnetic probe and diamagnetic loop [30]

Parameters	Magnetic probe	Diamagnetic loop
R (Resistivity)	33 Ω	100 Ω
L (Inductance)	1.5 mH	20 mH
n (Turns)	500	170
S (Sensitivity)	0.7 mV/G	0.5 V/G
f (Frequency response)	22 kHz	5 kHz
Effective nA	0.022 m^2	16 m^2
d (Wire diameter)	0.1 mm	0.2 mm
d_m (Coil average radius)	3 mm	175 mm

circulating in the poloidal plane, particularly the toroidal field coil current, eddy currents in the conducting vacuum chamber induced during transient changes in the plasma energy, and plasma current. In other words, the diamagnetic loop consists of a simple loop that links the plasma column, ideally located in a poloidal direction in order to minimize detecting the poloidal field. The parameters of the magnetic probes and diamagnetic loop installed on IR-T1 Tokamak are summarized in Table 8.5.

Determination of the Toroidal Field Ripple and Shafranov Parameter by Discrete Magnetic Probes

The toroidal magnetic field can be analyzed by the following simple relationship [30]:

$$B_{\varnothing}(\theta, \varnothing) = B_0(1 - \rho \cos \theta - A \cos N\varnothing) \tag{8.13}$$

where B_0, θ and $\varnothing$ indicate the toroidal magnetic field at the center of the chamber, and poloidal and toroidal angles, respectively. Also ρ and N are the inverse aspect

ratio and the number of toroidal field coils (TFCs), respectively. The amplitude of the toroidal field ripple, A, is determined as follows:

$$A = \frac{\delta B}{\langle B_{\varnothing} \rangle} \approx \frac{B_{\mathrm{Max}} - B_{\mathrm{Min}}}{B_{\mathrm{Max}} + B_{\mathrm{Min}}} \tag{8.14}$$

In IR-T1 Tokamak, $N = 16$ and $\rho = 0.278$. The amplitude of the toroidal field ripple depends on the poloidal angle, so to determine the amplitude of the toroidal field ripple it is necessary to calculate the average value of it as follows:

$$A = \frac{1}{4}\left(\frac{B_{\emptyset}(\theta = 0, \emptyset = \pi/N) - B_{\emptyset}(\theta = 0, \emptyset = 0)}{B_0} + \frac{B_{\emptyset}(\theta = \pi, \emptyset = \pi/N) - B_{\emptyset}(\theta = \pi, \emptyset = 0)}{B_0}\right) \tag{8.15}$$

This equation shows that the toroidal magnetic field is determined using four probes in four different poloidal angles. The measurements performed by the magnetic pick-up coils on the outer surface of the IR-T1 Tokamak demonstrate that the amplitude of the toroidal field ripple on the sensor position is 0.01. This result is consistent with the result of modeling given in Fig. 8.25.

The Shafranov parameter can be calculated by the distribution of tangential and normal components of the magnetic field around the plasma current [31]:

$$B_{\theta} = \frac{\mu_0 I_{\mathrm{p}}}{2\pi b} - \frac{\mu_0 I_{\mathrm{p}}}{4\pi R_0} \times \left\{ \ln \frac{a}{b} + 1 - \left(\Lambda + \frac{1}{2}\right)\left(\frac{a^2}{b^2} + 1\right) - \frac{2R_0\Delta_{\mathrm{s}}}{b^2} \right\} \cos\,\theta \tag{8.16}$$

$$B_{\mathrm{r}} = -\frac{\mu_0 I_{\mathrm{p}}}{4\pi R_0} \times \left\{ \ln \frac{a}{b} + \left(\Lambda + \frac{1}{2}\right)\left(\frac{a^2}{b^2} - 1\right) + \frac{2R_0\Delta_{\mathrm{s}}}{b^2} \right\} \sin\,\theta \tag{8.17}$$

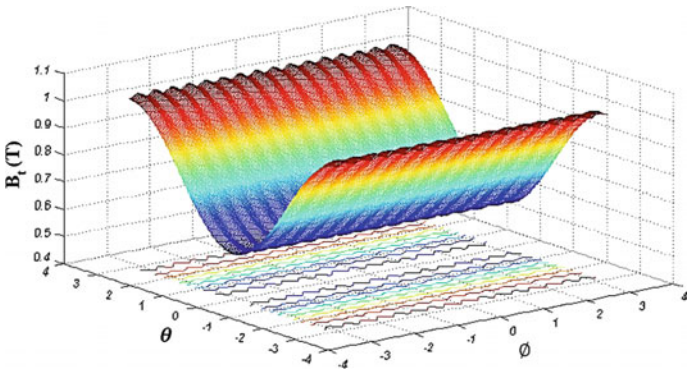

Fig. 8.25 Dependence of the toroidal field on the poloidal and toroidal angles (TF ripple)

where in these relations R_0, Δ_s, I_p, a, and b are the major radius of the vacuum vessel, Shafranov shift, plasma current, the minor radius of the plasma and chamber, respectively.

$$\Lambda = \beta_p + \frac{l_i}{2} - 1 = \ln\frac{a}{b} + \frac{\pi R_0}{\mu_0 I_p}(B_\theta + B_r) \tag{8.18}$$

$$\langle B_\theta \rangle = B_\theta(\theta = 0) - B_\theta(\theta = \pi) \tag{8.19}$$

$$\langle B_r \rangle = B_r\left(\theta = \frac{\pi}{2}\right) - B_r\left(\theta = \frac{3\pi}{2}\right) \tag{8.20}$$

Here, l_i and β_p represent the plasma internal inductance and poloidal beta, respectively. In this experiment, we assume that the minor radius of the plasma and amplitude of the toroidal field ripple at different poloidal angles are constant. Since toroidal flux is a variable parameter at different toroidal angles, we need field lines which loop back on themselves, in which case we require localized poloidal currents.

Measurements of the Poloidal Beta and Internal Inductance with the Diamagnetic Loop

The toroidal diamagnetic flux that relates to the perpendicular thermal energy of the plasma is measured using the diamagnetic loop. When measuring the diamagnetic flux, poloidal beta is obtained by the following relation [31]:

$$\beta_p = 1 - \frac{8\pi B_\varnothing}{\mu_0^2 I_p^2}\Delta\Phi_D \tag{8.21}$$

The diamagnetic flux $\Delta\Phi_D$ is equal to $\Phi_{total} - \Phi_{vacuum}$.

$$\Phi_{vacuum} = \Phi_{Toroidal} + \Phi_{Vertical} + \Phi_{Ohmic} + \Phi_{Eddy} \tag{8.22}$$

$\Phi_{Toroidal}$, $\Phi_{Vertical}$ and Φ_{Ohmic} are the toroidal flux due to toroidal field coils, the flux passing through the loop due to possible misalignment between the diamagnetic loop and vertical field, and the ohmic field, respectively. Φ_{Eddy} is toroidal flux due to eddy current in the chamber. The compensation coil in Fig. 8.24, can compensate for these fluxes. The compensation coil of the diamagnetic loop that is wrapped around the plasma current can only receive toroidal flux (Figs. 8.23 and 8.24). Substituting Eq. (8.13) into Eq. (8.21), we can write:

$$\beta_{\mathrm{p}} = 1 - \frac{8\pi B_0(1 - \rho\ \cos\ \theta - A\ \cos\ N\varnothing)}{\mu_0^2 I_{\mathrm{p}}^2}\Delta\Phi_{\mathrm{D}} \tag{8.23}$$

And from Eq. (8.18):

$$\frac{l_{\mathrm{i}}}{2} = \left(1 - \beta_{\mathrm{p}} + \Lambda\right) \tag{8.24}$$

$$l_{\mathrm{i}} = 2\ln\frac{a}{b} + \frac{2\pi R_0}{\mu_0 I_{\mathrm{p}}}\left(\langle B_\theta\rangle + \langle B_{\mathrm{r}}\rangle\right) + \frac{16\pi B_0(1 - \rho\ \cos\ \theta - A\ \cos\ N\varnothing)}{\mu_0^2 I_{\mathrm{p}}^2}\Delta\Phi_{\mathrm{D}} \tag{8.25}$$

Moreover, the Shafranov shift is obtained from Eq. (8.16):

$$\Delta_{\mathrm{s}} = \frac{\pi b^2}{\mu_0 I_{\mathrm{p}}}\langle B_\theta\rangle + \frac{b^2}{2R_0} \times \left\{\ln\frac{a}{b} + 1 - \left(\frac{a^2}{b^2} + 1\right)\left(\beta_{\mathrm{p}} + \frac{l_{\mathrm{i}}}{2} - \frac{1}{2}\right)\right\} \tag{8.26}$$

According to the above discussion, the IR-T1 group has done many experiments to investigate the toroidal field ripple effects on the poloidal beta, internal inductance, and Shafranov shift [30, 31]. The experimental results were illustrated in Figs. 8.26, 8.27 and 8.28. Figure 8.26 illustrates the plasma parameters in the absence of toroidal field ripple. The time evolution of plasma current is seen in Fig. 8.26a. As shown in Fig. 8.26b, the measured poloidal beta is close to one which is acceptable for ohmically heated Tokamaks such as IR-T1 Tokamak. The time evolution of measured internal inductance and Horizontal Displacement (H.D.) of the plasma column can be observed in Fig. 8.26c, d. The effect of toroidal field ripple amplitude on DBetap (the difference of poloidal beta with and without toroidal field ripple) at different poloidal angles is presented in Fig. 8.27a–d. The results show that DBetap is on the order of 10^{-4}. DBetap is negative in the high field side region ($\theta = 180°$) whereas it is positive in the low field side ($\theta = 0°$). The effect of toroidal field ripple amplitude on Dli (the difference in internal inductance with and without Toroidal field ripple) is on the order of 10^{-2}, as observed in Fig. 8.28a–d. It is noticeable that in the high field side region ($\theta = 180°$), unlike the poloidal beta case, Dli is positive while in the low field side ($\theta = 0°$) Dli is negative. As shown in Fig. 8.29a–d, no observable change is found in Shafranov shift [Horizontal Displacement (H.D.)] due to the toroidal field ripple at different poloidal angles.

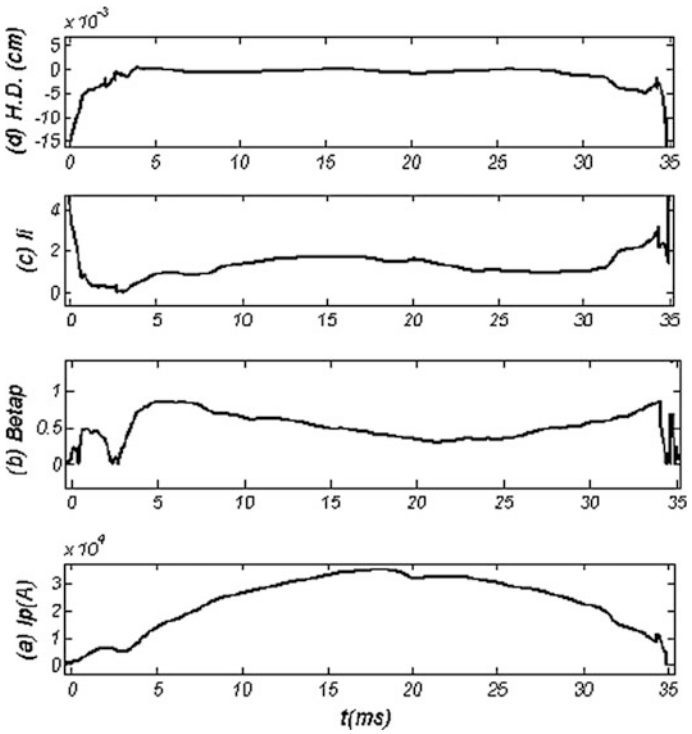

Fig. 8.26 The time evolution of **a** Plasma current, **b** Poloidal beta, **c** Internal inductance, and **d** horizontal displacement (H.D.) in the absence of toroidal field ripple

The Effect of Cold Limiter Biased System on the Plasma Internal Inductance in IR-T1 Tokamak

As mentioned in an earlier section, poloidal beta is an important parameter in Tokamaks. With the measurement of poloidal beta, we can obtain other important parameters of a plasma such as plasma pressure (P), plasma thermal energy (U), plasma temperature (T), plasma resistance (R), and plasma internal inductance (l_i). The volume averaged plasma kinetic pressure $\langle P \rangle$ can be directly determined from poloidal beta by the following relation [32]:

$$\langle P \rangle = \beta_p \frac{B_\theta^2(a)}{2\mu_0} = \frac{\mu_0 I_p^2 \beta_p}{8\pi^2 a^2} \tag{8.27}$$

Also, Eqs. (8.28) and (8.29) can be used to determine the plasma thermal energy (U) and also plasma temperature (T):

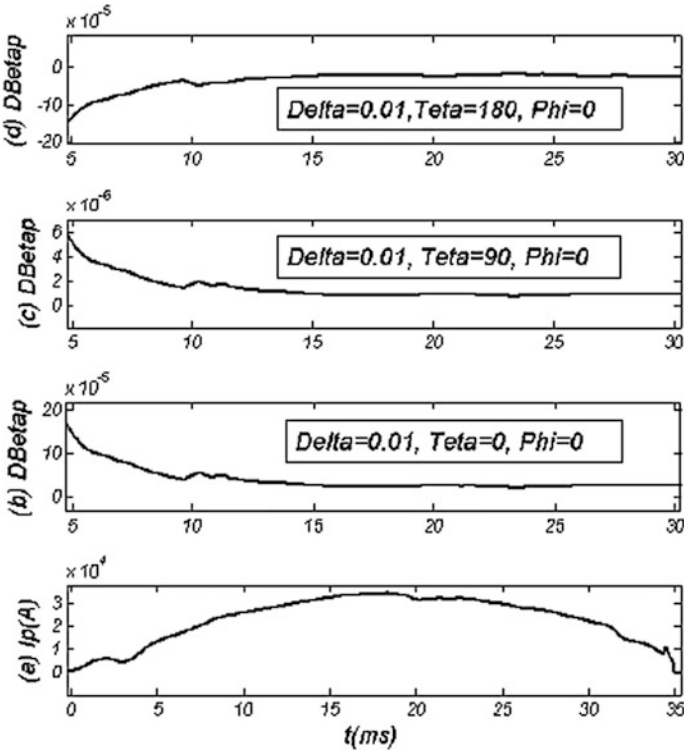

Fig. 8.27 Effects of the equal TF ripple amplitude on the difference in poloidal beta with and without TF ripple (DBetap) at different poloidal angles

$$U = \frac{3}{2}\left(\sum_{\alpha} n_{\alpha} T_{\alpha}\right) V = \frac{3}{2}\langle P \rangle V \tag{8.28}$$

$$\overline{T}_{\alpha} = \frac{U}{3 n_{\alpha} V} \tag{8.29}$$

where V and n are the plasma volume and plasma density and subscript α indicates the plasma species. Moreover, the plasma specific resistance in the steady state plasma can be written as:

$$\rho_{\mathrm{p}} = \frac{1}{\sigma_{\mathrm{p}}} = \frac{A}{l} R_{\mathrm{p}} = \frac{a^2}{2R_0} \frac{V_{\mathrm{R}}}{I_{\mathrm{p}}} \tag{8.30}$$

where σ_{p}, R_{p} and V_{R} are the plasma conductivity, the plasma resistance and the resistive component of the loop voltage (poloidal flux loop), respectively.

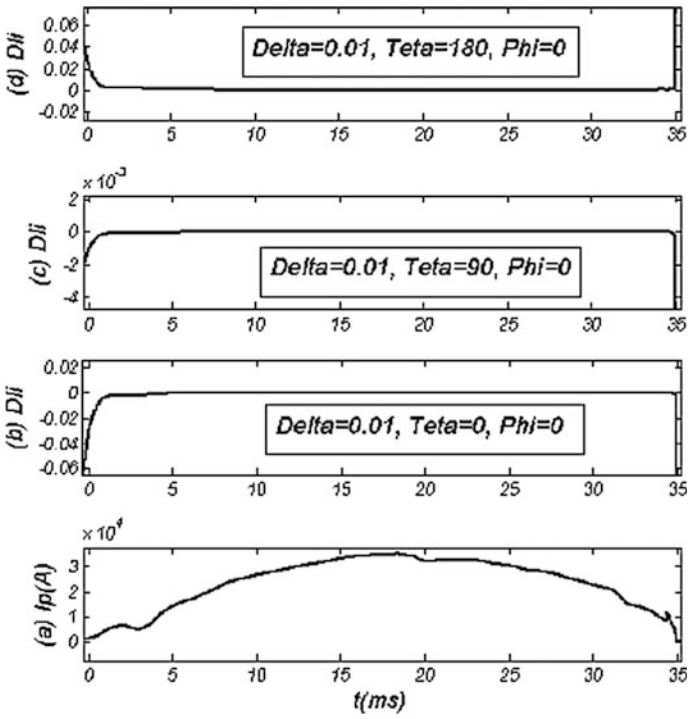

Fig. 8.28 Effects of the equal TF ripple amplitude on the difference in internal inductance with and without TF ripple (Dli) at different poloidal angles

In the following, the time evolution of plasma parameters is calculated using the above procedure and the effects of the biased limiter are presented. Figure 8.30 illustrates the time evolution of plasma current (I_p), loop voltage (V_{loop}), poloidal beta (β_p), plasma pressure (P), plasma energy (U), plasma resistance (R), plasma temperature (T), plasma displacement, Shafranov parameter (Λ), and plasma internal inductance (l_i) without biased voltage. As can be seen from this figure, all of these parameters turn into the steady state (after 10 ms) when the plasma current is in the equilibrium state. The results show that the plasma temperature and plasma displacement calculated using the diamagnetic loop are around 140 eV and 5×10^{-3} m. The effects of the cold biased limiter with different voltages (+200 V and +320 V) on these parameters is seen in Figs. 8.31 and 8.32. It can be observed that plasma current increases as a result of applying the cold biased limiter with voltage +200 V. Also, the plasma current profile is flattened in the presence of a +200 V biasing voltage. The +200 V biasing voltage increases poloidal beta, plasma pressure, plasma energy, and plasma temperature and decreases plasma resistance, plasma displacement, and plasma internal inductance.

It can be concluded that applying +200 V biasing voltage to the plasma could be effective for improving the quality of the Tokamak plasma discharge by creating

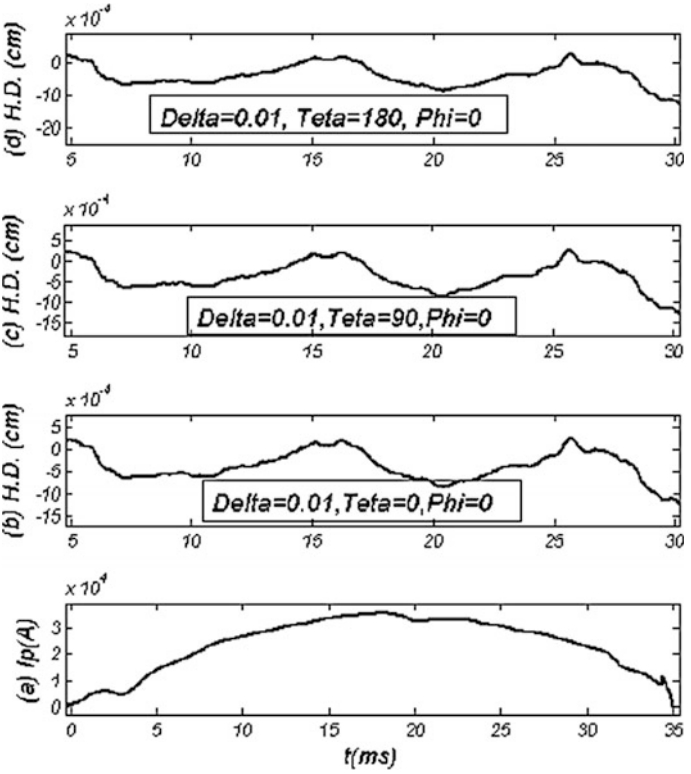

Fig. 8.29 Effects of the equal TF ripple amplitude on the horizontal displacement (H.D.) at different poloidal angles

steady state plasma. The +200 V biasing voltage significantly increases the magnitude of the radial electric field in the region inside the fixed limiters. Also, one of the results of improving the particle and energy confinement is that the plasma displacement is decreased (from 8 mm to around 1 mm). The plasma current, plasma pressure, plasma energy, and plasma temperature increase as a result of applying the cold biased limiter with voltage +320 V and then decreases rapidly. Also, reduction of plasma displacement is not steady after applying biased voltage +320 V. These results show that the cold biased limiter with voltage +320 V is not effective for improving the plasma confinement.

8.5.2 Electrical Probes

The scrape-off layer (SOL) and edge plasma which are the closest regions to the chamber walls have been extensively studied in recent fusion research. In general,

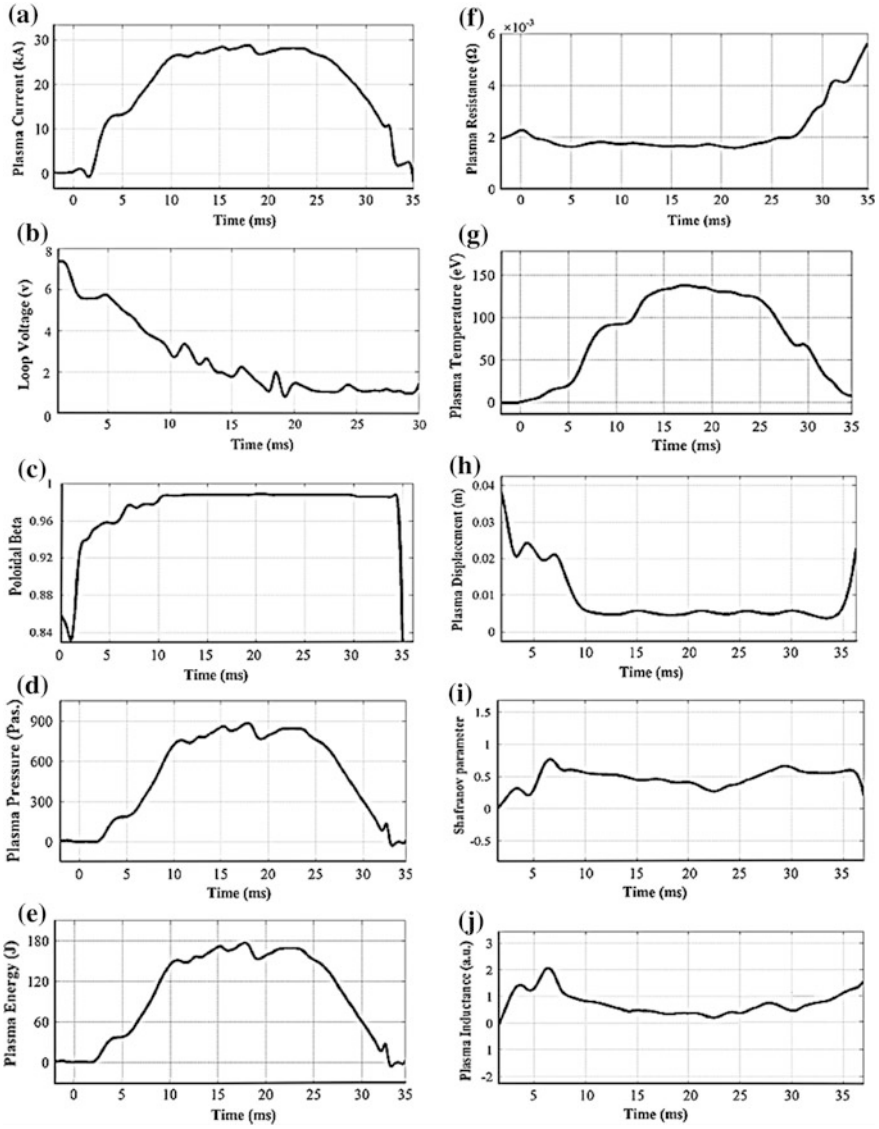

Fig. 8.30 Time evolution of **a** plasma current, **b** loop voltage, **c** poloidal beta, **d** plasma pressure, **e** plasma energy, **f** plasma resistance, **g** plasma temperature, **h** plasma displacement, **i** Shafranov parameter and **j** plasma internal inductance without applying biasing voltage

the critical conditions of edge plasma relate to interactions with the wall and impurity transport. The measurement of parameters is essential for the study and control of edge plasma behavior. The easiest, most practical, and accurate tool for

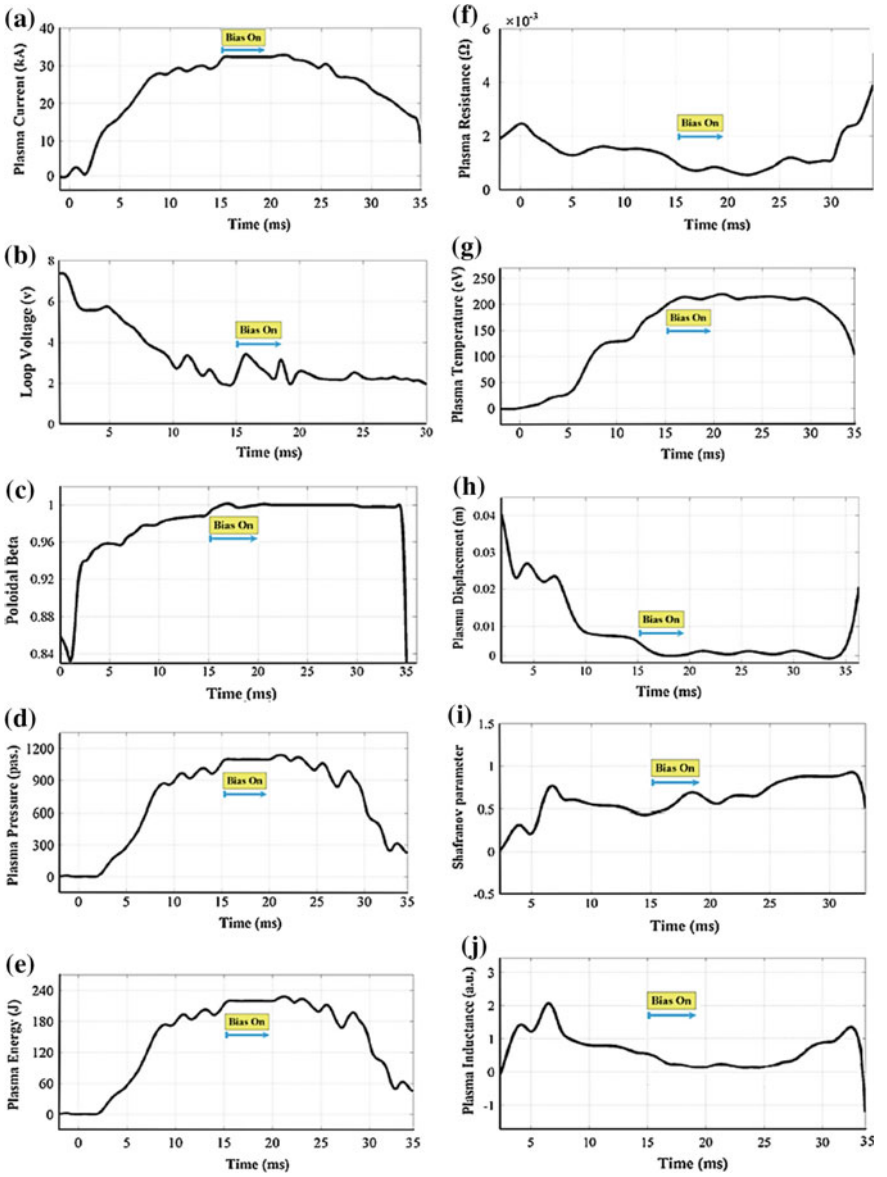

Fig. 8.31 Time evolution of **a** plasma current, **b** loop voltage, **c** poloidal beta, **d** plasma pressure, **e** plasma energy, **f** plasma resistance, **g** plasma temperature, **h** plasma displacement, **i** Shafranov parameter and **j** plasma internal inductance in the presence of a biasing voltage (+200 V)

measuring local plasma parameters is the electrical probe. To minimize destruction of the probe and impurity transport into the plasma, the electrical probes can only be placed at the plasma edge. This probe includes one or more electrodes in

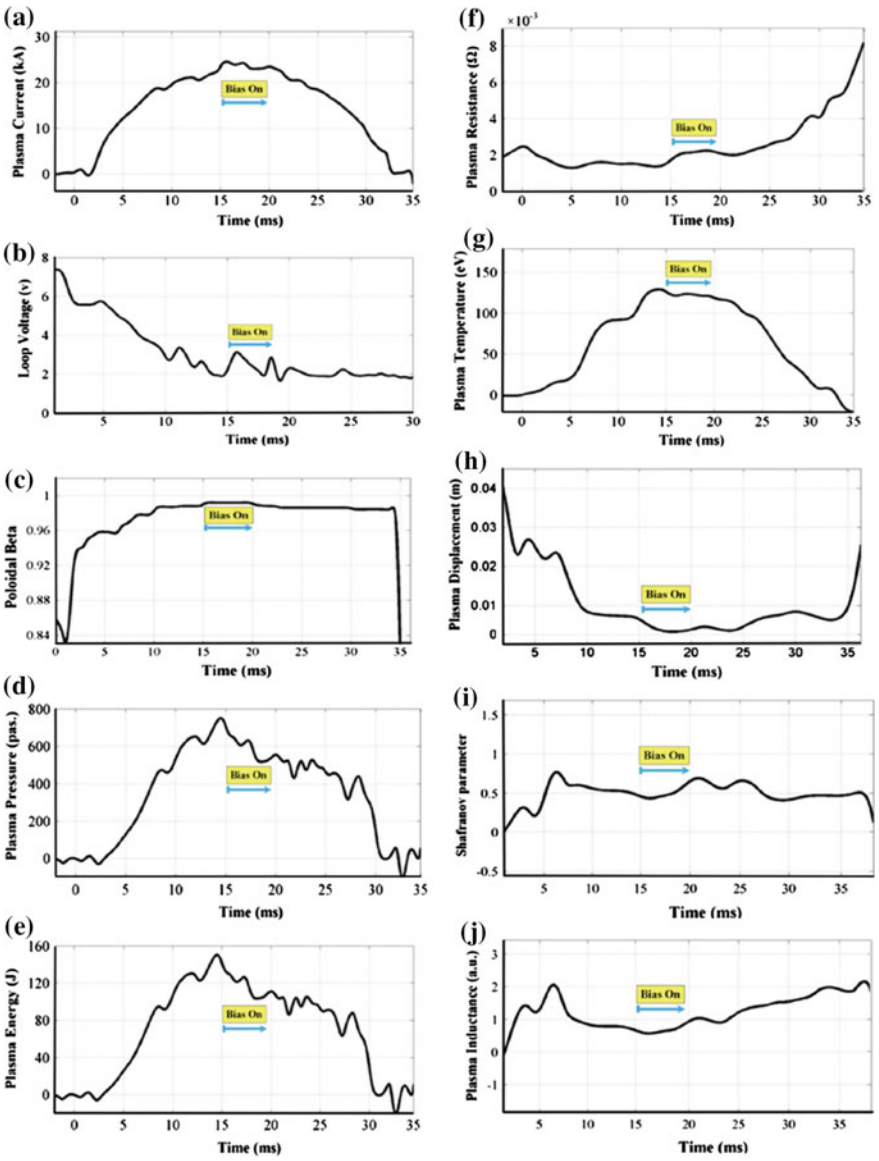

Fig. 8.32 Time evolution of **a** plasma current, **b** loop voltage, **c** poloidal beta, **d** plasma pressure, **e** plasma energy, **f** plasma resistance, **g** plasma temperature, **h** plasma displacement, **i** Shafranov parameter and **j** plasma internal inductance in the presence of a biasing voltage (+320 V)

different forms based on the required measurements. For measuring parameters, an external voltage is applied to the electrodes and the current or voltage response detected by the electrodes is measured as output data.

8.5.2.1 Principles of Langmuir Probe Operation

The oldest and simplest electrical probe is the Langmuir probe that was invented by Arving Langmuir in 1924. The Langmuir probe is a diagnostic tool for the measurement of electron density, electron temperature, and floating potential at the plasma edge and SOL region. In general, an electrode is inserted into the plasma and is connected to a defined voltage to collect ions and electrons. For different applications, Langmuir probes are constructed in different configurations such as: single Langmuir probe, double Langmuir probe, Mach probe, radial array of Langmuir probes (rake probe), and poloidal array of Langmuir probes.

8.5.2.2 Single Langmuir Probe

A single Langmuir probe includes an electrode that is placed at the plasma edge. By applying an external voltage to the electrode and measuring the current collected by the electrode, it is possible to determine *I–V* characteristics of the plasma discharge. A typical *I–V* characteristic curve for plasma with Maxwellian energy distribution is illustrated in Fig. 8.33. Since the plasma is a quasi-neutral gas of ions and electrons, the *I–V* characteristic curve includes two currents for ion current (I_i) and electron current (I_e).

When the potential of the probe is greater than the plasma potential (V_p), electrons are preferentially collected by the probe (relative to ions), so the electron current increases to reach an electron saturation current (I_{es}). When the probe reaches the electron saturation current, electrons are repelled from the probe and no more electrons are collected by the probe. On the other hand, if the probe potential is less than the plasma potential, more ions are collected than electrons. To attract these ions and increase the ion current, the probe is positively charged until ions are repelled from probe. In this situation, the probe current is equal to the ion saturation current (I_{is}). The floating potential is the potential at which the probe is electrically

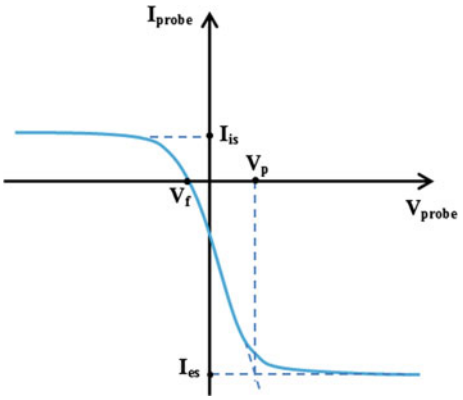

Fig. 8.33 *I–V* characteristic curve for the Langmuir probe

insulated from the chamber. Electron temperature can be obtained from the following relation:

$$V_p = V_f + T_e \ln\left(\frac{I_{es}}{I_{is}}\right) \tag{8.31}$$

where V_p, V_f, and T_e are the plasma potential, floating potential, and electron temperature, respectively.

There are two different arrays of Langmuir probes in IR-T1 Tokamak. A radial array of 16 single Langmuir probes (Rake probe), separated radially by 2.5 mm from each other, is inserted vertically from the top of the Tokamak into the chamber, as presented in Fig. 8.34. This movable array is used to measure the radial electric fluctuations. Probe tips are made of molybdenum and are 3.3 mm in length and 0.6 mm in diameter. The other probe is a poloidal array of four single Langmuir probes placed in the poloidal direction on two poloidal surfaces to determine the poloidal electric fluctuations. Two of the four probes are shorter in length than the other two probes. In order to prevent the probes from producing shadows on each other, the shorter probes are located in the first surface and the longer probes are placed in the second surface. The tips are made of tungsten with a diameter of 0.6 mm and a length of 3.9 mm (see Fig. 8.35). These probes are used to determine the edge plasma fluctuations and associated transport in IR-T1 Tokamak experiments.

The Control of Turbulent Transport in IR-T1 Tokamak by External Resonant Fields

In this experiment [11, 33], the effect of a cold biased limiter with voltages of +200 and −200 V on turbulence and transport of the particles at the edge of the plasma are investigated. Figures 8.36a–e and 8.37a–e display the influence of cold biased limiter voltage with positive and negative polarity, respectively, on the temporal

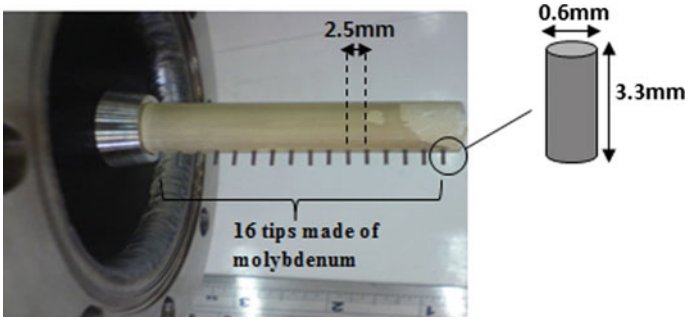

Fig. 8.34 Photo of the Rake probe in IR-T1 Tokamak

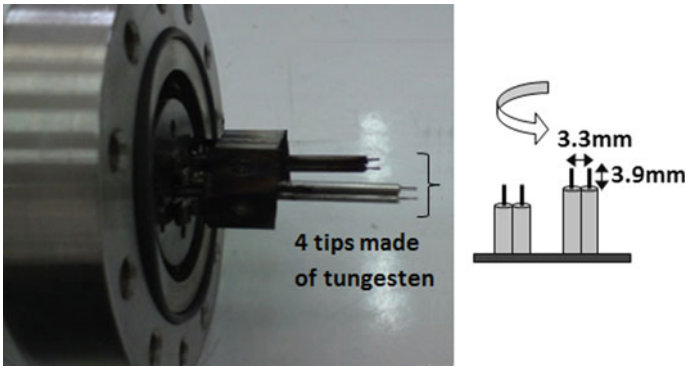

Fig. 8.35 Photo of a poloidal array of Langmuir probes in IR-T1 Tokamak

evolution of plasma parameters. These parameters include the plasma current, radial and poloidal electric field, and the radial and poloidal turbulent transport. The measurements were taken at the plasma edge using the radial and poloidal Langmuir probe arrays mentioned earlier.

It is noticeable that the radial particle flux (Γ_r) and poloidal particle flux (Γ_p) can be calculated by $\Gamma_r(t) = n(t)\, E_p(t)$ and $\Gamma_p(t) = n(t)\, E_r(t)$, respectively. $n(t)$, $E_p(t)$ and $E_r(t)$ are the fluctuations of electron density, poloidal electric field, and radial electric field as determined by Langmuir probes. As presented in Figs. 8.36a and 8.37a, the plasma current increases after applying the cold biased limiter with positive voltage while it reduces as a result of the presence of the negative biased voltage. Additionally, Fig. 8.37a demonstrates the reduction of confinement time after applying the biasing voltage with negative polarity. One possible explanation for this is the radial current (J) produced by the cold biased limiter, which can create the $\vec{J} \times \vec{B}$ force to balance the gradient of kinetic pressure in the plasma. Figures 8.36b and 8.37b confirm the results as the radial electric field in the plasma edge increases with the application of the positive biased voltage and reduces as a result of the presence of the negative biased voltage. The poloidal electric field decreases in the presence of a biasing voltage with positive polarity, while the negative biased voltage increases it (see Figs. 8.36c and 8.37c).

These results show that the $\vec{J} \times \vec{B}$ force produced by the positive biased voltage is in the opposite direction to the gradient of kinetic pressure. In contrast, it can be guessed that the negative biased voltage produces the $\vec{J} \times \vec{B}$ force in the direction of the gradient of kinetic pressure. So we can predict that the biased voltage with positive polarity can reduce the radial particle flux and increase the poloidal particle flux, as shown in Fig. 8.36d, e. Also, Fig. 8.37d, e demonstrate that the negative biased voltage causes an increase in the radial particle flux and the reduction of poloidal particle flux. These results show that the cold biased limiter with positive voltage improves plasma confinement while negative voltage reduces it. Figure 8.38a–c illustrate the effects of biasing voltage (+200 and −200 V) on the

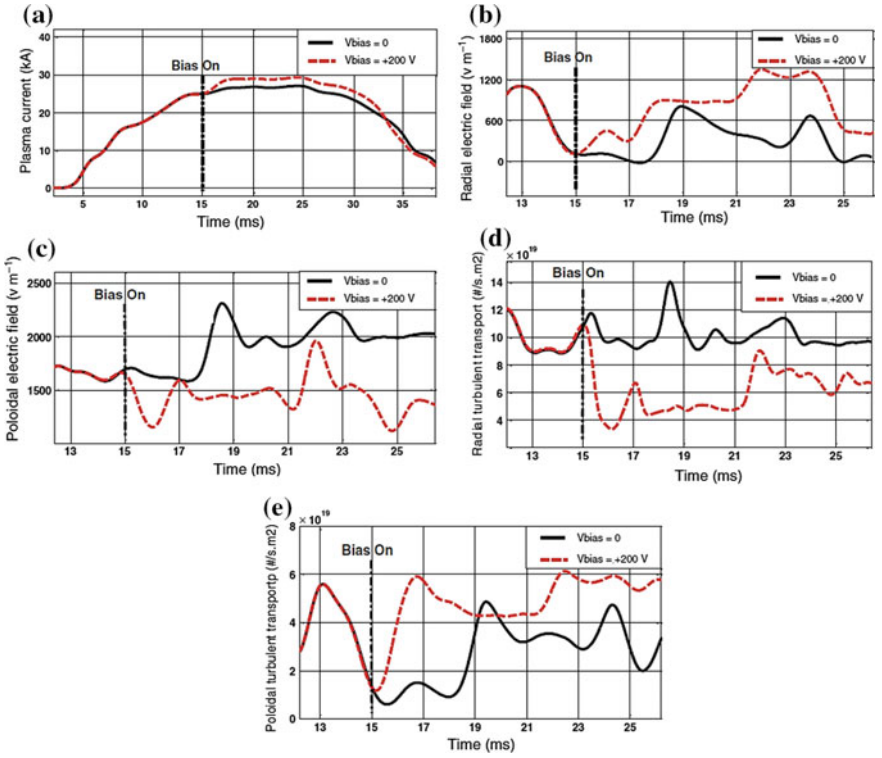

Fig. 8.36 The temporal evolution of **a** plasma current, **b** radial electric field, **c** poloidal electric field, **d** radial turbulent transport and **e** poloidal turbulent transport in the absence of the cold biased limiter voltage and in the presence of the cold biased limiter voltage with positive polarity (+200 V)

temporal evolution of *H*-alpha radiations, energy, and confinement time of plasma in IR-T1 Tokamak. It can be observed that the energy and confinement time of the plasma increases in the presence of the positive biasing voltage and reduces after applying the negative biasing voltage. It can be concluded that the polarity of the biasing voltage has a key role in improving plasma confinement.

In the following, the influence of both the cold biased limiter with positive polarity (+200 V) and RHF ($L = 2$ and $L = 3$) and the time order of applying them to the IR-T1 Tokamak plasma are investigated. For this purpose, the experiments have been performed in three steps: first, the biasing voltage and RHF were applied at $t = 15$ ms and $t = 20$ ms, respectively and continue until the end of the shot. In the next step, RHF and biasing voltage were applied at $t = 15$ ms and $t = 20$ ms, respectively, until the end of the shot. In the final step, RHF and biasing voltage were applied simultaneously at $t = 15$ ms until the end of the shot. As mentioned earlier, turbulent transport depends on fluctuations of the density and the potential, so a description of their statistical properties can be useful in studying turbulent

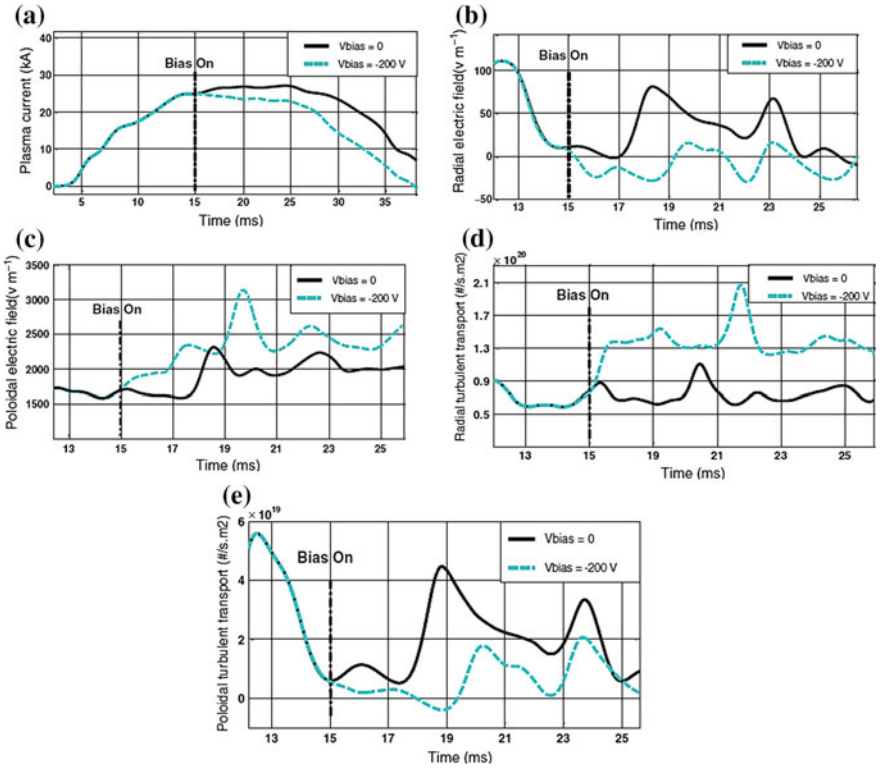

Fig. 8.37 The temporal evolution of **a** plasma current, **b** radial electric field, **c** poloidal electric field, **d** radial turbulent transport and **e** poloidal turbulent transport in the absence of the cold biased limiter voltage and in the presence of the cold biased limiter voltage with negative polarity (−200 V)

transport. It is noticeable that the auto-power spectrum of the parameter u can be estimated by [34, 35]:

$$S_u(\omega_j) = \left\langle \left| u(\omega_j) \right|^2 \right\rangle \tag{8.32}$$

where the brackets <…> denote ensemble averaging, showing the frequency distribution of the power of the fluctuations. For two fluctuating quantities, u and v, the cross-power spectrum reveals information on the correlation between two different quantities in the Fourier domain. It is given by:

$$P_{uv} = \left\langle u(\omega_j)^* v(\omega_j) \right\rangle \tag{8.33}$$

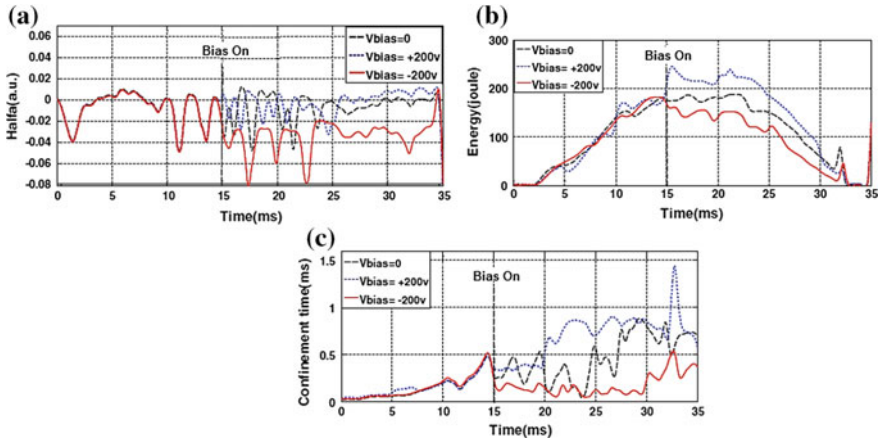

Fig. 8.38 The time evolution of **a** *H*-alpha radiation, **b** energy and **c** confinement time of plasma in both the absence of biasing voltage and the presence of biasing voltages (+200 V and −200 V)

the asterisk denotes the complex conjugation. The cross-phase spectrum can be determined by:

$$\varphi_{uv} = \tan^{-1}\left(\frac{\text{Image}\,(P_{uv}(\omega))}{\text{Real}\,(P_{uv}(\omega))}\right) \tag{8.34}$$

Furthermore, the cross-coherence is defined as:

$$\gamma_{uv}(\omega_j) = P_{uv}(\omega_j) \Big/ \sqrt{S_u(\omega_j) S_v(\omega_j)} \tag{8.35}$$

Which is limited to [0, 1], where 0 and 1 indicate phase incoherence and coherence, respectively, and the values between them indicate the partial phase coherence.

Diffusion is a factor in plasma particle transport and is produced by pressure gradients and different types of collisions from the high density regions to the low density regions, both along and across the magnetic field lines. The flux of the diffusing particles is given by [36]:

$$\Gamma = \mu n E - D\nabla n \tag{8.36}$$

μ and D represent the mobility and diffusion coefficients, respectively. If either the mobility or electric field is zero, this equation is called the Fick's low and is expressed by:

$$\Gamma = -D\nabla n \tag{8.37}$$

So, the measurements of the particle flux and density gradient can determine the diffusion coefficient. Figure 8.39a–d present the effect of the cold biased limiter and RHF on the power spectrum of the ion saturation current (I_{sat}) and gradient of floating potential. It is necessary to express that when the temperature is assumed to be constant, we can presume $n \propto I_{sat}$. As seen from Fig. 8.39a, the power spectrum of the amplitudes of I_{sat} and ∇V_f are the same at $t < 15$ ms, but they change as a result of applying the biasing voltage and RHF to the plasma. They have a broadband turbulent character, i.e., there is no reproducible or persistent peak in the spectra. When the biasing voltage and RHF are applied at $t = 15$ ms and $t = 20$ ms, respectively, at low frequency ($f \leq 10$ kHz) and in the time interval $20 < t < 22$ ms, the spectrum of I_{sat} varies in the range of $0 <$ spectrum of $I_{sat} \leq 1.2 \times 10^{-9}$. In the other range, it was reduced and when $f > 60$ kHz it was near zero (Fig. 8.39b).

In the opposite situation, i.e., when RHF and biasing voltage are applied at $t = 15$ ms and $t = 20$ ms, respectively, in the time interval $20 < t < 22$ ms, the fluctuations of the power spectrum of I_{sat} are more than the fluctuations in the other conditions. At the low frequency interval ($f \leq 10$ kHz), the spectrum of I_{sat} varies in the range of $0 \leq$ spectrum of $I_{sat} \leq 2 \times 10^{-9}$ but at the frequencies beyond 10 Hz, it decreases about 90%. To apply the RHF and biasing simultaneously, the range of the spectrum of the I_{sat} was restricted to $0 \leq$ spectrum of $I_{sat} \leq 1.1 \times 10^{-9}$. Its fluctuations are less than the fluctuations observed under the other conditions. The analysis was repeated in the time interval $13 < t < 15$ ms. The spectrum of the signals is identical in all the conditions (Fig. 8.39a, c).

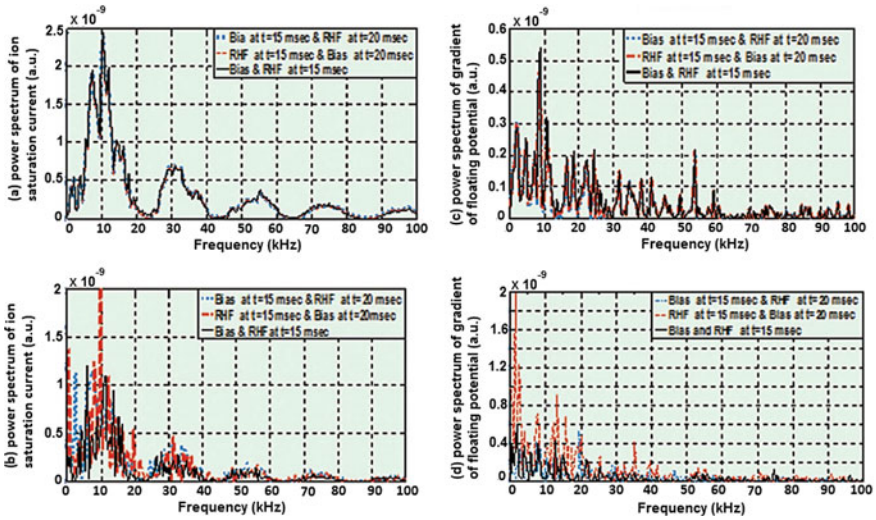

Fig. 8.39 Superposition of **a** power spectrum of I_{sat} during 2 ms ($13 < t < 15$ ms), **b** power spectrum of I_{sat} during 2 ms ($20 < t < 22$ ms), **c** power spectrum of ∇V_f during 2 ms ($13 < t < 15$ ms), **d** power spectrum of ∇V_f during 2 ms ($20 < t < 22$ ms)

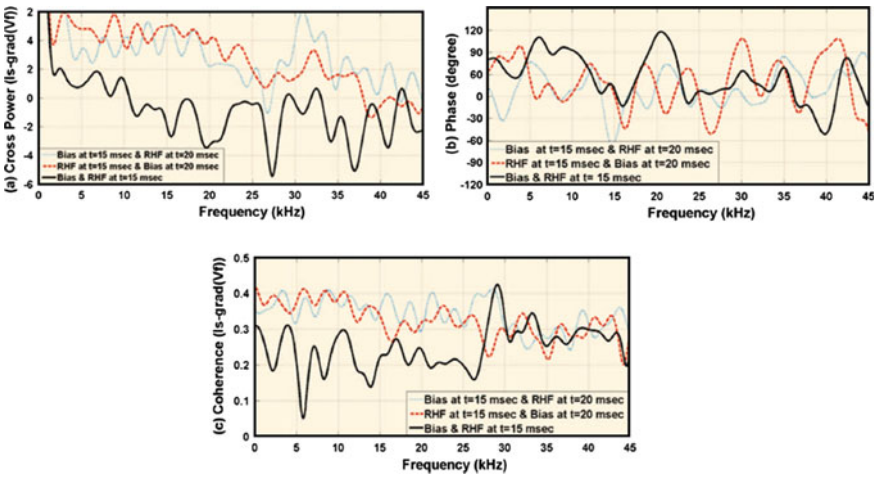

Fig. 8.40 Analysis of fluctuation spectra during 2 ms ($20 < t < 22$ ms), includes **a** cross-power spectrum of ($\nabla V_f - I_{sat}$); **b** phase between ($\nabla V_f - I_{sat}$); **c** coherence of ($\nabla V_f - I_{sat}$)

The same results are obtained from the spectrum of ∇V_f (Fig. 8.39d). The power spectrum of ∇V_f becomes smoother as a result of exerting the biasing voltage and RHF at $t = 15$ ms. The analysis proceeds by calculating the cross power, phase, and the coherence between ∇V_f and I_{sat}. The cross power of ∇V_f and I_{sat} by applied RHF and biasing voltage at $t = 15$ ms, $t = 20$ ms, and vice versa, is more than the cross power when biasing voltage and RHF are applied at $t = 15$ ms simultaneously (see Fig. 8.40). The cross power decreases with increasing frequency in all conditions. The coherence between ∇V_f and I_{sat} (Fig. 8.40c) depends on the time order of applying the RHF and biasing voltage. The results show that this coherence reduces when biasing voltage and RHF are applied simultaneously.

Figure 8.41a–d present the effects of biasing voltage and RHF on the temporal evolution of the plasma current, radial particle flux, gradient of particle density, and diffusion coefficient. The results show that when simultaneously applying the biasing voltage and RHF at $t = 15$ ms, the radial particle flux, radial particle density gradient, and the diffusion coefficient decrease by around 60, 50, and 55%, respectively. We can conclude that applying the biasing voltage and RHF simultaneously at $t = 15$ ms has the most effect on plasma confinement improvement. Table 8.6 presents the average values of the diffusion coefficient, radial particle flux and the particle density gradient at different time intervals.

8.5.2.3 Ball-Pen Probe

Due to fluctuating electron temperatures (T_e) during measurement, it is very difficult to calculate T_e with sufficient accuracy. Moreover, in a strong magnetic field, the ratio between the ion and the electron saturation currents I_{es}/I_{is} cannot always be

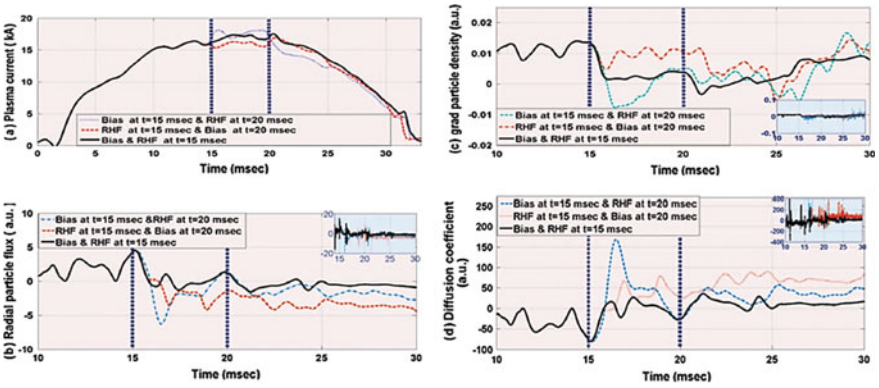

Fig. 8.41 The time evolution of **a** plasma current; **b** radial particle flux; **c** radial particle density and **d** particle diffusion coefficient at plasma edge. No smoothed version of the diagrams was plotted at the corner of each diagram

determined precisely [37]. Moreover, the Langmuir probe obtains incorrect results for the plasma potential. This can be attributed to electron drift or runaway electrons with velocity distribution functions that deviate from the Maxwellian velocity distribution function. To avoid this problem, there are probes such as the ball-pen and emissive which can directly measure the plasma potential as explained in the following. *I–V* curve becomes symmetric for both the ball-pen probe and emissive probe as explained in the following (see Fig. 8.42).

The ball-pen probe is a simple probe for the direct measurement of plasma potential. This probe is based on the Katsumata probe which is supposed to only be sensitive to ions [38, 39]. The difference between Larmor radii of ions and electrons in a strong magnetic field forms the basis of the probe's operation. The Katsumata probe consists of a movable collector and an insulating tube that surrounds the collector. Within a strong magnetic field, the electron Larmor radius is much smaller than the ion Larmor radius, and thus the insulator tube can shield the collector from electrons. To measure the plasma potential, electron saturation current has to be equal to ion saturation so the part of electron current must shield collector. For this purpose, Adamek et al. improved the Katsumata probe and invented the ball-pen probe [38,40]. In contrast to the original Katsumata probe, the collector of this probe has a conical tip to transit smoothly from full electron collection to no electron collection. When the electron saturation current decreases to become equal to the ion saturation current, the second part of the right side of relation (8.31) becomes equal to zero and the floating potential becomes equal to the plasma potential and the *I–V* characteristic curve becomes symmetric.

Direct measurement of electron temperature can be achieved by adding a single Langmuir probe to the ball-pen probe as shown in Fig. 8.43. The collector of the ball-pen probe can measure plasma potential as mentioned above and the Langmuir ring probe can measure the floating potential because it is in direct contact with the plasma. The electron temperature can now be calculated using Eq. (8.31).

Table 8.6 Average values of the diffusion coefficient, radial particle flux and the particle density gradient at different time intervals

Order of biasing and RHF applied	Time interval (ms)	Average value of radial particle flux (a.u.) 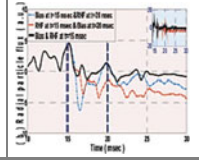	Average value of gradient of particle density (a.u.) 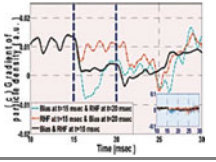	Average value of diffusion coefficient (a.u.) 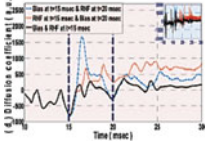
Bias applied at t = 15 ms and RHF applied at t = 20 ms	10 < time < 15	1.8329	0.0116	−158.0027
	15 < time < 20	−1.0571	0.00316	333.9051
	25 < time < 30	−1.0367	0.0021	492.9769
RHF applied at t = 15 ms and bias applied at t = 20 ms	10 < time < 15	1.8329	0.0116	−158.0027
	15 < time < 20	−1.0786	0.0097	150.1958
	20 < time < 25	−3.0437	0.0055	553.4000
Bias and RHF applied at t = 15 ms	10 < time < 15	1.8329	0.0116	−158.0027
	15 < time < 20	0.4723	0.0021	−224.4369
	20 < time < 25	−0.5390	0.00329	163.4034

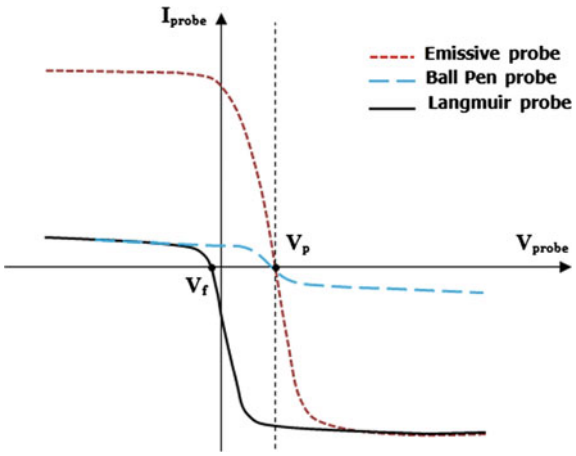

Fig. 8.42 *I–V* characteristic curves obtained by a Langmuir probe (the *solid line*), ball-pen probe (the *dash line*) and emissive probe (the *dotted line*)

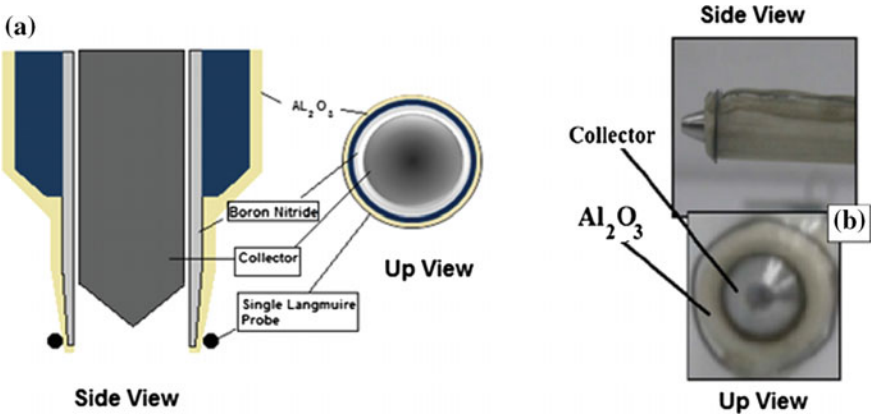

Fig. 8.43 The **a** schematic and **b** photo of Langmuir ball-pen probe in IR-T1 Tokamak

The schematic and photo of the Langmuir ball-pen probe in IR-T1 Tokamak are illustrated in Fig. 8.43a, b, respectively. The probe consists of a conically shaped collector, which is shielded by an insulating tube made of alumina (Al_2O_3).

Study of Electron Temperature by the Langmuir Ball-Pen Probe

In this study [41], we investigated the results of direct measurement of the plasma potential and electron temperature using the Langmuir Ball-pen probe. Moreover, the influence of external fields [cold biased limiter with different voltages

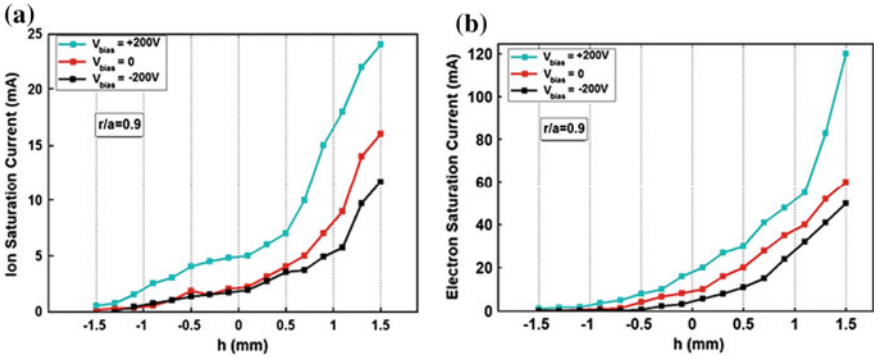

Fig. 8.44 Dependence of **a** ion and **b** electron saturation currents on the collector position in the IR-T1 plasma edge for different biasing voltages

(V =+200 V and V = −200 V) and resonant helical magnetic field (RHF) with different modes (L = 2 and L = 3)] on plasma parameters is studied. Dependence of ion and electron saturation current (I_{sat}^{+} and I_{sat}^{-}) on the collector position in edge plasma for different biasing voltages ($V_{biasing}$ = +200 V, $V_{biasing}$ = 0 V and $V_{biasing}$ = −200 V) is displayed in Fig. 8.44a, b.

It can be seen that when the collector retracts into the tube, both I_{sat}^{+} and I_{sat}^{-} decrease. Reduction of electron saturation current (I_{sat}^{-}) is steeper than in case of ion saturation current (I_{sat}^{+}) because the electrons have smaller Larmor radii compared to the ions. Very small displacement of collector causes to shield more electrons compared to ions. Also, the results obtained from experiments demonstrate a significant increase in ion and electron saturation currents after applying the positive biasing voltage ($V_{biasing}$ = +200 V) while the biasing voltage with negative polarity ($V_{biasing}$ = −200 V) decreases them, as shown in Fig. 8.32. Also, Fig. 8.45a, b show that RHF with both modes L = 3 and L = 2 increase ion and electron saturation currents. It is clear that the decrease of electron and ion saturation currents when retracting the collector into the tube is much greater when RHF is applied to plasma. One of the possible reasons for this reduction can be explained by an increase in the magnetic field. As we know, with an increasing magnetic field the Larmor radius of both electrons and ions decrease.

As mentioned earlier, by retracting the collector into the tube fewer electrons are collected by the collector until the number of electrons collected by the collector becomes equal to the number of ions. A comparison between the electron saturation current and ion saturation current shows that the ion saturation current and electron saturation could be very close to one another when the collector retracts into the tube by about 0.7 mm. So R is approximately equal to 1 for position h = −0.7 mm as seen in Fig. 8.46. But this is just in the case of no external field biasing being applied to the plasma. As a result, the floating potential is almost equal to the plasma potential in this collector position. To study the influence of resonant external fields on the plasma potential, the dependence of R on the collector

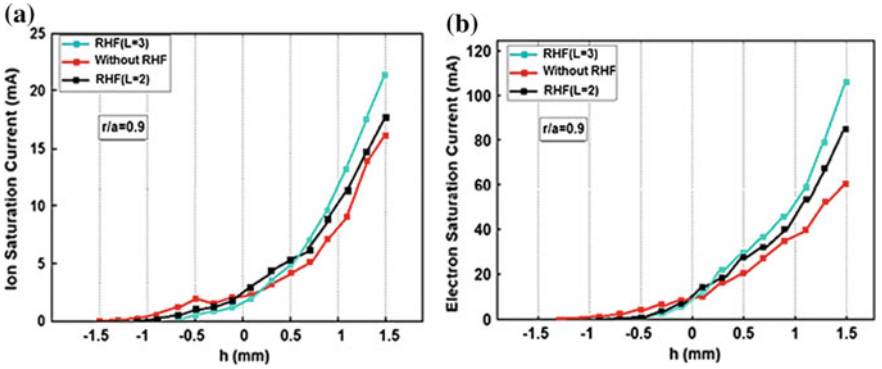

Fig. 8.45 Dependence of **a** ion and **b** electron saturation currents on the collector position in the IR-T1 plasma edge for different modes of RHF

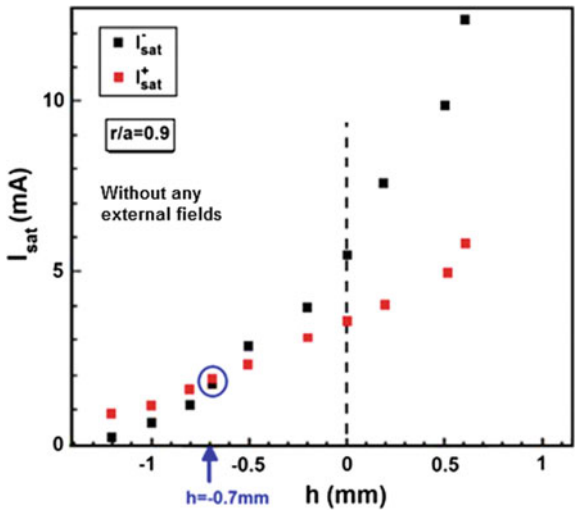

Fig. 8.46 The ion and electron saturation currents in different collector positions. The measurements were performed in IR-T1 plasma edge without external fields

position was investigated in the presence of external fields. The results demonstrate that $R \cong 1$ in $h = -1.1$ mm and $h = -0.6$ mm in the presence of biasing voltages of +200 and −200 V, respectively. On the other hand, the floating potential can be assumed to be the same as the plasma potential in these positions.

Also, $R \cong 1$ in $h = -0.5$ mm and $h = -0.6$ mm for RHF with $L = 3$ and $L = 2$, respectively. Figure 8.47a, b correspond to the influence of external fields on the time evolution of the plasma potential measured by the ball-pen probe. As seen from these figures, plasma potential increases after applying the biasing voltage with positive polarity, and decreases for negative polarity. Furthermore, RHF with both modes $L = 3$ and $L = 2$ increases the plasma potential however mode $L = 3$ is

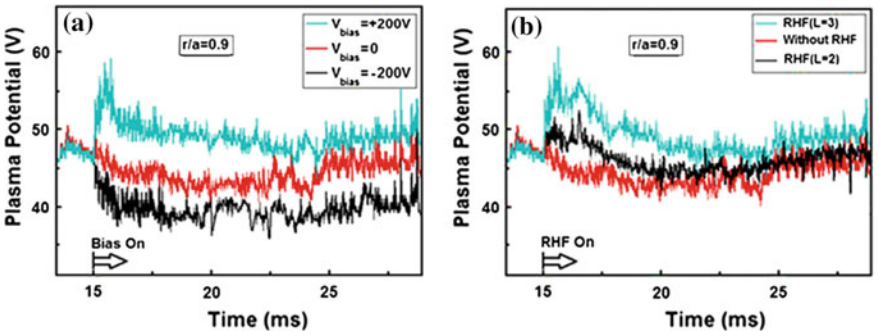

Fig. 8.47 Time evolution of the edge plasma potential for **a** different biasing voltages and **b** different modes of RHF

more effective than $L = 2$. As the Eq. (8.31) implies, the electron temperature can be directly calculated from the difference between the plasma potential and floating potential:

$$T_e = \frac{V_p - V_f}{\ln R} \tag{8.38}$$

Figure 8.48a, b illustrate the temporal evolution of electron temperature measured by the Langmuir ball-pen probe and the influence of external fields on it. According to the results in Fig. 8.48a, biased limiter with positive voltage causes an increase in electron temperature while the electron temperature decreases quickly in the presence of the negative biasing voltage. On the other hand, the negative biasing voltage reduces confinement time, as seen in Fig. 8.48a. The electron temperature grows when the resonant helical magnetic field with different modes ($L = 3$ and $L = 2$) acts on the plasma. The electron temperature growth with RHF in mode $L = 3$ is much more significant than for $L = 2$ (seen Fig. 8.48b).

8.5.2.4 Emissive Probe

Usually, an emissive probe includes a tungsten half-loop with its two ends placed into the bores of a double-bore ceramic. The schematic of an emissive probe is seen in Fig. 8.49. This probe can emit electrons when is inserted into the plasma and heated to a high temperature (around 3000 K). With electron emission, the *I–V* characteristic curve becomes symmetric because the electron current emitted by the probe is in the direction of the positive ion current that flows to the probe. Therefore, the ion saturation current increases to become equal to the electron saturation current. An emissive probe can calculate the potential of a Maxwellian plasma using the relation (8.39):

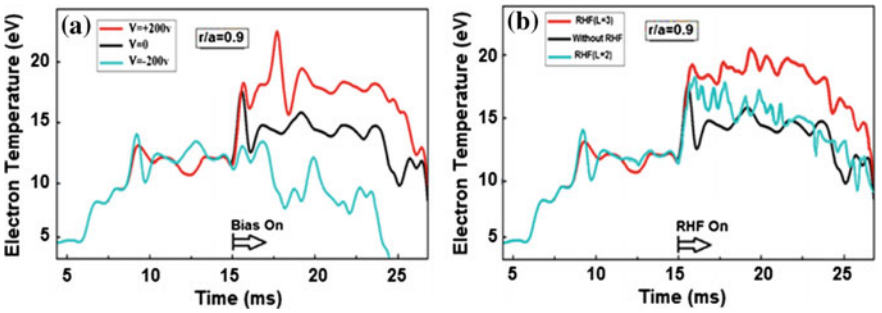

Fig. 8.48 Time evolution of the electron temperature in the plasma edge of IR-T1 Tokamak for **a** different biasing voltages and **b** different modes of RHF

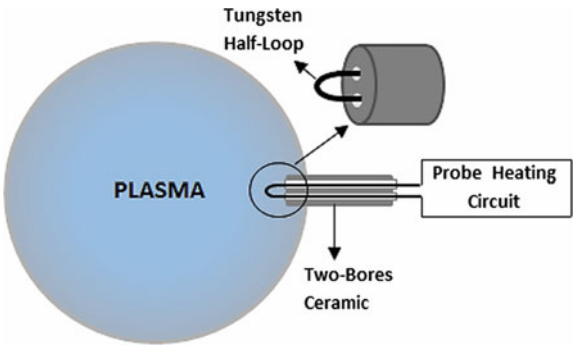

Fig. 8.49 Schematic representation of an emissive probe

$$V_{\mathrm{p}} = V_{\mathrm{f,em}} + T_{\mathrm{e}} \ln\left(\frac{I_{\mathrm{es}}}{I_{\mathrm{is}} + I_{\mathrm{em}}}\right) \tag{8.39}$$

$V_{\mathrm{f,em}}$ is a real floating potential that depends on the emission current I_{em}. The probe can emit electrons for so long as the probe potential is more negative than the plasma potential [42].

One of the disadvantages of emissive probes is their technical limitation to reach the temperature of around 3000 K. Also, the high power of the electron saturation current can destroy the probe. There is a new type of emissive probe that is heated by a laser, called the laser-heated emissive probe. For first time, a laser-heated emissive probe was designed in the Max Planck Institute in Germany that consists of a cylindrical electrode made of LaB_6 [43]. A molybdenum wire connects the electrode to copper threads passing from a single-bore ceramic. An infrared high-voltage diode laser heats the electrode to a high temperature and the probe begins to emit electrons. The schematic of the laser-heated emissive probe is seen in Fig. 8.50.

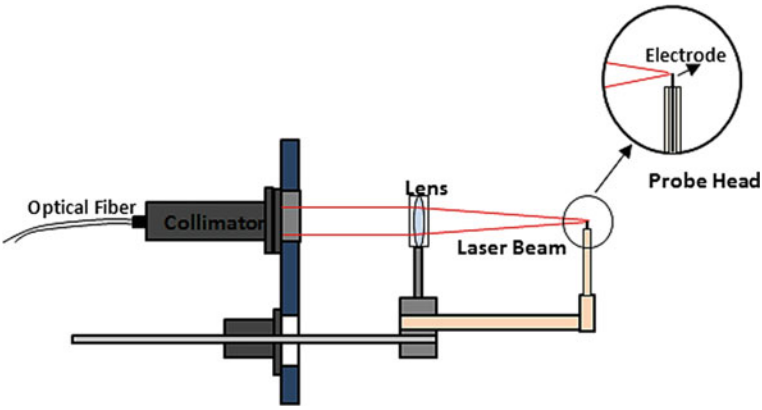

Fig. 8.50 Schematic of the laser-heated emissive probe [44]

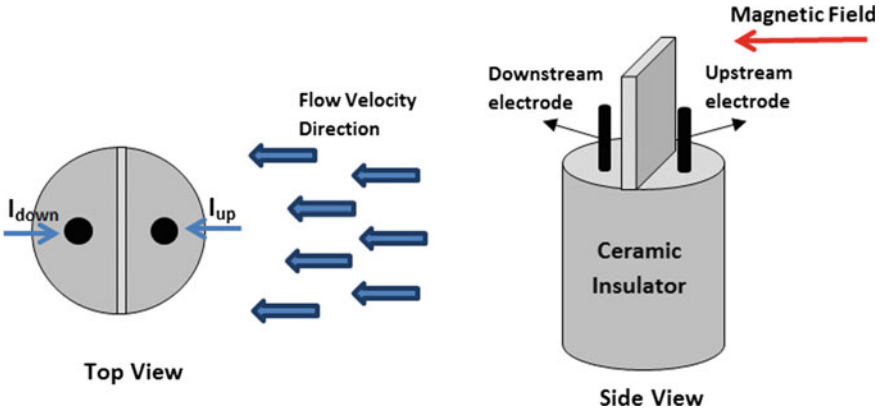

Fig. 8.51 Schematic of the double sided Mach probe

8.5.2.5 Mach Probe

The study of plasma flow velocity is of specific interests to Tokamaks, and particularly Tokamaks with a divertor [42]. The plasma rotation velocity can be determined by the Mach probe, which is a type of Langmuir probe. The simplest configuration of a Mach probe is composed of two electrodes separated from each other by an insulator (double sided Mach probe) as shown in Fig. 8.51. When the probe is exposed to a plasma flow as observed in Fig. 8.51, the current drawn by the upstream facing electrode (electrode facing the plasma flow) is more than that of the downstream facing electrode (electrode facing away from the flow). If I_{up} and I_{down} are currents drawn by upstream electrode and downstream electrode respectively, then the relation between them can be expressed by:

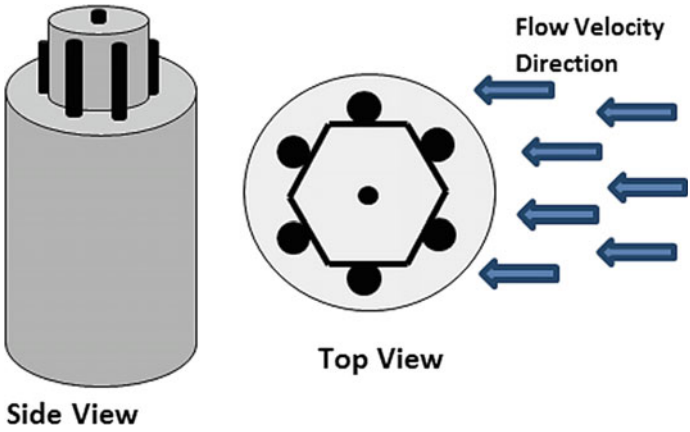

Fig. 8.52 Schematic of a multi-sided Mach probe (Gundestrup probe)

$$I_{\mathrm{up}}/I_{\mathrm{down}} = \mathrm{e}^{kM} \tag{8.40}$$

where $M = \frac{V_{\mathrm{flow}}}{C_s}$ is the Mach number of the plasma flow and $C_{\mathrm{s}} = \sqrt{\frac{2T_{\mathrm{e}}}{m_{\mathrm{i}}}}$ and k are sound velocity and a constant that is determined by the model used, respectively [45].

The picture is complicated by the need to consider the extent to which ion collection is impacted by the presence of the magnetic field. If the ion gyro radius (ρ_{i}), is much greater than the characteristic dimension of the probe (r_{p}), ions are considered to be unmagnetized. If the opposite limit holds, the ions are considered to be magnetized. For the highly magnetized case ($\rho_{\mathrm{i}}/r_{\mathrm{p}} \ll 1$), the magnetized model by Hutchinson is by far the most widely used. Double-sided Mach probes only measure the flow velocity along the magnetic line, so to measure the total flow velocity, this probe must be rotated from one shot to another shot. Multi-sided Mach probes are the best solution to this problem. These probes consist of four or more electrodes that are separated from each other by an insulator. One type of multi-sided Mach probe is the Gundestrup probe that can be seen in Fig. 8.52. The Mach probe in IR-T1 Tokamak is a four-sided probe as shown in Fig. 8.53.

The Influence of the Biased Electrode System on the Rotation Velocity of Plasma

In this part, the experimental results of the biased electrode effect on rotation velocity measured by a Mach probe are investigated [47]. For this purpose, a biasing voltage of +300 V is applied to the plasma edge (r = 11.5 cm) from t = 12.5 ms to t = 27 ms. Figure 8.54a–d illustrate the temporal evolution of the

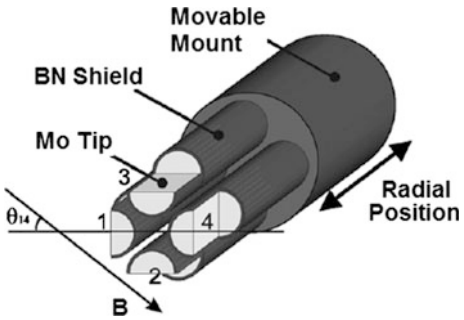

Fig. 8.53 Four-sided Mach probe in IR-T1 Tokamak [46]

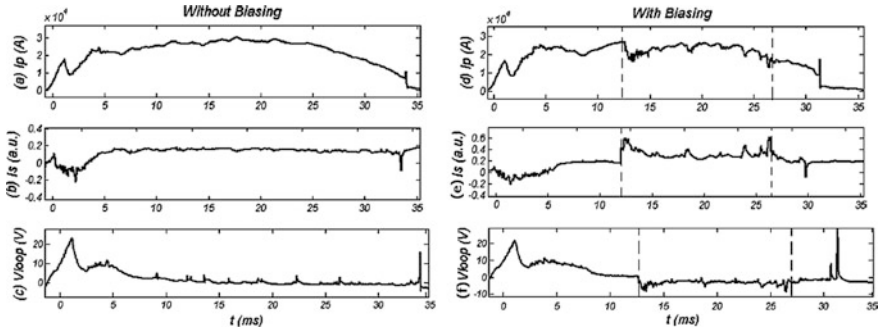

Fig. 8.54 Temporal evolution of the plasma current (I_p), ion saturation current (I_s) and loop voltage (V_{loop}) in both the absence and presence of the biasing voltage

plasma current (I_p), ion saturation current (I_s), and loop voltage (V_{loop}) at the plasma edge in both the absence and presence of the biasing voltage.

It can be observed that the ion saturation current increases during biasing. Theoretical models have been derived to describe the Mach probe's data in unmagnetized and magnetized plasmas, using fluid, particle, and kinetic models [11,48]. Figure 8.55a–d show the time profile of ion saturation currents collected by the toroidal Mach probes, the ratio of upstream to downstream current, and the resulting Mach number.

These figures demonstrate that the electrode biasing voltage causes a significant increment in the ion saturation currents in the upstream and downstream Mach probe signals. The ratio of upstream to downstream current signal (R) is as high as 8 during the bias induced improvement phase. For toroidal flow, the Mach number approaches 1.1 during electrode biasing, corresponding to a toroidal velocity of 5.58×10^4 m/s (T_i = 10 eV).

Figure 8.56a–d present the ion saturation currents measured by the poloidal Mach probes and the current ratio in the plasma edge. According to the model of Hutchinson, the peak poloidal velocity is around 3×10^3 m/s. The obtained results indicate that the biasing electrode voltage has an important role in the improvement of both the toroidal and poloidal edge plasma rotation. It must be mentioned that the

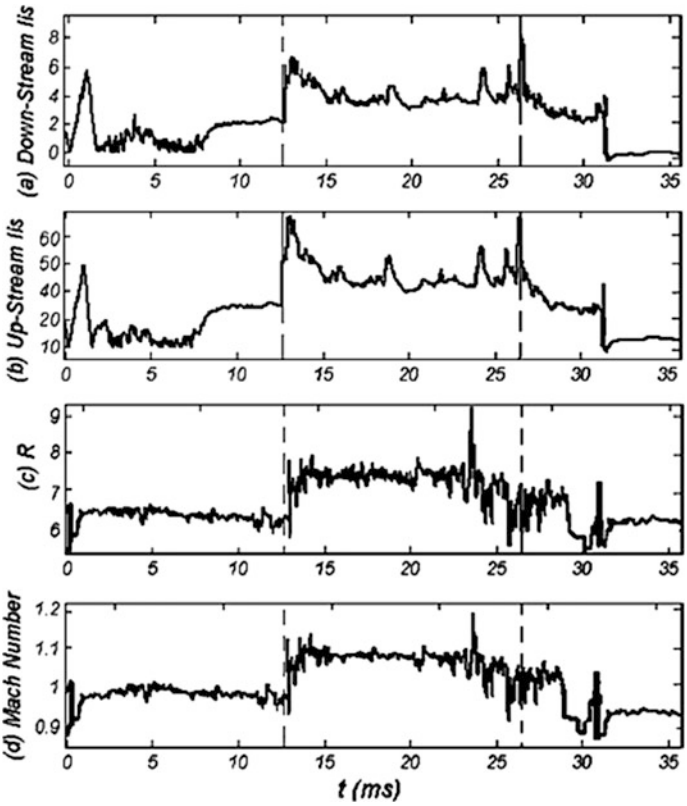

Fig. 8.55 Time evolution of **a** downstream ion saturation current, **b** upstream ion saturation current, **c** ratio of ion saturation currents, and **d** toroidal Mach number. The biasing voltage of +300 V is applied to the plasma edge (r = 11.5 cm) from t = 12.5 ms to t = 27 ms

poloidal velocity measured by the Mach probes is much smaller than the toroidal velocity, whereas in the experiments described, the poloidal magnetic field is very weak, $B_p \ll B_{tor}$. This means that $E \times B$ drift is mainly poloidal. It seems that another unknown phenomenon affects plasma toroidal rotation. The increase in the radial electric field due to the applied biasing voltage slowly reduces the poloidal rotation in the electron diamagnetic drift direction, i.e., to speed up rotation in the ion diamagnetic drift direction. An increased toroidal rotation velocity has the opposite effect on the poloidal rotation. The experimental uncertainty in our measurements can be attributed to: (1) the discrepancies in design, construction, and installing of the Mach probe, (2) excessive noises do not become zero during compensation of the Mach probe data, and (3) the Hutchinson model (which is not 100% compatible with our experiments).

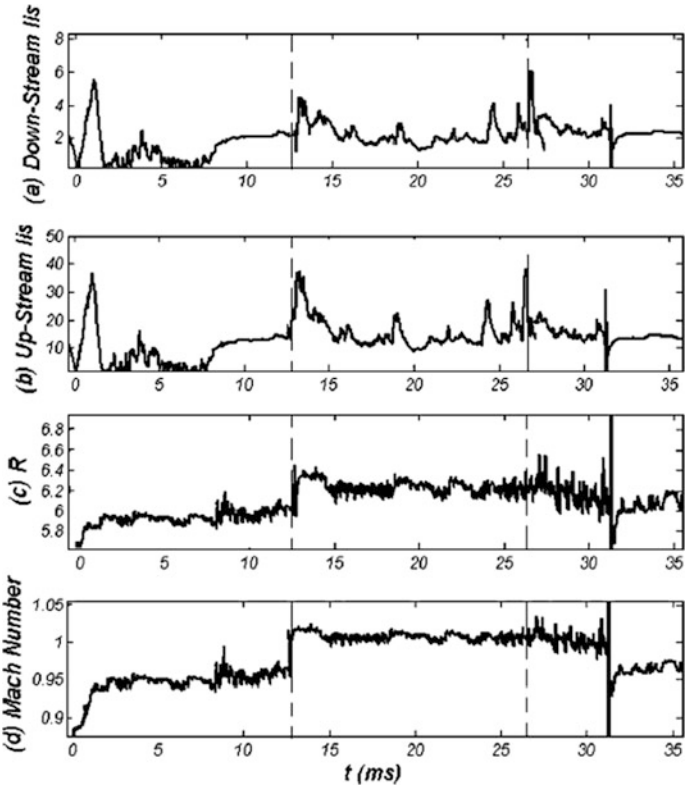

Fig. 8.56 Time evolution of **a** downstream ion saturation current, **b** upstream ion saturation current, **c** ratio of ion saturation currents, and **d** poloidal Mach number. The biasing voltage of +300 V is applied to the plasma edge (r = 11.5 cm) from t = 12.5 ms to t = 27 ms

The Study of Plasma Flow Rotation in the Presence of a Resonant Helical Magnetic Field

As mentioned earlier, RHF in IR-T1 Tokamak is an external magnetic field which can improve the plasma confinement. In this experiment, the RHF effect on the rotation of plasma flow in IR-T1 Tokamak is investigated. The DC current pulse through the helical windings is applied 100–400 A, which is very low compared to the plasma current itself (20–30 kA). The dominant mode in IR-T1 plasma Tokamak is often m = 3. The typical time evolution of the polar mode structure, plasma current, and Mirnov oscillations and diagnostics positioned around the chamber are shown in Fig. 8.57.

During the discharges, RHF current pulses of about 2, 3 ms and continuously until end of discharge were applied during active MHD oscillations. In most discharges the parameters were: Ip = 20 kA, $V_{\text{loop}} < 3$ V and $q(a) = 3.7$. In this experiment, the current in the RHF coil is about 400 A.

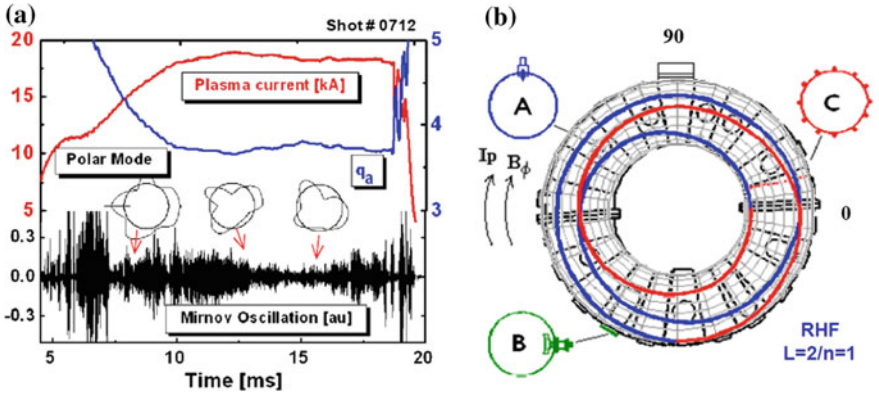

Fig. 8.57 **a** Time evolution of the polar mode structure, plasma current, and Mirnov oscillations. **b** A typical schematic of the $L = 2/1$ RHF winding coil, *A* Mach probe, *B* Biasing limiter and *C* Mirnov coils positioned around the chamber

The main effect of RHF on the discharge is the significant change in plasma rotation velocity and MHD fluctuation signals. As seen from Fig. 8.58, the poloidal velocity increases with positive biasing voltage but it decreases in the presence of RHF. Toroidal velocity does not exhibit considerable change and the poloidal Mach decreases as a result of applying the biasing voltage. It is clear that RHF decreases the toroidal rotation velocity to a significant extent. Figure 8.58a illustrates the temporal evolution of the poloidal and toroidal velocity of plasma rotation in the presence of RHF ($L = 3$) and positive limiter biasing voltage. RHF and positive limiter biasing voltage are applied at 7.7 and 10 ms, respectively. The first response of the plasma to the biasing voltage is a significant decrease in plasma poloidal rotation. During this reduction, in a matter of less than 0.5 ms, the edge electrostatic and magnetic fluctuations are strongly suppressed and the pressure gradient increases. The direction of this rotation usually corresponds to a negative direction of E_r. When applying the positive limiter biasing voltage after RHF with $L = 2$, a rapid increase in poloidal rotation is found and in this situation, the toroidal rotation became smooth (see Fig. 8.58b). This figure shows that by applying RHF, the plasma rotation fluctuation increases while both poloidal and toroidal rotation becomes smooth. The significant reduction of Mirnov oscillations, and toroidal and poloidal rotation velocity can be found in Fig. 8.58c as a result of applying RHF with $L = 3$.

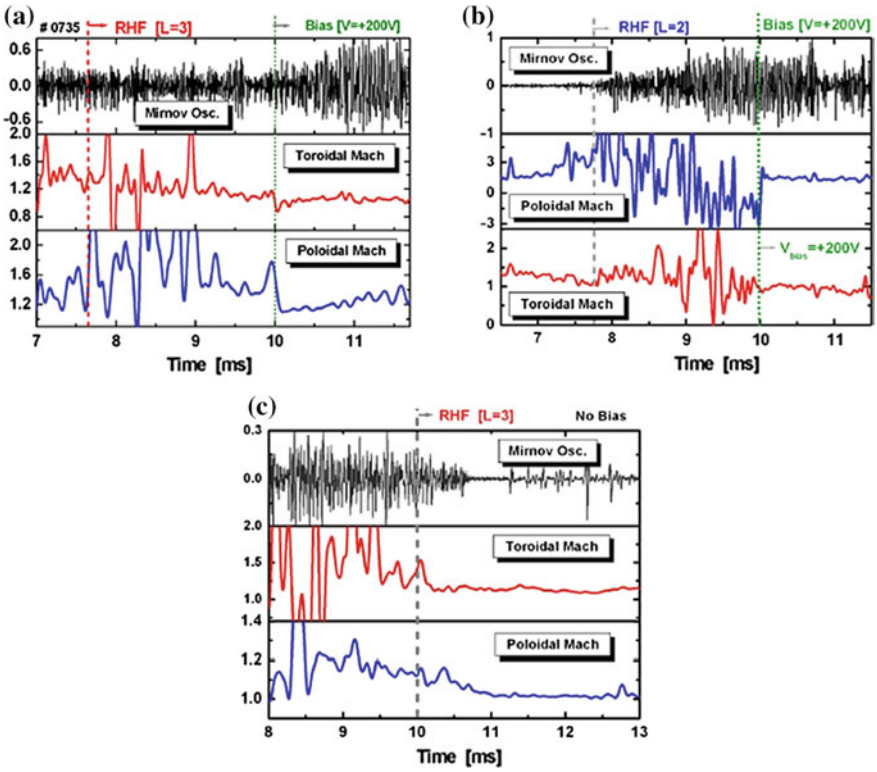

Fig. 8.58 **a** Time evolution of poloidal and toroidal rotation in the presence of RHF ($L = 3$) and positive limiter biasing voltage (+200 V), **b** Time evolution of Mirnov oscillations and poloidal and toroidal Mach number in the presence of RHF ($L = 2$) and positive limiter biasing voltage (+200 V) and **c** Time evolution of Mirnov oscillations and poloidal and toroidal Mach number in the presence of RHF ($L = 3$). RHF and biasing voltage are applied at 7.7 and 10 ms respectively

8.6 Conclusion

Nuclear fusion can possibly be a boundless, clean, and safe type of energy resource. It may require scientific and technological discoveries to reach our goals. Tokamaks are the devices used for magnetic confinement fusion, and over 198 Tokamaks have been built in the world. Large Tokamaks such as Tore Supra, and several smaller projects, notably the spherical Tokamak experiments such as MAST and NSTX, have paved the way for a next-generation project, ITER. The ITER project is expected to create ten times more energy that the energy consumed in heating the plasma. An extensive diagnostic system will be installed on the ITER machine to provide the measurements necessary to control, evaluate, and optimize plasma performance and to further the understanding of plasma physics. These include temperature, density, impurity concentration, and particle and energy confinement

time measurements. There are different Tokamaks with different sizes. CASTOR, ISTTOK, STOR-M, and IR-T1 are active small Tokamaks around the world and they are all lending a helping hand to the ITER project. The group of IR-T1 Tokamak has performed many experimental studies on the exact measurement of plasma parameters using different diagnostic techniques. In order to improve the plasma confinement, IR-T1 group designed and fabricated a biasing systems and resonant helical magnetic field. The experimental results demonstrate that the external resonant fields can control MHD activities and improve the plasma confinement.

Acknowledgements The authors thank the IR-T1 group for their great efforts. Also, the authors gratefully acknowledge support and encouragement for fusion research provided by the Coordinated Research Projects (CRP) No. 17001 of the International Atomic Energy Agency (IAEA) in Vienna.

References

1. World Population Prospects: The 2004 Revision (United Nations, Department of Economic and Social Affairs, Population Division, New York, 2005), https://esa.un.org/unpd/wpp/. Accessed 24 Feb 2005
2. International Energy Annual 1995 (U.S. Department of Energy, Washington, 1995), http://www.eia.doe.gov/emeu/world/contents.html. Accessed Dec 1996
3. UD-Led Team Sets Solar Cell Record (University of Delaware, Delaware, 2007), http://www.udel.edu/PR/UDaily/2008/jul/solar072307.html. Accessed 23 July 2007
4. Magic Solar Milestone Reached (UNSW Australia, 2008), http://www.unsw.edu.au/news/pad/articles/2008/nov/Solarrecord.html. Accessed 4 Nov 2008
5. K. Miyamoto, *Plasma Physics for Nuclear Fusion*, Revised edn. (MIT Press, Cambridge, 1987)
6. J. Wesson, *Tokamaks*, 3rd edn. (Clarendon Press, Oxford, 2004)
7. K. Niu, *Nuclear Fusion* (Cambridge University Press, Cambridge, 2009)
8. Inertial Confinement Fusion (Wikipedia, last modified on 27 July 2016), https://en.wikipedia.org/wiki/Inertial_confinement_fusion
9. Inertial Electrostatic Confinement Fusion (University of Wisconsin, Madison, 2007), http://iec.neep.wisc.edu/operation.php
10. M. Kikuchi, K. Lackner, M.Q. Tran (eds.), *Fusion Physics* (International Atomic Energy Agency press, Vienna, 2012)
11. S. Meshkani, M. Ghoranneviss, M. Lafouti, A.S. Elahi, Analysis of the radial and poloidal turbulent transport in the edge tokamak plasma. J. Plasma Phys. **79**, 647–655 (2013). doi:10.1017/S002237781300010X
12. I.A. Huchinson, *Principles of Plasma Diagnostics*, 2nd edn. (Cambridge University Press, New York, 2002)
13. M. Ghasemloo, M. Ghoranneviss, M.K. Salem, R. Arvin, S. Mohammadi, A. Nik Mohammadi, The effect of emissive biased limiter on the magnetohydrodynamic modes in the IR-T1 tokamak. Phys Plasmas **20**, 032503 (2013). doi:10.1063/1.4791658
14. R.R. Weynants, G. Van Oost, G. Bertschinger, J. Boed, H. Euringer, K.H. Finken, D.S. Gray, J.D. Hey, D.L. Hillis, J.T. Hogan, L. Konen, R. Leners, A.M. Messiaen, A. Pospieszczyck, U. Samm, R.P. Schorn, B. Schweer, G. Telesca, R.V. Nieuwenhove, P.E. Vandenplas, P. Brays, T. Delvigen, K.H. Dippel, F. Durodie, Confinement and profile changes induced by the

presence of positive or negative radial electric fields in the edge of the TEXTOR tokamak. Nucl. Fusion **32**, 837–853 (1992)
15. C. Silva, I. Nedzelskiy, H. Figueiredo, C. Varandas, Comparison of limiter and emissive electrode bias on the Tokamak ISTTOK. J. Nucl. Mater. **415**, 337–339 (2005). doi:10.1016/j.jnucmat.2004.10.106
16. H.W. Lu, J.R. Luo, F.C. Zhong, X.J. Zha, L.Q. Hu, HT-7 team, suppression of MHD activity with limiter biasing in the HT-7 Tokamak. Eur. Phys. J. D **66**, 213–217 (2012). doi:10.1140/epjd/e2012-30283-1
17. K.M. Lau, H. Weng, Climate signal detection using wavelet transform: how to make a time series sing. Bull. Am. Math. Soc. **76**, 2391–2402 (1995). doi:10.1175/1520-0477(1995)076<2391:CSDUWT>2.0.CO;2
18. C. Eckart, G. Young, A principal axis transformation for non-hermitian matrices. Bull. Am. Math. Soc. **45**, 118–121 (1939). doi:10.1090/S0002-9904-1939-06910-3
19. V.P. Budaev, I.M. Pankratov, S. Takamura, N. Ohno, M. Takagi, H. Matsuno, M. Okamoto, S.K. Saha, The effect of the rotating helical fields on the plasma edge in the HYBTOK-II Tokamak. Nucl. Fusion **46**, S175–S180 (2006). doi:10.1088/0029-5515/43/6/302
20. M. Jakubowski, R. Fonck, J.S. Kim, G. McKee, Application of wavelet spectral analysis to plasma fluctuation measurements using beam emission spectroscopy. J. Rev. Sci. Instrum. **70**, 874–877 (1999)
21. C. Nardone, Multichannel fluctuation data analysis by the singular value decomposition method. Application to MHD modes in JET. J Plasma Phys. Controlled Fusion **34**, 1447–1465 (1992)
22. S. Saadat, M.K. Salem, M. Goranneviss, P. Khorshid, Comparison study of fourier and SVD method for plasma mode analysis in Tokamaks. J. Fusion Energy **30**, 100–104 (2011). doi:10.1007/s10894-010-9349-0
23. D.F. Escande, M. Ottaviani, Simple and rigorous solution for the nonlinear tearing mode. J. Phys. Lett. A **323**, 278–284 (2004). doi:10.1016/j.physleta.2004.02.010
24. B.P. Van Milligen, A.C.A.P. van Lammeren, N.J.L. Cardozo, F.C. Schüller, M. Verreck, Gradients of electron temperature and density across m = 2 magnetic islands in RTP. J. Nucl. Fusion **33**, 1119–1132 (1993)
25. J.A.C. Cabral, C.A.F. Varandas, M.P. Alonso, P. Belo, R. Canário, H. Fernandes, R. Gomes, A. Malaquias, P. Malinov, F. Serra, F. Silva, A. Soares, Enhancement of the ISTTOK plasma confinement and stability by negative limiter biasing. J. Plasma Phys. Control. Fusion **40**, 1001–1009 (1998)
26. M. Dreval, C. Xiao, D. Trembach, A. Hirose, S. Elgriw, A. Pant, D. Rohraff, T. Niu, Simultaneous evolution of plasma rotation, radial electric field, MHD activity and plasma confinement in the STOR-M tokamak. J. Plasma Phys. Control. Fusion **50**, 095014–095026 (2008). doi:10.1088/0741-3335/50/9/095014
27. R.B. White, Resistive instabilities and field line reconnection, in *Handbook of Plasma Physics* (Amsterdam, Netherlands: North Holland, 1983)
28. H.P. Furth, J. Killeen, M.N. Rosenbluth, Finite-resistivity instabilities of a sheet pinch. Phys. Fluids **6**, 459–484 (1963)
29. M. Ghoranneviss, A. Hogabri, S. Kuhn, MHD activity at low q(a) in Iran tokamak1 (IR-T1). J. Nucl. Fusion **43**, 210–215 (2003)
30. A.S. Elahi, M. Ghoranneviss, Theoretical and experimental investigation of effects of Toroidal field ripple on Poloidal beta, internal inductance and Shafranov shift in IR-T1 Tokamak. J. Nucl Part Phys **2**, 112–118 (2012). doi:10.5923/j.jnpp.20120205.02
31. M. Emami, M. Ghoranneviss, A.S. Elahi, A.R. Rad, Analytical and experimental approach in plasma displacement measurement in IR-T1 Tokamak. J. Plasma Phys. **76**, 1–8 (2009). doi:10.1017/S0022377809008034
32. S. Meshkani, M. Ghoranneviss, M. Lafouti, A.S. Elahi, Plasma internal inductance in the presence of external resonant fields in IR-T1 Tokamak. J. Fusion Energy **33**, 619–626 (2014)
33. M. Lafouti, M. Ghoranneviss, S. Meshkani, A.S. Elahi, Low MHD activity using resonant helical field and limiter biasing in IR-T1 tokamak. J. Plasma Phys. **79**, 765–770 (2013)

34. M. Lafouti, M. Ghoranneviss, S. Meshkani, A.S. Elahi, Modification of tokamak edge plasma turbulence and transport by biasing and resonant helical magnetic field. J. Rev. Sci. Instrum. **84**, 053504 (2013). doi:10.1063/1.4805066
35. R.B. Randall, B. Tech, *Frequency Analysis*, 3rd edn. (Bruël and Kjær, Nærum, 1987)
36. W.F. Smith, *Foundations of Materials Science and Engineering*, 3rd edn. (McGraw-Hill, New York, 2004)
37. R. Schrittwieser, J. Adamek, P. Balan, M. Hron, C. Ionita, K. Jakubka, L. Kryska, E. Martines, J. Stockel, M. Tichy, G. Van Oost, Measurements with emissive probes in the CASTOR tokamak. J. Plasma Phys. Control Fusion **44**, 567–578 (2002)
38. J. Adamek, J. Stockel, M. Hron, J. Ryszawy, A novel approach to direct measurement of the plasma potential. Czech J. Phys. **54**, C95–C99 (2004)
39. I. Katsumata, A review of ion sensitive probes. J. Contrib. Plasma Phys. **36**, 73–80 (1996)
40. J. Adamek, P. Balan, M. Hron, C. Ionita, E. Martines, J. Ryszawy, R. Schrittwieser, J. Stöckel, M. Tichy, G. Van Oost, Direct plasma potential measurements by a novel probe. Paper presented at the 31st EPS conference on plasma physics, London, 28 June–2 July (2004)
41. S. Meshkani, M. Ghoranneviss, A.S. Elahi, M. Lafouti, Design and fabrication of comparative Langmuir Ball-Pen Probe (LBP) for the Tokamak. J. Fusion Energy **34**, 394–397 (2015)
42. M. Keilhacker, E. Deksnis, P. Harbour, P.H. Rebut, R. Simonini, A. Taroni, G.C. Vlases, M. L. Watkins, Modeling impurity control by plasma flows in the JET pumped divertor, in *Proceeding of the Thirteenth International Conference on Plasma Physics and Controlled Nuclear Fusion Research*, 345–364 (1990)
43. R. Madani, C. Ionita, R. Schrittwieser, G. Amarandei, P. Balan, T. Klinger, A laser-heated emissive probe for fusion applications. Paper presented at the 31st EPS conference on plasma physics, London, 28 June–2 July (2004)
44. R. Schrittwieser, R. Stärz, C. Ionita, R. Gstrein, T. Windisch, O. Grulke, T. Klinger, A radially movable laser-heated emissive probe. J. Plasma Fusion Res. **8**, 632–635 (2009)
45. M. Lafouti, M. Ghoranneviss, A.S. Elahi, S. Meshkani, Novel design of multi-purpose probe for the measurement of plasma density gradient, flow and transport. J. Fusion Energy **34**, 273–276 (2015)
46. F. Hedayatian, M. Ghoranneviss, A.S. Elahi, Measurement of magnetic field fluctuations and plasma rotation speed. J. Nucl. Part. Phys. **4**, 123–128 (2014). doi:10.5923/j.jnpp.20140404.02
47. M. Ghoranneviss, S. Mohammad, A.S. Elahi, R. Arvin, Tokamak edge plasma rotation in the presence of the biased electrode. J. Fusion Eng. Des. **88**, 94–99 (2013). doi:10.1016/j.fusengdes.2012.12.001
48. I.H. Hutchinson, Ion collection by probes in strong magnetic fields with plasma flow. J. Phys. Rev. A **37**, 4358 (1988). doi:10.1103/PhysRevA.37.4358

Chapter 9
Cost-Effective Plasma Experiments for Developing Countries

Rattachat Mongkolnavin, Siriporn Damrongsakkul, Oi Hoong Chin, Deepak Subedi and Chiow San Wong

9.1 Introduction

Plasma technology is a backbone technology for most of all modern industries, including electronics, agricultural, medical, and environmental remediation industries. However, due to the high initial capital cost required to set up plasma systems for related industrial processes, the potential for plasma technology to enhance productivity and effectiveness cannot be fully realized in industry. Thus, we believe there is a need to emphasize the importance of developing cost-effective plasma devices to perform industrial processes that are currently relying on expensive plasma systems.

There are two major cost factors in setting up most plasma systems. First is the requirement of low or ultra-low operating pressure. The creation of high vacuum means that a large budget is needed to purchase expensive high vacuum equipment, which consists of the pumping system, pressure gauges, as well as an assortment of vacuum valves, couplings, and connection pipes. It is for this reason that the development of atmospheric pressure discharge has attracted much research effort in recent years [1, 2]. The second factor is the power source. Compared to RF,

R. Mongkolnavin
Department of Physics, Faculty of Science,
Chulalongkorn University, Bangkok 10330, Thailand

S. Damrongsakkul
Department of Chemical Engineering, Faculty of Engineering,
Chulalongkorn University, Bangkok 10330, Thailand

O.H. Chin · C.S. Wong (✉)
Plasma Technology Research Centre, Department of Physics, Faculty of Science,
University of Malaya, 50603 Kuala Lumpur, Malaysia
e-mail: wongchiowsan@gmail.com

D. Subedi
Department of Natural Science, Kathmandu University, Dhulikhel, Nepal

R.S. Rawat (ed.), *Plasma Science and Technology for Emerging Economies*,
DOI 10.1007/978-981-10-4217-1_9

microwave or even DC power sources, one relatively cheap power source is the 50 Hz AC power supply which can be obtained directly from the domestic power source via a step-up transformer. The effectiveness of using relatively less-expensive and simple plasma devices for industrial processes must of course be verified before they can be implemented in industry. This opens up a broad range of opportunities for research which may be undertaken by small laboratories such as those among the member institutions of the Asian African Association for Plasma Training (AAAPT) [3].

Another category of plasma devices that can be considered by small laboratories due to their low initial and subsequent maintenance costs is small pulsed plasma devices such as the plasma focus, vacuum spark, and pulsed capillary discharge. These devices are not yet being used for industrial application, but they are being widely studied for possible applications as high-energy particle beams and soft to hard X-ray radiation sources. These devices are capable of producing plasmas with high temperatures up to tens of keV and particle densities close to solid density. The plasma focus is the subject of several chapters of the current book, and hence it will not be covered in this chapter. The operating principles and applications of the 50 Hz glow discharge, dielectric barrier discharge, nonthermal plasma jet, vacuum spark, pulsed capillary discharge, and exploding wire will be discussed in the following sections.

9.2 Plasma Devices and Their Applications

9.2.1 50 Hz AC Glow Discharge

Glow discharge plasma is well known to be used in many industrial applications. It can be produced by a high-voltage power source that is coupled to a pair of electrodes. A 50 Hz AC power source is relatively cheap in comparison to the RF, microwave, or DC power sources that are commonly used in industrial systems. The 50 Hz AC power source is provided through domestic power outlets. For higher voltage application, a step-up transformer can be used, such as in the case of neon lighting. A simple milliammeter or a multimeter can be used to monitor the discharge current. A voltmeter coupled with a resistive voltage divider can be used to measure the discharge voltage which is expected to be in the kV region. An example of the setup of a 50 Hz AC glow discharge system is shown in Fig. 9.1 [4].

The system consists of a discharge chamber evacuated by using a rotary pump, a gas flow control system, a pair of circular stainless steel plates as electrodes that are connected to a 50 Hz AC power supply consisting of basically a variac, and a neon transformer. The system operation is straight forward and the discharge current can be controlled by using a current-limiting resistor such that the current is within the operating range of a glow discharge, which is normally in the mA region. The voltage across the electrodes can be adjusted from 3 to 16 kV. Before each

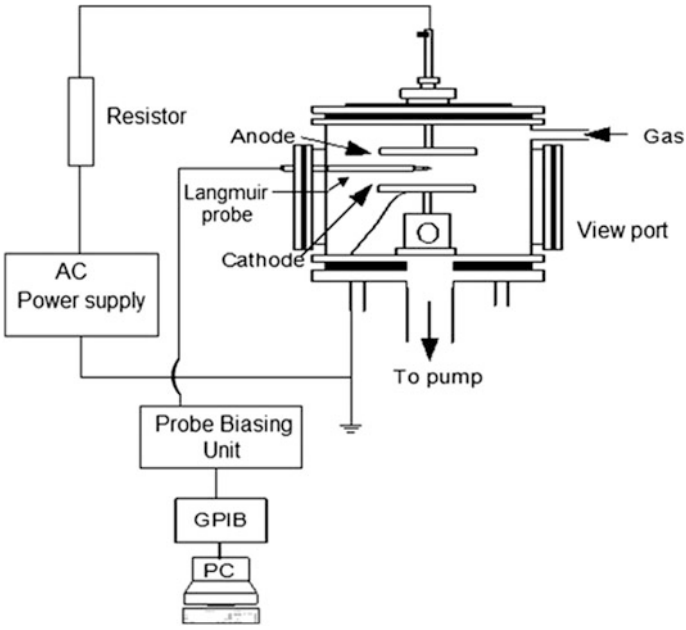

Fig. 9.1 Schematic of a typical 50 Hz AC glow discharge system [4]

operation, the chamber must be evacuated to less than 0.3 mbar before the operating gas is filled to the required pressure. After the pressure stabilizes at 1 mbar, glow discharge plasma can be initiated by applying a sufficiently high AC voltage across the electrodes. The average power (W) can be calculated according to Eq. (9.1):

$$W = \frac{1}{T}\int_{t}^{t+T} I(t)V(t)dt, \tag{9.1}$$

where W is the average power, I is the discharge current, V is the applied voltage, and T is the cycle time.

In a series of experiments [4] where the interelectrode distance was set to 2 cm and the working pressure was varied from 0.3 to 0.6 mbar, argon glow discharge plasma was produced by using a discharge voltage of 16 kV peak-to-peak. Various sets of I–V characteristics were obtained with the Langmuir probe placed at the center of the plasma column. These I–V characteristics can be used to determine the electron temperature and density of the plasma produced by the system. The variations of electron density and electron temperature with pressure for this example are shown in Fig. 9.2. It can be seen that the electron density increases when the operating pressure increases, while the electron temperature decreases. The maximum electron density and electron temperature obtained are found to be 3.58×10^{16} m^{-3} and 5.98 eV, respectively. The increase of electron density with

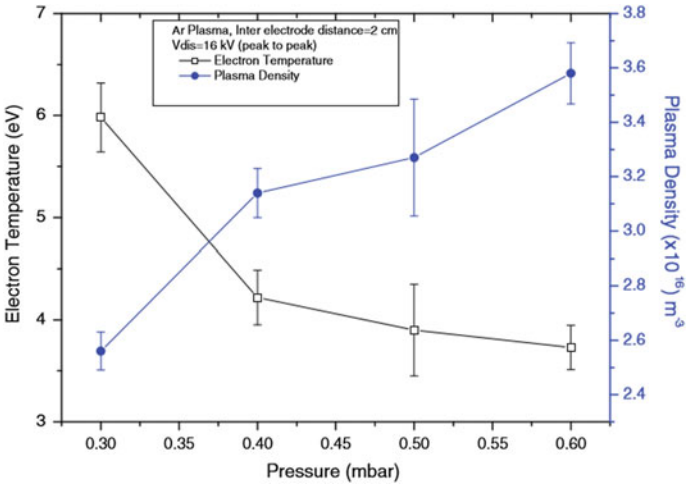

Fig. 9.2 Variation of electron temperature and electron density with operating pressure of a 50 Hz AC glow discharge [4]

pressure is believed to be due to more ionization. Since an increase in pressure increases the neutral particle density, the probability of plasma electron energy loss due to collisions with neutral particles also increases. This, in turn, leads to a decrease in electron energy, i.e., electron temperature decreases with increase in pressure. However, it has been noticed that decrease in interelectrode distance for a particular pressure caused a decrease in plasma density but an increase in electron temperature, while the reverse trend occurred for the case of widening interelectrode distance. It is believed that when the interelectrode distance is greater, the electrons can undergo more collisions resulting in an increase in plasma density. However, because there are more collisions, electrons also lose more energy, resulting in a decrease in electron temperature.

In another series of experiments, Optical Emission Spectroscopy (OES) has been used to monitor the excited plasma reactive species generated by a 50 Hz AC plasma. The optical emission analysis can explicate the reactions of reactive species that may contribute to plasma surface modification. The emission spectra of 50 Hz AC plasmas generated using nitrogen, oxygen, and dry air are presented in Fig. 9.3. The results showed that nitrogen plasma mainly consisted of the nitrogen molecule radical ($N_2^{\cdot}$) and nitrogen molecule ion (N_2^{+}) as indicated by the strong peaks at the wavelengths of 315.9, 337.13, and 357.8, 391.44 nm, respectively. For oxygen plasma, strong peaks were observed at the wavelengths of 777.42 and 844.56 nm corresponding to the oxygen radical ($O^{\cdot}$) [5]. For air plasma, both nitrogen and oxygen species were observed. In addition, the hydrogen radical ($H_{\alpha}^{\cdot}$) was noticed at the wavelength of 656.30 nm, when all types of plasma were generated. With measurable and known plasma characteristics, the 50 Hz AC glow discharge plasma has been used successfully to treat biomaterials such as gelatin and Thai silk fibroin to improve the wettability of their surfaces [5–9].

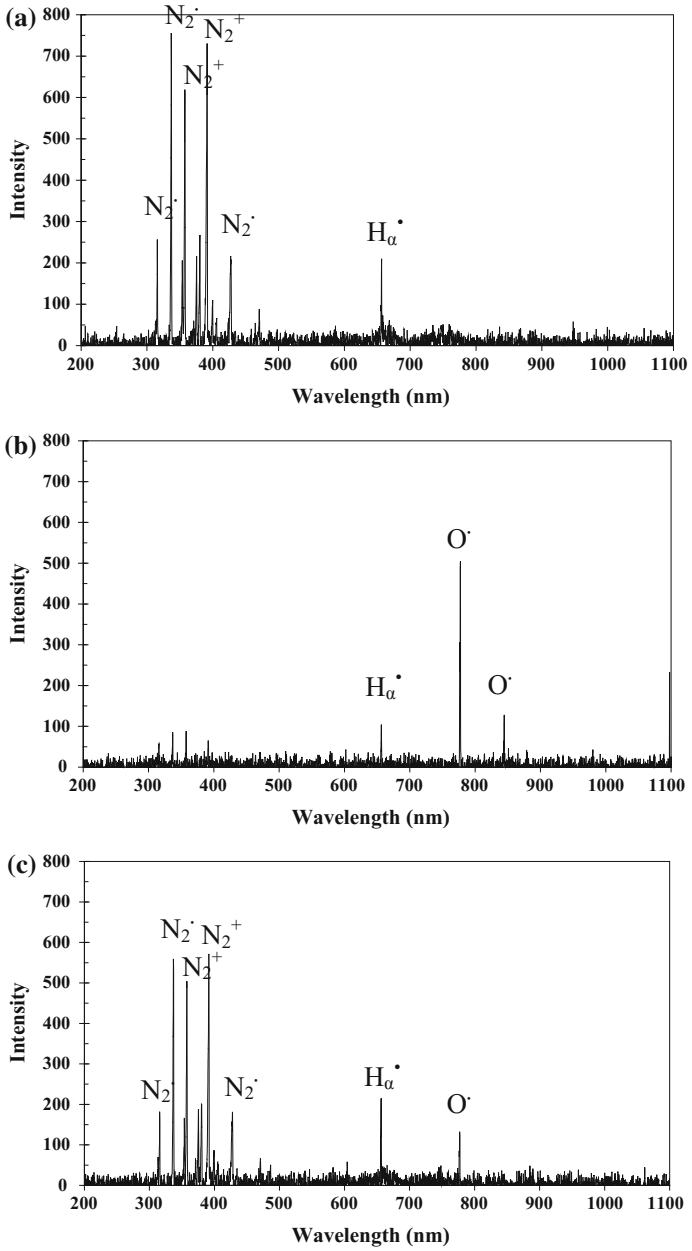

Fig. 9.3 Optical emission spectrum of **a** nitrogen plasma, **b** oxygen plasma, and **c** air plasma generated by 50 Hz AC glow discharge [5]

9.2.1.1 Application of 50 Hz Plasma System for Graft Polymerization of Polyimide Film to Improve Adhesion of Copper by Electroless Plating

The fabrication of flexible printed circuits in the microelectronics industry requires the use of copper metallized polyimide (PI) film. Electroless plating of metal from solution onto PI film is one of the most frequently used industrial processes for copper metallization. However, the adhesion strength of the electrolessly plated copper or nickel to the pristine PI film is found to be weak for practical applications. The PI surfaces have to be pretreated by various methods such as chemical treatment, [10–12] plasma treatment, [13], and laser treatment [14] to enhance the adhesion with the electrolessly deposited metals.

The utilization of the 50 Hz AC glow discharge for pretreatment of PI film to enhance adhesion strength of copper plating has been tested [15]. The procedure for plasma treatment of the PI film may involve three processes: (i) plasma cleaning of the polymer surface by an argon plasma; (ii) polymer surface activation to improve wettability by an oxygen plasma; and (iii) polymerization of the PI surface by using the 1-vinlyimidazole (VIDz) monomer to produce the adhesion promotion layer for electroless plating of Cu on the PI film. This procedure produced an average adhesion strength of 9–10 N/cm, as compared to the 7 N/cm adhesion strength reported earlier [15, 16].

9.2.1.2 Application of a 50 Hz AC Glow Discharge for Surface Modification of Biomedical Materials

Materials and biomaterials developed for biomedical applications need to be biocompatible with cells and living tissues. The materials could be designed to serve required functions in specific applications. For example, to be applied as tissue engineered scaffolds, biodegradable materials are required to support tissue formation. They have to be not only biocompatible but mechanically stable and biodegradable with an appropriate rate, corresponding to the rate of tissue formation. To accomplish this, the morphology and properties of scaffolds are very important. This includes the surface properties of biomaterials used to fabricate scaffolds as surface properties play a major role in determining the fate of cells. Generally, cells can interact well with some selective surfaces that are favorable to cell adhesion, initiating an initial stage of cell growth. If cells can interact well with the surface, they can subsequently adhere, migrate, proliferate, and eventually differentiate. Cell-material interaction therefore is a crucial factor for the initial stage of cell growth. Preferable surface properties for great cell–material interactions include, for example, appropriate surface wettability, surface charge, surface topology, and surface functional groups. Various surface modifications are thus introduced to create such a surface to support this process. Plasma treatment is an effective tool to modify surfaces of various materials used in biomedical applications. The treatment can induce changes in surface wettability and topology,

introduce selective functional groups, and change electrostatic charges on the surface. The treated surface could be ready for use "as is", or may be subjected to further treatment with other techniques. The plasma process gas is chosen based on the desired surface functionality.

Examples of biomaterials treated with various types of plasma for biomedical applications in the past decades are summarized in Table 9.1. The plasma is usually generated by a radio-frequency power supply at a frequency of 13.56 MHz. AC and DC power supplies are less frequently applied, in particular, 50 Hz AC glow discharge. Biodegradable materials both natural and synthetic were of more interests compared to nonbiodegradable materials. Among biodegradable materials applied for biomedical technology, naturally derived materials are more popular due to their biocompatibility. Reports on the plasma treatment effects on natural biodegradable materials include proteins (gelatin, silk) [7–9, 23–31] and polysaccharides (chitosan and cellulose) [17–22, 32]. Recently, only three reports have used a 50 Hz AC power supply to treat naturally derived biomaterials, such as gelatin and silk fibroin [7–9]. Prasertsung et al. [7, 8] first introduced 50 Hz AC plasma to treat the surface of gelatin, one of the most interesting biodegradable materials due to its affordable cost and excellent peptide sequence for cell recognition. The treatment aimed to improve the biocompatibility of dehydrothermal-crosslinked gelatin films using three types of plasma gases, including nitrogen, oxygen, and air. They showed that the N-containing functional groups generated by nitrogen and air plasma, and O-containing functional groups generated by oxygen and air plasmas were incorporated onto the surface, resulting in a more hydrophilic surface. The functional groups were found to increase with increasing treatment time. An in vitro cell culture using rat bone marrow-derived stem cells revealed that the number of cells attached to plasma-treated gelatin films was significantly increased compared to untreated samples. Among the three types of plasmas used, nitrogen plasma treatment provided the best cell attachment on the gelatin surface.

To enhance the biocompatibility of Thai silk fibroin surfaces, Amornsudthiwat et al. [9] have used low-energy nitrogen plasma generated by a 50 Hz AC power source. Surface wettability and cell adhesion on the Thai silk fibroin surfaces were improved after plasma treatment. X-ray photoelectron spectroscopy (XPS) revealed that amine, hydroxyl, ether, and carboxyl groups were created on the Thai silk fibroin surfaces after plasma treatment. After 90s plasma treatment, the water contact angle was reduced to 20°, compared to 70° for the untreated surface (Fig. 9.4). The early cell adhesion of L929 mouse fibroblasts was accelerated on a 90s plasma-treated silk fibroin surface. L929 cells only took 3 h to reach 100% cell adhesion and showed a more developed F-actin on 90s nitrogen plasma-treated surfaces, while less than 50% cell adhesion was observed on the untreated Thai silk fibroin surfaces as shown in Fig. 9.5. This demonstrated that the 50 Hz AC plasma system enhanced early L929 mouse fibroblast adhesion on Thai silk fibroin surfaces without any significant change in surface topography and bulk chemistry.

The only report on the use of AC plasma to treat nonbiodegradable (synthetic) polymers was by Anderson et al. [39]. They used a phase shifted 100 Hz power

Table 9.1 Examples of biomaterials treated with various types of plasma for biomedical applications

Type of material	Material	Plasma gas	No. of reports	Type of plasma generator					
				AC	DC	Conventional RF	Microwave RF	Dielectric barrier discharge (DBD)	Unidentified
Biodegradable materials (natural and synthetic)	Chitosan	Ar, O_2, air, N_2	4			1 [17]		1 [18]	2 [19, 20]
	Chitosan/gelatin/poly (*L*,*L*-lactide) blend		1		1 [21]				
	Corn starch-based biomaterial (SBB) blend	O_2	1			1 [22]			
	Gelatin	O_2, air, N_2	4	2 [7, 8]	1 [23]				1 [24]
	Silk fibroin	Ar, O_2, N_2	8	1 [9]		2 [26, 27]	3 [25, 28, 29]		2 [30, 31]
	Cellulose	Alkaline, O_2, NH_4	1			1 [32]			
	Polycaprolactone	Air	1			1 [33]			
	Poly (lactide-co-glycolide), PLGA		3			3 [34–36]			
	Poly-l-lactide, PLLA		2			1 [37]			1 [38]
	Total 25			3	2	11	2	1	6

(continued)

Table 9.1 (continued)

Type of material	Material	Plasma gas	No. of reports	Type of plasma generator					
				AC	DC	Conventional RF	Microwave RF	Dielectric barrier discharge (DBD)	Unidentified
Nonbiodegradable materials (synthetic)	Silicone rubber	Ar	1	1 [39]					
	316L Stainless steel	NH_3, Ar, Allylamine	1			1 [40]			
	Titania nanotube	Allylamine	1			1 [41]			
	Titanium	NH_3, Ar, Allylamine, H_2, N_2, O_2	4		2 [42, 43]		1 [44]		1 [45]
	Glass slip	Allylamine & Hexane	1			1 [46]			
	Biphasic calcium phosphate	N_2, air	1						1 [47]
	Total 9			1	2	3	1		2

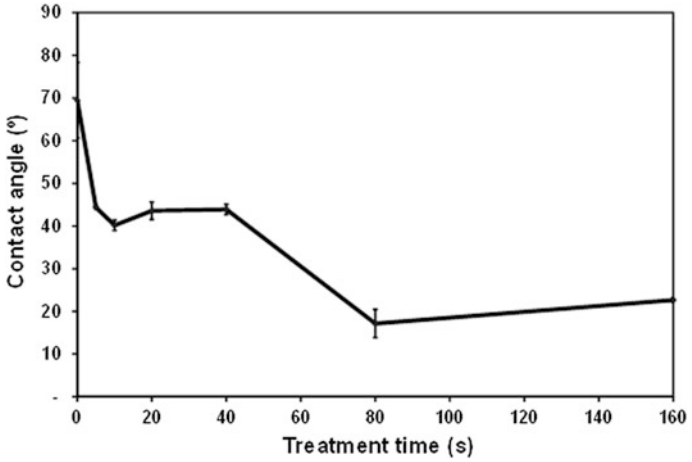

Fig. 9.4 The water contact angle of nitrogen plasma-treated Thai silk fibroin films as a function of treatment time. Reprinted from Ref. [9], Copyright (2013), with permission from Elsevier

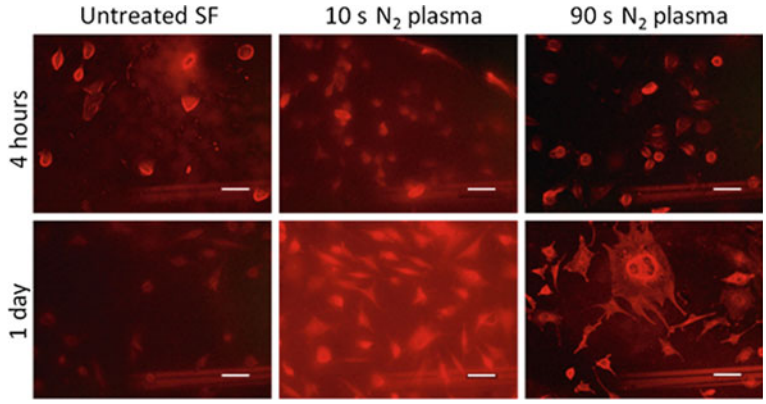

Fig. 9.5 F-actin cell cytoskeleton of L929 on untreated and plasma-treated Thai silk fibroin surface after the culture period of 4 h and 1 day (the scale bar is 100 m in length). Reprinted from Ref. [9], Copyright (2013), with permission from Elsevier

supply to generate argon plasma for the polymerization of 1-vinyl-2-pyrrolidone (VP) on a silicon rubber surface to reduce the activation of blood coagulation.

This compares to silk fibroin, which is one of the most studied natural biomaterials of this decade. RF microwave plasma treatment of this material has been explored in three reports by Amornsudthiwat et al. [25], Baek et al. [28], and Jin et al. [29]. Amornsudthiwat et al. introduced microwave oxygen plasma etching to create different degrees of stiffness in the silk fibroin surface and to investigate the effects of differing surface stiffness on the cell–substrate interaction [25]. In vitro

culture using mouse fibroblasts (L929) and human Mesenchymal Stem Cells (hMSC) as distinct model cells showed that the increased stiffness of plasma-treated silk fibroin affected only L929 adhesion, and not that of hMSC. L929 cell attachment and spreading were better on the stiffer surface than on the untreated surface, while hMSC could spread well on both stiff (plasma-treated) and soft (untreated) silk fibroin surfaces. Microwave plasma was also reported to treat silk fibroin surfaces to improve biocompatibility and chondrogenic responses of articular chondrocytes [28, 29].

Regarding the type of plasma generators, microwave plasma can generally provide higher plasma power on the order of hundreds of W to kW, while the AC plasma provides much lower plasma power (2–12 W) [7, 8, 25]. This proves that AC plasma, especially 50 Hz AC glow discharge, is a cost-effective plasma that can be efficiently employed as a surface modification tool for biomaterials in biomedical technology.

9.2.2 Dielectric Barrier Discharge (DBD)

Dielectric Barrier Discharges (DBDs) have gained much attention in the last few decades due to their wide range of potential applications in industry, medicine, ozone generation, and other forms of pollution control. The interest in these atmospheric pressure plasmas has been emphasized in practical applications because they minimize the need for vacuum systems and enable the continuous treatment of materials [48]. DBDs are formed using one or more insulating layers between two metal electrodes with different planner, cylindrical, or annular configurations, and have been used for material processing and polymer surface modification. The filamentary DBD is an excellent source of micro-discharges containing energetic electrons. It is believed that micro-discharges in DBD strike randomly; however, this is not always true. Under certain conditions, micro-discharges interact with each other and arrange themselves into a regular pattern. The micro-discharge pattern affects the performance of DBD treatment, especially in applications where spatial uniformity is required, because it results in superior quality of the treated surface. Usually, uniform plasma treatment is desired but it is necessary to emphasize that the requirement for uniform plasma treatment does not always necessitate uniform discharge. The first atmospheric pressure plasma device built at Kathmandu University, Nepal in 2005 was a DBD system operated by an HV power supply with frequency ranging from 10 to 30 kHz [49]. The discharge was generated within two cylindrical electrodes of spacing 2 mm. The power supply was built at the Department of Electrical & Electronics Engineering, Kathmandu University. Although the cost of fabrication was much lower than that of commercial HF frequency power supplies, it was still more expensive than a line frequency HV power supply. Realizing this, a HV power supply at 50 Hz was built using a step-up transformer and a varactor.

9.2.2.1 Parallel-Plate DBD System

In 2008, atmospheric pressure DBD was generated using the 50 Hz AC power supply with a parallel-plate electrode system at Kathmandu University, Nepal (Fig. 9.6). It consisted of a discharge chamber made of polycarbonate, step-up transformer, variac, and gas supply system with flow meter. The electrodes were the two rectangular copper plates. The lower electrode was coupled to a traveling microscope in order to vary the interelectrode distance very precisely. This electrode was covered by a glass or polycarbonate plate. A picture of the typical discharge obtained is shown in Fig. 9.7. The system has been tested to improve the hydrophilicity of different types of polymers, namely, High Density Polyethylene (HDPE), Polyethylene (PET), Polypropylene (PP), and Polyamide (PA). The samples were obtained from Goodfellow, UK. Plasma treatment was found to be effective in reducing the contact angle of water on the surface while increasing the surface free energy. This system has been used to investigate the effect of DBD treatment on the surface properties of polymers.

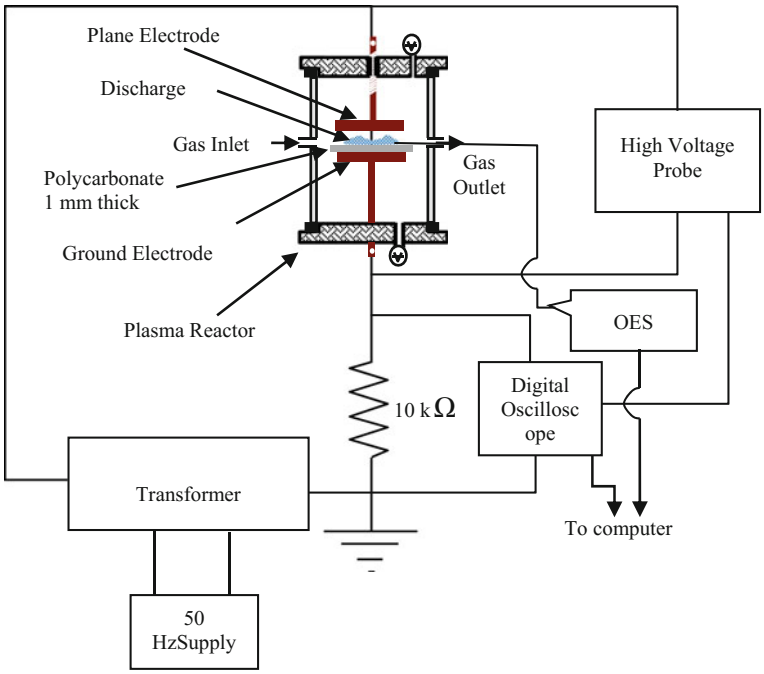

Fig. 9.6 Schematic diagram of a DBD system using the 50 Hz AC power supply built at Kathmandu University, Nepal

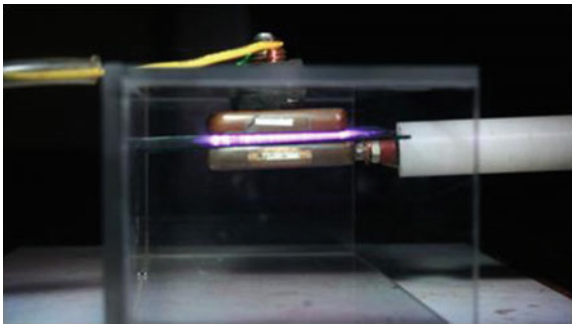

Fig. 9.7 Photograph of the parallel-plate DBD plasma in air generated by a 50 Hz AC power supply

9.2.2.2 Tubular DBD System with Coaxial Electrodes

We have also carried out work to develop a tubular DBD system with cylindrical coaxial electrodes. The discharge is powered by a 50 Hz 230 V AC mains supply stepped up to 15 kV peak voltage by a transformer. Transient filamentary discharges consisting of energetic electron streamers known as micro-discharges will occur near to both positive and negative peak voltages (shown in Fig. 9.8). Each discharge current pulse has a duration of nano-seconds. The current and voltage waveforms of a typical discharge are shown in Fig. 9.8. Also shown in the figure is the time-integrated end-on image of the discharge showing the occurrence of the micro-discharges. Chemical reactions will be activated in the gas flowing through the discharge gap.

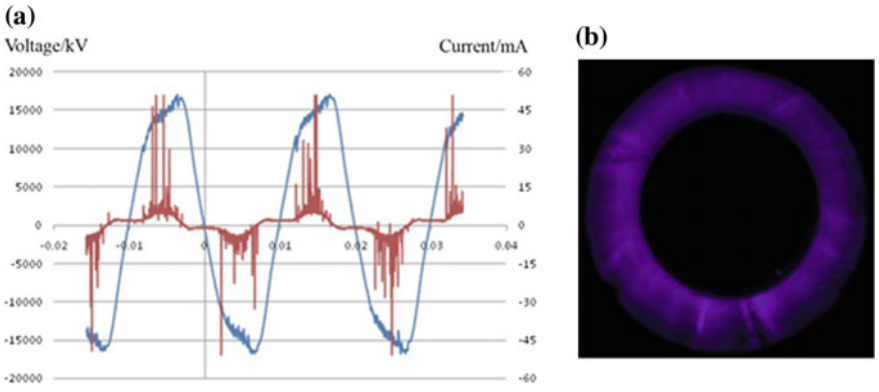

Fig. 9.8 **a** The voltage and current waveforms of a tubular DBD with coaxial electrodes. **b** End-on time-integrated image of the tubular DBD

9.2.2.3 Applications of Parallel-Plate Atmospheric Pressure DBD for Polymer Surface Treatment

Figure 9.9 shows the images of water drops on the surface of untreated and plasma-treated PP. It is evident that there is a decrease in water contact angle on the surface of the polymer after the DBD treatment. Figure 9.10 shows the variation of contact angle as a function of treatment time for different polymers. The figure shows that wettability of the polymers strongly depends on the treatment time. It is interesting to note that the nature of dependence of contact angle on treatment time is identical for all polymers.

Figure 9.11 shows the SEM micrographs of untreated and plasma-treated samples of PP. As can be seen from the figure, the surface of the air plasma-treated PP is changed, with increased roughness of the surface compared to the untreated PP [50].

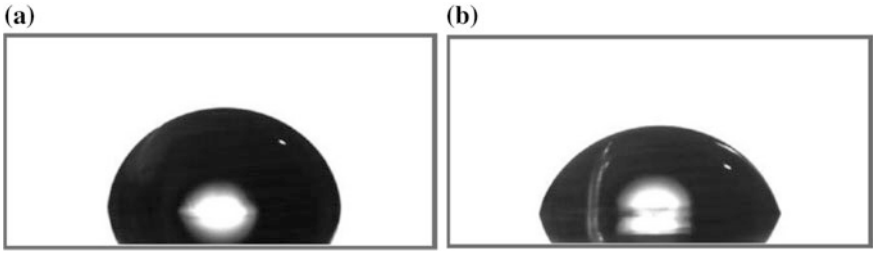

Fig. 9.9 Images of water drop on the surface of PP **a** untreated **b** after treatment by 50 Hz DBD in air

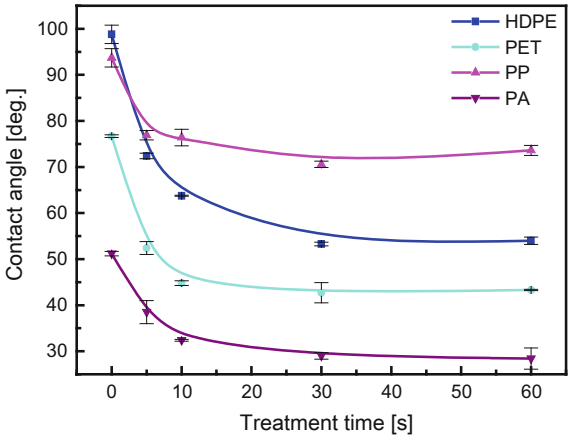

Fig. 9.10 The decrease of water contact angle on the surface of HDPE, PET, PP, and PA after treatment by 50 Hz AC DBD in air

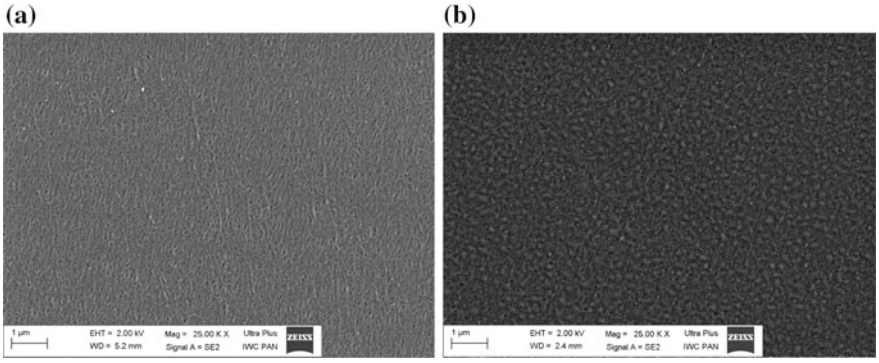

Fig. 9.11 SEM images of PP surfaces **a** untreated **b** treated in air plasma for 60 s

9.2.2.4 Applications of the Tubular DBD as a Chemical Reactor

The tubular DBD with cylindrical coaxial electrodes configuration is ideal for use as a chemical reactor in various applications. A well-established example of such applications is the DBD-based ozonizer [51–53]. Another interesting application of the tubular DBD as a chemical reactor is for remediation of engine exhaust gas. Fossil fuel burning from activities such as power generation and transportation is known to release large amount of environmental pollutants such nitrogen oxides (NOx) into the atmosphere. Emission of NOx may be minimized by improving the combustion process through the use of low NOx burners, improved gas circulation, and staged combustion. Post-combustion removal of pollutants can be done by using techniques such as selective catalytic reduction (SCR). In recent years, discharge-based techniques for engine pollutants remediation have attracted much research interest worldwide [54, 55]. In particular, the DBD has been tested to be effective in removing the nitric oxide from a gas stream containing a mixture of nitrogen and nitric oxide. A removal rate of better than 99% can be achieved [55].

9.2.3 Nonequilibrium Atmospheric Pressure Plasma Jets

It is known that discharges operated at atmospheric pressure tend toward thermal equilibrium because the high collisional rate will result in effective exchange in energy between the colliding partners (electrons, ions, and neutral molecules) such that the electron, ion, and neutral temperatures equalize, that is, $T_e \cong T_i \cong T_n$. Hence, these atmospheric pressure discharges cause gas heating and are usually operated in the high current regime, for example, the thermal torches that are used for metal cutting and welding [56, 57]. For treatment of heat-sensitive materials such as polymers, living cells, and tissues, it is necessary to avoid thermal equilibrium. Instead, the nonthermal or nonequilibrium plasmas, in which the electrons

are markedly more energetic than the ions and the neutral atoms or molecules, are desired [58–60]. Another advantage of the nonequilibrium plasma is the possibility of manipulating the relative populations of the various species in the plasma necessary for the specific application by generally tuning the electron energy distribution through altering operating parameters such as the applied electric field and gas mixtures [61, 62].

There are many arrangements of atmospheric pressure discharges, but the focus here is on the nonequilibrium plasma jet. The primary discharge in a nonequilibrium atmospheric pressure plasma jet (APPJ) is usually produced internally between the electrodes. A gas flow administered at rates of typically several l/min is necessary to launch the plasma jet or plume into the surrounding environment external to the device. The operating conditions necessary for generating these plasma jets are described below. Many configurations have been used and are often categorized in terms of electrical excitation frequency, types of discharges, and applications that could be obtained from the many review articles available [58, 59, 63, 64] and the references given therein. It is also important to determine the plasma jet properties and some important diagnostics will be briefly described. The usefulness and potential use of these nonequilibrium APPJs will be demonstrated through selected applications that have been performed.

9.2.3.1 Conditions to Operate Nonequilibrium Discharges at Atmospheric Pressure

There are various methods to generate nonequilibrium discharges at atmospheric pressure. Basically, one needs to prevent gas heating by limiting the discharge current density below the threshold for the glow-to-arc transition. This threshold demarcates the glow discharge mode from the arc discharge mode. Glow discharges are characterized by low current density (usually below 10^{-1} A/cm^2) but high cathode fall potential (hundreds of volts), while arc discharges are sustained at high currents (typically 10^2–10^4 A/cm^2) but low cathode fall (typically the ionization potential of the gas). Operating a discharge at high pressure is accompanied by increased collision frequency and intensified exchange of energy between electrons and heavier particles (neutrals, ions). This leads to enhanced gas heating resulting in discharge instability. When a local increase in gas temperature occurs, the gas density drops due to thermal expansion. The electron temperature that depends on the ratio of electric field to the gas number density *E/N* is increased. Ionization is enhanced, hence, resulting in local increase in current density as well as release of Joule heat. Thermal instability sets in, as gas heating is further enhanced, and the glow discharge can transform to the arc mode. Gas heating from collisional energy transfer occurs in the characteristic time of 10^{-2}–10^{-3} s, slower than other collision kinetics such as ionization, attachment, excitation, and recombination [65]. If the discharge is operated above the threshold, then fast pulsed power (typically nanosecond pulses) can be applied to shorten the duration of the discharge pulse (or discharge maintenance time) such that it is below the characteristic time for

instabilities to build up to the said transition. One commonly used configuration is the dielectric barrier discharge (DBD) described in Sect. 9.2.2 [66, 67]. Charges tend to build up on the dielectric surface, and eventually extinguish the discharge before a thermal arc column can be formed. The dielectric barrier discharge often operates in the filamentary mode. The current carried by an individual filament may be low, but the localized electron temperature and density can be high. Hence, dissociation and ionization of a small but significant fraction of the gas occur. The neutral particles, however, remain close to room temperature. DC nanosecond pulse excitation is efficient in generating nonequilibrium discharges in comparison to AC sinusoidal voltage-powered devices [68]. In continuous DC-powered configuration, a ballast resistor is inserted in the circuit to limit the current [69].

Another method is to confine the plasma to sub-millimeter dimensions such that it is too small for thermal equilibrium to be established, with cooling being achieved by the large surface-to-volume ratio [70]. These atmospheric pressure discharges are known as micro-discharges, and have been demonstrated to be stable and useful in nanoscale materials synthesis [71]. Mariotti and Sankaran [70] considered power balance under steady-state conditions (i.e., no gas flow) and the following relationship was deduced:

$$p \propto \frac{\sqrt{T_g^3}}{L^2 \varepsilon(T_e) n_e K_e(T_e)}, \tag{9.2}$$

where p is the pressure, T_g is the gas temperature, L represents the dimension of the plasma, $\varepsilon(T_e)$ is the average energy exchanged in a collision, n_e is the electron density, and $K_e(T_e)$ is the collision rate. Both ε and K_e depend on the effective electron temperature T_e, and generally increase monotonically with T_e within the range of electron energies of interest. It was assumed that the heating and cooling mechanisms were mainly due to collisional processes and conduction in the gas phase, respectively. The relation in Eq. (9.2) shows that gas heating is high at higher pressure. However, by maintaining the plasma at small dimension and low electron density, gas heating can be reduced.

Forced convection by flowing gas through the discharge volume at a sufficient rate is another method to carry the heat dissipated in the gas due to the current density. Helium is commonly used as the carrier gas in atmospheric pressure nonequilibrium discharge configurations [72, 73]. Among the noble gases, helium has the highest thermal conductivity of 0.153 Wm^{-1} K^{-1} at 300 K [74]; the thermal conductivity decreases with increase in the atomic number of these noble gases. Besides that, the applied voltage used to produce an electrical breakdown at high pressure is lower when helium gas is used. This can be seen from the Paschen curves shown in Fig. 9.12. External cooling (e.g., water-cooled electrodes) would be necessary when nonequilibrium plasmas are maintained at large volume under atmospheric pressure.

Sustaining a corona discharge that occurs in the vicinity of a sharp pin or thin wire, where the electric field is greatly enhanced, can also be employed to generate

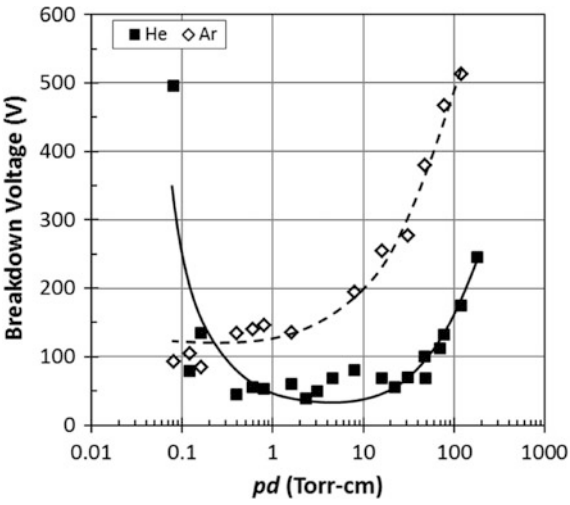

Fig. 9.12 Paschen curves for helium and argon RF discharges [75]. Reproduced from Journal of Applied Physics 96, M. Moravej et al., Physics of high-pressure helium and argon radio-frequency plasmas, 7011, Copyright (2004), with the permission of AIP Publishing

nonequilibrium discharges at atmospheric pressure [76]. This discharge is also known as partial discharge as it normally does not extend to the counter-electrode, and the current can be maintained at a low level.

9.2.3.2 Some Configurations of Nonequilibrium Plasma Jets

Sample configurations employed to limit the energy deposition into the gas are shown in Figs. 9.13 and 9.14. The various APPJs are different mainly in their electrode configurations, excitation schemes, operating frequency, and gas compositions. Figure 9.13a depicts one of the first reported stable nonequilibrium APPJs that were blown into the ambient air by Koinuma et al. [77]; it was called "microbeam plasma". The primary discharge was sustained at 13.56 MHz between two coaxial electrodes with a quartz tubing barrier between them. Gases used included pure He and admixtures with He as the carrier with a typical flow rate of 70 sccm producing a plasma jet 2 mm in diameter. Figure 9.13b shows the schematic of an RF-powered plasma needle used extensively in biomedical applications by Kieft et al. [78]. Figure 9.13c–e depict devices powered by AC sinusoidal voltages (9–30 kHz) tuned to match the capacitive load. DC pulse excitation was used in configurations as shown in Fig. 9.14a–c with arrangements of double electrodes (with the applied field oriented axially or transversely to the plasma jet flow) and single electrodes. The configuration in Fig. 9.14d was powered by DC high voltage with ballasting. The microplasma jet in Fig. 9.14e is DC powered with current control and forms a component of the electrical circuit in which charge conduction occurs through an aqueous solution. The gases used in the plasma jet devices above were not limited to noble gases only, with molecular gases such as N_2, O_2, H_2, CF_4, and air also being utilized depending on the intended applications.

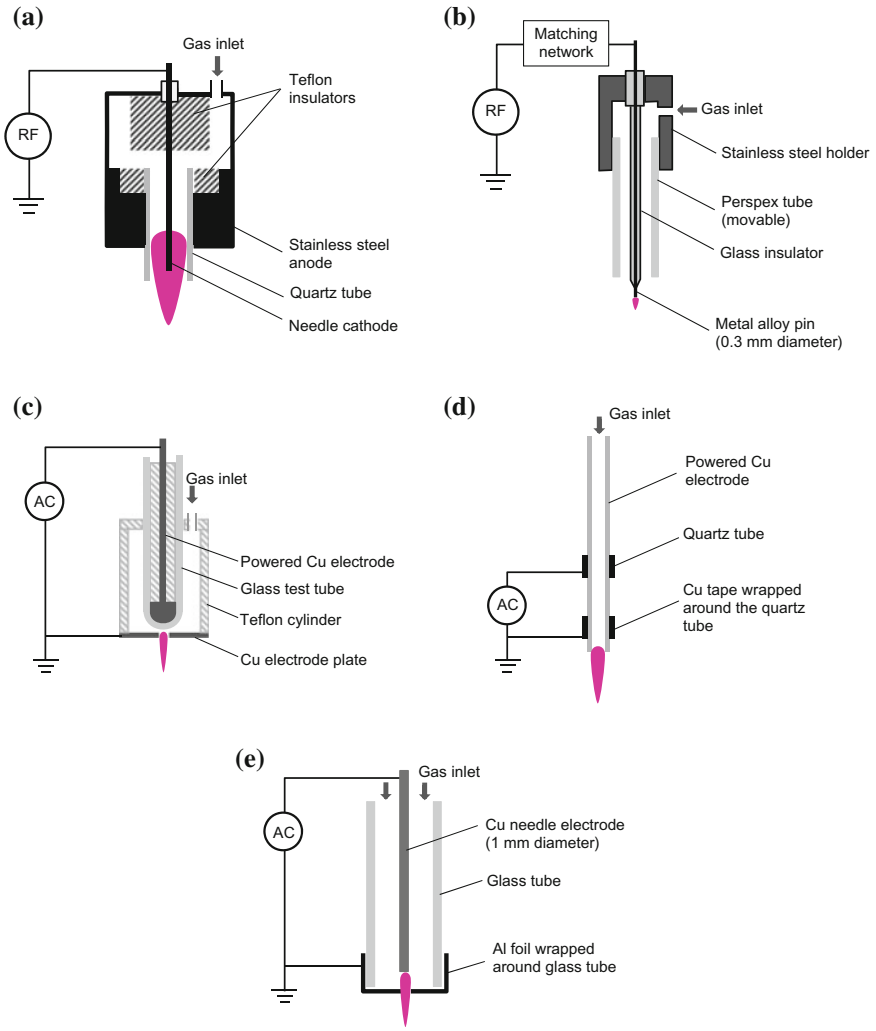

Fig. 9.13 Examples of APPJs with RF or AC excitation reported in literature. **a** RF excitation, Microbeam plasma generator [77]. **b** RF excitation, glow discharge [78]. **c** AC sinusoidal voltage (9 kHz) [79]. **d** AC sinusoidal voltage (11 kHz) [80, 81]. **e** AC sinusoidal excitation (10–30 kHz) [82]

9.2.3.3 Characteristics of Nonequilibrium APPJs

The nonequilibrium APPJ is characterized by the discharge geometry determined by the electrode arrangement and field direction (some of these are shown in Figs. 9.13 and 9.14), electrical properties (voltage and current waveforms, power dissipation, discharge mode), spectral emission (deduction of active species), and

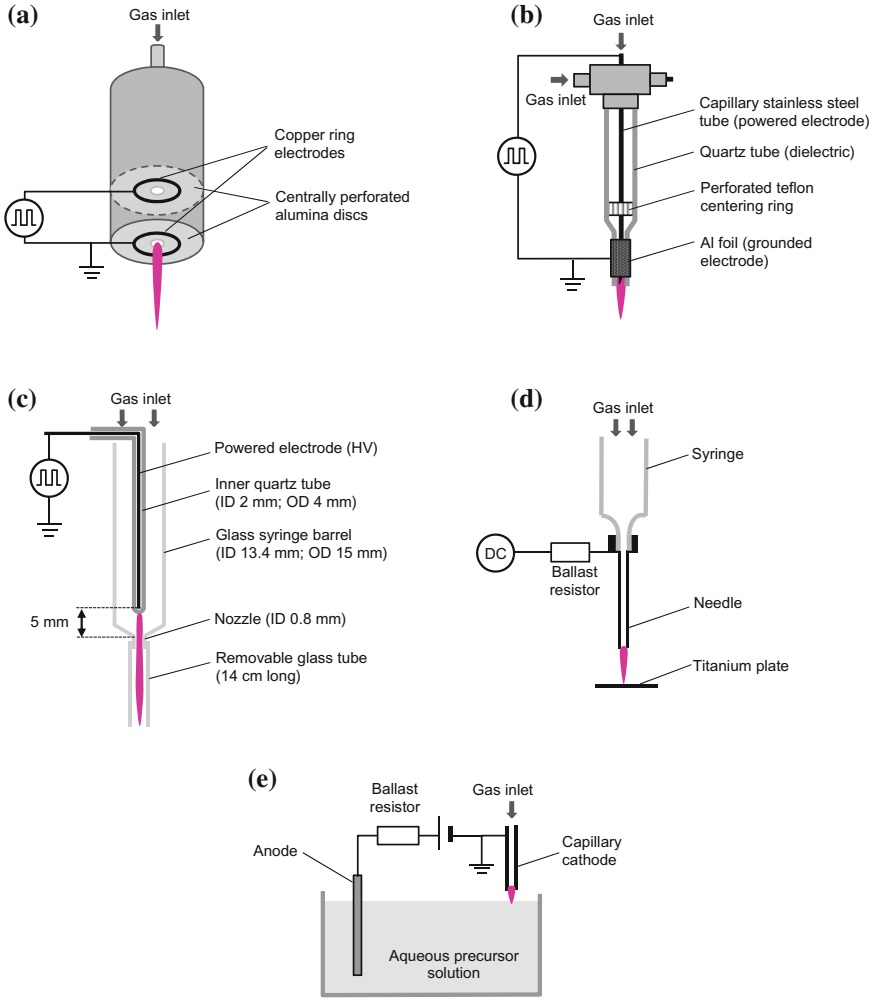

Fig. 9.14 Various APPJs with DC excitation reported in literature. **a** Handheld plasma pencil—DC pulse excitation, axial field [83]. **b** DC pulse excitation, transverse field [84]. **c** DC pulse excitation, single electrode [85, 86]. **d** DC voltage (0–20 kV) with ballast resistor to limit discharge current [69]. **e** DC excitation with ballast resistor [87, 88]

jet structure (length, plasma "bullets", turbulent/laminar flow). These characteristics are dependent on the configuration of the APPJ device and operating conditions such as the type of gas, gas flow rate, applied voltage, and excitation frequency.

A common configuration of the APPJ is the dielectric barrier discharge (DBD) plasma jet (all except Figs. 9.13b, e, and 9.14d, e), and the double electrode configuration of Fig. 9.13d with a linear field along the direction of the gas flow is one of the simplest to set up. Figure 9.15 shows typical current and voltage

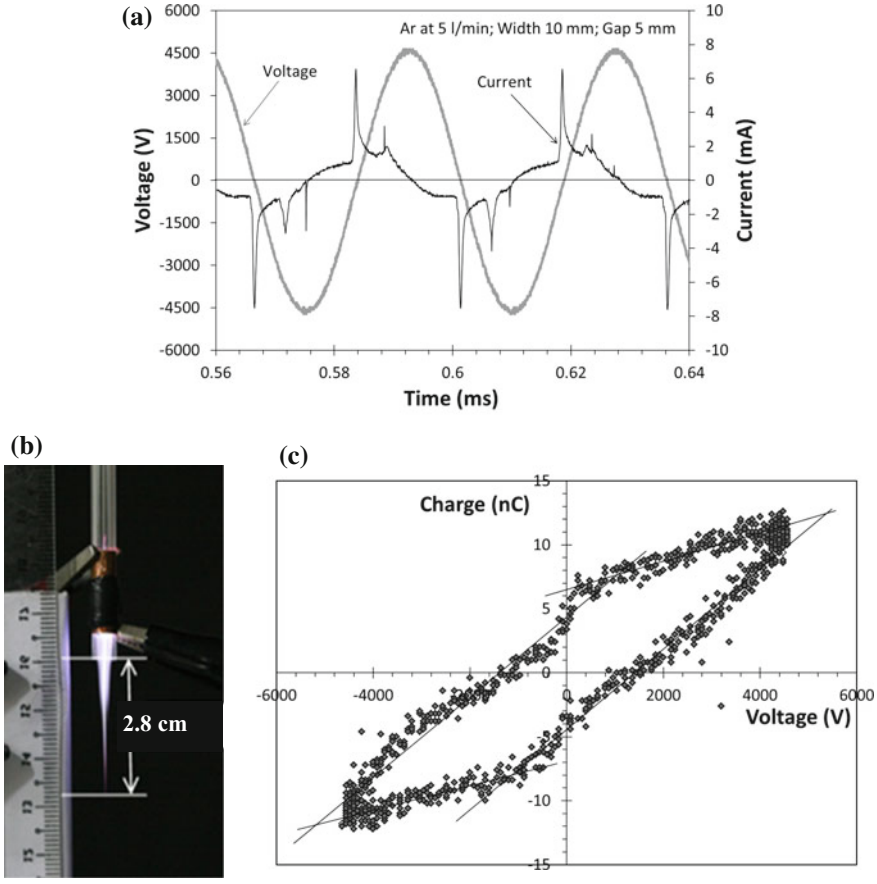

Fig. 9.15 APPJ with active electrode width 10 mm, counter-electrode width 2 mm, gap separation 5 mm, and argon gas flow at 5 l/min. **a** Current and voltage waveforms. **b** Image of the jet. **c** *Q*–*V* Lissajous plot (average energy dissipated per discharge cycle is 0.103 mJ, average power dissipation is 2.97 W at 28.8 kHz)

waveforms, an image of the APPJ with argon gas flow, and the charge–voltage (*Q*–*V*) Lissajous diagram. The charge *Q* transferred in the DBD is measured by the potential drop across a capacitor connected in series to the DBD. In AC excitation, shown in Fig. 9.15a, sharp current pulses typically occur in the first and the third quadrants of the voltage waveform and two strong sharp pulses are observed in each cycle. The sharp current pulse is due to rapid rise in gas conductivity upon plasma ignition, and subsequent extinction of the current due to charge accumulation on the dielectric surface that distorts the field. Walsh et al. [89] identified three distinct operating modes in a similar linear field arrangement characterized approximately by the current waveforms:

- chaotic mode with non-periodic current waveforms (occur just after breakdown at low-input power),
- plasma bullet mode, periodic current signals with at least one strong sharp pulse every cycle, and
- continuous mode in which the current peaks become broader in duration, occurring at higher input power.

Therefore, it is speculated that the Ar APPJ shown in Fig. 9.15a depicts the plasma bullet mode. The average power dissipation in the discharge is 3 W (deduced from the area of the *Q–V* Lissajous parallelogram). Figure 9.16 shows the current waveform for He APPJ which resembles that for the continuous mode.

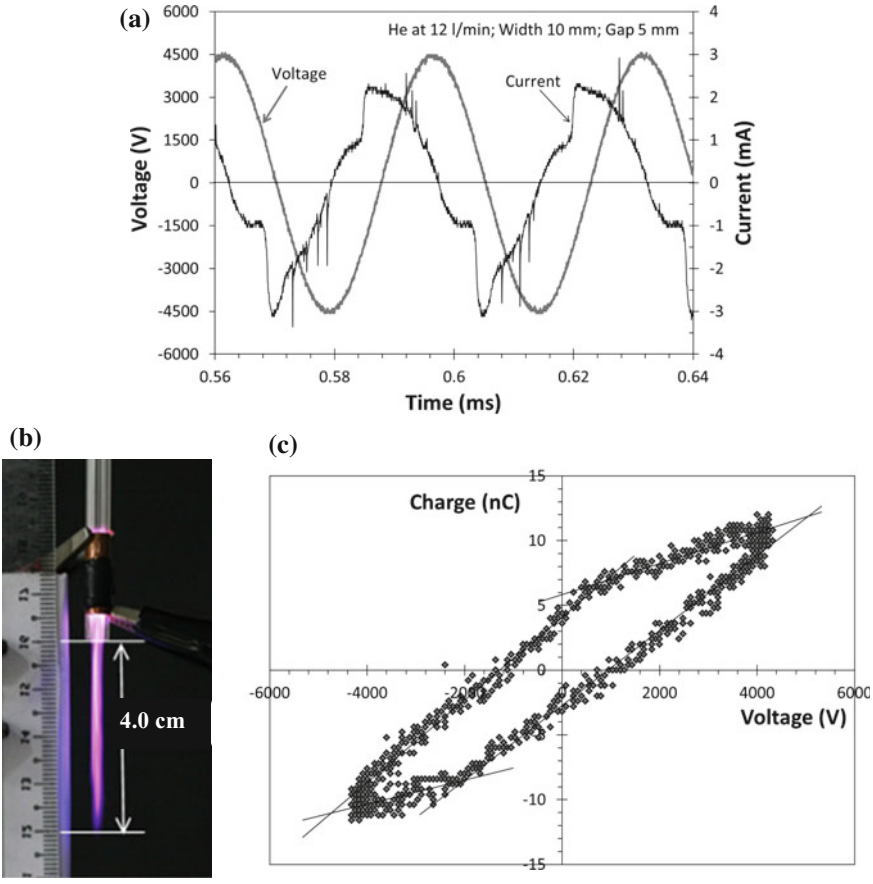

Fig. 9.16 APPJ with active electrode width 10 mm, counter-electrode width 2 mm, gap separation 5 mm, and helium gas flow at 12 l/min. **a** Current and voltage waveforms. **b** Image of the jet. **c** Q-V Lissajous plot (average energy dissipated per discharge cycle is 0.103 mJ, average power dissipation is 2.94 W at 28.6 kHz)

Lu et al. showed a He APPJ that can extend up to 11 cm into ambient air [90], and flexibility to apply it to two- and three-dimensional samples with an array of jets [91]. APPJ length is controlled by the discharge parameters (e.g., applied voltage, pulse width, pulse frequency, working gas flow rate, and diameter of the dielectric tube) and ambient air (open air or within an enclosure). For example, adding a 10-cm-long quartz tube to the exit nozzle produces a longer jet length [85]. Figure 9.17 shows variation in the length of APPJ for two discharge voltages of 8.8–11 kV (peak-to-peak value) for different gas flow rates for (a) He and (b) Ar. The critical Reynolds number that delineates laminar and turbulent fluid flow is 2320 [92]. With a hydraulic diameter of 4 mm, laminar flow is maintained when the flow rate is below 6.2 l/min for Ar and 53.5 l/min for He. In Ar gas (density = 1.661 kg/m^3), which is heavier than air, the flow status is maintained when Ar APPJ is blown out into ambient air. Length of the Ar APPJ increases with flow rate until about 6 l/min when turbulence sets in producing flow directions that are not parallel to the axial direction, resulting in a decrease in the APPJ length. However, in the lighter He (0.1664 kg/m^3), the maximum APPJ length is obtained at 15–19 l/min which is much lower than the critical value for the transition to turbulent flow. This indicates that the buoyancy of ambient air strongly influences the He APPJ length. Both Ar and He APPJ are directed vertically downward.

Larger voltage amplitude results in higher energy and an increase in the number of excitation and ionization particles produced in the DBD and carried by jet; hence, the APPJ extends to a longer length. This is evident in Ar APPJ (Fig. 9.17b). However, the length of the He APPJ is independent of the applied voltage, implying that it is strongly influenced by ambient air.

Optical emission spectroscopy is widely used as it is a convenient noninvasive method to determine several characteristics of the plasma. Figure 9.18a, b show emission spectra from the respective Ar and He APPJs. In addition to the atomic emission lines from the carrier gases, Ar and He, other emission lines detected are listed in Table 9.2. Though 99.999% purity carrier gases are used, the APPJ discharges into ambient air, and hence, plasma chemistry involving nitrogen–oxygen–hydrogen is observed.

The strong intensity of OH radicals drops rapidly as the APPJ propagates into ambient air. The main possible mechanism that produces OH is the direct electron impact dissociative excitation of water molecules (humid air and few ppm of water content in the carrier gas tank), and is given as [93]

$$H_2O(X) + e \rightarrow OH(A) + H + e, \tag{9.3}$$

while the main loss mechanism of the OH(A) state is through quenching by N_2 and O_2. For the $N_2(C)$ state, the main process contributing to their population is direct electron impact excitation [93, 94] with a threshold level of 11.03 eV:

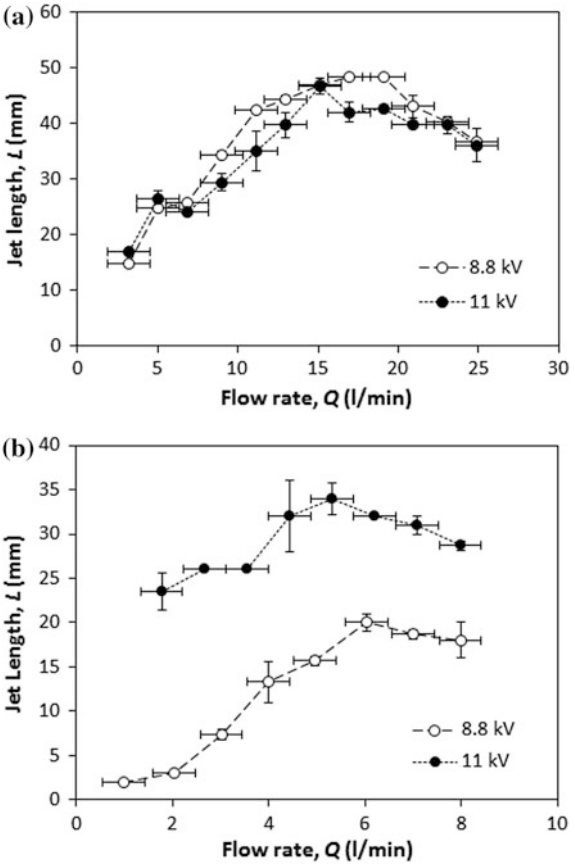

Fig. 9.17 Length of APPJ at a different flow rate Q for **a** helium and **b** argon at discharge voltages of 8.8 and 11 kV (peak-to-peak value). Frequency of the applied AC voltage is 11 kHz [80]. Reproduced from Journal of Science and Technology in the Tropics 10, Y.T. Lau et al., Dependence of dielectric barrier jet length on gas flow rate and applied voltage, 131, Copyright (2014), with permission from COSTAM)

$$N_2 + e_{fast} \rightarrow N_2^*\left(C^3\Pi_u\right) + e_{slow}. \tag{9.4}$$

In He APPJ, the first negative system (FNS) from the molecular ion, $N_2{}^+(B)$, requires a higher threshold energy of 18.7 eV. Production is mainly through penning ionizing collisions with He metastables given by

$$He(2^3P) + e \rightarrow He(3^3S)(19.8\ \text{eV}) + e, \tag{9.5}$$

(transition from He(3^3S) to He(2^3P) emits at 706.5 nm), and

$$He^* + N_2 \rightarrow N_2{}^+(B^2\Sigma_u{}^+) + He. \tag{9.6}$$

The $N_2{}^+(B)$ is quenched by N_2 and O_2 along the APPJ and the radiative transition,

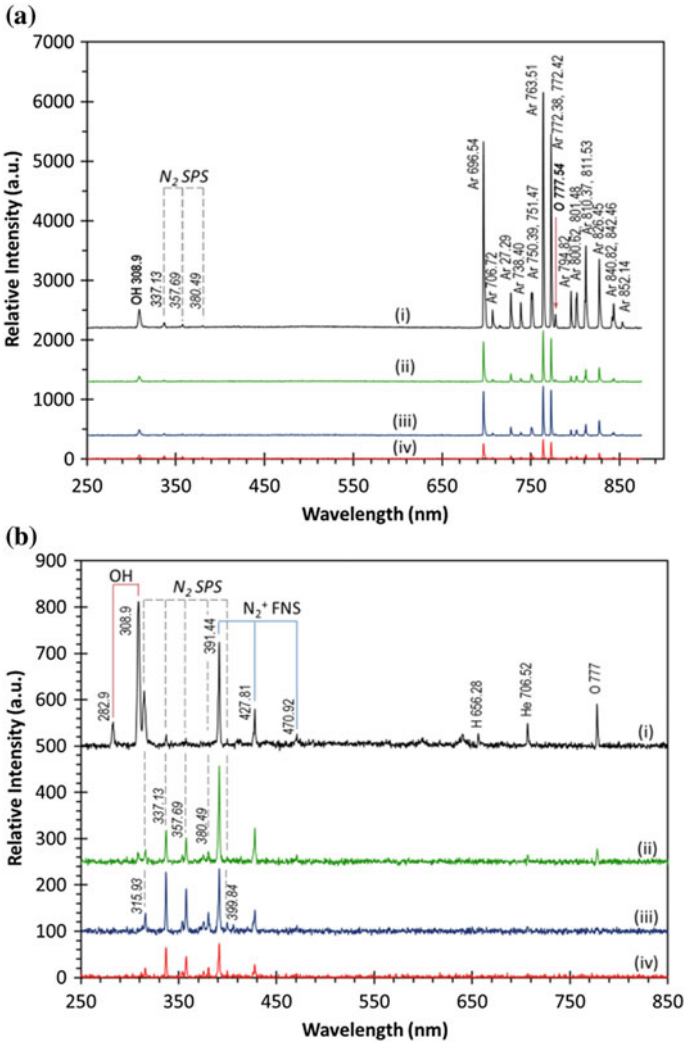

Fig. 9.18 Optical emission spectra of the **a** Ar and **b** He APPJ. The emission was measured at *i* the gap between the electrodes, *ii* the open end (edge) of the quartz tube, *iii* the middle of the jet, and *iv* the tip (or end) of the jet

$$N_2{}^+(B) \rightarrow N_2{}^+(X) + hf. \tag{9.7}$$

The possible mechanisms for production of atomic oxygen O are dissociation of molecular oxygen by direct electron impact and collision with excited Ar or He, namely [95],

Table 9.2 Transitions other than those for the carrier gases (Ar and He) contributing to the optical emission spectra of the APPJ

Species	Wavelength (nm)	Transition
OH	282.9, 308.9	$A^2\Sigma^+ \rightarrow X^2\Pi$ (v', v'') = (1, 0), (0, 0)
N_2 (SPS)	315.93, 337.13, 353.67, 357.69, 375.54, 380.49, 399.84	$C^3\Pi_u \rightarrow B^3\Pi_g$ (v', v'') = (1, 0), (0, 0), (1, 2), (0, 1), (1, 3), (0, 2), (1, 4)
N_2^+ (FNS)	391.44, 427.81, 470.92	$C^2\Sigma_u^+ \rightarrow X^2\Sigma_u^+$ (v',v'') = (0, 0), (0, 1), (0, 2)
H	656.28	H_α (3 → 2)
O	777.17, 777.42, 777.54	$^5P_{3,2,1} \rightarrow {}^5S_2^0$

$$e + O_2 \rightarrow e + 2\,O, \tag{9.8}$$

$$\begin{aligned} &Ar^*(^4S[^3P_2]) + O_2 \rightarrow 2\,O + Ar; \\ &He^* + O_2 \rightarrow 2\,O + He. \end{aligned} \tag{9.9}$$

The reactive species produced in the APPJ are important to the efficacy of plasma applications discussed in the following section.

9.2.3.4 Applications of Nonequilibrium Plasma Jets

Plasma jets operated under nonequilibrium (non-LTE/nonthermal/cold plasma) conditions have gas temperatures ranging from room temperature to 1000 K, while the electron temperature is at least one order of magnitude higher. Electron densities are typically 10^{19} m^{-3} or lower [63]. These properties support high plasma chemical activity and produce charged particles, neutral metastable species, reactive radicals, and energetic photons as described in the preceding section. The jets discharge into atmospheric air with a moderate bulk temperature, which makes these plasma jets well suited for biological applications such as sterilization, wound healing, blood coagulation, and cancer treatment [58, 96–98]. They are also suitable for surface modification of polymers [99, 100] and for the fabrication of nanomaterials [87, 88, 101].

Inactivation of Bacteria

Evaluation of bacteria inactivation efficacy can be done quantitatively by (a) enumerating the colony forming units or (b) measuring the size of the inactivation zone after being exposed to plasma and followed by an incubation period. Figure 9.19 shows the growth of the inhibition zone with treatment time. The inhibition zone denotes the region in which the bacteria were inactivated and were unable to form a colony when incubated after the plasma treatment. The opening of the 4-mm-diameter quartz tube was kept 2 cm above the culture, and the jet was held

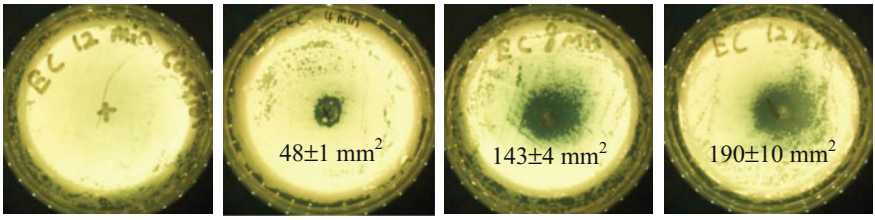

(a) Untreated (b) 4 min (c) 8 min (d) 12 min

Fig. 9.19 Gram-negative *E. coli* culture treated with argon APPJ for various time durations. The average area of the clear inhibition zone was calculated from three samples

static over the same spot during the treatment. The agar plate contains Luria Bertani (LB) nutrient medium. For the plasma treatment, 100 µl of 0.5 McFarland standard (1.5×10^8 CFU/ml) of bacterial suspension in 0.85% saline solution was pipetted and spread over each agar plate. Killing efficacy is known to depend on characteristics of the samples to be treated such as the type of the bacteria (Gram positive or Gram negative), the initial concentration of bacteria, and the support medium for the bacteria [102, 103]. In addition, the inactivation process can be impacted by the plasma and its treatment conditions, e.g., type of exposure (direct or remote) and exposure time, contribution of UV radiation, operating gas mixture, etc.

Inactivation agents include heat, charged particles, UV radiation, and reactive species. An increase of temperature by 8 °C above the room temperature was recorded when the APPJ was in direct contact with the bulb of a mercury thermometer for 1.5 min. This macroscopic mean temperature rise is unlikely to kill the *E. coli* bacteria as effective killing of *E. coli* in water requires at least 70 °C [104]. However, Gazeli et al. showed that the gas temperature of He APPJ varies with time, peaking at the beginning of each DC pulse of width 2 µs applied at 10 kHz with a predicted value about 4 times higher than room temperature [105]. Hence, the time evolution of the gas temperature of APPJ must be considered, especially when applied to biological samples such as living tissues. Charges can accumulate on the outer surface of the bacterial cell membrane, creating an electrostatic force that overcomes the tensile strength of the membrane causing its rupture and cell death. This is more likely to occur for gram-negative bacteria with irregular features on their cell membrane [106, 107]. UVC, the short-wave range (100–280 nm) of ultraviolet (UV) radiation, is known to be bactericidal with lethal doses of several mW s cm^{-2}. The UV radiation causes damage to the DNA strands of the bacteria by dimerization of the thymine bases, inhibiting their ability to replicate properly and leading to apoptosis (programmed cell death in which the integrity of the cell membrane is maintained and pro-inflammatory intracellular contents are prevented from leakage). As the emission spectra of Fig. 9.18 did not exhibit UV emission from 280 nm down to the detection limit of 178 nm, possibly very little bactericidal UV radiation was produced in the He and Ar APPJ. Ar has emission lines at 104.82 and 106.67 nm [108], but wavelengths below 200 nm, will not propagate through

ambiance at atmospheric pressure. Hence, UV radiation does not play a major role in the inactivation process. The most important inactivating agents are the reactive species. Atomic oxygen and OH radicals have been detected. These can attack the unsaturated fatty acids in the lipid bilayers of the cell membranes, compromising the ability of the membrane lipids to transport biochemical by-products across the membrane. Protein molecules can be oxidized by the reactive oxygen species (ROS), affecting their function in controlling the transport of macromolecules in and out of the cell.

Treatment on Malignant Cells

Another example is the application of He APPJ to malignant cells, e.g., human breast cancer cells MDA-MB-231 and MCF7 in RPMI-1640 culture medium. MDA-MB-231 cells are estrogen receptor (ER)—negative, and are known to be more invasive (can spread to normal, healthy tissues) and more sensitive to drug treatment. Cell viability is assessed post-treatment and MDA-MB-231 cells recorded higher cell death as shown in Fig. 9.20 [109]. Prolonged doses of exposure resulted in lower cell viability, and the APPJ treatment was more effective at killing MDA-MB-231 cells than MCF7 cells. Barekzi and Laroussi demonstrated dose-dependent inhibition of the progression of CCRF-CEM leukemia cells by He APPJ, and the effect may not be immediate but delayed [110]. Low-temperature APPJs have been shown to be able to induce apoptosis which is favored over necrosis (premature unprogrammed cell death induced by external factors that cause inflammation and damage to neighboring tissues) [111]. Plasma treatment

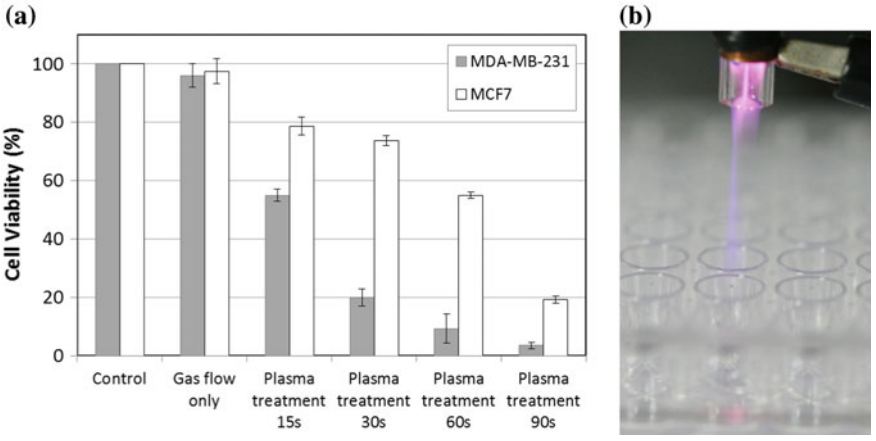

Fig. 9.20 **a** Cell viability post-plasma treatment on human breast cancer cells (Cell lines, MDA-MB-231 and MCF7 in culture medium RPMI-1640). **b** He APPJ applied to cancer cells cultured in a 96-well cell culture plate, with each well containing 10^4 cells

demonstrated selectivity in killing cancer cells in vitro (treatment of cells grown in well plates) and in vivo (treating cancer induced mice), providing a promising practical solution to anticancer therapy [112].

Brulle et al. have shown promising enhancement of cancer treatment with a combined mode of plasma and gemcitabine (chemotherapeutic) treatment of pancreatic cancer model [113]. These nonthermal plasma plumes have been applied directly to the cancer cells locally, with the challenge now being to apply them to the internal site of cancer growth. One clinical possibility is to use the plasma as a complementary tool, for example, to treat the surrounding incised site when the malignant tumor is removed surgically.

The effective plasma treatment is related to an ROS-based mechanism [114]. Cancer cells have a raised level of ROS when compared to normal cells. Plasma treatment enhances the level of ROS in both types of cells, but the oxidative stress in cancer cells is raised to "overload" leading to cell death. Normal cells that are not above the critical oxidative stress level could recover when the plasma treatment is removed, and hence, selective killing is made possible.

Surface Modification

Application of APPJ to surfaces results in changes in wettability. Figure 9.21a shows an increase in the hydrophilicity of Mylar (biaxially oriented polyethylene terephthalate) film after being treated by the APPJ shown in Fig. 9.13c with nitrogen and argon flow [115]. Enhancing the hydrophilic surface property of a substrate would result in better adhesion strength leading to a more durable adhesive joint. However, the change in wettability is not totally permanent as shown in Fig. 9.21b, in which the water contact angle increased by 75% after 1 h post-treatment and stabilized at this level over 1 week. To be effective, the plasma treatment should be incorporated as a pretreatment step immediately before the adhesive bonding process [116].

Synthesis of Nanoparticles

In the synthesis of nanoparticles, the microplasma jet becomes the cathode that is coupled with an aqueous solution as shown in Figs. 9.14e and 9.22a. In the plasma-assisted electrochemical cell, the metal salt is reduced and a colloidal dispersion of nanoparticles is produced [88, 117]. To avoid thermal equilibrium, the atmospheric plasma has to be miniaturized to below 1 mm in at least one of the dimensions and helium of high thermal conductivity is used as the carrier gas. DC voltage (up to 2000 V) is applied with current limited to 5 mA and below. For surfactant-free synthesis of the gold and silver nanoparticles, a low concentration (0.5 mM and below) of the aqueous metal precursor salts is necessary. The respective metal precursors are gold (III) chloride trihydrate ($HAuCl_4.3H_2O$) and silver nitrate ($AgNO_3$). The gold and silver nanoparticles of sizes ranging from 50

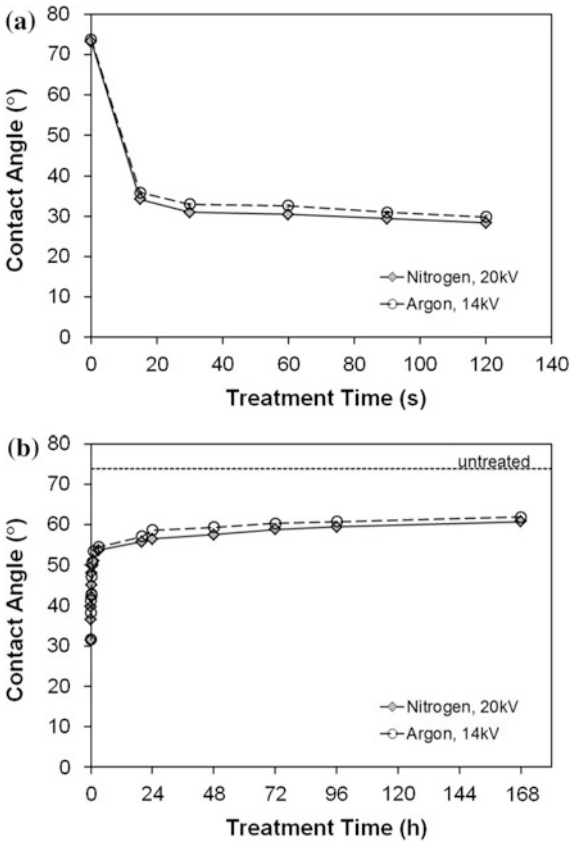

Fig. 9.21 **a** Water contact angle of Mylar surfaces treated with the APPJ shown in Fig. 9.13c in N_2 (discharge voltage at 20 kV peak-to-peak value) and Ar (14.4 kV) flow at 6 l/min for different time durations. **b** Aging effect of the treated PET samples

to 100 nm synthesized using a discharge current of 5 mA with He flow rate of 53 sccm and 0.5 mM of the respective aqueous metal precursor salts are shown in Fig. 9.22b–f.

Gas-phase plasma induces chemical reactions in the aqueous solution to produce hydrogen peroxide (H_2O_2) which is known to be a reducing agent for the gold precursor, possibly through the following reactions [87]:

(i) dissociative electron attachment near the liquid/vapor interface by energetic electrons produced in the plasma:

$$e_{gas} + H_2O \rightarrow \ OH^* + H^-. \tag{9.10}$$

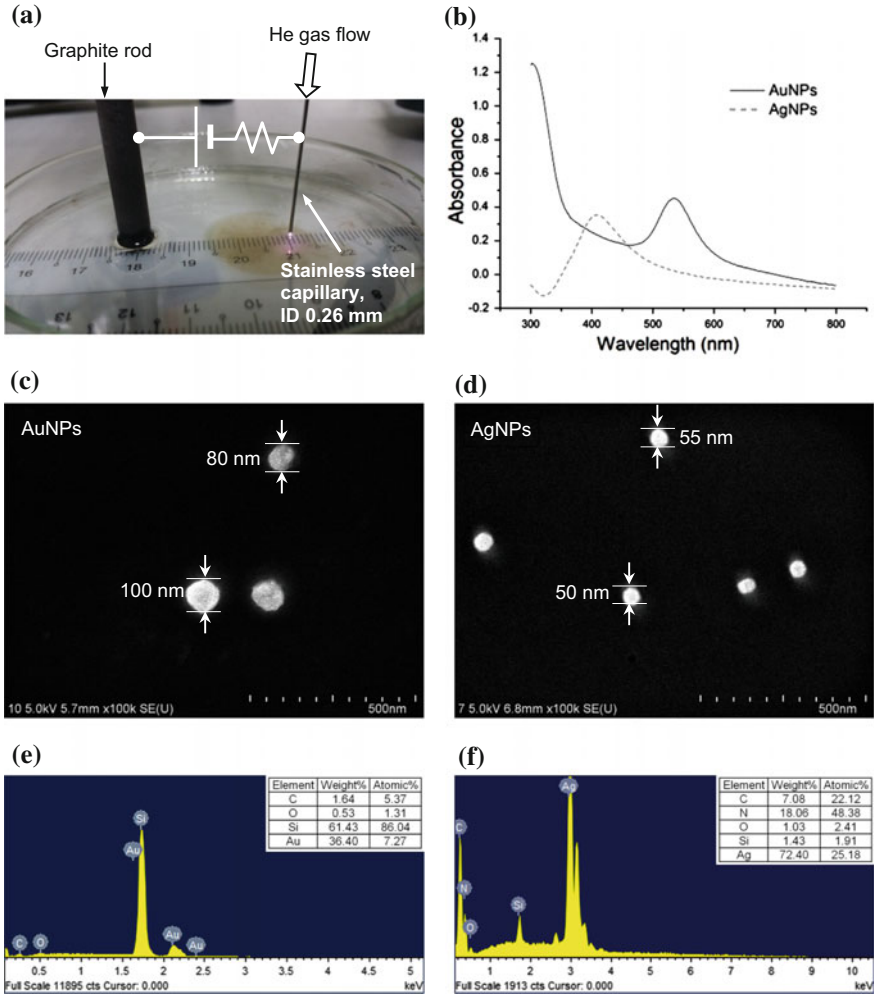

Fig. 9.22 **a** Photograph of the DC He microplasma during the synthesis process of silver nanoparticles. **b** UV–Vis absorbance spectra of colloidal Au and Ag nanoparticles with the respective "signature" surface plasmon resonance (SPR) peaks at 530 and 410 nm. **c** and **d** show the FESEM images of the synthesized Au and Ag nanoparticles, respectively, both at a magnification of 100 K. **e** and **f** are the EDX spectra confirming the presence of Au and Ag nanoparticles (The colloidal nanoparticles were air dried on silicon substrate)

(ii) H^- is believed to be too short-lived to play an active role in the synthesis process, and the reaction in the bulk liquid would likely be

$$2OH^* \rightarrow H_2O_2. \tag{9.11}$$

(iii) followed by the reduction process with hydrogen peroxide:

$$3\ H_2O_2 + 3\,OH^- + Au^{3+} \rightarrow Au^0 + 3\,HO_2 + 3\ H_2O. \tag{9.12}$$

and subsequent nucleation and growth of Au nanoparticles. OH^- could be produced by hydrated electrons and water.

The Ag nanoparticles are possibly synthesized via a multistep process as follows [118]:

$$2\ H_2O - 4\ e \rightarrow O_2 \uparrow + 4\ H^+, \tag{9.13}$$

resulting in oxygen being released at the anode. Below the microplasma cathode, reduction of silver ions takes place and hydrogen gas is released:

$$Ag^{+1} + e \rightarrow Ag^0, \tag{9.14}$$

$$2\ H_2O + 2\,e \rightarrow H_2 \uparrow + 2\,OH^-. \tag{9.15}$$

Immediately after ignition of the microplasma, a yellow-brownish patch is formed in the aqueous solution just below the cathode and it spreads outward. This indicates the formation of Ag nanoparticles. The silver and hydrogen ions (Ag^+ and H^+) migrate quickly to the cathode, and Ag nanoparticles are formed via nucleation and growth.

The examples of APPJ applications presented above have been carried out at the Plasma Technology Research Centre, Department of Physics, University of Malaya. These are only a small number of the vast and varied applications of the APPJs published in the literature.

9.2.4 Vacuum Spark and Flash X-Ray Tube

9.2.4.1 Introduction

X-ray and EUV radiations from hot plasmas have been widely investigated since the early 1900s [119, 120]. Several plasma devices including z-pinch, plasma focus, vacuum spark, and capillary discharge have been developed to be utilized as

possible sources of these radiations. Among these devices, the vacuum spark has long been known as a compact pulsed plasma source capable of producing intense X-ray from metallic plasmas. In the earlier work carried out on the vacuum spark, one of the main aims was to generate spectra from highly charged metallic ions in the regions of vacuum ultraviolet and soft X-ray [121–123]. Recently, one important area of research interest is to generate EUV emission at a 13.5 nm wavelength by using vacuum spark with suitable anode materials.

The vacuum spark is a linear high-voltage discharge operated in high vacuum, normally at pressures of 10^{-4} mbar and below. It is capable of producing dense plasma ($n_e > 10^{20}$ cm^{-3}) consisting of ions from the metallic electrode materials. The plasma generated is hot and highly ionized, with electron temperature T_e typically greater than 1 keV [122, 124, 125]. Intense X-rays are emitted from the highly ionized plasma due to the high discharge current of between 60 [126] and 600 kA [127]. Multiple bursts of X-ray radiation with intensity that increases proportionally with the discharge current are also frequently observed.

In the mid-60s, there were efforts to produce a low-inductance vacuum spark, with lower voltage of about 20 kV and lower inductance of 160 nH [128]. It was also reported that in a low-inductance vacuum discharge, the X-ray originates predominantly from the regions of concentrated plasma with spot structure or micropinches. These plasma spots are the sources of extraordinary bright X-rays, which are of great importance for a number of applications. They are formed from phenomena associated with the pinch effect and sausage instability ($m = 0$) leading to particle outflow and intense radiative energy losses [129–131]. Based on the Radiative Collapse Model, the plasma column between the electrodes is assumed to be electromagnetically compressed to an extremely small dimension when the discharge current exceeds a critical value during the main breakdown. During this moment, an increase in plasma density and temperature occurs and is then followed by multiple ionizations of ions. The inhomogeneity between the plasma column and the magnetic field leads to the occurrence of $m = 0$ magnetohydrodynamic instability. The final stage of the micropinch is characterized by the emission of H-like and He-like ionization of the electrode material. The hot spots were reported to have typical dimensions of 1–300 μm, electron densities of 10^{21}–10^{23} cm^{-3}, and electron temperatures of 1–10 keV [125, 130, 132–136]. These plasma parameters depend greatly on the atomic number Z of the anode material [137] and electrode shape [136].

One advantage of the vacuum spark as compared to other plasma X-ray sources is that it offers flexibility in the selection of characteristic X-ray emission wavelengths, as various metals can be used for the anode material. These materials range from high to low Z elements which include copper, iron, zinc, nickel, tungsten, titanium, and molybdenum [128, 133, 138–141] and lighter elements such as aluminum, magnesium, lithium, and carbon [135, 142, 143]. In addition, rare earth elements such as cerium, samarium, gadolinium, and dysprosium were also used in studying the X-ray spectra [144, 145].

Conventionally, the ignition of the vacuum spark discharge is initiated by heating the tip of the anode material using a high-powered and highly focused pulsed laser

beam [127, 144]. It can also be ignited by an auxiliary sliding spark at the surface of the cathode [146, 147]. Recently, an electron beam generated by the transient hollow cathode region [148] has been utilized to trigger the vacuum spark discharge [122, 149]. The transient hollow cathode discharge electron beam has been shown to be an effective triggering method in comparison to the sliding spark and laser triggered system. A hot spot with an electron temperature of 1–2 keV and an electron density of 10^{23} cm^{-3} has been reported for this type of device using the main input energy of less than 1 kJ [122]. The hollow cathode discharge electron beam is also utilized to enhance the X-ray emission from low-energy X-ray sources [150].

The vacuum spark has been considered for various applications including spectroscopic source of highly charged ions [142, 151, 152], pulsed X-ray point source for X-ray microscopy and radiography [153, 154], ion source for film deposition [155], and pump source for X-ray laser [156]. Early investigations of the device were focused on the X-ray spectra of highly stripped ions due to the demand to identify and simulate the spectral lines emitted during solar flares. For example, ion species from highly ionized plasmas such as Fe-XXVI, Ti-XII, Ni-XXVII, and Mo-XLII had been reported in the literature [121, 122, 125, 131, 146, 157, 158]. The vacuum spark is also being developed as an X-ray source for possible application in X-ray lithography. Images of X-ray test masks with dimensions of down to 0.4 μm were obtained by using a vacuum spark with an average X-ray output of 50 W operated in a 10 Hz repetitive mode [141]. Recently, a vacuum spark system with an operating frequency of up to several tens of kilohertz has been achieved by Xu et al. at ALFT. Such a high repetitive mode is required to provide the desired X-ray throughput for the microlithography industry [159].

For possible application as an EUV source in EUV lithography, tin has been widely reported as the most promising candidate for fuel (target) material. Hence, the study of emission spectra from tin plasma has recently attracted increasing interest from many researchers because the spectra of the ions in the states of Sn^{7+}, Sn^{8+}, Sn^{9+}, Sn^{10+}, Sn^{11+}, and Sn^{12+} are strongly peaked around the 13.5 nm spectral region in the form of unresolved transition arrays (UTAs) [160, 161]. The concept of using tin vapor in the vacuum spark was introduced by Koshelev and Pereira [130]. This work was later continued by Kieft et al. [162, 163] in the ASML EUV laboratory in The Netherlands. They estimated the electron density of the vacuum spark tin plasma to be up to 1×10^{24} m^{-3} and temperature to be over 30 eV. They also demonstrated that various ionization stages of tin from Sn^{7+} to Sn^{10+} were found in the plasma.

9.2.4.2 An Example of a Low-Cost Vacuum Spark System

The first vacuum speak system set up at the Plasma Technology Research Centre (formally the Plasma Research Laboratory) at the Physics Department, Faculty of Science, University of Malaya is the UMVS-1 as reported by Wong and Lee [127]. This system was powered by a capacitor bank rated at 60 kV, 22 μF. For the operation of the UMVS-1, the capacitor bank was normally discharged at 20 kV

(4.4 kJ). The discharge was initiated by using an MW ruby laser beam focused onto the anode tip. The electron temperature of the plasma produced was estimated to be about 8 keV [164].

A compact version of vacuum spark was designed with a single 60 kV, 1.85 μF capacitor which is 1/12 of the energy capacity of UMVS-1 [122]. In this system, the discharge is triggered by using the transient hollow effect induced by electron beam incorporated into the system [148]. This triggering scheme had been shown to be effective and together with the use of just a single capacitor, the construction and maintenance costs of the device have been significantly reduced. This makes the compact vacuum spark a cost-effective pulsed plasma device to be considered for a small research laboratory in developing countries. Furthermore, the basic diagnostics required for the start include a magnetic pickup coil for discharge current measurement, BPX65 PIN diode for X-ray detection in the wavelength range of 30–300 nm, and XRD for ultra soft X-ray [4].

The oscilloscope signals for the rate of change of current, PIN diode X-ray, and XRD obtained for a typical 20 kV discharge of the compact vacuum spark [165] are shown in Fig. 9.23. In this discharge, the X-ray signal is off scale due to strong X-ray emission. The severe dip in the d*I*/d*t* signal indicates strong transient electromagnetic phenomena probably caused by a strong pinching of the plasma column. The XRD signal indicates the presence of the hot plasma, with its peak

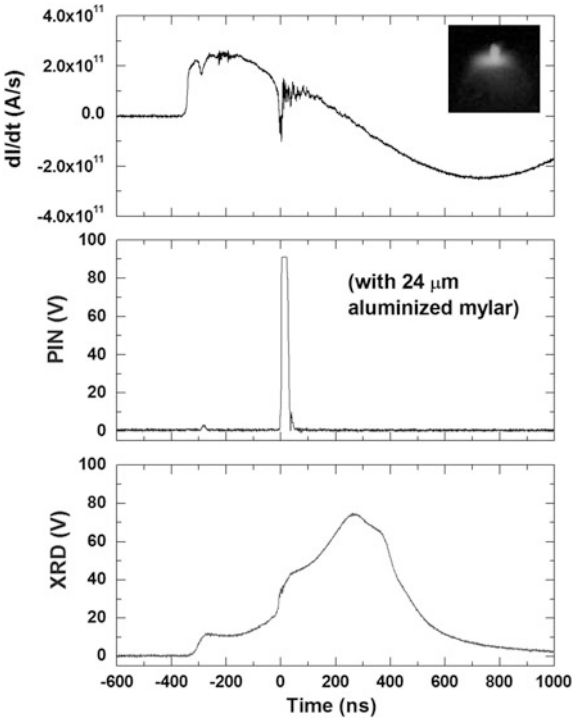

Fig. 9.23 The oscilloscope signals for magnetic pickup coil, PIN diode and XRD of a typical vacuum spark discharge [165]

coinciding with the peak of the discharge current (at the point when the d*I*/d*t* crosses the zero point of the horizontal time axis). The X-ray pinhole image of the plasma produced is also shown. The X-ray is observed to be concentrated at a spot-like structure above the anode, surrounded by a plasma cloud.

9.2.4.3 The Flash X-Ray Tube (UMFX)

The input energy of the vacuum spark system can be further scaled down by using a capacitor with a capacitance of 21.6 nF. With a low-input electrical energy of only 4.3 J, the plasma produced is expected to be cold and thus will not be able to emit in the X-ray region. However, the pre-breakdown transient hollow cathode electron beam bombardment at the anode tip is found to be able to produce the K_α line radiation of the anode material. Thus, the low-energy vacuum spark can be utilized as a flash X-ray source, which is named as UMFX [166].

Figure 9.24 shows the picture of the flash X-ray tube (UMFX) and the soft X-ray pinhole image of the plasma for a typical 20 kV discharge. Comparing this X-ray pinhole image with that shown in Fig. 9.23, the X-ray is observed to be mainly emitted from the tip of the anode. The X-ray emission of the discharge is produced by the Transient Hollow Cathode Discharge (THCD) electron beam bombardment of the anode and its spectrum is found to be dominated by the K_α line radiation of the anode material, as shown in Fig. 9.25. For aluminum (Al), the K_α lines at λ = 14.9 nm together with the continuum are observed, while for molybdenum (Mo) and tungsten (W), the L_α lines are shown. The discharge current,

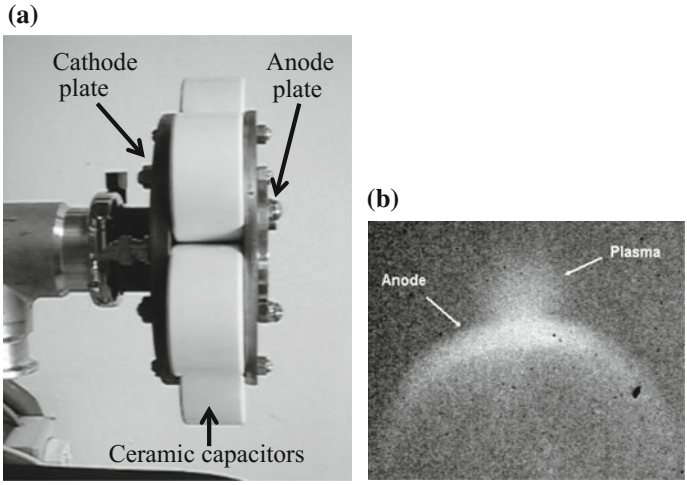

Fig. 9.24 **a** A picture of the scaled down 4.3 J vacuum spark, UMFX. **b** Pinhole X-ray image of the anode tip bombarded by high-energy electron beam

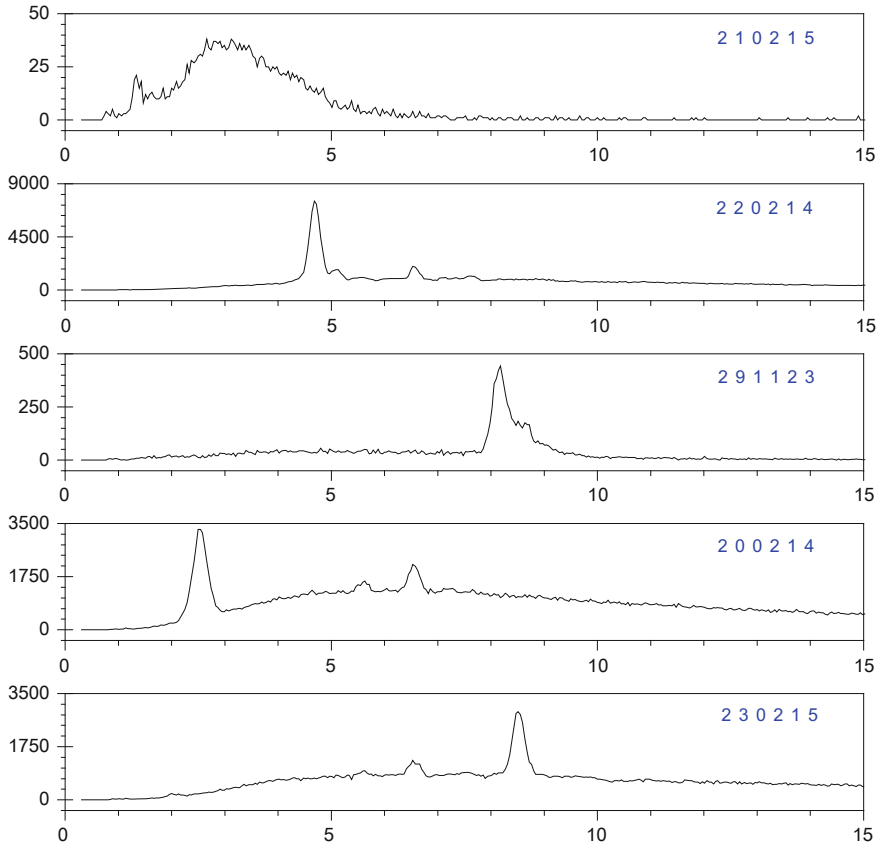

Fig. 9.25 X-ray emission spectra of a series of 20 kV discharges of UMFX operated with anodes of different materials. From *top* Al, Ti, Cu, Mo, W

pre-breakdown X-ray, and XRD waveforms of a typical 20 kV discharge are shown in Fig. 9.26, showing the temporal evolution of the plasma formation.

9.2.4.4 Applications of the UMFX Pulsed X-Ray Source

The UMFX flash X-ray source can be utilized for X-ray radiography of small objects. One example of such an application is the radiography of a live lizard as shown in Fig. 9.27.

To obtain this radiograph, the small lizard was kept inside a small plastic bag and placed at the mylar output window of the UMFX flash X-ray source, while the X-ray film in a light tight envelope was placed directly above the plastic bag. Hence, a direct print of the X-ray image of the lizard was obtained at a close

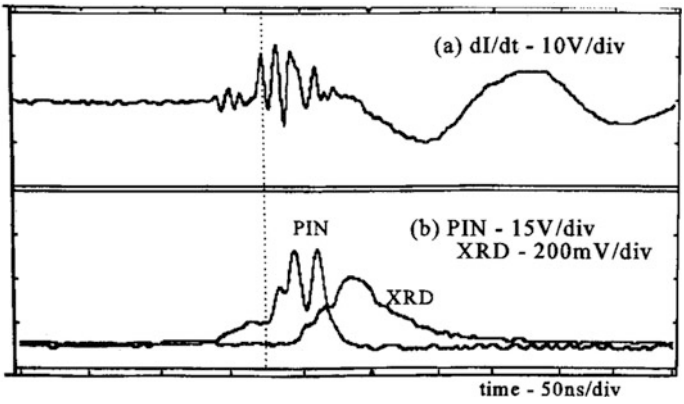

Fig. 9.26 The discharge current (*dI/dt*), X-ray (PIN), and EUV (XRD) waveforms of a typical discharge UMFX

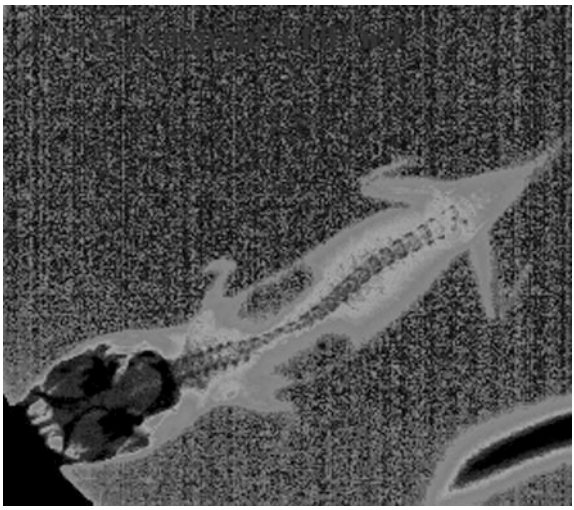

Fig. 9.27 X-ray radiograph of a live lizard taken using UMFX

distance from the source (<3 cm). The UMFX X-ray source is practically a point source since it is produced by electron beam bombardment at the tip of the anode.

In another application, the UMFX is used as the pulsed X-ray source for a high school demonstration experiment or a university-level radiation experiment. In this case, the UMFX is packaged as a bench top unit as shown in Fig. 9.28.

Besides the demonstration of X-ray radiography, the half thickness method of estimating the X-ray photon energy can also be carried out by the student. This experiment has been used by Year 3 Physics students at the University of Malaya since 1992. The UMFX pulsed plasma X-ray source has been awarded a Malaysian Patent in 2007 (MY-145318-A).

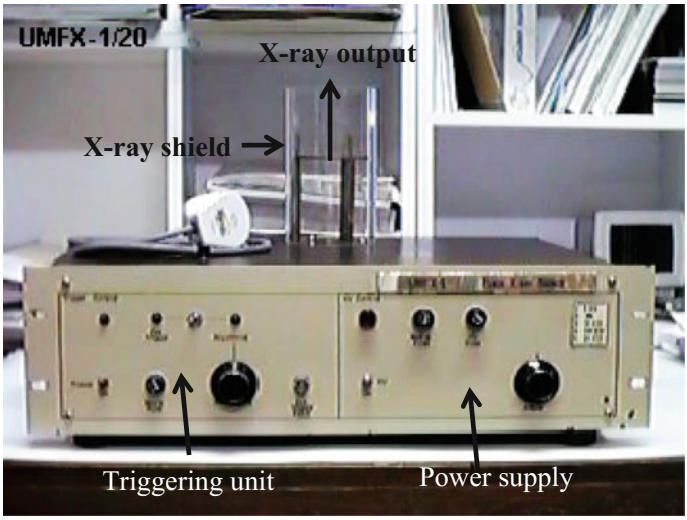

Fig. 9.28 Bench top UMFX unit used as the pulsed X-ray source for radiation experiment at the university level

9.2.5 Synthesis of Nanoparticles by the Wire Explosion Technique

9.2.5.1 Introduction

The wire explosion technique is a simple technique for the synthesis of nanoparticles. In this method, a thin metallic wire is disintegrated by passing a high-power pulsed current through it to generate a supersaturated vapor. The pulsed current can be generated by charging and discharging a capacitor. Due to the current flow through the wire, the wire will be heated by the Joule heating effect. The solid wire will be melted and vaporized if sufficient heat is deposited, forming a supersaturated vapor. Subsequently, nucleation will occur in the supersaturated vapor and it is followed by the growth of the nuclei. Nanoparticles are then formed from the growth of the nuclei.

The use of the wire explosion process in scientific research can be back dated to Nairne's work in 1774 [167]. Research related to the wire explosion phenomenon during the early years from 1774 to 1966 had been reviewed and published in New Scientist (1963) and Physics Today (1964) by Chace [168, 169]. Bennett published a review on the use of wire explosion to produce matter in the high-temperature state in 1968 [170]. Recently, Lebedev and Savvatimskii have published another review on wire explosion which focused on the change of thermophysical properties of the wire when it was heated by intense pulsed current [171].

In recent years, the wire explosion phenomenon had received growing research interest due to its various potential applications. For example, its ability to generate

matters at different states from solid to plasma has enabled the study of thermophysical properties of certain materials in the different states [172]. In the X-pinch experiment, the plasma is generated by exploding two wires arranged in an "X" shape and it is able to generate intense pulsed X-rays [173]. The wire explosion phenomenon is also acting as a fuse in electrical circuits [174], used for the detonation of explosives [175] as well as the synthesis of nanopowders [176].

According to Phalen [177], the wire explosion technique had been used to produce fine particles by Abrams as early as 1946 to study the aerosols of Al, U, and Pu. From the study, it was found that the particles produced by the wire explosion had a mean diameter of 200 nm, and agglomerated particles were observed [177]. In 1962, Karioris and Fish reported the production of various aerosols by exploding Ag, Al, Au, Cu, Fe, Mg, Mo, Ni, Pb, Pt, Sn, Ta, Th, U, and W wires in the air [178]. Spherical particles forming chains and agglomerates were observed. In the following years, more works were done to investigate the effects of various circuit parameters on the particles being produced. Besides that, attempts were made to synthesize fine powders of iodides, sulfides, carbides, oxides, and nitrides for a wide variety of elements. Kotov presented two reviews in 2003 and 2009 regarding the production of nanopowders by the wire explosion technique [176, 179]. Circuit parameters and the ambient conditions that affect the particle characteristics were discussed.

9.2.5.2 The Wire Explosion System at University of Malaya [180]

The wire explosion chamber was designed based on the vacuum spark system. Instead of the interelectrode spacing of the vacuum spark, the electrodes are connected by a wire of the specific material to be studied, as illustrated in Fig. 9.29. The discharge is powered by the same 1.85 μF capacitor as in the case of the vacuum spark. Annealed copper wire with a diameter of 125 μm and length of 6 cm was used for the experiments described here.

In order to investigate the discharge characteristics of the exploding wire system, a series of experiments have been conducted with various ambient pressures from 50 to 1000 mbar. The signals obtained from nitrogen and air wire explosion at the same pressure are generally observed to be similar. The typical current, voltage, and visible light signals recorded for an exploding wire discharge are shown in Fig. 9.30 for ambient air pressures of 1000, 500, 100, and 50 mbar. For wire explosion at ambient pressures of 1000 and 500 mbar in air, the signals are almost the same. After the first current pulse, interruption of current is observed for a few microseconds where the current is maintained at a near zero level. An underdamped sinusoidal waveform occurs at the end of this current pause, indicating the initiation of the discharge leading to the formation of the plasma. The deposited energy at the first current peak is calculated to be about 10 J for these cases. It is suggested that the wire has been fully melted at the peak of the first current pulse and a dense vapor of the wire material with high resistance is formed thus causing the current to

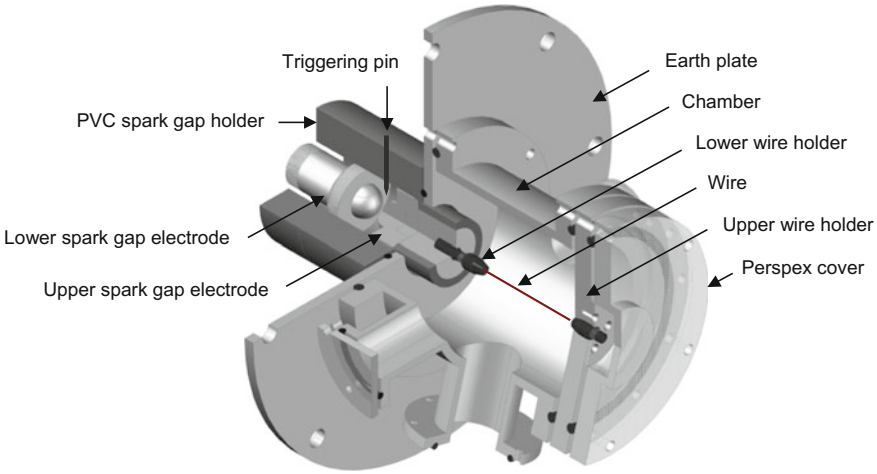

Fig. 9.29 Schematic diagram of the exploding wire chamber and electrodes setup [180]

stop flowing. At this stage, the liquid and vapor phases of the wire material coexist between the wire holders.

At the lower air ambient pressure of 100 mbar, no current pause is observed. The underdamped sinusoidal waveform occurs at an earlier time before the end of the first current pulse. While for the case of 50 mbar, the underdamped sinusoidal waveform occurs immediately at the peak of the first current pulse. For these two low-pressure cases, it is suggested that breakdown of the ambient gas has occurred before the melting of wire. The occurrence of the ambient gas breakdown prior to the melting of the wire has been observed using a high-speed camera [181]. The total energy deposited before the occurrence of plasma has been calculated to be approximately 25 J for the case of 100 mbar and about 16 J for the case of 50 mbar.

9.2.5.3 Syntheses of Nanopowder by Wire Explosion

The wire explosion system has been tested for the synthesis of copper nanoparticles. During the discharge, silicon substrates are placed at the NW64 flange at the bottom port of the chamber to collect the nanoparticles after each discharge. To allow the nanoparticles to be deposited on the silicon substrate, the vacuum of the chamber is released about 15 min after the discharge before the sample collection flange is removed carefully from the port. Figure 9.31 shows the FESEM image of the nanoparticles collected after one discharge. The median diameter and geometrical standard deviation of the size distribution of the nanoparticles are summarized in Table 9.3. The trend shown suggests that nanoparticles of smaller size are obtained at lower ambient pressure.

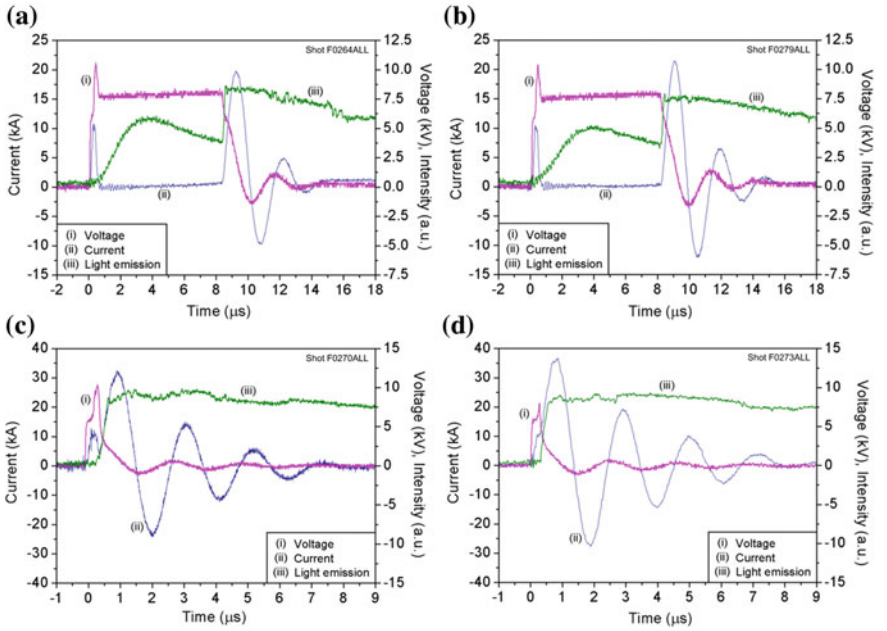

Fig. 9.30 Typical current, voltage, and light emission signals obtained from wire explosion in air and nitrogen at different pressures. **a** 1 bar, **b** 500 mbar, **c** 100 mbar, and **d** 50 mbar [180]

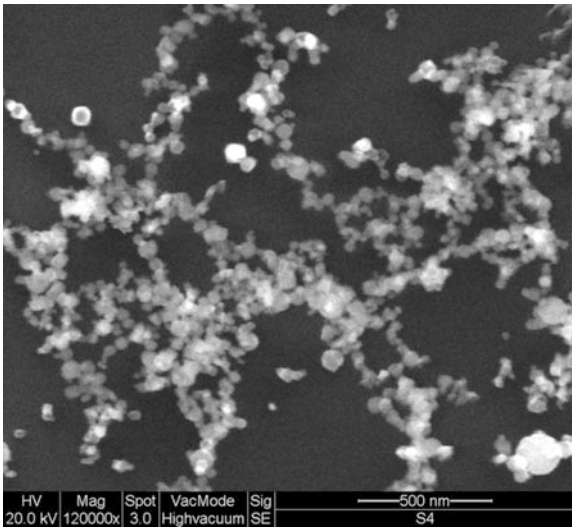

Fig. 9.31 Typical FESEM image of agglomerated nanoparticles [180]

Table 9.3 Particle size analysis for nanopowders produced by wire explosion in air at different pressures

Pressure (mbar)	Median diameter (nm)	Geometrical standard deviation (nm)
1000	31.3	1.6
500	31.0	1.5
100	26.4	1.6
50	23.6	1.6

9.3 Conclusion

The plasma experiments described in this chapter are examples of experiments that can be set up with a low budget by researchers working in small laboratories in developing countries. In particular, experiments such as the 50 Hz glow discharge, the dielectric barrier discharge, and the plasma jet are collaborative projects undertaken jointly by three institutions, namely Chulalongkorn University, Kathmandu University, and University of Malaya, which are all very active member institutions of AAAPT network. Besides reducing the cost of the experiments, an important strategy that can be adopted by small research group is to work together by sharing resources in order to enhance their research output.

Acknowledgements We wish to acknowledge University of Malaya, Chulalongkorn University, and Kathmandu University for their supports in the form of research grants, human resources, and infrastructure to carry out the reseach projects described in this chapter.

References

1. R.B. Tyata, D.P. Subedi, R. Shrestha, C.S. Wong, Generation of uniform atmospheric pressure argon glow plasma by dielectric barrier discharge. Pramana **80**, 507–517 (2013)
2. O. Goossens et al., Application of atmospheric pressure dielectric barrier discharges in deposition, cleaning and activation. Surf. Coat. Technol. **142–144**, 474–481 (2001)
3. Asian African Association on Plasma Training (AAAPT) web site at http://aaapt.org
4. C.S. Wong, R. Mongkolnavin, *Elements of Plasma Technology*. Springer Briefs in Applied Sciences and Technology (2016)
5. I. Prasertsung, in *Improvement of crosslinked gelatin for in vitro cell culture by plasma surface treatment*, PhD thesis, Chulalongkorn University (2010)
6. I. Prasertsung, S. Kanokpanont, R. Mongkolnavin, C.S. Wong, J. Panpranot, S. Damrongsakkul, Plasma enhancement of in vitro attachment of rat bone-marrow-derived stem cells on cross-linked gelatin films. J. Biomater. Sci. Polym. Ed. **23**, 1485–1504 (2012)
7. I. Prasertsung, R. Mongkolnavin, S. Damrongsakkul, C.S. Wong, Surface modification of dehydrothermal crosslinked gelatin film using a 50 Hz oxygen glow discharge. Surf. Coat. Technol. **205**, S133–S138 (2010)
8. I. Prasertsung, S. Kanokpanont, R. Mongkolnavin, C.S. Wong, J. Panpranot, S. Damrongsakkul, Comparison of the behavior of fibroblast and bone marrow-derived mesenchymal stem cell on nitrogen plasma-treated gelatin films. Mater. Sci. Eng., C **33**, 4475–4479 (2013)

9. P. Amornsudthiwat, R. Mongkolnavin, S. Kanokpanont, J. Panpranot, C.S. Wong, S. Damrongsakkul, Improvement of early cell adhesion on thai silk fibroin surface by low energy plasma. Colloids Surf. B **111**, 579–586 (2013)
10. T.H. Baum, D.C. Miller, T.R. O'Toole, Photoselective catalysis of electroless copper solutions for the formation of adherent copper films onto polyimide. Chem. Mater. **3**, 714–720 (1991)
11. K.W. Lee, A. Viehbeck, Wet-process surface modification of dielectric polymers: adhesion enhancement and metallization. IBM J. Res. Develop. **38**, 457–474 (1994)
12. T.N. Vorobyova, Adhesion interaction between electrolessly deposited copper film and polyimide. J. Adhes. Sci. Technol. **11**, 167–182 (1997)
13. G. Rozovskis, J. Vinkevicius, J. Jaciauskiene, Plasma surface modification of polyimide for improving adhesion to electroless copper coatings. J. Adhes. Sci. Technol. **10**, 399–406 (1996)
14. H. Niino, A. Yabe, Excimer laser polymer ablation: formation of positively charged surfaces and its application into the metallization of polymer films. Appl. Surface Sci. **69**, 1–6 (1993)
15. C.S. Wong, S.P. Lem, B.T. Goh, C.W. Wong, Electroless plating of copper on polyimide film modified by 50 Hz plasma graft polymerization with 1-Vinylimidazole. Jpn. J. Appl. Phys. **48**, 036501 (2009)
16. W.C. Wang, E.T. Kang, K.G. Neoh, Electroless plating of copper on polyimide films modified by plasma graft copolymerization with 4-vinylpyridine. Appl. Surface Sci. **199**, 52–66 (2000)
17. Y.-C. Wu, T.-M. Lee, J.-C. Lin, S.-Y. Shaw, C.-Y. Yang, Argon-plasma-treated chitosan: surface characterization and initial attachment of osteoblasts. J. Biomaterials Sci. **21**, 563–579 (2010)
18. R. Molina, P. Jovancic, S. Vilchez, T. Tzanov, C. Solans, In situ chitosan gelation initiated by atmospheric plasma treatment. Carbohyd. Polym. **103**, 472–479 (2014)
19. X. Jing, H.-Y. Mi, J. Peng, X.-F. Peng, L.-S. Turng, Electrospun aligned poly(propylene carbonate) microfibers with chitosan nanofibers as tissue engineering scaffolds. Carbohyd. Polym. **117**, 941–949 (2015)
20. K. Inthanon, N. Saranwong, W. Wongkham, P. Wanichapichart, K. Prakrajang, D. Suwannakachorn, L.D. Yu, PIII-induced enhancement and inhibition of human cell attachment on chitosan membranes. Surf. Coat. Technol. **229**, 112–119 (2013)
21. T. Demina, Z.-Z. Daria, M. Yablokov, A. Gilman, T. Akopova, E. Markvicheva, A. Zelenetskii, DC discharge plasma modification of chitosan/gelatin/PLLA films: surface properties, chemical structure and cell affinity. Surf. Coat. Technol. **207**, 508–516 (2012)
22. C.M. Alves, Y. Yang, D.L. Carnes, J.L. Ong, V.L. Sylvia, D.D. Dean et al., Modulating bone cells response onto starch-based biomaterials by surface plasma treatment and protein adsorption. Biomaterials **28**, 307–315 (2007)
23. I. Prasertsung, R. Mongkolnavin, S. Kanokpanont, S. Damrongsakkul, The effects of pulsed inductively coupled plasma (PICP) on physical properties and biocompatibility of crosslinked gelatin films. Int. J. Biol. Macromol. **46**, 72–80 (2010)
24. R. Safaeijavan, M. Soleimani, A. Divsalar, A. Eidi, A. Ardeshirylajimi, Biological behavior study of gelatin coated PCL nanofiberous electrospun scaffolds using fibroblasts. J. Paramedical Sci. **5**(1), 67–73 (2014)
25. P. Amornsudthiwat, S. Damrongsakkul, Oxygen plasma etching of silk fibroin alters surface stiffness: a cell-substrate interaction study. Plasma Processes Polym. **11**(8), 763–776 (2014)
26. A.J. Choudhury, D. Gogoi, R. Kandimalla, S. Kalita, Y.B. Chaudhari, M.R. Khan, J. Kotoky, J. Chutia, Penicillin impregnation on oxygen plasma surface functionalized chitosan/Antheraea assama silk fibroin: studies of antibacterial activity and antithrombogenic property. Mater. Sci. Eng., C **60**, 475–484 (2016)
27. R. Uchida, U.K. Bhawal, H. Kiba, K. Arai, Y. Tanimoto, N. Kuboyama, T. Asakura, N. Nishiyama, Effect of plasma-irradiated silk fibroin in bone regeneration. J. Biosci. Bioeng. **118**(3), 333–340 (2014)

28. H.S. Baek, Y.H. Park, C.S. Ki, J.-C. Park, D.K. Rah, Enhanced chondrogenic responses of articular chondrocytes onto porous silk fibroin scaffolds treated with microwave-induced argon plasma. Surf. Coat. Technol. **202**, 5794–5797 (2008)
29. S.C. Jin, H.S. Baek, Y.I. Woo, M.H. Lee, J.-S. Kim, J.-C. Park, Beneficial effects of microwave-induced argon plasma treatment on cellular behaviors of articular chondrocytes onto nanofibrous silk fibroin mesh. Macromol. Res. **17**, 703–708 (2009)
30. A.J. Choudhury, D. Gogoi, J. Chutia, R. Kandimalla, S. Kalita, J. Kotoky, Y.B. Chaudhari, M.R. Khan, K. Kalita, Controlled antibiotic-releasing Antheraea assama silk fibroin suture for infection prevention and fast wound healing. Surgery **159**, 539–547 (2016)
31. M. Liang, J. Yao, X. Chen, L. Huang, Z. Shao, Silk fibroin immobilization on poly(ethylene terephthalate) films: comparison of two surface modification methods and their effect on mesenchymal stem cells culture. Mater. Sci. Eng., C **33**(3), 1409–1416 (2013)
32. P. Zdenka, M. Uroš, P. Tanja, M. Tina, V. Alenka, M. Miran, S.-K. Karin, Novel cellulose based materials for safe and efficient wound treatment. Carbohyd. Polym. **100**, 55–64 (2014)
33. S.D. Valencen, J.-C. Tille, C. Chaabane, R. Gurny, M.-L. Bochaton-Piallat, B.H. Walpoth, M. Möller, Plasma treatment for improving cell biocompatibility of a biodegradable polymer scaffold for vascular graft applications. Eur. J. Pharm. Biopharm. **85**(1), 78–86 (2013)
34. H. Shen, X. Hu, J. Bei, S. Wang, The immobilization of basic fibroblast growth factor on plasma-treated poly(lactide-co-glycolide). Biomaterials **29**, 2388–2399 (2008)
35. H. Shen, X. Hu, F. Yang, J. Bei, S. Wang, Combining oxygen plasma treatment with anchorage of cationized gelatin for enhancing cell affinity of poly(lactide-co-glycolide). Biomaterials **28**, 4219–4230 (2007)
36. X. Qu, W. Cui, F. Yang, C. Min, H. Shen, J. Bei, S. Wang, The effect of oxygen plasma pretreatment and incubation in modified simulated body fluids on the formation of bone-like apatite on poly(lactide-co-glycolide) (70/30). Biomaterials **28**, 9–18 (2007)
37. Z. Ding, J. Chen, S. Gao, J. Chang, J. Zhang, E.T. Kang, Immobilization of chitosan onto poly-l-lactic acid film surface by plasma graft polymerization to control the morphology of fibroblast and liver cells. Biomaterials **25**, 1059–1067 (2004)
38. Y. Wan, C. Tu, J. Yang, J. Bei, S. Wang, Influences of ammonia plasma treatment on modifying depth and degradation of poly(L-lactide) scaffolds. Biomaterials **27**, 2699–2704 (2006)
39. T.E. Andersen, Y. Palarasah, M.-O. SkjØdt, R. Ogaki, M. Benter, M. Alei et al., Decreased material-activation of the complement system using low-energy plasma polymerized poly (vinyl pyrrolidone) coatings. Biomaterials **32**, 4481–4488 (2011)
40. Z. Yang, J. Wang, R. Luo, M.F. Maitz, F. Jing, H. Sun et al., The covalent immobilization of heparin to pulsed-plasma polymeric allylamine films on 316L stainless steel and the resulting effects on hemocompatibility. Biomaterials **31**, 2072–2083 (2010)
41. K. Vasilev, Z. Poh, K. Kant, J. Chan, A. Michelmore, D. Losic, Tailoring the surface functionalities of titania nanotube arrays. Biomaterials **31**, 532–540 (2010)
42. M. Hirano, M. Yamane, N. Ohtsu, Surface characteristics and cell-adhesion performance of titanium treated with direct-current gas plasma comprising nitrogen and oxygen. Appl. Surf. Sci. **354**, 161–167 (2015)
43. K.K. Alicja, K.B. Małgorzata, P. Elżbieta, S. Wojciech, Electrochemical and biological characterization of coatings formed on Ti–15Mo alloy by plasma electrolytic oxidation. Mater. Sci. Eng., C **43**, 172–181 (2014)
44. B. Finke, F. Luethen, K. Schroeder, P.D. Mueller, C. Bergemann, M. Frant et al., The effect of positively charged plasma polymerization on initial osteoblastic focal adhesion on titanium surfaces. Biomaterials **28**, 4521–4534 (2007)
45. H. Kawai, Y. Shibata, T. Miyazaki, Glow discharge plasma pretreatment enhances osteoclast differentiation and survival on titanium plates. Biomaterials **25**, 1805–1811 (2004)
46. M. Zelzer, R. Majania, J.W. Bradley, F.R.A.J. Rose, M.C. Davies, M.R. Alexandera, Investigation of cell-surface interactions using chemical gradient formed from plasma polymers. Biomaterials **29**, 172–184 (2008)

47. Y.-R. Choi, J.-S. Kwon, D.-H. Song, E.-H. Choi, Y.-K. Lee, K.-N. Kim, K.-M. Kim, Surface modification of biphasic calcium phosphate scaffolds by non-thermal atmospheric pressure nitrogen and air plasma treatment for improving osteoblast attachment and proliferation. Thin Solid Films **547**, 235–240 (2013)
48. T. Nozaki, K. Okazaki, Materials processing at atmospheric pressure: nonequilibrium effects on nanotechnology and mega-industries. Pure Appl. Chem. **78**, 1157–1172 (2006)
49. G. Shrestha, P. Freere, S.M. Basnet, W.T. Jewel, D.P. Subedi, in *Development of a cold plasma generator for atmospheric pressure dielectric barrier discharge*. IEEE Region Technical Conference, pp. 432–435 (2007)
50. U.M. Joshi, D.P. Subedi, Surface treatment of polypropylene (PP) film by 50 Hz dielectric barrier discharge produced in air and argon/air mixture at atmospheric pressure. AIP Conf. Proc. **1588**, 109–114 (2014)
51. D.P. Subedi, R.B. Tyata, A. Khadgi, C.S. Wong, Physicochemical & microbiological analysis of drinking water treated by using ozone. Sains Malaysiana **41**, 739–745 (2012)
52. R.K. Ramasamy, N.A. Rahman, C.S. Wong, Effect of temperature on the ozonation of textile waste effluent. Color. Technol. **117**, 95–97 (2001)
53. A.N. Yusilawati, M. Maizirwan, I. Sopyan, M.S. Hamzah, K.H. Ng, C.S. Wong, Surface modification of polystyrene beads by uv/ozone treatment. Adv. Mater. Res. **264–265**, 1532–1537 (2011)
54. X. Xu, Dielectric barrier discharge: properties and applications. Thin Solid Films **390**, 237–242 (2001)
55. S.A. Hashim, C.S. Wong, M.R. Abas, K.Z. Hj, Dahlan, discharge based processing systems for nitric oxide (NO) remediation. Sains Malaysiana **39**, 981–987 (2010)
56. S. Ramakrishnan, M.W. Rogozinski, Properties of electric arc plasma for metal cutting. J. Phys. D Appl. Phys. **30**, 636–644 (1997)
57. P. Bertrand, M. Ignatiev, G. Flamant, I. Smurov, Pyrometry applications in thermal plasma processing. Vacuum **56**, 71–76 (2000)
58. G.Y. Park, S.J. Park, M.Y. Choi, I.G. Koo, J.H. Byun, J.W. Hong, J.Y. Sim, G.J. Collons, J. K. Lee, Atmospheric-pressure plasma sources for biomedical applications. Plasma Sources Sci. Technol. **21**, 043001 (2012)
59. M. Laroussi, T. Akan, Arc-free atmospheric pressure cold plasma jets: a review. Plasma Process. Polym. **4**, 777–788 (2007)
60. D. Mariotti, T. Belmonte, J. Benedikt, T. Velusamy, G. Jain, V. Švrček, Low-temperature atmospheric pressure plasma processes for 'green' third generation photovoltaics. Plasma Process. Polym. **13**, 70–90 (2016)
61. E.E. Kunhardt, Generation of large-volume, atmospheric-pressure, nonequilibrium plasmas. IEEE Trans. Plasma Sci. **28**, 189–200 (2000)
62. S.Y. Moon, J. Han, W. Choe, Control of radio-frequency atmospheric pressure argon plasma characteristics by helium gas mixing. Phys. Plasmas **13**, 013504 (2006)
63. C. Tendero, C. Tixier, P. Tristant, J. Desmaison, P. Leprince, Atmospheric pressure plasmas: a review. Spectrochim. Acta B **61**, 2–30 (2006)
64. A.P. Napartovich, Overview of atmospheric pressure discharges. Plasmas Polym. **6**, 1–14 (2001)
65. Yu.P. Raizer, *Gas Discharge Physics* (Springer-Verlag, Berlin Heidelberg, 1991), pp. 214–287
66. U. Kogelschatz, Dielectric-barrier discharges: their history, discharge physics, and industrial applications. Plasma Chem. Plasma P. **23**, 1–46 (2003)
67. F. Massines, P. Ségur, N. Gherardi, C. Khamphan, A. Ricard, Physics and chemistry in a glow dielectric barrier discharge at atmospheric pressure: diagnostics and modelling. Surf. Coat. Tech. **174–175**, 8–14 (2003)
68. S. Zhang, W.C. Wang, P.C. Jiang, D.Z. Yang, L. Jia, S. Wang, Comparison of atmospheric air plasmas excited by high-voltage nanosecond pulsed discharge and sinusoidal alternating current discharge. J. Appl. Phys. **114**, 163301 (2013)

69. Z. Xiong, X. Lu, Y. Cao, Q. Ning, K. Ostrikov, Y. Lu, X. Zhou, J. Liu, Room-temperature, atmospheric plasma needle reduces adenovirus gene expression in HEK 293A host cells. Appl. Phys. Lett. **99**, 253703 (2011)
70. D. Mariotti, R.M. Sankaran, Microplasmas for nanomaterials synthesis. J. Phys. D Appl. Phys. **43**, 323001 (2010)
71. R.M. Sankaran, K.P. Giapis, Hollow cathode sustained plasma microjets: characterization and application to diamond deposition. J. Appl. Phys. **92**, 2406–2411 (2002)
72. Q. Xiong, A.Y. Nikiforov, M.A. Gonzalez, C. Leys, X.P. Lu, Characterization of an atmospheric helium plasma jet by relative and absolute optical emission spectroscopy. Plasma Sources Sci. Technol. **22**, 015011 (2013)
73. S.A. Norberg, E. Johnsen, M.J. Kushner, Helium atmospheric pressure plasma jets touching dielectric and metal surfaces. J. Appl. Phys. **118**, 013301 (2015)
74. Tables of Physical & Chemical Constants (16th edition 1995), 2.3.7 Thermal conductivities (Kaye & Laby Online, Version 1.0, National Physical Laboratory (UK), 2005), http://www.kayelaby.npl.co.uk. Accessed 15 Feb 2016
75. M. Moravej, X. Yang, G.R. Nowling, J.P. Chang, R.F. Hicksa, S.E. Babayan, Physics of high-pressure helium and argon radio-frequency plasmas. J. Appl. Phys. **96**, 7011–7017 (2004)
76. T. Kuwahara, T. Kuroki, K. Yoshida, N. Saeki, M. Okubo, Development of sterilization device using air nonthermal plasma jet induced by atmospheric pressure corona discharge. Thin Solid Films **523**, 2–5 (2012)
77. H. Koinuma, H. Ohkubo, T. Hashimoto, K. Inomata, T. Shiraishi, A. Miyanaga, S. Hayashi, Development and application of a microbeam plasma generator. Appl. Phys. Lett. **60**, 816 (1992)
78. I.E. Kieft, D. Darios, A.J. Roks, E. Stoffels, Plasma treatment of mammalian vascular cells: a quantitative description. IEEE Trans. Plasma Sci. **33**, 771–775 (2005)
79. C.Y. Choo, O.H. Chin, Study of non-thermal plasma jet with dielectric barrier configuration in nitrogen and argon. AIP Conf. Proc. **1588**, 191–195 (2014)
80. Y.T. Lau, K.K. Jayapalan, M.E. Pam, O.H. Chin, C.S. Wong, Dependence of dielectric barrier jet length on gas flow rate and applied voltage. J. Sci. Technol. Tropics **10**, 131–138 (2014)
81. K.L. Lai, K.K. Jayapalan, O.H. Chin, P.F. Lee, C.S. Wong, Investigating the characteristics of a coplanar-coaxial atmospheric pressure dielectric barrier discharge jet in argon. AIP Conf. Proc. **1657**, 150002 (2015)
82. R.B. Tyata, D.P. Subedi, A. Shrestha, D. Baral, Development of atmospheric pressure plasma jet in air. Kathmandu Univ. J. Sci. Eng. Technol. **8**, 15–22 (2012)
83. M. Laroussi, X. Lu, Room-temperature atmospheric pressure plasma plume for biomedical applications. Appl. Phys. Lett. **87**, 113902 (2005)
84. H.M. Joh, J.Y. Choi, S.J. Kim, T.H. Chung, T.H. Kang, Effect of additive oxygen gas on cellular response of lung cancer cells induced by atmospheric pressure helium plasma jet. Sci. Rep. **4**, 6638 (2014)
85. Q. Xiong, X. Lu, K. Ostrikov, Z. Xiong, Y. Xian, F. Zhou, C. Zou, J. Hu, W. Gong, X, Jiang, Length control of He atmospheric plasma jet plumes: effects of discharge parameters and ambient air. Phys. Plasmas **16**, 043505 (2009)
86. X.P. Lu, Z.H. Jiang, Q. Xiong, Z.Y. Tang, Y. Pan, A single electrode room-temperature plasma jet device for biomedical applications. Appl. Phys. Lett. **92**, 151504 (2008)
87. J. Patel, L. Němcová, P. Maguire, W.G. Graham, D. Mariotti, Synthesis of surfactant-free electrostatically stabilized gold nanoparticles by plasma-induced liquid chemistry. Nanotechnology **24**, 245604 (2013)
88. Y.L. Thong, O.H. Chin, B.H. Ong, N.M. Huang, Synthesis of silver nanoparticles prepared in aqueous solutions using helium dc microplasma jet. Jpn. J. Appl. Phys. **55**, 01AE19 (2016)

89. J. Walsh, F. Iza, N. Janson, V. Law, M. Kong, Three distinct modes in a cold atmospheric pressure plasma jet. J. Phys. D Appl. Phys. **43**, 075201 (2010)
90. X. Lu, Z. Jiang, Q. Xiong, Z. Tang, X. Hu, Y. Pan, An 11 cm long atmospheric pressure cold plasma plume for applications of plasma medicine. Appl. Phys. Lett. **92**, 081502 (2008)
91. Z. Cao, J. Walsh, M. Kong, Atmospheric plasma jet array in parallel electric and gas flow fields for three-dimensional surface treatment. Appl. Phys. Lett. **94**, 021501 (2009)
92. X. Shao, G. Zhang, J. Zhan, H. Mu, Investigation on spurt length of atmospheric-pressure plasma jets. IEEE Trans. Plasma Sci. **39**, 2340–2341 (2011)
93. K. Gazeli, P. Svarnas, P. Vafeas, P. Papadopoulos, A. Gkelios, F. Clement, Investigation on streamers propagating into a helium jet in air at atmospheric pressure: electrical and optical emission analysis. J. Appl. Phys. **114**, 103304 (2013)
94. P. Cullen, V. Milosavljević, Spectroscopic characterization of a radio-frequency argon plasma jet discharge in ambient air. Prog. Theor. Exp. Phys. **2015**, 063J01 (2015)
95. T. Takamatsu, K. Uehara, Y. Sasaki, H. Miyahara, Y. Matsumura, A. Iwasawa, N. Ito, T. Azuma, M. Kohno, A. Okino, Investigation of reactive species using various gas plasmas. RSC Adv. **4**, 39901 (2014)
96. M. Pervez, A. Begum, M. Laroussi, Plasma based sterilization: overview and the stepwise inactivation process of microbial by non-thermal atmospheric pressure plasma jet. International Journal of Engineering & Technology IJET-IJENS **14**, 7–16 (2014)
97. D. Dobrynin, G. Fridman, G. Friedman, A. Fridman, Physical and biological mechanisms of direct plasma interaction with living tissue. New J. Phys. **11**, 115020 (2009)
98. G. Morfill, M. Kong, J. Zimmermann, Focus on plasma medicine. New J. Phys. **11**, 115011 (2009)
99. K. Kostov, T. Nishime, A. Castro, A. Toth, L. Hein, Surface modification of polymeric materials by cold atmospheric plasma jet. Appl. Surf. Sci. **314**, 367–375 (2014)
100. O.H. Chin, C.K. Lai, C.Y. Choo, C.S. Wong, R.M. Nor, K.L. Thong, Atmospheric pressure dielectric barrier discharges for sterilization and surface treatment. AIP Conf. Proc. **1657**, 030008 (2015)
101. D. Mariotti, R. Sankaran, Perspectives on atmospheric-pressure plasmas for nanofrabrication. J. Phys. D Appl. Phys. **44**, 174023 (2011)
102. M. Laroussi, E. Karakas, W. Hynes, Influence of cell type, initial concentration, and medium on the inactivation efficiency of low-temperature plasma. IEEE Trans. Plasma Sci. **39**, 2960–2961 (2011)
103. M. Laroussi, Low-temperature plasma jet for biomedical applications: a review. IEEE Trans. Plasma Sci. **43**, 703–712 (2015)
104. C.D. Groh, D.W. MacPherson, D.J. Groves, Effect of heat on the sterilization of artificially contaminated water. J. Travel. Med. **3**, 11–13 (1996)
105. K. Gazeli, C. Noel, F. Clement, C. Dauge, P. Svarnas, T. Belmonte, A study of helium atmospheric-pressure guided streamers for potential biological applications. Plasma Sources Sci. Technol. **22**, 025020 (2013)
106. D.A. Mendis, M.A. Rosenberg, F. Azam, A note on the possible electrostatic disruption of bacteria. IEEE Trans. Plasma Sci. **28**, 1304–1306 (2000)
107. M. Laroussi, D.A. Mendis, M. Rosenberg, Plasma interaction with microbes. New J. Phys. **5**, 41 (2003)
108. A. Kramida, Y. Ralchenko, J. Reader, N.A. Team, NIST Atomic Spectra Database (Ver. 5.3). (National Institute of Standards and Technology, 2015), http://physics.nist.gov/PhysRefData/ASD/lines_form.html. Accessed 1 Mar 2016
109. K.L. Lai, *unpublished data*
110. N. Barekzi, M. Laroussi, Dose-dependent killing of leukemia cells by low-temperature plasma. J. Phys. D Appl. Phys. **45**, 422002 (2012)
111. K. Kong, G. Kroesen, G. Morfill, T. Nosenko, T. Shimizu, J. van Dijk, J. Zimmermann, Plasma medicine: an introductory review. New J. Phys. **11**, 115012 (2009)
112. J. Schlegel, J. Koritzer, V. Boxhammer, Plasma in cancer treatment. Clin. Plasma Med. **1**, 2–7 (2013)

113. L. Brullé, M. Vandamme, D.M. Riès, E. Robert, S. Lerondel, V. Trichet, S. Richard, J.M. Pouvesle, A. Le Pape, Effects of non thermal plasma treatment alone or in combination with gemcitabine in a MIE PaCa2-luc orthotopic pancreatic cancer model. PLoS One **7**, e52653 (2012)
114. D.B. Graves, Low temperature plasma biomedicine: a tutorial review. Phys. Plasmas **21**, 080901 (2014)
115. C.Y. Choo, in *Characterization of dielectric barrier discharge jet for surface treatment*, MSc thesis, University of Malaya (2013)
116. U. Lommatzsch, D. Pasedag, A. Baalmann, G. Ellinghorst, H.E. Wagner, Atmospheric pressure plasma jet treatment of polyethylene surfaces for adhesion improvement. Plasma Process. Polym. **4**, S1041–S1045 (2007)
117. Y.L. Thong, in *Synthesis of gold and silver nanoparticles assisted by dc helium microplasma jet at atmospheric pressure*, MSc thesis, University of Malaya (2016)
118. R. Wang, S. Zuo, W. Zhu, S. Wu, W. Nian, J. Zhang, J. Fang, Microplasma-assisted growth of colloidal silver nanoparticles for enhanced antibacterial activity. Plasma Process. Polym. **11**, 44–51 (2014)
119. R.A. Millikan, R.A. Sawyer, Extreme ultra-violet spectra of hot sparks in high vacua. Proc. Am. Phys. Soc. **12**(2), 167–170 (1918)
120. B. Edlén, Early observations of highly charged ions. *Phys. Scrip.,* **T3**: 5–6 (1983)
121. R.C. Elton, T.N. Lie, Laboratory-produced radiation related to the solar flare emission. Space Sci. Rev. **13**, 747–760 (1972)
122. C.S. Wong, C.X. Ong, S.P. Moo, P. Choi, Characteristics of a vacuum spark triggered by the transient hollow cathode discharge electron beam. IEEE Trans. Plasma Sci. **23**(3), 265–269 (1995)
123. F. Wu, W.C. Tang, K.W. Witpszo, E. Panarella, The vacuum spark and spherical pinch X-Ray/EUV point sources. Proc. SPIE **3676**, 410–420 (1999)
124. S. Morita, J. Fujita, X-Ray spectroscopy of highly ionized atoms of Ti through Zn in a dense plasma. Nuc. Instr. Meth. Phys. Res. **B9**, 713–723 (1985)
125. J.J. Turechek, H.J. Kunze, Time resolved spectroscopic observation of a high temperature, high density plasma in a vacuum spark. Zeits. Phys. A **273**, 111–121 (1975)
126. A.N. Dolgov, G.K. Salakhutdinov, Material transport in a low-inductance vacuum spark. Fiz. Plazmy **29**(9), 757–763 (2003)
127. C.S. Wong, S. Lee, Vacuum spark as a reproducible X-Ray source. Rev. Sci. Instrum. **55**, 1125–1128 (1984)
128. L. Cohen, U. Feldman, M. Swartz, J.H. Underwood, Study of the X Rays produced by a vacuum spark. J. Opt. Soc. Am **58**(6), 843–846 (1968)
129. J.W. Shearer, Contraction of Z-pinches actuated by radiation losses. Phys. Fluids **19**(9), 1426–1428 (1976)
130. K.N. Koshelev, N.R. Pereira, Points and radiative collapse in vacuum sparks. J. Appl. Phys. **69**(10), R21–R44 (1991)
131. C.R. Negus, N.J. Peacock, Local regions of a high-pressure plasma in a vacuum spark. J. Phys. D Appl. Phys. **12**, 91–111 (1979)
132. J. Christiansen, Ch. Schultheiss, Production of high current particle beams by low pressure spark discharge. Z. Physik A **290**, 35–41 (1979)
133. P.S. Antsiferov, K.N. Koshelev, A.E. Kramida, A.M. Panin, Two regimes of micropinching in a low-inductance vacuum spark. J. Phys. D Appl. Phys. **22**, 1073–1077 (1989)
134. M. Hebach, A. Engel, A. Schulz, R. Lebert, H.J. Kunze, Time evolution of the X-Ray emission from a micropinch in a vacuum spark discharge. Europhys. Lett. **21**(3), 311–316 (1993)
135. A. Schulz, M. Hebach, H.J. Kunze, F.R. Rosmej, F. Walden, Investigations of micropinches with comparison to the predictions of the radiative collapse model. J. Quant. Spectrosc. Radiat. Transfer **51**(1/2), 341–348 (1994)

136. C.K. Erber, O.H. Herzog, A. Schulz, E.J. Clothiaux, F. Walden, H.J. Kunze, Optimization of micropinch plasmas produced by vacuum spark discharges. Plasma Sources Sci. Techno. **5**, 436–441 (1996)
137. A. Schulz, M. Hebach, F. Walden, F.B. Rosmej and H.J. Kunze, in *Z-scaling of K_α-radiation from micropinches in low-inductance vacuum sparks*. Proceedings XXI International Conference on Phenomena in Ionized Gases, **1**, 347–353 (1993)
138. M. Klapisch, P. Mandelbaum, J.L. Schwob, A.B. Shalom and N. Schweitzer, 3d-4p transitions in the soft X-Ray spectra of Mo XIV and of isoelectronic Y to Ag ions, from a low-inductance vacuum spark. Phys. Lett. **84 A** (4),177–181 (1981)
139. P. Beiersdorfer, E.J. Clothiaux and G. Bell, axial magnetic field measurements and the stability of a vacuum spark plasma. J. Phys. D Appl. Phys. **16**, 1635–1642 (1983)
140. Y.V. Sidelnikov, E.Y. Kononov, K.N. Koshelev, X-Ray diagnostics of hot dense plasma in low-inductance vacuum spark. Nuc. Instr. Meth. Phys. Res. **B9**, 724–726 (1985)
141. O.G. Semyonov, A.E. Gurey, A.P. Kanavin, A.A. Tikhomirov, Applications of micropinch X-ray source. J. Vac. Sci. Technol., B **19**(4), 1235–1240 (2001)
142. N.K. Podder, E.J. Clothiaux, Carbon and lithium spectra from a vacuum spark. J. Appl. Phys. **86**, 725–730 (1999)
143. C.K. Erber, K.N. Koshelev, H.J. Kunze, Time development of Mg micropinches in a low-inductance vacuum spark discharge. J. Quant. Spectrosc. Radiat. Transfer **65**, 195–206 (2000)
144. P.G. Burkhalter, D.J. Nagel, R.R. Whitlock, Laser-produced rare-earth X-ray spectra. Phys. Rev. A **9**(6), 2331–2336 (1974)
145. M. Finkenthal, D. Stutman, A.B. Shalom, Electron density of the prepinched phase of a cerium (Z = 58) vacuum spark plasma obtained from line emission measurements around 1 keV. J. Appl. Phys. **65**(10), 3786–3789 (1989)
146. T.N. Lie, R.C. Elton, X radiation from optical and inner-shell transitions in a highly ionized dense plasma. Phys. Rev. A **3**(3), 865–871 (1971)
147. S. Lee, H. Conrads, Measurements of neutrons and X-rays from a vacuum spark. Phys. Lett. A **57** (3), 233–237 (1976)
148. C.S. Wong, Pulsed electron beams generated by transient hollow cathode discharge. Malaysian J. Science **15B**, 61–66 (1994)
149. C.S. Wong, C.X. Ong, S. Lee, P. Choi, Observation of enhanced pre-breakdown electron beams in a vacuum spark with a hollow-cathode configuration. IEEE Trans. Plas. Sc. **20**(4), 405–409 (1992)
150. M. Skowronek, P. Roméas, J. Larour, P. Choi, X-ray measurements in a low energy vacuum spark. AIP Conf. Proc. **195**, 395–404 (1989)
151. W.A. Cilliers, R.U. Datla, H.R. Griem, Spectroscopic measurements on vacuum spark plasmas. Phys. Rev. A **12**, 1408–1418 (1975)
152. E.V. Aglitsky, E.Y. Golts, Y.A. Levykin, A.M. Livshits, Spectra of Ne-like ions of Ag, Cd, In and Sn. J. Phys. B: Mol. Phys. **14**, 1549–1552 (1981)
153. N. Georgescu, C.G. Serbănescu, G. Sandolache, Reproducibility conditions for the pulsed X-ray emission in a vacuum spark discharge. Proc. NUKLEONIKA **46**, S17–S20 (2001)
154. A.E. Gurey, O.G. Semyonov, A.A. Tikhomirov, Micropinches X-ray source and its applications. Proc. SPIE **4144**, 59–67 (2000)
155. T. Schuelke, T. Witke, H.J. Scheibe, P. Siemroth, B. Schultrich, O. Zimmer, J. Vetter, Comparison of DC and AC arc thin film deposition techniques. Surf. Coat. Techno. **120–121**, 226–232 (1999)
156. D. Stutman, M. Finkenthal, Investigation of the low-inductance vacuum spark as a source of soft X-ray atomic quasi-continua for optical pumping. J. Phys. B: At. Mol. Opt. Phys. **30**, 951–961 (1997)
157. J.L. Schwob, B.S. Fraenkel, X-ray spectra from highly ionized iron and nickel. Space Sci. Rev. **13**, 589–591 (1972)
158. T.N. Lee, Solar-flare and laboratory plasma phenomena. Astrophys. J. **190**, 467–479 (1974)

159. M. Xu, Y. Rubin, X. Guo, Y. Antoshko, S. Drew, I. Ahtik, J. Orzechowski, E. Panarella, The vacuum spark discharge soft X-ray source. Proc. SPIE **4502**, 55–61 (2001)
160. A. Cummings, G. O'Sullivan, P. Dunne, E. Sokell, N. Murphy, J. White, Conversion efficiency of a laser-produced Sn plasma at 13.5 nm, simulated with a one-dimensional hydrodynamic model and treated as a multi-component blackbody. J. Appl. Phys. **38**, 604–616 (2005)
161. J. White, P. Hayden, P. Dunne, A. Cummings, N. Murphy, P. Sheridan, G. O'Sullivan, Simplified modeling of 13.5 nm unresolved transition array emission of a Sn plasma and comparison with experiment. J. Appl. Phys. **98**, 113301 (2005)
162. E.R. Kieft, J.J.A.M. Van der Mullen, G.M.W. Kroesen, Time-resolved pinhole camera imaging and extreme ultraviolet spectrometry on a hollow cathode discharge in Xenon. Phys. Rev. E **68**, 056403 (2003)
163. E.R. Kieft, J.J.A.M. Van der Mullen, G.M.W. Kroesen, Collective thomson scattering experiments on a Tin vapor discharge in the prepinch phase. Phys. Rev. E **70**, 056413 (2004)
164. C.S. Wong, in *Experimental and numerical studies of a laser-initiated vacuum spark*, PhD thesis, University of Malaya (1983)
165. S.H. Chew, in *X-ray and euv emission characteristics of a vacuum spark*, MSc thesis, University of Malaya (2007)
166. C.S. Wong, H.J. Woo, S.L. Yap, A low energy tunable pulsed X-ray source based on the pseudospark electron beam. Laser Part. Beams **25**, 497–502 (2007)
167. E. Nairne, Electrical experiments by Mr. Edward Nairne. Philosophical Transactions of the Royal Society **64**, 79–89 (1774)
168. W.G. Chace, Exploding wires and their uses. New Scientist **18**, 386–388 (1963)
169. W.G. Chace, Exploding wires. Phys. Today **17**, 19–24 (1964)
170. F.D. Bennett, High-temperature exploding wires. In C. A. Rouse (Ed.), Progress in high temperature physics and chemistry (Vol. 2, pp. 1–63). Oxford: Pergamon Press (1968)
171. S.V. Lebedev, A.I. Savvatimskii, Metals during rapid heating by dense currents. Soviet Physics Uspekhi **27**(10), 749–771 (1984)
172. H. Hess, A. Kloss, A. Rakhel, H. Schneidenbach, Determination of thermophysical properties of fluid metals by wire-explosion experiments. Int. J. Thermophys. **20**(4), 1279–1288 (1999)
173. T.A. Shelkovenko, D.B. Sinars, S.A. Pikuz, D.A. Hammer, Radiographic and spectroscopic studies of X-pinch plasma implosion dynamics and X-ray burst emission characteristics. Phys. Plasmas **8**(4), 1305–1318 (2001)
174. K.H. Schoenbach, M. Kristiansen, G. Schaefer, A review of opening switch technology for inductive energy storage. Proc. IEEE **72**(8), 1019–1040 (1984)
175. J.O. Chae, Y.J. Jeong, V.M. Shmelev, A.A. Denicaev, V.M. Poutchkov, V. Ravi, Plasma discharge initiation of explosives in rock blasting application: a case study. Plasma Sci. Technol **8**(4), 443–446 (2006)
176. Y.A. Kotov, Electric explosion of wires as a method for preparation of nanopowders. J. Nanopart. Res. **5**, 539–550 (2003)
177. R.F. Phalen, Evaluation of an exploded-wire aerosol generator for use in inhalation studies. Aerosol Science **3**, 395–406 (1972)
178. F.G. Karioris, B.R. Fish, An exploding wire aerosol generator. J. Colloid Sci. **17**, 155–161 (1962)
179. Y.A. Kotov, The electrical explosion of wire: a method for the synthesis of weakly aggregated nanopowders. Nanotechnol. Russ. **4**(7), 415–424 (2009)
180. Y.S. Lee, in *Syntheses of nanoparticles by wire explosion technique*, MSc thesis, University of Malaya (2011)
181. B. Bora, S.S. Kausik, C.S. Wong, O.H. Chin, S.L. Yap, L. Soto, Observation of the partial reheating of the metallic vapor during the wire explosion process for nanoparticle synthesis. Appl. Phys. Lett. **104**, 223108 (2014)

Chapter 10
Radio Frequency Planar Inductively Coupled Plasma: Fundamentals and Applications

Kanesh Kumar Jayapalan, Oi Hoong Chin and Chiow San Wong

10.1 Introduction

10.1.1 Introduction to Inductively Coupled Plasmas (ICPs)

Plasmas can be produced in electric fields with frequencies ranging from DC, low-frequency AC (50 Hz–1 MHz), radio frequency (1–500 MHz), and microwave frequency (0.5–10 GHz). With DC excitation, plasma is sustained by a conduction current in the form of ions and electrons flowing between the electrodes. At radio frequencies, whereby the period of the applied field is comparable to the time taken by electrons or ions (in particular) to traverse the sheath between the electrode and the plasma, the applied power interacts with the plasma through displacement currents. Radio frequency (RF) plasma reactors are popular in the materials processing industry, and 13.56 MHz and its harmonics are widely used. These radio frequencies are chosen basically because they are allocated for industrial, scientific, and medical (ISM) applications under the International Telecommunication Union Radio Regulations to avoid interference with telecommunications bands [1]. RF plasma for industrial applications is still thriving since about half a century ago and many review articles and books have been published on these sources [2–6]. These RF plasma sources generally fall into three main categories in terms of energy transfer coupling: (i) capacitively coupled plasma (CCP), (ii) inductively coupled plasma (ICP), and (iii) helicon wave (HWP) plasma [7]. The topic of RF plasmas is extremely wide and impossible to contain within one chapter. Therefore, the scope of this chapter will be limited to ICP using planar coil configuration.

K.K. Jayapalan · O.H. Chin (✉) · C.S. Wong
Plasma Technology Research Centre, Department of Physics, Faculty of Science, University of Malaya, 50603 Kuala Lumpur, Malaysia
e-mail: ohchin@um.edu.my

K.K. Jayapalan
e-mail: kane.karnage@gmail.com

R.S. Rawat (ed.), *Plasma Science and Technology for Emerging Economies*,
DOI 10.1007/978-981-10-4217-1_10

10.1.2 Brief Historical Development of the Inductive Discharge

The inductive ring-shaped discharge was first observed by Hittorf [8] in 1884 using a Leyden jar to discharge to a wire coiled around an evacuated glass tube. This was followed by several decades of disputes on the mechanism of the plasma production with externally placed electrodes (i.e., the electrodeless discharge). Sir Thomson [9, 10] proposed that the discharge was ignited by the oscillating e.m.f. induced in the tube by the time-varying magnetic field of the external coil. Townsend and Donaldson [11], however, contended that the discharge was due to the 'electric forces' across the low- and high-voltage ends of the coil and this was later supported by Brasefield [12, 13]. MacKinnon [14] reconciled the two explanations by showing electromagnetic induction was possible at large coil currents, while at low currents the large electric field across the ends of the coils was responsible for the discharge. Later in 1947, Babat [15] distinguished the two discharges as the E-discharge (electric phenomenon) in which the plasma conductance currents are divergent and the H-discharge (electromagnetic phenomenon) in which the plasma conductance currents are in the closed loop.

The next milestone in the development of ICP technology was in 1961 when Reed [16, 17] showed that an ICP closely achieving local thermodynamic equilibrium could be sustained in an open tube with the gas flow. This led to the development of the open-air induction torch for use in spectroscopy. In 1963, Greenfield and co-workers [18] demonstrated the preliminary use of ICP for elemental analysis, through optical emission spectroscopy (OES). The commercial ICP-OES system was launched in 1974 by Fassel's group [19, 20]. Combining the ICP (as an ion source) with a mass spectrometer, this forms another analytical tool for elemental analysis, first published in 1980 [21]. PerkinElmer introduced the first ICP-MS in 1983. An account on the development of ICP-MS is given by Potter [22]. Another important application is RF induction plasma spraying technology [23–26]. A patented design of the induction plasma torch with water-cooled ceramic confinement tube was filed in 1991 by Boulos and Jurewicz [27].

The demand for high-rate, uniform large area single-wafer processing in the integrated circuit (IC) fabrication industries led to concerted efforts in the 1990s to develop low-pressure ICP sources producing plasmas with high densities of ions, electrons, and reactive species, low and controllable ion energies as well as low contamination [4]. Ogle [28] from Lam Research, Coultas and Keller [29, 30] as well as Cuomo, Guarnieri, and Hopwood [24] from IBM patented some of the early low-pressure high-density plasma systems for semiconductor processing. In planar induction plasma coupling, ion densities of 10^{16}–10^{18} m^{-3} at low pressure (0.13–2.67 Pa) can be produced. These fall within the range desirable for most single-wafer processing [29].

The development of the theoretical treatment and simulation of the inductive discharges progressed in sync with the experiments, and it is presented chronologically in Table 10.1 [31].

Table 10.1 Chronological summary of the theoretical development and simulation of electrodeless discharges and ICPs

Research by (year)	Configuration	Model (type)	Motivation
Thomson (1927) [32]	Infinitely long cylindrical tube with helical coil (inductive fields)	Solenoid model (analytical)	Development of new inductive discharge theory based on electromagnetic induction
Thomson (1930) [33]	Cylindrical tube with external electrodes (capacitive fields)	Parallel plate model (analytical)	Study of the conditions required to sustain an inductive discharge
Townsend (1932) [34]	Spherical bulb/infinitely long cylindrical tube between two parallel plate electrodes	Parallel plate model (analytical)	Development of new inductive discharge theory based on capacitive fields
Kunz (1932) [35]	Infinitely long cylindrical tube with external electrodes (both inductive and capacitive fields)	Circuit model (analytical)	Development of new circuit theory to derive inductive discharge properties
Eckert (1962) [36]	Infinitely long, coaxial, cylindrical discharge tube and coil with circular cross-sections	ICP diffusion theory model (analytical)	Development of Schottky diffusion theory (electron-loss mechanism) for an inductive discharge
Henriksen et al. (1971) [37]	Infinitely long, cylindrical discharge tube within an infinitely long coil	1D H mode EM field model (analytical)	Development of electromagnetic field model with complex (previously assumed as real) plasma conductivity
Vahedi et al. (1995) [38]	Planar ICP system seeded with Ar gas	2D power deposition model with effective collision frequency (analytical)	Development of power deposition model with effective collision frequency valid for both collisional and collisionless plasma regimes
Li et al. (1995) [39]	Planar ICP system seeded with Ar and O_2 gases and Ar/CF_4/O_2 gas mixture	Self-consistent, time-averaged 2D fluid model (analytical)	Development of a 2D fluid model to simulate plasma transport properties valid at a specific pressure range
Gudmundsson and Lieberman (1998) [40]	Planar ICP system seeded with Ar gas	Global model and transformer circuit model with effective collision frequency (analytical)	Development of a global (volume-averaged) model and transformer (circuit) model; in which calculations were comparable to measured values

(continued)

Table 10.1 (continued)

Research by (year)	Configuration	Model (type)	Motivation
El-Fayoumi and Jones (1998) [41]	Planar ICP system seeded with Ar gas	2D H mode EM field models (analytical and numerical)	Derivation of the analytical and numerical electromagnetic fields for H mode inductive discharge
El-Fayoumi et al. (1998) [42]	Planar ICP system seeded with Ar gas	Power balance model and 2D E mode EM field model (analytical)	Derivation of the power balance equations for calculation of the working path of an inductive discharge and description of discharge hysteresis between E–H mode transitions
Turner and Lieberman (1999) [43]	Planar ICP system seeded with Ar gas	Nonlinear power balance model (analytical)	Derivation of nonlinear power balance factors contributing to E–H mode transition hysteresis in an inductive discharge
Nanbu (2000) [44]	High-density, low-pressure systems including ICPs; various atomic and molecular gases for specific calculations	2D PIC-MCC model (numerical)	Review of development of 2D numerical model for prediction of spatial properties of the inductive discharge including kinetic and collision theory
Nam and Economou (2004) [45]	Miniature ICP (mICP) with planar source and seeded with Ar gas	2D self-consistent fluid model (analytical)	Development of 2D analytical fluid model for a miniaturized ICP system
Takao et al. (2010) [46]	Miniature ICP (mICP) with planar source and seeded with Ar gas	2D PIC-MCC model (numerical)	Development of 2D numerical model for a miniaturized ICP system

10.2 Fundamentals

10.2.1 Configurations of the Inductive Source

In practice, the inductive source used for generation of an RF ICP comes in two principal configurations, namely, the helical coil configuration and the planar coil configuration (Fig. 10.1).

The helical coil configuration uses a solenoid wound across the z-axis of a cylindrical dielectric chamber typically at lower than atmospheric pressures [Fig. 10.1a(i)]. RF current, I_{RF} is passed through the solenoid creating a

high-frequency magnetic field in the direction of the chamber axis [Fig. 10.1a(ii)]. The temperature-resistant dielectric material used in chamber construction (typically glass or quartz) allows contactless permeation of the magnetic fields into the chamber for interaction with the designated gases. In earlier material-processing designs, the ICP was first generated within the region of the coil windings before being directed onto a biased substrate for deposition or etching [47]. More recent designs employ the planar coil configuration, which consists of a flat spiral coil buffered by a dielectric plate which is mounted onto a metal chamber at vacuum pressure [Fig. 10.1b(i)]. The ICP is generated near the plate and across the coil radius via a circular magnetic field [Fig. 10.1b(ii)]. The advantage of the planar coil

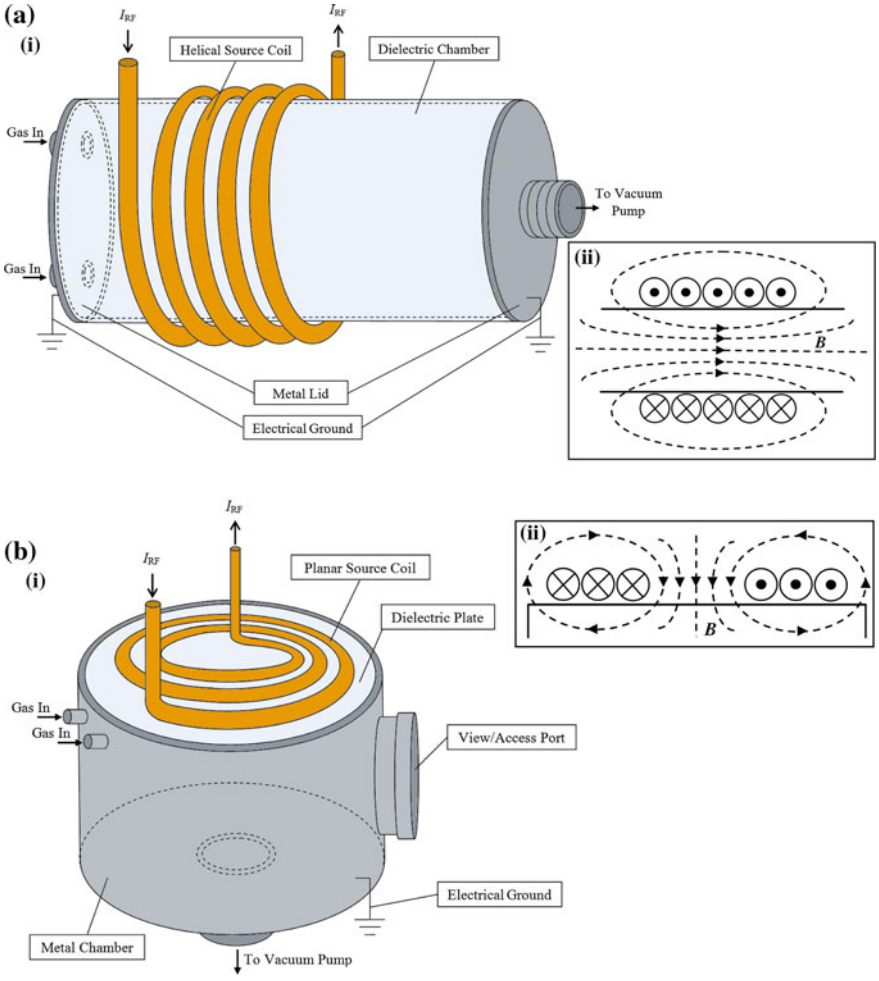

Fig. 10.1 Two types of coil configurations used in ICP design, that is, **a** (i) helical and **b** (i) planar. The respective directions of the coil magnetic fields, *B* are shown in **a** (ii) and **b** (ii)

configuration over the helical coil configuration is the increased uniformity in density distribution of the ICP formed across the coil dimensions. In material etching and deposition applications, higher uniformity would give better process control and reproducibility of results [28, 48].

10.2.2 Impedance Matching

Impedance matching is necessary for RF circuitry. The maximum power transfer theorem in DC circuits states that maximum power from the source is transferred to the load when the load resistance is equal or "matched" to the source resistance. In AC circuits, both the source impedance and load impedance must be matched for maximum power transfer, too. In this case, the reactance component of the source impedance and the load impedance must cancel each other out. This means the matching load impedance must be equal to the complex conjugate of the source impedance, $Z_L = Z_S^*$. Figure 10.2 illustrates the matched condition for maximum power transfer, whereby, R_S, R_L, X_S, and X_L are the source resistance, load resistance, source reactance and load reactance, respectively, in Ω. Reactance is frequency dependent, hence, the source and load impedance are perfectly matched only at a single frequency.

Besides consideration for power efficiency, another factor is the safety issue relating to the build-up of standing waves in the transmission line when the power is reflected in an unmatched RF circuit. The forward and reflected waves can add up or cancel out depending on their relative phase. If the resultant wave is positioned on the transmission line in such a way that maximum voltage or current is applied to the power electronics in the RF source, the RF source can be damaged.

The typical Thevenin equivalent resistance of an RF power source is 50 Ω at 13.56 MHz. The coaxial cable that connects the source to the load can affect the power coupling. This cable becomes a transmission line if it has length larger than $\lambda/8$ at operating frequency. If the line impedance is mismatched to the source and load impedances, standing waves will develop along the line resulting in reflected

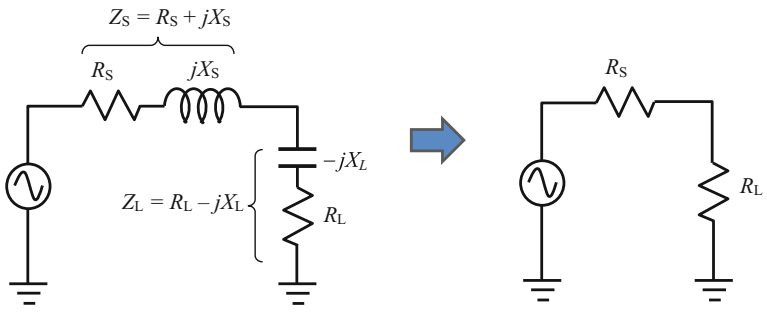

Fig. 10.2 Requirement for impedance matching in AC circuit, and the resulting equivalent circuit

power. At 13.56 MHz, λ = 22.1 m, so keeping the cable length below 2.8 m will minimize this problem.

Figure 10.3 shows the equivalent circuit of a capacitive matching network for an inductive discharge [5, 49].

V_S and R_S are the source voltage and resistance. The impedance at the inductive coil terminals, when the plasma is turned on is constituted by the inductance L_{CP} in series with resistance R_{CP}. The admittance at the terminals *a–b* (toward the right) is expressed by

$$Y_{ab} \equiv G_{ab} + jB_{ab} \equiv \frac{1}{Z_{ab}} = [R_{CP} + j(X_1 + X_{CP})]^{-1}, \tag{10.2.2.1}$$

where the conductance (real component) is

$$G_{ab} = \frac{R_{CP}}{R_{CP}^2 + (X_1 + X_{CP})^2}, \tag{10.2.2.2}$$

and the susceptance (imaginary component) is

$$B_{ab} = -\frac{X_1 + X_{CP}}{R_{CP}^2 + (X_1 + X_{CP})^2}. \tag{10.2.2.3}$$

For matched conditions, the conductance, G_{ab} is made to be equal to $(R_S)^{-1}$ and the susceptance is canceled through $B_{ab} = -B_2 = -\omega C_2$. Hence, solving for Eqs. (10.2.2.2) and (10.2.2.3), the matching condition is achieved when the capacitors C_1 and C_2 are tuned to

$$C_1 = \frac{1}{\omega\left(\omega L_{CP} - \sqrt{R_S R_{CP} - R_{CP}^2}\right)}, \tag{10.2.2.4a}$$

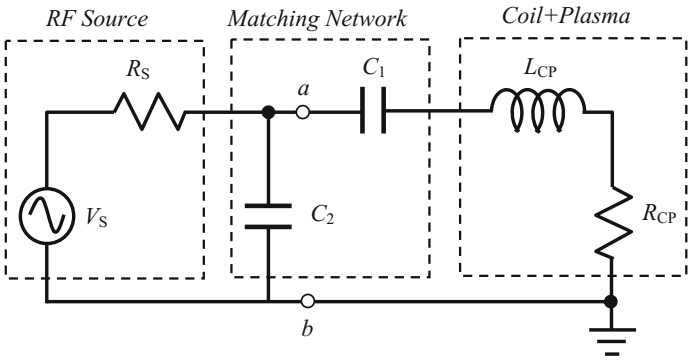

Fig. 10.3 Equivalent circuit for matching the RF source to the inductive plasma (load)

and

$$C_2 = \frac{1}{\omega}\sqrt{\frac{1}{R_S R_{CP}} - \frac{1}{R_S^2}}. \tag{10.2.2.4b}$$

A configuration commonly used in practical RF matching networks is to make $R_s = R_{CP}$, then C_2 becomes negligible (can be removed) and the circuit is in the resonance condition when C_1 is tuned to

$$\omega C_1 = \frac{1}{\omega L_{CP}}. \tag{10.2.2.5}$$

For inductive plasma, R_{CP} is $\sim 1\ \Omega$ [50]. With $R_s' = 50\ \Omega$ for 13.56 MHz commercial sources, the large impedance mismatch can be aptly solved by introducing a step-down transformer as shown in Fig. 10.4. The number of turns required to reduce the source impedance, Z_S, to a value closer to the load impedance, Z_L, is given by

$$\frac{Z_S}{Z_L} = \frac{L_1}{L_2} = \frac{N_1^2}{N_2^2}. \tag{10.2.2.6}$$

Here, N_1 and N_2 are the number of windings on the primary and secondary transformer coils respectively. For the source–load impedance ratio, Z_S:Z_L = 50:1, the ratio of the number of turns required for impedance matching is, N_1:$N_2 \approx$ 7:1 [51].

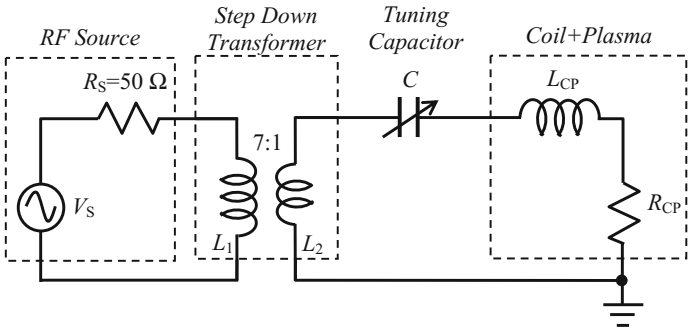

Fig. 10.4 A step-down transformer (L_1:L_2) is introduced between the load and the source for impedance matching. L_1 and L_2 are the primary and secondary coils of the transformer respectively

10.2.3 Modes of Operation and Hysteresis

10.2.3.1 E Mode and H Mode

ICPs have two means of power coupling, that is, capacitive coupling and inductive coupling, which together contribute toward the formation of the plasma. The primary mode (or H mode) of the plasma is formed mainly by inductive coupling of the magnetic fields of the source coil. The secondary mode (or E mode) of the plasma is formed mainly by capacitive coupling from the electric fields of the source coil. These electric fields are produced by the oscillating potential difference across the gaps between the windings of the coil. The terminology of E and H were first introduced in 1947 by Babat [15]; taking the commonly used notations for hollow metal waveguides to identify the electric and magnetic waves, respectively.

The E mode plasma is generally formed at lower input powers in which power coupling of the source magnetic fields is low and insufficient to trigger an induction current in the discharge. The E mode and H mode plasmas can be identified by prominent differences in plasma density and luminosity (Fig. 10.5). The H mode plasma is highly luminous and has a plasma density in the order of 10^{16}–10^{18} m^{-3}. The E mode plasma is low in luminosity and has a plasma density in the order of 10^{13}–10^{15} m^{-3}.

In applications, the mode of interest is typically the H mode at which high electron density and discharge purity give more precise results in material deposition and etching. The E mode is generally characterized for better understanding of discharge dynamics [5].

10.2.3.2 Mode Transitions and Hysteresis

Switching between E and H modes can occur either seamlessly or in discontinuous "jumps" depending on gas type, gas pressure, and impedance matching. At low pressures, E to H mode transitions are typically seamless with discontinuity occurring

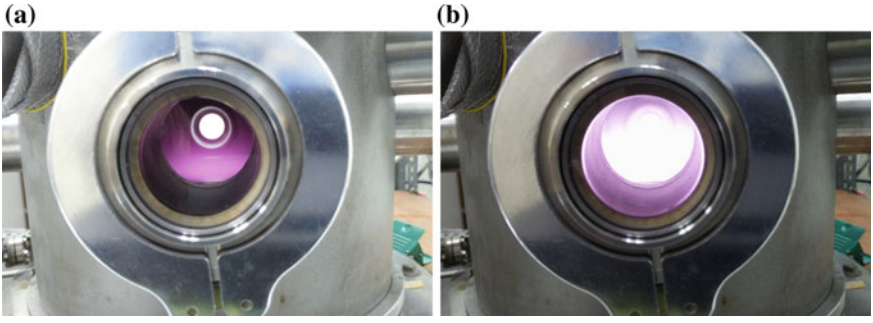

Fig. 10.5 Laboratory 13.56 MHz RF argon ICP operating at **a** E mode and **b** H mode at 10 Pa

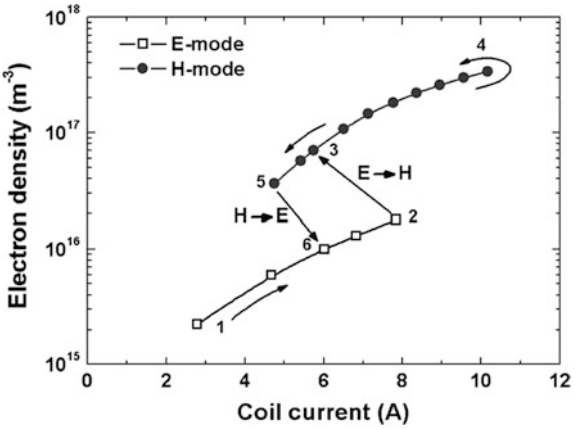

Fig. 10.6 The calculated electron density (m^{-3}) versus coil current (A) at 100 mTorr argon pressure. The current required to cause a transition from E to H mode is higher (point 2, ~8 A) than the power required for maintaining H mode (point 5, ~5 A). © IOP Publishing. Reproduced with permission from [54]. All rights reserved

mainly due to the impedance mismatch of the matching network [52]. At higher pressures, however, impedance matching alone does not negate discontinuity between E to H mode transitions; nonlinearity in power absorption and power loss of the plasma electrons becomes an important factor [53]. Nonlinearity in power absorption also causes an additional hysteresis effect, in which the coil current (corresponding to the input RF power) required for the transition from E to H mode is different from the coil current required for the transition from H to E mode (Fig. 10.6).

Properties of ICP mode transitions were first observed by Kortshagen et al. [55] whereby a trace of the photon multiplier tube signal versus coil current obtained from the experiment showed discontinuity in light emission at the points of transition between E and H modes.

10.2.4 Power Balance in RF Planar ICPs

Maintenance of an ICP at a certain operating state can be fundamentally attributed to the balance points between the total power coupled into the discharge and discharge power loss. In low-temperature discharges such as ICPs, most of the discharge power is deposited into the plasma electrons. Phenomena such as mode transitions and hysteresis can also be effectively simulated by calculating the nonlinearity in the power utilized and dissipated by the plasma electrons. As such, the state at which the plasma exists can be appropriately described by the total absorbed electron power, P_{abs} and electron power loss, P_{loss}. For a stable discharge to occur at a given electron density, n_e, the following power balance conditions need to be fulfilled [42, 56]:

$$P_{abs} = P_{loss} \tag{10.2.4.1}$$

and

$$dP_{abs}/dn_e < dP_{loss}/dn_e. \quad (10.2.4.2)$$

In the following sections, a theoretical model (i.e., power balance model) will be presented to further explain the relevance of these conditions in determining a stable operating state of an ICP reactor at 13.56 MHz RF frequency seeded with argon gas.

10.2.4.1 Power Balance Model

In this model, a reactor in planar coil configuration (Fig. 10.7) will be simulated. The planar coil configuration is chosen due to its wide use in material-processing applications. The reactor is taken to be an azimuthally symmetric cylinder with radius, b in m and height, L in m. A six-turn planar source coil is mounted above the reactor and has a radius of a in m. The total distance between the source coil and the surface of the dielectric plate in contact with the plasma is given by D in m. A summary of the reactor dimensions and specifications are given in Table 10.2. Calculations are made in cylindrical coordinates using the notations r, θ and z.

The model employs several assumptions in the solutions of the reactor electromagnetic fields [equation sets (10.2.5.66a)–(10.2.5.66i) and (10.2.5.106a)–(10.2.5.106j)] which are required to calculate P_{abs}.

They are:

(a) The source coil is assumed to be an infinitesimally thin disc with the surface current density,

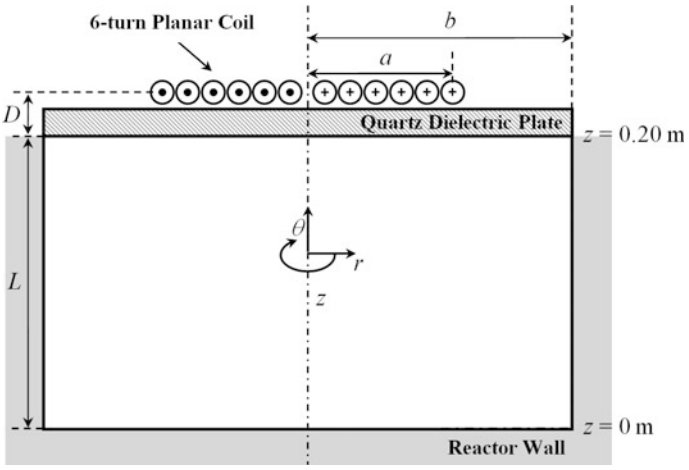

Fig. 10.7 Model diagram of the simulated planar coil ICP reactor

Table 10.2 Dimensions and specifications of the simulated planar coil ICP reactor

Reactor dimensions/specifications						
Drive frequency, f (Hz)	Chamber height, L (m)	Coil-Chamber distance, D (m)	Chamber radius, b (m)	Planar coil radius, a (m)	Number of turns in planar coil	Planar coil inductance, L_o (H)
13.56×10^6	0.20	0.02	0.15	0.05	6	2×10^{-6}

$$K_\theta = \frac{NI_p}{a}, \tag{10.2.4.3}$$

and average electric field across the surface,

$$E_o = \frac{V_p}{a}. \tag{10.2.4.4}$$

Here, N is the number of turns of the coil, I_p is the peak coil current in A, and V_p is the peak coil voltage in V. V_p is given by

$$V_p = I_p \omega L_o, \tag{10.2.4.5}$$

where ω is the RF angular drive frequency, that is, $\omega = 2\pi f$ with f being the RF drive frequency in Hz. L_o is the planar coil inductance in H.

(b) At the source coil surface, $z = L + D$, the radial magnetic field, B_r and the radial electric field, E_r are given by,

$$B_r = \begin{cases} -\frac{\mu_o K_\theta}{2} & 0 \le r \le a \\ 0 & a < r \le b \end{cases} \tag{10.2.4.6a}$$

and

$$E_r = \begin{cases} E_o = \frac{V_p}{a} & 0 \le r \le a \\ 0 & a < r \le b \end{cases} \tag{10.2.4.6b}$$

where μ_o is the vacuum permeability in NA^{-2}. Further details on the application of these assumptions and boundary conditions for the calculation of the electromagnetic field components used in this model will be discussed in Sect. 10.2.5.

10.2.4.2 Total Absorbed Electron Power, P_{abs}

The total absorbed electron power, P_{abs} is defined as the sum of contributive component powers absorbed by the plasma electrons via various mechanisms of

power coupling from the source coil. Three important components that contribute to P_{abs} are the H mode field power, P_h, the E mode field power, P_e and power from stochastic heating of the plasma capacitive sheath, P_{stoc}. Aptly, P_{abs} can be expressed as,

$$P_{abs} = P_h + P_e + P_{stoc}. \tag{10.2.4.7}$$

Contributions from the H mode (P_h) and E mode (P_e) fields are calculated by taking the integration of the time-averaged Poynting vector, P_{ave} [57],

$$P_{ave} = 1/2\mu_o \mathrm{Re}(\boldsymbol{E}\times\boldsymbol{B}^*), \tag{10.2.4.8}$$

over the induction coil area, $d\boldsymbol{S} = 2\pi r(-\boldsymbol{z})dr$ at the coil surface, that is, $z = L + D$. Here, $\boldsymbol{E}$ and $\boldsymbol{B}^*$ are the electric field and complex conjugate of the magnetic field and $\boldsymbol{z}$ is the unit vector for the axial coordinate, respectively. For an azimuthally symmetric reactor, the H mode and E mode fields can be delineated to the following scalar components (Table 10.3):

In view of the boundary conditions and assumptions given in Sect. 10.2.5 and the field components shown in Table 10.3, integration of P_{ave} with $d\boldsymbol{S}$ for P_h and P_e would subsequently yield the following results:

$$P_h = \mathrm{Re}\left(-\pi K_\theta \int_0^a rE_\theta(r, L+D)dr\right) \tag{10.2.4.9}$$

and

$$P_e = \mathrm{Re}\left(-\frac{2\pi}{\mu_o}E_o \int_0^a rB_\theta^*(r, L+D)dr\right). \tag{10.2.4.10}$$

Here, B_θ^* is the complex conjugate of the azimuthal magnetic field in T. At lower RF powers, the measured electron density may be experimentally lower than the densities predicted by the effects of E mode power coupling and H mode power coupling alone. Dominant capacitive coupling from the source coil produces a thick plasma sheath which dampens the effective absorption of power by the plasma electrons. Simulation of the sheath in the power balance model is done by adding a simplified, time-averaged sheath thickness, S to the coil-chamber distance, D when

Table 10.3 H mode and E mode component scalar fields for azimuthal symmetry

	Electric fields, E			Magnetic fields, B		
	Radial	Azimuthal	Axial	Radial	Azimuthal	Axial
H mode fields	0	E_θ	0	B_r	0	B_z
E mode fields	E_r	0	E_z	0	B_θ	0

calculating P_h and P_e; making the effective distance between the field power and plasma electrons larger in calculation, that is, effective distance represented by $(L + D + S)$. S is derived from Child's Law for a collisionless capacitive sheath, which is shown in detail by Lieberman and Lichtenberg [5]. It is expressed as

$$S = \frac{1}{a}\int_0^a \frac{5J_s^3(r)}{12e^2\omega^3\varepsilon_o n_e^2 T_e}dr. \tag{10.2.4.11}$$

J_s represents the first harmonic component of current density through the sheath and is defined by,

$$J_s^2(r) \approx 1.73\, e\, \varepsilon_o \omega^2 n_e (T_e V_s(r))^{1/2}, \tag{10.2.4.12}$$

where $V_s(r)$ is the first harmonic component of voltage across the plasma sheath at the coil–dielectric interface. The subsequent harmonics for the current density and voltage are not considered due to their negligible contribution in derivation. The electron charge e is in C, ε_o is the vacuum permittivity in Fm^{-1}, ω is the RF angular drive frequency in $rads^{-1}$ and T_e is the electron temperature in eV. For the source coil,

$$V_s(r) = \frac{V_p}{a} r. \tag{10.2.4.13}$$

The plasma sheath is known to oscillate at the RF drive frequency. This can produce an additional heating effect in which the field oscillation of the sheath accelerate and de-accelerate plasma electrons, producing collisions which contribute to power transfer. This effect is known as stochastic power coupling, P_{stoc}. For a single capacitive sheath in which the motion of oscillation is slower than the thermal velocity of the electrons, P_{stoc} is approximated by

$$P_{stoc} \approx 0.9\pi\varepsilon_o\omega^2\left(\frac{m_e T_e}{e}\right)^{1/2}\int_0^a rV_s(r)dr. \tag{10.2.4.14}$$

10.2.4.3 Electron Power Loss, P_{loss}

Electron power loss in an ICP is mainly due to energy consumed for the formation and maintenance of ion–electron pairs in the plasma. In simpler derivations, the

power dissipation, P_{loss} is typically taken to be directly proportional to the electron density, n_e (that is, $P_{\text{loss}} \propto n_e$). However, for more accurate simulation of the power balance seen in experiments, nonlinearities in the power loss curve have to be considered. In the power balance model, the contribution of electron–electron collisions or Coulomb collisions is considered; with the transition from Druyvestyen to Maxwellian electron energy density function (EEDF) being representative of the nonlinearity in the electron power loss. This equation for P_{loss} can be written as [43]

$$P_{\text{loss}} = n_e u_B A_{\text{eff}} \varepsilon_T \left(\frac{\varepsilon_{cD}}{\varepsilon_{cM}}\right)^{1/(1+C_{D-M} n_e/n_g)} \tag{10.2.4.15}$$

where u_B is the Bohm velocity in ms^{-1}; given by

$$u_B = (eT_e/M_{Ar})^{1/2} \tag{10.2.4.16}$$

with M_{Ar} being the argon ion mass in kg and T_e the electron temperature in eV. A_{eff} is the effective surface area for particle loss in the reactor in m^2 and ε_T is the total energy lost per electron–ion pair created by the discharge in J. A_{eff} for a simple cylindrical chamber [5] is defined as,

$$A_{\text{eff}} = 2\pi b(bh_l + Lh_r). \tag{10.2.4.17}$$

Here, h_l and h_r are the radial and axial plasma diffusion terms when approaching the sheath edge, that is,

$$h_l \approx 0.86(3 + L/2\lambda_{in})^{-1/2} \tag{10.2.4.18}$$

and

$$h_r \approx 0.80(4 + b/\lambda_{in})^{-1/2}. \tag{10.2.4.19}$$

L and b are the effective chamber height and radius in m. The ion-neutral mean free path, λ_{in}, is related to the neutral gas density, n_g, and the ion-neutral collision cross section, σ_{in}, through the expression

$$\lambda_{in} = \left(\frac{1}{n_g \sigma_{in}}\right). \tag{10.2.4.20}$$

ε_T (calculated in terms of eV) is defined as the sum of the collisional energy loss per ion–electron pair, ε_c, the mean kinetic energy lost per ion, ε_i, and the mean kinetic energy lost per electron, ε_e, given by

$$\varepsilon_{\mathrm{T}}(\mathrm{eV}) = \varepsilon_{\mathrm{c}} + \varepsilon_i + \varepsilon_{\mathrm{e}}. \tag{10.2.4.21}$$

For argon plasma, the kinetic energy lost per ion and per electron is approximated by, $\varepsilon_i \approx 5.2T_{\mathrm{e}}$ and $\varepsilon_{\mathrm{e}} \approx 2T_{\mathrm{e}}$, respectively. The collisional energy lost per ion–electron pair, ε_{c}, itself comprises of the total collisional losses due to ionization, excitation, and elastic scattering of electrons with neutrals. It is expressed as

$$\varepsilon_{\mathrm{c}} = \varepsilon_{\mathrm{iz}} + \frac{K_{\mathrm{ex}}}{K_{\mathrm{iz}}}\varepsilon_{\mathrm{ex}} + \frac{K_{\mathrm{el}}}{K_{\mathrm{iz}}}\frac{3m_{\mathrm{e}}}{M_{\mathrm{Ar}}}T_{\mathrm{e}}. \tag{10.2.4.22}$$

Here, $\varepsilon_{\mathrm{iz}}$ (=15.76 eV) is the argon ionization threshold energy and $\varepsilon_{\mathrm{ex}}$ (=12.14 eV) is the argon excitation threshold energy. K_{iz}, K_{ex}, and K_{el} are the argon ionization, excitation, and elastic scattering rate constants ($\mathrm{m^3 s^{-1}}$) given, respectively, by [5, 58],

$$K_{\mathrm{iz}} = 2.34\times10^{-14}T_{\mathrm{e}}^{0.59}\exp(-17.44/T_{\mathrm{e}}), \tag{10.2.4.23}$$

$$K_{\mathrm{ex}} = 2.48\times10^{-14}T_{\mathrm{e}}^{0.33}\exp(-12.78/T_{\mathrm{e}}), \tag{10.2.4.24}$$

and

$$K_{\mathrm{el}} = 2.336\times10^{-14}T_{\mathrm{e}}^{1.609}\exp(0.0618\ln(T_{\mathrm{e}})^2 - 0.1171\ln(T_{\mathrm{e}})^3). \tag{10.2.4.25}$$

The term $(\varepsilon_{\mathrm{cD}}/\varepsilon_{\mathrm{cM}})^{1/(1+C_{\mathrm{D-M}}n_{\mathrm{e}}/n_{\mathrm{g}})}$ in Eq. (10.2.4.15) accounts for the nonlinear effect of transition in electron energy distribution function (EEDF) from Druyvesteyn to Maxwellian when approaching higher electron densities. The exponential factor $C_{\mathrm{D-M}}$, adjusts for the experimental discrepancy (due to random and systematic errors) of the transition point between Druyvesteyn and Maxwellian EEDFs [59, 60]; which is concurrent with the transition of the discharge from E mode to H mode [61]. n_{g} is the neutral gas density in $\mathrm{m^{-3}}$ given by,

$$n_{\mathrm{g}} = \frac{P}{k_{\mathrm{B}}T_{\mathrm{n}}}. \tag{10.2.4.26}$$

Here, k_{B} is the Boltzmann constant in $\mathrm{JK^{-1}}$ and T_{n} is the neutral gas temperature in K. $\varepsilon_{\mathrm{cD}}/\varepsilon_{\mathrm{cM}}$ is the ratio of the Druyvesteyn and Maxwellian electron–electron collision energy loss factors which is approximated as [43, 62]

$$\frac{\varepsilon_{\mathrm{cD}}}{\varepsilon_{\mathrm{cM}}} \approx 1.27 + \frac{9.73}{T_{\mathrm{e}}}. \tag{10.2.4.27}$$

10.2.4.4 Mode Transition Dynamics and Hysteresis in an ICP Discharge

If the absorbed electron power, P_{abs} and electron power loss, P_{loss} parameters are plotted against electron density, n_e, they would intersect at certain points. These intersecting points [based on the first power balance condition given by Eq. (10.2.4.1)] represent the plausible operating states of the ICP system as shown in Fig. 10.8.

The second power balance condition [given by Eq. (10.2.4.2)] determines if these plausible operating states are stable. For an operating state to be observed in an experiment, the rate of change of absorbed power with electron density must be less than the rate of change of power loss with electron density [56, 63]. In Fig. 10.8, points **I** and **III** represent the stable and observable H and E mode operations, respectively, in which both power balance conditions are fulfilled. The plasma mode is determined by identifying the power coupling mechanism which is dominant in the simulation. Point **II** represents an unstable state which is not observable experimentally.

One of the important characteristics for optimization of the ICP discharge is the input power (represented by the peak coil current, I_p) at which the mode transition between E and H mode occurs. At certain ICP operating parameters, the currents at which the E mode transitions to H mode and H mode transitions to E mode are largely different; indicating the effect of hysteresis. To demonstrate this effect in simulation, a 3D plot of total absorbed electron power, P_{abs} and electron power loss, P_{loss} versus peak coil current, I_p and electron density, n_e is visualized (Fig. 10.9). Values used in the plot are taken from measurements at 20 Pa argon pressure [63].

The lighter surface of the 3D plot represents the evolution of absorbed electron power, P_{abs} whereas the darker surface represents the evolution of electron power loss, P_{loss}. In this case, the intersections between the two surfaces (at which the

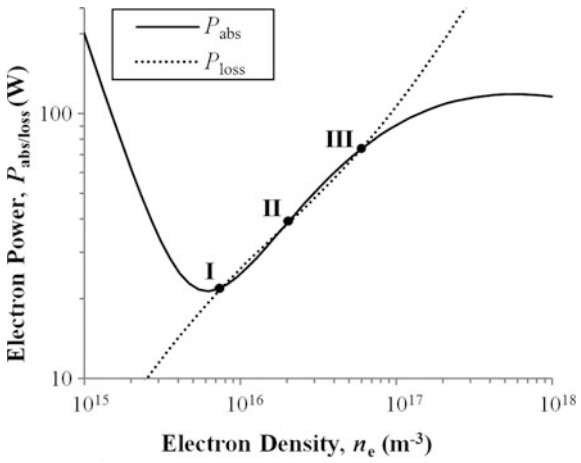

Fig. 10.8 Simulated electron absorbed power and electron power loss versus electron density for I_p = 8.7 A peak RF coil current at 20 Pa argon pressure. **I**, **II**, and **III** represent the E mode, unstable operation, and H mode, respectively. Electron temperature, T_e, neutral gas temperature, T_n, and the factor C_{D-M} were set at 2 eV, 800 K and 10^5, respectively

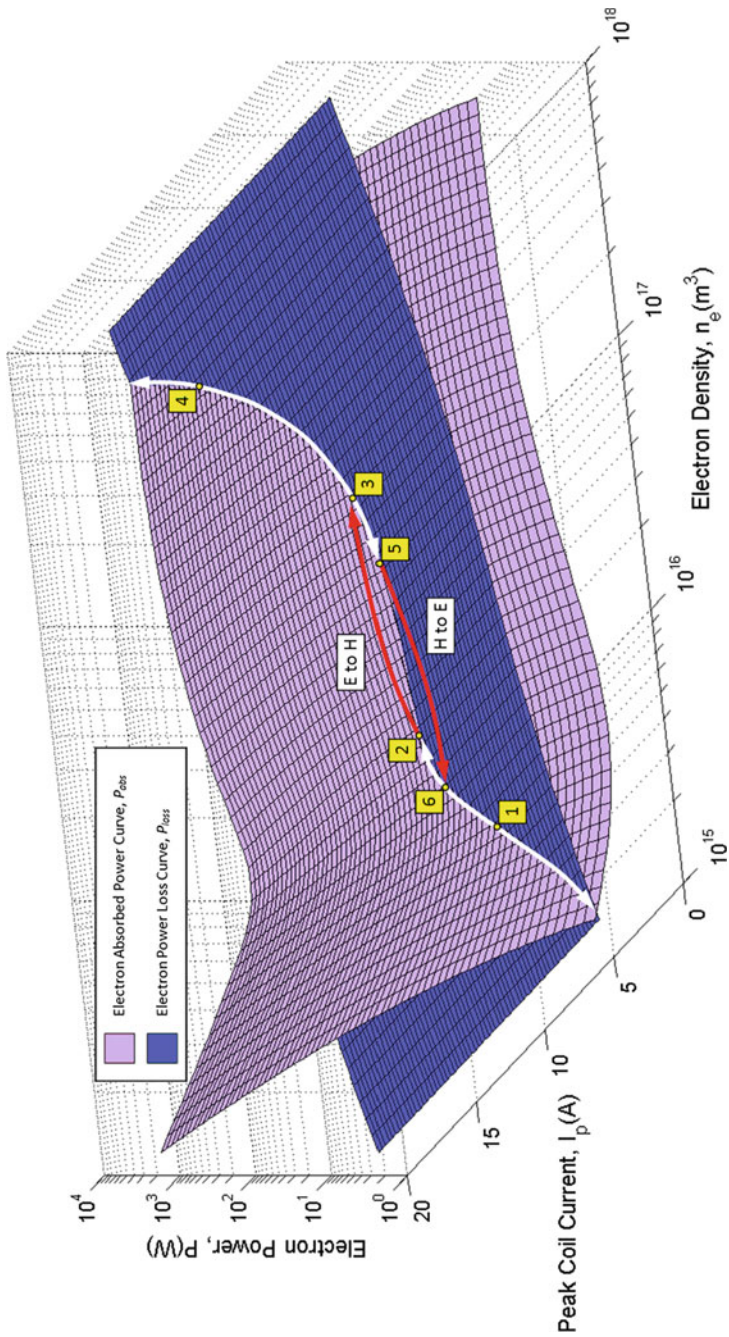

Fig. 10.9 A 3D plot of absorbed electron power, P_{abs} (*lighter surface*) and electron power loss, P_{loss} (*darker surface*) versus electron density, n_e and peak coil current, I_p at 20 Pa argon pressure. Electron temperature, T_e was set at 2 eV, neutral gas temperature, T_n set at 800 K, and $C_{D-M} = 10^5$. The *white arrows* indicate the working path of the system, whereas the *darker arrows* indicate mode transitions

power balance conditions hold) represent the working path of the ICP system. From the input coil current of zero, the operating state of the system moves towards point 1 as current (or RF power) is gradually introduced to the discharge (Fig. 10.9).

At point 1, the low-intensity E mode plasma is observed (Figs. 10.9 and 10.10). A further increase in current would move the operating state of the system to point 2. Point 2 is the threshold at which any further increase in coil current would trigger a transition from E to H mode (Figs. 10.9 and 10.11).

From point 2, the system jumps to point 3 which switches it to H mode operation. The electron density and coil current at which point 3 occurs depend mainly on the experimental setup and is largely affected by the sensitivity and accuracy of the impedance matching circuit [42, 43, 61]. Further increase in coil current at point 3 would bring the system operation state to point 4 (Figs. 10.9 and 10.10) which is a higher density plasma in H mode. When coil current is decreased from point 4, the system follows the H mode operation path until point 5. Point 5 is the threshold at which a further decrease in coil current would trigger a transition from H to E mode (Figs. 10.9 and 10.11). The disparity between E to H mode transition and H to E mode transition currents denotes the effect of hysteresis in the working path of the system. From point 5, a decrease in coil current shifts the system state to point 6 which is in E mode operation.

10.2.5 Electromagnetic Field Distributions in RF Planar ICPs

Knowledge of the electromagnetic source field distributions in an ICP reactor enables further insight on the formation and maintenance of the discharge. Besides calculation of mode operation state and hysteresis, intrinsic attributes of the plasma such as electron density [41] and neutral gas temperature are also inferable from the source field [63]. Hence, simulation of these fields would be useful in understanding the plasma interaction dynamics occurring in an ICP reactor and for the development of ICP-based systems.

As the source coil provides two types of power coupling, that is, inductive (H mode) and capacitive (E mode), the source fields can be more systematically simulated by separating both coupling components into mode specific models, i.e., the H mode field model and the E mode field model. In the following sections, the H mode and E mode ICP fields will be derived in cylindrical coordinates ($-r$, $-\theta$ and $-z$) for a planar coil ICP reactor with specifications described in Fig. 10.7 and Table 10.2. Both models are based on the works of El-Fayoumi [64], El-Fayoumi and Jones [41] and Jayapalan [31] and will be solved analytically by the separation of variables method [65–67] with the required boundary conditions (Fig. 10.12). Some key results from the simulation will be discussed in Sect. 10.2.5.5.

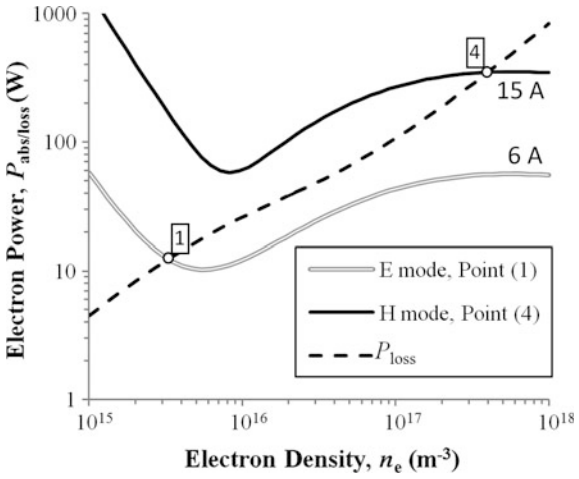

Fig. 10.10 The simulated absorbed electron power (*solid line*) and power loss (*dashed line*) curves depicting the current at which either E mode [6 A—(1)] or H mode operation [15 A—(4)] alone occurs

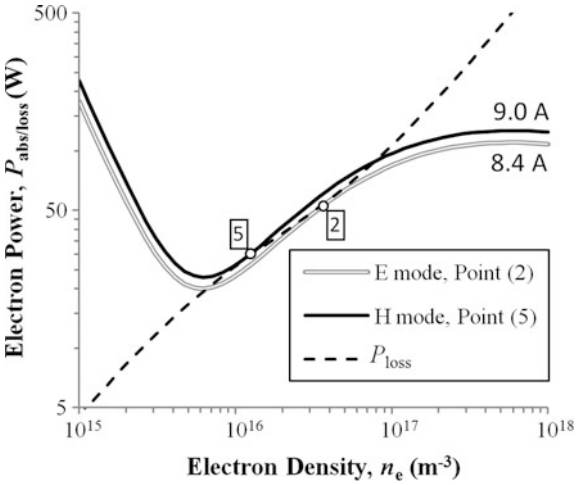

Fig. 10.11 The simulated absorbed electron power (*solid line*) and power loss (*dashed line*) curves depicting the threshold currents for E→H [9.0 A—(2)] and H→E [8.4 A—(5)] mode transitions

10.2.5.1 Electromagnetic Field Equations

The H mode and E mode fields are derived from the standard Maxwell's equations given by

$$\nabla \times \mathcal{E}(r,\theta,z,t) = -\frac{\partial \mathcal{B}(r,\theta,z,t)}{\partial t}, \tag{10.2.5.1}$$

$$\nabla \cdot \mathcal{E}(r,\theta,z,t) = \frac{\rho}{\varepsilon_o}, \tag{10.2.5.2}$$

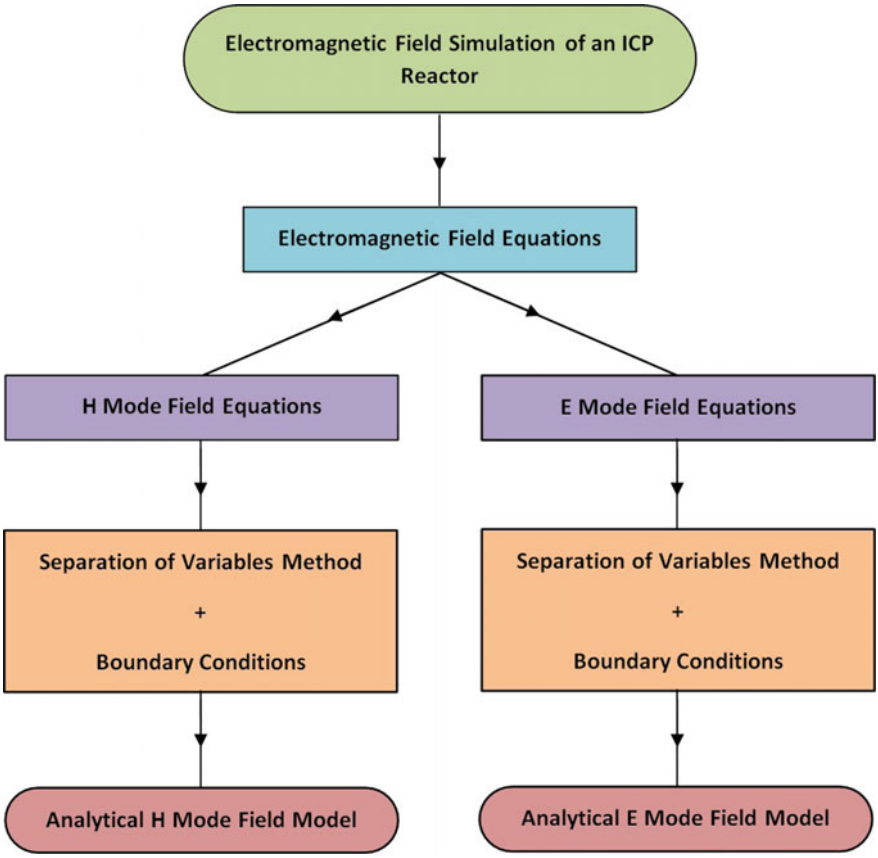

Fig. 10.12 Flowchart illustrating the gist of the H mode field model and E mode field model derivations, which will be detailed in the following sections

$$\nabla \times \mathcal{B}(r,\theta,z,t) = \mu_{\mathrm{o}}\left(\mathcal{J}(r,\theta,z,t) + \varepsilon_{\mathrm{o}}\frac{\partial \mathcal{E}(r,\theta,z,t)}{\partial t}\right), \tag{10.2.5.3}$$

and

$$\nabla \cdot \mathcal{B}(r,\theta,z,t) = 0, \tag{10.2.5.4}$$

with the following base assumptions:

(i) The reactor is azimuthally symmetric, that is, the fields only vary in the $-r$ and $-z$ directions.

(ii) The plasma consists mostly of low-energy electrons and immobile ions. Thus, this satisfies the local Ohm's Law criterion,

$$\mathcal{E}(r,\theta,z,t) = \frac{m_e}{n_e e^2}\left(\nu\mathcal{J}(r,\theta,z,t) + \frac{\partial\mathcal{J}(r,\theta,z,t)}{\partial t}\right), \tag{10.2.5.5}$$

where m_e is the electronic mass in kg, e is the electronic charge in C, n_e is the electron density in m^{-3}, and ν is the electron collision frequency in s^{-1}.

(iii) In free space, the charge density term, $\rho = 0$, thus, reducing Eq. (10.2.5.2) to,

$$\nabla \cdot \mathcal{E}(r,\theta,z,t) = 0. \tag{10.2.5.6}$$

(iv) The steady-state temporal term ($\sim t$) of the RF field is represented as a variation of frequency, that is, $\exp(j\omega t)$, where ω is the RF angular frequency (rad/s), given as, $\omega = 2\pi \times 13.56 \times 10^6$ rads^{-1}.

Here, $\mathcal{E}$, $\mathcal{B}$ and $\mathcal{J}$ are the time-varying electric field in Vm^{-1}, magnetic field in T and current density in Am^{-2}, respectively. μ_o is the free space permeability in Hm^{-1} and ε_o is the free space permittivity in Fm^{-1}.

These base assumptions allow for simplification of an otherwise complex set of solutions. Equations (10.2.5.1)–(10.2.5.5) are subsequently reduced to

$$\nabla\times\boldsymbol{E}(r,z) = -j\omega\boldsymbol{B}(r,z), \tag{10.2.5.7}$$

$$\nabla \cdot \boldsymbol{E}(r,z) = 0, \tag{10.2.5.8}$$

$$\nabla\times\boldsymbol{B}(r,z) = \mu_o\boldsymbol{J}(r,z) + j\varepsilon_o\mu_o\omega\boldsymbol{E}(r,z), \tag{10.2.5.9}$$

$$\nabla \cdot \boldsymbol{B}(r,z) = 0, \tag{10.2.5.10}$$

and

$$\boldsymbol{J}(r,z) = \frac{\varepsilon_o\omega_p^2}{\nu + j\omega}\boldsymbol{E}(r,z), \tag{10.2.5.11}$$

where ω_p is the plasma frequency in s^{-1} and is given by

$$\omega_p = \left(\frac{n_e e^2}{\varepsilon_o m_e}\right)^{1/2}. \tag{10.2.5.12}$$

The equation set (10.2.5.7)–(10.2.5.12) will be solved analytically in Sects. 10.2.5.2 and 10.2.5.3 using further case-specific assumptions and boundary conditions for H mode and E mode fields.

10.2.5.2 H Mode Field Equations

To derive the H mode fields from Eqs. (10.2.5.7) to (10.2.5.12) for the described reactor, further assumptions and boundary conditions are first required:

(a) The displacement current term in Eq. (10.2.5.9) is neglected (that is, $j\varepsilon_o\mu_o\omega \boldsymbol{E}(r, z) = 0$). This is due to the higher free excitation wavelength ($\sim$22 m for 13.56 MHz) as compared to the chamber dimensions. Equation (10.2.5.9) then reduces to

$$\nabla\times\boldsymbol{B}(r,z) = \mu_o\boldsymbol{J}(r,z). \tag{10.2.5.13}$$

(b) The planar coil is assumed to be an infinitesimally thin disc of moving uniform charge and has a surface current density of

$$K_\theta = \frac{NI_p}{a}, \tag{10.2.5.14}$$

where I_p is the peak coil current in A, N is the number of turns in the coil and a is the coil radius in m.

(c) The chamber (from boundaries $-b < r < b$ and $0 < z < L$) has a uniform electron density, n_e, collision frequency, v and electron temperature, T_e. Externally, these parameters are equal to zero.

(d) At the boundaries between the quartz plate and the plasma, the tangential electric fields and tangential and normal magnetic fields are continuous.

(e) At the boundaries between the chamber walls and the plasma, the tangential electric fields and normal magnetic fields are equal to zero.

Next, by taking the curl of Eq. (10.2.5.7) and by further substitutions of Eqs. (10.2.5.11) and (10.2.5.13), we arrive at the following key expressions

$$\nabla\times\boldsymbol{E}(r,z) = -j\omega\boldsymbol{B}(r,z) \tag{10.2.5.15}$$

and

$$\nabla\times\nabla\times\boldsymbol{E}(r,z) = -\left(\frac{\mu_o\varepsilon_o\omega_p^2}{1-jv/\omega}\right)\boldsymbol{E}(r,z). \tag{10.2.5.16}$$

The term $\mu_o\varepsilon_o\omega_p^2/(1-jv/\omega)$ in Eq. (10.2.5.16) is the quantified interaction between the electromagnetic fields and plasma and can be more conveniently expressed as the spatial conductivity parameter, α^2, given by

$$\alpha^2 = \frac{\mu_o n_e e^2}{m_e[1-jv/\omega]}. \tag{10.2.5.17}$$

α^2 is highly dependent on the electron collision frequency, ν and thus, calculation of this important parameter will be separately discussed in Sect. 10.2.5.4. With α^2 defined, Eq. (10.2.5.16) can be written as,

$$\nabla\times\nabla\times\boldsymbol{E}(r,z) = -\alpha^2\boldsymbol{E}(r,z). \tag{10.2.5.18}$$

With the assumption of azimuthal symmetry of the chamber, the solution to the H mode electromagnetic fields would only have the scalar azimuthal electric field, E_θ component, that is, $\boldsymbol{E}$ = [0, E_θ, 0] and the scalar radial magnetic field, B_r and axial magnetic field, B_z components, $\boldsymbol{B}$ = [B_r, 0, B_z] (Table 10.3). Lastly, in scalar form, Eqs. (10.2.5.15) and (10.2.5.16) can be rewritten as the field equations,

$$\frac{1}{r}\frac{\partial}{\partial r}\left(r\frac{\partial E_\theta}{\partial r}\right) - \frac{E_\theta}{r^2} + \frac{\partial^2 E_\theta}{\partial z^2} = \alpha^2 E_\theta, \tag{10.2.5.19}$$

$$B_\mathrm{r} = -\frac{j}{\omega}\frac{\partial E_\theta}{\partial z}, \tag{10.2.5.20}$$

and

$$B_\mathrm{z} = \frac{j}{\omega}\frac{1}{r}\left(\frac{\partial(rE_\theta)}{\partial r}\right). \tag{10.2.5.21}$$

for $0 \le z \le L + D$.

Equations (10.2.5.19)–(10.2.5.21) constitute the general field equations required to solve the H mode fields for an ICP reactor. This set of equations can be solved both anayltically and numerically as required in simulation.

Separation of Variables Method for the H Mode Field Model

For analytical solution of the field with Eqs. (10.2.5.19)–(10.2.5.21), the separation of variables method is used [65–67]. In this method, a multivariable function is split and solved separately as single variable functions. These single variable functions are linked together using an introduced expression known as a separation constant. For the present case, the multivariable azimuthal electric field, E_θ (r, z) is defined to be the product of two single variable functions, $R(r)$ and $Z(z)$, namely

$$E_\theta = Z(z)R(r). \tag{10.2.5.22}$$

The defined Eq. (10.2.5.22) is next substituted into Eq. (10.2.5.19) yielding,

$$\frac{1}{R(r)}\left(\frac{1}{r}\frac{\partial R(r)}{\partial r} + \frac{\partial^2 R(r)}{\partial r^2} - \frac{R(r)}{r^2} - \alpha^2 R(r)\right) + \frac{1}{Z(z)}\frac{\partial^2 Z(z)}{\partial z^2} = 0. \tag{10.2.5.23}$$

By introducing a separation constant, k^2, Eq. (10.2.5.23) is separated into two equations. They are written as

$$\frac{1}{R(r)}\left(\frac{1}{r}\frac{\partial R(r)}{\partial r}+\frac{\partial^2 R(r)}{\partial r^2}-\frac{R(r)}{r^2}-\alpha^2 R(r)\right)=-k^2 \tag{10.2.5.24}$$

and

$$\frac{1}{Z(z)}\frac{\partial^2 Z(z)}{\partial z^2}=k^2. \tag{10.2.5.25}$$

By rearranging Eqs. (10.2.5.24) and (10.2.5.25) to be representative of common closed-form solutions, we arrive at

$$r^2\frac{\partial^2 R(r)}{\partial r^2}+r\frac{\partial R(r)}{\partial r}+[\lambda^2 r^2-1]R(r)=0, \tag{10.2.5.26}$$

and

$$\frac{\partial^2 Z(z)}{\partial z^2}=k^2 Z(z). \tag{10.2.5.27}$$

Here, λ^2 and k^2 are separation constants and are related by

$$k^2=\lambda^2+\alpha^2. \tag{10.2.5.28}$$

Looking at the boundary conditions (b)–(e) in Sect. 10.2.5.2, we are able to deduce several important relations for the component fields:

(i) At the plane of the coil ($z = L + D$), the total radial magnetic field emitted by an infinitesimally thin disc of surface current density, K_θ is given by,

$$B_{\mathrm{r}}(r,L+D)_{-}-B_{\mathrm{r}}(r,L+D)_{+}=\mu_{\mathrm{o}}K_{\theta}, \tag{10.2.5.29}$$

where $B_r(r, L + D)_-$ and $B_r(r, L + D)_+$ are the radial magnetic field emissions below and above the plane of the coil. Taking the point that $B_r(r, L + D)_- = -B_r(r, L + D)_+$, the radial magnetic field traversing into the plasma at the coil plane can be deduced as,

$$B_{\mathrm{r}}=\begin{cases}-\frac{\mu_{\mathrm{o}}K_{\theta}}{2} & 0\le r\le a\\ 0 & a<r\le b\end{cases} \tag{10.2.5.30}$$

or in relation to Eq. (10.2.5.20)

$$\left.\frac{\partial E_\theta}{\partial z}\right|_{z=L+D} = \begin{cases} -\frac{j\omega\mu_o K_\theta}{2} & 0 \le r \le a \\ 0 & 0 < r \le b \end{cases}. \tag{10.2.5.31}$$

Here, a is the radius of the coil and b is the radius of the chamber.

(ii) The tangential electric field and tangential and normal magnetic field components between the quartz plate and plasma would be continuous; giving the following relations:

$$E_\theta(r, L_+) = E_\theta(r, L_-), \tag{10.2.5.32}$$

$$B_r(r, L_+) = B_r(r, L_-), \tag{10.2.5.33}$$

and

$$B_z(r, L_+) = B_z(r, L_-). \tag{10.2.5.34}$$

In terms of the azimuthal electric field, Eqs. (10.2.5.33) and (10.2.5.34) are written, respectively as,

$$\left.\frac{\partial E_\theta}{\partial z}\right|_{z=L_+} = \left.\frac{\partial E_\theta}{\partial z}\right|_{z=L_-} \tag{10.2.5.35}$$

and

$$\left.\frac{1}{r}\frac{\partial r E_\theta}{\partial r}\right|_{z=L_+} = \left.\frac{1}{r}\frac{\partial r E_\theta}{\partial r}\right|_{z=L_-}. \tag{10.2.5.36}$$

(iii) The tangential electric field and normal magnetic field components at the chamber walls are zero, yielding,

$$E_\theta(b, z) = 0, \tag{10.2.5.37}$$

$$B_r(b, z) = 0, \tag{10.2.5.38}$$

$$E_\theta(r, 0) = 0, \tag{10.2.5.39}$$

and

$$B_z(r, 0) = 0. \tag{10.2.5.40}$$

(iv) The spatial conductivity parameter $\alpha^2 = 0$ for $L < z < L + D$.

From the deduced field boundaries (i)–(iv), the general solutions for Eqs. (10.2.5.22), (10.2.5.26), and (10.2.5.27) are determined as

$$R(r) = A_1 J_1(\lambda r), \tag{10.2.5.41}$$

$$Z(z) = B_1 \sinh(kz), \tag{10.2.5.42}$$

and

$$E_\theta = A \sinh(kz) J_1(\lambda r), \tag{10.2.5.43}$$

for $0 \le z \le L$, and

$$R(r) = A_2 J_1(\lambda r), \tag{10.2.5.44}$$

$$Z(z) = B_2 \exp(-\lambda z) + C_2 \exp(\lambda z), \tag{10.2.5.45}$$

and

$$E_\theta = [B \exp(-\lambda z) + C \exp(\lambda z)] J_1(\lambda r), \tag{10.2.5.46}$$

for $L < z \le L + D$.

A, B, and C in Eqs. (10.2.5.43) and (10.2.5.46) are boundary constants to be defined and $A = A_1 B_1$, $B = A_2 B_2$, and $C = A_2 C_2$. To obtain the radial magnetic field, B_r and axial magnetic field, B_z [as per Eqs. (10.2.5.20) and (10.2.5.21)], Eqs. (10.2.5.43) and (10.2.5.46) are differentiated, that is,

$$B_r(r,z) = \begin{cases} -\frac{j}{\omega} Ak \cosh(kz) J_1(\lambda r) & 0 \le z \le L \\ -\frac{j}{\omega} [C \exp(\lambda z) - B \exp(-\lambda z)] \lambda J_1(\lambda r) & L < z \le L + D \end{cases} \tag{10.2.5.47}$$

$$B_z(r,z) = \begin{cases} \frac{j}{\omega} A\lambda \sinh(kz) J_0(\lambda r) & 0 \le z \le L \\ \frac{j}{\omega} [B \exp(-\lambda z) + C \exp(\lambda z)] \lambda J_0(\lambda r) & L < z \le L + D \end{cases} \tag{10.2.5.48}$$

It is noted that in Eq. (10.2.5.37), $E_\theta(b,z) = 0$ at the radial boundaries of the chamber. Thus, in obtaining a valid solution for the value of λ, the Bessel function nth root, μ_n (which forms a set of eigenvalues) has to be a multiple of the chamber radius, b, that is,

$$\lambda_n b = \mu_n \tag{10.2.5.49}$$

or

$$\lambda_n = \frac{\mu_n}{b}. \tag{10.2.5.50}$$

Consequently, we get k_n as

$$k_n = \sqrt{\lambda_n^2 + \alpha^2}. \tag{10.2.5.51}$$

The form of the differential Eqs. (10.2.5.26) and (10.2.5.27) is generally the form of the Sturm–Liouville problem in which the solution constitutes the sum of a set of orthogonal eigenfunctions [68, 69]. Hence, the full solution for the analytical H mode fields can be appropriately written as the eigenfunction series

$$E_\theta(r,z) = \begin{cases} \sum_{n=1}^{\infty} A_n \sinh(k_n z) J_1(\lambda_n r) & 0 \le z \le L \\ \sum_{n=1}^{\infty} [B_n \exp(-\lambda_n z) + C_n \exp(\lambda_n z)] J_1(\lambda_n r) & L < z \le L + D \end{cases} \tag{10.2.5.52}$$

$$B_r(r,z) = \begin{cases} -\frac{j}{\omega} \sum_{n=1}^{\infty} A_n k_n \cosh(k_n z) J_1(\lambda_n r) & 0 \le z \le L \\ -\frac{j}{\omega} \sum_{n=1}^{\infty} [C_n \exp(\lambda_n z) - B_n \exp(-\lambda_n z)] \lambda_n J_1(\lambda_n r) & L < z \le L + D \end{cases} \tag{10.2.5.53}$$

$$B_z(r,z) = \begin{cases} \frac{j}{\omega} \sum_{n=1}^{\infty} A_n \lambda_n \sinh(k_n z) J_0(\lambda_n r) & 0 \le z \le L \\ \frac{j}{\omega} \sum_{n=1}^{\infty} [B_n \exp(-\lambda_n z) + C_n \exp(\lambda_n z)] \lambda_n J_0(\lambda_n r) & L < z \le L + D \end{cases} \tag{10.2.5.54}$$

Solving the Boundary Constants for H Mode Field Model

The next step is to derive closed-form expressions for the boundary constants A_n, B_n, and C_n. Using the boundary conditions at the coil-chamber boundary, L, as given by Eqs. (10.2.5.32) and (10.2.5.33), we are able to obtain the following simultaneous equations for derivation:

$$A_n \sinh(k_n L) = B_n \exp(-\lambda_n L) + C_n \exp(\lambda_n L), \tag{10.2.5.55}$$

and

$$A_n k_n \cosh(k_n L) = -\lambda_n [B_n \exp(-\lambda_n L) - C_n \exp(\lambda_n L)]. \tag{10.2.5.56}$$

For a more convenient solution, it would be apt to define an additional constant,

$$v_n = C_n \exp(\lambda_n(L+D)) - B_n \exp(-\lambda_n(L+D)). \tag{10.2.5.57}$$

From simultaneous solving of Eqs. (10.2.5.55), (10.2.5.56) and (10.2.5.57) for A_n, B_n and C_n, we finally get

$$A_n = \frac{v_n \lambda_n}{\lambda_n \sinh(\lambda_n D)\sinh(k_n L) + k_n \cosh(\lambda_n D)\cosh(k_n L)}, \tag{10.2.5.58}$$

$$B_n = \frac{A_n}{2\lambda_n} e^{\lambda_n L}[\lambda_n \sinh(k_n L) - k_n \cosh(k_n L)], \tag{10.2.5.59}$$

$$C_n = \frac{A_n}{2\lambda_n} e^{-\lambda_n L}[\lambda_n \sinh(k_n L) + k_n \cosh(k_n L)]. \tag{10.2.5.60}$$

To complete the solution set for the H mode fields, an independent expression for the constant v_n is required. By replacing the field boundary condition at $(L + D)$ given in Eq. (10.2.5.31) and the constant v_n defined in Eq. (10.2.5.57) into Eq. (10.2.5.53), we get the piecewise continuous relationship,

$$\sum_{n=1}^{\infty} v_n \lambda_n J_1(\lambda_n r) = \begin{cases} -\frac{j\omega\mu_o K_\theta}{2} & 0 \le r \le a \\ 0 & a < r \le b \end{cases} \tag{10.2.5.61}$$

Multiplying both sides of Eq. (10.2.5.61) with the eigenfunction $rJ_1(\lambda_n r)$ and by integration across the chamber radius, $0 \le r \le b$; due to orthogonality of the Sturm–Liouville problem, we would subsequently get the equation

$$v_n \lambda_n \int_0^b r J_1^2(\lambda_n r)\mathrm{d}r = -\frac{j\omega\mu_o K_\theta}{2} \int_0^a r J_1(\lambda_n r)\mathrm{d}r, \tag{10.2.5.62}$$

and thus, the solution for v_n is,

$$v_n = -\frac{j\omega\mu_o K_\theta}{2} \frac{\int_0^a r J_1(\lambda_n r)\mathrm{d}r}{\lambda_n \int_0^b r J_1^2(\lambda_n r)\mathrm{d}r}. \tag{10.2.5.63}$$

Using the Bessel function identity for orthogonality [65] in Eq. (10.2.5.63), that is,

$$\int_0^b r J_p(\lambda_n r) J_p(\lambda_n r)\mathrm{d}r = \frac{b^2}{2} J_{p+1}^2(\lambda_n b) = \frac{b^2}{2} J_{p-1}^2(\lambda_n b) = \frac{b^2}{2} J_p'^2(\lambda_n b), \tag{10.2.5.64}$$

in which, p is the Bessel function order; v_n is then simplified to

$$v_n = -j\omega\mu_o K_\theta \frac{\int_0^a rJ_1(\lambda_n r)\mathrm{d}r}{\lambda_n b^2 J_1'^2(\lambda_n b)}. \tag{10.2.5.65}$$

The analytical solutions and corresponding derived constants for the H mode fields for the case of an ICP reactor of height, L and radius, b with the coil radius, a and the coil-chamber distance, D can be summarized as the following equation set:

$$E_\theta(r,z) = \begin{cases} \sum_{n=1}^{\infty} A_n \sinh(k_n z) J_1(\lambda_n r) & 0 \le z \le L \\ \sum_{n=1}^{\infty} [B_n \exp(-\lambda_n z) + C_n \exp(\lambda_n z)] J_1(\lambda_n r) & L < z \le L + D \end{cases} \tag{10.2.5.66a}$$

$$B_r(r,z) = \begin{cases} -\frac{j}{\omega} \sum_{n=1}^{\infty} A_n k_n \cosh(k_n z) J_1(\lambda_n r) & 0 \le z \le L \\ -\frac{j}{\omega} \sum_{n=1}^{\infty} [C_n \exp(\lambda_n z) - B_n \exp(-\lambda_n z)] \lambda_n J_1(\lambda_n r) & L < z \le L + D \end{cases} \tag{10.2.5.66b}$$

$$B_z(r,z) = \begin{cases} \frac{j}{\omega} \sum_{n=1}^{\infty} A_n \lambda_n \sinh(k_n z) J_0(\lambda_n r) & 0 \le z \le L \\ \frac{j}{\omega} \sum_{n=1}^{\infty} [B_n \exp(-\lambda_n z) - C_n \exp(\lambda_n z)] \lambda_n J_0(\lambda_n r) & L < z \le L + D \end{cases} \tag{10.2.5.66c}$$

$$k_n = \sqrt{\lambda_n^2 + \alpha^2} \tag{10.2.5.66d}$$

$$\lambda_n = \frac{\mu_n}{b} \tag{10.2.5.66e}$$

$$v_n = -j\omega\mu_o K_\theta \frac{\int_0^a rJ_1(\lambda_n r)\mathrm{d}r}{\lambda_n b^2 J_1'^2(\lambda_n b)} \tag{10.2.5.66f}$$

$$A_n = \frac{v_n \lambda_n}{\lambda_n \sinh(\lambda_n D)\sinh(k_n L) + k_n \cosh(\lambda_n D)\cosh(k_n L)} \tag{10.2.5.66g}$$

$$B_n = \frac{A_n}{2\lambda_n} \exp(\lambda_n L)[\lambda_n \sinh(k_n L) - k_n \cosh(k_n L)] \tag{10.2.5.66h}$$

$$C_n = \frac{A_n}{2\lambda_n}\exp(-\lambda_n L)[\lambda_n \sinh(k_n L) + k_n \cosh(k_n L)] \tag{10.2.5.66i}$$

This equation set will be used to simulate the H mode fields in Sect. 10.2.5.5.

10.2.5.3 E Mode Field Equations

For deriving the analytical E mode fields, a similar set of assumptions and boundary conditions as the H mode fields are first applied to Eqs. (10.2.5.7)–(10.2.5.12):

(a) The coil (at $-a \leq r \leq a$) is assumed to be an infinitely thin disc with a uniform radial electric field, E_o of magnitude,

$$E_o = \frac{V_p}{a}. \tag{10.2.5.67}$$

where V_p is the peak coil voltage in V given by, $V_p = I_p \omega L_o$. L_o is the source coil inductance in H.

(b) The chamber is an azimuthally symmetric cylinder of radius, b and effective height, L with a coil radius of a. The coil-chamber spacing is D.

(c) The chamber (from boundaries $-b < r < b$ and $0 < z < L$) has a uniform electron density, n_e, collision frequency, ν and electron temperature, T_e. Externally, these parameters are equal to zero.

(d) At the boundaries between the chamber walls and the plasma, the normal magnetic fields and tangential electric fields are equal to zero.

(e) At the boundaries between the quartz plate and the plasma, the normal magnetic fields and tangential electric fields are continuous.

Due to the assumption of azimuthal symmetry for the chamber, the solutions for the E mode fields would be limited to the radial and axial electric field components, that is, $\boldsymbol{E} = [E_r, 0, E_z]$ and azimuthal magnetic field component, that is, $\boldsymbol{B} = [0, B_\theta, 0]$ (Table 10.3). The displacement current term, $j\varepsilon_o\mu_o\omega\boldsymbol{E}(r, z)$ in Eq. (10.2.5.9) for the E mode fields, however, is not ignored due to the presence of a time-varying electric field through the dielectric plate.

Next, by substitution of Eq. (10.2.5.11) into Eq. (10.2.5.9), we get,

$$\nabla \times \boldsymbol{B}(r,z) = \frac{j\omega}{c^2}\left(1 - \frac{\left(\omega_p^2/\omega^2\right)}{1 - j\nu/\omega}\right)\boldsymbol{E}(r,z), \tag{10.2.5.68}$$

in which the term $1 - \left(\omega_p^2/\omega^2\right)/(1 - j\nu/\omega)$ represents the permittivity of the plasma medium, ε_p. Equation (10.2.5.68) can be thus simplified as,

$$\nabla \times \boldsymbol{B}(r,z) = \frac{j\omega}{c^2}\varepsilon_{\mathrm{p}}\boldsymbol{E}(r,z) \tag{10.2.5.69}$$

where $c\left(=\sqrt{1/\mu_{\mathrm{o}}\varepsilon_{\mathrm{o}}}\right)$ is the speed of light in ms^{-1}.

For the E mode fields inside the dielectric quartz plate ($L < z \leq L + D$) the plasma permittivity term, ε_{p} in Eq. (10.2.5.69) is replaced by the dielectric constant, ε_{r}. This yields a field equation set for two boundaries, that is,

$$\nabla \times \boldsymbol{B}(r,z) = \begin{cases} \frac{j\omega}{c^2}\varepsilon_{\mathrm{p}}\boldsymbol{E}(r,z) & 0 \leq z \leq L \\ \frac{j\omega}{c^2}\varepsilon_{\mathrm{r}}\boldsymbol{E}(r,z) & L < z \leq L+D \end{cases} \tag{10.2.5.70}$$

For the quartz plate used in the laboratory reactor, the dielectric constant, $\varepsilon_{\mathrm{r}} = 3.8$. Then, by taking the curl of the equation set (10.2.5.70) and substituting the field Eq. (10.2.5.7), we obtain the simplified single-term magnetic field expressions

$$\nabla \times \nabla \times \boldsymbol{B}(r,z) = \begin{cases} \varepsilon_{\mathrm{p}}\frac{\omega^2}{c^2}\boldsymbol{B}(r,z) & 0 \leq z \leq L \\ \varepsilon_{\mathrm{r}}\frac{\omega^2}{c^2}\boldsymbol{B}(r,z) & L < z \leq L+D \end{cases} \tag{10.2.5.71}$$

Lastly by solving Eqs. (10.2.5.70) and (10.2.5.71) for only the electromagnetic field components and taking into account the assumption of azimuthal symmetry [boundary condition (b)], we arrive at the following set of scalar equations:

$$\frac{1}{r}\frac{\partial}{\partial r}\left(r\frac{\partial B_\theta}{\partial r}\right) - \frac{B_\theta}{r^2} + \frac{\partial^2 B_\theta}{\partial z^2} = -\varepsilon_{\mathrm{p}}\left(\frac{\omega}{c}\right)^2 B_\theta, \tag{10.2.5.72}$$

$$E_{\mathrm{r}} = \frac{jc^2}{\omega\varepsilon_{\mathrm{p}}}\frac{\partial B_\theta}{\partial z}, \tag{10.2.5.73}$$

and

$$E_{\mathrm{z}} = -\frac{jc^2}{\omega\varepsilon_{\mathrm{p}}}\frac{1}{r}\left(\frac{\partial(rB_\theta)}{\partial r}\right). \tag{10.2.5.74}$$

for $0 \leq z \leq L$;

$$\frac{1}{r}\frac{\partial}{\partial r}\left(r\frac{\partial B_\theta}{\partial r}\right) - \frac{B_\theta}{r^2} + \frac{\partial^2 B_\theta}{\partial z^2} = -\varepsilon_{\mathrm{r}}\left(\frac{\omega}{c}\right)^2 B_\theta, \tag{10.2.5.75}$$

$$E_{\mathrm{r}} = \frac{jc^2}{\omega\varepsilon_{\mathrm{r}}}\frac{\partial B_\theta}{\partial z}, \tag{10.2.5.76}$$

and

$$E_z = -\frac{jc^2}{\omega\varepsilon_r}\frac{1}{r}\left(\frac{\partial(rB_\theta)}{\partial r}\right). \tag{10.2.5.77}$$

for $L < z \leq L + D$.

Equations (10.2.5.72)–(10.2.5.77) give the general field equations required to solve the E mode fields for an ICP reactor. Both analytical and numerical solutions can be obtained by this set of equations.

Separation of Variables Method for the E Mode Field Model

As with the H mode fields in Sect. 10.2.5.2, the separation of variables method is used to solve field Eqs. (10.2.5.72)–(10.2.5.77). The boundary conditions (a)–(e) in Sect. 10.2.5.3 would yield the following relations for the component E mode fields:

(i) At the plane of the coil ($z = L + D$), the radial electric field is given by,

$$E_r = \begin{cases} E_o = \frac{V_p}{a} & 0 \leq r \leq a \\ 0 & a < r \leq b \end{cases} \tag{10.2.5.78}$$

(ii) The tangential electric field and normal magnetic field between the quartz plate and plasma would be continuous, thus,

$$E_r(r, L_+) = E_r(r, L_-), \tag{10.2.5.79}$$

(iii) At the chamber boundaries, applying boundary condition (d), we get,

$$E_z(b, z) = 0, \tag{10.2.5.80}$$

and

$$E_r(r, 0) = 0. \tag{10.2.5.81}$$

For the axial electric field at the boundary between the plasma and the dielectric plate, E_z (r, L), an additional relationship,

$$\varepsilon_p E_z(r, L_+) = \varepsilon_r E_z(r, L_-), \tag{10.2.5.82}$$

is introduced. The electric fields $E_z(r, L_+)$ and $E_z(r, L_-)$ given in Eq. (10.2.5.82) are discontinuous. This accounts for the abrupt change between media (plasma–dielectric plate) of the traversing electric fields. Solving for the E mode fields with the same steps shown in Sect. 10.2.5.2, we get,

$$B_\theta(r,z) = \begin{cases} D\cosh(qz)J_1(\lambda r) & 0 \le z \le L \\ [E\exp(sz) + F\exp(-sz)]J_1(\lambda r) & L < z \le L+D \end{cases} \tag{10.2.5.83}$$

$$E_r(r,z) = \begin{cases} \frac{jc^2}{\omega\varepsilon_p} qD\sinh(qz)J_1(\lambda r) & 0 \le z \le L \\ \frac{jc^2}{\omega\varepsilon_r} s[E\exp(sz) + F\exp(-sz)]J_1(\lambda r) & L < z \le L+D \end{cases} \tag{10.2.5.84}$$

and

$$E_r(r,z) = \begin{cases} \frac{-jc^2}{\omega\varepsilon_p} \lambda D\cosh(qz)J_0(\lambda r) & 0 \le z \le L \\ \frac{-jc^2}{\omega\varepsilon_r} \lambda[E\exp(sz) + F\exp(-sz)]J_0(\lambda r) & L < z \le L+D \end{cases} \tag{10.2.5.85}$$

Here, λ, q and s are the separation constants related by,

$$q^2 = \lambda^2 - \varepsilon_p\left(\frac{\omega}{c}\right)^2, \tag{10.2.5.86}$$

and

$$s^2 = \lambda^2 - \varepsilon_r\left(\frac{\omega}{c}\right)^2 \tag{10.2.5.87}$$

D, E and F are constants to be defined.

Applying the boundary condition for the radial walls of the chamber [Eq. (10.2.5.80)] to Eqs. (10.2.5.83)–(10.2.5.87), a valid solution can only be obtained if $J_0(\lambda b) = 0$. Thus, it can be deduced that the separation constant, λ would be a solution set consisting of the ratios of the eigen Bessel function roots, μ_n and the chamber radius, that is,

$$\lambda_n = \frac{\mu_n}{b}. \tag{10.2.5.88}$$

Rewriting Eqs. (10.2.5.83)–(10.2.5.85) as a sum of the set of orthogonal eigenfunctions with the deduction given in Eq. (10.2.5.88), we subsequently get,

$$B_\theta(r,z) = \begin{cases} \sum_{n=1}^{\infty} D_n\cosh(q_n z)J_1(\lambda_n r) & 0 \le z \le L \\ \sum_{n=1}^{\infty} [E_n\exp(s_n z) + F_n\exp(-s_n z)]J_1(\lambda_n r) & L < z \le L+D \end{cases} \tag{10.2.5.89}$$

$$E_{\mathrm{r}}(r,z)=\begin{cases}\frac{jc^2}{\omega\varepsilon_{\mathrm{p}}}\sum_{n=1}^{\infty}q_nD_n\ \sinh(q_nz)J_1(\lambda_nr) & 0\le z\le L\\ \frac{jc^2}{\omega\varepsilon_{\mathrm{r}}}\sum_{n=1}^{\infty}s_n[E_n\exp(s_nz)-\ F_n\exp(-s_nz)]J_1(\lambda_nr) & L\ <z\le L+D\end{cases} \tag{10.2.5.90}$$

and

$$E_{\mathrm{z}}(r,z)=\begin{cases}\frac{-jc^2}{\omega\varepsilon_{\mathrm{p}}}\sum_{n=1}^{\infty}\lambda_nD_n\ \cosh(q_nz)J_0(\lambda_nr) & 0\le z\le L\\ \frac{-jc^2}{\omega\varepsilon_{\mathrm{r}}}\sum_{n=1}^{\infty}\lambda_n[E_n\exp(s_nz)+\ F_n\exp(-s_nz)]J_0(\lambda_nr) & L\ <z\le L+D\end{cases} \tag{10.2.5.91}$$

with,

$$q_n^2=\lambda_n^2-\varepsilon_{\mathrm{p}}\left(\frac{\omega}{c}\right)^2 \tag{10.2.5.92}$$

and

$$s_n^2=\lambda_n^2-\varepsilon_{\mathrm{r}}\left(\frac{\omega}{c}\right)^2. \tag{10.2.5.93}$$

Solving the Boundary Constants for E Mode Field Model

By taking the field relationships given in Eqs. (10.2.5.79) and (10.2.5.82), the expressions for the solution of boundary constants D_n, $E_{n,}$ and F_n are determined as

$$D_n\cosh(q_nL)=E_n\exp(s_nL)+F_n\exp(-s_nL) \tag{10.2.5.94}$$

and

$$\varepsilon_{\mathrm{r}}q_nD_n\sinh(q_nL)=\varepsilon_{\mathrm{p}}s_n[E_n\exp(s_nL)-F_n\exp(-s_nL)]. \tag{10.2.5.95}$$

For the convenience of solving D_n, $E_{n,}$ and F_n using simultaneous equations, an additional constant, u_{n} is introduced:

$$u_n=E_n\exp(s_n(L+D))-F_n\exp(-s_n(L+D)). \tag{10.2.5.96}$$

With subsequent replacement in Eqs. (10.2.5.94) and (10.2.5.95), the following solutions are met:

$$D_n = \frac{u_n \varepsilon_p s_n}{\varepsilon_p s_n \cosh(q_n L)\sinh(s_n D) + \varepsilon_r q_n \sinh(q_n L)\cosh(s_n D)}, \tag{10.2.5.97}$$

$$E_n = \frac{D_n}{2\varepsilon_p s_n}\exp(-s_n L)\left[\varepsilon_p s_n \cosh(q_n L) + \varepsilon_r q_n \sinh(q_n L)\right], \tag{10.2.5.98}$$

and

$$F_n = \frac{D_n}{2\varepsilon_p s_n}\exp(s_n L)[\varepsilon_p s_n \cosh(q_n L) - \varepsilon_r q_n \sinh(q_n L)], \tag{10.2.5.99}$$

At the plane of the coil ($L + D$), the radial electric field, $E_r(r, L + D)$ can be expressed in terms of u_n as

$$E_r(r, L+D) = \frac{jc^2}{\omega\varepsilon_r}\sum_{n=1}^{\infty} s_n u_n J_1(\lambda_n r). \tag{10.2.5.100}$$

Applying the boundary conditions given by the piecewise continuous Eq. (10.2.5.78) from the chamber center to the coil radius, a and chamber radius, b, to Eq. (10.2.5.100), we get,

$$\frac{jc^2}{\omega\varepsilon_r}\sum_{n=1}^{\infty} s_n u_n J_1(\lambda_n r) = \begin{cases} E_o & 0 \le r \le a \\ 0 & a < r \le b \end{cases}. \tag{10.2.5.101}$$

To obtain a calculable expression for u_n, Eq. (10.2.5.101) is first multiplied with r and differentiated. This yields the following equation

$$\frac{jc^2}{\omega\varepsilon_r}\sum_{n=1}^{\infty} s_n u_n \lambda_n r J_0(\lambda_n r) = \begin{cases} E_o & 0 \le r \le a \\ 0 & a < r \le b \end{cases}. \tag{10.2.5.102}$$

Next, by multiplying both sides of the equation with $J_0(\lambda_n r)$ and integrating across the chamber radius $0 \le r \le b$ (with the orthogonal properties Sturm–Liouville problem), we eventually get,

$$\frac{jc^2 s_n u_n \lambda_n}{\omega\varepsilon_r}\int_0^b r J_0^2(\lambda_n r)\mathrm{d}r = E_o \int_0^a J_0(\lambda_n r)\mathrm{d}r, \tag{10.2.5.103}$$

which can be rewritten as,

$$u_n = -\frac{j\omega\varepsilon_r E_o}{c^2 s_n \lambda_n}\frac{\int_0^a J_0(\lambda_n r)\mathrm{d}r}{\int_0^b r J_0^2(\lambda_n r)\mathrm{d}r}. \tag{10.2.5.104}$$

Equation (10.2.5.104) can be further simplified with the Bessel function identity given in Eq. (10.2.5.64), yielding,

$$u_n = -\frac{2j\omega\varepsilon_r E_o}{b^2 c^2 s_n \lambda_n} \frac{\int_0^a J_0(\lambda_n r)\mathrm{d}r}{J_1^2(\lambda_n b)}. \tag{10.2.5.105}$$

The analytical solutions and corresponding derived constants for the E mode fields for the ICP chamber (height, L; radius, b; coil radius, a and the coil-chamber distance, D) can be summarized as the following equation set:

$$B_\theta(r,z) = \begin{cases} \sum_{n=1}^{\infty} D_n \cosh(q_n z) J_1(\lambda_n r) & 0 \le z \le L \\ \sum_{n=1}^{\infty} [E_n \exp(s_n z) + F_n \exp(-s_n z)] J_1(\lambda_n r) & L < z \le L + D \end{cases} \tag{10.2.5.106a}$$

$$E_r(r,z) = \begin{cases} \frac{jc^2}{\omega\varepsilon_p} \sum_{n=1}^{\infty} D_n q_n \sinh(q_n z) J_1(\lambda_n r) & 0 \le z \le L \\ \frac{jc^2}{\omega\varepsilon_r} \sum_{n=1}^{\infty} [E_n \exp(s_n z) - F_n \exp(-s_n z)] s_n J_1(\lambda_n r) & L < z \le L + D \end{cases} \tag{10.2.5.106b}$$

$$E_z(r,z) = \begin{cases} -\frac{jc^2}{\omega\varepsilon_p} \sum_{n=1}^{\infty} D_n \lambda_n \cosh(q_n z) J_0(\lambda_n r) & 0 \le z \le L \\ -\frac{jc^2}{\omega\varepsilon_r} \sum_{n=1}^{\infty} [E_n \exp(s_n z) + F_n \exp(-s_n z)] \lambda_n J_0(\lambda_n r) & L < z \le L + D \end{cases} \tag{10.2.5.106c}$$

$$q_n^2 = \lambda_n^2 - \varepsilon_p \left(\frac{\omega}{c}\right)^2 \tag{10.2.5.106d}$$

$$s_n^2 = \lambda_n^2 - \varepsilon_r \left(\frac{\omega}{c}\right)^2 \tag{10.2.5.106e}$$

$$\lambda_n = \frac{\mu_n}{b} \tag{10.2.5.106f}$$

$$u_n = -\frac{2j\omega\varepsilon_r E_o}{b^2 c^2 s_n \lambda_n} \frac{\int_0^a J_0(\lambda_n r)\mathrm{d}r}{J_1^2(\lambda_n b)} \tag{10.2.5.106g}$$

$$D_n = \frac{u_n \varepsilon_p s_n}{\varepsilon_p s_n \cosh(q_n L) \sinh(s_n D) + \varepsilon_r q_n \sinh(q_n L) \cosh(s_n D)} \tag{10.2.5.106h}$$

$$E_n = \frac{D_n}{2\varepsilon_p s_n}\exp(-s_n L)[\varepsilon_p s_n \cosh(q_n L) + \varepsilon_r q_n \sinh(q_n L)] \quad (10.2.5.106i)$$

$$F_n = \frac{D_n}{2\varepsilon_p s_n}\exp(s_n L)[\varepsilon_p s_n \cosh(q_n L) - \varepsilon_r q_n \sinh(q_n L)] \quad (10.2.5.106j)$$

This equation set will be used to simulate the E mode fields in Sect. 10.2.5.5.

10.2.5.4 Calculation of Electron Collision Frequency, *v*

The electron collision frequency, v, denotes the rate of collision between electrons and other plasma particles. Since low-temperature plasmas are predominantly due to ionization and excitation of electrons, v becomes an important plasma parameter in determining the extent of interaction between an ICP and the source fields. v ideally, includes all particle collisions occurring in the plasma. However, for simulation, the effects of the three largest collision frequencies are used to estimate v, that is, the electron-neutral collision frequency, v_{en}, electron–ion collision frequency, v_{ei}, and stochastic collision frequency, v_{st} [40, 70]. v, thus, is expressed as,

$$v = v_{en} + v_{ei} + v_{st}. \quad (10.2.5.107)$$

The electron-neutral collision frequency, v_{en} is obtained from the electron momentum transfer collision frequency and electron energy density function (EEDF) [71, 40], that is,

$$v_{en} + j\omega_{eff} = -\frac{3}{2}\left[\int_0^\infty \frac{\varepsilon^{3/2}}{v_c(\varepsilon) + j\omega}\frac{df(\varepsilon)}{d\varepsilon}d\varepsilon\right]^{-1}, \quad (10.2.5.108)$$

with ε being the electron energy in J, ω_{eff} being the effective drive frequency in rads^{-1}, $v_c(\varepsilon)$ is the differential collision frequency term for electron momentum transfer and $f(\varepsilon)$ is the EEDF. For simplicity, a Maxwellian EEDF can be used and is defined as

$$f(\varepsilon) = \frac{2}{\sqrt{\pi}}\frac{1}{(eT_e)^{3/2}}\exp\left[-\frac{\varepsilon}{T_e}\right] \quad (10.2.5.109)$$

where T_e is the electron temperature in eV. The collision frequency term,$v_c(\varepsilon)$ is given by

$$v_c(\varepsilon) = n_g \sigma_c(\varepsilon)\sqrt{\frac{2e\varepsilon}{m_e}} \quad (10.2.5.110)$$

Here, $\sigma_c(\varepsilon)$ is the collision cross section for the momentum transfer in m^2 (for argon gas, $\sigma_c(\varepsilon)$ is obtainable from Hayashi [72]); the neutral gas density, n_g is given by Eq. (10.2.4.26).

The electron–ion collision frequency, ν_{ei} is calculated using the Coulomb logarithm, ln Λ [73] and is expressed as [40],

$$\nu_{ei} = \frac{n_e e^4 \ln \Lambda}{4\pi\varepsilon_o^2 m_e^{1/2} (eT_e)^{3/2}}, \tag{10.2.5.111}$$

Since the RF field in an ICP reactor is spatially inhomogeneous, an interaction known as the anomalous skin effect may cause changes to electron velocities and trajectories; much like collisions with particles. The contribution of this effect (which is a significant at lower gas pressures) is represented by the stochastic collision frequency, ν_{st}. ν_{st} is derived from the average thermal velocity of the electrons and the anomalous skin depth of the RF fields and is expressed as [38],

$$\nu_{st} \approx \frac{1}{4}\frac{\bar{v}_e}{\delta}, \tag{10.2.5.112}$$

$\bar{v}_e$ denotes the average electron velocity, which in the Maxwellian case is,

$$\bar{v}_e = \left(\frac{8eT_e}{\pi m_e}\right)^{1/2}, \tag{10.2.5.113}$$

in ms^{-1}. δ_a is the anomalous skin depth approximated by,

$$\delta_a = \left(\frac{c}{\omega_p}\right)\left(\frac{\bar{v}_e \omega_p}{2c\omega}\right)^{1/3}, \tag{10.2.5.114}$$

with ω_p being the plasma angular frequency given in Eq. (10.2.5.12) calculated with the n_e.

10.2.5.5 Electromagnetic Field Characteristics in RF Planar ICPs

The H mode magnetic field and E mode electric field flux generated by the source coil at peak current ($\omega t = 0$) for different gas pressures can be visualized by streamline plots[1] as shown in Fig. 10.13. These plots use the following time-varying field equations:

(a) H mode:

$$B_r(r, z, t) = |B_r(r, z)| \cos(\omega t + \phi_{B_r}) \tag{10.2.5.115a}$$

[1]Plotted with MATLAB "streamslice" function.

(a) H Mode Fields

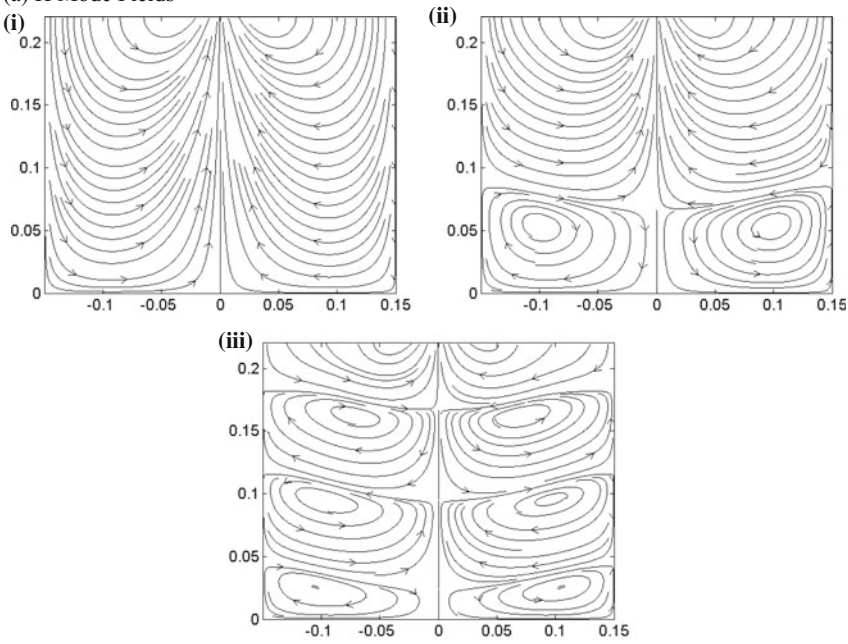

(b) E Mode Fields

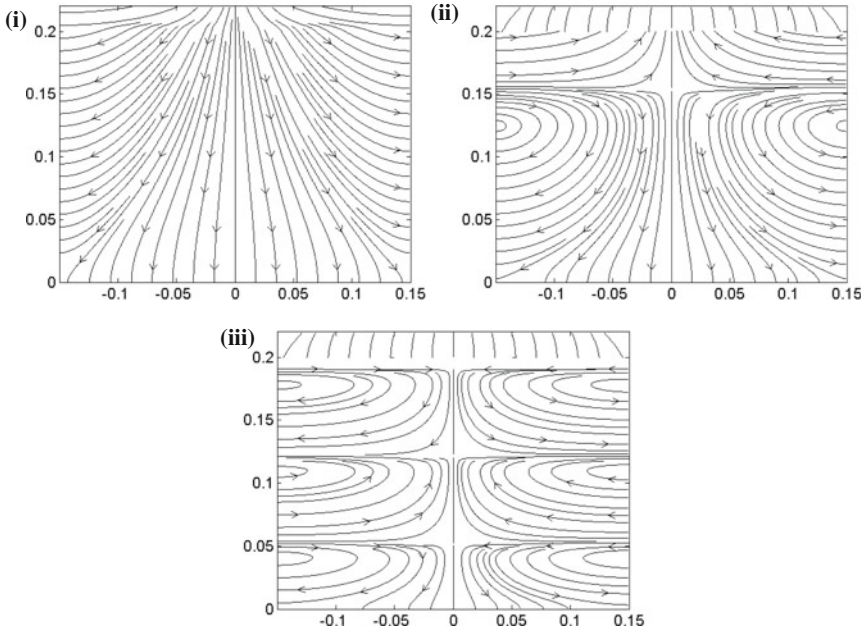

◂**Fig. 10.13** **a** H mode magnetic *field lines* and the **b** E mode electric *field lines* due to the source coil for an (i) evacuated chamber and for (ii) 5 Pa and (iii) 20 Pa argon pressure at $\omega t = 0$. The direction of the fields is indicated by the *line arrows*. In these plots, the distance between the *field lines* does not represent the field strength. The source coil is at the *top* of each plot

$$B_z(r,z,t) = |B_z(r,z)|\cos(\omega t + \phi_{B_z}) \tag{10.2.5.115b}$$

(b) E mode:

$$E_r(r,z,t) = |E_r(r,z)|\cos(\omega t + \phi_{E_r}) \tag{10.2.5.116a}$$

$$E_z(r,z,t) = |E_z(r,z)|\cos(\omega t + \phi_{E_z}) \tag{10.2.5.116b}$$

ϕ_{Br}, ϕ_{Bz}, $\phi_{Er,}$ and ϕ_{Ez} are the phase angles for the radial magnetic, axial magnetic, radial electric and axial electric fields respectively, and are calculated with,

$$\phi_{M_x} = \tan^{-1}\left(\frac{\mathrm{Im}\,(M_x)}{\mathrm{Re}\,(M_x)}\right), \tag{10.2.5.117}$$

in which M and x are the associated fields and directions, respectively, that is, $M = E$, B and $x = r$, z.

The ICP input parameters required for simulation of the H mode and E mode fields described in this section are summarized in Table 10.4. These values are based on the measurement range given by Jayapalan and Chin [63].

In a vacuum chamber at pressures below the threshold for ICP ignition (that is, evacuated condition with $\varepsilon_p = 0$), penetration of both the H mode magnetic fields and E mode electric fields occur across the chamber dimensions [Fig. 10.13a(i), b (i), respectively] without any changes in axial phase angle, ϕ_{Mz}; as shown in Fig. 10.14.

The H mode magnetic field lines in Fig. 10.13a(i) are seen as curls oscillating in the $-r$ and $-z$ directions as a result of the azimuthal, $-\theta$, source current. The E

Table 10.4 ICP input parameters used in simulation of the H mode and E mode fields

ICP input parameters	Argon pressure, P(Pa)		
	Evacuated	5	20
Coil current, I_p(A)	20	15	13
Electron density, $n_e(m^{-3})$	0	5×10^{16}	5×10^{17}
Electron temperature, T_e(eV)	0	3	2
Neutral gas temperature, T_n(K)	300	500	800
Electron collision frequency, $\nu(s^{-1})$	0	1.27×10^8	1.84×10^8

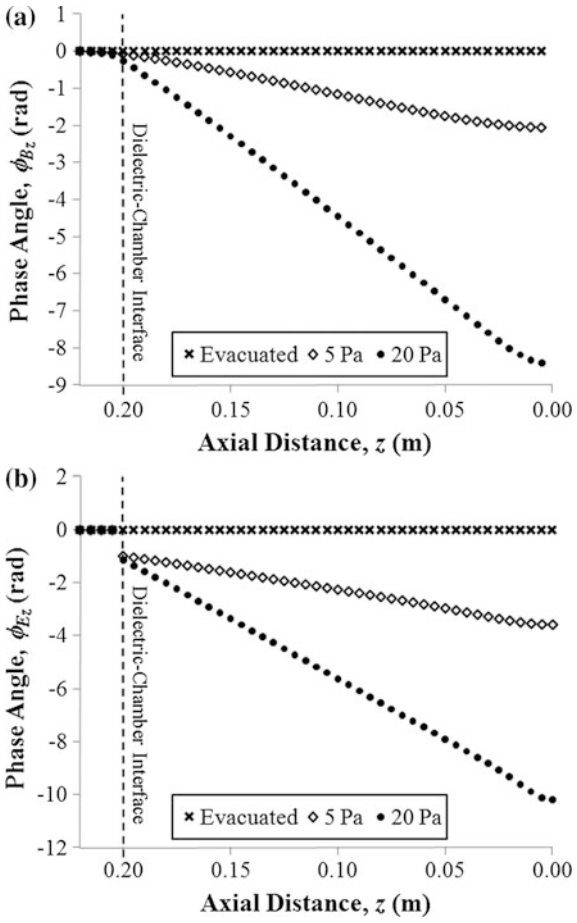

Fig. 10.14 The phase angles for the **a** H mode axial magnetic field, B_z and **b** E mode axial electric field, E_z at the chamber axis, $r = 0$, across the axial distance, z. The phase shifts are taken at $r = 0$ for reference

mode electric field lines in Fig. 10.13b(i), on the other hand, are divergent fields in the $-r$ and $-z$ directions generated by the radial potential difference along the coil radius. In the presence of plasma, the H mode magnetic fields and E mode electric fields are seen to both dampen and oscillate in propagation as they traverse the chamber length in the axial direction; with these effects increasing as argon pressure is increased from 5 to 20 Pa (Figs. 10.13a(ii), (iii), b(ii), (iii) and 10.14). This observation is attributed to the permittivity of the plasma medium, ε_p (represented by spatial decay parameter, α^2 for the H mode fields) which is complex in value. The imaginary component of ε_p is dependent on the ratio of collision frequency,ν [Eq. (10.2.5.107)] and drive frequency, ω, which denotes a causal relationship between collisional processes in the plasma and field oscillation frequency. Thus, as the source fields propagate through the plasma medium, their energy is coupled by the plasma electrons and redistributed to other particles via collisional interactions, consequently, resulting in field dampening and phase shift. The extent of field

Table 10.5 Plasma skin depth, δ_p (m) at different pressures for the H mode and E mode fields

	Skin depth, δ_p (m)		
Pressure, P (Pa)	Evacuated	5	20
H Mode	∞	0.068	0.022
E Mode	∞	0.036	0.014

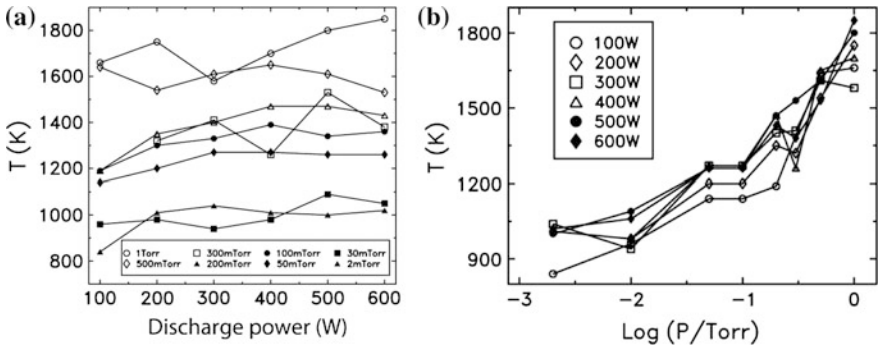

Fig. 10.15 Measured neutral gas temperature versus **a** discharge power and **b** logarithm of pressure for an argon discharge using AOES. The highest neutral gas temperature obtained was 1850 K at 600 W [80]. Reprinted from [80], with permission from the Department of Physics & Engineering Physics, University of Saskatchewan

dampening for the H mode and E mode fields can be quantified by the plasma skin depth, δ_p (Table 10.5). δ_p is calculable via,

$$\delta_p = \mathrm{Im}\,(\alpha^2)^{-1/2} = -\omega^2/c^2 \mathrm{Im}\,\varepsilon_p^{-1/2}. \qquad (10.2.5.118)$$

Since the plasma increases in density, n_e and collision frequency, ν with higher pressure (Table 10.4), dampening and oscillation of the source fields are most pronounced at 20 Pa.

10.2.6 Neutral Gas Heating in RF Planar ICPs

Neutral gas (or background gas) heating is a well-recognized and documented phenomenon which occurs especially in high-density discharges such as ICPs [74–79]. It is caused mainly by collisional energy transfer with other charged particles such as elastic collisions between electrons and ions with neutrals and de-excitation of highly energetic ions [63]. At higher pressures, heating of the neutrals can be very significant; with measured temperatures reaching up to 1850 K for some ICP systems (Fig. 10.15).

10.2.6.1 The Effects of Neutral Gas Heating on ICP Characteristics

As the neutral gas temperature in an ICP is elevated, the dynamics of particle transport and collisions occurring within the plasma medium are also changed. With neutral gas heating, transport of the plasma particles is nonlinearly enhanced [75, 76], via convection, from the denser region of the discharge (most heating) towards the reactor walls (least heating); following a temperature and pressure gradient [77]. As a result, several interesting observations have been seen in both measurement and simulation:

(i) Neutral gas depletion

At higher pressures, a non-negligible effect of neutral gas heating is neutral gas depletion; in which the neutral gas density at the region of the discharge which has the most heating is lower as compared to the surrounding areas [78, 79]. Heating of the neutrals creates a convective flux which causes the particles to travel towards the walls. For a simple axis-symmetric design, this usually occurs near the coil center; producing a characteristic well-shaped density profile across the chamber radius as seen in Fig. 10.16.

(ii) Electron density drift

For ICPs using a planar coil, the H mode electron density is typically expected to be highest near the proximity of the coil, whereby the power coupling from the source magnetic fields is the highest. However, in measurements reported by El-Fayoumi and Jones [41] and Stittsworth and Wendt [81], a displacement is seen between the power dissipation of the source field and the region of maximum electron density (Fig. 10.17).

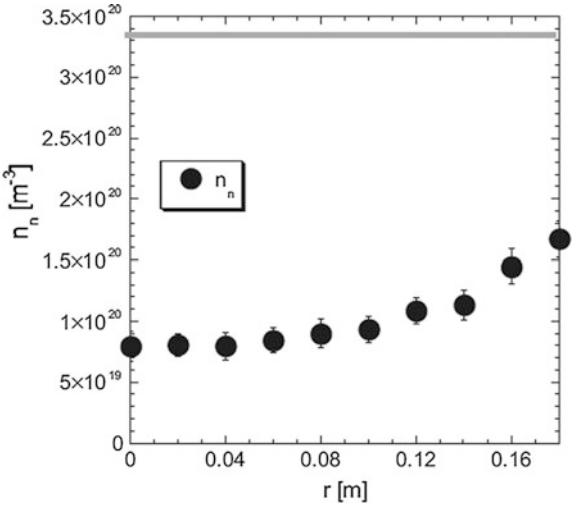

Fig. 10.16 Measured neutral gas density (labeled as n_n [m^{-3}], *black circles*) versus radius (labeled as r [m]) for an ICP reactor operating at 10 mTorr argon pressure and 2000 W power [79]. Neutral gas depletion is seen nearing the discharge center at $r = 0$ m. The *gray line* shows the initial neutral gas density before discharge ignition.

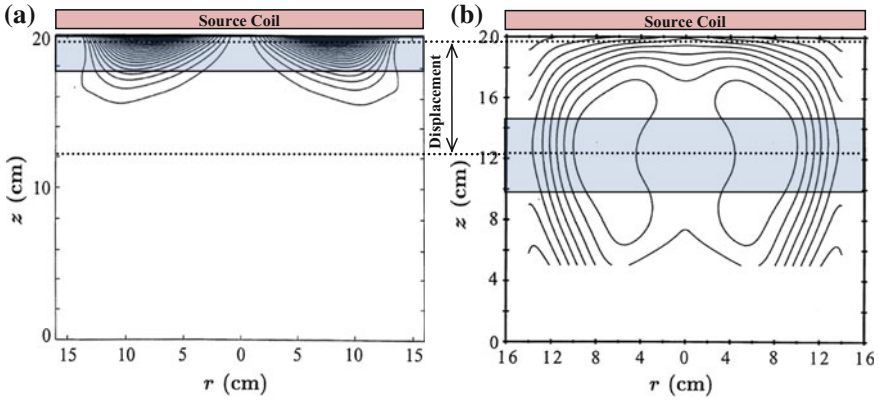

Fig. 10.17 Contour plots of the **a** measured power dissipation (ΔP = 1000 Wm^{-3}) and **b** measured electron density (maximum $n_e = 1.46 \times 10^{18}$ m^{-3}, line separation = 1.46×10^{18} m^{-3}) for an axis-symmetric, planar coil, ICP reactor at 120 mTorr argon pressure and peak coil current of 11.8 A [41]. Displacement between the regions of maximum discharge power dissipation and maximum electron density is labeled.

As aforementioned, heating of the neutral gas at the high-density regions of the discharge would cause an enhancement in transport of plasma particles via a temperature gradient; pushing the particles away from the discharge source towards the chamber walls. The resulting steady state flux of the moving particles and background heating would together form the observed displacement of electron density.

(iii) E mode and H mode transitions

In predictive simulation of E mode and H mode transitions [59], neutral gas heating has been shown to increase the threshold currents required to initiate E mode and H mode transitions at low pressures (Fig. 10.18).

At higher pressures, however, the threshold currents required for E mode and H mode transitions are lower. At lower pressures, heating of the neutrals diffuses the particles in the plasma in accordance with the ideal gas law [78, 82]. Since the plasma is diffused, higher input current is required to generate sufficient plasma ionization and reach threshold electron density to initiate E mode and H mode transitions [75]. At higher pressures, the neutral gas density in the plasma is sufficiently high enough such that heating of the neutral particles increases the power transfer efficiency by assisting plasma collisional processes [5, 83]. This reduces the input current required for E mode and H mode transitions.

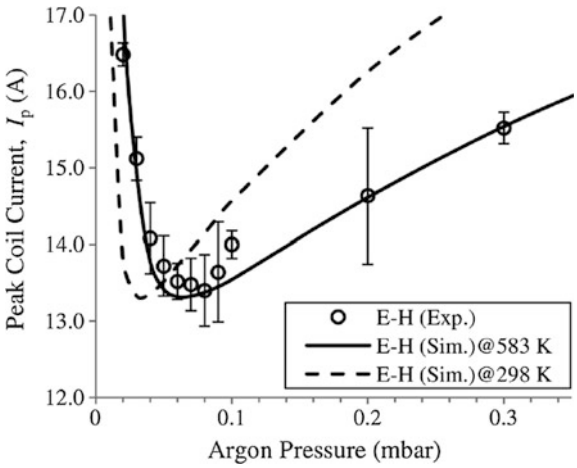

Fig. 10.18 Simulated (Sim.) and measured (Exp.) **a** E–H mode peak transition currents at 0.02–0.3 mbar argon pressure for a planar coil ICP reactor. Simulation was run at two neutral gas temperatures, that is, 583 K (elevated) and 298 K (ambient); with elevated temperatures more closely matching measured values [59]. Reproduced from [59] with the permission of AIP Publishing

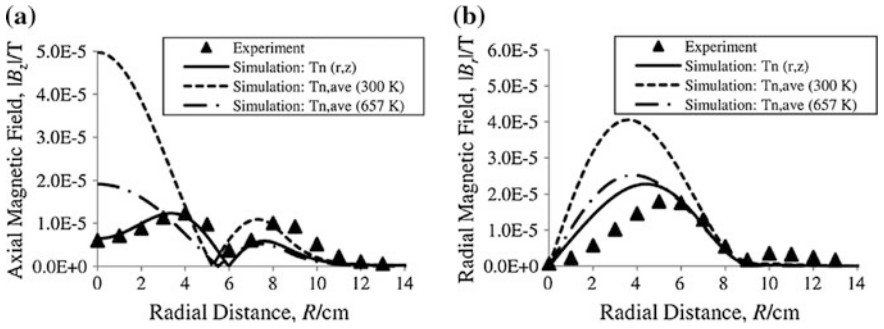

Fig. 10.19 Measured and simulated magnitudes of the **a** axial magnetic fields, $|\mathrm{Re}(B_z)|$ and **b** radial magnetic fields, $|\mathrm{Re}(B_r)|$ for 0.2 mbar argon pressure at 180 W RF power at 3.2 cm axial distance from the dielectric plate [63]. Fields were simulated for averaged ambient neutral gas temperature (300 K), averaged elevated neutral gas temperature (657 K) and spatially resolved elevated neutral gas temperature, $T_n(r, z)$; with closer fit to measurement only when temperature is elevated. Reproduced from [63] with the permission of AIP Publishing

(iv) Phase and magnitude of the source magnetic fields

In predictive simulation of the source magnetic fields [63], neutral gas heating is shown to play an important role in more accurately fitting the phase and magnitude of simulated fields with experiment (Fig. 10.19).

With neutral gas depletion occurring at the denser region of the plasma due to heating, a localized environment in which less energy is required to sustain ion–

electron pairs is created; whereby particle mean free path is longer and thus more energetic particles exist [76]. This allows for more efficient coupling of the source fields, subsequently affecting both phase and magnitude. For simulation without neutral gas heating, the phase and magnitude of the fields would not sufficiently match the measured fields.

10.2.6.2 Measurement of ICP Neutral Gas Temperature with AOES

Measurement of neutral gas temperature is usually indirect and noninvasive. This is due to the inert nature of the gas particles and the reactivity of the discharge toward temperature probes (such as thermocouples), which will introduce significant errors. As such, estimation of the neutral gas temperature can be made by analyzing the spectral broadening of select emission peaks of the discharge and fitting with theoretical derivatives. A simple yet widely used method of this form of measurement is actinometry optical emission spectroscopy (AOES).

In the AOES method, the plasma is seeded with trace amounts (<5% for minimal interaction with plasma) of a chemically inert probe gas. The probe gas used for neutral temperature measurement is typically a molecular gas with well-defined ground state emission peaks and with minimal dissociative interactions with the discharge gas; for example, nitrogen gas actinometer for argon plasma [74, 79, 84–86]. A high-resolution spectrometer is used to measure a selected ground state emission peak for analysis of spectral broadening (Fig. 10.20).

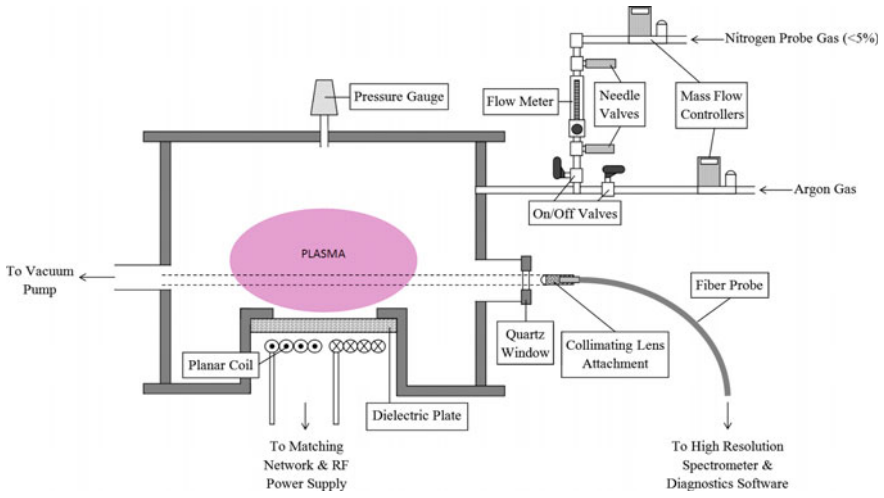

Fig. 10.20 A typical AOES setup for measurement of argon-neutral gas temperature with nitrogen probe gas (or actinometer). The collimating lens attachment on the fiber probe enables the probe to measure the line-averaged emission of the discharge at a particular axial height, as indicated by the *dashed lines*

An increase in spectral broadening of the emission peak corresponds to the elevation in the rotational temperature, $T_{rot,probe}$ of the probe gas neutrals. This increase is quantified by statistically fitting the experimentally measured peak with a theoretically modeled peak which considers all relevant mechanisms of spectral broadening including instrumental broadening; by which $T_{rot,probe}$ can be found. $T_{rot,probe}$ can be equated to the neutral gas temperature of the plasma, T_n in conditions for which the following assumptions hold [31, 80, 87]:

(i) The rotational temperature of the probe gas emission peaks, $T_{rot,probe}$ is analogous to the translational temperature of the probe gas neutrals, $T_{trans,probe}$ that is, $T_{trans,probe} \equiv T_{rot,probe.}$
(ii) The species population of the rotational ground state molecules of the probe gas emission peaks is in thermal equilibrium.
(iii) The probe gas neutral temperature, $T_{trans,probe}$ is equal and representative of the plasma neutral gas temperature, T_n, that is, $T_n \equiv T_{trans,probe}$.

As aforementioned, $T_{rot,probe}$ is calculated by taking an appropriate emission peak from the measured spectra and retrofitting it with a simulated spectrum obtained from theory. Selection criteria for the emission peak are as follows [31, 80, 87]:

(i) The peak should involve a ground state transitions that would represent the ground state temperature of the molecules.
(ii) The peak should be of resolvable intensity and free from peak impurities due to overlapping emissions that would affect the accuracy of the fit.

Estimation of Neutral Gas Temperature of an Argon ICP Using the Nitrogen Second Positive System ($N_2C^3\Pi_u - B^3\Pi_g$)

For estimation of the neutral gas temperature of an argon plasma, $T_{n,Ar}$, miniscule amount of nitrogen probe gas (<5%) is seeded into the discharge. This results in the distinct observation of the nitrogen second positive system ($N_2C^3\Pi_u - B^3\Pi_g$) during measurement of the plasma emission spectra (Fig. 10.21).

The emission peaks for the nitrogen second positive system are the result of excitation of neutral nitrogen molecules by low energy thermal electrons (2–3 eV) from the $X^1\Sigma_g^+$ ground state to the $C^3\Pi_u$ state and subsequent photon emission during de-excitation to the $B^3\Pi_g$ state. Thus, analysis of these emission peaks would allow for evaluation of the rotational temperature of the nitrogen ground-state molecules.

The governing relations for these emission transitions are given by

$$e + N_2(X^1\Sigma_g^+) \rightarrow N_2(C^3\Pi_u) + e \qquad (10.2.6.1)$$

$$N_2(C^3\Pi_u) \rightarrow N_2(B^3\Pi_g) + h\nu \qquad (10.2.6.2)$$

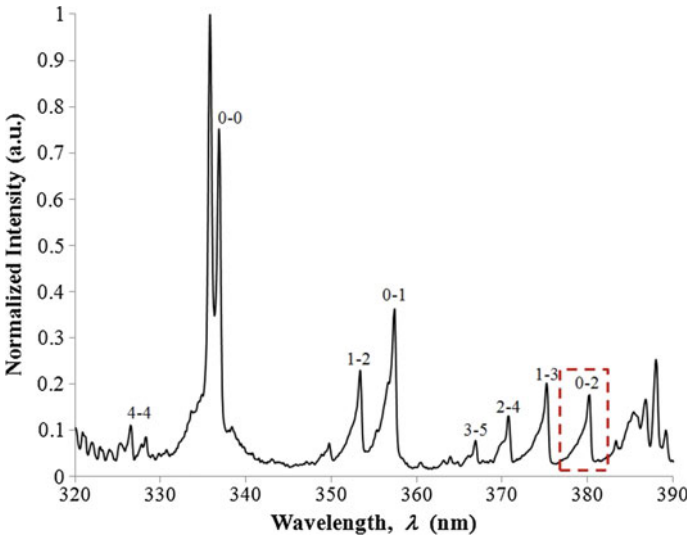

Fig. 10.21 Sample emission spectra showing the nitrogen second positive system ($N_2C^3\Pi_u - B^3\Pi_g$) for a planar coil ICP system at 0.1 mbar pressure (~95% Ar/~5% N_2) and 200 W RF power measured with a 0.1 nm resolution spectrometer [31]. The chosen ground state emission peak (0–2) is indicated

Each emission peak seen in Fig. 10.21 is a result of a transition between the upper $C^3\Pi_u$ vibrational state and the lower $B^3\Pi_g$ vibrational state; i.e., the notation (0–0) shows that the peak is due to the transition from the zeroth upper $C^3\Pi_u$ vibrational state ($v' = 0$) to the zeroth lower $B^3\Pi_g$ vibrational state ($v'' = 0$). Discrete transitions from numerous rotational states within each vibrational state form a discrete emission band which is observed as a continuous emission peak (also known as a vibro-rotational emission peak) due to the effects of spectral broadening [87].

With consideration of the selection criteria given in Sect. 10.2.6.2, it is noted that the (0–2) emission peak (highlighted in Fig. 10.21) is a ground-state transition of both resolvable intensity and free from overlap impurity with other peaks. Thus, this peak is suitable to be used to estimate $T_{n,Ar}$ [74, 79, 85]. In assuming that the argon neutral gas temperature is equal to the nitrogen rotational temperature, ($T_{n,Ar} = T_{rot,N_2}$; as described Sect. 10.2.6.2) $T_{n,Ar}$ can be determined in three steps [31, 80, 87]:

(i) *Calculation of the discrete rotational line positions and intensities of the selected* $N_2C^3\Pi_u - B^3\Pi_g$ emission band

All possible rotational line positions and intensities are calculated as prescribed by atomic/molecular physics theory. The discrete rotational line positions of a single vibrational emission band for an electronic state transition (i.e., $N_2C^3\Pi_u - B^3\Pi_g$) is expressed as

$$\lambda_i(v', v'', J', J'') = \frac{1}{v_i(v', v'', J', J'')n_{\text{air}}}. \quad (10.2.6.3)$$

Here, n_{air} is the refractive index of air, v_i is the transitional vibro-rotational wavenumber of the spectral line in cm^{-1}, v is the vibrational quantum number and J is the rotational quantum number. The superscript notations $'$ and $''$ indicate the upper and lower transition states, respectively, e.g. for the 0–2 vibrational emission peak, $v' = 0$ is the upper state ($C^3\Pi_u$) vibrational quantum number and $v'' = 2$ is the lower state ($B^3\Pi_g$) vibrational quantum number. For each rotational line position, the corresponding line intensity is given by

$$I(J', T_{\text{rot,N}_2}) = C_{\text{spec}} S_J(J') \exp\left[\frac{-hcF_v(J')}{k_B T_{\text{rot,N}_2}}\right], \quad (10.2.6.4)$$

where C_{spec} is a constant dependent on spectroscopic parameters (normalized intensities are typically used for temperature estimation, thus, C_{spec} can be taken as 1), S_J is the line strength of the rotational transition, h is Planck's constant in Js^{-1}, c is the speed of light in cms^{-1}, $F_v(J')$ is the upper state rotational term in cm^{-1}, k_B is the Boltzmann constant in JK^{-1} and $T_{\text{rot,N}_2}$ is the rotational temperature of nitrogen in K. Calculation of all contributing line positions and intensities would give a band of discrete rotational lines which represents the theoretical (0–2) emission peak (Fig. 10.22).

(ii) *Convolution of the discrete rotational lines with instrumental broadening*

The modeled discrete rotational lines of the (0–2) vibrational emission transition in Fig. 10.22 are observed as a continuous peak in the measured spectra due to the effect of instrumental broadening; caused by mechanical and design limitations of the spectrometer in resolving different wavelengths of emission. As such, to incorporate instrumental broadening, the amount of peak broadening is first measured by using standard sources with line emissions at the wavelength of interest. For the nitrogen second positive band system which is in the UV region, an

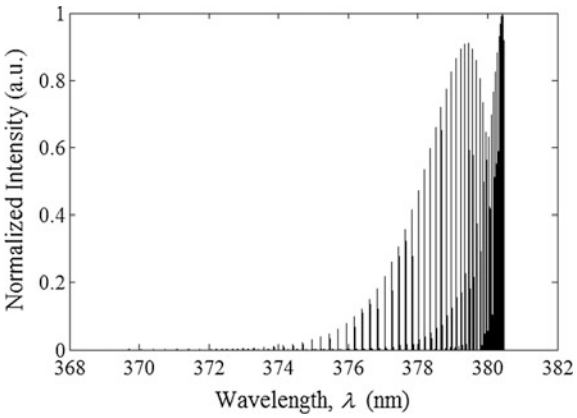

Fig. 10.22 Discrete rotational lines for the 0–2 vibrational emission transition of the nitrogen second positive system $N_2C^3\Pi_u - B^3\Pi_g$ at $T_{\text{rot,N}_2} = 600$ K

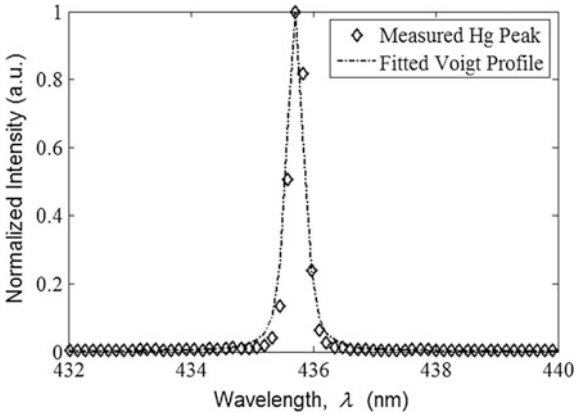

Fig. 10.23 Voigt profile fitted to the measured Hg peak at 435.8 nm

appropriate standard source for measurement would be the Hg vapor source which has several strong discrete emission transitions in the same wavelength range [31].

A suitable Hg emission peak (as close as possible to the wavelength of the (0–2) vibrational emission peak) is then chosen and fitted with a spectral function (Fig. 10.23), typically the normalized Voigt profile [88].

Both the discrete rotational spectra in Fig. 10.22 and Voigt profile in Fig. 10.23 are convolved with the convolution theorem,

$$I_{\text{conv}}(\lambda) = \int_{-\infty}^{\infty} I(\lambda') \cdot f(\lambda - \lambda')\mathrm{d}\lambda'. \qquad (10.2.6.22)$$

Here, $I_{\text{conv}}(\lambda)$ is the convolved intensity at wavelength λ, $I(\lambda')$ is the intensity at the integration wavelength λ' and $f(\lambda - \lambda')$ is the Voigt profile with peak wavelength λ at displacement λ'. The convolution results in a continuous spectrum shown in Fig. 10.24c. It resembles the measured spectral peak around 380 nm in Fig. 10.21.

(iii) *Statistical fitting of the theoretical peak with measurement to estimate* $T_{\text{n,Ar}}$

After incorporating the effects of instrumental broadening, both the theoretical and measured peaks are statistically fitted by using the minimum chi squared (χ^2) analysis. By varying $T_{\text{rot,N}_2}$, the minimum χ^2 value is found. It is noted that higher $T_{\text{rot,N}_2}$ will result in overall increased peak broadening. This minimum χ^2 value corresponds to the minimum statistical variance between the modeled spectra and measured peak and thus, yields the best fit. With the assumptions provided in Sect. 10.6.2, $T_{\text{n,Ar}}$ can be estimated from the value of $T_{\text{rot,N}_2}$ at this point (Fig. 10.25). For the sample spectra seen in Fig. 10.21, $T_{\text{n,Ar}}$ = 600 K.

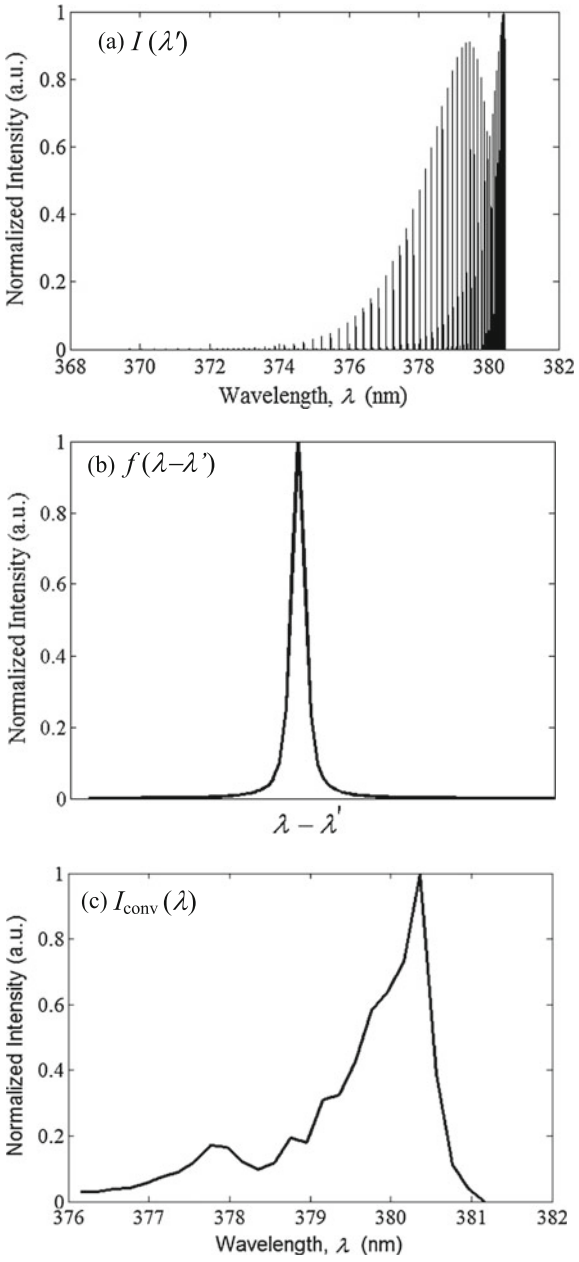

Fig. 10.24 The discrete rotational line spectra **a** is convolved with instrumental broadening **b** via the Voigt function resulting in the convolved theoretical spectrum **c**. The convolved theoretical spectrum takes the shape of the experimentally measured 0–2 vibro-rotational peak seen in Fig. 10.21

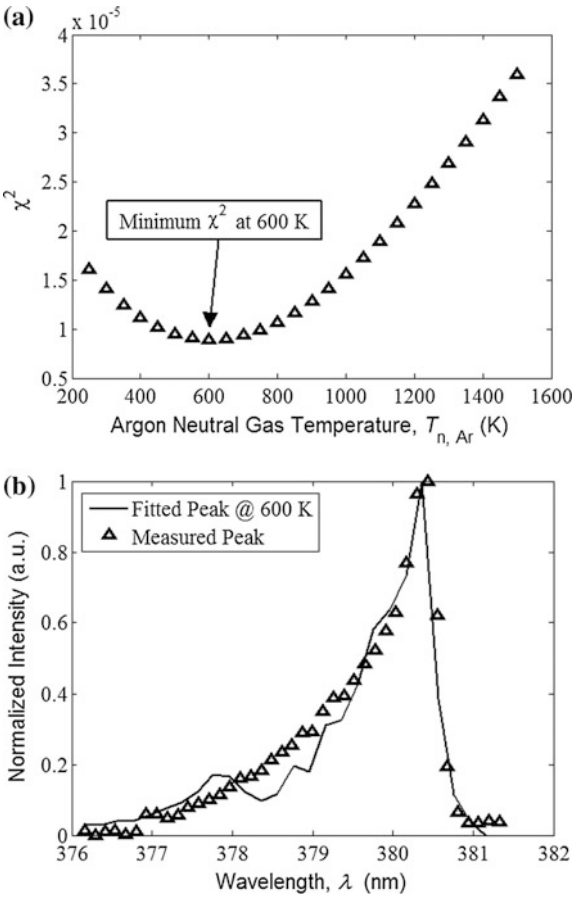

Fig. 10.25 **a** χ^2 plot showing minimum fitting value at 600 K. **b** Experimental 0–2 vibro-rotational peak at 0.1 mbar Ar/N_2 pressure and 200 W RF power fitted with the convolved theoretical spectrum at 600 K

10.3 Applications of ICPs

10.3.1 Inductive Lamp

One of the earliest applications found for ICPs was for electrodeless illumination. A decade after the initial discovery of the electrodeless discharge by Hittorf [8], the inductive lamp made its public debut at the 1893 Chicago World's Columbian Exposition via renowned inventor and industrialist, Nikola Tesla. Tesla's demonstration lamps were externally powered by the magnetic fields of another one of his exhibits, a large Tesla coil [89]. Further development of the inductive lamp was later made by Hewitt [90]. Hewitt experimented with various types of lamp designs, including the double sphere and single sphere lamps and also developed the first mercury vapor induction lamp (Fig. 10.26a).

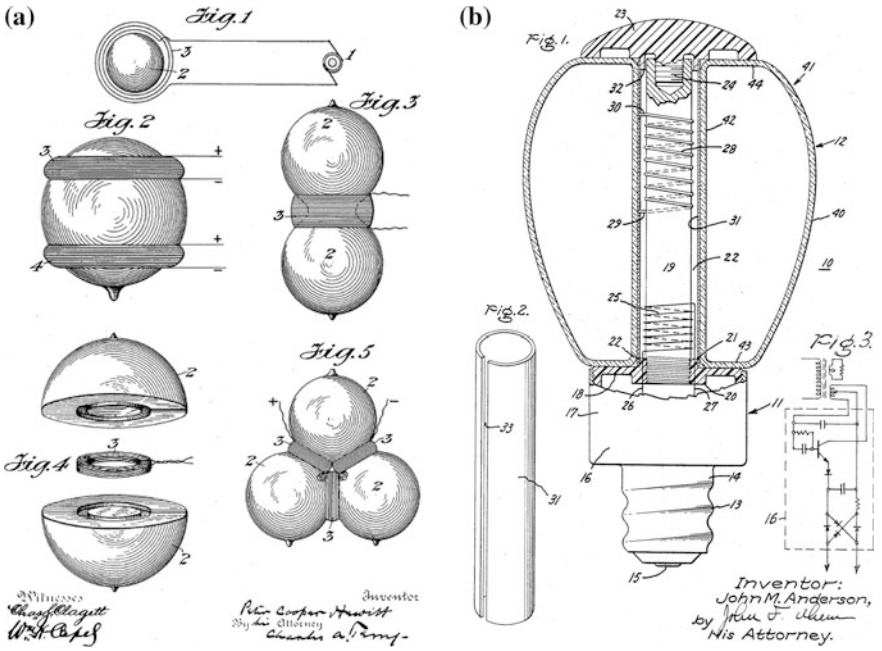

Fig. 10.26 **a** Various early inductive lamp designs [90] and **b** a commercially viable inductive lamp designed for existing fixtures [91]

Despite various theoretical and experimental developments on inductive discharges for the next 65 years, inductive lamps designs were still not safe or practical for commercial applications. The first marketable inductive lamp was designed by Anderson [91]. The argon–mercury lamp had a self-contained radio frequency oscillator for ignition and was able to fit into existing fixtures made for incandescent lamps (Fig. 10.26b). It was not until the mid 1990s, however, that inductive lamps became commercially available; with companies such as Phillips and Osram coming out with the 2.65 MHz QL and 250 kHz Endura lamps, respectively [92]. Lack of commercialization of inductive lamps in the past was mainly due to the much lower cost of fluorescent lighting and issues with electromagnetic interference. However, the increasing demand for more energy efficient and longer lasting lighting solutions has brought the inductive lamp into better perspective for future applications [92]. Some of the more recent innovations for inductive lamps include the development of a miniaturized microwave lamp with dielectric waveguide [93] and a brightness control mechanism [94].

10.3.2 Inductively Coupled Plasma Mass Spectrometry (ICP-MS)

Inductively coupled plasma mass spectrometry (ICP-MS) is a sensitive element analysis technique used to detect trace concentrations (up to one part per trillion) of chemical elements in sample materials. The sample is typically ionized by an inductively coupled argon plasma jet and a mass spectrometer is used to detect and quantify the ionic composition of the sample via charge-to-mass ratio [18, 95]. A typical ICP-MS setup consists of several elaborate components including a sample introduction system, an ICP torch, a vacuum system, a plasma–spectrometer interface, ion-focusing lenses, a quadrupole mass spectrometer, an ion detector, and a data diagnostics system [96]. ICP-MS is commonly used to detect contaminant levels and bio-toxicity in products for various industries including semiconductor, environmental, pharmaceutical, and food and beverage [97]. Prior to the advent of ICP-MS, other techniques including flame atomic absorption spectroscopy (FAAS) and DC arc and AC spark atomic emission spectroscopy (AES) were typically used for elemental analysis [98]. The practicality of the inductively coupled plasma as an emission source for AES was first demonstrated by Greenfield et al. [99]. In comparison with DC arc and AC spark sources, the inductively coupled source had easier operability, lack of contamination from electrodes, multi-element analysis capability and low background emissions. Greenfield et al. also reported that the inductively coupled source had the combined qualities of stability of an AC spark source and sensitivity of a DC arc source. The use of an inductively coupled source for mass spectrometry was later introduced by Houk et al. [21]. By coupling an argon inductively coupled source with a quadrupole mass spectrometer, Houk et al. were able to identify the ionic constituents found in the plasma at the correct relative concentrations. Sensitivity of element analysis using a mass spectrometer was also found to be relatively higher with detection limits in the range of 0.002–0.06 μg/ml for the elements studied. It was only 3 years after Houk's publication that the first commercial ICP-MS device, the ELAN 250 ICP-MS Elemental Analysis System was produced by Douglas et al. at Sciex Inc., Ontario [100]. The ELAN 250 had a dynamic range of 10^6 (two orders higher than commercial ICP-AES systems available at the time) and was able to analyze more than 90% of the elements in the periodic table at concentrations ranging from 0.5 to 10 parts per billion. Innovations in ICP-MS that followed the ELAN 250 include the first computer controlled system, PMS 100 by Yokogawa Electric Corp. in 1987, the first benchtop system, the 4500 ICP-MS by Agilent in 1994, the first system with time-of-flight charge-to-mass ratio, the Renaissance TOF-ICP-MS by LECO Corp. in 1997 and the first system with an interference removal device (that is, a dynamic reactive cell or DRC), the ELAN 6100 DRC by PerkinElmer in 1999 [96].

10.3.3 Plasma-Enhanced Chemical Vapor Deposition (ICP-PECVD)

Plasma-Enhanced Chemical Vapor Deposition (PECVD) is a deposition process which uses plasma ionized material gases to coat a substrate with thin layers of solid-state material. The substrate is typically biased with a negative voltage to allow bombardment of material ions at a controlled rate [5]. PECVD is widely used in the semiconductor industry for fabrication of electronic circuits and components. Early study of PECVD by inductive coupling (ICP-PECVD) was done by Chittick, Alexander and Sterling [101] using silane gas to deposit thin amorphous silicon layers on substrates at 25–650 °C. The deposited films were found to have properties which varied with deposition temperature and had an appreciably higher resistivity (up to 10^{14} Ω cm at 21 °C) compared to films deposited by vacuum evaporation or sputtering [102] thus, being advantageous to component fabrication. Shuskus and Cowher [47] patented a PECVD technique of fabricating high purity thin semiconductor films on alkali halide substrates demonstrated using a helical inductively coupled plasma system (Fig. 10.27).

The technique eliminated contamination of the thin films from substrate sublimation by reducing the required substrate temperature for deposition. The novel production of diamond thin films (that is, for high-temperature semiconductor devices, abrasion protection, optical window, and heat sink applications) with RF ICP PECVD was investigated by Meyer et al. [103]. RF ICP PECVD offered

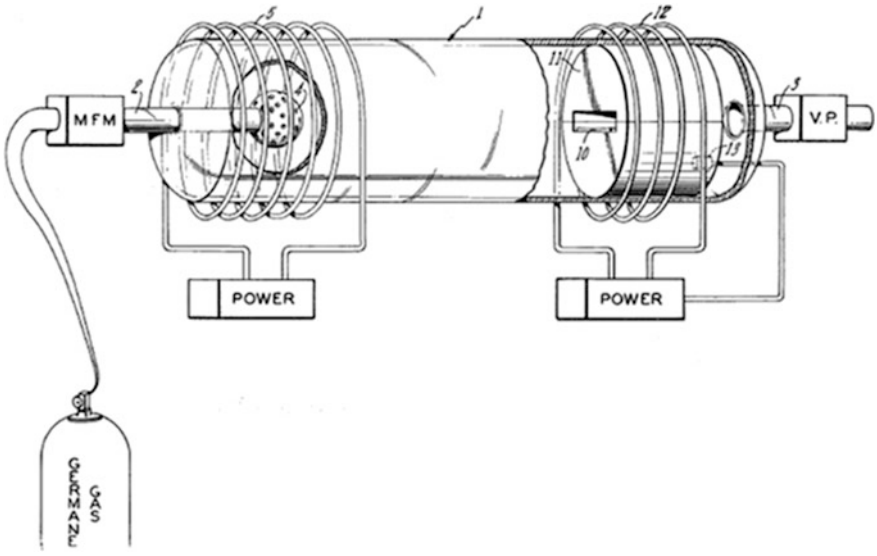

Fig. 10.27 The helical ICP-PECVD system by Shuskus and Cowher used for low temperature deposition of *thin films* on alkali halide substrates [47]

the advantage of easier production volume and power scalability as compared to microwave fabrication systems which were extensively researched. The films were fabricated using a mixture of methane and hydrogen on silicon substrates with various surface treatments, that is, a diamond-like carbon (DLC) coating, scratched by sanding and polished. It was found that the substrates treated with a DLC coating had better diamond nucleation, film uniformity and shorter deposition times in comparison to the scratched and unmodified substrates. Liew [104] fabricated DLC films using a 13.56 MHz RF ICP with similar gas admixture of methane and hydrogen on silicon substrates. A glass funnel was used in the reactor to confine the plasma, allowing for higher electron density and neutral gas temperature at lower input power. The percentage of methane mixed with hydrogen showed significant effects on the morphology of the DLC film with better quality films being produced with less than 1% methane admixture (Fig. 10.28).

Xu et al. [105] were able to fabricate highly uniform, large area, vertically aligned carbon nanofibers (VACNF) using a high-density and low-frequency inductively coupled plasma source in an $Ar/H_2/CH_4$ discharge. Research on deterministic fabrication of carbon nanofibers is of high interest due to their applications in scanning microscopy, field emission devices, and in the emerging fields of nanoelectronics and nanobiology [106]. The VACNFs were grown by Xu et al. [105] on lightly doped silicon (100) substrates which have been predeposited with nanometer-layered Ni/Fe/Mn catalysts. Growth morphology, crystalline structure and chemical states of the nanofibers were found to be highly dependent on substrate preparation, temperature and bias voltage. Ng [107] studied on hydrogenated amorphous carbon (a-C:H) films deposited on glass and silicon substrates by ICP PECVD using the admixture of acetylene (C_2H_2)-argon gas. The deposited films were characterized to be polymeric and homogeneous, having thicknesses from 0.45 to 1.2 μm. Post annealing of the films increased adhesion of the films on the substrate, however, with some compromise to the microstructure of

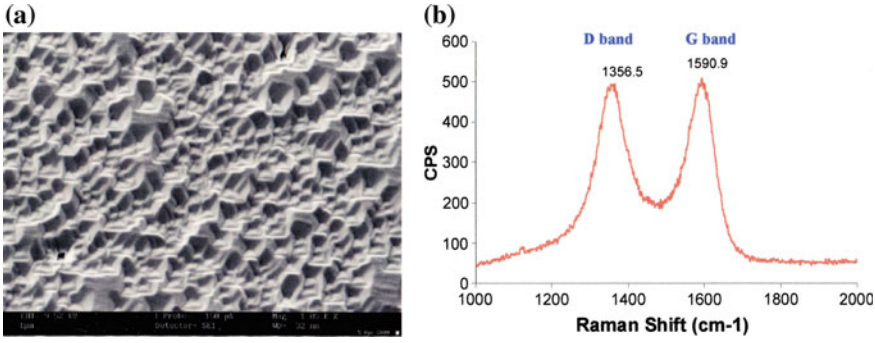

Fig. 10.28 **a** SEM surface morphology and **b** Micro-Raman spectrum of a DLC film deposited with 0.8% methane and 99.2% hydrogen admixture. The polygonal crystalline structure in **a** indicates the increased formation of sp3-hybridized carbon (*diamond*) bonds. The D and G bands in **b** are characteristic peaks, typically seen for DLC films

the film. At present, research with ICP-PECVD includes the fabrication and characterization of material nanostructures, that is, silicon nanowires [108], tin oxide nanorods [109] and carbon nanowalls [110].

10.3.4 Reactive Ion Etching (RIE)

Reactive Ion Etching (RIE) is a dry etching process, which uses highly ionized reactive gases to etch a circuit or pattern on a prepared substrate. The substrate is typically applied with a photoresist layer which is imprinted with the desired photolithographic pattern before etching [5]. Compared to wet etching, that is, in which the substrate is immersed in highly corrosive chemicals to etch unwanted material, RIE poses the advantage of better process control for pattern transfer, higher etching resolution, reduced usage and handling of hazardous chemicals and having both isotropic and anisotropic etching capability [111]. Before the potential of RIE for pattern transfer and anisotropic etching was fully uncovered in the late 1970s, most dry etching research focused on plasma etching, that is, a similar process which used volatile plasma at low ion energies for isotropic chemical etching. One of the earliest patents for an inductively coupled plasma etching system for semiconductor manufacturing was filed by Jacob [112]. The helical coil system was able to etch passivation layers (e.g., SiO, SiO_2 and Si_3N_4) at a rate of 3000 A/min and various metals (e.g., tungsten, tantalum and molybdenum) at 2000 A/min without degradation of the photoresist (organic) mask. In an effort to make plasma etching a faster process, Hosokawa et al. [113] showed that positive ions at higher energies were able to enhance plasma etching via physical bombardment and removal. The directional nature shown by the ion bombardment at high energies eventually led to the discovery of anisotropic plasma etching; aptly termed "reactive ion etching" due to the involvement of both physical ion bombardment and volatile chemical etching [114, 115]. In 1987, Keeble [116] filed a patent of a helical inductively coupled system with both RIE and PECVD capabilities. The system is able to generate a largely uniform, low pressure, high ion density discharge for even etching and deposition. A novel, separately adjustable voltage bias is also added to the substrate plate to draw ion flux independently from the power supply allowing improved control of the process. Further plasma uniformity and process control was later achieved with the use of a planar coil system [28] in which the plasma is generated by using a flat spiral coil (Fig. 10.29).

In a planar coil system, the ion flux is nondirectional (that is, parallel to the substrate) and thus, the ions do not bombard or react with the substrate unless a voltage bias is applied. The plasma is also generated more uniformly across the radius of the coil as compared to a helical coil system. Bell et al. [117] investigated the selective etching of SiO_2–Si layers using a mixture of fluorocarbon (CHF_3, $C2F_4$, and C_3F_6) and hydrogen gases in an inductively coupled plasma system.

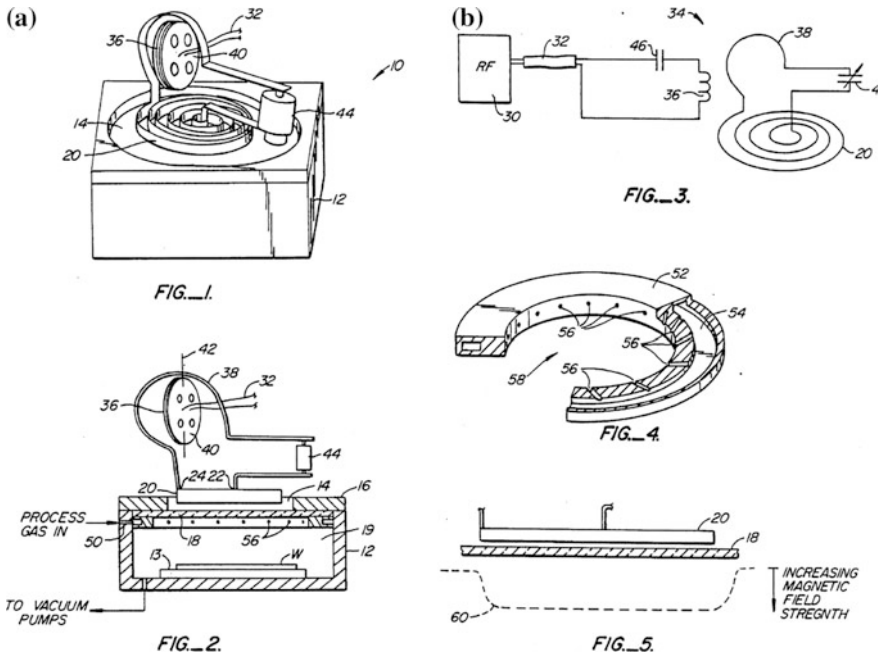

Fig. 10.29 A planar coil ICP system for both PECVD and RIE applications patented by Ogle (1990). **a** FIG_1 and FIG_2 illustrates the system assembly whereas, **b** FIG_3, FIG_4, and FIG_5 illustrates the circuit and coil assembly

From experiments, it was found that C_3F_6 (without the addition of hydrogen) gave the highest SiO_2 etching rate of 830 nm/min at the RF bias power of 350 W. The addition of hydrogen for all the gases reduced the etch rate of both SiO_2 and Si layers with the drop of etch rate for Si being considerably higher; thus, showing better selectivity. The highest selectivity of 45 (etch rate of SiO_2/etch rate of Si) was shown by C_2F_4 when 30% hydrogen was added into the discharge. Yu et al. [118] developed a new method of fabricating gallium nitride (GaN) nanorods for nano-optoelectronic devices by using ICP-RIE. The nanorods were etched out of a GaN epitaxial film which was grown on a sapphire substrate by metal-organic chemical vapor deposition. A fixed Cl_2/Ar flow rate of 10/25 sccm and an ICP/substrate bias power of 200/200 W was used to fabricate nanorod arrays with densities of 10^8–10^{10} cm^{-2} and with dimensions of up to 20–100 nm; scaled by varying the chamber pressure from 10 to 30 mTorr. More recent research of ICP-RIE includes etching zinc oxide (ZnO) photonic crystals using nanosphere lithography [119] and cryogenically enhanced (deep) ICP-RIE for etching of nanostructures [120].

10.4 Chapter Summary

The fundamentals of RF ICPs have been thoroughly discussed in this chapter with emphasis toward the planar coil configuration. The plasma exists in two modes of operation, namely the E mode and H mode. Hysteresis between mode transitions has been quantified in the form a power balance model, which also maps out the stable operating path of the RF discharge at different input coil currents. The source electromagnetic fields traversing the plasma medium has also been modeled for the E and H modes; showing larger phase difference of both E and H mode fields for increasing filling pressure in the presence of plasma. Detailed derivation of the electromagnetic field equations in both the E and H modes has been presented for ease of reference. The effects of neutral gas heating on the plasma characteristics have been also discussed. Heating of the neutrals causes significant changes to plasma particle transport dynamics which include depletion of neutral particles at the most intense region of the discharge and drift of electrons away from the source coil. Measurement of the ICP neutral gas temperature using the AOES technique was also discussed along with an example of temperature determination for argon plasma with nitrogen as seed gas. The chapter ends with various applications of RF ICPs which include induction lamps, mass spectrometry, and materials processing.

References

1. B. Chapman, *Glow Discharge Processes: Sputtering and Plasma Etching* (John Wiley & Sons Inc, New York, 1980)
2. P. Chabert, N. Braithwaite, *Physics of Radio-Frequency Plasmas* (Cambridge University Press, Cambridge, 2011)
3. C. Hollenstein, A.A. Howling, P. Guittienne, I. Furno, Industrial plasmas in academia. Plasma Phys. Control. Fusion **57**(1), 014010 (2015). doi:10.1088/0741-3335/57/1/014010
4. J. Hopwood, Review of inductively coupled plasmas for plasma processing. Plasma Sources Sci. Technol. **1**(2), 109–116 (1992). doi:10.1088/0963-0252/1/2/006
5. M.A. Lieberman, A.J. Lichtenberg, *Principles of Plasma Discharges and Materials Processing*, 2nd edn. (John Wiley & Sons Inc, Hoboken, 2005)
6. J.R. Roth, *Industrial Plasma Engineering: Volume 2-Applications to Nonthermal Plasma Processing* (IOP Publishing Ltd., Bristol, 2001)
7. F.F. Chen, in *Advanced Plasma Technology*, ed. by R. d'Agostino, P. Favia, Y. Kawai, H. Ikegami, N. Sato, F. Arefi-Khonsari (Wiley-VCH Verlag, Weinheim, 2008), pp. 99–115
8. W. Hittorf, Ueber die electricitätsleitung der gase. Ann. Phys. **257**(1), 90–139 (1884). doi:10.1002/andp.18842570105
9. J.J. Thomson, XLI. On the discharge of electricity through exhausted tubes without electrodes. Philos. Mag. Ser. 5. **32**(197), 321–336 (1891). doi:10.1080/14786449108620192
10. J.J. Thomson, C.I. The electrodeless discharge through gases. Lond. Edinb. Dubl. Phil. Mag. **4**(25), 1128–1160 (1927). doi:10.1080/14786441108564414
11. J.S. Townsend, R.H. Donaldson, XVI. Electrodeless discharges. Lond. Edinb. Dubl. Phil. Mag. **5**(27), 178–191 (1928). doi:10.1080/14786440108564455
12. C.J. Brasefield, The conductivity of a high frequency discharge in hydrogen. Phys. Rev. **35** (9), 1073–1079 (1930). doi:10.1103/physrev.35.1073

13. C.J. Brasefield, High frequency discharges in mercury, helium and neon. Phys. Rev. **37**(1), 82–86 (1931). doi:10.1103/physrev.37.82
14. K.A. MacKinnon, LXVI. On the origin of the electrodeless discharge. Lond. Edinb. Dubl. Phil. Mag. **8**(52), 605–616 (1929). doi:10.1080/14786441108564921
15. G.I. Babat, Electrodeless discharges and some allied problems. J. Inst. Electr. Eng. 3. **94**(27), 27–37 (1947). doi:10.1049/ji-3-2.1947.0005
16. T.B. Reed, Induction-coupled plasma torch. J. Appl. Phys. **32**(5), 821–824 (1961). doi:10.1063/1.1736112
17. T.B. Reed, U.S. Patent 3,324,334, 6 Jun 1967
18. S. Greenfield, Invention of the annular inductively coupled plasma as a spectroscopic source. J. Chem. Educ. **77**(5), 584–591 (2000). doi:10.1021/ed077p584
19. *Liberty Series II Analytical Methods Book* (Varian (Agilent Technologies), Victoria, Australia, 1999), http://www.agilent.com/cs/library/usermanuals/public/1500.pdf. Accessed 6 Feb 2016
20. R.H. Wendt, V.A. Fassel, Induction-coupled plasma spectrometric excitation source. Anal. Chem. **37**(7), 920–922 (1965). doi:10.1021/ac60226a003
21. R.S. Houk, V.A. Fassel, G.D. Flesch, H.J. Svec, A.L. Gray, C.E. Taylor, Inductively coupled argon plasma as an ion source for mass spectrometric determination of trace elements. Anal. Chem. **52**(14), 2283–2289 (1980). doi:10.1021/ac50064a012
22. D. Potter, A commercial perspective on the growth and development of the quadrupole ICP-MS market. J. Anal. At. Spectrom. **23**(5), 690–693 (2008). doi:10.1039/b717322a
23. M.I. Boulos, RF induction plasma spraying: state-of-the-art review. J. Therm. Spray Technol. **1**(1), 33–40 (1992). doi:10.1007/bf02657015
24. J.J. Cuomo, C.R. Guarnieri, J.A. Hopwood, U.S. Patent 5,433,812, 18 Jul 1995
25. P.L. Fauchais, J.V.R. Heberlein, M.I. Boulos, *Thermal Spray Fundamentals: From Powder to Part* (Springer Science + Business Media, New York, 2014). doi:10.1007/978-0-387-68991-3
26. T. Okada, H. Hamatani, T. Yoshida, Radio-frequency plasma spraying of ceramics. J. Am. Ceram. Soc. **72**(11), 2111–2116 (1989). doi:10.1111/j.1151-2916.1989.tb06040.x
27. M.I. Boulos, J. Jurewicz, U.S. Patent 5,200,595, 6 Apr 1993
28. J.S. Ogle, U.S. Patent 4,948,458, 14 Aug 1990
29. J.H. Keller, Inductive plasmas for plasma processing. Plasma Sources Sci. Technol. **5**(2), 166–172 (1996). doi:10.1088/0963-0252/5/2/008
30. D.K. Coultas, J.H. Keller, U.S. Patent 5,304,279, 19 Apr 1994
31. K.K. Jayapalan, *Study of the Effects of Neutral Gas Heating in a Radio Frequency Inductively Coupled Plasma*, Ph.D. thesis (University of Malaya, 2015)
32. J.J. Thomson, The electrodeless discharge through gases. Proc. Phys. Soc. **40**(1), 79–89 (1927). doi:10.1088/0959-5309/40/1/314
33. J. Thomson, XXII. On the mechanism of the electrodeless discharge. Lond. Edinb. Dubl. Phil. Mag. **10**(63), 280–291 (1930). doi:10.1080/14786443009461574
34. J.S. Townsend, LXX. Electrodeless discharges. Lond. Edinb. Dubl. Phil. Mag. **13**(86), 745–759 (1932). doi:10.1080/14786449209461981
35. J. Kunz, X.C. Theory of electromagnetic and electrostatic induction in electrodeless discharges. Lond. Edinb. Dubl. Phil. Mag. **13**(87), 964–975 (1932). doi:10.1080/14786443209462002
36. H.U. Eckert, Diffusion theory of the electrodeless ring discharge. J. Appl. Phys. **33**(9), 2780–2788 (1962). doi:10.1063/1.1702549
37. B.B. Henriksen, D.R. Keefer, M.H. Clarkson, Electromagnetic field in electrodeless discharge. J. Appl. Phys. **42**(13), 5460–5464 (1971). doi:10.1063/1.1659964
38. V. Vahedi, M.A. Lieberman, G. DiPeso, T.D. Rognlien, D. Hewett, Analytic model of power deposition in inductively coupled plasma sources. J. Appl. Phys. **78**(3), 1446–1458 (1995). doi:10.1063/1.360723

39. M. Li, H.-M. Wu, Y. Chen, Two-dimensional simulation of inductive plasma sources with self-consistent power deposition. IEEE Trans. Plasma Sci. **23**(4), 558–562 (1995). doi:10.1109/27.467975
40. J.T. Gudmundsson, M.A. Lieberman, Magnetic induction and plasma impedance in a planar inductive discharge. Plasma Sources Sci. Technol. **7**(2), 83–95 (1998). doi:10.1088/0963-0252/7/2/002
41. I.M. El-Fayoumi, I.R. Jones, Theoretical and experimental investigations of the electromagnetic field within a planar coil, inductively coupled RF plasma source. Plasma Sources Sci. Technol. **7**(2), 162–178 (1998). doi:10.1088/0963-0252/7/2/011
42. I.M. El-Fayoumi, I.R. Jones, M.M. Turner, Hysteresis in the E- to H-mode transition in a planar coil, inductively coupled rf argon discharge. J. Phys. D Appl. Phys. **31**(21), 3082–3094 (1998). doi:10.1088/0022-3727/31/21/014
43. M.M. Turner, M.A. Lieberman, Hysteresis and the E-to-H transition in radiofrequency inductive discharges. Plasma Sources Sci. Technol. **8**(2), 313–324 (1999). doi:10.1088/0963-0252/8/2/312
44. K. Nanbu, Probability theory of electron-molecule, ion-molecule, moleculemolecule, and Coulomb collisions for particle modeling of materials processing plasmas and cases. IEEE Trans. Plasma Sci. **28**(3), 971–990 (2000). doi:10.1109/27.887765
45. S.K. Nam, D.J. Economou, Two-dimensional simulation of a miniaturized inductively coupled plasma reactor. J. Appl. Phys. **95**(5), 2272–2277 (2004). doi:10.1063/1.1644043
46. Y. Takao, N. Kusaba, K. Eriguchi, K. Ono, Two-dimensional particle-in-cell Monte Carlo simulation of a miniature inductively coupled plasma source. J. Appl. Phys. **108**(9), 093308–093309 (2010). doi:10.1063/1.3506536
47. A.J. Shuskus, M.E. Cowher, U.S. Patent 4,421,592, 20 Dec 1983
48. R. Patrick, F. Bose, P. Schoenborn, H. Toda, U.S. Patent 5,401,350, 28 Mar 1995
49. C.S. Wong, R. Mongkolnavin, *Elements of Plasma Technology* (Springer, Singapore, 2016)
50. I.M. El-Fayoumi, I.R. Jones, The electromagnetic basis of the transformer model for an inductively coupled RF plasma source. Plasma Sources Sci. Technol. **7**(2), 179–185 (1998). doi:10.1088/0963-0252/7/2/012
51. S.P. Chew, *Plasma Enhanced Physical Vapor Deposition of Titanium Nitride Thin Film*, M.Sc. dissertation. (University of Malaya, 2002)
52. A.M. Daltrini, S.A. Moshkalev, T.J. Morgan, R.B. Piejak, W.G. Graham, Plasma power measurement and hysteresis in the E–H transition of a RF inductively coupled plasma system. Appl. Phys. Lett. **92**(6), 061504 (2008). doi:10.1063/1.2844885
53. H.-C. Lee, C.-W. Chung, Effect of Electron energy distribution on the hysteresis of plasma discharge: theory, experiment, and modeling. Sci. Rep. **5**, 15254 (2015). doi:10.1038/srep15254
54. N. Kang, F. Gaboriau, Simple modeling of the E–H mode transition and hysteresis in low pressure argon ICP discharges for direct comparison with experiments. J. Phys. D Appl. Phys. **44**(44), 442001 (2011). doi:10.1088/0022-3727/44/44/442001
55. U. Kortshagen, N.D. Gibson, J.E. Lawler, On the E–H mode transition in RF inductive discharges. J. Phys. D Appl. Phys. **29**(5), 1224–1236 (1996). doi:10.1088/0022-3727/29/5/017
56. K.P. Shamrai, V.P. Pavlenko, V.B. Taranov, Excitation, conversion and damping of waves in a helicon plasma source driven by an $m = 0$ antenna. Plasma Phys. Control. Fusion **39**(3), 505–529 (1997). doi:10.1088/0741-3335/39/3/011
57. M. Sadiku, *Elements of electromagnetics*, 3rd edn. (Oxford University Press, New York, 2001)
58. J.T. Gudmundsson, *Notes on the Electron Excitation Rate Coefficients for Argon and Oxygen Discharge* (Report RH-21-2002, University of Iceland, 2002)
59. K.K. Jayapalan, O.-H. Chin, The effects of neutral gas heating on H mode transition and maintenance currents in a 13.56 MHz planar coil inductively coupled plasma reactor. Phys. Plasmas **19**(9), 093501 (2012). doi:10.1063/1.4750055

60. K.N. Ostrikov, I.B. Denysenko, E.L. Tsakadze, S. Xu, R.G. Storer, Diagnostics and two-dimensional simulation of low-frequency inductively coupled plasmas with neutral gas heating and electron heat fluxes. J. Appl. Phys. **92**(9), 4935–4946 (2002). doi:10.1063/1.1510598
61. G. Cunge, B. Crowley, D. Vender, M.M. Turner, Characterization of the E–H transition in a pulsed inductively coupled plasma discharge with internal coil geometry: bi-stability and hysteresis. Plasma Sources Sci. Technol. **8**(4), 576–586 (1999). doi:10.1088/0963-0252/8/4/309
62. H. Amemiya, Sheath formation criterion and ion flux for non-Maxwellian plasma. J. Phys. Soc. Jpn. **66**(5), 1335–1338 (1997). doi:10.1143/JPSJ.66.1335
63. K.K. Jayapalan, O.-H. Chin, Effect of neutral gas heating on the wave magnetic fields of a low pressure 13.56 MHz planar coil inductively coupled argon discharge. Phys. Plasmas **21**(4), 043510 (2014). doi:10.1063/1.4872004
64. I.M. El-Fayoumi, *The Electrical and Electromagnetic Properties of a Low Frequency, Inductively Coupled RF Plasma Source*, Ph.D. thesis. (Flinders University of South Australia, 1996)
65. M. Boas, *Mathematical Methods in Physical Sciences*, 2nd edn. (John Wiley & Sons, Hoboken, 1983)
66. E. Kreyszig, *Advanced Engineering Mathematics*, 8th edn. (John Wiley & Sons, Hoboken, 1998)
67. M. Sadiku, *Numerical Techniques in Electromagnetics with MATLAB*, 3rd edn. (CRC Press, Boca Raton, 2009)
68. R. Herman, *A Second Course in Ordinary Differential Equations: Dynamical Systems and Boundary Value Problems* (2008), http://people.uncw.edu/hermanr/mat463/ODEBook/Book/ODE_Main.pdf. Accessed 3 Jan 2016
69. F. Atkinson, A. Mingarelli, *Multiparameter Eigenvalue Problems Sturm-Liouville Theory* (CRC Press, Boca Raton, 2011)
70. C.Y.M. Maurice, *Inductively Coupled Plasmas: Ion Dynamics and Interactions with Bone Tissue*, Ph.D. thesis. (Technische Universiteit Eindhoven, 2003)
71. G.G. Lister, Y.M. Li, V.A. Godyak, Electrical conductivity in high-frequency plasmas. J. Appl. Phys. **79**(12), 8993–8997 (1996). doi:10.1063/1.362631
72. M. Hayashi, *Recommended Values of Transport Cross Sections for Elastic Collision and Total Collision Cross Section of Electrons in Atomic and Molecular Gases* (IPPJ-AM-19, Nagoya University, 1981)
73. D.L. Book, *NRL Plasma Formulary. Revision (No . NRL-PUB-177-4405)* (Naval Research Lab, Washington D.C., 1990)
74. H. Li, C. Xiao, E. Zhang, A.K. Singh, A. Hirose, Measurement of neutral gas temperature in inductively coupled plasmas. Radiat. Eff. Defect. S. **166**(6), 399–407 (2011). doi:10.1080/10420150.2011.566876
75. A. Fruchtman, Neutral depletion in a collisionless plasma. IEEE Trans. Plasma Sci. **36**(2), 403–413 (2008). doi:10.1109/tps.2008.918777
76. A. Fruchtman, G. Makrinich, P. Chabert, J.M. Rax, Enhanced plasma transport due to neutral depletion. Phys. Rev. Lett. **95**(11), 115002 (2005). doi:10.1103/physrevlett.95.115002
77. L. Liard, J.L. Raimbault, J.M. Rax, P. Chabert, Plasma transport under neutral gas depletion conditions. J. Phys. D Appl. Phys. **40**(17), 5192–5195 (2007). doi:10.1088/0022-3727/40/17/026
78. D. O'Connell, T. Gans, D.L. Crintea, U. Czarnetzki, N. Sadeghi, Neutral gas depletion mechanisms in dense low-temperature argon plasmas. J. Phys. D Appl. Phys. **41**(3), 035208 (2008). doi:10.1088/0022-3727/41/3/035208
79. M. Shimada, G.R. Tynan, R. Cattolica, Neutral gas density depletion due to neutral gas heating and pressure balance in an inductively coupled plasma. Plasma Sources Sci. Technol. **16**(1), 193–199 (2007). doi:10.1088/0963-0252/16/1/024

80. H. Li, *Measurements of Electron Energy Distribution Function and Neutral Gas Temperature in an Inductively Coupled Plasma*, M.Sc. dissertation. (University of Saskatchewan, 2006)
81. J.A. Stittsworth, A.E. Wendt, Reactor geometry and plasma uniformity in a planar inductively coupled radio frequency argon discharge. Plasma Sources Sci. Technol. **5**(3), 429–435 (1996). doi:10.1088/0963-0252/5/3/011
82. M. Shimada, G.R. Tynan, R. Cattolica, Neutral depletion in inductively coupled plasmas using hybrid-type direct simulation Monte Carlo. J. Appl. Phys. **103**(3), 033304 (2008). doi:10.1063/1.2836938
83. K. Suzuki, K. Nakamura, H. Ohkubo, H. Sugai, Power transfer efficiency and mode jump in an inductive RF discharge. Plasma Sources Sci. Technol. **7**(1), 13–20 (1998). doi:10.1088/0963-0252/7/1/003
84. G.P. Davis, R.A. Gottscho, Measurement of spatially resolved gas-phase plasma temperatures by optical emission and laser-induced fluorescence spectroscopy. J. Appl. Phys. **54**(6), 3080–3086 (1983). doi:10.1063/1.332514
85. V.M. Donnelly, M.V. Malyshev, Diagnostics of inductively coupled chlorine plasmas: measurements of the neutral gas temperature. Appl. Phys. Lett. **77**(16), 2467–2469 (2000). doi:10.1063/1.1318727
86. J. Wormhoudt, A.C. Stanton, A.D. Richards, H.H. Sawin, Atomic chlorine concentration and gas temperature measurements in a plasma etching reactor. J. Appl. Phys. **61**(1), 142–148 (1987). doi:10.1063/1.338846
87. M. Shimada, *Experimental and Numerical Studies of Neutral Gas Depletion in an Inductively Coupled Plasma*, Ph.D. thesis. (University of California San Diego, 2006)
88. E.E. Whiting, An empirical approximation to the Voigt profile. J. Quant. Spectrosc. Radiat. Transfer **8**(6), 1379–1384 (1968). doi:10.1016/0022-4073(68)90081-2
89. J.P. Barrett, *Electricity at the Columbian Exposition* (R.R. Donnelley, Ann Arbor, Michigan, 1894)
90. P.C. Hewitt, U.S. Patent 843,533, 5 Feb 1907
91. J.M. Anderson, U.S. Patent 3,521,120, 21 Jul 1970
92. D.O. Wharmby, Electrodeless lamps for lighting: a review. IEE Proc-A **140**(6), 465–473 (1993). doi:10.1049/ip-a-3.1993.0071
93. F.M. Espiau, C.J. Joshi, Y. Chang, U.S. Patent 7,362,056, 22 Apr 2008
94. B. Zhang, X.-Q. Yu, U.S. Patent 20,100,171,443, 8 Jul 2010
95. A. Kraj, D.M. Desiderio, N.M. Nibbering, *Mass Spectrometry: Instrumentation, Interpretation, and Applications*, ed. By R. Ekman, J. Silberry, A.M. Westman-Brinkmalm (John Wiley & Sons Inc., Hoboken, 2009)
96. J. Hunt, *Celebrating 25 Years of Inductively Coupled Plasma-Mass Spectrometry* (American Laboratory, 2008), http://www.americanlaboratory.com/913-Technical-Articles/764-Celebrating-25-Years-of-Inductively-Coupled-Plasma-Mass-Spectrometry/. Accessed 30 Jan 2016
97. K. Morton, Agilent ICP-MS Literature at a Glance. Agilent ICP-MS J. **14**, 6–7 (2011). https://www.agilent.com/cs/library/periodicals/Public/5990_7194EN.pdf. Accessed 30 Jan 2016
98. H.E. Taylor, *Inductively coupled plasma-mass spectrometry: practices and techniques* (Academic Press, San Diego, 2001)
99. S. Greenfield, I.L. Jones, C.T. Berry, High-pressure plasmas as spectroscopic emission sources. Analyst **89**, 713–720 (1964). doi:10.1039/an9648900713
100. T.H. Maugh, The 1983 Pittsburgh conference: A special instrumentation report: quadrupoles appears in new instruments. Science **220**(4593), 178–179 (1983). doi:10.1126/science.220.4593.178
101. R.C. Chittick, J.H. Alexander, H.F. Sterling, The preparation and properties of amorphous silicon. J. Electrochem. Soc. **116**(1), 77–81 (1969). doi:10.1149/1.2411779
102. P.G. Le Comber, W.E. Spear, Electronic transport in amorphous silicon films. Phys. Rev. Lett. **25**(8), 509–511 (1970). doi:10.1103/PhysRevLett.25.509

103. D.E. Meyer, Radio-frequency plasma chemical vapor deposition growth of diamond. J. Vac. Sci. Technol. A **7**(3), 2325–2327 (1989). doi:10.1116/1.575936
104. W.S. Liew, *Diamondlike Carbon Thin Film Deposition Using a RF Planar Coil Inductively Coupled Plasma System*, M.Sc. dissertation. (University of Malaya, 2001)
105. S. Xu, Z. Tskadze, J.D. Long, K. Ostrikov, N. Jiang, in *COMMAD 2002: Low Temperature Growth of Vertically Aligned Carbon Nanofibres in a Low Frequency Inductively Coupled Plasma Reactor*, ed. M. Gal. 2002 Conference on Optoelectronic and Microelectronic Materials and Devices, Sydney, December 2002. COMMAD 2002 Proceedings (IEEE Inc., 2002), pp. 177–180. doi:10.1109/commad.2002.1237221
106. V.I. Merkulov, A.V. Melechko, M.A. Guillorn, M.L. Simpson, D.H. Lowndes, J.H. Whealton, R.J. Raridon, Controlled alignment of carbon nanofibers in a large-scale synthesis process. Appl. Phys. Lett. **80**(25), 4816–4818 (2002). doi:10.1063/1.1487920
107. K.H. Ng, *Development of a Planar Coil Radio Frequency Inductively Coupled Plasma System for Material Processing*, Ph.D. thesis. (University of Malaya, 2008)
108. Y. Qin, F. Li, D. Liu, H. Yan, J. Wang, D. He, The structure and optical properties of silicon nanowires prepared by inductively coupled plasma chemical vapor deposition. Mater. Lett. **65**(7), 1117–1119 (2011). doi:10.1016/j.matlet.2011.01.033
109. H. Huang, Y.C. Lee, O.K. Tan, W. Zhou, N. Peng, Q. Zhang, High sensitivity SnO_2 single-nanorod sensors for the detection of H_2 gas at low temperature. Nanotechnology **20** (11), 115501 (2009). doi:10.1088/0957-4484/20/11/115501
110. H.G. Jain, H. Karacuban, D. Krix, H.-W. Becker, H. Nienhaus, V. Buck, Carbon nanowalls deposited by inductively coupled plasma enhanced chemical vapor deposition using aluminum acetylacetonate as precursor. Carbon **49**(15), 4987–4995 (2011). doi:10.1016/j.carbon.2011.07.002
111. B.K. Gale, *Dry Etching*, http://www.eng.utah.edu/~gale/mems/Lecture%208%20Dry%20Etching.pdf. Accessed 12 Jan 2016
112. A. Jacob, U.S. Patent 3,795,557, 5 Mar 1974
113. N. Hosokawa, R. Matsuzaki, T. Asamaki, RF Sputter-etching by fluoro-chloro-hydrocarbon gases. Jpn. J. Appl. Phys. **13**(S2–1), 435–438 (1974). doi:10.7567/jjaps.2s1.435
114. V. Srivastav, R. Pal, B.L. Sharma, A. Naik, D.S. Rawal, V. Gopal, H.P. Vyas, Etching of mesa structures in HgCdTe. J. Electron. Mater. **34**(11), 1440–1445 (2005). doi:10.1007/s11664-005-0203-5
115. M. Lieberman, *Plasma Processing for Nanoelectronics—History and Prospects* (2010), http://www.eecs.berkeley.edu/~lieber/LiebGEC100831crop.pdf. Accessed 24 Jan 2016
116. F. Keeble, U.S. Patent 4,844,775, 4 Jul 1989
117. F.H. Bell, O. Joubert, G.S. Oehrlein, Y. Zhang, D. Vender, Investigation of selective SiO_2-to-Si etching in an inductively coupled high-density plasma using fluorocarbon gases. J. Vac. Sci. Technol. A **12**(6), 3095–3101 (1994). doi:10.1116/1.578942
118. C.-C. Yu, C.-F. Chu, J.-Y. Tsai, H.W. Huang, T.-H. Hsueh, C.-F. Lin, S.-C. Wang, Gallium nitride nanorods fabricated by inductively coupled plasma reactive ion etching. Jpn. J. Appl. Phys. **41**(8B), L910–L912 (2002). doi:10.1143/jjap.41.l910
119. S.-J. Chen, C.-M. Chang, J.-S. Kao, F.-R. Chen, C.-H. Tsai, Fabrication of ZnO photonic crystals by nanosphere lithography using inductively coupled-plasma reactive ion etching with $CH_4/H_2/Ar$ plasma on the ZnO/GaN heterojunction light emitting diodes. J. Vac. Sci. Technol. A **28**(4), 745–749 (2010). doi:10.1116/1.3357282
120. Ü. Sökmen, A. Stranz, S. Fündling, S. Merzsch, R. Neumann, H.H. Wehmann, E. Peiner, A. Waag, Shallow and deep dry etching of silicon using ICP cryogenic reactive ion etching process. Microsyst. Technol. **16**(5), 863–870 (2010). doi:10.1007/s00542-010-1035-7

Chapter 11
Plasma Polymerization: Electronics and Biomedical Application

Avishek Kumar, Daniel Grant, Surjith Alancherry, Ahmed Al-Jumaili, Kateryna Bazaka and Mohan V. Jacob

11.1 Introduction

Polymer thin films have received great interest in recent past because of their wide range of physical, chemical, mechanical, electrical and biological properties, which make them well suited for innumerable applications in fields of mechanics, optics, and electronics [1–3]. Polymer thin films can be fabricated using a variety of methods. Based on the nature of the fabrication process, these methods can be broadly divided into two categories: "wet" solution-based processing, e.g., spin coating and dip coating, or "dry" methods, e.g., physical vapor deposition (PVD) and chemical vapor deposition (CVD). Plasma polymerization is a type of CVD used extensively to synthesize polymer thin films from organic and inorganic precursors, where plasma discharge is used to catalyze the chemical reactions leading to formation of the polymer structure [4, 5]. Hence, plasma polymers can be generally defined as thin films of material which are formed as a result of interaction of monomer (organic and inorganic) vapor in the plasma (glow) discharge [6]. Although the word *polymer* is used, this special class of material differs from conventional polymers in several respects. Most notably, plasma polymers generally lack regular repeating unit, their chains are often short, randomly branched, and highly cross-linked. As the result of their unique chemical structure, these polymers generally do not exhibit distinct glass transition temperatures and have high elastic moduli, excellent mechanical, thermal and chemical stability, and outstanding adhesion to a variety of substrates [5]. Their chemical composition and thickness can be easily controlled by controlling the deposition parameters and the nature of

A. Kumar · D. Grant · S. Alancherry · A. Al-Jumaili · K. Bazaka · M.V. Jacob (✉)
Electronics Materials Lab, College of Science and Engineering,
James Cook University, 4811 Townsville, QLD, Australia
e-mail: Mohan.Jacob@jcu.edu.au

K. Bazaka
Queensland University of Technology, Brisbane, QLD, Australia

R.S. Rawat (ed.), *Plasma Science and Technology for Emerging Economies*,
DOI 10.1007/978-981-10-4217-1_11

the precursor, affording much greater degree of versatility and control compared to other synthesis methods. Furthermore, even polymers that have limited solubility can be deposited as thin films using this method. Not surprisingly, plasma polymers have found a host of applications [7], from bioactive to chemically inert coatings for medical devices [8–10], to anti-corrosion coatings for metals [11, 12], to dielectric and encapsulating layers in thin film electronics devices [13–15].

The distinct properties of plasma polymers arise from the mechanism of polymerization in plasma environment being distinctly different from conventional thermochemical polymerization. Under plasma conditions, the polymer formation follows atomic or elemental polymerization, whereas conventional polymerization is molecular in nature [16]. Monomers under the plasma are fragmented partially or fully to their individual constituents and polymerization proceeds by recombination of these fragments on a surface, whereas conventional polymerization proceeds by addition of monomers to growing polymer chain. Plasma polymerization involves reaction among surface species and between plasma and surface species [17, 18]. Depending on the processing conditions, polymer formation can take place via (1) plasma-state polymerization, and (2) plasma-induced polymerization [19]. The mechanism of plasma-state polymerization is similar to atomic or elemental polymerization, i.e., when passing through glow discharge, precursor units are fragmented partially or completely into individual atoms, which get reassembled into a polymer-like structure, e.g., by free radical termination reactions on the substrate surface. Plasma-induced or plasma-initiated polymerization refers to a mechanism in which monomers having polymerizable structures, such as double bond, triple bond, or cyclic structures undergo polymerization initiated by plasma. It is similar to conventional polymerization in terms of polymer growth, yet it is triggered by unconventional plasma-generated reactive species. One of the key differences between these mechanisms of plasma polymerization is that in the case of plasma-state polymerization, gaseous phase by-products are formed, whereas theoretically in plasma-induced polymerization, there should be no by-products. However it is unlikely that all of the feed can be converted to polymers in plasma-induced mechanism. The polymerization in plasma-enhanced chemical vapor deposition (PECVD) involves both plasma-induced and plasma-state polymerization.

The physicochemical properties of plasma polymer films can be easily tailored by independently controlling the deposition parameters such as excitation frequency and power, deposition pressure, temperature, monomer flow rate, and reactor geometry [20, 21]. Indeed, plasma forms a highly reactive environment suitable for processing of virtually any type of organic precursor and conductive, dielectric and insulating substrates. Furthermore, the technique is a low-temperature process which realizes the fabrication of polymer thin films directly on various types of temperature-sensitive flexible plastic substrates with excellent quality of interface characteristics [22]. In addition, the process is single step, solvent free, human health and environmental friendly, and can be easily scaled up [23].

This chapter aims to present a concise review of PECVD technique, with a more in-depth discussion of the principles of plasma generation, mechanisms of plasma

polymer formation, and their dependence on most common processing variables. Selected examples of plasma polymers are presented to highlight the areas where plasma polymers have found or have the potential to find applications, focusing particularly on biomedical and electronics fields.

11.2 Generation of Plasma

Plasma polymerization requires relatively low processing temperatures, as higher temperature deposition may be detrimental to the quality of the film as well as limiting with regard to the substrate. Plasmas for polymerization are most commonly generated at low pressures by exposing neutral gas molecules or monomer precursor vapor to an electric field [24, 25]. The benefits of low-pressure polymerization include even distribution of plasma inside the deposition chamber which allows for highly uniform treatment of three-dimensional objects, the ability to treat oxidation-sensitive substrates, including metals and organic thin film electronic devices. One of the key disadvantages of low-pressure systems lies in the requirement for complex and expensive vacuum technology, which significantly limits its integration into roll-to-roll processing or other high-throughput systems. The size of the reactor may also place restrictions on the scalability of the process. Atmospheric-pressure discharges provide a more promising alternative for integration into existing manufacturing processes, as they do not require vacuum or deposition reactor. However, unless plasma arrays are used, the deposition area is limited to approximately 8–12 mm^2, which may on one hand facilitate local treatment, yet may also prove to be a hindrance if uniform coating or deposition in deep grooves is desired.

The chemical, physical, and electrical effects generated in plasma will differ between different plasma systems. In general, plasmas represent partially or fully ionized state of a gas and are comprised of free electrons, ions, free radicals, photons, and atoms in the ground and excited states [26]. When significant amount of energy is delivered into the system dissociation of neutral gas molecules takes place, with the degree of dissociation directly linked to the input energy. The minimum amount of energy required is to be greater or equal than the bond dissociation energy of precursor's monomer molecules. The energy can be delivered through thermal excitation, adiabatic compression, excitation using charged beams or by application of an electric field [24]. The latter is regarded as the most convenient way of generating and sustaining plasma in laboratory, with the process generally known as the glow discharge technique [27]. Generally, the glow discharge plasma operates at a lower pressure and uses a direct current (DC), radio frequency (RF), or microwave (MW) frequency signal for exciting the free electron and reactant molecule to generate the plasma [19]. It is worth noting that the characteristic behavior of plasmas differs depending on the type of source used to generate the glow discharge. These characteristics will be discussed in more detail in Sect. 2.2.

The key mechanism behind the generation of plasma is the inelastic collision of free electrons and the resultant transfer of energy from the highly energetic electrons to the reactant molecules, which in turn leads to subsequent molecule dissociation, rearrangement, and recombination with other species within the plasma volume. The ignition and stability of plasmas is therefore dependent on the balance of input energy and species. Plasmas used for polymerization are non-equilibrium, with low degree of ionization and low ion temperature (ranging from fractions to few tens of electron volt). These plasmas are regarded as "cold". Increasing the input energy shifts plasma towards the thermodynamic equilibrium. Such plasmas have a very high degree of ionization as well as high electron and ion temperature, and are considered "hot" ($T_{gas} > 5000$ K) [28]. The excessively high temperatures of hot plasmas preclude their use for polymer fabrication, and as such any further discussion is outside the scope of this chapter.

Cold plasmas have received considerably more attention than hot plasma, with vast number of applications stretching from material synthesis, surface modification, volume related transformation, carrier functions, and particle sources, to name a few [24].

11.2.1 Mechanisms of Plasma Polymerization

Physical and chemical environment in plasma reactor determines the film growth process. As briefly mentioned in Sect. 11.1, mechanisms of plasma polymerization generally differ from that observed in conventional thermochemical polymerization [17, 29]. First, plasma polymerization is initiated by the impact of highly energetic electrons generated by the applied electric field. Second, there are fundamental differences in the nature of building units from which polymers are formed. In conventional polymerization, intact monomer units are the primary building blocks for the growing polymer; whereas in plasma polymerization, the monomer units often undergo significant fragmentation, rearrangement, and reassembly prior to being incorporated into the polymer chain. This leads to a significant degree of heterogeneity among the building blocks, and consequently a relatively high degree of nanoscale non-uniformity in the assembled plasma polymer structure. Plasma deposition mechanism can be of neutral species grafting or ion adsorption. The dominant mechanism depends strongly on the chemical structure of the monomers [30]. In low-pressure plasma, following deposition modes can be found

(a) **Radical chain growth polymerization**: Neutral species consists of both radicals and intact monomers. This type of polymerization is initiated by radicals created by exposing monomer molecules to plasma. The radicals are generated by bond scission, C–C or C–H in case of hydrocarbon monomers, and are highly reactive with short lifetimes. This type of polymerization proceeds by continuous addition or grafting of neutral (N) species [31]:

$$\begin{array}{lcll} N + \text{Plasma} & \rightarrow & \text{Fragments}^{\cdot} & \rightarrow \text{Initiation} \\ \text{Fragments}^{\cdot} + N & \rightarrow & \text{Fragment} - N^{\cdot} & \\ \text{Fragments} - N^{\cdot} + N & \rightarrow & P^{\cdot} & \rightarrow \text{Propagation} \\ 2\,P^{\cdot} & \rightarrow & P{-}P & \rightarrow \text{Termination} \end{array}$$

This mechanism is dominant in polymerization of unsaturated monomers particular at low power [32]. The neutrals arrive at surface with relatively lower energy than ions and they react with surface radical sites by either radical–radical termination or radical propagation. Surface radical sites are created by UV radiation or ion impact. Chain termination takes place by free radical recombination, disproportionation, or radical transfer. Recombination of radicals and plasma-generated UV irradiation give rise to cross-linking in plasma polymers. The formed polymers are short and branched, with a relatively low value of the kinetic chain length. Kinetic chain length (v) is a ratio of rate of chain propagation to chain termination, which provides an indication of the number of monomer units added before the chain terminates. The rate of chain termination increases with increasing initiator concentration and decreases with increasing monomer concentration [33]. In the case of low pressure plasma, the concentration of initiator is high and that of the monomer is low, which leads to short kinetic chain length [34].

(b) **Fragmentation and recombination plasma polymerization**: In this type of plasma polymerization, bombardment with high-energy particles and radiation result in significant fragmentation of monomer molecules. The resulting reactive fragments then recombine to form polymers of random composition and high degree of irregularity.

$$\begin{array}{lcl} \text{ABCDEF} + \text{Plasma} & \rightarrow & \text{A} + \text{B} + \text{C} + \text{DE} + \text{F}\,(\text{Fragmentation}) \\ \text{n}\,(\text{A} + \text{B} + \text{C} + \text{DE} + \text{F}) & \rightarrow & (\text{FADEC})_{\text{n}}(\text{Recombination}) \end{array}$$

The degree of fragmentation is directly related to the energy invested per monomer molecule, and as such is influenced by both the input energy and the monomer flow [35]. Typical reactions include H_2, CO_2, and CO abstraction, and aromatic ring opening [36].

(c) **Ionic plasma polymerization**: This type of polymer synthesis involves formation of mainly C^+ ions or ion pair formation [37]. These species are created by inelastic collision of monomer molecules with electrons. Ion energy plays an important role in deposition of saturated monomers, as the ion energy is reduced the deposition rate falls [38]. Sticking probability of ions is dependent on their energy and increases with increase in energy [39]. Ions arrive at surface with higher energy which aides them in chemical reaction with surfaces without any preexisting radical sites. Ionic mechanism is dominant when saturated monomers are polymerized [32]. The cationic mechanism is one of the most probable mechanisms of chain propagation in plasma polymerization model

founded on an ionic mechanism [40]. The cationic mechanism proceeds in the following manner:

$$\begin{aligned} C + e^- &\rightarrow C^+ + e^- + e^- \quad \text{(Initiation)} \\ C^+ + C &\rightarrow CC^+ \\ CC^+ + nC &\rightarrow C\,[C_n]\,C^+ \quad \text{(Chain propagation)} \end{aligned}$$

Additional positive charges are created in polymer by collision with energetic plasma-generated particles, e.g., ions and electrons. These charge sites serve as locations for monomer grafting, which results in cross-linking. Termination takes place by ion–electron recombination or charge transfer to another monomer. Nucleophilic monomers have been shown to polymerize by cationic mechanism [41].

The energy with which depositing species arrive at the surface determines structure of resulting polymer films. In deposition by ionic mechanism by, high-energy impacts lead to random, highly cross-linked structure whereas the film formed by radical mechanism are more dense and less cross-linked [32]. Both radical chain growth polymerization and fragmentation-recombination polymerization are in competition with each other. High energy per unit monomer leads to fragmentation-recombination polymerization. The radical mechanism is most applicable in radiofrequency range whereas in low-frequency region, ionic mechanism should dominate as ions can follow the changing electric field [31]. In polymerization of unsaturated monomers increasing, the RF power shifts the mechanism from radical to ionic deposition because of the increased fragmentation of monomers. Which mechanism dominates also depends on the relative concentration of radicals to ions in a given plasma system.

11.2.2 Types of Glow Discharge

Plasma glow discharge can be generated by different techniques and sources in a reactor. The types of plasma discharge can be classified according to frequency used for generation of glow discharge

(a) **Direct current plasma discharge**: The conventional DC plasma reactor comprises two parallel plate electrodes arranged inside a vacuum chamber powered with DC electric signal. A DC discharge is formed only when DC voltage of sufficient strength (i.e., able to form a continuous current between the electrodes) is applied between cathode and anode. By regulating the voltage of the input DC signal, various types of discharges such as Townsend discharge, subnormal glow discharge, normal discharge, arc discharge, etc. could be created inside the discharge tube [24]. Figure 11.1 shows the various kinds of DC discharge and the relationship between voltage and current.

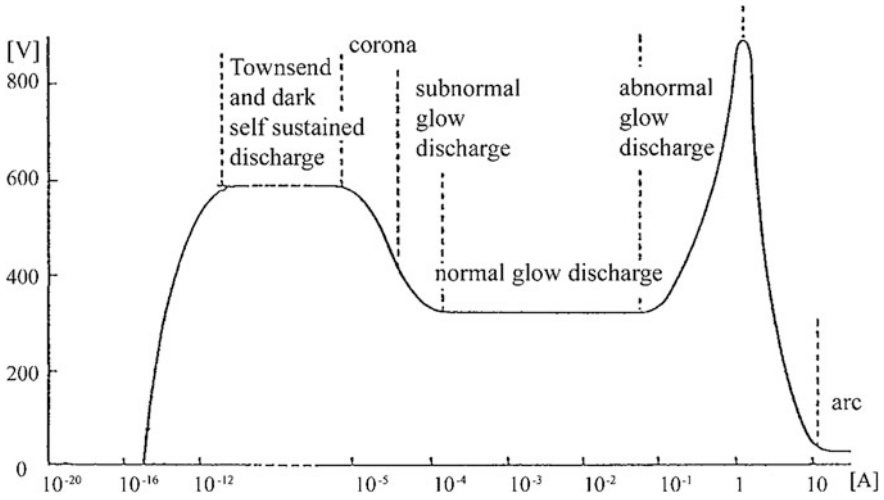

Fig. 11.1 The dependence of voltage upon current for various kinds of dc discharges. Reproduced from previous work with permission from Ref. [24]

A DC signal of sufficient strength will accelerate electrons within the gas, resulting in inelastic collisions between the electrons and the neutral molecules, and consequently excitation and ionization of the gas molecules. The ionization creates electrons and ions which sustain the discharge, whereas the de-excitation of excited species creates the characteristic glow. Apart from this, the secondary ions liberated from the cathode as a result of collisions between electrons and cathode help sustain the plasma. However, when the potential is sufficiently high, the ion bombardment can release atoms of cathode material along with the secondary electrons through sputtering.

A low-pressure DC glow discharge produces characteristic luminous bands. The bands are identified as cathode dark space (region close to cathode having strong electric field), negative glow (characterized by constant and slightly positive potential), Faraday dark space (slightly negative electric field), positive column (slightly negative electric filed), and anode glow inside the discharge volume. However DC glow discharge is not commonly used in polymer synthesis applications due to several reasons. First, in a DC discharge, more energy is consumed for accelerating ions than for creating reactive species [42]. Also, DC discharges are characterized by high-energy ion collisions that may damage the substrate as well as the growing structure [43]. As the power is directly coupled to the electrode, there is no provision to independently control the substrate bias and reduce the effect of ion collisions.

(b) **Alternating current plasma discharge**: Electrode polarity gets alternated every half cycle which determines the mechanism of plasma discharge. At lower frequency (below 100 Hz), it is principally DC discharge with alternating

polarity. As the frequency increases, the movement of ions cannot follow the change in polarity of electrodes. At the frequency above 500 kHz, electrode polarity never maintains itself for sufficiently long for the ions and electrons to be swept entirely across the inter-electrode region. The positive ions are massive and cannot follow the changing electrode polarity. However, as the electrons are much lighter, they are swept through inter-electrode space in vicinity of driving electrode in positive half cycle. Thus, an electron deficient region that is formed as a result of this process (termed plasma sheath) results in negative voltage on the walls of electrode with respect to plasma body [19, 44].

Discharges excited at high frequency of current are of utmost importance for technical and industrial application. Most of the plasma polymerization systems work at RF frequency of 13.56 MHz. Microwave frequency (MW) plasmas have become of great interest in recent years in applications where high deposition rate and high fragmentation of precursor material are required [45]. In order to sustain the high-frequency plasmas in RF and MW frequency region, the wavelength of the exciting signal should be comparable with the dimensions of the plasma reactor. However, the operational frequencies for RF and MW systems are restricted by the International Telecommunications Union-approved, Industrial, Scientific and Medical (ISM) frequencies [46].

A typical RF plasma system should have three necessary components to generate plasma. They are the RF generator, impedance matching network and reactor chamber with electrodes. The matching network minimizes the reflected RF power by matching the impedance of the generator to that of the discharge [47]. There are mainly two types of RF discharges classified based on the nature of coupling of RF power to the reactor. They are capacitively coupled configuration (CCP) and inductively coupled configuration (ICP).

The CCP configuration comprises of internal parallel electrodes in contact with the plasma or external electrodes outside the discharge tube. The presence of "self-bias" field is the unique feature of CCP discharge [48]. The CCP configuration can generate electron densities up to 10^9–10^{10} cm^{-3} and plasma density 10^{11} cm^{-3} [49].

The inductively coupled configuration (ICP) uses magnetic field generated by a transformer from a RF current in a conductor to excite the plasma [24]. The advantages of ICP over CCP are the very high electron density (10^{12} cm^{-3}) and plasma density (10^{14} cm^{-3}), electrodeless discharge, and independent control over substrate bias [42, 49].

The MW plasma systems use electromagnetic signals within the microwave regime (frequency above 300 MHz) to generate discharge. The most commonly used excitation frequency for microwave discharge is 2.45 GHz. In order to create MW plasma, the following components are essentially required: a microwave power source, circulator, directional couplers, matching circuit, and microwave to plasma applicator. There are mainly two types of microwave plasma-enhanced chemical vapor deposition (MWPECVD) systems commonly used for fabricating carbon nanostructures. They are NIRIM (National Institute of Research of Organic

Materials) type and ASTex (Applied Science and Technology, Inc.) type [50]. However, the detailed discussion of these is outside the scope of this chapter.

The MW discharge are electrodeless and can operate at pressures from 10^{-5} Torr to atmospheric pressure and power ranging from several watts to hundreds of kilo watts [51]. The microwave plasma produces high electron densities of 10^{13} cm^{-3} and high degree of ionization compared to low-frequency plasma [52]. Apart from this, microwave plasma exhibits intense emission in near ultra violet region which triggers the simultaneous action of plasma-chemical and photochemical processes, which realize high growth rate together with remarkable properties of the deposited material [53]. The absorbed power depends on the electron neutral collision frequency, and is very high, at up to 90% of the incident power [51].

Wertheimer and Moisan [54] compared the behavior of microwave and lower frequency plasma and reported that the former have significantly higher fraction of high-energy electrons and very high deposition rate (about ten times higher) compared to the latter. According to Musil et al. [53] the electron energy distribution and activation of plasma inside the plasma volume is determined by the ratio υ/ω, where υ is the electron neutral collisional frequency and ω is the angular frequency of the applied electromagnetic field. However, the plasma created by the low frequency and microwave have entirely different υ/ω and electron energy distribution. For $\upsilon/\omega \geq 1$ (RF and AC region), many collisions occur per oscillation, whereas when $\upsilon/\omega \leq 1$ (MW region) many oscillations of the electron occur before collision [19]. The theoretical studies of Ferreira and Loureiro proposed that the electron energy distribution of microwave plasmas is Maxwellian ($\upsilon/\omega \leq 1$) whereas of other like RF, DC, AC plasmas are not Maxwellian distribution ($\upsilon/\omega \geq 1$) [55]. Hence, microwave plasma is different from other plasmas.

(c) **Pulse plasma discharge**: Plasma polymerization leads to the highly cross-linked films due to extensive fragmentation of monomer molecules. The control over the film chemistry is poor. The functional group in monomer can be lost or incorporated in a random manner in the polymer film. For the fabrication of functional coating with desired properties the retention of specific functional group is of utmost importance.

To overcome this limitation of plasma polymerization, the pulse plasma technique was devised for better control over the chemistry of plasma polymers [56, 57]. In pulse plasma polymerization, the plasma is activated intermittently according to pulse frequency. Duty cycle gives relationship between on and off time of plasma and is given by

$$\Delta = \tau_{on}/\tau_{on} + \tau_{off},$$

where τ_{on} is the time during which plasma is active and τ_{off} is the time during which plasma is switched off. The average power P_{mean} delivered during plasma on cycle is given by

$$P_{\text{mean}} = \Delta \times P_{\text{peak}},$$

where P_{peak} is the peak power delivered during $\tau_{\text{on.}}$

The plasma activation time is few μs during which radicals are generated and plasma polymerization is initiated. Pulse off time varies from μs to ms during which radicals initiate the radical chain reaction. The composition of pulse plasma polymers depend on the duty cycle. Apart from duty cycle P_{mean} is another parameter which effects the chemical structure of polymers [58]. Larger plasma off-period than on-period leads to better chemical control of films. Monomers which can polymerize by radical chain growth mechanism are suited for pulse plasma polymerization. Amine-based monomers have been used extensively in pulse plasma polymerization. Of all the monomers, allylamine has been used extensively because of its biomedical use [59–61]. Monomers such as ethylene, propylene, etc., have been used in pulse plasma polymerization but resultants polymers were highly cross-linked and irregular [62].

11.2.3 Plasma Polymerization Apparatus

Plasma polymerization process is a low-temperature- and low-pressure phenomenon. Atmospheric-pressure plasma polymerization has also got overwhelming interest in past decade for both economic and technological reasons [63]. A great number of geometries are used for the low-pressure plasma deposition [35, 44]. The most commonly used reactor geometries can be classified as: (a) an internal electrode system, (b) an external electrode system, and (c) an electrodeless system. The schematics of commonly used plasma polymerization reactor are shown in Fig. 11.1.

(a) **Reactor with internal electrodes**

The widely used configuration in the class is bell jar type reactor with internal parallel plate electrode arrangement [64]. The main features of this arrangement include a vacuum pump connected to the base of the bell jar; the monomer can be introduced into the reactor at the base, over the electrodes, or through the center of the electrodes. The electrodes may be oriented horizontally or vertically. The plasma can be initiated by DC, AC, or RF voltage. Uniform electric filed can be achieved in this set up if the electrodes have a large area and are very close to each other. This type of the system is generally used in industrial applications as it gives uniform surface property in resultant plasma polymers.

(b) **External electrode system**

There are a number of possible configurations that can be used to deliver the energy to the reactor. Power can be supplied to the gas either by capacitive coupling [65, 66] or inductive coupling [67]. In most cases, the coupling is of capacitive nature.

In one of the arrangements, external electrode system uses curved electrodes to match the cylindrical geometry of the reactor. The created electric filed is perpendicular to the axis of the cylinder. Another commonly used configuration involves two cylindrical electrodes wrapped around cylindrical reactor; here, the electric field parallel to the axis of the cylinder is created. In another type of setup, an external coil is wrapped around the cylindrical reactor. This arrangement is also known as inductive coupling.

The aforementioned electrode arrangements can be fitted external to a cylindrical vessel, which is generally a tube made of glass, quartz or alumina. The monomer can be fed from one end and by-products can exit from the other. The substrate can be placed inside plasma or downstream of plasma. The position of monomer inlet with respect to plasma activating electrode can be varied. To prevent the monomer exposure to most intense part of plasma, the monomer inlet is placed downstream the plasma activating electrodes [68].

It is worth noting that as the system is closed it is possible to capture by-products.

(c) **Electrodeless system**

This type of system is microwave-powered. Tubular reactors made of Pyrex or silica and by resonant cavity are coupled to microwave power supply of 2.45 GHz [69]. The plasma is generated in the cavity region; a substrate is placed downstream from plasma, where the polymer is created. Polymer films obtained using this type of system are free from impurities as no impurities can be sputtered off from electrodes and embedded in the film (Fig. 11.2).

11.2.4 Effect of Process Variables on Polymerization

Plasma process parameters affect the deposition rate of polymers for a given monomer. Physical, chemical, structural, and compositional property of plasma polymers depend on various plasma parameters. These include

(a) Monomer flow rate,
(b) Plasma pressure,
(c) Substrate temperature,
(d) Geometrical configuration of reactor,
(e) Effect of substrate,
(f) Frequency of exciting power,
(g) Excitation power, and
(h) Effect of monomer.

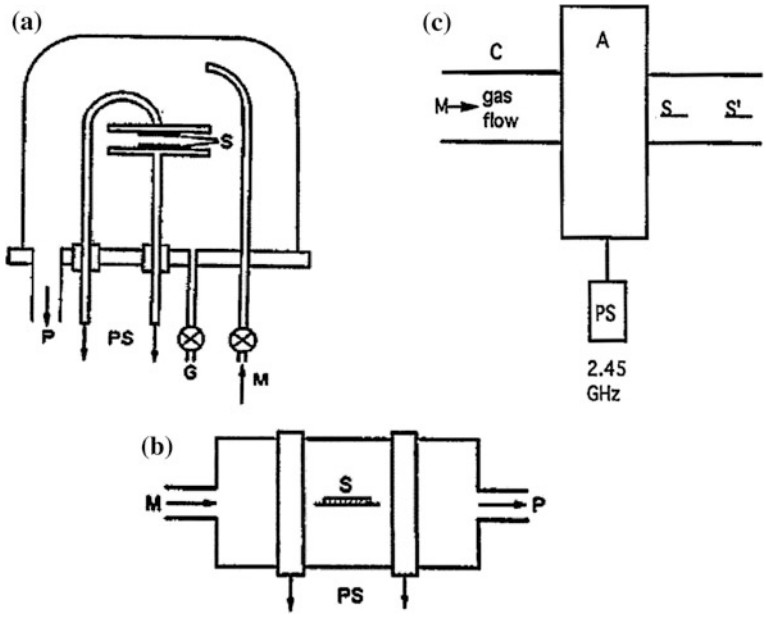

Fig. 11.2 Reactor configuration used for plasma polymerization. (*P* pumps; *PS* power supply; *S* substrate; *M* feed gas inlet; *G* vacuum gauge; *A* resonant cavity; *C* tubular reactor): **a** bell jar reactor with parallel plate metal electrodes (internal reactor); **b** external electrode reactors; **c** electrodeless microwave reactor. Reproduced from previous work with permission from Ref. [44]

(a) **Monomer flow rate**: Residence time is defined as the average time for which molecule stay in a reactor before getting pumped out. The residence time depends on the monomer flow rate (F), volume of glow discharge (V) and total pressure (P) in the plasma chamber [70]. The residence time (τ) can be given by

$$\tau = V\,P/F$$

Residence time of the monomer in plasma decreases with increase in flow rate. When other parameters (pressure, power, etc.) are kept constant, deposition rate at first increases with the flow rate because of fresh supply of feed gases. However, once the flow rate exceeds a certain value, deposition rate decreases as not all the monomer molecules can be excited and even some of the excited species can be drawn away from the deposition site. The direction of flow of monomer also has influence on the property of deposited material [68].

(b) **Reactor Pressure**: The ambient gas/monomer pressure in plasma reactor has strong influence on deposition rate. The effects of pressure on plasma polymerization include

(a) Effect on residence time: it increases with increasing pressure.
(b) Effect on average electron energy: Average electron energy (e_g) is proportional to E/p in RF plasma, where E is electric field initiating the plasma and p is the gas/monomer pressure.
(c) Effect on mean free path. The mean free path of a molecule in gas is given by

$$\lambda = \frac{1}{4}\pi r^2 D,$$

where r is the radius of the molecule and D is density of gas. The operating pressure affects the density of the gas, which in turn affects the mean free path of the molecules. The width of the active plasma zone increases with the increasing pressure; this in turn increases the energy input for plasma polymerization [71]. Mean free path of molecules is inversely proportional to pressure. The thickness of plasma sheath depends inversely on the pressure for the given excitation frequency, power, and monomer [70].

Low mean free path, long resident time, and high electron energy are the requirements for formation of plasma polymers. Thus, high pressure (p) is one of the key requirements of plasma polymerization; however, with the increasing pressure the deposition rate distribution become inhomogeneous [72]. It was found that with increasing pressure, powder formation occurs and formation of polymer in gaseous phase takes place [37]. The plasma expansion changes with the gas pressure [73]. For low gas pressures, expansion of the glow discharge takes place with increasing power. For higher pressures, the glow discharge is more concentrated between the electrodes, especially in the front of driving electrode [74].

Plasma polymer properties and deposition rate are dependent on incident particle flux (J_i) and sticking probability of depositing species. The incident particle flux J_i is related to pressure exerted by corresponding species P_i

$$\mathrm{J_i} = \frac{P_i}{\sqrt{2\pi K_B m_i T}},$$

where m_i is mass of species i, K_B is the Boltzmann constant, and T is the temperature of the gas.

(c) **Substrate temperature**: Surface reactions at the substrate are influenced by the thermal conditions at the substrate [16]. This in turn affects the deposition rate of polymers. At low substrate temp (near room temperature), the polymerization rate depends on the monomer flow rate, while at higher temperature the monomer coverage n/n_0 is the limiting factor [75]. Here, n is the surface concentration of monomer molecules and n_0 is the surface density of the substrate. The monomer surface concentration is given by

$$\frac{dn}{dt} = \gamma j\,(1 - \frac{n}{\mathrm{no}}) - \frac{n}{t} - n\sigma j_x$$

Here, j is the monomer flux density, γ the monomer sticking probability, t the residence time of monomer, σ the reaction cross section, and j_x the energetic particle flux (ions and electrons). The term $n\sigma j_x$ gives the polymerization rate P. Solving above equations gives

$$n = \mathrm{n}_0 \gamma j / y\, j + \mathrm{n}_0\,(1/t + \sigma j_x)$$

$$P = \mathrm{n}_0 \gamma j\, \sigma j_x / y\, j + \mathrm{n}_0\,(1/t + \sigma j_x)$$

The coverage n/n_0 depends on the residence time of monomer molecules (t) and monomer flux (j). The monomer flux j depends on the surface temperature (T_s) of the substrate

$$J = \sqrt{\frac{k}{2\pi M}}\, N\sqrt{Ts}$$

where k is Boltzmann constant, M molecular mass of monomer, N volume concentration of monomer gas.

Substrate temperature has strong influence on thin film structure and morphology. Increase in surface roughness with increasing substrate temperature was found for PECVD deposition of poly(2,2,3,4,4,4-hexafluorobutyl acrylate) thin films [76]. Enhanced cross-linking density with increasing substrate temperature was reported for poly(methyl methacrylate) thin films fabricated via atmospheric plasma deposition [77].

(d) **Geometrical configuration**: The energy invested per monomer particle *W/M F* (Deposition power/Monomer flow rate × Monomer Molecular weight) through active plasma zone affects the plasma polymer deposition [71]. The location in the reactor where plasma deposition process takes, affects the property of deposited polymer. The location is relative to the electric field generating electrodes and monomer inlet. The location of deposition, i.e., where the substrate is placed has minimal effect in systems that use flat electrodes and those that are capacitively coupled discharges. However, the location effect becomes an important factor in systems which are inductively coupled or those that use cylindrical reactors.

In inductively coupled plasmas, there is a wide difference in electron density environments across the plasma volume, with a maximum occurring under the coil. This type of plasma system produces plasma polymers which have inhomogeneous longitudinal property [78].

Plasma polymers deposited in capacitively coupled systems may show variable properties along the inter-electrode axis [79]. This variance in property is attributed to the presence of sheath near the driving electrode.

The Yasuda factor (W/MF) represents the energy input per monomer particle [80]. This factor accounts for the deposition rate, plasma kinetics, and functional group retention. The use of Yasuda factor as similarity parameter for scaling relies on its relation with activation energy (E_a) for polymerization [71, 81]:

$$\frac{R_m}{F} = \mathrm{G}\ \exp\left(-\frac{E_a}{W/F}\right),$$

where R_m is mass deposition rate, G is a reactor-dependent factor, F is monomer flow rate, W is deposition power and E_a is apparent activation corresponding to monomer used. Yasuda factor cannot be applied to reactors of different geometry [82, 83]. The technological parameters which control plasma processes vary from reactor to reactor and require proper scaling factors [70, 84]. The power applied to the deposition reactor is not consumed completely in active plasma zone and also not all of the monomer passes through active plasma zone. Thus, the true value of energy consumed per monomer particle is necessary in order to determine the actual deposition rate (W/F_{dep}) [85]. A similarity factor (S) was introduced to take into account the geometrical configuration of the reactor [71]

$$S = \frac{W}{F_{dep}} = \frac{W}{F}\frac{d_{act}V_{gas}}{d_{gas}V_{dis}},$$

where W is the applied power, F is the monomer flow rate, d_{act} is the length of active plasma zone; V_{gas} is the volume occupied by the gas; d_{gas} is the distance between the deposition area and the monomer inlet; and V_{dis} is the volume occupied by the glow discharge [81].

The electron ion energy has impact on the deposition rate at constant ion flux. It is shown in recent studies [86] that ion flux is a better parameter for characterizing deposition rate and functional group retention than the RF power.

(e) **Effect of substrate**: Sticking probability and adatom mobility on the substrate affects the initial growth of plasma polymers and initial chemistry of plasma films. The ion sticking probability varies with the surface chemistry of the substrate. Thus, the initial film growth may be affected by the nature of the substrate until film thickness reaches a point where it masks the substrate effect. The sticking probability or monomer grafting rate was found to depend more on organic substrates than on metal substrates [87]. After the deposition of few nanometers of the film, the effect of the substrate becomes insignificant. The underlying substrate also has effect on stability of plasma films [88].

(f) **Frequency of excitation power**: DC is rarely used in modern days [42, 43]. In the frequency range from 100 Hz to 500 kHz there is a presence of negative glow, which results from the ion bombardment of cathode. The density of

activated species and ions is greater near cathode than the positive column, which leads to higher deposition rate at the cathode below 500 kHz. At frequency above 500 kHz, the positive glow discharge column forms.

Most of the plasma polymerization systems work at RF frequency of 13.56 MHz. Ion bombardment of electrode also takes place in RF frequency, but is relatively low. This potential difference between the sheath and the positive column results in ion bombardment of the electrodes.

In the plasma system coupled to microwave discharge, it is found that the rate of plasma polymerization is much higher than that in the RF frequency systems. The plasma intensity is also very balanced over large area. The high deposition rate can be attributed to more efficient transfer of power to plasma which results in more energetic electrons than in the RF system.

Discharge frequency is closely related to electron energy distribution function (EEDF) and electron density. If the wavelength of applied signal and the characteristic length of the reactor are of similar range, standing waves can be generated in reactor, which cause non-uniform growth of polymer films because of interference pattern of electric field [89].

Frequency also effects the position of glow discharge. The position of the plasma in the reactor is important as deposition takes place in active zone of the plasma. The discharge frequency affects the critical sheath frequency v_{sh} which is the inverse of transit time taken by ion to cross sheath thickness. When the discharge frequency is lower than v_{sh}, the discharge shifts closer to the electrodes; and when it is higher than v_{sh}, the plasma shifts towards the center of the reactor. The v_{sh} for RF discharges is 1 MHz, thus RF discharges are formed away from the driving electrode.

Dual frequency discharges are used to independently control the ion flux and energy during film growth. This type of dual frequency discharge has led to the coating with improved surface properties [90, 91].

(g) **Excitation power**: Potential drop across electrodes and current density on electrodes increases with increase in power. In DC or alternating DC discharge, there is an increase in density of energetic electrons and ion bombardment of electrodes with increasing power.

In RF discharges, an increase in power increases the current, which leads to higher electron density. At low powers, the glow discharge in confined between the electrodes and its expansion takes place as the power is increased, keeping other variables constant.

Increasing the power yields more energetic particles, which leads to more plasma dissociation. Increase in plasma dissociation creates more nucleation sites, increasing the deposition rate. However, due to sputtering, reduced deposition rate can also be observed.

Electrode geometry determines the electric field distribution at the electrode surface.

(h) **Effect of monomer**: The chemistry of the monomer has an influence on the deposition rate of the polymer. The energy required to dissociate the monomer molecule (activation energy) is related to the radical formation of that monomer. This activation energy is found to be independent of reactor geometry, monomer flow rate, and pressure. The activation energy is found to be closely related to the bond dissociation energy of various monomers and the mechanism of dissociation of the bonds [71]. For monomers having double and triple bonds, the main radical formation mechanism takes place by bond rupture, as well as hydrogen abstraction as the power in increased. For monomers such as acrylic acid, complex growth mechanisms exist. At lower powers, there is breaking of carbon double bonds, whereas at higher powers, there is more fragmentation and removal of CO_2 which as reactive agent influences the film growth [92].

Rate of plasma polymer deposition from monomers from homologue series was found to be dependent on the molar mass and the degree of unsaturation of the monomer. The deposition rate of unsaturated monomers was negligibly influenced by increasing power whereas the deposition rate for saturated precursor increases linearly with increasing power.

11.2.5 Feed Gases Used in Plasma Polymerization

(a) **Hydrocarbons**: This class of monomers can be classified into three subclasses based on their saturation and structure: (1) triple bond containing monomers (including benzene), (2) double bond containing monomers and cyclic structures, and (3) saturated structures. Hydrocarbons such as ethane, methane, cyclohexane, etc., which cannot be polymerized using conventional techniques can be polymerized using plasma technique. The deposition rate for all the subclasses is different for similar molecular weight gases under identical conditions.

Hydrocarbons containing polar groups yield more polar plasma polymers. Monomer gases such as pyridine and allylamine are included in this group. Additional feed gases can be introduced into the deposition reactor to get desired property in plasma polymers. For example, addition of N_2 and H_2O during plasma polymerization of acetylene yields more hydrophilic polymers.

(b) **Fluorocarbons**: Fluorocarbon monomers are used for deposition of plasma polymers of composition of CF_x or to perform fluorination or etching of inorganic and organic materials. Fluoroalkanes (C_nF_{2n+2}), alkenes, alkynes, cyclic, and aromatic fluorocarbons are some of the commonly used monomer feeds for the synthesis of fluorocarbon coatings. These coating are highly adherent to substrates. F atoms and CF_x radicals are main etching and deposition species in fluorocarbon plasma and their density ratio F/CF_x determines

whether deposition or etching will take place [93]. Fluorocarbons are used for plasma etching in microelectronic systems [94].

Addition of O_2 gas to fluorocarbon plasma increases the number of F atoms, creating more favorable conditions for etching due to reaction of CF_x radicals with the oxygen atoms as follows

$$CF_x + O\,(O_2) \rightarrow CO\,(CO_2) + xF$$

While addition of H_2 gas increases the CF_x density and favors the deposition. The hydrogen atoms abstract the F atoms from plasma and form the radicals by following reactions:

$$H(H_2) + F \rightarrow HF + (HF)$$

$$H(H_2) + CF_x \rightarrow CF_{x-1} + HF + (H)$$

Dry HF which is formed in this reaction does not affect surface reactions.

(c) **Silicon-containing polymers**: The feed monomer gas includes linear and cyclic siloxanes and silanes. Although a wide range of organosilicon molecules are available, only few members from the group are commonly used because of their compatibility with PECVD. The key selection criterion for the precursor material is the ease of evaporation at room temperature and pressure. For this reason, mostly gas and liquid precursor are used. Furthermore, the liquid precursor should have enough vapor pressure at room temperature so that the vapors can be conveniently introduced in the reaction chamber. This further restricts the choice of monomers that have one or two Si atoms or four atoms as in cyclic molecules.

Tetraethoxysilane (TEOS) and hexamethyldisiloxane (HMDSO) are two of the most common monomer materials [95]. Both of these materials are liquid at room temperature and pressure and are cheap. Few of the other molecules used are tetramethyldisiloxane (TMDSO), divinyl tetramethyldisiloxane (DVTMDSO), and tetramethylsilane (TMS). Oxygen and nitrogen gas are often added as carrier gas in polymerization of these monomers.

(d) **Metal plasma polymer films**: Metal-containing plasma polymers can be made by various deposition methods, such as simultaneous plasma polymerization and incorporation of metal atoms by sputtering of the metal target. The metal target is placed on the excitation electrode and the substrate is attached to the earthed electrode. Halocarbons (e.g., CF_4) are used to facilitate the sputter etching of the target metals (e.g., Au, Cu, or Mo).

Another way is simultaneous plasma polymerization and incorporation of metal by evaporation. The metal is placed into metal evaporator (in the plasma reactor) which is then heated. Metal atomic vapors get embedded into the growing plasma

polymer. In this method, both evaporation of metal atoms and deposition of polymeric component can be controlled independently.

Plasma polymerization of metalorganic compounds is another way of fabricating metal/organic plasma polymers. The metal content in these films can be controlled by variation of power density, substrate temperature, and monomer flow rate. Plasma polymerization of ferrocene, iron pentacarbonyl, copper phthalocyanine, and many others has been successfully attempted.

Generally in metal/polymer films, metal particles form clusters in the film and there is no bond formation between metal and carbon atoms. However, it has been shown that metalorganic complexes can be formed while using transition metal under certain circumstances [96].

(e) **Plasma polymerization from natural precursors**: Plasma polymerization from natural precursors has received significant interest in modern times. Natural precursors have wide range of chemical compositions, for example the tea tree oil has 16 chemical components [97]. Fabrication of plasma polymer films from various essential oils like lavender oil, tea tree oil, orange oil, and their components has been reported [98]. The essential oils can easily evaporate at room temperature, which make these precursors compatible to PECVD process. The plasma polymer films fabricated from essential oil at low power are generally transparent [99]. The chemical structure analysis by FTIR shows that irrespective of the starting precursor material, the FTIR spectra of deposited plasma polymers possess similar chemical features.

Plasma-polymerized films from essential oils have been studied for their application in the biological field, e.g., as coatings for medical implants [100] and in organic electronics, e.g., as dielectrics [101].

11.2.6 Plasma Polymerization Process: Challenges and Issues

Reproduction or duplication of the scientific data is the cornerstone of scientific process. One of the major challenges in plasma processing of thin films has been the consistency of the result of one reactor to another setup [102, 103] using external parameters such as power, flow rate, and pressure. The issue of scale up becomes more important in case of deposition of functional polymer film, where retention of certain chemical moieties is necessary.

Yasuda parameter ($Y = W/FM$) has been used as scaling factor from one system to another since 1982. This parameter is quite reasonable for the polymerization in a single set up but does not transfer well to another plasma deposition system.

Another scaling factor known as similarity parameter was given by Hegemann et al. [71] more recently. This parameter is based on the actual energy consumed in the active plasma zone, which determines the measured deposition rate. This

scaling parameter also takes into account the different geometry of the reactor used for plasma polymerization. However, this approach does not transfer well when the deposition of functional polymer coating is required, where the retention of certain chemical moieties in necessary. Indeed, the correlation between retention of functional group and similarity factor is not straightforward.

In a transfer of deposition process from one reactor to another in polymerization of acrylic acid, it was found that the value of (W/F) is a good scaling parameter when the width of the active plasma zone is comparable between reactors and similarity parameter S is an appropriate scaling parameter when the residence time of monomer is comparable [104].

Fabrication of functional thin films has been a major focus of plasma polymerization. The deposition rate which has often been used as a scaling parameter may not directly correlate with the properties of functional plasma-polymerized films. Chemical properties and deposition rate may not scale on the same basis [105].

The source of variation in plasma processing of material can include variation in efficiency of power coupling, geometry, monomer flow rate, and pressure from one reactor to another [105]:

- Actual plasma power: Actual plasma power delivered to the reactor can vary from reactor to reactor. The power transfer efficiency increases with decreasing symmetry of the reactor [106].
- Flow rate measurement: Change in pressure during fixed time and ideal gas equation have been used to calculate the flow rate [107]. However, this approach relies on the treatment of monomers as ideal gases, which may not be appropriate in every instance.
- Reactor geometry: Dependence of plasma properties on geometry of the reactor has not been established until now. The geometry has an influence on the deposition rate as it is found to be different for different reactor geometries [105].

11.3 Properties of Plasma Polymers

Plasma polymer thin films are high molecular weight systems. The properties of these thin films depend on the nature of deposition conditions in which they are formed [108]. Such films are generally formed without any macroscopic defects such as pinholes, cracks, or porosity. The thickness of the film obtained ranges from few nanometers to few micrometers. These films have generated considerable interest in modern science applications. These thin films have great advantages as they require less amount of processing materials.

Plasma polymers do not possess the definite molecular structure. The generation of each chemical entity in plasma determines the chemical, structural, optical, and electronic property of the resultant thin films. The desired properties of plasma

polymers can be tailored if the correlation between deposition conditions—chemical structure—electronic structure—electronic property—optical properties is established for a particular precursor material.

11.3.1 Optical Properties

Possessing good transparency, optical nonlinearity, physical stability, and intimate connection with substrate, polymer films are extensively beneficial to optical applications. These include protective coating on solar cells and optical devices, such as light sensors, to name but a few [109–111]. Plasma polymerization is a well-known technique to fabricate uniform organic thin films for optical applications, such as optical filters and optical waveguides [112]. In particular, optical properties of the fabricated plasma polymer thin films include transparency, the spectral dependence of the refractive index, band gap energy, Raman polarization, and absorption, which are vital in the optics-related industries [113–115].

In optical applications, it is very important to specify the material refractive index (n), which describes how light propagates through that medium. The refractive index for conventional polymer films is found to be between 1.30 and 1.70, which is relevant for several uses, such as anti-reflective coatings [116, 117]. However, there are several organic materials that have higher refractive index, for instance, polythiophene ($n = 2.12$) and aromatic conjugated polymers ($n \approx 2.7$) [118]. High refractive index is often required for specific applications such as light emitting diodes (LEDs) and image sensors. In this regard, it has been reported that the incorporation of a dopant, such as sulfur atom, into polymer films can increase the refractive index, caused by its large atomic refraction [119]. Saloum et al. [120] used plasma polymerization technique to modify refractive index of polymer films by changing the process gas from a rare gas (argon) to a reactive molecular gas (nitrogen) in the reactor; this led to an increase of refractive index from 1.59 to 1.69 at 500 nm.

Sang et al. investigated the influence of nitrogen flow rate on the refractive index of thiophene and found that n was decreasing dramatically with increasing N_2 flow rate. The study revealed that the density of the plasma polymer thin film decreased with increasing N_2 flow rate due to the disturbances that lead to the formation of a high density cross-link between the thiophene molecules in the plasma polymer (Fig. 11.3) [121]. However, the refractive index is highly dependent on the frequency of the light beam as well.

Generally, polymers are transparent in the visible region and have high absorption in the infrared region if the incident photons have energies equivalent to C–C bond or C=O bond. Then, the absorbed energy could be transformed to various forms called radiative transition, such as florescence, or non-radiative transition, such as heat effect [122].

Researchers suggested that the absorption in polymer films can be classified as either intrinsic or extrinsic. As long as the absorption occurs in the UV region, it is

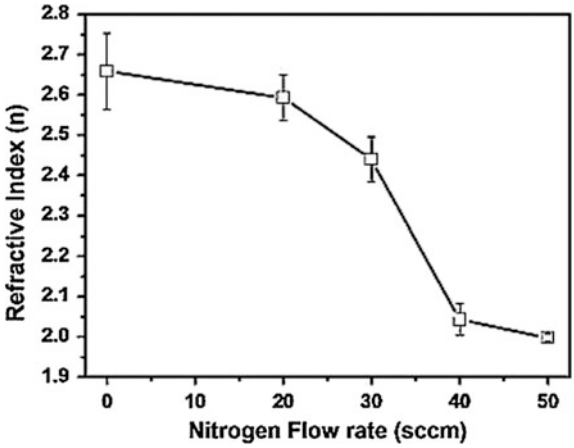

Fig. 11.3 Refractive indices of ThioPP and N-ThioPP with N_2 flow rate. Reproduced from previous work with permission from Ref. [121]

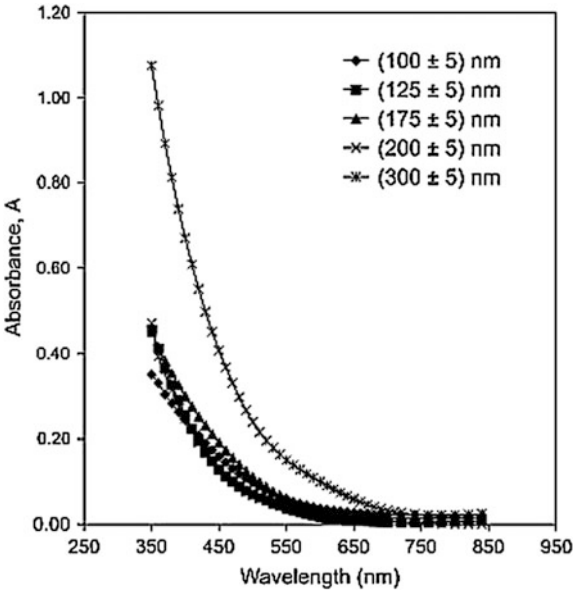

Fig. 11.4 Wavelength versus absorbance plot for different PPOMA thin films. Reproduced from previous work with permission from Ref. [124]

intrinsic loss that is related to the electronic excitations of chromophores in repeating units of polymer.

However, the extrinsic absorption takes place in the near IR region which is associated with vibrational overtone absorption of C–H [123].

It is experientially found that the absorbance of numerous polymer films decreases exponentially with increasing wavelength; as illustrated in Fig. 11.4 [124]. The absorption tendency in various amorphous materials is found to follow the Tauc relation which is employed to determine the energy gap as well. Tauc relation is described as

$$\alpha h\upsilon = B(h\upsilon - E_o)^p,$$

where α is the absorption, $h\upsilon$ is the energy of light, B is related to the length of localized state tails, E_o is the optical band gap and p is a constant that determines the type of transmission (p = ½ for direct, p = 2 for indirect).

The relationship between optical properties and plasma polymerization parameters has been widely investigated. In this regard, it has been reported that thin films of plasma-polymerized γ-terpinene at lower power up to 100 W are optically transparent. The refractive index and extinction coefficient of these films show very little dependence on RF power and film thickness [125]. Similarly, another study indicated that refractive index of 3,7-dimethyl-1,6-octadien-3-ol thin films was found to be independent of RF power and thickness, ranging from 1.54 to 1.57 at 500 nm while the optical band gap decreased linearly from 2.81 eV for 15 W to 2.64 eV for 75 W [101]. Conversely, Cho et al. [126] discussed that the refractive index of ethyl-cyclohexane thin films increased when the RF power was increased.

Also, it has been found that changing the carrier gas in plasma polymerization process has a noticeable effect on the optical properties of grown films. When the carrier gas of plasma reactor was changed from argon to nitrogen in plasma deposition of hexamethyldisilazane compound, the energy band gap decreased from 4.00 to 3.88 eV as well as the dielectric constant increased from 2.74 to 2.88 [120]. Sajeev et al. [127] studied the effect of iodine doping on aniline thin films prepared by AC and RF plasma polymerization. It was reported that the iodine doping decreases the optical band gap from 3.6 to 2.8 eV and 2.2 to 1.9 eV in the case of AC and RF plasma films, respectively. Espideto et al. hypothesized that absorption changes which occur when RF power increase is related to the enhancement in both the dissociation of molecules and the ion bombardment on the formed film. This can cause more branching and cross-linking in the film structure, constructing a denser film with a π-electron delocalization in wide band states and a drop in the band gap [128].

Within this area, Mohammed et al. reported that the absorbance increases with the increase of thickness of the plasma-polymerized o-methoxyaniline thin films which may be interpreted as an increase in the scattering loss with the increase in the film thickness and the electronic transition occurs from bulk of the samples which need more energy [124]. Further, Wang informed that the refractive index of PP-heptadecafluoro-1-decen increases slightly with increasing film thickness, due to inhomogeneity in the densification and the cross-linking density in plasma polymer films [129]. Table 11.1 refers to the refractive index of plasma-polymerized thin films from various precursor materials.

Table 11.1 Refractive index of some polymer thin films

Precursor	Refractive index (*n*)	Wavelength (*nm*)	Reference
1-isopropyl-4-methyl-1,4 cyclohexadiene	1.57–1.58	500	[125]
Cis-β-ocimene	1.57	500	[98]
Hexamethyldisilazane	1.69	500	[120]
Lavandula angustifolia oil	1.53–1.54	500	[279]
Linalyl acetate	1.53	500	[98]
Linalyl acetate	1.55–1.58	589	[280]
Imidothioethers	1.68–1.62	632.8	[121]
Terpinen-4-ol	1.54–1.55	500	[99]
Melaleuca alternifolia oil	1.56	500	[281]
Tetraethoxysilane and toluene, 1:10	1.68	632	[143]
Thiophene	1.7–2.7	400–600	[282]

11.3.2 Electrical Properties

There is a consensus among scientists that the electrical properties of the polymers are fundamentally dependent on their structural parameters. Research interest in electroactive polymers started in 1977, when Heeger et al. demonstrated that the conductivity of polyacetylene can be improved through functionalization with appropriate oxidizing compounds, namely dopants [130]. Polymer thin films have a wide range of electrical properties. As such, they can be classified according to their conductivity into insulating dielectric films (conductivity $\sigma < 10^{-1}$ S cm^{-1}), semiconductive films ($10^{-2} < \sigma < 10^{-2}$ S cm^{-1}), and conductive films ($\sigma < 10^{-2}$ S cm^{-1}) [109]. In other words, depending on the number and type of valence electrons involved in the chemical bonding, organic materials can be commonly categorized into either saturated or conjugated types. In saturated polymers, the valence electrons of the carbon atoms in the main chain are hybridized in sp^3 configuration with carbon bonded to four atoms. Consequently, these polymers are characterized with a low dielectric property. Polymers with high insulating properties toward electrical charge and signal are essential in the engineering of high density, high-speed microelectronics chips. Based on the saturated organic materials, Giordano et al. utilized plasma polymerization to fabricate oxygen-containing fluoropolymer films from the C_2F_4 monomer. These polymer films have low dielectric constant of approximately 2.6, which is relevant for manufacturing of integrated circuits [131].

On the other hand, conjugated polymers have the carbon orbitals in the sp^2p_x, which leads to one unpaired π-electron per atom [132]. These electrons are positioned in the π orbital and they are vertical to the σ bond. Yet, doping materials such as HCl, iodine and CSA (camphor sulfonic acid) can lead to a significant increase in the electrical conductivity of a number of polymers [133]. A doping

process may increase the conductivity of an organic film up to fifteen orders of magnitude, because of the creation of extended energetic states in a polymer chain. However, it has been hypothesized that the formation of the energetic states in the forbidden gap of the electronic structure is associated with induced conformational defect [134, 135]. Kim et al. [136] fabricated plasma-polymerized polythiophene films, which exhibited insulating behavior, having sheet resistance of $10^{10–12}$ Ω/m^2. The conductivity was immediately increased up to 10 Ω/m^2 when doped with O_2 plasma, producing conductive layers suitable for applications requiring semiconductor films.

The dominant charge transport mechanisms found in plasma-polymerized thin films include Schottky effect, Poole–Frenkel effect, direct tunneling effect, and space charge limited conduction [137–140]. Sajeev U. et al. [122] described that the electron transition occurs through the following processes: (i) through the conduction band, (ii) by tunneling, (iii) through impurity bands, (iv) space charge limited process, and (v) by ionic transport. In the plasma polymerization process, a large variation of electrical properties of films can be reached by utilizing different precursors and different growth conditions. Jae et al. reported that plasma-polymerized films of styrene and vinyl acetate display low operation voltage of −10 V and low threshold voltage of −3 V [141]. Saloum et al. [120] demonstrated that plasma-deposited films from hexamethyldisilazane compound exhibit relatively high electrical resistivity (10^{13}–10^{14} Ω cm) that is inversely proportional to the film thickness. Anderson et al. [142] verified that the conductivity of plasma-polymerized linalyl acetate thin films decreased at higher RF power levels. The author proposed the increased cross-linking in the film at higher RF powers which decreased the carrier mobility through the film and consequently increased the resistivity. Sang-Jin et al. found a change in the leakage current densities with various tetraethoxysilane (TEOS)/tolune ratio due to the influence of the film density. Consequently, leakage current density was 10^{-9} A/cm^2 at 1 MV/cm for all the films fabricated at different ratio of toluene/TEOS, demonstrating that the hybrid plasma-polymerized film had a noticeable insulating properties [143]. Bae et al. [144] described that when the plasma power was increased from 20 to 50 W, the leakage current density decreased, and breakdown did not appear below 1 MV. This reveals that the films had a compact structure with high density and pinhole-free layers that are well known to have a lower leakage current density and a higher breakdown field. Table 11.2 presents the electrical conductivity of plasma-polymerized thin films from various precursor material.

Table 11.2 Electrical conductivity of several polymer films

Polymerized films	Electrical conductivity S/cm	Reference
Polylinalyl acetate	10^{-10}	[280]
PolyAniline/iodine	10^{-9}	[283]
PolyPyrrole/iodine	10^{-9}–10^{-10}	[283]
PolyPicoline	2.2×10^{-14}	[145]
PolyAniline	2.8×10^{-16}	[145]

11.3.3 Chemical and Structural Properties

Plasma polymerization creates polymer chains that are largely different in the structure and chemical properties from those of the precursor material. The polymerized structure consists of amorphous structure containing cross-linked units and units fragmented or rearranged from monomer molecules [145]. Fundamentally, the organic molecules are held together by strong covalent bonds, while a solid polymer they form is held together via weak van der Waals forces [146]. The formed chains are short, randomly ranched, and terminated with a high degree of cross-linking, as well as a large amount of free radicals are trapped within a growing film on the substrate [147]. These chains and other active species in the plasma reactor are deposited on a substrate as thin films, fine particles, or viscous liquids [148]. Hence, the polymerized films can be considered as a single amorphous macromolecule comprising of the tridimensional system with attached side units, such as hydrogen atoms and functional groups [5].

It has been suggested that the fragmentation of precursor molecules in the vapor phase and cross-linking during polymer assembly influence films characteristics that can range from soft or highly functional films to hard materials [149]. Yasuda H. hypothesized that the chemical structure of the monomer largely determines the quantity of free radicals trapped in the plasma polymer, which affects the overall properties of the formed martial [150]. A large fraction of radicals usually recombines to form a complex branched and cross-linked three-dimensional net whereas the remaining radicals are trapped in the generated polymer [151].

In several applications, the presence of trapped free radicals within the formed films is unfavorable and cause considerable problems, such as uncontrollable surface oxidation that occurs inevitably in aerobic conditions [152]. In another applications, free radicals are beneficial; for example, a remarkable increase in both water flux and salt rejection with time observed for reverse-osmosis membranes prepared by plasma polymerization is highly desired [150]. However, the chemical and structural properties of formed plasma polymers are not solely dependent on the monomer used, with other growth parameters, such as pressure, power level, temperature, frequency and flow rate, known to significantly influence the films [129].

Generally, X-ray photoelectron spectroscopy (XPS) is employed to analyze the surface composition of polymerized films. XPS relies on the photoelectric effect, in which X-ray radiation removes an electron from an atom within the films structure, provided that the photon has sufficient energy [153]. The kinetic energy and the number of electrons that escape from the films are measured, providing information regarding the chemical configuration of the analyzed material. In this regard, Luis and Renate utilized XPS to investigate plasma polymerization of Zinc acetylacetonate hydrate ($Zn(acac)_2$) and found that depositing at low input power (20 and 50 W) resulted in an O/C ratio of around 0.25, while depositing at higher input power (100 W) showed an increase in the O/C ratio to $\sim$0.5. At the same time, an increase in the amount of zinc was observed with an increase in input power. The

authors supposed that the higher input power leads to a higher degree of fragmentation of the precursor, accompanied by the loss of hydrocarbon components due to increased ion bombardment and etching, and thus the relative increase in zinc and oxygen [154]. Moreover, S. Schiller et al. [155] studied the chemical structure of maleic anhydride films. XPS results revealed that after pulse plasma polymerization at duty cycle 1/40, 100 W, the total oxygen concentration is reduced from O/C = 0.43 in the monomer molecule to O/C = 0.33 in the polymerized films. Other plasma conditions lead to O/C ratios ranging between 0.27 and 0.35, as seen in Fig. 11.5.

Fourier transform infrared spectroscopy (FTIR) is widely used to identify the chemical composition of organic polymer films. FTIR irradiates film surface by an IR radiation beam, and measures how much of that beam is absorbed and transmitted by the sample. The result is a spectrum that represents the molecular absorption and transmission, creating a molecular fingerprint of the sample. A study carried out by Ahmad et al. used FTIR spectra to investigate chemical properties of plasma-polymerized 1-isopropyl-4-methyl-1,4-cyclohexadiene (pp-GT) thin films. The spectrum revealed that the number of absorption peaks in the spectra has reduced significantly upon polymerization, particularly in the fingerprint region of the spectrum (1500 cm^{-1} and below). Peaks also broadened for the pp–GT thin

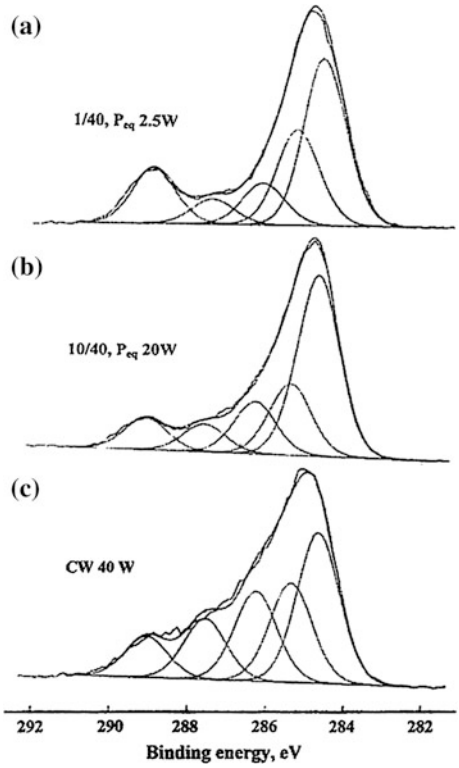

Fig. 11.5 XPS C (1 s) spectra of plasma-polymerized maleic anhydride using **a** on/off ratio of 1/40, **b** on/off ratio of 10/40, and **c** 40 W continuous wave. Reproduced from previous work with permission from Ref. [155]

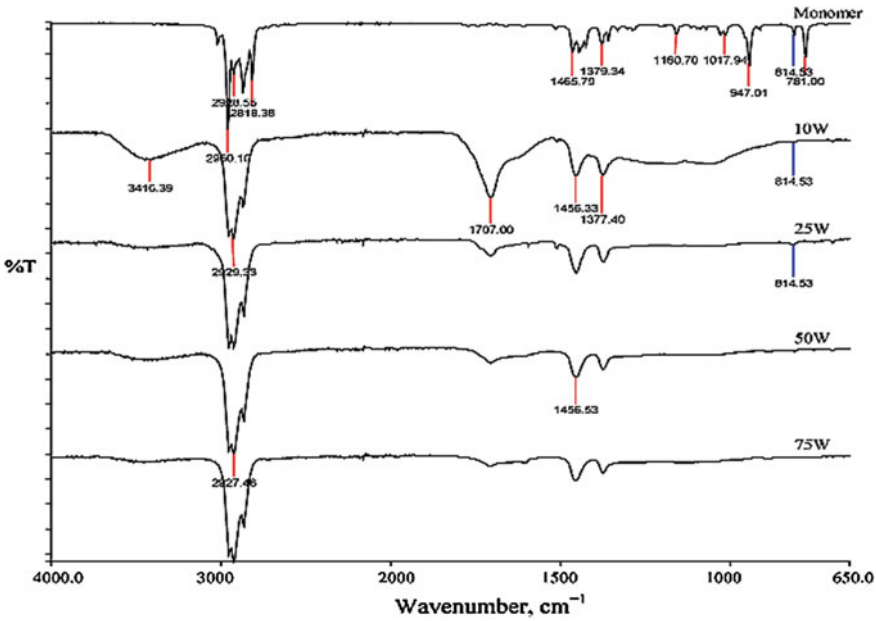

Fig. 11.6 FTIR spectra (% transmittance vs. wavenumber, cm^{-1}) for γ-terpinene monomer and pp–GT thin film. Reproduced from previous work with permission from Ref. [156]

films, indicating very high degrees of polymerization as well as disappearance of the =C–H vibration at (3088 cm^{-1}), as illustrated in Fig. 11.6 [156]. This proved that the fabricated polymers are structurally dissimilar to their monomer and highly cross-linked, where the loss of original functional groups and the degree of cross-linking increased with deposition power.

It has been reported that the irregularity of the chemical structure of the plasma polymer may improve chemical and mechanical characteristics of the film, including its resistance against oxidation, aging, and shrinking. Yet, the regularity of plasma polymers can be improved using pulsed plasma polymerization [157]. Moreover, it has been found that the use of high power in pulsed-PECVD technique has led to more efficient plasma chemistry, where a higher amount of the precursor molecules are utilized for the thin film deposition [158].

The influence of pulsed discharge may be related to the association between deposition pressure parameter and deposition rate [159]. Also it has been found that the effect of the pulse is varied for different monomer structures conditional to whether or not they include an olefinic double bond and/or a triple bond. Specifically, in monomers containing these bonds additional polymerization mechanism may take place during the off-period of the pulsed discharge. Furthermore, the concentration and lifetime of free radicals generated from these monomers will be significantly different to monomers that do not contain these chemical functionalities [160, 161].

11.3.4 Surface Properties

The surface of plasma-polymerized films can be functionalized by changing the growth conditions as well as the chemistry of the monomer. The selected monomer is an important factor in the overall surface properties, providing the chemical composition and the amount of free radicals. Yasuda reported that the surface energies of plasma polymers of hydrocarbons are usually higher than those of common hydrocarbon polymers because of the existence of oxygen-containing groups, such as carbonyl, that are incorporated onto the formed surface by interaction of free radicals with atmospheric O_2 [150]. Siow et al. indicated that plasma polymer surfaces that contain amide groups show good ability to support cell colonization for bio-interface applications [162]. It is well known that surfaces rich in non-polar groups (e.g., $–CH_x$, with x = 1–3) have low surface energies and, thus, are hydrophobic, while surfaces with a high density of polar groups (e.g., –OH or –C=O) are characterized by high surface energies and are hydrophilic [156]. The degree of hydrophobicity (water repelling) and degree of hydrophilicity (water loving) are determined from the contact angle that forms between the surface and the liquid drop. If the drop spreads forming a contact angle of less than 90°, the surface is considered hydrophilic, whereas if the contact angle is more than 90° the surface is hydrophobic. Chemical functionalities and the surface features in range of 0.5–1 nm effects the contact angle measurements [163, 164]. Moreover Sung et al. investigated plasma-polymerized allylamine films and demonstrated that with increasing input power, the surface free energy decreases and the contact angle increases; therefore, the hydrophobicity of the films increased [148]. Jacob and his colleagues studied different plasma polymer films fabricated from lavender oil, linalyl acetate, linalool acetate, terpene-4-ol, and cis-β-ocimene and found that water contact angle values ranged from 68.5° to 94.1°. This indicates that the polymers ranged from hydrophilic to mildly hydrophobic. The contact angle data demonstrated that the polymer thin films were stable while in contact with water [98]. Super hydrophobic surfaces are reported to be less prone to colonization by microorganisms compared to macroscopically and microscopically rough surfaces, where higher surface area provides extra attachment points for microorganisms to stick. Polyterpenol antibacterial coatings fabricated by PECVD process has demonstrated a significant decrease in the pathogen adhesion as the substrate average surface roughness (R_a) reduced from approximately 0.4 to 0.25 nm [165].

The atomic force microscopy (AFM) is commonly used to determine film topography at micro- and nanoscales. AFM uses a mechanical probe to magnify surface features up to 100,000,000 times, and it produces 3-D images of the surface. AFM images of PECVD-deposited silicon dioxide films on silicon substrate using tetraethylorthosilicate as silicon source showed that increase in the argon flow corresponds to an increase in the roughness of the silicon surface due to the additional bombardment of species present in the plasma; additionally, structural defects appear on the surface [166]. Bazaka et al. [111] fabricated pp-terpene-4-ol films and used AFM to demonstrate that the polymerized films were smooth and

free of defects, suggesting that polymerization process occurred predominantly on the surface of the substrate (glass) rather than in the gas phase. Ianova et al. [167] demonstrated that *P. aeruginosa* and *S. aureus* cells attached to surfaces containing regularly spaced pits of 1 and 2 μm in size but not to surfaces containing irregularly spaced pits of 0.2 and 0.5 μm. Figure 11.7 shows AFM images of several plasma polymer thin films fabricated from essential oils for electronic and biomedical applications. The roughness of most of these thin film surfaces was found to be less than 1 nm except for cis- β-ocimene which has roughness of 14.2 nm [98].

11.4 Plasma Polymer Thin Films for Electronic Applications

Nano-engineering of organic polymers on various substrates is the crucial part of organic electronics. It essentially requires an efficient technique to fabricate polymer thin films having desired properties on various substrates. Foreseeing the huge demand and potential applications, efforts are being made not only to develop materials with well-defined properties but also to get efficient synthesis methods that can be easily scaled-up for large-scale production. A large number of articles were published on the synthesis of polymer thin films through solution processing techniques [168–170]. Though solution-based processing of polymer thin films is

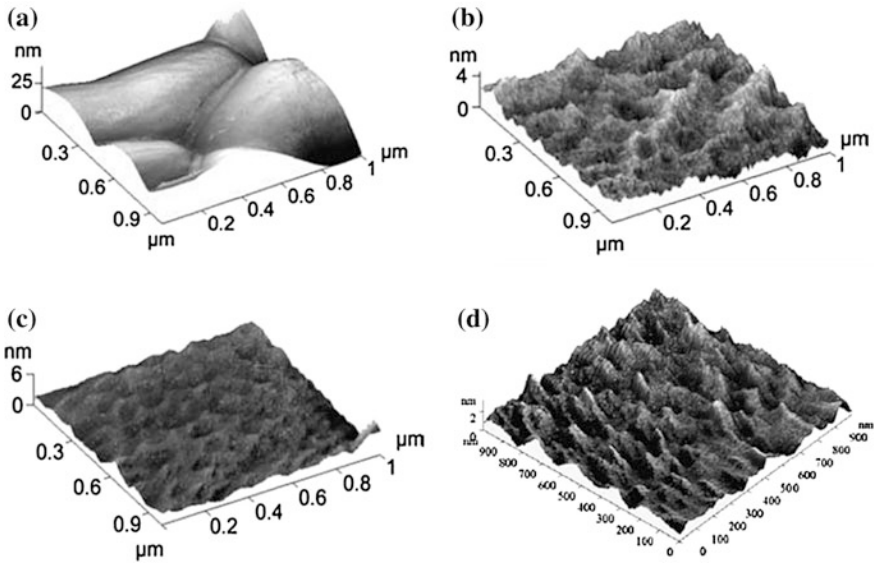

Fig. 11.7 AFM images of polymer thin film fabricated from various essential oil precursor: **a** cis-β-ocimene, **b** linalool, **c** linalyl acetate, **d** terpene-4-ol. Reproduced from previous work with permission from Ref. [98]

widely accepted, the unwanted reactions of the solvents with already existing layers, inability to pattern the device and scalability still remain as major hurdles [171]. In this context, plasma polymerization gained much attention for fabricating polymer thin films. The major advantages of plasma polymerization which makes it excellent fabrication tool in electronics are

- Highly cross-linked and pinhole-free polymer thin films having excellent chemical, mechanical, and thermal properties.
- Excellent control over physicochemical properties.
- Low-temperature processing and compatibility with microelectronic packaging.
- Susceptible to almost all organic precursors and conductive, dielectric and insulating substrates.
- Single step, solvent free, less toxic and large area production.

Modern microelectronics is heavily dependent to the semiconductor technology. It is anticipated that the present technology will reach its fundamental limit in miniaturization very soon due to the ever increasing number of components incorporated into a single processor [172]. Also, concerns are growing due to the large consumption of energy during the production stage (embodied energy), inability to cope with flexible applications and material scarcity [173]. The search for an effective substitute technology paved the way to so-called organic electronics, based on the conjugated polymers and small molecules. The organic electronics mainly rely on polymers having excellent conducting, semiconducting, and insulating properties. The field of organic electronics has made its entry into the research during 1977 when Shirikawa et al. [174] synthesized electrically conducting polyacetylene polymers. Since then, immense amount of research has been carried out in exploring electronic properties of various types of organic polymers and specific applications that incorporate these materials. Major applications for organic polymer thin films include organic thin film transistors (OTFTs), organic photovoltaics (OPV), organic light emitting diodes (OLEDs), sensors and large area displays [175–177].

11.4.1 Various Roles of Plasma-Deposited Thin Films in Thin Film Transistor (TFT) Technology

Thin film transistors (TFTs) gained considerable research impetus in the area of flexible electronics [178]. TFTs became the essential component of various devices such as flat panel displays, smart cards, electronic paper, radio frequency identification (RFID) tags, etc. [179, 180]. A typical TFT design contains an active semiconducting layer, a dielectric layer and metal contacts (source, gate, and drain). Figure 11.8 shows the schematic diagram of a flexible thin film transistor. In a TFT device structure, the semiconducting layer is separated from the gate metal contact by a gate insulating layer. The basic principle behind the functioning of a TFT is

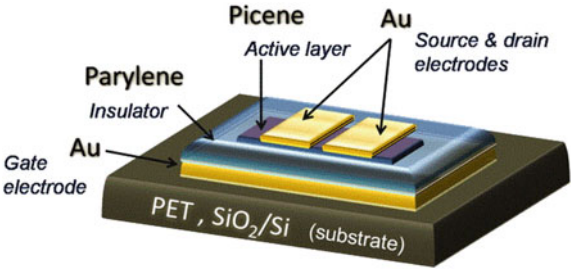

Fig. 11.8 Schematic of TFT (flexible) in bottom-gate staggered configuration. Reproduced from previous work with permission from Ref. [275]

that, by applying a sufficient gate voltage the charge density of the semiconducting layer can be altered, which leads to the control of the current flowing through the transistor [181]. There are four different ways of arranging layers within a TFT device structure. They are (i) bottom-gate (inverted) staggered TFT, (ii) bottom-gate (inverted) coplanar TFT, (iii) top-gate staggered TFT, and (iv) top-gate coplanar TFTs [182]. It is worth noting that, the selection of metal contact, gate dielectric material and organic semiconducting layer critically affects the performance of TFTs [183, 184]. Hence, considerable amount of research has been carried out in developing novel materials having better properties to meet the existing demand.

11.4.1.1 Plasma Polymer Thin Films as Gate Dielectric Material

The choice of the gate dielectric material has a significant influence on the performance of TFTs [185]. Mainly, the dielectric constant and the thickness of the gate dielectric layer determine the device operating voltage, whereas the quality of the interface with the semiconducting layer regulates the filed mobility [186]. Hence, an ideal gate dielectric material should have good insulating properties, smooth morphology, and easy processing conditions. Polymer thin films are excellent choice to serve as the gate dielectric material in TFTs. Unlike the conventional inorganic gate dielectrics like silicon dioxide, silicon nitride, aluminum oxide, etc., polymer gate dielectrics have the advantage of better interface characteristics as well as easy integration into the device architecture [187].

Plasma polymerization is a very useful technique to create ultra-thin films with excellent control over the process and the properties. Hence, thin films having various thicknesses (ranging from few nanometers to micrometers) and diverse dielectric constant can be easily fabricated using this technique. To illustrate, Senda et al. [188] reported the fabrication of ultra-thin (2–10 nm) plasma-polymerized hydrocarbon films with consistent properties suited for various electronic applications. A number of reports have also been published on the dielectric properties of plasma-polymerized hexamethyldisilazane, fluorocarbons, polyaniline, organic and organosilicon polymer thin films [189–192]. It is worth mentioning that, pp-hexamethyldisilazane fabricated through microwave discharge exhibited dielectric breakdown strength of 12.5×10^8 MV/cm comparable with that of

inorganic SiO_2 dielectric material [193]. Even though the dielectric constant values of polymer thin film dielectrics are generally lower compared to the inorganic dielectrics, former have the advantage of flexibility and suit the niche foldable applications.

A novel approach for realizing high-k dielectric polymer thin films was established by Bhattacharryya et al. [194] through successive plasma polymerization of vinyl acetic acid and allylamine. At 1 MHz, a dielectric constant of 5.7–6.2 was measured for the prepared polymer thin film samples. The high dielectric constant obtained here is attributed to the unique layered structure of the polymer film incorporating polar $–COO^-$ and $–NH3^+$ groups. Followed by this work, Yoon et al. [195] reported the performance of a TFT fabricated with a multistack gate dielectric layer material. In this study, a 10-layer polymer film of thickness of 60 nm has been made from allylamine and vinyl acetic acid monomers using pulsed radio frequency plasma polymerization. The multilayered dielectric possessed a relatively high dielectric constant of 4.4 and the TFT tested exhibited a low-voltage operation and moderate field effect mobility of 3×10^{-2} cm^2/Vs. Furthermore, the gate dielectric showed a breakdown field larger than 4 MV/cm and leakage current density of 7.34×10^{-6} A/cm^2. Another work reported the fabrication of very high permittivity gate dielectrics from dichlorotetramethyldisiloxane (DCTMDS) monomer [196]. The measured dielectric constant was found to be $\sim$7–10 and was associated with the high polarizability of DCTMDS monomer. The authors also tested a poly (3-hexathiophene) FET using a 85 nm pp-DCTMDS as gate dielectric material. It was observed that, the high dielectric constant of the gate material facilitated a high gate capacitance, which reduced the device operating voltage [197]. Lim et al. [198] reported the fabrication as well as the gate dielectric performance of plasma-polymerized methylmethacrylate (pp-MMA) thin films (Fig. 11.9). One interesting observation is that pp-MMA showed a higher dielectric constant than that of the conventionally processed polymethylmethacrylate film. In this study, a dielectric constant of 3.86 was obtained for pp-MMA thin films whereas a dielectric constant of 2.5–2.9 is reported for conventional films [199]. Interestingly, a 100 nm thick pp-MMA film shows good dielectric strength and minimum leakage current density of the order of 10^{-8} A/cm^2. On the other hand, the conventionally processed PMMA layers exhibit much higher leakage current density, greater than 10^{-4} A/cm^2 [199]. Figure 11.9d, e compares the J-E characteristics of plasma-polymerized and conventionally processed PMMA films. The improved performance of pp-MMA is ascribed to the highly cross-linked and pinhole-free nature of pp-MMA. This study also evaluated the behavior of pp-MMA dielectric in an AU/pentacene/pp-MMA/ITO OTFT device. The device showed a field effect mobility of 0.08 ± 0.02 cm^2/Vs, lower threshold voltage -3 ± 0.15 V and an on/off current ratio of 1.0×10^4.

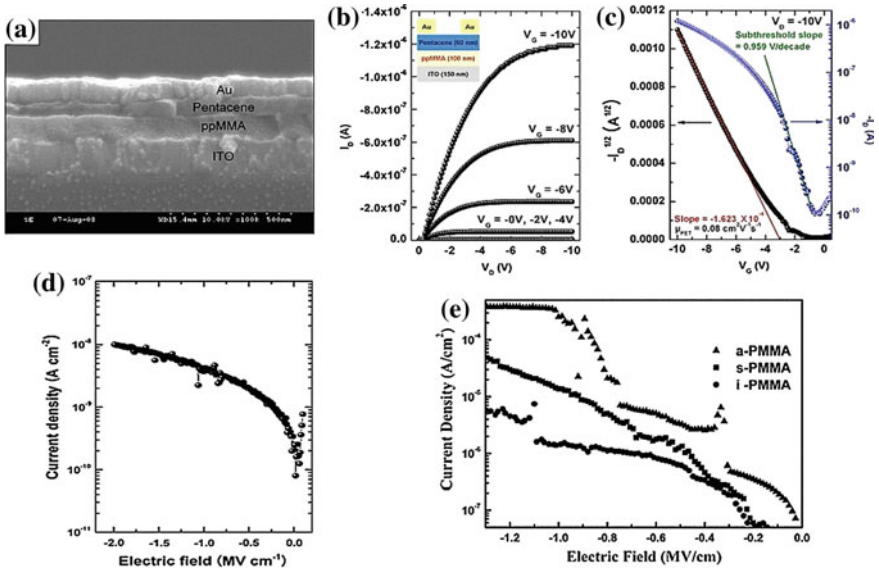

Fig. 11.9 **a** SEM image of the ITO/pp-MMA/pentacene/Au TFT device taken from one side. **b** Drain current-drain voltage characteristics of TFT (ITO/pp-MMA/pentacene/Au) with plasma-polymerized methylmethacrylate gate dielectric film. **c** Transfer characteristics (drain current Vs gate voltage) for the same. Reproduced with permission from [198]. **d** and **e** compares the J-E characteristics plasma-polymerized and conventionally processed PMMA films. The PP-MMA films exhibited good dielectric strength as well as minimum leakage current compared to the conventional films. Reproduced from previous work with permission from Ref. [198, 199]

11.4.1.2 Hybrid Gate Dielectric Thin Films

Organic–inorganic hybrid materials constitute an important class of materials used in TFTs as gate dielectrics. Hybrid films deposited from a mixture of hexamethyldisiloxane (HDMSO) and O_2 gained considerable research interest as gate dielectrics. Noteworthy is that film properties of the hybrid film can be easily varied from an organic to inorganic SiO_2 nature by precisely controlling the stoichiometry of the reactant gas mixture [200–202]. Han et al. [203] introduced the use of plasma-deposited hybrid film developed from HDMSO/O_2 mixture as a new gate dielectric material for amorphous silicon (a-Si:H) thin film transistor. The hybrid film exhibited a dielectric constant of 4 and the thin film transistor demonstrated a high field mobility of 2 and 0.1 cm^2/Vs for electrons and holes respectively. Another work by the same authors realized ultra-flexible a-Si:H thin film transistor by replacing both silicon nitride barrier layer and gate dielectric layer by plasma-deposited silicon dioxide-silicon hybrid polymer material. In this study, the transistor showed a bending down to 0.5 mm radius in tension and down to 1 mm radius in compression, with potential applications in pull-out display screen. A remarkable 10-fold increase in maximum tensile strength $\varepsilon_{critical}$ is recorded for

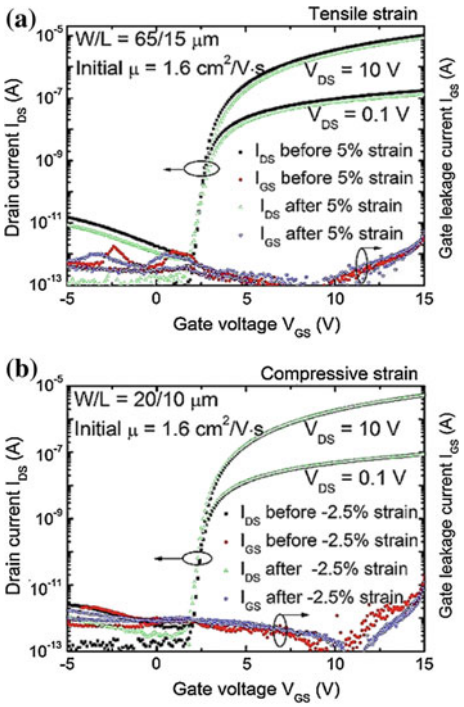

Fig. 11.10 Transfer characteristics of ultra-flexible a-Si:H thin film transistors using hybrid gate dielectric layer. Drain current (I_D) and gate leakage current (I_{GS}) showed consistent behaviors with and without **a** tensile strain and **b** compressive strain. Reproduced with the permission from Ref. [204]

hybrid TFTs (5%) compared to the conventional SiN_x TFTs [204]. The study conducted by Han and coworkers [205] observed that the hybrid dielectric (Si–SiO_2) film have enhanced the performance of a-Si:H thin film transistor to the level needed for AM-OLED pixel circuits. The study revealed a reasonably good electron mobility of 1.5 cm^2/Vs and on-off current ratio of 10^7. Also, compared to the conventional a-SiH/silicon nitride transistor, the threshold voltage was found to reduce by one-half (Figure 11.10).

11.4.1.3 Plasma Polymer Buffer Layers for Conventional Inorganic Dielectric Films

The field effect mobility of the TFT is highly dependent to the dielectric semiconducting interface behavior [206, 207]. In order to have high field mobility, the dielectric layer should form a good interface with the semiconducting layer. Yildirim et al. [208] reported the effect of gate dielectric interface on the performance TFT using various dielectric materials. Though inorganic materials have better dielectric properties than organic polymers, they generally suffer from poor interface with semiconducting channel [209]. However, the interface characteristics of inorganic dielectrics can be tailored by modifying the surface features through employing a buffer layer. Tang et al. [210] used plasma-polymerized fluorocarbon film as coating

layer for SiO_2 dielectric layer in a pentacene organic transistor. Interestingly, the dielectric surface modification enhanced the field effect mobility from 0.015 to 0.22 cm^2/Vs and also reduced the threshold voltage from −14 to −9.9 V. A comparison between drain current and drain voltage for both configurations is depicted in Fig. 11.11. The improvement in transistor performance is mainly attributed to improvement in interface characteristics (manipulation of electronic structure at the SiO_2/pentacene interface) provided by the pp–CF_x coating. Also, the hydrophilic nature of pp–CF_x film prevents the moisture absorption, which is considered an additional advantage. Another advantage of plasma polymerization is its compatibility to wide range of precursor materials. There are published studies on the fabrication of polymer thin films from natural precursor sources through plasma polymerization [125, 211, 212]. Synthesis of a non-synthetic polymer dielectric having relatively good dielectric constant was reported by Jacob et al. [213]. Using RF plasma polymerization, the authors were able to synthesize polymer thin films from a natural precursor, terpene-4-ol. The films exhibited a dielectric constant of 3.4. In addition, the film was implemented as a gate modifying layer in pentacene/SiO_2 TFT. The OFET device performance with polyterpenol gate modifying layer showed a significant reduction in threshold voltage from +20 to −3 V and an improvement in switching property from 10^4 to 10^7.

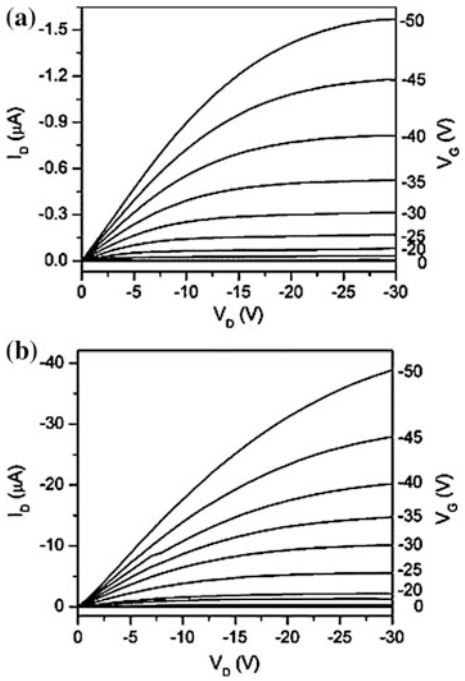

Fig. 11.11 I_D Vs V_D characteristics of pentacene transistors at various gate voltages having **a** SiO_2 dielectric layer, **b** SiO_2 dielectric layer coated with pp-CF_x polymer layer. The device with CF_x layer showed a larger drain current, higher saturation current and a 10-fold increase in the mobility compared to transistor with bare SiO_2 Reproduced from previous work with permission from Ref. [210]

11.4.2 Plasma Polymers for Organic Light Emitting Diodes (OLEDs) Applications

Organic light emitting diodes (OLEDs) have received significant attention in large area flexible displays. A typical OLED has a single or multilayered structure composed of an anode electrode, a hole injection layer (HIL), a hole transport layer (HTL), an electron transport (ETL) layer, an emitting layer, and a cathode electrode [214]. A schematic of OLED structure is shown in Fig. 11.12. It is reported that the difference in the electron mobility and hole mobility in ETL and HTL is a major problem in OLEDs and leads to lower efficiency [215]. One of the approaches to circumvent the issue is to improve the charge injection efficiency at the anode/organic layer interface by modifying the electrostatic condition, for instance, through the introduction of a buffer layer. However, selection of the buffer layer is very important since any defects/impurities in the layer, a mismatch or poor interlayer adhesion will adversely affect the device performance. It is noted that plasma polymers are one of the best suited material choices to tune the surface characteristics of electrodes to enhance the charge injection in OLEDs [215–217]. Hung et al. [218] studied the effect of anode modification of OLEDs using plasma-polymerized CHF_3 films. The authors observed that OLEDs with modified anode exhibited enhanced hole injection as well as operational stability compared to unmodified devices. Tang et al. [216] reported an improvement in the hole injection and operational stability of OLEDs where the anode was coated with plasma-polymerized fluorocarbon (CF_x) films. The improved hole injection could be attributed to the reduction in the barrier height (energy difference between E_{HOMO} of the hole transporting layer and Fermi level (E_F) of the anode) and better energy level alignment between anode/organic interface facilitated by the polar CF_x layer. The ultraviolet photo emission spectroscopy (UPS) measurement revealed that the introduction of fluorocarbon films has substantially reduced the barrier potential to 0.56 eV (Fig. 11.13), which boosted the hole injection. The J–V measurements performed on Au/CF_x/NPB/Alq_3/MgAg devices revealed that the current density drastically increased from 0.35 to 94 mA/cm^2 when the interface CF_x layer was incorporated. It is also observed that the presence of CF_x layer protects the anode from atmospheric moisture and provide high operational stability. Hence CF_x layer coated ITO anode characterized with good operational stability by avoiding reduced luminosity decay of less than 5% (duration 300 h).

Park et al. [217] has achieved improved hole injection efficiency for ITO/ppTh/TPD/Alq_3/Al OLED device by modifying the O_2-plasma-treated indium tin oxide (ITO) anode using RF plasma-polymerized polythiophene (ppTH). The introduction of ppTH buffer layer provided a better interface between anode and the hole transporting layer (TPD), reduced the hole mobility and thereby improved the electron–hole recombination in the emitting layer. On comparing the luminosity characteristics, the device incorporated with ppTH buffer layer exhibited brightness higher than 4600 cd/m^2. On the other hand, the device without the ppTH layer showed a decreased brightness of 3400 cd/m^2. Another work illustrates that

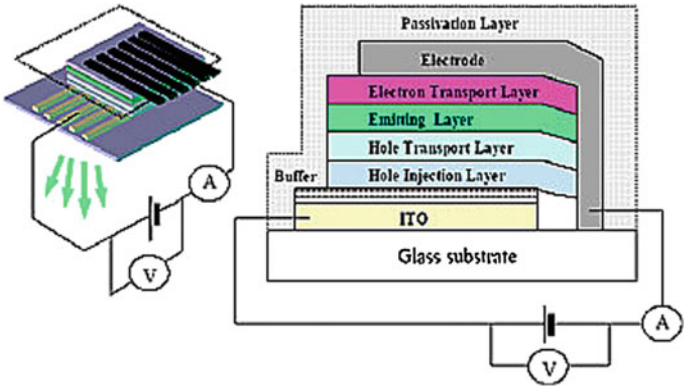

Fig. 11.12 Schematic of a multilayered OLED. Reproduced from previous work with permission from Ref. [214]

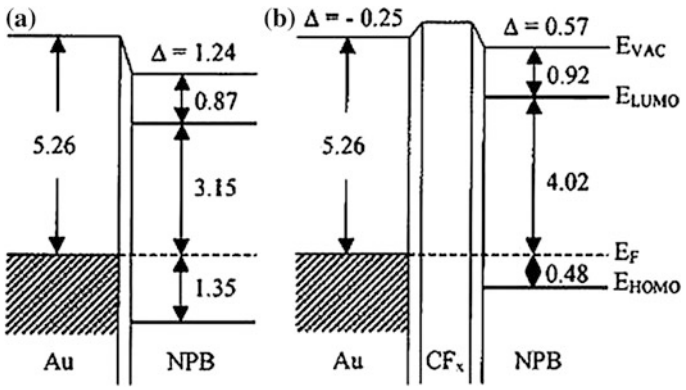

Fig. 11.13 Schematic energy diagram of the interface derived from UPS spectra **a** Au/NPB/Alq_3/MgAg with Au anode and **b** Au anode surface modified with 0.3 nm pp-CF_x thin film. The former exhibits a very high barrier height of 1.35 eV which virtually block the hole injection whereas the latter exhibited a significantly lower barrier height of 0.48 eV, enabled by the pp-CFx interface and therefore resulted in considerable improvement in OLED performance (as equal as that of surface treated ITO anode). Reproduced from previous work with the permission from Ref. [216]

incorporation of plasma-polymerized methyl methacrylate (pp-MMA) layer into OLEDs (ITO/pp-MMA/TPD/Alq_3/Al) resulted in a lower turn-off voltage and very high luminescence of 6800 cd/m^2. Furthermore, the pp-MMA-modified anode was found to be smooth, with lower surface roughness ($\sim$1.6 nm) and good adhesion to the electrode [215]. All these reports confirm the ability of plasma polymers to serve as an excellent anode coating in OLEDs (Fig. 11.14).

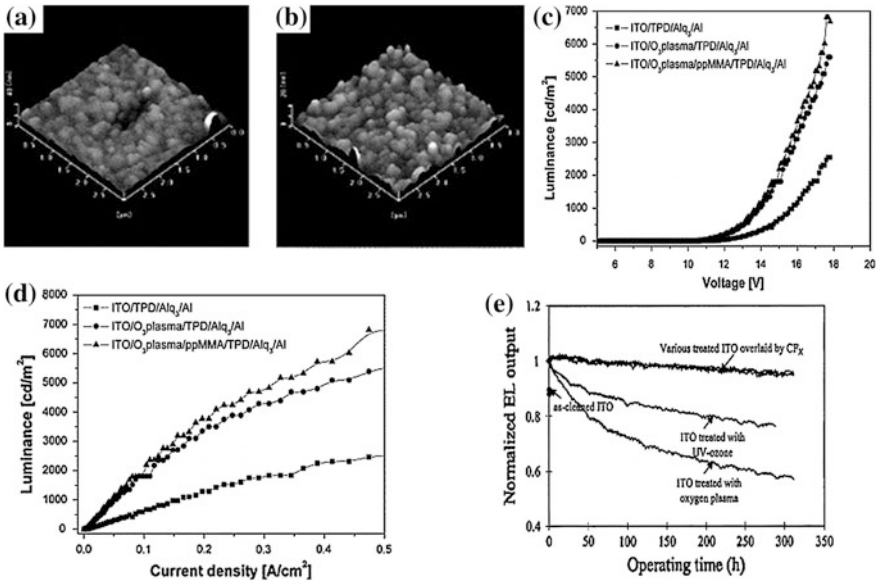

Fig. 11.14 **a** and **b** Represents 3 × 3 μm 3-D AFM image of bare ITO anode surface and the surface of ITO anode coated with pp-MMA buffer layer. The pp-MMA layer forms a smooth pinhole-free buffer layer and hence provides a significantly better interface with hole transporting layer. **c** and **d** Depicts the performance evaluation of OLEDs with bare ITO, O_3 plasma-treated ITO, and O_3 plasma-treated ITO coated wtih PP-MMA layer. Incorporation of pp-MMA layer improved the L-V and L-J characteristics of the device considerably. Reproduced with the permission from [215]. **e** Displays the operational stability of OLED employing a pp-CF*x* buffer layer. Reproduced from previous work with permission from Ref. [216]

11.4.3 Plasma Deposited Films for Device Encapsulation

One of the greatest challenges faced by organic electronics is the poor stability of the devices due to absorption of water from the ambient atmosphere [219]. The moisture/oxygen can degrade the polymer layers and the metal contacts thereby significantly affecting the device efficiency as well as the lifetime. In order to prevent the moisture/oxygen permeation, the device needs to be encapsulated with suitable barrier coatings. The most commonly used encapsulation methods are (i) encapsulation through glass lid or metal coating, (ii) barrier coated flexible lids, and (iii) thin films barrier coatings [220]. The two major parameters taken into consideration when judging the barrier performance of an encapsulating layer are the water vapor transmission rate (WVTR) and oxygen transfer rate (OTR) [221]. Organic electronic devices generally demand a very low WVTR ($\sim 10^{-6}$ gm^{-2} day^{-1}) and OTR ($\sim 10^{-3}$ cm^3 m^{-2} day^{-1}) [222]. The barrier coating should also be flexible and transparent, and be deposited using low-temperature, simple processes.

PECVD is highly efficient in realizing highly uniform and large area films with excellent barrier properties. Plasma polymers can either act as barrier layers by

themselves or perform as interlayers in a multilayer barrier coating structure [223, 224] (Fig. 11.15a). Li et al. [223] reported the environmental stability of a solar cell encapsulated with single layer of plasma-derived hybrid barrier layer and compared it with that of an uncoated device. Noteworthy is that the former demonstrated no decline in efficiency for 3000 h when exposed to air whereas the latter showed a drastic reduction in efficiency. Here, the barrier layer is created from hexadimethylsiloxane (HDMSO)/O_2 mixture and showed transmittance $\geq 90\%$ together with a low WVTR of 3.6×10^{-6} gm^{-2} day^{-1}. Another work by Mandlik et al. [225] reported an improvement in the OLED lifetime (3000 h) when coated with hybrid barrier film created through RF-PECVD of HDMSO and O_2 mixtures. Thus fabricated SiO_2-like hybrid film (80% SiO_2 and 20% pp-HDSMO) showed better micro hardness compared to thermally grown SiO_2 of the same thickness. Plasma-deposited silicon nitride (SiN_x) and oxide coatings are also extensively studied for barrier coating applications [226–229]. Recently, Qit et al. [230] reported the shelf-life improvement of solar cells covered with plasma-deposited SiO_x layers. The study used transparent polyethyleneterephtalate (125 μm) coated with SiO_x layer as barrier coatings for an inverted solar cell (ITO/Al_2O_3/P_3HT:PCBM/MoO_3/Ag). In this study, PET + SiO_x combination exhibited a WVTR of 1.1×10^{-3} gm^{-2} day^{-1} and OTR less than 0.05 cm^3 m^{-2} day^{-1}. Furthermore, the encapsulation has improved the shelf-life of the device to 500 h with 50% retained efficiency.

In order to cope with the flexible electronic applications, the encapsulating layers should be as flexible as possible. Even though metal oxide thin films such as Al_2O_3, ZrO_2, and TiO_2 are superior over polymer films in terms of barrier performance, they are highly brittle in nature [231]. However, multilayer structures composed of alternating organic–inorganic layers were shown to have excellent flexibility and barrier properties [15, 224]. Lee et al. [224] reported an excellent retention of WVTR properties of an oxide multilayer permeation barrier PET/Al_2O_3/SiO_x ($x = 1.8$). The barrier layer was fabricated by successively depositing Al_2O_3 (Atomic Layer Deposition, ALD) and SiO_x (PECVD) on PET substrate. The WVTR of PET/Al_2O_3 (90 nm)/SiO_x (10 nm) was measured to be less than 5×10^{-3} gm^{-2} day^{-1} after 1000 bending cycles at 35 mm bending radius. A recent work by Seo et al. [15] reported an extremely bendable multistack encapsulating layer composed of Al_2O_3 and plasma-polymerized hexane interlayers. The authors could fabricate the multilayer structure within the same chamber using trimethyl aluminum and hexane as the precursor source for ALD and PECVD, respectively. The performance evaluation of the OLED device before and after encapsulation revealed that the coating process did not alter the device properties (Fig. 11.16a). It is observed that bending property increased with number of layers and moisture absorption rate decreased with increasing the number of interlayers. In addition, the multilayer barrier with 200 periodic structures showed a WVTR of $\sim 10^{-4}$ gm^{-2} day^{-1} initially and change was less than 20% even after 10,000 times of bending.

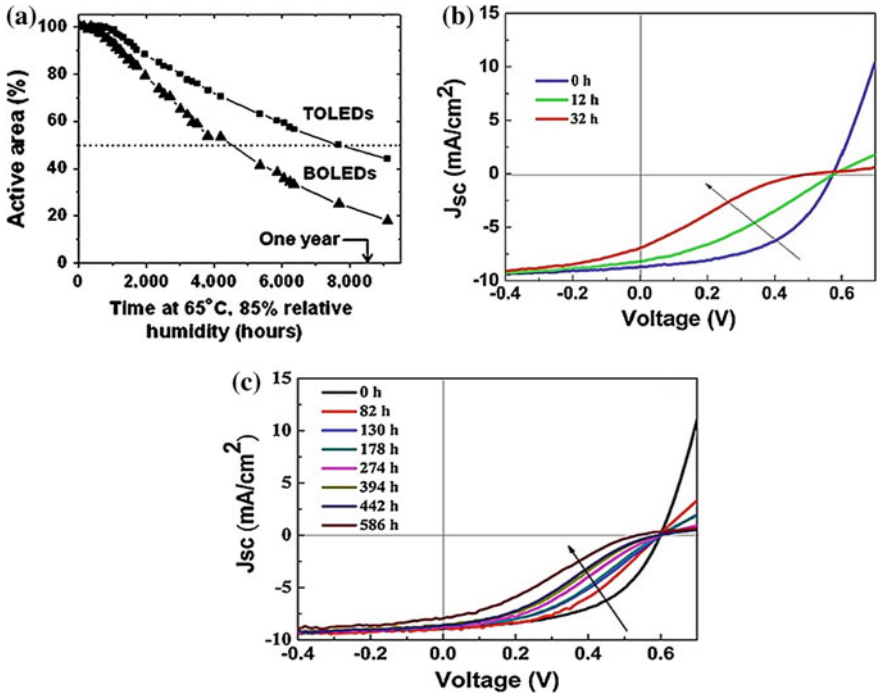

Fig. 11.15 **a** Average active pixel area versus duration of accelerated storage for top emitting OLEDs (TOLED) and bottom emitting OLEDs (BOLEDs) coated with plasma-derived hybrid coatings. The devices exhibited a lifetime up to 7500 h (TOLEDs) and 4500 h (BOLEDs), far higher than the industrial requirement of 1000 h. Reproduced with permission from Ref. [225]. J–V curves of solar cells under ambient environment **b** un-encapsulated **c** encapsulated (plasma-deposited SiO_x layer). The former showed a drastic reduction in the conversion efficiency (2.62–0.74%) within 32 h of storage time whereas the latter has improved the shelf-life of the device to 500 h with 50% retained efficiency. Reproduced from previous work with permission from Ref. [230]

11.5 Plasma Polymer Thin Films for Biomedical Applications

Materials employed within the biomedical field are subjected to a significant number of design constraints. From an operational perspective they must exhibit specific mechanical, biocompatibility, and degradation characteristics. These properties must be further overlaid with economical and process related considerations extending to their reproducibility, ease of manufacturing, and scalability. It is common to employ a two-step process in order to fabricate biomedical materials or devices that can satisfy all of these criteria.

First, a bulk material is selected for its mechanical properties (elasticity, strength, density, and so on). This material is then subject to a surface treatment procedure,

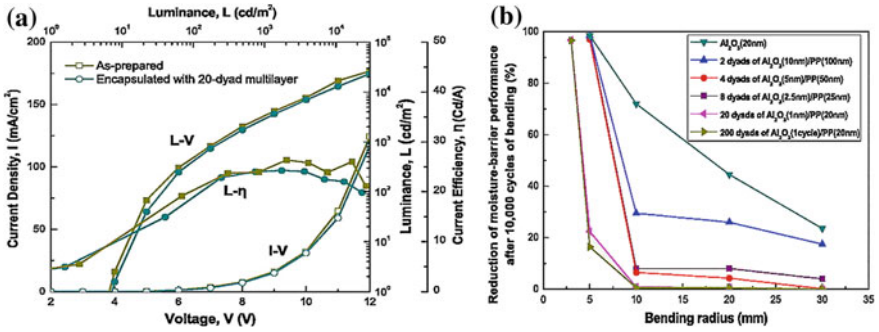

Fig. 11.16 **a** Comparison of the OLED performance coated with multilayer barrier coatings. The resemblance in the behavior confirms that the encapsulation process does not degrade the OLEDs. **b** The reduction of moisture barrier property after 10,000 cycles of bending with various bending radii. Samples with more dyads (20 and 200) tend to keep the barrier property even with a bending radius of 5 mm. Reproduced from previous work with permission from Ref. [15]

either directly or via thin film deposition, in order to present a surface with the appropriate chemical and morphological features needed to interact with the external biological environment. Desirable responses often include minimal immunogenic reactions, and the elicitation of specific cellular responses (e.g., adhesion, proliferation, and differentiation). This surface modification process should induce no variations in the mechanical properties of the underlying bulk material.

Cold plasmas have been applied to the biomedical field to accomplish three particular objectives, namely: the sterilization of surfaces, the direct treatment of tissue and cells, and the fabrication of surfaces with specific chemical and morphological properties. This final objective can be accomplished either vie direct plasma treatment of the surface, or by the deposition of a plasma polymer thin film.

Regardless of the specific biomedical application under consideration, plasma polymer thin films demonstrate a number of properties that serve to enhance their biomedical utility. To begin with, the physicochemical properties of the thin films can be tuned by controlled variation in any number of process parameters, such as monomeric precursor species, deposition time, applied power, species of carrier gas, and so on. The fabrication of pinhole-free films with strong adhesion to conformationally irregular substrata (a generic characteristic of plasma polymers) also enhances their suitability for biomedical applications. These films also tend to be chemically stable and physically durable [232].

There exists a persistent need for the development of surface-fabrication technologies that can keep pace with the inherent adaptability of medically relevant pathogens, and enable the future development of new biomedical devices. The remainder of this subsection addresses the dominant fields in which plasma polymers are presently being studied for their capacity to satisfy this need in the biomedical domain.

11.5.1 Drug Encapsulation and Controlled Release

Pharmaceutical drugs are subject to a number of constraints relating to both their own unique chemistry, and the biological environment in which they operate. These factors may cause the drug to be rapidly metabolized and subsequently eliminated from the organism, imposing the need for repeated administration (coupled with a consummate increase in treatment cost).

By matching the rate of drug release to the rate of drug elimination, the efficacy of the drug can be enhanced, while simultaneously minimizing the corresponding impact of harmful side effects. Furthermore, maintaining the drug's concentration within its corresponding therapeutic window can also lead to a reduction in the frequency of drug administration, leading to increased consumer convenience and compliance with administration schedules [233].

Technologies employed to control the release rate of pharmaceutical products can be discriminated into two broad camps; those which seek to control the temporal rate of drug release, and those which work to control the spatial distribution of drug release. In the first instance the objective is to either provide a consistent rate of drug release, or to ensure that the drug release is subject to a delay of precise duration.

Controlled drug release can be achieved via three approaches, including: delayed drug dissolution, diffusion control, and controlled drug solution flow [234]. The first of these approached, delayed drug dissolution, typically takes the form of encapsulating the drug in a biodegradable layer (or layers), and has been achieved using a variety of techniques. The temporal control of drug release can be achieved via three approaches, including: delayed drug dissolution, diffusion control, and controlled drug solution flow [234]. The first of these approaches, delayed drug dissolution, typically takes the form of encapsulating the drug in a biodegradable layer (or layers), and has been achieved using a variety of techniques that typically center around the application of a polymeric coating, for which plasma polymerization is particularly well suited to. Because the films in plasma polymerization method can be applied in a single low-temperature and solvent-less step the chemical properties of the bulk drug material are not subjected to incidental modification. Furthermore, films of precise thickness can be fabricated by simple regulation of the deposition time, and the extent of cross-linking can be easily controlled by variation of the applied power. The implication being that the film thickness and cross-linking can be modified to control the duration of its biodegradation and subsequent release of drug payload.

Complete encapsulation of drug particles has been accomplished by the utilization of rotating plasma reactor vessels, the tumbling motion of which ensures uniform conformational coverage of the particles with the plasma polymers. These systems also often employ pulsed mode deposition at low power to minimize UV photon-induced photochemical dissociation of the drug molecules. Using these techniques, the first application of a plasma polymer using allyl alcohol precursor was deposited on acetylsalicyclic acid (aspirin) in 2004 [235]. The release profiles

of these polyallylalcohol coated aspirin crystals in pH 1 HCl solution (to simulate gastric fluid) are presented in Fig. 11.17 for differing deposition conditions. These findings indicated that the drug release rate can be reduced by increasing the deposition power (increasing polymer cross-linking and impermeability), time (thicker films), and duty cycle (again, increased cross-linking).

In addition to applying plasma polymers to discrete drug particles, plasma polymerization may also be employed to encapsulate comparatively larger surfaces (such as those of an indwelling implant) to which a pharmaceutical product has previously been applied. This approach often utilizes a layered technique, with the underlying substrate first receiving a plasma polymer coating that is primarily tasked with enhancing the adhesion of the drug to the device. Following the application of the pharmaceutical product, a final plasma polymer layer is deposited to control the rate of drug release [236–238].

Beyond controlled drug dissolution, it has been shown that plasma polymers can effect drug diffusion control by taking advantage of their preferential adherence to the rims of pores (with comparatively small amounts of the polymer penetrating into the interior of the pore). This opens up the possibly of using plasma polymers to either constrict the diameter of pore rims, or to effect complete encapsulation of drug-loaded porous devices. This dry approach to drug encapsulation is particularly attractive because it guarantees that there will be no elution of the drug payload

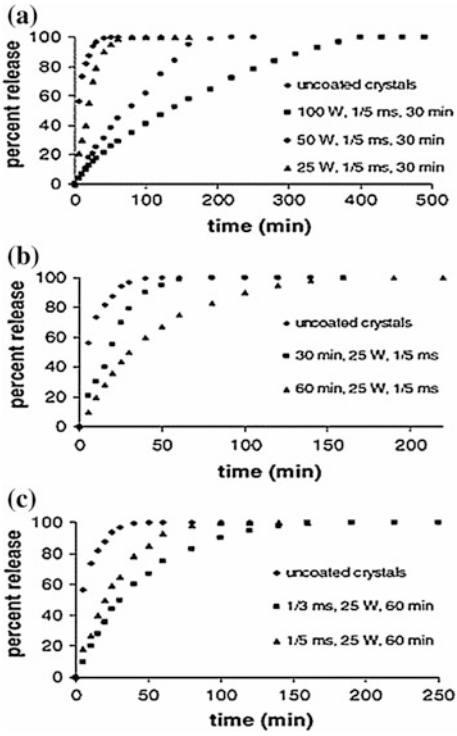

Fig. 11.17 Time-dependent release rate of plasma polymer coated aspirin crystals for coatings produced under varying **a** peak power, **b** deposition time, and **c** plasma duty cycle. Reproduced from previous work with permission from Ref. [276]

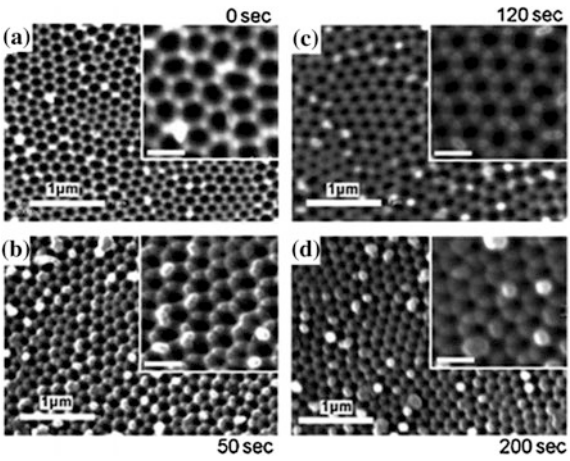

Fig. 11.18 SEM images of **a** pristine anodic alumina oxide, and anodic alumina oxide modified with allylamine plasma polymer with deposition times of **b** 50 s, **c** 120 s; and **d** 200 s. Insert *scale bar* = 200 nm. Reproduced from previous work with permission from Ref. [277]

during the encapsulation process, and its efficacy has been demonstrated on a number of porous media such as alumina, titania, and silicon as shown in Fig. 11.18 [239, 240].

11.5.2 Antibacterial Coatings

Hundreds of millions of patients in both developing and developed countries are affected by nosocomial (i.e., in-hospital acquired) infections each year, resulting in hundreds of thousands of deaths. A portion of these infections are related to the use of invasive devices and implants, which also harbor the potential to increase patient distress and impose economic penalties on both the patient and their extended network (including their family, employer, and the health system) [241].

While synthetic antibiotics have been utilized as the go-to method for controlling bacterial infections, their use is subject to a number of limitation. For example, antibiotics often exhibit an action that is specific to a particular type of bacteria. Furthermore, certain bacteria are resistant to the action of antibiotics (or produce a biofilm that effectively grants resistance), and many bacteria are strenuously developing antibiotic resistances [242].

The development of antibacterial films that are resistant to the adhesion, proliferation, and eventual spread of bacteria represents one of the most promising methods for curtailing the pervasiveness of bacterial infections. The antibacterial actions of these films are often achieved by careful selection of their surface chemistry and nanoscale structures, and/or by the incorporation of antibacterial agents (e.g., silver nanoparticles) into their structure. These films have been produced using plasma polymerization where the cold plasma environment utilized in the polymerization process has the added benefit of being a rich source of ions, electrons, UV photons, and other reactive species. The presence of these species

imbues the process with an inherent capacity for destroying spores, bacteria, and biomolecules, rendering the underlying substrate and final film surface sterile [243, 244].

11.5.2.1 Antibacterial Coatings—Surface Functionalization

The ultimate fate of an indwelling implant (i.e., whether it is ultimately accepted or rejected by the host) is strongly dependent upon early interactions between the device's surface and its surrounding biological medium. Specifically, the adhesion and subsequent colonization of the surface is a competitive process between host cells (e.g., fibroblasts, endothelial cells, etc.) and microorganisms. This competitive process is itself a function of the status and composition of the conditioning film of extracellular matrix (ECM) proteins that coat the surface shortly after implantation.

Functional groups present on the surface of a biomaterial influence its hydrophobicity and surface free energy. These factors, coupled with the presence of functional groups, serve to control the adhesion of various biologically relevant proteins. These proteins, in turn, mediate the adhesion (or repulsion) of mammalian and pathogenic cells. Plasma polymerization may be employed in the fabrication of functionalized coatings that serve as attachment sites for biocidal or bacteriostatic molecules (such as collagen, fibronectin, and ARg-Gly-ASP) that serve to regulate cell-surface interactions [245].

One example of developing surfaces for enhanced endothelialisation, (i.e., formation of endothelial tissues) involves the utilization of fibronectin functionalized plasma-polymerized acrylic acid films [246]. In this instance, covalent immobilization of fibronectin (an adhesion promoting protein) to carboxyl groups present within the plasma polymer has been successfully demonstrated. The utility of this development was shown in the enhanced adhesion and proliferation of human umbilical vein endothelial cells (HUVECs) to the treated surface as shown in Fig. 11.19. This specific example demonstrates the promotion of HUVEC adhesion and proliferation on the plasma-polymerized surface relative to the stainless steel control. This, coupled with the increased elongation and coverage of the cells in question highlights the potential for utilizing approaches such as this for the development of plasma polymerization surface modification for the fabrication of vascular devices, where the enhanced endothelialisation may inhibit the onset of thrombosis and restenosis [247].

In addition to promoting the adhesion of desirable mammalian cells, plasma polymerization can also be used to introduce surface functionalities that serve to inhibit the attachment of bacterial cells. Non-synthetic antibacterial precursors such as monoterpene alcohols have also been used, and have been shown to inhibit the adhesion of pathogens such as the biomedically relevant *Pseudomonas aeruginosa* as shown in Fig. 11.20. It is interesting to note here that minimal bacterial adhesion and proliferation is achieved for the film fabricated at the lowest applied power.

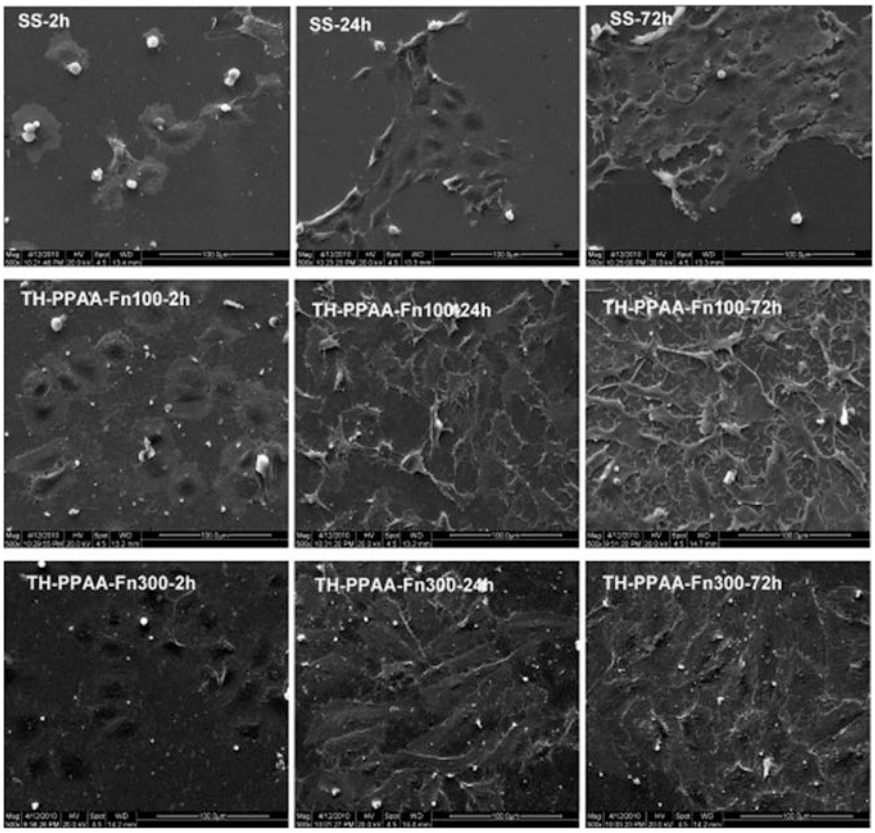

Fig. 11.19 HUVEC cells seeded on stainless steel (SS), and thermal treated plasma-polymerized acrylic acid pretreated with immersion in a 100 μg/mL fibronectin biomolecule solution (TH-PPAA-Fn100) at 2, 24, and 72 h. Reproduced from previous work with permission from Ref. [246]

This is a property common to many plasma polymers, and can be attributed to the increased incorporation of the precursor monomer (either via physisorption or an inherently decreased extent of monomer fragmentation) and its antibacterial functionalities. For this reason, functionalized antibacterial plasma polymers are typically fabricated utilizing low applied power or pulsed plasma approaches, both of which tend to lead to an increase in the retention of whole (or minimally fragmented) monomeric units. Plasma polymers may also been employed to indirectly inhibit bacterial adhesion by covalently immobilizing various antimicrobial peptides such as nisin, Trp11, LL37, and 4 K-$C1_6$ to epoxide and aldehyde surface functionalities [248, 249].

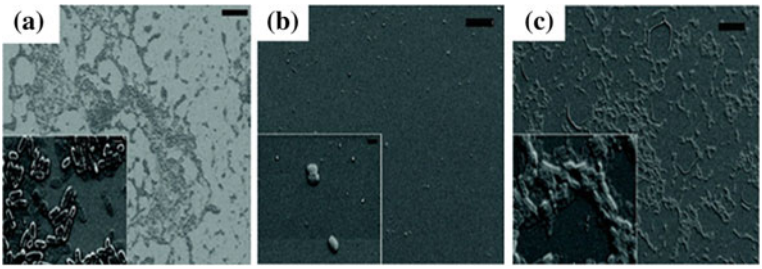

Fig. 11.20 *P. aeruginosa* growth patterns after 18 h on (**a**) glass, and polyterpenol plasma polymer deposited at (**b**) 10 W, and (**c**) 25 W (500 × magnification for images at *left*, *bar* = 20 μm). Reproduced from previous work with permission from Ref. [278]

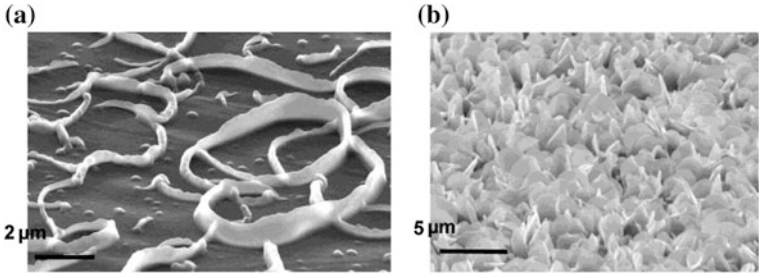

Fig. 11.21 Ribbon-like and petal nanostructured fluorocarbon coatings. Reproduced from previous work with permission from Ref. [251]

11.5.2.2 Antibacterial Coatings—Surface Nanostructuring

Cells possess the ability to sense the chemistry and morphology of surfaces prior to initiating adhesion to said surface [250]. In addition to interacting with randomly disordered surface features, it has also been demonstrated that cells respond to geometrically ordered surface features (such as grooves, pits, spheres, etc.). This response can take the form of directed adhesion, growth, or migration (with the latter two often being directed along fibers, edges, or ridges). Advanced materials can now be fabricated with micro- and nanoscale features that can be effectively employed to either regulate cellular adhesion, or promote guided cell growth and migration.

Teflon-like coatings have been developed using fluorocarbon precursor monomers [251]. The hydrophobic, inert, and low-friction characteristics have shown a capacity to render the films biocompatible. Various cell lines (such as osteoblasts, fibroblasts, and chondrocytes) have been grown on these nano- and micro-structured Teflon-like fluorocarbon surfaces exhibiting different topographies. The diversity of some of these topographies is demonstrated in the scanning electron microscopy (SEM) images depicted in Fig. 11.21.

These films, and others of a similar nature, demonstrate the capacity for utilizing surface structuring to enhance cell proliferation (relative to that exhibited by cells on smooth surfaces). This is demonstrated in Fig. 11.22, where osteoblasts exhibit preferential spreading and grown on a textured surface (relative to a perfectly smooth surface).

Another common method for the production of nanostructured surface features is to incorporate nanoparticles into the deposited film. An ideal candidate for this approach is gold nanoparticles which can be produced with tightly controlled size distributions, and when greater than around 5 nm produce minimal oxidation products (rendering them biologically inert for the most part) [252]. An example of the surfaces that can be prepared in this manner are presented in Fig. 11.23, where gold nanoparticles of varying size and number density gradients have been prepared using immersion of a substrate coated with a functional plasma polymer into a solution of gold nanoparticles. It must be noted that the incorporation of

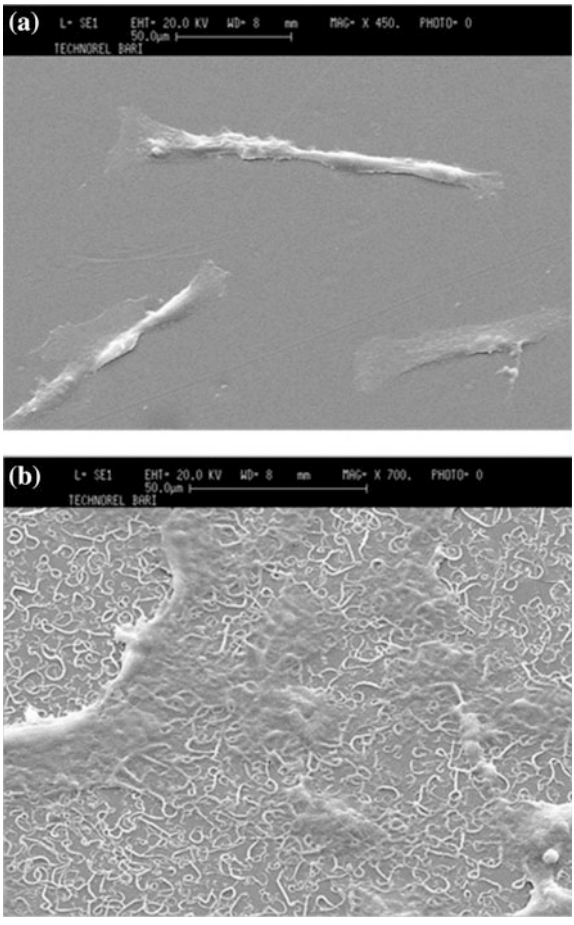

Fig. 11.22 MG63 osteoblast cell lines grown on plasma-deposited fluorocarbon surfaces on **a** a flat substrate; and **b** a substrate with ribbon-like features as detailed in Fig. 11.21. Reproduced from previous work with permission from Ref. [251]

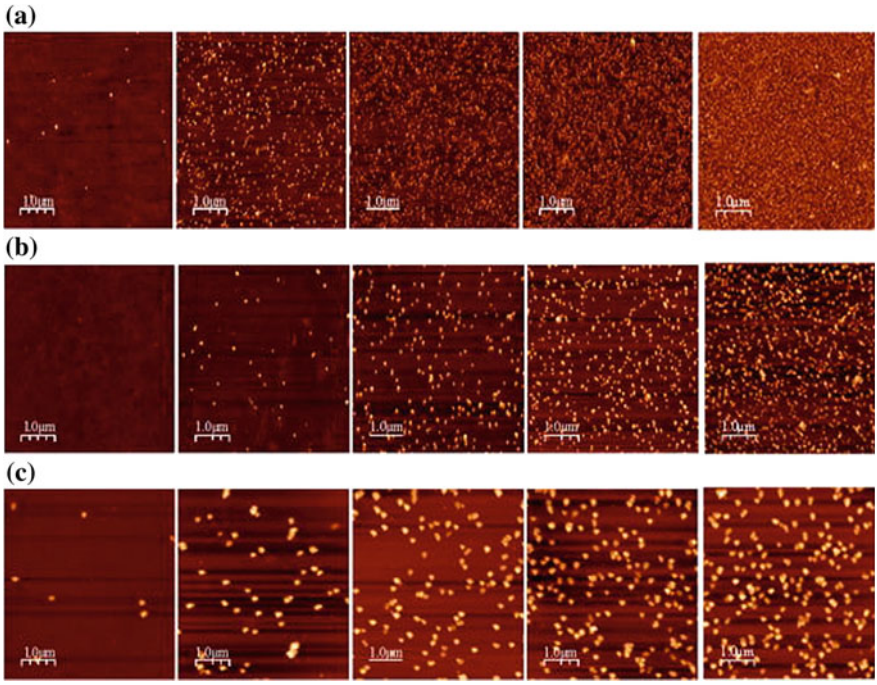

Fig. 11.23 Atomic force microscopy images of the number density gradients of gold nanoparticles of sizes **a** 16 nm, **b** 38 nm, and **c** 68 nm. The length of micronbar is 10 μm in each AFM image. Reproduced from previous work with permission from Ref. [252]

nanoparticles such as these present not only a nanoparticle density gradient, but also a surface chemistry gradient. In the interests of studying cellular response to the purely physical aspects of these nanostructured surface, these nanoparticles may be coated with a ultra-thin plasma polymer layer (<10 nm) which serves to both preserve the underlying topography of the nanoparticles, whilst simultaneously presenting a uniform surface chemistry across the entirety of the sample area [253]. Nanostructured surfaces prepared in this manner have a demonstrated ability to influence the adhesion and proliferation behavior of various cell types [254].

11.5.2.3 Antibacterial Coatings—Nanoparticle Incorporation

Certain metal ions and nanoparticles (particularly those originating from silver, copper, and zinc) have shown great promise for reducing the presence of bacterial infections in a number of biomedical applications [255–258]. The antibacterial properties of these nanoparticles have been predominantly attributed to their capacity to form metallic ions when exposed to an aqueous environment. These ions disrupt cellular functions by binding to and blocking biomolecule functional

groups, displacing other metals in enzymes, or participating in chemical reactions that induce structural changes in bacteria cell walls and nuclear membranes, all of which ultimately lead to cell death [259, 260]. A number of processes have been developed to incorporate these ions into thin film coatings and surfaces. Unfortunately, common processes such as ion beam implantation/assisted deposition, chemical vapor deposition, and electrochemistry often suffer from a number of characteristic imperfections including limited treatment area and complications relating to the toxicity of the films thus formed [261–263].

To this end, plasma polymerization techniques have been employed to fabricate thin films incorporating nanoparticles which, in addition to displaying the requisite antibacterial behavior, also exhibit the cytotoxicity properties needed to facilitate the adhesion and growth of mammalian cells. This ability to regulate the cytotoxicity of plasma polymer films incorporating nanoparticles is believed to be attributable to the ability to control both the amount of nanoparticles contained within the films, as well as the release rate of these particles (through manipulation of the degree of cross-linking and film thickness). Furthermore, the ability to apply ultra-thin plasma polymer layers (down to the order of tens of nanometers) ensures that the bulk mechanical properties of the underlying device, such as the flexibility of a catheter, is not inhibited.

11.5.3 Protective Coating

In addition to the utilization of biodegradable plasma polymer coatings for enabling controlled drug release, numerous studies have been undertaken to demonstrate the anti-corrosion protective properties of plasma polymers on several biomedically relevant metals such as gold, iron, and steel [264, 265].

For biosensors that use implanted stimulating or recording electrodes, one issue centers around the difficulty of applying conventional polymer coatings to the underlying metal substrate. These polymeric coatings are essential to protecting the electrodes from the penetration of the electrolyte-rich aqueous media which may serve to alter the characteristic electrical impedance of the device and induce corrosion. The unique properties of plasma polymers, including that of their low permeability, make them ideal for acting as barrier coatings for bulk implant materials. Plasma polymers have been employed to protect these devices from biomolecule-induced poisoning, whereby the presence of such molecules may induce undesirable variation in device performance (e.g., sensor drift, decreased sensitivity, etc.). The efficacy of this approach was demonstrated early in the 1980s with the application of oxygen-soluble propylene plasma polymers to polarographic sensors used to detect oxygen concentration in biological media [266].

Beyond using plasma polymers as the primary mechanism for combating corrosion, these films have also been used to circumvent the inherent difficulties encountered in applying other forms of organic coatings to metal substrates (specifically, poor substrate adhesion). In these instances, the plasma polymer is

relegated to the role of serving as an adhesion promoting interface between the underlying substrate and the primary external organic coating [232, 267].

11.5.4 Biosensing

Decision-making within the medical domain often finds its basis in the accurate collection and analysis of specific biomarkers. These biomarkers include various peptides, proteins, and other biomolecules that play important roles in mediating molecular recognition, cell adhesion, immune responses, and so on. The detection of these biomarkers can be indicative of a variety of diseases (such as Alzheimer's), or the presence of certain pathogenic cells [268]. To this end, devices collecting data pertinent to enzymes, hormones, DNA, and the immune system have been developed [269]. At their core, these devices rely on the specific and reproducible immobilization of various biomolecules to surface functionalities such as $–NH_2$, –COOH, or –OH. Furthermore, the utility of these devices is strongly dependent upon their analyze selectivity, and the density of bound biomolecules that they can achieve [270, 271]. These requirements in turn feed into the method of operation for the techniques that are subsequently used to quantify the presence of these biomolecules, including quartz crystal microbalances (QCM), surface plasmon resonance (SPR), or other processes relying on unique optical, electronic, or magnetic properties for transducing the presence of these biomolecules into usable signals.

The binding of these biomolecules is typically accomplished using biomolecule immobilization via wet chemistry, electrochemistry, or chemical vapor deposition. These approaches suffer from a number of drawbacks, including UV degradation of tethering bonds, excessive time required to organize the binding layers, or poor stability (resulting in low signal-to-noise ratios) [270]. This binding can, however, be implemented via plasma polymerization by creating bio-interfaces or surfaces with chemically reactive functional groups that can covalently immobilize biomolecules [272]. This has been demonstrated with cyclopropylamine plasma polymerization that was used to fabricate amine rich thin films deposited on QCM biosensors for the detection of the antibody specific to human serum albumin [273, 274].

11.6 Conclusion

Plasma polymerization or plasma-enhanced chemical vapor deposition is an excellent method for fabrication of polymer films with desired physical and chemical properties. Plasma polymer films find wide range of application from electronics to biomedical field. The solvent-free processing enables the integration of plasma thin films in micro- and nano-devices for improved performance. Plasma polymers as dielectric material in organic thin film transistor (OTFT) have shown

significant improvement in performance of device. Use of plasma polymers as buffer layer and encapsulation material in microelectronics and food packaging has gained importance in recent times. Also the inherent properties of plasma polymer films make them ideal materials for incorporation in biomedical applications. To this end, intensive research has been undertaken to develop and eventually commercialize their utilization in antibacterial coatings, controlled drug release coatings, and coatings that employ nanostructuring properties to control cellular responses.

Overall plasma polymer thin films are superior in electrical and chemical properties and exhibits defect free surfaces. Also the devices fabricated using polymer thin films are environmentally friendly and cheap to fabricate.

References

1. H. Tobushi et al., Thermomechanical properties in a thin film of shape memory polymer of polyurethane series. Smart Mater. Struct. **5**(4), 483 (1996)
2. M. Ibn-Elhaj, M. Schadt, Optical polymer thin films with isotropic and anisotropic nano-corrugated surface topologies. Nature **410**(6830), 796–799 (2001)
3. C.D. Dimitrakopoulos, P.R. Malenfant, Organic thin film transistors for large area electronics. Adv. Mater. **14**(2), 99–117 (2002)
4. J. Goodman, The formation of thin polymer films in the gas discharge. J. Polym. Sci. **44** (144), 551–552 (1960)
5. H. Biederman, *Plasma polymer films* (World Scientific, Singapore, 2004)
6. L. Cademartiri, A. Ghadimi, G.A. Ozin, Nanocrystal plasma polymerization: from colloidal nanocrystals to inorganic architectures. Acc. Chem. Res. **41**(12), 1820–1830 (2008)
7. K. Bazaka, M.V. Jacob, K. Ostrikov, Sustainable life cycles of natural-precursor-derived nanocarbons. Chem. Rev. **116**(1), 163–214 (2016)
8. S.J. McInnes et al., "Thunderstruck": plasma-polymer-coated porous silicon microparticles as a controlled drug delivery system. ACS Appl. Mater. Interfaces. **8**(7), 4467–4476 (2016)
9. M.C. Vasudev et al., Exploration of plasma-enhanced chemical vapor deposition as a method for thin-film fabrication with biological applications. ACS Appl. Mater. Interfaces. **5** (10), 3983–3994 (2013)
10. I. Melnichuk et al., Direct covalent coupling of proteins to nanostructured plasma polymers: a route to tunable cell adhesion. Appl. Surf. Sci. **351**, 537–545 (2015)
11. D.-C. Jeong et al., Low-temperature plasma polymerization of dicyclopentadiene for anti-corrosion properties. Polymer **92**, 133–139 (2016)
12. R.-G. Hu et al., Recent progress in corrosion protection of magnesium alloys by organic coatings. Prog. Org. Coat. **73**(2), 129–141 (2012)
13. L.K. Joy et al., Large enhanced dielectric permittivity in polyaniline passivated core-shell nano magnetic iron oxide by plasma polymerization. Appl. Phys. Lett. **104**(12), 121603 (2014)
14. H.J. Seo et al., Device characteristics and mechanical flexibility simulation of plasma-polymer gate dielectrics based organic thin film transistors. Sci. Adv. Mater. **8**(3), 665–668 (2016)
15. S.-W. Seo et al., Extremely bendable thin-film encapsulation of organic light-emitting diodes. Appl. Phys. Lett. **102**(16), 161908 (2013)
16. H. Yasuda, C. Wang, Plasma polymerization investigated by the substrate temperature dependence. J. Polym. Sci. Polym. Chem. Ed. **23**(1), 87–106 (1985)

17. D.L. Flamm, O. Auciello, R. d'Agostino, in *Plasma deposition, treatment, and etching of polymers: the treatment and etching of polymers*, ed. by R.d. Agostino (Elsevier, Amsterdam, 2012)
18. H. Biederman, Y. Osada, Plasma chemistry of polymers. Polym. Phys. **95**, 57–109 (1990)
19. Y. Osada, *Plasma polymerization processes*, vol. 3 (Elsevier Science Ltd., Amsterdam, 1992)
20. R. Morent et al., Influence of operating parameters on plasma polymerization of acrylic acid in a mesh-to-plate dielectric barrier discharge. Prog. Org. Coat. **70**(4), 336–341 (2011)
21. D. Hegemann et al., Densification of functional plasma polymers by momentum transfer during film growth. Appl. Phys. Lett. **101**(21), 211603 (2012)
22. A.M. Coclite et al., Single-chamber deposition of multilayer barriers by plasma enhanced and initiated chemical vapor deposition of organosilicones. Plasma Process. Polym. **7**(7), 561–570 (2010)
23. C. Corbella et al., Up-scaling the production of modified aC: H coatings in the framework of plasma polymerization processes. Solid State Sci. **11**(10), 1768–1772 (2009)
24. H. Conrads, M. Schmidt, Plasma generation and plasma sources. Plasma Sources Sci. Technol. **9**(4), 441 (2000)
25. R. Prat et al., Polymer deposition using atmospheric pressure plasma glow (APG) discharge. Polymer **41**(20), 7355–7360 (2000)
26. M.A. Lieberman, A.J. Lichtenberg, *Principles of Plasma Discharges and Materials Processing* (Wiley, New York, 2005)
27. H. Yasuda, *Plasma Polymerization* (Academic press, London, 1985)
28. K. Ostrikov, A. Murphy, Plasma-aided nanofabrication: where is the cutting edge? J. Phys. D Appl. Phys. **40**(8), 2223 (2007)
29. A. Choukourov et al., Mechanistic studies of plasma polymerization of allylamine. J. Phys. Chem. B **109**(48), 23086–23095 (2005)
30. A. Michelmore et al., On the effect of monomer chemistry on growth mechanisms of nonfouling PEG-like plasma polymers. Langmuir **29**(8), 2595–2601 (2013)
31. S. Morita, G. Sawa, M. Ieda, Thin Polymer Films by the Glow-Discharge Indirect Method. J. Macromol. Sci. Chem. **10**(3), 501–517 (1976)
32. A. Michelmore et al., The link between mechanisms of deposition and the physico-chemical properties of plasma polymer films. Soft Matter **9**(26), 6167–6175 (2013)
33. A.M. Coclite, K.K. Gleason, Initiated PECVD of organosilicon coatings: a new strategy to enhance monomer structure retention. Plasma Process. Polym. **9**(4), 425–434 (2012)
34. M. Gürsoy et al., Initiation of 2-Hydroxyethyl Methacrylate polymerization by Tert-Butyl Peroxide in a planar PECVD system. Plasma Process. Polym. **13**, 438–446 (2015)
35. H.K. Yasuda, Some important aspects of plasma polymerization. Plasma Process. Polym. **2** (4), 293–304 (2005)
36. M. Rajabi et al., Electroluminescence and photoluminescence of conjugated polymer films prepared by plasma enhanced chemical vapor deposition of naphthalene. Plasma Chem. Plasma Process. **33**(4), 817–826 (2013)
37. J. Friedrich, Mechanisms of plasma polymerization–Reviewed from a chemical point of view. Plasma Process. Polym. **8**(9), 783–802 (2011)
38. D. Barton et al., The effect of ion energy upon plasma polymerization deposition rate for acrylic acid. Chem. Commun. **3**, 348–349 (2003)
39. A. Choukourov et al., Growth of primary and secondary amine films from polyatomic ion deposition. Vacuum **75**(3), 195–205 (2004)
40. A. Fridman, *Plasma chemistry* (Cambridge University Press, Cambridge, 2008)
41. J.P. Kim et al., Synthesis and optical properties of fluorinated poly (arylene ether phosphine oxide) s. J. Polym. Sci. Part A Polym. Chem. **41**(10), 1497–1503 (2003)
42. M. Meyyappan, A review of plasma enhanced chemical vapour deposition of carbon nanotubes. J. Phys. D Appl. Phys. **42**(21), 213001 (2009)
43. A. Bogaerts et al., Gas discharge plasmas and their applications. Spectrochim. Acta, Part B **57**(4), 609–658 (2002)

44. F.F. Shi, Recent advances in polymer thin films prepared by plasma polymerization synthesis, structural characterization, properties and applications. Surf. Coat. Technol. **82**(1–2), 1–15 (1996)
45. M. Liehr, M. Dieguez-Campo, Microwave PECVD for large area coating. Surf. Coat. Technol. **200**(1–4), 21–25 (2005)
46. M. Moisan, M. Wertheimer, Comparison of microwave and rf plasmas: fundamentals and applications. Surf. Coat. Technol. **59**(1–3), 1–13 (1993)
47. M. Hirose, *Plasma-Deposited Films: Kinetics of Formation, Composition, and Microstructure. Plasma Deposited Films* (CRC publishing, Boca Raton FL, 1986)
48. H. Butler, G. Kino, Plasma sheath formation by radio frequency fields. Phys. Fluids (1958–1988). **6**(9), 1346–1355 (1963)
49. O.A. Popov, *High Density Plasma Sources: Design, Physics and Performance* (Elsevier, Amsterdam, 1996)
50. M. Hiramatsu, M. Hori, *Carbon Nanowalls: Synthesis and Emerging Applications* (Springer Science & Business Media, Berlin, 2010)
51. Y.A. Lebedev, Microwave discharges: generation and diagnostics. J. Phys: Conf. Ser. **257** (1), 012016 (2010)
52. J. Musil, Microwave plasma: its characteristics and applications in thin film technology. Vacuum **36**(1–3), 161–169 (1986)
53. J. Musil, Deposition of thin films using microwave plasmas: present status and trends. Vacuum **47**(2), 145–155 (1996)
54. M. Moisan et al., Radio frequency or microwave plasma reactors? Factors determining the optimum frequency of operation. J. Vac. Sci. Technol. B **9**(1), 8–25 (1991)
55. M. Wertheimer, M. Moisan, Comparison of microwave and lower frequency plasmas for thin film deposition and etching. J. Vac. Sci. Technol. A **3**(6), 2643–2649 (1985)
56. R.B. Timmons, A.J. Griggs, Pulsed plasma polymerizations. Plasma polym. Films **1**, 217–245 (2004)
57. R. Förch, Z. Zhang, W. Knoll, Soft plasma treated surfaces: tailoring of structure and properties for biomaterial applications. Plasma Processes Polym. **2**(5), 351–372 (2005)
58. L. Denis et al., Synthesis of allylamine plasma polymer films: correlation between plasma diagnostic and film characteristics. Plasma Processes Polym. **6**(3), 199–208 (2009)
59. Z. Yang et al., The covalent immobilization of heparin to pulsed-plasma polymeric allylamine films on 316L stainless steel and the resulting effects on hemocompatibility. Biomaterials **31**(8), 2072–2083 (2010)
60. L. Denis et al., Deposition of functional organic thin films by pulsed plasma polymerization: a joint theoretical and experimental study. Plasma Process. Polym. **7**(2), 172–181 (2010)
61. A. Hoene et al., In vivo investigation of the inflammatory response against allylamine plasma polymer coated titanium implants in a rat model. Acta Biomater. **6**(2), 676–683 (2010)
62. K.G. Donohoe, T. Wydeven, Plasma polymerization of ethylene in an atmospheric pressure-pulsed discharge. J. Appl. Polym. Sci. **23**(9), 2591–2601 (1979)
63. V. Hopfe, D.W. Sheel, Atmospheric-pressure PECVD coating and plasma chemical etching for continuous processing. Plasma Sci. IEEE Trans. **35**(2), 204–214 (2007)
64. H. Biederman, D. Slavınská, Plasma polymer films and their future prospects. Surf. Coat. Technol. **125**(1), 371–376 (2000)
65. E. Kay, A. Dilks, Plasma polymerization of fluorocarbons in rf capacitively coupled diode system. J. Vac. Sci. Technol. **18**(1), 1–11 (1981)
66. N. Puač et al., Low pressure RF capacitively coupled plasma reactor for modification of seeds, polymers and textile fabrics. Mater. Sci. Forum. (2005) (Trans Tech Publications, Switzerland)
67. J. Hopwood, Review of inductively coupled plasmas for plasma processing. Plasma Sources Sci. Technol. **1**(2), 109 (1992)

68. H. Jiang et al., The growth and chemical structure of thin photonic films formed from plasma copolymerization. Part II. Effect of monomer feed location. Polymer **46**(19), 8178–8184 (2005)
69. M. Wertheimer, J. Klemberg-Sapieha, H. Schreiber, Advances in basic and applied aspects of microwave plasma polymerization. Thin Solid Films **115**(2), 109–124 (1984)
70. C. Corbella, Upscaling plasma deposition: the influence of technological parameters. Surf. Coat. Technol. **242**, 237–245 (2014)
71. D. Hegemann et al., Macroscopic description of plasma polymerization. Plasma Process. Polym. **4**(3), 229–238 (2007)
72. H. Yasuda, T. Hsu, Some aspects of plasma polymerization investigated by pulsed RF discharge. J. Polym. Sci. Polym. Chem. Ed. **15**(1), 81–97 (1977)
73. B. Kim, K. Park, D. Lee, Use of neural network to model the deposition rate of PECVD-silicon nitride films. Plasma Sources Sci. Technol. **14**(1), 83 (2005)
74. J. Trieschmann, D. Hegemann, Plasma polymerization at different positions in an asymmetric ethylene discharge. J. Phys. D Appl. Phys. **44**(47), 475201 (2011)
75. H. Deutsch et al., On the temperature dependence of plasma polymerization. Contrib. Plasma Phys. **28**(2), 149–155 (1988)
76. M. Karaman, E. Yenice, Plasma enhanced chemical vapor deposition of poly (2, 2, 3, 4, 4, 4-hexafluorobutyl acrylate) thin films. Chem. Vap. Depos. **21**(7-8-9), 188–195 (2015)
77. G. Scheltjens, G. Van Assche, B. Van Mele, Effect of Substrate Temperature on Thermal Properties and Deposition Kinetics of Atmospheric Plasma Deposited Methyl (methacrylate) Films. Plasma Process. Polymer. (2016)
78. D. Rice, D. O'Kane, Glow discharge polymerization of tetrafluoroethylene, 1, 1 difluoroethylene, and chlorotrifluoroethylene. J. Electrochem. Soc. **123**(9), 1308–1312 (1976)
79. N. Morosoff et al., Plasma polymerization of tetrafluoroethylene. II. Capacitive radio frequency discharge. J. Appl. Polym. Sci. **23**(12), 3449–3470 (1979)
80. H. Yasuda, Glow discharge polymerization. in Thin Film Processes. (Academic Press, New York, 1978), pp. 361–396
81. D. Hegemann, Macroscopic investigation of reaction rates yielding plasma polymer deposition. J. Phys. D Appl. Phys. **46**(20), 205204 (2013)
82. A. von Keudell, J. Benedikt, A physicist's perspective on "views on macroscopic kinetics of plasma polymerisation". Plasma Process. Polym. **7**(5), 376–379 (2010)
83. H. Biederman, O. Kylián, Some remarks to macroscopic kinetics of plasma polymerization. Plasma Processes Polym. **8**(6), 475–477 (2011)
84. D. Hegemann, D. Cameron, *Plasma Polymer Deposition and Coatings on Polymers* (Elsevier Ltd., Oxford, UK, 2014), pp. 201–228
85. D. Hegemann, M.M. Hossain, Influence of non-polymerizable gases added during plasma polymerization. Plasma Process. Polym. **2**(7), 554–562 (2005)
86. A. Michelmore et al., Defining plasma polymerization: new insight into what we should be measuring. ACS Appl. Mater. Interfaces. **5**(12), 5387–5391 (2013)
87. K. Vasilev et al., Substrate influence on the initial growth phase of plasma-deposited polymer films. Chem. Commun. **24**, 3600–3602 (2009)
88. D.E. Robinson et al., The substrate and composition dependence of plasma polymer stability. Plasma Process. Polym. **7**(2), 102–106 (2010)
89. Y.-X. Liu et al., Electromagnetic effects in high-frequency large-area capacitive discharges: a review. J. Vac. Sci. Technol. A **33**(2), 020801 (2015)
90. C. Corbella et al., Modified DLC coatings prepared in a large-scale reactor by dual microwave/pulsed-DC plasma-activated chemical vapour deposition. Thin Solid Film. **517** (3), 1125–1130 (2008)
91. E. Schüngel et al., Evaluation of the electrical asymmetry effect by spectroscopic measurements of capacitively coupled discharges and silicon thin film depositions. Thin Solid Film. **574**, 60–65 (2015)

92. D. Hegemann, E. Körner, S. Guimond, Plasma polymerization of acrylic acid revisited. Plasma Process. Polym. **6**(4), 246–254 (2009)
93. E. Kay et al., Topics in current chemistry. Plasma Chem. **94**, 1–42 (1980)
94. T.J. Cotler, M.E. Elta, Plasma-etch technology. Circ. Devices Mag. IEEE **6**(4), 38–43 (1990)
95. R.P. Mota et al., HMDSO plasma polymerization and thin film optical properties. Thin Solid Film. **270**(1), 109–113 (1995)
96. N. Morosoff et al., Preparation of tris (η 5-cyclopentadienylcobaltmonocarbonyl) cluster complex by a plasma technique. Inorg. Chim. Acta **83**(2), 137–141 (1984)
97. F. Mondello et al., In vivo activity of terpinen-4-ol, the main bioactive component of *Melaleuca alternifolia Cheel* (tea tree) oil against azole-susceptible and-resistant human pathogenic Candida species. BMC Infect. Dis. **6**(1), 1 (2006)
98. M.V. Jacob et al., RF plasma polymerised thin films from natural resources. Int. J. Mod. Phys. Conf. Ser. **7**, 1–11 (2014)
99. K. Bazaka, M.V. Jacob, B.F. Bowden, Optical and chemical properties of polyterpenol thin films deposited via plasma-enhanced chemical vapor deposition. J. Mater. Res. **26**(08), 1018–1025 (2011)
100. K. Bazaka et al., Anti-bacterial surfaces: natural agents, mechanisms of action, and plasma surface modification. Rsc Advances **5**(60), 48739–48759 (2015)
101. M.V. Jacob et al., Plasma polymerised thin films for flexible electronic applications. Thin Solid Films **546**, 167–170 (2013)
102. D. Hegemann, C. Oehr, A. Fischer, Design of functional coatings. J. Vac. Sci. Technol. A **23** (1), 5–11 (2005)
103. V. Sciarratta et al., *Plasma Processes and Polymers* (Wiley-VCH, Weinheim, 2005), p. 39
104. V. Sciarratta et al., Upscaling of plasma processes for carboxyl functionalization. Plasma Process. Polym. **1**, 39–49 (2006)
105. J.D. Whittle et al., Variability in plasma polymerization processes—an international round-robin study. Plasma Process. Polym. **10**(9), 767–778 (2013)
106. D. Hegemann et al., Deposition of functional plasma polymers influenced by reactor geometry in capacitively coupled discharges. Plasma Processes Polym. **13**, 279–286 (2015)
107. A.J. Ward, R.D. Short, A tofsims and xps investigation of the structure of plasma polymers prepared from the methacrylate series of monomers: 2. The influence of the WF parameter on structural and functional group retention. Polymer **36**(18), 3439–3450 (1995)
108. M. Drabik et al., Influence of deposition conditions on structure and aging of C:H:O plasma polymer films prepared from acetone/CO2 mixtures. Plasma Process. Polym. **11**(5), 496–508 (2014)
109. F.F. Shi, Recent advances in polymer thin films prepared by plasma polymerization synthesis, structural characterization, properties and applications. Surf. Coat. Technol. **82**(1), 1–15 (1996)
110. S. Yurish, *Sensors and Biosensors, MEMS Technologies and its Applications* (Lulu. com, North Carolina, US, 2014)
111. K. Bazaka, *Fabrication and Characterization of Plasma Polymer Thin Films From Monoterpene Alcohols for Applications in Organic Electronics and Biotechnology* (James Cook University, Australia, 2011)
112. L. Martinu, D. Poitras, Plasma deposition of optical films and coatings: a review. J. Vac. Sci. Technol. A **18**(6), 2619–2645 (2000)
113. X.-Y. Zhao, M.-Z. Wang, J. Xiao, Deposition of plasma conjugated polynitrile thin films and their optical properties. Eur. Polymer J. **42**(9), 2161–2167 (2006)
114. M. Losurdo et al., Spectroscopic ellipsometry for characterization of organic semiconductor polymeric thin films. Synth. Met. **138**(1), 49–53 (2003)
115. A. Alias et al., Optical characterization and properties of polymeric materials for optoelectronic and photonic applications. Int. J. Appl. Sci. Technol. **3**(5), 11–38 (2013)
116. J.-G. Liu, M. Ueda, High refractive index polymers: fundamental research and practical applications. J. Mater. Chem. **19**(47), 8907–8919 (2009)

117. J.A. Hiller, J.D. Mendelsohn, M.F. Rubner, Reversibly erasable nanoporous anti-reflection coatings from polyelectrolyte multilayers. Nat. Mater. **1**(1), 59–63 (2002)
118. C. Lü, B. Yang, High refractive index organic–inorganic nanocomposites: design, synthesis and application. J. Mater. Chem. **19**(19), 2884–2901 (2009)
119. H.-J. Yen, G.-S. Liou, A facile approach towards optically isotropic, colorless, and thermoplastic polyimidothioethers with high refractive index. J. Mater. Chem. **20**(20), 4080–4084 (2010)
120. S. Saloum, B. Alkhaled, Structural, optical and electrical properties of plasma deposited thin films from hexamethyldisilazane compound. Acta Phys. Pol., A **119**(3), 369–373 (2011)
121. S.-J. Cho, J.-H. Boo, A study on the characteristics of plasma polymer thin film with controlled nitrogen flow rate. Nanoscale Res. Lett. **7**(1), 1–4 (2012)
122. U. Sajeev, M. Anantharaman, Plasma polymerised organic thin films-a study on the structural, electrical and nonlinear optical properties for possible applications. Department of Physics (2006)
123. D.L. Wise et al., *Photonic Polymer Systems: Fundamentals: Methods, and Applications* (CRC Press, Boca Raton, FL, 1998)
124. M.J. Rahman, A. Bhuiyan, Structural and optical properties of plasma polymerized o-methoxyaniline thin films. Thin Solid Films **534**, 132–136 (2013)
125. J. Ahmad, K. Bazaka, M.V. Jacob, Optical and surface characterization of radio frequency plasma polymerized 1-isopropyl-4-methyl-1, 4-cyclohexadiene thin films. Electronics **3**(2), 266–281 (2014)
126. S.-H. Cho et al., Physical and optical properties of plasma polymerized thin films deposited by PECVD method. Surf. Coat. Technol. **174**, 1111–1115 (2003)
127. U. Sajeev et al., On the optical and electrical properties of rf and ac plasma polymerized aniline thin films. Bull. Mater. Sci. **29**(2), 159–163 (2006)
128. E. Vassallo et al., Characterization of Poly (3-Methylthiophene)-like Films Produced by Plasma Polymerization. Plasma Processes Polym. **4**(S1), S801–S805 (2007)
129. X. Wang, G. Grundmeier, *Thin Functional Plasma Polymer and Metal/Plasma Polymer Nanocomposite Films*, Ruhr-Universität, Fakultät Maschinenbau, Institut für Werkstoffe Bochum, Germany (2007)
130. S. Palaniappan, A. John, Polyaniline materials by emulsion polymerization pathway. Prog. Polym. Sci. **33**(7), 732–758 (2008)
131. P.J. Giordano, G.W. Prohaska, R.C. Smierciak, *Fluoropolymer thin film coatings and method of preparation by plasma polymerization*. Google Patents (1990)
132. Z.R. Li, *Organic Light-Emitting Materials and Devices* (CRC Press, Boca Raton, FL, 2015)
133. J.L. Yagüe Marrón, *Development of a New Chemical Sensor Based on Plasma Polymerized Polypyrrole Films.* 2010
134. R.M. Faria, O. Oliveira Jr., Exploiting the electrical properties of thin films of semiconducting polymers. Braz. J. Phys. **29**(2), 360–370 (1999)
135. P. Langley, J. Hulliger, Nanoporous and mesoporous organic structures: new openings for materials research. Chem. Soc. Rev. **28**(5), 279–291 (1999)
136. T.-W. Kim et al., Deposition andin-situ plasma doping of plasma-polymerized thiophene films using PECVD. Macromol. Res. **17**(1), 31–36 (2009)
137. M.C. Joseph, et al., *Mechanism of Electrical Conduction in Plasma Polymerized Furfural Thin Films.* (2002)
138. A.S. Jalal et al., On the conduction mechanism in plasma polymerized m-xylene thin films. Thin Solid Films **295**(1), 125–130 (1997)
139. R.B. Sarker, A. Bhuiyan, Electrical conduction mechanism in plasma polymerized 1-Benzyl-2-methylimidazole thin films under static electric field. Thin Solid Films **519** (18), 5912–5916 (2011)
140. N. Nagaraj et al., DC conduction mechanism in polyvinyl alcohol films doped with potassium thiocyanate. J. Power Sources **112**(1), 326–330 (2002)

141. J.S. Lim, B.J. Lee, Regular paper: organic thin film transistors with gate dielectrics of plasma polymerized styrene and vinyl acetate thin films. Trans. Electr. Electron. Mater. (TEEM) **16** (2), 95–98 (2015)
142. L. Anderson, M. Jacob, Electrical characterisations of plasma polyermised linalyl acetate. Mater. Sci. Eng., B **177**(3), 311–315 (2012)
143. S.-J. Cho, D. Jung, J.-H. Boo, A low dielectric study on hybrid plasma-polymer thin films of different ratio between toluene and TEOS. J. Nanosci. Nanotechnol. **11**(6), 5323–5327 (2011)
144. I. Bae et al., Characterization of organic polymer thin films deposited using the PECVD method. J.-Korean Phys. Soc. **50**(6), 1854 (2007)
145. N. Inagaki, *Plasma Surface Modification and Plasma Polymerization* (CRC Press, Boca Raton, FL, 1996)
146. A.M. Fox, *Optical Properties of Solids*, vol. 3 (Oxford University Press, Oxford, 2001)
147. E.A. Favret, *Functional Properties of Bio-Inspired Surfaces: Characterization and Technological Applications* (World Scientific, Singapore, 2009)
148. S.W. Myung, H.S. Choi, Chemical structure and surface morphology of plasma polymerized-allylamine film. Korean J. Chem. Eng. **23**(3), 505–511 (2006)
149. M.M. Hossain, *Plasma Technology for Deposition and Surface Modification*, vol. 4 (Logos Verlag Berlin GmbH, Berlin, 2009)
150. H. Yasuda, *Plasma Polymerization* (Academic press, London, 2012)
151. S. Ershov et al., Free radical generation and concentration in a plasma polymer: the effect of aromaticity. ACS Appl. Mater. Interfaces. **6**(15), 12395–12405 (2014)
152. S. Ershov et al., Free radical-induced grafting from plasma polymers for the synthesis of thin barrier coatings. RSC Advances **5**(19), 14256–14265 (2015)
153. R. White, J. Wolstenholme, X-ray photoelectron spectroscopy (xps) for energy-related device characterization. Life Sci. Instrum **5**, 010 (2010)
154. L. Duque, R. Förch, Plasma polymerization of zinc acetyl acetonate for the development of a polymer-based zinc release system. Plasma Process. Polym. **8**(5), 444–451 (2011)
155. S. Schiller et al., Chemical structure and properties of plasma-polymerized maleic anhydride films. Chem. Mater. **14**(1), 235–242 (2002)
156. J. Ahmad et al., Wetting, solubility and chemical characteristics of plasma-polymerized 1-isopropyl-4-methyl-1, 4-cyclohexadiene thin films. Coatings **4**(3), 527–552 (2014)
157. C. Wen, *Surface Coating and Modification of Metallic Biomaterials* (Woodhead Publishing, Cambridge, 2015)
158. D. Lundin, J. Jensen, H. Pedersen, Influence of pulse power amplitude on plasma properties and film deposition in high power pulsed plasma enhanced chemical vapor deposition. J. Vac. Sci. Technol. A **32**(3), 030602 (2014)
159. A. Bousquet et al., Influence of plasma pulsing on the deposition kinetics and film structure in low pressure oxygen/hexamethyldisiloxane radiofrequency plasmas. Thin Solid Films **514** (1), 45–51 (2006)
160. J. Ebdon, G.C. Eastmond, *New methods of Polymer Synthesis* (Springer, Berlin, 1995)
161. S. Morita, S. Hattori, Applications of plasma polymerization. Pure Appl. Chem. **57**(9), 1277–1286 (1985)
162. K.S. Siow et al., Plasma methods for the generation of chemically reactive surfaces for biomolecule immobilization and cell colonization-a review. Plasma Process. Polym. **3**(6–7), 392–418 (2006)
163. D. Öner, T.J. McCarthy, Ultrahydrophobic surfaces. Effects of topography length scales on wettability. Langmuir **16**(20), 7777–7782 (2000)
164. A. Tuteja et al., Designing superoleophobic surfaces. Science **318**(5856), 1618–1622 (2007)
165. K. Bazaka et al., The effect of polyterpenol thin film surfaces on bacterial viability and adhesion. Polymers **3**(1), 388–404 (2011)
166. C.E. Viana et al., Analysis of SiO_2 thin films deposited by PECVD using an oxygen-TEOS-argon mixture. Braz. J. Phys. **31**(2), 299–303 (2001)

167. E.P. Ivanova et al., Differential attraction and repulsion of *Staphylococcus aureus* and *Pseudomonas aeruginosa* on molecularly smooth titanium films. Scientific reports **1**, 165 (2011)
168. J. Smith et al., Solution-processed small molecule-polymer blend organic thin-film transistors with hole mobility greater than 5 cm^2/Vs. Adv. Mater. **24**(18), 2441–2446 (2012)
169. J. Li et al., A stable solution-processed polymer semiconductor with record high-mobility for printed transistors. Sci. Rep **2**, 754 (2012)
170. K. Fukuda et al., Fully solution-processed flexible organic thin film transistor arrays with high mobility and exceptional uniformity. Sci. Rep. **4**, 3947 (2014)
171. S.R. Forrest, The path to ubiquitous and low-cost organic electronic appliances on plastic. Nature **428**(6986), 911–918 (2004)
172. F. Schwierz, Graphene transistors. Nat. Nanotechnol. **5**(7), 487–496 (2010)
173. M. Irimia-Vladu, "Green" electronics: biodegradable and biocompatible materials and devices for sustainable future. Chem. Soc. Rev. **43**(2), 588–610 (2014)
174. H. Shirakawa et al., Synthesis of electrically conducting organic polymers: halogen derivatives of polyacetylene, (CH). J. Chem. Soc., Chem. Commun. **16**, 578–580 (1977)
175. Y. Lin, Y. Li, X. Zhan, Small molecule semiconductors for high-efficiency organic photovoltaics. Chem. Soc. Rev. **41**(11), 4245–4272 (2012)
176. P. Sonar et al., A low-bandgap diketopyrrolopyrrole-benzothiadiazole-based copolymer for high-mobility ambipolar organic thin-film transistors. Adv. Mater. **22**(47), 5409–5413 (2010)
177. A. Fujiki et al., Enhanced fluorescence by surface plasmon coupling of Au nanoparticles in an organic electroluminescence diode. Appl. Phys. Lett. **96**(4), 043307 (2010)
178. K. Nomura et al., Room-temperature fabrication of transparent flexible thin-film transistors using amorphous oxide semiconductors. Nature **432**(7016), 488–492 (2004)
179. L. Qiu et al., Versatile use of vertical-phase-separation-induced bilayer structures in organic thin-film transistors. Adv. Mater. **20**(6), 1141–1145 (2008)
180. K.-L. Lin, Use of thin film transistor liquid crystal display (TFT-LCD) waste glass in the production of ceramic tiles. J. Hazard. Mater. **148**(1), 91–97 (2007)
181. G. Horowitz, Organic thin film transistors: from theory to real devices. J. Mater. Res. **19**(07), 1946–1962 (2004)
182. E. Fortunato, P. Barquinha, R. Martins, Oxide semiconductor thin-film transistors: a review of recent advances. Adv. Mater. **24**(22), 2945–2986 (2012)
183. Z. Bao, Materials and fabrication needs for low-cost organic transistor circuits. Adv. Mater. **12**(3), 227–230 (2000)
184. R.P. Ortiz, A. Facchetti, T.J. Marks, High-k organic, inorganic, and hybrid dielectrics for low-voltage organic field-effect transistors. Chem. Rev. **110**(1), 205–239 (2009)
185. A. Facchetti, M.H. Yoon, T.J. Marks, Gate dielectrics for organic field-effect transistors: new opportunities for organic electronics. Adv. Mater. **17**(14), 1705–1725 (2005)
186. S.E. Fritz, T.W. Kelley, C.D. Frisbie, Effect of dielectric roughness on performance of pentacene TFTs and restoration of performance with a polymeric smoothing layer. J. Phys. Chem. B **109**(21), 10574–10577 (2005)
187. H. Klauk et al., High-mobility polymer gate dielectric pentacene thin film transistors. J. Appl. Phys. **92**(9), 5259–5263 (2002)
188. K. Senda et al., 2–10 nm scale plasma polymerized organic films. J. Appl. Phys. **74**(10), 6425–6426 (1993)
189. Y. Matsumoto, M. Ishida, The property of plasma-polymerized fluorocarbon film in relation to CH_4/C_4 F 8 ratio and substrate temperature. Sens. Actuators A **83**(1), 179–185 (2000)
190. C.J. Mathai et al., Characterization of low dielectric constant polyaniline thin film synthesized by ac plasma polymerization technique. J. Phys. D Appl. Phys. **35**(3), 240 (2002)
191. S.H. Lee, D.C. Lee, Preparation and characterization of thin films by plasma polymerization of hexamethyldisiloxane. Thin Solid Films **325**(1), 83–86 (1998)

192. G. Borvon et al., Analysis of low-k organosilicon and low-density silica films deposited in HMDSO plasmas. Plasmas Polym. **7**(4), 341–352 (2002)
193. T. Ramu, M. Wertheimer, Dielectric properties of plasma-polymerized hexamethyldisiloxane films: 2 dielectric breakdown. IEEE Trans. Electr. Insul. **4**, 557–563 (1986)
194. D. Bhattacharyya et al., Plasma-polymerized multistacked organic bipolar films: a new approach to flexible high-κ dielectrics. Adv. Mater. **20**(12), 2383–2388 (2008)
195. W.-J. Yoon et al., Plasma-polymerized multistacked bipolar gate dielectric for organic thin-film transistors. Org. Electron. **11**(11), 1767–1771 (2010)
196. Y. Xu et al., High-k polymerized dichlorotetramethyldisiloxane films deposited by radio frequency pulsed plasma for gate dielectrics in polymer field effect transistors. in *MRS Proceedings* Cambridge Univ Press, Cambridge, 2005
197. Y. Xu et al., Pulsed plasma polymerized dichlorotetramethyldisiloxane high-k gate dielectrics for polymer field-effect transistors. J. Appl. Phys. **99**(1), 014104 (2006)
198. J.-S. Lim et al., Plasma polymerized methyl methacrylate gate dielectric for organic thin-film transistors. Org. Electron. **11**(5), 951–954 (2010)
199. J.H. Park et al., Studies on poly (methyl methacrylate) dielectric layer for field effect transistor: influence of polymer tacticity. Thin Solid Films **515**(7), 4041–4044 (2007)
200. F. Fanelli et al., Insights into the atmospheric pressure plasma-enhanced chemical vapor deposition of thin films from methyldisiloxane precursors. Plasma Process. Polym. **9**(11–12), 1132–1143 (2012)
201. D.S. Wavhal et al., Investigation of gas phase species and deposition of SiO_2 films from HMDSO/O_2 plasmas. Plasma Processes Polym. **3**(3), 276–287 (2006)
202. L. Han et al., Properties of a permeation barrier material deposited from hexamethyl disiloxane and oxygen. J. Electrochem. Soc. **156**(2), H106–H114 (2009)
203. L. Han et al., Amorphous silicon thin-film transistors with field-effect mobilities of 2 cm^2/V s for electrons and 0.1 cm^2/V s for holes. Appl. Phys. Lett. **94**(16), 162105 (2009)
204. L. Han et al., Ultraflexible amorphous silicon transistors made with a resilient insulator. Appl. Phys. Lett. **96**(4), 042111 (2010)
205. L. Han, P. Mandlik, S. Wagner, A new gate dielectric for highly stable amorphous-silicon thin-film transistors with electron field-effect mobility. Electron Device Lett. IEEE **30**(5), 502–504 (2009)
206. S.Y. Park, M. Park, H.H. Lee, Cooperative polymer gate dielectrics in organic thin-film transistors. Appl. Phys. Lett. **85**(12), 2283–2285 (2004)
207. J. Veres et al., Gate insulators in organic field-effect transistors. Chem. Mater. **16**(23), 4543–4555 (2004)
208. F. Yildirim et al., Gate insulators and interface effects in organic thin-film transistors. Org. Electron. **9**(1), 70–76 (2008)
209. W.C. Shin et al., Low-voltage high-performance pentacene thin-film transistors with Ultrathin PVP/High-HfLaO hybrid gate dielectric. Electron Device Lett. IEEE **31**(11), 1308–1310 (2010)
210. J. Tang et al., Enhanced electrical properties of pentacene-based organic thin-film transistors by modifying the gate insulator surface. Appl. Surf. Sci. **254**(23), 7688–7692 (2008)
211. M. Jacob et al., Fabrication of a novel organic polymer thin film. Thin Solid Films **516**(12), 3884–3887 (2008)
212. K. Bazaka, M. Jacob, Synthesis of radio frequency plasma polymerized non-synthetic Terpinen-4-ol thin films. Mater. Lett. **63**(18), 1594–1597 (2009)
213. M.V. Jacob et al., Fabrication and characterization of polyterpenol as an insulating layer and incorporated organic field effect transistor. Thin Solid Films **518**(21), 6123–6129 (2010)
214. N. Thejokalyani, S. Dhoble, Novel approaches for energy efficient solid state lighting by RGB organic light emitting diodes–A review. Renew. Sustain. Energy Rev. **32**, 448–467 (2014)
215. J.-S. Lim, P.-K. Shin, Improved performance of organic light-emitting devices with plasma treated ITO surface and plasma polymerized methyl methacrylate buffer layer. Appl. Surf. Sci. **253**(8), 3828–3833 (2007)

216. J. Tang et al., Anode/organic interface modification by plasma polymerized fluorocarbon films. J. Appl. Phys. **95**(8), 4397–4403 (2004)
217. S.-M. Park et al., Enhanced performance of the OLED with plasma treated ITO and plasma polymerized thiophene buffer layer. Curr. Appl. Phys. **7**(5), 474–479 (2007)
218. L. Hung, L. Zheng, M. Mason, Anode modification in organic light-emitting diodes by low-frequency plasma polymerization of CHF_3. Appl. Phys. Lett. **78**, 673 (2001)
219. M. Schaer et al., Water vapor and oxygen degradation mechanisms in organic light emitting diodes. Adv. Func. Mater. **11**(2), 116–121 (2001)
220. J.S. Lewis, M.S. Weaver, Thin-film permeation-barrier technology for flexible organic light-emitting devices. IEEE J. Sel. Top. Quantum Electron. **10**(1), 45–57 (2004)
221. W.J. Potscavage Jr. et al., Encapsulation of pentacene/C_{60} organic solar cells with Al_2O_3 deposited by atomic layer deposition. Appl. Phys. Lett. **90**, 253511 (2007)
222. G. Dennler et al., A new encapsulation solution for flexible organic solar cells. Thin Solid Films **511**, 349–353 (2006)
223. Y.-S. Li et al., Single-layer organic–inorganic-hybrid thin-film encapsulation for organic solar cells. J. Phys. D Appl. Phys. **46**(43), 435502 (2013)
224. G.-H. Lee et al., Investigation of brittle failure in transparent conductive oxide and permeation barrier oxide multilayers on flexible polymers. Thin Solid Films **518**(11), 3075–3080 (2010)
225. P. Mandlik et al., A single-layer permeation barrier for organic light-emitting displays. Appl. Phys. Lett. **92**(10), 103309 (2008)
226. D.S. Wuu et al., Transparent barrier coatings for flexible organic light-emitting diode applications. Chem. Vap. Deposition **12**(4), 220–224 (2006)
227. W. Huang et al., Low temperature PECVD SiN*x* films applied in OLED packaging. Mater. Sci. Eng. B **98**(3), 248–254 (2003)
228. H. Lin et al., Moisture-resistant properties of SiN_x films prepared by PECVD. Thin Solid Films **333**(1–2), 71–76 (1998)
229. N. Inagaki, S. Tasaka, T. Nakajima, Preparation of oxygen gas barrier polypropylene films by deposition of SiO_x films plasma-polymerized from mixture of tetramethoxysilane and oxygen. J. Appl. Polym. Sci. **78**(13), 2389–2397 (2000)
230. L. Qi, C. Zhang, Q. Chen, Performance improvement of inverted organic solar cells by adding ultrathin Al_2O_3 as an electron selective layer and a plasma enhanced chemical vapor deposition of SiO_x encapsulating layer. Thin Solid Films **567**, 1–7 (2014)
231. P. Carcia et al., Ca test of Al_2O_3 gas diffusion barriers grown by atomic layer deposition on polymers. Appl. Phys. Lett. **89**(3), 031915 (2006)
232. H. Yasuda, M. G, Biomedical applications of plasma polyermization and plasma treatment of polymer surfaces. Biomaterials **3**, 10 (1981)
233. K.E. Uhrich, S.M.C. Robert, S. Langer, K.M. Shakesheff, Polymeric systems for controlled drug release. Chem. Rev. **99**, 18 (1999)
234. C.T.R. Gilbert, S. Banker (eds), *Modern Pharmaceutics*. 4th ed. Drugs and the pharmaceutical sciences (Marcel Dekker, New York, 2002)
235. C. Susut, R.B. Timmons, Plasma enhanced chemical vapor depositions to encapsulate crystals in thin polymeric films: a new approach to controlling drug release rates. Int. J. Pharm. **288**(2), 253–261 (2005)
236. Sung-Woon Myung, S.-C. J, Byung-Hoon Kim, Immobilization and controlled release of drug using plasma polymerized thin film. Thin Solid Films **584**, 5 (2015)
237. Stefano Zanini, E. G, Claudia Riccardi, Development of controlled releasing surfaces by plasma deposited multilayers. Mater. Chem. Phys. **138**, 6 (2013)
238. K. Vasilev et al., Controlled release of levofloxacin sandwiched between two plasma polymerized layers on a solid carrier. ACS Appl. Mater. Interfaces. **3**(12), 4831–4836 (2011)
239. J.P.M. Steven, E.J. Szili, S.A. Al-Bataineh, J. Xu, M.E. Alf, K.K. Gleason, R.D. Short, N.H. Voelcker, Combination of iCVD and porous silicon for the development of a controlled drug delivery system. ACS App. Mater. Interfaces. **4**(7), 9 (2012)

240. Krasimir Vasilev, Z. P, Krishna Kant, Joseph Chan, Andrew Michelmore, Dusan Losic, Tailoring the surface functionalities of titania nanotube arrays. Biomaterials **31**, 9 (2010)
241. World Health Organization, *WHO Guidelines on Hand Hygiene in Health Care: a Summary*. (2009)
242. Krasimir Vasilev, V. S, Karine Anselme, Chi Ndi, Mihaela Mateescu, Bjorn Dollmann, Petr Martinek, Hardi Ys, Lydia Ploux, Hans J. Griesser, Tunable antibacterial coatings that support mammalian cell growth. Nano Lett. **10**, 6 (2009)
243. Tobias G. Klampfl, G. I, Tetsuji Shimizu, Yang-Fang Li, Julia L. Zimmermann, Wilhelm Stolz, Jurgen Schlegel, Gregor E. Morfill, Hans-Ulrich Schmidt, Cold atmospheric air plasma sterilization against spores and other microorganisms of clinical interest. Appl. Environ. Microbiol. **78**, 6 (2012)
244. Richard A. Venezia, M. O, Edward Houston, Shu-Min Yin, Yelena Y. Naumova, Lethal activity of nonthermal plasma sterilization against microorganisms. Infect. Control Hosp. Epidemiol. **29**, 7 (2008)
245. Krasimir Vasilev, S.S. G, Hans J. Griesser, Antibacterial surfaces and coatings produced by plasma techniques. Plasma Process. Polym. **8**, 14 (2011)
246. Tingting He, Z. Y, Rui Chen, Jin Wang, Yongxiang Leng, Hong Sun, Nan Huang, Enhanced endothelialization guided by fibronectin functionalized plasma polymerized acrylic acid film. Mater. Sci. Eng., C **32**, 7 (2012)
247. Norio Tada, R. V, Gordon Grant, Lauren Barlett, Alexander Black, Claudia Clavijo, Uwe Christians, Ron Betts, Doug Savage, Shih-Horng Su, John Shulze, Saibal Kar, Polymer-free biolimus A9-coated stent demonstrates more sustained intimal inhibition, improved healing, and reduced inflammation compared with a polymer-coated sirolimus-eluting cypher stent in a porcine model. Circ. Cardiovasc. Interv. **3**, 11 (2010)
248. Christelle Vreuls, G. N, Benjamin Thierry Zejchvb, Geoffrey Garitte, Stefani S. Griesser, Catherine Archambeau, Cecile van de Weerdt, Joseph Martial, Hans Griesser, Prevention of bacterial biofilms by covalent immobilization of peptides onto plasma polymer functionalized substrates. J. Mater. Chem. **20**, 7 (2010)
249. Bryan R. Coad, M. J, Stefani S. Griesser, Hans J. Griesser, Controlled covalent surface immobilisation of proteins and peptides using plasma methods. Surf. Coat. Technol. **223**, 9 (2013)
250. Eloisa Sardella, P. F, Roberto Gristina, Marina Nardulli, Riccardo d'Agostino, Plasma-aided micro- and nanopatterting processes for biomedical applications. Plasma Process. Polym. **3**, 14 (2006)
251. P. Favia, Plasma deposited coatings for biomedical materials and devices: fluorocarbon and PEO-like coatings. Surf. Coat. Technol. **211**, 50–56 (2012)
252. K. Vasilev, Nanoengineering plasma polymer films for biomaterial applications. Plasma Chem. Plasma Process. **34**, 14 (2014)
253. Renee V. Goreham, A. M, Madelene Pierce, Robert D. Short, Shima Taheri, Akash Bachhuka, Alex Cavallaro, Louise E. Smith, Krasimir Vasilev, A substrate independent approach for generation of surface gradients. Thin Solid Films **528**, 5 (2013)
254. R.V. Goreham, G. M, L. Muscariello, G. Cafiero, P. Favia, E. D'Aloia, R. D'Agostino, A. Barbarisi, Small surface nanotopgraphy encourages fibroblast and osteoblast cell adhesion. RSC Adv. **3**, 9 (2006)
255. D.M. Caruso, K.N. Foster, M.H.E. Hermans, C. Rick, Aquacel Ag in the management of partial-thickness burns: results of a clinical trial. J. Burns Care Rehabil. **25**, 9 (2004)
256. Eric J. Tobin, R. B, Silver coating of dialysis catheters to reduce bacterial colonization and infection. Ther. Apheresis Dial. **7**, 6 (2003)
257. S. Hardman et al., An in vitro model to compare the antimicrobial activity of silver-coated versus rifampicin-soaked vascular grafts. Ann. Vasc. Surg. **18**(3), 308–313 (2004)
258. M. O'donnell et al., Optimisation of the long-term efficacy of dental chair waterline disinfection by the identification and rectification of factors associated with waterline disinfection failure. J. Dent. **35**(5), 438–451 (2007)

259. Mahendra Rai, A. Y, Aniket Gade, Silver nanoparticles as a new generation of antimicrobials. Biotechnol. Adv. **27**, 8 (2009)
260. Jon L. Hobman, L.C. C, Bacterial antimicrobial metal ion resistance. J. Med. Microbiol. **64**, 27 (2014)
261. Milena Ignatova, S. V, Bernard Gilbert, Nadya Markova, Damien Cossement, Rachel Gouttebaron, Robert Jerome, Christine Jerome, Combination of electrografting and atom-transfer radical polymerization for making the stainless steel surface antibacterial and protein antiadhesive. Langmuir **22**, 8 (2006)
262. Jeom Sik Song, S. L, Gook Chan Cha, Sung Hee Jung, Seo Yoon Choi, Kyung Hoon Kim, Mu Seong Mun, Surface modification of silicone rubber by ion beam assisted deposition (ibad) for improved biocompatibility. J. Appl. Polym. Sci. **96**, 7 (2005)
263. T.P. Martin, S.E. K, S.H. Chang, K.L. Sedransk, K.K. Gleason, Initiated chemical vapor deposition of antimicrobial polymer coatings. Biomaterials **28**, 7 (2007)
264. G. Grundmeier, P. T, J. Carpentier, V. Barranco, Tailored thin plasma polymers for the corrosion protection of metals. Surf. Coat. Technol. **174–175**, 6 (2003)
265. W.J. van Ooij, D. S, H.K. Yasuda, Plasma-polyermized coatings of trimethysilane deposited on cold-rolled steel substrates Part 2. Effect of deposition conditions of corrosion performance. Prog. Org. Coat. **25**, 19 (1995)
266. A.W. Hahn, M.F. N, A.K. Sharma, E.W. Hellmuth, *Glow Discharge Polymer Coated Oxygen Sensors. Biomedical and Dental Applications of Polymers* (Plenum Press, New York, 1981)
267. R.K. Sadhir, W.J. J, H.K. Yasuda, A.K. Sharma, M.F. Nichols, A.W. Hahn, The adhesion of glow-discharge polymers, silastic and parylene to implantable platinum electrodes: results of tensile pull tests after exposure to isotonic sodium chloride. Biomaterials **2**(4), 5 (1981)
268. R.D. Ajeet Kaushik, R.D. J, Sneham Tiwari, Arti Vashist, Madhavan Nair, Nano-biosensors to detect beta-amyloid for Alzheimer's disease management. Biosens. Bioelectron. **80**, 15 (2016)
269. B. Derkus, Applying the miniaturization technologies for biosensor design. Biosens. Bioelectron. **79**, 13 (2016)
270. S. Babacan, P. P, S. Letcher, A. Rand, Evaluation of antibody immobilization methods for piezoelectric biosensor application. Biosens. Bioelectron. **15**, 7 (2000)
271. P. Peluso, D.S. W, D. Do, H. Tran, M. Venkatasubbaiah, D. Quincy, B. Heidecker, K. Poindexter, N. Tolani, M. Phelan et al., Optimizinng antibody ammobilization strategies for the construction of protein microarrays. Ann. Biochem. **312**, 12 (2003)
272. Kim Shyong Siow, L. B, Sunil Kumar, Hans J. Griesser, Plasma methods for the generation of chemically reactive surfaces for biomolecule immobilization and cell colonization—A review. Plasma Processes Polym. **3**, 27 (2006)
273. Anton Manakhov, P. S, David Necas, Jan Cechal, Josef Polcak, Marek Elias, Lenka Zajickova, Cyclopropylamine plasma polymers deposited onto quartz crystal microbalance for biosensing application. Phys. Status Solidi A **211**, 8 (2014)
274. Anton Manakhov, E. M, Petr Skladal, David Necas, Jan Cechal, Lukas Kalina, Marek Elias, Lenka Zajickova, The robus bio-immobilization based on pulsed plasma polymerization of cyclopropylamine and glutaraldehyde coupling chemistry. Appl. Surf. Sci. **360**, 9 (2016)
275. N. Kawasaki et al., Flexible picene thin film field-effect transistors with parylene gate dielectric and their physical properties. Appl. Phys. Lett. **96**(11), 113305 (2010)
276. Ceren Susut, R.B. T, Plasma enhanced chemical vapor depositions to encapsulate crystals in thin polymeric films: a new approach to controlling drug release rates. Int. J. Pharm. **288**, 9 (2005)
277. S. Simovic, D. Losic, K. Vasilev, Controlled drug release from porous materials by plasma polymer deposition. Chem. Commun. **46**(8), 1317–1319 (2010)
278. Kateryna Bazaka, M.V. J, Vi Khanh Truong, Feng Wang, Wickrama Arachchilage Anoja Pushpamali, James Y. Wang, Amanda V. Ellis, Christopher C. Berndt, Russel J. Crawford, Elena P. Ivanova, Plasma-enhanced synthesis of bioactive polymeric coatings from

monoterpene alcohols: a combined experimental and theoretical study. Biomacromolecules **11**, 11 (2010)
279. C. Easton, *Development of Lavender Oil Based Polymer Films for Emerging Technologies* (James Cook University, Australia, 2009)
280. L.J. Anderson, *Investigations into Plasma Deposited Linalyl Acetate Thin Films for Applications in Organic Electronics* (James Cook University, Australia, 2013)
281. M. Jacob, K. Bazaka, Fabrication of Electronic Materials from Australian Essential Oils. Australian Government: Rural Industries Research and Development Corporation (2010)
282. M. Kim et al., High-rate deposition of plasma polymerized thin films using PECVD method and characterization of their optical properties. Surf. Coat. Technol. **169**, 595–599 (2003)
283. J. Morales et al., Electronic conductivity of pyrrole and aniline thin films polymerized by plasma. J. Polym. Sci., Part B: Polym. Phys. **38**(24), 3247–3255 (2000)

Chapter 12
Cold Atmospheric Plasma Sources—An Upcoming Innovation in Plasma Medicine

Dheerawan Boonyawan and Chanchai Chutsirimongkol

12.1 Introduction

In terms of physics and chemistry, plasma is a completely or partially ionized gas with ions, electrons, and uncharged particles such as atoms, molecules, and radicals, regarded as the fourth state of matter. The other states of matter are liquid, gas, and solid. Plasma does not have a definite shape or volume as gas; however, it will form structures when put under a magnetic field, which is not seen in gas. From a macroscopic point of view, plasma is electrically neutral. However, plasma is electrically conductive and a lot of free charge carriers are contained in it (Fig. 12.1).

Depending on amounts of energy transferred to plasmas, the plasma properties change in terms of electron density and electron temperature. These two parameters define plasmas into two categories: thermal equilibrium plasma or thermal plasma and nonthermal equilibrium plasma or cold plasma.

- Thermal plasma, transitions, and chemical reactions are mainly controlled by plasma particles collisions, not by radiative processes. Moreover, collision phenomena are micro-reversible in thermal plasma, suggesting that each kind of collision is balanced by its inverse such as excitation/de-excitation; ionization/recombination; and kinetic balance [1]. Therefore, in thermal plasma, the plasma temperature is equal to the gas temperature.
- Cold plasma can be described by two temperatures: electron temperature (T_e) and ion temperature (T_i). Because of the huge mass difference between electrons

D. Boonyawan (✉)
Plasma and Beam Physics Research Facility, Science Faculty,
Chiang Mai University, Chiang Mai 50200, Thailand
e-mail: dheerawan.b@cmu.ac.th

C. Chutsirimongkol
Photo Bio Care Co. Ltd, Nonthaburi 11120, Thailand

R.S. Rawat (ed.), *Plasma Science and Technology for Emerging Economies*,
DOI 10.1007/978-981-10-4217-1_12

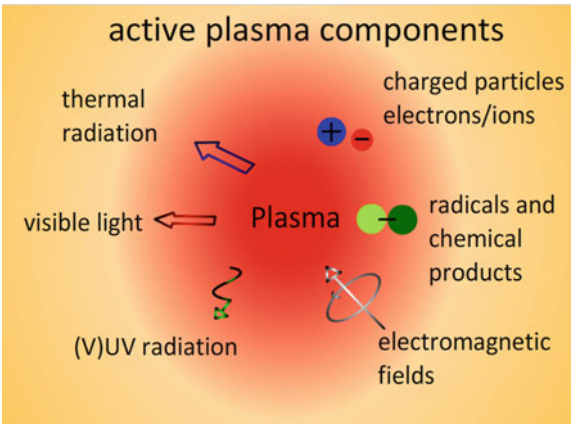

Fig. 12.1 The typical compositions of a plasma

and ions, the plasma temperature or gas temperature is determined by ion temperature. On the other hand, the electron-induced de-excitation rate of the atom is generally lower than the corresponding electron-induced excitation rate because of a significant radiative de-excitation rate. Therefore, the density distribution of excited atoms in cold plasma is possible to depart from Boltzmann distribution, saying that the plasma temperature is much lower than the electron temperature [2–5] (Fig. 12.2).

- **Plasma in Medical Sciences**

Plasma has been used for a long time in medical field and it can generally be classified according to temperature of the plasma gas. Thermal plasma is used in medical procedures such as tissue removal, cauterization, cut, and sterilization of thermally stable medical materials and even for cosmetic tissue restructuring [6–9]. Since the high flux of heat can reach temperatures above 80 °C, it causes several damages on living tissue. The nonthermal atmospheric-pressure plasma, or cold

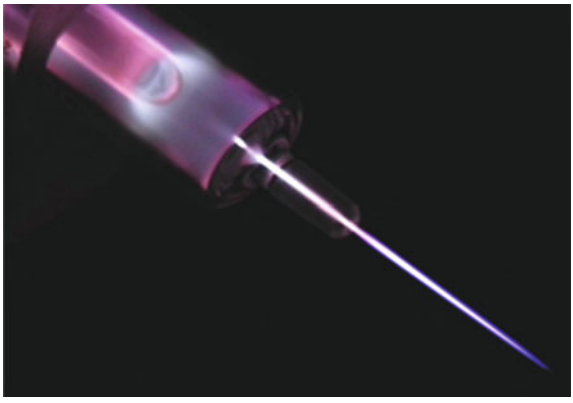

Fig. 12.2 A plasma needle operated at PBP research center

plasma, is delivered at near room temperature, which results in less damaging effects on living tissue, while still has the efficacy in disinfection and sterilization. Many studies proved that it is able to inactivate gram-negative and gram-positive bacteria, fungi, virus, spore, various parasites, and foreign organisms or pathogens without harming tissue [6–9]. Moreover, cold plasma has been used effectively in medical field such as dental use, inducing apoptosis of malignant cells [10], stopping bleeding [11], promoting wound healing and tissue regeneration by increasing cell proliferation by the release of growth factors such as fibroblast growth factor-2 (FGF2), and by activating plasma-produced reactive oxygen species [6, 7, 12, 13] (Fig. 12.3).

Dielectric barrier discharge (DBD) generates cold plasma at atmospheric pressure of air or other gas. DBD, moreover, has been used to treat cell culture medium to induce cell proliferation in vitro [12, 14] and treat liquid for antimicrobial effect [15, 16]. The plasma treatment of cell culture medium causes interaction with medium components such as protein and amino acids leading to the production of long-lived reactive organic hydroperoxide. This in turn induces cell expression and release of cytokines and growth factors for cell recovery [12].

Cold atmospheric plasma generates reactive oxygen species (ROS), reactive nitrogen species (RNS), UV radiation, and electric field. Most of plasma's effects on biological system are related to reactive nitrogen–oxygen species (RNOS) including H_2O_2, O_3, O_2^-, NO, NO_2, N_2^-, and OH which may enhance wound healing [12, 13, 17]. It has been known that reactive species, free radicals, and some ground state molecules are produced by mammalian immune system cells, macrophages, and neutrophils, defense bacterial and virus, and also regulate cellular functions. Furthermore, reactive species are involved in the regulation of signal pathways such as growth factor and cytokine receptors [9]. In physiological processes, reactive species play a role in the regulation of vascular contraction, blood coagulation, angiogenesis, inflammation, immune system response, and nerve impulse transmission. As well as at cellular level, reactive species regulate cell differentiation, division, migration, and apoptosis by controlling cell-to-cell

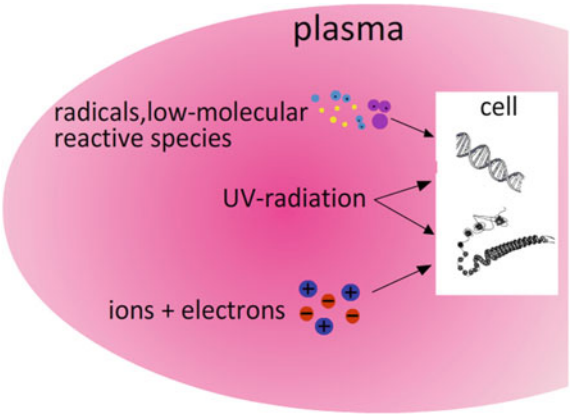

Fig. 12.3 Plasma medicine is a branch of plasma bioscience regarding human cells and tissues

adhesion, biosynthesis of growth factors, and collagen production [9]. However, the effect of plasma on cells is dose dependent. Short-time treatment has stimulating effect such as increasing cell proliferation and migration, while long plasma treatment time or treatment with higher intense plasma induces lethal effect, DNA damage, cell apoptosis, and necrosis [9, 18].

- **Wounds and Skin**

Wound healing is a complex dynamic process, requiring the cooperation of different cell types including cytokines, chemokines, and components of the renin–angiotensin system, which stimulate proliferation and migration of mesenchymal and non-mesenchymal cells to promote wound healing after skin or another body injury [19]. The process is divided into three distinct phases: proceeding from the inflammatory phase to the proliferative phase and to the remodeling phase [20]. In the inflammation phase, platelets that form initial thrombus release growth factor to induce chemotaxis and proliferation of neutrophils and macrophages in order to remove necrotic tissue, debris, and bacteria in wound area. Afterward, fibroblasts play a key role in the proliferative phase by producing collagen which provides the wound structure. In this phase, angiogenesis of new blood vessels to sustain cells and tissues is found and epithelialization also form keratocytes to cover wound surface. The remodeling phase begins when wound has filled in and resurfaced. Collagen fibers reorganize, remodel, and mature to give wound tensile strength forming scar tissue. Cellular activity reduces and a number of blood vessels in the wounded area regress and decrease. In chronic wound, the duration may be interrupted and overlapped in one or more of the phases of wound healing which will inhibit and decrease effective normal healing [18, 20] (Fig. 12.4).

Fig. 12.4 Plasma skin treatment conducted at PBP research center

Dermal fibroblasts are the dermis layers of skin cells, related to connective tissue regeneration and skin recovery. After skin is wounded, keratinocyte growth factor (KGF) or fibroblast growth factor-7 (FGF7) is rapidly induced from dermal fibroblasts and blind to FGFR2IIIb receptor on keratinocytes [21] stimulating interleukin-1(IL-1) and transforming growth factor-β (TGF-β) release. The IL-1 and TGF-β induce fibroblasts to release various growth factors and cytokines and stimulate keratinocyte proliferation and differentiation [17, 21]. After skin is wounded, fibroblasts Endothelin-1 (ET-1) and TGF-β, released from activated fibroblasts, stimulate themselves proliferate and differentiate into myofibroblasts which orient themselves along lines of tension and pull collagen fiber together in order to contract the wound margin [21, 22]. These activities can lead to sublethal cell membrane damage or cell death [12]. The injury due to sublethal damage of the cell membrane will further increase inflammatory cytokine levels and exaggerate ROS generation to prolong myofibroblast activation to induce collagen accumulation and fibrotic scar [13]. In addition to a wound, mechanical force, radiation, and electromagnetic fields can induce sublethal cell membrane damage and lead to growth factors release [9, 12, 23]. This method, however, harms the surrounding tissue and also needs an extensive setup to generate safety to living tissue. Cold plasma, however, provides a novel and safer process that induces growth factors release. High concentration of ROS from cold plasma damages endothelial cell membrane and the subsequent release FGF-2 from endothelial cell enhanced wound healing through increased angiogenesis [23]. These artificial ROS species appear to be related to intracellular and extracellular produced by neutral plasma component [12, 23]. Therefore, ROS which generated by cold plasma may enhance wound healing by stimulating activities of fibroblast cells in vitro model.

12.2 CAP: Principles and Design

For a typical plasma, Fig. 12.5 shows the dependence of gas pressure on electron temperature (T_e) and gas temperature (T_g). At a lower pressure, such as 10^{-4} to 10^{-2} kPa, gas temperature is much lower than electron temperature. Operating gas atoms or molecules are excited or ionized through inelastic collisions with energetic electrons, driven by external electric field. These inelastic collisions do not raise the temperature of ions/molecules in the plasma.

However, collisions in the plasma are enhanced at a higher gas pressure where particles mean free path are short. These led to both mechanisms, plasma chemistry from inelastic collisions, and plasma particles heating from elastic collisions to take place inside the plasma. The difference between T_e and T_g decreases, and plasma state is then close to the thermal equilibrium state. To avoid a plasma gas from being heated, which later generate a thermal plasma at atmospheric pressure [24], it was found that the density of the driving power affects the transition to reach thermal equilibrium at a large extent. Namely, a high density of driving power

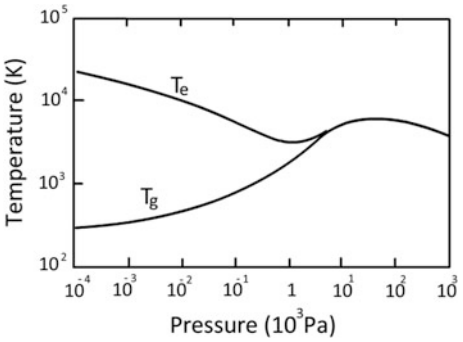

Fig. 12.5 Electron and gas temperature as a function of gas pressure in a plasma

produces the atmospheric-pressure thermal plasma, e.g., arc plasma whilst a low density of driving power produce the atmospheric-pressure nonthermal plasma.

- **Dielectric barrier discharges (DBDs)**

DBD was first reported by Siemens in 1857 [25]. They concentrated on the generation of ozone using DBDs. Nowadays, DBDs are widely used to generate atmospheric-pressure nonequilibrium plasmas in a controllable way. Generally, planar and cylindrical electrode arrangements are utilized in DBDs. This plasma source may consist of two flat metal electrodes that are covered with dielectric material. Having an insulator prevents current buildup between two electrodes to create safe plasma without a large number of hot gasses which is appropriate to be directed at biological systems as treatment (Fig. 12.6).

One can see that a dielectric arrangement over electrode is employed, and the presence of one or more dielectric layers between the two electrodes across the gap is important for a gas discharge. First, the dielectric is able to limit the discharge current and can avoid transition to arc plasma. And finally, the dielectric randomly distributes micro-discharges or streamers all over the electrode surface since the formation of micro-discharges is due to electrons accumulation on the dielectric layer.

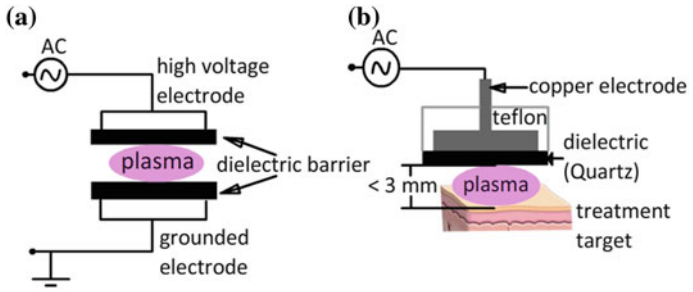

Fig. 12.6 Configuration of DBDs. **a** DBD, **b** FE-DBD

Typical materials for dielectric barriers which can hold temperature rise for a long period of discharge are glass, quartz, and ceramics. Materials such as plastic foils, silicone tube, Teflon plates, and other insulators can be used as well [26].

- **Filamentary mode barrier discharges**

There are two different modes of DBDs: filamentary mode and diffuse mode [27–34]. In general, DBD is operated in the filamentary mode. When the local electric field strength in discharge gap reaches the gas breakdown level, the discharge takes place, known as streamers or filamentary or micro-discharges. Micro-discharges are easily observed in most gasses when the gas pressure is in the order of 10^2 kPa. The development of micro-discharges may divide into three steps [26, 35]:

– The pre-breakdown. Space charge of electrons or negative ions due to electron attachment is accumulated over the anode. This phase generally lasts for at least 0.5 ms. Then, a high local electric field strength built up in front of the anode. When it reaches a certain critical level, the discharge starts from the anode surface.
– The propagation. This phase is controlled by an ionization wave in the direction to the cathode. Pairs of ions and electrons are produced on the way of the ionization wave. This phase typically takes 1–2 ns.
– The decay. This phase is characterized by charge accumulation on dielectric surface in the way to compensate the external electric field. Both the emission radiation and current pulses of the micro-discharges decay in this phase. The micro-discharges are of nanosecond time duration. They are uniformly distributed over the dielectric surface. In the next half cycle of the applied voltage, the formation of micro-discharges renews inversely. The dielectric barrier limits the amount of the transferred charge and the energy deposited in a single micro-discharge channel. Therefore, nonthermal equilibrium plasma is able to be generated at atmospheric pressure by DBD.

Figure 12.7 shows the effect of the time constants on the relevant processes in the filamentary DBDs. One can see that the development of micro-discharge channels, which is initiated by the production of energetic electrons, takes place in the range of nanosecond. Subsequently, the plasma chemical reactions phase typically starts within the millisecond time scale by atoms, radicals, excited species, and short wave radiation. The active species production from gas media is controlled by properties of the micro-discharges, namely by the reduced local electric field strength and electron density. The properties of the micro-discharges in filamentary DBDs do not depend on the external driving electric field, e.g., frequency, voltage, and waveform over a wide range of operation conditions. They are mainly controlled by the feed gas composition (Fig. 12.8).

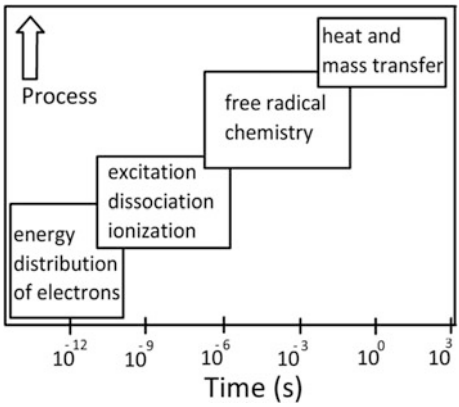

Fig. 12.7 Timescales of relevant processes in filamentary barrier discharges

Fig. 12.8 A filamentary mode barrier discharge of Argon in air taken at PBP research center

- **Diffuse or glow mode barrier discharges**

A diffuse or glow mode of DBD can be obtained under certain operating conditions. Donohoe investigated a uniform glow discharge with pulsed excitation in helium/ethylene mixtures [36]. Okazaki and coworkers proposed the term "APGD": atmospheric-pressure glow discharge by using a barrier glow discharge setup at 50 Hz sinusoidal voltage with two metal foils covered by a special metal mesh and ceramic dielectrics electrode configuration using helium, nitrogen, and air [37–39]. Massines and coworkers investigated barrier glow discharges in helium and nitrogen in detail [40–42]. The stable diffuse DBD generation at atmospheric pressure requires special operation conditions, which primarily depend on the properties of feed gas. Compared to the filamentary mode DBD conditions, effective pre-ionization, Penning ionization via metastables, and primary ionization in the low electric field condition are very important for the generation of diffuse mode

DBD [26]. Hence, the driving voltage frequency plays an important role in the transition to the diffuse mode. Some dielectric materials can keep considerable numbers of charges uniformly on the surface. When the electric field changes its polarity, the charge carriers are expelled from the surface and start a diffuse discharge [43]. Until now, substantial works were made to better understand the formation of diffuse DBD.

The basic mechanisms of diffuse DBD are strongly affected by properties of the feed gas. This can be illustrated by the comparison of the DBD in helium and nitrogen, which are quite different. In helium plasma, effective ionization and excitation processes take place in the cathode electric field region through direct collisions of atoms with energetic electrons or through three body processes, generating He^+ and He_2^+ ions [44, 45]. On the contrary, in nitrogen, plasma ions and electrons are probably generated through another mechanism. Kinetic models of diffuse DBD in the nitrogen plasma come to the conclusion that Penning ionization through two body collisions of metastable nitrogen molecules and surface electrons are very important [46, 47]. In the mixtures of nitrogen and oxygen, the nitrogen metastable molecules are quenched considerably by molecular oxygen, which results in a significant decreased in the densities of nitrogen metastables. Therefore, in nitrogen gas with an addition of a trace of oxygen gas, the direct ionization of nitrogen molecules ($E \approx 18.7$ eV) in the ground state by energetic electrons is dominant [48]. This process requires electrons with energy at least of 18.7 eV. Therefore, when most of the nitrogen metastables are quenched, there is no other way for the discharge development. It well explains that diffuse mode transits to filamentary mode when a trace of O_2 gas is added into the nitrogen plasma [48].

- **The design**

There are many reports of different types of nonthermal atmospheric-pressure plasma sources for biomedical applications. However, DBD atmospheric pressure, room air plasma has great potential for acne and skin surface improvement. In his report, Fridman et al. have confidently concluded that the direct plasma or filamentary DBD is much more potent in bacterial eradication than the indirect plasma or glow DBD type [7, 12, 23]. Nevertheless, the direct plasma source using the DBD technique can work only at very small millimeters distance, the gap between the powered or floating electrode and skin as second or ground electrode. The problem with using a DBD electrode on a nonuniform skin surface is that the geometry and variation of skin electrical properties make it difficult to apply the flat planar floating electrode clinically. It is difficult to maintain and fix small-millimeter gap distances to create a uniform and stable homogeneous plasma beam without uncontrollable streamer discharge.

We have developed a novel CAP device operated in mixed filamentary and glow discharge using the FE-DBD configuration by Photo Bio Care, Thailand as shown schematically in Fig. 12.9. The device can create a low-temperature, sustained, homogeneous microfilament beam (23) that emits from the, round shape designed, dielectric floating electrode (22) when it comes in direct contact with a dry or

mildly moist skin surface, e.g., wounds (24). The round shape of the dielectric electrode tip can be varied from a few millimeters up to 25 mm. The electrode used in this study is 18 mm in diameter. Such geometry creates regular, small gap distances once the electrode is mildly pressed to the skin surface and is moved constantly.

The power generator (25) drives high-frequency pulse waves in the range of 15–20 kHz. Peak-to-peak voltage is ~6–7 kV, delivered as pulsing and adjustable rate from 10 to 110 Hz. The maximum input power from a normal household socket is 40 watts. Power intensity is adjustable from 1 to 10. The plasma power output is in the range of 0.2–1 watts, adjustable according to intensity and repetitive pulse setting. The automatic preset is at level 05 intensity at 50 Hz, with average CAP power of 0.62 watts. The system is set at a duration limit of 20 min per treatment. Also, it is equipped with Argon feed gas (26) to perform a hybrid mode operation (Fig. 12.10).

The system has a small compact movable platform using room air as the discharge gas medium in filamentary DBD mode. Uniform, homogeneous micro-plasma streamers are generated by ionizing surrounding air on electrode surface and discharging it directly to target the skin tissue with direct skin contact.

As shown in Fig. 12.11 the powered electrode also can be applied without direct contact with skin, and by retaining a floating gap of 1–3 mm, a hybrid plasma mode can be conducted. With a flow of Argon feed gas, an intense and strong glow plasma of 2–6-mm in beam size reach the skin surface, creating a very high power density spot. This technique is used to coagulate superficial skin lesions, such as pustular acne, with few seconds of repeated strokes on the lesion.

Electronics and pulse power generator system as shown in Fig. 12.12, the circuit, consist of power supply that supplies a controller or MCU circuit (in dash-line

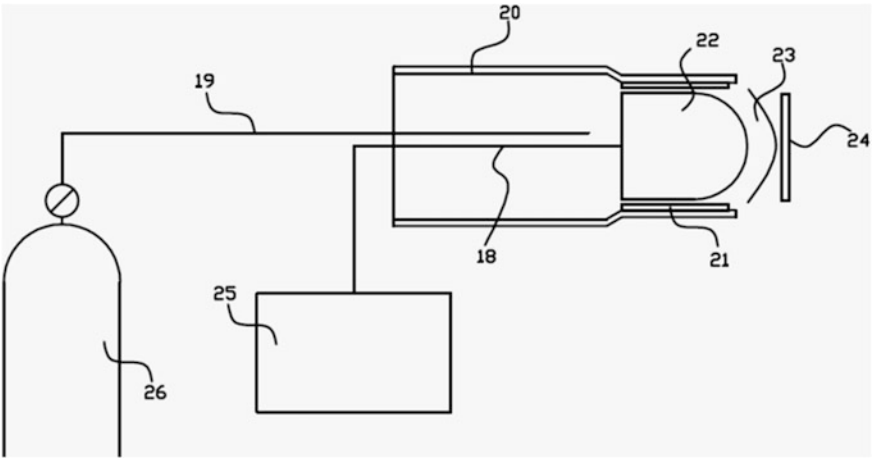

Fig. 12.9 A FE-DBD plasma device developed for biomedical treatment

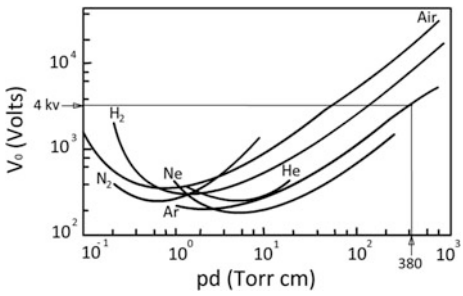

Fig. 12.10 The peak pulse voltage needed for Argon as a working gas in hybrid mode

Fig. 12.11 Photo of the hybrid CAP®

box). This circuit produces variable frequency, pulse signal for a driver circuit through the DBD plasma head via high-voltage transformer circuit (in dash-line circle). Furthermore, MCU circuit adjusts rate of pulse repetition for plasma dose control. Operating time of this system is controlled by a timer, which is settable up to 20 min maximum per treatment.

High-voltage transformer circuit transforms pulse signal from low driving pulse voltage to 6–7.5 kV, which suffices for plasma production in a hybrid DBD plasma mode. This power driving circuit is limited by a current-limited resistor in order to prevent excess of power to the transformer and excess of CAP power density, afterward. A foot switch is utilized for easy access and unit operation.

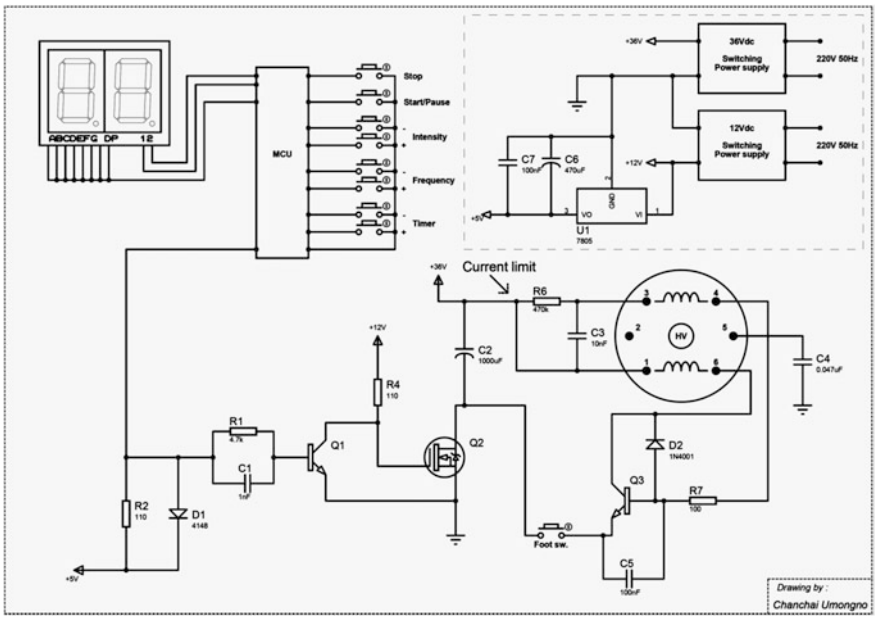

Fig. 12.12 Diagram of **e**lectronics and pulse power generator, limited at 40 watts input power

12.3 Characteristics of the Hybrid CAP®

Measurement of electrical signals at the output of pulse power circuit, directly connected to the DBD plasma head, was carried out (Fig. 12.13).

It was found that plasma was generated by a pulse voltage of 3.5–4.5 kV, a tunable frequency between 16 and 19 kHz. The dose of CAP can be controlled by duty cycle of the pulse train which is 10, 50, and 100%, respectively. The following figure shows the relation between intensity or dose level and pulse repetition rate at 20 Hz.

12.3.1 CAP Power Determination and Skin Contact Temperature

Assuming that all micro-discharges have nearly identical properties in every current pulse, then $\Delta Q \approx nq$, where n is the number of micro-discharges in a series and q is the charge transferred by one single micro-discharge. The quantity of charge transfer is mainly determined by the categories of dielectric and the width of gap spacing [26].

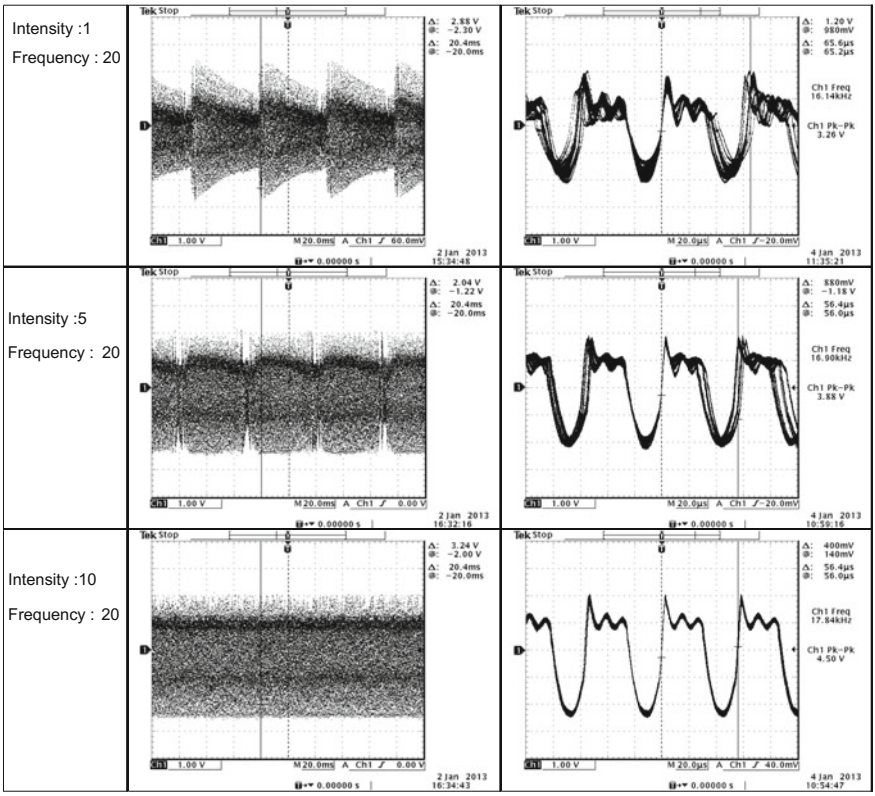

Fig. 12.13 Driving pulse train at 20 Hz with 10, 50, and 100% duty cycle, respectively

By using above assumption, the CAP power measurement can be determined using voltage–charge (V–Q) Lissajous method. The voltage difference of modulator (Vx) is measured by using high-voltage probe, which connected with x–y display oscilloscope as shown in Fig. 12.14. This oscilloscope is also used of capacitor voltage (Vy) determination and electrical charge is estimated from this voltage. The voltages Vx and Vy are displayed on x-axis and y-axis of oscilloscope, respectively, and the area within Lissajous pattern indicates power of the CAP, which generated from plasma head due to charge $Q = CVy$, where C is capacitance of the capacitor, energy of plasma $W = QVx$ and plasma power per one period of pulse signal $P = W/T = Wf$, where f is the signal frequency.

The measured dose or CAP power per unit area at different settings is summarized in Table 12.1, performed under IEC60601-1 medical standard.

To overcome a real sense of the CAP power which will be applied directly to skin or wounds, a liquid crystal thermometer strip was also used with volunteer's skin. Figure 12.15 shows series of photos when CAP was applied to arm skin and temperature strip was measured, afterward. The skin temperature was collected and

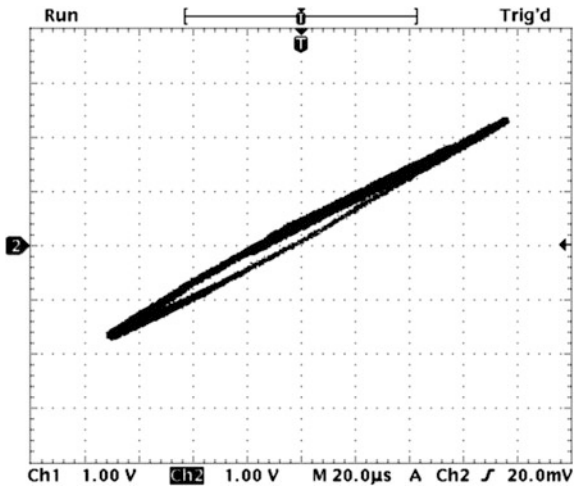

Fig. 12.14 A hybrid CAP® power in a pulse determined by *V–Q* Lissajous method

Table 12.1 CAP dose (W/cm^2) measured at different settings

Setting	Rate 10	Rate 50	Rate 110
Dose 1	0.25	0.56	0.80
Dose 5	0.30	0.62	0.81
Dose 10	0.27	0.65	0.84

the sense of power with CAP application time also be recorded as shown in Table 12.2.

12.3.2 Radicals and UV Determination

- **Optical emission and UV absorption spectroscopy**

In CAP, feed or air gas molecules are excited and ionized through the collisions with energetic electrons. And most of them are responding by electron-induced excitation mode in the nonequilibrium plasma. Therefore, the active species such as excited molecules, atoms, and ions in CAP emit light through a significant radiative de-excitation. Optical emission spectroscopy (OES) is well known as a noninvasive and non-disturbing technique for general plasma diagnostics [49–53] (Fig. 12.16).

In the OES measurement, light emitted from active species in the plasma is collected through a spectrometer. One can explore the mechanism of plasma chemical reactions by monitoring the emission intensities of active species. Assuming that CAP is in a local thermodynamic equilibrium, the gas temperature is equal to the rotational temperature of a certain active species. Therefore, OES can also utilize for gas temperature evaluation from emission spectral profile shape of a certain molecular active species, e.g., N_2 or NO [54, 55]. Recently, several research

Fig. 12.15 CAP was applied to arm skin and temperature strip was measured, afterward, from *left* to *right*, *top* to *bottom*. The setting was 5/50 at 24 °C 50% RH

Table 12.2 Skin temperature and sense of power of volunteers with CAP application time

Application time (s)	–	2	3	4	5
Measured temp (°C)	26.5	29.5	32.0	35.5	39.0
Sense of volunteer	–	Feel warm	Warm	Quite warm	Hot

groups [56–59] focused on spatially and temporally resolved spectroscopic measurements (Fig. 12.17).

Series of spectra in Fig. 12.18 show emission band 308 nm of hydroxyl (OH) radical, band 350 nm of nitrogen positive system, and a group of Ar emission lines. The OES result indicates that this plasma was operated in air. And as well known that CAP temperature is then defined by the surrounding nitrogen which carries plasma heat by rotation and vibration of theirs molecule.

At high Argon flow rate, OH radicals are highly suppressed while the band of N_2 positive system becomes higher. This mechanism explains by the ionization cross sections and ionization potentials are nearly the same for Argon and N_2 which is $\sim 2.5 \times 10^{-20}$ m^2 and ~ 15.7 eV, respectively. A known mechanism is increasing the pressure of the plasma component more dense that redound the mean free path of energetic electron to decrease, and the ability to excite other components such as water molecule to produce OH radical decreases.

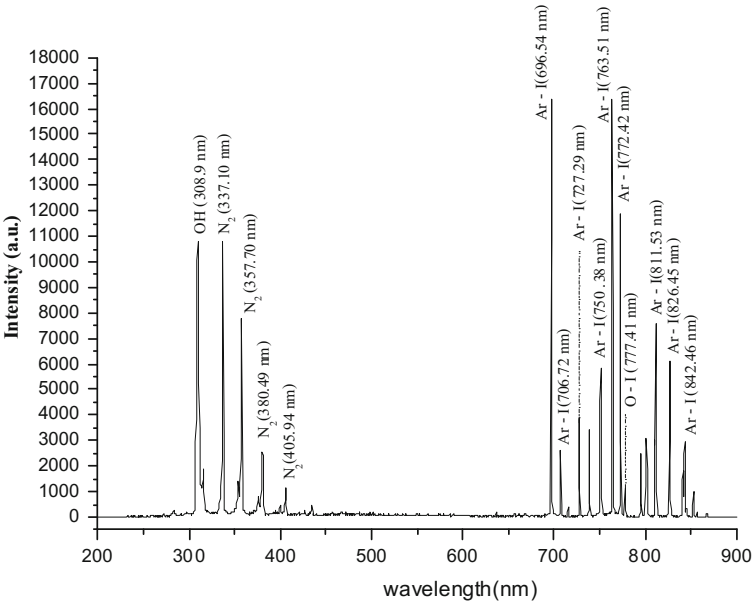

Fig. 12.16 Typical OES of Ar DBD plasma operated in air. Emission spectral profile shape of N_2 is resolved in 3–400 nm wavelength

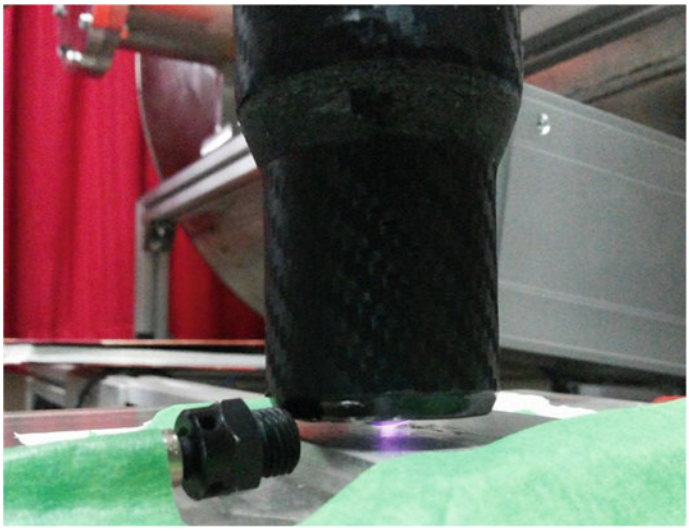

Fig. 12.17 Setup for OES measurement of hybrid CAP®. The setting was 5/50 at 24 °C 65% RH

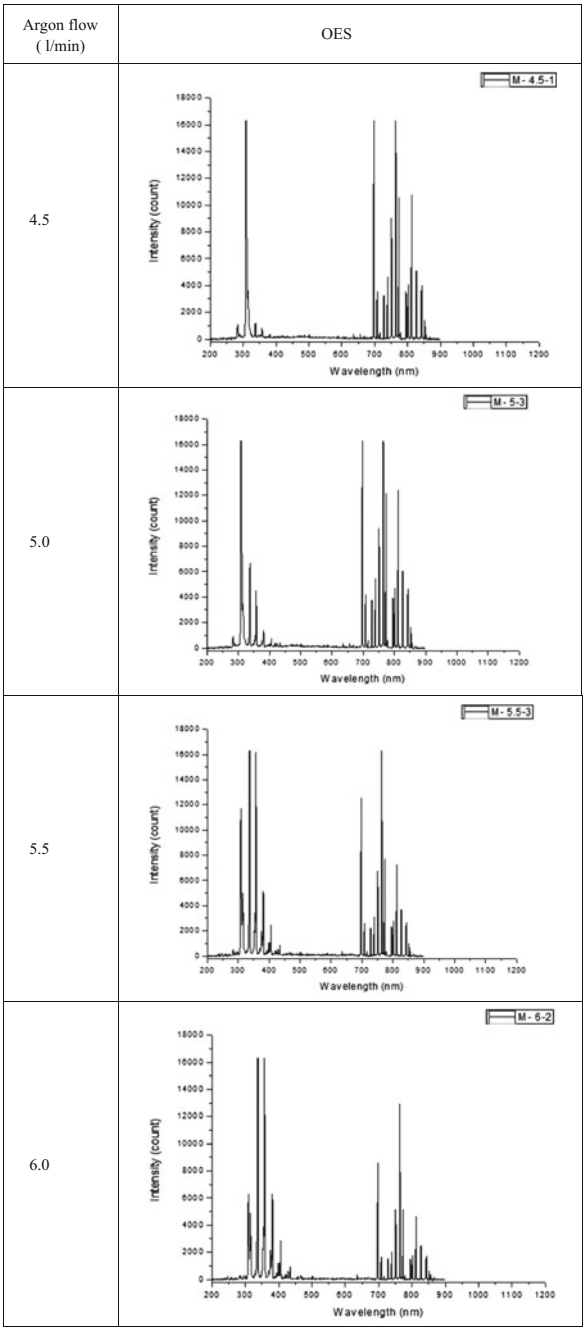

Fig. 12.18 Series of OES at different Argon flow rates from 4.5 to 6.0 slm

To determine the number of radicals particularly in this CAP, the spectroscopy can be rearranged from OES to UV absorption spectroscopy. And the density of ground state hydroxyl OH radicals, [OH], could be carried out by UV absorption spectroscopy using the Lambert–Beer's law:

$$[\mathrm{OH}] = -\frac{1}{\sigma \cdot l}\ln\left(\frac{I^{t+p} - I^{p}}{I^{s}}\right),$$

where σ is the attenuation cross section of $1.03 \times 10^{-16}\,\mathrm{cm}^2$ for absorbing species of OH radical [57, 58], and l is the plasma spatial depth which is the UV beam passed through. Whereas I^{t+p} is the total light intensity or the sum of the transmitted light and plasma light measured with UV lamp and plasma on, I^{p} is the plasma intensity with the source off and I^{s} is the intensity of the source with the plasma off.

The numbers of OH radical based on the absorbed band head at 306.4 nm from electronic transition $A^2\Sigma \rightarrow X^2\Pi$ have been investigated versus Argon flow rate with some settings of the hybrid CAP® and summarized in Table 12.3.

In an Ar-CAP, the OH radical is primarily ascribed by electrons and Ar metastables (Ar^m) induced by dissociation of water molecules in the ambient air. Two dominant mechanisms are $e^- + H_2O \rightarrow OH + H + e^-$, $k_1 = 2 \times 10^{-18 \sim -16}\ m^3\ s^{-1}$ and $Ar^m + H_2O \rightarrow OH + H + Ar$, $k_2 = 4.5 \times 10^{-16}\ m^3\ s^{-1}$, where k_1 is estimated at typical conditions for low-temperature plasma, i.e., low ionization degree ($\sim 10^{-4}$) and an electron temperature of 1–2 eV. The yield of OH radical, as shown in Fig. 12.19, is clearly due to the second reaction by the Ar^m density. The Argon metastable $1s_5$ state density estimated by using the 811.53 nm line obviously presents the OES results.

- **Erythemally weighted irradiance of ultraviolet**

Biological weighting function is an action spectrum for the UV spectrum in an integration of the monochromatic UV irradiance which describes the relative effect of UV energy at different wavelengths in producing a certain biological response. These effects may occur at a molecular level, such as DNA damage, or at the level of the whole organism, such as damaged burns. Consider UV range of A, B, and C type emissions from CAP and by using total erythemally weighted irradiance equals $\Sigma\ P_{\mathrm{eff}}(\lambda) \times \Delta\lambda\ \mathrm{w/m}^2$ [6]. The accumulation can be carried out by a number of counts of all peaks in each range of UV as shown in Fig. 12.20

Table 12.3 Numbers of OH radical from hybrid CAP® at some settings

OH radicals ($10^{15}\ \mathrm{cm}^{-3}$) flow/setting	5/10	5/50	5/110
@ Ar 4.5 lpm	0.74	1.8	2.2
@ Ar 5 lpm	0.68	1.7	2.0
@ Ar 6 lpm	0.42	0.76	0.95

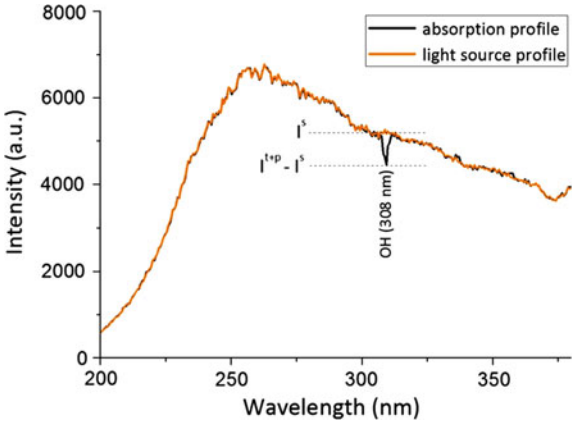

Fig. 12.19 The yield of OH radical in hybrid CAP® accumulated from UV absorption at 308 band head

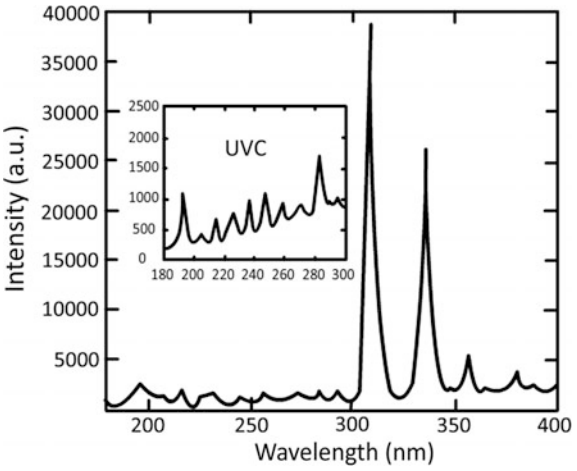

Fig. 12.20 OES of UV A, B, and C covered 200–400 nm range from typical atmospheric plasma

Assuming UV-A (315–400 nm) are from N_2 molecules, UV-B (280–315 nm) are from OH radicals, and UV-C (100–280 nm) are from NO radicals, we can summarize Table 12.4 from the previous OES data of the hybrid CAP®. From the table, one can see that the hybrid CAP® generates high level of UV-A at the high Argon flow rate. In contrast, this maximum value is rather low compared to

Table 12.4 UV power exposure on animal skin for 1 min from hybrid CAP®

UV power ($\mu W/cm^2$)	UV-C	UV-B	UV-A
Sun ray	1–2.5	30–50	600
@ Ar 4.5 lpm	0.5	15	5
@ Ar 5 lpm	0.3	13	20
@ Ar 6 lpm	0.15	7.5	115

exposure by the sun ray. 1 min of hybrid CAP® treatment gives the 5–10 time less UV-C than that of the sun exposure dose.

For UV-B, 1 min of treatment is equivalent to 4–6 time of sun exposure dose less. For UV-A, 1 min of treatment corresponds to 10 s of the sun exposure dose, where WHO–ICNIRP standard regulation defines maximum allowed dose of 50 W/cm^2.

Nevertheless, for the open wounds or unprotected skin, they are allowed to extend the total erythemally weighted irradiance for 5–10 times the normal skin.

12.4 The Hybrid CAP® Case Studies

12.4.1 Disinfection Measure

Disinfection and decontamination procedures are essential in medicine and dentistry [60]. Prostheses have been cited as a potential source of cross-contamination and cross-infection between patients and dental personnel [61]. The incidence of contamination increases through constant exposure to debris, plaque, blood, and saliva which contain pathogenic organisms which adhere to prostheses [62] and can be transmitted through various routes, such as dental burs, handpieces, casts, impressions, contaminated hands, and skin [63].

Various bacteria can be transmitted through the aforementioned process [63, 64]. Methicillin-resistant *Staphylococcus aureus* (MRSA), the *Staphylococcus aureus* with resistance to a wide range of antibiotics [65–67], is one of the organisms of most concern due to its pathogenicity and its resistance to drying, heat and some groups of disinfectants [68]. Furthermore, it is often found colonizing in common areas of the body, such as the oral cavity, nose, throat, and skin [69], so it can frequently be found contaminating on dental instruments and denture surfaces [69, 70].

Several methods of disinfection have been recommended to ensure infection control in dental practice, such as chemical soaking, heat treatment, ionizing, and non-ionizing irradiation [60, 71–74]. However, there are disadvantages and limitations to those methods, for examples, inability to kill certain pathogenic organisms [71]; leaving residual chemicals that can cause tissue injury [72]; not being environmentally friendly [63]; and, more importantly, taking a relatively long time to disinfect. The gold standard for chemical disinfection is 2% chlorhexidine digluconate soaking, for at least 10 min [63, 71, 75, 76], which is considered a long time in medical procedures.

To overcome the problems associated with previous disinfection measures, a trial demonstrates the use of CAP for MRSA disinfection on the surface of acrylic resin specimen compared to the traditional chemical (2% chlorhexidine digluconate) soaking. Pilot studies were conducted, using various durations of plasma treatment (120, 90, 30, 15, and 5 s), to determine the shortest treatment time needed

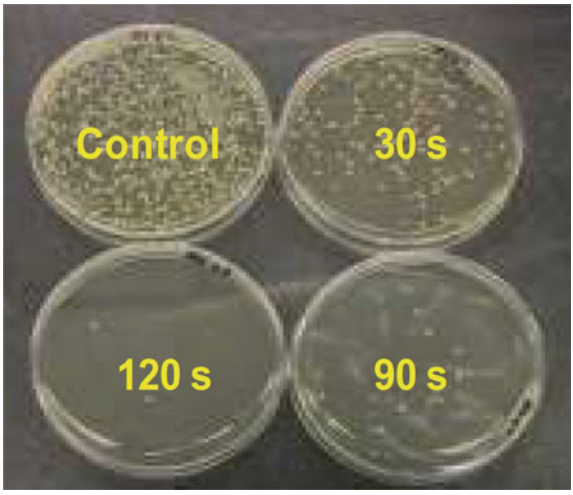

Fig. 12.21 MRSA of $N_0 = 10^6$ cfu/ml disinfected using CAP, living colony with treatment time

to kill the bacteria as effectively as, or even more effectively than, does ten-minute immersion in the chlorhexidine solution.

The result is shown in Fig. 12.21. Each treatment time significantly reduced the CFU counts, but the 15–20 s treatment time was the shortest with effectiveness not less than that of the gold standard.

Effect of heat from plasma treatment is a factor of concern to some investigator [77, 78]. The gas flow at 80 °C without plasma ignition was fired at contaminated specimens under the same conditions as used with plasma treatment. As shown in Fig. 12.22, 80 °C gas flow did not effectively eliminate the bacteria, compared to the plasma method, indicating that the heat from the plasma is not a major agent in the disinfection of MRSA, especially at treatment times of 30 s and lower.

Chlorhexidine, a cationic biguanide (Fig. 12.23), is an important disinfectant. Its antimicrobial effects [79–81] are associated with the attractions between chlorhexidine (cation) and negatively charged bacterial cell wall which disrupting

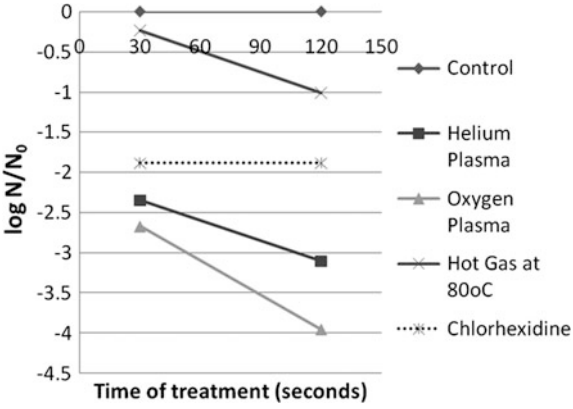

Fig. 12.22 A dose–response curve: treatment time and log N/N_0

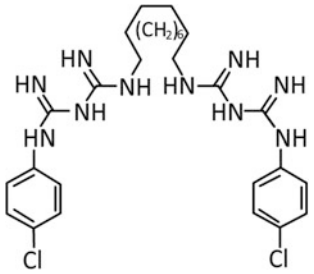

Fig. 12.23 Chemical molecular structure of chlorhexidine

the integrity of cell membrane and causing leakage of intracellular components of the organisms.

Possible mechanisms of bacterial death and injury by the CAP method can be discussed as follows:

– **Desiccation**

Gas flow and the temperature from the plasma flume can cause further evaporation of the remaining liquid, leaving the bacteria to desiccate. However, the results of the CFU counts indicate survivability of MRSA after being left desiccated. Besides, several studies have shown *S. aureus*' tolerance to desiccation, under various conditions, so it can be assumed that desiccation is not a major agent for the killing of MRSA [82, 83].

– **Thermal**

The aforementioned pilot study is evidence supportive of the assumption that thermal damage is not an important mechanism of the disinfection. Also, most plasma systems are designed to operate at ambient temperature, at least below a value known to cause cell damage [71].

– **UV radiation**

UV radiation is known to be a very potent disinfection method only if its wavelength is within the killing range (220–280 nm) [84] and its dose is high enough. However, UV radiation poses the danger of DNA damage to normal cells; therefore, plasma sources are usually thoroughly designed so as to limit the emission of such UV radiation [72, 78, 83].

– **Charged particles**

Much less attention is given to charged species. Most researchers in this field have neglected to investigate the role, if any, of the electrons and ions in the process. The bacterial cell wall carries a natural negative charge, because it consists of strongly electronegative components [78]. These components make bacteria sensitive to changes in their surface charge. By considering that the changes violate the wall integrity, lowering of the natural charge might cause the cells to leak and eventually

die. This mechanism is plausible to contribute the killing of the MRSA directly exposed to the plasma [72, 78, 83].

– **Reactive species**

Disinfection of MRSA by reactive species generated in the plasma effluent is then considered to be the main disinfection mechanism in the experiments [72, 78, 83]. Though the exact role of electrons and ions is not yet fully resolved, there are several indications of their importance. Through the oxidation process, chemically ROS are known to be effective in the disruption of the bacterial cell wall. The role of oxygen radicals in plasma sterilization has been also demonstrated: the rate of bacterial inactivation in the oxygen plasma group was greater than that in the helium plasma group. This is due to the presence of oxygen-based active species, such as atomic oxygen, the metastable singlet state of oxygen, and ozone (O_3). Also, in the presence of moisture, the hydroxyl-radical, OH, is expected to play a significant role by chemically attacking the outer structures of bacterial cells. The presence of such reactive species is verified by the OES of the plasma flume. Peaks in the spectral region between 777.1 and 777.6 nm, as shown as a combined peak OI (777.48 nm) in Fig. 12.24, are the signature of atomic oxygen spectral lines.

This role also affirmed by the ATR-FTIR spectra of MRSA specimens in Fig. 12.25. In gram-negative bacteria like *E.coli* main mechanism comes from hydroxyl radicals (·OH) in the form of carboxylic acid. In this case, ·OH is strong and effects in disrupting an integrity of phospholipids layer (P=O: phosphine oxide) of cell membrane. The effect is clearer when <0.5% oxygen was added and oxygen radicals (O–) enhanced damage via increment of alcohol (C–O).

At this stage of discussion, the plasma method offers an alternative way of disinfection with equal efficacy, but with much less time required. By using the proper combination of parameters and feed gas compositions, the CAP device is capable of operating as a uniform, nonthermal discharge at atmospheric pressure. It

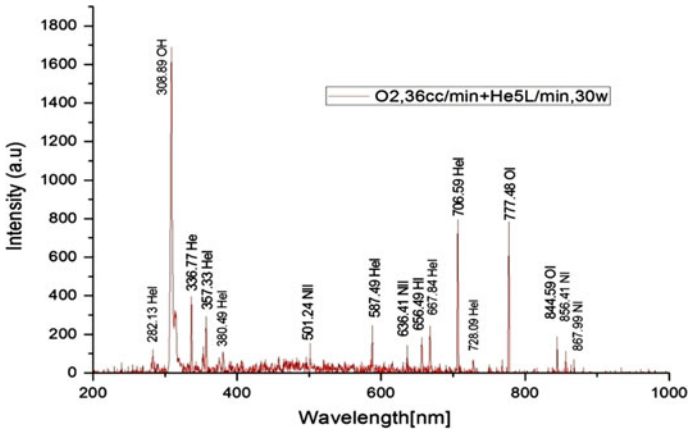

Fig. 12.24 Combined atomic oxygen spectral line from He + O_2 plasma

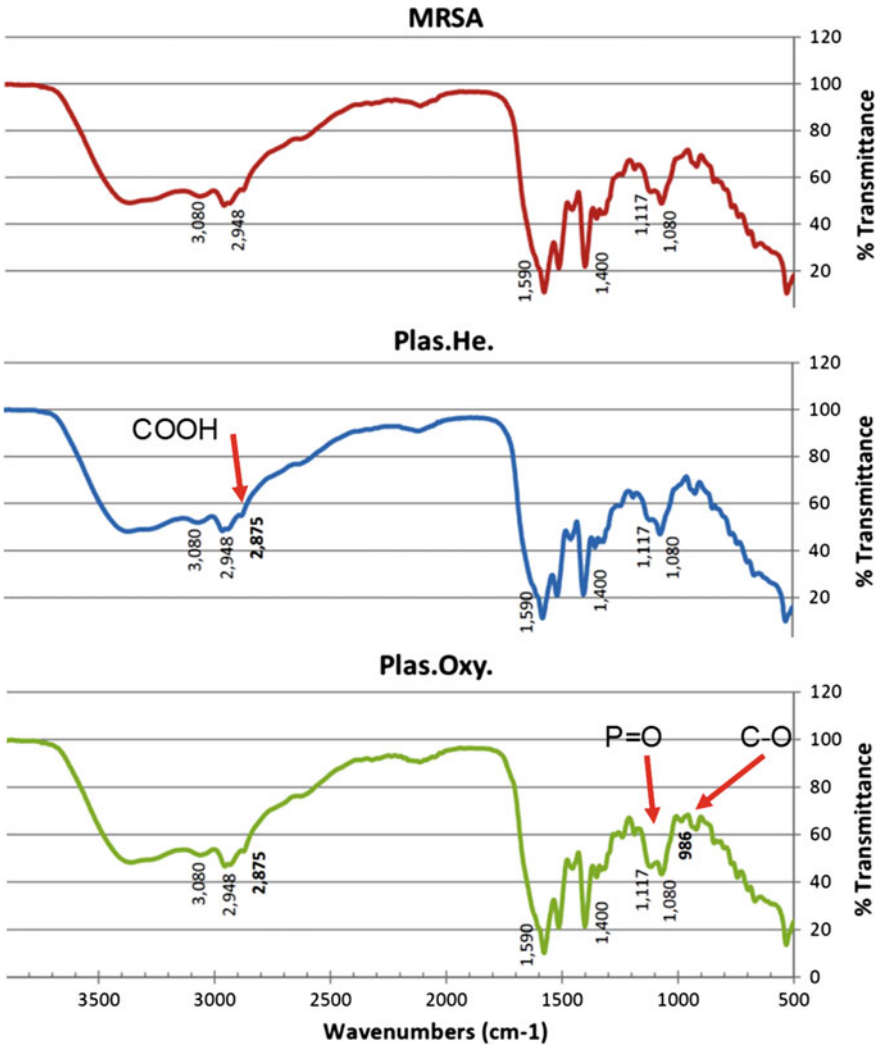

Fig. 12.25 ATR-FTIR spectra of MRSA specimens revealed reactive species in He/O_2-CAP interact with phospholipids layer

produces high-density reactive species at relatively low temperature. Because of its numerous advantages, more research efforts have been put into the issue.

- **SEM and Live/Dead results**

Scanning electron micrographs in Fig. 12.26 is the instant effect of CAP treatment on *C. albicans* and *E. faecalis* biofilms. It can clearly see that cell walls show ruptures or shrinkage for all over. These unhealthy cells in biofilm are unable to proliferate.

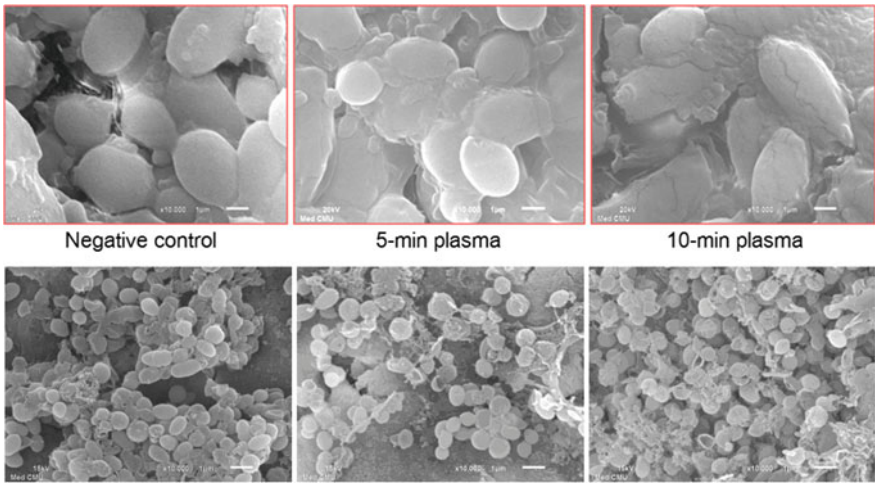

Fig. 12.26 Instant effect of CAP treatment on *C. albicans* (*top*) and *E. faecalis* (*bottom*)

Live/Dead assay

In Fig. 12.27, specimens with *C. albicans* and *E. faecalis* biofilm, aged 7 days, were exposed to the CAP for 5 and 10 min, and then stained with dye to observe the viability rate. Within 5–10 min of plasma exposure, it shows a high rate of cell death, (Cells that stained orange/yellow color) compared to the dark green as a negative control. The biofilm of *E. faecalis*, aged 7 days, also shows the proportion of cells killed when exposed to the CAP with greater efficacy compared to the *C. albicans*.

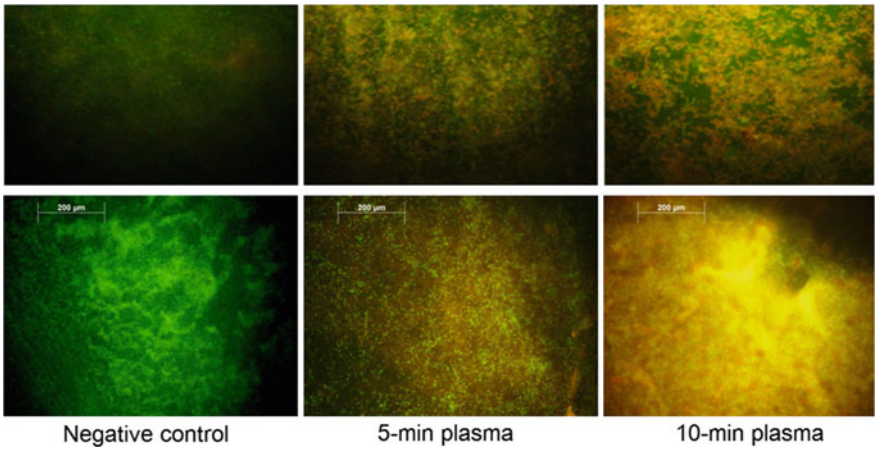

Fig. 12.27 Live/Dead stain of CAP exposed on 7 days biofilm of *C. albicans* (*top*) and *E. faecalis* (*bottom*)

12.4.2 Infected Wound

Pressure sores are soft tissue injuries resulting from an unrelieved pressure of soft tissue over a bony prominence. Pressure sore prevalence is around 9% of all hospitalized patients. Most of them will turn to a chronic wound stage with multiple drug-resistant bacterial superimposed infections. Wound tends to have poor circulation with unhealthy granulating tissue and difficult to heal. Such wound usually becomes heavy exudative forming biofilm and necrotic tissue debris. It also has poor epithelialization wound coverage which exposed tissue to further injury and infection. A chronic wound such as bed sore or pressure sore is one of the illnesses that create a heavy and chronic burden to patient and healthcare service system.

Patients were invited to participate in the study if they had chronic pressure ulcer grade 3 or 4 that did not heal within 3 weeks despite proper wound care. We used National Pressure Ulcer Advisory Panel 2007 (NPUAP) for grading of pressure ulcers in this study.

- **Case results**

Patients were divided into two groups randomly by using computer-generated list with nQuery Advisor 6.01 program, Block randomized technique. Patients in the control group were received standard wound care (debridement, proper wound dressing, etc.) as usual. In addition to the standard wound care, the hybrid CAP® was used in the study group patients.

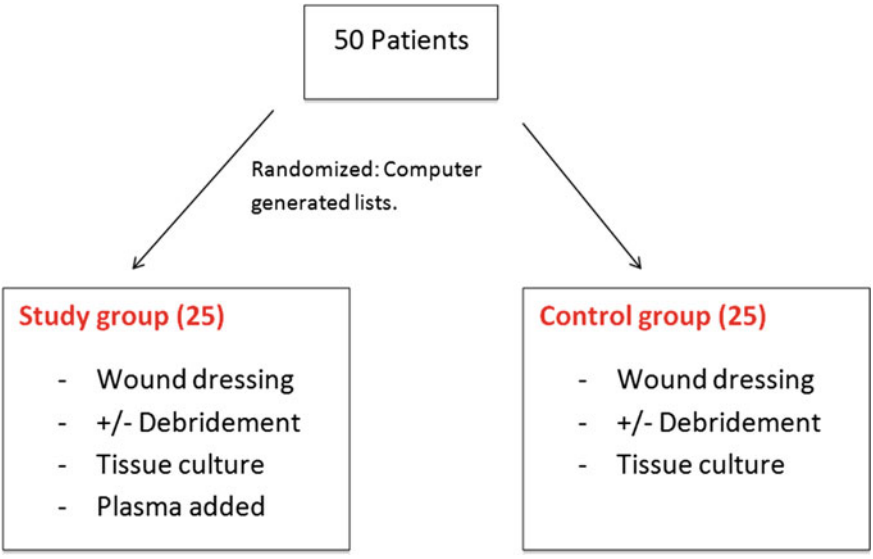

A total of 42 patients completed the study: 23 patients, 26 pressure ulcers in plasma group, and 19 patients, 23 pressure ulcers in the control group. Patient demographics and wound characteristics are summarized in Table 12.5.

Clinical outcomes of wound healing

Figure 12.29 shows the development of wound healing by the Ar-hybrid CAP® treatment. PUSH score is used to evaluate the wound healing process in three aspects (wound size, exudate, and wound base). The number of wounds that reduce in size compared to the initial assessment were statistically different at second week after two treatments (46.2% in plasma, 8.7% in control group; $p = 0.003$). The number of wounds that reduce in amount of exudate compared to the initial assessment was statistically different at first week after one treatment (26.9% in

Table 12.5 Patient demographic data and wound characteristics

	Plasma (23 pts, 26 wounds)	Control (19 pts, 23 wounds)	*p* value
Age	70.75 ± 17.5	74.53 ± 11.6	0.658
Sex male	7 (30.4%)	6 (31.6%)	1
female	16 (69.6%)	13 (68.4%)	
Underlying disease			
Hypertension	11/23 (47.8%)	10/19 (52.6%)	1
Diabetes	7/23 (30.4%)	8/19 (42.1%)	0.644
Dyslipidemia	9/23 (39.1%)	3/19 (15.8%)	0.186
Old CVA	5/23 (21.7%)	4/19 (21.1%)	1
Spinal cord injury	3/23 (13%)	1/19 (5.3%)	0.239
CKD	4/23 (17.4%)	1/19 (5.3%)	0.114
Antibiotic use (IV/oral)	2 (7.7%)	4 (17.4%)	0.4
Smoking (>10 pack-year)	4/23 (17.4%)	5/19 (26.3%)	0.707
Pressure ulcer grading			
grade 3	14/26 (53.8%)	9/23 (39.1%)	0.457
grade 4	12/26 (46.2%)	14/23 (60.9%)	
Site			
Ischial	4 (15.4%)	3 (13%)	0.459
Greater trochanter	3 (11.5%)	5 (21.7%)	
Sacrum	17 (65.4%)	15 (65.2%)	
Others	2 (7.7%)	0 (0%)	
Chronic wound duration			
3–4 weeks	12 (46.2%)	5 (21.7%)	0.271
5–12 weeks	2 (7.7%)	3 (13%)	
3–6 months	7 (26.9%)	11 (47.8%)	
>6 months	5 (19.2%)	4 (17.4%)	
Initial PUSH score	14 ± 1.4	15 ± 1.6	1

plasma, 0% in control group; $p = 0.015$). The number of wounds that improve tissue type of wound base compared to the initial assessment was statistically different at second week after two treatments (57.7% in plasma, 8.7% in control group; $p = 0.002$). The number of wounds that is improved in overall wound healing process (total PUSH score) compared to the initial assessment was statistically different at first week after one treatment (57.7% in plasma, 4.3% in control group; $p = 0.015$).

In summary, total PUSH score and amount of exudates improved with statistic significant after 1 plasma treatment. Wound size and wound base were improved with statistic significant after two plasma treatments as shown in Table 12.6.

Table 12.6 Results of treatment in wound size and exudate reduction wound base improvement and PUSH score results

	Plasma-treated group ($n = 26$)	Control group ($n = 23$)	p value
Wound size reduction (size score week0)–(score week 1, 2, 3, …) $\geq$ 1	Number of wounds that reduced in size compared to the initial assessment.		
wk 1	5 (19.2%)	0 (0%)	0.052
wk 2	12 (46.2%)	2 (8.7%)	***0.003***
wk 4	19 (73.1%)	6 (26.1%)	***<0.001***
wk 8	23 (88.5%)	12 (52.2%)	***<0.001***
Exudate reduction (exudate score week 0)–(score week 1, 2, 3, …) $\geq$ 1	Number of wounds that reduced in the amount of exudate compared to the initial assessment.		
wk 1	7 (26.9%)	0 (0%)	***0.015***
wk 2	18 (69.2%)	1 (4.3%)	***<0.001***
wk 4	18 (69.2%)	3 (13%)	***<0.001***
wk 8	21 (80.8%)	7 (30.4%)	***<0.001***
Wound base improvement (wound base score week 0)–(score week 1, 2, 3, …) $\geq$ 1			
wk 1	5 (19.2%)	1 (4.3%)	0.08
wk 2	15 (57.7%)	2 (8.7%)	***0.002***
wk 4	18 (69.3%)	4 (17.3%)	***0.001***
wk 8	20 (76.9%)	7 (30.4%)	***0.007***
Total PUSH score improvement (wound healing) (total PUSH score week 0)–(total PUSH score week 1, 2, 3, …) $\geq$ 1			
wk 1	15 (57.7%)	1 (4.3%)	***0.001***
wk 2	23 (88.5%)	2 (8.7%)	***<0.001***
wk 4	25 (96.2%)	7 (30.4%)	***<0.001***
wk 8	25 (96.2%)	12 (52.2%)	***<0.001***

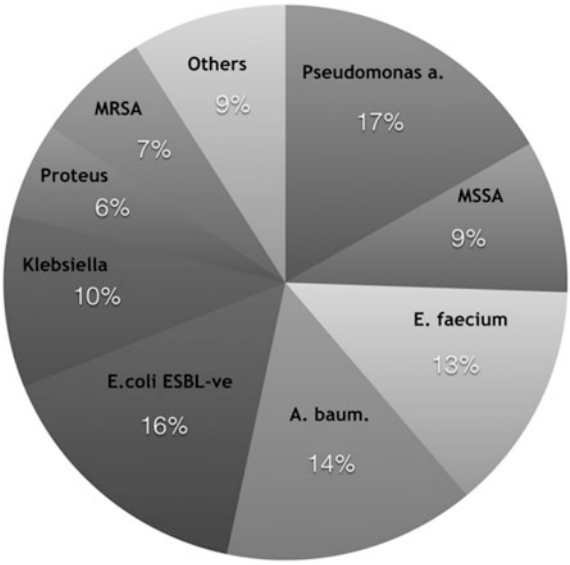

Fig. 12.28 Bacterial culture distribution of control group (others are Coryneform bacteria, Streptococcus and Yeast)

Table 12.7 Bacterial load reduction

	Plasma-treated group (n = 26)	Control group (n = 23)	p value
Bacterial load reduction (tissue culture score week 0)–(score week 1, 2, 3, …) $\geq$ 1	Number of wounds with less bacterial load		
wk 1	18 (69.2%)	4 (17.3%)	***0.001***
wk 4	19 (73.1%)	11 (47.8%)	***0.001***
wk 8	23 (88.5%)	19 (82.7%)	***0.002***

Outcomes of bacterial reduction

The distribution of bacterial culture detected on wounds by weekly tissue culture before treatments is shown in Fig. 12.28. The bacterial load was significantly reduced at first week after one treatment, regardless of the species of bacteria identified, (69.2% in plasma, 17.3% in control group; p = 0.001) as summarized in Table 12.7 (Fig. 12.29).

This was the first RCT study in vivo to demonstrate the wound healing effect of CAP. The CAP seems to support the clinical healing process of chronic pressure ulcer wounds in humans, reduce wound size/exudate, improve wound base, and reduce bacterial load. Applying this method, no relevant side effects have been observed so far, and the available in vitro experimental and this in vivo clinical results may allow the conclusion that CAP is a promising new option for the treatment of chronic wounds.

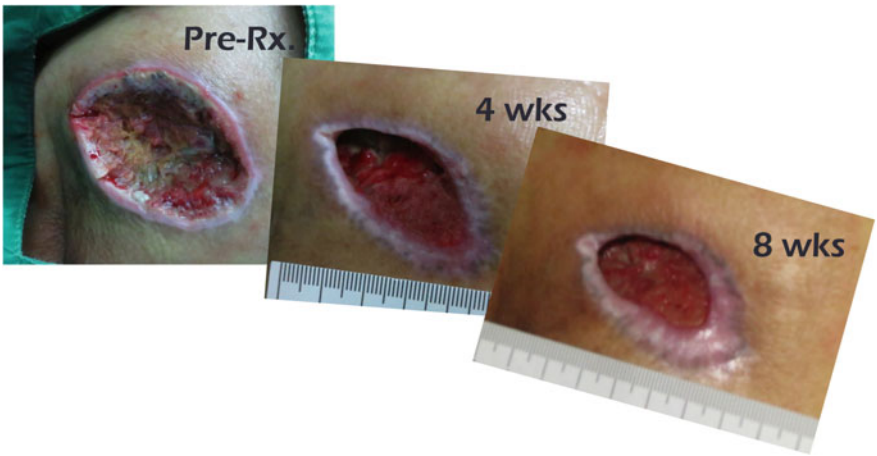

Fig. 12.29 Photograph of pressure ulcer, infected wound for 4 weeks of Ar-hybrid CAP® treatment. Courtesy of Prof. A. Chuangsuwanich

Acknowledgements Authors would like to express our sincere thanks to Y. Thana, S. Klinhom, S. Chinsawananon, S. Khemaleelakul, and Prof. A. Chuangsuwanich M.D. for their devoted efforts and all contributions in the chapter. We also thank Chiang Mai University, Thailand Center of Excellence in Physics (ThEP), and Thailand Center of Excellence for Life Sciences (TCELS) for their supports to the plasma bio/medicine project.

References

1. M. Moisan, M.D. Calzada, A. Gamero, A. Sola, J. Appl. Phys. **80**, 46 (1996)
2. R.H. Huddlestone, S.L. Leonard, *Plasma Diagnostic Techniques* (Academic Press, New York, 1965)
3. H.R. Griem, *Plasma Spectroscopy* (McGraw-Hill, New York, 1964)
4. W. Lochte-Holtgreven, *Plasma Diagnostics* (North-Holland, Amsterdam, 1968)
5. M. Mitchner, C.H. Kruger, *Partially Ionized Gases* (Wiley, New York, 1973)
6. J. Heinlin, G. Isbary, W. Stolz, G. Morfill, M. Landthaler, T. Shimizu et al., Plasma applications in medicine with a special focus on dermatology. J. Eur. Acad. Dermatol. Venereol. **25**(1), 1–11 (2011)
7. S. Kalghatgi, C.M. Kelly, E. Cerchar, B. Torabi, O. Alekseev, A. Fridman et al., Effects of non-thermal plasma on mammalian cells. PLoS ONE **6**(1), e16270 (2011)
8. B.B. Lopes, M.B.P.L. de Kraft, J. Rehder, F.R.X. Batista, M.B. Puzzi, The interactions between non-thermal atmospheric pressure plasma and ex-vivo dermal fibroblasts. Proc. Eng. **59**, 92–100 (2013)
9. M.G. Kong, G. Kroesen, G. Morfill, T. Nosenko, T. Shimizu, J. van Dijk et al., Plasma medicine: an introductory review. New J. Phys. **11**(11), 115012 (2009)
10. C. Hoffmann, C. Berganza, J. Zhang, Cold Atmospheric Plasma: methods of production and application in dentistry and oncology. Med Gas Res. **3**(1), 21 (2013)
11. S. Arndt, P. Unger, E. Wacker, T. Shimizu, J. Heinlin, Y.-F. Li et al., Cold atmospheric plasma (CAP) changes gene expression of key molecules of the wound healing machinery and improves wound healing in vitro and in vivo. PLoS ONE **8**(11), e79325 (2013)

12. S. Kalghatgi, G. Friedman, A. Fridman, A.M. Clyne, Endothelial cell proliferation is enhanced by low dose non-thermal plasma through fibroblast growth factor-2 release. Ann. Biomed. Eng. **38**(3), 748–757 (2010)
13. P. Brun, S. Pathak, I. Castagliuolo, G. Palù, P. Brun, M. Zuin et al., Helium generated cold plasma finely regulates activation of human fibroblast-like primary cells. PLoS ONE **9**(8), e104397 (2014)
14. I. Trizio, T. Ilaria, S. Eloisa, F. Edda, D. Giorgio, R. Vito et al. Investigation of air-DBD effects on biological liquids for in vitro studies on eukaryotic cells. Clin. Plasma Med. (2015). Available from: http://dx.doi.org/10.1016/j.cpme.2015.09.003
15. K. Oehmigen, M. Hähnel, R. Brandenburg, C. Wilke, K.-D. Weltmann, T. von Woedtke, The role of acidification for antimicrobial activity of atmospheric pressure plasma in liquids. Plasma Process Polym. **7**(3–4), 250–257 (2010)
16. T. Von Woedtke, O. Katrin, B. Ronny, H. Tomáš, W. Christian, H. Marcel et al., Plasma-liquid interactions: chemistry and antimicrobial effects. In: *NATO Science for Peace and Security Series A: Chemistry and Biology* (2011), pp. 67–78. Available from: http://dx.doi.org/10.1007/978-94-007-2852-3_6
17. A. Barton, B. Annemarie, W. Kristian, B. Lena, H. Sybille, S. Anke et al., Nonthermal plasma increases expression of wound healing related genes in a keratinocyte cell line. Plasma Medicine. **3**(1–2), 125–136 (2013)
18. B. Haertel, T. von Woedtke, K.-D. Weltmann, U. Lindequist, Non-thermal atmospheric-pressure plasma possible application in wound healing. Biomol Ther. **22**(6), 477–490 (2014)
19. S. Werner, R. Grose, Regulation of wound healing by growth factors and cytokines. Physiol. Rev. **83**(3), 835–870 (2003)
20. A. Hsu, H. Andrew, T.A. Mustoe, The principles of wound healing. In: *Plastic Surgery Secrets Plus* (2010), pp. 3–7. Available from: http://dx.doi.org/10.1016/b978–0-323-03470-8.00001-6
21. S. Werner, T. Krieg, H. Smola, Keratinocyte-fibroblast interactions in wound healing. J Invest Dermatol. **127**(5), 998–1008 (2007)
22. S. McDougall, J. Dallon, J. Sherratt, P. Maini, Fibroblast migration and collagen deposition during dermal wound healing: mathematical modelling and clinical implications. Philos. Trans. A Math. Phys. Eng. Sci. **364**(1843), 1385–1405 (2006)
23. S.U. Kalghatgi, A. Fridman, G. Friedman, A.M. Clyne, Cell proliferation following non-thermal plasma is related to reactive oxygen species induced fibroblast growth factor-2 release. Conf Proc IEEE Eng Med Biol Soc. **2009**, 6030–6033 (2009)
24. M.I. Boulos, P. Fauchais, E. Pfender, *Thermal Plasmas: Fundamental and Applications*, vol. I (Plenum Press, New York, 1994), 452, p. 19. ISBN: 0-306-44607-3
25. U. Kogelschatz, Plasma Chem. Plasma Process. **23**, 1 (2003)
26. H.-E. Wagner, R. Brandenburg, K.V. Kozlov, A. Sonnenfeld, P. Michel, J.F. Behnke, Vacuum **71**, 417 (2003)
27. B. Eliasson, U. Kogelschatz, IEEE Trans. Plasma Sci. **19**, 309 (1991)
28. V.I. Gibalov, G.J. Pietsch, J. Phys. D Appl. Phys. **33**, 2618 (2000)
29. G.J. Pietsch, Contrib. Plasma Phys. **41**, 620 (2001)
30. B. Eliasson, M. Hirth, U. Kogelschatz, J. Phys. D Appl. Phys. **20**, 1421 (1987)
31. D. Braun, U. Kuchler, G.J. Pietsch, J. Phys. D Appl. Phys. **24**, 564 (1991)
32. D. Braun, V. Gibalov, G. Pietsch, Plasma Sources Sci. Technol. **1**, 166 (1992)
33. V.I. Gibalov, V.G. Samoilovich, Y.V. Filippov, Russ. J. Phys. Chem. **55**, 471 (1981)
34. K. Yoshida, H. Tagashira, Memoirs Kitami Inst. Technol. **18**, 11 (1986)
35. K.V. Kozlov, H.-E. Wagner, R. Brandenburg, P. Michel, J. Phys. D Appl. Phys. **34**, 3164 (2001)
36. K.G. Donohoe, PhD thesis, California Institute of Technology, Pasadena, CA (1976)
37. S. Kanazawa, M. Kogoma, T. Moriwaki, S. Okazaki, International Symposium on Plasma Chemistry, Tokyo (Japan), 1987, 1844, p. 20
38. S. Kanazawa, M. Kogoma, T. Moriwaki, S. Okazaki, J. Phys. D Appl. Phys. **21**, 838 (1988)

39. S. Okazaki, M. Kogoma, M. Uehara, Y. Kimura, J. Phys. D Appl. Phys. **26**, 889 (1993)
40. F. Massines, C. Mayoux, R. Messaoudi, A. Rabehi, P. Segur, *International Conference on Gas Discharges and Their Applications*, Swansea (UK), 1992, p. 730
41. F. Massines, A. Rabehi, P. Decomps, R.B. Gadri, P. Segur, C. Mayoux, J. Appl. Phys. **83**, 2950 (1998)
42. N. Gherardi, G. Gouda, A. Ricard, F. Massines, Plasma Sources Sci. Technol. **9**, 340 (2000)
43. J. Tepper, M. Lindmayer, J. Salge, *Proceedings of the Sixth International Symposium on High Pressure Low Temperature Plasma Chemistry*, *HAKONE VI*, Cork (Ireland), 1998, p. 123
44. A. Ricard, P. Decomps, F. Massines, Surf. Coatings **112**, 1 (1999)
45. Y.B. Golubovski, A. Maiorov, J. Behnke, J.F. Behnke, *Proceedings of the Eighth International Symposium on High Pressure, Low Temperature Plasma Chemistry, HAKONE VIII*, Puhajarve (Estonia), 2002, p. 48
46. P. Segur, F. Massines, *Proceedings of the International Conference on Gas Discharges and Their Applications*, Glasgow (UK), 2000, p. 15
47. Y.B. Golubovskii, V.A. Maiorov, J. Behnke, J.F. Behnke, J. Phys. D Appl. Phys. **35**, 751 (2002)
48. H.-E. Wagner, R. Brandenburg, P. Michel, F. Massines, K.V. Kozlov, *Proceedings of the seventh International Symposium on High Pressure Low Temperature Plasma Chemistry, HAKONE VII*, Greifswald (Germany), 2000, p. 93
49. A. Ricard, T. Czerwiec, Thin Solid Films **341**, 1 (1999)
50. A. Fateev, F. Leipold, Plasma Process. Polym. **2**, 193 (2005)
51. A. Simon, S.D. Anghel, Nucl. Instr. Methods in Phys. Res. B **267**, 438 (2009)
52. J.R. Roberts, J. Res. Natl. Inst. Stand. Technol. **100**, 353 (1995)
53. P. Jamroz, W. Zyrnicki, Vacuum **84**, 940 (2010)
54. J.K. Rhee, D.B. Kim, Thin Solid Films **515**, 4909 (2007)
55. Y. Kubota, R. Ichiki, T. Hara, J. Plasma Fusion Res. Series **8**, 740 (2009)
56. C. Hudon, R. Bartnikas, M.R. Wertheimer, IEEE Trans. Electr. Insul. **28**, 1 (1993)
57. R. Brandenburg, K.V. Kozlov, N. Gherardi, P. Michel, C. Khampan, H.-E. Wagner, F. Massines, *Proceedings of the Eighth International Symposium on High Pressure, Low Temperature Plasma Chemistry, HAKONE VIII*, Puhajarve (Estonia), 2002, p. 28
58. D. Trunec, R. Brandenburg, P. Michel, D. Pasedag, H.-E. Wagner, Z. Navratil, *Proceedings of the International Symposium on High Pressure, Low Temperature Plasma Chemistry, HAKONE VIII*, Puhajarve (Estonia), 2002, p. 63
59. V. Poenariu, M.R. Wertheimer, R. Bartnikas, Plasma Process. Polym. **3**, 17 (2006)
60. L.N. Dovigo, A.C. Pavarina, D.G. Ribeiro, J.A. de Oliveira, C.E. Vergani, A.L. Machado, Microwave disinfection of complete dentures contaminated in vitro with selected bacteria. J Prosthodont. **18**(7), 611–617 (2009)
61. J.A. Bell, S.L. Brockmann, P. Feil, D.A. Sackuvich, The effectiveness of two disinfectants on denture base acrylic resin with an organic load. J. Prosthet. Dent. **61**(5), 580–583 (1989)
62. A.L. Chassot, M.I. Poisl, S.M. Samuel, In vivo and in vitro evaluation of the efficacy of a peracetic acid-based disinfectant for decontamination of acrylic resins. Braz Dent J. **17**(2), 117–121 (2006)
63. F.C. da Silva, E.T. Kimpara, M.N. Mancini, I. Balducci, A.O. Jorge, C.Y. Koga-Ito, Effectiveness of six different disinfectants on removing five microbial species and effects on the topographic characteristics of acrylic resin. J Prosthodont. **17**(8), 627–633 (2008)
64. A. Falah-Tafti, A.A. Jafari, M.H. Lotfi-Kamran, Comparison of the effectiveness of sodium hypochlorite and dentamize tablet for denture disinfection. World J Med Sci. **3**(1), 10–14 (2008)
65. R.M. Klevens, R.J. Gorwitz, A.S. Collins, Methicillin-resistant *Staphylococcus aureus*: a primer for dentists. J. Am. Dent. Assoc. **139**(10), 1328–1337 (2008)
66. N. Lewis, *MRSA and Dentures—Should we be worried?* (University Colledge of London Hospital, London, 2009)

67. M. Zimmerli, A.F. Widmer, M. Dangel, A. Filippi, R. Frei, J. Meyer, Methicillin-resistant *Staphylococcus aureus* (MRSA) among dental patients: a problem for infection control in dentistry? Clin Oral Investig. **13**(4), 369–373 (2009)
68. P.J. Bremer, G.C. Fletcher, C. Osborne, *Staphylococcus aureus* (New Zealand Institute for Crop & Food Research Limited Christchurch, New Zealand, 2004)
69. P.D. Marsh, R.S. Percival, S.J. Challacombe, The influence of denture-wearing and age on the oral microflora. J. Dent. Res. **71**(7), 1374–1381 (1992)
70. N. Siriwong, E. Chukeatirote, Antibiotic *Resistance in Staphylococcus aureus and Controling* (School of Science, Mae Fah Luang University, Chiang Rai, Thailand, 2009)
71. H.W. Herrmann, I. Hennis, J. Park, G.S. Selwyn, Decontamination of chemical and biological warfare (CBW) agents using an atmospheric pressure plasma jet (APPJ). Phys. Plasmas **6**(5), 2284–2289 (1999)
72. S.P. Kuo, Plasma assisted decontamination of bacterail spores. Open Biomed. Eng. J. **2**, 36–42 (2008)
73. H.F. Paranhos, C.H. Silva-Lovato, R.F. de Souza, P.C. Cruz, K.M. de Freitas-Pontes, E. Watanabe et al., Effect of three methods for cleaning dentures on biofilms formed in vitro on acrylic resin. J Prosthodont. **18**(5), 427–431 (2009)
74. A. Baysan, R. Whiley, P.S. Wright, Use of microwave energy to disinfect a long-term soft lining material contaminated with *Candida albicans* or *Staphylococcus aureus*. J. Prosthet. Dent. **79**(4), 454–458 (1998)
75. R.F. Hicks, *Atmospheric-Pressure Plasma Cleaning of Contaminated Surfaces* (University of California, Los Angeles, 1999), pp. 1–131
76. J. Goree, I. Member, Bin Liu, David Drake, Stoffels E. Killing of *S. mutans* Bacteris using a plasma needle at atmospheric pressure. IEEE T Plasma Sci. **34**(4):1317–24 (2006)
77. Y.C. Hong, W.S. Kang, Y.B. Hong, W.J. Yi, H.S. Uhm, Atmospheric pressure air-plasma jet evolved from microdischarges: eradication of *E. coli* with the jet. Physics of Plasmas. **16**(12) (2009)
78. E. Stoffels, Y. Sakiyama, D.B. Graves, Cold atmospheric plasma: charged species and their interactions with cells and tissues. IEEE Trans. Plasma Sci. **36**(4), 1441–1457 (2009)
79. F.J. de Souza-Filho, J. Soares Ade, M.E. Vianna, A.A. Zaia, C.C. Ferraz, B.P. Gomes, Antimicrobial effect and pH of chlorhexidine gel and calcium hydroxide alone and associated with other materials. Braz Dent J. **19**(1), 28–33 (2008)
80. C.C. Ferraz, B.P. Gomes, A.A. Zaia, F.B. Teixeira, F.J. Souza-Filho, Comparative study of the antimicrobial efficacy of chlorhexidine gel, chlorhexidine solution and sodium hypochlorite as endodontic irrigants. Braz Dent J. **18**(4), 294–298 (2007)
81. P.C. Komori, D.H. Pashley, L. Tjaderhane, L. Breschi, A. Mazzoni, M.F. de Goes et al., Effect of 2% chlorhexidine digluconate on the bond strength to normal versus caries-affected dentin. Oper Dent. **34**(2), 157–65 (2009)
82. P. Chaibenjawong, S.J. Foster, Desiccation tolerance in *Staphylococcus aureus*. Arch Microbiol. **193**(2), 125–135 (2011)
83. O. Tolba, A. Loughrey, C.E. Goldsmith, B.C. Millar, P.J. Rooney, J.E. Moore, Survival of epidemic strains of nosocomial- and community-acquired methicillin-resistant *Staphylococcus aureus* on coins. Am. J. Infect. Control **35**(5), 342–346 (2007)
84. Laroussi, M., Nonthermal decontamination of biological media by atmospheric-pressure plasma: review, analysis, and prospects. IEEE T Plasma Sci. **30**(4):1409–15 (2002)

Chapter 13
Dielectric Barrier Discharge (DBD) Plasmas and Their Applications

Deepak Prasad Subedi, Ujjwal Man Joshi and Chiow San Wong

13.1 Introduction

Gas discharge plasmas, also known as low-temperature plasmas, have drawn much attention in past few decades because of their importance in many technological developments. The use of plasma for industrial purposes began more than 100 years ago with the use of plasma sources for generation of ozone and also as light sources [1]. Since then, plasma processes have been utilized in a wide range of technological and research areas, including microelectronics, gas lasers, polymers treatments [2–4], synthesis of novel materials [5, 6], protective coatings [7–9], etc. Plasma processes are now commonly used in air cleaning systems, and treatment of food containers, fruits, meat, vegetables, fabrics, and medical devices [10]. New areas of application of plasma processes have also been established in recent years. This includes plasma nanotechnology that involves plasma-based production and modification of nanomaterials [11], plasma ignition, and plasma aerodynamics. Recent development in the production of atmospheric pressure plasma jet has extended the use of nonthermal plasma in biology and medicine for various applications such as dental treatment, wound healing, decontamination of surfaces, treatment of cancer cells, and other skin diseases [10, 12].

Among various sources of plasma, the dielectric barrier discharge (DBD) offers one of the most cost-effective nonthermal plasma sources. This type of discharge is known to be effective in the initiation of chemical and physical processes in gases [13]. DBD has been extensively studied in past few years because of its potential

D.P. Subedi (✉) · U.M. Joshi
Department of Natural Sciences, School of Science, Kathmandu University, Dhulikhel, Nepal
e-mail: deepaksubedi2001@yahoo.com

C.S. Wong
Physics Department, Faculty of Science, Plasma Technology Research Centre, University of Malaya, 50603 Kuala Lumpur, Malaysia

R.S. Rawat (ed.), *Plasma Science and Technology for Emerging Economies*,
DOI 10.1007/978-981-10-4217-1_13

application in many different areas. It covers not only material processing but also applications in the field of energy and environment due to its ability to form highly reactive plasma at near room temperature with low energy consumption using simple reactor system at atmospheric pressure condition [14].

The first application of DBD plasma was in water treatment by ozone after Siemens proposed his novel idea to use DBD for ozone generation in 1857. It was reported in his paper that discharge initiated in an annular gap between two coaxial glass tubes could generate ozone from atmospheric pressure oxygen or air [1]. This invention led to the large-scale industrial production of ozone for the treatment of drinking water around 1900 in Europe. Novel application of DBDs in the production of flat panel television screens using AC plasma, reported in 1996, also drew much attraction [15]. The list of applications of DBD has been extended recently to at least two more fields of interest: airflow control and medicine [16].

The most important characteristic, which has made DBD profoundly useful in material processing, is its nonthermal equilibrium nature (refer Fig. 13.1). This nonthermal equilibrium plasma conditions can be established in DBDs in a much simpler way than with other alternatives such as low-pressure discharges, fast-pulsed high-pressure discharges, or by electron beam injection.

Figure 13.1 shows the dependence of electron temperature (T_e) and neutral temperature (T_g) on the pressure of mercury and rare gas mixture DBD plasma discharge. It is evident that there is a large difference between T_e ($\sim$10,000 K) and T_g ($\sim$300 K) at a pressure of about 1 m Torr resulting in a nonthermal equilibrium plasma [17]. The difference in temperature between these two species arises due to low collision frequency between electron and neutral molecules at low pressure. However, at a pressure above 5 Torr, these two temperatures merge together to an average value of about 5000 K. The nonthermal equilibrium nature of these discharges has made them suitable for material processing.

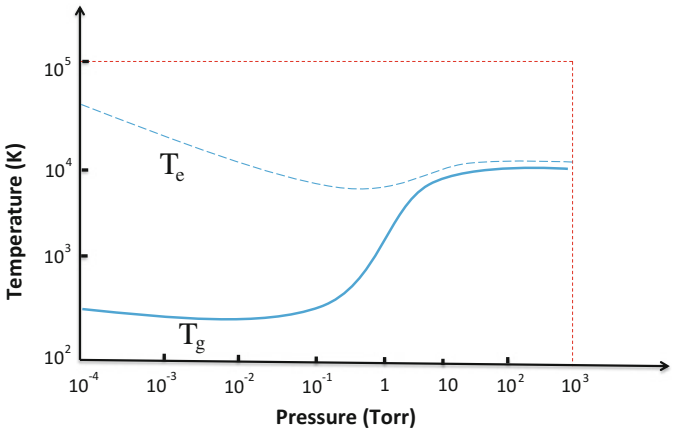

Fig. 13.1 Variation of electron and heavy particle temperature with pressure

13.2 Various Types of Plasmas Useful in Industry

There are various types of plasmas which are generated in research laboratories and many of them have been employed in industry. Classification of these wide range of plasmas can be made mainly on the basis of power supply used to generate them, pressure of the working gas, geometry of the electrode, and nature of the discharge. In the following sections, some low-pressure plasmas based on different power supplies will be discussed. This will be followed by a brief introduction to some plasmas which are generated in atmospheric pressure and are classified based on their discharge characteristics.

13.2.1 Low-Pressure Plasmas

There are many ways to generate a low-pressure plasma. The simplest and the oldest method is the DC glow discharge [18]. DC discharge is useful for sputter deposition of thin films of metals. It has a large potential drop at the conductive cathode producing an energetic bombardment of positive ions on cathode which sputter materials from the metallic cathode. However, they cannot be used to sputter dielectric materials or to deposit dielectric films since insulating surfaces become charged in opposition to the applied field. This problem is overcome using radio frequency (RF) or microwave (MW) discharges so that the positive charges accumulated during the one half cycle can be neutralized by electron bombardment during the next half cycle [19].

High-frequency (HF) plasma sources can be classified according to the type of external energy input used to sustain them. Plasma processing tools generally use RF and microwave power to sustain the plasma. Most commonly RF power is available at 13.56 MHz and microwave power is available at 2.45 GHz. Many types of HF plasma sources exist for processing applications and these are generally classified into capacitive, inductive, and types of EM wave sources used [20]. The latter two are also referred to as high density sources with electron density n_e 10^{17} m^{-3}. A brief review of low-pressure DC, RF, and microwave discharges will be presented in the following sections.

13.2.1.1 DC Discharge

DC glow discharge at low pressure is one of the most familiar of gaseous discharges because of the ease with which it can be generated and maintained and because of its distinctive appearance [21]. This is also one of the earliest forms of laboratory plasma originally studied by Faraday, Crookes, and others working on cathode ray

experiments. The appearance of the discharge is composed of several dark and luminous regions as shown in Fig. 13.2. The light emitted from luminous zones has specific colors which is the characteristic of the gas used. The discharge is produced by applying a DC voltage across two metal electrodes placed inside a glass tube evacuated and filled with a gas to a pressure in the range of 0.1–10 Torr. In a typical DC glow discharge, the voltage is of the order of few hundreds of volts, and the current is of the order of several milliamps [20]. The breakdown voltage V_B is a function of the pressure p of the gas inside the tube and the interelectrode distance d as expressed by Eq. 13.2.1 which is known as Paschen law.

$$V_B = f(pd) \tag{13.2.1}$$

The voltage (V) along the discharge is found experimentally to vary as shown in the lower part of Fig. 13.2. The associated curve for the axial electric field (E) can readily be found from the voltage distribution. If the distance between the two electrodes is reduced keeping the pressure constant, it is found that the reduction in length is taken up entirely by the positive column of the discharge. The positive column constitutes a plasma which is an ionized gas with no net space charge. A detailed description of the different dark and luminous regions in the discharge tube can be found in earlier work [21].

In fact, most of the modern plasma devices are the modified version of the low-pressure glow discharge tube. In practical applications of the discharge for material processing, the electrode area is enlarged whereas the interelectrode distance is reduced. When the distance between the electrodes is made much smaller compared to the dimension of the electrode, most of the discharge will be occupied by the positive column providing a bulk of stable and homogeneous plasma.

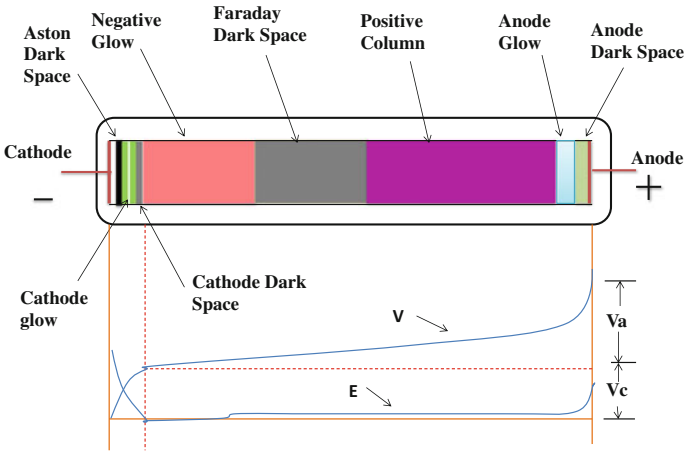

Fig. 13.2 Schematic diagram of the luminous zones and dark spaces in a low-pressure DC glow discharge

13.2.1.2 RF Discharge

When an alternating electric field is applied to a gas, the DC breakdown characteristics are still applicable if the frequency is below about 1 kHz. In this low frequency range, the time for one cycle of the applied AC field is much longer than the ion transit time in the plasma. However, for higher frequencies, AC breakdown takes place at peak voltages differing from the corresponding DC values [21]. At frequencies of the order of 100 kHz, the breakdown voltage is not only a function of (pd) as in the case of DC discharge but also depends on (fd) as represented by the following equation:

$$V_B = f'(pd, fd), \tag{13.2.2}$$

where f is frequency of the RF source. Radio frequency discharge is one of the most widely used discharge types in application for thin film deposition because of its ability to generate a large volume of stable and homogenous plasma. The commercially available RF power supplies are operated at a frequency of 13.56 MHz. Based on the method of coupling, the high-frequency power with the load, the high-frequency discharges are usually classified into two types: (i) capacitive coupling and (ii) inductive coupling.

The capacitively coupled internal electrode type which is also referred as parallel-plate or diode RF system has been widely used as production-level plasma reactors. The main reason for their wide application is due to its ease of scale-up [22]. The schematic drawing of a typical capacitively coupled *RF* plasma reactor is shown in Fig. 13.3.

A plasma is formed in the space between the electrodes due to the applied electric field. The region between the plasma and both the electrodes and the walls

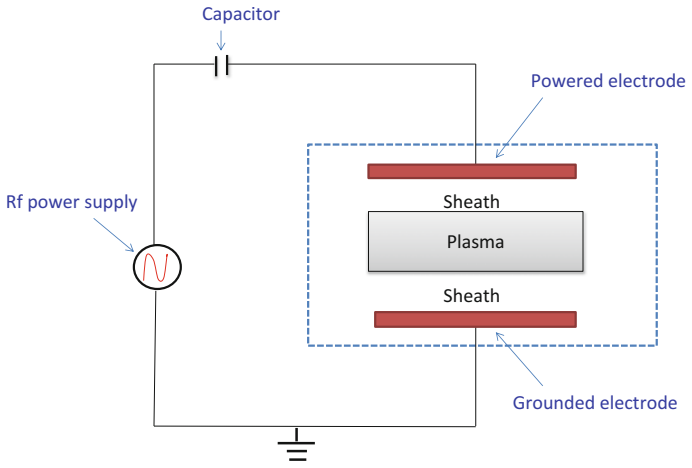

Fig. 13.3 Schematic diagram of AC-coupled RF plasma reactor

of the reactor is known as the sheath. The sheath plays an important role in the use of plasma for various applications because it is the region where the charged particles gain kinetic energy to bombard the surfaces to be treated by plasma. The reactors are said to be capacitively coupled because the radio frequency currents and voltages that sustain the plasma are introduced through the sheath, which acts like a capacitive element in an electrical circuit [23]. These sources employ one or more electrodes to produce plasma, with typical electrode voltages of 100–1000 V and typical RF powers of 100–1000 W. Low-pressure RF discharges are widely used for deposition of thin films by plasma-enhanced chemical vapor deposition (PECVD). Zajickova et al. [8] used PECVD based on hexamethyldisiloxane (HMDSO) monomers to deposit SiO_2 protective films on polycarbonate (PC). Dependence of the sputtering of PC on the applied RF power and the self-bias voltage in argon plasma was also investigated in this study. It was found that the sputtering rate is proportional to these two discharge parameters.

A more detailed investigation on the surface treatment of polycarbonate substrate by low-pressure RF discharge and its effect on film deposition can also be found in an earlier work by Zajickova et al. [9]. This study revealed that treatment of the substrate in argon discharge prior to the deposition of the thin film considerably increased the adhesion of the film to the substrate.

At low pressures, a stable glow discharge can be easily generated, whereas it is difficult to get a stable homogeneous glow discharge at atmospheric pressure. Recently, RF power sources are also used to generate stable glow discharge in atmospheric pressure plasma using DBD configuration. Moon et al. [24] performed a feasibility study of controlling plasma at atmospheric pressure by investigating the role of helium gas in an argon glow plasma using 13.56 MHz radio frequency power. This study suggests that mixing of the supply gas is a useful way of controlling the plasma characteristics that may be utilized for applications with specific required discharge conditions.

13.2.1.3 Microwave Discharge

Microwave discharges are widely used for generation of quasi-equilibrium and nonequilibrium plasma for different applications. Microwave plasma can be generated at pressures from 10^{-5} Torr up to atmospheric pressure in the pulse and continuous wave regimes at incident powers ranging between several watts and hundreds of kW [25].

At this range of frequency of the power supply, ions and subsequently the electrons also can no longer reach the electrodes as they are unable to follow the rapidly oscillating field. No secondary electron emission is required to sustain the discharge. This makes it possible to have electrode less discharge. Therefore, the power can be concentrated to a localized volume and thus a high-density plasma can be generated [20]. The density of ions in such a plasma can be more than 3×10^{11} cm^{-3}. The most commonly used frequency of the microwave power

supply is 2.45 GHz corresponding to a wavelength of 12.24 cm which is roughly comparable to the dimension of a typical microwave reactor [26].

In 2012, Hoskinson et al. [27] demonstrated a novel array of micro-plasma sources consisting of microwave resonators arranged in a two-dimensional grid. This study verified the electromagnetic behavior of the array through application of analytic coupled mode theory, electromagnetic modeling, and observation of the generated plasma structures. Their investigations showed that the device in specific mode could be useful for applications in material and surface modifications. Microwave resonator-based discharges offer several advantages compared to DC or low-frequency micro-plasma discharges.

A topical review on the methods of microwave plasma generation, general features of microwave plasma, and selected aspects of microwave plasma diagnostics can be found in an earlier work [25].

13.2.2 Atmospheric Pressure Plasma

Atmospheric pressure nonequilibrium plasmas have made a remarkable progress in plasma generation techniques recently, including atmospheric pressure glow discharge (APGD) [28–32], dielectric barrier discharge (DBD) [1], corona discharge [33, 34], surface discharge [35–37], pulsed discharge [14, 38, 39], etc. This has led to an expansion of their applications into the field of energy and environment as well as material conversion processes [14]. The widespread application of these discharges is driven mainly by virtue of their special advantage of forming a highly reactive plasma at near room temperature condition with low energy consumption using simple reactor system at atmospheric pressure.

An extended review of atmospheric pressure discharges producing nonthermal plasma has been presented in a paper by Navartovich [15] which reports the classification of such discharges with respect to their properties, and an overview of their possible applications. Several research papers have been published reporting new developments in the form and applications of atmospheric pressure plasmas in past one and a half decade.

In the following sections, corona discharge, arc discharge, surface barrier discharge (SBD), dielectric barrier discharge (DBD), and atmospheric pressure glow discharge (APGD) are briefly reviewed with some recent developments and their new areas of applications.

13.2.2.1 Corona Discharge

Generally, a corona discharge is obtained when the discharge current is limited to the micro-ampere level after electrical breakdown has been achieved. A specific form of corona discharge at atmospheric pressure is the luminous glow localized in space around a point tip in a highly nonuniform electric field [17]. Figure 13.4

shows the schematic diagram of a typical point-to-plane corona discharge. In this type of discharge, the geometry of the electrode confines the gas ionizing process to high-field ionization region around the active pointed electrode. Usually, the corona geometry is named positive, negative, bipolar, AC, or high frequency (HF), according to the polarity of the active electrode. The space between the active pointed electrode and the plane electrode can be divided into two regions: (i) the ionization region and (ii) the drift region. The ionization region is concentrated very close to the pointed electrode. The region outside this is the drift region where ions and electrons react with the neutrals but with too low energy to ionize and too low density to react with other ionized particles [33]. The application of corona discharge in processing of materials is limited due to the restricted area of the discharge. However, several attempts have been made to overcome this limitation using two-dimensional arrays of electrodes. Main applications of corona discharge are in the fields of surface modification of polymers, ozone generation, particle precipitation, and enhancement of SiO_2 growth during thermal oxidation of silicon wafers [17]. Schutze et al. reported that for a positive point-to-plane corona discharge operating in air at 760 Torr, the plasma was ignited at 2–5 kV and produced extremely small current of the order of 10^{-10}–10^{-5} A.

Akishev et al. [34] investigated the phenomenology of a high-current negative point-to-plane corona in nitrogen. They found that the structure and current–voltage characteristic of the corona change significantly when the working gas is slowly blown through the discharge cell. They also studied the time evolution of the radial profile of the current density at the anode under different experimental conditions.

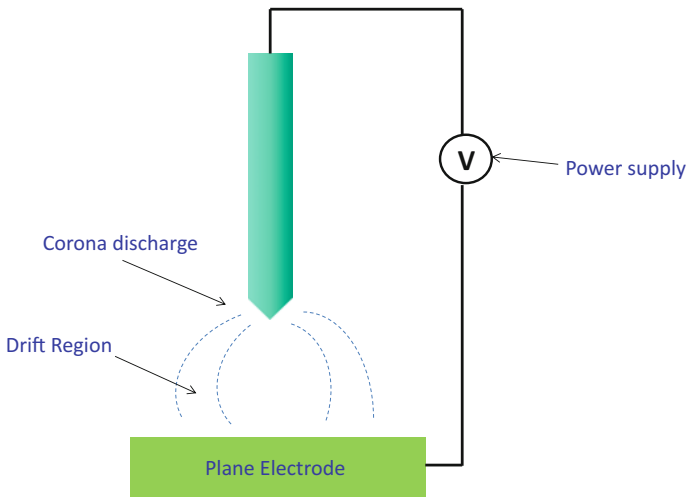

Fig. 13.4 Schematic diagram of a point-to-plane corona discharge

13.2.2.2 Arc Discharge

An arc discharge is obtained when the discharge current is maintained at above ampere level after an electrical breakdown of a gas has occurred. A thermal arc discharge will be produced when the filling gas pressure is sufficiently high.

Figure 13.5 shows the current–voltage characteristics of a gas discharge showing the Townsend (Dark) discharge, corona discharge, glow discharge, and arc discharge regions. It is evident from the figure that an arc discharge can be maintained by a lower voltage than a glow discharge. Further details on current–voltage characteristics of gas discharge can be found in an open source [40].

Arc discharges are commonly used in metallurgical processes, e.g., to melt rocks containing Al_2O_3 to produce aluminum and synthesis of carbon nanoparticles [41]. Fanara et al. [42] made a detailed investigation on the properties of atmospheric pressure arc by means of electric exploration of the plasma column and the anode region. A multi-wire apparatus, operating for arc currents in the range 50–200 A has been described and the ion current density and temperature maps are also shown in their study.

In order to obtain a nonthermal plasma at atmospheric pressure discharge, the first step is to avoid the formation of an arc. This can be achieved by limiting the current flowing through the discharge. Use of dielectric barrier between the electrodes can be made to limit the current in the discharge thereby converting it into high-voltage, low-current discharge. This type of discharge system in which either one or both of the electrodes are covered by dielectric barrier is called a dielectric barrier discharge (DBD).

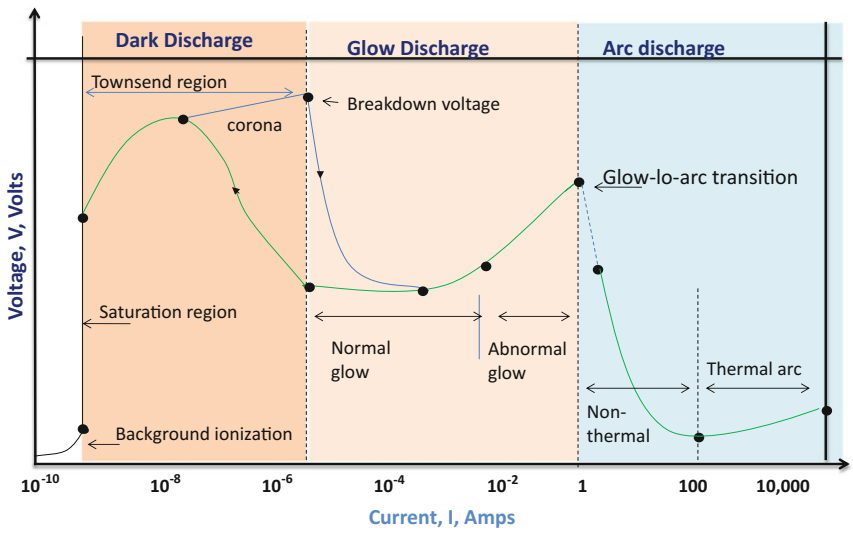

Fig. 13.5 Current voltage characteristics of gas discharge showing the Townsend (*Dark*) discharge, corona discharge, and arc discharge regions

13.2.2.3 Dielectric Barrier Discharge (DBD)

In the study of gaseous discharge, there are two main ways to prevent the transition of a discharge from corona to spark. One approach is to use a nanosecond pulse power supply [43]. The other approach is to insert a dielectric barrier in the discharge gap. The insertion of dielectric material in the discharge gap is to limit the discharge current thereby preventing the formation of complete breakdown. The schematic diagram of a DBD system is shown in Fig. 13.6. Due to the absence of complete breakdown, DBD is sometimes called silent discharge.

The dielectric barrier discharge (DBD) has a number of possible industrial applications and has been a subject of research for many years [44]. It possesses potential advantages in atmospheric pressure surface processing and plasma chemistry. The most important characteristic of DBD is that a nonthermal equilibrium plasma condition can be achieved in a much simpler way compared to other alternatives like low-pressure discharges, fast-pulsed high-pressure discharges, or electron beam injection. The flexibility with respect to geometrical configuration, operating medium, and operating parameters is another important advantage of atmospheric pressure DBD.

Moreover, the conditions optimized in laboratory experiments can easily be scaled up to large industrial installations [45]. In 2004, Laroussi and Lu [38] presented a study on the power consideration in the pulsed dielectric barrier discharge at atmospheric pressure. Pulsed operation with pulse widths in the range of nanoseconds has been suggested to enhance the plasma chemical processes. This study reports on a specially designed, dielectric barrier discharge-based diffuse-pulsed discharge and its electrical characteristics. Their results indicated that the mechanism in this system would lead to a much improved power transfer to the plasma.

In a recent study by Gibalov and Pietsch [16], dynamics of dielectric barrier discharges in different arrangements has been investigated. Based on experimental results, they have performed numerical investigations of DBDs in three basic configurations: volume, coplanar, and surface discharge arrangements. This study found that the anode- and cathode-directed streamers appear with a highly

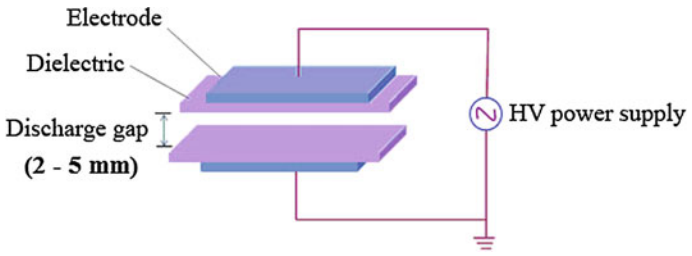

Fig. 13.6 Schematic diagram of a parallel-plate DBD

conductive channel in between. The interaction of the streamers with conductive and dielectric surfaces determines the filamentary or homogeneous appearance of the discharge and its properties.

13.2.2.4 Surface Barrier Discharge (SBD)

There are several terms used in literature to describe surface discharge. They are often named as sliding discharge and/or creeping discharge. A surface discharge is called dielectric barrier discharge (DBD) when one or both the electrodes are covered by dielectric material. SBDs are commonly used for surface treatment of materials, ozone generation, aerodynamics, etc. Schematics of typical surface barrier discharge systems are shown in Fig. 13.7.

A detailed investigation of SBD generation and its application for surface modification of polypropylene nonwoven fabrics has been reported in an earlier work by Cernakova et al. [35]. An experimental study of a SBD for the active control of subsonic airflow has been made by Dong et al. [36]. This study also performed complementary and coherent electrical, optical, and aerodynamic measurements as a function of various parameters and geometries. They have investigated the influence of the frequency and applied voltage of the discharge on the dissipated power. Their investigation resulted in an empirical formula to calculate the dissipated power and the energy lost in the dielectric.

In 2009, Cech et al. [46] reported on the influence of electrode gap width on plasma properties of diffuse coplanar surface barrier discharge in nitrogen. They studied the plasma parameters by means of time- and space-resolved optical emission spectroscopy and oscilloscopic measurements which provided a spatial and temporal distribution of the luminosity of the discharge. An elaborated description on SBD can also be found in an earlier report [37].

13.2.2.5 Atmospheric Pressure Glow Discharge (APGD)

The APGDs are closely related to DBDs and they are operated in a similar discharge configuration with high-voltage electrodes that are covered by dielectric barriers that lead to self-quenching of the micro-discharges and prevention of spark formation [47].

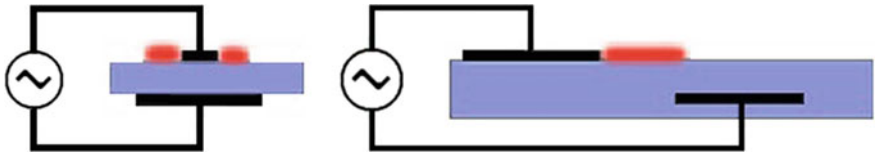

Fig. 13.7 Examples of surface DBD configurations. Reprinted from Kogelschatz [37] with permission

The DBD at atmospheric pressure usually has a filamentary nonhomogeneous form. The first step to get a homogeneous discharge at atmospheric pressure consists of avoiding the formation of a streamer and then of a micro-discharge. The origin of the streamer is a large electronic avalanche creating enough ions to localize the electrical field. The streamer formation is observed when the gas gap becomes large compared with the electron mean free path. At room temperature, the transition between the Townsend and the streamer breakdown occurs when the product of the gas gap and the pressure (*pd*) becomes around 100 Torr cm. An easy solution to avoid streamer formation at atmospheric pressure has been suggested by Massines et al. The solution consists of using micro-plasmas made in micrometric cells. Another solution consists of heating the gas in order to decrease its density [48]. Several researchers have tried to obtain the homogeneous DBD at atmospheric pressure [49, 50]. Okazaki et al. [50] were able to show that a uniform DBD could be generated under specific condition of power supply and electrode configuration. They named such discharge as APGD. Their study showed that DBD can be made homogeneous, if the frequency of the power supply is higher than 1 kHz and if helium or argon with a small admixture of acetone is used. A new technique of stabilizing the homogeneous glow discharge at atmospheric pressure by 50 Hz source in any gas was reported by Okazaki et al. [50]. Due to the possibility of using line frequency power supply, this system could be more cost-effective compared to the systems which work with power supplies of frequencies in the range of kHz or MHz.

In 2001, Trunec et al. [49] reported the generation of atmospheric pressure glow discharge in neon. They investigated the electrical characteristics of APGD in neon for different voltages and frequencies of power supply and different gas flows. This study also made a comparison of electrical properties of the discharges in neon with that of the discharge in argon and in the mixture of neon with argon.

Chen et al. [30] presented a preliminary discharging characterization of a novel APGD plume and its application in organic contaminant degradation. They were able to generate an atmospheric pressure glow discharge plume (APGD-p) using a dielectric barrier discharge reactor with one conductive liquid electrode. Their results showed that the APGD reactor produced a cold plasma plume with temperature not higher than 320 K at power of 5–50 W.

In another work reported in 2007, Buntat et al. [31] reported the generation of a homogeneous glow discharge in air at atmospheric pressure. They have experimentally investigated the discharge using two different electrode configurations of a perforated aluminum sheet and stainless steel wire mesh. This study showed that the perforated material shows a better glow discharge stabilization than that of stainless steel wire mesh.

13.3 Generation and Characterization of DBD

13.3.1 Introduction

DBD systems can be made in many configurations. The most convenient is the planar-type DBD using parallel plates separated by a dielectric material. Cylindrical DBDs are also widely used for ozone generation. This system is made using coaxial tubes with a dielectric material between them. The schematics of planar and cylindrical DBDs are shown in Fig. 13.8 [1]. This discharge requires alternating voltage for operation due to the presence of a dielectric barrier between electrodes. The interelectrode distance may considerably depend upon the type of DBD. In plasma displays, it is less than 0.1 mm where as it can be up to several millimeters in ozone generators and up to several centimeters in the case of CO_2 lasers. In the DBD systems described here, the interelectrode distance is varied from 1 to 3 mm.

13.3.2 Principle and Operation of DBD

As a consequence of the presence of at least one dielectric barrier, the DBD acts as a capacitor. Its capacitance is contributed by both the dielectric and the air/gas space. The capacitance, in combination with the time derivative of the applied

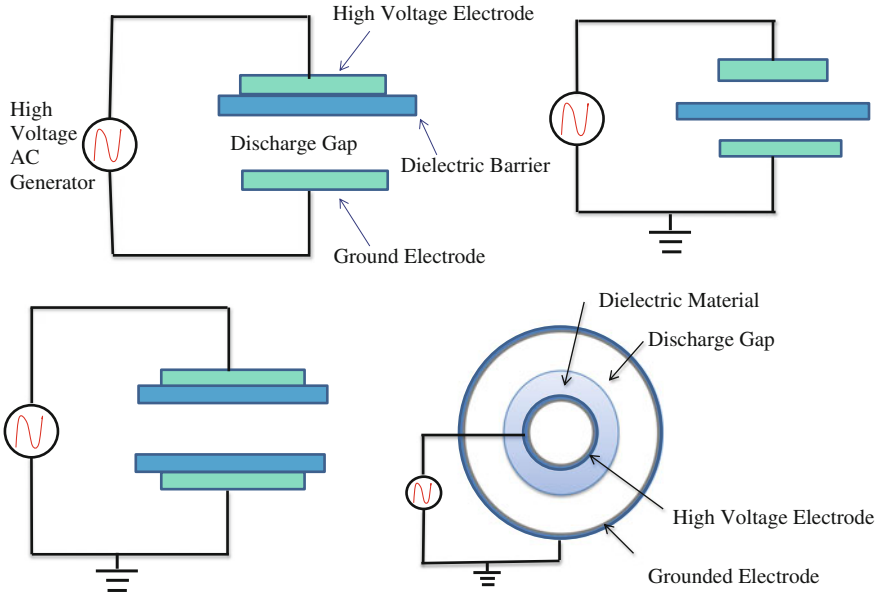

Fig. 13.8 Common dielectric barrier discharge configurations

voltage determine the amount of displacement current that can be passed through the DBD. The main discharge current flows through the DBD when the electric field is high enough to cause breakdown in the discharge gap. In most applications, the dielectric limits the average current density in the gas space. It thus acts as a ballast which, in ideal case, does not consume energy. Preferred materials for the dielectric barrier are glass, quartz, ceramics, thin enamel, or polymer layers or other materials of low dielectric loss and high breakdown strength. In some applications, additional protective or functional coatings are applied. At very high frequencies, the current limitation by the dielectric becomes less effective. For this reason, DBDs are normally operated between line frequency and 10 MHz. When the electric field in the discharge gap is high enough to cause the breakdown, in most gases a large number of micro-discharges are observed when the pressure is of the order of 10^5 Pa (atmospheric pressure). This is a preferred pressure range for ozone generation, pollution control as well as material processing and polymer surface modification.

To generate a discharge, one of the electrodes is connected to the high-voltage power supply with voltages in the range of a few hundred volts to several hundred kilovolts (operated between line frequency and about 10 MHz as mentioned above) through a ballast resistor (5–20 MΩ) in series to limit the current which prevents the electric puncture in case of material processing and polymer surface modification. Another electrode is grounded through a shunt resistor of 10 kΩ across which the discharge current is measured. The voltage applied to the electrodes can be measured by a high-voltage probe. In case of atmospheric pressure DBD, the most common electrical diagnostic consists of the measurement of the voltage applied to the electrodes and the discharge current. The voltage across the shunt resistor connected in series to ground yields the discharge current. The current and voltage waveforms can be recorded with the help of a digital oscilloscope. From these observations, current–voltage characteristics and breakdown characteristics can be obtained. The characteristics of the breakdown and the formation of the discharge are sensitive to the electrode gap, applied voltage, and ballast resistor which affect the uniformity in its applications such as material processing, polymer surface modification, etc. For optical characterization, the optical emission spectroscopy (OES) method is commonly used.

When the electric field in the discharge gap is high enough to cause breakdown, in most gases a large number of micro-discharges are observed when the pressure is of the order of 10^5 Pa (atmospheric pressure). Figure 13.9 (left) shows the micro-discharges in a 1-mm gap containing atmospheric pressure air, photographed through a transparent electrode. In this filamentary mode, plasma formations resulting in electrical conductivity are restricted to the micro-discharges. The gas in between is not ionized and serves as a background reservoir to absorb the energy dissipated in the micro-discharges and to collect and transport the long-lived species created.

The dielectric is the key for the proper functioning of the discharge. Once ionization occurs at a location in the discharge gap, the transported charges accumulate on the dielectric. The field due to the accumulated charges reduces the field

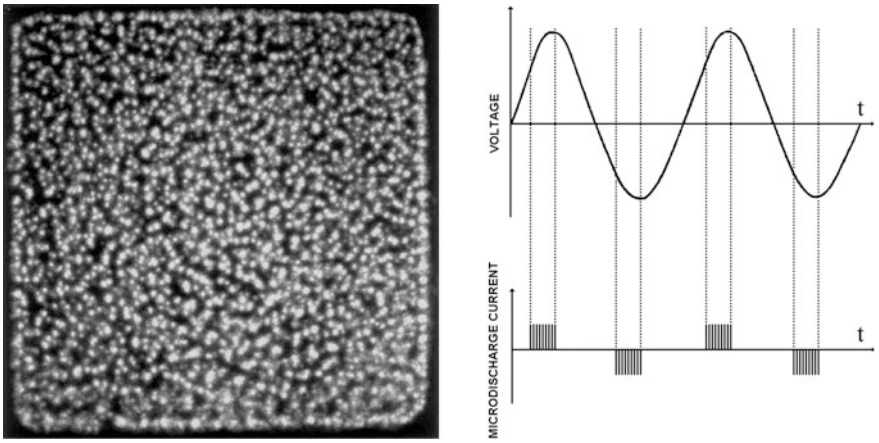

Fig. 13.9 End-on view of micro-discharges (*left*) and schematic diagram of bursts of micro-discharges (*right*) (Eliason 1997)

in the gap and interrupts the current flow after a few nanoseconds. The duration of the current pulse depends on the pressure and the effective ionization characteristics of the gas as well as on the dielectric properties. By applying a sinusoidal voltage of sufficient amplitude, a large number of such micro-discharges of nanosecond duration are formed. They are randomly distributed in space and time. The DBD produced at atmospheric pressure usually has nonhomogeneous filamentary nature. At the maximum and minimum of the applied voltage, the displacement current is zero and the micro-discharge activity stops, only to start again when the breakdown field is reached in the gap during the next half cycle (Fig. 13.9). The dielectric serves two functions: it limits the amount of charge transported by a single micro-discharge, and ensures that the micro-discharges present are distributed over the entire electrode area.

13.3.3 Generation of DBD Plasma in Different Configurations

The geometry of electrodes plays significant role in determining the value of potential and the electric field strength between the interelectrode spacing where the DBD plasma is formed. The interelectrode distance and thickness of dielectric barrier have equally important role in the production of DBD plasma. DBDs generated using different types of electrodes are briefly described in the following sections.

13.3.3.1 Parallel-Plate Electrode System

The schematic diagram of a parallel-plate DBD system is shown in Fig. 13.10. The discharge is generated between two symmetric electrodes. The electrodes are made of brass with smooth surface. They have 50 mm diameter and 10 mm thickness. The lower electrode is fixed and the upper one is movable with a pitch of 0.5 mm. Glass plate of 2 mm thickness is used as the dielectric barrier. A high-voltage AC power supply is used and the applied voltage is in the range of 1–2 kV at a frequency of 30 kHz. The gap between the electrodes can be varied from 0.5 to 2 mm and Ar is fed at a flow rate of 1 l/min. The experiments are carried out for gap spacing of 0.5, 1–2 mm.

This system was studied by electrical and optical measurements. Electron temperature and electron density in the discharge were measured by power balance method and line intensity ratio method. Effect of this plasma treatment on the surface property of polymers was also investigated by contact angle measurement. Contact angle measurement on untreated and plasma-treated samples showed that this discharge effectively improves the wettability of the polymer surface [51].

13.3.3.2 Cylindrical Electrode System

The schematic of a typical DBD system with cylindrical electrodes is shown in Fig. 13.11a. Two electrodes are held parallel to each other horizontally in stand. The electrode consists of glass tube filled with fine brass powder with a central wire inside. The internal diameter of the tube is 12.6 mm and external diameter is 14.9 mm with 1.2 mm thick glass as dielectric barrier. The electrodes are 126.2 mm in length. They are separated by 2.9 mm distance where DBD is produced. The fine metallic powder packed inside the glass tube serves as electrode to produce electric discharge. The photograph of the discharge is depicted in Fig. 13.11b.

The electrodes used in this system are designed for an easy passage of long rolls of textiles and other materials for continuous treatment in plasma. As an example, a

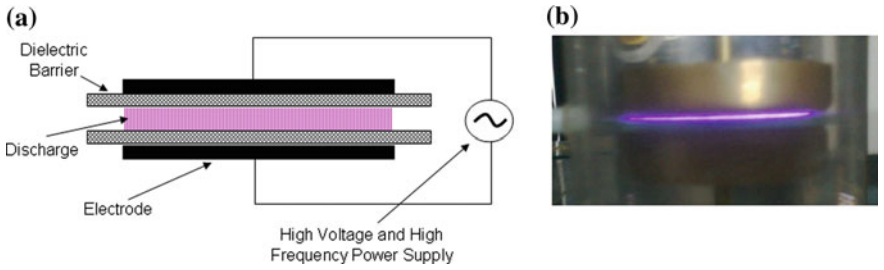

Fig. 13.10 Schematic diagram DBD with parallel-plate electrodes with double barrier (**a**) and photograph of the discharge (**b**) [51]

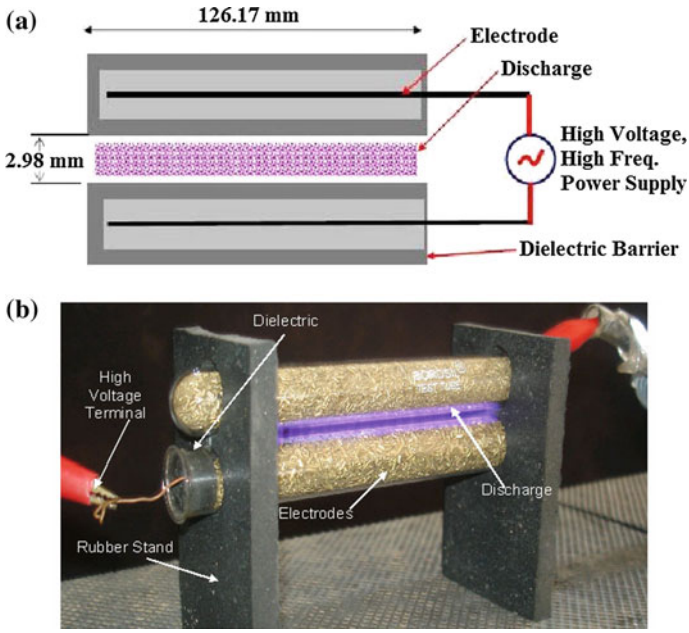

Fig. 13.11 **a** Schematic diagram of DBD with cylindrical electrodes. **b** Photograph of the discharge

cotton fabric driven by an electric motor was passed through the discharge between the electrodes and the improvement in wettability of the sample was investigated by contact angle measurement. Figure 13.12 shows the image of water drops on the untreated and plasma-treated samples. It was observed that the cotton sample which was hydrophobic before treatment turned into hydrophilic after 20 cycles of treatment through the discharge.

13.3.3.3 Coaxial Electrode System

DBD with coaxial cylindrical electrode system is mainly used for chemical syntheses such as generation of ozone and treatment of engine exhaust gas. It is designed to provide an annular gap between two coaxial tubes and a radial electric field is applied by a high-voltage AC power supply. It causes an electrical breakdown of the flowing gas in the annular gap. Early experiments conducted in such a system showed that some oxygen molecules in the air flowing through the discharge gap between the glass tubes are converted to ozone. In the present experiment, a HV power supply of amplitude 18 kV operating at line frequency of 50 Hz is applied across the two cylindrical electrodes. The central electrode is made of brass rod (diameter is 3 mm, length 65 mm) and enclosed by an inner cylindrical glass tube. The outer electrode is made of aluminum foil which wraps around the

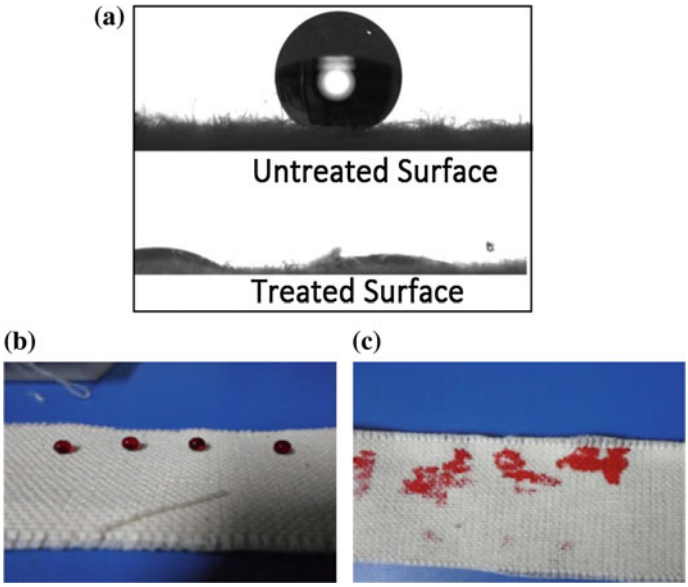

Fig. 13.12 Images of water drops on untreated and plasma-treated surface of cotton fabric (**a**, **b**). A complete wetting was obtained after 20 cycles of treatment (**c**) Image reproduced from the permission of authors: doi:10.1063/1.4993084

outer cylindrical glass tube. The gap between the two dielectric layers is 3 mm through which air or water can easily flow. In our experiments, we used the system for direct treatment of water by electric discharge. Figure 13.13 shows the cross-sectional view of the coaxial electrode system in a DBD. The main objective of the work was to develop a system in which water could be passed through the annular gap between the electrodes making the treatment more effective. Water from different sources such as river, well, stone spout, and tap was treated by this method. The general evaluation of the efficiency of the treatment for water disinfection was made. The experimental results show that the qualities of water such as pH, conductivity, chlorides, and total hardness of water changed slightly after treatment. However, the coliforms and chemical oxygen demand (COD) were significantly reduced in the treated samples. A remarkable increase in the amount of dissolved oxygen (DO) was also observed after the treatment [52].

13.3.3.4 Atmospheric Pressure Plasma Jet (APPJ)

In the previous sections, we mentioned that the atmospheric pressure plasma can be generated in various configurations. The main problem with these systems is that the working space is often limited because of the small gap between the electrodes.

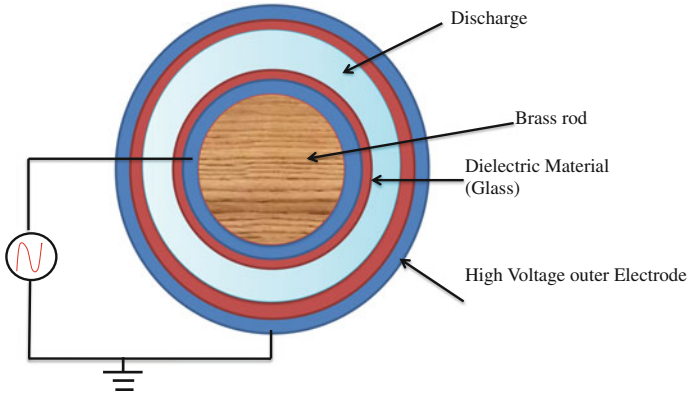

Fig. 13.13 Cross-sectional view of the coaxial electrode system in a DBD

In an atmospheric pressure plasma jet, the plasma constituents are expelled through an orifice by a gas flow which makes the treatment of large objects possible. Forster et al. [53] reported an atmospheric pressure plasma jet in a DBD configuration. This type of discharge can be operated under high gas flow rate. In 2003, Toshifuji et al. [54] reported a relatively cold arc plasma jet produced under atmospheric pressure having potential application for surface modification. Recently, Takemura et al. [55] developed an APPJ with long flame which can be used to modify polymer film with a work distance of over 200 mm. Similarly, a double-layered APPJ had also been reported in 2009 [56]. It consists of an additional part in the jet system for introduction of nitrogen gas into the outer nozzle between the inner and outer tubes boosting the plasma plume which results in a brighter and longer plasma torch. This system is supposed to have more radicals which may broaden the application range of atmospheric pressure plasma jets. Kuwabara et al. have presented a detailed investigation on the effects of electrode positioning on the atmospheric pressure plasma torch based on DBD configuration [57]. In this work, the authors also discussed the factors which determine the length of plasma jet.

In our study, a nonthermal nitrogen plasma jet was generated using a high-voltage power supply with output frequency of 10–30 kHz under atmospheric pressure. The experimental setup used to generate atmospheric pressure plasma jet is shown in Fig. 13.14. The dependence of the length of plasma jet on the gas flow rate was investigated and application of this plasma jet to the surface modification of polymer material was also demonstrated.

Figure 13.15 shows that the length of plasma jet can be enhanced up to 75 mm by increasing the gas flow rate from 1 to 4 l/min. However, there was no further change in length beyond this flow rate.

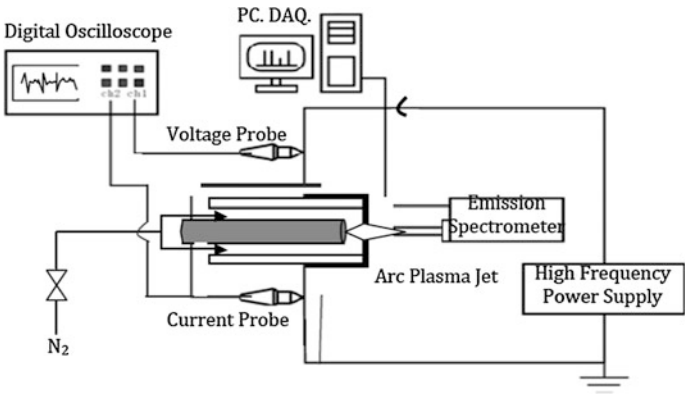

Fig. 13.14 Schematic diagram of atmospheric pressure plasma jet system. Reproduced from Subedi et al. [58] with permission from the editor

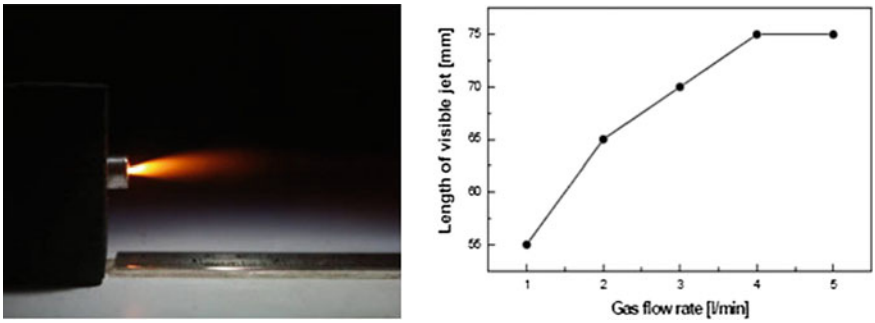

Fig. 13.15 Photograph of plasma jet and the dependence of jet length on gas flow rate. Reproduced from Subedi et al. [58] with permission from the editor

13.3.4 Characterization of DBD

Different methods are available to measure the electron density and electron temperature in a plasma. The most commonly used methods are: Langmuir probe, microwave interferometer, Laser Thomson Scattering [LTS], optical emission, and absorption spectroscopy [59].

Characterization of the discharge by analyzing the emission spectra is a powerful tool for the diagnostic of plasma.

To determine the electron temperature (T_e) and electron density (n_e) in low-pressure plasma, probe method is widely used but the application of probe method to atmospheric pressure plasma is difficult due to small discharge gap distance [60]. Alternatively, a powerful tool widely used for the plasma diagnostic is optical emission spectroscopy (OES), which is nonintrusive and gives rich

information about the plasma species. By analyzing and interpreting the plasma spectra, we can obtain the important properties of the plasma, such as temperature, density of chemical species, and ionization state [61].

13.3.4.1 Electrical Characterization

In DBD, electric current (i) flows between the electrodes through a defined plasma volume with cross section A and there is no current loss to the surrounding. This makes it possible to use the measured current as a diagnostic tool for plasma generated at atmospheric pressure. The current density (j) is a function of electron density (n_e) and drift velocity (v_d) of electrons according to Eq. 13.3.1 which in turn is a function of electric field.

$$j = n_e e v_d \tag{13.3.1}$$

In order to determine n_e from Eq. 13.3.1, values of v_d for different electric field values can be found from literature. Alternatively, it is also possible to use the measured values of applied voltage and average discharge current to estimate the electron density n_e. This method is termed as power balance method and is described by the following equation:

$$n_e = \frac{P_{av}}{2Av_b E_{lost}}, \tag{13.3.2}$$

where P_{av} is the average power, A is the area of the electrode, v_b is Bohm velocity, and E_{lost} is the energy lost by the system per electron–ion pair. In a recent study, Eq. 13.3.2 was used to estimate the electron density in argon discharge produced in parallel-plate DBD [62]. A high-voltage probe was used to measure the voltage applied across the electrodes while the discharge current was measured using a shunt resistor at the earth side of the discharge tube.

The signals were recorded using a Tektronix TDS2002 digital oscilloscope. Figure 13.16 shows the applied voltage and discharge current waveforms obtained in an argon discharge.

Taking Bohm velocity $v_b = 2 \times 10^3$ m/s and energy lost $E_{lost} = 50$ eV; and using the values of electrode area $A = 17.5 \times 10^{-4}$ m^2, applied voltage $V_{rms} = 13$ kV, and average discharge current $I_{rms} = 3.86 \times 10^{-5}$ A from the current waveform shown in Fig. 13.16 and substituting in Eq. (13.3.2), the electron density in air plasma was found to be equal to $n_e = 8.97 \times 10^{11}$ cm^{-3} which is in fairly good agreement with the values of electron density in low-temperature plasmas.

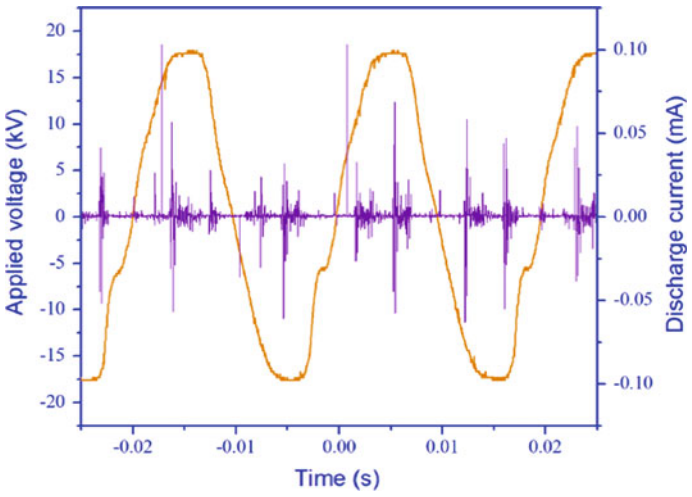

Fig. 13.16 Applied voltage and discharge current waveforms obtained in argon discharge

13.3.4.2 Optical Characterization

To understand the generation of reactive species in the plasma, it is important to measure the electron temperature and the density of the plasma. Conventional plasma diagnostics such as an electrostatic probe and a microwave interferometer are not applicable for atmospheric plasma [63]. Several attempts have been made to characterize atmospheric pressure DBD using OES technique to measure electron temperature and density [24, 47, 63–69].

OES analyzes the light emitted from the plasma. The light originates from the excited states decaying to lower energy levels in atoms and molecules due to various processes. OES can be used to identify the types of excited species present in the plasma. It can also be used to estimate the temperature of such species which is obtained from the analysis of the energy distributions of particles and their respective population. The transitions between electronic energy levels correspond to wavelength of light in ultraviolet to visible range. Therefore, the monochromator and photoelectron multiplier which are sensitive over a range of 200–900 nm can be employed. The resolution required for monochromator depends on the aim of the diagnostic. Normally, it is sufficient to resolve the vibrational structure of emission spectra of molecules with resolution of about 0.1 nm.

The typical optical emission spectrum in the range of 190–850 nm, recorded by a HORIBA Jobin Yvon UV–Vis Spectrometer, for DBD discharge in air is shown in Fig. 13.17. Its focal length is 140 mm and the grating used is 1200 per mm. Optical fiber with 100 μm diameter core and resolution of 2.3 nm is used to transmit the light from the source to the monochromator. The spectrum is recorded on the computer via SMA connector.

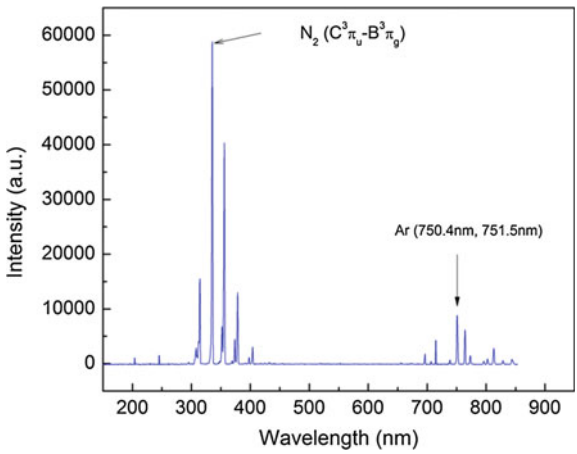

Fig. 13.17 Optical emission spectra of atmospheric DBD in air in the range of 190–850 nm

Measurement of electron temperature and electron density by line intensity ratio method

The electron temperature can be obtained by line intensity ratio method using the equation given below

$$\frac{R_1}{R_2} = \frac{I_1/I_2}{I_3/I_4} = \left(\frac{A_{pq}}{A_{xy}}\right)\left(\frac{g_p}{g_x}\right)\left(\frac{\lambda_{xy}}{\lambda_{pq}}\right)\left(\frac{A_{uv}}{A_{rs}}\right)\left(\frac{g_u}{g_r}\right)\left(\frac{\lambda_{rs}}{\lambda_{uv}}\right)\exp\left[-\frac{E_p - E_x - E_r + E_u}{kT_e}\right], \tag{13.3.3}$$

where R_1 is the ratio of the intensity of a pair of lines (p → q) and (x → y), assuming that (p → q) is originated from neutral species (atom) while the transition (x → y) is produced by singly ionized ion. Similarly, R_2 is the ratio of the intensity of another pair of lines (r → s) and (u → v), assuming that (r → s) is originated from neutral species (atom) while the transition (u → v) is produced by singly ionized ion. I is the intensity of the spectral line, λ_{ij} and A_{ij} are wavelength and transition probability, respectively. g_i is the statistical weight of the upper level, E_i is the energy of the upper level, k is the Boltzmann constant, and T_e is electron temperature. The values of λ and I are obtained from the optical emission spectra, and the values of A_{ij}, g_i, and E_i are obtained from the NIST atomic spectra database. Electron temperature T_e is then used to calculate the electron density n_e using Eq. (13.3.4).

$$n_e = 2\left(\frac{I_1}{I_2}\right)\left(\frac{A_{xy}}{A_{pq}}\right)\left(\frac{g_x}{g_p}\right)\left(\frac{\lambda_{pq}}{\lambda_{xy}}\right)\left(\frac{2\pi\, m_e\, kT_e}{h^2}\right)^{3/2}\exp\left[\frac{E_i + E_p - E_x}{kT_e}\right] \tag{13.3.4}$$

Four suitable nitrogen lines, two for NII and two for NIII, are chosen from the spectrum and the electron temperature T_e is estimated using the line intensity ratio method.

Considering two NII lines with wavelengths 204.02 and 655.85 nm, and two NIII lines with wavelengths 245.21 and 378.57 nm, we obtain the intensities (from OES) and parameters from NIST Atomic Spectra Database which are listed in Table 13.1.

Substituting the above data in Eq. 13.3.3, we get

$$\frac{R_1}{R_2} = 0.506 \exp\left(\frac{2.78}{T_e}\right) \tag{13.3.5}$$

Taking different electron temperatures, we obtain the corresponding intensity ratio as given in Table 13.2.

Figure 13.18 is the graph plotted between electron temperature T_e and corresponding intensity ratio R_1/R_2. This graph is used to determine the electron temperature using the value of R_1/R_2 obtained from the intensity ratio [70]. Since $R_1/R_2 = 9.16$, it corresponds to electron temperature 0.97 eV in Fig. 13.18.

The electron temperature T_e determined from above is then used to calculate the electron density n_e using Eq. 13.3.4. Considering two nitrogen lines NI (402.45 nm) and NII (397.98 nm), we obtain the intensities as given in Table 13.3 (from OES) and parameters from NIST Atomic Spectra Database.

Using the above data in Eq. 13.3.4 with electron temperature $T_e = 0.97$ eV and ionization potential of nitrogen $E_i = 14.53$ eV, we obtain the electron density $n_e = 3.46 \times 10^{17}$ m^{-3}.

Similarly, the electron temperature and electron density in argon/air mixture plasma can be obtained.

Measurement of Electron Density by Stark Broadening Method

One of the most reliable techniques to determine the electron number density is using the measured Stark broaden line profile of an isolated line of either neutral atom or singly charged ion. Stark broadening is caused by the Coulomb interaction between the radiator (in this case argon atom) and the charged particles present in the plasma.

The Stark broadening appearing due to collision of charged species is the primary mechanism influencing the width of Ar emission line. The stark broadened line is assumed to have the Lorentz profile. The electron number density (n_e) related

Table 13.1 Selected NII lines intensities (from OES) and parameters from NIST atomic spectra database

Nitrogen lines	Intensity (a. u.)	A_{ij}	g_i	E_i
NII (204.02 nm)	$I_1 = 1568.65$	$A_{pq} = 2.11 \times 10^6$	$g_p = 5$	$E_p = 21.62$ eV
NII (655.85 nm)	$I_2 = 528.47$	$A_{xy} = 1.43 \times 10^6$	$g_x = 5$	$E_x = 41.73$ eV
NIII (245.21 nm)	$I_3 = 1809.92$	$A_{rs} = 1.21 \times 10^7$	$g_r = 6$	$E_r = 23.26$ eV
NIII (378.57 nm)	$I_4 = 5589.23$	$A_{uv} = 2.40 \times 10^6$	$g_u = 5$	$E_u = 40.59$ eV

Table 13.2 Electron temperature for different values of R calculated in accordance with Eq. 13.3.5

Electron temperature (T_e)	R_1/R_2
0.9	11.1045
1	8.15387
1.1	6.33311
1.2	5.13052
1.3	4.29315
1.4	3.68507
1.5	3.22819
1.6	2.87514

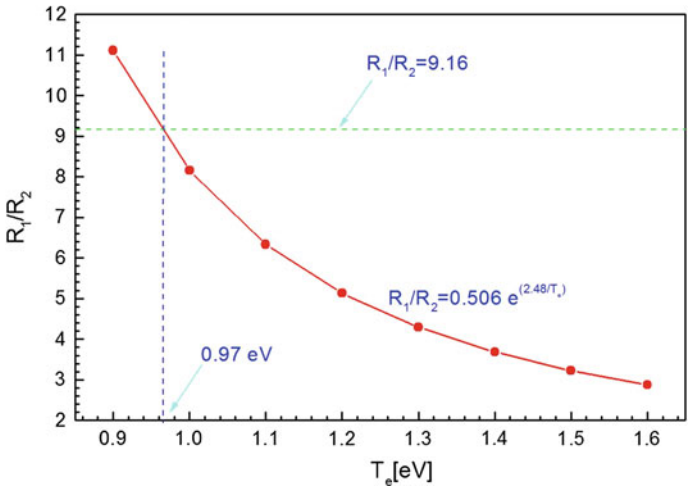

Fig. 13.18 Plot of R_1/R_2 as a function of T_e

Table 13.3 Spectroscopic constants for the two emission lines of nitrogen NI (402.45 nm) and NII (397.98 nm)

Nitrogen lines	Intensity (a. u.)	A_{ij}	g_i	E_i
NI (402.45 nm)	I_1 = 1649.07	$A_{pq} = 1.14 \times 10^6$	$g_p = 4$	E_p = 10.71 eV
NII (397.98 nm)	I_2 = 1478.17	$A_{xy} = 7.79 \times 10^7$	$g_x = 5$	E_x = 18.51 eV

to the full width at half maximum (FWHM) of the Stark broaden line is given by the expression [36].

$$\Delta\lambda_{\text{Stark}} = 2\omega\left[\frac{n_e}{10^{16}}\right] + 3.5\,\alpha\left[\frac{n_e}{10^{16}}\right]^{1/4} \times \left[1 - \frac{3}{4}N_D^{-1/3}\right]\omega\left[\frac{n_e}{10^{16}}\right], \qquad (13.3.6)$$

where ω is the electron impact width parameter (nm); α is the ion broadening parameter (nm); n_e is the electron density (cm^{-3}); N_d is the number of particles in the Debye sphere. The first term in Eq. (13.3.6) refers to the broadening due to the

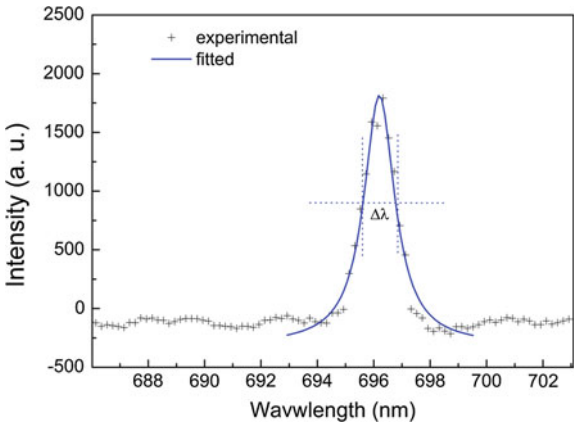

Fig. 13.19 Emission line of argon/air plasma at 696.23 nm showing FWMH

electron contribution and the second term to the ion broadening contribution. Since the contribution of the ionic broadening is normally very small, therefore, it can be neglected and Eq. (13.3.6) can be reduced to a simple form:

$$\Delta\lambda_{\text{Stark}} = 2\omega\frac{n_e}{10^{16}} \tag{13.3.7}$$

Values of both ω and α for different temperatures are reported in [36]. Hence n_e can be expressed as

$$n_e = \left[\frac{\Delta\lambda_{\text{stark}}}{2\times 10^{-11}}\right]^{\frac{3}{2}} \tag{13.3.8}$$

Equation 13.3.8 is an equation for determining the electron density in dielectric barrier discharge in argon by measuring the full width at half maximum (FWHM) of the emission line. The emission line of argon/air plasma at wavelength 696.23 nm is shown in Fig. 13.19.

The use of stark broadening of this line to estimate electron density in the discharge has also been reported in earlier papers [51, 61, 62].

The calculated value of electron density is $n_e = 6.04 \times 10^{16}$ cm^{-3}. This value is slightly higher than the results obtained by Balcon et al. [71] by Stark broadening on an argon line.

13.4 Application of DBD

The increasing application of DBD in industries is motivated by the possibility of treatment of pressure-sensitive objects and materials which cannot be treated using a low-pressure system. For example, treatment of living tissues, as in case of

medical treatment, is possible only with plasma devices which operate at atmospheric pressure.

Filamentary discharges controlled by dielectric barriers have been used for a long time in the fields of surface treatment and ozone production. This section will deal with some examples of DBD application for ozone generation, polymer surface modification, and plasma medicine. The surface modification of polymer material and the characterization of the modified polymer surface will be presented in more detail with special reference to contact angle and surface free energy analyses. The DBD was produced between electrodes with insulating layers of glass or polymer on the metal electrodes. An AC driving voltage of approximately 10 kV was used to create the discharge at DBD gap spacing of a few mm.

13.4.1 Ozone Generation

Many technical ozone generators make use of cylindrical discharge tube with diameter of about 20–50 mm and length of 1–2 m. Glass tubes are mounted inside stainless steel tube to form a narrow annular discharge space of about 0.5–1 mm. The high-voltage electrode is formed by a conductive coating (such as a thin aluminum film) on the inside of the glass tubes whereas the outer steel tubes serve as ground electrode. The preferred dielectric material is borosilicate glass. Other dielectrics such as ceramic tubes are also increasingly used. In advanced ozone generators, layered enamel coatings with optimized dielectric characteristics are also used. The ground electrode is cooled on the outside by a transverse water flow in a heat exchanger configuration. Since the efficiency of ozone formation decreases strongly with rising temperature, the ozone generator generally has narrow discharge gaps to ensure efficient heat removal. Previously, ozone generators were operated at line frequency. For smaller and low-cost ozone installation, this technique is still used. Modern high-power ozone generators use power semiconductors to generate square-wave currents with a frequency range of 0.5–5 kHz. Higher operating frequencies can deliver the desired power density at much lower operating voltages. The lower voltage results in less electrical stress on the dielectrics. Large ozone generators use several hundred discharge tubes and produce up to 100 kg of ozone per hour.

For industrial purposes, ozone is exclusively generated in large installations using dielectric barrier discharges. Ozone is a potent germicide and one of the strongest known oxidants. In many applications, it can replace chlorine thus causing less environmental concern. Although ozone itself is toxic, ozone treatment leaves no toxic residues in the medium that has to be treated or disposed of. The traditional application of ozone is for water treatment. About 100 years ago, it was realized that the germicidal and viricidal effects of ozone can provide safe drinking water in areas previously endangered by cholera. The first major ozone installation used in drinking water plant for disinfection was built around the beginning of the last century in Paris (1897) and Nice (1904), France; and in St. Petersburg, Russia

(1910). Although up to recently many countries have preferred chlorine for water treatment because of its lower cost, there is a strong tendency now to switch to ozone. The major targets for using ozone in water treatment are disinfection, color, odor, and iron removal. Another important growing large-scale use of ozone is in the paper industry. By combining oxygen, ozone, and hydrogen peroxide bleaches, pulp can be treated in a closed circuit without using chlorine. Extended reviews on ozone generation and their applications can be found in earlier works [72–75].

In this section, we present a small-scale ozone generator based on dielectric barrier discharge scheme. An attempt has been made to find out the optimum condition for higher ozone yield in coaxial cylindrical electrode. The schematic diagram of ozone generating system is shown in Fig. 13.20. Discharge from dielectric barrier was generated using high-voltage AC power supply operating at 50 Hz. The central electrode was made of a brass rod fixed inside a glass tube of thickness 1 mm. The gap between two glass layers was 2 mm. A sheet of aluminum wrapped outside of the tube acted as the outer electrode. The gas was passed inside the tube through the gap between the anode and the glass tube. It was supplied by air pump (ATEC Aquarium, AR-8500). The flow rate of air was 4 l/min. The concentration of ozone produced was measured by an ozone analyzer (Ozone Analyzer BMT 964, MESSTECHNIK GMBH Germany).

Effect of applied voltage on ozone concentration

Figure 13.21 shows the variation of ozone concentration as a function of applied voltage for a fixed air flow rate of 2 l/min at 2 mm gap with double barrier [77]. It is evident that ozone concentration increases as the applied voltage increases. It is due to the reason that the increase in voltage increases the electrical energy density, i.e., more energy transferred to the electrons, thereby increasing the possibility of collision of the air molecules in the chamber. However, supplied energy may not always be sufficient for recombination of ions, radicals, etc.

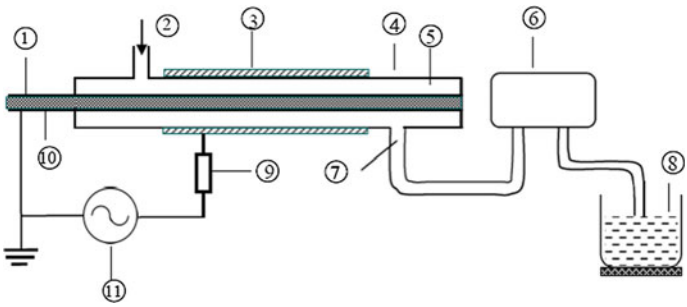

Fig. 13.20 Schematic diagram of ozonizer, *1* dielectric material, *2* gas inlet, *3* aluminum Sheet, *4* glass tube, *5* gap, *6* ozone analyzer, *7* outlet (mixture of air and ozone), *8* beaker with water, *9* resistance 10 kΩ, *10* central electrode, *11* power supply (18 kV, 50 Hz) [76]

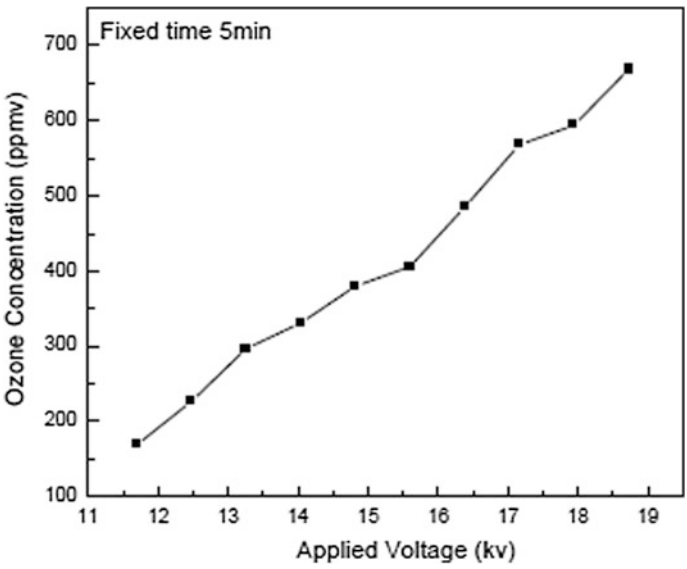

Fig. 13.21 Ozone concentration versus applied voltage for double barrier ozonizer with air flow rate of 2 l/min

13.4.2 Material Processing—Polymer Surface Modification

Polymers are used in a wide variety of applications including packaging and labeling, textile, stationary, automotive, laboratory equipment, etc. A low surface energy may be desirable in them for several applications, but for other applications it is a disadvantage, which has to be overcome [78]. As the surface energy of polymers is quite low, its surface properties such as hydrophilicity, adhesivity, and printability do not often meet the requirement for industrial applications. In order to extend its application range, different methods have been developed to modify its surface properties [79, 80]. Among them, atmospheric pressure nonthermal plasma treatment is a convenient and environmentally friendly way to obtain these modifications by introducing new chemical groups at the surface without affecting the bulk properties. However, most of such processes are conducted at low pressure and high frequency, which needs expensive vacuum equipment and batch treatments, and therefore it is difficult to apply these processes to large-scale objects, especially under the condition of continuous treatment. This environmentally friendly dry treatment can modify the surface properties of materials without changing the chemical and physical bulk properties [81].

The result of atmospheric pressure dielectric barrier discharge is similar to that obtained in low-pressure discharges, that is, to produce a substantial increase of surface free energy. It is reported that the surface free energy of untreated polymers changes from 20–30 to 50–70 mJ/m^2 after the treatment by atmospheric pressure

DBD (APDBD) [82] making material surface more wettable. APDBD thus enhances the adhesion, printability, and dye uptake of material surface. Recent investigations also include the upgrading of wool and textiles and the plasma treatment of insulated wires and cables.

During surface activation, radicals formed in the plasma disrupt chemical bonds in the surface layer causing the formation of new species with different properties. This results in a modification of the near-surface region without changing the desirable bulk properties of the material. In air plasmas, the active species are identified as oxygen atoms resulting in the buildup of oxygenated carbon centers in the surface layer.

Several studies carried out in plasma surface modification had shown that the modified surface is not stable for long time [8, 83, 84]. The treated polymer recovers a significant fraction of its hydrophobic property with the storage time after treatment. Figure 13.22 shows a schematic representation of a possible situation during surface modification of a polymer containing only carbon and hydrogen atoms such as polyethylene exposed to oxygen plasma. It also shows the mechanism responsible for the hydrophobic recovery (aging) in plasma-treated polymers. Inelastic collisions, mainly involving energetic electrons in the discharge and species on the polymer surface, can result in chemical bonds breakage creating free radicals in the material. Reactions between free radicals and atomic oxygen can add peroxides to the surface as shown in Fig. 13.22. Chemical reactions involving peroxides and species, such as atomic hydrogen originated from the polymer or atmospheric contaminants, can incorporate hydrophilic groups to the polymer surface. This modification enhances the surface energy.

The experimental DBD setup used for polymer treatment is shown in Fig. 13.23. For the discharge, two rectangular copper electrodes with dimensions 5 cm 3.5 cm × 1 cm are used. The lower electrode is covered by a polycarbonate (PC) plate with dimensions 10 cm × 8 cm × 0.2 cm as a dielectric barrier, separated by a gap between two electrodes. The discharge was generated via line frequency (50 Hz), high-voltage (maximum peak-to-peak value of 50 kV) power supply. The plasma surface treatment was performed by placing the polymer samples with dimensions 3 cm × 2.5 cm on the dielectric material, i.e., the polycarbonate (PC) plate in between the two electrodes at room temperature. Dry ambient air and a mixture of air and argon are used as plasma gas. Argon with a flow rate of about 2 l per minute is used in case of air and argon mixture. The plasma treatment time varied from 5 to 60 s. Surface treatments are performed by setting the electrode gap to 3.5 mm with applied voltage 13 kV rms and ballast

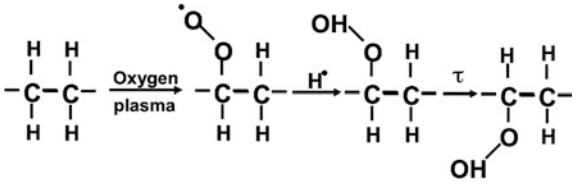

Fig. 13.22 Schematic representation of a possible mechanism responsible for the hydrophobic recovery in plasma treated polymer [83]

resistor 20 MΩ. Commercially available four different types of polymer films, namely high-density polyethylene (HDPE), polyethylene terephthalate (PET), polypropylene (PP), and polyamide 6,6 (PA), from Goodfellow Cambridge Limited, UK with dimensions 3 cm × 2.5 cm were used as samples for plasma treatment. Before the DBD plasma treatment, the samples were washed in isopropyl alcohol and then washed in distilled water, and ultrasonicated for 10 min and dried at room temperature.

Surface characterization of plasma-treated polymers

Polymer samples before and after the treatment are studied using contact angle measurements, surface free energy calculations, scanning electron microscopy (SEM), and atomic force microscopy (AFM).

Measurement of contact angle of liquid with the solid surface permits a rapid and qualitative evaluation of surface free energy of polymers. Analysis of the surface free energy of the untreated and plasma-treated samples has been made by measuring its surface free energy (γ), its dispersion part (γ^{LW}), and its acid–base part (γ^{AB}) along with the electron–donor component (γ^{+}) and the electron–acceptor component (γ^{-}) of the acid–base interaction.

In case of sessile drop method, values of contact angles are recorded for a few test liquids with well-defined surface tension and its components described as polar part and dispersive part. The interaction between a single droplet and tested surface in the most general form can be expressed by Young's equation [83–85]:

$$\gamma_S = \gamma_{SL} + \gamma_L \cos\,\theta, \tag{13.4.1}$$

where γ_S is the unknown surface free energy (SFE) of tested surface, γ_{SL} is the surface tension of solid–liquid interface, γ_L is the surface tension of a test liquid, and θ is the contact angle between the solid and the test liquid as shown in

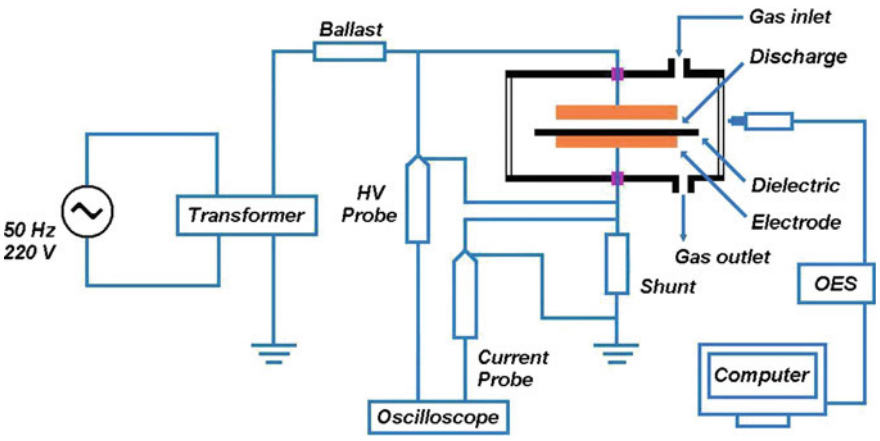

Fig. 13.23 Schematic diagram of the experimental setup

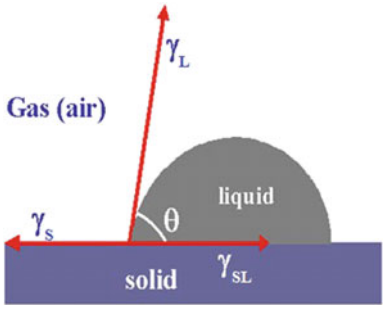

Fig. 13.24 Schematic diagram contact angle and interfacial tensions of three surfaces

Fig. 13.24. It comes out from Eq. (13.4.1) that the difference $\gamma_S - \gamma_{SL}$ can be obtained from the experimental values of γ_L and θ.

On the other hand, the work of adhesion for a liquid and a solid in contact, W_{SL}, is given, according to Young–Dupre equation by Refs. [78, 86–90],

$$W_{SL} = \gamma_S + \gamma_L - \gamma_{SL} \tag{13.4.2}$$

In addition, it has been proposed that two different interactions of the work of adhesion W_{SL} can be obtained: W_{SL}^{LW} derived from London dispersive forces, i.e., from apolar or dispersive or Lifschitz–van der Waals (LW) interactions and W_{SL}^{AB} derived from nondispersive interactions, i.e., from acid–base (AB) interactions or electron–acceptor/electron–donor interactions (deriving from hydrogen bonding, dipole–dipole interactions, etc.) [91]:

$$W_{SL} = W_{SL}^{LW} + W_{SL}^{AB}$$

The total surface free energy can be written as [89]

$$\gamma_S = \gamma^{LW} + \gamma^{AB}$$

W_{SL}^{LW} can be expressed by the geometric mean of the dispersion components [88]:

$$W_{SL}^{LW} = 2(\gamma_S^{LW} \cdot \gamma_L^{LW})^{1/2}$$

However, the acid–base interactions do not obey the geometric mean combining rule because they are complementary rather than symmetrical. For this reason, the acid–base term, γ^{AB}, should be split into an electron acceptor surface parameter, γ^+, and an electron donor surface parameter, γ^-, in such a way that $\gamma^{AB} = 2(\gamma^+ \cdot \gamma^-)^{1/2}$. The acid–base contribution to the work of adhesion between the solid and the liquid is thus given by,

$$W_{SL}^{AB} = 2(\gamma_S^+ \cdot \gamma_L^-)^{1/2} + 2(\gamma_S^- \cdot \gamma_L^+)^{1/2}$$

For the total work of adhesion, the sum of LW and AB contributions is given by,

$$W_{SL} = 2(\gamma_S^{LW} \cdot \gamma_L^{LW})^{1/2} + 2(\gamma_S^+ \cdot \gamma_L^-)^{1/2} + 2(\gamma_S^- \cdot \gamma_L^+)^{1/2} \quad (13.4.3)$$

From Eqs. (13.4.1), (13.4.2), and (13.4.3), we get

$$\gamma_L(1 + \cos\theta) = 2(\gamma_S^{LW} \cdot \gamma_L^{LW})^{1/2} + 2(\gamma_S^+ \cdot \gamma_L^-)^{1/2} + 2(\gamma_S^- \cdot \gamma_L^+)^{1/2},$$

which allows the determination of LW and AB components of the surface tension of a solid surface from contact angle measurements of three testing liquids with known values of the surface tension components. Table 13.4 shows the surface tension and its polar and dispersive part of three test liquids used for the contact angle measurements.

Contact angle measurement and wettability

Static contact angle measurements are made before the treatment and immediately after the treatment by dropping 4 μl of distilled water (H_2O), glycerol ($C_3H_8O_3$), and diiodomethane (CH_2I_2) on the surface. Different liquid drops on the polymer surface were imaged using CCD camera and the contact angles were measured by ramé-hart Model 200 contact angle goniometer. The values of the static contact angle were the average of three measured values. It is seen that a rapid decrease in the static water contact angle takes place with the treatment time up to 10 s which shows that a strong increase of wettability in the polymer surface is induced by DBD treatment. After 10 s of DBD treatment in air, the static water contact angle of untreated HDPE, PET, PP, and PA changed from (i) 92.8° to 63.7°, (ii) 76.7° to 44.8°, (iii) 93.7° to 76.4°, and (iv) 51.2° to 32.4°, respectively. Similarly, after 10 s of DBD treatment in argon/air mixture, the static water contact angle of untreated HDPE, PET, PP, and PA changed from (i) 92.8° to 51.4°, (ii) 76.7° to 36.5°, (iii) 93.7° to 66.0°, and (iv) 51.2° to 25.2°, respectively. This shows that DBD treatment in argon/air mixture decreased the static water contact angle more than DBD treatment in air with the same treatment time which clearly proved that a significant increase of wettability in the polymer surface can be induced by introducing a small amount of argon in the discharge gas environment. Figure 13.25

Table 13.4 Surface tension and its polar and dispersive part of three test liquids used for the contact angle measurements

Liquid	Total (γ_L)	Dispersive (γ_L^{LW})	Polar (γ_L^{AB})	Polar + (γ_L^+)	Polar − (γ_L^-)
Water	72.8	21.8	51.0	25.5	25.5
Glycerol	63.9	37.5	26.4	3.9	57.4
Diiodomethane	50.8	50.8	0	0	0

shows the variation of the static water contact angle on the surface of the PET film with DBD treatment time, both in air and in argon/air mixture. The results show that for PET film the treatment time longer than 10 s is not helpful as the decrease in contact angle becomes stable.

From the results mentioned above, it has been verified that atmospheric pressure dielectric barrier discharge (DBD) can be successfully used for the surface hydrophilization. It has been shown that different polymer surfaces can be treated to achieve high hydrophilicity with relatively short treatment time (up to 10 s). Longer exposure time do not cause significant changes in static contact angle values which means that saturation of plasma effect occurs. The contact angles are measured over an extended area of the treated sample and show a dispersion lower than 2.5° which is within the limit of experimental error. This implies that the surface treatment is uniform despite the fact that the discharge consists of a series of micro-discharges randomly distributed over the electrode/sample surface. The steep diminution of the contact angles on treated samples compared to the untreated one shows the significantly increased wettability induced by DBD even after such short treatment times. This behavior can be attributed to strong surface oxidation. The molecular oxygen in the contacting air is activated, ionized, and dissociated in the discharge to give extremely reactive oxygen species that react readily with the substrate surface.

Surface free energy results

The static contact angles between the three test liquids and different polymers are measured in order to determine the total surface free energy using sessile drop technique and three-liquid model. The surface free energy is calculated from Young–Dupre equation using the contact angle. It is seen that after 10 s of DBD treatment in air, the surface free energy of untreated HDPE, PET, PP, and PA changed from (i) 35.0 to 43.6 mJ/m^2, (ii) 44.5 to 53.6 mJ/m^2, (iii) 36.7 to 43.5 mJ/m^2, and (iv) 49.4 to 54.2 mJ/m^2, respectively. Similarly, after 10 s of DBD

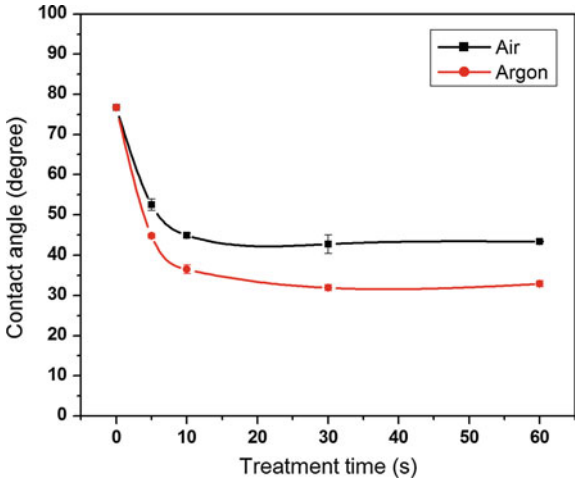

Fig. 13.25 Variation of water contact angle with treatment time (PET)

treatment in argon/air mixture, the surface free energy of untreated HDPE, PET, PP, and PA changed from (i) 35.0 to 48.2 mJ/m^2, (ii) 44.5 to 55.4 mJ/m^2, (iii) 36.7 to 42.8 mJ/m^2, and (iv) 49.4 to 61.0 mJ/m^2, respectively. Further treatment of polymers after 10 s, for both ambiences, does not lead to any significant changes in the surface free energy. DBD treatment in argon/air mixture increases the surface free energy more than DBD treatment in air. Figure 13.26 shows the dependence of surface free energy and its components on treatment time of PET in air plasma.

Scanning electron microscopy (SEM)

In order to compare the polymer surface modifications in air plasma and argon/air mixture plasma, SEM imaging is performed using Leo 500 scanning electron microscope for surface topography characterization. Figure 13.27a shows the SEM micrograph of untreated sample of PET and profile of a water droplet on the surface, showing measured contact angle of 76.7°. Figure 13.27b shows the SEM micrograph of PET sample that has been treated in air plasma for 60 s and profile of a water droplet on the surface, showing measured contact angle of 43.2°. Figure 13.27c shows the SEM micrograph of PET surface treated in argon/air mixture plasma for 60 s and profile of a water droplet on the surface, showing measured contact angle of 32.9°. The topography of the treated polymers appears to be quite different from the untreated one. It is seen that the surface of the air plasma-treated polymer has slightly increased surface roughness compared to the untreated polymer surface. The surface of the argon/air mixture plasma-treated polymer, however, is changed drastically with highly increased surface roughness compared to both the untreated and air plasma-treated polymers. This is caused by the dominant etching effect of the argon plasma treatment. The main species in the plasma which are responsible for the etching effect are positive ions and photons,

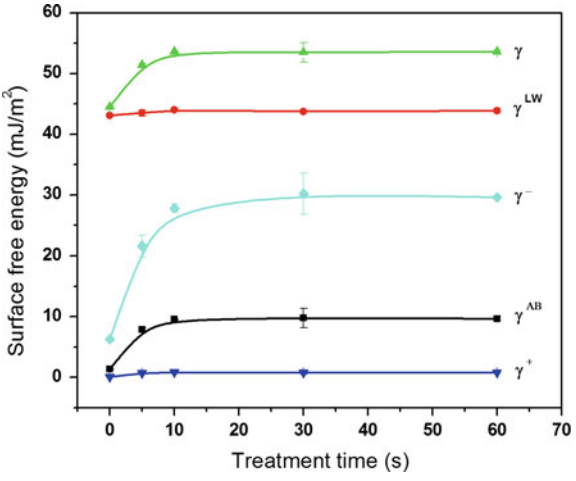

Fig. 13.26 Variation of surface free energy and its components with treatment time for PET in air plasma. γ is the surface free energy, γ^{LW} is its dispersion part, and γ^{AB} is its acid–base part. γ^+ is the electron–donor component and γ^- is the electron–acceptor component of the acid–base interaction

with the ability of breaking primary chemical bonds and introducing cross-linking. It is quite interesting to note that the roughness of the polymer treated in argon/air mixture plasma is more prominent than in the case of air plasma treatment. The air plasma has only a slight effect on the topography of the polymers.

Atomic force microscopy (AFM)

In order to compare the polymer surface modifications in air plasma and argon/air mixture plasma, AFM imaging is also performed using Nanoscope III SPM atomic

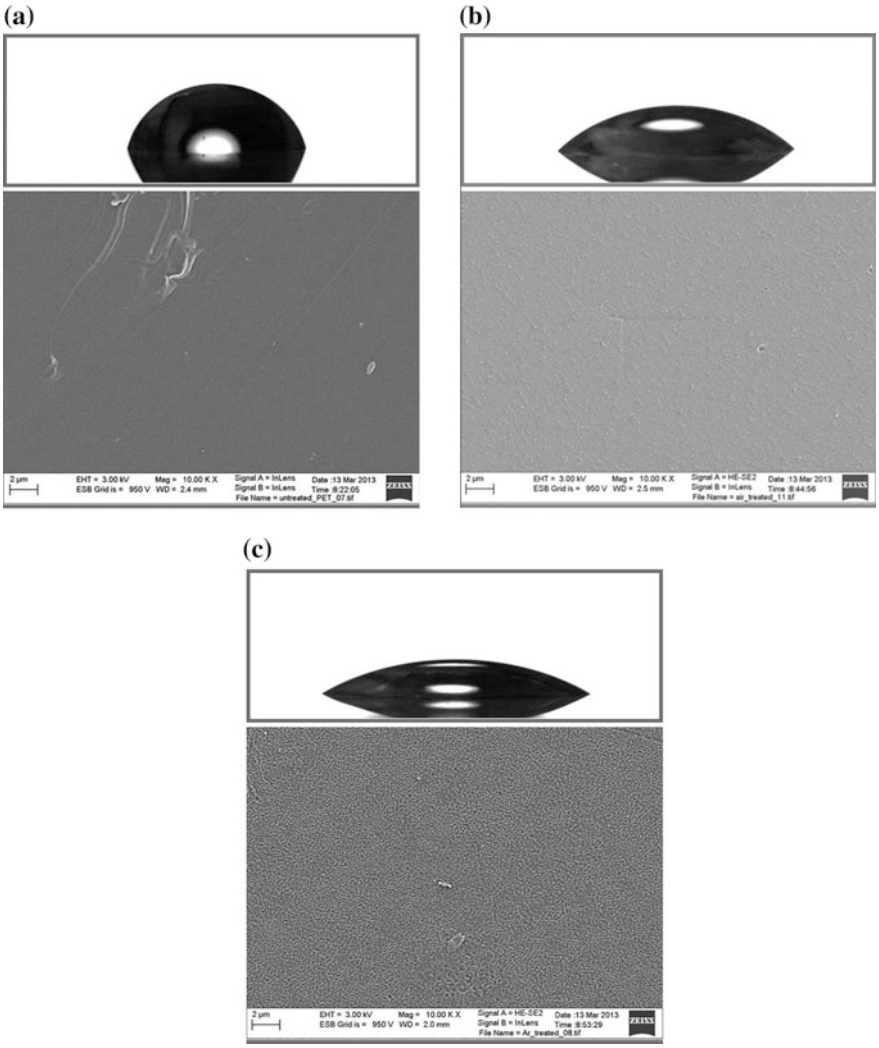

Fig. 13.27 SEM image and profile of a water droplet on the surface of untreated PET (**a**), treated in air plasma for 60 s (**b**) treated in argon/air mixture plasma for 60 s (**c**)

force microscope for surface morphology characterizing of polymer. It is seen that the argon/air mixture plasma-treated polymer samples are most pronounced than untreated and air plasma-treated samples. It is known that the argon plasma does not allow incorporation of new chemical species into the polymer chains. Despite this, argon/air plasma-treated surface gets much more oxygen-containing polar groups than the untreated and air plasma-treated surface. This phenomenon can be explained as argon has lower breakdown potential than air. The blending of it can make the discharging more symmetrical which can lead to ample plasma ionization. Figure 13.28a shows the 2-D AFM image of untreated sample of HDPE and profile of a water droplet on the surface, showing measured contact angle of 92.8°. The morphology of the untreated HDPE appears comparatively smooth. Figure 13.28b shows the 2-D AFM image of HDPE sample that has been treated in air plasma for 60 s and profile of a water droplet on the surface, showing measured contact angle of 54.0°. As can be seen from the figure, the surface of the air plasma-treated HDPE has only slightly increased surface roughness compared to the untreated HDPE. Figure 13.28c shows the 2-D AFM of HDPE surface treated in argon/air mixture plasma for 60 s and profile of a water droplet on the surface, showing measured contact angle of 46.1°. It is also clearly seen that the surface of the argon/air mixture plasma-treated HDPE has been changed drastically with highly increased surface roughness compared to both the untreated HDPE and air plasma-treated HDPE. As can be seen, the air plasma has only a slight effect on the morphology of HDPE. These results can also be observed in 3-D AFM images presented in Figs. 13.29a, b and 13.30.

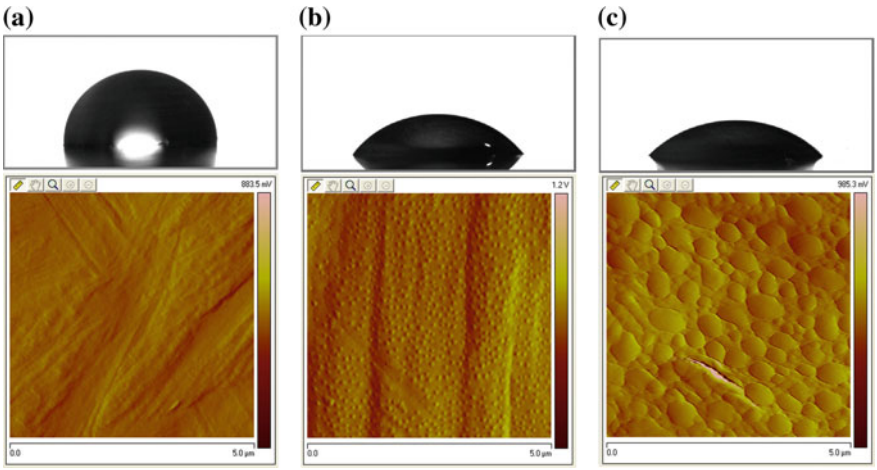

Fig. 13.28 **a** 2-D AFM image of untreated HDPE; **b** AFM image of HDPE treated in air plasma for 60 s; and **c** AFM image of HDPE treated in argon/air mixture plasma for 60 s

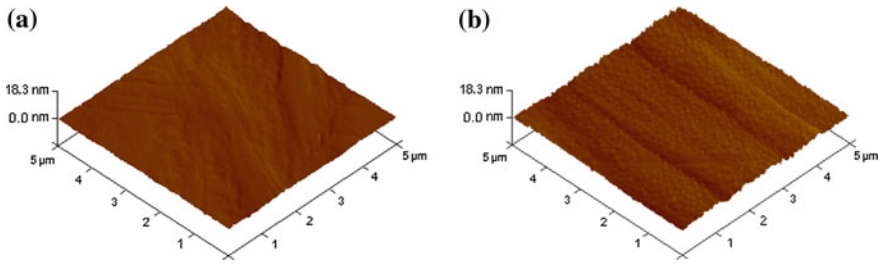

Fig. 13.29 3-D AFM image of **a** untreated HDPE and **b** HDPE surface treated in air plasma for 60 s

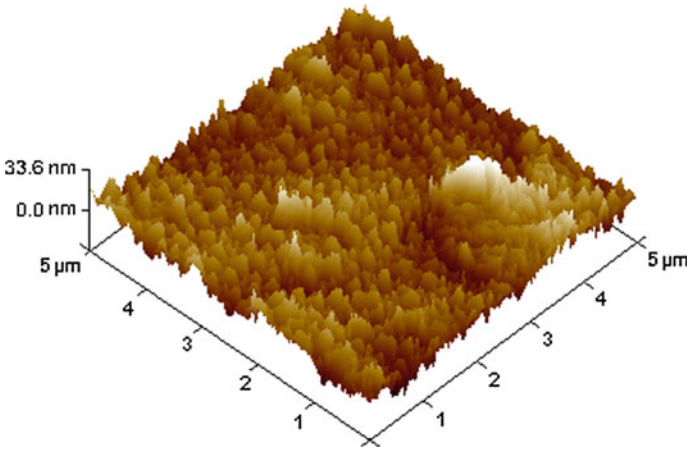

Fig. 13.30 3-D AFM image of HDPE surface treated in argon/air mixture plasma for 60 s

13.4.3 Plasma Medicine

Some of the earlier applications of plasma in medicine relied mainly on the thermal effects of plasma. Heat and high temperature have been exploited in medicine for a long time for the purpose of tissue removal, sterilization, and cauterization. Recently, research on applications of plasma in medicine has shifted to the exploitation of nonthermal effects [43]. Nonthermal atmospheric pressure plasma sources offer efficient means for the production of chemically active radicals under low thermal loading conditions. The ability of these devices to operate outside vacuum chambers not only reduces the overall operation and installation costs, but also permits the treatment of mechanically sensitive materials, such as biomaterials and human tissues [92]. Nonequilibrium plasmas are found to be nondestructive to tissue, safe, and effective in inactivation of various parasites and foreign organisms [43]. Various types of atmospheric pressure plasma sources have been designed for

a wide range of biomedical and industrial applications, like plasma needle, floating-electrode DBD, microhollow cathode discharge air plasma jet, and various other forms of plasma jets [12, 43, 77, 92–96]. Atmospheric pressure plasma jets have been established as suitable sources of low-temperature and nonequilibrium atmospheric pressure plasmas. The plasma jet devices generate plasma plumes in open space rather than in confined discharge gaps only. Thus, they can be used for direct treatment and there is no limitation on the size of the object to be treated [77].

As an example, a recent work on the application of atmospheric pressure plasma jet for the inactivation of prokaryotic cells (*Escherichia coli*, *Staphylococcus aureus,* etc.) and eukaryotic cells (*Candida albicans*, *Saccharomyces cerevisae*, etc.) to obtain >4 log10 reduction in *E. coli* and <2000 cells reduction in eukaryotic microalgae *C. vulgaris* is briefly discussed in this section.

An atmospheric pressure single-electrode argon/oxygen plasma jet was generated between a high-voltage (3.5 kV, 27 kHz) electrode and the surrounding room air for treatment of the cells. The micro-plasma jet device operated with an electrical power less than 10 W exhibited a long plasma jet of about 8.0 cm with temperature near 300 K, not causing any harm to human skin. Optical emission spectra measured in the range of 200–900 nm showed that various reactive species such as O, OH, N_2^+, Ar^+, etc., are present in the plasma plume. The schematic diagram of the experimental setup used in the present work is depicted in Fig. 13.31.

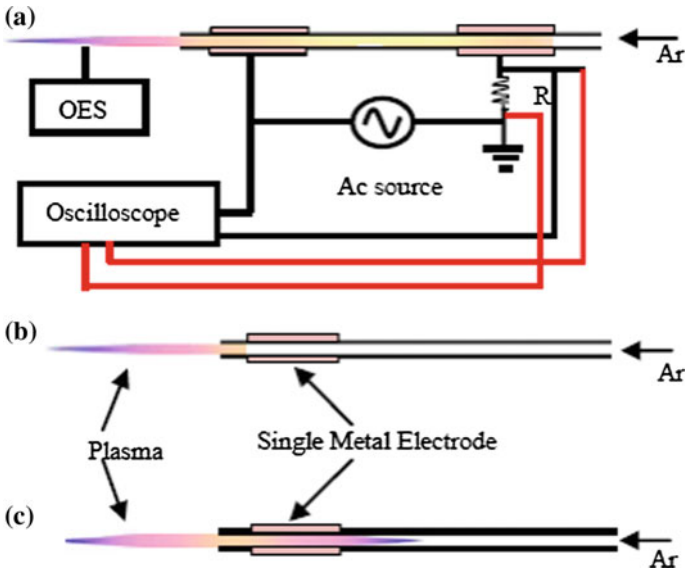

Fig. 13.31 Schematic diagram of the experimental setup used for the treatment of the cells. The discharge was generated by a high-voltage power supply with V_{ap} = 3.5 kV, f = 27 kHz and gas flow rate Q = 2 l/min

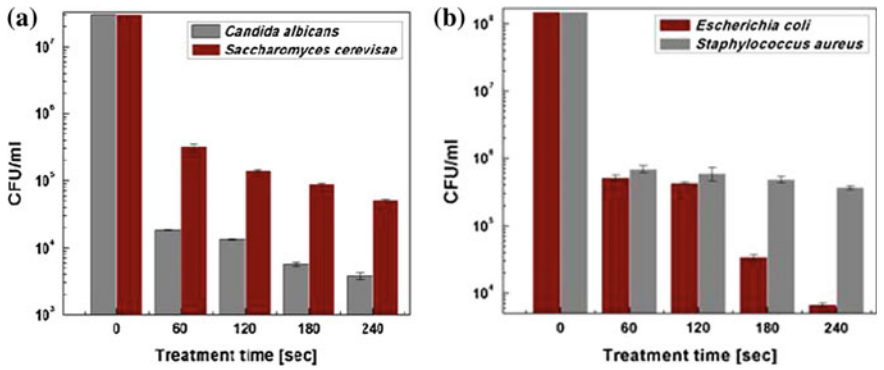

Fig. 13.32 CFU in **a** eukaryotic yeast cells **b** prokaryotic bacteria cells as a function of treatment time in APPJ. The treatments were carried out at distance of 3.5 cm from nozzle in 12 well plates [77]

In order to demonstrate that plasma species are solely responsible for inactivating living cells, the effect of plasma jet in pH and temperature of cell culture medium was also investigated.

Colony Forming Unit (CFU) analysis was done to investigate the number of dead cells and number of viable (live) cells. Treated and untreated samples were diluted by 10–10^4 times. 100 µl of diluted sample was spread on Plate Count Agar (PCA) using sterile bent glass rod. Then, the samples were incubated for 24 h at 37° C. After incubation, viable colony of microbes were counted using Quebec Colony Counter (QCC). By spread plate technique, viable cell colony was counted using QCC. More than 4 log reductions were observed in *E. coli*, *Staphylococcus*, *C. albicans,* and *S. cerevisae*. In eukaryotic microalgae, more than 2000 cells were killed by jet at a maximum treatment time of 240 s, as measured using UV–Vis spectrophotometer taking into account the absorbance of the cell suspension before and after treatment.

Figure 13.32a, b indicates that plasma jet is responsible for the killing of prokaryotic and eukaryotic cells. The inactivation and killing of both prokaryotic and eukaryotic cells increased as the treatment time increased with argon as carrier gases.

13.5 Summary

An overview of low-temperature, nonthermal plasma with focus on dielectric barrier discharge has been presented. Low-pressure gaseous discharges which can be generated by DC, RF, or MW power sources have been briefly described before introducing different types of atmospheric pressure plasmas. This chapter mainly

focused on atmospheric pressure DBD, its generation, characterization, and application in some selected fields.

Although the field of low-pressure plasma has been studied for quite a long time, the field of atmospheric pressure plasma is still very young. In the past few decades, new and interesting applications are emerging rapidly and hence interest in this field of research is growing in the same rate. One of the most challenging topics of research for the coming years will be to generate a larger volume of stable and homogenous plasma at atmospheric pressure so that material processing which originally used to be carried out in low pressure could be possible at atmospheric pressure thereby significantly reducing the cost of installation, operation, and maintenance. This will demand a better understanding of the discharge process at atmospheric pressure mainly, the nature of micro-discharges and the associated plasma chemical reactions in such systems. Numerous attempts have been made in this direction by improving existing diagnostics tools and also by introducing new methods. This will not only increase our understanding but will also pave the way for development of new applications of these cost-effective plasmas.

Acknowledgements The authors would like to thank Dr. Raju Bhai Tyata, Dr. Rajendra Shrestha, Mr. Amit Shrestha, Ms. Arati Khadgi, Ms. Rita Bhatta, and Mr. Jyoti Gurung for their contribution in this work. The authors would also like to thank Prof. Andrzej Huczko from Department of Chemistry, University of Warsaw, Poland for AFM and SEM analysis. We would also like to thank Mr. Suraj Sharma, for his assistance in drawing the schematic diagrams of plasma systems.

References

1. U. Kogelschatz, B. Eliasson, W. Egli, From ozone generators to at television screens: history and future potential of dielectric-barrier discharges. Pure Appl. Chem. **71**(10), 1828 (1999)
2. J. Janca, P. Stahel, J. Buchta et al., A plasma surface treatment of polyester textile fabrics used for reinforcement of car tires. Plasmas Polym. **6**(1/2), (2001)
3. P. Stahel, J. Janca, D.P. Subedi, Surfaceactivation of non-fabricated polymeric textile by means of low temperature plasmas at atmosphericpressure. Czechoslovak J. Phys. **52** (2002)
4. D.P. Subedi, L. Zajickova, V. Bursikova et al., Surface modification of polycarbonate (bisphenol A) by low pressurerf plasma. Him. J. Sci. **1**(2), 115–118 (2003)
5. S. Starostin, E. Aldea, H. de Vries et al., Application of atmospheric pressure glow discharge (APGD) for deposition of thin silica-like films on polymeric webs, in *28th ICPIG*, Prague, Czech Republic, 2007
6. Y. Yin, L. Dongping, L. Dongming et al., Surface properties of silicon oxide films deposited using low-pressure dielectric barrier discharge. Appl. Surf. Sci. **18628**, 1–5 (2009). doi:10.1016/j.apsusc.2009.04.142
7. V. Bursikova, L. Zajickova, P. Dvorak et al., Plasma enhanced chemical vapor deposition of silicon incorporated diamond like carbon films, in *Proceeding XVth Europhysics Conference on Atomic and Molecular Physics of Ionized Gases, Miscolc-lillafured*, Hungary 2000, pp. 408–409
8. L. Zajickova, V. Bursikova, V. Perina et al., Plasma modifications of polycarbonates. Surf. Coat. Technol. **142–144**, 449–454 (2001)

9. L. Zajickova, D.P. Subedi, V. Bursikova et al., Study of argon plasma treatment of polycarbonate substrate and its effect on film deposition. Acta Phys. Slovacca. **53**(6), 489–504 (2003)
10. G. Fridman, G. Friedman, A. Gutsol et al., Applied plasma medicine. Plasma Process. Polym. **5** (2008)
11. M.S. Bell, B.K.T. Kenneth, G.L. Rodrigo et al., Carbon nanotubes by plasma-enhanced chemical vapor deposition. Pure Appl. Chem. **78**(6), 1117–1125 (2006)
12. P. Rajasekaran, P. Mertmann, N. Bibinov et al., DBD plasma source operated in single-filamentary mode for therapeutic use in dermatology. J. Phys. D Appl. Phys. **42** (2009). doi:10.1088/0022-3727/42/22/225201
13. G. Borcia, C.A. Anderson, N.M.D. Brown, Dielectric barrier discharge for surface treatment: application to selected polymers in film and fibre form. Plasma Sources Sci. Technol. **12**, 335–344 (2003)
14. K. Okazaki, T. Nozaki, Ultrashort pulsed barrier discharges and Applications. Pure Appl. Chem. **74**(3), 447–452 (2002)
15. A.P. Napartovich, Overview of atmospheric pressure discharges producing non-thermal plasma. Plasmas Polym. **6**(1–2), (2001)
16. V.I. Gibalov, G.J. Pietsch, Dynamics of dielectric barrier discharges in different arrangements. Plasma Sources Sci. Technol. **21** (2012)
17. A. Schutze, J.Y. Jeong, S.E. Babayan et al., The atmospheric-pressure plasma jet: a review and comparison to other plasma sources. IEEE Trans. Plasma Sci. **26**(6), (1998)
18. B. Graham, Technological plasmas. Phys. World. 31–36 (2001)
19. E. Stoffels, W. Stoffels, *Electrons, Ions and Dust in a Radio Frequency Discharge*, (Edindhoven, 1994)
20. M. Konuma, *Film Deposition by Plasma Techniques*, (Stuttgart, 1991)
21. A.M. Howatson, *An Introduction to Gas Discharges* (Pergamon Press, Frankfurt, 1976)
22. L. Zajickova Thin films prepared by radio frequency PECVD. PhD thesis, Department of Physical Electronics, Masaryk University, Brno, Czech Republic, 1999
23. J.L. Cecchi, *Introduction to Plasma Concepts and Discharge Configurations*, (Noyes Publications, New Jersey, 1990), pp. 14–69
24. S.Y. Moon, J. Han, W. Choeb, Control of radio-frequency atmosphericpressure argon plasma characteristics by helium gas mixing. Phys. Plasmas. **13** (2006)
25. Y.A. Lebedev, Microwave discharges: generation and diagnostics. J. Phys. Conf. Ser. **257** (2010). doi:10.1088/1742-6596/257/1/012016
26. H. Conrads, M. Schmidt, Plasma generation and plasma sources. Plasma Sources Sci. Technol. **9**, 441–454 (2000)
27. A.R. Hoskinson, J. Hopwood, A two-dimensional array of microplasmas generated using microwave resonators. Plasma Sources Sci. Technol. **21** (2012)
28. K. Tanaka, M. Kogoma, Application of spray-type atmospheric pressure glow plasma reactor: ashing of organic compounds. Plasmas Polym. **6**(1–2), (2001)
29. L. Peng, Z. Ru-juan, W. Xiac-hui et al., An experimental study on atmosphericpressure glow discharge in different gases. Plasma Sci. Technol. **4**(3), (2002)
30. G. Chen, S. Chen, M. Zhou et al., The preliminary discharging characterization of a novel APGD plume and its application in organic contaminant degradation. Plasma Sources Sci. Technol. **15**, 603–608 (2006). doi:10.1088/0963-0252/15/4/002
31. Z. Buntat, I.R. Smith, N.A.M. Razali, Ozone generation using atmospheric pressure glow discharge in air. J. Phys. D: Appl. Phys. **42** (2009)
32. L. Mangolini, C. Anderson, J. Heberlein et al., Effects of current limitation through the dielectric in atmospheric pressure glows in helium. J. Phys. D Appl. Phys. **37**, 1021–1030 (2003)
33. M. Goldman, A. Goldman, R.S. Sigmond, The corona discharge, its properties and specific uses. Pure Appi. Chem. **57**(9), 1353–1362 (1985)
34. Y.S. Akishev, G.I. Aponin, V.B. Karal'nik, Phenomenology of a high-current negative point-to-plane corona in nitrogen. Plasma Phys. Rep. **30**(9), 779–787 (2004)

35. L. Cernakova, D. Kovacik, A. Zahoranova et al., Surface modification of polypropylenenon-wovenfabrics by atmospheric-pressure plasma activation followed by acrylic acid grafting. Plasma Chem. Plasma Process. **25**(4), (2005)
36. B. Dong, J.M. Bauchire, J.M. Pouvesle et al., Experimental study of a DBD surface discharge for the active control of subsonic airflow. J. Phys. D Appl. Phys. **41** (2008)
37. U. Kogelschatz, Collective phenomena in volume and surface barrier discharges. J. Phys.: Conf. Ser. **257** (2010) 012015, in *25th Summer School and International Symposium on the Physics of Ionized Gases—SPIG 2010*, IOP Publishing, 2010
38. M. Laroussi, X. Lu, V. Kolobov et al., Power consideration in the pulsed dielectric barrier discharge at atmospheric pressure. J. Appl. Phys. **96**(51), (2004)
39. N. Balcon, A. Aanesland, R. Boswell, *Pulsed rf Discharge, Glow and Filamentary Mode At atmospheric Pressure in Argon*, vol. 16, (IOP Publishing Ltd., 2006)
40. https://www.plasma-universe.com/Electric_glow_discharge (14 Sept 2016)
41. Y. Ando, X. Zhao, Synthesis of carbon nanotubes by arc discharge method. New Diam. Front. Carbon Technol. **16**(3), (2006)
42. C. Fanara, L. Vilarinho, Electrical characterization of atmospheric pressure arc plasmas. Eur. Phys. J. D **28**, 241–251 (2004)
43. A. Fridman, *Plasma Chemistry* (Cambridge University Press, Cambridge, 2008)
44. A. Chirokov, A. Gutsol, A. Fridman, Atmospheric pressure plasma of dielectric barrier discharges. Pure Appl. Chem. **77**(2), 487–495 (2005)
45. U. Kogelschatz, B. Eliasson, W. Egli, Dielectric-barrier discharges: principle and applications. J. Phys. IV France, **7** (1997)
46. J. Cech, P. Stahel, Z. Navratil, The influence of electrode gap width on plasma properties of diffuse coplanar surface barrier discharge in nitrogen. Eur. Phys. J. D **54**, 259–264 (2009)
47. C. Anderson, M. Hur, P. Zhang et al., Two-dimensional space-time-resolved emission spectroscopy on atmospheric pressure glows in helium with impurities. J. Appl. Phys. **96**(4), (2004)
48. F. Massines, N. Gherardi, N. Naude, Glow and Townsend dielectric barrier discharge in various atmosphere. Plasma Phys. Control. Fusion **47**, B577–B588 (2005). doi:10.1088/0741-3335/47/12B/S42
49. D. Trunec, A. Brablec, J. Buchta, Atmosphericpressure glow discharge in neon. J. Phys. D: Appl. Phys. **34**, 1697–1699. (2001). www.iop.org/Journals/jd, PII: S0022-3727(01)21705-7
50. S. Okazaki, M. Kogoma, M. Uehara et al., Appearance of stable glow discharge in air, argon, oxygen and nitrogen at atmosphericpressure using a 50 Hz source. J. Phys. D Appl. Phys. **26**, 889–892 (1993)
51. R.B. Tyata, D.P. Subedi, R. Shrestha et al., Generation of uniform atmosphericpressure argon glow plasma by dielectric barrier discharge. Pramana, J. Phys. Indian Acad. Sci. **8**(3), 507–517 (2012)
52. D.P. Subedi, R.B. Tyata, A. Khadgi et al., Treatment of water by dielectric barrier discharge. J. Sci. Technol. Trop. **5**, 117–123 (2009)
53. S. Foster, C. Mohr, W. Viol, Investigations of an atmospheric pressure plasma jet by optical emission spectroscopy. Surf. Coat. Technol. **200**, 827 (2005)
54. J. Tioshifuji, T. Katsumata, H. Takikawa et al., Cold arc-plasma jet under atmosphericpressure for surface modification. Surf. Coat. Tech. **171**, 302 (2003)
55. Y. Takemura, Y. Kubota, N. Yamaguchi et al., Development of atmospheric plasma jet with long flame. Trans. Plasma Sci. **26**, 1604 (2009)
56. J. Choi, K. Matsuo, H. Yoshida et al., Double-layered atmospheric pressure plasma jet. Japanese J. Appl. Phys. 48 (2009)
57. A. Kuwabara, S. Kuroda, H. Kubot, Effects of electrodepositioning on the atmospheric-pressure DBD plasma torch. Plasma Process. Polym. **2**, 305–309 (2005). doi:10.1002/ppap.200400089
58. D.P. Subedi, R.B. Tyata, A. Shrestha et al., An atmospheric pressure non-thermal plasma jet in nitrogen for surface modification of polyethylene. J. Sci. Technol. Trop. **6**, 49–52 (2010)
59. Y. Zhang, X.H. Wen, W.H. Yang, Plasma Sources Sci. Technol. **16**, 441–447 (2007)

60. X.M. Zhu, W. Cong-Che, Y.K. Pu, Using OES to determine electron temperature and density in low-pressure nitrogen and argon plasmas. J. Phys. D: Appl. Phys. **41** (2008)
61. D.P. Subedi, R.B. Tyata, R. Shrestha et al., An experimental study of atmospheric pressure dielectric barrier discharge (DBD) in argon. AIP Conf. Proc. **103** (2014)
62. U.M. Joshi, Surface modification of polymers by 50 Hz dielectric barrier discharge produced in air and argon at atmospheric pressure. Ph.D. thesis, Kathmandu University, Nepal, 2013
63. J.H. Kim, Y.H. Choi, Y.S. Hwang, Electron density and temperature measurement method by using emission spectroscopy in atmospheric pressure nonequilibrium nitrogen plasmas. Phys. Plasmas. **13** (2006)
64. O.A. Omarov, S.S. El'darov, A.M. Gadzhiev et al., An investigation of the optical characteristics of a pulse discharge in argon at atmospheric pressure in an external magnetic field. High Temp. **41**(2), 161–165 (2003)
65. L. Dong, J. Ran, Z. Mao, Direct measurement of electron density in microdischarge at atmospheric pressure by Stark broadening. Appl. Phys. Lett. **86**, 161501–161503 (2005)
66. S.J. Kang, V.M. Donnelly, Optical absorption and emission spectroscopy studies of ammonia-containing plasmas. Plasma Sources Sci. Technol. **16**, 265–272 (2007). doi:10.1088/0963-0252/16/2/008
67. N. Britun, M. Gaillard, A. Ricard et al., Determination of the vibrational, rotational and electron temperatures in N_2 and Ar–N_2 rf discharge. J. Phys. D Appl. Phys. **40**, 1022–1029 (2007). doi:10.1088/0022-3727/40/4/016
68. J. Tynan, V.J. Law, P. Ward et al., Comparison of pilot and industrial scale atmospheric pressure glow discharge systems including a novel electro-acoustic technique for process monitoring. Plasma Sources Sci. Technol. **19** (2010)
69. D. Xiao, C. Cheng, J. Shen et al., Electron density measurements of atmospheric-pressurenon-thermal N_2 plasma jet by Stark broadening and irradiance intensity methods. Phys. Plasmas. **21** (2014)
70. C.S. Wong, R. Mongkolnavin, *Elements of Plasma Technology* (Springer, Berlin, 2016)
71. N. Balcon, atmospheric pressure radio frequency discharges, diagnostic and numerical modeling. Ph.D. thesis, Australian National University, Australia, 2007
72. D.T. Burns, Earlyproblems in the analysis and the determination of ozone. Fresenius J. Anal. Chem. **357**, 178–183 (1997)
73. M.B. Rubin, The history of ozone. Bull. Hist. Chem. **26**(1), 1839–1868 (2001)
74. J. Grundmann, S. Muller, R.J. Zahn, Treatment of soot by dielectric barrier discharges and ozone. Plasma Chem. Plasma Process. **25**(5), (2005)
75. Z. Buntat, I.R. Smithand, N.A.M. Razali, Ozone generation using atmospheric pressure glow discharge in air. J. Phys. D: Appl. Phys. **42** (2009)
76. R. Bhatta, R. Kayastha, D.P. Subedi et al., Treatment of wastewater by ozone produced in dielectricbarrier discharge. J. Chem. **2015** (2015)
77. R. Shrestha, U.M. Joshi, D.P. Subedi, Experimental study of ozone generation by atmospheric pressure dielectric barrier discharge. Int. J. Recent Res. Rev. **VIII**(4), (2015)
78. M. Sira, D. Trunec, P. Stahel et al., Surface modification of polyethylene and polypropalene in atmospheric pressure glow discharge. J. Phys. D Appl. Phys. **38**, 621 (2005)
79. S.K. Oiseth, A. Krozer, B. Kasemo et al., Surface modification of spin-coated high-density polyethylene films by argon and oxygen glow discharge plasma treatments. Appl. Surf. Sci. **202**, 92–103 (2002)
80. P. Svarnas, N. Spyrou, B. Held, Polystyrene thin films treatment under DC point-to-plane low-pressure discharge in nitrogen for improving wettability. Eur. Phys. J. Appl. Phys. **28**, 105–112 (2004)
81. F. Zhi, Q. Yuchang, W. Hui, Surface treatment of polyethylene terephthalate film using atmospheric pressure glow discharge in air. Plasma Sci. Technol **6**, 2576 (2004)
82. U. Kogelschatz, Dielectric-barrier discharges: their history, discharge physics, and industrial applications. Plasma Chem. Plasma Process. **23** (2003)
83. E.C. Rangel, G.Z. Gadioli, N.C. Cruz, Investigations on the stability of plasma modified silicone surfaces. Plasmas Polym. **9**(1), 35–48 (2004)

84. D.P. Subedi, D.K. Madhup, K. Adhikari et al., Low pressure plasma treatment for the enhancement of wettability of polycarbonate. Indian J. Pure Appl. Phys. **46**, 540–544 (2008)
85. B. Luepakdeesakoon, C. Saiwan, J.F. Scamehorn, Contact angle of surfactant solutions on precipitated surfactant surfaces. J. Surfactants Deterg. **9**(2), 125–136 (2006)
86. H.W. Fox, W.A. Zisman, The spreading of liquids on low energy surfaces. I. polytetrafluoroethylene. J. Colloid Sci. **5**, 514–531 (1950)
87. J. Drelich, J.D. Miller, Examination of Neumann's equation-of-state for interfacial tensions. J. Colloid Interface Sci. **167**, 217–220 (1994)
88. N.T. Correia, J.J.M. Ramos, B.J.V. Saramago et al., Estimation of the surface tension of a solid: application to a liquid crystalline polymer. J. Colloid Interface Sci. **189**, 361–369 (1997)
89. D.Y. Kwok, C.N.C. Lam, A. Li et al., Measuring and interpreting contact angles: a complex issue. Colloids Surfaces A: Physiochem. Eng. Asp. **142**, 219–235 (1998)
90. M. Sira, P. Stahel, V. Bursikova et al., Activation of polyethylene and polypropylene in atmospheric pressure glow discharge. Czech J. Phys. **54**, 835–839 (2004)
91. R. Mahlberg, H.E.M. Niemi, F. Denes et al., Effect of oxygen and hexamethyldisiloxane plasma on morphology, wettability and adhesion properties of polypropylene and lignocellulosics. Int. J. Adhes. Adhes. **18**, 283–297 (1998)
92. S. Coulombe, V. Léveillé, S. Yonson et al., Miniature atmosphericpressure glow discharge torch (APGD-*t*) for local biomedical applications. Pure Appl. Chem. **78**(6), 1147–1156 (2006)
93. G. Fridman, M. Peddinghaus, H. Ayan et al., Blood coagulation and living tissue sterilization by floating-electrodedielectric barrier discharge in air. Plasma Chem. Plasma Process. **26**, 425–442 (2006)
94. M. Leduc, D. Guay, R.L. Leask et al., Cell permeabilization using a non-thermal plasma. New J. Phys. **11** (2009)
95. L. Xue-Chen, J. Peng-Ying, Y. Ning et al., Aspects of the upstreamregion in a plasma jet with dielectric barrier discharge configurations. Chin. Phys. B **21**(4), 1–6 (2012)
96. R. Foest, E. Kindel, A. Ohl et al., RF capillary jet—a tool for localized surface treatment. Contrib. Plasma Phys. **47**, 72–77 (2007)

Chapter 14
Carbon-Based Nanomaterials Using Low-Temperature Plasmas for Energy Storage Application

Bo Ouyang and Rajdeep Singh Rawat

14.1 Introduction

Energy can be conveniently stored as chemical energy from which it can also be retrieved easily. Currently, a large fraction of energy, about 85%, used by mankind for various activities is usually derived from fossil fuels. Fossil fuels are most favoured energy resources as energy can be extracted and distributed at comparatively low expense. Nonetheless, the combustion of fossil fuels delivers pollutants in our environment raising concerns of global warming [1]. Moreover, the natural reserves for fossil fuels are rather limited and at the current rate of exploitation they will not last longer and hence long-term sustainable energy resources are required. Another dimension of energy research is the energy storage. Many types of energy resources store energy directly into them which can be used when required, e.g., energy stored in coal, oil and gas (fossil fuels which are depleting fast) can be extracted when needed. But in many situations we do not have the control over the availability of energy as they are intermittently available, particularly for renewable energy resources such as solar, wind, tidal, hydroelectric energy. If we do not store these energies they will be wasted. There are several methods of energy storage among which electrochemical energy storage (EES) methods/systems have received considerable attention to store these intermittent renewable energy. The EES systems are not only for energy storage, but also capable of delivering the easily transportable energy such as portable devices including cell phones, laptops, vehicles, electrical vehicles, etc. The EES devices should have certain key features which include (i) being capable of providing high energy (for them to last longer)

B. Ouyang (✉) · R.S. Rawat
NSSE, National Institute of Education, Nanyang Technological University, Singapore 637616, Singapore
e-mail: N15OU80BO@e.ntu.edu.sg

R.S. Rawat
e-mail: rajdeep.rawat@nie.edu.sg

R.S. Rawat (ed.), *Plasma Science and Technology for Emerging Economies*,
DOI 10.1007/978-981-10-4217-1_14

and power densities (for them to provide sufficient current to operate the loading device), and (ii) with longer cyclic life (i.e., we can re-charge them several times for reuse).

Sustainable energy storage and conversion materials, together with the corresponding devices, have been in great demand. Because of that, the above issues can be solved in two approaches. First, energy can be efficiently converted from other infinite resources, such as the solar power and water into the useful forms such as fuel and electricity. In order to achieve this goal, fuel cells, water splitting catalysts as well as solar cells have received considerable research interest [2, 3]. Second, energy storage devices have been required to deliver the properties of environmental friendliness, cost-efficiency, and efficient performance, which is essentially due to the sporadic characters of most sustainable energy sources. Lithium-based batteries, including lithium-ion, lithium-sulfur and lithium-air, can be the most promising and useful devices toward these storage purposes, especially for the lithium-ion batteries (LIBs) [4–6]. Another efficient and promising device for energy storage is the supercapacitor (SC), which is capable of storing and releasing energy rapidly [3, 7].

The LIBs and SCs, two major energy storage devices, have received the global research interests since they serve as predominant energy sources for portable electronics such as laptops and cell phones. Despite different definitions, both of them belong to the electrochemical devices and deliver lots of similarities in configuration. In principle, both integrated SC and LIB devices contain three indispensable components: a positive electrode (cathode), an electrolyte (aqueous or non-aqueous solution), and a negative electrode (anode). During charging process, cations (H^+, Li^+, Na^+, K^+, etc.) or anions (OH^-, etc.) from electrolyte or either one electrode move across the electrolyte and adsorb onto/insert into the other electrode, delivering polarization within the electrochemical device [8]. Reversibly, the discharging process is a depolarization process during which ions desorb/extract from the electrode and return to the other electrode. Meanwhile, the electrons pass through the external circuit. In spite of many common characters, SCs and LIBs can also deliver several differences within the charge storage mechanism. For instance, SCs can be typically classified into two kinds: pseudocapacitors as well as electric double-layer capacitors (EDLCs), both of which can only store charges on the surface or in a thin-layer region of active materials (several tens of nanometers from the surface) through absorbing/desorbing ions to achieve electric double layers or utilizing reversible surface/near-surface redox reactions (a chemical reaction in which the oxidation states of atoms are changed) [9]. Hence, SCs are capable of delivering considerable charge/discharge capacitance (resulting in highly power densities) due to the ion diffusion while delivering depressed energy density ($\sim$5–20 W h kg^{-1}) because of the inadequate utilization of entire active materials (for pseudocapacitors) or limited active surface areas (for EDLCs). For comparison, LIBs are able to store charges through the intercalating lithium ions both in the bulk and on the surface of active materials. Resultantly, LIBs can achieve a considerably enhanced energy density ($\sim$120–150 W h kg^{-1}, usually two orders of magnitude higher than the capabilities of SCs) [10]. Nonetheless, they always experience

extensive kinetic issues because of the gradual diffusion of lithium ions into the bulk active materials, resulting in the comparatively lower power densities.

Because of the rapid development of nanoscience and technology, the requirement toward innovation in the techniques of nanostructural fabrication has been largely increased [11]. In comparison with excited neutrals and charged particles, plasma can deliver a distinct environment toward material fabrication and chemical process, which are quite different from normal gas, liquid, and solid phases. In terms of this approach, novel nanostructure seems to be fabricated. The definition of plasma was first given by Erving Langmuir during 1928 [12]. Nine decades have witnessed the continuous progress of plasma as well as plasma-enhanced technologies which have currently served as the essential candidate towards the numerous applications and are fundamentally indispensable in different areas, such as information technologies, materials sciences, environmental sciences, life and medical science, as well as energy sciences. In the field of material fabrication and processing, plasma-based strategies have been observed to achieve significant applications in thin-film deposition, etching and surface modifications [13, 14]. In particular, the synthesis of microstructure on the basis of plasma etching serves as an indispensable part in microelectronics [15].

Even though plasma-based approaches have currently been introduced into fabricating structures with reduced scales, the micro-to-nano conversion still needs considerable control towards the strategies. The preparation of microstructure is conventionally dependent upon patterned masks achieved via lithography. However, as the dimension of micro-architecture is decreased towards the nano-metered size, considerable interest has been attracted to investigate a bottom-up preparation approach rather than the conventional top-down method on the basis of lithography. Novel ideas toward fabrication strategies need to be found, particularly for the nanostructures fabrication without lithography, which enables plasma-enhanced fabrication toward nanoarchitectures to be an exciting interdisciplinary field containing surface science, solid-state and materials physics, chemistry and physics of plasmas and gaseous discharges, nanoscience and technology, and corresponding engineering techniques. Thin-film depositions have been the most commonly utilized approach through the plasma-assisted strategy, with predominant investigation towards carbon- and silicon-based species. Currently, nanoarchitectures with low dimensions such as nanoparticles, nanowires, nanotubes, and nanobelts have rapidly gained tremendous attention due to the novel structural and functional features within these systems. Resultantly, extension in both types of materials and nanostructure morphologies has been serving as essential issues. Recently, the application toward plasma-enhanced methods have been largely investigated in both types of materials as well as the morphologies of nanoarchitecture, but much more investigations are required towards further exploiting such field.

In this chapter, we will describe the fundamental information about energy storage devices, especially lithium-ion batteries and supercapacitors. Additionally, typical low-temperature plasma system including inductively coupled plasma and

capacitively coupled plasma will be illustrated. Furthermore, the low-temperature plasma-assisted approaches using these two devices are summarized with two critical carbon-based materials (carbon nanotubes and vertically oriented graphene nanosheets) as instances. In a word, we are trying to deliver that plasma-based methods can serve as one of the most promising candidates for energy storage applications.

Short definitions of key words that will be routinely used throughout the chapter:

Electrochemical Energy Storage (EES): A method used to store electrical energy in a chemical form. This storage technique benefits from the fact that both electrical and chemical energy share the same carrier, the electron. The typical electrochemical energy storage systems are lithium-ion batteries (LIBs) and supercapacitors (SCs).

Cathode: An electrode from which a conventional current leaves a polarized electrical device. A conventional current describes the direction in which positive electronic charges move.

Anode: An electrode through which the conventional current flows into a polarized electrical device.

Redox: A chemical reaction in which the oxidation states of atoms change. Any such reaction involves both a reduction process and a complementary oxidation process, two key concepts involved with electron transfer processes.

Intercalation: Insertion of ions into layered solids such as graphite.

Charging: The process of storing the electrical energy in the form of chemical energy in a battery or a supercapacitor.

Discharging: The process of releasing the stored chemical energy in the form of electrical energy.

Faradic process: A reaction governed by Faraday's law (i.e., the amount of chemical reaction caused by the flow of current is proportional to the amount of electricity passed).

Capability: The ability of an electrochemical system to store electric energy via chemical energy, especially in relation to the overall energy it can store.

Electrochemical capacity: The amount of electric charge which a battery can deliver per unit mass of battery at the rated voltage (A h kg^{-1}).

Specific capacitance: The specific capacitance is defined as the capacitance per unit mass (F kg^{-1}) or capacitance per unit volume F m^{-3}) of a supercapacitor. Since the capacitance is also defined as the ability to store charge, so the specific capacitance can also be defined as the ability of a device to store electric charge per unit of mass with units of W h kg^{-1}.

Specific surface area (SSA): A property of solids defined as the total surface area of a material per unit mass or bulk volume.

Capacity fading: A phenomenon observed in rechargeable battery usage where a battery can deliver the decreased amount of charge at the rated voltage with use.

Coulombic efficiency: The efficiency with which charges (electrons) are transferred in a system facilitating an electrochemical reaction.

Cycling: Repeating the charging and the discharging processes for a rechargeable battery or a supercapacitor to measure their capacity fading.

Cyclic stability: An evaluation to determine the extent of capacity fading during the cycling process.

Cyclic voltammetry: A type of potentio-dynamic electrochemical measurement. In a cyclic voltammetry (CV) experiment, the working electrode potential is ramped linearly versus time. After the set potential is reached in a CV experiment, the working electrode's potential is ramped in the opposite direction to return to the initial potential. The current at the working electrode is plotted versus the applied voltage to give the cyclic voltammogram trace.

14.2 Lithium-Ion Battery

First, it is better for us to discuss what batteries are before entering our predominant part. Batteries are the chemical devices which are capable of storing energy. Even though several ancient societies might have first developed these kinds of devices (the so-called Baghdad Battery might be dated back to 200 BC), its intrinsic "invention" within modern society can be attributed to Alessandro Volta during the earlier 19th century [16]. At least 200 years have witnessed the continuous progress of battery technology and enabled the constant development of portable electronics. Currently, the limited accessibility of energy sources has inspired the concern towards considering sustainable energies and therefore batteries have been fostered to be able to store energy from the intermittent resources. Moreover, the requirement towards forecasted raises in fuel expenses and reducing emissions of greenhouse gases have paved the pathway toward the continuous progress on hybrid electric vehicles (HEVs) [17–19]. Hence, batteries currently act on the most promising candidate in powering them.

14.2.1 Primary Versus Secondary Batteries

Even though the term "battery" has intrinsically been referred to a mass of cells, nowadays it is still utilized to identify as an individual electrochemical cell. An integrated battery can be composed of two electrochemically active components: the electrodes which have been separated and an electrolyte which serves as an ion-conductive and electronically insulating medium. During charging–discharging processes, electrons can be driven to move from one electrode towards the other via the external circuit and simultaneously electro-neutrality can be ensured through ion transport across the electrolyte, as shown in Fig. 14.1. After one of the redox processes is completed, the electron flow can stop. Once the above process is reversed by introducing the external current, the battery is able to re-charge. The rechargeable batteries are named as the secondary batteries and meanwhile,

non-rechargeable batteries are referred as the primary batteries. An essential part towards setting up a favorable battery system is to select the most suitable composites for a battery electrode. Noticeably, the electrochemical capability (typically provided in A h kg^{-1}) of the specific electrode material is dependent upon the number of exchanged electrons as well as the related molar weight. Additionally, the voltages of batteries rely upon the difference between the potentials of two involved faradic processes. The standards towards selecting the battery for the typical utilization are the energy amount (energy density: W h l^{-1} or W h kg^{-1}) as well as the electric power (power density: W l^{-1} or W kg^{-1}) [20], mass and size, durability, reliability, expenses, and safety [21].

In terms of their specific usage, many types of batteries with a wide range of stored energies have been introduced into our daily lives. For instance, the battery can be utilized for powering watches (0.1–0.5 W h), electric cars (5–10 kW h), laptop computers (30–100 W h), and even serves as an uninterrupted power supply (UPS) towards entire cities [10]. Notably, the biggest battery all over the world, which has been established in Fairbanks of Alaska, provides the capability to deliver the power of 40 MW for 7 min [16].

14.2.2 Rechargeable Battery Chemistries

The number of rechargeable batteries available for commercial utilization is comparatively lower as compared to primary batteries. Rechargeable batteries can be divided into two types: (i) the aqueous electrolyte-based system (lead–acid, alkaline nickel–cadmium, and nickel–metal hydride-based cells), and (ii) nonaqueous

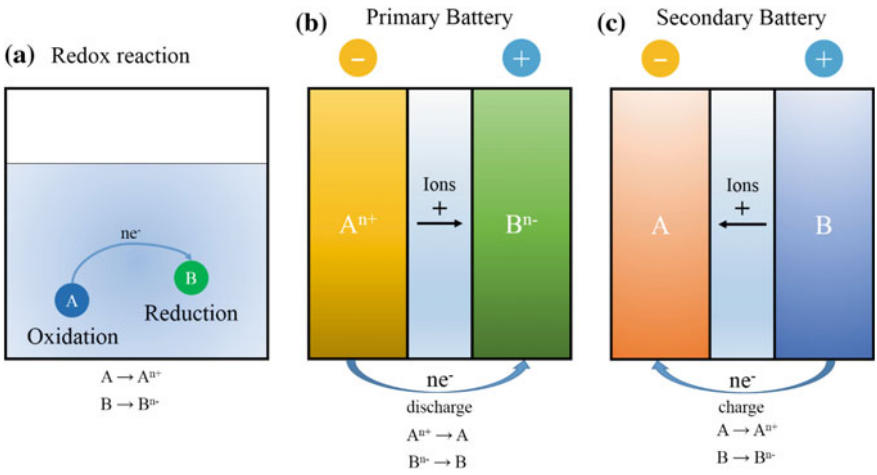

Fig. 14.1 Schematic diagrams of **a** a redox reaction, **b** a primary (non-rechargeable) battery discharging process and **c** a secondary (rechargeable) battery charging process

Table 14.1 The voltage, theoretical capability values (considering only the mass of the active materials in the electrodes), values achieved in practice and energy densities for the major battery systems (there is a large range of values for lithium-ion batteries owing to the great variety of available electrode materials, both for the cathodes and anodes)

Battery chemistry	Type	Voltage (V)	Theoretical capability (W h kg^{-1})	Practical capability (W h kg^{-1})	Practical energy density (W h dm^{-3})
Zn–MnO_2 (alkaline)	Primary	1.5	358	145	400
Li–I_2	Primary	2.8	560	245	900
Pb–acid	Secondary	2.1	252	35	70
Ni–Cd	Secondary	1.3	244	35	100
Ni–MH	Secondary	1.3	240	75	240
Na–S	Secondary	2.1	792	170	345
Na–$NiCl_2$ (ZEBRA)	Secondary	2.6	787	115	190
Lithium-ion	Secondary	4.1	410	150	400

electrolyte-based system (lithium-based batteries and sodium-ion batteries), both of which have dominated the market, according to their different size and value. The theoretical and practical energy densities have been provided in Table 14.1. During the end of the nineteenth century, lead–acid technology was firstly investigated along with granted patents. It uses lead-based redox couple (lead-based compound as a cathode and metallic lead as an anode, termed as Pb–Pb^{4+}) into two electrodes and during the discharging process the electrolyte utilizes the active components into reactions by achieving lead sulfate. The lead–acid batteries are the most utilized secondary batteries in our society, especially in starting, lightning, and ignition (SLI) in cars, as well as occupies at least 70% of the global lead production.

The first granted patents towards nickel-based batteries appeared in the nineteenth century with either iron or cadmium as the anode and nickel hydroxide as the cathode. Batteries introducing hydrogen as the anode have been particularly investigated toward spacecraft utilizations from 1970s to 1980s, which has also inspired the progress of the nickel–metal hydride technology, largely applied to portable electronics and recently introduced into commercial HEVs. Besides, the chemical process behind those batteries, particularly with respects to the cathode, is not straightforward, whereas its fundamental investigation has led to the deeper level of understanding towards different phases that may occur during charging–discharging processes, relying on the operating conditions. This can be the indispensable part for the broad utilization of nickel-based batteries [22].

Progress towards batteries on the basis of the utilization of alkali metals (typically lithium, sodium, and potassium) as the anode occurred later in time and, therefore, largely benefited from the scientific knowledge of previous investigations towards other batteries. Their advantage is derived from the relatively lower atomic weight, resulting in highly capabilities: such as capacities of 3860 A h kg^{-1} for lithium and 1170 A h kg^{-1} for sodium [1]. Moreover, because of their remarkable

standard reducing potentials, large battery voltages can be achieved by integrating these electrodes with relatively lower standard reducing potential species. Therefore, theoretical capabilities can be larger than that obtained from the above nickel-based and lead–acid battery systems. Noticeably, the achievement of batteries through utilizing alkali metals requires the absence of aqueous agents, because they are not stable electrochemically at the operation potentials of aqueous media. The utilization toward nonaqueous electrolytes introduces enhanced complication for the system, since electrochemistry in these agents has been quite less investigated. In addition, battery preparation is required to build the cells under the moisture-free condition. Besides, the development of sodium-based batteries has been targeted at delivering high capability with the easily accessible non-strategic precursor. The initial prototypes, investigated by the Ford Motor Company, had sulfur as the cathode material and the sodium β"-Al_2O_3 as the solid electrolyte. Such cell has delivered a spinel-related framework and is normally formulated as $Na_2O_{5.33}Al_2O_3$, in spite of the existence of several extra ions which enhance the thermodynamic stability. Such species is the electrical insulator, which delivers ionic conductivity of 20 S m^{-1} at $\sim$300 °C, comparable to the values of numerous aqueous electrolytes. In terms of its surprising features, such investigation delivering with high temperature and introducing the operation of liquid sodium and sulfur has been developed for more than four decades [16]. Currently, a large-scale battery system (8 MW power density and 40 MW h energy density) has been achieved and further established in Japan, which has successfully been operated for massive stationary storage applications. As the Coulombic efficiency (a ratio between discharging and charging capacity of the battery) of such system is near 100%, efforts have been devoted to extend its utilization. The products based on this technology, named as the ZEBRA battery, has been evaluated later towards automotive utilization, delivering the predominance of being assembled during the discharged phase and therefore preventing the requirement towards introducing liquid sodium [16].

In stark contrast with the above scenarios, in which progress has been driven by specific applications and has been involved in a comparatively smaller number of compound integration, lithium-based batteries depend upon a wide variety of chemistries. Notably, even though only a few of them have been in commercial utilization, the exploitation towards promising electrode species is considerably extensive. Electrolytes ranging from the most utilized lithium salt solutions in organic solvents to ionic conductive polymers, along with even molten salts have been used. Noticeably, the firstly developed lithium-based cells were primary batteries, with metallic lithium as the anode, whereas it was soon realized that reversible features of most faradic processes were capable of delivering the pathway towards developing the secondary batteries [4, 5]. Actually, most of the cathode materials could be lithium-intercalation composites, achieved via inserting lithium ions into the interlayers of the host species. Several lithium-based secondary batteries with such type have already reached the market. However, they have rapidly been withdrawn because of the safety problems derived from the dendritic growth of metallic lithium during re-charging process, which may pierce the separator,

resulting in the cell shortcut and subsequent heating, even causing a hazardous explosion [2, 23]. In order to solve this challenge, the concept of "lithium ion", which is associated with substituting cathodic metallic lithium using an alternative intercalation composite, has been investigated during 1980s. In spite of the subsequent decrease of capacity, such strategy has been efficiently conducted and further dominated the market of portable electronics.

14.2.3 Conventional LIB

As already discussed, the exploitation of LIBs has been boosted due to their natural evolution from lithium metal technology. The primary lithium batteries have been used as a commercial product since the 1970s [24]. Their characterization and categorization have been considerably described in numerous publications and hundreds of books. Efforts toward developing rechargeable lithium batteries with metallic lithium anodes have accompanied with the investigation of lithium batteries from their early stages. Nonetheless, several commercially available secondary lithium (metal) batteries came into existence during the early 1990s [25]. These products were composed of Li–MoS_2, Li–Li_xMnO_2 and Li–TiS_2 systems (metallic lithium as an anode; MoS_2, Li_xMnO_2 & TiS_2 as cathodes). The Li–Li_xMnO_2 system, which has been investigated by Tadiran Inc. (Israel) during the mid-1990s, was used in commercial AA batteries utilized for powering cellular phones. In comparison, Li–TiS_2 and Li–MoS_2 systems could not perform as the commercial products because of the safety issues. Even though the Li-Li_xMnO_2 system has been regarded to be safe because of the intrinsic safety mechanisms, it cannot be broadly utilized owing to the prolonged charging duration to obtain the extended cycle life (several hours per cycle). From the early stages of investigation towards LIBs, it has been apparent that transition metal oxides (TMOs) and sulfides (TMSs) are capable of acting as extraordinary reversible anode materials for rechargeable lithium-ion batteries [18, 26–29]. The evolution of LIB technology, which allowed the commercialization of the rechargeable, high-performance batteries to dominate the market, has been achieved because of the introduction of graphite as the anode material rather than metallic lithium along with the utilization of lithiated transition metal oxide as the cathode materials ($LiMO_2$ as the lithium source within the cell).

Among these emerging systems, graphite-$LiCoO_2$ served as the predominant LIB system which even currently powers most of the portable electronic devices such as laptops, cellular phone, and digital cameras [18, 30]. Within this cell, the $LiCoO_2$ electrode is used as the cathode and graphite as the anode, together with $LiPF_6$ dissolved into the mixture of propylene carbonate and diethyl carbonate as the electrolyte. Figure 14.2 shows the oversimplified schematic of the LIB, where the electrodes are composed of the active species (C or $LiCoO_2$), a metal current collector and the additives (usually different kinds of carbon) which can enhance the electric conductivity, mechanical strength, adhesion and increased

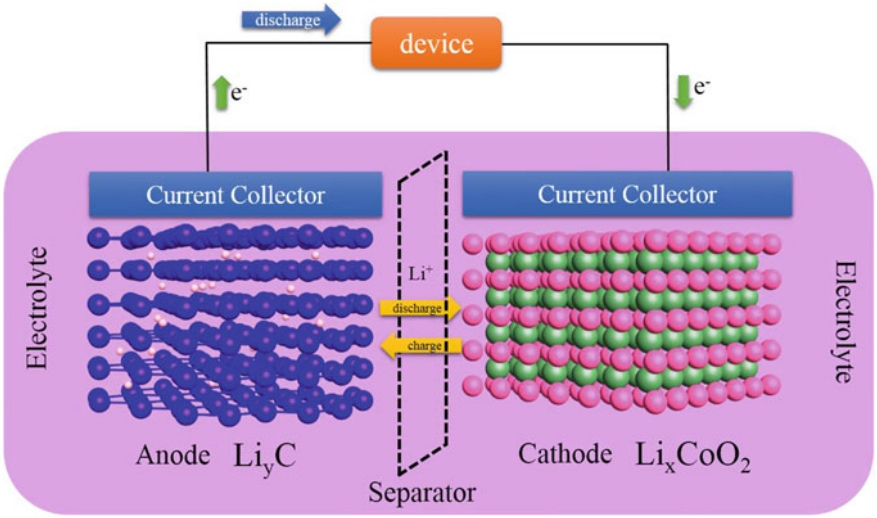

Fig. 14.2 The operation principle of the first commercialized lithium-ion batteries. Lithium ions migrate back and forth between the anode and cathode electrodes upon discharging–charging processes via the electrolyte, electrons doing so similarly via the outer electrical circuit

processability. The electrodes have been separated through the microporous polypropylene or polyethylene film and the entire system has been filled with the electrolyte.

Figure 14.2 shows the basic LIB system where the typical reactions are the reversible lithium-ion intercalation-extraction reactions between two layered composites of the anode and the cathode. The cathode reactions can be:

$$\mathrm{LiCoO_2} \rightleftharpoons \frac{1}{2}\mathrm{Li^+} + \frac{1}{2}\mathrm{e^-} + \mathrm{Li_{0.5}CoO_2} \tag{14.1}$$

The upper potential of the delithiation toward $LiCoO_2$ is restricted to 4.2 V (vs. Li/Li^+), which indicates that only half of the cathodic theoretical capacity ($\sim$140 mA h g^{-1}) is extracted from the reaction which is mainly first-order phase transition between $Li_{0.5}CoO_2$ and $LiCoO_2$ [6]. As discussed above, the lithium source in these LIBs is the cathode material, which leads to a remarkably prolonged shelf life as well as outstanding safety property, in comparison with metallic lithium-based batteries. The first process within the battery is usually the charging process, namely, delithiation and oxidation of the $LiCoO_2$ cathode in parallel with the lithiation and reduction of the graphite anode. Graphite reversibly intercalates with lithium ion to achieve LiC_6 as the final product through the following process:

$$C_6 + Li^+ + e^- = LiC_6 \tag{14.2}$$

The lithium-ion insertion into graphite takes place in stages including LiC_{24}, $LiC_{27,}$ and LiC_{12} through first-order phase transition reactions between the various stages [16]. During the charging–discharging processes, lithium ions are forced to be shuttled between the anode and the cathode through the nonaqueous electrolyte which is sandwiched between two electrodes (Fig. 14.2). During the discharging process, lithium ions are extracted from the cathode material, whose working potential is usually higher than 2.0 V (vs. Li/Li^+), and are inserted into the anode material, whose working potential is typically lower than 3.0 V (vs. Li/Li^+). Within an ideal LIB, lithium ions are reversibly shuttled between the anode and the cathode with 100% efficiency, and there are no side reactions during the charging–discharging processes. However, in reality, the columbic efficiency is generally lower than 100%, and some side reactions between the electrode and electrolyte always take place during normal cell operation and abuse conditions. For example, as the battery is charged, an oxidative transition metal oxide can be achieved on the anode, and the reductive lithiated graphite is formed on the cathode [31]. These side reactions can deliver several negative impacts on the battery performance. Firstly, they consume available lithium ions as well as the active electrode materials, leading to the gradual decrease of overall capability. Such phenomenon is technically named as capacity fading. Additionally, several by-products which deposit onto the active electrode material typically increase the energy barrier toward the charge-transfer process at the surface of electrode, leading to the capacity fading during the high rate process. Lastly, these side reactions are able to be kinetically promoted with enhanced temperatures or under execrable conditions and deliver large amounts of heat within a short period of duration. In such situation, fire or even explosion can possibly take place. Therefore, within the practical LIBs, such side reactions should be kinetically slow within ambient conditions to enable an appropriate battery lifespan as well as thermal stability.

14.2.4 Electrode Materials for LIBs

Considerable efforts have been made toward enhancing the already incomparable LIB performance at all level. Resultantly, this technology is desirable to enter into novel applications, along with enhancing its market share in portable electronics. Generally, continuous improvements typically depend upon electronics and engineering breakthroughs which are essentially derived from novel materials as well as chemical reactions [32, 33].

14.2.4.1 Insertion Electrodes

Metal oxides for Cathode—Researches toward insertion composites have been considerably investigated, in which major efforts have been made towards cathode materials [34]. Besides the composites present within the first generation of LIBs, two novel electrode materials have currently been realized into commercial products: $LiFePO_4$ as the cathode as well as $Li_4Ti_5O_{12}$ at the anode [35]. Even though they cannot overcome the drawback of one electron per active 3d metal, both species also deliver significant predominance in terms of cost, safety, and toxicity. $LiFePO_4$ was first found to be a potential electrode material during 1997. Subsequently, it received the fastest development from the research to commercialization. Such compound delivers an olivine framework comprised of $PO4^{-3}$ tetrahedra with divalent iron in corner-shared octahedral positions and lithium ion located in chains of edge-shared octahedra. Even though the redox property of such compound is dependent upon the Fe^{2+}/Fe^{3+} couples, its operating potential ($\sim$3.4 V vs. Li/Li^+) can be remarkably higher in comparison to that of iron oxide because of the enhanced energy of the M–O covalent bonds, providing enhanced energy at the Fermi level. $FePO_4$ can be formed after the oxidizing process, within a two-phase reaction which leads to the capability of $\sim$160 mA h g^{-1}, with little capacity fading after prolonged cycling processes. Although the original lower electronic conductivity of $LiFePO_4$ has been regarded as a barrier toward its practical utilization, such problem has been resolved via coating the carbon thin film on the surface of $LiFePO_4$ particles. The tremendous enhancement in performance at high current densities has allowed the $LiFePO_4$ to be the commercial LIB electrode material as well as the extension toward lithium-ion technique for the application of portable electronics. Due to the fact that LIB safety is dependent upon the thermodynamic stability of electrode materials in terms of the electrolyte, electrode materials undergoing at the mild potential can be initially safer. Regarding that, the relatively lower operating potential of $LiFePO_4$, along with its lower toxicity, enables it to be an extraordinary cathode material in LIBs. Additionally, similar attention has also been drawn towards $Li_4Ti_5O_{12}$. Such compound delivers a defect spinel framework which can be expressed as $Li[Li_{1/3}Ti_{5/3}]O_4$ and can accommodate lithium ions reversibly toward achieving the rock salt-type phase $Li_2[Li_{1/3}Ti_{5/3}]O_4$ within a heterogeneous process occurring at the potential of 1.55 V (vs. Li/Li^+). With its cell parameters almost equal to those of $Li[Li_{1/3}Ti_{5/3}]O_4$, such composite has been named as the zero-strain insertion material. In spite of its lower capacity ($\sim$150 mA h g^{-1}) in comparison with graphite, the great capability at high current densities, along with the safety enhancement because of the higher potential without formation of SEI layer, makes it an attractive material for practical LIB application for transport applications. Besides the above-discussed composites, other phosphates, including $LiMnPO_4$ and $LiCoPO_4$, and spinel derivatives, such as $LiNi_{0.5}Mn_{1.5}O_4$, silicates, including $LiFeSiO_4$, and other titanium oxides, containing all polymorphs of TiO_2 can be insertion electrode materials that have currently received the research interest of the LIB scientific community [36].

Both $Li_4Ti_5O_{12}$ and $LiFePO_4$ exhibit a heterogeneous insertion reaction mechanism, which induces that their potential remains constant within the entire operation range. Nonetheless, the question whether heterogeneous insertion mechanisms can be intrinsically better towards utilizations has still not been thoroughly solved. Generally, homogeneous processes are initially inclined to achieve rapid kinetics as well as architectural stability with the composition-dependent potential as the trade-off. Nonetheless, such potential variation can possibly serve as an expectable property toward large-scale LIBs, because the detection towards the state of battery charge can be much easier and hence the electronic devices for battery management can be much simpler. In terms of that, it is noticeable that the redox mechanism is not required to be regarded as the intrinsic invariable toward the specific composite. For instance, a conversion from heterogeneous toward homogeneous intercalation-deintercalation mechanisms can be achieved via modifying the particle diameter as well as ion ordering.

Nano-carbons for anode—Carbonaceous materials serve as the most favorable anode materials for LIBs, especially graphite. They are capable of avoiding the formation of lithium dendrite via reversible intercalation of lithium ion into carbon host lattice, which delivers great safety and cyclability toward LIBs. Nonetheless, graphite can only deliver a limited theoretical capacity of 372 mA h g^{-1} since most Li-intercalated graphite only provides a stoichiometry of LiC_6. In order to enhance the energy and power densities of LIBs, nanostructured carbonaceous materials, typically including one-dimensional (1D), two-dimensional (2D), and three-dimensional (3D) porous carbon-based anodes, have been developed to achieve more active sites for lithium ion storage.

The development of 1D carbon materials, especially carbon nanotubes (CNTs), is stimulated because of the high specific surface area (SSA) and extraordinary surface activities for high-performance LIBs. It has been found that CNTs can provide lithium ion intercalation between graphitic layers of the CNT walls. The capacity of CNT anodes can be higher than 460 mA h g^{-1} and achieve 1116 mA h g^{-1} via various treatments [37–39]. Nonetheless, the Coulombic efficiency of CNTs was found to be lower as compared with that of graphite due to the introduction of a large amount of structural defects. To date, various CNTs via different approaches have been applied as LIB anodes. The Columbic efficiencies of these anodes were enhanced by the high lithium ion intercalation towards CNT walls, the large number of active sites and fast electron transfer rate.

Graphene, a single-layer carbon sheet with a hexagonal lattice, has also received considerable interests for utilization of LIB anode materials due to its intriguing mechanical, physical, and chemical features, especially its ultrahigh SSAs, excellent thermal and electronic conductivities, structural flexibility, and unique porous structure. Additionally, graphene holds a remarkable Li-storage capability, since lithium ions are able to be bound not only on both sides of graphene, but also on the defects and edges of graphene. Hence, it has been found that graphene and graphene-based composites can deliver improved LIB performances than that of graphite. Currently, the LIB performances of graphene have been largely investigated. For instance, Guo and co-workers [40] utilized chemically fabricated

graphene as LIB anodes to evaluate the electrochemical property. These 2D anodes can be preserved at about 502 mA h g^{-1} after 30 cycles [40].

Porous carbons with various pore sizes serve as favorable anode materials for LIBs because of the high SSAs and porous architectures. The attractive features of such materials are the effective diffusion pathways for Li ions due to the formation of percolation networks from interconnected nano-pores, reasonable electrical conductivity provided by the well-interconnected carbon walls, large amounts of active sites for Li storage, and minimized mechanical stress for volume expansion/contraction during Li intercalation/deintercalation. Because of these unique merits, porous carbons often show prominently increased capacities in comparison with traditional graphitic carbons. There are three types of porous carbons, i.e., microporous (pore size < 2 nm), mesoporous (2 nm < pore size < 50 nm), and macroporous (pore size > 50 nm) carbons. Among them, microporous carbons have delivered higher capacities than conventional graphitic carbons. Mesoporous carbons have also been applied as anode materials for LIBs. Zhou and co-workers fabricated 3D-ordered mesoporous carbon structures with a reversible capacity of 1100 mA h g^{-1}, which was ascribed to the localized graphitic structure and the ordered porous architecture [41]. Su and co-researchers have also synthesized ordered macroporous carbons via template-based methods. Such anodes delivered the capacity of 320 mA h g^{-1} with capacity retention of 98% over 60 cycles [42].

Alloying

Besides the development of insertion materials, other electrode compounds which react with lithium ions through different mechanisms have also been considerably investigated. The major advantage of these reactions can be the remarkable enhancement of electrochemical capability, but the major disadvantage is that those values can be realized with the sacrifice of essential architectural expansion. Moreover, it is difficult for the related electrode materials to accommodate such changes, even after introducing sophisticated additives and binders. Thus, it will lead to the performance penalties, including a quite short cycling lifespan and a considerable potential hysteresis. Here, we will introduce the electrode compounds with different insertion–extraction mechanisms.

The illustration that electrochemical alloying process between metallic/semimetallic elements and lithium can be possible at mild condition within nonaqueous electrolytes has been proposed simultaneously with the extensive investigations for intercalation materials during the 1970s. Several decades later, the progress towards both kinds of composites in practical utilizations has been considerably different. In spite of the fact that the capabilities based upon alloying processes can reach the excellent values of 4.2 A h g^{-1} and 8.5 A h cm^{-3} for silicon, their practical application towards secondary batteries is largely prevented due to the remarkable volume expansion which are accompanied with the alloying reaction [43]. For instance, the reaction between lithium and tin to achieve $Li_{4.4}Sn$

induces the 440% of increase towards the number of atoms within each particle, which results in a large volume expansion and subsequently leads to the contact loss between the current collector and the grains, as well as the disintegration of the electrodes, therefore causing considerably depressed cycling performance [44].

The most intriguing anode materials, because of their cost-efficiency, high abundance, and highly theoretical capability, are typically tin- and silicon-based composites. Typically efficient cycling process, with the compromise of subsequently lower capabilities, has been delivered via various methods which are usually aimed at restricting volume expansion. These researches are not supposed to be neglected in terms of the applications because they have realized tin electrodes towards entering the market. Recently commercialized LIB consists of Sn–Co nanoparticles wrapped via amorphous carbon as the anodic material. Such framework relieves the considerable volume expansion due to the alloying reaction of lithium ions with tin, whereas the cobalt introduction can be advantageous in inhibiting the formation of crystalline phase [45]. Such LIB delivers the 30% enhancement in capability and better rate performance as compared with traditional LIB technology, but still suffers from lower cyclability.

Conversion

The term "conversion" reaction is typically utilized to define the reaction containing the binary transition metal composite, M_aX_b (M = transitional metal and X = N, O, F, P, S etc.), with lithium to achieve metallic nanoparticles embedded into a matrix of Li_yX. These reactions are involved in the entire reduction of the transitional metal ion towards its metallic phase, providing higher capabilities. The research interests towards compounds for conversion reactions have been rapidly enhanced recently after their high reversibility and cycling stability have been demonstrated during the 2000s [46]. Noticeably, a large number of transition metal composites which cannot deliver vacant sites within their framework to enable the intercalation of lithium ion have not been considered as the electrode materials. Nonetheless, they have been demonstrated to achieve tremendously higher capabilities which are attributed to conversion processes.

The reaction potential increases with the M–X ionic bonding intensity, which is typically in the range from 0.5 to 1 V. Fluorides serve as the major exception, which can react at the considerably high potential value of $\sim$3 V, allowing their utilization as the cathode materials. Generally speaking, the essential disadvantage towards the practical utilization of those binary composites should be the enlarged potential hysteresis, which can be observed during charging–discharging process, resulting in inferior Coulombic efficiency. Even though the comparative thermodynamic and kinetic contributions of such hysteresis have not been demonstrated yet, the corresponding magnitude has been investigated to enhance with the increased anionic electronegativity and to reduce with the decreased ionic conductivity of the lithiated framework. Such impact can be more predominant during the first cycle, possibly associated with the enhanced crystallinity of the intrinsic

material in terms of the amorphous feature of the binary hybrid achieved after the first charging process [47]. The above-discussed challenges serve as the essential obstacle towards the practical utilization of conversion electrode materials into commercial products, along with their mild cyclic lifespan. However, it can be obvious that, in comparison with alloying and insertion materials, such composites have just drawn the research interests recently, which seems to bring about approaches to circumvent these issues [48]. For example, the mixture containing conductive components into the electrode fabrication has enabled the total application of badly conductive fluorides as the electrode materials, whereas the introduction of nano-structural current collectors has delivered excellent power densities via applying Fe_3O_4 as an electrode material [49].

14.3 Supercapacitors (SCs)

Recently, SCs have received considerable research interest, typically because of their outstanding power density, prolonged cyclic lifespan, as well as bridging nature towards the gap between conventional dielectric capacitors with high power density and batteries with high energy storage [50]. The earliest electrochemical storage (ES) has been patented during 1957. Nonetheless, SCs began to receive a few interests for the hybrid electric vehicles (HEVs) application from the 1990s [51]. Generally, it has been observed that the major function of SCs can rapidly charge the battery within HEVs to deliver the necessary power for acceleration and brake [52]. Further investigations have contributed to the recognition that SC can serve as an essential candidate towards complementing batteries during their energy storage utilization through delivering spare power supplies for protecting against power disruptions. Resultantly, the US Department of Energy has proposed that SCs can become essential as batteries towards the next-generation energy storage devices [53]. Most other governments as well as enterprises have also devoted resources and efforts in exploiting, investigating, and progressing SC-based technology and science. Recent decades have witnessed considerable development of SC in both theoretical and experimental researches, as indicated by a tremendous number of technical reports and research articles. Meanwhile, the disadvantages of SC, such as relatively lower energy density as well as higher processing expenses, have already been suggested as the major obstacle towards the promotion of SC technologies.

In order to address the above challenges, one of the most promising strategies is to develop novel materials for SC electrodes. Among all the investigated materials, carbon-based electrodes are the most favorable candidate, which delivers large SSAs for charge storage. However, despite high SSAs, the charges stored physically onto the carbon particles within porous electrode layers are disappointingly restricted. Such kind of SC, named as electrostatic double-layer capacitor (EDLC), delivers the limited specific capacitance and relatively lower energy density. Further methods for enhancing the SC energy density has been provided via hybridizing the

electrode materials through introducing electrochemically active materials for the electrode layer based upon carbon particles or totally replacing the carbon-based materials with electrochemically active species. SCs with electrochemically active composites as the electrodes are typically named as pseudocapacitors or faradic capacitors (FCs). Noticeably, it has readily been proven that FCs and hybrid SCs are capable of delivering considerably enhanced capacitances along with higher energy densities as compared with that of EDLCs [54].

In terms of the novel SC composites, metal oxides containing manganese oxides and ruthenium oxides have been regarded as the most promising materials for the future SC. Hence, we will pay specific attention towards metal oxides as well as their utilization in SC electrodes but firstly we provide some basic information about the SC.

14.3.1 Fundamentals of Supercapacitors (SCs)

Since SC belongs to one type of charge storage devices which is quite similar with LIBs in designing and producing. As exhibited in Fig. 14.3, the SC is composed of an electrolyte and two electrodes, together with the separator which electrically separates both electrodes. Generally, the most essential part of the SC should be the electrode material. The SC electrodes can be prepared through nano-sized materials which can deliver large specific surface area as well as highly porous architecture. It can be observed in Fig. 14.3 that charges are accumulated and isolated at the interface between the electrolyte and the conductive particles such as metal oxide particles and carbon particles. Such interface has been considered as the capacitor with the electrostatic double-layer (EDL) capacitance, with the capacitance given by the following equation:

$$C = \frac{A\varepsilon}{d} \tag{14.3}$$

where A is the surface area of the electrode, which needs be the active surface area of the electrode; ε is the dielectric constant of the electrolyte, which is equal to 1 for the vacuum and larger than 1 for any other medium; and d denotes the effective EDL thickness.

As already mentioned, there are two kinds of SCs. One can be the EDLC, within which the electrode materials, especially carbon particles, are electrochemically inert. Therefore, no electrochemical reaction takes place on the electrode material during the charging–discharging processes, and there is only physical charge accumulation at the interface between the electrode and electrolyte. The other type with the electrochemically active material electrode, typically based on metal oxides, is capable of storing charges directly during the cycling processes [55].

The capacitance of the electrode in an EDLC can be ascribed to an accumulation of electrostatic charges at the interface between the carbon particle and the

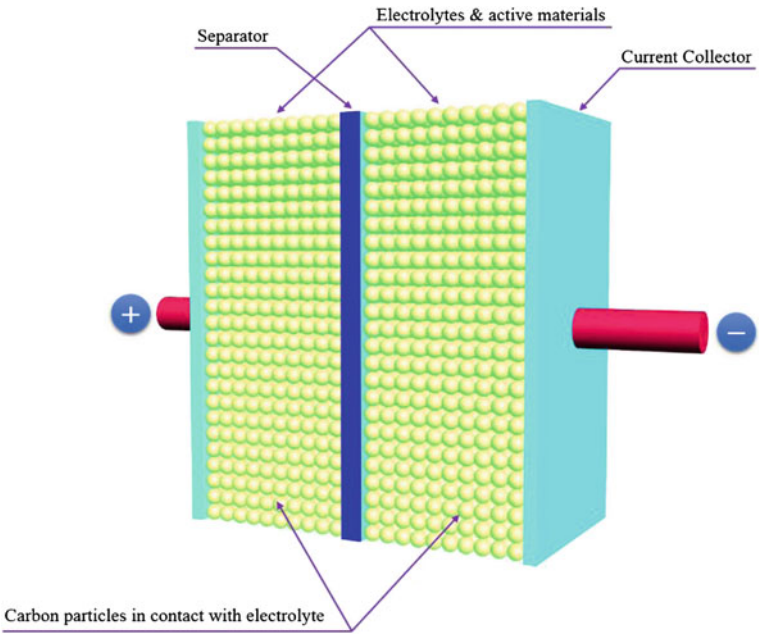

Fig. 14.3 Schematic of a single-cell double-layer capacitor

electrolyte, which is dependent on the electrode potential. The mechanism towards charge generation onto the electrode surface can be the surface dissociation and ion adsorption from both the crystal lattice defects and electrolyte [53]. These processes can be achieved via the electrostatic storage of surface charges. According to Fig. 14.3, such EDL capacitance is derived from electrode materials, particularly at the interface between the electrolyte and carbon particles, where excessive charges can be stored onto the surfaces of electrodes. Meanwhile, electrolyte ions with counter-balancing charges can be delivered onto the electrolyte to achieve electro-neutrality. During the charging process, electrons move from the cathode toward the anode via an external circuit. Additionally, cations travel to the anode and simultaneously anions travel to the cathode in the electrolyte. During the discharging process, the reverse processes can occur. Within such kind of SC, no charge transfer takes place across the interface between the electrolyte and the electrode, and no excessive ion exchanges occur between the electrolyte and the electrode. This induces that during charging–discharging processes, ion concentration of the electrolyte keeps constant. In terms of that, energy can be accumulated into the double-layer interface.

If the surfaces of two electrodes can be written as S_{C1} and S_{C2}, a cation as C^+, an anion as A^-, and the interface between the electrode and electrolyte as //. Hence, the electrochemical processes towards charging–discharging process can be shown through the following reactions [56].

$$S_{C1} + A^- \overset{\text{charging}}{\rightarrow} S_{C1}^+ // A^- + e^- \tag{14.4}$$

$$S_{C1}^+ // A^- + e^- \overset{\text{discharging}}{\rightarrow} S_{C1} + A^- \tag{14.5}$$

On the other electrode (negative electrode):

$$S_{C2} + C^+ + e^- \overset{\text{charging}}{\rightarrow} S_{C2}^- // C^+ \tag{14.6}$$

$$S_{C2}^- // C^+ \overset{\text{discharging}}{\rightarrow} S_{C2} + C^+ + e^- \tag{14.7}$$

And the overall charging–discharging process can be exhibited as the following reactions:

$$S_{C1} + S_{C2} + A^- + C^+ \overset{\text{charging}}{\rightarrow} S_{C1}^+ // A^- + S_{C2}^- // C^+ \tag{14.8}$$

$$S_{C1}^+ // A^- + S_{C2}^- // C^+ \overset{\text{discharging}}{\rightarrow} S_{C1} + S_{C2} + A^- + C^+ \tag{14.9}$$

On the other hand, the FCs are totally different from the EDLCs. When a potential is introduced toward a FC, reversible and rapid redox reactions will occur onto the electrode materials and are involved in the charge exchanges across the double layer, which is similar to the charging–discharging processes within LIBs, leading to the faradaic current passing through the overall SC. Materials processing these redox reactions contain conducting polymers as well as several metal oxides such as RuO_2, Co_3O_4, and MnO_2 [57–59]. Three kinds of faradaic processes can take place at FC electrodes: (i) reversible adsorption such as hydrogen adsorption on the platinum/gold surface, (ii) redox reactions of transition metal oxides such as RuO_2, and (iii) reversible electrochemical doping and de-doping within conductive polymer-containing electrodes.

As considerably investigated, those faradaic reactions can both extend the operating potential as well as enhance the capacitance of the overall SCs [60]. Due to the fact that the electrochemical processes take place not only on the surface but also in the bulk near the solid electrode surface, the FC can deliver much higher capacitance values as well as energy density than that of the EDLC. As investigated by Conway and co-workers, the capacitance of an FC can be usually 10–100 times higher than the value of an EDLC [61]. Nonetheless, FCs typically experience comparatively decreased power density as compared to EDLC since non-faradaic processes are usually faster than faradaic processes. Additionally, since redox processes take place at the electrode, the FC is often short of stability during cycling, which is similar to LIBs [62].

Noticeably, the hybrid SC with the asymmetrical conformation, in which one electrode is comprised of the faradaic capacitance material and the other contains the electrostatic carbon material) have been tremendously investigated currently to make the most of the advantages of both electrode materials in enhancing entire

voltages, powers, and energy densities [63]. In such kind of hybrid SC, both the faradaic capacitance and EDL capacitance mechanisms simultaneously occur, whereas one of these mechanisms serves as the major part. Within both mechanisms, suitable pore-size distribution, large SSA, and high conductivity act as crucial features of the electrode materials to deliver highly specific capacitance.

14.3.2 Advantages and Challenges of SCs

14.3.2.1 Advantages of SCs

In comparison with LIBs, SCs are capable of providing the following advantages:

(i) *Higher power density*—Fig. 14.4 exhibits the comparison between power density and energy density of current energy storage devices. It has been observed that SCs can provide a considerably higher power delivery from 1 to 10 kW kg^{-1} as compared with that of LIBs ($\sim$150 W kg^{-1}). Due to the fact that SC can accumulate charges both in the bulk close to the electrode surface as well as at the electrode surface, instead of in the total electrode, charging–discharging processes cannot be restricted through ionic transfer into the inner components. Therefore, the charging–discharging rates can be remarkably faster as compared to the faradic processes within LIBs. These ultrafast rates are able to display high power density of SC. The SC is able to be totally charged just in several seconds ($\sim$30 s), and the charged energy can be rapidly extracted from it ($\sim$0.1 s) [64].

(ii) *Longer life expectancy*—The electrochemical energy storage within LIBs can be achieved via redox processes, which is usually involved in the irreversible conversion of the electrolyte and the electrode. Comparatively, in terms of energy, within the SC, only little amounts of redox reactions are associated with charging–discharging processes, so that the SC is capable to displaying almost unrestricted cyclability. Moreover, SCs require little maintenance during their lifespans and can tolerate a large number of

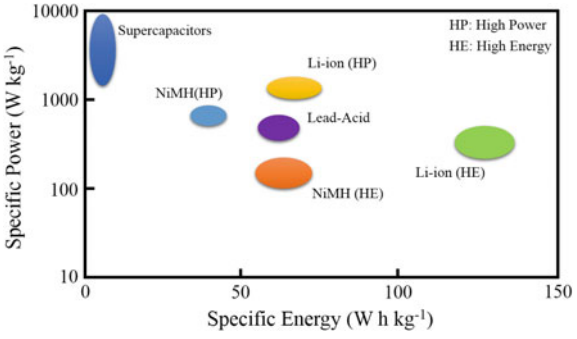

Fig. 14.4 Specific power versus specific energy of modern storage devices

charging–discharging processes even up to 1×10^6 cycles. The SC is capable of undergoing with high current density discharges for about 5×10^5–1×10^6 cycles with the little conversion of their features. LIBs cannot achieve such longevity even though the discharging depth can be achieved as low as 10–20% of the total energy. Moreover, the SC lifespan has been evaluated to be at least three decades, much longer than that of LIBs with only 5–10 years. Even for FCs, although the rapid faradic processes are associated during cycling processes, their lifespan can still be considerably longer as compared to LIBs [60, 65, 66].

(iii) *Longer shelf life*—Long shelf life also serves as one of the essential advantages in SCs. Most LIBs can become useless once let without usage for several months because of self-discharging process along with corrosion. For comparison, SCs are capable of preserving their capacitance and therefore can be recharged towards their intrinsic condition, although the self-discharging process for a long duration can result in the lower potential. It has been demonstrated that SCs can be located without any usage for several years but still maintain close to their initial capability [66].

(iv) *High efficiency*—The charging and discharging processes within ESs are reversible through their entire operating potential range, and the energy loss toward heat generation during cycling is comparatively smaller and can be neglected, which indicates that the cyclic efficiency of SC is much higher even with operating power density above 1 kW kg^{-1}.

(v) *Broad operating temperature range*—SCs are capable of working efficiently at extensively low and high temperatures. The particular operating temperature of SC is in the range of −40–+70 °C, beneficial towards military applications, in which dependable energy storage has been demanded undertaking specific electronic devices within any conditions.

(vi) *Environmental friendliness*—Generally, SCs contain little toxic and hazardous species, and the corresponding waste materials can be readily disposed.

(vii) *Safety*—Within common conditions, SCs can be significantly safer than LIBs.

14.3.2.2 Challenges for SCs

Even though SCs can provide lots of advantages over LIBs, they also suffer from several drawbacks at the current technological stage.

(i) *Lower energy density*—SCs typically suffer from inhibited energy density ($\sim$5 W h kg^{-1}) in comparison to LIBs (>50 W h kg^{-1}), as exhibited in Fig. 14.4. Commercial SCs only deliver energy densities of $\sim$3–4 W h kg^{-1}. When the higher energy capability is demanded towards a specific application, the larger SC needs to be used, considerably increasing the expenses. Therefore, lower energy density serves as an essential issue towards SC utilization within the short future.

(ii) *Higher expenses*—The expenses of materials and the related manufacturing have still been the primary issue towards SC commercialization. The critical costs of the SC are derived from the electrode materials. Currently, in terms of practical applications, RuO_2 and carbon materials serve as the most commonly utilized electrode materials for commercial SC. Nonetheless, carbon architecture, particularly those with high SSAs, are currently quite expensive ($50–100 per kg), even without mentioning the costs of rare metal oxides including RuO_2. Additionally, the electrolyte and the separator can also largely enhance the expenses. Notably, if organic electrolytes are applied into SC, the entire expenses will be even more.

(iii) *Highly self-discharging rate*—SCs can only display a relatively lower charge storage duration because of the high self-discharging rate (10–40% per day) [67]. In term of some specific applications, this can be regarded as the critical obstacle toward their practical utilization.

(iv) *Industrial criteria toward commercialization*—At present, carbon-based SCs achieving the capacitances from 50 to 5000 F have been accessible for commercial applications and the corresponding electrolyte utilized in these types of SCs is acetonitrile, delivering the typical energy density of 4 W h kg^{-1} with the cell voltage of 2.7 V. Even though such type of SC can be commercially accessible, it should be essential to provide generally available industrial criteria including electrode architecture, capability, porosity, and electrode thickness. Nevertheless, because of limited commercial products along with various applications, general industrial standards of SC have not been formulated. Typically, Gore's commercial electrode can possibly provide us several ideas what the reasonable standards are. Gore's electrode, fabricated via coating the activated carbon (AC)-PTFE hybrid onto the etched aluminum collector, can deliver the BET surface density of $\sim$1800 m^2 g^{-1}, the thickness of 0.3 mm as well as the average pore diameter of $\sim$2 nm [68]. As a matter of fact, the requirement towards electrode thicknesses is supposed to be largely based upon the SC applications. In power sensitive utilization, the thickness can possibly be $\sim$100 μm whereas in energy sensitive utilization, the coating can be controlled at $\sim$150 μm. Hence, it is indispensable to devote considerable efforts on SC standard establishment for various applications.

14.3.3 Electrode Materials

As already mentioned, the specific capacitance of SC mainly relies upon the selected electrode materials. Hence, further development of novel materials with highly specific capacitance and enhanced cycling performance is the most promising strategy to resolve these issues [69].

Noticeably, the specific capacitance of SC remarkably relies upon the SSA of the electrode materials. Due to the fact that not all the SSA is electrochemically available as the material is connected with the electrolyte, the practical capacitance of different materials cannot enhance linearly with the increased SSAs. Therefore, for those electrochemically available SSAs, the definition named as the active surface area should be much more accurate towards expressing the electrode capacitance. Moreover, the pore size distribution within the electrode material serves as the essential candidate towards the active surface area. According to Largeot and co-workers, the pore size within electrode materials which could achieve the highest EDL capacitance should be almost equal to the ionic size within the electrolyte, and both smaller and larger pore sizes result in a tremendous drop in capacitance [50]. The increase of the pore size will also enhance the average length between the center of ions and pore walls, achieving the decreased capacitance with larger pores. Both pore sizes and pore-size distribution affect the overall SSA and hence the capacitance of the electrode.

Generally, the electrode materials within SCs can be divided into three kinds [70]: (i) carbon materials with high SSAs [71], (ii) conducting polymers [72, 73], as well as (iii) metal oxides, including MnO_2, RuO_2, NiO, SnO_2, Co_3O_4, Fe_2O_3, and MoO_3 [74–78].

14.3.3.1 Carbon Materials

Carbon materials have been regarded as the promising SC electrode materials towards industrialization as they deliver advantages such as abundance, cost-efficiency, easy processability, nontoxicity, higher SSAs, great electric conductivity, high chemical inertness, as well as broad operation temperature range [60]. Apparently, carbon-based SCs are quite close to EDLCs. Typically, carbon architectures can accumulate charges largely via the EDL achieved at the electrode–electrolyte interfaces, instead of collecting them within the bulk of carbon materials. Thus, the specific capacitance tremendously relies upon the SSAs which are available to the electrolyte ions. The essential parts which affect their electrochemical performance are the pore-size distribution, SSAs, pore structure and shape, electric conductivity, and surface functionalization. Among these, pore-size distribution and SSAs are the two indispensable characteristics impacting the overall capability of carbon structures for SC. As investigated, the carbon for double-layer type supercapacitors must deliver three features: (i) high SSAs of at least 1000 $m^2\ g^{-1}$, (ii) great conductivity in porous architectures, and (iii) intriguing electrolyte accessibility of carbon materials. In terms of these features, the rule to select electrode materials is to achieve highly accessible SSAs with excellent conductivity.

CNTs, graphene and porous carbon serve as crucial carbon architectures with high SSAs. The performances of these structures as SC electrode materials have

been largely investigated. Generally, carbon materials with larger SSAs deliver higher capabilities for charge accumulation at the interface between electrode and electrolyte. Various approaches have been tried to enhance SSAs, such as alkaline treatment, steam activation, thermal treatment, and plasma treatment. These strategies can efficiently introduce defects and micro-pores onto the surface of carbon materials, resulting in increased SSAs. Sometimes, specific capacitance is not directly proportional to the SSA. It has been reported that pore sizes between 0.4 and 0.7 nm are suitable for aqueous electrolytes [79] while the pore sizes of $\sim$0.8 nm are better for organic electrolytes [80]. The optimal capacitance can be achieved via matching ion size with pore size. Besides highly SSA and proper pore size, surface functionalization has also been regarded as an efficient method to enhance the specific capacitance of carbon architectures. Surface functional groups can contribute to the ion adsorption and thus improve the hydrophilicity of the carbon materials, resulting in rapid ion transport and improved wettability. Hence, the introduction of surface functional groups onto the surface of carbonaceous materials seems to be an efficient strategy to improve the specific capacitance. The functional groups present in carbon matrices usually contain boron [81], nitrogen [82], oxygen [83] and sulfur [84]. Typically, nitrogen introduction has been extensively investigated.

To sum up, carbon materials with high SSAs and appropriate pore sizes are ideal architectures for SCs for high specific capacitance and enhanced cyclic stability. However, their high internal resistances of carbon nanostructures lead to reduced SC performance. Additionally, the surface area inaccessible to electrolyte also restricts the performance of carbon architectures, leading to limited capacitance. It can be believed that future carbon materials are largely developed to achieve higher SSAs, rational pore distribution, as well as moderate surface modification to optimize overall capacitance.

14.3.3.2 Faradaic Materials

As already discussed, electrode materials dependent upon the EDL mechanism can preserve the restricted specific capacitance, especially within the range from 10 to 50 mF cm^{-2} toward the surface of electrodes. Since pseudo-capacitance of FCs can achieve 10–100 times larger than that of EDL-based capacitance, SC composed of redox-active materials are considerably favorable as the future commercial SC [85]. FCs cannot only accumulate charges based on the EDL mechanism, analogues to the traditional SC electrodes, but undertake rapidly reversible faradic reactions on the electrode surface. Hence, tremendous efforts have been provided currently towards investigating electrode materials with pseudo-capacitive property. Such type of material can be typically classified into two kinds: conductive polymers (CPs) and metal oxides/hydroxides.

Conductive Polymers (CPs)

CPs have displayed various advantages, which enables them as the suitable materials for FCs, including cost-effectiveness, higher environmental friendliness, great conductivity during the doped state, wide potential window, excellent capability, as well as controllable reactivity via chemical modification [86–88]. CPs provide capacitive features through the faradic process such as polyaniline (PANI) [89], polypyrrole (PPy) [90] and poly[3,4-ethylenedioxythiophene] (PEDOT) [91]. Once the oxidation process occurs, ions will travel towards the polymeric backbone, and as the reducing process takes place, the ions will be extracted from the backbone to the electrolyte. Such faradic processes within CPs are achieved through the entire materials, not only on their surface. Since the charging–discharging processes are not involved in any structural changes, particularly phase conversion, these processes can be highly reversible.

CPs are able to be negatively or positively charged with ionic insertion into the polymer framework to balance the inserted charge, such as poly(cyclopenta [2,1-b;3,4-b′]dithiophen-4-one)] [92]. Therefore, electronic conductivity can be promoted within these kinds of polymers through reduction and oxidation processes, achieving delocalized π-electrons on the polymeric chains. The oxidizing-reducing processes within the polymers have been defined as "doping-dedoping processes". The positively charged polymers, achieved via oxidizing the polymeric chains, can be named as "p-doped", whereas negatively charged polymers formed through reducing process are defined as "n-doped". Noticeably, the potentials of those processes largely depend upon the electronic state of π electrons.

Metal Oxides/Hydroxides

Generally, metal oxides are capable of delivering larger energy density for SC as compared to traditional carbon materials and higher electrochemical stability than polymer materials. These materials can both accumulate energy like electrostatic carbon materials and deliver faradaic processes between electrolyte ions and electrode materials with proper voltage windows [93].

The typical advantages of metal oxides in SC applications are: (i) they are supposed to deliver outstanding electronic conductivity, (ii) the oxidation states of metal ions should be at least +2, which coexists within a continuous range without phase transition associated with irreversible structural changes of the 3D architecture, and (iii) the protons can enter into the lattice of metal oxides during reducing process and extract from the lattice during oxidizing process without restriction, enabling easy inter-conversion between O^{2-} and OH^{-}. Currently, these largely investigated materials contain ruthenium oxide (RuO_x), cobalt oxide (CoO_x), vanadium oxide (VO_x), nickel oxide (NiO) as well as manganese oxide (MnO_x).

14.4 Low-Temperature Plasma for Syntheses of Energy Materials

Plasmas are generated by providing energy to neutral gas, resulting in the generation of charge carriers (Fig. 14.5) [94]. Ions and electrons can be produced within the gas phase as the photons or electrons with sufficient energy collide with the neutral molecules and atoms of the gas, which can be technically named as the photo-ionization or electron-impact ionization, respectively. A variety of strategies have been achieved to provide enough energy for plasma formation towards the neutral gas. The introduction of thermal energy is one typical approach, particularly in flames, in which exothermic chemical reactions of the molecules can be utilized as the prime energy source. Adiabatic compression of the gas is also able to heat up the molecules and atoms to the ignition point for plasma formation. Another important approach for generating plasma is to supply energy to the gas via energetic neutral beams. Beams composed of neutral particles can deliver the advantage of being unperturbed by magnetic and electric fields, which has been essentially applied for maintaining plasmas as well as heating plasma in fusion devices.

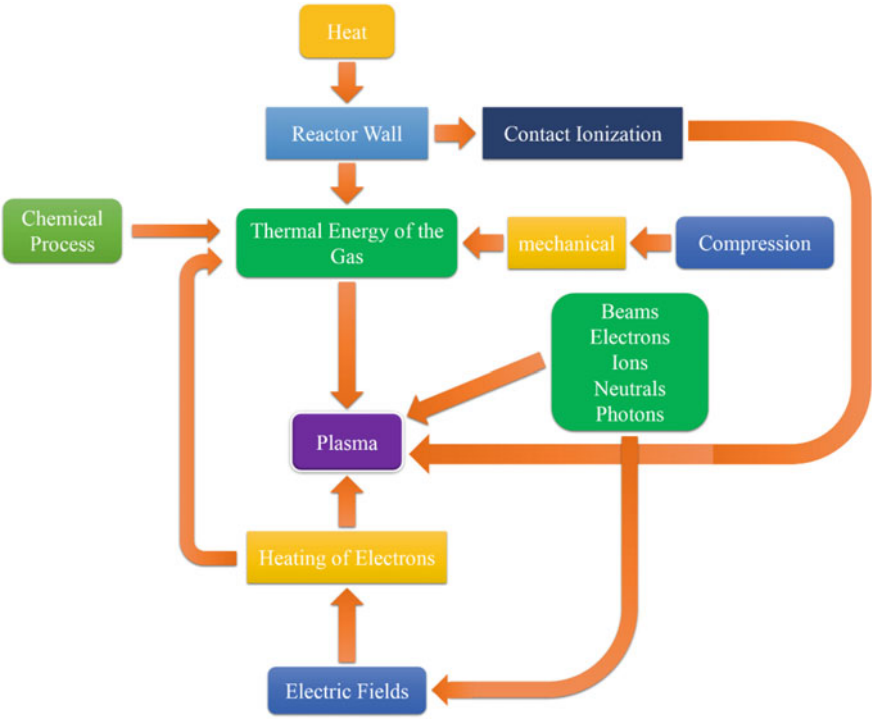

Fig. 14.5 Methods of plasma generation

The most favorable approach towards generating and maintaining a low-temperature plasma for the practical application is via introducing an electric field, either dc or alternating field, to a neutral gas. Almost all the volumes of neutral gases usually include some ions and electrons that are formed, typically, resulting from the interaction of radioactive radiation or cosmic rays with gases. Such free charge carriers can be facilitated via the electric field and new charged particles can possibly be generated when these charge carriers gain energy from the applied electric field and then collide with molecules and atoms within the gas or with the electrode surfaces. This results in a large number of charged particles which can be finally balanced by the loss of charge carriers to form stable plasma.

Plasmas have been used for various applications which are listed in Fig. 14.6. However, different applications require different types of plasma sources with different plasma parameters. For example, plasma source for producing integrated circuits is quite different from plasma source needed for remediating exhaust gases from power stations. There are extensive differences in (i) the physical shape of various plasma sources, (ii) plasma parameters such as density, temperature and ion species and (iii) the temporal plasma behaviors which are achieved in different sources. Figure 14.7 summarizes required technical characters, which are essential for selecting a suitable plasma source for a particular application. In this book, several chapters have already discussed the various methods of producing plasma. So we only very briefly touch upon the production of plasma using varying RF electric field in capacitively and inductively coupled modes, which are most commonly used for applications in material synthesis and processing.

14.4.1 Plasma Production Using Electric Fields

The most broadly utilized approach toward plasma generation uses the electric breakdown of the neutral gas through an externally applied electric field. The charge carriers facilitated within the electric field supply their energy to the plasma through collision with other particles. Electrons can preserve most of the energies during elastic collisions with molecules and atoms due to their small mass and transfer their energies mainly through inelastic collisions. Discharges can be classified as direct current (DC) discharges, alternative current (AC) discharges, and pulsed discharges, which is based upon the temporal characteristics of the exciting electric field.

14.4.2 Radio Frequency (RF) Discharge

Discharges activated and preserved through high-frequency electromagnetic fields are called as RF discharges and have received considerable attention for industrial and technical applications [95].

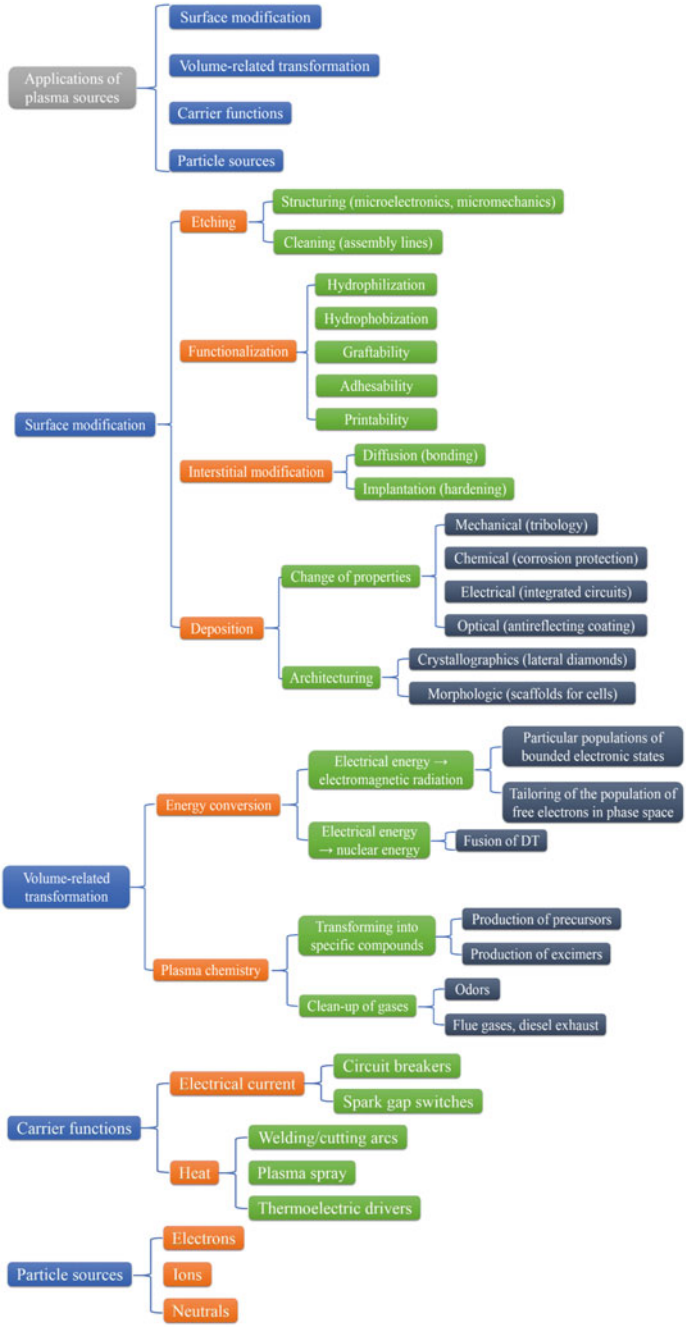

Fig. 14.6 Various applications of low-temperature plasma sources

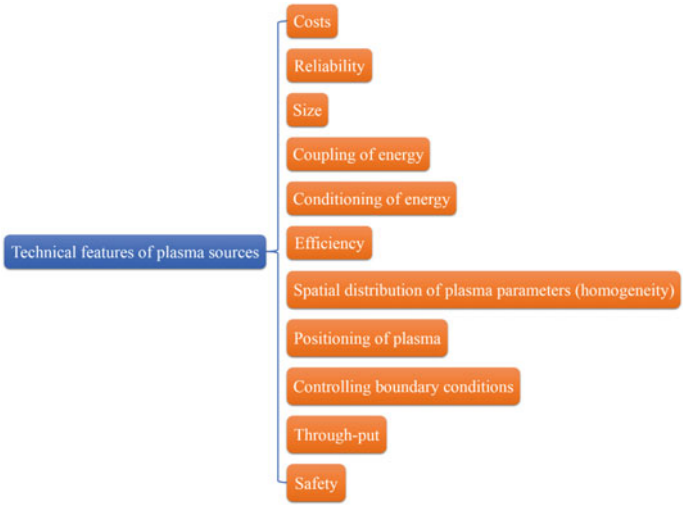

Fig. 14.7 Features of plasma sources for any application

RF plasma discharges are commonly undertaken in the frequency range of 1–100 MHz with the corresponding wavelengths of about 300–3 nm which are much larger in comparison to the dimensions of the plasma reactor. At lower frequencies, the ions facilitated in the field travel towards the electrodes and provide secondary electrons. At higher frequency, the ions and electrons cannot enter onto the electrode surface during the accelerating phase of the external field. The power coupling within RF discharges can be achieved in different methods, including (i) capacitively coupled plasma (CCP) discharges, named as 'E' discharge; and (ii) inductively coupled plasma (ICP) discharges, designated as 'H' discharges.

14.4.2.1 Capacitively Coupled Plasma (CCP) Discharge

The vessel of a CCP is typically built with interior circular disc-shaped parallel electrodes which are separated by the distance of several centimeters. They can be either in contact with the discharge or insulated from it with a dielectric. In terms of insulating chamber walls, the outer electrodes, particularly on the outside of the vessel, have been typically applied. The corresponding gas pressures are usually ranging from 1 to 10^3 Pa. A traditional RF system for preserving a discharge is established in the reactor with the electrodes and a RF generator which is connected to electrodes via an impedance matching network unit. The generator type is required to be licensed according to the frequency band toward commercial usage. A matching network is essential for matching the impedance of the generator to the impedance of the load. This is to ensure that the power can be transferred from the generator to the discharge with the maximum efficiency, in which the reflected RF

power can be minimized, as shown in Fig. 14.8 [94]. The electrodes within the RF discharge are occupied by the sheath regions while the space between two electrodes is covered by the bulk plasma. Within moderate pressures, capacitively coupled RF discharges can be achieved in two types: the α and the γ mode [96]. The α mode corresponds to lower currents and a positive voltage–current characteristic. On the contrary, the γ mode is achieved through higher currents and a negative voltage–current characteristic. Notably, the sheath regions in front of the electrodes are entirely different with the above two modes. The concentration of charge carriers and the electric conductivity within the sheath of α mode are relatively smaller as compared to the γ sheath. In the α mode, there is a weakly luminous region in the center of the gap between two electrodes with the maximum glow intensity in contrast to other regions, while the emission of the γ mode is typically much more intensive. The 'positive column' at the gap center is isolated from the bright 'negative glows' via the 'Faraday dark spaces'. The designations of α and γ modes are provided by the Townsend's first ionization coefficient α toward an avalanche of charge carriers in the volume and the coefficient γ toward releasing secondary electrons from a target surface via the exciting positive ions, respectively.

The alleged self-bias is a unique feature of such kind of plasma. This self-bias, a negative DC potential, can be evolved between the smaller sized powered electrode and the plasma, because of the utilization of a coupling capacitor between the powered electrode and the RF generator as well as the utilization of properly shaped

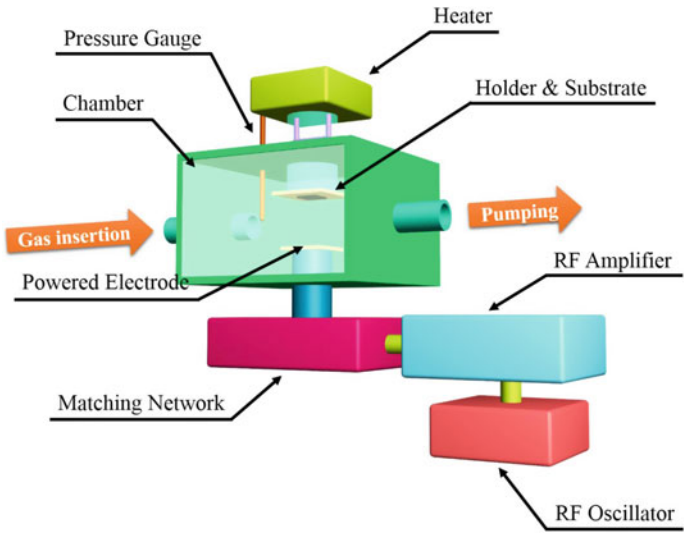

Fig. 14.8 Schematic diagram of a deposition apparatus with capacitively coupled RF discharge. The RF power is transmitted to the electrodes from RF generator via a matching network. The substrate can be on the powered or grounded electrode

areas of the larger grounded electrode and the smaller powered electrode. Such characteristic can ensure the equal currents from the plasma towards both electrodes. The enhanced current density with the reduced size of power electrode is required to achieve via a higher voltage between the electrode and plasma. In other plasma devices, an additional RF bias introduced towards the sample holder provides a self-bias with larger ion energies.

Within the capacitively coupled RF discharge, the electron density typically ranges from 10^9 to 10^{10} cm^{-3} and higher density of 10^{11} cm^{-3} can possibly be achieved with higher frequencies [97]. The ion energy close to the powered electrode is capable of reaching several hundred electron-volts (eV) because of the self-bias. These discharges can be usually introduced into plasma etching and thin-film deposition, along with the sputtering for insulating materials.

A hollow cathode effect is also able to be found for RF discharges and can be applied for designing plasma reactors. Such a process has been utilized within a supersonic RF plasma jet, which was considerably applied into the plasma etching and thin-film deposition.

14.4.2.2 Inductively Coupled Plasma (ICP) Discharge

An ICP is achieved via an electric field which is generated by a transformer from the RF current in a conductor. The varying magnetic field of such conductor activates an electric field where the plasma species are facilitated. Different ICP systems are shown in Fig. 14.9. The current-carrying wire or coil can be either inside or outside the plasma system. In terms of the coil, its shape can be designed as a helix (Fig. 14.9a, b) or as a spiral (Fig. 14.9c). A ring-shaped plasma volume can also be applied as a single-turn secondary winding of a transformer (Fig. 14.9d). The impact of the electric field of the wire can be shielded, leading to a restriction of capacitive coupling.

ICPs are capable of delivering higher electron densities ($n_e = 10^{12}$ cm^{-3}) at relatively lower ionic energies. Some specific applications that are investigated using ICP include plasma etching, thin-film deposition as well as ion sources for mass spectrometric analysis.

The helicon discharge serves as a particular kind of inductively coupled discharge. Such plasma is typically achieved within a cylindrical vacuum vessel in a longitudinal homogeneous magnetic field with intensities of 100, 300 G, or even higher. Noticeably, the electromagnetic energy can be transferred towards the plasma source with frequency ranges from 1 to 50 MHz, typically with 13.56 MHz for processing plasma. Helicon waves are achieved within the plasma column via specially designed antennas. Such kind of discharge provides electron densities of 10^{12}–10^{13} cm^{-3} at the pressure of 0.1 Pa.

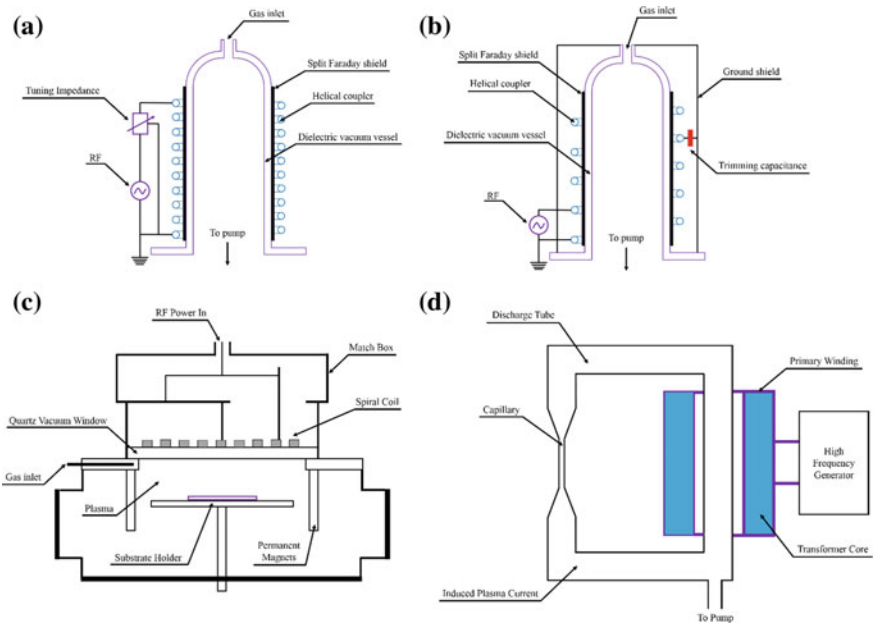

Fig. 14.9 Diagrams of various ICP reactors: **a** helical coupler, **b** helical resonator, **c** spiral coupler, and **d** transformer-coupled plasma. The Faraday shield in devices **a** and **b** avoids capacitively coupling from the coil to the plasma. The permanent magnets **c** confine the plasma, enhance the uniformity, and increase the plasma density

14.5 Low-Temperature Plasma-Based Carbon Materials for Energy Storage Performance

As mentioned earlier advanced technologies for both energy storage (e.g., LIBs and SCs) and conversion (such as solar and fuel cells) and are being extensively studied around the world. The tremendous progress and development in nanoscience and nanotechnology has opened up new frontiers in materials science and engineering to meet this challenge. In particular, carbon nanomaterials and nanotechnologies have been demonstrated to be an enabling technology for creating high-performance energy-conversion and storage devices. It is because carbon-nanostructured infused electrodes possess some unusual size-/surface-dependent properties such as greater accessible surface area, favorable reaction kinetics, superior mechanical strengths, better charge transport properties at the edges of nanostructures which are highly useful in enhancing energy-conversion and storage performance. Specifically, considerable efforts have been made to utilize the unique properties of fullerenes, carbon nanotubes (CNTs), and graphene as energy materials, and tremendous progress has been achieved in developing various methods of synthesizing and functionalizing carbon nanomaterials for high-performance energy-conversion and storage devices.

The carbon nanostructures for energy applications have been synthesized using various methods which include arc discharge [98], sono-chemical or hydrothermal [99], electrolysis [100], laser ablation [101], and most extensively studied chemical vapor deposition [102]. In addition to these methods plasma-enhanced or plasma-assisted chemical vapor depositions have also been used actively for carbon nanostructure synthesis and functionalization, but much more investigations are required for further exploiting such field.

The following section will describe current progress in nano-structural fabrication via plasma-enhanced strategy, providing the utilization of specific features of plasma towards nano-architectural preparation, through describing critical instances in recent publications. This section will concentrate on the specificity of plasma-enhanced techniques in nano-structural fabrication as well as suitable utilization of these strategies to realize controllable, morphologies, structures, and properties for carbon-based nanostructured frameworks especially for CNTs and vertically oriented graphene nanosheets that have been actively used as electrode materials for energy storage and conversion applications.

14.5.1 Advantages of Plasma-Assisted Strategies in Nano-Structural Preparation

A plasma produces a plethora of different precursor species (molecules, atoms, and radicals), in a large number of different energetic states (ionized, excited, metastable, and ground states) compared to solid, liquid, or gaseous precursors [103]. The basic premise of nanoscale plasma engineering is that these plasma precursors can be produced, transported and self-organized to assemble into nano-solid objects with quite different atomic arrangements that are not so easily possible in other synthesis methods. Plasmas feature a higher degree of complexity that allows nanoscale synthesis, efficient functionalization by simply mixing plasma precursors or by post deposition plasma treatment, defect engineering and surface nano-structuring by imping ions and plasma sheath-accelerated energetic electrons. Diverse activated species within the plasma can enable the inherently high chemical reactivity in comparison with traditional reaction. Furthermore, the excellent reactivity is capable of achieving high reaction rates, typically named or termed as “plasma enhancement”. Even though most current researches toward nanostructure fabrication focus on exact control instead of highly output, considerable production efficiency is however usually expected, particularly for the purpose of commercialization. Another advantage of the high reactivity of plasma species is that it enables researchers to choose much more types of precursors, even including several precursors that remain inert during conventional chemical processes. For instance, toxic and difficultly-handled ammonia is always utilized to deliver activated nitrogen during conventional chemical processes but it can be substituted by easily available and nontoxic molecular nitrogen gas during plasma-enhanced

processes because of the nitrogen activation via the plasma. The wider choice for starting materials for plasma-enhanced processes is able to provide advantages of reduced costs and enhanced flexibility during the fabrication process.

With charged species, plasma can possibly deliver electric fields since local fluctuation may be deviated from the equilibrium of charges. Typically within the cold plasma, the vertically oriented electric field on the substrate surface can be achieved at the interface between the plasma and substrate, which is named as the plasma sheath field. Such sheath field is derived from the various mobility of ions and electrons onto the substrate surface. Noticeably, zero net-charge flux onto the substrate surface with charge equilibrium can be achieved by the lower electric potential of the substrate surface in comparison to that of the plasma. This will retard the electrons with higher kinetics as well as accelerate the cations with lower mobility. Moreover, the sheath electric field can usually be directed vertically towards the substrate surface. Within the cold-ion and non-collision sheath model, the sheath potential can be expressed by Eq. (5.1) [104].

$$\Phi_w = -\frac{T_e}{e}\mathrm{In}\left(\frac{M}{2\pi m}\right)^{1/2} \tag{14.10}$$

where Φ_w denotes the sheath potential, T_e refers to the electron temperature and M and m are masses of ions and electrons, respectively. As exhibited, the sheath potential will be higher for increased electron temperature as well as for an enhanced ion mass. The typical thickness of the sheath can be several hundred micrometers for representative cold plasmas.

The sheath potential can lead to a bombardment of ions on the substrate surface by promoting the cations acceleration, which will further be accelerated through external bias. Bombardment of ions can cause etching and sputtering of the substrate surface, which serves as an important approach for accommodating the surface structure into specific nanostructures. Additionally, the electric field can also deliver impact on the growth orientations and directions during the growth of nano-architecture.

The large degree of freedom within plasma include different electron and ion temperatures, plasma density, multiple species within the plasma, plasma life-time, and dimensions, allowing the plasma-assisted strategies to achieve syntheses and processing for various materials, at the moderate to high reactor zone temperature. The heating effect delivered to the substrate surface is weak in cold plasmas but the high chemical reactivity of precursor species can be achieved, which results in the high surface selectivity during fabrication and processing. Additionally, the bulk material is not essentially affected by the weak heating effect, but the material surface can be considerably shaped via the excited species within the plasma. The thermal plasmas can be applied in terms of the energetic heating effect, the highly dense reactive species, and a tremendous temperature gradient between the cold surroundings and the plasma region, which can be introduced to fabricate nanostructures with metastable phase architectures as well as high crystallinity. The

specificity of plasma-assisted strategies in nanostructure processing has been demonstrated by numerous successful instances in literatures and their advantages are not restricted to the above discussed examples. Currently, a practical challenge is how to totally make use of these advantages to deliver great control towards the attractive features through proper experimental approaches.

14.5.2 Classifications of Plasma-Assisted Approaches for Nanostructure Fabrication

The nanostructured material syntheses and processing based on currently reported plasma-assisted approaches can be assorted mainly into the following four types (Fig. 14.10).

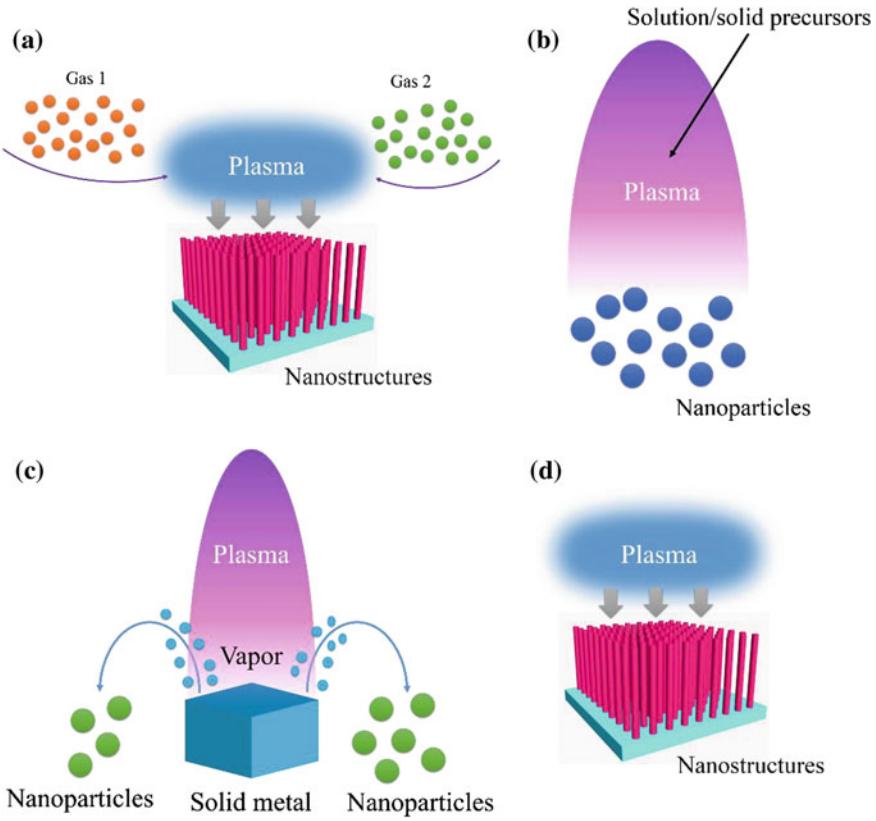

Fig. 14.10 Schematic illustrations of four plasma-assisted material preparation processes: **a** PECVD, **b** thermal plasma sintering, **c** thermal plasma evaporation and condensation, and **d** plasma treatment of solid phases

(i) *Plasma-enhanced chemical vapor deposition (PECVD)*: Similar to chemical vapor deposition (CVD) processes, the precursors are inserted in the reaction zone as the form of vapors or gases. Subsequently, plasma discharge is initiated into the reaction zone for activating the precursors. The substrate can be located either inside the plasma zone or outside the plasma region, for enhancing or preventing some typical plasma effects including ion bombardment. PECVD can undertake with a wide range of temperature and pressure, enabling huge diversity in fabrication and related property. The precursors for PECVD are required to be volatile, delivering partial limitations towards the fabrication strategy for some materials.

(ii) *Thermal plasma processing with liquid and solid precursors*: In this approach, the precursors can be selected as liquids, solids, or even solutions, which are directly introduced into the high-temperature and typical high-density thermal plasma zone typically created in atmospheric-pressure plasma torch. Products can be achieved after the conversion within the high-temperature plasma region. Such approach can supply a large number of choices for the precursors. For instance, nano-architectures with highly crystalline phases are usually achieved because of the intense heating effect.

(iii) *Thermal and Nonthermal plasma evaporation and condensation*: In this approach, the precursors are evaporated through the strong heating effect of thermal plasma or the sputtering effects of energetic nonthermal plasma on the solid target material. Once departing from the high-temperature plasma region, the vapors will be condensed into nano-architectures. Reactive gaseous species can also be injected into the plasma for tailoring chemical composition.

(iv) *Plasma treatment of solid phases*: In this case, the product can be fabricated by directly exposing the solid precursor by plasmas through the interaction between solid and plasma. The advantage of this strategy is simple and not complicated. Additionally, the conditions of solid phases such as external bias and temperature can be largely controlled by such system, which is appropriate towards solid-plasma interactions.

14.5.3 Nanostructures Fabricated by PECVD

PECVD is the most frequently utilized approach towards plasma-assisted material fabrication [105, 106]. Within this section, several typical carbon-based nano-architectures fabricated via PECVD are reviewed. Currently, numerous materials including several forms of carbon have been fabricated with various nano-architecture using PECVD approach and hence, we will mainly concentrate our attention on two typical systems of carbon-based structures: carbon nanotubes (CNTs) and vertically oriented graphene nanosheets (VGNSs); both of which are crucial materials for energy storage applications in LIBs and SCs.

14.5.3.1 Carbon Nanotubes (CNTs)

CNTs, the one-dimensional nanomaterials, can be fabricated either as single-walled carbon nanotube (SWCNT) which is a one-layer graphene rolled into a cylindrical tube or as multiwalled carbon nanotube (MWCNT) by rolling multilayer graphene. CNTs have been increasingly becoming popular in energy storage applications due to its excellent electrochemical properties with 10^6 S m^{-1} at 300 K for SWCNTs and $>10^5$ S m^{-1} for MWCNTs, electrode reactivity and interfacial capacitance. CNTs are widely used in LIBs, both as the anode material and as the conductive additive in the composite electrodes.

The CNT growth has been a well-developed field of PECVD application, in which some typical phenomena associated with plasma effects are found. The typical precursors for CNT synthesis are hydrocarbon species, mostly CH_4 and C_2H_2, which are decomposed via plasma to provide carbon. The CNT growth is catalyzed through metal nanoparticles, usually Co, Fe, and Ni, which has been demonstrated to be capable of promoting decomposition of hydrocarbon precursors efficiently. Catalytic metallic nanoparticles are commonly deposited via sputter coating or salt decomposition accompanied with in situ reduction within CNT growth environment. The diameter and density of the resultant CNTs are controlled through the size and density of the catalyst nanoparticles on the substrate surface. Catalyst particles with larger size can lead to the obtained CNTs with a larger diameter but lower length and density. The deposition of CNTs can be achieved onto many types of substrates including quartz, glass, and silicon [107, 108].

Electrically Guided Alignment of Carbon Nanotubes

A typical characteristic of PECVD grown CNTs has been frequently found as the vertically aligned arrays, which are proven to be electrically directed due to either the externally imposed bias or the sheath electrical field. Bower and co-researchers have investigated the CNT growth through microwave plasma-assisted CVD onto unbiased substrates [109]. The growth direction of CNTs is always perpendicular to the substrate surface, even with the curved substrate, since the direction of the sheath electric field is typically vertically oriented to the substrate. Additionally, the CNT growth mechanism is considerably different between the thermal growth and the plasma-enhanced growth. The thermally grown CNTs usually deliver curly structure whereas the plasma-assisted growth can provide straight architecture. The typical growth mechanism further indicates that the vertical orientation is triggered by the sheath electric field in PECVD. Merkulov and co-workers [101] have demonstrated that the CNTs grown at the boundary of the substrate holder have also shown curved shapes due to the curved electric field. The capability of guiding the CNT growth direction via electric field allows large freedom in controlling CNT morphologies through external bias. Hence, the growth direction of CNT arrays can be essentially manipulated through the external electric field. The extent of alignment has been observed to be enhanced with increased substrate bias. For instance,

AuBuchon and co-researchers have conducted multi-step CNT growth with different bias directions at different stages. Once the bias direction has been changed by 90°, the CNT growth direction was also adjusted accordingly, leading to the achievement of zigzag CNTs [110]. Additionally, Law and co-researchers have applied the plasma-assisted surface charging effect to generate an electric field which is almost parallel to the substrate surface. Resultantly, lateral CNT growth onto the substrate surface has been displayed [111].

The alignment of electrically directed CNTs has still been an attractive issue for simulation studies. Several theoretical and simulation works have indicated that the electric field strength is increased within the area above the CNT tips, achieving a large force towards directing the nanotube growth. For instance, Merkulov and co-researchers have found that the vertically aligned CNTs are typically based on the tip-growth mode [112]. The catalyst nanoparticles are situated in the CNT tips. According to their model, the electric field can generate stress at the interface between the catalyst and CNT (Fig. 14.11a, b). Within this mode, the stress at the interface can straighten the CNTs, once bending processes have occurred because of the spatial fluctuation (Fig. 14.11c). Moreover, if the catalyst particles are situated at the bottom of CNTs, the bending degree will be further enhanced via the stress at the catalyst–CNT interface (Fig. 14.11d). Nonetheless, the electric field-directed growth can possibly be CNT-specific, along with a few other 1D nano-architectures [113]. One possible explanation is that within most crystalline frameworks, bending or twisting the lattice needs a quite high energy which is much beyond the electric force. CNTs can deliver a flexible architecture which allows a typical degree of bending. Hence, the electric field serves as a crucial aspect towards the growth direction.

Amorphous Carbon Removal and Related Plasma Chemistries

The PECVD strategy leads to an improved CNT growth rate as compared to the thermal growth [114]. Nonetheless, the high deposition rate is not usually expected. Amorphous carbon is always observed with a high concentration of carbon precursors. The generation of amorphous carbon is not based on metallic catalysts and therefore does not occur selectively onto the catalyst surface. Resultantly, the amorphous carbon deposition can also take place onto the side walls of the as-obtained CNTs, with the absence of the catalyst, resulting in the structural change of the as-obtained CNTs. Therefore, rough surfaces are usually found in CNTs grown with high growth rates, because of the deposition of amorphous carbon onto the CNTs surface.

Hence, avoiding and removal of amorphous carbon serves as the critical issue to obtain CNTs with excellent quality. Notably, the amorphous carbon displays less stability than that of CNTs, which delivers coiled graphitic frameworks, and can be removed preferentially via chemicals with etching capability. NH_3 or H_2 are typically applied into the plasma as the etching species for selectively removing

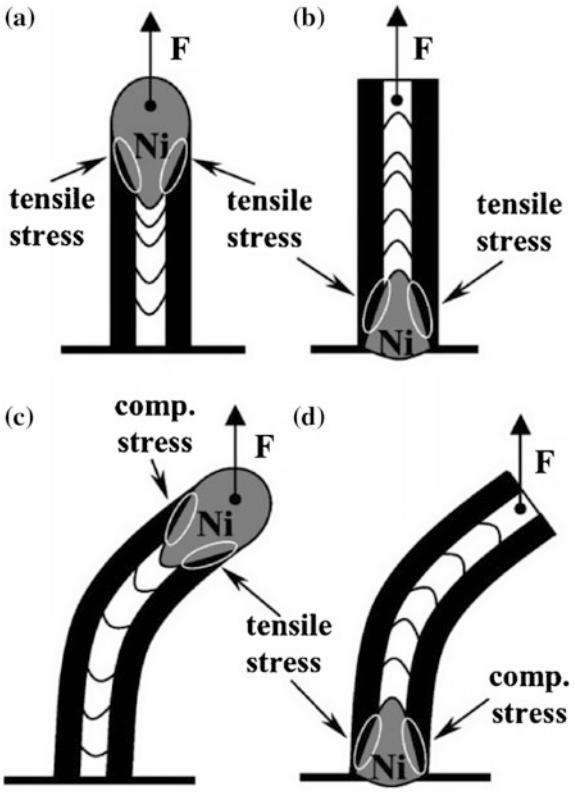

Fig. 14.11 The tensile distribution based mechanism for CNT alignment by electric fields proposed by Merkulov and co-workers: **a** top growth mode, undisturbed, **b** bottom growth mode, undisturbed, **c** top growth mode, bending due to perturbation, **d** bottom growth mode, bending due to perturbation. Reprinted from Merkulov et al. [112] Copyright (2001), with permission from AIP Publishing

amorphous carbon [115]. For instance, CNT growth conducted within NH_3–C_2H_2 plasma exhibits that the growth rate of CNTs enhances with the C_2H_2 proportion less than 30% in the system [116]. Further increasing C_2H_2 contents can result in the decrease of the CNT growth rate as well as the architectural changes of a small fraction of CNTs from the cylindrical structures to the cone shapes (Fig. 14.12). The cone-shaped carbon nano-architectures achieved with high C_2H_2 content can be due to amorphous carbon deposition onto the CNT side walls. Even though the deposition rate of carbon species enhances with increased carbon precursor concentration within the plasma, the deposition of amorphous carbon on side walls largely decreases the axial growth rate with highly C_2H_2 concentration. The favorable C_2H_2 proportion towards CNT growth has been observed to be $\sim$20%, in terms of previous investigations [107].

The reactive agents essentially associated with the removal of amorphous carbon is considered to be atomic hydrogen species. Simulations on the basis of the surface-diffusion model have exhibited that the amorphous carbon can be totally removed through etching it with a proper hydrogen flux during plasma processes. In comparison to H_2, ammonia serves as a more effective supplier of atomic hydrogen. Typically, the plasma chemistry and the corresponding CNT growth characteristics

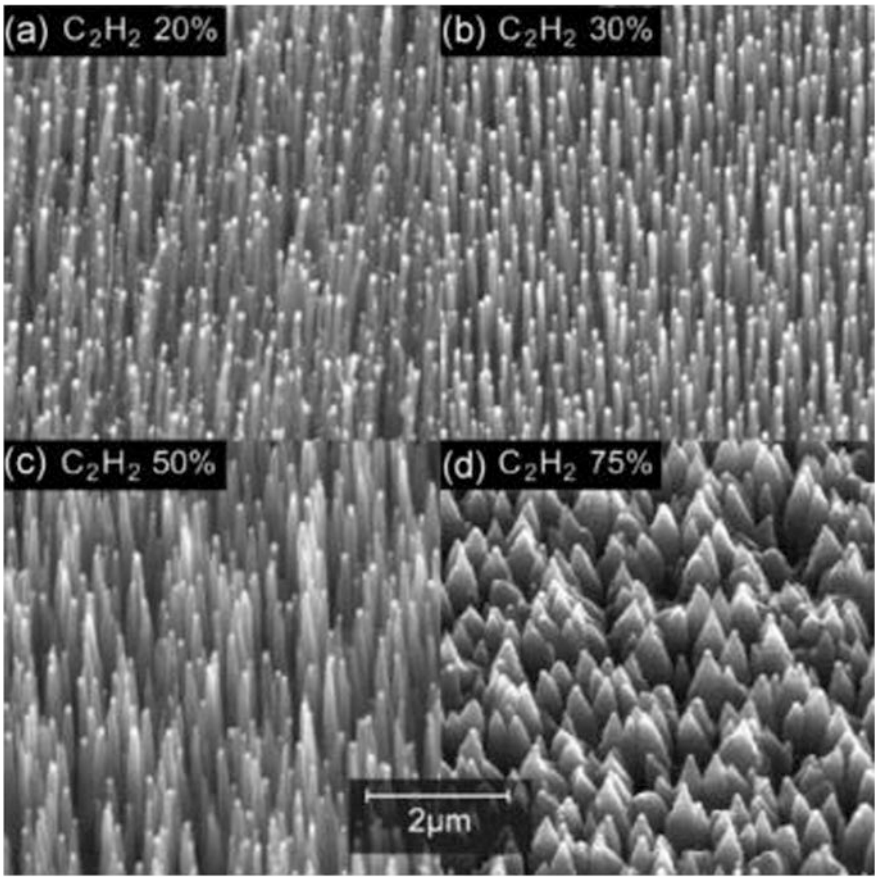

Fig. 14.12 SEM images of CNTs grown at different concentrations of C_2H_2. Reprinted from Chhowalla et al. [107] Copyright (2001), with permission from AIP Publishing

within ammonia-containing plasma has been considerably studied via mass spectroscopy (MS) and in situ optical emission spectroscopy (OES) [117].

By introducing in situ MS diagnostics, Bell and co-workers investigated the plasma composition for preferable CNT growth [118]. The ionized and neutral species have been simultaneously detected via secondary ion MS and residue gas analysis, respectively. The formation of HCN was observed because of the amorphous carbon etched by ammonia. Obvious HCN generation could be found as the NH_3 content was higher than 20%, as suggested by both OES and MS investigations [119]. Hydrogen serves as another essential neutral part, derived from the decomposition of either C_2H_2 or NH_3. The interaction of two different mechanism leads to the lower H_2 concentration with 20% C_2H_2 content within the gas precursor, which occurs simultaneously with the optimal composition of the gas precursor towards CNT growth. It was exhibited that the decomposition of C_2H_2 with

the existence of NH_3 was inhibited, because of the lower N–H bonding energy in comparison with that of C–H bonds. Moreover, the sufficiency of carbon-based cations including C_2H^+ and $C_2H_2^+$ within the plasma has been observed to interact with the amorphous carbon deposition. These carbon-based cations could be much more reactive as compared to C_2H_2 molecules, leading to a nonselective carbon deposition. Noticeably, in situ OES diagnostics of the plasma have recognized more reactive species within the plasma. H atoms and CH_x radicals were always observed and their existence has further been identified via numerical simulation. Within the C_2H_2–NH_3-based growth, several nitrogen-based species including NH and CN radicals have also been found. Integrating the MS techniques with the OES approach, Woo and co-workers investigated the growth process of CNTs within the H_2–NH_3–CH_4 system and attempted to understand the growth characteristic with the plasma diagnostics results [120]. The emission lines from CN radicals and H atoms were the dominant components of the optical emission spectra. Both of them become more intensive with the increasing proportion of NH_3 within the plasma till saturation as the NH_3 content reached to the same concentration as that of CH_4, indicating that most species are derived from the plasma-triggered chemical processes between NH_3 and CH_4. The formation of HCN, detected via MS technique, has exhibited the same variation tendency with the NH_3 content. Even though CH_4 has been applied as the carbon source, C_2H_2 acted as the major growth precursor, as identified via the specific peak within the MS spectra. With the capability to inhibit the deposition, NH_3 has also been observed to restrict the formation of C_2H_2 if CH_4 was introduced as the carbon source.

Moreover, MS diagnostics of the growth plasma along with simulation have demonstrated that the dissociation degree of both NH_3 and C_2H_2 could reach more than 50% at highly plasma power. However, a significant amount of carbon species are presented as the form of HCN, without contribution towards CNT growth [121]. It was observed that with high plasma power, the endothermic interaction between cations and neutrals should be considered for a better evaluation toward the densities of plasma species [122].

Post treatment of CNTs with etching species is capable of enhancing their several properties. Because of the highly chemical stability of carbon-based materials as well as the high aspect ratio (ratio of length to diameter) of the CNTs, vertically aligned CNT arrays serve the quite promising role in field-emission applications. The field-emission properties of vertical CNT arrays can be improved by post-plasma treatment. Zhi and co-researchers have demonstrated that the hydrogen plasma treatment of 5 min considerably decreased the turn-on field of the species [123]. The hydrogen plasma treatment inhibits the surface dangling bonds, as suggested by the presence of C–H bands after post treatment. The potential drop on the surface C–H dipole is advantageous to decrease the surface work function. The ion bombardment can lead to the generation of surface defects, which is indicated to be preferable sites towards electron emission. Additionally, plasma treatment can eliminate the metallic nanoparticle catalysts at the CNT tips and sharpen the tip (Fig. 14.13). Similar removal of the metallic nanoparticle catalysts can be achieved through post argon plasma treatment. Nonetheless, longer

treatment duration can lead to the structural deformation of CNTs and therefore was undesirable to enhance the iron properties. The favorable treatment duration is usually from 5 to 10 min [124]. Currently, the transition from metal to semiconductor within single-walled CNTs in field-effect transistors triggered via hydrogen plasma treatment has been observed [125].

In spite of the existence of the etching agents such as NH_3, an amorphous carbon layer can still be deposited during the short thermal growth duration once the plasma is switched off. As the metallic nanoparticle catalysts are covered by an amorphous carbon layer, they are deactivated and cannot further catalyze the growth of CNTs. With hydrogen plasma treatment, AuBuchon and co-researchers [110] have removed the shell structure of amorphous carbon and the renascent nanoparticle catalysts are capable of catalyzing the second-stage CNT growth. The authors have further utilized such approach to fabricate zigzag CNTs with many bends.

Energy Application of CNTs

CNTs for LIBs

MWCNTs have the hollow structure of multilayers coaxial circular tubes of hexagonally arranged sp^2 hybridized carbon atoms. The interlayer distance between neighboring coaxial layers of CNTs is 0.34 nm and the diameter of CNTs can range from 2 to 20 nm. The low density of carbon atom and the layered structure of CNTs allow the imbedding of Li-ion. Moreover, the structural defects on the surface and edges of CNTs as well as the interlayer spacing allow Li-ions to imbed anywhere

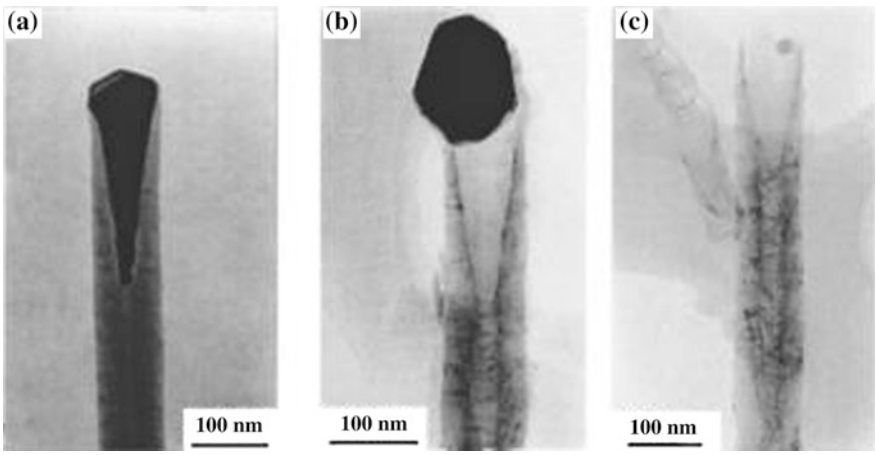

Fig. 14.13 TEM images showing the effect of hydrogen plasma treatment of a CNT with a Ni catalyst particle at the tip: **a** untreated, **b** transitional during treatment, and **c** after plasma treatment. Reprinted from Zhi et al., [123] Copyright (2002), with permission from AIP Publishing

on the CNT walls or between the layers [126]. It is reported that it is easy for Li/Li^+ to spread along the wall inside CNTs; however, it is easier for Li/Li^+ to imbed on the location of C_6 on the surface outside; thus in order to spread Li/Li^+ along wall inside the CNT an effective opening at the end of CNTs or adding more defects will be a useful strategy [127]. For LIBs, the CNTs can be used (i) directly alone as anode materials, (ii) composite of CNTs as the anode materials, and (iii) in cathode material.

CNTs alone as Anode Materials: The graphite structure of CNTs allows it to be used as the anode material in the place of graphite. The specific capacity of SWCNT is about 400–490 mA h g^{-1}, but it can reach above 1000 mA h g^{-1} after introducing defects on the surface. The solid electrolyte interface (SEI) can be formed at around 0.9 V, which can remarkably reduce the specific capacity during the first electrochemical cycle. Notably, both the inner and outer tubules of CNTs are electrochemically active for Li^+ intercalation. Indeed, CNT morphology as well as the degree of graphite crystallinity serves essential roles in largely affecting both the capability and cyclic stability of CNTs. It was found that the cyclability of highly graphitized CNTs is better than that of slightly graphitized CNTs, as the slightly graphitized CNTs provide a higher capacity than the highly graphitized CNTs [128]. Zhang et al. [129] used the CNT array as anode and obtained the specific capacity of 373 mA h g^{-1} with good cyclability. They believed that the graphite in the inner layer provides better conducting passages so as to avoid the loss of active material in the process of charge and discharge leading to good cyclability. There are a large number of defects on CNTs. For example, the top open ends (edges) of CNTs are defects and similarly there can be many defects on the outer planar surface of graphene layer on CNT surface. During the charging process, the Li^+ can insert between graphite layers through these defects, which will deform the carbon layer close to these defects as shown in Fig. 14.14. The deformation is more obvious at the open end of CNTs as more defects are formed during nucleation growth of CNTs.

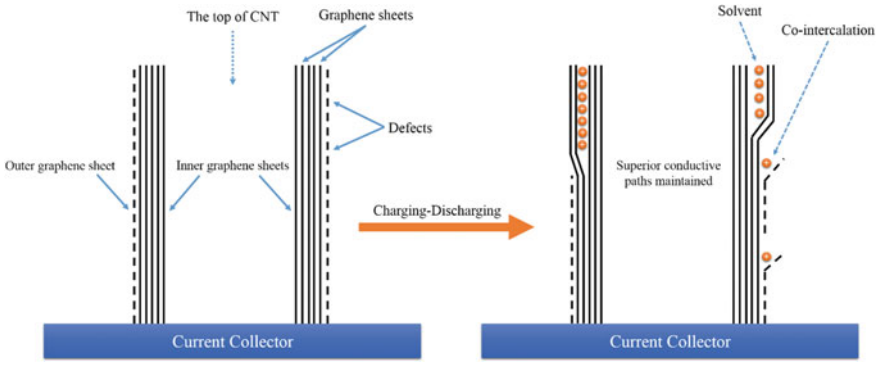

Fig. 14.14 Schematic representation of Li^+ insertion and energy storage characteristics of the CNT anodes

However, there is an issue due to the relatively higher resistance of CNT array of about 1–5 $k\Omega\ cm^{-2}$ which impedes the electron transportation along with significant heat loss. The possible solution to circumvent this issue is the direct growth of CNTs on the current collector. Chen et al. [130] grew CNTs on the carbon layer loaded on the metal foil. The resistance between carbon and copper foil was only 1–2 Ω which could be ignored. They reported that after 100 cycles, the specific capacity was 572 mA h g^{-1} and the compound between Li and graphite layer was $Li_{1.6}C_6$. Lahiri et al. [131]. grew CNTs on Ti–Ni thin catalyst layer (20–25 nm) on copper foil through CVD method to produce the LIB electrode free of adhesive. The CNTs were tightly connected to the copper foil which was used as the current collector of LIB providing the specific capacity 900 mA h g^{-1} at 1 C which is three times as that of graphite. Even at high charge/discharge current densities of 3 C rate, the electrode kept good curve showing negligible capacity decay with capacity retention of 99% after 50 cycles. Hence the results were very promising.

However, critical difficulties also exist in CNTs including their highly irreversible capacity and challenges in controlling their morphology and structure during fabrication. In terms of that, it is difficult for pure CNTs to replace graphite in LIB anodes.

Composite of CNTs as the anode material: Instead of applying CNTs alone as the anode material, investigations have also been focused on incorporating CNTs with other high capacity compounds to achieve core-shell structures (CNTs as core and other components as shell) as anodes for enhancing overall performance [132]. This is due to higher conductivities and SSAs of CNTs than graphite. The advantages of such composites are attributed to the enhanced capacity of metal-containing components (typically transition metal oxides (TMOs)) as well as CNT scaffolds to inhibit crumbling and pulverization in the anode. A hybrid made of both TMOs and CNTs has two Li^+ storage mechanisms including intercalation and conversion [133]. Besides enhanced capability and better cyclability, CNTs can also serve as conductive substrates to transport electrons from the coating, especially when the CNTs are coated with non-conductive TMOs. Reddy and co-researchers reported an approach, where MnO_2 layer is coated onto CNT outer surface with reversible capacity of 500 mA h g^{-1} (50 mA g^{-1}) over 15 cycles [134]. Zhang and co-workers described the formation of cross-stacked CNTs uniformly anchored with SnO_2 nanoparticles with the reversible capability of 850 mA h g^{-1} (40 mA g^{-1}) over 85 cycles [135]. In addition to the core-shell configuration, the CNT composites with other active materials (for example with $LiCoO_2$ for cathode and with graphitic carbon particles for anode) with CNTs acting as additives provide effective interweaving links between active material particles with significantly improved conductivity, as shown in Fig. 14.15. This helps in providing higher power ability and prolonged cyclability of LIBs. Such types of composite frameworks provide alternative architectures in LIBs.

CNTs in cathode materials: Cathode material in LIBs is the source of Li^+. Most commonly explored cathode materials are the inorganic salts such as $LiCoO_2$

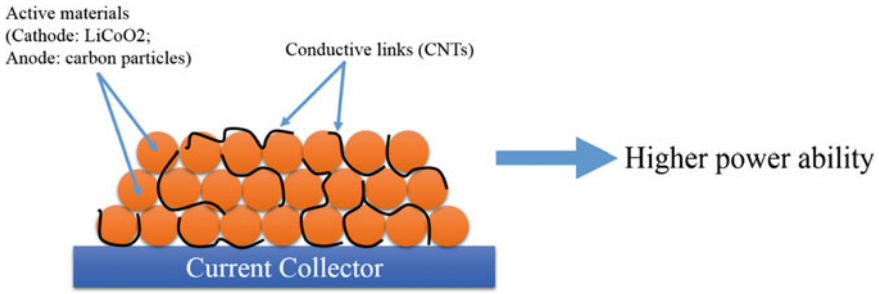

Fig. 14.15 CNTs as additive providing conductive links between active materials on cathodes or anodes

(hexagonal layered structure), $LiMn_2O_4$ (spinel structure), and $LiFePO_4$ (olivine structure). $LiFePO_4$ is one of the widely studied and applied cathode materials because of its low price, environmental compatibility, high theoretical specific capacity (170 mA h g^{-1}) and proper working voltage (3.42 V vs. Li^+/Li). However, the crystal structure of $LiFePO_4$ slows down the spread of Li ions influencing the intercalation of Li-atom and de-Li atom. The lack of a continuous network of the octahedron in $LiFePO_4$ also lowers the electronic conductivity of $LiFePO_4$. Jin et al. [136] reported the conductivity enhancement for $LiFePO_4$–CNT composite with 1.08×10^{-1} S cm^{-1}, 8 times as that of pure $LiFePO_4$. The CNTs addition not only improved the electronic conductivity but also improved the Li^+ diffusion coefficient, reducing the crystallite size and transportation resistance. It has been found that CNTs play critical role in electron transportation and in inhibition of the oxidization of Fe^{2+}. Similarly, $LiMn_2O_4$–MWCNTs composites have been produced by sol-gel method [137] and hydrothermal method [138]. Once again CNT composite cathode were found (i) to have better electron transport resulting in higher conductivity of composite compared to that of pure $LiMn_2O_4$ spinel structure, (ii) to help in higher cycle stability and capacity retention in composites compared to that of pure $LiMn_2O_4$, and (iii) to have effectively reduced agglomeration of $LiMn_2O_4$ nanoparticles which get well crystallized and uniformly distributed in the CNT matrix providing structural and long-term stability.

In short, the CNTs have promising prospect as an electrode material for LIBs. Although, a large amount of work has been done in this field and much progress has been made but there is great potential as a lot more can be done. This includes: (i) better understanding of lithium storage mechanism of CNTs, e.g., understanding the influence of the CNT length, diameter, number of walls, and defects on lithium storage which is crucial to minimize the loss of specific capacity after the formation of SEI and to improve the cycle performance, and (ii) greater effort on a wider variety of composites containing CNTs as LIBs electrode.

CNTs for SCs

CNTs with large SSAs have been tremendously investigated in SCs, with specific capacitances from 4 to 180 F g^{-1} in a solution of acid or alkaline, superior to that of traditional carbon [139–141]. Surface areas and pore sizes of CNTs largely affect the specific capacitances. Notably, Niu and co-researchers reported MWCNTs with SSA of 430 m^2 g^{-1}, delivering a specific capacitance of 113 F g^{-1} using the electrolyte of 38 wt% H_2SO_4 [141]. An and co-workers provided a specific capacitance of 180 F g^{-1} with a large power density of 20 kW kg^{-1} via enhancing the pore distribution and surface area [142]. Researchers have also tried to treat the CNT surfaces with NH_3, alkaline, or HNO_3 to introduce oxygen-containing functional groups to improve the electrochemical behaviors of electrodes [143–145]. Yoon and co-researchers reported the specific capacitance of the CNT electrode from 38.7 to 207.3 F g^{-1} via surface functionalization through NH_3 plasma [143]. The specific power of SCs is $P_{max} = V^2/4R$ (V: the working voltage; R: the equivalent series resistance). Hence, the features of electrode materials and the type of synthesized electrode serve as the essential factors for extraordinary performance, including the density of CNTs. Several strategies have been applied to enhance the SCs' performances. (1) Direct deposition of CNTs on the current collectors (such as Ni, Ni-alloy, Al, and other metals) as electrodes, decreasing the contact resistance [146–148]. The formation of such binder-free CNT electrode can improve its supercapacitive performance as lesser impurities have been introduced by the polymer binders. (2) The combination of CNTs with TMOs (including RuO_2, MnO_2, NiO, In_2O_3, etc.) or conductive polymers (CPs), such as PANI, PPy, and PEDOT [149–152]. Currently, such composites are more favorable since they can combine two components to obtain the highest capacitance through dual storage mechanisms (EDLC and FC). Within such hybrid systems, CPs or TMOs can deliver higher specific capacitances (such as 480 F g^{-1} for PPy, 775 F g^{-1} for PANI and 1000 F g^{-1} for MnO_2) [88, 153, 154], delivering most of the capacitance, whereas CNTs play the good conductor and backbone for composites during cycling. As reported, Au-anchored MnO_2@CNTs composites have been prepared for high-power SCs, in which CNTs enhance conductivity and Au tips between MnO_2@CNTs and current collector decrease the contact resistance [155].

14.5.3.2 Vertically Oriented Graphene Nanosheets (VGNSs)

VGNSs are composed of a stack of graphene nanosheets grown perpendicularly onto the substrate surface. In spite of the normal hexagonal carbon frameworks, VGNSs are different from the traditionally horizontal, randomly directed graphene in many fields. Their typical structure and morphology toward micro- and nano-scales are expressed in Fig. 14.16, as compared with horizontal graphene. These characteristics are determinant factors for numerous distinctive electronic,

chemical, electrochemical, optoelectronic and mechanical properties for a broad range of applications.

One of the important features within VGNSs is the vertically orientated structure on the substrate that enhances mechanical stability and higher reactivity. Even though VGNS framework can deliver turnstile-, petal-, cauliflower-, and maze-like morphologies, each VGNS typically stands for a self-supported rigid architecture [156]. Such structure can achieve the mechanical stability of 2D graphene without collapsing with each other along random directions, partially because of the strong van der Waals forces. With respect to the optoelectronic, electronic, and electrochemical applications, the optimization towards the enhanced charge transport at the sharp edges accompanied with the highly conductive graphene planes within the devices can deliver the improved efficiency. The vertically orientated architecture of VGNS also promotes the SEM imaging because of their lateral dimensions being remarkably larger than the thicknesses.

Additionally, VGNS can provide a non-agglomerated framework with a very high surface-to-volume ratio and reactive passages between the sheets, enabling the much higher amounts of VGNSs readily available for interaction with other species towards electrochemical and other applications. The considerable attention for graphene applications is because of the one to the varied thickness from single to a few layers and the high SSAs. The collapse and stacking of horizontal graphene result in the tremendous decrease of the available SSAs. Such issue can be addressed to some degree via utilizing VGNSs as the substitute. According to the growth parameters and plasma-based process, the interlayer spacing between the adjacent VGNSs is different with the range from a few tens to several hundred nanometers. Benefiting from such non-agglomerated framework, the SSAs of the VGNS structures is capable of reaching the high value of $\sim 1100\ m^2\ g^{-1}$ [157].

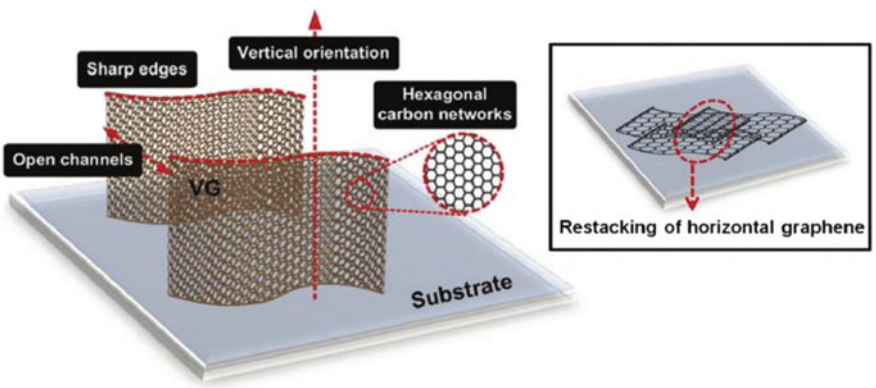

Fig. 14.16 Schematic representing VGNSs' structural and morphological features. *Inset* illustrates the restacking of horizontal graphene nanosheets. Reprinted from Bo et al., [158] RSC Publishing, Open Access paper

Moreover, VGNSs provide densely exposed reactive graphene edges, favorable for applications which depend upon the edge reactivity. Each VGNS can usually deliver a tapered morphology, with several graphene layers stacked at the bottom and an atomically thin graphene layer at the top. These thin carbon layers, typically with the interlayer spacing from 0.34 to 0.39 nm, can form the Bernal AB configuration [159]. Nonetheless, disordered stacking frameworks are always observed in multilayer graphene. It has recently been indicated that most VGNS edges are composed of the folded seamless graphene nanosheets and only a comparatively small proportion of edges keep opening during the plasma-assisted growth [160]. Such reactive edges can largely optimize the electrochemical activity of VGNS towards energy storage applications.

These particular morphological and structural characteristics allow VGNSs to be one of the most promising candidates towards various emerging applications. For instance, the largely available SSAs and high in-plane electric conductivity can contribute to the application of VGNS in SCs, LIBs, solar cells, and fuel cells [161, 162]. The high density of reactive edges with controllable defects is able to improve the electrochemical activity in many applications, including energy storage devices [163].

Plasma-Assisted Growth

In addition to the fabrication using arc discharges and cutting from stacked graphene film, VGNSs with remarkable quality have been synthesized via the PECVD [164]. Through controlling the growth conditions, the VGNSs with controlled architectures and features can be prepared within highly efficient, lower temperature, and catalyst-free conditions. Here, recent development of the VGNS growth via PECVD and the corresponding growth mechanism will be discussed.

VGNS Growth on Different Substrates

Actually, VGNS growth via PECVD can be achieved on many substrates from foam-like, cylindrical, and macro-sized planar shapes to micrometer- and nanometer-scaled frameworks. Such capability, along with the controllable VGNS architecture, enables the facile synthesis of various VGNS-based devices for different applications.

VGNS growth via PECVD onto planar substrates has been extensively investigated [165]. Requiring no catalyst serves as one of the essential advantages of the plasma-assisted growth, allowing the growth to be available on different materials including Al_2O_3 and SiO_2, semi-conductive silicon, conductive carbon and a variety of metallic substrates such as copper, nickel, tungsten, aluminum, titanium, platinum, as well as stainless steel. For instance, Fig. 14.17a, b exhibit SEM images of VGNSs deposited onto the planar n-type silicon substrate [165]. The gaseous mixture of H_2 and CH_4 was utilized as the precursor and the fabrication was

achieved within the 13.56 MHz RF-PECVD reactor. The resultant VGNS frameworks without metallic contamination have been obtained with considerably sharp graphitic edges (∼1 nm) and the uniform height distribution (standard deviation of <10%).

Figure 14.17c exhibits the SEM image of VGNSs deposited onto the macroporous nickel foam [166]. During the process, the commercial Ni foam was firstly compressed and chemically treated via HCl solution for removing surface oxides. Subsequently, the substrate was etched via H_2 plasmas and VGNSs were generated through utilizing CH_4 as the carbon resource through the microwave PECVD. The SEM image apparently exhibits that VGNSs with the height of several

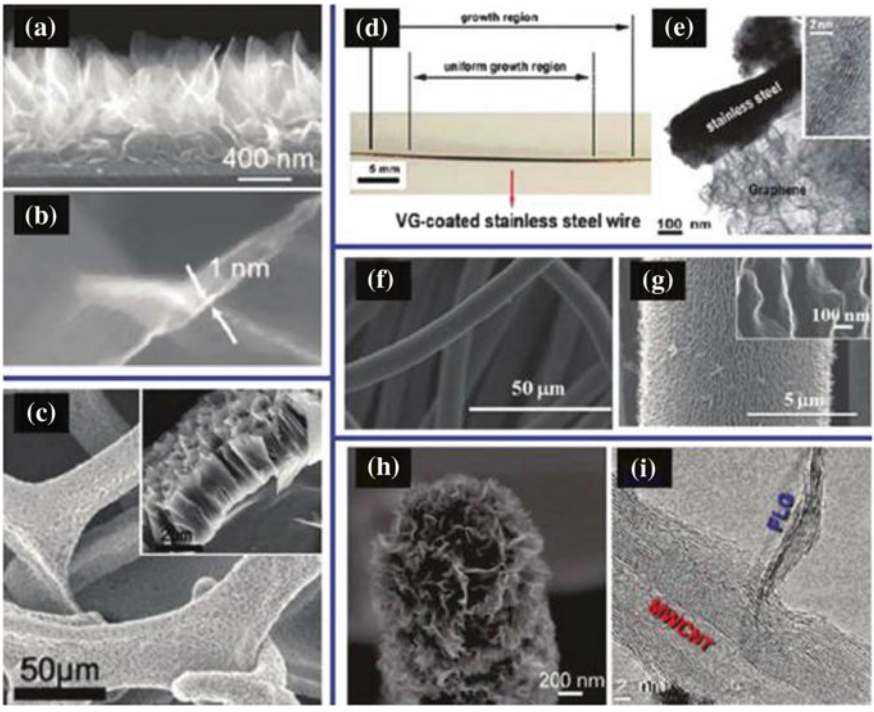

Fig. 14.17 VGNSs grown on various substrates: **a** cross-sectional SEM of VGNS networks and **b** magnified SEM image of an individual VGNS grown on planar Si. [165] **c** *Top-view* and cross-sectional (*inset*) SEM images of VGNSs on 3D porous Ni substrate. [166] **d** A photograph and **e** a TEM micrograph of VGNSs on a stainless steel wire. [167] **f** Low- and **g** high-magnification SEM images of VGNSs on carbon cloth (*inset* shows the VGNS edges). [168] **h** SEM and **i** TEM images of VGNS seamlessly integrated with a CNT. [169] **a** and **b** Reprinted from Wang et al., [165], 183108, Copyright (2006), with permission from AIP Publishing; **c** Reprinted from Ren et al., [166] Copyright (2014), with permission from Elsevier Ltd; **d** and **e** Reprinted from Bo et al., [167] Copyright (2011), with permission from RSC Publishing; **f** and **g** Reprinted from Chang et al., [168] Copyright (2012), with permission from Elsevier Ltd.; and **h** and **i** Reprinted from Yu et al., [169] Copyright (2011), with permission from ACS Publications. **a–i** Reprinted from Bo et al., [158] RSC Publishing, Open Access paper

micrometers were deposited perpendicularly around the nickel scaffold on both outer and inner surfaces. The oxygen-containing contamination within VGNSs is also relatively lower because of the utilization of highly purified carbon resource and the low-pressure plasma process.

VGNSs can also be deposited onto cylindrical substrates including metallic wires, which has been achieved via the atmospheric-pressure glow discharge with carbon sources of CH_4–H_2O–Ar mixture [167]. The VGNSs fabricated via such approach exhibited great uniformity in both axial and circumferential directions (Fig. 14.17d), partially because of the utilization of the rotating stage. The transmission electron microscopy (TEM) image in Fig. 14.17e exhibits a strong contact at the interface between the VGNSs and the metallic substrate.

VGNSs can also be achieved onto micrometer- and nanometer-scaled substrates. Figure 14.17f, g exhibit SEM images of VGNS deposited onto carbon cloth (CC) through RF magnetron sputtering of the carbon target in the gaseous mixture of Ar–H_2 at the temperature of 350 °C [168]. The lateral dimension and thickness of VGNSs were about 300 nm and 5–10 nm, respectively. Analogical to the Ni foam, the fibrous and porous architecture of the CC allows the densely distributed VGNS framework with large SSAs. VGNSs can also be achieved onto the lateral surfaces of CNTs, as exhibited in Fig. 14.17h [169]. Figure 14.17i illustrates that VGNSs are seamlessly combined with the outer walls of the individual MWCNT through generating sp^2 covalent bonding. The substrate-independent and catalyst-free growth of VGNSs can result in the direct combination of VGNSs with different functional devices. For instance, VGNSs grown onto conductive planar metallic substrates exhibited the attractive performance as anode materials in LIBs. The VGNSs growth onto metallic cylindrical electrodes assisted in providing atmospheric corona discharges. The growth of VGNSs onto Ni foams allowed 3D framework to integrate the benefits of vertically orientated feature with the highly loading density of active materials toward high-performance SCs and the resultant VGNS-CNT hybrid architecture showed improved gas sensing and optoelectronic properties in comparison with the randomly mixed CNTs and graphene. However, it has been found that even though the growth is substrate-independent, the final crystallinity and structure of the VGNSs are different for diverse substrates. This can result in the overall performance enhancement of VGNS-based devices.

VGNS Growth Using Different Precursors

Gaseous precursors have been the most commonly utilized precursors towards the VGNS growth during PECVD processes, mainly containing hydrocarbons (such as CH_4, C_2H_2, C_2H_4), fluorocarbons (such as CF_4, C_2F_6, CHF_3), and carbon monoxide or dioxide. Additionally, these carbon-containing gases are always diluted via Ar, H_2O, H_2 to enhance the plasma stability and to achieve better control for the VGNS crystallinity and architecture. The catalyst-free growth of VGNSs in plasma-enhanced methods suggests that precursor dissociation via the plasma serves as an essential candidate towards the VGNS nucleation. However, because

of the complication of the plasma chemistry, it will be quite difficult to recognize which species devote mostly towards the VGNS growth. Numerous ions, free radicals, and other active species achieved from gaseous precursors collide inelastically with other species within the plasma. Typically, within C_2H_2 RF plasmas, $C_2H_2^+$, $C_4H_2^+$, H_2, $C_4H_3^+$, C_2 dimers, C_2H radical, C_4H_3 radicals, C_4H_2 neutrals, and $C_{2n}H_2$ polyacetylenes are formed and contribute to the formation of VGNSs [170].

The growth rate of VGNSs is largely associated with the gaseous dissociation energy as well as the generation of reactive C_2 dimers within the plasma. It has been found that it is easier to achieve carbon dimers via dissociating the C_2H_2 molecules instead of CH_4 precursor, mainly due to the C≡C bonding strength within C_2H_2 species. Therefore, during RF-PECVD processes, VGNSs can grow much more rapidly using C_2H_2 rather than CH_4. If fluorocarbon precursors are used such as C_2F_6 and CF_4, VGNS will display the thicker and straighter structure than during the CH_4-based process. Additionally, a little amount of oxidizing species, including water and oxygen, is typically introduced towards improving the VGNS crystalline structure.

Recent progress in utilizing liquid and solid natural precursors to achieve graphene has inspired cost-effective, environmentally friendly, and massive production of such material. In principle, VGNSs can also be fabricated via liquid and solid natural precursors, including sugar [171], honey [172], cookies [173], eggs [174], natural and plastic waste [173] and tea tree oil (TTO) extract [175, 176] by applying a rapid reformation within low-temperature H_2 or H_2–Ar plasmas without metal catalysts or external heat treatment. VGNSs achieved from those liquid and solid precursors can also exhibit vertical orientation, opening framework, and densely reactive edges, analogous to that derived from gaseous hydrocarbon precursors [172].

One specific advantage of using liquid and solid precursors is the potential transformation from biomass (particularly natural wastes) into useful VGNS structures for device production. Current chemical- and thermal-based approaches towards utilizing biomass are both precursor-specific and time-, resource-, energy-, and cost-consuming. In contrast, the plasma-based reformation stands for an energy-effective, eco-friendly, and cost-efficient strategy. Additionally, structural parameters including surface functional groups, reactive edge density, purities, adhesion, and crystallinity of VGNSs can be manipulated during PECVD process by selecting different liquid and solid precursors, which can possibly pave a novel pathway towards the massive production of VGNS frameworks for practical applications.

Growth Mechanisms of VGNSs

In spite of considerable efforts, the growth mechanisms of VGNSs are still elusive. Actually, apart from the effects of precursors and substrates, other parameters including the plasma power and source, plasma discharge duration, surface

temperature, etching rate, as well as pre-treatment can also have substantial impact on the final architecture [159]. The vapor–liquid–solid (VLS) (also called as vapor–solid–solid (VSS)) mechanisms broadly utilized for explaining the 1D nanostructure growth are not suitable to deduce the mechanism for plasma-assisted VGNS growth since no catalyst is needed. The nucleation mechanism for thin-film deposition also displays restricted relevance since it illustrates continuous layers instead of vertically oriented frameworks like VGNSs. Recent developments in techniques of microanalysis and time-resolved growth have enabled further investigation and several plausible growth mechanisms have been raised as described below.

The growth process of VGNSs can be divided into three steps: (i) firstly, a buffer layer is achieved onto the substrate surface with dangling bonds and irregular cracks, which becomes nucleation sites towards VGNS growth; (ii) subsequently, graphene begins to grow vertically under the influence of localised electric field due to plasma sheath and stress, and dissociated carbon species are constantly introduced into open edges; and (iii) VGNS growth eventually stops due to the closure of reactive edges which is controlled by the competition between etching effects and material deposition within the plasma.

The buffer layer achieved within the nucleation step is typically composed of either carbide or amorphous carbon. The carbide layer is generated if the substrates' material is able to react with carbon atoms, whereas amorphous carbon can be achieved if there is considerable mismatch between the graphite and the lattice parameters of the substrate. The carbon onion-like graphitic layer can be achieved between the amorphous carbon layer and the VGNSs, as exhibited in Fig. 14.18a. A proper amount of OH radicals and hydrogen atoms are found to be capable of etching the amorphous carbon and assisting in the VGNS growth. When the buffer layer is generated and the graphene begin to grow, VGNSs will not exhibit any substrate-dependent characteristics, leading to the similar morphology on any other substrate [177].

The next crucial issue is why VGNSs can grow vertically in plasma-assisted environment rather than remaining as horizontal graphene nanosheet which is typically observed in other growth methods. This is because of three possible aspects, typically, the internal stress, the electric field, as well as the anisotropic growth effects, which will be discussed below.

Internal stress effects—Internal stresses are derived from the ion bombardment, lattice mismatch, and temperature gradients between the graphitic material and the substrate. All these sources of internal stresses are possible in a plasma environment and they can possibly lead to buckling and defects within the buffer layer. The generated defects can act as nucleation sites for the VGNS growth. The intrinsic horizontal growth of 2D graphitic layers is finally converted to upward growth of graphene nanosheets, releasing the stress accumulated during the initial growth process. Subsequently, the dissociated species within the plasma constantly deliver carbon ions, neutrals, and radicals toward reactive sites of vertically oriented hexagonal lattices in VGNSs.

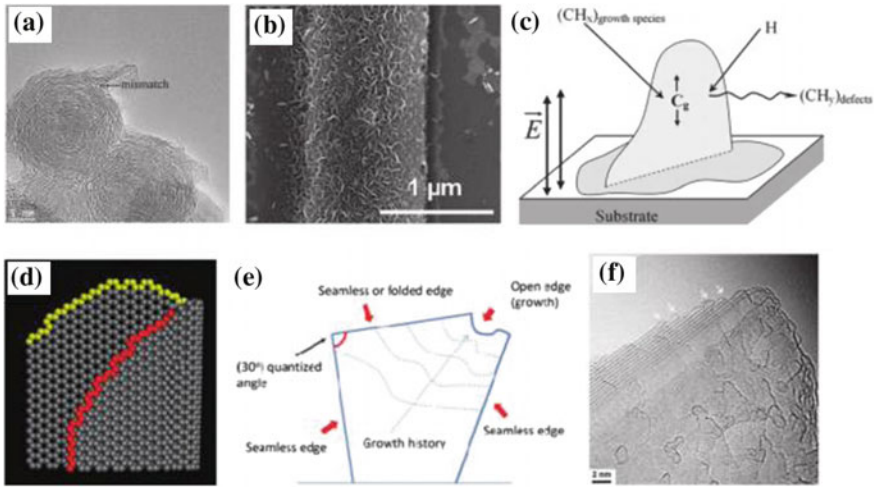

Fig. 14.18 VG growth mechanism: **a** TEM image of a carbon onion with mismatched graphitic layers at the surface, which may initialize the VGNS growth. [160] **b** SEM image of VGNSs grown on an Au stripe due to the electric field effect. [178] **c** A schematic of VGNS growth controlled by the electric field and carbon surface diffusion. [179] **d** Atomistic model of a curved vertical graphene with active growing edges (highlighted in *color*). [160] **e** Schematic representation of VGNS with folded/seamless and open edges. [102] **f** TEM image of a VGNS nanosheet with the tapered shape. Folded edges are shown by the *arrow*. [160] **a, d,** and **f** Reprinted from Zhao et al., [160] Copyright (2014), with permission from ACS Publications; **b** Reprinted from Yu et al., [178] Copyright (2011), with permission from ACS Publications; **c** Reprinted from Zhu et al., [179] Copyright (2007), with permission from Elsevier Ltd; **e** Reprinted from Davami et al., [102] Copyright (2014), with permission from Elsevier Ltd. **a–f** Reprinted from Bo et al., [158] RSC Publishing, Open Access paper

Electric field effects—The electric field within the plasma sheath contributes to the growth of diversely oriented nano-architecture such as CNTs and VGNSs on the substrate surface. The growth direction of VGNSs and the corresponding spatial distribution are largely influenced by the electric field within the plasma sheath. With the conductive substrates, the electric field can be achieved onto the surface of substrates and is relatively stronger close to the sharp points and edges. Such localized electric field on the substrate surface can be used for manipulating the orientation and density of the VGNS framework [178]. As exhibited in Fig. 14.18b, VGNSs was grown on the Au stripe with the high density whereas both VGNSs and amorphous carbon were not observed on the neighboring SiO_2 surface [178]. This phenomenon was explained by the relatively stronger electric field on the Au strip as compared with that on the SiO_2 substrate. Therefore, adjusting the electric field distribution on the surface can pave a novel pathway to pattern VGNSs for practical applications. Additionally, if the substrate is nonconductive as well as disconnected

from the external electrical circuit within the plasma, the comparatively lower electric field will cause much more random and irregular VGNS frameworks [163].

Anisotropic growth effects—The vertically orientated growth of VGNSs has also been attributed to the anisotropic growth effect. It has been reported that growth rates in the directions perpendicular and parallel to the graphene layer are different. In addition, the VGNSs oriented normally to the substrate grow relatively faster than the randomly oriented VGNSs, partially because of the surface diffusion of carbon species (Fig. 14.18c) [7]. Carbon-based species onto the surface of growing nanosheets move rapidly along the nanosheet surface to reach the upper edges, and subsequently achieve covalent bonding with the edge atoms before desorbing from the nanosheet surface. In comparison, carbon-based species diffusing onto the substrate can be desorbed from the surface due to the weak interaction of the species with the substrate. Additionally, more carbon species can be preferentially promoted towards growing edges of VGNSs because of their sharp characteristics which can display enhanced localized electric fields. Resultantly, the growth rate along the vertical direction is relatively higher than that along the lateral direction.

Currently, a dynamic model accompanied with experimental results has exhibited that the VGNS growth can be regarded as the step-flow process during which the nucleation occurs at the bottom [102, 160]. In terms of such a model, the VGNS nucleation can be facilitated via the graphitic layer mismatches at either the carbon onions or the buffer layer which has been generated on the substrate surface. Subsequently, the growth of individual graphene nanosheet can be controlled by the diffusion rate of carbon species towards each layer and the number of layers nucleated at the bottom (Fig. 14.18d). Additionally, VGNS growth can only take place at open edges rather than at seamless or folded edges, as illustrated in Fig. 14.18e. Since the neighboring layers are capable of achieving a closure and restricting the growth, tapered VGNS can be generated (Fig. 14.18f).

Although the growth mechanism of VGNSs based on gaseous precursors has attracted considerable attention, no unambiguous explanation towards the VGNS growth from liquid and solid precursors has currently been proposed. There are several obvious similarities in the growth dynamics for VGNSs synthesized using gaseous, liquid, or solid precursors. First, the plasma works on the liquid or solid natural precursors through dehydrating them because of the plasma-based heating process. Subsequently, the plasma converts the dehydrated natural precursors into smaller carbon-based species, regardless of the intrinsic precursor, via interacting with the plasma-achieved ions, neutrals, and radicals. Furthermore, these species serve as the fundamental parts towards the VGNS growth. However, some challenges still remain, such as why VGNS based on different precursors can deliver different adhesive property towards the substrate, and how to exactly control the surface reconstructions via the plasma for the optimized VGNS growth along the perpendicular direction. Since the understanding towards growth mechanism is fundamental to the controllable growth of VGNSs, and even related to their device performance, much more investigations are still required in such direction.

14.5.3.3 Energy Application of VGNSs

VGNSs for Supercapacitors (SCs)

As discussed above, SCs are novel electrochemical devices for energy storage which need frequent charging–discharging processes to achieve high power and energy densities. These devices can also deliver a much improved capacitance as compared to regular capacitors, partially because of the introduction of novel nano-architectures. Here we will describe recent development of VGNSs and VG-based composites in SC applications.

VGNS-based active materials for Electric Double-Layer Capacitors (EDLCs) —The specific capacitances of EDLCs are essentially ascribed to the utilization of electrode materials with the high SSAs. Therefore, the features of electrode materials serve as an essential candidate in determining the performance of EDLCs. A favorable EDLC electrode material should satisfy the following criteria: (i) a highly active surface area for the efficient ion adsorption to deliver high specific capacitance and high energy density; (ii) a proper architecture for the facile ion diffusion to achieve high rate capability; and (iii) the minimum resistances within the bulk of the material and at the interface between the current collector and the material towards the rapid charge transport to deliver the high power density.

The typical features of VGNSs seem to fulfill the above requirements. Firstly, the VGNS frameworks exhibit a non-agglomerated architecture with densely exposed edges which accelerate the surface utilization towards energy storage. The graphene-based EDLC electrodes are usually prepared using reduced graphene oxides (RGOs) through chemical method, accompanied with the assembly of these structures onto current collectors by applying binders. Because of the van der Waals interactions and the introduction of binders, typical restacking of horizontal graphene usually results in the tremendous decrease of available SSAs towards charge adsorption. Comparatively, the non-agglomerated feature of VGNSs can deliver the larger electrochemically available surface area, and hence a higher specific capacitance. Additionally, the numerous edges of VGNSs are also able to improve the charge storage capability, because the edges can deliver a much larger SSAs for improved specific capacitance in comparison with the basal planes [157].

Second, with VGNSs applied as electrode materials, the large ionic resistance attributed to the distributed charge storage within the porous structure can be largely decreased, which enables such electrode material to be utilized in the high current density application. Moreover, as mentioned in one of the previous sections on EDLC, the electrolyte accessible into porous structures serves as the essential part in determining the rate capability of EDLC. Remarkable ionic resistance can be achieved if the porous sizes are too small, resulting in the depressed capacitive performance, particularly with relatively higher current density. Such issue occurs not only in activated carbons, one of the most commonly utilized porous architectures for practical EDLCs, but also in horizontal graphene in which porous structure is mainly derived from the 2D interlayers. In terms of VGNSs (Fig. 14.19a), the open inter-sheet channels and vertical orientation are capable of

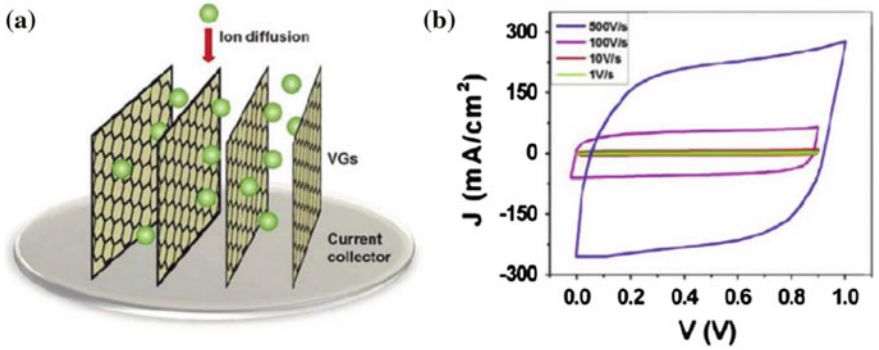

Fig. 14.19 Recent applications of VGNSs in SCs. **a** Schematic of ion diffusion within VGNSs [158]. **b** CV curves of a VGNS-based EDLC electrode (VGNS grown on a nickel foam) at scanning rates of 1, 10, 100 and 500 V s^{-1} [166]. **a** Reprinted from Bo et al., [158] RSC Publishing, Open Access Paper; and **b** Reprinted from Ren et al., [166] Copyright (2014), with permission from Elsevier Ltd

accelerating the ionic migration between the layers and largely decreasing the negative porosity effects [157].

Third, the series resistance within EDLC can be minimized and hence the rate capabilities can be significantly improved by using VGNSs. The vertically orientated feature of VGNSs with the outstanding initial in-plane electronic conductivity accelerates the charge transport within electrode materials. On the other hand, the direct growth of VGNSs without the typically utilized binder can decrease the contact resistance between the electrode material and the current collector. Furthermore, the novel EDLC electrode has also been reported with VGNS deposited onto the nickel foam current collectors. The introduction of the foam-type collector rather than the foil-type counterpart can result in a higher loading density of electrode materials, since VGNSs can be totally covered onto the 3D metallic substrate. Notably, most EDLCs are measured with the highest scanning rate of 1 V s^{-1}. As exhibited in Fig. 14.19b, with increasing scanning rate from 1 to 500 V s^{-1}, the cyclic voltammetry curves still remain quasi-rectangular shapes, which considerably indicates the high rate performance of VGNSs-based EDLCs.

The capacitive performance of VGNSs-based SCs can be controlled by tailoring their structure and morphology during the PECVD process, which can be achieved by tuning plasma sources, growth precursors, and growth conditions. Typically, the density of VGNSs edges and the graphitization degree largely influence the resultant performance [180]. Thinner edges particularly result in the higher specific capacitance, because of the much larger SSAs derived from edge planes than basal planes. Moreover, a higher sp^2 proportion can also enhance the charge storage capability, because the sp^3-type carbon can only increase the charge-transfer resistance and hence provide a little contribution towards the charge storage. The favorable specific capacitance of VGNSs-based EDLCs is capable of achieving the high value of 230 F g^{-1}, typically $\sim$23 mF cm^{-2} at the scanning rate of 10 mV s^{-1}.

The specific capacitance can be largely enhanced by introducing the VGNS-based hybrid architectures, such as CNT-VGNS. Such a combination between 1D and 2D nano-architectures can further enhance the SSA and improve the electron transport property of active materials, resulting in the highly specific capacitance of 278 F g^{-1}, typically ~36 mF cm^{-2}, at the scanning rate of 10 mV s^{-1} and great cyclability (99% capacitance retention after initial 8000 cycles) [181].

VGNS-based active materials for pseudocapacitors—As compared to the EDLCs' dependence on physical ionic adsorption, the pseudocapacitors largely rely on reversible redox charge transfer in electrodes. Because of the existence of redox processes, pseudocapacitors commonly provide a higher capacitance with the compromise of the lower power density and depressed cyclability as compared to the EDLC devices [7]. Through the integration of advantages of VGNSs with electrically conducting polymers or transitional metal oxides, high-performance pseudocapacitors can be achieved. VGNSs with both the high SSA and the outstanding electric conductivity can synergistically optimize the supercapacitive performance of faradic active materials. Actually, VGNSs can increase the loading density of active materials for the enhanced energy density and also improve the charge transport property between the substrate and active materials for higher power density and rate capacitance, and also optimize the adhesive feature of the active materials for the better cyclability.

For example, the electrochemical performance of pseudocapacitors constructed using VGNS-MnO_2 hybrid nano-structured electrode can be much better than that of EDLCs. VGNSs deposited onto a nickel foil have been applied as conductive templates for depositing MnO_2 nano-flowers. The exposed SSA and high conductivity of VGNSs can enhance electrochemical properties of MnO_2. At the scanning rate of 10 mV s^{-1}, the VGNS-MnO_2 electrode has delivered the high specific capacitance of 1060 F g^{-1}. Additionally, the VGNS-MnO_2 electrode has delivered a considerable capacitance retention (497%) after initial 1000 cycles, which can be associated with the strong adhesion between the VGNSs and the MnO_2 [180]. On the basis of density functional theory calculations, it has been shown that the sharp edge planes and vertical orientation of VGNSs accelerate the ion diffusion with lower energy barriers, whereas the covalent bonding between graphene and MnO_2 results in the effective charge transfer. Similar applications of VGNS-MnO_2 with various morphologies and other transitional metal oxides have also been investigated [182]. These investigations have indicated the crucial roles of VGNSs in reducing internal resistance, improving the specific capacitance, and enhancing the cyclability.

Hierarchical electrodes comprised of carbon cloth (CC), polyaniline (PANI), and VGNSs were found to further enhance the SC performance [183]. The SSA of the carbon cloth, which displays an open and flexible substrate, has been found to increase with the decoration of VGNSs. At the scanning rate of 2 mV s^{-1}, the specific capacitance of the hierarchical architecture of CC–VGNSs–PANI composite was almost three times higher than that of the CC–PANI electrode. Additionally, the CC–VGNS–PANI electrode exhibited the specific capacitance of 2000 F g^{-1} and the areal capacitance of 2.6 F cm^{-2}. The presence of VGNSs can

also enhance the electron transport feature, resulting in higher energy and power densities as compared to the previously investigated values towards PANI-based electrodes. For instance, a high-performance all-solid-state flexible SC with the CC–VGNS–PANI electrode and the H_2SO_4-PVA polymer electrolyte has been obtained. Such SC can provide the energy density of ten times as high as that of the commercially available one and is comparable to the upper potential of 4 V in LIBs, and the corresponding power density can be $\sim$2 orders of magnitude larger than that of LIBs.

In the recently reported work done by authors' group [175], via controlling plasma discharge duration, the optimized fully covered VGNS (f-VGS) with large surface area and large amounts of reactive edges, shown in Fig. 14.20, have been grown using environmentally friendly sustainable carbon precursor using a simple homemade PECVD setup discussed in the later section and shown in Fig. 14.21. The dense and uniform nanostructure of f-VGS can be observed in Fig. 14.20b with fully covered VGNSs on the surface of the graphite-type flake, in comparison with separated seldom VGNS structures on mostly horizontal multilayer graphene nanosheets (h-GS) seen in Fig. 14.20a. Notably in Fig. 14.21a, most of the outer surface of the Ni foam substrate is covered by multilayered horizontal graphene architecture with a little amount of VGNS nanostructures. The VGNS substrate template was then loaded with MnO_2 as the active material using hydrothermal method. In Fig. 14.20c, MnO_2 nanocrystals on h-GS have relatively subdued perpendicular architecture due to a few VGNSs on h-GS substrate, which severely decrease the overall SSA. Comparatively, MnO_2 thin-film assembled in nanocrystalline morphology is uniformly and strongly orthogonally anchored on the surface of VGNSs on f-VGS surface (Fig. 14.20d). Such corresponding 3D hierarchical composite still maintains its initial structure of f-VGS, which is capable of accelerating ion transfer and minimizing structural rearrangements during redox reaction. The supercapacitive performances of MnO_2@h-GS and MnO_2@f-VGS were further compared. The galvanostatic charge–discharge curves of MnO_2@f-VGS sample present enhanced performance and limited voltage drop with higher capacitance of 290 F g^{-1} at 2 A g^{-1} and 203 F g^{-1} at 10 A g^{-1}, as compared with that of MnO_2@h-GS sample (163 F g^{-1} and 82 F g^{-1}) (Fig. 14.20e). Additionally, for all the current densities from 1 to 20 A g^{-1}, the specific capacitance of MnO_2@f-VGS composite is significantly higher than that of MnO_2@h-GS (more than twice at current densities $\geq$5 A g^{-1}) (Fig. 14.20f), also confirming the enhanced synergistic effect of f-VGS than that of h-GS. Our results indicate that an increase in the amount of VGNSs on the substrate improves the overall capacitive performance of composites.

VGNSs for LIBs

The specific features of VGNSs also allow them to be highly suitable for other energy storage applications especially LIBs. As one of the most commonly utilized rechargeable batteries, LIBs can accumulate charges via the reversible

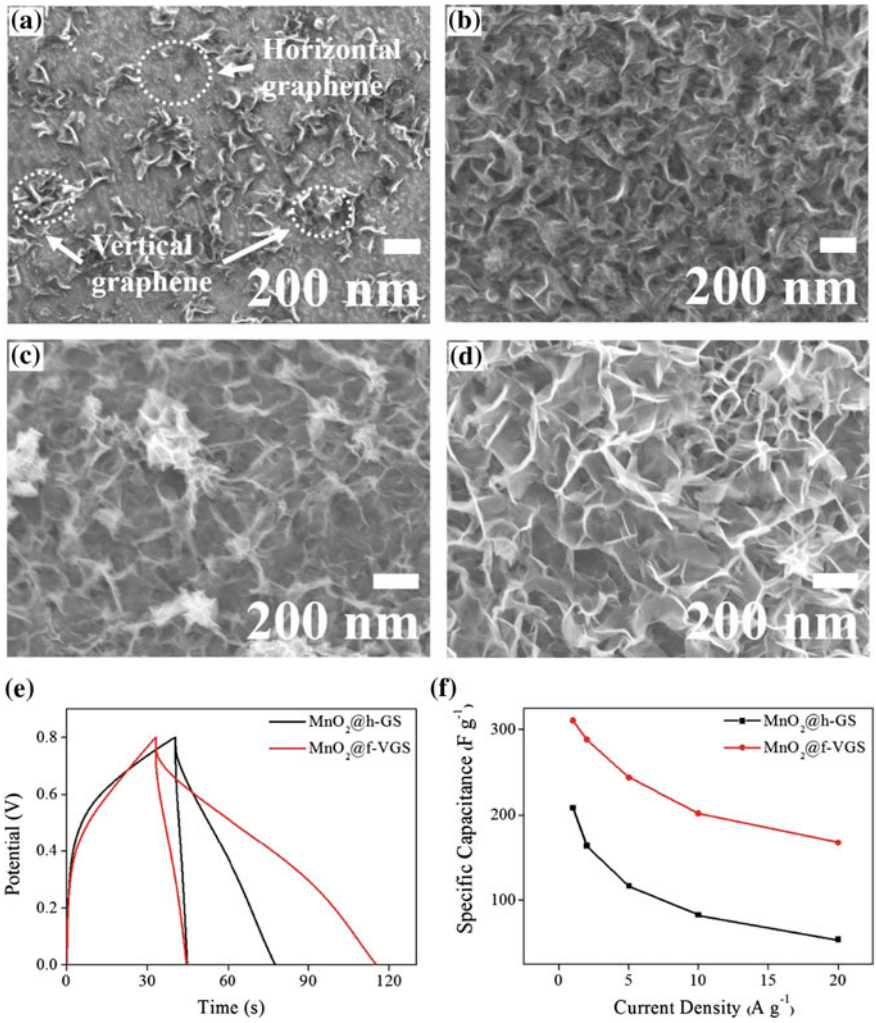

Fig. 14.20 **a** and **b** SEM images of h-GS and f-VGS; **c** and **d** SEM images of MnO_2@h-GS and MnO_2@f-VGS; **e** Galvanostatic discharge comparison at the current densities of 2 and 10 A g^{-1}; **f** Galvanostatic charge–discharge capacitance at different discharge current densities. Reprinted from Ouyang et al., [175] Copyright (2016), with permission from RSC Publications. *Note* Authors own work, permission not needed and hence not submitted but acknowledgment is necessary (delete this later)

intercalation-extraction of lithium ions between redox-active materials. Highly reversible lithium ion storage capability as well as the outstanding cyclability are expected characteristics of the anode materials. VGNSs directly deposited onto nano-structured current collectors serve as the promising anode materials in LIBs. VGNSs with the exposed edge planes and graphene surfaces are capable of

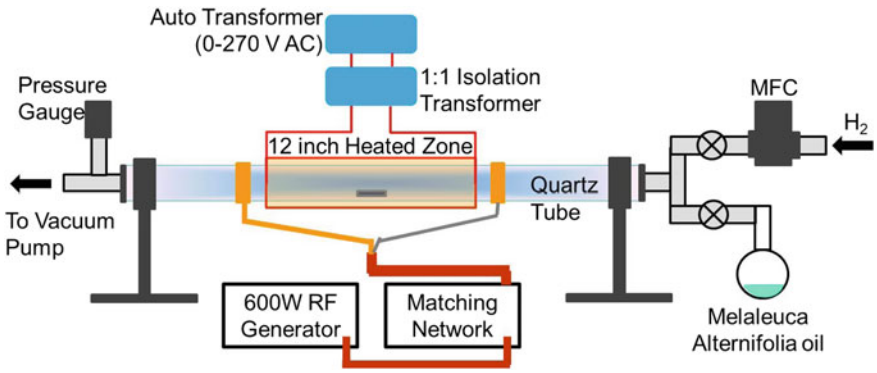

Fig. 14.21 Schematic diagram of our homemade PECVD

providing significantly increased active sites for capturing lithium ions. Additionally, the open inter-sheet passages, vertical orientation, and outstanding electrical connection of the VGNS substrates can tremendously decrease the transport resistance of lithium ions, the inherent resistance within the anode, as well as the contact resistance between the anode and the current collector, respectively, which is why LIBs utilizing VGNSs as anode materials can deliver the highly reversible capability and excellent cyclability. In addition, the integration of VGNS with lithium alloying materials (including GeO_x) can further enhance the lithium storage capability. For instance, VGNSs can serve as rapid electron transport passages and also enable smooth lithium diffusion routes within the VGNS@GeO_x sandwich nano-structural anode [162]. The VGNS@GeO*x* anode can deliver the stable capability of 1008 mA h g^{-1} at the current density of 550 mA g^{-1} (capacity retention of 96% over 100 cycles), the capability of 545 mA h g^{-1} at 15 C, and the capability retention of 92% with the current density recovered to 550 mA g^{-1}. Such features are regarded quite competitive in comparison with other lithium alloying material based LIBs [162].

In our own work [176], we synthesized three-dimensional vertical graphene (3DVG) using a low-cost, nontoxic, renewable and environment-friendly natural organic material, *M. alternifolia* essential oil, instead of hazardous and costly hydrocarbon gases in our homemade RF-PECVD system shown in Fig. 14.21. In comparison with three-dimensional graphene (3DG), 3D vertical graphene (3DVG) shown in Fig. 13.22a grown by the PECVD strategy retains hierarchical structure, resulting in many edges and ensuring direct contact and superior ion/electron transportation between active materials and the conductive substrate. It also exhibits the typical extent of VG to be the order of two to three hundred nanometers and thus holds large amounts of edges. As shown in Fig. 14.22b, the highly interconnected 3D nanoflower-like structures are composed of dense and numerous nanosheets of MoS_2, deposited onto 3DVG surface with uniform distribution. Notably, the nanosheets are randomly connected with the adjacent nanosheets to assemble into cross-linked 3D nanostructure. The LIB performance of MoS_2

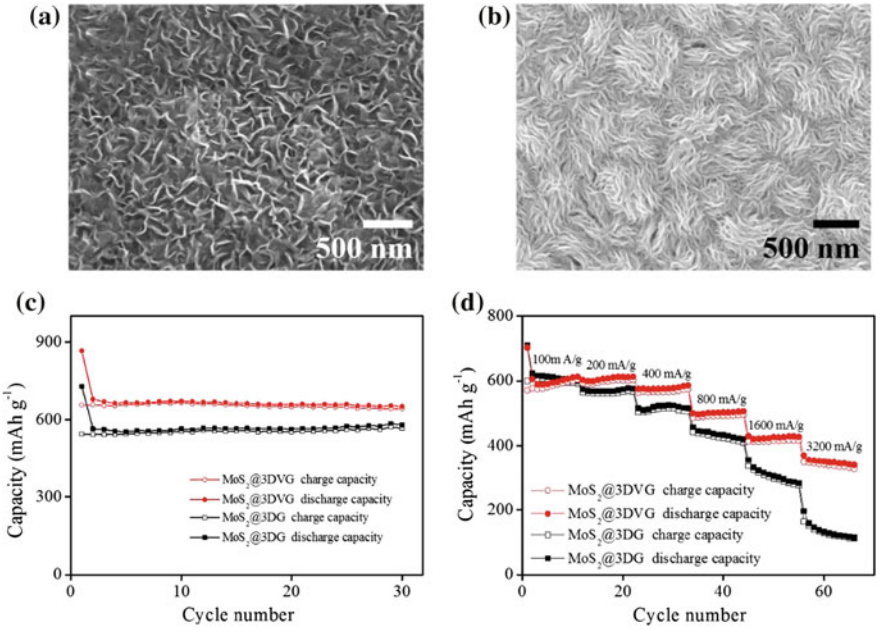

Fig. 14.22 **a** and **b** SEM images of 3DVG and MoS_2@3DVG; **c** and **d** cycling performance of MoS_2@3DVG and MoS_2@3DG at 100 mA g^{-1}; **d** Rate capability of MoS_2@3DVG and MoS_2@3DG. Reprinted from Ouyang et al., [176] Copyright (2016), with permission from Elsevier Ltd

anchored 3DVG surface (MoS_2@3DVG) is compared to MoS_2 anchored 3DG (MoS_2@3DG). As shown in Fig. 14.22c, the capacity of the MoS_2@3DVG is stable at ~670 mA h g^{-1} over 30 cycles at 100 mA g^{-1}, superior than that of MoS_2@3DG (550 mA h g^{-1}). In Fig. 14.22d, the capacities of the MoS_2@3DVG electrode are higher than those of MoS_2@3DG from 200 to 3200 mA g^{-1}. Due to the much lower density of 3DVG as compared to MoS_2 nanosheets, the 3DVG substrate occupied only about 8% fraction of total mass density. Hence, most of the capacity is attributed to MoS_2 nanosheets, which further helps to indicate lower charge-transfer resistance of MoS_2@3DVG than that of MoS_2@3DG. Therefore, we certainly ensure the advantage of the 3DVG and further demonstrate its contribution for developing nanocomposites based electrode.

14.6 Conclusions and Outlook

Plasma-enhanced strategy has delivered typical advantages in nanostructure fabrications and therefore enhanced energy storage performance, as exhibited in the numerous instances in this chapter. Nonetheless, the impact of plasma onto

nano-structural synthesis is not only restricted to the above-described components. As an intriguing inter-disciplinary direction, numerous aspects still require to be investigated in energy storage application.

Carbon-based nanostructures especially CNTs and VGNSs are two of the well-investigated materials using plasma-enhanced fabrication and functionalization. However, a deeper understanding of plasma-assisted synthesis is still lacking and more investigations and efforts are required. The utilization of plasma-based approaches for synthesis and processing of materials for energy storage applications is still a relatively less explored field and more efforts can possibly bring about more attractive results. The relationship between the plasma features or plasma parameters and material properties serves as one of key areas of research and development to achieve nano-architectures with desired enhanced performance from plasma-assisted syntheses/processing. The number of research investigations or efforts to study the influence of plasma parameters onto material features/characteristics is highly insufficient even in the comparatively well-explored carbon-based systems such as VGNSs and CNTs. Therefore, both case-specific studies and general plasma diagnostics which concentrate on the material characteristics are required in near future.

Moreover, the combination of plasma-assisted approaches with other nano-structural fabrication strategies is capable of stimulating the emergence of new novel fabrication methods, which can possibly deliver novel properties. Typically, plasma-based approaches alone can hardly achieve materials with excellent features. Therefore, a suitable evaluation towards the plasma-based approaches is usually required, understanding both their advantages and disadvantages. Nano-structural fabrication is an interdisciplinary field which requires different fields of knowledge as well as techniques. Proper integration of plasma-based strategies with other existent approaches can pave a novel pathway for unique nano-structural synthesis for energy storage application.

References

1. N.-S. Choi, Z. Chen, S.A. Freunberger, X. Ji, Y.-K. Sun, K. Amine, G. Yushin, L.F. Nazar, J. Cho, P.G. Bruce, Angew. Chem. Int. Ed. **51**, 9994–10024 (2012)
2. J. Jiang, Y. Li, J. Liu, X. Huang, C. Yuan, X.W. Lou, Adv. Mater. **24**, 5166–5180 (2012)
3. G. Wang, L. Zhang, J. Zhang, Chem. Soc. Rev. **41**, 797–828 (2012)
4. V. Etacheri, R. Marom, R. Elazari, G. Salitra, D. Aurbach, Energy Environ. Sci. **4**, 3243–3262 (2011)
5. C. Liu, F. Li, L.-P. Ma, H.-M. Cheng, Adv. Mater. **22**, E28–E62 (2010)
6. S.L. Candelaria, Y. Shao, W. Zhou, X. Li, J. Xiao, J.-G. Zhang, Y. Wang, J. Liu, J. Li, G. Cao, Nano Energy **1**, 195–220 (2012)
7. L.L. Zhang, X.S. Zhao, Chem. Soc. Rev. **38**, 2520–2531 (2009)
8. T. Lin, I.-W. Chen, F. Liu, C. Yang, H. Bi, F. Xu, F. Huang, Science **350**, 1508–1513 (2015)
9. G. Wang, H. Wang, X. Lu, Y. Ling, M. Yu, T. Zhai, Y. Tong, Y. Li, Adv. Mater. **26**, 2676–2682 (2014)
10. J.B. Goodenough, Y. Kim, Chem. Mater. **22**, 587–603 (2010)

11. Z. Liu, L. Jiao, Y. Yao, X. Xian, J. Zhang, Adv. Mater. **22**, 2285–2310 (2010)
12. I. Langmuir, Proc. Natl. Acad. Sci. **14**, 627–637 (1928)
13. H. Abe, M. Yoneda, N. Fujiwara, Jpn. J. Appl. Phys. **47**, 1435 (2008)
14. D. Schram, J. Van der Mullen, M. Van de Sanden, Plasma Phys. Controlled Fusion **36**, B65 (1994)
15. N. Layadi, J.I. Colonell, J.T.C. Lee, Bell Labs Tech. J. **4**, 155–171 (1999)
16. M.R. Palacin, Chem. Soc. Rev. **38**, 2565–2575 (2009)
17. W. Ai, Z. Du, Z. Fan, J. Jiang, Y. Wang, H. Zhang, L. Xie, W. Huang, T. Yu, Carbon **76**, 148–154 (2014)
18. J. Zhu, K. Sakaushi, G. Clavel, M. Shalom, M. Antonietti, T.-P. Fellinger, J. Am. Chem. Soc. **137**, 5480–5485 (2015)
19. J. Xu, Y. Lin, J.W. Connell, L. Dai, Small **11**, 6179–6185 (2015)
20. M. Park, X. Zhang, M. Chung, G.B. Less, A.M. Sastry, J. Power Sources **195**, 7904–7929 (2010)
21. P. Verma, P. Maire, P. Novák, Electrochim. Acta **55**, 6332–6341 (2010)
22. J.R. Owen, Chem. Soc. Rev. **26**, 259–267 (1997)
23. Y. Wang, G. Cao, Adv. Mater. **20**, 2251–2269 (2008)
24. Y. Nishi, Chem. Rec. **1**, 406–413 (2001)
25. P. Hagenmuller, J. Power Sources **90**, 9–12 (2000)
26. G. Zhang, S. Hou, H. Zhang, W. Zeng, F. Yan, C.C. Li, H. Duan, Adv. Mater. **27**, 2400–2405 (2015)
27. B. Liu, J. Zhang, X. Wang, G. Chen, D. Chen, C. Zhou, G. Shen, Nano Lett. **12**, 3005–3011 (2012)
28. H. Liu, W. Li, D. Shen, D. Zhao, G. Wang, J. Am. Chem. Soc. **137**, 13161–13166 (2015)
29. N.D. Trinh, M. Saulnier, D. Lepage, S.B. Schougaard, J. Power Sources **221**, 284–289 (2013)
30. K.T. Lee, X. Ji, M. Rault, L.F. Nazar, Angew. Chem. Int. Ed. **48**, 5661–5665 (2009)
31. D. Chao, X. Xia, J. Liu, Z. Fan, C.F. Ng, J. Lin, H. Zhang, Z.X. Shen, H.J. Fan, Adv. Mater. **26**, 5794–5800 (2014)
32. M. Armand, J.-M. Tarascon, Nature **451**, 652–657 (2008)
33. P.G. Bruce, B. Scrosati, J.M. Tarascon, Angew. Chem. Int. Ed. **47**, 2930–2946 (2008)
34. M.S. Whittingham, Chem. Rev. **104**, 4271–4302 (2004)
35. R. Castaing, Y. Reynier, N. Dupré, D. Schleich, S. Jouanneau, Si Larbi, D. Guyomard and P. Moreau. J. Power Sources **267**, 744–752 (2014)
36. P. Gibot, M. Casas-Cabanas, L. Laffont, S. Levasseur, P. Carlach, S. Hamelet, J.-M. Tarascon, C. Masquelier, Nat. Mater. **7**, 741–747 (2008)
37. B. Gao, C. Bower, J. Lorentzen, L. Fleming, A. Kleinhammes, X. Tang, L.E. Mcneil, Y. Wu, O. Zhou, Chem. Phys. Lett. **327**, 69–75 (2000)
38. J. Eom, H. Kwon, J. Liu, O. Zhou, Carbon **42**, 2589–2596 (2004)
39. X.X. Wang, J.N. Wang, H. Chang, Y.F. Zhang, Adv. Funct. Mater. **17**, 3613–3618 (2007)
40. P. Guo, H. Song, X. Chen, Electrochem. Commun. **11**, 1320–1324 (2009)
41. H. Zhou, S. Zhu, M. Hibino, I. Honma, M. Ichihara, Adv. Mater. **15**, 2107–2111 (2003)
42. F. Su, X. Zhao, Y. Wang, J. Zeng, Z. Zhou, J.Y. Lee, J. Phys. Chem. B **109**, 20200–20206 (2005)
43. M. Thackeray, J. Vaughey, C. Johnson, A. Kropf, R. Benedek, L. Fransson, K. Edstrom, J. Power Sources **113**, 124–130 (2003)
44. D. Larcher, S. Beattie, M. Morcrette, K. Edstroem, J.-C. Jumas, J.-M. Tarascon, J. Mater. Chem. **17**, 3759–3772 (2007)
45. A. Todd, R. Mar, J. Dahn, J. Electrochem. Soc. **154**, A597–A604 (2007)
46. P. Poizot, S. Laruelle, S. Grugeon, L. Dupont, J. Tarascon, Nature **407**, 496–499 (2000)
47. O. Delmer, P. Balaya, L. Kienle, J. Maier, Adv. Mater. **20**, 501–505 (2008)
48. F. Badway, A. Mansour, N. Pereira, J. Al-Sharab, F. Cosandey, I. Plitz, G. Amatucci, Chem. Mater. **19**, 4129–4141 (2007)
49. P.-L. Taberna, S. Mitra, P. Poizot, P. Simon, J.-M. Tarascon, Nat. Mater. **5**, 567–573 (2006)

50. C. Largeot, C. Portet, J. Chmiola, P.-L. Taberna, Y. Gogotsi, P. Simon, J. Am. Chem. Soc. **130**, 2730–2731 (2008)
51. R. Kötz, M. Carlen, Electrochim. Acta **45**, 2483–2498 (2000)
52. R. Kötz, S. Müller, M. Bärtschi, B. Schnyder, P. Dietrich, F. Büchi, A. Tsukada, G. Scherer, P. Rodatz, O. Garcia, Electrochem. Soc. Proc. **21**, 564–574 (2001)
53. P. Simon, Y. Gogotsi, Nat. Mater. **7**, 845–854 (2008)
54. K.H. An, W.S. Kim, Y.S. Park, J.-M. Moon, D.J. Bae, S.C. Lim, Y.S. Lee, Y.H. Lee, Adv. Funct. Mater. **11**, 387–392 (2001)
55. B. Babakhani, D.G. Ivey, Electrochim. Acta **55**, 4014–4024 (2010)
56. J. Zheng, J. Huang, T. Jow, J. Electrochem. Soc. **144**, 2026–2031 (1997)
57. M.-S. Wu, P.-C.J. Chiang, Electrochem. Solid-State Lett. **7**, A123–A126 (2004)
58. W. Sugimoto, H. Iwata, Y. Murakami, Y. Takasu, J. Electrochem. Soc. **151**, A1181–A1187 (2004)
59. X. Dong, W. Shen, J. Gu, L. Xiong, Y. Zhu, H. Li, J. Shi, J. Phys. Chem. B **110**, 6015–6019 (2006)
60. Y. Zhang, H. Feng, X. Wu, L. Wang, A. Zhang, T. Xia, H. Dong, X. Li, L. Zhang, Int. J. Hydrogen Energy **34**, 4889–4899 (2009)
61. B. Conway, V. Birss, J. Wojtowicz, J. Power Sources **66**, 1–14 (1997)
62. C.-M. Chuang, C.-W. Huang, H. Teng, J.-M. Ting, Energy Fuels **24**, 6476–6482 (2010)
63. M. Kisacikoglu, M. Uzunoglu, M. Alam, Int. J. Hydrogen Energy **34**, 1497–1507 (2009)
64. A. Kusko, J. Dedad, Industry Applications Magazine. IEEE **13**, 66–72 (2007)
65. M. Inagaki, H. Konno, O. Tanaike, J. Power Sources **195**, 7880–7903 (2010)
66. A. Burke, J. Power Sources **91**, 37–50 (2000)
67. H. Chen, T.N. Cong, W. Yang, C. Tan, Y. Li, Y. Ding, Prog. Nat. Sci. **19**, 291–312 (2009)
68. J. Garche, C.K. Dyer, P.T. Moseley, Z. Ogumi, D.A. Rand, B. Scrosati, *Encyclopedia of Electrochemical Power Sources* (Newnes, 2013)
69. A.S. Arico, P. Bruce, B. Scrosati, J.-M. Tarascon, W. Van Schalkwijk, Nat. Mater. **4**, 366–377 (2005)
70. H. Lee, M.S. Cho, I.H. Kim, J. Do Nam, Y. Lee, Synth. Met. **160**, 1055–1059 (2010)
71. E. Frackowiak, S. Delpeux, K. Jurewicz, K. Szostak, D. Cazorla-Amoros, F. Beguin, Chem. Phys. Lett. **361**, 35–41 (2002)
72. C. Peng, S. Zhang, D. Jewell, G.Z. Chen, Prog. Nat. Sci. **18**, 777–788 (2008)
73. C. Peng, J. Jin, G.Z. Chen, Electrochim. Acta **53**, 525–537 (2007)
74. Y.R. Ahn, M.Y. Song, S.M. Jo, C.R. Park, D.Y. Kim, Nanotechnology **17**, 2865 (2006)
75. V. Patake, C. Lokhande, O.S. Joo, Appl. Surf. Sci. **255**, 4192–4196 (2009)
76. C.-C. Hu, Y.-H. Huang, K.-H. Chang, J. Power Sources **108**, 117–127 (2002)
77. J. Yan, T. Wei, J. Cheng, Z. Fan, M. Zhang, Mater. Res. Bull. **45**, 210–215 (2010)
78. J. Jiang, A. Kucernak, Electrochim. Acta **47**, 2381–2386 (2002)
79. R.K. Kalluri, M.M. Biener, M.E. Suss, M.D. Merrill, M. Stadermann, J.G. Santiago, T.F. Baumann, J. Biener, A. Striolo, Phys. Chem. Chem. Phys. **15**, 2309–2320 (2013)
80. N.L. Torad, R.R. Salunkhe, Y. Li, H. Hamoudi, M. Imura, Y. Sakka, C.-C. Hu, Y. Yamauchi, Chem. Eur. J. **20**, 7895–7900 (2014)
81. Y. Cao, H. Yu, J. Tan, F. Peng, H. Wang, J. Li, W. Zheng, N.-B. Wong, Carbon **57**, 433–442 (2013)
82. D. Guo, R. Shibuya, C. Akiba, S. Saji, T. Kondo, J. Nakamura, Science **351**, 361–365 (2016)
83. S. Chen, J. Duan, M. Jaroniec, S.Z. Qiao, Adv. Mater. **26**, 2925–2930 (2014)
84. A.M. El-Sawy, I.M. Mosa, D. Su, C.J. Guild, S. Khalid, R. Joesten, J.F. Rusling, S.L. Suib, Adv. Energy Mater. **6**, 1501966 (2016)
85. C.-C. Hu, C.-C. Wang, K.-H. Chang, Electrochim. Acta **52**, 2691–2700 (2007)
86. K.R. Prasad, K. Koga, N. Miura, Chem. Mater. **16**, 1845–1847 (2004)
87. Y.-K. Zhou, B.-L. He, W.-J. Zhou, J. Huang, X.-H. Li, B. Wu, H.-L. Li, Electrochim. Acta **49**, 257–262 (2004)
88. L.-Z. Fan, J. Maier, Electrochem. Commun. **8**, 937–940 (2006)

89. C. Peng, D. Hu, G.Z. Chen, Chem. Commun. **47**, 4105–4107 (2011)
90. J. Zang, S.-J. Bao, C.M. Li, H. Bian, X. Cui, Q. Bao, C.Q. Sun, J. Guo, K. Lian, J. Phys. Chem. C **112**, 14843–14847 (2008)
91. R. Liu, S.I. Cho, S.B. Lee, Nanotechnology **19**, 215710 (2008)
92. F. Fusalba, N. El Mehdi, L. Breau, D. Bélanger, Chem. Mater. **11**, 2743–2753 (1999)
93. D.-D. Zhao, S.-J. Bao, W.-J. Zhou, H.-L. Li, Electrochem. Commun. **9**, 869–874 (2007)
94. H. Conrads, M. Schmidt, Plasma Sources Sci. Technol. **9**, 441 (2000)
95. D. Korzec, F. Werner, R. Winter, J. Engemann, Plasma Sources Sci. Technol. **5**, 216 (1996)
96. M. Turner, M. Lieberman, Plasma Sources Sci. Technol. **8**, 313 (1999)
97. O.A. Popov, *High Density Plasma Sources: Design, Physics and Performance* (Elsevier, 1996)
98. M. Inagaki, Carbon **50**, 3247–3266 (2012)
99. Q. Tian, Y. Tian, Z. Zhang, L. Yang, S.-I. Hirano, J. Power Sources **280**, 397–405 (2015)
100. H. Wu, Z. Li, D. Ji, Y. Liu, L. Li, D. Yuan, Z. Zhang, J. Ren, M. Lefler, B. Wang, Carbon **106**, 208–217 (2016)
101. A. Al-Hamaoy, E. Chikarakara, H. Jawad, K. Gupta, D. Kumar, M.R. Rao, S. Krishnamurthy, M. Morshed, E. Fox, D. Brougham, Appl. Surf. Sci. **302**, 141–144 (2014)
102. K. Davami, M. Shaygan, N. Kheirabi, J. Zhao, D.A. Kovalenko, M.H. Rümmeli, J. Opitz, G. Cuniberti, J.-S. Lee, M. Meyyappan, Carbon **72**, 372–380 (2014)
103. K. Ostrikov, E. Neyts, M. Meyyappan, Adv. Phys. **62**, 113–224 (2013)
104. M.A. Lieberman, A.J. Lichtenberg, *Principles of plasma discharges and materials processing* (Wiley, 2005)
105. M. Meyyappan, J. Phys. D Appl. Phys. **42**, 213001 (2009)
106. Z. Ren, Z. Huang, J. Xu, J. Wang, P. Bush, M. Siegal, P. Provencio, Science **282**, 1105–1107 (1998)
107. M. Chhowalla, K. Teo, C. Ducati, N. Rupesinghe, G. Amaratunga, A. Ferrari, D. Roy, J. Robertson, W. Milne, J. Appl. Phys. **90**, 5308–5317 (2001)
108. Y.C. Choi, Y.M. Shin, Y.H. Lee, B.S. Lee, G.-S. Park, W.B. Choi, N.S. Lee, J.M. Kim, Appl. Phys. Lett. **76**, 2367–2369 (2000)
109. C. Bower, O. Zhou, W. Zhu, D. Werder, S. Jin, Appl. Phys. Lett. **77**, 2767–2769 (2000)
110. J.F. AuBuchon, L.-H. Chen, S. Jin, J. Phys. Chem. B **109**, 6044–6048 (2005)
111. J. Law, C. Koo, J. Thong, Appl. Phys. Lett. **91**, 243108 (2007)
112. V.I. Merkulov, A.V. Melechko, M.A. Guillorn, D.H. Lowndes, M.L. Simpson, Appl. Phys. Lett. **79**, 2970–2972 (2001)
113. X. Liu, X. Wu, H. Cao, R. Chang, J. Appl. Phys. **95**, 3141–3147 (2004)
114. D. Hash, M. Meyyappan, J. Appl. Phys. **93**, 750–752 (2003)
115. J. Caughman, L.R. Baylor, M.A. Guillorn, V.I. Merkulov, D.H. Lowndes, L. Allard, Appl. Phys. Lett. **83**, 1207–1209 (2003)
116. K. Teo, M. Chhowalla, G. Amaratunga, W. Milne, D. Hasko, G. Pirio, P. Legagneux, F. Wyczisk, D. Pribat, Appl. Phys. Lett. **79**, 1534–1536 (2001)
117. I. Denysenko, S. Xu, J. Long, P. Rutkevych, N. Azarenkov, K. Ostrikov, J. Appl. Phys. **95**, 2713–2724 (2004)
118. M. Bell, R. Lacerda, K. Teo, N. Rupesinghe, G. Amaratunga, W. Milne, M. Chhowalla, Appl. Phys. Lett. **85**, 1137–1139 (2004)
119. S.H. Lim, H.S. Yoon, J.H. Moon, K.C. Park, J. Jang, Appl. Phys. Lett. **88**, 033114 (2006)
120. Y.S. Woo, D.Y. Jeon, I.T. Han, N.S. Lee, J.E. Jung, J.M. Kim, Diam. Relat. Mater. **11**, 59–66 (2002)
121. D.B. Hash, M.S. Bell, K.B. Teo, B.A. Cruden, W.I. Milne, M. Meyyappan, Nanotechnology **16**, 925 (2005)
122. B.A. Cruden, M. Meyyappan, J. Appl. Phys. **97**, 084311 (2005)
123. C. Zhi, X. Bai, E. Wang, Appl. Phys. Lett. **81**, 1690–1692 (2002)
124. K.S. Ahn, J.S. Kim, C.O. Kim, J.P. Hong, Carbon **41**, 2481–2485 (2003)
125. G. Zheng, Q. Li, K. Jiang, X. Zhang, J. Chen, Z. Ren, S. Fan, Nano Lett. **7**, 1622–1625 (2007)

126. X. Han, G. Qing, J. Sun, T. Sun, Angew. Chem. Int. Ed. **51**, 5147–5151 (2012)
127. A. Udomvech, T. Kerdcharoen, T. Osotchan, Chem. Phys. Lett. **406**, 161–166 (2005)
128. G. Wu, C. Wang, X. Zhang, H. Yang, Z. Qi, P. He, W. Li, J. Electrochem. Soc. **146**, 1696–1701 (1999)
129. H. Zhang, G. Cao, Z. Wang, Y. Yang, Z. Shi, Z. Gu, Electrochim. Acta **55**, 2873–2877 (2010)
130. J. Chen, A.I. Minett, Y. Liu, C. Lynam, P. Sherrell, C. Wang, G.G. Wallace, Adv. Mater. **20**, 566–570 (2008)
131. I. Lahiri, S.-W. Oh, J.Y. Hwang, S. Cho, Y.-K. Sun, R. Banerjee, W. Choi, ACS Nano **4**, 3440–3446 (2010)
132. H. Zhang, H. Song, X. Chen, J. Zhou, H. Zhang, Electrochim. Acta **59**, 160–167 (2012)
133. G. Wang, X. Shen, J. Yao, D. Wexler, J.-H. Ahn, Electrochem. Commun. **11**, 546–549 (2009)
134. A.L.M. Reddy, M.M. Shaijumon, S.R. Gowda, P.M. Ajayan, Nano Lett. **9**, 1002–1006 (2009)
135. H.X. Zhang, C. Feng, Y.C. Zhai, K.L. Jiang, Q.Q. Li, S.S. Fan, Adv. Mater. **21**, 2299–2304 (2009)
136. B. Jin, E.M. Jin, K.-H. Park, H.-B. Gu, Electrochem. Commun. **10**, 1537–1540 (2008)
137. X.-M. Liu, Z.-D. Huang, S. Oh, P.-C. Ma, P.C. Chan, G.K. Vedam, K. Kang, J.-K. Kim, J. Power Sources **195**, 4290–4296 (2010)
138. H. Xia, K.R. Ragavendran, J. Xie, L. Lu, J. Power Sources **212**, 28–34 (2012)
139. S. Pandey, U.N. Maiti, K. Palanisamy, P. Nikolaev, S. Arepalli, Appl. Phys. Lett. **104**, 233902 (2014)
140. Z. Zhu, Y. Hu, H. Jiang, C. Li, J. Power Sources **246**, 402–408 (2014)
141. D. Ma, J. Cai, X. Wu, H. Xu, Y. Tian, H. Zhao, J. Renew. Sustain. Energy **8**, 014101 (2016)
142. K.H. An, W.S. Kim, Y.S. Park, H.J. Jeong, Y.C. Choi, J.-M. Moon, D.J. Bae, S.C. Lim, Y. H. Lee, S. Saito, AIP Conf. Proc. **590**, 241–244 (2001)
143. B.-J. Yoon, S.-H. Jeong, K.-H. Lee, H.S. Kim, C.G. Park, J.H. Han, Chem. Phys. Lett. **388**, 170–174 (2004)
144. Z. Huang, J. Xu, Z. Ren, J. Wang, M. Siegal, P. Provencio, Appl. Phys. Lett. **73**, 3845–3847 (1998)
145. E. Frackowiak, F. Beguin, Carbon **39**, 937–950 (2001)
146. C. Du, J. Yeh, N. Pan, Nanotechnology **16**, 350 (2005)
147. L. Gao, A. Peng, Z.Y. Wang, H. Zhang, Z. Shi, Z. Gu, G. Cao, B. Ding, Solid State Commun. **146**, 380–383 (2008)
148. C. Emmenegger, J.-M. Bonard, P. Mauron, P. Sudan, A. Lepora, B. Grobety, A. Züttel, L. Schlapbach, Carbon **41**, 539–547 (2003)
149. J.Y. Lee, K. Liang, K.H. An, Y.H. Lee, Synth. Met. **150**, 153–157 (2005)
150. P.-C. Chen, G. Shen, S. Sukcharoenchoke, C. Zhou, Appl. Phys. Lett. **94**, 043113 (2009)
151. K.H. An, K.K. Jeon, J.K. Heo, S.C. Lim, D.J. Bae, Y.H. Lee, J. Electrochem. Soc. **149**, A1058–A1062 (2002)
152. J. Zhang, L.-B. Kong, B. Wang, Y.-C. Luo, L. Kang, Synth. Met. **159**, 260–266 (2009)
153. V. Gupta, N. Miura, Mater. Lett. **60**, 1466–1469 (2006)
154. J. Yan, Z. Fan, T. Wei, J. Cheng, B. Shao, K. Wang, L. Song, M. Zhang, J. Power Sources **194**, 1202–1207 (2009)
155. A.L.M. Reddy, M.M. Shaijumon, S.R. Gowda, P.M. Ajayan, J. Phys. Chem. C **114**, 658–663 (2009)
156. Y. Wu, P. Qiao, T. Chong, Z. Shen, Adv. Mater. **14**, 64–67 (2002)
157. J.R. Miller, R. Outlaw, B. Holloway, Science **329**, 1637–1639 (2010)
158. Z. Bo, S. Mao, Z.J. Han, K. Cen, J. Chen, K.K. Ostrikov, Chem. Soc. Rev. **44**, 2108–2121 (2015)
159. Z. Bo, Y. Yang, J. Chen, K. Yu, J. Yan, K. Cen, Nanoscale **5**, 5180–5204 (2013)
160. J. Zhao, M. Shaygan, J. r. Eckert, M. Meyyappan, M.H. Rümmeli, Nano Lett. **14**, 3064–3071 (2014)

161. C. Zhang, J. Hu, X. Wang, X. Zhang, H. Toyoda, M. Nagatsu, Y. Meng, Carbon **50**, 3731–3738 (2012)
162. S. Jin, N. Li, H. Cui, C. Wang, Nano Energy **2**, 1128–1136 (2013)
163. M. Cai, R.A. Outlaw, S.M. Butler, J.R. Miller, Carbon **50**, 5481–5488 (2012)
164. Y. Ando, X. Zhao, M. Ohkohchi, Carbon **35**, 153–158 (1997)
165. S. Wang, J. Wang, P. Miraldo, M. Zhu, R. Outlaw, K. Hou, X. Zhao, B.C. Holloway, D. Manos, T. Tyler, Appl. Phys. Lett. **89**, 183103 (2006)
166. G. Ren, X. Pan, S. Bayne, Z. Fan, Carbon **71**, 94–101 (2014)
167. Z. Bo, K. Yu, G. Lu, S. Cui, S. Mao, J. Chen, Energy Environ. Sci. **4**, 2525–2528 (2011)
168. H.-C. Chang, H.-Y. Chang, W.-J. Su, K.-Y. Lee, W.-C. Shih, Appl. Surf. Sci. **258**, 8599–8602 (2012)
169. K. Yu, G. Lu, Z. Bo, S. Mao, J. Chen, J. Phys. Chem. Lett. **2**, 1556–1562 (2011)
170. M. Cai, R.A. Outlaw, R.A. Quinlan, D. Premathilake, S.M. Butler, J.R. Miller, ACS Nano **8**, 5873–5882 (2014)
171. M.V. Jacob, R.S. Rawat, B. Ouyang, K. Bazaka, D.S. Kumar, D. Taguchi, M. Iwamoto, R. Neupane, O.K. Varghese, Nano Lett. **15**, 5702–5708 (2015)
172. D.H. Seo, A.E. Rider, Z.J. Han, S. Kumar, K.K. Ostrikov, Adv. Mater. **25**, 5638–5642 (2013)
173. G. Ruan, Z. Sun, Z. Peng, J.M. Tour, ACS Nano **5**, 7601–7607 (2011)
174. J. Wang, C.F. Wang, S. Chen, Angew. Chem. **124**, 9431–9435 (2012)
175. B. Ouyang, Y. Zhang, Z. Zhang, H.J. Fan, R. Rawat, RSC Adv. **6**, 23968–23973 (2016)
176. B. Ouyang, Y. Wang, Z. Zhang, R. Rawat, Electrochim. Acta **194**, 151–160 (2016)
177. A. Malesevic, R. Vitchev, K. Schouteden, A. Volodin, L. Zhang, G. Van Tendeloo, A. Vanhulsel, C. Van Haesendonck, Nanotechnology **19**, 305604 (2008)
178. K. Yu, P. Wang, G. Lu, K.-H. Chen, Z. Bo, J. Chen, J. Phys. Chem. Lett. **2**, 537–542 (2011)
179. M. Zhu, J. Wang, B.C. Holloway, R.A. Outlaw, X. Zhao, K. Hou, V. Shutthanandan, D.M. Manos, Carbon **45**, 2229–2234 (2007)
180. D.H. Seo, Z.J. Han, S. Kumar, K.K. Ostrikov, Adv. Energy Mater. **3**, 1316–1323 (2013)
181. D.H. Seo, S. Yick, Z.J. Han, J.H. Fang, K.K. Ostrikov, Chemsuschem **7**, 2317–2324 (2014)
182. G. Xiong, K. Hembram, R. Reifenberger, T.S. Fisher, J. Power Sources **227**, 254–259 (2013)
183. G. Xiong, C. Meng, R.G. Reifenberger, P.P. Irazoqui, T.S. Fisher, Adv. Energy Mater. **4**, 1300515 (2014)